Transactions of the ASME®

Technical Editor, **LEWIS T. WHEELER**

Department of Mechanical Engineering,
University of Houston,
Houston, TX 77204-4792

APPLIED MECHANICS DIVISION

Chairman, **C. T. HERAKOVICH**
Secretary, **T. HUGHES**
Associate Technical Editors,
J. R. BARBER
J. L. BASSANI
R. C. BECKER
R. C. BENSON
M. M. CARROLL
I. M. DANIEL
W. J. DRUGAN
A. A. FERRI
J. T. JENKINS
J. W. JU
V. K. KINRA
S. KYRIAKIDES
S. LICHTER
W. K. LIU
M. ORTIZ
N. C. PERKINS
M.-J. PINDERA
K. T. RAMESH
J. N. REDDY
D. A. SIGINER
M. TAYA

BOARD ON COMMUNICATIONS

Chairman and Vice-President
R. MATES

OFFICERS OF THE ASME
President, **K. B. THAYER**
Executive Director, **D. L. BELDEN**
Treasurer, **J. A. MASON**

PUBLISHING STAFF
Managing Director, Engineering
CHARLES W. BEARDSLEY
Director, Technical Publishing
PHILIP DI VIETRO
Managing Editor, Technical Publishing
CYNTHIA B. CLARK
Managing Editor, Transactions
CORNELIA MONAHAN
Production Coordinator
JUDITH SIERANT
Production Assistant
MARISOL ANDINO

Transactions of the ASME, Journal of Applied Mechanics (ISSN 0021-8936) is published quarterly (Mar., June, Sept., Dec.) for $210.00 per year by The American Society of Mechanical Engineers, 345 East 47th Street, New York, NY 10017.

Periodicals postage paid at New York, NY and additional mailing office. POSTMASTER: Send address changes to Transactions of the ASME, Journal of Applied Mechanics, c/o THE AMERICAN SOCIETY OF MECHANICAL ENGINEERS, 22 Law Drive, Box 2300, Fairfield, NJ 07007-2300.

CHANGES OF ADDRESS must be received at Society headquarters seven weeks before they are to be effective. Please send old label and new address. **PRICES:** To members, $40.00; to nonmembers, $230.00; single issue, $92.00. Add $40.00 (airmail $60.00) for postage to countries outside the United States and Canada.

STATEMENT from By-Laws. The Society shall not be responsible for statements or opinions advanced in papers or . . . printed in its publications (B7.1, Para. 3), **COPYRIGHT © 1998** by The American Society of Mechanical Engineers. Authorization to photocopy material for internal or personal use under circumstances not falling within the fair use provisions of the Copyright Act is granted by ASME to libraries and other users registered with the Copyright Clearance Center (CCC). Transactional Reporting Service provided that the base fee of $3.00 per article is paid directly to CCC, Inc., 222 Rosewood Drive, Danvers, MA 01923. Request for special permission or bulk copying should be addressed to Reprints/Permission Department. **INDEXED** by Applied Mechanics Reviews and Engineering Information, Inc. Canadian Goods & Services Tax Registration #126148048.

Journal of Applied Mechanics

Published Quarterly by The American Society of Mechanical Engineers

VOLUME 65 • NUMBER 2 • JUNE 1998

TECHNICAL PAPERS

293 **Dynamic Fracture Criteria for Crack Growth Along Bimaterial Interfaces**
M. Kavaturu and A. Shukla

300 **The Hypersingular Boundary Contour Method for Three-Dimensional Linear Elasticity**
S. Mukherjee and Y. X. Mukherjee

310 **Singular Integral Equation Method for Interaction Between Elliptical Inclusions**
Nao-Aki Noda and Tadatoshi Matsuo

320 **On Random Field Discretization in Stochastic Finite Elements**
B. A. Zeldin and P. D. Spanos

328 **Thermal Stresses in a Freezing Sphere and its Application to Cryobiology**
Y. Rabin and P. S. Steif

334 **Refined Dynamic Stability Theory of Laminated Isotropic Circular Plates**
G. Krizhevsky and Y. Stavsky

341 **Free-Vibration Analysis of Clamped Antisymmetrically Laminated Elliptical Plates**
K. Hosokawa, Y. Yamada, and T. Sakata

346 **Transient Residual Stresses in Thermal Barrier Coatings: Analytical and Numerical Results**
S. Q. Nusier and G. M. Newaz

354 **A Basic Problem in Thermoelasticodynamics and its Solution**
Xiangzhou Zhang

362 **Decomposition of the Deformation Gradient in Thermoelasticity**
A. Imam and G. C. Johnson

367 **An Inverse Problem for Determination of Transient Surface Temperature From Piezoelectric Sensor Measurement**
Fumihiro Ashida and T. R. Tauchert

374 **Stress and Deformation Fields Around a Cylindrical Cavity Embedded in a Pressure-Sensitive Elastoplastic Medium**
I. D. R. Bradford and D. Durban

380 **Linear and Nonlinear Elasticity of Granular Media: Stress-Induced Anisotropy of a Random Sphere Pack**
D. L. Johnson, L. M. Schwartz, D. Elata, J. G. Berryman, B. Hornby, and A. N. Norris

389 **Rigid Stamp Indentation on a Curvilinear Hole Boundary of an Anisotropic Elastic Body**
C. W. Fan and Chyanbin Hwu

398 **Probabilistic Representation and Transmission of Nonstationary Processes in Multi-Degree-of-Freedom Systems**
S. F. Masri, A. W. Smyth, and M.-I. Traina

410 **Mechanics of Polishing**
V. H. Bulsara, Y. Ahn, S. Chandrasekar, and T. N. Farris

417 **The Jamb (Self-Locking) Process in Three-Dimensional Collisions**
J. A. Batlle and S. Cardona

424 **Guided Circumferential Waves in a Circular Annulus**
Guoli Liu and Jianmin Qu

431 **Interaction and Microfracturing Pattern for Successive Origination (Introduction) of Pores in Elastic Bodies: Finite Deformation**
V. A. Levin and K. M. Zingerman

436 **Response of a Nonconservative Continuous System to a Moving Concentrated Load**
A. V. Pesterev and L. A. Bergman

445 **How the Raleigh Flow Transits to Blasius Numerically**
G. N. Sarma

(Contents continued on outside back cover)

This journal is printed on acid-free paper, which exceeds the ANSI Z39.48-1992 specification for permanence of paper and library materials.♾ ™

♻ 85% recycled content, including 10% post-consumer fibers.

Downloaded 04 May 2010 to 171.66.16.52. Redistribution subject to ASME license or copyright; see http://www.asme.org/terms/Terms_Use.cfm

CONTENTS (CONTINUED)

454 **Stress Singularities at the Apex of a Dissimilar Anisotropic Wedge**
Y. Y. Lin and J. C. Sung

464 **Physical Restrictions on the Impulse Acting During Three-Dimensional Impact of Two "Rigid" Bodies**
M. B. Rubin

470 **Steady Sliding of Two Elastic Half-Spaces With Friction Reduction due to Interface Stick-Slip**
G. G. Adams

476 **The Problem on Dynamical Loading of Plane Elastic Regions With Irregular Boundaries**
N. Morozov and I. Sourovtsova

479 **Effects of Flexibility and Damping on Momentum Transfer During Locking of Two Moving Links, Part I: Numerical Simulation**
W. Szyszkowski and K. Fielden

485 **Effects of Flexibility and Damping on Momentum Transfer During Locking of Two Moving Links, Part II: Analytical Approach**
W. Szyszkowski and K. Fielden

489 **Boundary Effects in Penetration or Perforation**
L. M. Keer, Yonglin Xu, and V. K. Luk

497 **Dynamic Response Control of Thin-Walled Beams to Blast Pulses Using Structural Tailoring and Piezoelectric Actuation**
L. Librescu and Sungsoo Na

505 **Dynamics of a Simple Model for a Wind-Loaded Nonlinear Structure: Bifurcations of Codimension One and Two**
K. Yagasaki

513 **Modeling and Identification of Inelastic Systems Using the Endochronic Model**
Dar-Yun Chiang

519 **On the Stability of Gyroscopic Systems**
P. Lancaster and P. Zizler

523 **Interactively Induced Localized Buckling in Sandwich Structures With Core Orthotropy**
M. Ahmer Wadee and G. W. Hunt

BRIEF NOTES

Cruciform Rigid Line Problem in an Infinite Plate 529
Y. Z. Chen

A Modified Element-by-Element Preconditioner for Elastostatics 531
M. Barboteu, P. Alart, and F. Lebon

Large Deflection of a Rigid-Plastic Circular Plate Pressed by a Sphere 533
Ge Wang, Hideomi Ohtsubo, and Kikuo Arita

On Love-Type Magnetoelastic Surface Waves 535
S. Chakraborty and M. Chattopadhyay

539 A Nonspectral Stability Criterion for Linear Conservative Gyroscopic Systems
R. M. Bulatovic

541 On the Stability of Schapery Beams
D. Touati and G. Cederbaum

544 Boundary Spectral Strip for Elastodynamics Using Analytical Integration Along a Circular Path
O. Michael, J. Avrashi, and G. Rosenhouse

BOOK REVIEW

548 ***Solution of Crack Problems: The Distributed Dislocation Technique,*** **by D. A. Hills, P. A. Kelly, D. N. Dai, and A. M. Korsunsky . . . Reviewed by L. M. Keer**

(Contents continued on p. 299)

Downloaded 04 May 2010 to 171.66.16.52. Redistribution subject to ASME license or copyright; see http://www.asme.org/terms/Terms_Use.cfm

CONTENTS (CONTINUED)

ANNOUNCEMENTS AND SPECIAL NOTICES

327	Fourth International Conference on Vibration Problems—Announcement and Call for Papers
340	Thermal Stresses '99—Call for Papers
366	Periodicals on ASMENET
397	SES Nominations Announcement
444	Change of Address Form
496	Fourth Asia-Pacific Conference on Computational Mechanics for the Next Millennium—Announcement and Call for Papers
528	Finite Element Books Bibliography on the Internet
547	20th International Congress of Theoretical and Applied Mechanics—Preliminary Announcement
549	Worldwide Mechanics Meetings Conference Listing
552	Information for Authors
553	1999 ASME Mechanics and Materials Conference—Announcement

Downloaded 04 May 2010 to 171.66.16.52. Redistribution subject to ASME license or copyright; see http://www.asme.org/terms/Terms_Use.cfm

Dynamic Fracture Criteria for Crack Growth Along Bimaterial Interfaces

M. Kavaturu
Mem. ASME

A. Shukla
Fellow ASME

Dynamic Photomechanics Laboratory,
Department of Mechanical Engineering
and Applied Mechanics,
University of Rhode Island,
Kingston, RI 02881

Dynamic fracture criteria based on experimental observations are proposed for subsonic crack growth along bimaterial interfaces. These criteria are based on the premise that the crack-face displacements at a point behind the crack tip increase exponentially with the instantaneous crack-tip velocity. This assumption establishes a generalized relationship between the dynamic energy release rate and the instantaneous crack-tip velocity. Experiments are performed on PSM-1/aluminum bimaterial systems for both shear dominated and opening-mode dominated crack growth to verify the proposed criteria. Two different bimaterial specimen geometries are employed to obtain the complete range of crack-tip speeds in the subsonic regime. The dynamic loading is achieved either by detonating two explosive charges on the specimen or by impacting the specimen in one-point bend configuration. Dynamic photoelasticity in conjunction with high-speed photography is used to analyze the fracture event. Explosive loading of the interface crack results in crack propagation speeds on the order of 65 percent of the shear wave speed of PSM-1 and the crack growth is observed to be stable and opening-mode dominated. In contrast, the impact loading results in very high crack propagation speeds on the order of shear wave speed of PSM-1 and the crack growth is observed to be shear dominated.

Introduction

In dynamic fracture mechanics problems, the knowledge of the idealized crack-tip stress fields provides a relationship between the dynamic stress intensity factor and the instantaneous crack-tip speed. The general form of this relationship is usually determined experimentally, or may even be obtained numerically. In homogeneous materials, this relationship was established as an empirical relation of the form (Kobayashi and Dally, 1977; Rosakis and Freund, 1982)

$$K_{ID} = \frac{K_{IA}}{1 - \left(\frac{\nu}{c_R}\right)^m}, \tag{1}$$

where K_{ID} is the dynamic stress intensity factor, K_{IA} is the arrest toughness, ν is the instantaneous crack-tip speed, c_R is Rayleigh wave speed of the material, and m is a parameter that depends on the material. This relationship suggests that the crack growth is stable, and it is impossible to drive the crack at the Rayleigh wave velocity for remotely loaded cracks. In bimaterial systems, however, it has been shown by Yang et al. (1991) that it takes only a finite amount of energy to maintain the crack propagation at the Rayleigh wave velocity of the more compliant material.

In recent years, there has been considerable interest in the study of the dynamic interfacial fracture. However, the majority of these studies have been either analytical or numerical in nature. There are only a few experimental studies that address some of the issues related to the dynamic fracture of bimaterial interfaces. The first experimental study on the dynamic interfacial fracture was conducted by Tippur and Rosakis (1991). They demonstrated that the crack growth along bimaterial interfaces can occur at speeds close to the Rayleigh wave speed of the more compliant material. This experimental study motivated a number of analytical and numerical investigations (Yang et al., 1991; Deng, 1993; Nakamura, 1991). Xu and Needleman (1996) analyzed dynamic interfacial crack growth along an interface using numerical methods. Their results indicated that the energy release rate versus crack speed relation for dynamic interfacial crack growth depends on the mismatch and on the bond line cohesive properties. A higher order asymptotic stress field equation for the fracture of bimaterial interfaces was provided by Liu et al. (1993). Lambros and Rosakis (1995a) employed coherent gradient sensing interferometry to study the bimaterial interface fracture in the subsonic regime. Based on the experimental observations, they proposed a criterion for dynamic crack propagation along bimaterial interfaces. It has been experimentally demonstrated that the interface crack can propagate intersonically with respect to the material with lower shear wave speed (Lambros and Rosakis, 1995b; Singh and Shukla, 1996a). The majority of these experimental studies dealt with specimen configurations that were loaded predominantly in shear. Recently, Shukla and Kavaturu (1997) performed a series of experiments to investigate the dynamic crack growth behavior in the velocity range, $0 < \nu/c_s < 0.65$ (c_s is the shear wave speed of the more compliant material). The bimaterial specimens were subjected to explosive loading that resulted in opening-mode dominated and stable crack growth.

This study proposes a generalized relationship between the dynamic energy release rate and the instantaneous crack-tip velocity for dynamic fracture of bimaterial systems in the subsonic regime. Experiments were performed on PSM-1/aluminum bimaterial specimens which were subjected to either explosive or impact loading. The complete range of crack-tip speeds in the subsonic regime were obtained by employing two different specimen geometries. The dynamic event was observed using photoelasticity and the full-field information was recorded by a high-speed camera. The experimental data was analyzed to verify the proposed criteria which were based on the premise

Contributed by the Applied Mechanics Division of THE AMERICAN SOCIETY OF MECHANICAL ENGINEERS for publication in the ASME JOURNAL OF APPLIED MECHANICS.

Discussion on the paper should be addressed to the Technical Editor, Professor Lewis T. Wheeler, Department of Mechanical Engineering, University of Houston, Houston, TX 77204-4792, and will be accepted until four months after final publication of the paper itself in the ASME JOURNAL OF APPLIED MECHANICS.

Manuscript received by the ASME Applied Mechanics Division, Mar. 17, 1997; final revision, Oct. 29, 1997. Associate Technical Editor: I. M. Daniel.

 Copyright © 1998 by ASME

Downloaded 04 May 2010 to 171.66.16.26. Redistribution subject to ASME license or copyright; see http://www.asme.org/terms/Terms_Use.cfm

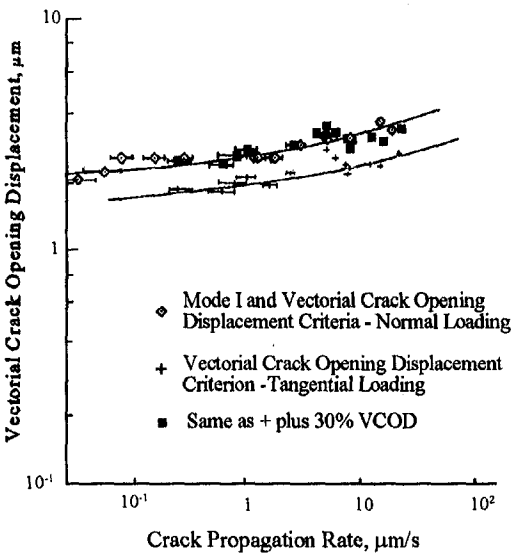


Fig. 1 The vectorial crack-opening displacement criterion of Liechti and Knauss (1982)

that the crack-face displacements at a point behind the crack tip increase exponentially with the instantaneous crack-tip velocity.

Review of Existing Interfacial Crack Growth Criteria

Liechti and Knauss (1982) have proposed a criterion for *quasi-static* crack growth along bimaterial interfaces. They employed optical interferometry to measure the crack opening profiles for interfacial cracks under remotely applied normal and tangential displacements. The primary objective of their study was to unify the experimental data into a master curve in the form of a criterion that would be independent of the applied loading. Three different parameters were proposed to formulate a crack growth criterion, namely,

- critical crack profile gradient,
- critical normal crack-opening displacement (δ_2),
- critical vectorial crack-face displacement ($(\delta_1^2 + \delta_2^2)^{1/2}$),

where δ_1 and δ_2 are the sliding and opening-mode displacements, respectively.

All these criteria were evaluated at a point $a = 2.5$ μm (0.5 percent of bond line thickness) behind the crack tip. The normal crack-opening displacement criterion and the crack profile gradient criterion provided very nearly the same results, differing essentially by a factor on the order of a. The results showed that the normal crack-opening displacement criterion did not achieve the objective of unifying the experimental data into a single master curve. This is not surprising as the normal crack-opening displacement data obtained under bond-normal loading can be expected to be higher than those resulting from bond-tangential loading.

The attention was then focussed on the vectorial crack-face displacement criterion. The tangential displacement (δ_1), which was essential to calculate the vectorial crack-face displacement, was unavailable from the adopted experimental technique. These bond-tangential displacements were therefore computed based on the linear analysis developed by Rice and Sih (1965) and a ten percent error was expected in the results for neglecting the nonlinearity in the displacements. The vectorial crack-face displacement criterion states that the rate of debonding ν is a function of the magnitude of the displacement vector,

$$\nu = \nu(s), \quad s = \sqrt{\delta_1^2 + \delta_2^2}, \tag{2}$$

where ν is the crack-tip speed, and δ_1 and δ_2 are the shearing and the opening displacements, respectively. The vectorial crack-face displacement criterion along with the experimental data is shown in Fig. 1. It is clear from the figure that the discrepancy between the data sets corresponding to normal and tangential loading is within the expected error of ten percent. It was concluded that the interfacial crack growth under combined loading is governed by the magnitude of the displacement vector.

Recently, Lambros and Rosakis (1995a) performed experiments on PMMA/aluminum and PMMA/steel bimaterial specimens to study the dynamic interfacial crack growth. The dynamic loading was achieved by impact loading the specimens either by drop weight tower or by means of a gas gun. They employed coherent gradient sensing interferometry to analyze the dynamic event. Based on these experimental observations, a criterion for dynamic crack propagation along bimaterial interfaces was proposed. According to this criterion, the crack growth along a bimaterial interface occurs in such a way as to keep the instantaneous shearing (δ_1) and opening (δ_2) crack-face displacements at a point behind the crack tip, constant at their initiation values. This criterion will be referred to as constant crack profile growth criterion in this paper. Figure 2 represents the sliding and the opening displacements at a point behind the crack tip.

The shearing and the opening displacements at a distance r behind the crack tip, δ_1 and δ_2, are given by (Yang et al., 1991)

$$\delta_2 + i\eta\delta_1 = \frac{H_{22}Kr^{i\epsilon}}{(1 + 2i\epsilon)\cosh \pi\epsilon}\sqrt{\frac{2r}{\pi}}, \tag{3}$$

where $i = \sqrt{-1}$, ϵ is the mismatch parameter, η is the traction resolution factor, and the function H_{22} is defined in Yang et al. (1991). The constant crack profile growth criterion has been proposed in two parts. The first part of the criterion which was based on the assumption that the ratio δ_1/δ_2 at a point a behind the crack tip remains constant ($\delta_1/\delta_2|_{r=a} = C_1$) leads to a relationship between the crack-tip velocity and the instantaneous mixity, ϕ, given by

$$\phi(\nu) = \arctan(C_1\eta(\nu)) + \arctan(2\epsilon(\nu)) - \epsilon(\nu)\ln a. \tag{4}$$

In addition to the constancy of the ratio, δ_1/δ_2, the fracture criterion also requires that the opening displacement, δ_2, at a point a behind the crack tip remain constant. This yields a functional relationship between the dynamic energy release rate and the crack-tip velocity and constitutes the second part of the criterion. Using Eq. (3), this can be expressed as

$$\delta_2|_{r=a} = \frac{H_{22}}{\cosh \pi\epsilon}\sqrt{\frac{2a}{\pi}}\frac{|K^d|}{\sqrt{1 + 4\epsilon^2}} \times \cos(\phi + \epsilon \ln a - \arctan(2\epsilon)) = C_2. \tag{5}$$

Equations (4) and (5) yield a functional relationship between the dynamic complex stress intensity factor and the crack-tip speed given by

$$|K^d| = C_2\frac{\sqrt{1 + 4\epsilon^2}\cosh \pi\epsilon}{H_{22}\cos(\arctan(C_1\eta))}\sqrt{\frac{\pi}{2a}}. \tag{6}$$

It is clear from Eq. (6) that $|K^d|$ is dependent on the constants C_1 and C_2. The constant C_1 can be obtained by fitting the experi-

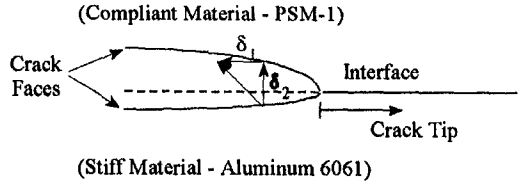


Fig. 2 Definitions of the shearing and opening displacements at a point behind the crack tip

Downloaded 04 May 2010 to 171.66.16.26. Redistribution subject to ASME license or copyright; see http://www.asme.org/terms/Terms_Use.cfm

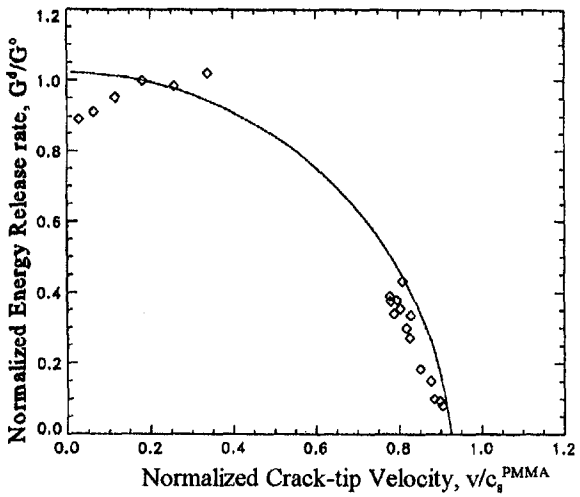


Fig. 3 Comparison of the experimental data from a PSM-1/aluminum steel drop weight tower experiment (Lambros and Rosakis, 1995)

mental data to Eq. (4). The constant C_2 is eliminated by normalizing Eq. (6) with some experimentally obtained data point with parameters ν_0, ϵ_0, η_0, H_{22}^0, and K_0^d as

$$\frac{|K^d|}{|K_0^d|} = \frac{\sqrt{1+4\epsilon^2}\cosh \pi\epsilon H_{22}^0 \cos(\arctan(C_1\eta_0))}{\sqrt{1+4\epsilon_0^2}\cosh \pi\epsilon_0 H_{22} \cos(\arctan(C_1\eta))}. \quad (7)$$

For dynamic interfacial crack growth, the dynamic energy release rate, G^d, was related to $|K^d|$ by Yang et al. (1991) as

$$G^d = F(\nu)\frac{|K^d|^2}{4\mu_1}, \quad (8)$$

where $F(\nu)$ is a function of crack-tip speed and material properties and μ_1 is the shear modulus of material-1. The factor F is shown to be finite at the Rayleigh wave speed of the compliant material by Yang et al. (1991). In contrast, this factor F is asymptotic to the Rayleigh wave speed for crack growth in homogeneous materials. Now, Eq. (7) may be expressed in terms of G^d/G_0 using Eq. (8). Figure 3 represents a comparison of the experimental data with the second part of the constant crack profile growth criterion for the PMMA-steel drop weight tower experiments. As can be seen from the figure, a good agreement between the experimental data and the criterion has been noticed. However, there is no intermediate speed data available to support the criterion.

In summary, the constant crack profile growth criterion in essence states that the crack-face profile at a point behind the crack tip is independent of the crack-tip velocity. Whereas, Liechti and Knauss criterion for quasi-static crack growth showed that the measured displacements do increase with the crack-tip velocity.

Proposed Dynamic Fracture Criteria

Exponential Crack Profile Growth Criterion. Recent experimental investigations by Singh et al. (1997) and Shukla and Kavaturu (1997) showed considerable disagreement of experimental data with the second part of the constant crack profile growth criterion for the velocities in the range of $0 < \nu < 0.65\ c_s$. They have observed that the dynamic energy release rate showed an increasing trend with the crack-tip velocity up to about 60 percent of the lower shear wave speed. This is unlike the decreasing trend predicted by the constant crack profile growth criterion. This necessitated the development of a criterion which yields a generalized relationship between the dynamic energy release rate and the instantaneous crack-tip velocity to describe crack propagation in the subsonic regime. A new criterion was obtained by assuming that the opening displacement at a point a behind the crack tip increases exponentially with the crack-tip velocity:

$$\delta_2|_{r=a} = C_2(\nu/c_s)^n, \quad (9)$$

where C_2 is a constant of proportionality, ν is the instantaneous crack-tip velocity, c_s is shear wave speed of the compliant material and n is a parameter that depends on the bimaterial and on the cohesive properties of the bond.

This assumption of exponential crack-face displacement is based on the experimental observations made by Liechti and Knauss (1982). It can be seen from Fig. 1 that the relation between $\ln(\delta_2)$ (δ_2 is the crack-opening displacement) and $\ln(\nu)$ (ν is the crack-tip velocity) can be approximated by means of a straight line as

$$\ln \delta_2 = n \ln \nu + \ln C_1$$

$$\text{or } \delta_2 = C_1\nu^n. \quad (10)$$

Thus, Liechti and Knauss (1982) experimentally observed that the crack-face displacement at a point behind the crack tip varies exponentially with the crack-tip velocity for quasi-static crack growth. This observation has been utilized to formulate the generalized criteria for dynamic crack growth.

Furthermore, in the case of dynamic interfacial fracture, it has been shown by Yang et al. (1991) that it takes only a finite amount of energy to maintain the crack propagation at lower Rayleigh wave speed. In other words, the energy release rate and hence the opening and the shearing displacements remain bounded at the lower Rayleigh wave speed:

$$\nu \to c_R, \quad \delta_1 \text{ and } \delta_2 \to C_2 \quad \text{(some finite value)}. \quad (11)$$

The experimental observations by Liechti and Knauss (1982) in combination with the energy constraint on the interfacial crack propagation (Eq. (11)) provides a relationship between the crack-face displacement at a point behind the crack tip and the crack-tip velocity given by equation (9).

In addition to this assumption, the exponential crack profile growth criterion also assumes that the ratio δ_1/δ_2 at a point a behind the crack tip remain constant ($\delta_1/\delta_2|_{r=a} = C_1$). This assumption is essentially the first part of the constant crack profile growth criterion. Using the Eq. (9) in Eq. (3) we get

$$\delta_2 = \frac{H_{22}}{\cosh \pi\epsilon}\sqrt{\frac{2a}{\pi}}\frac{|K^d|}{\sqrt{1+4\epsilon^2}}\cos(\phi + \epsilon \ln a - \arctan(2\epsilon))$$

$$= C_2(\nu/c_s)^n. \quad (12)$$

Using Eqs. (4) and (12), $|K^d|$ may be expressed as

$$|K^d| = C_2(\nu/c_s)^n \frac{\sqrt{1+4\epsilon^2}\cosh \pi\epsilon}{H_{22}\cos(\arctan(C_1\eta))}\sqrt{\frac{\pi}{2a}}. \quad (13)$$

The constant C_2 was eliminated by normalizing the Eq. (13) with some experimentally determined stress intensity factor $|K_o^d|$ and the experimental data was also normalized with the corresponding value. Equation (13) may be expressed in terms of G^d/G_o using Eq. (8). Thus, the assumption that the crack-face displacements increase exponentially with the crack-tip speed leads to a generalized relationship between the dynamic energy release rate and the instantaneous crack-tip speed.

Equation (13) shows that the stress intensity factor depends on the constant C_1 and hence depends on the nature of loading present at the crack tip. In order to understand the dependence of the G^d versus ν relation on $\delta_1/\delta_2(=C_1)$, Eq. (13) for PSM-1/aluminum bimaterial is plotted as a function of C_1 for $n = 0.15$ in Fig. 4. It is clear from the figure that G^d versus ν relation is a weak function of C_1, especially at low velocities up to 60 percent of the shear wave velocity of the compliant material.

Downloaded 04 May 2010 to 171.66.16.26. Redistribution subject to ASME license or copyright; see http://www.asme.org/terms/Terms_Use.cfm

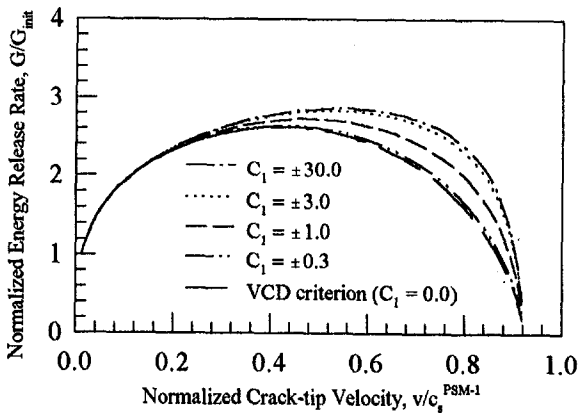


Fig. 4 Dependence of the G^d versus v relation on the constant C_1 for crack growth along PSM-1/aluminum interface

Vectorial Crack-face Displacement Criterion. A simple and generalized relationship between the dynamic energy release rate and the instantaneous crack-tip velocity was obtained by assuming that the vectorial crack-face displacement at a point behind the crack tip increases exponentially with the crack-tip velocity:

$$\sqrt{\delta_2^2 + (\eta\delta_1)^2}|_{r=a} = C_3(v/c_s)^n, \qquad (14)$$

where C_3 is a constant of proportionality and n is a parameter that depends on the bimaterial and the cohesive properties of the bond. Equations (3) and (14) yield a functional relationship between $|K^d|$ and v:

$$|K^d| = C_3(v/c_s)^n \frac{\sqrt{1+4\epsilon^2}\cosh \pi\epsilon}{H_{22}} \sqrt{\frac{\pi}{2a}}, \qquad (15)$$

The constant C_3 can be eliminated by normalizing $|K^d|$ with respect to some experimentally determined stress intensity factor. It is interesting to note that this $|K^d|$ versus v relation is independent of the nature of loading at the crack tip (δ_1/δ_2) and depends on the mismatch parameter (ϵ) and the crack-tip velocity. Equation (15) may be expressed in terms of dynamic energy release rate, G^d, using Eq. (8). This criterion reduces to the exponential crack profile growth criterion when the constant C_1 is zero. The vectorial crack-face displacement criterion for PSM-1/aluminum bimaterial is also plotted in Fig. 4 for $n = 0.15$.

Experimental Procedure

Bimaterial Specimens. The bimaterial specimens used in this study were made of a stiff aluminum half bonded to a compliant PSM-1 half (a birefringent polymer supplied by the Measurements Group, Inc., NC, USA). The mechanical properties of the bimaterial constituents are shown in Table 1. This bimaterial combination provides a significant (elastic) mismatch of properties across the interface to produce intensified interfacial effects at the crack tip. The procedure for the specimen preparation is described in detail in Singh et al. (1997).

Explosive Loading Experiments. The schematic of the bimaterial specimen used in this series of experiments is shown in Fig. 5. The interface was dynamically loaded by detonating two explosive charges containing 200 mg of lead azide explosive in the specimen as shown in Fig. 5. A stiff steel spacer was introduced between the side arms of the aluminum specimen and the explosive holder to further increase the loading rate. The detonation initiates a compressive wave in the side arms of the aluminum half of the bimaterial which reflects off the opposite free surface as a tensile wave. This tensile wave propagates down the aluminum half and develops a planar front before reaching the interface. The planar tensile wave loads the interface crack resulting in initiation, propagation and arrest, all in the same experiment.

Table 1 Material properties of the bimaterial interface constituents.

Property	PSM-1	Al
Young's Modulus, E (GPa)	2.76	71
Poisson's Ratio, ν	0.38	0.33
Density, ρ (kg/m³)	1200	2770
P-Wave Velocity , c_l (m/s)	1640	5430
S-Wave Velocity, c_s (m/s)	913	3100
Rayleigh Velocity, c_R (m/s)	857	2890
Fracture Toughness, K_{ic} (MPa√m)	3.1	29
Material Fringe Value, f_o (kN/m)	6.8	----
Mismatch Parameter, ϵ	0.0936	

The entire event of dynamic fracture was observed by dynamic photoelasticity and the full field information in the PSM-1 half was recorded using a Cranz-Schardin type multiple spark high-speed camera. A typical set of isochromatic fringe patterns obtained for the dynamic fracture of a PSM-1/aluminum bimaterial interface inclined at an angle of 10 deg is shown in the Fig. 6. Time $t = 0$ represents the time of incidence of the planar wave on the interface.

Impact Loading Experiments. The schematic of the bimaterial specimen used to study the interfacial fracture under impact loading is shown in Fig. 7. The aluminum half of the bimaterial specimen was subjected to impact by a projectile fired from a gas gun at low speeds on the order of 5 m/s. The impact sets up a compressive wave in the aluminum half which traverses the width of the specimen and reflects off the free surface as a tensile wave. This tensile wave loads the interface crack, primarily in shear, resulting in crack initiation and subsequent propagation. A sequence of photographs obtained in a typical experiment is shown in Fig. 8. Time $t = 0$ corresponds to the time of impact on the bimaterial specimen. It can be noticed from Figs. 6 and 8 that the stress field surrounding the crack tip in impact experiments is completely different from that of explosive loading experiments indicating a totally different loading situation in these two experiments.

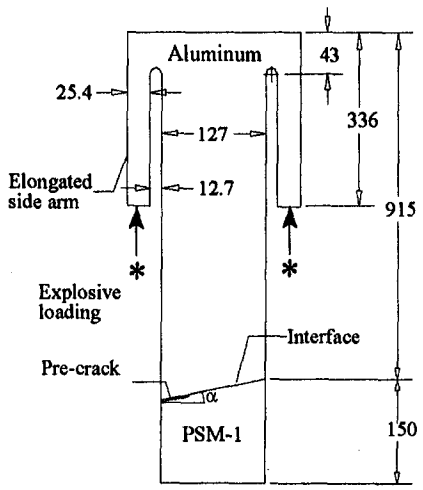


Fig. 5 Schematic of the bimaterial specimen used to study the interface fracture under explosive loading

Downloaded 04 May 2010 to 171.66.16.26. Redistribution subject to ASME license or copyright; see http://www.asme.org/terms/Terms_Use.cfm

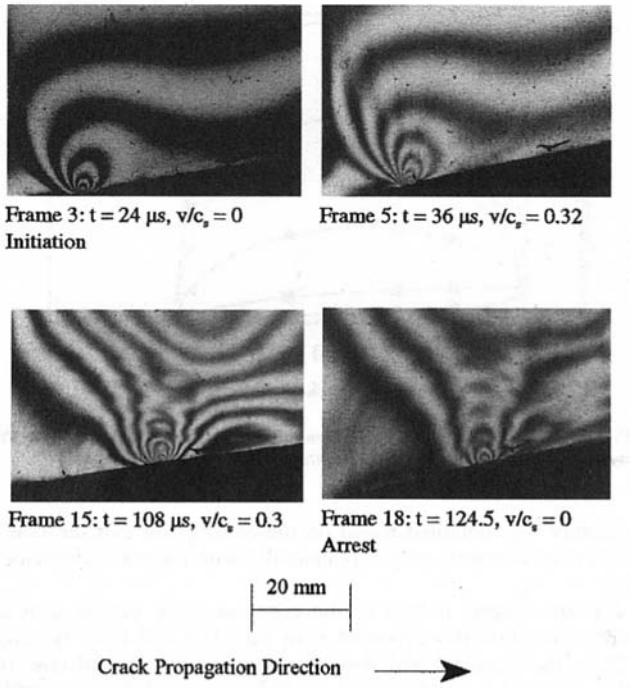


Fig. 6 Isochromatic fringe patterns due to a crack propagating along a PSM-1/aluminum interface (α = 10 deg) subjected to explosive loading (t is the post-incidence time)

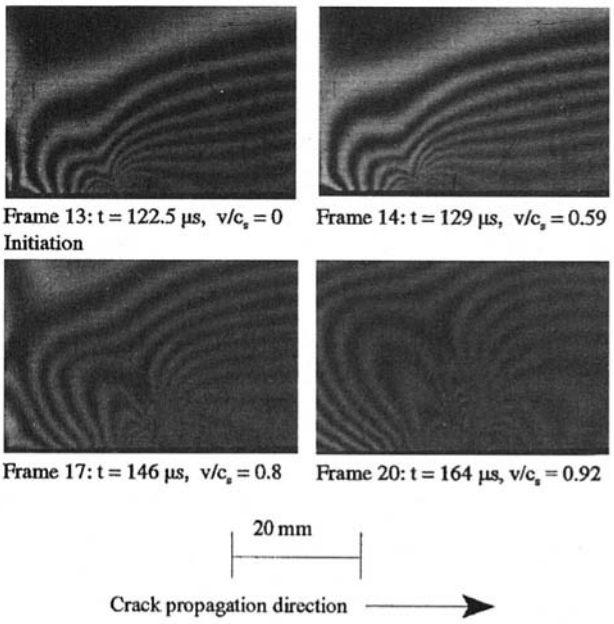


Fig. 8 Isochromatic fringe patterns for fracture a PSM-1/aluminum interface subjected to impact loading (t is the post-impact time)

The isochromatic fringe patterns obtained from the explosive and the impact loading experiments were analyzed to evaluate fracture parameters such as crack-tip velocity, the dynamic complex stress intensity factor, the dynamic energy release rate, and the instantaneous mixity. The crack-tip velocity history was obtained directly from the photographs from the knowledge of the crack-tip location as a function of time. The crack-tip velocity remained subsonic for the duration of the crack propagation in all these experiments. The histories of the dynamic complex stress intensity factor, the dynamic energy release rate, and the mixity were evaluated using the steady-state singular stress field equations developed by Yang et al. (1991). Mixity was evaluated at a characteristic length scale of L = 1 m to maintain consistency with the previous results (Lambros and Rosakis, 1995a, b; Singh et al., 1997; Shukla and Kavaturu, 1997). The analysis procedure involved a nonlinear least-squares method based on Newton-Raphson technique. Singh and Shukla (1996b) provide the details and also establish the validity of the analysis procedure. The fracture parameters extracted using these singular stress field equations are valid only when the experimental data is collected from K^d-dominant zone surrounding the crack tip. It has been shown by Sinha et al. (1997) that there exists such a zone of K^d-dominance outside the region of three-dimensional deformation. The experimental data was carefully sampled from these K^d-dominant zones for the purpose of analysis.

Experimental Verifications of the Proposed Criteria

The experimental data obtained was utilized to verify these criteria. The value of parameter C_1 in Eq. (13) which was essential in the evaluation of the exponential crack profile growth criterion, was obtained by fitting the experimental data to the first part of the constant crack profile growth criterion (Eq. (4)). Experimentally determined mixity is plotted as a function of the crack-tip velocity in Fig. 9 to determine the constant C_1. In this figure, the solid circles correspond to the results obtained from a typical explosive loading experiment and the open circles correspond to those of impact experiment. In order to maintain consistency with the previous results (Lambros and Rosakis, 1995a, b; Singh et al., 1997; Shukla and Kavaturu, 1997), the value of the ratio δ_1/δ_2 was evaluated

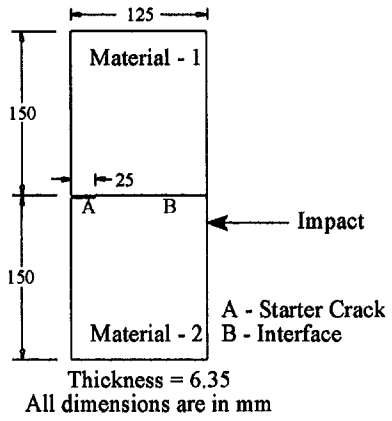


Fig. 7 Schematic of the bimaterial used in the impact loading experiments (material-1: PSM-1 and material-2: aluminum)

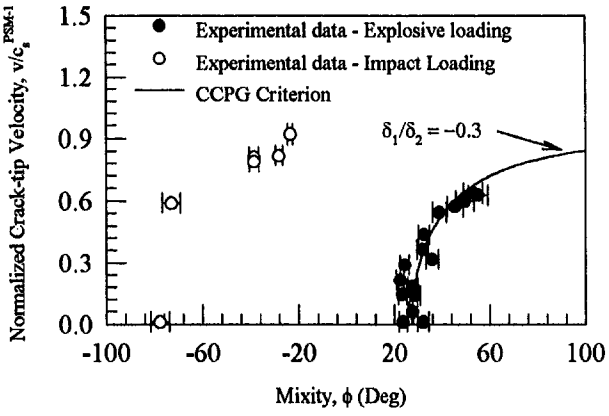
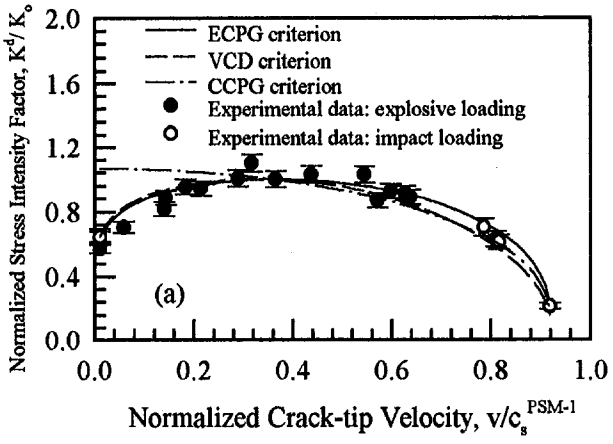


Fig. 9 Fit of Eq. (4) with the experimental data obtained from dynamic loading of PSM-1/aluminum interface inclined at −10 deg

Downloaded 04 May 2010 to 171.66.16.26. Redistribution subject to ASME license or copyright; see http://www.asme.org/terms/Terms_Use.cfm



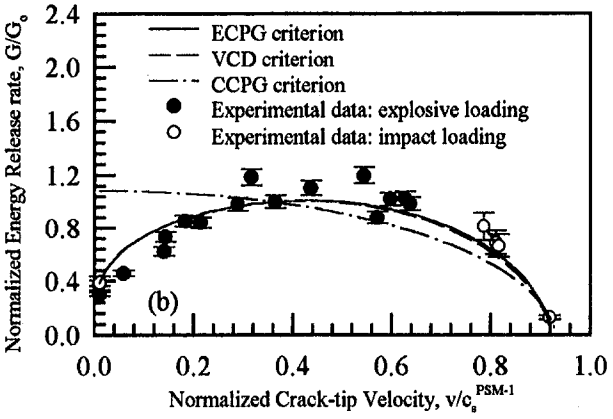


Fig. 10 Variation of the (*a*) normalized K^d (*b*) normalized G^d with the crack-tip velocity. Fit of the experimental data with the predictions of the proposed criteria and the Lambros and Rosakis criterion.

at a point 2 mm behind the crack tip. From the data fitting, the value of the constant C_1 was determined to be -0.3 for the explosive loading experiment. This suggests that the crack growth is opening-mode dominated as the crack-face opening is 3.3 times the crack-face sliding.

At this point, an attempt was made to fit the analytical relation between ν and ϕ (Eq. (4)) resulting from the first part of the constant crack profile growth criterion to the experimental data obtained from the impact experiment. For the purpose of comparison of the two experiments, Eq. (4) was again evaluated at a point 2 mm behind the crack tip. However, at a point 2 mm behind the crack tip, it was found that there was no finite value of C_1 that would fit the data. This is an artifact of the length scale of 1 m chosen to evaluate the mixity. This could possibly be eliminated by choosing a smaller length scale.

However, as mentioned earlier, since G^d versus ν relation resulting from exponential crack profile growth criterion is relatively a weak function of the constant C_1, its dependence on the constant C_1 was ignored and was evaluated for $C_1 = -0.3$. A comparison of the experimental data with the proposed criteria in the form of $|K^d|$ versus ν and G^d versus ν is presented in Fig. 10. The experimental data is normalized (as required by the criteria) with respect to a data point corresponding to $\nu = 350$ m/s. It is clear from the figure that these criteria fit very well with the experimental data in the subsonic regime. It can thus be inferred that the crack-face displacements vary exponentially with the crack-tip velocity for dynamic fracture along bimaterial interfaces.

Discussion on the Criteria

In the preceding sections, a generalized relationship between the dynamic energy release rate and the instantaneous crack-tip velocity was obtained based on the assumption that the crack face displacements vary exponentially with the crack-tip velocity.

These criteria reduce to the constant crack profile growth criterion when the exponent n in Eqs. (9) and (14) is zero. Thus, the Lambros and Rosakis criterion is a special case of the proposed generalized criteria. The exponential crack profile growth criterion reduces to the vectorial crack profile growth criterion for small values of δ_1/δ_2. The vectorial crack profile growth criterion leads to a G^d versus ν relation that is independent of the nature of loading (δ_1/δ_2) present at the crack tip. The exponential crack profile growth criterion, on the other hand, yields a G^d versus ν that exhibits a dependence on the nature of loading at the crack tip, especially at higher crack-tip velocities in the range of 65 percent to 80 percent of the lower shear wave speed (Fig. 4(*a*)). As can be seen from Fig. 4, the G^d versus ν resulting from the proposed criteria predict that the dynamic energy release rate increases with the crack-tip velocity up to about 50 percent of the lower shear wave speed indicating that the crack propagation is stable in this velocity range ($dG^d/d\nu > 0$). The dynamic energy release rate after reaching a peak shows a decreasing trend up to the Rayleigh wave velocity of the more compliant material. This decreasing trend in the energy release rate with the crack-tip velocity is characteristic of unstable crack growth behavior ($dG^d/d\nu < 0$). Also, the criteria predict that the dynamic energy release rate is finite in the limit of the Rayleigh wave velocity of the compliant material.

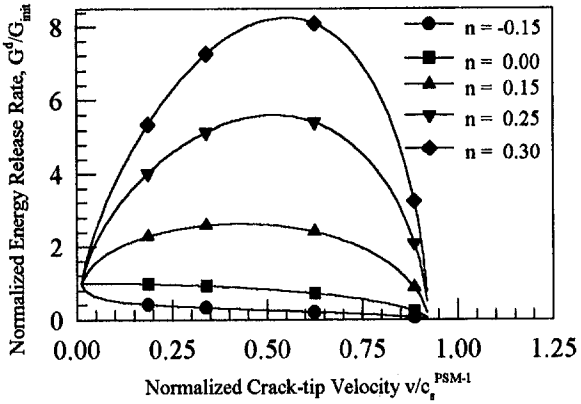


Fig. 11 Dependence of the G^d versus ν relation on the constant n for dynamic fracture along PSM-1/aluminum bimaterial interface

In order to study the effect of the exponent on the dynamic energy release rate and the crack-tip velocity relationship, G^d versus ν relation was evaluated for PSM-1/aluminum bimaterial from Eq. (15) (vectorial crack-face displacement criterion) is plotted as a function of exponent n in Fig. 11. The figure shows that as the exponent increases the slope of the curve ($dG^d/d\nu$) in the stable portion of the crack growth ($dG^d/d\nu > 0$) increases. Thus the exponent governs the degree of stability of the crack growth in the stable crack growth regime. Furthermore, the peak of the G^d versus ν relation also increases as the exponent increases. From Fig. 11, it can be seen that the peak value of $G^d(\nu)/G_{init}$ for a typical value of exponent $n = 0.3$ is about 8. This implies that the peak value of dynamic energy release rate is eight times greater than the initiation toughness. It is physically possible for an interface crack to achieve such high values of energy before any branching into the constituent materials occurs since interfaces can be much weaker than either of the constituents.

Closure

The principal objective of the study was to develop dynamic interfacial fracture criteria that establish a generalized relation-

Downloaded 04 May 2010 to 171.66.16.26. Redistribution subject to ASME license or copyright; see http://www.asme.org/terms/Terms_Use.cfm

ship between the dynamic energy release rate and the instantaneous crack-tip velocity in the subsonic regime of crack growth. Experiments were conducted on PSM-1/aluminum bimaterial systems in two different loading configurations. Based on the experimental observations, two criteria, namely, exponential crack profile growth criterion and vectorial crack-face displacement criterion were proposed. These criteria are based on the premise that the crack-face displacements at a point behind the crack tip increase exponentially with the crack-tip velocity. This assumption establishes a generalized relationship between the dynamic energy release rate and the instantaneous crack-tip velocity. The experimental data fit very well with the proposed criteria and therefore do verify these criteria.

Acknowledgment

The support of the National Science Foundation under grant number CMS 9424114 is gratefully acknowledged.

References

Deng, X. 1992, "Complete Complex Series Expansions of Near-Tip Fields for Steadily Growing Interface Cracks in Dissimilar Isotropic Materials," *Engineering Fracture Mechanics,* Vol. 42, No. 2, pp. 237–242.

Kobayashi, Y., and Dally, J. W., 1977, "The Relation Between the Crack Velocity and the Stress Intensity Factor in Birefringent Polymers," ASTM STP 627, pp. 257–273.

Lambros, J., and Rosakis, A. J., 1995a, "Development of a Dynamic Decohesion Criterion for Subsonic Fracture of the Interface Between Two Dissimilar Materials," *Proceedings of the Royal Society, London,* Vol. A451, pp. 711–736.

Lambros, J., and Rosakis, A. J., 1995b, "Shear Dominated Transonic Crack Growth in Bimaterials, Part I: Experimental Observations," *Journal of Mechanics and Physics of Solids,* Vol. 43, No. 2, pp. 169–188.

Liechti, K. M., and Knauss, W. G. 1982, "Crack Propagation at Material Interfaces: II Experiments on Mode Interaction," *Experimental Mechanics,* Vol. 22, pp. 383–391.

Liu, C., Lambros, J., and Rosakis, A. J., 1993, "Highly Transient Elastodynamic Crack Growth in a Bimaterial Interface: Higher Order Asymptotic Analysis and Optical Experiments," *Journal of the Mechanics and Physics of Solids,* Vol. 41, No. 12, pp. 1857–1954.

Nakamura, T. 1991, "Three-Dimensional Stress Fields of Elastic Interface Cracks," ASME JOURNAL OF APPLIED MECHANICS, Vol. 32, No. 2, pp. 418–423.

Rice, J. R., and Sin, G. C., 1965, "Plane Problems of Cracks in Dissimilar Media," ASME JOURNAL OF APPLIED MECHANICS, Vol. 32, pp. 418–423.

Rosakis, A. J., and Freund, L. B., 1982, "Optical Measurements of the Plain Strain Concentration at a Crack Tip in a Ductile Steel Plate," ASME *Journal of Engineering Materials and Technology,* Vol. 104, pp. 115–120.

Shukla, A., and Kavaturu, M., 1997, "Opening-mode dominated crack growth along inclined interfaces," *International Journal of Solids and Structures,* Vol. 83, pp. 291–304.

Singh, R. P., and Shukla, A., 1996a, "Subsonic and Transonic Crack Growth Along a Bimaterial Interface," ASME JOURNAL OF APPLIED MECHANICS, Vol. 63, pp. 919–924.

Singh, R. P., and Shukla, A., 1996b, "Characterization of Isochromatic Fringe Patterns for a Dynamic Propagating Interface Crack," *International Journal of Fracture,* Vol. 76, pp. 293–310.

Singh, R. P., Kavaturu, M., and Shukla, A., 1997, "Initiation, Propagation and arrest of a bimaterial interface crack subjected to controlled stress wave loading," *International Journal of Fracture,* to appear.

Sinha, J. K., Tippur, H., and Xu, L., 1997, "An Interferometric and Finite Element Investigation of Interfacial Crack-tip Fields: Role of Mode-mixity on 3-d Stress Variations," *International Journal of Solids and Structures,* Vol. 34, No. 6, pp. 741–754.

Tippur, H. V., and Rosakis, A. J., 1991, "Quasi-static and Dynamic Crack Growth Along Bimaterial Interfaces: A Note on Crack-tip Field Measurements Using Coherent Gradient Sensing," *Experimental Mechanics,* Vol. 31, pp. 243–251.

Xu, X.-P., and Needleman, A., 1996, "Numerical Simulations of Dynamic Crack Growth along an Interface," *International Journal of Fracture,* Vol. 74, pp. 289–324.

Yang, W., Suo, Z., and Shih, C. H., 1991, "Mechanics of Dynamic Debonding," *Proceedings of the Royal Society, London,* Vol. A433, pp. 679–697.

Downloaded 04 May 2010 to 171.66.16.26. Redistribution subject to ASME license or copyright; see http://www.asme.org/terms/Terms_Use.cfm

The Hypersingular Boundary Contour Method for Three-Dimensional Linear Elasticity

S. Mukherjee
Professor,
Department of Theoretical and Applied Mechanics,
Cornell University,
Kimball Hall,
Ithaca, NY 14853
Fellow ASME

Y. X. Mukherjee
President,
DeHan Engineering Mechanics,
95 Brown Road,
Box 1016,
Ithaca, NY 14850
Mem. ASME

A variant of the usual boundary element method, called the boundary contour method, has been presented in the literature in recent years. In the boundary contour method in three-dimensions, the surface integrals on boundary elements of the usual boundary element method are transformed, through an application of Stokes' theorem, into line integrals on the bounding contours of these elements. The boundary contour method employs global shape functions with the weights, in the linear combinations of these shape functions, being defined piecewise on boundary elements. A very useful consequence of this approach is that stresses at points on the boundary of a body, where they are continuous, can be easily obtained from the boundary contour method. The hypersingular boundary element method has many important applications in diverse areas such as wave scattering, fracture mechanics, symmetric Galerkin formulations, and adaptive analysis. This paper first presents the derivation of a regularized hypersingular boundary contour method for three-dimensional linear elasticity. This is followed by a discussion of special cases of the general formulation, as well as some numerical results.

Introduction

The usual boundary element method for three-dimensional linear elasticity requires numerical evaluations of surface integrals on boundary elements on the surface of a body (see, for example, Mukherjee, 1982). Nagarajan et al. (1994, 1996) have recently proposed a novel approach, called the boundary contour method, that achieves a further reduction in dimension! The boundary contour method, for three-dimensional linear elasticity problems, only requires numerical evaluation of line integrals over the closed bounding contours of the usual (surface) boundary elements.

The central idea of the boundary contour method is the exploitation of the divergence-free property of the usual boundary element method integrand and a very useful application of Stokes' theorem, to analytically convert surface integrals on boundary elements to line integrals on closed contours that bound these elements. Lutz (1991) first proposed an application of this idea for the Laplace equation. Nagarajan et al. (1994) generalized this idea to linear elasticity. Numerical results for two-dimensional problems, with linear boundary elements, are presented in Nagarajan et al. (1994), while results with quadratic boundary elements appear in Phan et al. (1997). Three-dimensional elasticity problems, with quadratic boundary elements, is the subject of Nagarajan et al. (1996) and Mukherjee et al. (1997). Sensitivity analysis for two-dimensional elasticity problems, based on the boundary contour method, is presented in Phan et al. (1998).

The focus of the present paper is the hypersingular boundary contour method. Hypersingular boundary element equations (please see Krishnasamy et al. (1992), Tanaka et al. (1994), and Paulino (1995) for recent surveys of the field) have diverse important applications and is the subject of considerable current research interest. Hypersingular boundary element equations, for example, have been employed for the evaluation of boundary stresses (e.g., Guiggiani et al., 1992), in wave scattering (e.g., Krishnasamy et al., 1990), in fracture mechanics (e.g., Gray et al., 1990; Lutz et al., 1992; Paulino, 1995; Gray and Paulino, 1998), to obtain symmetric Galerkin boundary element formulations (e.g., Bonnet, 1995; Gray et al., 1995; Gray and Paulino, 1997), and adaptive analysis (e.g., Paulino et al., 1996; Menon, 1996; Menon et al., 1998). There is a lively ongoing debate on smoothness requirements of shape functions for boundary displacements, for collocating a hypersingular boundary element equation on the boundary of a body (Martin and Rizzo, 1996; Cruse and Richardson, 1996).

As explained later in this paper, boundary stresses can be easily obtained accurately from the usual boundary contour method without the need for the hypersingular boundary contour method or differentiation of boundary shape functions. Hypersingular boundary contour equations (and the corresponding hypersingular boundary contour methods), however, are very important, in their own rights, from both a theoretical as well as a practical applications point of view. Hypersingular boundary contour equations, for example, can, in principle, be used instead of hypersingular boundary element equations to solve the diverse classes of problems that are described in the previous paragraph.

This paper is organized as follows. The usual boundary contour method for three-dimensional linear elasticity is briefly reviewed first. This is followed by a discussion of evaluating boundary stresses from the boundary contour method. Then, starting from a regularized hypersingular boundary element equation (Krishnasamy et al., 1992; Cruse and Richardson, 1996), a regularized hypersingular boundary contour equation is derived. This equation can be collocated at any point on the boundary of a body as long as the stress is continuous there.

Further developments related to the subject follow. An integral representation of the displacement gradient, at a point inside a body, is derived next. This is followed by the derivation of a hypersingular boundary contour equation at a regular off-contour boundary point. This equation is derived by regularizing the Hadamard Finite Part integral (Eq. (22)) following the procedure outlined in Toh and Mukherjee (1994). Finally, nu-

Contributed by the Applied Mechanics Division of THE AMERICAN SOCIETY OF MECHANICAL ENGINEERS for publication in the ASME JOURNAL OF APPLIED MECHANICS.

Discussion on this paper should be addressed to the Technical Editor, Professor Lewis T. Wheeler, Department of Mechanical Engineering, University of Houston, Houston, TX 77204-4792, and will be accepted until four months after final publication of the paper itself in the ASME JOURNAL OF APPLIED MECHANICS.

Manuscript received by the ASME Applied Mechanics Division, Jan. 28, 1997; final revision, Oct. 30, 1997. Associate Technical Editor: M. Ortiz.

 Copyright © 1998 by ASME

Downloaded 04 May 2010 to 171.66.16.26. Redistribution subject to ASME license or copyright; see http://www.asme.org/terms/Terms_Use.cfm

merical results are presented for a simple illustrative example—the calculation of stresses in a hollow sphere subjected to internal pressure (the Lamé problem). One-eighth of the hollow sphere is modeled as a fully three-dimensional problem and the numerical results from the boundary contour method are compared against the analytical solution.

Boundary Surface and Boundary Contour Integral Equations

A regularized form of the standard boundary integral equation (Rizzo, 1967), for three-dimensional linear elasticity, can be written as

$$0 = \int_{\partial B} [U_{ik}(P, Q)\sigma_{ij}(Q) - \Sigma_{ijk}(P, Q)\{u_i(Q) - u_i(P)\}]\mathbf{e}_j \cdot d\mathbf{S}(Q) \equiv \int_{\partial B} \mathbf{F}_k \cdot d\mathbf{S}(Q). \quad (1)$$

Here, ∂B is the bounding surface of a body B with infinitesimal surface area $d\mathbf{S} = dS\mathbf{n}$, where $\mathbf{n}$ is the unit outward normal to ∂B at a point on it. The stress tensor is $\boldsymbol{\sigma}$, the displacement vector is $\mathbf{u}$, and $\mathbf{e}_j$ ($j = 1, 2, 3$) are global Cartesian unit vectors. The boundary element method Kelvin kernels are written in terms of (boundary) source points P and field points Q. These are

$$\Sigma_{ijk} = -\frac{1}{8\pi(1-\nu)r^2}[(1-2\nu)(r_{,i}\delta_{jk} + r_{,j}\delta_{ik} - r_{,k}\delta_{ij}) + 3r_{,i}r_{,j}r_{,k}] \quad (2)$$

$$U_{ik} = \frac{1}{16\pi\mu(1-\nu)r}[(3-4\nu)\delta_{ik} + r_{,i}r_{,k}] \quad (3)$$

in terms of r, the Eucledian distance between the source and field points P and Q, and the shear modulus μ and Poisson's ratio ν of the isotropic elastic solid. Also, $\boldsymbol{\delta}$ is the Knonecker delta and $_{,i} = \partial/\partial x_i(Q)$. The range of indicies in these and all other equations in this section is 1, 2, 3, unless specified otherwise.

It has been shown (Nagarajan et al., 1994, 1996; Mukherjee et al., 1997), that the integrand vector $\mathbf{F}_k$ in Eq. (1) is divergence free (except at the point of singularity $P = Q$) and that the surface integral in it, over an open surface patch $S \in \partial B$, can be converted to a contour integral around the bounding curve C of S, by applying Stokes' theorem. Therefore, vectors $\mathbf{V}_k$ exist such that

$$\int_S \mathbf{F}_k \cdot d\mathbf{S} = \oint_C \mathbf{V}_k \cdot d\mathbf{r}. \quad (4)$$

Since the vectors $\mathbf{F}_k$ contain the unknown fields $\mathbf{u}$ and $\boldsymbol{\sigma}$, shape functions must be chosen for these variables, and potential functions derived for each linearly independent shape function, in order to determine the vectors $\mathbf{V}_k$. Also, since the kernels in Eq. (1) are functions only of $x_k = x_k(Q) - x_k(P)$ (and not of the source and field coordinates separately), these shape functions must also be written in the coordinates x_k in order to determine the potential vectors $\mathbf{V}_k$. Finally, these shape functions are global in nature and are chosen to satisfy, a priori, the Navier-Cauchy equations of equilibrium. The weights, in linear combinations of these shape functions, however, are defined piecewise on boundary elements.

One writes

$$x_1 = x - x_0, \quad x_2 = y - y_0, \quad x_3 = z - z_0 \quad (5)$$

where (x, y, z) and (x_0, y_0, z_0) are the Cartesian coordinates of a field and source point, respectively. Quadratic shape functions are used in this work. One has, on a boundary element,

$$u_i = \sum_{\alpha=1}^{27} \beta_\alpha \bar{u}_{\alpha i}(x, y, z) = \sum_{\alpha=1}^{27} \hat{\beta}_\alpha \bar{u}_{\alpha i}(x_1, x_2, x_3) \quad (6)$$

$$\sigma_{ij} = \sum_{\alpha=1}^{27} \beta_\alpha \bar{\sigma}_{\alpha ij}(x, y, z) = \sum_{\alpha=1}^{27} \hat{\beta}_\alpha \bar{\sigma}_{\alpha ij}(x_1, x_2, x_3) \quad (7)$$

where $\bar{u}_{\alpha i}$, $\bar{\sigma}_{\alpha ij}$ (with $i = 1, 2, 3$ and $\alpha = 1, 2, \ldots, 27$) are the shape functions and β_α are the weights in the linear combinations of the shape functions. Each boundary element has, associated with it, 27 constants β_α which will be related to physical variables on that element. This set of β's differ from one element to the next.

The displacement shape functions for $\alpha = 1, 2, 3$ are constants, those for $\alpha = 4, \ldots, 12$ are of first degree and those for $\alpha = 13, \ldots, 27$ are of second degree. There are a total of 27 linearly independent (vector) shape functions $\bar{\mathbf{u}}_\alpha$. The shape functions for the stresses are obtained from those for the displacements through the use of Hooke's law. The shape functions $\bar{u}_{\alpha i}$ and $\bar{\sigma}_{\alpha ij}$ are given in Mukherjee et al. (1997).

Consequences of Eqs. (6) and (7) are

$$u_i(P) = \hat{\beta}_i^P, \quad i = 1, 2, 3 \quad (8)$$

$$\lim_{Q \to P} u_{i,j}(Q) = u_{i,j}(P) = \hat{\beta}_k^P, \quad k = 4, 5, \ldots, 12, \quad j = \left\lfloor \frac{k-1}{3} \right\rfloor, \quad i = k - 3j \quad (9)$$

where the symbol $\lfloor n \rfloor$, called the floor of n, denotes the largest integer less than or equal to n.

It is easy to show that the coordinate transformation (5) results in the constants $\hat{\beta}_j$ being related to the β_α's as follows:

$$\hat{\beta}_i = \sum_{\alpha=1}^{27} S_{i\alpha}\beta_\alpha, \quad i = 1, 2, 3 \quad (10)$$

$$\hat{\beta}_k = \sum_{\alpha=1}^{27} R_{n\alpha}\beta_\alpha, \quad k = 4, 5, \ldots 12, \quad n = k - 3 \quad (11)$$

$$\hat{\beta}_\alpha = \beta_\alpha, \quad \alpha = 13, 14, \ldots, 27 \quad (12)$$

where

$$S_{i\alpha} = \bar{u}_{\alpha i}(x_0, y_0, z_0), \quad i = 1, 2, 3, \quad \alpha = 1, 2, \ldots, 27$$

$$R_{k\alpha} = \left.\frac{\partial \bar{u}_{\alpha l}(x, y, z)}{\partial x_j(Q)}\right|_{(x_0, y_0, z_0)}, \quad k = 1, 2, \ldots, 9, \quad \alpha = 1, 2, \ldots, 27$$

with $j = 1 + \lfloor (k-1)/3 \rfloor$ and $l = k - 3j + 3$.

It is useful to note that the matrices $\mathbf{S}$ and $\mathbf{R}$ are functions of only the source point coordinates (x_0, y_0, z_0).

The procedure for designing boundary elements in the three-dimensional boundary contour method is discussed in detail in Nagarajan et al. (1996) and Mukherjee et al. (1997). A set of primary physical variables a_k, whose number must match the number (here 27) of artificial variables β_k on a boundary element, are chosen first. The first step in the boundary contour method solution procedure is to determine the unspecified primary physical variables in terms of those prescribed from the boundary conditions. Later, secondary physical variables as well as stresses, at boundary points, are obtained from a simple post-processing procedure.

Downloaded 04 May 2010 to 171.66.16.26. Redistribution subject to ASME license or copyright; see http://www.asme.org/terms/Terms_Use.cfm

A square invertible transformation matrix $\mathbf{T}$ relates the vectors $\mathbf{a}$ and $\boldsymbol{\beta}$ on element m according to the equation

$$\overset{m}{a} = \overset{m}{T}\beta. \tag{13}$$

The CIM9 boundary element, shown in Fig. 1(*c*) in Nagarajan et al. (1996), is used in the present work. The displacement $\mathbf{u}$ is the primary physical variable at the three corner nodes C_i and the three midside nodes M_i, while tractions are primary variables at the internal nodes I_i. Thus, there are a total of 27 primary variables. The boundary contour method equations are collocated at the six peripheral nodes as well as at the centroid of the element. In a typical discretization procedure, some of the peripheral nodes may lie on corners or edges, while the internal nodes are always located at regular points where the boundary ∂B is locally smooth. It is of obvious advantage to have to deal only with displacement components, that are always continuous, on edges and corners, while having traction components only at regular boundary points. This approach avoids well known problems in the usual boundary element method at corners and edges that are associated with discontinuous tractions, for example, the standard boundary element method algorithm fails if, at an edge or a corner, all the displacement components are prescribed from the boundary conditions. The boundary contour method can easily handle Dirichlet problems with $\mathbf{u}$ prescribed all over the boundary of a body (Mukherjee et al., 1997). It is also important to restate that the boundary contour method is versatile enough to handle any well-posed problem in linear elasticity—all the secondary variables can be easily determined by simple post-processing once the primary boundary contour method equations are solved.

Details of the shape functions and intrinsic coordinates, that are used to define the geometry of the boundary elements, are available in Mukherjee et al. (1997). Also, the procedure for obtaining the vector potentials $\mathbf{V}_k$, for nonsingular as well as singular integrands, are available in Nagarajan et al. (1996) and Mukherjee et al. (1997). Finally, the regularized boundary element equation, Eq. (1), is converted into a regularized boundary contour equation that can be collocated (as in the usual boundary element method) at any point (including those on edges and corners). This equation is

$$\begin{aligned} 0 = \tfrac{1}{2}\sum_{m=1}^{M}\sum_{\alpha=13}^{27}\left[\oint_{L_m}(\bar{\sigma}_{\alpha ij}U_{ik} - \bar{u}_{\alpha i}\Sigma_{ijk})\epsilon_{jst}x_s dx_t\right][\overset{m}{T}^{-1}\overset{m}{a}]_\alpha \\ + \sum_{m=1}^{M}\sum_{\alpha=4}^{12}\left[\oint_{L_m}(\bar{\sigma}_{\alpha ij}U_{ik} - \bar{u}_{\alpha i}\Sigma_{ijk})\epsilon_{jst}x_s dx_t\right][\overset{m}{R}\overset{m}{T}^{-1}\overset{m}{a}]_{\alpha-3} \\ + \sum_{\substack{m=1\\ m\notin S}}^{M}\sum_{\alpha=1}^{3}\left[\oint_{L_m}D_{\alpha jk}dx_j\right]\left[S\left(\overset{m}{T}^{-1}\overset{m}{a} - \overset{P}{T}^{-1}\overset{P}{a}\right)\right]_\alpha \end{aligned} \tag{14}$$

with

$$\begin{aligned} \oint_{L_m}D_{\alpha jk}dx_j &= -\int_{S_m}\Sigma_{\alpha jk}\mathbf{e}_j\cdot d\mathbf{S} \\ &= \frac{1}{8\pi(1-\nu)}\oint_{L_m}\epsilon_{kij}\frac{r_{,\alpha}r_{,i}}{r}dx_j \\ &\quad + \frac{1-2\nu}{8\pi(1-\nu)}\oint_{L_m}\epsilon_{\alpha kj}\frac{1}{r}dx_j + \frac{\Theta}{4\pi}\delta_{\alpha k}. \end{aligned} \tag{15}$$

Here L_m is the bounding contour of the surface element S_m. In the above, Θ is the solid angle (subtended by a surface element m at a collocation point P), which is defined as

$$\Theta = \int_{S_m}\frac{\mathbf{r}\cdot d\mathbf{S}}{r^3}. \tag{16}$$

Also, $\overset{m}{T}$ and $\overset{m}{a}$ are the transformation matrix and primary physical variable vectors on element m, $\overset{P}{T}$ and $\overset{P}{a}$ are the same quantities evaluated on any element that belongs to the set S of elements that contain the source point P, and ϵ_{ijk} is the usual alternating symbol.

Note that the first and second integrals of Eq. (14) are regular. They are of $O(r)$ and $O(1)$, respectively, and can be easily evaluated by routine Gaussian quadrature. The third integrand is potentially strongly singular ($O(1/r)$), but this integral only needs to be evaluated on nonsingular elements. Therefore, standard Gaussian quadrature again suffices. The solid angle subtended by a flat element can be easily computed from a well-known algebraic formula (see, for example, Mantič, 1993). Contour integral formulae for evaluating the solid angle, subtended at a point by a curved boundary element, have been derived (Nagarajan et al., 1996) but computational algorithms based on these formulae have proved to be somewhat fragile in general applications for three-dimensional bodies of complex shape. The surface integral formula (16), however, is very easy to implement in a computer code, and has been used to obtain most of the numerical results reported in this paper. An exception is the evaluation of the solid angle on a singular boundary element as may be required for some boundary stress calculations. This issue is discussed later in this paper. Please note that the solid angle calculation from Eq. (16) is purely geometrical and does not involve any physical variables. This is the only time that a surface integral is evaluated in the boundary contour method.

The assembled, discretized boundary contour equation (Eq. (14)) has the usual form

$$Ka = 0 \tag{17}$$

which is written as

$$Ax = By \tag{18}$$

where $\mathbf{x}$ contains the unknown and $\mathbf{y}$ the known (from the boundary conditions) values of the primary physical variables on the surface of the body. Once these equations are solved, the vector $\mathbf{a}$ is completely known. Now, at a post-processing step, $\overset{m}{\beta}_\alpha$ can be easily obtained on each boundary element from Eq. (13).

Boundary Stresses

First, a few preliminaries. This paper is concerned with boundary (surface) points at which the stress is continuous. A point at an edge or corner is called a corner point while at a regular point the boundary is locally smooth. Also, a boundary point can lie on or away from a boundary contour. The former is called a contour point, the latter an off-contour point. A point inside a body is called an internal point.

A very useful consequence of using global shape functions is that, once the standard boundary contour method is solved, it is very easy to obtain the stress at any point on the bounding surface of a body. First, one obtains $\overset{m}{\beta}_\alpha$ from Eq. (13), then uses Eq. (11) to get $\hat{\beta}^m_\alpha$, $\alpha = 4, 5, \ldots, 12$. Finally, Eq. (9), whose explicit form is

$$[u_{i,j}(P)] = \begin{bmatrix}\hat{\beta}_4 & \hat{\beta}_7 & \hat{\beta}_{10}\\ \hat{\beta}_5 & \hat{\beta}_8 & \hat{\beta}_{11}\\ \hat{\beta}_6 & \hat{\beta}_9 & \hat{\beta}_{12}\end{bmatrix}_P \tag{19}$$

can be used to find the displacement gradients at P. Hooke's law would then give the stress $\sigma_{ij}(P)$. An alternative approach is to use Eq. (7) together with all the β_α on an element.

It should be noted that the simple approach, described above, cannot be used to find internal stresses since the constants $\overset{m}{\beta}_\alpha$

Downloaded 04 May 2010 to 171.66.16.26. Redistribution subject to ASME license or copyright; see http://www.asme.org/terms/Terms_Use.cfm

are only meaningful on the boundary of a body. Therefore, an internal point representation of the differentiated boundary contour equation, for the internal displacement gradients $u_{i,j}(p)$, is necessary. It is also of interest to examine the limiting process of a differentiated boundary contour equation as an internal point p approaches a boundary point P. This issue is of great current interest in the boundary element method community in the context of the standard and hypersingular boundary element equations (see, for example, Martin and Rizzo (1996) and Cruse and Richardson (1996)). Further, the hypersingular boundary contour equation must be understood if one wishes to collocate the hypersingular boundary contour equation as the primary integral equation, as may be necessary, for example, in applications such as fracture mechanics, symmetric Galerkin formulations or adaptive analysis (please see the Introduction section of this paper). This topic is the subject of the next two sections of this paper.

Hypersingular Boundary Integral Equations

One starts from an internal point representation of Eq. (1)

$$u_k(p) = \int_{\partial B} [U_{ik}(p, Q)\sigma_{ij}(Q) - \Sigma_{ijk}(p, Q)u_i(Q)]n_j(Q)dS(Q). \quad (20)$$

Differentiating this equation at a source point p gives

$$u_{k,n}(p) = -\int_{\partial B} [U_{ik,n}(p, Q)\sigma_{ij}(Q) - \Sigma_{ijk,n}(p, Q)u_i(Q)]n_j(Q)dS(Q) \quad (21)$$

where, as usual, the derivatrives of the kernels with respect to $x_n(p)$ have been converted, by a sign change, to those with respect to $x_n(q)$. As shown by Krishnasamy et al. (1990) and Toh and Mukherjee (1994), the limiting value of Eq. (21) as p approaches a regular point P on ∂B, (provided that $\mathbf{u} \in C^{1,\alpha}$ at P for some $\alpha > 0$), is

$$u_{k,n}(P) = -\oint\!\!\!\!\!\!=_{\partial B} [U_{ik,n}(P, Q)\sigma_{ij}(Q) - \Sigma_{ijk,n}(P, Q)u_i(Q)]n_j(Q)dS(Q) \quad (22)$$

where $\oint\!\!\!\!\!\!=$ denotes the Hadamard finite part of the integral. The Hadamard finite part is interpreted in this paper in the sense of Toh and Mukherjee (1994). Please note that if the displacement field is $C^{1,\alpha}$ at P, then the stress field is $C^{0,\alpha}$ at that point.

A very useful computable regularized form of Eq. (22) (see, for example, Krishnasamy et al. (1992), Lutz et al. (1992), and Cruse and Richardson, (1996)) is

$$0 = \int_{\partial B} U_{ik,n}(P, Q)[\sigma_{ij}(Q) - \sigma_{ij}(P)]n_j(Q)dS(Q) - \int_{\partial B} \Sigma_{ijk,n}(P, Q)[u_i(Q) - u_i(P) - u_{i,l}(P)(x_l(Q) - x_l(P))]n_j(Q)dS(Q). \quad (23)$$

Cruse and Richardson (1996) have recently proved that the above equation is valid even at a corner point P provided that the stress is continuous there.

Hypersingular Boundary Contour Equations

The first task at hand is to transform Eq. (23) into a boundary contour form. The integrands in Eq. (23), without $n_j(Q)dS(Q)$, are first evaluated at an internal field point q very near Q (i.e., on a surface ∂_B inside the body, very near and parallel to ∂B), the derivatives are transferred from the kernels to the quantities inside the square brackets by the product rule, and then the limit $q \to Q$ is taken again. This is possible since the integrals in Eq. (23) are regular. The result is

$$0 = \int_{\partial B} [U_{ik}(P, Q)[\sigma_{ij}(Q) - \sigma_{ij}(P)] - \Sigma_{ijk}(P, Q)[u_i(Q) - u_i^{(L)}]]_{,n}n_j(Q)dS(Q) - \int_{\partial B} [U_{ik}(P, Q)\sigma_{ij,n}(Q) - \Sigma_{ijk}(P, Q)[u_{i,n}(Q) - u_{i,n}(P)]]n_j(Q)dS(Q) \quad (24)$$

where

$$u_i^{(L)} = u_i(P) + u_{i,l}(P)(x_l(Q) - x_l(P)).$$

Note also that

$$u_{i,n}^{(L)} = u_{i,n}(P)$$

Therefore, the linear displacement field $u_i^{(L)}$ gives the stress field $\sigma_{ij}(P)$, so that the stress field $\sigma_{ij}(Q) - \sigma_{ij}(P)$ is obtained from the displacement field $u_i(Q) - u_i^{(L)}$.

The bounding surface ∂B is now considered to be the union of open surfaces (boundary elements) S_m. Using the identity (Nagarajan et al., 1996)

$$\mathbf{v}_{,n} = \nabla \times (\mathbf{v} \times \mathbf{e}_n) \quad (25)$$

(which is valid if the vector field $\mathbf{v}$ is divergence free) and Stokes' theorem, the first integral in Eq. (24), over S_m, is converted to the contour integral

$$I_1 = \oint_{L_m} [U_{ik}(P, Q)[\sigma_{ij}(Q) - \sigma_{ij}(P)] - \Sigma_{ijk}(P, Q)[u_i(Q) - u_i^{(L)}]]\epsilon_{jnt}dx_t. \quad (26)$$

An explicit form of Eq. (26) is derived in Appendix A.

Next, it is noted from Eqs. (8) and (10) that

$$u_{i,n}(P) = [\overset{P}{S}_{,N}\beta]_i \quad (27)$$

where, $N \equiv \partial/\partial x_n(P)$.

Further, as proved in Appendix B,

$$u_{i,n}(Q) = [\overset{m}{S}_{,N}\beta]_i + \sum_{\alpha=4}^{12} [\overset{m}{R}_{,N}\beta]_{\alpha-3}\bar{u}_{\alpha i}(x_1, x_2, x_3). \quad (28)$$

Now, the second integral (called I_2) in Eq. (24) is written as

$$I_2 = -\int_{\partial B} [U_{ik}(P, Q)\sigma_{ij,n}(Q) - \Sigma_{ijk}(P, Q)u_{i,n}(Q)]n_j dS - u_{i,n}(P)\int_{\partial B} \Sigma_{ijk}(P, Q)n_j dS. \quad (29)$$

The next steps involve writing $\partial B = \cup S_m$, separating the constant and linear parts of $u_{i,n}$ in the first integrand above, and using Eq. (28). This sets the stage for converting I_2 into two contour integrals. Details are given in Appendix C.

The final result is a contour integral form (hypersingular boundary contour equation) of the regularized hypersingular boundary element equation (23). This equation is valid at any point on the boundary ∂B as long as the stress is continuous there. This includes edge, corner, and regular points that lie on or off contours.

Downloaded 04 May 2010 to 171.66.16.26. Redistribution subject to ASME license or copyright; see http://www.asme.org/terms/Terms_Use.cfm

The regularized hypersingular boundary contour equation is

$$0 = -\sum_{m=1}^{M}\sum_{\alpha=13}^{27}\left[\oint_{L_m}(\bar{\sigma}_{\alpha ij}U_{ik} - \bar{u}_{\alpha i}\Sigma_{ijk})\epsilon_{jnt}dx_t\right][{}^{m}_{T^{-1}}{}^{m}_{a}]_{\alpha}$$
$$+\sum_{m=1}^{M}\sum_{\alpha=4}^{12}\left[\oint_{L_m}(\bar{\sigma}_{\alpha ij}U_{ik} - \bar{u}_{\alpha i}\Sigma_{ijk})\epsilon_{jst}x_s dx_t\right][R_N{}^{m}_{T^{-1}}{}^{m}_{a}]_{\alpha-3}$$
$$-\sum_{\substack{m=1\\ m\notin S}}^{M}\sum_{\alpha=4}^{12}\left[\oint_{L_m}(\bar{\sigma}_{\alpha ij}U_{ik} - \bar{u}_{\alpha i}\Sigma_{ijk})\epsilon_{jnt}dx_t\right]$$
$$\times\left[R\left({}^{m}_{T^{-1}}{}^{m}_{a} - {}^{P}_{T^{-1}}{}^{P}_{a}\right)\right]_{\alpha-3}$$
$$+\sum_{\substack{m=1\\ m\notin S}}^{M}\sum_{\alpha=1}^{3}\left[\oint_{L_m}D_{\alpha jk}dx_j\right]\left[S_N\left({}^{m}_{T^{-1}}{}^{m}_{a} - {}^{P}_{T^{-1}}{}^{P}_{a}\right)\right]_{\alpha}$$
$$+\sum_{\substack{m=1\\ m\notin S}}^{M}\sum_{\alpha=1}^{3}\left[\oint_{L_m}\Sigma_{\alpha jk}\epsilon_{jnt}dx_t\right]\left[S\left({}^{m}_{T^{-1}}{}^{m}_{a} - {}^{P}_{T^{-1}}{}^{P}_{a}\right)\right]_{\alpha} \quad (30)$$

where, as before, S is the set of boundary elements that contain the source point P. In the above equation, the integrands in the first two terms are regular ($O(1)$). The third and fourth (potentially strongly singular, $O(1/r)$) as well as the fifth (potentially hypersingular, $O(1/r^2)$) need to be evaluated only on nonsingular elements.

Equation (30) can be used as the primary integral equation for obtaining the unspecified boundary tractions and displacements. If, however, one is interested (in a post-processing step) to obtain the displacement gradient at a point P where it is continuous, after the standard boundary contour equation (Eq. (14)) has been solved, then the fourth term in Eq. (30) must be replaced by the term

$$I_4 = \sum_{\substack{m=1\\ m\notin S}}^{M}\sum_{\alpha=1}^{3}\left[\oint_{L_m}D_{\alpha jk}dx_j\right][(S_N{}^{m}_{T^{-1}}{}^{m}_{a})_{\alpha} - u_{\alpha,n}(P)]. \quad (31)$$

Internal Stresses

At this stage, it is a simple matter to derive an equation for the displacement gradient at a point inside a body. A comparison of the surface integral representation for the internal displacement gradient (Eq. (21)) and the regularized hypersingular boundary element equation (23) reveals the extra terms in the latter equation that have been necessary in order to obtain the regularized hypersingular boundary element equation. Removing the contour integrals from the hypersingular boundary contour equation (30) that correspond to these extra terms, leaves the desired equation. This is

$$\gamma u_{k,n}(p)$$
$$= -\sum_{m=1}^{M}\sum_{\alpha=13}^{27}\left[\oint_{L_m}(\bar{\sigma}_{\alpha ij}U_{ik} - \bar{u}_{\alpha i}\Sigma_{ijk})\epsilon_{jnt}dx_t\right][{}^{m}_{T^{-1}}{}^{m}_{a}]_{\alpha}$$
$$+\sum_{m=1}^{M}\sum_{\alpha=4}^{12}\left[\oint_{L_m}(\bar{\sigma}_{\alpha ij}U_{ik} - \bar{u}_{\alpha i}\Sigma_{ijk})\epsilon_{jst}x_s dx_t\right][R_N{}^{m}_{T^{-1}}{}^{m}_{a}]_{\alpha-3}$$
$$-\sum_{m=1}^{M}\sum_{\alpha=4}^{12}\left[\oint_{L_m}(\bar{\sigma}_{\alpha ij}U_{ik} - \bar{u}_{\alpha i}\Sigma_{ijk})\epsilon_{jnt}dx_t\right][R{}^{m}_{T^{-1}}{}^{m}_{a}]_{\alpha-3}$$
$$+\sum_{m=1}^{M}\sum_{\alpha=1}^{3}\left[\oint_{L_m}D_{\alpha jk}dx_j\right][S_N{}^{m}_{T^{-1}}{}^{m}_{a}]_{\alpha}$$
$$+\sum_{m=1}^{M}\sum_{\alpha=1}^{3}\left[\oint_{L_m}\Sigma_{\alpha jk}\epsilon_{jnt}dx_t\right][S{}^{m}_{T^{-1}}{}^{m}_{a}]_{\alpha} \quad (32)$$

with $\gamma = 1$. Hooke's law is now used to obtain the internal stress from the internal displacement gradient.

The Hypersingular Boundary Contour Equation at a Regular Off-Contour Boundary Point

The hypersingular boundary contour equation (30) is valid at any boundary point at which the stress in continuous. Nevertheless, it is of interest to derive a different regularized hypersingular boundary contour equation for the special case when the point P is a regular off-contour boundary point. The idea here is to derive the limiting form of Eq. (32) as an internal point p approaches a regular off-contour boundary point. The adopted procedure is to regularize the Hadamard finite part in Eq. (22) using the method outlined in Toh and Mukherjee (1994).

It is sufficient to consider the Hadamard finite part on a singular element only. One has

$$I_{kn} = -\oint\!\!\!\!\!\!-_{S_P}[U_{ik,n}(P, Q)\sigma_{ij}(Q) - \Sigma_{ijk,n}(P, Q)u_i(Q)]n_j(Q)dS(Q)$$
$$\equiv I^{(2)}_{kn} + I^{(1)}_{kn}. \quad (33)$$

Using the regularization scheme presented in Toh and Mukherjee (1994), with the exclusion zone set equal to the entire surface S_P, one gets

$$I^{(1)}_{kn} = \int_{S_P}\Sigma_{ijk,n}(P, Q)[u_i(Q) - u_i(P) - u_{i,l}(P)(x_l(Q) - x_l(P))]n_j(Q)ds(Q) + A_{ikn}(S_P)u_i(P) + B_{iknl}(S_P)u_{i,l}(P) \quad (34)$$

and

$$I^{(2)}_{kn} = -\int_{S_P}U_{ik,n}(P, Q)[\sigma_{ij}(Q) - \sigma_{ij}(P)]n_j(Q)dS(Q) - C_{iknj}(S_P)\sigma_{ij}(P). \quad (35)$$

It is proved in Appendix D that

$$A_{ikn}(S_P) = \oint_{L_P}\Sigma_{ijk}\epsilon_{jnt}dx_t \quad (36)$$

$$B_{iknl}(S_P) = \oint_{L_P}\epsilon_{jnt}\Sigma_{ijk}(x_l(Q) - x_l(P))dx_t + \delta_{nl}\oint_{L_P}D_{ijk}dx_j + \int_{S_P}\Sigma_{ilk}n_n dS \quad (37)$$

$$C_{iknj}(S_P) = \oint_{L_P}\epsilon_{jnt}u_{ik}dx_t + \int_{S_P}U_{ik,j}n_n dS \quad (38)$$

where L_P is the bounding contour for S_P.

Now, it can be shown that

$$A_{\alpha kn}(S_P)u_{\alpha}(P) = \text{the fifth term in Eq. (32) on a singular element,} \quad (39)$$

$$B^{(1)}_{iknl}(S_P)u_{i,l}(P) - C^{(1)}_{iknj}(S_P)\sigma_{ij}(P) = \text{the third term in Eq. (32) on a singular element,} \quad (40)$$

$$B^{(2)}_{\alpha knl}(S_P)u_{\alpha,l}(P) = \text{the fourth term in Eq. (32) on a singular element,} \quad (41)$$

Downloaded 04 May 2010 to 171.66.16.26. Redistribution subject to ASME license or copyright; see http://www.asme.org/terms/Terms_Use.cfm

and

$$B^{(3)}_{iknl}(S_P)u_{i,l}(P) - C^{(2)}_{iknj}(S_P)\sigma_{ij}(P) = 0. \qquad (42)$$

The regularized integrals from Eq. (33) (i.e., the sum of the integrals in Eqs. (34) and (35), immediately give the first and second terms in Eq. (32) on a singular element. (Please see Eqn. (30) and note that its third, fourth, and fifth terms vanish on a singular element.)

Finally, the form of Eq. (32), when P is a regular off-contour boundary point, changes in the following ways:

1 The internal point p is replaced by the boundary point P.

2 The solid angle Θ in the expression for $D_{\alpha jk}$ (see the second term in Eq. (37), the fourth term in Eq. (32) and also Eq. (15)) must be evaluated on the singular element. This is best done from a contour integral formula for Θ written in local coordinates, normal and tangential to ∂B at P. Details are given in Appendix E.

3 The scalar $\gamma = \frac{1}{2}$. The reason for this is also explained in Appendix E.

The resulting equation at a regular off-contour boundary point, called Eq. (32) ($p \to P$) for reference purposes, is useful for a boundary contour method formulation, for example for three-dimensional fracture mechanics, if nonconforming elements are used (see Lutz et al. (1992) for the corresponding boundary element method version). Of course, integrals on both a singular element and its twin must be regularized when a crack is modeled with two geometrically identical surfaces, but the present approach can be easily modified in order to carry this out.

An alternative way to derive Eq. (32) ($p \to P$) is to regularize the hypersingular boundary element equation (21) only on a singular element as $p \to P$. This gives (see Eq. (33))

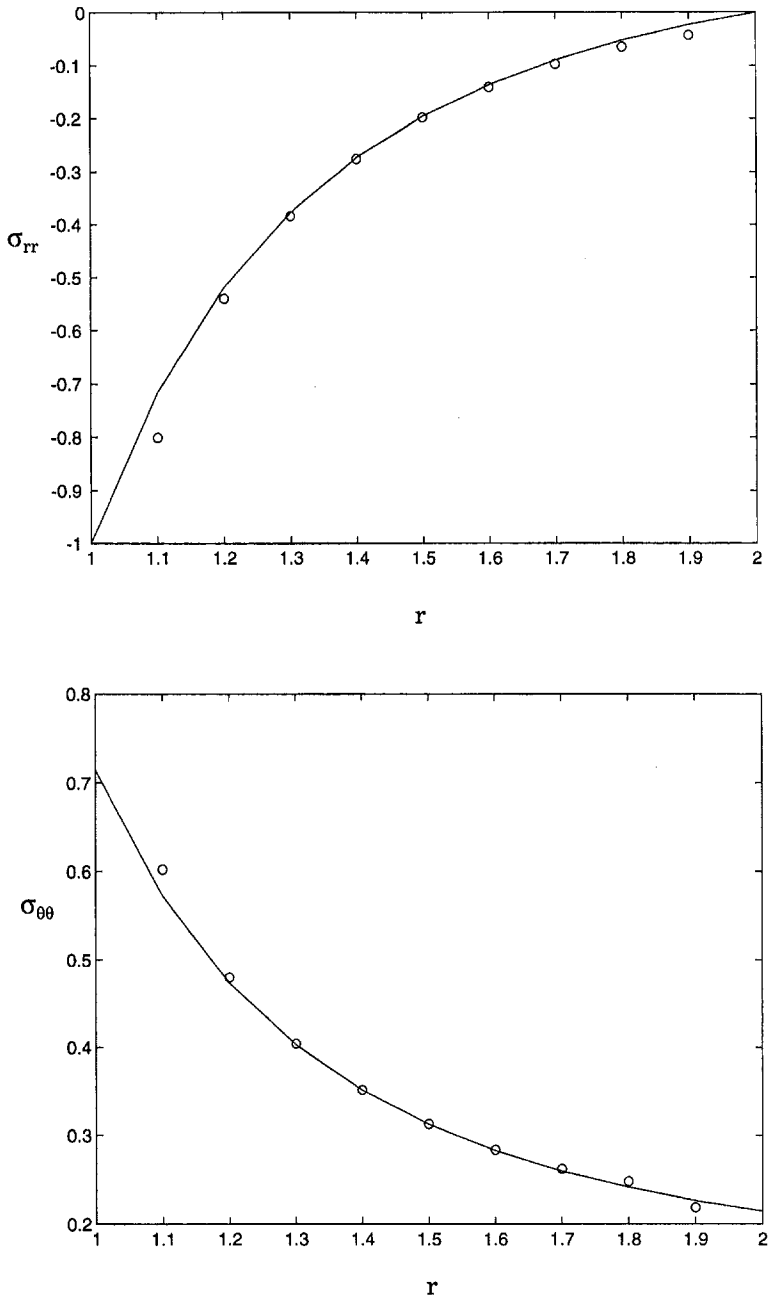


Fig. 1 Internal stresses in a one-eighth sphere as functions of radius, along the line $x = y = z$; ——: exact solution, ○○○: numerical solution

Downloaded 04 May 2010 to 171.66.16.26. Redistribution subject to ASME license or copyright; see http://www.asme.org/terms/Terms_Use.cfm

$$I_{kn} = -\int_{S_P} U_{ik,n}(P, Q)[\sigma_{ij}(Q) - \sigma_{ij}(P)]n_j(Q)dS(Q)$$
$$+ \int_{S_P} \Sigma_{ijk,n}(P, Q)[u_i(Q) - u_i(P)$$
$$- u_{i,l}(P)(x_l(Q) - x_l(P))]n_j(Q)ds(Q)$$
$$+ u_i(P) \int_{S_P} \Sigma_{ijk,n}(P, Q)n_j(Q)dS(Q)$$
$$+ u_{i,l}(P) \int_{S_P} \Sigma_{ijk,n}(P, Q)(x_l(Q) - x_l(P))n_j(Q)dS(Q)$$
$$- \sigma_{ij}(P) \int_{S_P} U_{ik,n}(P, Q)n_j(Q)dS(Q). \quad (43)$$

Now, from Appendix D, one can easily identify the integrals in the added back terms with **A**, **B**, and **C**, respectively, in Eqs. (36)–(38), so that Eq. (32) ($p \to P$) follows. (Please compare Eq. (43) with Eqs. (33)–(35).)

Numerical Results for a Sphere

A computer program, capable of solid modeling, and meshing the curved surfaces of the solid with triangular boundary elements, has been used in this research. This computer program is based on transfinite mapping. An example of a mesh produced by this package is given in Mukherjee et al. (1997).

The numerical example considered in this work is a hollow elastic sphere under internal pressure. The internal and external radii of the sphere are 1 and 2 units, respectively. The applied internal pressure is unity and the Poisson's ratio of the material is 0.3.

One-eighth of the sphere is modeled here to take advantage of symmetry and also to include corners in the model. Of course, the problem is treated as fully three-dimensional in order to test the three-dimensional boundary contour method code. The mesh consists of a total of 54 (curved, triangular CIM9) boundary elements. Of these, nine elements are placed on each of the curved surfaces and 12 are placed on each of the flat surfaces of the one-eighth sphere. A similar mesh, with 92 boundary elements, is shown in Mukherjee et al. (1997).

The first step in the boundary contour method analysis is to solve the primary problem, Eq. (14), for the unspecified components of boundary tractions and displacements. Numerical results for some components of displacements and tractions are given in Mukherjee et al. (1997) and are not repeated here.

The primary focus of the present work is the calculation of stresses, both inside and on the surface of a body. Internal displacement gradients are calculated from Eq. (32) and internal stresses are then obtained from Hooke's law. Numerical results from the boundary contour method are compared with Lamé's solution (Timoshenko and Goodier, 1970) in Fig. 1. This figure shows radial and circumferential ($\sigma_{\theta\theta}$) stresses as functions of radius. The numerical result for the stress component $\sigma_{\phi\phi}$ is practically identical to $\sigma_{\theta\theta}$ and is not shown here. It is seen from Fig. 1 that the analytical and numerical solutions are in excellent agreement sufficiently inside ($r = 1.2$ to $r = 1.8$) the sphere. There is some disagreement between the results closer to the surface of the sphere. This is typical of results from the usual boundary element method and is related to the loss of numerical accuracy from numerical integration of nearly singular integrals. One remedy is to employ quadrature rules that account for the distance between a collocation point and integration element (e.g., Lutz, 1991), but this has not yet been done in the present work.

Table 1 Boundary stresses on a flat surface ($x = 0$) of the one-eighth sphere, at the centroids of boundary elements

points (x=0) y	z	σ_{kk} exact: 3/7	% error
1.2659,	0.24993	0.429003	1.007
1.0692,	0.42044	0.418230	2.473
1.7733,	0.34111	0.425490	0.724
1.5099,	0.58320	0.427855	0.167
0.97115,	0.84929	0.426139	0.571
0.89873,	0.71589	0.422310	1.485
1.3647,	1.1820	0.436910	1.946
1.0158,	1.2599	0.422019	1.553
0.41951,	1.2212	0.426787	0.418
0.17051,	1.1366	0.413199	3.720
0.59104,	1.7058	0.435103	1.524
0.24993,	1.5992	0.429831	0.294

Table 2 Boundary stresses on curved surfaces (inside and outside) of the one-eighth sphere, at representative centroids of boundary elements

points	σ_{rr}		$\sigma_{\theta\theta}$		$\sigma_{\phi\phi}$	
(x,y,z)	numerical	% error	numerical	% error	numerical	% error
inside	exact solution: 1		exact solution: 5/7		exact solution: 5/7	
0.17821 0.96654 0.17821	-0.92409	7.5913	0.75097	5.1352	0.75106	5.1485
0.37923 0.84068 0.37923	-0.95317	4.6835	0.75154	5.2162	0.74930	4.9015
0.69332 0.69332 0.19201	-0.94676	5.3236	0.75222	5.3111	0.75289	5.4044
outside	exact solution: 0		exact solution: 3/14		exact solution: 3/14	
0.35646 1.9331 0.35646	0.0063744		0.21697	1.2519	0.21692	1.2278
0.75847 1.6813 0.75847	0.0095049		0.22466	4.8409	0.22424	4.6449
0.13867 1.3867 0.38401	0.0047842		0.22191	3.558	0.21737	1.4407

Next, surface stresses are calculated at regular off-contour boundary points (centroids of the CIM9 elements) from Eq. (32) ($p \to P$). Results are compared with Lamé's solution in Tables 1 and 2. Table 1 compares numerical and analytical results for the trace of the stress tensor, σ_{kk}, on the 12 element centroids on the plane $x = 0$. The worst error is seen to be less than four percent. Very similar results are obtained on the other flat surfaces $y = 0$ and $z = 0$.

Table 2 shows similar results on the curved surfaces (inside and outside) of the sphere. Three representative element centroids are chosen on each surface. This time, most of the errors are around five percent. Results on the rest of the centroids are very similar. The accuracy is expected to improve with mesh refinement. Since the primary motivation of this paper is theoretical rather than numerical, mesh refinement studies are postponed to a future paper.

Conclusions

In this work, a hypersingular boundary element method has been transformed, using Stokes' theorem, to a corresponding hypersingular boundary contour method. The general hypersingular boundary contour method, which is valid at any boundary point at which the stress is continuous, as well as a special version, that is valid for regular off-contour boundary points, are completely regularized. Numerical results for an illustrative sphere problem demonstrate the ease of using this approach for the calculation of boundary stresses.

Acknowledgments

This research has been supported by two NSF SBIR grants to DeHan Engineering Numerics. These are DMI-9460263 (SBIR–Phase I) and DMI-9629076 (SBIR–Phase II).

References

Bonnet, M., 1995, "Regularized Direct and Indirect Symmetric Variational BIE Formulations for Three-Dimensional Elasticity," *Engineering Analysis with Boundary Elements,* Vol. 15, pp. 93–102.

Downloaded 04 May 2010 to 171.66.16.26. Redistribution subject to ASME license or copyright; see http://www.asme.org/terms/Terms_Use.cfm

Cruse, T. A., and Richardson, J. D., 1996, "Non-singular Somigliana Stress Identities in Elasticity," *International Journal for Numerical Methods in Engineering,* Vol. 39, pp. 3273–3304.

Gray, L. J., Martha, L. F., and Ingraffea, A. R., 1990, "Hypersingular Integrals in Boundary Element Fracture Analysis," *International Journal for Numerical Methods in Engineering,* Vol. 29, pp. 1135–1158.

Gray, L. J., Balakrishna, C., and Kane, J. H., 1995, "Symmetric Galerkin Fracture Analysis," *Engineering Analysis with Boundary Elements,* Vol. 15, pp. 103–109.

Gray, L. J., and Paulino, G. H., 1997, "Symmetric Galerkin Boundary Integral Formulation for Interface and Multi-Zone Problems," *International Journal for Numerical Methods in Engineering,* Vol. 40, pp. 3085–3101.

Gray, L. J., and Paulino, G. H., 1998, "Crack Tip Interpolation, Revisited," *SIAM Journal on Applied Mathematics,* Vol. 58, pp. 428–455.

Guiggiani, M., Krishnasamy, G., Rudolphi, T. J., and Rizzo, F. J., 1992, "A General Algorithm for the Numerical Solution of Hypersingular Boundary Integral Equations," ASME JOURNAL OF APPLIED MECHANICS, Vol. 59, pp. 604–614.

Kaplan, W., 1984, *Advanced Calculus,* 3rd ed., Addison-Wesley, Reading, MA.

Krishnasamy, G., Schmerr, L. W., Rudolphi, T. J., and Rizzo, F. J., 1990, "Hypersingular Boundary Integral Equations: Some Applications in Acoustics and Elastic Wave Scattering," ASME JOURNAL OF APPLIED MECHANICS, Vol. 57, pp. 404–414.

Krishnasamy, G., Rizzo, F. J., and Rudolphi, T. J., 1992, "Hypersingular Boundary Integral Equations: Their Occurrence, Interpretation, Regularization and Computation," *Developments in Boundary Element Methods,* Vol. 7, P. K. Banerjee and S. Kobayashi, eds., Elsevier Applied Science, London, pp. 207–252.

Lutz, E. D., 1991, "Numerical Methods for Hypersingular and Near-Singular Boundary Integrals in Fracture Mechanics," Ph.D. dissertation, Cornell University, Ithaca, NY.

Lutz, E. D., Ingraffea, A. R., and Gray, L. J., 1992, "Use of 'Simple Solutions' for Boundary Integral Methods in Elasticity and Fracture Analysis," *International Journal for Numerical Methods in Engineering,* Vol. 35, pp. 1737–1751.

Mantič, V., 1993, "A New Formula for the C-Matrix in the Somigliana Identity," *Journal of Elasticity,* Vol. 33, pp. 191–201.

Martin, P. A., and Rizzo, F. J., 1996, "Hypersingular Integrals: How Smooth Must the Density Be?," *International Journal for Numerical Methods in Engineering,* Vol. 39, pp. 687–704.

Menon, G., 1996, "Hypersingular Error Estimates in Boundary Element Methods," M.S. thesis, Cornell University, Ithaca, NY.

Menon, G., Paulino, G. H., and Mukherjee, S., 1998, "Analysis of Hypersingular Residual Error Estimates in Boundary Element Methods for Potential Problems," *Computer Methods in Applied Mechanics and Engineering,* in press.

Mukherjee, S., 1982, *Boundary Element Methods in Creep and Fracture,* Elsevier Applied Science, London.

Mukherjee, Y. X., Mukherjee, S., Shi, X., and Nagarajan, A., 1997, "The Boundary Contour Method for Three-Dimensional Linear Elasticity with a New Quadratic Boundary Element," *Engineering Analysis with Boundary Elements,* Vol. 20, pp. 35–44.

Nagarajan, A., Lutz, E., and Mukherjee, S., 1994, "A Novel Boundary Element Method for Linear Elasticity With No Numerical Integration for Two-Dimensional and Line Integrals for Three-Dimensional Problems," ASME JOURNAL OF APPLIED MECHANICS, Vol. 61, pp. 264–269.

Nagarajan, A., Mukherjee, S., and Lutz, E., 1996, "The Boundary Contour Method for Three-Dimensional Linear Elasticity," ASME JOURNAL OF APPLIED MECHANICS, Vol. 63, pp. 278–286.

Paulino, G. H., Gray, L. J., and Zarkian, V., 1996, "Hypersingular Residuals—A New Approach for Error Estimation in the Boundary Element Method," *International Journal for Numerical Methods in Engineering,* Vol. 39, pp. 2005–2029.

Paulino, G. H., 1995, "Novel Formulations of the Boundary Element Method for Fracture Mechanics and Error Estimation," Ph.D. dissertation, Cornell University, Ithaca, NY.

Phan, A.-V., Mukherjee, S., and Mayer, J. R. R., 1997, "The Boundary Contour Method for Two-Dimensional Linear Elasticity With Quadratic Boundary Elements," *Computational Mechanics,* Vol. 20, pp. 310–319.

Phan, A.-V., Mukherjee, S., and Mayer, J. R. R., 1998, "A Boundary Contour Formulation for Design Sensitivity Analysis in Two-Dimensional Linear Elasticity," *International Journal of Solids and Structures,* Vol. 35, pp. 1981–1999.

Rizzo, F. J., 1967, "An Integral Equation Approach to Boundary Value Problems of Classical Elastostatics," *Quarterly of Applied Mathematics,* Vol. 25, pp. 83–95.

Tanaka, M., Sladek, V., and Sladek, J., 1994, "Regularization Techniques Applied to Boundary Element Methods," ASME *Applied Mechanics Reviews,* Vol. 47, pp. 457–499.

Timoshenko, S. P., and Goodier, J. N., 1970, *Theory of Elasticity,* 3rd ed., McGraw-Hill, New York.

Toh, K.-C., and Mukherjee, S., 1994, "Hypersingular and Finite Part Integrals in the Boundary Element Method," *International Journal of Solids and Structures,* Vol. 31, pp. 2299–2312.

APPENDIX A

An Explicit Form of Eq. (26)

Using the equations

$$u_i(Q) = \sum_{\alpha=1}^{27} \hat{\beta}_\alpha^m \bar{u}_{\alpha i}(x_1, x_2, x_3)$$

$$u_i(P) = \sum_{\alpha=1}^{3} \hat{\beta}_\alpha^P \bar{u}_{\alpha i}(x_1, x_2, x_3)$$

$$u_{i,l}(P)[x_l(Q) - x_l(P)] = \sum_{\alpha=4}^{12} \hat{\beta}_\alpha^P \bar{u}_{\alpha i}(x_1, x_2, x_3)$$

(the last equation above can be proved from Eq. (19)), the integral in Eq. (26) can be written as

$$I_1 = \oint_{L_m} U_{ik}(P, Q)[\sum_{\alpha=4}^{12} (\hat{\beta}_\alpha^m - \hat{\beta}_\alpha^P)\bar{\sigma}_{\alpha ij} + \sum_{\alpha=13}^{27} \hat{\beta}_\alpha^m \bar{\sigma}_{\alpha ij}]\epsilon_{jnt} dx_t$$

$$- \oint_{L_m} \Sigma_{ijk}(P, Q)[\sum_{\alpha=1}^{12} (\hat{\beta}_\alpha^m - \hat{\beta}_\alpha^P)\bar{u}_{\alpha i} + \sum_{\alpha=13}^{27} \hat{\beta}_\alpha^m \bar{u}_{\alpha i}]\epsilon_{jnt} dx_t$$

where the fact that $\bar{\sigma}_{\alpha ij} = 0$ for $\alpha = 1, 2, 3$ has been used.

APPENDIX B

Proof of Eq. (28)

$$u_i(Q) = \sum_{\alpha=1}^{27} \hat{\beta}_\alpha^m \bar{u}_{\alpha i}(x_1, x_2, x_3)$$

$$u_{i,n}(Q) = \sum_{\alpha=4}^{27} \hat{\beta}_\alpha^m \bar{u}_{\alpha i,n}(x_1, x_2, x_3)$$

since $\bar{u}_{\alpha i}$, $\alpha = 1, 2, 3$, are constant.

Now

$$u_{i,n}(Q)_{\text{constant}} \equiv \sum_{\alpha=4}^{12} \hat{\beta}_\alpha^m \bar{u}_{\alpha i,n} = [S_N \overset{m}{\beta}]_i$$

where the last equality is obtained by observing Eq. (27).

Let

$$u_{i,n}(Q)_{\text{linear}} \equiv \sum_{\alpha=13}^{27} \hat{\beta}_\alpha^m \bar{u}_{\alpha i,n}(x_1, x_2, x_3)$$

$$= \sum_{\alpha=13}^{27} \overset{m}{\beta}_\alpha \bar{u}_{\alpha i,n}(x_1, x_2, x_3).$$

Now, with $n = 1$,

$$\sum_{\alpha=13}^{27} \overset{m}{\beta}_\alpha \bar{\mathbf{u}}_{\alpha,1} = 2(\overset{m}{\beta}_{13} + \overset{m}{\beta}_{20})\bar{\mathbf{u}}_4 + 2\overset{m}{\beta}_{15}\bar{\mathbf{u}}_5 + 2\overset{m}{\beta}_{18}\bar{\mathbf{u}}_6 + , \ldots ,$$

$$+ (K_2\overset{m}{\beta}_{19} + K_1\overset{m}{\beta}_{20})\bar{\mathbf{u}}_{12} = \sum_{\alpha=4}^{12} [R_{,1}\overset{m}{\beta}]_{\alpha-3}\bar{\mathbf{u}}_\alpha(x_1, x_2, x_3).$$

Similar expressions can be obtained for $n = 2, 3$.

In the above, a vector displacement shape function is defined as

$$\bar{\mathbf{u}}_\alpha = [\bar{u}_{\alpha 1}, \bar{u}_{\alpha 2}, \bar{u}_{\alpha 3}]^T$$

(where T denotes the transpose of the vector), and the constants K_1 and K_2 are defined in Table 1.

APPENDIX C

Conversion of Eq. (29)

$$\overset{m}{I}_2 = -\sum_{\alpha=4}^{12} \left[\int_{S_m} [U_{ik}(P, Q)\bar{\sigma}_{\alpha ij} - \Sigma_{ijk}(P, Q)\bar{u}_{\alpha i}]n_j dS \right]$$

$$\times [R_N \overset{m}{\beta}]_{\alpha-3} + \sum_{\alpha=1}^{3} \left[\int_{S_m} \Sigma_{\alpha jk}(P, Q) n_j dS \right] [S_N \overset{m}{\beta}]_\alpha$$

$$- \sum_{\alpha=1}^{3} u_{\alpha,n}(P) \int_{S_m} \Sigma_{\alpha jk}(P, Q) n_j dS$$

Downloaded 04 May 2010 to 171.66.16.26. Redistribution subject to ASME license or copyright; see http://www.asme.org/terms/Terms_Use.cfm

Applying Kaplan (1984)'s formula (see Nagarajan et al. (1996) Mukherjee et al. (1997)) to the first term above (its integrand is $O(1/r)$), one gets the contour integral

$$\overset{m}{I}_{2_1} = -\sum_{\alpha=4}^{12}\left[\oint_{L_m}(\bar{\sigma}_{\alpha ij}U_{ik} - \bar{u}_{\alpha i}\Sigma_{ijk})\epsilon_{jst}x_s dx_t\right][R_{,N}\overset{m}{\beta}]_{\alpha-3}.$$

The remaining terms cancel on a singular element (see Eq. (27)), while, on a nonsingular element, one gets (see Eq. (15)):

$$\overset{m}{I}_{2_2} = -\sum_{\alpha=1}^{3}\left[\oint_{L_m} D_{\alpha jk}dx_j\right][S_{,N}(\overset{m}{\beta} - \overset{P}{\beta})]_\alpha.$$

APPENDIX D

Proof of Eqs. (36) – (42)

(See Toh and Mukherjee, 1994.)

With $\hat{S} \subset S_P$

$$A_{ikn}(S_P) - A_{ikn}(\hat{S}) = \int_{S_P\setminus\hat{S}}\Sigma_{ijk,n}n_j dS = \oint_{L_P\setminus\hat{L}}\Sigma_{ijk}\epsilon_{jnt}dx_t$$

so that

$$A_{ikn}(S_P) = \oint_{L_P}\Sigma_{ijk}\epsilon_{jnt}dx_t$$

which proves Eq. (36).

$$B_{iknl}(S_P) - B_{iknl}(\hat{S}) = \int_{S_P\setminus\hat{S}}\Sigma_{ijk,n}(x_l(Q) - x_l(P))n_j dS$$

$$= \int_{S_P\setminus\hat{S}}[\Sigma_{ijk}(x_l(Q) - x_l(P))]_{,n}n_j dS - \delta_{nl}\int_{S_P\setminus\hat{S}}\Sigma_{ijk}n_j dS$$

The second term in the above equation is

$$I_2 = \delta_{nl}\oint_{L_P\setminus\hat{L}}D_{ijk}dx_j$$

while the first can be written as

$$I_1 = \int_{S_P\setminus\hat{S}}\{[\Sigma_{ijk}(x_l(Q) - x_l(P))]_{,n}n_j - [\Sigma_{ijk}(x_l(Q) - x_l(P))]_{,j}n_n\}dS + \delta_{lj}\int_{S_P\setminus\hat{S}}\Sigma_{ijk}n_n dS.$$

Applying Stokes' theorem to the first integral, one has

$$I_1 = \oint_{L_P\setminus\hat{L}}\epsilon_{jnt}\Sigma_{ijk}(x_l(Q) - x_l(P))dx_t + \int_{S_P\setminus\hat{S}}\Sigma_{ilk}n_n dS.$$

This proves Eq. (37).

Also

$$C_{iknj}(S_P) - C_{iknj}(\hat{S}) = \int_{S_P\setminus\hat{S}}U_{ik,n}n_j dS$$

$$= [U_{ik,n}n_j - U_{ik,j}n_n]dS + \int_{S_P\setminus\hat{S}}U_{ik,j}n_n dS$$

$$= \oint_{L_P\setminus\hat{L}}\epsilon_{jnt}U_{ik}dx_t + \int_{S_P\setminus\hat{S}}U_{ik,j}n_n dS$$

which proves Eq. (38).

Proof of Eq. (39) is obvious when one refers to Eqs. (36), (8), (10), and (13).

Proof of Eq. (40) follows from Eqs. (37), (38), (11), and (13), together with the third equation in Appendix A.

Proof of Eq. (41) follows from Eqs. (37), (8), (10), and (13).

Finally, Eq. (42) follows from Hooke's law applied to both the physical and the Kelvin fields, i.e.:

$$\sigma_{ij} = E_{ijmn}u_{m,n}$$

$$\Sigma_{ijk} = E_{ijmn}U_{mk,n}$$

where, for isotropic elastic solids,

$$E_{ijmn} = \lambda\delta_{ij}\delta_{mn} + G(\delta_{im}\delta_{jn} + \delta_{in}\delta_{jm})$$

in terms of the Lamé constants λ and G.

APPENDIX E

Computation of the Solid Angle on a Singular Element

Let P be a regular off-contour boundary point on an element S_P (Fig. 2). Of interest is the evaluation of the solid angle Θ_P subtended by S_P at P. The general expression for the solid angle is

$$\Theta_P = \int_{S_P}\frac{\mathbf{r}(P, Q)\cdot\mathbf{n}(Q)}{r^3}dS(Q).$$

First consider an internal point p, which does not lie on S_P, but is close to P. For convenience, let it lie on the normal $\mathbf{n}$ to S_P at P.

Let

$$I = \int_{S_P}\frac{\mathbf{r}(p, Q)\cdot\mathbf{n}(Q)}{r^3}dS(Q)$$

$$= \int_{S_P\setminus S_0}\frac{\mathbf{r}(p, Q)\cdot\mathbf{n}(Q)}{r^3}dS(Q) + \int_{S_0}\frac{\mathbf{r}(p, Q)\cdot\mathbf{n}(Q)}{r^3}dS(Q)$$

$$= I_1 + I_2.$$

The second integral is regular and vanishes as $S_0 \to 0$.

The first integral can be converted, by using Stokes' theorem, into the form (Nagarajan et al., 1996)

$$I_1 = \oint_{L_P\setminus L_0}\mathbf{V}\cdot d\mathbf{r}.$$

It can be shown that as $L_0 \to 0$,

$$I_1 = \oint_{L_P}\mathbf{V}\cdot d\mathbf{r} + 2\pi$$

$$= I + 2\pi.$$

This integral is continuous as $p \to P$. By definition, $\lim_{p\to P} I = \Theta_P$ is the solid angle on a singular element. (Note that the solid angle subtended by a sphere at a point inside it is 4π while that subtended by the same sphere at a point on it is 2π.) The factor 2π above changes the value of γ from 1 to $\frac{1}{2}$ in Eq. (32).

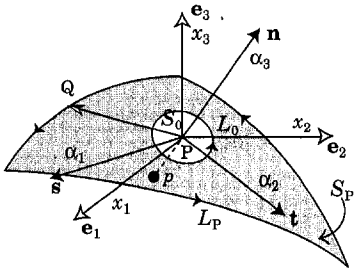


Fig. 2

Downloaded 04 May 2010 to 171.66.16.26. Redistribution subject to ASME license or copyright; see http://www.asme.org/terms/Terms_Use.cfm

It is convenient to evaluate Θ_P in local coordinates $(\alpha_1, \alpha_2, \alpha_3)$ along the base vectors $(\mathbf{s}, \mathbf{t}, \mathbf{n})$ at P. Here, $\mathbf{n}$ is the unit outward normal to S_P at P and $\mathbf{s}$ and $\mathbf{t}$ are unit tangent vectors to S_P at P. With s_k, t_k, and n_k, $k = 1, 2, 3$, the Cartesian components of the appropriate vectors, one has

$$\begin{bmatrix} \alpha_1 \\ \alpha_2 \\ \alpha_3 \end{bmatrix} = \begin{bmatrix} s_1 & s_2 & s_3 \\ t_1 & t_2 & t_3 \\ n_1 & n_2 & n_3 \end{bmatrix} \begin{bmatrix} x_1 \\ x_2 \\ x_3 \end{bmatrix}.$$

Finally, in local coordinates,

$$\Theta_P = \oint_{L_P} \frac{\alpha_3(\alpha_2 d\alpha_1 - \alpha_1 d\alpha_2)}{r(\alpha_1^2 + \alpha_2^2)}$$

which is valid as long as $\mathbf{n}$ does not intersect S_P again. This should not be a problem as long as the boundary element S_P is reasonably small in size.

The value of Θ_P, computed from the equation above, must be used in the expression for D_{ijk} (see Eq. (15)) in the fourth term in Eq. (32) ($p \to P$) at a regular off-contour boundary point.

Downloaded 04 May 2010 to 171.66.16.26. Redistribution subject to ASME license or copyright; see http://www.asme.org/terms/Terms_Use.cfm

Singular Integral Equation Method for Interaction Between Elliptical Inclusions

Nao-Aki Noda
Department of Mechanical Engineering,
Kyushu Institute of Technology,
Kitakyushu 804-8550, Japan

Tadatoshi Matsuo
Department of Mechanical Engineering,
Fukushima National College of Technology,
Iwaki 970-8034, Japan

This paper deals with numerical solutions of singular integral equations in interaction problems of elliptical inclusions under general loading conditions. The stress and displacement fields due to a point force in infinite plates are used as fundamental solutions. Then, the problems are formulated as a system of singular integral equations with Cauchy-type or logarithmic-type singularities, where the unknowns are the body force densities distributed in infinite plates having the same elastic constants as those of the matrix and inclusions. To determine the unknown body force densities to satisfy the boundary conditions, four auxiliary unknown functions are derived from each body force density. It is found that determining these four auxiliary functions in the range $0 \leqq \phi_k \leqq \pi/2$ is equivalent to determining an original unknown density in the range $0 \leqq \phi_k \leqq 2\pi$. Then, these auxiliary unknowns are approximated by using fundamental densities and polynomials. Initially, the convergence of the results such as unknown densities and interface stresses are confirmed with increasing collocation points. Also, the accuracy is verified by examining the boundary conditions and relations between interface stresses and displacements. Randomly or regularly distributed elliptical inclusions can be treated by combining both solutions for remote tension and shear shown in this study.

1 Introduction

Elliptical inclusions can be regarded as a general model of defects because they cover a wide variety of particular cases, such as line and circular defects. The stress concentration due to two or more defects differs from that due to an isolated defect. Interaction among cracks can be treated using singular integral equations using the related Green's function for an edge dislocation (Erdogan et al., 1972). In this paper, the general solution for elliptical inclusions will be discussed. To formulate the problem, the body-force method is applied.

In the conventional body-force method, the unknown functions of the body-force densities have been approximated by the products of the fundamental density functions and weight functions. Here,

(a) the fundamental density function is an exact density of body force to express a two-dimensional single elliptical hole, and
(b) the weight function is chosen to be a "step function," which takes a constant value along each segment into which a whole boundary is discretized (Nisitani, 1963, 1967).

In previous papers, numerical solutions of the singular integral equation of the body-force method for elliptical holes was discussed (Noda-Matsuo, 1995a, b, 1997). Then it was found that in the conventional method, unknown body-force densities distributed in two directions in plates do not converge with increasing collocation points. The reason was indicated that conventional two-type body-force densities cannot represent the actual density distributions enough especially near the apex of elliptical boundaries. To overcome this difficulty, eight fundamental densities were newly introduced, and the body-force densities were approximated by a linear combination of fundamental densities and polynomials.

The objects of this paper are follows:

1 to show the solution of elliptical inclusions that can be regarded as a general model of defects. The method is essentially based on the solution proposed for solving elliptical holes. However, the applicability of several fundamental densities proposed previously to inclusion problems is not obvious and therefore it should be confirmed in this study.

2 to explain the meaning of the new fundamental densities proposed by the authors more clearly. It has been told that the discussion of the theory shown in previous papers is of little pedagogical value because it cryptically presents the governing equations with no derivation. In this paper, therefore, auxiliary functions will be derived from original unknown densities of the singular integral equations. Then it will be shown that new fundamental densities are useful for approximating these auxiliary functions. Finally, original unknown densities will be expressed from obtained auxiliary functions.

2 Singular Integral Equations of the Body Force Method for Inclusion Problems

Consider an infinite plate with two elliptical inclusions ($x = \pm d + a \cos\theta$, $y = b \sin\theta$) under remote tension or shear as shown in Figs. 1 or 2 to explain the numerical solution. This method may be applied to regular or random distribution of inclusions. The problem can be formulated in terms of singular integral equations by using the stress and displacement fields due to a point force in two infinite plates "M" and "I". Here, the infinite plate "M" has the same elastic constants as those of the matrix (E_M, ν_M) and the infinite plate "I" has the same ones as those of the inclusions (E_I, ν_I). The integral equations are expressed in Eqs. (1) and (2), where the body-force densities distributed in the infinite plates M and I in the x, y-directions are unknown functions (see Fig. 3).

Contributed by the Applied Mechanics Division of THE AMERICAN SOCIETY OF MECHANICAL ENGINEERS for publication in the ASME JOURNAL OF APPLIED MECHANICS.

Discussion on the paper should be addressed to the Technical Editor, Professor Lewis T. Wheeler, Department of Mechanical Engineering, University of Houston, Houston, TX 77204-4792, and will be accepted until four months after final publication of the paper itself in the ASME JOURNAL OF APPLIED MECHANICS.

Manuscript received by the ASME Applied Mechanics Division, Feb. 13, 1995; final revision, Mar. 2, 1998. Associate Technical Editor: X. Markenscoff.

 Copyright © 1998 by ASME

Downloaded 04 May 2010 to 171.66.16.26. Redistribution subject to ASME license or copyright; see http://www.asme.org/terms/Terms_Use.cfm

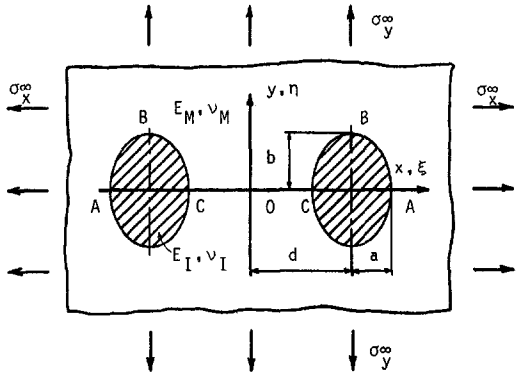


Fig. 1 Two elliptical inclusions in an infinite plate under remote tension

$$
\begin{aligned}
&-(1/2)\{\rho_{xM}^*(\theta_i)\cos\theta_{i0}+\rho_{yM}^*(\theta_i)\sin\theta_{i0}\}\\
&-(1/2)\{\rho_{xI}^*(\theta_i)\cos\theta_{i0}+\rho_{yI}^*(\theta_i)\sin\theta_{i0}\}\\
&+\sum_{k=1}^{2}\int_0^{2\pi}K_{nnM}^{Fx}(\phi_k,\theta_i)\rho_{xM}^*(\phi_k)ds\\
&+\sum_{k=1}^{2}\int_0^{2\pi}K_{nnM}^{Fy}(\phi_k,\theta_i)\rho_{yM}^*(\phi_k)ds\\
&-\sum_{k=1}^{2}\int_0^{2\pi}K_{nnI}^{Fx}(\phi_k,\theta_i)\rho_{xI}^*(\phi_k)ds\\
&\qquad-\sum_{k=1}^{2}\int_0^{2\pi}K_{nnI}^{Fy}(\phi_k,\theta_i)\rho_{yI}^*(\phi_k)ds=-\sigma_n^\infty\\
&-(1/2)\{-\rho_{xM}^*(\theta_i)\sin\theta_{i0}+\rho_{yM}^*(\theta_i)\cos\theta_{i0}\}\\
&-(1/2)\{-\rho_{xI}^*(\theta_i)\sin\theta_{i0}+\rho_{yI}^*(\theta_i)\cos\theta_{i0}\}\\
&+\sum_{k=1}^{2}\int_0^{2\pi}K_{ntM}^{Fx}(\phi_k,\theta_i)\rho_{xM}^*(\phi_k)ds\\
&+\sum_{k=1}^{2}\int_0^{2\pi}K_{ntM}^{Fy}(\phi_k,\theta_i)\rho_{yM}^*(\phi_k)ds\\
&-\sum_{k=1}^{2}\int_0^{2\pi}K_{ntI}^{Fx}(\phi_k,\theta_i)\rho_{xI}^*(\phi_k)ds\\
&\qquad-\sum_{k=1}^{2}\int_0^{2\pi}K_{ntI}^{Fy}(\phi_k,\theta_i)\rho_{yI}^*(\phi_k)ds=-\tau_{nt}^\infty\quad i=1,2\quad(1)\\
&\sum_{k=1}^{2}\int_0^{2\pi}K_{uM}^{Fx}(\phi_k,\theta_i)\rho_{xM}^*(\phi_k)ds\\
&+\sum_{k=1}^{2}\int_0^{2\pi}K_{uM}^{Fy}(\phi_k,\theta_i)\rho_{yM}^*(\phi_k)ds\\
&-\sum_{k=1}^{2}\int_0^{2\pi}K_{uI}^{Fx}(\phi_k,\theta_i)\rho_{xI}^*(\phi_k)ds\\
&\qquad-\sum_{k=1}^{2}\int_0^{2\pi}K_{uI}^{Fy}(\phi_k,\theta_i)\rho_{yI}^*(\phi_k)ds=-U^\infty\\
&\sum_{k=1}^{2}\int_0^{2\pi}K_{vM}^{Fx}(\phi_k,\theta_i)\rho_{xM}^*(\phi_k)ds\\
&+\sum_{k=1}^{2}\int_0^{2\pi}K_{vM}^{Fy}(\phi_k,\theta_i)\rho_{yM}^*(\phi_k)ds\\
&-\sum_{k=1}^{2}\int_0^{2\pi}K_{vI}^{Fx}(\phi_k,\theta_i)\rho_{xI}^*(\phi_k)ds\\
&-\sum_{k=1}^{2}\int_0^{2\pi}K_{vI}^{Fy}(\phi_k,\theta_i)\rho_{yI}^*(\phi_k)ds=-V^\infty\quad i=1,2\quad(2)
\end{aligned}
$$

where

$$
\begin{aligned}
\sigma_n^\infty&=\sigma_x^\infty\cos^2\theta_{i0}+\sigma_y^\infty\sin^2\theta_{i0},\\
\tau_{nt}^\infty&=(\sigma_y^\infty-\sigma_x^\infty)\sin\theta_{i0}\cos\theta_{i0},\\
U^\infty&=(\sigma_x^\infty-\nu_M\sigma_y^\infty)x/E_M,\\
V^\infty&=(\sigma_y^\infty-\nu_M\sigma_x^\infty)y/E_M\quad\text{(for Fig. 1)};\\
\sigma_n^\infty&=2\tau_{xy}^\infty\sin\theta_{i0}\cos\theta_{i0},\quad\tau_{nt}^\infty=\tau_{xy}^\infty(\cos^2\theta_{i0}-\sin^2\theta_{i0}),\\
U^\infty&=2(1+\nu_M)\tau_{xy}^\infty y/E_M,\\
V^\infty&=2(1+\nu_M)\tau_{xy}^\infty x/E_M\quad\text{(for Fig. 2)};\\
-d\xi&=a\sin\phi_k d\phi,\quad d\eta=b\cos\phi_k d\phi,\\
ds&=\sqrt{a^2\sin^2\phi_k+b^2\cos^2\phi_k}\,d\phi,\\
\tan\theta_{i0}&=(a/b)\tan\theta_i\qquad(3)
\end{aligned}
$$

Here, θ_{i0} is the angle between x-axis and the normal direction at the point (x, y) on the elliptical hole.

The body-force densities $\rho_{xM}^*(\phi_k)$, $\rho_{yM}^*(\phi_k)$, $\rho_{xI}^*(\phi_k)$, $\rho_{yI}^*(\phi_k)$ are defined as follows:

$$
\rho_{xM}^*(\phi_k)=\frac{dF_\xi}{ds},\quad\rho_{yM}^*(\phi_k)=\frac{dF_\eta}{ds},
$$

$$
\rho_{xI}^*(\phi_k)=\frac{dF_\xi}{ds},\quad\rho_{yI}^*(\phi_k)=\frac{dF_\eta}{ds},\qquad(4)
$$

where dF_ξ, dF_η are the components of the resultant of the body force in the x and y-directions acting on the infinitesimal arc length ds, respectively.

Suppose that σ_{nM}, τ_{ntM}, U_M, V_M denote the stress and displacement along the imaginary boundary of elliptical hole in the infinite plate "M." In addition, σ_{nI}, τ_{ntI}, U_I, V_I denote the stress and displacement along the imaginary boundary of elliptical inclusions in the infinite plate "I." Equations (1), (2) enforce the boundary conditions at the connecting boundary of matrix and inclusion; that is, $\sigma_{nM}-\sigma_{nI}=0$, $\tau_{ntM}-\tau_{ntI}=0$, $U_M-U_I=0$, $V_M-V_I=0$. The first and second terms of Eqs. (1) represent the stress due to the body force distributed on "minus boundary". Here "minus boundaries" means the imaginary boundary composed of the internal points that are infinitesimally apart from the initial boundary (Nisitani, 1967). Taking

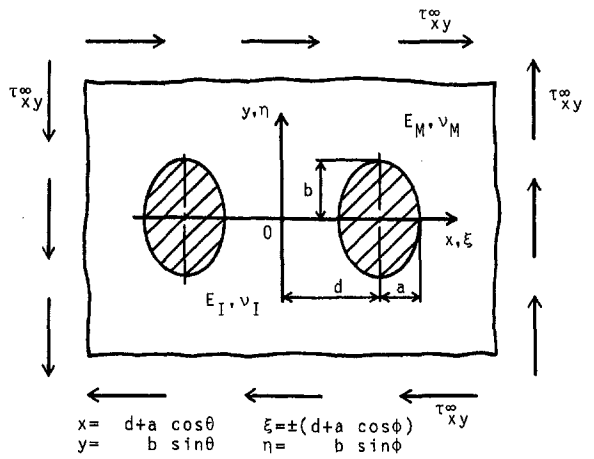


Fig. 2 Two elliptical inclusions in an infinite plate under remote shear

Downloaded 04 May 2010 to 171.66.16.26. Redistribution subject to ASME license or copyright; see http://www.asme.org/terms/Terms_Use.cfm

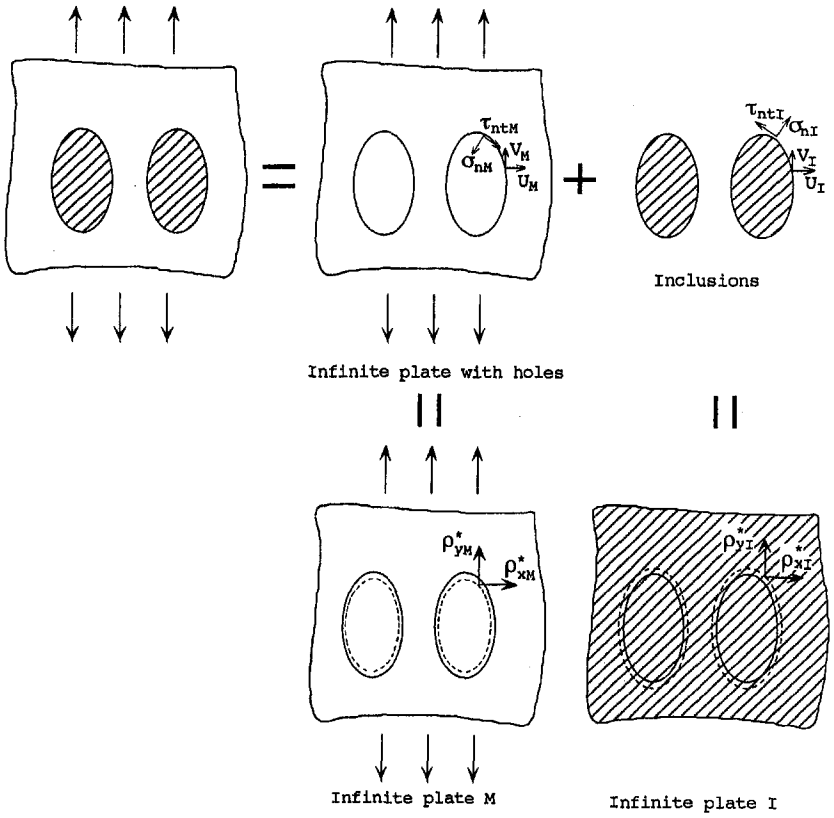


Fig. 3 Formulation of the singular integral equation based on the body-force method

$K^{Fx}_{nnM}(\phi_k, \theta_i)$ for example, the notation means the normal stress σ_n induced at the point when the body force with unit density in the x-direction is acting at the infinitesimal arc length on the kth elliptical hole in the infinite plate "M." In the calculation of displacement $K^{Fx}_{uM}(\phi_k, \theta_i)$, etc., the relative displacement with respect to a certain point outside inclusion is considered (Nisitani-Chen, 1987). Equations (1) and (2) include the Cauchy-type and logarithmic-type singularities, respectively, when $i = k$. Therefore, when $\theta = \phi$ and $k = i$, the integration in Eq. (1) should be interpreted as the meaning of Cauchy's principle values.

3 How to Determine Unknown Body Force Densities

3.1 Definition of Auxiliary Functions. To solve Eqs. (1), (2) is to determine the body-force densities $\rho^*_{xM}(\phi_k)$, $\rho^*_{yM}(\phi_k)$, $\rho^*_{xI}(\phi_k)$, $\rho^*_{yI}(\phi_k)$ in the range $0 \leqq \phi_k \leqq 2\pi$. Here, by taking examples $\rho^*_{xM}(\phi_k)$, $\rho^*_{yM}(\phi_k)$ how to determine unknown functions will be explained. Consider auxiliary functions $\rho^*_{xM1}(\phi_k) \sim \rho^*_{xM4}(\phi_k)$, and $\rho^*_{yM1}(\phi_k) \sim \rho^*_{yM4}(\phi_k)$ defined by Eqs. (5), (6) instead of $\rho^*_{xM}(\phi_k)$, $\rho^*_{yM}(\phi_k)$.

$$\rho^*_{xM1}(\phi_k) = \{\rho^*_{xM}(\phi_k) + \rho^*_{xM}(\pi - \phi_k) + \rho^*_{xM}(\pi + \phi_k) + \rho^*_{xM}(-\phi_k)\}/4 \quad (5a)$$

$$\rho^*_{xM2}(\phi_k) = \{\rho^*_{xM}(\phi_k) + \rho^*_{xM}(\pi - \phi_k) - \rho^*_{xM}(\pi + \phi_k) - \rho^*_{xM}(-\phi_k)\}/4 \quad (5b)$$

$$\rho^*_{xM3}(\phi_k) = \{\rho^*_{xM}(\phi_k) - \rho^*_{xM}(\pi - \phi_k) - \rho^*_{xM}(\pi + \phi_k) + \rho^*_{xM}(-\phi_k)\}/4 \quad (5c)$$

$$\rho^*_{xM4}(\phi_k) = \{\rho^*_{xM}(\phi_k) - \rho^*_{xM}(\pi - \phi_k) + \rho^*_{xM}(\pi + \phi_k) - \rho^*_{xM}(-\phi_k)\}/4 \quad (5d)$$

$$\rho^*_{yM1}(\phi_k) = \{\rho^*_{yM}(\phi_k) + \rho^*_{yM}(\pi - \phi_k) + \rho^*_{yM}(\pi + \phi_k) + \rho^*_{yM}(-\phi_k)\}/4 \quad (6a)$$

$$\rho^*_{yM2}(\phi_k) = \{\rho^*_{yM}(\phi_k) + \rho^*_{yM}(\pi - \phi_k) - \rho^*_{yM}(\pi + \phi_k) - \rho^*_{yM}(-\phi_k)\}/4 \quad (6b)$$

$$\rho^*_{yM3}(\phi_k) = \{\rho^*_{yM}(\phi_k) - \rho^*_{yM}(\pi - \phi_k) - \rho^*_{yM}(\pi + \phi_k) + \rho^*_{yM}(-\phi_k)\}/4 \quad (6c)$$

$$\rho^*_{yM4}(\phi_k) = \{\rho^*_{yM}(\phi_k) - \rho^*_{yM}(\pi - \phi_k) + \rho^*_{yM}(\pi + \phi_k) - \rho^*_{yM}(-\phi_k)\}/4 \quad (6d)$$

These new functions $\rho^*_{xM1}(\phi_k) \sim \rho^*_{xM4}(\phi_k)$ and $\rho^*_{yM1}(\phi_k) \sim \rho^*_{yM4}(\phi_k)$ must satisfy Eqs. (7), (8) because of the definition (5), (6).

$$\rho^*_{xM1}(\phi_k) = \rho^*_{xM1}(\pi - \phi_k) = \rho^*_{xM1}(\pi + \phi_k) = \rho^*_{xM1}(-\phi_k) \quad (7a)$$

$$\rho^*_{xM2}(\phi_k) = \rho^*_{xM2}(\pi - \phi_k) = -\rho^*_{xM2}(\pi + \phi_k) = -\rho^*_{xM2}(-\phi_k) \quad (7b)$$

$$\rho^*_{xM3}(\phi_k) = -\rho^*_{xM3}(\pi - \phi_k) = -\rho^*_{xM3}(\pi + \phi_k) = \rho^*_{xM3}(-\phi_k) \quad (7c)$$

$$\rho^*_{xM4}(\phi_k) = -\rho^*_{xM4}(\pi - \phi_k) = \rho^*_{xM4}(\pi + \phi_k) = -\rho^*_{xM4}(-\phi_k) \quad (7d)$$

$$\rho^*_{yM1}(\phi_k) = \rho^*_{yM1}(\pi - \phi_k) = \rho^*_{yM1}(\pi + \phi_k) = \rho^*_{yM1}(-\phi_k) \quad (8a)$$

$$\rho^*_{yM2}(\phi_k) = \rho^*_{yM2}(\pi - \phi_k) = -\rho^*_{yM2}(\pi + \phi_k) = -\rho^*_{yM2}(-\phi_k) \quad (8b)$$

$$\rho^*_{yM3}(\phi_k) = -\rho^*_{yM3}(\pi - \phi_k) = -\rho^*_{yM3}(\pi + \phi_k) = \rho^*_{yM3}(-\phi_k) \quad (8c)$$

$$\rho^*_{yM4}(\phi_k) = -\rho^*_{yM4}(\pi - \phi_k) = \rho^*_{yM4}(\pi + \phi_k) = -\rho^*_{yM4}(-\phi_k) \quad (8d)$$

It should be noted that determining four auxiliary functions $\rho^*_{xM1}(\phi_k) \sim \rho^*_{xM4}(\phi_k)$ and $\rho^*_{yM1}(\phi_k) \sim \rho^*_{yM4}(\phi_k)$ in the range $0 \leqq$

Downloaded 04 May 2010 to 171.66.16.26. Redistribution subject to ASME license or copyright; see http://www.asme.org/terms/Terms_Use.cfm

$\phi_k \leqq \pi/2$ is equivalent to determining original unknown densities $\rho^*_{xM}(\phi_k)$ and $\rho^*_{yM}(\phi_k)$ in the range $0 \leqq \phi_k \leqq 2\pi$. In other words, if the auxiliary functions $\rho^*_{xM1}(\phi_k) \sim \rho^*_{xM4}(\phi_k)$ and $\rho^*_{yM1}(\phi_k) \sim \rho^*_{yM4}(\phi_k)$ are given in the range $0 \leqq \phi_k \leqq \pi/2$, original unknown functions $\rho^*_{xM}(\phi_k)$ and $\rho^*_{yM}(\phi_k)$ are expressed in the range $0 \leqq \phi_k \leqq 2\pi$ using Eqs. (9), (10).

$$\rho^*_{xM}(\phi_k) = \rho^*_{xM1}(\phi_k) + \rho^*_{xM2}(\phi_k) + \rho^*_{xM3}(\phi_k) + \rho^*_{xM4}(\phi_k) \quad (9a)$$

$$\rho^*_{xM}(\pi - \phi_k) = \rho^*_{xM1}(\phi_k) + \rho^*_{xM2}(\phi_k) - \rho^*_{xM3}(\phi_k) - \rho^*_{xM4}(\phi_k) \quad (9b)$$

$$\rho^*_{xM}(\pi + \phi_k) = \rho^*_{xM1}(\phi_k) - \rho^*_{xM2}(\phi_k) - \rho^*_{xM3}(\phi_k) + \rho^*_{xM4}(\phi_k) \quad (9c)$$

$$\rho^*_{xM}(-\phi_k) = \rho^*_{xM1}(\phi_k) - \rho^*_{xM2}(\phi_k) + \rho^*_{xM3}(\phi_k) - \rho^*_{xM4}(\phi_k) \quad (9d)$$

$$\rho^*_{yM}(\phi_k) = \rho^*_{yM1}(\phi_k) + \rho^*_{yM2}(\phi_k) + \rho^*_{yM3}(\phi_k) + \rho^*_{yM4}(\phi_k) \quad (10a)$$

$$\rho^*_{yM}(\pi - \phi_k) = \rho^*_{yM1}(\phi_k) + \rho^*_{yM2}(\phi_k) - \rho^*_{yM3}(\phi_k) - \rho^*_{yM4}(\phi_k) \quad (10b)$$

$$\rho^*_{yM}(\pi + \phi_k) = \rho^*_{yM1}(\phi_k) - \rho^*_{yM2}(\phi_k) - \rho^*_{yM3}(\phi_k) + \rho^*_{yM4}(\phi_k) \quad (10c)$$

$$\rho^*_{yM}(-\phi_k) = \rho^*_{yM1}(\phi_k) - \rho^*_{yM2}(\phi_k) + \rho^*_{yM3}(\phi_k) - \rho^*_{yM4}(\phi_k) \quad (10d)$$

3.2 Fundamental Density Functions as Examples of Auxiliary Functions. The fundamental density functions for the body forces in the x and y-directions $w_x(\phi_k)$, $w_y(\phi_k)$ are defined by the following expressions (Noda-Matsuo, 1995a, 1995b):

$$w_{x1}(\phi_k) = n_x(\phi_k)/\cos\phi_k \quad (11a)$$

$$w_{x2}(\phi_k) = n_x(\phi_k)\tan\phi_k \quad (11b)$$

$$w_{x3}(\phi_k) = n_x(\phi_k) \quad (11c)$$

$$w_{x4}(\phi_k) = n_x(\phi_k)\sin\phi_k \quad (11d)$$

$$w_{y1}(\phi_k) = n_y(\phi_k)/\sin\phi_k \quad (12a)$$

$$w_{y2}(\phi_k) = n_y(\phi_k) \quad (12b)$$

$$w_{y3}(\phi_k) = n_y(\phi_k)\cot\phi_k \quad (12c)$$

$$w_{y4}(\phi_k) = n_y(\phi_k)\cos\phi_k \quad (12d)$$

where

$$n_x(\phi_k) = \frac{b\cos\phi_k}{\sqrt{a^2\sin^2\phi_k + b^2\cos^2\phi_k}} = \cos\theta_{k0}$$

$$n_y(\phi_k) = \frac{a\sin\phi_k}{\sqrt{a^2\sin^2\phi_k + b^2\cos^2\phi_k}} = \sin\theta_{k0}. \quad (13)$$

The fundamental densities $w_{x1}(\phi_k) \sim w_{x4}(\phi_k)$ and $w_{y1}(\phi_k) \sim w_{y4}(\phi_k)$ are good examples of continuous auxiliary functions because each satisfies one of Eqs. (7a), . . . , (8d). Here it should be noted that $w_{x3}(\phi_k)$, $w_{y2}(\phi_k)$ are exact densities of body force to express a single elliptical inclusion under remote tension. Also, $w_{x2}(\phi_k)$, $w_{y3}(\phi_k)$ are exact densities of body force to express a single elliptical inclusion under remote shear. Using Eqs. (11), (12), original body-force densities are expressed as shown in Eqs. (14), (15).

$$\rho^*_{xMj}(\phi_k) = \rho_{xjM}(\phi_k)w_{xj}(\phi_k) \quad j = 1, 2, 3, 4 \quad (14)$$

$$\rho^*_{yMj}(\phi_k) = \rho_{yjM}(\phi_k)w_{yj}(\phi_k) \quad j = 1, 2, 3, 4 \quad (15)$$

where $\rho_{x1}(\phi_k) \sim \rho_{x4}(\phi_k)$ and $\rho_{y1}(\phi_k) \sim \rho_{y4}(\phi_k)$ are unknown functions, which have been called weight functions. Then all $\rho_{x1}(\phi_k) \sim \rho_{x4}(\phi_k)$ and $\rho_{y1}(\phi_k) \sim \rho_{y4}(\phi_k)$ must satisfy Eq. (16).

$$f(\phi_k) = f(\pi - \phi_k) = f(\pi + \phi_k) = f(-\phi_k)$$

$$f(\phi_k) : \rho_{x1}(\phi_k) \sim \rho_{y4}(\phi_k). \quad (16)$$

Finally, original unknown densities $\rho^*_{xM}(\phi_k)$, $\rho^*_{yM}(\phi_k)$, $\rho^*_{xI}(\phi_k)$, $\rho^*_{yI}(\phi_k)$ can be expressed in Eq. (17) as a linear combination of the fundamental densities and the weight functions. The discussion for $\rho^*_{xI}(\phi_k)$, $\rho^*_{yI}(\phi_k)$ can be made in a similar way of $\rho^*_{xM}(\phi_k)$, $\rho^*_{yM}(\phi_k)$.

$$\rho^*_{xM}(\phi_k) = \sum_{j=1}^{4} \rho_{xjM}(\phi_k)w_{xj}(\phi_k)$$

$$\rho^*_{yM}(\phi_k) = \sum_{j=1}^{4} \rho_{yjM}(\phi_k)w_{yj}(\phi_k)$$

$$\rho^*_{xI}(\phi_k) = \sum_{j=1}^{4} \rho_{xjI}(\phi_k)w_{xj}(\phi_k)$$

$$\rho^*_{yI}(\phi_k) = \sum_{j=1}^{4} \rho_{yjI}(\phi_k)w_{yj}(\phi_k) \quad (17)$$

4 Numerical Solutions for Singular Integral Equations

4.1 Two Elliptical Inclusions Under Remote Tension as Shown in Fig. 1. In this case, by considering the x-axis symmetry of the problem, $w_{x1}(\phi_k)$, $w_{x3}(\phi_k)$ and $w_{y2}(\phi_k)$, $w_{y4}(\phi_k)$ are suitable. Unknown function $\rho^*_{xM}(\phi_k) \sim \rho^*_{yI}(\phi_k)$ can be expressed by the following equations.

$$\rho^*_{xM}(\phi_k) = \rho_{x1M}(\phi_k)w_{x1}(\phi_k) + \rho_{x3M}(\phi_k)w_{x3}(\phi_k)$$

$$\rho^*_{yM}(\phi_k) = \rho_{y2M}(\phi_k)w_{y2}(\phi_k) + \rho_{y4M}(\phi_k)w_{y4}(\phi_k)$$

$$\rho^*_{xI}(\phi_k) = \rho_{x1I}(\phi_k)w_{x1}(\phi_k) + \rho_{x3I}(\phi_k)w_{x3}(\phi_k)$$

$$\rho^*_{yI}(\phi_k) = \rho_{y2I}(\phi_k)w_{y2}(\phi_k) + \rho_{y4I}(\phi_k)w_{y4}(\phi_k). \quad (18)$$

Here all unknown weight functions can be approximated as shown in Eqs. (19) $\sim$ (21) because all of these must satisfy Eq. (16).

$$\rho_{x1M}(\phi_k) = \sum_{n=1}^{M/2} a_{nM}t_n(\phi_k) \quad \rho_{y2M}(\phi_k) = \sum_{n=1}^{M/2} c_{nM}t_n(\phi_k)$$

$$\rho_{x3M}(\phi_k) = \sum_{n=1}^{M/2} b_{nM}t_n(\phi_k) \quad \rho_{y4M}(\phi_k) = \sum_{n=1}^{M/2} d_{nM}t_n(\phi_k) \quad (19)$$

$$\rho_{x1I}(\phi_k) = \sum_{n=1}^{M/2} a_{nI}t_n(\phi_k) \quad \rho_{y2I}(\phi_k) = \sum_{n=1}^{M/2} c_{nI}t_n(\phi_k)$$

$$\rho_{x3I}(\phi_k) = \sum_{n=1}^{M/2} b_{nI}t_n(\phi_k) \quad \rho_{y4I}(\phi_k) = \sum_{n=1}^{M/2} d_{nI}t_n(\phi_k) \quad (20)$$

$$t_n(\phi_k) = \cos\{2(n-1)\phi_k\} \quad (21)$$

Downloaded 04 May 2010 to 171.66.16.26. Redistribution subject to ASME license or copyright; see http://www.asme.org/terms/Terms_Use.cfm

where M is the number of the collocation points in $0 \leqq \phi \leqq 2\pi$.

Using the approximation method mentioned above, we obtain the following system of linear equations for determining the coefficients a_{nM}, b_{nM}, c_{nM}, d_{nM}, a_{nI}, b_{nI}, c_{nI}, d_{nI}.

$$\sum_{n=1}^{M/2} (a_{nM}A_{nM} + b_{nM}B_{nM} + c_{nM}C_{nM} + d_{nM}D_{nM} + a_{nI}A_{nI} + b_{nI}B_{nI} + c_{nI}C_{nI} + d_{nI}D_{nI}) = -(\sigma_x^\infty \cos^2 \theta_{i0} + \sigma_y^\infty \sin^2 \theta_{i0})$$

$$\sum_{n=1}^{M/2} (a_{nM}E_{nM} + b_{nM}F_{nM} + c_{nM}G_{nM} + d_{nM}H_{nM} + a_{nI}E_{nI} + b_{nI}F_{nI} + c_{nI}G_{nI} + d_{nI}H_{nI}) = -(\sigma_y^\infty - \sigma_x^\infty) \sin \theta_{i0} \cos \theta_{i0} \quad (22)$$

$$\sum_{n=1}^{M/2} (a_{nM}I_{nM} + b_{nM}J_{nM} + c_{nM}K_{nM} + d_{nM}L_{nM} + a_{nI}I_{nI} + b_{nI}J_{nI} + c_{nI}K_{nI} + d_{nI}L_{nI}) = -(\sigma_x^\infty - \nu_M\sigma_y^\infty)x/E_M$$

Table 1 Convergence of the unknown functions (a/b = 1, a/d = 0.648, σ_x^∞ = 1, σ_y^∞ = 0, E_I/E_M = 0.5, $\nu_I = \nu_M$ = 0.3, under plane stress in Fig. 1)

θ (deg.)	M	ρx3M	ρy2M	ρx1M	ρy4M
0	8	0.6938	0.0276	0.0282	-0.0420
	12	0.6938	0.0288	0.0283	-0.0440
	16	0.6938	0.0288	0.0283	-0.0440
20	8	0.7027	0.0205	0.0172	-0.0378
	12	0.7027	0.0208	0.0171	-0.0382
	16	0.7027	0.0208	0.0171	-0.0382
40	8	0.7186	0.0063	-0.0018	-0.0272
	12	0.7186	0.0061	-0.0016	-0.0269
	16	0.7186	0.0061	-0.0016	-0.0269
60	8	0.7291	-0.0042	-0.0127	-0.0182
	12	0.7292	-0.0040	-0.0128	-0.0186
	16	0.7292	-0.0040	-0.0128	-0.0186
80	8	0.7340	-0.0083	-0.0169	-0.0158
	12	0.7337	-0.0083	-0.0168	-0.0148
	16	0.7337	-0.0083	-0.0168	-0.0148
90	8	0.7348	-0.0087	-0.0174	-0.0157
	12	0.7342	-0.0088	-0.0172	-0.0144
	16	0.7342	-0.0088	-0.0172	-0.0144

θ (deg.)	M	ρx3I	ρy2I	ρx1I	ρy4I
0	8	1.4370	-0.0852	-0.3303	0.0898
	12	1.4377	-0.0853	-0.3313	0.0892
	16	1.4377	-0.0853	-0.3313	0.0892
20	8	1.3905	-0.0657	-0.2695	0.0738
	12	1.3899	-0.0653	-0.2686	0.0735
	16	1.3899	-0.0653	-0.2686	0.0735
40	8	1.3057	-0.0323	-0.1615	0.0464
	12	1.3061	-0.0326	-0.1622	0.0467
	16	1.3061	-0.0326	-0.1622	0.0467
60	8	1.2494	-0.0131	-0.0939	0.0295
	12	1.2491	-0.0129	-0.0935	0.0292
	16	1.2491	-0.0129	-0.0936	0.0292
80	8	1.2242	-0.0053	-0.0652	0.0214
	12	1.2244	-0.0053	-0.0653	0.0220
	16	1.2244	-0.0053	-0.0653	0.0220
90	8	1.2210	-0.0043	-0.0615	-0.0202
	12	1.2215	-0.0045	-0.0621	-0.0212
	16	1.2215	-0.0045	-0.0621	-0.0212

Table 2 Convergence of the stresses (a/b = 1, a/d = 0.9, τ_{xy}^∞ = 1, E_I = 0 in Fig. 2)

θ (deg.)	M	σt	σn	τnt
40	16	-4.5587	-2.2×10^{-5}	-3.3×10^{-4}
	24	-4.5626	1.5×10^{-6}	1.9×10^{-6}
	32	-4.5627	6.9×10^{-6}	-9.1×10^{-6}
	40	-4.5627	2.2×10^{-7}	-5.7×10^{-6}
	48	-4.5627	4.9×10^{-7}	-1.7×10^{-7}
80	16	-2.7643	1.0×10^{-3}	2.7×10^{-3}
	24	-2.7675	3.9×10^{-5}	2.0×10^{-5}
	32	-2.7676	-1.0×10^{-6}	1.2×10^{-5}
	40	-2.7676	-2.9×10^{-6}	5.6×10^{-6}
	48	-2.7676	7.6×10^{-7}	-1.8×10^{-6}
90	16	-1.6283	-1.5×10^{-3}	-3.1×10^{-3}
	24	-1.6272	-9.6×10^{-5}	-3.2×10^{-5}
	32	-1.6272	-1.4×10^{-5}	1.9×10^{-5}
	40	-1.6272	-3.9×10^{-6}	8.9×10^{-6}
	48	-1.6272	-1.5×10^{-6}	4.2×10^{-6}
120	16	1.5923	-1.8×10^{-3}	1.7×10^{-3}
	24	1.5958	-1.7×10^{-4}	4.4×10^{-5}
	32	1.5959	8.6×10^{-6}	-2.3×10^{-5}
	40	1.5959	1.9×10^{-6}	-9.2×10^{-6}
	48	1.5959	-1.4×10^{-6}	8.3×10^{-6}
159.6	16	4.8794	-6.1×10^{-3}	3.7×10^{-4}
	24	4.8842	1.9×10^{-4}	-6.6×10^{-4}
	32	4.8863	-8.2×10^{-6}	1.3×10^{-5}
	40	4.8858	-2.9×10^{-7}	-1.3×10^{-5}
	48	4.8859	1.3×10^{-7}	-1.0×10^{-6}
160	16	4.8791	-5.6×10^{-3}	4.6×10^{-4}
	24	4.8828	1.5×10^{-4}	-5.3×10^{-4}
	32	4.8853	2.5×10^{-6}	-3.3×10^{-5}
	40	4.8847	-4.8×10^{-7}	-2.2×10^{-5}
	48	4.8848	3.5×10^{-7}	-2.9×10^{-6}

$$\sum_{n=1}^{M/2} (a_{nM}M_{nM} + b_{nM}N_{nM} + c_{nM}O_{nM} + d_{nM}P_{nM} + a_{nI}M_{nI} + b_{nI}N_{nI} + c_{nI}O_{nI} + d_{nI}P_{nI}) = -(\sigma_y^\infty - \nu_M\sigma_x^\infty)y/E_M$$

$$A_{nM} = (-1/2)t_n(\theta_i) \cos^2 \theta_{i0}/\cos \theta_i + \int_0^{2\pi} K_{nnM}^{Fx}(\phi_k, \theta_i)t_n(\phi_k)bd\phi \quad (23)$$

$B_{nM}, \ldots, P_{nI}$ can be expressed in a similar manner.

The stresses at an arbitrary point are represented by a linear combination of the coefficients $a_{nM} \sim d_{nI}$, which is determined from the boundary conditions of suitably chosen collocation points shown in Eq. (24) and the influence coefficients corresponding to $A_{nM} \sim P_{nI}$.

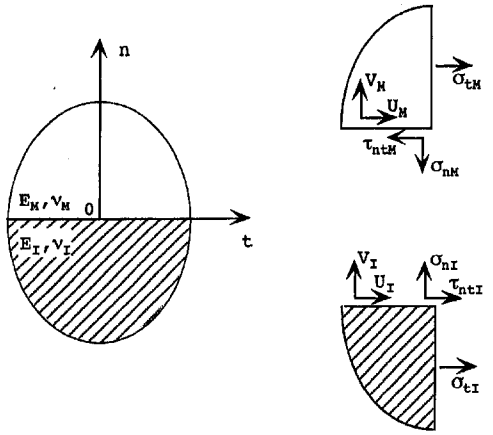


Fig. 4 Model of interface

Downloaded 04 May 2010 to 171.66.16.26. Redistribution subject to ASME license or copyright; see http://www.asme.org/terms/Terms_Use.cfm

Table 3 Examination of Eq. (4) ($a/b = 1$, $a/d = 0.648$, $\sigma_x^\infty = 1$, $\sigma_y^\infty = 0$, $E_I/E_M = 0.5$, $\nu_I = \nu_M = 0.3$, under plane stress in Fig. 1)

θ (deg.)	σtM	σtM	τntM	σtI Eqn(29)	σtI
0	-0.22567	0.72212	0.00000	-0.00452	-0.00452
20	-0.02518	0.63484	-0.23653	0.08264	0.08264
40	0.48086	0.41443	-0.35990	0.30259	0.30259
60	1.05059	0.16591	-0.31044	0.55018	0.55018
80	1.40880	0.00864	-0.11077	0.70569	0.70569
86	1.44392	-0.00732	-0.03464	0.72086	0.72086
90	1.44619	-0.00884	0.01658	0.72177	0.72177
94	1.43116	-0.00292	0.06874	0.71514	0.71514
100	1.37722	0.01946	0.14301	0.69153	0.69153
120	0.96634	0.19264	0.32461	0.51207	0.51207
140	0.38968	0.43394	0.34175	0.25993	0.25993
160	-0.04557	0.61103	0.20178	0.06887	0.06887
180	-0.18578	0.66556	0.00000	0.00695	0.00695

$$\theta_i = \pm \frac{2\pi(i-0.5)}{M}, \quad \pi \pm \frac{2\pi(i-0.5)}{M},$$

$$i = 1, 2, \ldots, M/4, \quad M = 4m \quad (m\text{: integer}) \quad (24)$$

4.2 Two Elliptical Inclusions Under Remote Shear as Shown in Fig. 2. In this case, by considering the x-axis skew-symmetry of the problem, $w_{x2}(\phi_k)$, $w_{x4}(\phi_k)$ and $w_{y1}(\phi_k)$, $w_{y3}(\phi_k)$ are suitable. Unknown function $\rho^*_{xM}(\phi_k) \sim \rho^*_{yI}(\phi_k)$ can be expressed by the following equations.

$$\begin{aligned}
\rho^*_{xM}(\phi_k) &= \rho_{x2M}(\phi_k)w_{x2}(\phi_k) + \rho_{x4M}(\phi_k)w_{x4}(\phi_k)\\
\rho^*_{yM}(\phi_k) &= \rho_{y1M}(\phi_k)w_{y1}(\phi_k) + \rho_{y3M}(\phi_k)w_{y3}(\phi_k)\\
\rho^*_{xI}(\phi_k) &= \rho_{x2I}(\phi_k)w_{x2}(\phi_k) + \rho_{x4I}(\phi_k)w_{x4}(\phi_k)\\
\rho^*_{yI}(\phi_k) &= \rho_{y1I}(\phi_k)w_{y1}(\phi_k) + \rho_{y3I}(\phi_k)w_{y3}(\phi_k) \quad (25)
\end{aligned}$$

Here, also, all unknown weight functions can be approximated in a similar manner to Eqs. (19)–(21), because all of these must satisfy Eq. (16).

5 Convergence of the Results

5.1 Convergence of Unknown Weight Functions. Table 1 shows the convergence of the unknown functions with increasing the collocation number M for two circular inclusions when $a/b = 1$, $a/d = 0.648$, $\sigma_x^\infty = 1$, $\sigma_y^\infty = 0$, $E_I/E_M = 0.5$, $\nu_I = \nu_M = 0.3$, under plane stress in Fig. 1. The weight unknown functions have almost the same convergence rate and the fifth digit accuracy when $M = 12$. Unknown body-force densities seem to be obtained in good accuracy in the numerical solution presented in the preceding paper.

5.2 Convergence of Interface Stresses for Inclusions Under Remote Shear Stress. In the conventional body-force method, interaction problems under remote tension has been mainly treated. Originally, Nisitani proposed a simple calculating method of stresses in an elastic body having several holes and inclusions (Nisitani, 1963, 1968). In his study, "additional stress fields" were considered when the tractions along an elliptical boundary are relieved in a plate under tension. The body-force method (Nisitani, 1967, 1974) was finally developed on the basis of this simple calculation. In this paper, interaction is also considered under remote shear that has not been treated by using body-force method.

Table 2 shows the convergence of the values of stress σ_n, σ_t, τ_{nt} along the hole boundary with increasing the collocation number M when $a/d = 0.9$, $E_I/E_M = 0.0$ in Fig. 2. In the present analysis, the boundary conditions ($\sigma_n = 0$, $\tau_{nt} = 0$), which should be zero along the boundary, are less than 10^{-4} even when $M = 24$. In the present analysis, therefore, the boundary requirements can be highly satisfied along the entire boundary when two holes are very close.

6 Examination of Relations Between Interface Stresses, Strains, and Displacement

Consider a perfectly bonded interface between a matrix (E_M, ν_M) and an inclusion (E_I, ν_I) as shown in Fig. 4. The interface stresses, strains, and displacements must satisfy the following conditions.

$$\sigma_{tM} \neq \sigma_{tI}, \quad \sigma_{nM} = \sigma_{nI}, \quad \tau_{ntM} = \tau_{ntI} \quad (26)$$

$$\epsilon_{tM} = \epsilon_{tI}, \quad \epsilon_{nM} \neq \epsilon_{nI}, \quad \gamma_{ntM} \neq \gamma_{ntI} \quad (27)$$

$$U_M = U_I, \quad V_M = V_I \quad (28)$$

Normal interface stresses in tangential direction must satisfy the following equation because of the continuity of tangential strains.

$$\sigma_{tI} = \frac{E_I}{E_M}\sigma_{tM} + \left\{\nu_I - \frac{E_I}{E_M}\nu_M\right\}\sigma_{nM} \quad \text{plane stress} \quad (29)$$

$$\sigma_{tI} = \frac{E_I(1-\nu_M^2)}{E_M(1-\nu_I^2)}\sigma_{tM} + \left\{\frac{\nu_I}{1-\nu_I} - \frac{E_I\nu_M(1+\nu_M)}{E_M(1-\nu_I^2)}\right\}\sigma_{nM}$$

$$\text{plane strain} \quad (30)$$

On the other hand, normal interface strains must satisfy the following equation because of the continuity of normal stresses and shear stresses.

$$\epsilon_{nI} = \frac{E_M}{E_I}\epsilon_{nM} + \left(\frac{\nu_M}{E_I} - \frac{\nu_I}{E_M}\right)\sigma_{tM} - \frac{\nu_I}{E_I}\left(\nu_I - \frac{E_I}{E_M}\nu_M\right)\sigma_{nM} \quad (31)$$

$$\gamma_{ntI} = \frac{G_M}{G_I}\gamma_{ntM} \quad (32)$$

Table 4 Examination of Eqs. (6) and (7) ($a/b = 1$, $a/d = 0.648$, $\sigma_x^\infty = 1$, $\sigma_y^\infty = 0$, $E_I/E_M = 0.5$, $\nu_I = \nu_M = 0.3$, plane stress in Fig. 1)

θ (deg.)	εtM	εnM	γntM	εnI Eqn(31)	εnI	γntI Eq(32)	γntI
0	-0.44231	0.78982	-0.00167	1.44696	1.44696	-0.00335	-0.00335
20	-0.21563	0.64239	-0.61498	1.22009	1.22009	-1.22995	-1.22995
40	0.35653	0.27017	-0.93575	0.64730	0.64730	-1.87150	-1.87150
60	1.00082	-0.14926	-0.80714	0.00172	0.00172	-1.61427	-1.61427
80	1.40621	-0.41400	-0.28801	-0.40614	-0.40614	-0.57601	-0.57601
86	1.44611	-0.44049	-0.09007	-0.44715	-0.44715	-0.18015	-0.18015
90	1.44885	-0.44270	0.04309	-0.45074	-0.45074	0.08619	0.08619
94	1.43204	-0.43227	0.17872	-0.43493	-0.43493	0.35744	0.35744
100	1.37138	-0.39371	0.37182	-0.37600	-0.37600	0.74364	0.74364
120	0.90855	-0.09727	0.84398	0.07803	0.07803	1.68796	1.68796
140	0.25950	0.31703	0.88856	0.71192	0.71192	1.77712	1.77712
160	-0.22888	0.62470	0.52464	1.18074	1.18074	1.04928	1.04928
180	-0.38544	0.72129	0.00134	1.32695	1.32695	0.00269	0.00269

Downloaded 04 May 2010 to 171.66.16.26. Redistribution subject to ASME license or copyright; see http://www.asme.org/terms/Terms_Use.cfm

Table 5 Values and positions of the maximum stress for two circular inclusions (a/b = 1, σ_x^∞ = 1, σ_y^∞ = 0, $\nu_I = \nu_M$ = 0.3, plane strain in Fig. 1)

		Matrix		Inclusion	
EI/EM	a/d	(deg.)	σmax	(deg.)	σmax
0.0	0.	90.0	3.0000		
	0.1	90.0	2.9804		
	0.2	89.7	2.9268		
	0.3	89.0	2.8531		
	0.4	88.0	2.7774		
	0.5	86.7	2.7065		
	0.6	85.9	2.6704		
	0.7	85.2	2.6419		
	0.8	84.7	2.6234		
	0.9	84.4	2.6114		
0.5	0.	90.0	1.5058	0~180	0.7573
	0.1	90.0	1.5034	0.	0.7562
	0.2	89.9	1.4966	0.	0.7533
	0.3	89.7	1.4868	0.	0.7492
	0.4	89.4	1.4759	0.	0.7442
	0.5	89.0	1.4659	33.5	0.7388
	0.6	88.6	1.4581	60.5	0.7338
	0.7	88.4	1.4532	76.0	0.7298
	0.8	88.2	1.4509	86.8	0.7274
	0.9	88.1	1.4510	94.3	0.7265
2.0	0	22.4,157.6	1.2149	0~180	1.1920
	0.1	157.6	1.2166	180.	1.1937
	0.2	157.8	1.2225	180.	1.1997
	0.3	158.0	1.2338	180.	1.2115
	0.4	158.8	1.2516	180.	1.2310
	0.5	160.7	1.2774	180.	1.2607
	0.6	163.6	1.3134	180.	1.3034
	0.7	169.3	1.3642	180.	1.3618
	0.8	180.0	1.4370	180.	1.4370
	0.9	180.0	1.5192	180.	1.5192
∞	0.	21.7158.3	1.5488	0~180	1.4778
	0.1	158.2	1.5546	180.	1.4833
	0.2	158.2	1.5747	180.	1.5025
	0.3	158.3	1.6135	180.	1.5433
	0.4	159.7	1.6776	180.	1.6131
	0.5	162.7	1.7777	180.	1.7263
	0.6	166.2	1.9348	180.	1.9055
	0.7	180.0	2.1932	180.	2.1932
	0.8	180.0	2.6900	180.	2.6933
	0.9	160.0	3.7657	180.	3.4197

Table 6 Values and positions of the maximum stress for two circular inclusions (a/b = 1, σ_x^∞ = 0, σ_y^∞ = 1, $\nu_I = \nu_M$ = 0.3, plane strain in Fig. 1)

		Matrix		Inclusion	
EI/EM	a/d	(deg.)	σmax	(deg.)	σmax
0.0	0	0.,180.	3.0000		
	0.1	0.	3.0005		
	0.2	0.	3.0043		
	0.3	0.	3.0147		
	0.4	0.	3.0345		
	0.5	0.	3.0642		
	0.6	180.	3.1162		
	0.7	180.	3.3807		
	0.8	180.	4.0340		
	0.9	180.	5.7993		
0.5	0.	0.,180.	1.5058	0.~180.	0.7573
	0.1	0.	1.5060	124.5	0.7576
	0.2	0.	1.5065	124.5	0.7584
	0.3	0.	1.5076	126.8	0.7602
	0.4	180.	1.5096	132.5	0.7635
	0.5	180.	1.5159	141.5	0.7694
	0.6	180.	1.5313	157.0	0.7796
	0.7	180.	1.5676	180.	0.8006
	0.8	180.	1.6495	180.	0.8436
	0.9	180.	1.8375	180.	0.9360
2.0	0	67.7,112.3	1.2149	0.~180.	1.1920
	0.1	67.6	1.2147	0.	1.1918
	0.2	67.6	1.2142	0.	1.1914
	0.3	67.6	1.2162	0.	1.1909
	0.4	67.5	1.2116	0.	1.1904
	0.5	67.4	1.2091	0.	1.1901
	0.6	67.2	1.2059	0.	1.1899
	0.7	67.0	1.2020	0.	1.1901
	0.8	66.7	1.1976	0.	1.1905
	0.9	66.4	1.1931	0.	1.1913
∞	0	68.3,111.7	1.5488	0.~180.	1.4778
	0.1	68.2	1.5488	0.	1.4775
	0.2	68.2	1.5490	0.	1.4778
	0.3	68.3	1.5491	0.	1.4800
	0.4	68.3	1.5487	0.	1.4852
	0.5	68.4	1.5479	0.	1.4945
	0.6	68.5	1.5467	0.	1.5093
	0.7	68.6	1.5456	0.	1.5308
	0.8	68.7	1.5455	0.	1.5612
	0.9	68.9	1.5474	0.	1.6098

First, to examine the accuracy of the present analysis, subtraction of interface stresses and displacements ($\sigma_{nM} - \sigma_{nI}$), ($\tau_{ntM} - \tau_{ntI}$), ($\epsilon_{tM} - \epsilon_{tI}$), ($U_M - U_I$), ($V_M - V_I$) are calculated for the problem when a/b = 1, a/d = 0.648, σ_x^∞ = 1, σ_y^∞ = 0, E_I/E_M = 0.5, $\nu_I = \nu_M$ = 0.3, under plane stress in Fig. 1. These values, that should be zero along the interface, are less than 10^{-5} even when M = 12. Table 3 shows interface stresses and values of Eq. (29). Table 4 shows interface strains and values of Eq. (31) and Eq. (32). It is found that the present method satisfy these conditions to the sixth digit. In the present analysis, therefore, the boundary requirements can be highly satisfied along the entire boundary.

7 Interaction Between Two Elliptical Holes Under Tension

Tables 5 and 6 show values and positions of maximum stress (principal stress) under plane strain for two circular inclusions. From the results of Tables 5 and 6, it is found that the values and positions of the maximum stress slightly varies with varying the shape and elastic ratio. The interaction effect is not very large unless the inclusions are extremely close ($a/d \geqq 0.8$) and elastic ratio between matrix and inclusion are extremely different (E_I/E_M = 0 or $E_I/E_M = \infty$). The calculations are carried out also for plane stress. The results of Shioya (1971) are in good agreement with the present results when a/d = 0.465, 0.648, and E_I/E_M = 0.5, 2.0.

Figures 5–8 show the stress distribution (σ_1, σ_n, σ_t, τ_{nt}) along the boundary of matrix when E_I/E_M = 0.0, 0.5, 2.0, ∞ under σ_x^∞ = 1, σ_y^∞ = 0. The solid line shows the stress distribution when a/d = 0.9 (E_I/E_M = 0.0, 0.5, 2.0) or a/d = 0.5 ($E_I/E_M = \infty$) and the broken line shows the stress distribution when $a/d \to 0$. The present method is useful for obtaining these smooth stress distributions.

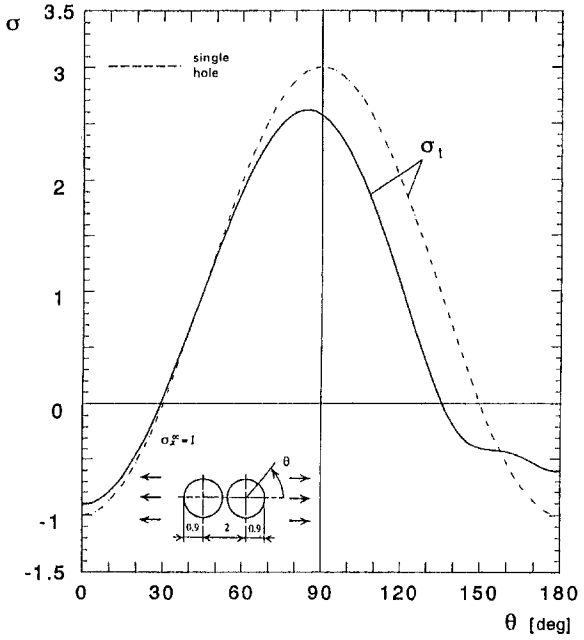


Fig. 5 Stress distribution of hole (σ_x^∞ = 1, σ_y^∞ = 0 in Fig. 1)

Downloaded 04 May 2010 to 171.66.16.26. Redistribution subject to ASME license or copyright; see http://www.asme.org/terms/Terms_Use.cfm

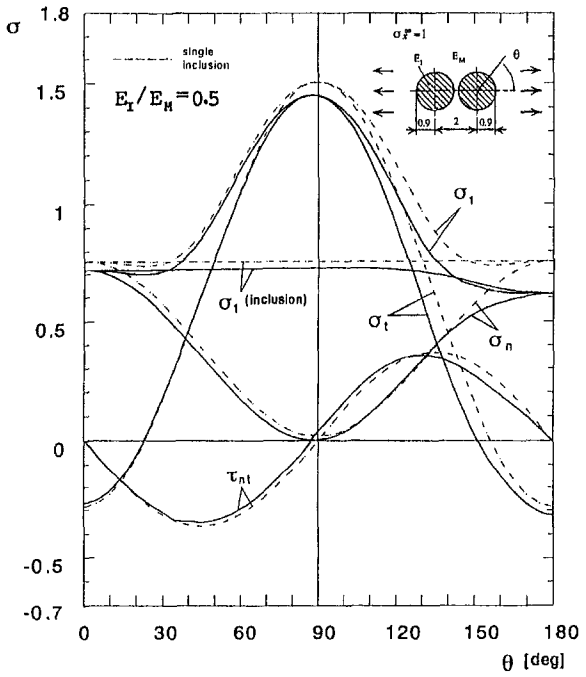


Fig. 6 Stress distribution of matrix ($\sigma_x^\infty = 1$, $\sigma_y^\infty = 0$, $E_I/E_M = 0.5$, $\nu_I = \nu_M = 0.3$, plane strain in Fig. 1)

8 Interaction Between Two Elliptical Inclusions Under Remote Shear

Table 7 shows the values and positions of maximum stress for two circular holes when a/d is changed in comparison with the results of Barrett et al. (1971), which were obtained from the chart in their paper. The results of Barrett et al. coincide with the present results when a/d is small. Their accuracy decreases with increasing a/d. The maximum stress has a peak value at $a/d = 0.82$ and after the peak it decreases as $a/d \rightarrow 1$. Figure 9 shows the stress distribution σ_t along the boundary

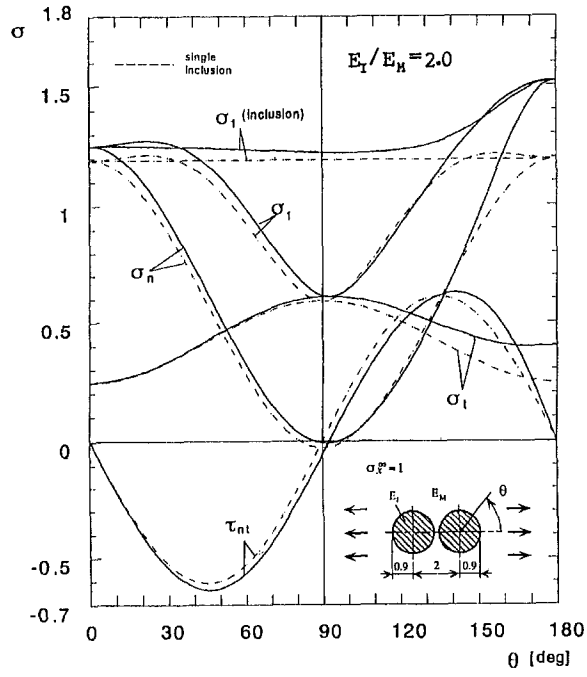


Fig. 7 Stress distribution of matrix ($\sigma_x^\infty = 1$, $\sigma_y^\infty = 0$, $E_I/E_M = 2.0$, $\nu_I = \nu_M = 0.3$, plane strain in Fig. 1)

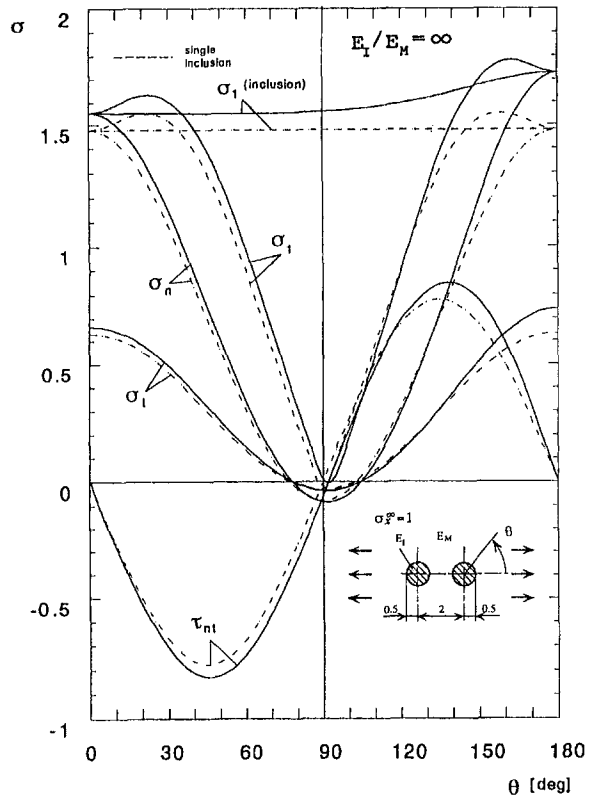


Fig. 8 Stress distribution of matrix ($\sigma_x^\infty = 1$, $\sigma_y^\infty = 0$, $E_I/E_M = \infty$, $\nu_I = \nu_M = 0.3$, plane strain in Fig. 1)

of circular hole under $\tau_{xy}^\infty = 1$. The solid line shows the stress distribution when $a/d = 0.9$ and the broken line shows the stress distribution when $a/d \rightarrow 0$.

Figures 10–12 show the stress distributions (σ_1, σ_n, σ_t, τ_{nt}) along the boundary of matrix when $E_I/E_M = 0.5$, 2.0, ∞. The solid line shows the stress distribution when $a/d = 0.5$ and the broken line shows the stress distribution when $a/d \rightarrow 0$.

9 Conclusion

In this paper, a singular integral equation method in the analysis of interaction of between elliptical inclusions was discussed. The conclusions were summarized as follows:

Table 7 Values and positions of the maximum stress for two circular holes ($a/b = 1$, $\tau_{xy}^\infty = 1$, $E_I = 0$ in Fig. 2)

a/d	Present analysis		Barrett
	θ (deg.)	σt max	σt max
0	135.	4.0000	4.00
0.1	135.0	4.0213	
1/6	135.2	4.0607	4.06
0.2	135.3	4.0883	4.08
1/4	135.6	4.1394	4.13
0.3	136.0	4.2014	4.20
1/3	136.5	4.2485	4.25
0.4	137.5	4.3549	4.35
0.5	140.0	4.5419	4.51
0.6	143.9	4.7615	4.78
2/3	147.3	4.9292	5.00
0.7	149.2	5.0189	5.08
0.8	154.9	5.2476	5.55
0.82	156.0	5.2605	5.76
0.84	157.0	5.2466	5.92
0.86	158.0	5.1923	6.11
0.88	158.9	5.0795	6.38
0.9	159.6	4.8859	6.50
0.92	160.0	4.5804	6.61

Downloaded 04 May 2010 to 171.66.16.26. Redistribution subject to ASME license or copyright; see http://www.asme.org/terms/Terms_Use.cfm

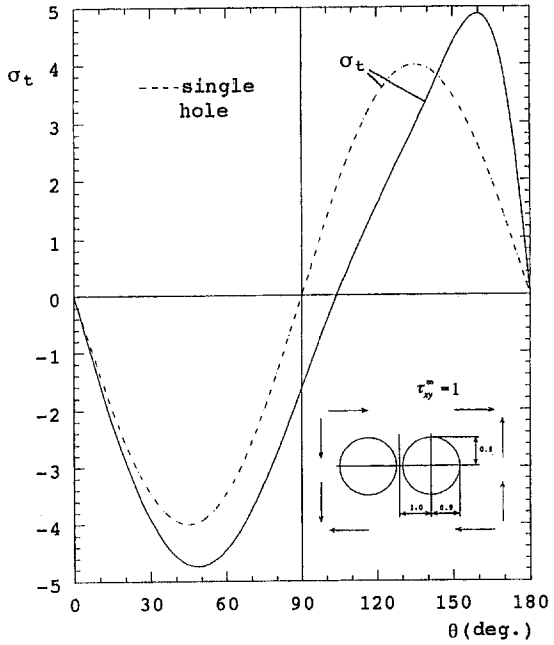


Fig. 9 Stress distribution of hole ($\tau^{\infty}_{xy} = 1$, $E_I = 0$ in Fig. 2)

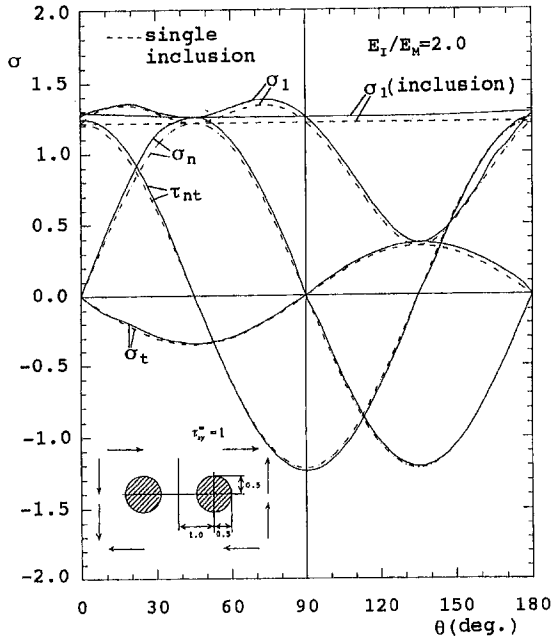


Fig. 11 Stress distribution of matrix ($\tau^{\infty}_{xy} = 1$, $E_I = E_M = 2.0$, $\nu_I = \nu_M = 0.3$, plane strain in Fig. 2)

1 The interaction problem between elliptical inclusion was formulated in terms of singular integral equations with Cauchy-type and logarithmic-type singularities. To formulate the problem, the body force method was applied, where the stress and displacement fields due to a point force were used as the fundamental solutions. The problem is reduced to determining the unknown body force densities distributed in infinite plates having the same elastic constants as those of the matrix and inclusions.

2 To determine the unknown body-force densities to satisfy the boundary conditions, four auxiliary unknown functions were defined from each body-force density. It is found that determining four auxiliary functions in the range $0 \leqq \phi_k \leqq \pi/2$ is equivalent to determining a original unknown density in the range $0 \leqq \phi_k \leqq 2\pi$. Namely, if the auxiliary functions are given in the range $0 \leqq \phi_k \leqq \pi/2$, the original unknown function is expressed in the range $0 \leqq \phi_k \leqq 2\pi$. Then, instead of determining body-force densities directly, these auxiliary unknowns were approximated by using known fundamental densities and unknown weight functions. Here, the fundamental density was defined as an example of continuous function holding the condition that the auxiliary function must satisfy. The solution presented in this paper will be applied to several problems in the following paper and the results and usefulness will be discussed.

3 Two elliptical inclusions under remote tension were considered. The accuracy of the present analysis was verified

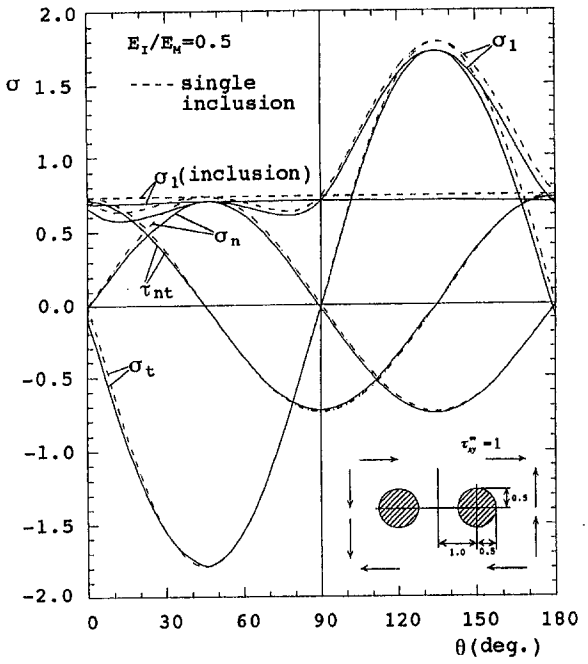


Fig. 10 Stress distribution of matrix ($\tau^{\infty}_{xy} = 1$, $E_I = E_M = 0.5$, $\nu_I = \nu_M = 0.3$, plane strain in Fig. 2)

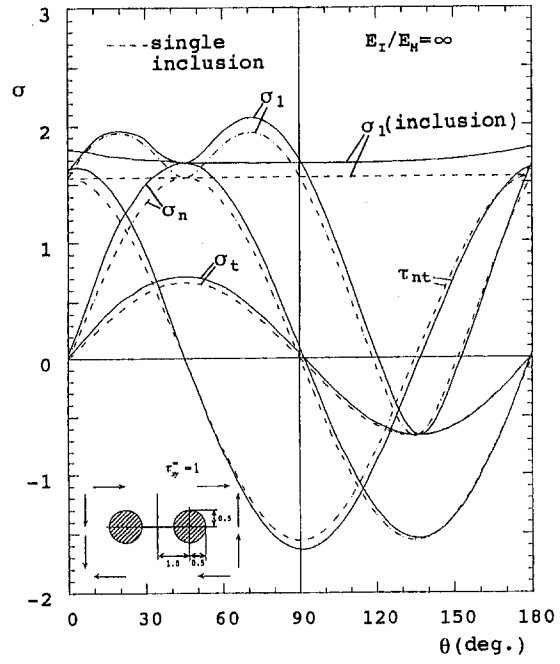


Fig. 12 Stress distribution of matrix ($\tau^{\infty}_{xy} = 1$, $E_I = E_M = \infty$, $\nu_I = \nu_M = 0.3$, plane strain in Fig. 2)

Downloaded 04 May 2010 to 171.66.16.26. Redistribution subject to ASME license or copyright; see http://www.asme.org/terms/Terms_Use.cfm

through examining the convergence of the results and necessary relations between interface stresses, strains, and displacements. The maximum stresses and stress distributions along the interface were shown in the tables and charts.

4 Two elliptical inclusions under remote shear were also considered. The results were shown in the tables and charts. With increasing a/d, the maximum stress for two circular holes has a peak value at a midpoint of a/d and it decreases as $a/d \to 1$.

5 The usefulness of the theory and solutions in the preceding paper was confirmed for the wide geometrical and elastic ranges of inclusions. The method may be applied to regular or random distributions of inclusions.

References

Barrett, R. F., Sheth, P. R., and Patel, G. C., 1971, "Effect of Two Circular Holes in a Plate Subjected to Pure Shear Stress," ASME JOURNAL OF APPLIED MECHANICS, Vol. 93, pp. 528–530.

Donnel, L. H., 1974, *Stress Concentration Factors,* R. E. Peterson, ed., John Wiley and Sons, New York, p. 223.

Erdogan, F., and Gupta, G. D., 1972, "On the Numerical Solution of Singular Integral Equations," *Quarterly Applied Mathematics,* Vol. 30, pp. 525–534.

Eshelby, J. D., 1957, "The Determination of the Elastic Field of an Ellipsoidal Inclusion, and Related Problems," *Proceedings Royal Society of London.,* Vol. A241, pp. 376–396.

Eshelby, J. D., 1959, "The Elastic Field Outside an Ellipsoidal Inclusion," *Proceedings Royal Society of London.,* Vol. A252, pp. 561–569.

Mura, T., 1987, *Micromechanics of Defects in Solids,* 2nd Ed., Martinus Nijhoff, Boston, MA, pp. 129–176.

Mura, T., 1988, "Inclusion Problems," ASME *Applied Mechanics Reviews,* Vol. 41, pp. 129–176.

Nisitani, H., 1963, "On the Tension of an Infinite Plate Containing an Infinite Row of Elliptical Holes," *Bull. Japan Soc. Mech. Eng.,* Vol. 6, pp. 635–638.

Nisitani, H., 1967, "The Two-Dimensional Stress Problem solved using an Electrical Digital Computer," *Jour. Japan Soc. Mech. Eng.,* Vol. 70, pp. 627–632. (*Bull. Japan Soc. Mech. Eng.,* Vol. 11, 1968, pp. 14–23).

Nisitani, H., 1968, "Method of Approximate Calculation for Interference Effects and Its Application," *J. Japan Soc. Mech. Eng.,* Vol. 11, pp. 725–738.

Nisitani, H., 1974, "Solution of Notch Problems by Body Force Method," *Stress Analysis of Notch Problem* G. C. Sih, ed., Leyden, pp. 1–68.

Nisitani, H., and Chen, D. H., 1987, *Taisekiryokuhou,* Baifukan, p. 89 (in Japanese).

Noda, N.-A., and Matsuo, T., 1995a, "Singular Integral Equation Method in the Analysis of Interaction between Crack and Defects," *Fracture Mechanics* ASTM STP 1220, F. Erdogan, ed., American Society for Testing and Materials, Philadelphia, pp. 591–605.

Noda, N.-A., and Matsuo, T., 1995b, "Singular Integral Equation Method in Optimization of Stress-Relieving Hole: A New Approach Based on the Body Force Method," *Int. Jour. Fract.,* Vol. 70, pp. 147–165.

Noda, N.-A., and Matsuo, T., 1997, "Numerical Solution of Singular Integral Equations in Stress Concentration Problems," *International Journal Solids Structures,* Vol. 34, No. 19, pp. 2429–2444.

Shioya, S., 1971, "On the Tension of an Infinite Thin Plate Containing a Pair of Circular Inclusions," *Bulletin of the JSME,* Vol. 14, No. 68. pp. 117–126.

APPENDIX

Fundamental Solutions

The kernel of stresses and displacement used in Eqs. (1), (2) are expressed by putting $F_x = 1$, $F_y = 1$ in Eq. (A1)–(A3).

(a) Stress:

$$K_{nn}^{Fx} = \sigma_n^{Fx} = \sigma_x^{Fx}\cos^2\theta + \sigma_y^{Fx}\sin^2\theta + 2\tau_{xy}^{Fx}\sin\theta\cos\theta$$

$$K_{nn}^{Fy} = \sigma_n^{Fy} = \sigma_x^{Fy}\cos^2\theta + \sigma_y^{Fy}\sin^2\theta + 2\tau_{xy}^{Fy}\sin\theta\cos\theta$$

$$K_{nt}^{Fx} = \tau_{nt}^{Fx} = (-\sigma_x^{Fx} + \sigma_y^{Fx})\sin\theta\cos\theta + 2\tau_{xy}^{Fx}(\cos^2\theta - \sin^2\theta)$$

$$K_{nt}^{Fy} = \tau_{nt}^{Fy} = (-\sigma_x^{Fy} + \sigma_y^{Fy})\sin\theta\cos\theta + 2\tau_{xy}^{Fy}(\cos^2\theta - \sin^2\theta) \quad \text{(A1)}$$

where

$$\sigma_x^{Fx} = -\frac{(x-\xi)\{\beta(x-\xi)^2 + \alpha(y-\eta)^2\}}{r^4}F_x$$

$$\sigma_x^{Fy} = \frac{(y-\eta)\{\alpha(y-\eta)^2 + (2\alpha-\beta)(x-\xi)^2\}}{r^4}F_y$$

$$\sigma_y^{Fx} = \frac{(x-\xi)\{\alpha(x-\xi)^2 + (2\alpha-\beta)(y-\eta)^2\}}{r^4}F_x$$

$$\sigma_y^{Fy} = \frac{(y-\eta)\{\beta(y-\eta)^2 + \alpha(x-\xi)^2\}}{r^4}F_y$$

$$\tau_{xy}^{Fx} = -\frac{(y-\eta)\{\beta(x-\xi)^2 + \alpha(y-\eta)^2\}}{r^4}F_x$$

$$\tau_{xy}^{Fy} = -\frac{(x-\xi)\{\beta(y-\eta)^2 + \alpha(x-\xi)^2\}}{r^4}F_y$$

$$r^2 = (x-\xi)^2 + (y-\eta)^2,$$

$$\alpha = \frac{1-\nu}{4\pi}, \quad \beta = \frac{3+\nu}{4\pi} \quad \text{(plane stress)}. \quad \text{(A2)}$$

(b) Displacement:

$$K_u^{Fx} = \left[2\gamma\log\frac{R}{r} + \delta\left\{\frac{(x-\xi)^2-(y-\eta)^2}{r^2} - \frac{\xi^2-\eta^2}{R^2}\right\}\right]F_x$$

$$K_u^{Fx} = 2\delta\left[\frac{(x-\xi)(y-\eta)}{r^2} - \frac{\xi\eta}{R^2}\right]F_y$$

$$K_V^{Fx} = 2\delta\left[\frac{(x-\xi)(y-\eta)}{r^2} - \frac{\xi\eta}{R^2}\right]F_x$$

$$K_V^{Fy} = \left[2\gamma\log\frac{R}{r} + \delta\left\{\frac{(x-\xi)^2-(y-\eta)^2}{r^2} - \frac{\xi^2-\eta^2}{R^2}\right\}\right]F_y$$

$$\gamma = \frac{(1+\nu)(3-\nu)}{8\pi E}, \quad \delta = \frac{(1+\nu)^2}{8\pi E},$$

$$R^2 = \xi^2 + \eta^2 \quad \text{(plane stress)}. \quad \text{(A3)}$$

Downloaded 04 May 2010 to 171.66.16.26. Redistribution subject to ASME license or copyright; see http://www.asme.org/terms/Terms_Use.cfm

B. A. Zeldin
Research Associate.

P. D. Spanos
Ryon Chair in Engineering,
Fellow ASME.

Department of Mechanical Engineering,
MS 321
George Brown School of Engineering,
Rice University,
Houston, TX 77005-1892

On Random Field Discretization in Stochastic Finite Elements

Several traditional methods for discretizing random fields in stochastic mechanics applications are considered; they are the midpoint method, the interpolation method, and the local averaging method. A simple and computationally convenient criterion for estimating the accuracy of these discretization methods is developed. Also, the Volterra series representation of nonlinear input/output relationships is utilized to assess the effect of the random field discretization methods on the response variability of stochastic mechanics problems. The theoretical developments are elucidated by a numerical example involving a beam problem.

1 Introduction

Considerable attention has been devoted in recent years to extending the deterministic finite element method for treating stochastic phenomena (Deodatis and Shinozuka, 1991; Ghanem and Spanos, 1991; Liu et al., 1986; Takada, 1990; Liu and Der Kiureghian, 1991). The stochastic finite element method involves discretization of random fields which are to be represented by a set of random variables. Random field discretization in the stochastic finite element method is a crucial step in the development of a reliable computational procedure capable of accurately predicting the response variability of stochastic mechanics problems.

Several random field discretization methods have been developed in this regard. They include the midpoint method (Der Kiureghian and Ke, 1988), the local averaging method (Vanmarcke and Grigoriu, 1983), the interpolation method (Liu et al., 1986), the weighted integral method (Takada, 1990; Deodatis and Shinozuka, 1991), and methods involving the Karhunen-Loeve expansion (Ghanem and Spanos, 1991) and expansion of random fields in terms of more general orthogonal bases (Elishakoff, 1979; Zhang and Ellingwood, 1994). Notably, rather few investigations have focused on estimating the errors resulting from these field discretization procedures. More importantly, even fewer studies are available regarding simple criteria for controlling the discretization error for an arbitrary random field. Note that currently convergence results with respect to the random field discretization are obtained by refining the discretization mesh for random fields in the stochastic finite element method or by introducing additional terms in the corresponding series expansions (Der Kiureghian and Ke, 1988; Ghanem and Spanos, 1991; Zhang and Ellingwood, 1994). This may be prohibitive from a computational resources perspective; in this regard, it is noted that computational requirements of the stochastic finite element method exceed considerably those of the deterministic finite element method.

The aforementioned issues associated with estimating the errors induced by several of the random field discretization procedures in the stochastic finite element method are the subject of this paper. The paper focuses on the midpoint, local averaging, and interpolation methods of random field discretization. It is shown that these methods can be considered as a rather special case of a more general discretization scheme by using the representation theory of shift-invariant subspaces (de Boor et al., 1994a).

2 Background on the Stochastic Finite Element Method

This paper focuses on linear stochastic mechanics problems. However, the approach can be readily extended for analyzing the discretization error of nonlinear problems, as well. Consider the equation

$$(L_0 + \tilde{L}_{\alpha(\mathbf{x},\theta)})(u(\mathbf{x})) = f_0(\mathbf{x}) + f(\mathbf{x}, \theta), \quad \mathbf{x} \in \Omega \subset \mathbf{R}^d, \quad (1)$$

where $\alpha(\mathbf{x}, \theta)$ and $f(\mathbf{x}, \theta)$ are zero-mean random fields describing the variability of the material properties and the external loading, respectively; the symbol θ indicates explicitly the dependence of pertinent quantities on the elements of the sample space. The spatial differential operator of the stochastic mechanics problem is split into two components. Specifically, L_0 denotes the deterministic linear differential operator, and $\tilde{L}_{\alpha(\mathbf{x},\theta)}$ expresses the corresponding random part. Similarly, $f_0(\mathbf{x})$ denotes the mean value of the external loading, whereas the component $f(\mathbf{x}, \theta)$ describes load variability around the mean value. Further, Eq. (1) is defined within the region Ω of d-dimensional spatial domain $\mathbf{R}^d$ and $\mathbf{x} = (x_1, \ldots, x_d)$; appropriate boundary conditions are appended.

Clearly, the response of the stochastic mechanics system $u(\mathbf{x})$ is, also, a random quantity. In fact, Eq. (1) defines an implicit relationship between $f_0(\mathbf{x})$, $f(\mathbf{x}, \theta)$, $\alpha(\mathbf{x}, \theta)$ and the unknown system response $u(\mathbf{x})$. The objective of the stochastic finite element method is to transform the stochastic differential Eq. (1) into a set of random algebraic equations which can be solved by using digital computers (Ghanem and Spanos, 1991; Der Kiureghian and Ke, 1988; Liu et al., 1986). The solution of Eq. (1) can be sought in the form

$$u(\mathbf{x}, \theta) = \sum_{k=1}^{N} c_k(\theta) v_k(\mathbf{x}), \quad (2)$$

where $v_k(\mathbf{x})$, $k = 1, \ldots, N$, are basis functions, and $c_k(\theta)$ are corresponding random variables; the accuracy of the stochastic finite element method approximation can be controlled by varying the number of basis elements N. In this regard, bases of polynomial splines are commonly used in finite element method applications; they lend themselves to the appealing interpretation of partitioning the spatial domain of the problem Ω into a set of finite elements which can be treated locally by "shape functions."

The unknown random coefficients $c_k(\theta)$ can be determined by substituting the approximation of Eq. (2) into Eq. (1) and

Contributed by the Applied Mechanics Division of THE AMERICAN SOCIETY OF MECHANICAL ENGINEERS for publication in the ASME JOURNAL OF APPLIED MECHANICS.

Discussion on this paper should be addressed to the Technical Editor, Professor Lewis T. Wheeler, Department of Mechanical Engineering, University of Houston, Houston, TX 77204-4792, and will be accepted until four months after final publication of the paper itself in the ASME JOURNAL OF APPLIED MECHANICS.

Manuscript received by the ASME Applied Mechanics Division, Feb. 18, 1997; final revision, Sept. 17, 1997. Associate Technical Editor: M. Shinozuka.

 Copyright © 1998 by ASME

Downloaded 04 May 2010 to 171.66.16.26. Redistribution subject to ASME license or copyright; see http://www.asme.org/terms/Terms_Use.cfm

making the resulting error orthogonal to another set of functions $w_k(\mathbf{x})$, also called test functions. Specifically, one may set

$$\sum_{k=1}^{N} c_k(\langle L_0(v_k(\mathbf{x})), w_j(\mathbf{x})\rangle + \langle \tilde{L}_{\alpha(\mathbf{x},\theta)}(v_k(\mathbf{x})), w_j(\mathbf{x})\rangle) = \langle f_0(\mathbf{x}), w_j(\mathbf{x})\rangle + \langle f(\mathbf{x}), w_j(\mathbf{x})\rangle, \quad (3)$$

where the scalar product $\langle f(\mathbf{x}), g(\mathbf{x})\rangle$ is defined as the integral over the entire spatial domain Ω. Also, integrating by parts the inner products of Eq. (3) involving the differential operators, the corresponding expressions can be written in the following symmetric form:

$$\langle L_0(v_k(\mathbf{x})), w_j(\mathbf{x})\rangle = \langle l_0(v_k(\mathbf{x})), l_0(w_j(\mathbf{x}))\rangle, \quad (4)$$

and

$$\langle \tilde{L}_{\alpha(\mathbf{x},\theta)}(v_k(\mathbf{x})), w_j(\mathbf{x})\rangle = \langle \alpha(\mathbf{x}, \theta) l(v_k(\mathbf{x})), l(w_j(\mathbf{x}))\rangle, \quad (5)$$

where l_0 and l are appropriate deterministic differential operators.

Denoting $\langle l_0(v_k), l_0(w_j)\rangle$ and $\langle \alpha(\mathbf{x}, \theta) l(v_k), l(w_j)\rangle$ by $[K_0]_{jk}$ and $[\tilde{K}]_{jk}$, respectively, and $\langle f_0, w_j\rangle$ and $\langle f, w_j\rangle$ by f_j^0 and $\tilde{f}_j$, respectively, leads to the following system of random algebraic equations

$$\sum_{k=1}^{N} ([K_0]_{jk} + [\tilde{K}]_{jk}) c_k = f_j^0 + \tilde{f}_j, \quad j = 1, \ldots, N. \quad (6)$$

In conjunction with the preceding development it is noted that the stochastic finite element method must resolve two important issues. The first relates to the representation of the associated random fields in calculating efficiently the probability structure of the random variables $[\tilde{K}]_{jk}$ and $\tilde{f}_j$; some of the pertinent discretization methods and the related approximation errors will be considered in the ensuing section. The second issue relates to the solution of the system of random algebraic Eqs. (6). In this regard, it is noted that often the first-order perturbation method constitutes a reasonable compromise between the numerical complexity of the stochastic finite element method and the accuracy of the derived results, if the level of engineering uncertainties is not quite high.

3 Discretization of Random Fields in the Stochastic Finite Element Method

3.1 Preliminary Remarks. A simple criterion is developed in this paper to evaluate the accuracy of the midpoint method, the local averaging method, and the interpolation method for random field discretization in conjunction with stochastic finite element method applications by introducing representation principles of the theory of shift-invariant subspaces generated by a single function (de Boor et al., 1994a). Note that the weighted integral method (Takada, 1990; Deodatis and Shinozuka, 1991) can be also analyzed by using the analytical concepts developed in the paper by invoking the theory of shift-invariant subspaces generated by several functions (de Boor et al., 1994b). The theory of shift-invariant space approximation is a well-established area of mathematical research. It has found application in a large class of problems such as wavelet analysis, spline approximation, etc. In this section, the corresponding formalism and notions are extended for stochastic mechanics applications. In this regard, it is assumed that the considered mesh of the random field discretization is uniform. This assumption is quite realistic in practical applications dealing with homogeneous random fields. Also, in the multidimensional case, the discretization of random fields is performed by using square elements of size h in order to simplify, somewhat, the corresponding notation. However, it is believed that extending the developed criterion for treating non-uniform meshes with the characteristic element size h is not an insurmountable task.

3.2 Several Traditional Approaches of Random Fields Discretization. The *midpoint discretization method* is a commonly used discretization methods (Deodatis, 1989; Der Kiureghian and Ke, 1988). In this case the mesh of the finite element method discretization is generated, and the values at the "center" of elements are used to represent the stochastic field. Specifically,

$$\tilde{\alpha}(\mathbf{x}, \theta) = \alpha_{\mathbf{k}}(\theta), \quad \mathbf{x} \in \Omega_{\mathbf{k}}, \quad (7)$$

where

$$\alpha_{\mathbf{k}}(\theta) = \alpha(\mathbf{x}_{\mathbf{k}}, \theta), \quad (8)$$

$\mathbf{x}_{\mathbf{k}}$ is the coordinate of the geometrical center of the $\mathbf{k}$th element, and $\mathbf{k} = (k_1, \ldots, k_d)$ is the multidimensional index numbering the discretization elements. Further, the correlation properties of the random variables $\alpha_{\mathbf{k}}(\theta)$ can be readily found from the equation

$$r_{\mathbf{kl}} = \mathbf{E}[\alpha_{\mathbf{k}}(\theta)\alpha_{\mathbf{l}}(\theta)] = R_\alpha(\mathbf{x}_{\mathbf{k}}, \mathbf{x}_{\mathbf{l}}). \quad (9)$$

Thus, the random field $\alpha(\mathbf{x}, \theta)$ is approximated by using the equation

$$\tilde{\alpha}(\mathbf{x}, \theta) = \sum_{\mathbf{k}} \alpha_{\mathbf{k}}(\theta)\phi_{h,\mathbf{k}}(\mathbf{x}), \quad (10)$$

where $\phi_{h,\mathbf{k}}(\mathbf{x}) = \phi((\mathbf{x}/h) - \mathbf{k})$ is the set function associated with the $\mathbf{k}$th element. That is,

$$\phi(\mathbf{x}) = \begin{cases} 1, & \mathbf{x} \in [0, 1]^d \\ 0, & \text{otherwise.} \end{cases} \quad (11)$$

The *interpolation method* was used by Liu et al. (1986) who argued that the mesh of random field discretization may not be equal to the mesh of the finite element method and, in fact, it can be determined using only the field correlation characteristics. For example, for random fields with large correlation length, the random field discretization mesh can be significantly coarser than the mesh of the finite element method; the number of random variables in stochastic finite element method computations is reduced. Thus, the random field can be represented by Eq. (10) where

$$\phi_{h,\mathbf{k}}(\mathbf{x}) = \prod_{l=1}^{d} \phi_{h,k_l}(x_l) = \prod_{l=1}^{d} \phi(x_l/h - k_l) \quad (12)$$

is the multidimensional linear shape function

$$\phi(x) = \begin{cases} 1 - |x|, & x \in [-1, 1] \\ 0, & \text{otherwise} \end{cases}, \quad (13)$$

and $\alpha_{\mathbf{k}}(\theta)$ is the nodal value of the random field at $\mathbf{x}_{\mathbf{k}}$, as in Eq. (8).

In the *local averaging method,* the properties of the random field $\alpha(\mathbf{x}, \theta)$ are characterized by analyzing its average values

$$\alpha_{\mathbf{k}}(\theta) = \frac{1}{|\Omega_{\mathbf{k}}|}\int_{\Omega_{\mathbf{k}}} \alpha(\mathbf{x}, \theta) d\mathbf{x} = \frac{1}{|\Omega_{\mathbf{k}}|}\int_{\Omega_{\mathbf{k}}} \alpha(\mathbf{x}, \theta)\phi_{h,\mathbf{k}}(\mathbf{x}) d\mathbf{x}, \quad (14)$$

where $\phi_{h,\mathbf{k}}(\mathbf{x})$ is the indicator function of the element $\Omega_{\mathbf{k}}$, Eq. (11). Vanmarcke (1994) argued that the stochastic finite element method discretization should be based on averaging since any field measurements are, in fact, representatives of the random variables $\alpha_{\mathbf{k}}(\theta)$ of Eq. (14) and they do not specify the random field $\alpha(\mathbf{x}, \theta)$. Vanmarcke and Grigoriu (1983) adapted random field averaging for the stochastic finite element method by describing random fields within a finite element by the corre-

Downloaded 04 May 2010 to 171.66.16.26. Redistribution subject to ASME license or copyright; see http://www.asme.org/terms/Terms_Use.cfm

sponding average values. Specifically, the random field is approximated by Eq. (10) where the correlation of the random variables $\alpha_k(\theta)$ can be readily found by using the equation

$$r_{kl} = E[\alpha_k(\theta)\alpha_l(\theta)] = \frac{1}{|\Omega_k||\Omega_l|}\int_{\Omega_k}\int_{\Omega_l} R_\alpha(\mathbf{x}_1, \mathbf{x}_2)d\mathbf{x}_1 d\mathbf{x}_2. \quad (15)$$

Approximate expressions for the integral of Eq. (15) have also been developed (Vanmarcke and Grigoriu, 1983).

3.3 A Unified Approach: Shift-Invariant Discretization Method.

3.3.1 Mathematical Representation. Clearly, the midpoint method, the interpolation method, and the local averaging method of random field discretization utilize similar principles. They can be readily grouped together by using the notion of shift invariant approximation. In this regard, the random field $\alpha(\mathbf{x}, \theta)$ can be approximated by using the equation

$$\tilde{\alpha}(\mathbf{x}, \theta) = \sum_{\mathbf{k}} \alpha_{\mathbf{k}}(\theta)\phi(\mathbf{x}/h - \mathbf{k}), \quad (16)$$

where the random variables $\alpha_k(\theta)$ are defined as the weighted averages of the random field $\alpha(\mathbf{x}, \theta)$. Specifically,

$$\alpha_{\mathbf{k}}(\theta) = \frac{1}{h^d}\int \alpha(\mathbf{x}, \theta)\psi(\mathbf{x}/h - \mathbf{k})dx. \quad (17)$$

Here, the interpolation function $\phi(\mathbf{x})$ and the sampling function $\psi(\mathbf{x})$ are arbitrary square integrable functions associated with a uniform rectangular mesh in the spatial domain. Note that the mesh of the random field discretization does not necessarily coincide with the elements of the associated finite element method.

The discretization introduced by Eqs. (16) and (17) can be called the shift-invariant discretization since the expansion basis is invariant under the transformation $\mathbf{x} \to \mathbf{x} + \mathbf{k}h$; it is a generalization of the function approximation by shift invariant subspaces adapted to the case of random fields. Analyzing Eqs. (16) and (17) it is seen that the midpoint method utilizes the interpolation function of Eq. (11) and the sampling function

$$\psi(\mathbf{x}/h) = \frac{1}{h^d}\,\delta\left(\frac{\mathbf{x} - \mathbf{x}_i}{h}\right), \quad (18)$$

where $\delta(x)$ the Dirac delta function. Similarly, the interpolation method utilizes the interpolation function of Eqs. (12) and (13) and the sampling Dirac delta function of Eq. (18). Finally, the local averaging method differs from the midpoint method by the sampling function which is equal to

$$\psi(\mathbf{x}/h) = \frac{1}{h^d}\,\phi\left(\frac{\mathbf{x}}{h}\right), \quad (19)$$

where $\phi(\mathbf{x})$ is the element set function of Eq. (11).

3.3.2 Spectral Matching Quality Assessment. The autocorrelation function of the discretized random field $\tilde{\alpha}(\mathbf{x}, \theta)$ can be readily determined from Eq. (16). Specifically,

$$R_{\tilde{\alpha}}(\mathbf{x}_1, \mathbf{x}_2) = \sum_{\mathbf{k},\mathbf{l}} r_{\mathbf{kl}}\phi(\mathbf{x}_1/h - \mathbf{k})\phi(\mathbf{x}_2/h - \mathbf{l}). \quad (20)$$

If $\alpha(\mathbf{x}, \theta)$ is a homogeneous random field, the covariance parameters $r_{kl} = E[\alpha_k(\theta)\alpha_l(\theta)]$ depend only on the difference of the indices $\mathbf{k} - \mathbf{l}$. That is, Eq. (20) can be rewritten in the form

$$R_{\tilde{\alpha}}(\mathbf{x}_1, \mathbf{x}_2) = \sum_{\mathbf{k}} r_{\mathbf{k}} \sum_{\mathbf{l}} \phi(\mathbf{x}_1/h - \mathbf{k} - \mathbf{l})\phi(\mathbf{x}_2/h - \mathbf{l}). \quad (21)$$

Note that the approximation $\tilde{\alpha}(\mathbf{x}, \theta)$ is not a homogeneous field since the right-hand side of Eq. (21) is not a function of $\mathbf{x}_2 - \mathbf{x}_1$ for a general interpolation function $\phi(\mathbf{x})$. In fact, the homogeneity of the approximation $\tilde{\alpha}(\mathbf{x}, \theta)$ can be satisfied only if one selects an interpolation function of the form

$$\phi(\mathbf{x}) = \prod_{j=1}^{d} \frac{\sin \pi x_j}{\pi x_j}. \quad (22)$$

Indeed, in this case

$$\sum_{\mathbf{l}} \phi(\mathbf{x}_1 - \mathbf{k} - \mathbf{l})\phi(\mathbf{x}_2 - \mathbf{l}) = \sum_{\mathbf{l}} \prod_{j=1}^{d} \frac{\sin \pi(x_{1,j} - k_j - l_j) \sin \pi(x_{2,j} - l_j)}{\pi^2(x_{1,j} - k_j - l_j)(x_{2,j} - l_j)} = \prod_{j=1}^{d} \frac{\sin \pi(x_{1,j} - x_{2,j} - k_j)}{\pi(x_{1,j} - x_{2,j} - k_j)} = \phi(\mathbf{x}_1 - \mathbf{x}_2 - \mathbf{k}). \quad (23)$$

In conjunction with the preceding development it is noted that the quantitative comparison of the auto-correlation functions $R_{\tilde{\alpha}}(\mathbf{x}_1, \mathbf{x}_2)$ and $R_\alpha(\mathbf{x}_1, \mathbf{x}_2)$ is computationally costly. Therefore, the concept of averaged spectrum can be used to evaluate the properties of $\tilde{\alpha}(\mathbf{x}, \theta)$ with respect to approximating the target random field $\alpha(\mathbf{x}, \theta)$, though the former is not formally stationary. The averaged spectrum associated with the multidimensional frequency vector $\boldsymbol{\omega} = (\omega_1 \ldots, \omega_d)$ can be defined as

$$\bar{S}_{\tilde{\alpha}}(\boldsymbol{\omega}) = \frac{1}{(2\pi)^d}\int_{-\infty}^{\infty}\left(\lim_{T\to\infty}\frac{1}{(2T)^d}\int_{-T}^{T} R_{\tilde{\alpha}}\left(\mathbf{x} + \frac{\mathbf{t}}{2}, \mathbf{x} - \frac{\mathbf{t}}{2}\right)d\mathbf{x}\right)e^{-i\boldsymbol{\omega}\mathbf{t}}d\mathbf{t}, \quad (24)$$

where $\boldsymbol{\omega}\mathbf{t}$ denotes the scalar product of the vectors ω and t.

Note that for a stationary process the averaged spectrum conforms with the conventional definition of the spectral density function. Substituting Eq. (21) into Eq. (24) one finds

$$\bar{S}_{\tilde{\alpha}}(\boldsymbol{\omega}) = h^d P(h\boldsymbol{\omega})|\hat{\phi}(h\boldsymbol{\omega})|^2, \quad (25)$$

where

$$P(\boldsymbol{\omega}) = \frac{1}{(2\pi)^d}\sum_{\mathbf{k}} r_{\mathbf{k}} e^{-i\boldsymbol{\omega}\mathbf{k}} \quad (26)$$

is the spectrum of the discrete random sequence $\alpha_k(\theta)$, and $\hat{\phi}(\boldsymbol{\omega})$ denotes the Fourier transform of the interpolation functions $\phi(\mathbf{x})$. That is,

$$\hat{\phi}(\boldsymbol{\omega}) = \int_{-\infty}^{\infty}\phi(\mathbf{x})e^{-i\boldsymbol{\omega}\mathbf{x}}d\mathbf{x}. \quad (27)$$

Further, the spectrum $P(\omega)$ of the discrete random sequence $\alpha_k(\theta)$ can be related to the spectrum $S_\alpha(\omega)$ of the continuous random field $\alpha(\mathbf{x}, \theta)$. Indeed, Eq. (17) yields

$$\begin{aligned} r_{\mathbf{k}} &= \frac{1}{h^{2d}}\iint R_\alpha(\mathbf{x}_1, \mathbf{x}_2)\psi(\mathbf{x}_1/h)\psi(\mathbf{x}_2/h - \mathbf{k})d\mathbf{x}_1 d\mathbf{x}_2 \\ &= \frac{1}{h^{2d}}\iint\left(\int_{-\infty}^{\infty} S_\alpha(\boldsymbol{\omega})e^{i\omega(\mathbf{x}_2 - \mathbf{x}_1)}d\boldsymbol{\omega}\right) \\ &\quad \times \psi(\mathbf{x}_1/h)\psi(\mathbf{x}_2/h - \mathbf{k})d\mathbf{x}_1 d\mathbf{x}_2 \\ &= \int_{-\infty}^{\infty} S_\alpha(\boldsymbol{\omega})|\hat{\psi}(\boldsymbol{\omega}h)|^2 e^{i\omega h\mathbf{k}}d\boldsymbol{\omega} \\ &= \int_{-\pi/h}^{\pi/h}\left(\sum_{\mathbf{l}=-\infty}^{\infty} S_\alpha\left(\boldsymbol{\omega} + \frac{2\pi\mathbf{l}}{h}\right)\right. \\ &\quad \left.\times\,|\hat{\psi}(h\omega + 2\pi\mathbf{l})|^2\right)e^{i\omega h\mathbf{k}}d\boldsymbol{\omega}. \end{aligned} \quad (28)$$

Downloaded 04 May 2010 to 171.66.16.26. Redistribution subject to ASME license or copyright; see http://www.asme.org/terms/Terms_Use.cfm

The correlation parameters $r_{\mathbf{k}}$ can be also expressed as the inverse Fourier transform of $P(\omega)$. Specifically,

$$r_{\mathbf{k}} = \int_{-\pi}^{\pi} P(\boldsymbol{\omega}) e^{i\boldsymbol{\omega}\mathbf{k}} d\boldsymbol{\omega} = h^d \int_{-\pi/h}^{\pi/h} P(\boldsymbol{\omega}h) e^{i\boldsymbol{\omega}h\mathbf{k}} d\boldsymbol{\omega}. \quad (29)$$

Comparing Eqs. (28) and (29) one derives

$$P(\boldsymbol{\omega}h) = \frac{1}{h^d} \sum_{\mathbf{l}=-\infty}^{\infty} S_\alpha\left(\boldsymbol{\omega} + \frac{2\pi\mathbf{l}}{h}\right) |\hat{\psi}(\boldsymbol{\omega}h + 2\pi\mathbf{l})|^2. \quad (30)$$

Finally the averaged spectrum of the approximation $\tilde{\alpha}(\mathbf{x}, \theta)$ is equal to

$$\bar{S}_{\tilde{\alpha}}(\boldsymbol{\omega}) = \sum_{\mathbf{l}=-\infty}^{\infty} S_\alpha\left(\boldsymbol{\omega} + \frac{2\pi\mathbf{l}}{h}\right) |\hat{\psi}(\boldsymbol{\omega}h + 2\pi\mathbf{l})|^2 |\hat{\phi}(h\boldsymbol{\omega})|^2. \quad (31)$$

In conjunction with Eq. (31), the quality of the spectral approximation of the traditional discretization procedures of Section 3.2 can be readily evaluated. The Fourier transforms of the interpolation function and the sampling function associated with the midpoint method are

$$|\hat{\phi}(\omega)|^2 = \prod_{l=1}^{d} \left[\frac{\sin(\pi\omega_l/2)}{\pi\omega_l/2}\right]^2, \text{ and } |\hat{\psi}(\omega)|^2 = 1, \quad (32)$$

respectively. Similarly, these functions are

$$|\hat{\phi}(\omega)|^2 = \prod_{l=1}^{d} \left[\frac{\sin(\pi\omega_l/2)}{\pi\omega_l/2}\right]^4 \quad \text{and} \quad |\hat{\psi}(\omega)|^2 = 1 \quad (33)$$

for the interpolation method, and

$$|\hat{\phi}(\omega)|^2 = \prod_{l=1}^{d} \left[\frac{\sin(\pi\omega_l/2)}{\pi\omega_l/2}\right]^2 \quad \text{and}$$

$$|\hat{\psi}(\omega)|^2 = \prod_{l=1}^{d} \left[\frac{\sin(\pi\omega_l/2)}{\pi\omega_l/2}\right]^2 \quad (34)$$

for the local averaging method.

Substituting Eq. (32) into Eq. (31) one can readily deduce that the averaged spectrum $S_{\tilde{\alpha}}$ associated with the midpoint method may significantly overestimate the target spectrum $S(\omega)$ for a coarse discretization mesh. Indeed, the sum in Eq. (31) induces aliasing of the spectrum increasing the averaged spectrum value at low frequencies; this is not compensated by the sampling function $\hat{\psi}(\boldsymbol{\omega})$ of Eq. (32). Due to this aliasing effect, the midpoint method may introduce a higher variability of the response quantities of the stochastic mechanics problem. This feature of the midpoint method was observed, for example, in reference Der Kiureghian and Ke (1988). Also, the Fourier transform of the interpolation function $\hat{\psi}(\boldsymbol{\omega})$ of Eq. (34) associated with the local averaging method eliminates the aliasing effect but, simultaneously, in combination with the corresponding interpolation function, it may cause underestimation of the target spectrum. This yields a lower level of variability of the response quantities for the stochastic mechanics problem obtained by incorporating the local averaging method. A numerical example of this phenomenon was also reported by Der Kiureghian and Ke (1988).

Finally, it is pointed out that the computational requirements of Eq. (31) are quite low; the Fourier transform of the interpolation and sampling functions are, as a rule, known analytically and the summation in Eq. (31) can be truncated beyond a few terms since random fields encountered in engineering applications have, often, quite rapidly decaying spectra. Thus, this equation may provide a useful criterion for assessing the quality of various discretization schemes.

3.4 Numerical Examples. A numerical example is considered to illustrate the preceding theoretical developments; it involves discretization of a homogeneous one-dimensional random field with the auto-correlation function

$$R_\alpha(x) = \exp(-|x|/a), \quad (35)$$

where a is a parameter commonly defined as the correlation length of the field $\alpha(x, \theta)$; in the numerical calculations of this example the length of correlation is $a = 1$. The target spectrum and the averaged spectra corresponding to the midpoint method, the interpolation method, and the local averaging method are plotted in Fig. 1. Clearly, for coarse mesh ($h = 2$) there are significant discrepancies between the various discretization approaches and the target field. Thus, the midpoint method overestimates the target spectrum in the region of low frequencies whereas the local averaging method, while eliminating aliasing, underestimates the target spectrum away from zero frequency. However, for $h = 0.5$, the discrepancies between the target and approximate spectra are minimal. A similar convergence result, which was, however, obtained by refining the discretization mesh and by solving repeatedly stochastic mechanics problems in conjunction with the stochastic finite element method, was reported previously by Der Kiureghian and Ke (1988).

4 Influence of the Random Field Discretization on the Solution Variability

Clearly, the discretizations of the random fields describing system and external loading in a stochastic mechanics problem influence, to a certain extent, the reliability of the derived expressions for the statistics of the solution of the stochastic finite element method. This issue is the subject of the current section.

4.1 Continuous Spatial Domain. As it has been alluded to previously, Eq. (1) constitutes a nonlinear implicit relationship between the response quantity of interest $u(\mathbf{x}, \theta)$ and the (random) functions $\alpha(\mathbf{x}, \theta)$ and $f(\mathbf{x}, \theta)$. This nonlinear relationship can be expressed, in the most general form, by using the Volterra series expansion (Rugh, 1981)

$$u(\mathbf{x}) = u_0(\mathbf{x}) + \int h_{1,0}(\mathbf{x}, \mathbf{y}) f(\mathbf{y}) d\mathbf{y} + \int h_{0,1}(\mathbf{x}, \mathbf{y}) \alpha(\mathbf{y}) d\mathbf{y}$$
$$+ \iint h_{2,0}(\mathbf{x}, \mathbf{y}_1, \mathbf{y}_2) f(\mathbf{y}_1) f(\mathbf{y}_2) d\mathbf{y}_1 d\mathbf{y}_2$$
$$+ \iint h_{1,1}(\mathbf{x}, \mathbf{y}_1, \mathbf{y}_2) f(\mathbf{y}_1) \alpha(\mathbf{y}_2) d\mathbf{y}_1 d\mathbf{y}_2$$
$$+ \iint h_{0,2}(\mathbf{x}, \mathbf{y}_1, \mathbf{y}_2) \alpha(\mathbf{y}_1) \alpha(\mathbf{y}_2) d\mathbf{y}_1 d\mathbf{y}_2 + \ldots, \quad (36)$$

where $h_{i,j}(\mathbf{x}, \mathbf{y}_1, \ldots, \mathbf{y}_{i+j})$ are corresponding Volterra kernels. It has been noted previously that the first-order perturbation method is utilized commonly in the stochastic finite element method for the approximate evaluation of the system response variability. Note that the higher order terms may provide only for minor improvements of the accuracy of the stochastic finite element method in the case of small variability of the stochastic field $\alpha(\mathbf{x}, \theta)$ while increasing significantly the required computational resources. Incorporating the perturbation approach for deriving analytically the kernels of the Volterra series of Eq. (36), the solution of the stochastic mechanics problem can be written as (Adomian, 1983)

$$u(\mathbf{x}) = u_0(\mathbf{x}) + u_1(\mathbf{x}) + \ldots \quad (37)$$

where

$$L_0(u_0(\mathbf{x})) = f_0(\mathbf{x}) \quad \text{and}$$
$$L_0(u_1(\mathbf{x})) = f(\mathbf{x}) - \tilde{L}_{(\alpha(\mathbf{x},\theta))}(u_0(\mathbf{x})). \quad (38)$$

Downloaded 04 May 2010 to 171.66.16.26. Redistribution subject to ASME license or copyright; see http://www.asme.org/terms/Terms_Use.cfm

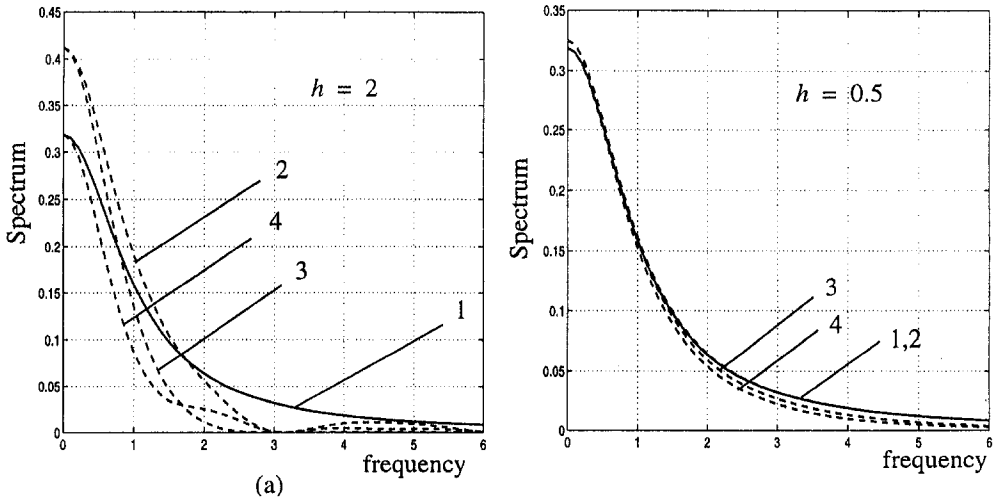


Fig. 1 Spectrum of the target homogeneous random field $S_\alpha(\omega) = (\alpha/\pi(1 + \omega^2\alpha^2))$ and averaged spectra of field approximations. Curve 1, target field. Curve 2, midpoint method. Curve 3, interpolation method. Curve 4, local averaging method.

Thus, the solution of Eq. (1) can be approximated as

$$u(\mathbf{x}) \approx u_0(\mathbf{x}) + \int G(\mathbf{x}, \mathbf{y}) f(\mathbf{y}) d\mathbf{y} - \int G(\mathbf{x}, \mathbf{y}) \tilde{L}_{(\alpha(\mathbf{y},\theta))}(u_0(\mathbf{y})) d\mathbf{y}, \quad (39)$$

where $G(\mathbf{x}, \mathbf{y})$ is the Green's function associated with the deterministic operator L_0; it satisfies the equation

$$L_0(G(\mathbf{x}, \mathbf{y})) = \delta(\mathbf{x} - \mathbf{y}) \quad (40)$$

with appropriate boundary conditions are appended. The first-order Volterra kernels $h_{1,0}(\mathbf{x}, \mathbf{y})$ and $h_{0,1}(\mathbf{x}, \mathbf{y})$ can be readily determined by comparing Eqs. (36) and (39). Specifically,

$$h_{1,0}(\mathbf{x}, \mathbf{y}) = G(\mathbf{x}, \mathbf{y}), \quad \text{and}$$
$$h_{0,1}(\mathbf{x}, \mathbf{y}) = -l(G(\mathbf{x}, \mathbf{y}))l(u_0(\mathbf{y})). \quad (41)$$

Note that the response $u(\mathbf{x})$ in Eq. (39) is obtained from integral expressions as if it is the response of a linear time (spatially)-varying dynamic system to random excitations $\alpha(\mathbf{x}, \theta)$ and $f(\mathbf{x}, \theta)$. Correspondingly, the kernels $h_{1,0}(\mathbf{x}, \mathbf{y})$ and $h_{0,1}(\mathbf{x}, \mathbf{y})$ can be viewed as the time (spatially)-varying impulse responses. Methods for analyzing time varying linear systems to stationary and nonstationary excitation are available in the literature (Priestley, 1981; Lin and Cai, 1995). In this context, it can be readily deduced that $u_0(\mathbf{x})$ is equal to the mean value of the random response $u(\mathbf{x})$. Further, the auto-covariance function of $u(\mathbf{x})$ can be found by using Eq. (39). Specifically,

$$R_u(\mathbf{x}_1, \mathbf{x}_2) = \iint h_{1,0}(\mathbf{x}_1, \mathbf{y}_1) h_{1,0}(\mathbf{x}_2, \mathbf{y}_2) R_f(\mathbf{y}_1, \mathbf{y}_2) d\mathbf{y}_1 d\mathbf{y}_2 + \iint h_{0,1}(\mathbf{x}_1, \mathbf{y}_1) h_{0,1}(\mathbf{x}_2, \mathbf{y}_2) R_\alpha(\mathbf{y}_1, \mathbf{y}_2) d\mathbf{y}_1 d\mathbf{y}_2, \quad (42)$$

where the random fields $\alpha(\mathbf{x}, \theta)$ and $f(\mathbf{x}, \theta)$ are assumed uncorrelated. Introducing the transfer function

$$H(\mathbf{x}, \omega) = \int h(\mathbf{x}, \mathbf{y}) e^{i\omega\mathbf{y}} d\mathbf{y}, \quad (43)$$

Eq. (42) yields

$$R_u(\mathbf{x}_1, \mathbf{x}_2) = \int [H_{1,0}(\mathbf{x}_1, \omega) H^*_{1,0}(\mathbf{x}_2, \omega) S_f(\omega) + H_{0,1}(\mathbf{x}_1, \omega) H^*_{0,1}(\mathbf{x}_2, \omega) S_\alpha(\omega)] d\omega, \quad (44)$$

where $(\,)^*$ denotes complex conjugation. Thus, an approximate expression for the variance of the response $u(\mathbf{x})$ of the stochastic mechanics problem can be obtained from Eq. (44). Specifically,

$$\text{Var}\,(u(\mathbf{x})) = \int [|H_{1,0}(\mathbf{x}, \omega)|^2 S_f(\omega) + |H_{0,1}(\mathbf{x}, \omega)|^2 S_\alpha(\omega)] d\omega. \quad (45)$$

Extending further the analogy between the stochastic mechanics problems and the random vibration problems, the space-frequency function $|H_{1,0}(\mathbf{x}, \omega)|^2 S_f(\omega) + |H_{0,1}(\mathbf{x}, \omega)|^2 S_\alpha(\omega)$ can be approximately treated as the evolutionary spectrum of the random field $u(\mathbf{x})$ if, of course, the Volterra transfer functions $|H_{1,0}(\mathbf{x}, \omega)|^2$ and $|H_{0,1}(\mathbf{x}, \omega)|^2$ are "slowly varying" functions in the spatial directions.

Note that the Volterra transfer functions $|H_{1,0}(\mathbf{x}, \omega)|^2$ and $|H_{0,1}(\mathbf{x}, \omega)|^2$ resemble "the response variability functions" (Deodatis and Shinozuka, 1991) introduced previously in the stochastic finite element method for obtaining sensible bounds on the response variability of stochastic mechanics problems without requiring any specific information regarding the spectral characteristics of the associated random fields. However, the Volterra transfer functions $|H_{1,0}(\mathbf{x}, \omega)|^2$ and $|H_{0,1}(\mathbf{x}, \omega)|^2$ of Eq. (45) are derived within a more general analytical framework by invoking the arguments of similarity between the stochastic mechanics and random vibration problems; they are associated with the kernels of the Volterra series representation of the solution of the stochastic mechanics problem.

Upon evaluating the Volterra transfer functions $|H_{1,0}(\mathbf{x}, \omega)|^2$ and $|H_{0,1}(\mathbf{x}, \omega)|^2$ by performing the Fourier transformation in Eq. (43) analytically or numerically, Eq. (45) yields a useful estimate of the error introduced by discretizing random fields in the stochastic finite element method. Specifically,

$$\text{Var}\,(u(\mathbf{x})) - \text{Var}\,(\tilde{u}(\mathbf{x})) \approx \int [|H_{1,0}(\mathbf{x}, \omega)|^2 (S_f(\omega) - \bar{S}_f(\omega))] d\omega + \int |H_{0,1}(\mathbf{x}, \omega)|^2 (S_\alpha(\omega) - \bar{S}_{\tilde{\alpha}}(\omega)) d\omega, \quad (46)$$

where $\tilde{u}(\mathbf{x})$ is the solution of the stochastic mechanics problem associated with the discrete random fields $\tilde{\alpha}(\mathbf{x}, \theta)$ and $\tilde{f}(\mathbf{x}, \theta)$.

Downloaded 04 May 2010 to 171.66.16.26. Redistribution subject to ASME license or copyright; see http://www.asme.org/terms/Terms_Use.cfm

Some issues related to the numerical computation of the Volterra transfer functions are discussed next.

4.2 Discretized Spatial Domain. The Green's function which is required for calculating the first-order Volterra kernels in Eq. (41) is not known analytically for most engineering applications. However, some elements of the deterministic finite element method can be introduced to evaluate them numerically. Specifically, the Green's function of Eq. (40) can be approximated by using the equation

$$G(\mathbf{x}, \mathbf{y}) = \sum_k g_k(\mathbf{y}) v_k(\mathbf{x}), \tag{47}$$

where $v_k(x)$ are basis functions of the deterministic finite element method, and $g_k(\mathbf{y})$ are the corresponding coefficients which depend on the coordinate of the concentrated force $\delta(\mathbf{x} - \mathbf{y})$ in Eq. (40). The coefficients $g_k(\mathbf{y})$ can be evaluated by substituting the approximation of Eq. (47) into Eq. (40) and making the resulting error orthogonal to a set of test functions $w_j(x)$. Specifically,

$$\sum_k g_k(\mathbf{y})(l_0(v_k(\mathbf{x})), l_0(w_j(x_0))) = \sum_k [K_0]_{jk} g_k(\mathbf{y}) = w_j(\mathbf{y}), \tag{48}$$

where K_0 is the stiffness matrix of the deterministic finite element method. Further, Eq. (48) shows that the coefficients $g_k(\mathbf{y})$ are equal to $\sum_j [K_0^{-1}]_{kj} w_j(\mathbf{y})$, yielding the following approximation of the Green's function

$$G(\mathbf{x}, \mathbf{y}) = \sum_{k,j} [K_0^{-1}]_{kj} w_j(\mathbf{y}) v_k(\mathbf{x}). \tag{49}$$

Further, the first-order Volterra kernels of Eq. (41) can be determined as

$$h_{1,0}(\mathbf{x}, \mathbf{y}) = \sum_{k,j} [K_0^{-1}]_{kj} w_j(\mathbf{y}) v_k(\mathbf{x}), \tag{50}$$

and

$$h_{0,1}(\mathbf{x}, \mathbf{y}) = -\sum_{k,j} [K_0^{-1}]_{kj} v_k(\mathbf{x}) l(w_j(\mathbf{y})) l(u_0(\mathbf{y})). \tag{51}$$

Correspondingly, the Volterra transfer functions are approximately equal to

$$H_{1,0} = \sum_{k,j} [K_0^{-1}]_{kj} \hat{w}_j(\omega) v_k(\mathbf{x}) \quad \text{and}$$

$$H_{0,1} = \sum_{k,j} [K_0^{-1}]_{kj} v_k(\mathbf{x}) \widehat{(l(w_j) l(u_0))}(\boldsymbol{\omega}). \tag{52}$$

Note that the Fourier transforms, $\hat{(\cdot)}$, of the finite element shape functions in Eq. (52) are, as a rule, known analytically. However, the determination of the inverse matrix K_0^{-1} involved in Eq. (52) can be computationally costly.

4.3 Numerical Example. A simple numerical example involving a shear beam with random rigidity is considered to elucidate the preceding theoretical concepts. The beam deflection is governed by the differential equation

$$-((1 + \alpha(x, \theta))u(x)')' = f_0(x), \quad x \in [0, 1], \tag{53}$$

where $\alpha(x, \theta)$ is the random field describing the fluctuation of the beam stiffness from its mean value equal to 1. The shape of the auto-correlation function of the field $\alpha(x, \theta)$ is given by Eq. (35), where the length of correlation a is taken equal to 0.125, and the standard deviation of the field $\alpha(x, \theta)$ is equal to 0.1. The boundary conditions are taken as

$$u(0) = u(1) = 0. \tag{54}$$

That is, the beam is statically indeterminate. Further, the deterministic external loading $f_0(x)$ is assumed to be equal to 1.

Random fluctuations of $u(x)$ approximated by using the first-order perturbation analysis is found equal to

$$u_1(x) = \int_0^1 h_\alpha(x, y)\alpha(y, \theta)dy, \tag{55}$$

where $h_\alpha(x, y) = \frac{1}{2}[1_+(x - y) - x](1 - 2y)$ and the function $1_+(x)$ is equal to 1 for $x \geq 0$ and is equal to 0 otherwise. Therefore, the Volterra transfer function for displacement is equal to

$$|H_\alpha(x, \omega)|^2 = \left| \left\{ \frac{(1 - 2x)e^{i\omega x} + xe^{i\omega} + x - 1}{2i\omega} + \frac{2(1 - x) + 2e^{i\omega x} - 2xe^{i\omega}}{2(i\omega)^2} \right\} \right|^2. \tag{56}$$

This function is shown in Fig. 2 for the spatial coordinate $x = 0.5$ in the middle of the shear beam. The "filtering" effect of the function $|H_\alpha(x, \omega)|^2$ can be discerned from Fig. 2. Also, plotted in Fig. 2 is the normalized spectrum of the random field $\alpha(x, \theta)$ so that one can identify the frequency components of the field $\alpha(x, \theta)$ that contribute significantly to the variability of $u(x = 0.5)$. Further, the absolute value of the discretization error evaluated by using Eq. (46) is shown in Fig. 3 as a function of the discretization mesh h. It is seen that the discretization with mesh size equal to the length of correlation of the field $\alpha(x, \theta)$, $h/a = 1$, yields an error in evaluating the variance of $u(x = 0.5)$ approximately equal to eight percent for the midpoint method, and four percent for the interpolation method; this may be considered acceptable for most engineering applications.

5 Selection of the Random Field Discretization Mesh

The preceding concepts facilitate the development of a reasonable strategy for selecting random field discretization meshes in stochastic finite element method applications without resorting to a costly mesh refinement procedure. The random field discretization mesh can be selected by using only certain information regarding the spectral characteristics of the random fields and the nature of the associated deterministic problem. Two features of the probabilistic mechanics problem are especially important in this regard.

First, the spectrum of the discrete random field $\tilde{\alpha}(\mathbf{x}, \theta)$ must match reasonably well the spectrum of the target random field $\alpha(\mathbf{x}, \theta)$. Equation (31) provides a useful criterion in this regard which requires minimal computational resources. According to Eq. (31) the size of the discretization mesh h must be inversely proportional to the cutoff frequency λ

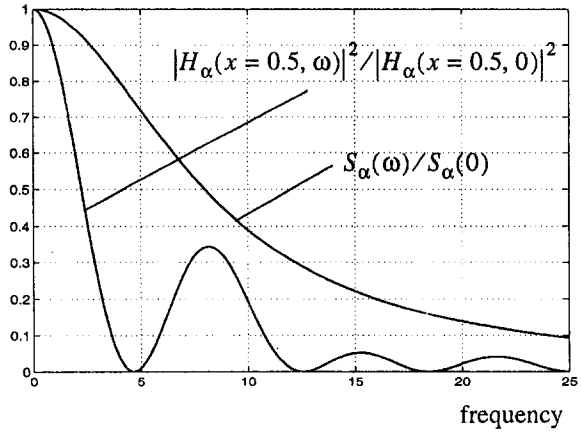
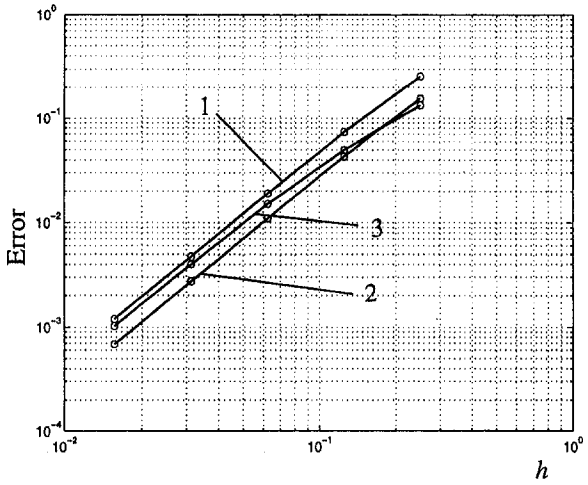


Fig. 2 Normalized Volterra transfer function for displacement at $x = 0.5$

Downloaded 04 May 2010 to 171.66.16.26. Redistribution subject to ASME license or copyright; see http://www.asme.org/terms/Terms_Use.cfm



Curve 1. Midpoint method
Curve 2. Interpolation method
Curve 3. Local averaging method

Fig. 3 An estimate of Eq. (46) of the discretization error of the response variance ($|\text{Var}(u(x)) - \text{Var}(\tilde{u}(x))|$)/ $\text{Var}(u(x))$ versus the size of the discretization mesh h at $x = 0.5$

$$h = \kappa \frac{\pi}{\lambda}, \tag{57}$$

where κ is a coefficient of proportionality. The cutoff frequency λ is selected so that

$$S_\alpha(\omega) \approx 0, \quad \text{for} \quad \omega > \lambda. \tag{58}$$

The parameter $\kappa \leq 1$ must be small enough to prevent the Fourier transform of the interpolation function $\hat{\phi}(h\omega)$ and of the sampling function $\hat{\psi}(h\omega)$ from compromising the spectral matching in Eq. (31); these functions must be approximately equal to a constant for $\omega < \lambda$.

In conjunction with the preceding discussion it is noted that currently the scale of fluctuation ϑ (Vanmarcke and Grigoriu, 1983) or the length of correlation, rather than the cutoff frequency λ, are used as the prime factors in the determination of the requisite mesh size. This practice is, perhaps, well justified for random fields for which a significant portion of the energy is associated with low frequencies and with the maximum of the spectral density function at $\omega = 0$. The spectra of such fields may be approximated by the spectral density function

$$S(\omega) = \begin{cases} S_0, & |\omega| < \lambda \\ 0, & \text{otherwise} \end{cases}. \tag{59}$$

In this case of clipped white noise the scale of fluctuation is proportional to the value of the spectrum at zero frequency since (Vanmarcke and Grigoriu, 1983)

$$\vartheta = \int R_\alpha(x)dx = 2\pi S_0. \tag{60}$$

Thus,

$$\vartheta = \frac{\pi R_\alpha(0)}{\lambda}. \tag{61}$$

Combining Eqs. (57) and (61) shows that

$$h = \frac{\kappa}{R_\alpha(0)}\vartheta. \tag{62}$$

That is, the scale of fluctuation, in this case, is a reasonable measure of h for a process resembling clipped white noise.

Note that stochastic fields with the spectra resembling Eq. (59) are quite common in stochastic mechanics applications. In particular, the spectrum used for the numerical example of Section 3 satisfies the above conditions; its energy is centered in the low-frequency region with the maximum of the spectral density function at $\omega = 0$. However, the scale of fluctuation can be a quite misleading criterion for selecting the discretization mesh when the spectral density function is shifted away from $\omega = 0$. As it has been pointed out previously, in this case the mesh size h must be selected initially by using λ as a criterion which then can be rectified by using Eq. (31).

The second feature which is important for the selection of the adequate value of h is the Volterra transfer functions indicating the frequency range that contributes towards the error of random field discretization in the stochastic finite element method, Eq. (46) elucidates this effect. Further, one can readily obtain an upper bound on the error of the response variance of the stochastic mechanics problem. Specifically,

$$\begin{aligned} &|\text{Var}(u(\mathbf{x})) - \text{Var}(\tilde{u}(\mathbf{x}))| \\ &= \max_\omega |S_f(\boldsymbol{\omega}) - \bar{S}_f(\boldsymbol{\omega})| \int |H_{1,0}(\mathbf{x}, \boldsymbol{\omega})|^2 d\boldsymbol{\omega} \\ &\quad + \max_\omega |S_\alpha(\boldsymbol{\omega}) - \bar{S}_\alpha(\boldsymbol{\omega})| \int |H_{0,1}(\mathbf{x}, \boldsymbol{\omega})|^2 d\boldsymbol{\omega}. \end{aligned} \tag{63}$$

Note, however, that the numerical determination of the Volterra transfer functions is computationally costly and, ultimately, is equivalent to solving the stochastic mechanics problem. Thus, this analysis can be used only at the finite stage of addressing the issue regarding the random field discretization mesh. In this context, Eq. (63) can provide a useful a posteriori bound on the response variability.

6 Concluding Remarks

The paper has presented an analysis of the error resulting from several discretization procedures for random fields in the stochastic finite element method. In this regard, the shift invariant discretization method has been proposed; it encompasses the midpoint method, the interpolation method, and the local averaging method which are commonly used in stochastic finite element method applications; the weighted integral method can be also analyzed within the proposed framework. A simple criterion of estimating the accuracy of these random field discretization schemes has been derived which can be used in numerical applications without resorting to a costly mesh refinement procedure. It has been shown that the developed criterion is computationally efficient and yields convergence estimates consistent with some of the results obtained numerically in the literature. Further, the influence of the random field dis-

Downloaded 04 May 2010 to 171.66.16.26. Redistribution subject to ASME license or copyright; see http://www.asme.org/terms/Terms_Use.cfm

cretization on the response variability of the stochastic mechanics problem has been investigated by using the Volterra series approach and deriving a useful a posteriori bound for the response variability. Numerical examples have been considered elucidating the usefulness of the developed estimates for stochastic mechanics applications.

References

Adomian, G., 1983, *Stochastic Systems,* Academic Press, New York.

De Boor, C., De Vore, R. A., and Ron, A., 1994a, "Approximation from Shift-Invariant Subspaces of $L_2(\mathbf{R}^d)$," *Transaction of the American Mathematical Society,* Vol. 341, No. 2, pp. 787–806.

De Boor, C., De Vore, R. A., and Ron, A., 1994b, "The Structure of Finitely Generated Shift-Invariant Spaces in $L_2(\mathbf{R}^d)$," *Journal of Functional Analysis,* Vol. 119, No. 1, pp. 37–78.

Deodatis, G., 1989, "Stochastic FEM Sensitivity Analysis of Nonlinear Dynamic Problems," *Probabilistic Engineering Mechanics,* Vol. 4, No. 3, pp. 135–141.

Deodatis, G., and Shinozuka, M., 1991, "The Weighted Integral Method. II: Response Variability and Reliability," *Journal of Engineering Mechanics,* Vol. 117, No. 8, pp. 1865–1877.

Der Kiureghian, A., and Ke, J.-B., 1988, "The Stochastic Finite Element Method in Structural Reliability," *Probabilistic Engineering Mechanics,* Vol. 3, No. 2, pp. 83–91.

Elishakoff, I., 1979, "Simulation of Space-Random Fields for Solution of Stochastic Boundary-Value Problems," *Journal of the Acoustical Society of America,* Vol. 65, No. 2, pp. 399–403.

Ghanem, R., and Spanos, P., 1991, *Stochastic Finite Elements: A Spectral Approach,* Springer-Verlag, New York.

Lin, Y. K., and Cai, G. Q., 1995, *Probabilistic Structural Dynamics: Advanced Theory and Applications,* McGraw-Hill, New York.

Liu, P.-L., and Der Kiureghian, A., 1991, "Finite Element Reliability of Geometrically Nonlinear Uncertain Structures," *Journal of Engineering Mechanics,* Vol. 117, No. 8, pp. 1806–1825.

Liu, W. K., Belytschko, T., and Mani, A., 1986, "Random Field Finite Elements," *International Journal for Numerical Methods in Engineering,* Vol. 23, pp. 1831–1845.

Priestley, M. B., 1981, *Spectral Analysis and Time Series,* Academic Press, London.

Rugh, W. L., 1981, *Nonlinear System Theory: The Volterra/Wiener Approach,* John Hopkins University Press, Baltimore, MD.

Takada, T., 1990, "Weighted Integral Method in Multi-dimensional Stochastic Finite Element Analysis," *Probabilistic Engineering Mechanics,* Vol. 5, No. 4, pp. 158–166.

Vanmarcke, E. H., 1994, "Stochastic Finite Elements and Experimental Measurements," *Probabilistic Engineering Mechanics,* Vol. 9, pp. 103–114.

Vanmarcke, E. H., and Grigoriu, M., 1983, "Stochastic Finite Element Analysis of Simple Beams," *Journal of Engineering Mechanics,* Vol. 109, No. 5, pp. 1203–1214.

Zhang, J., and Ellingwood, 1994, "Orthogonal Series Expansion of Random Fields in Reliability Analysis," *Journal of Engineering Mechanics,* Vol. 120, No. 12, pp. 2660–2677.

Downloaded 04 May 2010 to 171.66.16.26. Redistribution subject to ASME license or copyright; see http://www.asme.org/terms/Terms_Use.cfm

Y. Rabin[1]
Department of Mechanical Engineering,
Carnegie Mellon University,
5000 Forbes Avenue,
Pittsburgh, PA 15213-3890
and
Department of Human Oncology,
Allegheny University of the
Health Sciences,
320 East North Avenue,
Pittsburgh, PA 15212-4772

P. S. Steif
Department of Mechanical Engineering,
Carnegie Mellon University,
5000 Forbes Avenue,
Pittsburgh, PA 15213-3890
Mem. ASME.

Thermal Stresses in a Freezing Sphere and its Application to Cryobiology

Thermal stresses in an inwardly solidifying sphere are studied analytically. A closed-form solution is given which accounts for thermal expansion associated with temperature gradients and volume changes associated with phase transition. Consistent with the target application of cryopreservation of biological solutions and tissues, the material is modeled as elastic-perfectly plastic. Parametric studies using appropriate material properties and typical cryopreservation protocols suggest that strains associated with phase transition lead to far higher stresses than those associated with thermal expansion, with important implications for cryopreservation procedures.

Introduction

It is well known that freezing biological tissues can introduce severe damage. Sometimes this damage is intentional and desired, as is the case in cryosurgery. In other situations, such as cryopreservation, this damage is an undesired byproduct. This paper arises from efforts to quantify the development of mechanical stresses in freezing biological solutions and tissues and to relate such stresses to tissue damage. While mechanical stress is one mechanism of tissue destruction in cryobiology applications (Ishiguro and Rubinsky, 1994; Hunt et al., 1994; Gao et al., 1995), there are other mechanisms related to crystal growth and to the kinetics of freezing at the cellular level (Meryman, 1974; Mazur, 1984; Taylor, 1987).

Mechanical stress development in this class of problems has been analyzed by a number of researchers. Analyses of thermal stress associated with cryopreservation and with water freezing have been reported by Rubinsky et al. (1980) and Rubinsky (1982), who modeled the frozen tissue as a linear elastic material. An inverse-engineering analysis has been performed by Lin et al. (1990) for the estimation of mechanical properties of frozen water by comparison of predicted strains and experimental measurements. Expansion of the analysis to aqueous solutions containing cryoprotectants has been reported by Gao et al. (1995). Analysis of thermal stresses during cryosurgery has been reported by Rabin and Steif (1996), assuming an elastic-perfectly plastic model for the freezing tissue.

In this paper we reconsider the inward freezing of a body and propose several alternative modeling assumptions. While these assumptions are at odds with some of the analyses in the literature, particularly those carried out by workers motivated by cryobiological applications, we will argue the physical sensibility of these assumptions. In particular, we propose: (i) that the pressure in the core liquid region is important and cannot be neglected; (ii) that the nonhydrostatic part of the stress in the just-frozen region must be zero; and (iii) that the volume strain associated with freezing cannot be neglected and, in fact, appears to produce stresses that overwhelm stresses due to other sources. We note that the first two assumptions have been well appreciated by workers in the area of metal solidification and casting (Boley and Weiner, 1963; Tien and Richmond, 1982; Heinlein et al., 1986; Zabaras and Ruan, 1990; Zabaras et al., 1991). The third assumption may not be significant in metal solidification; however, in contrast to metals, aqueous solutions, and presumably biological tissues, expand severely upon solidification.

The purpose of this paper, therefore, is primarily to present a credible set of modeling assumptions, which are new to the calculation of freezing solutions and tissues, and to show that these assumptions radically change the accepted picture of stress development during cryopreservation. We note that the solution is based on the highly idealized spherically symmetric problem, which, with respect to the nonsymmetric freezing problem, likely leads to upper bounds on stresses and pressures. Nevertheless, the spherical symmetry simplifies the solution and allows the analysis and discussion to focus on the new approach to calculating mechanical stresses in freezing materials.

Analysis

The material domain under consideration is the sphere occupying the region $0 < r < R$, as illustrated in Fig. 1. The entire domain is initially liquid at the phase transition temperature, and a freezing front then starts to propagate inwards. The freezing front location, h_f, as well as the temperature distribution, are assumed to be determined purely by the heat transfer problem, which is discussed in the next section.

Solid Mechanics Problem. Within the material domain, the usual field equations of continuum mechanics, specialized to the spherically symmetric geometry, are assumed to prevail. These equations include mechanical equilibrium

$$\frac{d\sigma_r}{dr} + \frac{2}{r}(\sigma_r - \sigma_\theta) = 0 \tag{1}$$

and the strain displacement relations

$$\epsilon_r = \frac{du}{dr}; \quad \epsilon_\theta = \frac{u}{r} \tag{2}$$

where σ is the stress, ϵ is the strain, and u is the radial displacement.

[1] To whom correspondence should be addressed. Currently at the Department of Mechanical Engineering, Technion-Israel Institute of Technology, Technion City, Haifa 32000, Israel. e-mail: yoed@tx.technion.ac.il.

Contributed by the Applied Mechanics Division of THE AMERICAN SOCIETY OF MECHANICAL ENGINEERS for publication in the ASME JOURNAL OF APPLIED MECHANICS.

Discussion on this paper should be addressed to the Technical Editor, Professor Lewis T. Wheeler, Department of Mechanical Engineering, University of Houston, Houston, TX 77204-4792, and will be accepted until four months after final publication of the paper itself in the ASME JOURNAL OF APPLIED MECHANICS.

Manuscript received by the ASME Applied Mechanics Division, Feb. 17, 1997; final revision, Aug. 11, 1997. Associate Technical Editor: S. A. Berger.

 Copyright © 1998 by ASME

Downloaded 04 May 2010 to 171.66.16.26. Redistribution subject to ASME license or copyright; see http://www.asme.org/terms/Terms_Use.cfm

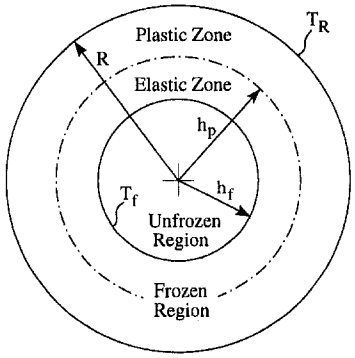


Fig. 1 Geometry of the phase transition problem of an inwardly freezing sphere, where R is the sphere outer surface, h_f is the freezing front, h_p is the interface between the elastic and plastic zones (also referred to as plastic front), T_f is the freezing temperature, and T_R is the forced temperature at the sphere outer surface

The constitutive relations are most conveniently expressed in terms of deviatoric and hydrostatic components of stress and strain. To that end, we define

$$\sigma_{ij} = S_{ij} - p\delta_{ij} \tag{3}$$

and

$$\epsilon_{ij} = \epsilon'_{ij} + \tfrac{1}{3}e\delta_{ij} \tag{4}$$

where S is the deviatoric stress, p is the hydrostatic pressure, ϵ' is the deviatoric strain, and e is the volume strain.

The liquid is assumed to be inviscid and therefore sustains only a hydrostatic pressure p, which is related to the volume strain according to

$$p = -\kappa(e - e_{th}) \quad 0 < r < h_f \tag{5}$$

where κ is the bulk modulus ($=E/[3(1-2\nu)]$) and the thermal strain is

$$e_{th} = \int^T \beta dT \tag{6}$$

where β is the thermal expansion coefficient.

The mechanical behavior of frozen biological tissues is very complex and not well understood. In the case of cryopreservation, it is common to employ cryoprotectants; these cause the unfrozen tissue to partly vitrify (become glassy) rather than freeze (transform to a crystalline solid). Vitrified material is likely to experience time-dependent deformation due to relaxation processes. Here, we ignore vitrification presuming solidification without cryoprotectants. There is evidence that the solid material, at least under compression and without cryoprotectants, deforms elastically until a critical level of stress at which point a pseudo-plasticity occurs, associated with the formation of microcracks (Rabin, et al., 1996). Therefore, we will consider two possible constitutive relations for the solid: either an elastic model or an elastic-perfectly plastic model.

A critical step in formulating the constitutive relation for the solid is to recognize that arbitrary deviatoric (volume preserving) strains could have occurred in the liquid state prior to solidification. The strains from which one calculates the deviatoric stress must be the total accumulated strains since the beginning of the contemplated process minus the strains accumulated up to the instant just after solidification. In the case of an elastic solid, the deviatoric stress can be written as

$$S_{ij} = 2G(\epsilon'_{ij} - \epsilon'^*_{ij}) \quad h_f < r < R \tag{7}$$

where ϵ'^*_{ij} is the deviatoric strain just after solidification, and G is the shear modulus ($=E/[2(1+\nu)]$). Consistent with the assumption of isotropy, we have presumed the thermal strains to have zero deviatoric part.

The hydrostatic pressure in the solid is given by

$$p = -\kappa[(e - e_{th}) - \Delta e] \quad h_f < r < R \tag{8}$$

where Δe is the volumetric strain upon freezing. The bulk modulus in the solid, κ, is assumed to be equal to the value in the liquid; more discussion of this assumption will be given below. As noted above, the volume strain upon freezing does not seem to have been incorporated previously, at least the context of cryobiology.

The boundary conditions consist of zero radial stress on the outer surface,

$$\sigma_r(R) = 0, \tag{9}$$

and continuity of radial stress and displacement at the freezing front, respectively,

$$\sigma_r(h_f)|_1 = \sigma_r(h_f)|_2, \tag{10}$$

and

$$\epsilon_\theta(h_f)|_1 = \epsilon_\theta(h_f)|_2 \tag{11}$$

where the indexes 1 and 2 indicate the unfrozen and frozen regions, respectively. The displacement continuity in Eq. (11) has been rewritten in terms of the hoop strain using the strain-displacement relations.

The forgoing equations are readily solved as follows. The liquid is initially at the phase transition temperature and, thus, the thermal strains in the liquid region are zero. The solution in liquid can be written in terms of the uniform liquid pressure p_1:

$$u = -\frac{p_1}{3\kappa} r \quad 0 < r < h_f. \tag{12}$$

It will be useful for the ensuing analysis to recast the condition of radial stress continuity as a condition on the radial strains; by combining Eqs. (5), (8), (10), and (11), one finds

$$\epsilon_r(h_f)|_2 = \epsilon_r(h_f)|_1 + \Delta e. \tag{13}$$

To derive an equation governing the displacement in the solid domain, it is necessary to evaluate the quantity ϵ'^*_{ij}, which for the case of spherical symmetry corresponds to $\epsilon_r - \epsilon_\theta$. From Eqs. (11)–(13), the difference $(\epsilon_r - \epsilon_\theta)^*$ is found to be simply

$$(\epsilon_r - \epsilon_\theta)^* = \epsilon_r(h_f)|_2 - \epsilon_\theta(h_f)|_2 = \Delta e. \tag{14}$$

We recapitulate the significance of this term: the liquid undergoes a deviatoric strain equal to Δe prior to becoming solid, and, as reflected in Eq. (7), this strain should not be counted in determining the deviatoric stresses in the solidified material.

It is now possible to express S_r and p in terms of the radial displacement, u, and the various other known quantities and substitute into the equation of equilibrium; the result is

$$\frac{4}{3}G\left[u'' - \left(\frac{u}{r}\right)'\right] + \kappa\left[u'' + 2\left(\frac{u}{r}\right)' - e'_{th}\right] + \frac{4G}{r}\left[u' - \frac{u}{r} - \Delta e\right] = 0. \tag{15}$$

The solution of this equation is

$$u = \frac{3\kappa}{4G + 3\kappa}\frac{1}{r^2}\int_{h_f}^{r} e_{th} r^2 dr + \frac{4G\Delta e}{4G + 3\kappa} r\left[\ln\left(\frac{r}{h_f}\right) - \frac{1}{3}\right] + B_1 r + \frac{B_2}{r^2} \quad h_f < r < R \tag{16}$$

Downloaded 04 May 2010 to 171.66.16.26. Redistribution subject to ASME license or copyright; see http://www.asme.org/terms/Terms_Use.cfm

where the integration constant B_1 is calculated from boundary condition (10), by expressing the hydrostatic pressure in the solid in terms of the displacement, while taking in account zero deviatoric stress in the solid region at the freezing front,

$$B_1 = \frac{1}{3}\left(\Delta e - \frac{p_l}{\kappa}\right). \tag{17}$$

The integration constant B_2 is determined from condition (11), by comparing Eqs. (12) and (16) at the freezing front,

$$B_2 = -\frac{h_f^3 \kappa \Delta e}{4G + 3\kappa}. \tag{18}$$

Note that the previous solutions related to cryobiology do not meet the assumption of zero deviatoric stress at the freezing front.

The solution now depends only on the liquid pressure p_l, via constant B_1. This quantity is determined by setting the radial stress equal to zero at the sphere outer surface, Eq. (9), which leads to

$$p_l = -\frac{4G\kappa}{4G + 3\kappa}\left\{\frac{3}{R^3}\int_{h_f}^{R} e_{th} r^2 dr + \Delta e\left[1 - 3\ln\left(\frac{R}{h_f}\right) - \left(\frac{h_f}{R}\right)^3\right]\right\}. \tag{19}$$

Final forms for the deviatoric stress and hydrostatic pressure in the solid region are, respectively,

$$S_r = -\frac{1}{2}S_\theta = \frac{4G\kappa}{4G + 3\kappa}\left[-\frac{3}{r^3}\int_{h_f}^{r} e_{th} r^2 dr + e_{th} + \Delta e\left(\frac{h_f^3}{r^3} - 1\right)\right] \tag{20}$$

and

$$p = \frac{4G\kappa}{4G + 3\kappa}\left[e_{th} - 3\Delta e \ln\left(\frac{r}{h_f}\right)\right] + p_l. \tag{21}$$

It is worth noting that the solution depends linearly both on the phase transition volume strain, Δe, and on the thermal strain, e_{th}. In the results and discussion presented below, two typical cases related to cryopreservation will be considered in order to study in a quantative manner the effects of the phase transition volume strain and of the thermal strain.

The solution assuming an elastic-perfectly plastic response in the solid turns out to be quite simple, assuming the Mises yield condition (Hill, 1950) specialized to spherical symmetry,

$$|\sigma_r - \sigma_\theta| = \tfrac{3}{2}|S_r| = \sigma_y, \tag{22}$$

where σ_y is the yield strength. As will be seen in the results and discussion section, the deviatoric stress S_r is maximal at the outer boundary, which is therefore where plasticity initiates. As the process continues, the plastic front, h_p, which separates the zones of elastic and plastic deformations, moves inwards from the outer surface, Fig. 1. Under the assumption that the flow stress remains constant independent of the pressure, one finds the stress distribution in the plastic zone to be fully determined by equilibrium, Eq. (1), by the yield condition, Eq. (22), and by the stress-free condition on the outer boundary, Eq. (9). Specifically, the pressure in the plastic region is given by

$$p = 2\sigma_y\left[\ln\left(\frac{R}{r}\right) - \frac{1}{3}\right] \quad h_p < r < R. \tag{23}$$

The location of the plastic front is also readily determined: the previous solution for the deviatoric stress in the elastic zone, Eq. (20), which was independent of the pressure in the liquid, p_l, remains valid. Thus, the location of the plastic front h_p is that position r at which the absolute value of S_r from Eq. (20) just reaches the yield value of $2\sigma_y/3$. The elastic-plastic interface merely progresses inwards as the freezing front moves inwards.

The pressure in the elastic zone is fully determined once the pressure in the liquid is known. The liquid pressure is chosen so as to match the pressure at the plastic front coming from the elastic side, Eq. (21), with the pressure from the plastic side, Eq. (23); the resulting equation is

$$p_l = 2\sigma_y\left[\ln\left(\frac{R}{h_p}\right) - \frac{1}{3}\right] + \frac{4G\kappa}{4G + 3\kappa}\left[3\Delta e \ln\left(\frac{h_p}{h_f}\right) - e_{th}\right]. \tag{24}$$

Heat Transfer Problem. A perturbation solution of the inward freezing sphere, initially at the phase-change temperature and subject to a step-like change of the outer surface temperature, has been given by Riley et al. (1974). The perturbation variable is the Stefan number, F, which is the ratio of sensible heat to latent heat for the phase-change process. With the following dimensionless variables and parameters

$$\eta = \frac{R - h_f}{R}; \quad \zeta = \frac{r}{R}; \quad F = \frac{C(T_f - T_R)}{L}; \quad \tau = \frac{\alpha t F}{R^2}; \quad \phi = \frac{T - T_R}{T_f - T_R}, \tag{25}$$

the dimensionless temperature distribution, ϕ, is given by

$$\phi = \frac{(1-\eta)(1-\zeta)}{\eta\zeta} + \frac{F(1-\zeta)}{6\zeta\eta(1-\eta)}\left[1 - \left(\frac{1-\zeta}{\eta}\right)^2\right] - \frac{F^2(1-\zeta)}{\zeta\eta(1-\eta)^3}\left\{\frac{1}{36}\left[1 - \left(\frac{1-\zeta}{\eta}\right)^2\right] + \frac{(3-4\eta)}{120}\left[1 - \left(\frac{1-\zeta}{\eta}\right)^4\right]\right\} + O(F^3) \tag{26}$$

where C is the specific heat, L is the latent heat, and α is the thermal diffusivity. The dependancy of the freezing front location on time is given implicitly by

$$\tau = \frac{3\eta^2 - 2\eta^3}{6} + \frac{\eta^2 F}{6} - \frac{\eta^2 F^2}{45(1-\eta)} + O(F^3). \tag{27}$$

The perturbation solution given here is accurate up to the third order, which provides a very good approximation for the purpose of the current study. This approximation is fairly good until the ratio of freezing front location to sphere radius, h_f/R, reaches the value of 0.2 (when more than 99 percent of the sphere volume has already changed phase). A modified solution has been derived by Riley et al. (1974) for the end of the phase-change process, a short period during which the freezing front approaches the origin.

Downloaded 04 May 2010 to 171.66.16.26. Redistribution subject to ASME license or copyright; see http://www.asme.org/terms/Terms_Use.cfm

Material Properties. It is widely assumed that soft biological tissues have physical properties similar to those of aqueous solutions. Recent experiments (Rabin et al., 1996) have shown that frozen tissues loaded in compression in cryogenic temperatures respond roughly like an elastic-perfectly plastic solid, with the plasticity apparently stemming from distributed microcracking (Rabin et al., 1997a). The thermal expansion was found (Rabin et al., 1997b) to be similar to that of water with the coefficient of thermal expansion being almost a linear function of temperature. These observations motivate the adoption of an elastic-perfectly plastic model for the frozen material, with the thermal expansion coefficient varying linearly with temperature. Since data is not available on the mechanical properties of biological tissues within the phase transition temperature range, we will assume that the behavior is similar to that of a pure material (freezing at a single temperature).

There are at least nine known different pure water ice phases (Fletcher, 1970). Ice *I* is the most relevant ice phase for the current study; this is the only phase in which water expands upon freezing. Solidification of ice *I* takes place between pressures of 5 kPa and 207 MPa, while the phase transition temperature decreases monotonously from 0.01°C to −22°C, respectively. At higher pressures water contracts upon freezing and the freezing temperature increases continually with pressure (up to at least 4.4 GPa and 440°C). Due to lack of relevant data for biological materials, the volume strain upon phase transition is assumed constant, and equal to that of water at standard conditions of temperature and pressure, that is, $\Delta e = 0.0907$. Other physical properties are assumed to be constant and uniformly distributed in each phase; relevant physical properties values for water, soft frozen biological tissues, and the chosen values for the current study, are listed in Table 1.

The assumption of equal bulk moduli in the liquid and solid phases is largely one of convenience. There is much uncertainty regarding the bulk modulus of ice, although if inferred from measured elastic moduli and a reasonable value of Poisson's ratio, it may be up to four times that of water at standard conditions. Choosing differing bulk moduli substantially complicates the constitutive description as well as the solution, since the strain difference at phase change $(\epsilon_r - \epsilon_\theta)^*$ will no longer be constant. Since rather strong qualitative conclusions are arrived at in this paper, we believed it unwise to introduce a second-order effect based on rather uncertain physical properties.

Finally, we note that biological tissues are composite materials which may have different physical properties in different orientations. The simplified analysis presented here presumes a homogeneous material only, which can be identified with, say, the average property values. The modeling of a biological tissue as a composite material is beyond the scope of this paper.

Table 1 Typical properties of polycrystalline ice water and soft frozen biological tissues

	Polycristalline Ice Water @ 101.3 kPa	Frozen Biological Tissues	Current Study
Poisson's Ratio, ν	0.31 - 0.36 (Fletcher, 1970)	-	0.33
Volume Strain of Phase Transition, Δe	0.0907 @ 0°C (Sohnel and Novotny, 1995)	-	0.0907
Thermal Expansion Coefficient: $\beta_3+\beta_4 T$ [1/°C]	$\beta_3=56.3\cdot10^{-6}$ $\beta_4=2.53\cdot10^{-7}$ -180°C<T<0°C (Powell, 1958)	$\beta_3=65\cdot10^{-6}$ $\beta_4=2.89\cdot10^{-7}$ -180°C<T<-20°C (Rabin et al., 1997b)	$\beta_3=60\cdot10^{-6}$ $\beta_4=2.5\cdot10^{-7}$
Elastic Modulus, E [GPa]	8.9 - 9.9 @ -5°C (Fletcher, 1970)	14 - 132 @ -196°C (Rabin et al., 1996)	10

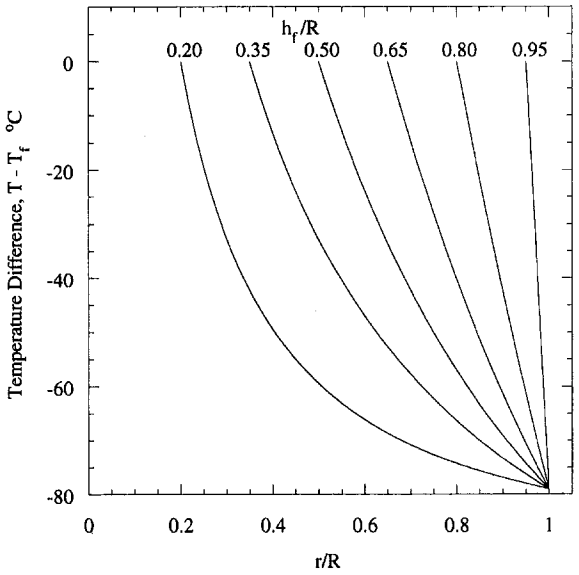


Fig. 2 Temperature distribution in case *A*, where a step-like temperature function is imposed at the sphere outer surface ($\Delta T = -79$°C)

Results and Discussion

Since the solution for the elastic response in the solid depends independently on the two "driving forces," that is, the thermal expansion in the solid state and the volume expansion due to phase transition, we consider these separately. Case A corresponds to neglecting the volume expansion due to phase transition and accounting for a temperature history which is the consequence of immersion in dry ice, i.e., a step-like temperature function is imposed at the sphere outer surface having a magnitude of −79°C. Case B, which approximates a typical cryopreservation protocol, corresponds to maintaining the material at nearly the phase transition temperature and allowing the phase transition to occur, presuming the volume strain is that which occurs at standard atmospheric pressure, i.e., $\Delta e = 0.0907$.

The temperature distribution for case A is shown in Fig. 2, where the corresponding Stephen number for pure water ice equals 0.27. As mentioned above, this solution is valid until the freezing front reaches 20 percent of the sphere radius (when more than 99 percent of the sphere volume is frozen). The deviatoric stresses and hydrostatic pressures for this case are shown in Figs. 3 and 4, respectively. Note first that the hydrostatic pressure in the liquid is by no means zero, and that it increases as the freezing process proceeds. Not surprisingly, this is at odds with the assumption that the pressure in the liquid is zero, as has been suggested previously for the analysis of a similar problem (Rubinsky et al., 1980). A second clear distinction between the current solution and previously reported solutions, most of which are for cryobiology applications (Rubinsky et al., 1980; Rubinsky, 1982; Lin et al., 1990; Gao et al., 1995; Rabin and Steif, 1996), is that the deviatoric stress here is zero at the freezing front (and increases monotonously as one approaches the sphere outer surface). This stems from the assumption that the deviatoric stress must be zero in recently solidified material, since no straining has yet occurred in the solid state. Finally, it is important to point to the magnitude of the predicted deviatoric stress: it is maximum at the initiation of the process, when the step-like temperature function is imposed at the sphere outer surface. This stress decreases with time, as the freezing front propagates inwards. The strains to initiate plasticity are in the order of 0.005 in frozen biological tissues (tested in compression; Rabin et al., 1996) and are not expected to exceed this value in polycrystalline water ice at low strain rates (Fletcher, 1970). It appears, in conclusion, that relative little plasticity would occur, if at all, during a sudden

Downloaded 04 May 2010 to 171.66.16.26. Redistribution subject to ASME license or copyright; see http://www.asme.org/terms/Terms_Use.cfm

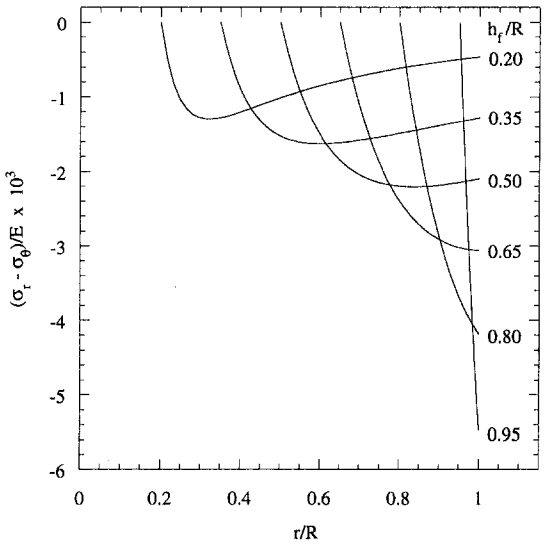


Fig. 3 Deviatoric stress distribution for case *A*, where no phase transition volume changes are included

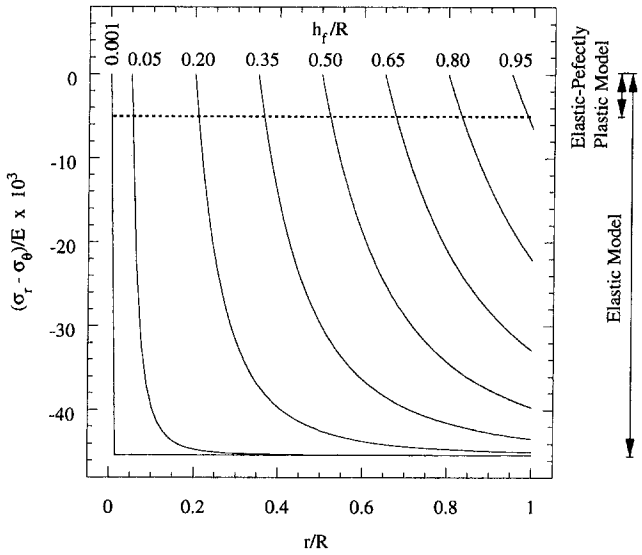


Fig. 5 Deviatoric stress distribution for case *B* ($\Delta e = 0.0907$; $\Delta T = 0$). The dashed line represents the extreme deviatoric stress in the case of an elastic-perfectly plastic model and a yield strain of 0.005.

cool down to dry ice temperatures, when volume straining due to phase transition is prevented. In practice, the stresses are expected to be somewhat lower in magnitude at the initiation of the process than those presented in Fig. 3. The idealized boundary condition of a step change in temperature produces infinite gradients initially, while in practice a finite time is necessary to bring the surface down to the lower temperature.

Consider now case B featuring only volume strain due to phase transition and no temperature gradients. With a linear elastic model for the solid, the stresses reach enormous values (Fig. 5); this might be expected given the rather large imposed strain associated with phase transition. Clearly, the linear elastic model for case B is unrealistic, considering a typical yield strain in the order on 0.005. The deviatoric stress, as in case A, varies from zero at the freezing front to a maximum at the sphere outer surface. This allows one to use the elastic-plastic solution derived above. The deviatoric strains for the case of an elastic-perfectly plastic solid is also presented in Fig. 5, assuming a yield strain of 0.005. The deviatoric stresses in the plastic zone are represented by the dashed line in Fig. 5. Note that almost the entire frozen region experiences plastic deformations as the freezing front approaches the origin.

The hydrostatic pressures for the more realistic case of elastic-plastic deformations are shown in Fig. 6. The analysis present in this study is valid for solidification of ice *I* only, which is the only case of volume expansion upon freezing. Taking into account the maximal hydrostatic pressure of ice *I*, i.e. 207 MPa, and assuming a typical elastic modulus of 10 GPa, one can see from Fig. 6 that the solution is not valid as the freezing front approaches the origin due to the high pressure magnitude. It was found that the hydrostatic pressure in this case reaches 207 MPa when the ratio of freezing front location to sphere radius reaches the value of 0.1 approximately, i.e., when 99.9 percent of the sphere volume is frozen, although the size of this region increases with the yield strength. The sequence of events after this late stage is unclear.

Finally, in case B freezing was assumed to occur when the temperature was held at the freezing point. However, it was

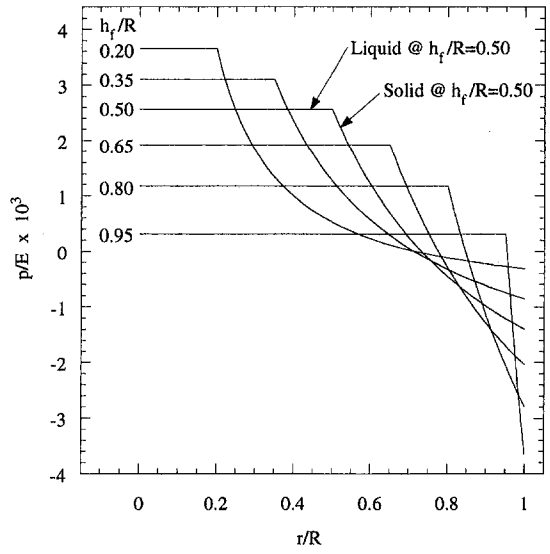


Fig. 4 Hydrostatic pressure distribution for case *A*

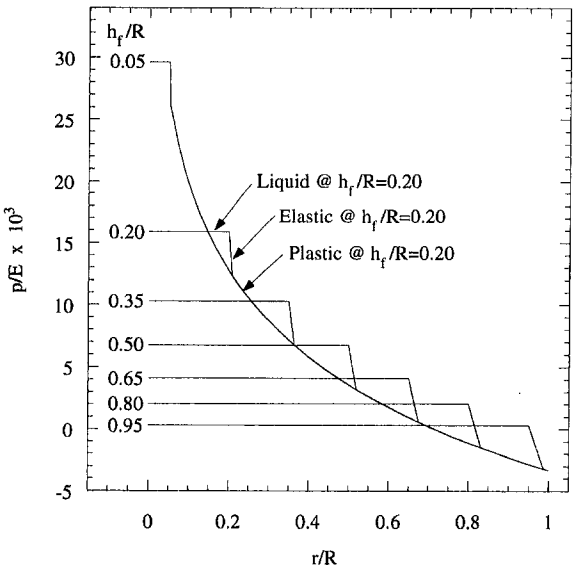


Fig. 6 Hydrostatic pressure distribution for case *B*, assuming an elastic-perfectly plastic model and yield strain of 0.005 ($\Delta e = 0.0907$; $\Delta T = 0$)

Downloaded 04 May 2010 to 171.66.16.26. Redistribution subject to ASME license or copyright; see http://www.asme.org/terms/Terms_Use.cfm

demonstrated that the hydrostatic pressures in the liquid may reach the critical pressure which corresponds to a transition temperature of −22°C. For this reason the imposed surface temperature will need to be reduced accordingly (but slowly) to complete freezing the sphere.

Summary and Conclusions

A closed-form solution for the thermal stresses in an inward solidifying sphere has been presented. The formulation accounts for thermal expansion associated with temperature gradients and volume changes associated with phase transition. The frozen medium is modeled as an elastic-perfectly plastic.

For physical properties similar to those of water, parametric studies have shown that the effect of volume expansion upon phase transition is much more significant than the effect of thermal expansion in generating stresses, at least in a typical cryopreservation protocol. It has been shown that a plastic zone is likely to occupy most of the frozen region after the completion of the freezing process. It follows that the attendant potential for tissue destruction is unavoidable regardless of how slowly the freezing is carried out, provided there is a substantial expansion associated with phase transition. Finally, the phase transition temperature may significantly decrease during the cryopreservation process, due to the elevated hydrostatic pressure in the unfrozen region.

References

Boley, B. A., and Weiner, J. H., 1963, "Elasto-Plastic Thermal Stress in a Solidifying Body," *J. Mech Phys Solids,* Vol. 11, pp. 145–154.

Fletcher, N. H., 1970, *The Chemical Physics of Ice,* Cambridge University Press, Cambridge, UK.

Gao, D. Y., Lin, S., Watson, P. F., and Critser, J. K., 1995, "Fracture Phenomena in an Isotonic Salt Solution During Freezing and Their Elimination Using Glycerol," *Cryobiology,* Vol. 32, pp. 270–284.

Heinlein, M., Mukherjee, S., and Richmond, O., 1986, "A Boundary Element Method Analysis of Temperature Fields and Stresses During Solidification," *Acta Mechanica,* Vol. 59, pp. 59–81.

Hill, R., 1950, *Mathematical Theory of Plasticity,* Oxford University Press, London.

Hunt, C. J., Song, Y. C., Bateson, A. J., and Pegg, E. D., 1994, "Fractures in Cryopreserved Arteries," *Cryobiology,* Vol. 31, pp. 506–515.

Ishiguro, H., and Rubinsky, B., 1994, "Mechanical Interaction Between Ice Crystals and Red Blood Cells During Directional Solidification," *Cryobiology,* Vol. 31, pp. 483–500.

Lin, S., Gao, D. Y., and Yu, X. C., 1990, "Thermal Stress Induced by Water Solidification in a Cylindrical Tube," ASME *Journal of Heat Transfer,* Vol. 112, pp. 1079–1082.

Mazur, P., 1984, "Freezing of Living Cells: Mechanisms and Implications," *Am J Physiol.,* Vol. 247, pp. C125–C142.

Meryman, H. T., 1974, "Freezing Injury and its Prevention in Living Cells," *Annual Review of Biophysics and Bioengineering,* Vol. 3, pp. 341–363.

Powell, R. W., 1958, "Thermal Conductivity and Expansion Coefficients of Water and Ice," *Adv. Phys.,* Vol. 7, pp. 276–297.

Rabin, Y., and Steif, S. P., 1996, "Analysis of Thermal Stresses Around Cryosurgical Probe," *Cryobiology,* Vol. 33, pp. 276–290.

Rabin, Y., Steif, S. P., Taylor, M. J., Julian, T. B., and Wolmark, N., 1996, "An Experimental Study of the Mechanical Response of Frozen Biological Tissues at Cryogenic Temperatures," *Cryobiology,* Vol. 33, pp. 472–482.

Rabin, Y., Olson, P., Taylor, M. J., Steif, P. S., Julian, T. B., and Wolmark, N., 1997a, "Gross Damage Accumulation in Frozen Rabbit Liver Due to Mechanical Stress at Cryogenic Temperatures," *Cryobiology,* Vol. 34, pp. 394–405.

Rabin, Y., Taylor, M. J., and Wolmark, N., 1997b, "Thermal Expansion Measurements of Frozen Biological Tissues at Cryogenic Temperatures," ASME *Journal of Biomechanical Engineering,* in press.

Riley, D. S., Smith, F. T., and Poots, G., 1974, "The Inward Solidification of Spheres and Circular Cylinders," *International J. of Heat and Mass Transfer,* Vol. 17, pp. 1507–1516.

Rubinsky, B., Cravalho, E. G., and Mikic, B., 1980, "Thermal Stress in Frozen Organs," *Cryobiology,* Vol. 17, pp. 66–73.

Rubinsky, B., 1982, "Thermal Stress During Solidification," ASME *Journal of Heat Transfer,* Vol. 104, pp. 196–199.

Sohnel, O., and Novotny, P., 1995, *Densities of aqueous solution of inorganic substances,* Elsevier, New York.

Taylor, M. J., 1987, "Physico-chemical Principles in Low Temperature Biology," *The Effect of Low Temperature on Biological Systems,* B. W. W. Grout, and G. J. Morris, eds., pp. 3–71.

Tien, R. H., and Richmond, O., 1982, "Theory of Maximum Tensile Stresses in the Solidifying Shell of a Constrained Rectangular Casting," ASME JOURNAL OF APPLIED MECHANICS, Vol. 49, pp. 481–486.

Zabaras, N., and Ruan, Y., 1990, "Front Tracking Thermomechanical Model for Hypoelastic-Viscoplastic Behavior in a Solidifying Body," *Computer Methods in Applied Mechanics and Engineering,* Vol. 81, pp. 333–364.

Zabaras, N., Ruan, Y., and Richmond, O., 1991, "On the Calculation of Deformations and Stresses During Axially Symmetric Solidification," ASME JOURNAL OF APPLIED MECHANICS, Vol. 58, pp. 865–871.

Downloaded 04 May 2010 to 171.66.16.26. Redistribution subject to ASME license or copyright; see http://www.asme.org/terms/Terms_Use.cfm

Refined Dynamic Stability Theory of Laminated Isotropic Circular Plates

G. Krizhevsky
Postdoctoral Researcher.

Y. Stavsky
Gerard Swope Professor of Mechanics, Mem. ASME.

Faculty of Aerospace Engineering, Technion-Israel Institute of Technology, Haifa 32000, Israel

Hamilton's variational principle is used for the derivation of transversally isotropic laminated circular plates motion. Nonlinear strain-displacements relations are considered. Linearized dynamic stability equations are obtained for circular plates subjected to the same uniformly distributed periodic radial loads. The effects of transverse shear and rotational inertia are included. The exact solutions of vibrations and buckling problems are given initially in the terms of Bessel, power, and trigonometric functions. The vibrational modal functions are used then as a basis in the Galerkin method that reduced the study of dynamic stability to investigation of bounds of instability of Mathieu's equations. Analytic expressions for the bounds of both principal and combination-type instability regions are obtained using the methods of Bolotin and Tamir. A new effect—sensitivity of certain instability regions to slight imperfections in the symmetry of lamination—is found out and discussed here.

1 Introduction

The stability problem for rectangular, circular, and annular plates subjected to the longitudinal periodic forces was solved first by Bodner (1938) applying series and Galerkin methods. The dynamic stability of thin isotropic clamped circular plate was studied analytically by Reckling (1953a). The dynamic stability of rectangular plates under various periodic force was studied by Bolotin (1964a) in geometrically nonlinear formulation with accounting of energy dissipation. Hutt and Salam (1971) have used the thin plate finite element model to study the dynamic stability of rectangular plates. Tani and Nakamura (1978) employed the Galerkin-Kantorovich method to investigate the dynamic stability of annular plates under periodic radial loads. The parametric resonance of orthotropic annular plates subjected to the periodic radial forces have been studied by Tani and Doki (1982). The dynamic stability and nonlinear response of parametrically excited rectangular plates are analized theoretically by Nguyen and Ostiguy (1989), and experimentally by Nguyen, Ostiguy, and Samson (1989) to reveal effect of boundary conditions. The dynamic stability of nonlinear antisymmetrically laminated rectangular plates under determinisic or stochastic membrane forces was investigated by Tylikowski (1989). The works named are concerned to the classical Kirchhoff plate model. The Mindlin plate finite element has used by Chen and Jang (1987) for the dynamic stability problem of a bimodulus moderately thick circular plate subjected to a combination of a pure dynamic bending and uniform dynamic extensional stress. The dynamic stability problem for composite laminated rectangular plates under uniaxial, harmonically varying, in-plane loads was solved by Moorthy, Reddy, and Plaut (1990); the transverse shear deformation was considered and the finite element formulation was used.

The purpose of the present paper is to determine the dynamic stability regions for the laminated transversally isotropic circular plates, subjected to uniformly distributed periodic radial loads based on the exact solution for the vibrations of the plate loaded by the constant constitutive of the excitation forces.

2 Problem Formulation

Let us consider a laminated circular plate composed of linearly elastic transversally isotropic layers with constant thickness compressed by the forces with intensity $\tilde{N}_0 + \tilde{N}_1 \cos 2\omega t$ uniformly distributed along the contour and acting in the reference surface. The elastic and inertia properties are assumed to be only thickness dependent.

The first-order shear deformation theory is accepted to describe displacements distribution through the plate

$$\{\tilde{u}_r, \tilde{u}_\theta, \tilde{w}\} = \{\tilde{u}_r^0, \tilde{u}_\theta^0, \tilde{w}^0\} + \tilde{z}\{\psi_1, \psi_2, 0\} \qquad (1)$$

where $\{z, r, u_r, u_\theta, w\} = \{\tilde{z}, \tilde{r}, \tilde{u}_r^0, \tilde{u}_\theta^0, \tilde{w}\}/a$, a–plate radius, $\{\tilde{r}, \theta\}$–polar coordinates (Fig. 1).

The strain-displacement relations utilized here take into account the second-order displacement terms associated with transverse deflection only.

The transverse normal stress σ_z has the order $(h/a)^2$ as compared with membrane normal stresses and assumed here to be equal to zero. Using the aforesaid, the linear stress-strain relations for transversally isotropic material may be rewritten as follows:

$$\begin{pmatrix}\sigma_r\\ \sigma_\theta\end{pmatrix} = \begin{pmatrix}E_{11} & E_{12}\\ E_{12} & E_{11}\end{pmatrix}\begin{pmatrix}\epsilon_r\\ \epsilon_\theta\end{pmatrix},$$

$$\begin{pmatrix}\sigma_{\theta z}\\ \sigma_{rz}\end{pmatrix} = \begin{pmatrix}G_z & 0\\ 0 & G_z\end{pmatrix}\begin{pmatrix}\epsilon_{\theta z}\\ \epsilon_{rz}\end{pmatrix}, \quad \sigma_{r\theta} = G\epsilon_{r\theta} \qquad (2)$$

where $E_{11} = E/(1-\nu^2)$, $E_{12} = \nu E_{11}$, $G = E/2(1+\nu)$.

E, G_i are Young and shear moduli, ν–Poisson's ratio which are assumed to be only thickness dependent.

Dynamic Equations. Using the Hamilton's variational principle applied to the three-dimensional functional of the plate energy, in view of (2) and then considering the small perturbations of the prebuckling stress-strain state which is found from the linear plate equations for the axisymmetric deformation, one obtains the following equations of motion in dimensionless form:

$$L_{ij}U_j = 0 \qquad (3)$$

($i, j = 1, 2, \ldots, 5$, summing on j is supposed here)

Contributed by the Applied Mechanics Division of THE AMERICAN SOCIETY OF MECHANICAL ENGINEERS for publication in the ASME JOURNAL OF APPLIED MECHANICS.

Discussion on this paper should be addressed to the Technical Editor, Professor Lewis T. Wheeler, Department of Mechanical Engineering, University of Houston, Houston, TX 77204-4792, and will be accepted until four months after final publication of the paper itself in the ASME JOURNAL OF APPLIED MECHANICS.

Manuscript received by the ASME Applied Mechanics Division, Apr. 15, 1994; final revision, July 21, 1994. Associate Technical Editor: W. K. Lin.

Downloaded 04 May 2010 to 171.66.16.26. Redistribution subject to ASME license or copyright; see http://www.asme.org/terms/Terms_Use.cfm

$$\{U_1, U_2, U_3, U_4, U_5\} = \{u_r, u_\theta, w, \psi_1, \psi_2\}, \quad (3a)$$

nonzero operators in (3) are

$$L_{11} \equiv L + \frac{\gamma_3}{r}\frac{\partial^2}{\partial\theta^2} + k_u r\frac{\partial^2}{\partial\tau^2}, \quad L \equiv r\frac{\partial^2}{\partial r^2} + \frac{\partial}{\partial r} - \frac{1}{r},$$

$$L_{12} \equiv \left((\gamma_1 + \gamma_3)\frac{\partial}{\partial r} - \frac{1+\gamma_3}{r}\right)\frac{\partial}{\partial\theta}$$

$$L_{14} \equiv \xi_1 L + \frac{\xi_3}{r}\frac{\partial^2}{\partial\theta^2} + k_\psi r\frac{\partial^2}{\partial\tau^2},$$

$$L_{15} \equiv \left((\xi_2 + \xi_3)\frac{\partial}{\partial r} - \frac{\xi_1+\xi_3}{r}\right)\frac{\partial}{\partial\theta}$$

$$L_{21} \equiv \left((\gamma_1 + \gamma_3)\frac{\partial}{\partial r} + \frac{1+\gamma_3}{r}\right)\frac{\partial}{\partial\theta},$$

$$L_{22} \equiv \gamma_3 L + \frac{1}{r}\frac{\partial^2}{\partial\theta^2} + k_u r\frac{\partial^2}{\partial\tau^2}$$

$$L_{24} \equiv \left((\xi_2 + \xi_3)\frac{\partial}{\partial r} + \frac{\xi_1+\xi_3}{r}\right)\frac{\partial}{\partial\theta},$$

$$L_{25} \equiv \xi_3 L + \frac{\xi_1}{r}\frac{\partial^2}{\partial\theta^2} + k_{\psi 1} r\frac{\partial^2}{\partial\tau^2}$$

$$L_{33} \equiv (1 - \bar{N}_0 - \bar{N}_1\cos 2\omega t) r(\nabla^2 + k_w)\frac{\partial^2}{\partial\tau^2},$$

$$\nabla^2 \equiv \frac{\partial^2}{\partial r^2} + \frac{1}{r}\frac{\partial}{\partial \mathrm{r}} + \frac{1}{r^2}\frac{\partial^2}{\partial\theta^2}$$

$$L_{34} \equiv r\frac{\partial}{\partial r} + 1, \quad L_{35} \equiv \frac{\partial}{\partial\theta},$$

$$L_{41} \equiv \eta_1 L + \frac{\eta_3}{r}\frac{\partial^2}{\partial\theta^2} + k_{u1} r\frac{\partial^2}{\partial\tau^2}$$

$$L_{42} \equiv \left((\eta_2 + \eta_3)\frac{\partial}{\partial r} - \frac{\eta_1+\eta_3}{r}\right)\frac{\partial}{\partial\theta}, \quad L_{43} \equiv -\zeta r\frac{\partial}{\partial r}$$

$$L_{44} \equiv L + \frac{\gamma_4}{r}\frac{\partial^2}{\partial\theta^2} - \zeta r + k_\psi r\frac{\partial^2}{\partial\tau^2},$$

$$L_{45} \equiv \left((\gamma_2 + \gamma_4)\frac{\partial}{\partial r} - \frac{1+\gamma_4}{r}\right)\frac{\partial}{\partial\theta}$$

$$L_{51} \equiv \left((\eta_2 + \eta_3)\frac{\partial}{\partial r} + \frac{\eta_1+\eta_3}{r}\right)\frac{\partial}{\partial\theta},$$

$$L_{52} \equiv \eta_3 L + \frac{\eta_1}{r}\frac{\partial^2}{\partial\theta^2} + k_{u1} r\frac{\partial^2}{\partial\tau^2}$$

$$L_{53} \equiv -\zeta\frac{\partial}{\partial\theta},$$

$$L_{54} \equiv \left((\gamma_2 + \gamma_4)\frac{\partial}{\partial r} + \frac{1+\gamma_4}{r}\right)\frac{\partial}{\partial\theta}$$

$$L_{55} \equiv \gamma_4 L + \frac{1}{r}\frac{\partial^2}{\partial\theta^2} - \zeta r + k_\psi r\frac{\partial^2}{\partial\tau^2} \quad (3b)$$

where

$$\xi_1 = B_{11}/A_{11}a, \quad \xi_2 = B_{12}/A_{11}a, \quad \xi_3 = B_{66}/A_{11}a,$$

$$\gamma_1 = A_{12}/A_{11}, \quad \gamma_2 = D_{12}/D_{11}, \quad \gamma_3 = A_{66}/A_{11},$$

$$\gamma_4 = D_{66}/D_{11}, \quad \eta_1 = B_{11}a/D_{11}, \quad \eta_2 = B_{12}a/D_{11},$$

$$\eta_3 = B_{66}a/D_{11}, \quad \zeta = \bar{A}a^2/D_{11}, \quad k_u = \lambda^2/\lambda_u, \quad k_\psi = \lambda^2/\lambda_\psi,$$

$$k_w = \lambda^2/\zeta, \quad k_{u1} = \lambda^2\lambda_{u1}, \quad k_{\psi 1} = \lambda^2\lambda_{\psi 1}, \quad \lambda_u = A_{11}a^2/D_{11},$$

$$\lambda_\psi = R_0 a^2/R_2, \quad \lambda_{u1} = R_1/R_0 a, \quad \lambda_{\psi 1} = \lambda_{u1}D_{11}/A_{11}a^2,$$

$$\lambda^2 = R_0 p^2 a^4/D_{11}, \quad \{\bar{N}_0, \bar{N}_1\} = \{\tilde{N}_0, \tilde{N}_1\}/\bar{A}, \tau = pt. \quad (3c)$$

$$\{A_{ij}, B_{ij}, D_{ij}\} = \int_{-h_0}^{h-h_0}\{1, \tilde{z}, \tilde{z}^2\}E_{ij}d\tilde{z},$$

$$\{R_0, R_1, R_2\} = \int_{-h_0}^{h-h_0}\{1, \tilde{z}, \tilde{z}^2\}\rho d\tilde{z} \quad (3d)$$

$E_{66} = G$, $E_{44} = G_z$, $\bar{A} = KA_{44}$, K—shear correction factor accepted here to be constant and $K = 5/6$, ρ is density of the material, p—scaling angular frequency (to be chosen appropriate to the concrete problem).

If the compressive load is the result of the effect of time-dependent temperature $T(\tilde{z}, t) = T_0(\tilde{z}, t) + T_1(\tilde{z}, t)\cos 2\omega t$, the constitutives $\{\tilde{N}_0, \tilde{N}_1\}$ in (3b) can be written as follows:

$$\tilde{N}_i = \int_{-h_0}^{h-h_0}\frac{\hat{\alpha}ET_i(\tilde{z})}{1-\nu}d\tilde{z} \quad (i = 0, 1) \quad (3e)$$

where $\hat{\alpha}$ is the coefficient of cubic expansion, h_0–distance from lower plate face to the reference surface, h–thickness.

Later on, it is assumed that a location of the reference surface is chosen to satisfy the condition

$$B_{11} = 0 \quad (\text{i.e., } \xi_1 = \eta_1 = 0). \quad (4)$$

3 Vibrations Solution

Let us consider a limiting case—$\bar{N}_1 = 0$—when the problem is degenerated into the quasi-free vibrations of the circular plate subjected to uniformly distributed radial forces with dimensionless intensity $\bar{N}_0$.

The solution of this problem satisfied the regularity requirements at the center can be found in closed form (scaling angular frequency p coincides here with eigenfrequency of the plate)

$$\{u_r, u_\theta, w, \psi_1, \psi_2\} = \{U_r, U_\theta, W, \Psi_1, \Psi_2\}\exp(i\tau) \quad (5)$$

$$U_r = \{\sum_{i=1}^{3} b_{1i}C_{1i}Z_n'(\mu_i r) + \frac{n}{r}\sum_{i=1}^{2} b_{2i}C_{2i}Z_n(\mu_{i+3}r)\}\cos n\theta \quad (6)$$

$$U_\theta = -\{\frac{n}{r}\sum_{i=1}^{3} b_{1i}C_{1i}Z_n(\mu_i r) + \sum_{i=1}^{2} b_{2i}C_{2i}Z_n'(\mu_{i+3}r)\}\sin n\theta \quad (7)$$

$$W = \sum_{i=1}^{3} b_{3i}C_{1i}Z_n(\mu_i r)\cos n\theta \quad (8)$$

$$\Psi_1 = \left\{\sum_{i=1}^{3} C_{1i}Z_n'(\mu_i r) + \frac{n}{r}\sum_{i=1}^{2} C_{2i}Z_n(\mu_{i+3}r)\right\}\cos n\theta \quad (9)$$

$$\Psi_2 = -\left\{\frac{n}{r}\sum_{i=1}^{3} C_{1i}Z_n(\mu_i r) + \sum_{i=1}^{2} C_{2i}Z_n'(\mu_{i+3}r)\right\}\sin n\theta \quad (10)$$

where $(\,)' \equiv (\,)_{,r}$, $Z_n(\mu_i r)$ and $\bar{Z}_n(\mu_i r)$ denote Bessel's functions of order n of the first and second kind, respectively (Watson, 1966); C_{ij} are arbitrary constants; $b_{1i} = k_{\psi 1}/(\mu_i^2 - k_u)$, $b_{3i} = \mu_i^2/[k_w - (1-\bar{N}_0)\mu_i^2]$, $b_{2j} = (k_{\psi 1} - \xi_3\mu_{j+3})/(\gamma_3\mu_{j+3} - k_u)$, $(i = 1, 2, 3; j, k = 1, 2; n = 0, 1, 2, \ldots)$.

Parameters μ_i $(i = 1, 2, 3)$ are the roots of the characteristic equation

$$a_0\mu^6 + a_1\mu^4 + a_2\mu^2 + a_3 = 0 \quad (11)$$

where

$$a_0 = 1 - \bar{N}_0, \quad a_1 = -k_w - (1-\bar{N}_0)(k_\psi + k_u) - \bar{N}_0\zeta$$

$$a_2 = k_w(k_\psi - \zeta) + k_u[(1-\bar{N}_0)k_\psi + k_w] - (1-\bar{N}_0)k_{u1}k_{\psi 1} + k_u\zeta\bar{N}_0$$

Downloaded 04 May 2010 to 171.66.16.26. Redistribution subject to ASME license or copyright; see http://www.asme.org/terms/Terms_Use.cfm

$$a_3 = k_w[k_u(\zeta - k_\psi) + k_{u1}k_{\psi 1}]. \quad (12)$$

The expressions for μ_4^2 and μ_5^2 are

$$\mu_{4,5}^2 = \frac{1}{2a_{45}}\left(-b_{45} \pm \sqrt{b_{45}^2 - 4a_{45}c_{45}}\right) \quad (13)$$

where $a_{45} = \gamma_3\gamma_4 - \xi_3\eta_3$, $b_{45} = \gamma_3(\zeta - k_\psi) + k_{u1}\xi_3 + \eta_3 k_{\psi 1} - k_u\gamma_4$, $c_{45} = k_u(k_\psi - \zeta) - k_{u1}k_{\psi 1}$.

The limiting case of symmetrically laminated plate ($k_{\psi 1} = k_{u1} = \xi_i = \eta_i = 0$) should be treated separately because of indeterminacy appeared in b_{ij} and the solution (6)–(10) can be rewritten as follows:

$$U_r = \left\{\bar{C}_{11}Z_n'(\mu_1 r) + \frac{n}{r}C_{21}Z_n(\mu_4 r)\right\}\cos n\theta \quad (14)$$

$$U_\theta = -\left\{\frac{n}{r}\bar{C}_{11}Z_n(\mu_1 r) + C_{21}Z_n'(\mu_4 r)\right\}\sin n\theta \quad (15)$$

$$W = \sum_{i=2}^{3} b_{3i}C_{1i}Z_n(\mu_i r)\cos n\theta \quad (16)$$

$$\Psi_1 = \left\{\sum_{i=2}^{3} C_{1i}Z_n'(\mu_i r) + \frac{n}{r}C_{22}Z_n(\mu_5 r)\right\}\cos n\theta \quad (17)$$

$$\Psi_2 = -\left\{\frac{n}{r}\sum_{i=2}^{3} C_{1i}Z_n(\mu_i r) + C_{22}Z_n'(\mu_5 r)\right\}\sin n\theta. \quad (18)$$

Let us choose as an example a clamped circular plate. Five conditions are given at the boundary $r = 1$:

$$u_r = u_\theta = w = \psi_1 = \psi_2 = 0. \quad (19)$$

The boundary conditions (19) are satisfied by equating to zero the Eqs. (4)–(10) at $r = 1$

$$[g_{ij}]\{c_j\} = 0 \quad (20)$$

where $\{c_j\}^T = \{C_{11}, C_{12}, C_{13}, C_{21}, C_{22}\}$

$$\bar{N}_1 = k_u = k_{u1} = k_w = k_\psi = k_{\psi 1} = 0. \quad (22)$$

There are two essentially different cases that should be considered separately: axisymmetric and asymmetric buckling.

The general solution of axisymmetric buckling equations satisfied the regularity requirements at the center and can be written as

$$u_r = C_1 r$$

$$\psi_1 = C_4 Z_0'(\alpha r)$$

$$w = -C_3 - (1 - \bar{N}_0)^{-1}\{C_4 Z_0(\alpha r)\} \quad (23)$$

where $\alpha^2 = \bar{N}_0\zeta/(1 - \bar{N}_0)$.

The general solution of asymmetric buckling equations satisfied the regularity requirements at the center and is

$$u_r = \{C_1 r^{n-1} + C_2 r^{1+n} - (n\xi_3/r\gamma_3)C_5 Z_n(\kappa r)\}\cos n\theta \quad (24)$$

$$u_\theta = \{-C_1 r^{n-1} + b_1 C_2 r^{1+n} - (\xi_3/\gamma_3)C_5 Z_n'(\kappa r)\}\sin n\theta \quad (25)$$

$$w = \{-C_3 r^n - (1 - \bar{N}_0)^{-1}C_4 Z_n(\alpha r)\}\cos n\theta \quad (26)$$

$$\psi_1 = \{nC_3 r^{n-1} + C_4 Z_n'(\alpha r) + (n/r)C_5 Z_n(\kappa r)\}\cos n\theta \quad (27)$$

$$\psi_2 = -\{nC_3 r^{n-1} + (n/r)C_4 Z_n(\alpha r) + C_5 Z_n'(\kappa r)\}\sin n\theta \quad (28)$$

where $\kappa^2 = -\zeta/(\gamma_4 - \eta_3\xi_3/\gamma_3)$, $(n = 1, 2, \ldots)$, $b_1 = [2 + (1 - \gamma_3)n]/[2\gamma_3 - (1 - \gamma_3)n]$, $b_2 = [(1 - \gamma_3)n - 2]/[2\gamma_3 + (1 - \gamma_3)n]$.

Let us consider as earlier the circular plate with a clamped edge. Five conditions (20) are set at the boundary $r = 1$.

The boundary conditions (20) are satisfied by equating to zero the three equations (23) for axisymmetric buckling ($u_\theta \equiv \psi_2 \equiv 0$) and Eqs. (24)–(28) for asymmetric case.

After certain reduction one has following eigenvalue equation:

$$[g_{ij}]^T = \begin{bmatrix} Z_n'(\mu_1) & nZ_n(\mu_1) & b_{11}Z_n'(\mu_1) & nb_{11}Z_n(\mu_1) & b_{31}Z_n(\mu_1) \\ Z_n'(\mu_2) & nZ_n(\mu_2) & b_{12}Z_n'(\mu_2) & nb_{12}Z_n(\mu_2) & b_{32}Z_n(\mu_2) \\ Z_n'(\mu_3) & nZ_n(\mu_3) & b_{13}Z_n'(\mu_3) & nb_{13}Z_n(\mu_3) & b_{33}Z_n(\mu_3) \\ nZ_n(\mu_4) & Z_n'(\mu_4) & b_{21}nZ_n(\mu_4) & b_{21}Z_n'(\mu_4) & 0 \\ nZ_n(\mu_5) & Z_n'(\mu_5) & b_{22}nZ_n(\mu_5) & b_{22}Z_n'(\mu_5) & 0 \end{bmatrix}, \quad (21)$$

for a generally laminated plate. The desired eigenvalue equation is obtained by setting the determinant of the matrix $[g_{ij}]$ equal to zero. After that the constants C_{ij} are determined from (20) by the traditional methods of linear algebra.

One can see that for the case of axisymmetric vibrations ($n = 0$) matrix $[g_{ij}]$ is separated into two blocks the lower of which is associated with torsional vibration modes, and they are found independently.

The eigenvalue equation and vibrational modes for symmetrically laminated plate are determined in the similar way using expressions (14)–(19).

The result predicted by classical-type plate theory is got from (4)–(21) by letting $\bar{A}$ go to infinity and rotational inertia term k_ψ to zero.

4 Static Buckling Solution

Another limiting case that can be solved in a closed analytical form is one for the static buckling, equations for which are obtained from (3) by setting there

$$Z_1(\alpha) = 0 \quad (29)$$

for axisymmetric, and the equation

$$\det[v_{ij}] = \begin{vmatrix} n & n & 1 \\ Z_n'(\alpha) & nZ_n(\alpha) & (1 - \bar{N}_0)^{-1}Z_n(\alpha) \\ nZ_n(\kappa) & Z_n'(\kappa) & 0 \end{vmatrix} = 0 \quad (30)$$

for axisymmetric buckling.

From (29) one obtains the explicit expression for the dimensionless buckling load

$$\zeta\bar{N}_0 = \alpha_1^2/(1 + \alpha_1^2/\zeta) \quad (31)$$

where $\alpha_1 = 3.8317\ldots$ is the first root of the Eq. (29).

Similarly to the foregoing, the result predicted by the classical Kirchhoff-type theory is obtained from the corresponding eigenvalue equations by letting $\bar{A}$ go to infinity.

It should be noted that for the clamped circular plate the buckling load associated with axisymmetric mode shape is minimal.

Downloaded 04 May 2010 to 171.66.16.26. Redistribution subject to ASME license or copyright; see http://www.asme.org/terms/Terms_Use.cfm

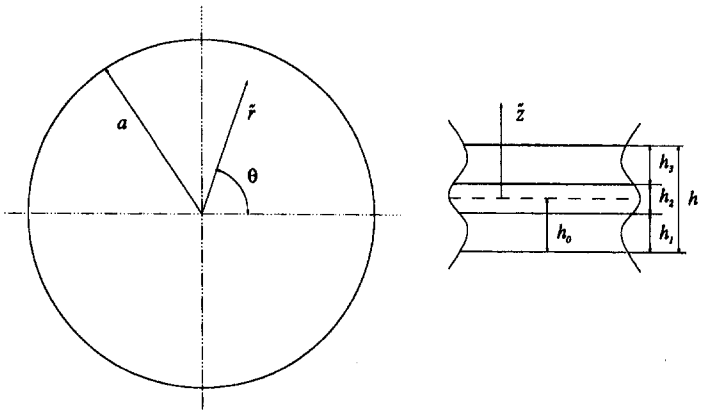


Fig. 1 Geometry of circular plate. Three-layer example.

5 Boundaries of Instability Regions

Let us represent solution of coupled Eqs. (3) in the form

$$\{u_r, u_\theta, w, \psi_1, \psi_2\} = \sum_{i=0}^{\infty}\sum_{n=0}^{\infty}\{U_r^{(in)}, U_\theta^{(in)}, W^{(in)}, \Psi_1^{(in)}, \Psi_2^{(in)}\} f_{in}(\tau) \quad (32)$$

where scaling angular frequency p is assumed to coincide with excitation frequency ω, $\{U_r^{(in)}, U_\theta^{(in)}, W^{(in)}, \Psi_1^{(in)}, \Psi_2^{(in)}\}$ is the eigenmode vector found in the part 3, n is the number of node diameters, and i is the ordinal number of eigenfrequency for the fixed n.

Following evident equality holds

$$L_{34}(\Psi_1^{(in)}) + L_{35}(\Psi_2^{(in)}) = -r[(1-\bar{N}_0)^{-1}\nabla^2 + k_w^{(in)}]W^{(in)}. \quad (33)$$

It can be shown that functions $W^{(in)}$ are orthogonal, i.e.,

$$\int_\Omega W^{(in)}W^{(mk)}d\Omega = 0 \quad \text{if} \quad (i \neq m \text{ or } n \neq k) \quad \text{for} \quad p_{in} \neq p_{mk} \quad (34)$$

where Ω means a full plate area.

Substitution of (32) and (33) into the third of the Eqs. (3) yields

$$\sum_{i=0}^{\infty}\sum_{n=0}^{\infty}\left[\bar{a}_{in}W^{(in)} + \frac{\bar{N}_1\zeta}{\lambda_\omega^2}\nabla^2 W^{(in)}\cos 2\tau + W^{(in)}\frac{\partial^2}{\partial\tau^2}\right]f_{in}(\tau) = 0 \quad (35)$$

where $\bar{a}_{in} = (p_{in}/\omega)^2$, $\lambda_\omega^2 = R_0\omega^2 a^4/D_{11}$.

Applying the Galerkin-Kantorovich method on $\{r, \theta\}$ —variables (Kantorovich and Krylov, 1958)—to (35) and utilizing (34), one obtains following differential equations set:

$$\frac{d^2 f_{kn}}{d\tau^2} + \bar{a}_{kn}f_{kn} + \frac{\bar{N}_1\zeta}{\lambda_\omega^2}\cos 2\tau\sum_{i=0}^{\infty} I_{ikn}f_{in} = 0 \quad (n, k = 0, 1, 2, \ldots) \quad (36)$$

where

$$I_{ikn} = \frac{\int_\Omega W^{(kn)}\nabla^2 W^{(in)}d\Omega}{\int_\Omega W^{(kn)}W^{(in)}d\Omega}. \quad (37)$$

Equations (36) are well-known Mathiue equations. The expressions for the boundaries of principal and combination type instability regions in the first approximation can be found following Bolotin (1964b) as

$$\frac{2\omega}{p_{in}+p_{kn}} = 1 \pm \frac{\bar{N}_1\zeta}{2(\lambda_{in}+\lambda_{kn})}\sqrt{\frac{I_{ikn}I_{kin}}{\lambda_{in}\lambda_{kn}}} \quad (i, n, k = 0, 1, 2, \ldots). \quad (38)$$

The expressions for the terms I_{mkn} are written in the form

$$I_{mkn} = -\sum_{i=1}^{3}\sum_{j=1}^{3}\mu_{i(mn)}^2 S_{ij}^{(mkn)}\Big(\sum_{i=1}^{3}\sum_{j=1}^{3}S_{ij}^{(mkn)}\Big)^{-1} \quad (39)$$

where

$$S_{ij}^{(mkn)} = \frac{1}{2}b_{3i}^{(mn)}b_{3j}^{(kn)}C_{1i}^{(mn)}C_{1j}^{(kn)} \times \int_0^1 Z_n(\mu_{i(mn)}r)Z_n(\mu_{j(kn)}r)rdr. \quad (40)$$

The integral here is expressed analytically in terms of Bessel functions (Prudnikov et al., 1983).

To determine the location of the secondary instability regions connected to principal ones, let us limit ourselves by the first approximation of Galerkin-Kantorovich procedure applied to (35). Then instead of the Eqs. (36) one has following set:

$$\frac{d^2 f_{kn}}{d\tau^2} + (\bar{a}_{kn} + 2q_{kn}\cos 2\tau)f_{kn} = 0 \quad (n, k = 0, 1, 2, \ldots) \quad (41)$$

where $q_{kn} = \bar{a}_{kn}\bar{N}_1\zeta I_{kkn}/2\lambda_{kn}^2$.

Let us represent solution of (41) in the form

$$f_{kn} = \exp(im\tau)P_{kn}(\tau) \quad (n, k = 0, 1, 2, \ldots) \quad (42)$$

where P_{kn} is a periodic function of τ, and m is the characteristic exponent. When m is real the solutions (42) are stable.

It is known (see work by Tamir (1962) where a convergence of the iterative process described below was proved) that all values of m can be found from following the fractional equation

$$y = R_0^+(y) + R_0^-(y) \quad (43)$$

where $y = m^2 - a_{in}$,

$$R_0^\pm(y) = \frac{q_{in}^2|}{4(1\pm m)+y} - \frac{q_{in}^2|}{|8(2\pm m)+y} - \ldots - \frac{q_{in}^2|}{|4l(l\pm m)+y} - \ldots (l = 2, 4, 6, \ldots). \quad (44)$$

Downloaded 04 May 2010 to 171.66.16.26. Redistribution subject to ASME license or copyright; see http://www.asme.org/terms/Terms_Use.cfm

Table 1 Angle of openness of principal instability regions Θ deg, $s = 0$

h/a	h_1/h	No	CL	i	n	$f = 1$ SH	i	n	ϵ percent	$f = 0.1$ SH	i	n	ϵ percent
0.1	0.445	1	1.885	0	0	1.937	0	0	2.8	2.320	0	0	23.1
		2	1.055	0	1	1.117	0	1	5.9	1.562	0	1	48.0
		3	0.686	0	2	0.752	0	2	9.6	1.215	0	2	77.1
		4	0.600	1	0	0.663	1	0	10.5	1.111	1	0	85.2
		5	0.486	0	3	0.554	0	3	14.0	1.020	0	3	109.9
		6	0.407	1	1	0.472	1	1	15.9	0.929	1	1	128.0
	0.0	1	0.880	0	0	0.930	0	0	5.6	1.325	0	0	50.5
		2	0.493	0	1	0.551	0	1	11.8	1.007	0	1	104.2
		3	0.321	0	2	0.382	0	2	19.1	0.850	0	2	164.9
		4	0.281	1	0	0.339	1	0	20.8	0.800	1	0	184.0
		5	0.227	0	3	0.290	0	3	27.5	0.755	0	3	232.2
		6	0.191	1	1	0.250	1	1	30.9	0.711	1	1	271.7
0.2	0.445	1	1.885	0	0	2.092	0	0	11.0	3.713	0	0	97.0
		2	1.055	0	1	1.299	0	1	23.2	3.146	0	1	198.1
		3	0.686	0	2	0.943	0	2	37.5	2.803	0	2	308.5
		4	0.600	1	0	0.845	1	0	40.8	2.677	1	0	346.1
		5	0.419*	1	1	0.748	0	3	78.5	2.581	0	3	516.6
		6	—	2	0	0.694*	1	1	—	2.484	1	1	—
	0.0	1	0.881	0	0	1.076	0	0	22.2	2.764	0	0	213.8
		2	0.495	0	1	0.723	0	1	46.1	2.585	0	1	422.7
		3	0.254*	1	1	0.561	0	2	121.0	2.401	0	2	845.9
		4	—	1	0	0.509	1	0	—	2.337	1	0	—
		5	0.324	0	2	0.429*	1	1	32.6	2.281	0	3	604.9
		6	0.283	2	0	—	2	0	—	2.237	1	1	690.6

The iterative procedure is employed to solve (43). Putting in (44) $m = 1, 2, \ldots$, one transforms (43) into the equation for bounds of mth instability region. To quicken the convergence of iterative process the averaging of the results (being simultaneously the initial value product for the next step of iterations) is used.

6 Results and Discussion

Preliminary testing dynamic stability problem was solved for the clamped thin isotropic homogeneous plate and has shown good agreement with the known result by Reckling (1953b).

Let us consider then a laminated circular plate composed of 2 outer layers 1, 3 made of the same material glued to an inner layer 2 made of another one. A correlations between properties of outer and inner layers are taken to be

$$E_{11}^{(1)} = E_{11}^{(2)} = E_{11}, \quad E_{11}^{(2)} = 10E_{11}, \quad \rho^{(1)} = \rho^{(2)} = \rho,$$

$$\rho^{(2)} = 1.25\rho, \quad \nu^{(1)} = \nu^{(2)} = 0.5,$$

$$\rho^{(2)} = 0.3, \quad f = G_z^{(k)}/G^{(k)} \quad (k = 1, 2, 3)$$

where the notation $(\ )^{(i)}$ means ith layer, f –shear moduli ratio to be varied. The ratio of inner layer thickness to a total one is set as $h_2/h = 0.1$.

The angles of openness of the principal instability regions associated with the first six natural frequencies in a dimensionless parameter space $\{p_{kn}/\omega, N_1\}$ $(N_1 = 12a^2\tilde{N}_1/h^3E_{11})$ are presented in Table 1. It should be noted that combination type instability regions do not appear within this frequency range. In the Table, "No" is the spectrum position number of correspondent frequency, n–number of node diameters, i–ordinal number of correspondent frequency for the fixed n, CL means classical, SH–Mindlin-type theory results, s is the ratio $\tilde{N}_0/\tilde{N}_c$ where $\tilde{N}_c$ is SH-critical buckling load, the relative error $\epsilon = (\Theta_{SH}/\Theta_{CL} - 1) \times 100$ percent. Values with asterisk are associated with predominantly longitudinal mode frequencies. Omitted values corresponds to the purely torsional mode frequencies ($n = 0$) and do not give instability regions.

Analysis of Table 1 shows that the relative error increase monotonically with rise in the spectrum position as the instability regions associated with the same wave numbers i, n are

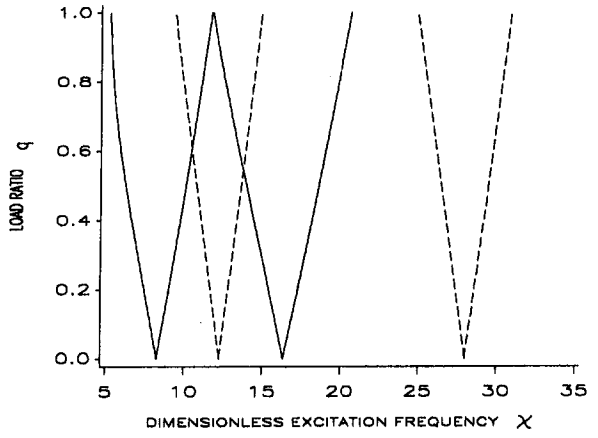


Fig. 2 First and second principal instability regions associated with natural frequencies p_{00} and p_{01}, respectively, $f = 0.1$, $h/a = 0.1$, $h_1/h = 0$, $s = 0.5$, solid lines–SH, dashed–CD

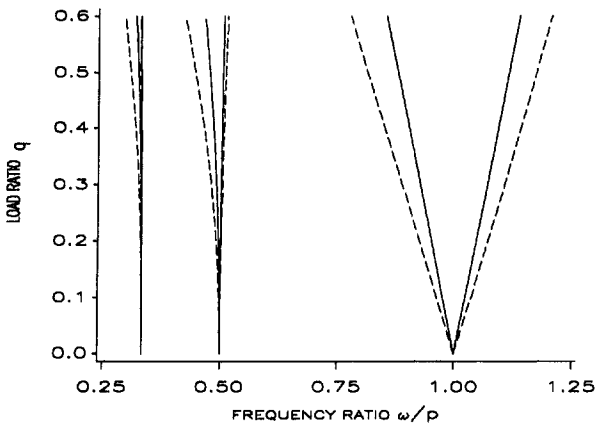


Fig. 3 Principal and two secondary instability regions associated with the lowest natural frequency p_{00}, $f = 0.1$, $h/a = 0.1$, $h_1/h = 0.45$, solid lines–$s = 0$, dashed–$s = 0.5$

Downloaded 04 May 2010 to 171.66.16.26. Redistribution subject to ASME license or copyright; see http://www.asme.org/terms/Terms_Use.cfm

considered. Similarly, growth in ϵ is observed with drop of shear moduli ratio f, with thickness rise and with increase in asymmetry of lamination ($h_1/h = 0.45$ corresponds to the symmetrical lamination). It can seen also that the openness of the instability regions associated with predominantly transverse mode frequencies decrease monotonically with progress in the spectrum position.

In Fig. 2, one can see a shift in location of two first principal instability regions computed by SH and CL theories in coordinates $\chi = \omega a^2 h\sqrt{12\rho/E_{11}}$, $q = \tilde{N}_1/\tilde{N}_c$.

An influence of the static component of the load on the openness of the principal and two secondary instability regions associated with the lowest natural frequency can be seen in Fig. 3. It is shown that the openness of both principal and secondary instability regions increases with static component of the load rise.

In Fig. 4, the principal instability regions associated with predominantly (for $h_1/h = 0.445$) and purely longitudinal (for $h_1/h = 0.45$) mode frequency p_{11} are shown for both SH and CL theories. One can see that for the symmetrical lamination ($h_1/h = 0.45$), the plate has simple resonance instead of the instability region. However, for the weakly asymmetrical lamination ($h_1/h = 0.445$), the instability region is opened at almost the same value of the frequency ($\chi = 45.16$). This limiting instability region is kept approximately the same for any small rate of the lamination asymmetry. It occurs because of the integral term (37) determined the openness of the instability region. For the asymmetrically laminated plate, we have mixed-mode shapes instead of purely transverse or in-plane modes. For slight asymmetry, the mode shape associated with frequency p_{11} has two components: small amplitude transverse and relatively large amplitude in-plane component. The peculiarity of the term (37) is that it does not depend on the amplitude of transverse deflection. That is why the openness of the instability region for the limiting case of weakly asymmetric lamination is determined by the mode shape only. Note that the last one, for this case, tends to the correspondent mode shape of symmetrically laminated plate. The phenomenon of sensitivity of instability regions to slight imperfections in symmetry of lamination causes necessity to consider the instability regions associated with in-plane mode frequencies for the symmetrically laminated plates (even for the isotropic homogeneous plates), excepting naturally purely torsional mode frequencies.

The dependences of the angles of openness of the first three principal instability regions on the shear moduli ratio f are shown in Fig. 5. It can be seen that decrease of f causes increase in the angles of openness. The intervals of weak and strong (f

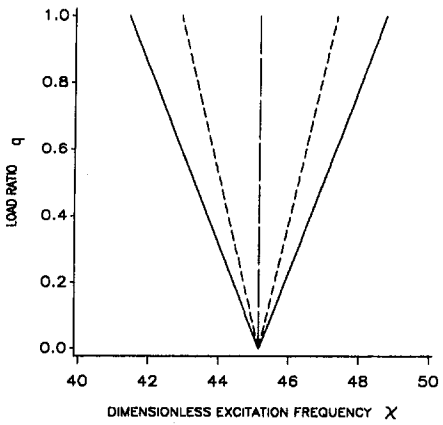


Fig. 4 Sensitivity of instability region associated with frequency p_{11} to slight imperfection in symmetry of lamination, $f = 1$, $h/a = 0.2$, $s = 0$, lines–[—— SH for $h_1/h = 0.445$, ---- CL for $h_1/h = 0.445$, — — SH and CL for $h_1/h = 0.45$]

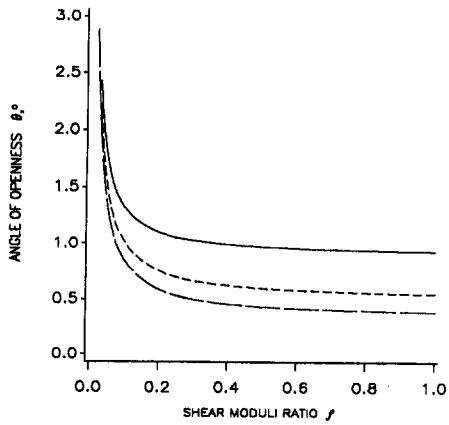


Fig. 5 Angle of openness of the first [——], second [----], and third [— —] principal instability regions associated with natural frequencies p_{00}, p_{01}, p_{02}, respectively, versus shear moduli ratio f. $h/a = 0.1$, $h_1/h = 0$, $s = 0$.

$\in [0, 0.1]$) sensitivity of Θ to shear moduli ratio change can be conditionally marked out.

Concluding Remarks

The dynamic stability regions for considered laminated circular plates under periodic radial loads, are studied in the present paper analytically using both classical (CL) and first-order shear deformation (SH) theories.

It is shown that the shift in location of principal instability regions computed by SH and CL theories increases essentially for the diminished value of the shear moduli ratio f.

The sensitivity phenomenon of certain instability regions to slight deviation in the symmetry of lamination is found.

Acknowledgments

The work of G. Krizhevsky was supported by the Center for Absorption in Science, Ministry of Immigrant Absorption, State of Israel and the Swope Chair of Mechanics. The work of Y. Stavsky was supported by the Swope Chair of Mechanics and the Technion Fund for Promotion of Research.

References

Bodner, V. A., 1938, "Stability of plates under the action of periodic forces," *Prikladnaya Matematika i Mekhanika,* Vol. 2, No. 1, pp. 87–94 (in Russian).

Bolotin, V. V., 1964, *The Dynamic Stability of Elastic Systems,* Holden-Day, San Francisco.

Chen, L. W., and Juang, D. P., 1987, "Axisymmetric dynamic stability of a bimodulus thick circular plate," *Computers and Structures,* Vol. 26, pp. 933–939.

Hutt, J. M., and Salam, A. E., 1971, "Dynamic stability of plates by finite elements," *Proceedings of the American Society of Civil Engineers,* Vol. EM97, pp. 879–899.

Kantorovich, L. V., and Krylov, V. I., 1958, *Approximate methods of higher analysis,* Interscience, New York and Noordhoff, Groningen, The Netherlands, pp. 304–327.

Moorthy, J., Reddy, J. N., and Plaut, R. H., 1990, "Parametric instability of laminated composite plates with transverse shear deformation," *J. Solids Structures,* Vol. 26, No. 7, pp. 801–811.

Nguyen, H., and Ostiguy, G. L., 1989, "Effect of boundary conditions on the dynamic instability and non-linear response of rectangular plates, Part 1: Theory," *Journal of Sound and Vibration,* Vol. 133, pp. 381–400.

Nguyen, H., Ostiguy, G. L., and Samson, L. P., 1989, "Effect of boundary conditions on the dynamic instability and non-linear response of rectangular plates, Part 2: Experiment," *Journal of Sound and Vibration,* Vol. 133, pp. 401–422.

Prudnikov, A. P., Brychkov, U. A., and Marichev, O. I., 1983, *Integrals and Series. Special Functions.* Nauka, Moscow, pp. 40–47 (in Russian).

Reckling, K. A., 1953, "Die dünne mit pulsierender randbelastung in ihrer mittelebene als stabilitätsproblem," *Ingenieur-Archiv,* Vol. 21, pp. 141–147.

Downloaded 04 May 2010 to 171.66.16.26. Redistribution subject to ASME license or copyright; see http://www.asme.org/terms/Terms_Use.cfm

Tamir, T., 1962, "Characteristical exponents of Mathieu functions," *Mathematics and Computations,* Vol. 16, No. 77, pp. 100–106.

Tani, J., and Nakamura, T., 1978, "Dynamic stability of annular plates under periodic radial loads," *Journal of the Acoustical Society of America,* Vol. 64, pp. 827–831.

Tani, J., and Nakamura, T., 1978, "Parametric resonance of annular plates under pulsating uniform internal and external loads with different periods," *Journal of Sound and Vibration,* Vol. 60, pp. 289–297.

Tani, J., and Doki, H., 1982, "Dynamic stability of orthotropic annular plate under pulsating radial loads," *Journal of the Acoustical Society of America,* Vol. 72, pp. 845–850.

Tylikowski, A., 1989, "Dynamic Stability of Nonlinear Antisymmetrically Laminated Cross-Ply Rectangular Plates," ASME JOURNAL OF THE APPLIED MECHANICS, Vol. 56, pp. 375–381.

Watson, G. N., 1966, *A Treatise on the Theory of Bessel Functions,* 2nd ed., Cambridge University Press, U.K.

Downloaded 04 May 2010 to 171.66.16.26. Redistribution subject to ASME license or copyright; see http://www.asme.org/terms/Terms_Use.cfm

K. Hosokawa
Lecturer,
Assoc. Mem. ASME.

Y. Yamada
Graduate Student

T. Sakata
Professor

Department of Mechanical Engineering,
Chubu University,
Kasugai, Aichi, 487, Japan

Free-Vibration Analysis of Clamped Antisymmetrically Laminated Elliptical Plates

In a previous paper, a numerical approach for analyzing the free vibration problem of an unsymmetrically laminated fiber-reinforced plastic composite plate was proposed by the authors. In the present paper, this approach is applied to the clamped antisymmetrically laminated elliptical plate. As numerical examples, the natural frequencies and the mode shapes of the circular and elliptical plates are estimated. The effects of the fiber orientation angle on natural frequency and mode shape are studied. Furthermore, the vibration tests of the clamped antisymmetrically laminated circular and elliptical plates made of carbon fiber-reinforced plastic are carried out, and the experimental natural frequency and mode shape are compared with the numerical results.

1 Introduction

Since a laminated plate is an important structural member, many studies on the free vibrations of a symmetrically laminated plate have been reported in the literature. However, studies on the vibrations of unsymmetrically and antisymmetrically laminated plates are limited. For example, Bert and Mayberry (1969) calculated the natural frequencies of laminated anisotropic rectangular plates using the Rayleigh-Ritz energy method. Jones (1973) presented an exact solution and numerical results for simply supported unsymmetrically laminated cross-ply rectangular plates. Natural frequencies of unsymmetrical cross-ply and antisymmetric angle-ply laminates with various boundary conditions were obtained by Lin and King (1974). Reddy (1979) presented a finite element formulation of the equations governing the laminated anisotropic plate theory of Yang, Norris, and Stavsky. To investigate the free vibration of antisymmetric angle-ply laminated plates, Khdeir (1988) developed an analytical procedure based on a generalized Levy-type solution. Free-vibration analysis was carried out for the annular and circular asymmetric composite plates having completely free edges by Sivakumaran (1989). As mentioned above, one can easily find published research on a rectangular plane-form. However, only a few reports can be found on the other plane-forms (circular, elliptical, etc.), or on experimental analyses of free vibrations of unsymmetrically and antisymmetrically laminated plates of such plane-forms.

The authors (Hosokawa et al., 1994) proposed a numerical approach for analyzing the free vibrations of an unsymmetrically laminated fiber-reinforced plastic composite plate. In the present paper, this approach is applied to a clamped antisymmetrically laminated elliptical plate. First, numerical examples are given that estimate the natural frequencies of the plate. Also, the convergence of the solution is investigated. The effects of the fiber orientation angle on natural frequency and mode shape are studied. Next, by vibration tests of clamped circular and elliptical plates, natural frequencies and mode shapes are obtained. By comparing with the experimental results, it follows that one can accurately estimate natural frequency and mode shape by using the numerical approach proposed by the authors.

2 Numerical Approach

2.1 Frequency Equation. On the basis of Chia's concept (1980), by neglecting the body force, rotatory effect, and in-plane inertia effect, the free transverse vibration of an antisymmetrically laminated plate is governed by

$$\left.\begin{aligned} L_1(u, v, w) &= 0 \\ L_2(u, v, w) &= 0 \\ L_3(u, v, w) + \rho h \ddot{w} &= 0 \end{aligned}\right\} \tag{1}$$

where h is the thickness, $u(x, y, t)$ and $v(x, y, t)$ are displacements with respect to the x and y-directions, respectively. $w(x, y, t)$ is the transverse deflection, $\ddot{w} = \partial^2 w/\partial t^2$; t is the time variable; ρ is the density; and $L_1(\ )$, $L_2(\ )$, and $L_3(\ )$ are the differential operators for the static bending problem of the plate given by Eqs. (2), (3), and (4), respectively.

$$L_1(u, v, w) = A_{11}\frac{\partial^2 u}{\partial x^2} + A_{66}\frac{\partial^2 u}{\partial y^2} + (A_{12} + A_{66})\frac{\partial^2 v}{\partial x \partial y} - 3B_{16}\frac{\partial^3 w}{\partial x^2 \partial y} - B_{26}\frac{\partial^3 w}{\partial y^3} \tag{2}$$

$$L_2(u, v, w) = A_{66}\frac{\partial^2 v}{\partial x^2} + A_{22}\frac{\partial^2 v}{\partial y^2} + (A_{12} + A_{66})\frac{\partial^2 u}{\partial x \partial y} - B_{16}\frac{\partial^3 w}{\partial x^3} - 3B_{26}\frac{\partial^3 w}{\partial x \partial y^2} \tag{3}$$

$$L_3(u, v, w) = D_{11}\frac{\partial^4 w}{\partial x^4} + D_{22}\frac{\partial^4 w}{\partial y^4} + 2(D_{12} + 2D_{66})\frac{\partial^4 w}{\partial x^2 \partial y^2} - 3B_{16}\frac{\partial^3 u}{\partial x^2 \partial y} - B_{26}\frac{\partial^3 u}{\partial y^3} - B_{16}\frac{\partial^3 v}{\partial x^3} - 3B_{26}\frac{\partial^3 v}{\partial x \partial y^2} \tag{4}$$

where A_{ij} are the extensional stiffnesses, B_{ij} are the coupling stiffnesses, and D_{ij} are the bending stiffnesses. These stiffnesses are evaluated from the moduli of elasticity E_1, E_2 in the direction of parallel and normal to the fiber, respectively, shear modulus G_{12}, Poisson's ratios ν_{12}, ν_{21}, and fiber orientation angle θ_r of each layer (see Fig. 1(*a*)). The solution of Eq. (1) is written as

Contributed by the Applied Mechanics Division of THE AMERICAN SOCIETY OF MECHANICAL ENGINEERS for publication in the ASME JOURNAL OF APPLIED MECHANICS.

Discussion on the paper should be addressed to the Technical Editor, Professor Lewis T. Wheeler, Department of Mechanical Engineering, University of Houston, Houston, TX 77204-4792, and will be accepted until four months after final publication of the paper itself in the ASME JOURNAL OF APPLIED MECHANICS.

Manuscript received by the ASME Applied Mechanics Division, Aug. 19, 1994; final revision, Mar. 7, 1998. Associate Technical Editor: W. N. Sharpe, Jr.

 Copyright © 1998 by ASME

Downloaded 04 May 2010 to 171.66.16.26. Redistribution subject to ASME license or copyright; see http://www.asme.org/terms/Terms_Use.cfm

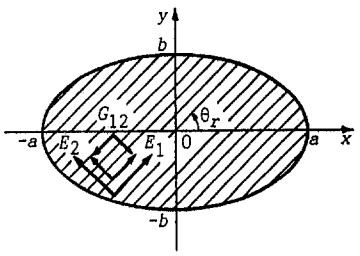


Fig. 1(*a*) *r*th layer

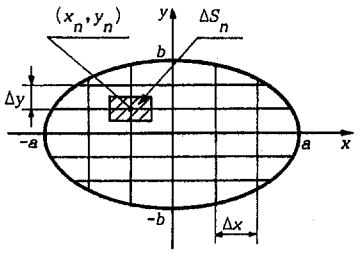


Fig. 1(*b*) Dividing pattern of elliptical plate

Fig. 1 Clamped laminated elliptical plate

$$\left.\begin{aligned} u &= -\iint \rho h\ddot{w}(\xi, \eta, t)G_1(x, y, \xi, \eta)d\xi d\eta \\ v &= -\iint \rho h\ddot{w}(\xi, \eta, t)G_2(x, y, \xi, \eta)d\xi d\eta \\ w &= -\iint \rho h\ddot{w}(\xi, \eta, t)G_3(x, y, \xi, \eta)d\xi d\eta \end{aligned}\right\} \quad (5)$$

where the functions $G_1(x, y, \xi, \eta)$, $G_2(x, y, \xi, \eta)$, and $G_3(x, y, \xi, \eta)$ satisfy the boundary condition and the differential equation represented by

$$\left.\begin{aligned} L_1(G_1, G_2, G_3) &= 0 \\ L_2(G_1, G_2, G_3) &= 0 \\ L_3(G_1, G_2, G_3) &= \delta(x - \xi)\delta(y - \eta) \end{aligned}\right\} \quad (6)$$

where $\delta(\ \ )$ is Dirac's delta function. Using the assumed plate transeverse deflection as

$$w(x, y, t) = W(x, y) \cos(\omega t), \quad (7)$$

from the third equation in Eq. (5), one has

$$W(x, y) = \omega^2 \iint \rho h W(\xi, \eta)G_3(x, y, \xi, \eta)d\xi d\eta, \quad (8)$$

where ω is the frequency in radians. Because it is difficult to solve analytically integral Eq. (8), the integration is carried out

Table 1 Mechanical properties of filamentary composite materials

Material	E_1(GPa)	E_2(GPa)	G_{12}(GPa)	ν_{12}
E-Glass/Epoxy	60.7	24.8	11.99	0.23
Boron/Epoxy	209	19	6.4	0.21
Graphite/Epoxy	138	8.96	7.1	0.30

approximately under the assumption that the integrand in Eq. (8) is constant in the small regions hatched in Fig. 1(*b*). Therefore, Eq. (8) is transformed as

$$W(x, y) = \omega^2 \sum_{n=1}^{N} \rho h G_3(x, y, x_n, y_n)\Delta S_n W(x_n, y_n), \quad (9)$$

where ΔS_n and (x_n, y_n) are the area and typical point of the nth small region of the plate shown in Fig. 1(*b*). By letting $x = x_m$ and $y = y_m$ in Eq. (9), the frequency equation is given by

$$\det|\delta_{m,n} - \omega^2 \rho h G_3(x_m, y_m, x_n, y_n)\Delta S_n| = 0$$
$$m, n = 1, 2, 3, \ldots, N \quad (10)$$

where $\delta_{m,n}$ is Kronecker's delta. Also, in the case in which the concentrated mass $\bar{p}$ is attached to the Ith dividing point (x_I, y_I) of the plate, from d'Alembert's principle, Eq. (10) is transformed as follows:

$$\det|\delta_{m,n} - \omega^2[\rho h + (\bar{p}/\Delta S_n)\delta_{n,I}]G_3(x_m, y_m, x_n, y_n)\Delta S_n| = 0$$
$$m, n = 1, 2, 3, \ldots, N \quad (11)$$

2.2 Estimation of Functions G_1, G_2, and G_3. The functions G_1, G_2, and G_3 are assumed in a power series form as the following equations, respectively:

$$G_1(x, y, \xi, \eta) = \sum_{i=1}^{I} A_i(\xi, \eta)\psi_1(x, y)x^k y^l \quad (12)$$

$$G_2(x, y, \xi, \eta) = \sum_{i=1}^{I} B_i(\xi, \eta)\psi_2(x, y)x^k y^l \quad (13)$$

$$G_3(x, y, \xi, \eta) = \sum_{i=1}^{I} C_i(\xi, \eta)\psi_3(x, y)x^k y^l \quad (14)$$

where $A_i(\xi, \eta)$, $B_i(\xi, \eta)$, and $C_i(\xi, \eta)$ are constants determined by the position (ξ, η) where unit load acts, and k and l are nonnegative integers determined according to the positive integer i. The functions $\psi_1(x, y)$, $\psi_2(x, y)$, and $\psi_3(x, y)$ are determined such that the functions G_1, G_2, and G_3 satisfy the boundary conditions of the plate, respectively. In case of the clamped elliptical plate shown in Fig. 1, the functions $\psi_1(x, y)$, $\psi_2(x, y)$, and $\psi_3(x, y)$ may be expressed as

Nomenclature

A_{ij}, B_{ij}, D_{ij} = extensional, coupling, and flexural rigidities of a laminated plate, $i, j = 1, 2, 6$
a, b = Semi-axes of an ellipse in the x and y-directions
E_1, E_2 = principal moduli of elasticity of an orthotropic layer in a laminated plate
G_{12} = modulus of rigidity of an orthotropic layer in a laminated plate
h = thickness of a laminated plate
L_1, L_2, L_3 = differential operators for a static bending problem of a laminated plate
t = time
u, v, w = displacement components in the x, y, z-directions, respectively
x, y, z = rectangular cartesian coordinates
ν_{12}, ν_{21} = Poisson's ratios of an orthotropic layer in a laminated plate
ρ = density of a laminated plate
θ_r = fiber orientation angle of the rth layer
ω = radian frequency

Other symbols are defined when they appear in the text.

Downloaded 04 May 2010 to 171.66.16.26. Redistribution subject to ASME license or copyright; see http://www.asme.org/terms/Terms_Use.cfm

Table 2 Convergence of natural frequencies $\omega_s/\sqrt{D_0/\rho ha^4}$ of clamped four layered circular plate; [30 deg/−30 deg/30 deg/−30 deg], $N = 225$, graphite/epoxy

Number of terms	$\omega_s/\sqrt{D_0/\rho ha^4}$			
I	s=1	s=2	s=3	s=4
3	6.3324	12.256	16.200	
6	6.2605	11.493	15.121	19.549
10	6.2500	11.141	14.725	18.419
15	6.2491	11.092	14.662	17.389
21	6.2489	11.082	14.652	17.258
28	6.2489	11.081	14.650	17.207
36	6.2489	11.080	15.650	17.200
45	6.2489	11.080	15.650	17.199
55	6.2489	11.080	15.650	17.199
66	6.2489	11.080	15.650	17.199

$$\psi_1(x, y) = \psi_2(x, y) = \frac{x^2}{a^2} + \frac{y^2}{b^2} - 1 \tag{15}$$

$$\psi_3(x, y) = \left(\frac{x^2}{a^2} + \frac{y^2}{b^2} - 1\right)^2. \tag{16}$$

By applying Galerkin's method to Eq. (6), one gets

$$\left.\begin{aligned} \iint L_1(G_1, G_2, G_3)\psi_1(x, y)x^{k'}y^{l'}dxdy = 0 \\ \iint L_2(G_1, G_2, G_3)\psi_2(x, y)x^{k'}y^{l'}dxdy = 0 \\ \iint \{L_3(G_1, G_2, G_3) - \delta(x - \xi)\delta(y - \eta)\} \\ \times \psi_3(x, y)x^{k'}y^{l'}dxdy = 0 \end{aligned}\right\} \tag{17}$$

$$k', l' = 0, 1, 2, \ldots.$$

From Eq. (17), one obtains a set of simultaneous equations with respect to $A_i(\xi, \eta)$, $B_i(\xi, \eta)$, and $C_i(\xi, \eta)$. By substituting $A_i(\xi, \eta)$, $B_i(\xi, \eta)$, and $C_i(\xi, \eta)$ estimated from the simultaneous equations into Eqs. (12), (13), and (14), respectively, one can obtain the functions G_1, G_2, and G_3.

3 Numerical Examples

To establish the convergence of the proposed approach, natural frequencies of a clamped antisymmetrically laminated circular plate are estimated. The plate is divided equally along the x and y-axes, respectively. The pattern for dividing a circular plate ($a = b$) is shown in Fig. 1(b). When all midpoints of the sides of a rectangular element are not included in the domain of the plate, the element is not used for the estimation of a numerical integration. The plate materials are assumed to be a fiber-reinforced plastic as shown in Table 1 (Vinson and Sierakowski, 1986). Table 2 shows the effect of the number of terms I of the functions G_j (j = 1, 2, 3) on the convergence of natural frequencies of a four-layered ([30 deg/−30 deg/30 deg/−30 deg]) circular plate. Graphite/epoxy has stronger orthotropy, so that it is used as a plate material. The effect of the number of divisions N on the convergence of natural frequencies is presented in Table 3. The plate is the same as the one used in Table 2. In these tables, a natural frequency is nondimensionalized by using the bending stiffness parameter $D_0 = E_1h^3/12(1 - \nu_{12}\nu_{21})$, where E_1 is the modulus of elasticity in the direction of the fiber. From Tables 2 and 3, it follows that one can obtain sufficiently converged values by using the number of terms $I = 66$ to estimate the functions G_j (j = 1, 2, 3) and by dividing the plate into 225 small regions. To investigate the accuracy of the results obtained by the proposed approach, this approach is applied to the clamped isotropic elliptical plate. Table 4 shows the lowest four natural frequencies of the plate. In the table, numerical results estimated by the other investigators also are tabulated for comparison. Judging from the comparison it follows that the values obtained by the presented approach are very accurate. As numerical examples, Table 5 shows the lowest four natural frequencies of four-layered ([30 deg/−30 deg/30 deg/−30 deg]) elliptical plates with various aspect ratios (a/b). The plate materials are three kinds of fiber-reinforced plastic as shown in Table 1. Figure 2 shows the effect of the fiber orientation angle on the natural frequency of a four-layered angle-ply ([θ/−θ/θ/−θ]) plate. In Fig. 2, (a) shows the natural frequencies and mode shapes of a circular plate and (b) shows those of an elliptical plate. Comparing with the numerical results of the elliptical plate, one can find that the natural frequency of the circular plate increases or decreases monoto-

Table 3 Convergence of natural frequencies $\omega_s/\sqrt{D_0/\rho ha^4}$ of clamped four-layered circular plate; [30 deg/−30 deg/30 deg/−30 deg], $I = 66$, graphite/epoxy

Division number	$\omega_s/\sqrt{D_0/\rho ha^4}$			
N	s=1	s=2	s=3	s=4
9	6.1611	10.549	12.942	13.564
21	6.2493	11.071	14.637	16.766
37	6.2511	11.097	14.667	17.234
69	6.2490	11.081	14.650	17.199
97	6.2490	11.081	14.650	17.200
137	6.2489	11.080	14.650	17.199
177	6.2489	11.080	14.650	17.199
225	6.2489	11.080	14.650	17.199

Table 4 Natural frequencies $\omega_s/\sqrt{D_0/\rho ha^4}$ of clamped isotropic elliptical plates; $I = 66$, $N = 225$

Aspect ratio	$\omega_s/\sqrt{D_0/\rho ha^4}$				
b/a	s=1	s=2	s=3	s=4	Remarks
1.0	10.216	21.261	21.261	34.880	Present
	10.216	21.260	21.260	34.879	Lam
	10.216	21.26	21.26	34.88	Carrington
	10.216	21.260	21.260	34.877	Kim
2.0	27.378	39.498	55.979	69.860	Present
	27.477	39.498	55.977	69.856	Lam
	27.5				Shibaoka
	27.378				Narita

Table 5 Natural frequencies $\omega_s/\sqrt{D_0/\rho hb^4}$ of clamped four-layered elliptical plates; [30 deg/−30 deg/30 deg/−30 deg], $I = 66$, $N = 225$

Aspect ratio	$\omega_s/\sqrt{D_0/\rho hb^4}$			
a/b	s=1	s=2	s=3	s=4
E-Glass/Epoxy				
1.0	8.1294	15.945	17.826	26.337
1.2	6.7302	13.562	14.429	22.387
1.5	5.6750	10.150	13.242	16.273
2.0	4.9364	7.6033	11.204	12.331
2.5	4.6173	6.4693	8.8890	11.911
3.0	4.4432	5.8542	7.6393	9.8241
4.0	4.2573	5.2120	6.3625	7.7235
Boron/Epoxy				
1.0	6.2734	11.226	14.619	17.409
1.2	4.9732	9.6750	10.956	15.393
1.5	3.9353	7.9485	8.4029	12.609
2.0	3.1607	5.6024	7.4049	8.6595
2.5	2.8165	4.5110	6.6178	6.9295
3.0	2.6320	3.9107	5.4752	6.6586
4.0	2.4445	3.2924	4.2958	5.4693
Graphite/Epoxy				
1.0	6.2489	11.080	14.650	17.199
1.2	4.9359	9.5392	10.941	15.243
1.5	3.8923	7.9018	8.2838	12.582
2.0	3.1198	5.5419	7.3067	8.6120
2.5	2.7800	4.4518	6.5558	6.8440
3.0	2.5992	3.8560	5.4113	6.5809
4.0	2.4162	3.2463	4.2377	5.4042

Downloaded 04 May 2010 to 171.66.16.26. Redistribution subject to ASME license or copyright; see http://www.asme.org/terms/Terms_Use.cfm

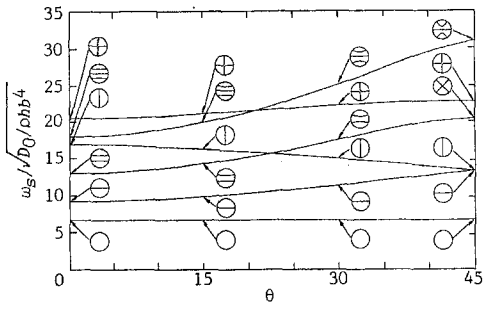


Fig. 2(*a*) Circular plate (*a*/*b* = 1.0)

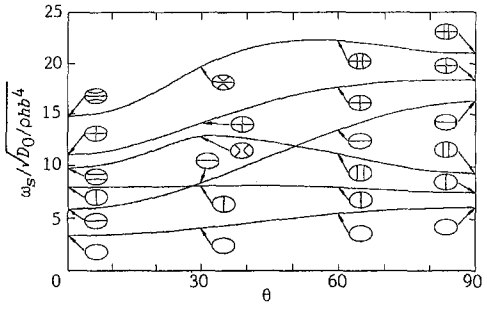


Fig. 2(*b*) Elliptical plate (*a*/*b* = 1.5)

Fig. 2 Effect of fiber orientation angle θ on natural frequency of clamped four-layered ([$\theta/-\theta/\theta/-\theta$]) plate; graphite/epoxy

nously versus the fiber orientation angle. Judging from the numerical results, the effect of the fiber orientation angle on the natural frequency is considerably influenced by the aspect ratio.

4 Experimental Results

To justify the numerical results, experimental studies are carried out for a plate laminated with four-layer angle plies with stacking sequence [30 deg/−30 deg/30 deg/−30 deg]. A circular plate ($a = b = 0.22$ m) and an elliptical plate ($a = 0.27$ m, $b = 0.18$ m) with plate thickness $h = 1.56 \times 10^{-3}$ m are used. Each layer material is carbon fiber-reinforced plastic. The measured material properties of the lamina are listed in Table 6. The plates are clamped to a rigid clamping fixture as shown in Fig. 3. Natural frequencies and mode shapes of the plates are obtained by using the experimental modal analysis. Table 7 presents the natural frequencies determined numerically and experimentally. A strain gage is affixed at the location where nodal lines disappear and an accelerometer is attached to the center of the plate. For the numerical results, the mass of an accelerometer (4.8 g) is considered as a concentrated mass. Therefore, to compute the natural frequency, Eq. (11) is used. From this table, one can see that the difference between experimental and numerical results is about eight percent at most. Figure 4 shows the mode shapes of the plates obtained numerically and experimentally. In Fig. 4, the narrow line represents the nodal line obtained by the experimental modal analysis and the heavy line shows those calculated by the numerical approach. The notation ● represents the location of the attached accelerometer, where it is different from the case of Table 7. For the natural frequencies, Fig. 4 shows that the difference is about ten percent at most. From this figure, we can see that the difference is large when the position of the accelerometer is close to the nodal line. From Table 7 and Fig. 4, it follows that one finds good agreement between the experimental and numerical results.

Table 6 Material properties of layer; carbon fiber-reinforced plastic

E_1(GPa)	E_2(GPa)	G_{12}(GPa)	ν_{12}	ρ(kg/m^3)
97.6	6.26	5.18	0.33	1535

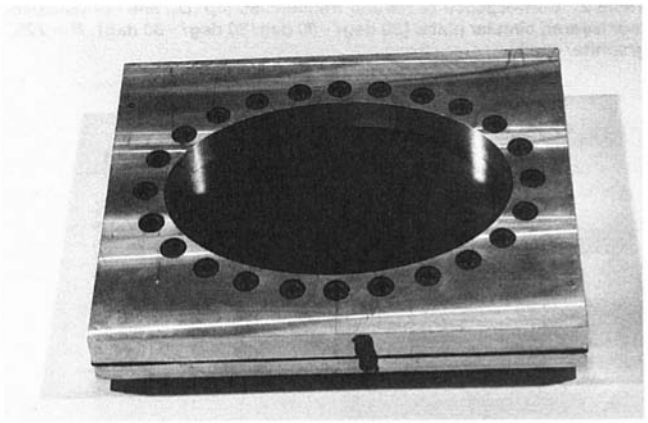


Fig. 3 Clamping fixture for elliptical plate

5 Conclusions

By applying free-vibration analysis using the functions for a static bending problem to the clamped antisymmetrically laminated elliptical plates, the convergence of natural frequencies was discussed. From the numerical examples, it follows that one can obtain sufficiently converged values by increasing the number of divisions of the plate. And, compared with the other investigators's numerical results, we can see that the accurate natural frequency is computed by the proposed approach. The effects of the fiber orientation angle on natural frequencies and mode shapes were investigated. From the changes of the fiber orientation angle, one can find that the variation of the natural frequency of the elliptical plate is more complicated than one of the circular plate. By the vibration tests of the clamped circular and elliptical plates, natural frequencies and mode shapes were obtained. From a comparison of experimental and numerical results, good agreement between these results is shown. Accordingly, it follows that one can accurately estimate natural frequencies and mode shapes by using the numerical approach proposed by the authors. In the present paper, full clamped elliptical plates were studied. However, by applying the energy method or Galerkin's method for the estimation of the functions for the static bending problem, free vibrations of the plates with various boundary conditions could be analyzed using the proposed approach. Also, using the similar approach proposed by the authors, one can obtain excellent results for the free vibration problem of the symmetrically laminated plates (Hosokawa et al., 1992, 1993). Therefore, the proposed approach is

Table 7 Natural frequencies of clamped four-layered elliptical plates; [30 deg/−30 deg/30 deg/−30 deg], carbon fiber-reinforced plastic

	Natural frequencies f_s(Hz)			
Order	Strain gage		Accelerometer	
s	Experiment	Analysis	Experiment	Analysis
Circular Plate (a/b=1.0)				
1	308	297	278	283
2	554	526	546	526
3	724	695	727	695
4	859	817	809	797
5	1082	1036	1080	1036
Elliptical Plate (a/b=1.5)				
1	299	276	270	268
2	599	560	590	560
3	635	588	615	588
4	949	892	927	890
5	1046	982	1008	982

Note: The accelerometer is attached to the center of the plate

Downloaded 04 May 2010 to 171.66.16.26. Redistribution subject to ASME license or copyright; see http://www.asme.org/terms/Terms_Use.cfm

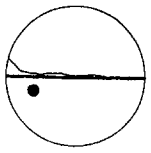
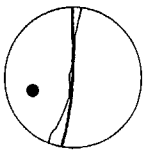
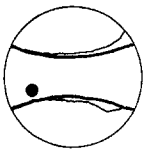
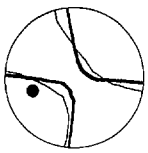
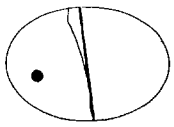
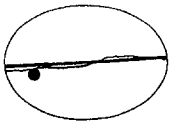
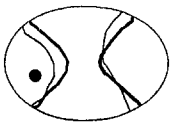
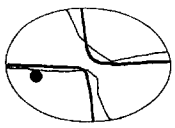
Modal order		2nd mode	3rd mode	4th mode	5th mode
Nodal pattern	Circular Plate a/b=1.0				
Natural frequency [Hz]	Analysis	524	680	814	1017
	Experiment	545	671	839	1021
Nodal pattern	Elliptical Plate a/b=1.5				
Natural frequency [Hz]	Analysis	552	587	874	975
	Experiment	565	643	866	1031

Fig. 4 Nodal patterns and natural frequencies of clamped four-layered elliptical plates; [30 deg/−30 deg/30 deg/−30 deg], carbon fiber-reinforced plastic

very useful for the analysis of the laminated composite plates with various boundary conditions and plane-forms.

References

Bert, C. W., and Mayberry, B. L., 1969, "Free Vibrations of Unsymmetrically Laminated Anisotropic Plates with Clamped Edges," *Journal of Composite Materials,* Vol. 3, pp. 282–292.

Carrington, H., 1925, "The Frequencies of Vibration of Flat Circular Plates Fixed at the Circumference," *Philosophical Magazine,* Vol. 50, pp. 1261–1264.

Chia, C., 1980, *Nonlinear Analysis of Plates,* McGraw-Hill, New York, p. 18.

Hosokawa, K., Yada, T., and Sakata, T., 1992, "Free Vibration Analysis of Clamped Symmetrically Laminated Plates (A Comparison between Numerical and Experimental Results)," *Transactions of the Japan Society of Mechanical Engineers,* Vol. 58, pp. 3184–3188 (in Japanese).

Hosokawa, K., Yada, T., and Sakata, T., 1993, "Free Vibrations Symmetrically Laminated Composite Plates," *JSME International Journal,* Vol. 36, Series C, pp. 296–300.

Hosokawa, K., Yamada, Y., and Sakata, T., 1994, "Free Vibration Analysis of Unsymmetrically Laminated Plates," *Transactions of the Japan Society of Mechanical Engineers,* Vol. 60, pp. 1904–1908 (in Japanese).

Jones, R. M., 1973, "Buckling and Vibration of Unsymmetrically Laminated Cross-Ply Rectangular Plates," *AIAA Journal,* Vol. 11, pp. 1626–1632.

Khdeir, A. A., 1988, "Free Vibration of Antisymmetric Angle-ply Laminated Plates Including Various Boundary Conditions," *Journal of Sound and Vibration,* Vol. 122, pp. 377–388.

Kim, C. S., and Dickinson, S. M., 1989, "On the Lateral Vibration of Thin Annular and Circular Composite Plates Subject to Certain Complicating Effects," *Journal of Sound and Vibration,* Vol. 130, pp. 363–377.

Lam, K. Y., Liew, K. M., and Chow, S. T., 1992, "Use of Two-Dimensionals for Vibration Analysis of Circular and Elliptical Plates," *Journal of Sound and Vibration,* Vol. 154, pp. 261–269.

Lin, C. C., and King, W. W., 1974, "Free Transverse Vibrations of Rectangular Unsymmetrically Laminated Plates," *Journal of Sound and Vibration,* Vol. 36, pp. 91–103.

Narita, Y., 1985, "Natural Frequencies of Free, Orthotropic Elliptical Plates," *Journal of Sound and Vibration,* Vol. 100, pp. 83–89.

Reddy, J. N., 1979, "Free Vibration of Antisymmetric, Angle-Ply Laminated Plates Including Transverse Shear Deformation by The Finite Element Method," *Journal of Sound and Vibration,* Vol. 66, pp. 565–576.

Shibaoka, Y., 1956, "On the Transverse Vibration of an Elliptic Plate with Clamped Edge," *Journal of the Physical Society of Japan,* Vol. 11, pp. 797–803.

Sivakumaran, K. S., 1989, "Free Vibration of Annular and Circular Asymmetric Composite Laminates," *Journal of Composite Structures,* Vol. 11, pp. 205–226.

Vinson, J. R., and Sierakowski, R. L., 1986, *The Behavior of Structures Composed of Composite Materials,* Martinus Nijhoff Dordrecht, The Netherlands, p. 303.

Downloaded 04 May 2010 to 171.66.16.26. Redistribution subject to ASME license or copyright; see http://www.asme.org/terms/Terms_Use.cfm

Transient Residual Stresses in Thermal Barrier Coatings: Analytical and Numerical Results

S. Q. Nusier
Assoc. Mem. ASME

G. M. Newaz
Assoc. Mem. ASME

Mechanical Engineering Department,
Wayne State University,
Detroit, MI 48202

Thermal barrier coatings (TBCs) provide thermal insulation to high-temperature superalloys. Residual stresses develop in TBCs during cool-down from processing temperatures due to the thermal expansion mismatch between the different layers (substrate, bond coat, and the ceramic TBC). These residual stresses can initiate microcracks at the bond coat/TBC interface which can lead to debonding at the bond coat/TBC interface. Elasticity-based modeling was used to determine the transient stresses in the TBC, bond coat, and the superalloy substrate with specific attention to the interfaces. For the steady-state case, finite element modeling was undertaken as well. Closed-form elasticity solutions correlated well with the finite element results for the steady-state case. The highest residual stresses occurred at the interface between the bond coat and the TBC. An important result of this investigation was that the TBC/bond coat interface was under biaxial stress field. An important result was that the residual stresses developed in the substrate are higher for the case of partly cooled specimen compared to the fully cooled specimen which can be rationalized due to the presence of higher temperature gradients at earlier times during cool-down from processing temperature.

Introduction

Thermal barrier coatings (TBCs) provide thermal insulation and the bond coat provides oxidation resistance at high temperatures. Ceramic matrix composites (CMCs) can be used for high-temperature application, whereas metallic substrate such as superalloys cannot perform at this high temperature without this ceramic layer, i.e., the TBC. Plasma-sprayed zirconia-yttria ceramic layer with a nickel-chromium-aluminum-yttrium bond coat on a substrate made of nickel-based superalloy (Chang et al., 1987) is a common superalloy/TBC system. Application of these superalloys can be found in aircraft engine (advanced gas turbines) parts such as ducts, vanes, and blades, etc. In automotive applications, the piston head for diesel engine is coated to achieve longer life time and higher performance in terms of fuel reduction and power. However, these coatings have durability problems, due to the material and thermal mismatch between the coating and the metallic substrate. Thermal residual stresses develop during cool down from processing temperatures. These residual stresses may initiate microcracks such as debonding and radial cracks and can have a profound effect on the response of the TBC and interfacial damage accumulation and failure. Their understanding is essential to predict the behavior of the coatings and their performance.

A quantitative determination of the stress states in a model thermal barrier coating as it cools down from the processing temperature (stress-free) to another lower temperature was studied by Chang, et al., (1987). Considering a three-layer concentric cylinder model and a plane-strain condition, they clearly illustrated the importance of the coefficient of thermal expansion of the bond coat and the Young's modulus of the TBC. The finite element approach was used by these authors. The experimental method and finite element approach was used by Holmes (1988) to study thermal fatigue of coated superalloys of a stepped-disk specimen. The results obtained for the various stress-strain histories clearly illustrate that both the compressive strains encountered on specimen heatup and the tensile strains encountered on cool-down can have a profound effect on useful coating life. An elastic-plastic finite element method was formulated to study residual stresses developed at graded ceramic-metal interfaces during cool-down by Williamson et al., (1993). The results demonstrate the importance of accounting for plasticity when comparing graded and nongraded interfaces. They studied the effects of different interlayer thicknesses and nonlinear composition profiles on strain and stress distributions established during cool down (Drake et al., 1993). Mikata and Taya (1985) studied the stress field in a coated continuous fiber composite subjected to thermomechanical loading, a four-layer concentric circular model was used. The displacement approach was used by Kardomateas (1989) to study the transient thermal stress problem for a hollow circular cylinder. He presented the variation of stresses as function of time and thickness. The effects of circumferential variation of the heat transfer coefficient and gas radiation in three concentric cylinders were studied by Chung et al. (1985). They determined the transient two-dimensional temperature distribution by using the finite element method. Transient thermal stresses in fully and partly cooled circular rings were investigated by Iwaki (1986). He showed that the thermal stress in the fully cooled circular ring is not always greater than that in the partly cooled circular ring. Thermal fracture of multilayer ceramic thermal barrier coatings was studied by Takenchi and Kokini (1994). Controlled experiments along with finite element modeling were used. Their work showed that surface cracks are formed as a result of tensile stresses that are created following stress relaxation in the TBC at steady-state high temperatures. The effect of a transient ther-

Contributed by the Applied Mechanics Division of THE AMERICAN SOCIETY OF MECHANICAL ENGINEERS for publication in the ASME JOURNAL OF APPLIED MECHANICS.

Discussion on the paper should be addressed to the Technical Editor, Professor Lewis T. Wheeler, Department of Mechanical Engineering, University of Houston, Houston, TX 77204-4792, and will be accepted until four months after final publication of the paper itself in the ASME JOURNAL OF APPLIED MECHANICS.

Manuscript received by the ASME Applied Mechanics Division, Oct. 3, 1995; final revision, Aug. 21, 1997. Associate Technical Editor: M. Taya.

 Copyright © 1998 by ASME

Downloaded 04 May 2010 to 171.66.16.26. Redistribution subject to ASME license or copyright; see http://www.asme.org/terms/Terms_Use.cfm

mal load on a coating which is bonded to a cylindrical substrate was studied by Kokini and Hornack (1988). The finite element method was used to obtain a solution for a circumferential edge crack normal to the coating. Their analysis showed that smaller heat transfer rates result in smaller stress intensity factors. The initial phase of transient thermal stresses due to general boundary thermal loads in an orthotropic hollow cylinder was studied by Kardomateas (1990). Kardomateas and Chung (1994) studied the case of orthotropic cylindrical shell loaded by an external pressure under imposed constant moisture concentrations on the inner and outer surfaces. They obtained an exact elasticity solution for stresses and displacements. The thermomechanical response of ceramically coated metal parts in elevated thermal environments were investigated by Padovan et al., (1984, 1985). A finite element algorithm was used in their analysis. The thermomechanical oxidation response of thermal barrier coatings was studied by Padovan et al., (1986). They solved the field equations with the associated boundary conditions numerically.

A thermal barrier coated high-temperature substrate in the form of a cylinder is a multilayer system with a number of interfaces. The substrate is first coated with a bond coat whose primary function is to provide oxidation protection and to enhance bonding of the thermal barrier coating (TBC) to the overall system. The TBC layer, the bond coat, and the substrate have different thermal expansion coefficients. As a result due to thermal loading and related excursion, each layer may experience residual thermal stresses. Prior to reaching a steady-state situation, the thermal residual stresses can vary significantly over time, particularly, at early times, say within the first 100 seconds of cooling. Therefore, the problem of transient residual stresses can become quite important and can affect the bond coat/TBC and the substrate/bond coat interfaces. Numerical solution techniques are often utilized for such problems provided that the geometry of the multilayer system is amenable to idealization. However, for TBC systems there no closed-form solutions available to determine the overall temperature field and subsequently to obtain the transient residual stress field. In the current work, a concentric cylinder model is taken for representating a realistic superalloy substrate coated with bond coat and TBC and to obtain an elasticity solution that describes the transient residual stress fields.

In our investigation, the primary focus was to analytically predict the transient thermal residual stress distribution at the various interfaces of the TBC/bond coat/superalloy system and compare the results with finite element stress analysis results. Evaluation of residual stresses is treated until it reaches a steady-state condition. These solutions provide an insight into the influence of thermal and material mismatch stresses at the interfaces in TBC coated superalloy systems, particularly in identifying conditions that lead to interfacial separation due to thermal loads.

Modeling Aspects

For the case of N concentric cylinders, it is possible to get an exact elasticity solution far away from the edges. This provides a better understanding of the type of stresses that exist, and also we will be able to verify these stresses with the finite element solution. The elasticity solution is developed as follows.

Transient Temperature Solution. Consider a one-dimensional multiphase region consisting of N concentric cylinders, where the outermost one is layer number one and the innermost one is solid and has a layer number N. Continuity of temperature and heat flux was assumed to be across the interfaces (perfect thermal contact between the layers at the interfaces). The governing equation for the transient temperature field is

$$\frac{\partial^2 T_i}{\partial r^2} + \frac{1}{r}\frac{\partial T_i}{\partial r} = \frac{1}{\alpha_i}\frac{\partial T_i}{\partial t}$$

$$i = 1, 2, \ldots, N \quad r_{i+1} < r < r_i \quad t > 0. \quad (1)$$

The boundary conditions are

$$T_{i+1}(r_{i+1}, t) = T_i(r_{i+1}, t) \quad i = 1, 2, \ldots, N-1 \quad t > 0 \quad (2)$$

$$k_{i+1}\frac{\partial T_{i+1}(r_{i+1}, t)}{\partial r} = k_i \frac{\partial T_i(r_{i+1}, t)}{\partial r}$$

$$i = 1, 2, \ldots, N-1 \quad t > 0 \quad (3)$$

$$hT_1(r_1, t) + k_1 \frac{\partial T_1(r_1, t)}{\partial r} = 0 \quad t > 0. \quad (4)$$

The initial condition is

$$T_i(r, 0) = T_0 \quad r_{i+1} < r < r_i \quad i = 1, 2, \ldots, N \quad t = 0, \quad (5)$$

where α_i is the thermal diffusivity, k_i is the thermal conductivity, t is the time, and h is the convection heat transfer coefficient. The above boundary value problem of heat conduction is solved by applying the orthogonal-expansion technique over multilayer regions (Ozisik, 1968; Tittle, 1965; Tittle and Robenson, 1965). The temperature function $T(r, t)$ can be represented in an infinite series of a separated space (r) and time (t) variables in the following form:

$$T(r, t) = \sum_{n=1}^{\infty} A_n \cdot X_{jn}(r) \cdot e^{-\alpha_j \omega_{jn}^2 t} \quad j = 1, 2, \ldots, N \quad (6)$$

where A_n are arbitrary constants and $X_{jn}(r)$ are the eigenfunctions associated with the above eigenvalue problem. The solution of this eigenvalue problem will have the form

$$X_{jn}(r) = B_{jn}[J_0(\omega_{jn} r) + C_{jn} Y_0(\omega_{jn} r)]$$

$$r_{i+1} < r < r_i \quad i = 1, 2, \ldots, N \quad (7)$$

where J_n and Y_n are Bessel function of the first and second kind, receptively. Since there is no energy storage in the infinitesimal thickness of the interface, the time behavior of the temperature at the interface should be the same on both sides. In mathematical form, this condition is written as

$$\alpha_{j-1}\omega_{(j-1)n}^2 = \alpha_j \omega_{jn}^2 \quad j = N-1, \ldots, 1. \quad (8)$$

For the case of uniform initial temperature (T_0) all over the regions, the coefficient A_n is written as

$$A_n = \frac{\sum_{j=1}^{N} \frac{k_j}{\alpha_j} \int_j T_0 \cdot X_{jn}(r) \cdot r \cdot dr}{\sum_{j=1}^{N} \frac{k_j}{\alpha_j} \int_j T_0 \cdot X_{jn}^2(r) \cdot r \cdot dr}. \quad (9)$$

By applying the boundary conditions, the coefficients B_{jn}, C_{jn} and the eigenvalues ω_{jn} can be evaluated.

Now, consider the case of the three concentric cylinders. The temperature functions for the layers are

$$T_1(r, t) = \sum_{n=1}^{\infty} A_n \cdot X_{1n}(r) \cdot e^{-\alpha_1 \omega_{1n}^2 t} \quad r_2 < r < r_1 \quad (10)$$

$$T_2(r, t) = \sum_{n=1}^{\infty} A_n \cdot X_{2n}(r) \cdot e^{-\alpha_2 \omega_{2n}^2 t} \quad r_3 < r < r_2 \quad (11)$$

$$T_3(r, t) = \sum_{n=1}^{\infty} A_n \cdot X_{3n}(r) \cdot e^{-\alpha_3 \omega_{3n}^2 t} \quad 0 < r < r_3. \quad (12)$$

The eigenfunctions are

$$X_{1n}(r) = B_{1n}[J_0(\omega_{1n} r) + C_{1n} Y_0(\omega_{1n} r)] \quad r_2 < r < r_1 \quad (13)$$

$$X_{2n}(r) = B_{2n}[J_0(\omega_{2n} r) + C_{2n} Y_0(\omega_{2n} r)] \quad r_3 < r < r_2. \quad (14)$$

Downloaded 04 May 2010 to 171.66.16.26. Redistribution subject to ASME license or copyright; see http://www.asme.org/terms/Terms_Use.cfm

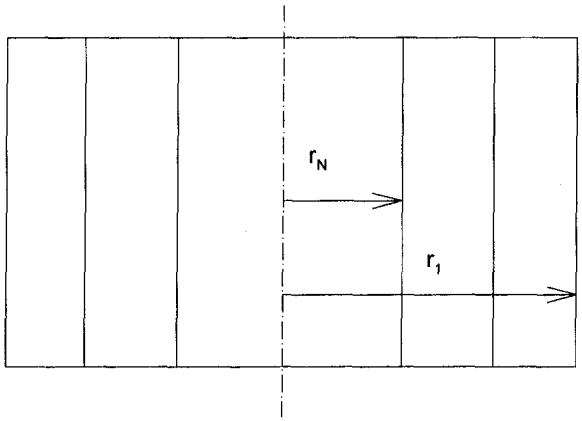


Fig. 1 *N*-phase concentric cylinder model

$$X_{3n}(r) = J_0(\omega_{3n}r) \quad 0 < r < r_3 \tag{15}$$

The eigenvalues are related by

$$\alpha_1\omega_{1n}^2 = \alpha_2\omega_{2n}^2 = \alpha_3\omega_{3n}^2. \tag{16}$$

By applying the boundary conditions (Eqs. (2), (3), (4)), one can get the following:

$$k_1\omega_{1n}[J_1(\omega_{1n}r_1) + C_{1n}Y_1(\omega_{1n}r_1)] = h[J_0(\omega_{1n}r_1) + C_{1n}Y_0(\omega_{1n}r_1)] \tag{17}$$

$$J_0(\omega_{3n}r_3) = B_{2n}[J_0(\omega_{2n}r_3) + C_{2n}Y_0(\omega_{2n}r_3)] \tag{18}$$

$$B_{2n}[J_0(\omega_{2n}r_2) + C_{2n}Y_0(\omega_{2n}r_2)] = B_{1n}[J_0(\omega_{1n}r_2) + C_{1n}Y_0(\omega_{1n}r_2)] \tag{19}$$

$$k_3\omega_{3n}J_1(\omega_{3n}r_3) = k_2\omega_{2n}B_{2n}[J_1(\omega_{2n}r_3) + C_{2n}Y_1(\omega_{2n}r_3)] \tag{20}$$

$$k_2\omega_{2n}B_{2n}[J_1(\omega_{2n}r_2) + C_{2n}Y_1(\omega_{2n}r_2)] = k_1\omega_{1n}B_{1n}[J_1(\omega_{1n}r_2) + C_{1n}Y_1(\omega_{1n}r_2)]. \tag{21}$$

Equations (17)–(20) along with Eq. (16) could be solved for the following unknowns, C_{1n}, C_{2n}, B_{1n}, B_{2n}, ω_{1n}, ω_{2n}, ω_{3n}.

The solution for these equations is obtained by eliminating all of the unknowns except ω_{1n}, the final equation is solved for the root ω_{1n} by using the bisection method. Finally, all the other unknowns were evaluated in terms of the known eigenvalue ω_{1n}. The coefficients A_n is evaluated by using Eq. (9) ($j = 3$ for this case). After integration and simplification, A_n is given by

$$A_n = \frac{2T_0}{r_3\omega_{3n}} \frac{J_1(\omega_{3n}r_3) + \sum_{i=1}^{2} \frac{k_{i+1}}{k_3}\left(\frac{\alpha_3}{\alpha_{3-i}}\right)^{0.5}\left[\frac{r_{3-i}}{r_3}Z_1(\omega_{(3-i)n}r_{3-i}) - Z_1(\omega_{(3-i)n}r_{4-i})\right]}{J_0^2(\omega_{3n}r_3) + J_1^2(\omega_{3n}r_3) + \sum_{i=1}^{2}\frac{k_{i+1}}{k_3}\left(\frac{\alpha_3}{\alpha_{3-i}}\right)\sum_{j=0}^{1}\frac{r_{3-i-j}^2}{r_3^2}[Z_j^2(\omega_{(3-i)n}r_{3-i}) - Z_j^2(\omega_{(3-i)n}r_{4-i})]} \tag{22}$$

where $Z_p(X_n) = B_n[J_p(X_n) + C_nY_p(X_n)]$. Finally, by using Eqs. (10)–(12) the temperature field is well defined.

Stress Field in *N* Concentric Cylinders Subjected to Thermal Loading. Consider the N concentric long circular cylinders shown in Fig. 1. The outermost cylinder radius is r_1 and the innermost cylinder radius is r_N. The entire model is subjected to axisymmetric temperature change $\Delta T(r, t)$. In general, all the materials are assumed to be transversely isotropic both in stiffness and thermal expansion, where (r, θ) is the transverse plane.

The equilibrium equations in the r, θ, and z directions are given by (Boley and Weiner, 1960; Manson, 1966; Hasselman and Heller, 1980; Timoshenko and Goodier, 1971),

$$\frac{\partial\sigma_{rr}}{\partial r} + \frac{1}{r}\frac{\partial\sigma_{r\theta}}{\partial\theta} + \frac{\partial\sigma_{rz}}{\partial z} + \frac{\sigma_{rr} - \sigma_{\theta\theta}}{r} = 0$$

$$\frac{\partial\sigma_{\theta r}}{\partial r} + \frac{1}{r}\frac{\partial\sigma_{\theta\theta}}{\partial\theta} + \frac{\partial\sigma_{\theta z}}{\partial z} + \frac{2\sigma_{r\theta}}{r} = 0$$

$$\frac{\partial\sigma_{zr}}{\partial r} + \frac{1}{r}\frac{\partial\sigma_{z\theta}}{\partial\theta} + \frac{\partial\sigma_{zz}}{\partial z} + \frac{\sigma_{rz}}{r} = 0. \tag{23}$$

The stress-strain relations are

$$\sigma_{rr} = C_{11}\epsilon_{rr} + C_{12}\epsilon_{\theta\theta} + C_{13}\epsilon_{zz} - \beta_1 T$$

$$\sigma_{\theta\theta} = C_{12}\epsilon_{rr} + C_{11}\epsilon_{\theta\theta} + C_{13}\epsilon_{zz} - \beta_1 T$$

$$\sigma_{zz} = C_{13}\epsilon_{rr} + C_{13}\epsilon_{\theta\theta} + C_{33}\epsilon_{zz} - \beta_3 T$$

$$\sigma_{rz} = 2C_{44}\epsilon_{rz}$$

$$\sigma_{\theta z} = 2C_{44}\epsilon_{\theta z}$$

$$\sigma_{r\theta} = (C_{11} - C_{12})\epsilon_{r\theta} \tag{24}$$

and

$$\beta_1 = (C_{11} + C_{12})\alpha_T + C_{13}\alpha_L$$

$$\beta_3 = 2C_{12}\alpha_T + C_{33}\alpha_L \tag{25}$$

where C_{ij} are elastic constants, and α_T and α_L are the thermal expansion coefficients along the transverse (r) and the longitudinal (z) directions, respectively. The strain-displacement relations are given by

$$\epsilon_{rr} = \frac{\partial u_r}{\partial r}, \quad \epsilon_{\theta\theta} = \frac{1}{r}\frac{\partial u_\theta}{\partial\theta} + \frac{u_r}{r}, \quad \epsilon_{zz} = \frac{\partial u_z}{\partial z},$$

$$\epsilon_{rz} = \frac{1}{2}\left(\frac{\partial u_z}{\partial r} + \frac{\partial u_r}{\partial z}\right)$$

$$\epsilon_{\theta z} = \frac{1}{2}\left(\frac{\partial u_\theta}{\partial z} + \frac{1}{r}\frac{\partial u_z}{\partial\theta}\right), \quad \epsilon_{r\theta} = \frac{1}{2}\left(\frac{1}{r}\frac{\partial u_r}{\partial\theta} + \frac{\partial u_\theta}{\partial r} - \frac{u_\theta}{r}\right) \tag{26}$$

where σ_{ij}, ϵ_{ij}, and u_i are components of stress, strain, and displacement, respectively. Due to the axisymmetry, the displacement field can be expressed as

$$u_r = u(r), \quad u_\theta = 0, \quad u_z = w(z). \tag{27}$$

A substitution of Eq. (27) into Eq. (26) yields to

$$\epsilon_{rr} = \frac{\partial u}{\partial r}, \quad \epsilon_{\theta\theta} = \frac{u}{r}, \quad \epsilon_{zz} = \frac{\partial w}{\partial z}, \quad \epsilon_{rz} = \epsilon_{\theta z} = \epsilon_{r\theta} = 0. \tag{28}$$

Substituting Eq. (28) into Eq. (24) gives

Downloaded 04 May 2010 to 171.66.16.26. Redistribution subject to ASME license or copyright; see http://www.asme.org/terms/Terms_Use.cfm

$$\sigma_{rr} = C_{11}\frac{\partial u}{\partial r} + C_{12}\frac{u}{r} + C_{13}\frac{\partial w}{\partial z} - \beta_1 T$$

$$\sigma_{\theta\theta} = C_{12}\frac{\partial u}{\partial r} + C_{11}\frac{u}{r} + C_{13}\frac{\partial w}{\partial z} - \beta_1 T$$

$$\sigma_{zz} = C_{13}\frac{\partial u}{\partial r} + C_{13}\frac{u}{r} + C_{33}\frac{\partial w}{\partial z} - \beta_3 T$$

$$\sigma_{rz} = \sigma_{\theta z} = \sigma_{r\theta} = 0. \tag{29}$$

Then the governing equations are obtained in terms of displacements from Eqs. (23) and (29)

$$C_{11}\frac{d^2u}{dr^2} - C_{11}\frac{u}{r^2} + \frac{C_{11}}{r}\frac{du}{dr} = \beta_1\frac{dT}{dr}, \frac{d^2w}{dz^2} = 0. \tag{30}$$

Now, for the case of three concentric long circular cylinders, the boundary conditions are given by

$$\sigma^1_{rr}(r_1) = 0$$

$$u_1 = u_2,\ w_1 = w_2,\ \sigma^1_{rr} = \sigma^2_{rr} \quad \text{at} \quad r = r_2$$

$$u_2 = u_3,\ w_2 = w_3,\ \sigma^2_{rr} = \sigma^3_{rr} \quad \text{at} \quad r = r_3$$

$$\int_0^{r_3} \sigma^3_{zz} r dr + \int_{r_3}^{r_2} \sigma^2_{zz} r dr + \int_{r_2}^{r_1} \sigma^1_{zz} r dr = 0. \tag{31}$$

The general solution to Eq. (30) is given by

$$u(r, t) = Ar + \frac{B}{r} + \frac{r}{2}\int g(r, t)dr - \frac{1}{2r}\int r^2 g(r, t)dr$$

$$w(z) = Ez + F \tag{32}$$

where

$$g(r, t) = \frac{\beta_1}{C_{11}}\frac{dT}{dr}. \tag{33}$$

$F = 0$, and substitution of Eq. (32) into Eq. (29), yields

$$\sigma^n_{rr} = C^n_{11}\left[A_n - \frac{B_n}{r^2} + C_n(r, t) - \frac{D_n(r, t)}{r^2}\right]$$

$$+ C^n_{12}\left[A_n + \frac{B_n}{r^2} + C_n(r, t) + \frac{D_n(r, t)}{r^2}\right]$$

$$+ C^n_{13}E - \beta^n_1 T_n(r, t)$$

$$\sigma^n_{\theta\theta} = C^n_{12}\left[A_n - \frac{B_n}{r^2} + C_n(r, t) - \frac{D_n(r, t)}{r^2}\right]$$

$$+ C^n_{11}\left[A_n + \frac{B_n}{r^2} + C_n(r, t) + \frac{D_n(r, t)}{r^2}\right]$$

$$+ C^n_{13}E - \beta^n_1 T_n(r, t)$$

$$\sigma^n_{zz} = 2C^n_{13}[A_n + C_n(r, t)] + C^n_{33}E - \beta^n_3 T_n(r, t), \tag{34}$$

where n is referred to as the cylinder under consideration, $n = 1$ is the outermost cylinder, $n = 2$ is the middle cylinder, and $n = 3$ is the innermost cylinder, and where

$$C_n(r, t) = \frac{1}{2}\int g_n(r, t)dr = \frac{\beta^n_1}{2C^n_{11}} T_n(r, t)$$

$$D_n(r, t) = \frac{-1}{2}\int r^2 g_n(r, t)dr = \frac{\beta^n_1}{2C^n_{11}}\sum_{m=1}^{\infty} A_m B_{nm} e^{-\alpha_n \omega^2_{nm} t}$$

$$\times [r^2[J_2(\omega_{nm} r, t) + C_{nm} Y_2(\omega_{nm} r, t)]]. \tag{35}$$

Now, when the materials are isotropic, both in stiffness and in thermal expansion, we have

$$C^1_{11} = C^1_{33} = 2\mu_1 + \lambda_1,\ C^1_{12} = C^1_{13} = \lambda_1$$

$$C^2_{11} = C^2_{33} = 2\mu_2 + \lambda_2,\ C^2_{12} = C^2_{13} = \lambda_2$$

$$C^3_{11} = C^3_{33} = 2\mu_3 + \lambda_3,\ C^3_{12} = C^3_{13} = \lambda_3$$

$$\beta^1_1 = \beta^1_3 = (2\eta_1 + 3\lambda_1)\alpha_1$$

$$\beta^2_1 = \beta^2_3 = (2\eta_2 + 3\lambda_2)\alpha_2$$

$$\beta^3_1 = \beta^3_3 = (2\eta_3 + 3\lambda_3)\alpha_3. \tag{36}$$

After substituting Eqs. (32), (34), and (36) into the boundary conditions, Eq. (31) yields

$$C^1_{11}\left[A_1 - \frac{B_1}{r_1^2} + C_1(r_1, t) - \frac{D_1(r_1, t)}{r_1^2}\right]$$

$$+ C^1_{12}\left[A_1 - \frac{B_1}{r_1^2} + C_1(r_1, t) - \frac{D_1(r_1, t)}{r_1^2}\right]$$

$$+ C^1_{13}E - \beta^1_1 T_1(r_1, t) = 0$$

$$A_1 r_2 + \frac{B_1}{r_2} + r_2 C_1(r_2, t) + \frac{D_1(r_2, t)}{r_2}$$

$$= A_2 r_2 + \frac{B_2}{r_2} + r_2 C_2(r_2, t) + \frac{D_2(r_2, t)}{r_2}$$

$$A_2 r_3 + \frac{B_2}{r_3} + r_3 C_2(r_3, t) + \frac{D_2(r_3, t)}{r_3}$$

$$= A_3 r_3 + r_3 C_3(r_3, t) + \frac{D_3(r_3, t)}{r_3}$$

$$C^3_{11}\left[A_3 + C_3(r_3, t) - \frac{D_3(r_3, t)}{r_3^2}\right]$$

$$+ C^3_{12}\left[A_3 + C_3(r_3, t) - \frac{D_3(r_3, t)}{r_3^2}\right]$$

$$+ C^3_{13}E - \beta^3_1 T_3(r_3, t)$$

$$= C^2_{11}\left[A_2 - \frac{B_2}{r_3^2} + C_2(r_3, t) - \frac{D_2(r_3, t)}{r_3^2}\right]$$

$$+ C^2_{12}\left[A_2 - \frac{B_2}{r_3^2} + C_2(r_3, t) - \frac{D_2(r_3, t)}{r_3^2}\right]$$

$$+ C^2_{13}E - \beta^2_1 T_2(r_3, t)$$

$$C^2_{11}\left[A_2 - \frac{B_2}{r_2^2} + C_2(r_2, t) - \frac{D_2(r_2, t)}{r_2^2}\right]$$

$$+ C^2_{12}\left[A_2 - \frac{B_2}{r_2^2} + C_2(r_2, t) - \frac{D_2(r_2, t)}{r_2^2}\right]$$

$$+ C^2_{13}E - \beta^2_1 T_2(r_2, t)$$

$$= C^1_{11}\left[A_1 - \frac{B_1}{r_2^2} + C_1(r_2, t) - \frac{D_1(r_2, t)}{r_2^2}\right]$$

$$+ C^1_{12}\left[A_1 - \frac{B_1}{r_2^2} + C_1(r_2, t) - \frac{D_1(r_2, t)}{r_2^2}\right]$$

$$+ C^1_{13}E - \beta^1_1 T_1(r_2, t)$$

Downloaded 04 May 2010 to 171.66.16.26. Redistribution subject to ASME license or copyright; see http://www.asme.org/terms/Terms_Use.cfm

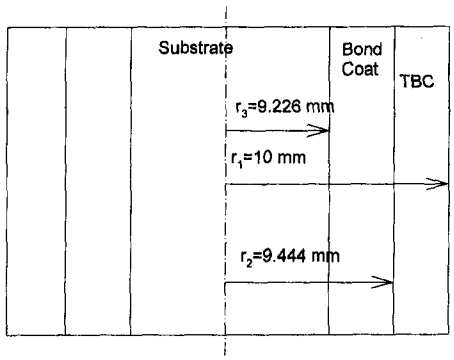


Fig. 2 Dimension of TBC layer in relation to bond coat and superalloy substrate

$$(2C^3_{13}A_3 + C^3_{33}E)\frac{r_3^2}{2} + (2C^2_{13}A_2 + C^2_{33}E) \times \frac{r_2^2 - r_3^2}{2}(2C^1_{13}A_1 + C^1_{33}E)\frac{r_1^2 - r_2^2}{2} + \left(\frac{C^3_{13}\beta^3_1}{C^3_{11}} - \beta^3_3\right)\sum_{n=1}^{\infty} A_nB_{3n}e^{-\alpha_3\omega^2_{3n}t}\left[\frac{r}{\omega_{3n}}[J_1(\omega_{3n}r, t) + C_{3n}Y_1(\omega_{3n}r, t)]\Big|_{r_3}^{r_2}\right] + \left(\frac{C^2_{13}\beta^2_1}{C^2_{11}} - \beta^2_3\right)\sum_{n=1}^{\infty} A_nB_{2n}e^{-\alpha_2\omega^2_{2n}t}\left[\frac{r}{\omega_{2n}}[J_1(\omega_{2n}r, t) + C_{2n}Y_1(\omega_{2n}r, t)]\Big|_{r_3}^{r_2}\right] + \left(\frac{C^1_{13}\beta^1_1}{C^1_{11}} - \beta^1_3\right)\sum_{n=1}^{\infty} A_nB_{1n}e^{-\alpha_1\omega^2_{1n}t}\left[\frac{r}{\omega_{1n}}[J_1(\omega_{1n}r, t) + C_{1n}Y_1(\omega_{1n}r, t)]\Big|_{r_2}^{r_1}\right] = 0. \quad (37)$$

Equation (37) has six linear equations with six unknowns (A_1, A_2, A_3, B_1, B_2, E), and after solving these equations, the stress field is fully defined at every r and t.

Finite Element Stress Analysis

The uncoated nickel-based superalloy specimen had a radius of 9.26 mm, the bond coat layer thickness is 0.184 mm, the TBC thickness is 0.556 mm, and the length of the specimen is 100 mm. These dimensions are shown in Fig. 2. The properties of these three layers are given in Table 1. We analyzed a model case where the specimen was plasma-sprayed in air with a thin zirconia-yttria (ZrO_2–8 wt% Y_2O_3) layer on a nickel-chromium-aluminum-zirconium bond coat, as in Chang et al. (1987). The specimen was cooled down from a processing temperature of 1000°C to a temperature of 0°C. A convection heat transfer coefficient (h) of a value 50 W/m^2/K was used in the analysis. The finite element model was used for the case of three concentric cylinders using ALGOR for a fully elastic analysis. A quarter model was used since the specimen is axisymmetric and also symmetry is maintained about the middle section. A four-node isoparametric element type was used; the total number of elements was 500. Along the longitudinal axis, the nodes can move in the axial direction only, and along the midsection symmetry line, the nodes can move in the radial direction only.

Results

The orthogonal-expansion technique over a multilayer region was used in order to determine the temperature distribution in the concentric cylinders. The first three roots (ω_{jn}) were found to be dominant in prescribing the temperature field. All other roots are weak and neglected. The axisymmetric condition was applied on the equilibrium equations along with stress-strain relations and strain-displacement relations, so the equilibrium equations reduce to two ordinary differential equations. The transient stress field was obtained by applying the boundary conditions to the solution obtained from those ordinary differential equations. Transient residual stresses have been evaluated for the case of three concentric cylinders by the finite element approach as well as by using the elasticity approach. Figure 3 shows the variation of stress-field components versus time at r = 2 mm in the substrate region, it is clear that the stresses are higher for the case of a partly cooled compared to a fully cooled case. Because of the high-temperature gradient in the superalloy, when the time reaches 16.5 seconds, the stresses are maximum. Figure 4 shows the variation of stress-field components versus time at r = 9.3 mm in the bond coat region. It is clear that the stresses are higher for the case of a fully cooled compared to that of a partly cooled case. Figure 5 shows the variation of stress-field components versus time at r = 9.6 mm in the TBC layer. It is clear that the stresses are higher for the case of a fully cooled compared to a partly cooled case because the temperature field has a high gradient at the earlier stages compared to latest stages. The temperature distribution as a function of time and radial distance is shown in Fig. 6. It is clear that the temperature field has a high gradient at the earlier stages compared to latest stages.

Figure 7 shows the variation of the radial stress versus the radial distance at different times. The peak value occurred close to the center at t = 16.5 seconds. Also, Fig. 7 shows that the radial stresses vanish at the outer surface. Radial stresses are not critical for this specimen configuration because of their low values. Note that the radial stress range is 0–25 MPa. Figure

Table 1 Material properties at 22, 566 and 1149°C (Wright, 1995)

Material	Young's modulus (GPa)	Poisson's ratio	Coefficient of thermal expansion (°C^{-1})	Coefficient of thermal conductivity (W/m/k)	Coefficient of thermal diffusivity (m^2/s)
Substrate	175.8	0.25	13.91×10^{-6}	7	2×10^{-6}
	150.4	0.2566	15.36×10^{-6}	13	3.4×10^{-6}
	94.1	0.3224	19.52×10^{-6}	22	2.64×10^{-6}
Bond coat	137.9	0.27	15.16×10^{-6}	25	8×10^{-6}
	121.4	0.27	15.37×10^{-6}	50	13.56×10^{-6}
	93.8	0.27	17.48×10^{-6}	65	15.52×10^{-6}
TBC	27.6	0.25	10.01×10^{-6}	1	5×10^{-7}
	6.9	0.25	11.01×10^{-6}	0.96	3.51×10^{-7}
	1.84	0.25	12.41×10^{-6}	1	3.43×10^{-7}

Downloaded 04 May 2010 to 171.66.16.26. Redistribution subject to ASME license or copyright; see http://www.asme.org/terms/Terms_Use.cfm

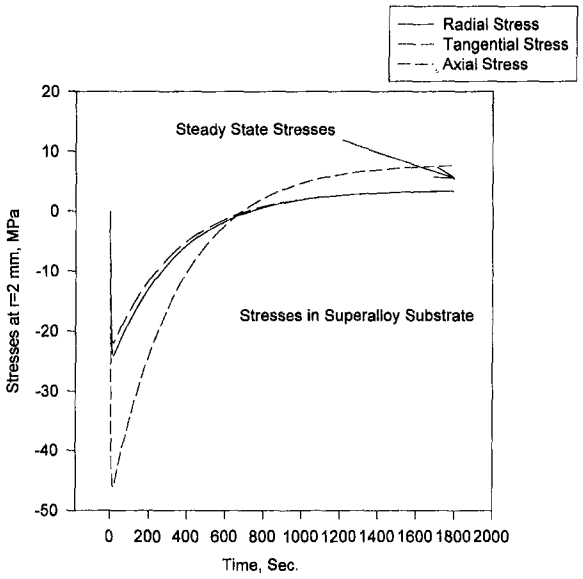


Fig. 3 Variation of stress-field components versus time in the superalloy substrate

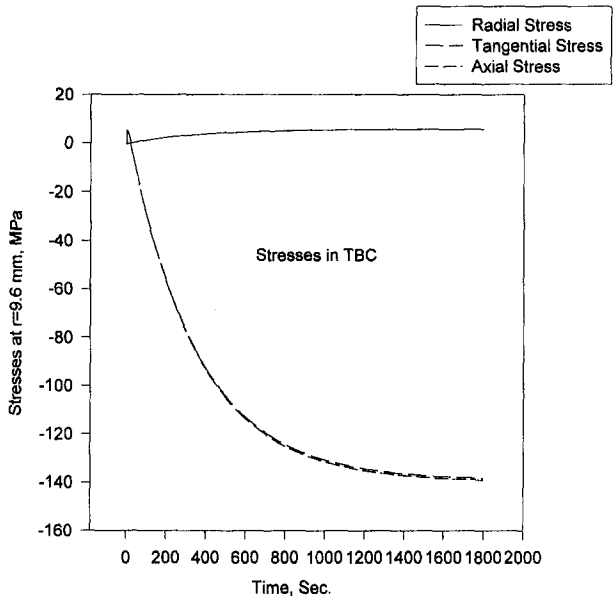


Fig. 5 Variation of stress-field components versus time in the TBC

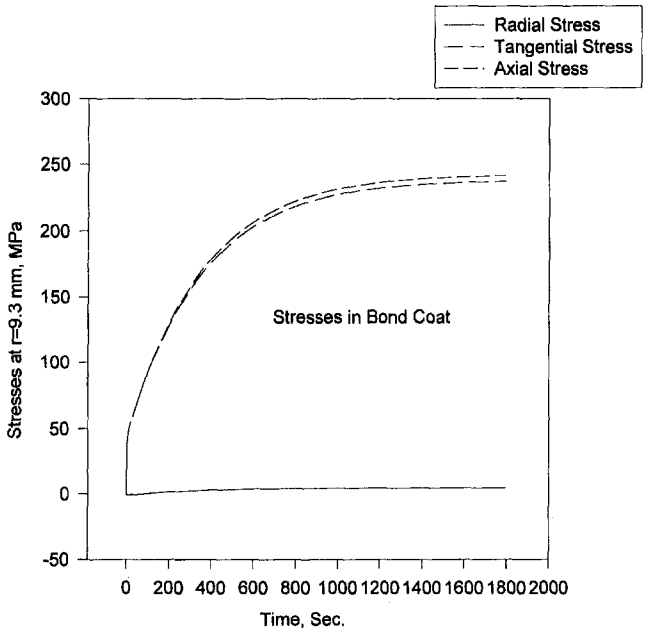


Fig. 4 Variation of stress-field components versus time in the bond coat

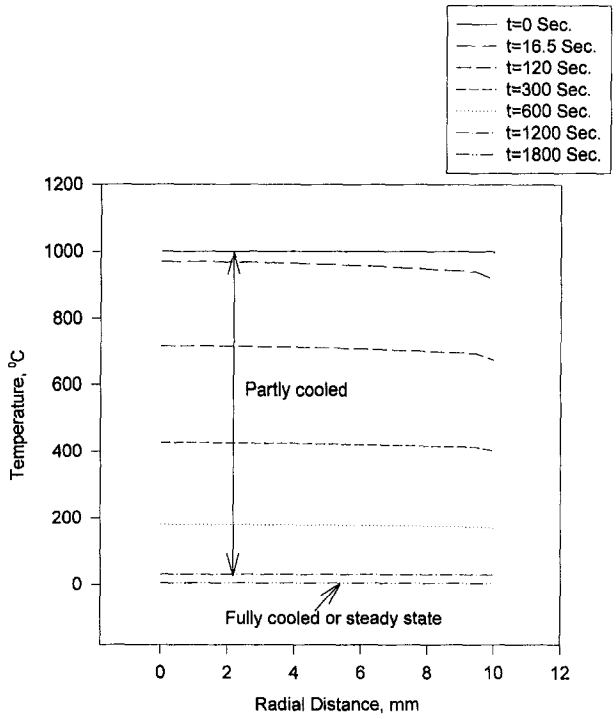


Fig. 6 Temperature versus radial distance at different time for the TBC/bond coat/superalloy system

8 shows the variation of the tangential stress versus the radial distance at different times. From this figure one can see that the maximum stress occurred in the bond coat. Figure 9 shows the variation of the axial stress versus the radial distance at different times, and is the same as in Fig. 8, the maximum axial stress occurred in the bond coat. These figures show excellent agreement between the finite element solution and the elasticity solution for the steady-state case. Bond coat/TBC interface is clearly under the biaxial stress field. The highest tensile stress is 242 MPa and the highest compressive stress is 132 MPa. Figure 10 shows the variation of the axial stress versus the radial distance at different times. In this figure, temperature-dependent properties were used and the results were obtained by using the finite element code ALGOR. By comparing this figure with Fig. 9, it is clear that using temperature-dependent properties, will increase the level of stresses by a factor of 1.7 and the trend will remain same. This effect of using temperature-dependent properties on the stresses variation for all of the other cases were the same.

Elasticity solution is not valid close to the free edge since the boundary conditions are not satisfied precisely at the free edge. The boundary conditions are subscribed in the average form at any cross section, which may not be precisely valid at the free edge.

Compressive stresses in the TBC play a major role in TBC failure. For example, a flaw size of 12 times the TBC thickness will buckle and spallation of the TBC may occur. The radial stress across the interface generates a driving force which may initiate an interface crack. Subsequently, the interface crack may propagate to failure.

Downloaded 04 May 2010 to 171.66.16.26. Redistribution subject to ASME license or copyright; see http://www.asme.org/terms/Terms_Use.cfm

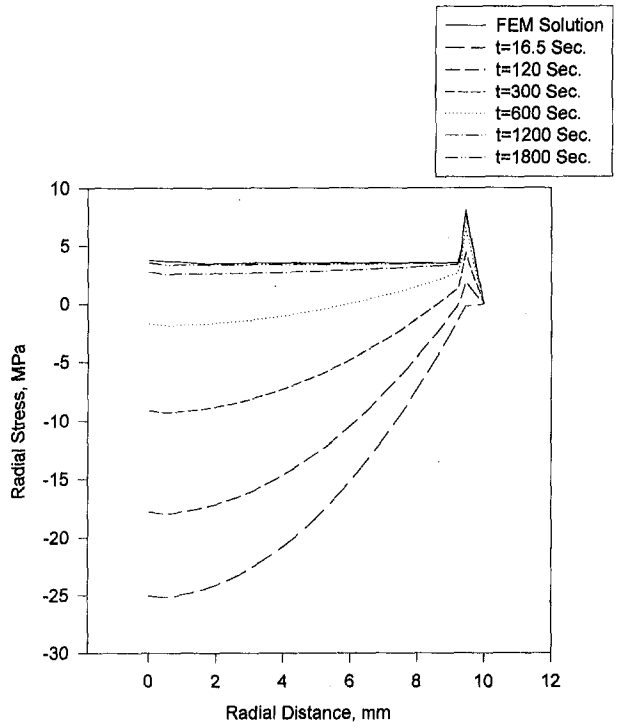


Fig. 7 Radial stress versus radial distance at different times for the TBC/bond coat/superalloy system

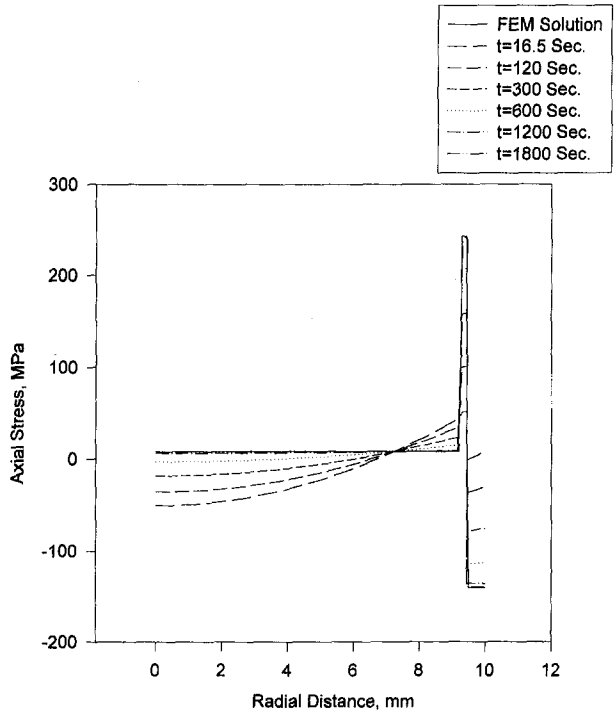


Fig. 9 Axial stress versus radial distance at different time for the TBC/bond coat/superalloy system

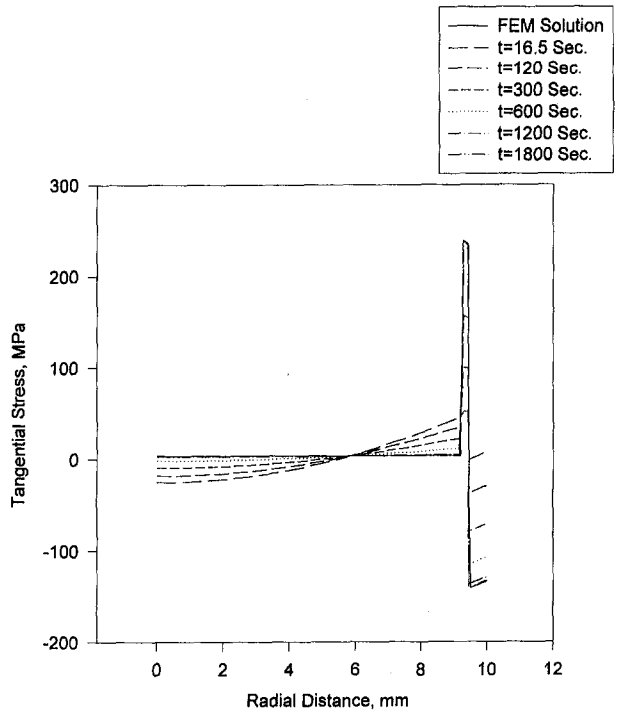


Fig. 8 Tangential stress versus radial distance at different times for the TBC/bond coat/superalloy system

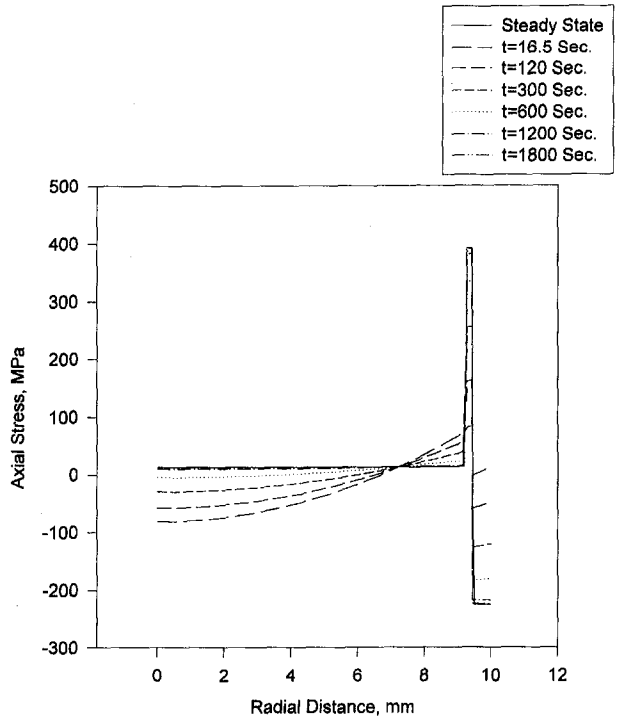


Fig. 10 Axial stress versus radial distance at different times for the TBC/bond coat/superalloy system with temperature-dependent properties

Summary and Conclusions

The orthogonal-expansion technique was utilized over a multilayer region to determine the true temperature field and subsequently to obtain the transient residual stress field. Analysis of the concentric cylinder model representing the TBC/bond coat/superalloy system showed that the elasticity solution and numerical results from finite element stress analyses (steady-state case only) correlate well in predicting thermal residual stresses in the various layers and at the interfaces. Because of the free-edge condition and stress singularity due to a material mismatch, the elasticity solution is not valid at the free edge of the concentric cylinders. The highest stresses were found to occur at the bond coat/TBC interface. At this interface, results indicate a biaxial stress field due to high axial and tangential

Downloaded 04 May 2010 to 171.66.16.26. Redistribution subject to ASME license or copyright; see http://www.asme.org/terms/Terms_Use.cfm

stress; the radial stress component was relatively small. For transient thermal residual analysis, the closed form-elasticity solution can be adequate except at the free edge. The residual stresses developed in the substrate are higher for the case of the partly cooled specimen compared to the fully cooled specimen because the temperature field has a high gradient at the earlier stages compared to later stages.

Acknowledgment

Funding for this research was provided through a grant (# F49620-95-1-0201) from the Air Force Office of Scientific Research (AFOSR). Dr. Walter Jones was the program monitor. Discussion and interaction with Dr. P. K. Wright of GEAE is gratefully acknowledged.

References

Boley, B. A., and Weiner, J. H., 1960, *Theory of Thermal Stress,* John Wiley and Sons, New York.

Chang, G. C., and Phucharoen, W., Miller, R. A., 1987, "Finite Element Thermal Stress Solutions for Thermal Barrier Coatings," *Surface and Coatings Technology,* Vol. 32, pp. 307–325.

Chung, B. T. F., Kermani, M. M., Braun, M. J., Padovan, J., and Hendricks, R. C., 1985, "Heat Transfer in Thermal Barrier Coated Rods with Circumferential and Radial Temperature Gradients," ASME *Journal of Engineering for Gas Turbines and Power,* Vol. 107, pp. 135–141.

Drake, J. T., Williamson, R. L., and Rabin, B. H., 1993, "Finite Element Analysis of Thermal Residual Stresses at Graded Ceramic-Metal Interfaces, Part II: Interface optimization for residual stress reduction," *J. Appl. Phys.,* Vol. 74, pp. 1321–1326.

Hasselman, D. P. H., and Heller, R. A., 1980, *Thermal Stresses in Severe Environments,* Plenum Press, New York.

Holmes, J. W., McClintock, F. A., O'Hara, K. S., and Conners, M. E., 1988, "Thermal Fatigue Testing of Coated Monocrystalline Superalloys," *Low Cycle Fatigue,* ASTM STP 942, pp. 672–691.

Iwaki, T., 1986, "Transient Thermal Stresses in Fully and Partly Cooled Circular Rings," *Exp. Mechs.,* pp. 163–168.

Kardomateas, G. A., 1989, "Transient Thermal Stresses in Cylindrically Orthotropic Composite Tubes," ASME JOURNAL OF APPLIED MECHANICS, Vol. 56, pp. 411–417.

Kardomateas, G. A., 1990, "The Initial Phase of Transient Thermal Stresses due to General Boundary Thermal Loads in Orthotropic Hollow Cylinders," ASME JOURNAL OF APPLIED MECHANICS, Vol. 57, pp. 719–724.

Kardomateas, G. A., and Chung, C. B., 1994, "Boundary Layer Transient Hygroscopic Stresses in Orthotropic Thick Shells Under External Pressure," ASME JOURNAL OF APPLIED MECHANICS, Vol. 61, pp. 161–168.

Kokini, K., and Hornack, T. R., 1988, "Transient Thermal Load Effects on Coatings Bonded to Cylindrical Substrates and Containing Circumferential Cracks," ASME *Journal of Engineering Materials and Technology,* Vol. 110, pp. 35–40.

Manson, S. S., 1966, *Thermal Stress and Low-Cycle Fatigue,* McGraw-Hill, New York.

Mikata, Y., and Taya, M., 1985, "Stress Field in a Coated Continuous Fiber Composite Subjected to Thermo-Mechanical Loadings," *J. of Comp. Mat.,* Vol. 19, pp. 554–578.

Ozisik, M. N., 1968, *Boundary Value Problems of Heat Conduction,* Dover, New York.

Padovan, J., Dougherty, D., Hendricks, B., Bratun, M. J., and Chung, B. T. F., 1984, "High Temperature Thermomechanical Analysis of Ceramic Coatings," *J. of Thermal Stresses,* Vol. 7, pp. 51–74.

Padovan, J., Dougherty, D., and Hendricks, B., 1986, "Inelastic High-Temperature Thermomechanical Response of Ceramic Coated Gas Turbine Seals," *J. of Thermal Stresses,* Vol. 9, pp. 31–43.

Padovan, J., Padovan, P., and Xiaru, Y., 1986, "Analysis of Thermomechanical Oxidation Fields in Thermal Barrier Coatings," *J. of Thermal Stresses,* Vol. 9, pp. 251–277.

Takeuchi, Y. R., and Kokini, K., 1994, "Thermal Fracture of Multilayer Ceramic Thermal Barrier Coatings," ASME *Journal of Engineering for Gas Turbines and Power,* Vol. 116, pp. 266–271.

Timoshenko, S. P., and Goodier, J. N., 1971, *Theory of Elasticity,* McGraw-Hill, New York.

Tittle, C. W., 1965, "Boundary-Value Problems in Composite Media: Quasi-Orthogonal Functions," *J. of App. Phy.,* Vol. 36, pp. 1486–1488.

Tittle, C. W., and Robenson, V. L., 1965, "Analytical Solution of Conduction Problems in Composite Media," ASME paper 65-WA-HT-52.

Williamson, R. L., Rabin, B. H., and Drake, J. T., 1993, "Finite Element Analysis of Thermal Residual Stresses at Graded Ceramic-Metal Interfaces, Part I: Model Description and Geometrical Effects," *J. Appl. Phys.,* Vol. 74, pp. 1310–1320.

Wright, P. K., 1995, private communication, General Electric Aircraft Engines, Evendale, OH.

Downloaded 04 May 2010 to 171.66.16.26. Redistribution subject to ASME license or copyright; see http://www.asme.org/terms/Terms_Use.cfm

A Basic Problem in Thermoelasticodynamics and its Solution

Xiangzhou Zhang
Department of Civil Engineering,
Shanghai Tiedao University,
Shanghai 200333, P.R.C.

Dynamic stresses in a solid sphere, brought about by a sudden temperature rise uniformly distributed over the whole volume of the sphere, is studied as a basic problem in thermoelasticodynamics. Using a simple reduction, the problem is first reduced to an isothermal dynamic response one. Exact solution to this dynamic response problem, for a hollow sphere with a fixed inner boundary, is developed with use of a solution in D'Alembert form and a technique of singularity extraction. This hollow sphere solution is further employed in a limit process, in which the inner radius of the sphere tends towards zero, with the objective of thereby creating a solution for the solid sphere. This limit process results in a solid sphere solution, which is exact and explicit, and takes various closed forms for each wave propagation and reflection. Numerical result and discussion regarding this solid sphere solution are given.

Introduction

An engineering component may undergoes a sudden temperature rise uniformly distributed over its whole volume, in case it is suddenly exposed to intensive radiation heating. The dynamic stress in a solid sphere caused by a sudden temperature rise uniformly distributed over the whole sphere volume is therefore a problem of interest in nuclear industry and high temperature engineering. This problem, which is a basic one in thermoelasticodynamics, and the problems it directly associates with, have been considered by Mann-Nachbar and Nachbar (1970), Ho (1976), Pao and Ceranoglue (1978), Hata (1991a, 1991b), and others. As indicated in the following section, by a simple reduction this problem can immediately and straightforwardly be reduced to that of a dynamic response one, in which the solid sphere is dynamically deformed by a normal traction uniformly and suddenly applied over its surface.

This reduced problem of dynamic response is a classic one in elastodynamics and of long-standing interest. Lamb studied the problem of free vibrations of a sphere and computed several first ones of the natural frequencies. Chree derived expressions of stresses and displacements in a sphere subject to harmonic surface tractions (Eringen and Suhubi, 1975). Grey and Eringen developed the complete solution of a sphere under the action of surface tractions, a part of their results can be seen in Eringen and Sububi (1975), where more information on the solution of this dynamic response problem is given. In Mann-Nachbar and Nachbar (1970), the stress-focusing effect in a suddenly heated sphere was originally investigated.

Despite of these research efforts, the dynamic response problem of a solid sphere to uniform normal tractions does not seem to have been finally settled. This may be mainly due to the difficulty in the numerical treatment of the solution. Though there is no dearth of formal solutions (Eringen and Suhubi, 1975), numerical results of the problem appear to be very few. In fact, no numerical data, either in tabular or graphic form, to this problem in elastodynamics, which is of fundamental significance and one of the simplest both in geometry and in external load, can be found in standard monographs by Achenbach (1973), Eringen and Suhubi (1975), Graff (1975), Milkowitz (1976), and Pao and Mow (1973).

Recently Hata (1991a) investigated the dynamic deformation in a solid sphere, induced by a temperature rise, uniformly distributed over the whole sphere volume, and varying with time in such a way that the temperature increases from zero linearly to a certain value, and remains in that value thereafter. Using the Laplace transform and the ray theory method, Hata obtained a solution to the reduced dynamic response problem, and provided numerical values of stresses for the case of a step temperature rise. Hata's solution will be discussed later.

The present article completely settles this basic problem in thermoelasticodynamics, mainly by providing an exact and explicit solution to the reduced dynamic response problem. The solution takes various closed forms for each wave propagation and reflection. A solution in the D'Alembert form and a technique of singularity extraction are employed in the development of the solution, first for a hollow sphere with a fixed inner boundary. The hollow sphere solution is subsequently used in a limit process, in which the inner radius of the sphere tends towards zero, and through this process the solution for the solid sphere is created. Numerical values of and discussion on the solid sphere solution are also given.

Problem and Reduction

Consider an elastic, solid sphere of radius b, initially at rest and of zero temperature such as

$$t < 0, \quad 0 \le r \le b,$$

$$\mathbf{u}(r, t) = \dot{\mathbf{u}}(r, t) = 0, \quad T(r, t) = 0; \tag{1}$$

while from $t \ge 0$ on, the temperature in the whole volume of the sphere is suddenly brought to a uniform increase, so that

$$t \ge 0, \quad T(r, t) = T_0(t), \tag{2}$$

where $T_0(t)$ is an arbitrary given function.

This is a basic problem of spherical symmetry in thermoelasticodynamics. To solve the problem, first suppose that simultaneously with the temperature increase, that is, for $t \ge 0$, a uniform normal traction

Contributed by the Applied Mechanics Division of THE AMERICAN SOCIETY OF MECHANICAL ENGINEERS for publication in the ASME JOURNAL OF APPLIED MECHANICS.

Discussion on this paper should be addressed to the Technical Editor, Professor Lewis T. Wheeler, Department of Mechanical Engineering, University of Houston, Houston, TX 77204-4792, and will be accepted until four months after final publication of the paper itself in the ASME JOURNAL OF APPLIED MECHANICS.

Manuscript received by the ASME Applied Mechanics Division, May 5, 1995; final revision, July 10, 1997. Associate Technical Editor: M. Taya.

 Copyright © 1998 by ASME

Downloaded 04 May 2010 to 171.66.16.26. Redistribution subject to ASME license or copyright; see http://www.asme.org/terms/Terms_Use.cfm

$$\sigma_0(t) = -\frac{\alpha E T_0(t)}{1-2\nu} \tag{3}$$

is applied on the sphere surface, where α denotes the coefficient of thermal expansion, E stands for the Young's modulus and ν is the Poisson's ratio of the material. Under the combining effect of the temperature and the traction, the deformation is strain free, and the nonvanishing displacement and stresses in the sphere, denoted by a superscript T, take the following simple form (Boley and Weiner, 1960):

$$u_r^T = 0, \quad \sigma_r^T = \sigma_\theta^T = \sigma_\varphi^T = \sigma_0(t). \tag{4}$$

To obtain the final solution to the problem, on the grounds of the principle of superposition, the solution to a dynamic response problem must be added to solution (4). This problem is prescribed by

$$t < 0, \quad 0 \le r \le b, \quad u_r^D = \dot{u}_r^D = 0, \quad T^D = 0, \tag{5}$$

$$t \ge 0, \quad r = b, \quad \sigma_r^D = -\sigma_0(t), \quad T^D = 0, \tag{6}$$

$$t \ge 0, \quad r = 0, \quad u_r^D = 0, \quad T^D = 0, \tag{7}$$

where the superscript D is used to denote that the affixed quantities are in association with the dynamic response problem.

Equations (5), (6), and (7) reduce the original problem to a dynamic response one, in which the deformation and the movement of the sphere are induced by a uniform normal traction. Note this reduction applies to elastic objects of any geometric shape, e.g., a solid or hollow ellipsoid.

Solution for a Hollow Sphere With a Fixed Inner Boundary

To prepare the solution for the solid sphere, we first consider the corresponding dynamic response problem for a hollow sphere with a fixed inner boundary. For brevity, in the following the superscript D, which appears in Eqs. (5)–(7), will be omitted.

The hollow sphere occupies the region $a \le r \le b$, the dynamic response problem to be solved is also prescribed by Eqs. (5), (6) and the following fixed boundary condition for the inner boundary is

$$t > 0, \quad r = a, \quad u_r = 0, \quad T = 0. \tag{8}$$

In addition, for definiteness in the subsequent development, in Eq. (6) it is assumed that

$$\sigma_0(t) = -A_0 e^{-\beta ct/b} \tag{9}$$

where A_0 and β are known constants and c stands for the longitudinal wave speed of the material. In case $\beta = 0$, σ_0 becomes the important form of a Heaviside step function.

Initial Propagation. Starting from the initial moment $t = 0$ an elastic wave issues from the boundary $r = b$ due to the application of the normal traction. The associated displacement u_r in the hollow sphere is governed by (Eringen and Suhubi, 1975)

$$t > 0, \quad a < r < b, \quad \frac{\partial^2 u_r}{\partial r^2} + \frac{2}{r}\frac{\partial u_r}{\partial r} - \frac{2u_r}{r^2} = \frac{1}{c^2}\frac{\partial^2 u_r}{\partial t^2}. \tag{10}$$

Introducing a solution in D'Alembert form (Eringen and Suhubi, 1975)

$$u_r = \frac{\partial \psi}{\partial r},$$

$$\psi(r,t) = \begin{cases} g(r-b+ct)/r, & r-b+ct \ge 0, \\ 0, & r-b+ct < 0, \end{cases} \tag{11}$$

and inserting it into Eq. (10), it is found that the governing equation and the initial condition (5) are automatically satisfied. Furthermore, by using (Eringen and Suhubi, 1975)

$$\sigma_r = (\lambda + 2\mu)\frac{\partial u_r}{\partial r} + 2\lambda\frac{u_r}{r}, \tag{12}$$

the boundary condition (6) is reduced to

$$(\lambda + 2\mu)b^2 g_b'' - 4\mu b g_b' + 4\mu b g_b = -b^3\sigma_0(t), \tag{13}$$

where λ and μ are Lame constants of the material, and

$$g_b = g(r-b+ct)|_{r=b}, \quad g_b' = \left.\frac{dg(r-b+ct)}{d(r-b+ct)}\right|_{r=b},$$

$$g_b'' = \left.\frac{d^2 g(r-b+ct)}{d(r-b+ct)^2}\right|_{r=b}. \tag{14}$$

The solution to the above ordinary differential Eq. (13) is easily obtainable (Ince, 1945), and from it we directly obtain

$$g(R) = Ce^{-\beta R/b} + e^{a_0 R}[A\sin(b_0 R) + B\cos(b_0 R)], \tag{15}$$

where

$$R = r - b + ct, \quad C = A_0 b^3/[(\lambda+2\mu)\beta^2 + 4\mu\beta + 4\mu],$$

$$a_0 = \frac{2\mu}{b(\lambda+2\mu)}, \quad b_0 = \frac{2\sqrt{\mu(\lambda+\mu)}}{b(\lambda+2\mu)}. \tag{16}$$

The unknown constants, A and B in Eq. (15), should be determined by singularity extraction as follows. The solution $g(R)$ contains singular components R^n, $n = 0, 1$. The component R^0 produces displacement and stress for a static solution

$$u_r = -1/r^2, \quad \sigma_r = 4\mu/r^3, \tag{17}$$

whereas the component R produces displacement and stress

$$u_r = (b-ct)/r^2, \quad \sigma_r = 4\mu(ct-b)/r^3 \tag{18}$$

for a solution with discontinuous displacement on the wave front. Therefore, both R^0 and R are singular components and should be extracted from $g(R)$. This gives

$$B = -C, \quad A = (\beta/b + a_0)C/b_0. \tag{19}$$

The displacement and stresses can be deduced from $g(R)$ by using Eqs. (11), (12), and the following formula (Eringen and Suhubi, 1975):

$$\sigma_\theta = \sigma_\varphi = \lambda\frac{\partial u_r}{\partial r} + 2(\lambda+\mu)\frac{u_r}{r}. \tag{20}$$

The result for u_r and σ_r is as follows:

$$u_r = -\{(1+\beta r/b)Ce^{-\beta R/b} + e^{a_0 R}[(A + A_1 r)\sin(b_0 R) + (B + B_1 r)\cos(b_0 R)]\}/r^2, \tag{21}$$

$$\sigma_r = \{[4\mu(1+\beta r/b) + (\lambda+2\mu)\beta^2 r^2/b^2]Ce^{-\beta R/b} + e^{a_0 R}[(A_2 + A_3 r + A_4 r^2)\sin(b_0 R) + [(B_2 + B_3 r + B_4 r^2)\cos(b_0 R)]\}/r^3, \tag{22}$$

where

$$A_1 = Bb_0 - Aa_0, \quad B_1 = -(Ab_0 + Ba_0),$$

$$A_2 = 4\mu A, \quad B_2 = 4\mu B, \quad A_3 = 4\mu A_1, \quad B_3 = 4\mu B_1,$$

$$A_4 = (\lambda+2\mu)[A(a_0^2 - b_0^2) - 2Ba_0 b_0],$$

$$B_4 = (\lambda+2\mu)[B(a_0^2 - b_0^2) + 2Aa_0 b_0]. \tag{23}$$

The inner boundary of the hollow sphere, $r = a$, remains at rest until the moment $t = (b-a)/c$.

Downloaded 04 May 2010 to 171.66.16.26. Redistribution subject to ASME license or copyright; see http://www.asme.org/terms/Terms_Use.cfm

Reflection From the Inner Surface. Once the initial propagating wave arrives at $r = a$ at the moment $t = (b - a)/c$, a reflected wave begins to propagate outwardly from the excited inner boundary to guarantee that the fixed boundary condition (8) is maintained. The displacement u_r associated with the reflected wave also obeys Eq. (10). Using a solution in D'Alembert form (see Eq. (11))

$$\psi(r, t) = \begin{cases} f^{(1)}(-r - b + 2a + ct)/r, & t \geq (b - a)/c, \\ & -r - b + 2a + ct \geq 0, \\ 0, \quad \text{otherwise}, \end{cases} \tag{24}$$

the governing Eq. (10) and the initial condition are automatically satisfied, while the fixed boundary condition (8) becomes

$$af_a^{(1)\prime} + f_a^{(1)} = a^2 u_{r0}, \tag{25}$$

where u_{r0} stands for the displacement expressed in Eq. (21) with $t \geq (b - a)/c$ and $r = a$, and

$$f_a^{(1)} = f^{(1)}(-r - b + 2a + ct)|_{r=a},$$
$$f_a^{(1)\prime} = \left.\frac{df^{(1)}(-r - b + 2a + ct)}{d(-r - b + 2a + ct)}\right|_{r=a}. \tag{26}$$

The solution to Eq. (25) is easily obtainable, and by the solution we directly obtain

$$f^{(1)}(S) = C^{(1)}e^{-\beta S/b} + e^{a_0 S}[A_0^{(1)} \sin(b_0 S) + B_0^{(1)} \cos(b_0 S)] + D_0^{(1)}e^{-S/a}, \tag{27}$$

where

$$S = -r - b + 2a + ct, \quad C^{(1)} = (\beta a/b + 1)C/(\beta a/b - 1),$$
$$A_0^{(1)} = [-(1 + aa_0)(A + A_1 a) - ab_0(B + B_1 a)]/\Delta,$$
$$B_0^{(1)} = [ab_0(A + A_1 a) - (1 + aa_0)(B + B_1 a)]/\Delta,$$
$$\Delta = (1 + aa_0)^2 + (ab_0)^2. \tag{28}$$

The coefficient $D_0^{(1)}$ should be fixed by the singularity extraction, to eliminate the component S^n, $n = 0$, in $f^{(1)}(S)$, namely

$$D_0^{(1)} = -(C_0^{(1)} + B_0^{(1)}). \tag{29}$$

It follows that the solution $f^{(1)}(S)$ becomes free from static elements. In the meantime it can easily be shown, either by a simple analysis or by some algebraic manipulations, that the singular component S automatically vanishes in solution (27).

Expressions for u_r and σ_r are obtained from Eqs. (11), (24), (27) and (12) as follows:

$$u_r = -\{C^{(1)}(1 - \beta r/b)e^{-\beta S/b} + e^{a_0 S}[(A_0^{(1)} + A_5 r)\sin(b_0 S) + (B_0^{(1)} + B_5 r)\cos(b_0 S)] + D_0^{(1)}(1 - r/a)e^{-S/a}\}/r^2, \tag{30}$$

$$\sigma_r = \{[4\mu - 4\mu\beta r/b + (\lambda + 2\mu)\beta^2 r^2/b^2]C^{(1)}e^{-\beta S/b} + e^{a_0 S}[4\mu(A_0^{(1)} + A_5 r) + (\lambda + 2\mu)A_6 r^2]\sin(b_0 S) + e^{a_0 S}[4\mu(B_0^{(1)} + B_5 r) + (\lambda + 2\mu)B_6 r^2]\cos(b_0 S) + [4\mu - 4\mu r/a + (\lambda + 2\mu)r^2/a^2]D_0^{(1)}e^{-S/a}\}/r^3, \tag{31}$$

where

$$A_5 = a_0 A_0^{(1)} - b_0 B_0^{(1)}, \; B_5 = a_0 B_0^{(1)} + b_0 A_0^{(1)},$$
$$A_6 = (a_0^2 - b_0^2)A_0^{(1)} - 2B_0^{(1)} a_0 b_0,$$
$$B_6 = (a_0^2 - b_0^2)B_0^{(1)} + 2A_0^{(1)} a_0 b_0. \tag{32}$$

Reflection From the Outer Surface. When the reflected wave from $r = a$ reaches $r = b$ at $t = 2(b - a)/c$, an inwardly going reflected wave begins to come out from the outer boundary. This reflected wave is governed by Eq. (10), the boundary condition (6), and the initial condition.

Analogously to that developed above, we take

$$\psi(r, t) = \begin{cases} g^{(1)}(r - 3b + 2a + ct)/r, & t \geq 2(b - a)/c, \\ & r - 3b + 2a + ct \geq 0, \\ 0, \quad \text{otherwise}. \end{cases} \tag{33}$$

This solution (33) inherently satisfies Eq. (10) and the initial condition. By employing Eq. (6), $g^{(1)}$ can be found from the following equation:

$$(\lambda + 2\mu)b^2 g_b^{(1)\prime\prime} - 4\mu b g_b^{(1)\prime} + 4\mu g_b^{(1)} = -b^3\sigma_{r0}, \tag{34}$$

where $g_b^{(1)}$, $g_b^{(1)\prime}$ and $g_b^{(1)\prime\prime}$ have the meanings similar to those expressed in equation (14), and σ_{r0} denotes the stress expressed in Eq. (31) with $t \geq 2(b - a)/c$ and $r = b$.

It is simple to find a solution for Eq. (34), and from the solution we directly obtain

$$g^{(1)}(R) = C^{(2)}e^{-\beta R/b} + e^{a_0 R}[(A_0^{(2)} + A_1^{(2)}R)\sin(b_0 R) + (B_0^{(2)} + B_1^{(2)}R)\cos(b_0 R)] + D_0^{(2)}e^{-R/a}, \tag{35}$$

where $R = r - 3b + 2a + ct$ and

$$C^{(2)} = \frac{4\mu\beta - 4\mu - (\lambda + 2\mu)\beta^2}{4\mu\beta + 4\mu + (\lambda + 2\mu)\beta^2} C^{(1)},$$
$$D_0^{(2)} = \frac{4\mu b/a - 4\mu - (\lambda + 2\mu)b^2/a^2}{4\mu b/a + 4\mu + (\lambda + 2\mu)b^2/a^2} D_0^{(1)},$$
$$A_1^{(2)} = B_7/[2b^2 b_0(\lambda + 2\mu)], \quad B_1^{(2)} = -A_7/[2b^2 b_0(\lambda + 2\mu)],$$
$$A_7 = -4\mu(A_0^{(1)} + A_5 b) - (\lambda + 2\mu)A_6 b^2,$$
$$B_7 = -4\mu(B_0^{(1)} + B_5 b) - (\lambda + 2\mu)B_6 b^2. \tag{36}$$

The remaining unknown constants, $A_0^{(2)}$ and $B_0^{(2)}$, must be determined by the singularity extraction. The result is

$$B_0^{(2)} = -(C^{(2)} + D_0^{(2)}),$$
$$A_0^{(2)} = -(B_0^{(2)} a_0 + B_1^{(2)} - \beta C^{(2)}/b - D_0^{(2)}/a)/b_0. \tag{37}$$

An expression for u_r can then be derived

$$u_r = -\{(1 + \beta r/b)C^{(2)}e^{-\beta R/b} + e^{a_0 R}[A_8(r, R)\sin(b_0 R) + B_8(r, R)\cos(b_0 R)] + (1 + r/a)D_0^{(2)}e^{-R/a}\}/r^2, \tag{38}$$

where

$$A_8(r, R) = A_0^{(2)} + (B_0^{(2)} b_0 - A_0^{(2)} a_0)r + A_1^{(2)}(R - r - a_0 Rr) + B_1^{(2)} b_0 Rr,$$
$$B_8(r, R) = B_0^{(2)} - (A_0^{(2)} b_0 + B_0^{(2)} a_0)r + B_1^{(2)}(R - r - a_0 Rr) - A_1^{(2)} b_0 Rr. \tag{39}$$

The expression for σ_r reads

$$\sigma_r = \{[4\mu(1 + \beta r/b) + (\lambda + 2\mu)\beta^2 r^2/b^2]C^{(2)}e^{-\beta R/b} + e^{a_0 R}[A_9(r, R)\sin(b_0 R) + B_9(r, R)\cos(b_0 R)] + [4\mu(1 + r/a) + (\lambda + 2\mu)r^2/a^2]D_0^{(2)}e^{-R/a}\}/r^3, \tag{40}$$

Downloaded 04 May 2010 to 171.66.16.26. Redistribution subject to ASME license or copyright; see http://www.asme.org/terms/Terms_Use.cfm

where

$$A_9(r, R) = (\lambda + 2\mu)[A_0^{(2)}(a_0^2 - b_0^2) - 2B_0^{(2)}a_0b_0 + (A_1^{(2)}a_0 - B_1^{(2)}b_0)(2 + a_0R) - (A_1^{(2)}b_0 + B_1^{(2)}a_0)b_0R]r^2 + 4\mu[A_0^{(2)} + (B_0^{(2)}b_0 - A_0^{(2)}a_0)r + A_1^{(2)}(R - r - a_0Rr) + B_1^{(2)}b_0Rr],$$

$$B_9(r, R) = (\lambda + 2\mu)[B_0^{(2)}(a_0^2 - b_0^2) + 2A_0^{(2)}a_0b_0 + (A_1^{(2)}b_0 + B_1^{(2)}a_0)(2 + a_0R) + (A_1^{(2)}a_0 - B_1^{(2)}b_0)b_0R]r^2 + 4\mu[B_0^{(2)} - (A_0^{(2)}b_0 + B_0^{(2)}a_0)r + B_1^{(2)}(R - r - a_0Rr) - A_1^{(2)}b_0Rr]. \quad (41)$$

Subsequent Reflections. Subsequent reflections take place at the boundaries $r = a$ and $r = b$, from $t = m(b - a)/c$, $m = 3, 5, \ldots$ and $t = n(b - a)/c$, $n = 4, 6, \ldots$, respectively. Using a procedure similar to that described above and employing well-known techniques for solving simple ordinary differential equations in the form of Eqs. (13) and (25), exact expressions for function $\psi(r, t)$, displacement u_r, and stress σ_r in each subsequent reflection can be obtained by an obviously straightforward way. Therefore, only the main result regarding these subsequent reflections is recorded in the following.

For the nth reflection taking place at the outer boundary $r = b$, which occurs from $t = 2n(b - a)/c$, $n = 1, 2, \ldots$, the function $\psi(r, t)$ can be written as

$$\psi(r, t) = \begin{cases} g^{(n)}(R)/r, & t \geq 2n(b - a)/c, \quad R \geq 0, \\ 0, & \text{otherwise}, \end{cases} \quad (42)$$

$$g^{(n)}(R) = C^{(2n)}e^{-\beta R/b} + e^{a_0R}[(A_0^{(2n)} + A_1^{(2n)}R + \ldots + A_n^{(2n)}R^n)\sin(b_0R) + (B_0^{(2n)} + B_1^{(2n)}R + \ldots + B_n^{(2n)}R^n)\cos(b_0R)] + (D_0^{(2n)} + D_1^{(2n)}R + \ldots + D_{n-1}^{(2n)}R^{n-1})e^{-R/a}, \quad (43)$$

where $R = r - (2n + 1)b + 2na + ct$, and $C^{(2n)}$, $A_0^{(2n)}, \ldots, B_0^{(2n)}, \ldots, D_0^{(2n)}, \ldots$ are known constants.

The subsequent reflection in the hollow sphere, namely the $(n + 1)$th reflection at the inner boundary $r = a$, occurs from $t = (2n + 1)(b - a)/c$, for which the function $\psi(r, t)$ can be written as

$$\psi(r, t) = \begin{cases} f^{(n+1)}(S)/r, & t \geq (2n + 1)(b - a)/c, \quad S \geq 0, \\ 0, & \text{otherwise}, \end{cases} \quad (44)$$

$$f^{(n+1)}(S) = C^{(2n+1)}e^{-\beta S/b} + e^{a_0S}[(A_0^{(2n+1)} + A_1^{(2n+1)}S + \ldots + A_n^{(2n+1)}S^n)\sin(b_0S) + (B_0^{(2n+1)} + B_1^{(2n+1)}S + \ldots + B_n^{(2n+1)}S^n)\cos(b_0S)] + D_0^{(2n+1)} + D_1^{(2n+1)}S + \ldots + D_n^{(2n+1)}S^n)e^{-S/a}, \quad (45)$$

where $S = -r - (2n + 1)b + 2(n + 1)a + ct$, and

$$C^{(2n+1)} = (\beta a/b + 1)C^{(2n)}/(\beta a/b - 1); \quad (46)$$

the constants $A_n^{(2n+1)}, \ldots$ and $B_n^{(2n+1)}, \ldots$ can be determined, consecutively, from the following simple linear equation systems:

$$(1 + aa_0)A_j^{(2n+1)} - ab_0B_j^{(2n+1)} = K_j^{(2n+1)},$$

$$ab_0A_j^{(2n+1)} + (1 + aa_0)B_j^{(2n+1)} = L_j^{(2n+1)},$$

$$K_j^{(2n+1)} = a[A_j^{(2n)}(a_0 - a^{-1}) - B_j^{(2n)}b_0 + (j + 1)(A_{j+1}^{(2n)} - A_{j+1}^{(2n+1)})],$$

$$L_j^{(2n+1)} = a[B_j^{(2n)}(a_0 - a^{-1}) + A_j^{(2n)}b_0 + (j + 1)(B_{j+1}^{(2n)} - B_{j+1}^{(2n+1)})], \quad (47)$$

where $j = n, n - 1, \ldots, 1, 0$. Besides

$$D_j^{(2n+1)} = (jD_j^{(2n)} - 2D_{j-1}^{(2n)}/a)/j, \quad (48)$$

where $j = 1, 2, \ldots, n$; finally

$$D_0^{(2n+1)} = -(C^{(2n+1)} + B_0^{(2n+1)}). \quad (49)$$

The next reflection in the hollow sphere, namely the $(n + 1)$th reflection taking place at the outer boundary $r = b$, occurs from $t = 2(n + 1)(b - a)/c$, for which the function $\psi(r, t)$ can be written as

$$\psi(r, t) = \begin{cases} g^{(n+1)}(R)/r, & t \geq 2(n + 1)(b - a)/c, \quad R \geq 0, \\ 0, & \text{otherwise}, \end{cases} \quad (50)$$

$$g^{(n+1)}(R) = C^{(2n+2)}e^{-\beta R/b} + e^{a_0R}[(A_0^{(2n+2)} + A_1^{(2n+2)}R + \ldots + A_{n+1}^{(2n+2)}R^{n+1})\sin(b_0R) + (B_0^{(2n+2)} + B_1^{(2n+2)}R + \ldots + B_{n+1}^{(2n+2)}R^{n+1})\cos(b_0S)] + (D_0^{(2n+2)} + D_1^{(2n+2)}R + \ldots + D_n^{(2n+2)}R^n)e^{-R/a}, \quad (51)$$

where $R = r - (2n + 3)b + 2(n + 1)a + ct$, and

$$C^{(2n+2)} = \frac{4\mu\beta - 4\mu - (\lambda + 2\mu)\beta^2}{4\mu\beta + 4\mu + (\lambda + 2\mu)\beta^2}C^{(2n+1)}; \quad (52)$$

the coefficients $A_{n+1}^{(2n+2)}, \ldots$ and $B_{n+1}^{(2n+2)}, \ldots$ can be determined consecutively from the following simple linear equations:

$$2(j + 1)(\lambda + 2\mu)b^2b_0A_{j+1}^{(2n+2)} = N_j^{(2n+2)} - (n + 1)(n + 2)(\lambda + 2\mu)b^2B_{j+2}^{(2n+2)},$$

$$2(j + 1)(\lambda + 2\mu)b^2b_0B_{j+1}^{(2n+2)} = -M_j^{(2n+2)} + (n + 1)(n + 2)(\lambda + 2\mu)b^2A_{j+2}^{(2n+2)},$$

$$M_j^{(2n+2)} = -4\mu[A_j^{(2n+1)} - b(B_j^{(2n+1)}b_0 - A_j^{(2n+1)}a_0 - (j + 1)A_{j+1}^{(2n+1)})] - (\lambda + 2\mu)b^2[A_j^{(2n+1)}(a_0^2 - b_0^2) - 2B_j^{(2n+1)}a_0b_0 + (j + 1)(j + 2)A_{j+2}^{(2n+1)} + 2(j + 1)(A_{j+1}^{(2n+1)}a_0 - B_{j+1}^{(2n+1)}b_0)],$$

$$N_j^{(2n+2)} = -4\mu[B_j^{(2n+1)} + b(B_j^{(2n+1)}a_0 + A_j^{(2n+1)}b_0 + (j + 1)B_{j+1}^{(2n+1)})] - (\lambda + 2\mu)b^2[B_j^{(2n+1)}(a_0^2 - b_0^2) + 2A_j^{(2n+1)}a_0b_0 + (j + 1)(j + 2)B_{j+2}^{(2n+1)} + 2(j + 1)(B_{j+1}^{(2n+1)}a_0 + A_{j+1}^{(2n+1)}b_0)], \quad (53)$$

where $j = n, n - 1, \ldots, 1, 0$. Besides

$$D_j^{(2n+2)} = \{P_j^{(2n+2)} - (\lambda + 2\mu)(j + 1)(j + 2)b^2D_{j+2}^{(2n+2)} + 2b(j + 1)[2\mu + (\lambda + 2\mu)b/a]D_{j+1}^{(2n+2)}\}/[4\mu + 4\mu b/a + (\lambda + 2\mu)b^2/a^2],$$

$$P_j^{(2n+2)} = [4\mu(b/a - 1) - (\lambda + 2\mu)b^2/a^2]D_j^{(2n+1)} - (j + 1)(j + 2)(\lambda + 2\mu)b^2D_{j+2}^{(2n+1)} + 2(j + 1)b[(\lambda + 2\mu)b/a - 2\mu]D_{j+1}^{(2n+1)}, \quad (54)$$

where $j = n, n - 1, \ldots, 1, 0$. Finally we have

Downloaded 04 May 2010 to 171.66.16.26. Redistribution subject to ASME license or copyright; see http://www.asme.org/terms/Terms_Use.cfm

$$B_0^{(2n+2)} = -(C^{(2n+2)} + D_0^{(2n+2)}),$$

$$A_0^{(2n+2)} = -(B_0^{(2n+2)}a_0 + B_1^{(2n+2)} - \beta C^{(2n+2)}/b - D_0^{(2n+2)}/a + D_1^{(2n+2)})/b_0. \quad (55)$$

For $n = 1$, the result has completely been given in Eqs. (35) – (41). By repeatedly using Eqs. (44) – (55), the function $\psi(r, t)$ for each subsequent reflection can exactly be determined. The displacement and stress in association with $\psi(r, t)$ can be obtained, in exact and explicit form, by employing Eqs. (11) and (12).

The solution for the hollow sphere concludes. The following additional brief remarks are useful in deriving a solution for the solid sphere from the hollow sphere solution.

It is easy to see that each of the coefficients, $C^{(i)}$, $A_j^{(i)}$, and $B_j^{(i)}$ in Eqs. (45) and (51) can be expressed by a power series in a. Consequently, the limit value of each of these coefficients, as $a \to 0$, can be obtained by simply putting $a = 0$ in the power series expression. For instance,

$$\lim_{a\to 0} A_j^{(i)} = A_j^{(i)}|_{n=0}. \quad (56)$$

By using Eqs. (48), (49), (54), and (55) and through algebraic manipulations, it is seen that the coefficients $D_j^{(i)}$'s in Eqs. (45) and (51) take the form of

$$D_j^{(i)} = a^{2-j}(d_{j,0}^{(i)} + d_{j,1}^{(i)}a + d_{j,2}^{(i)}a^2 + \ldots), \quad (57)$$

where $d_{j,0}^{(i)}$, $d_{j,1}^{(i)}$, ... are constants. Obviously, the following limit values

$$\lim_{a\to 0}\frac{D_0^{(i)}}{a^2} = \left.\frac{D_0^{(i)}}{a^2}\right|_{a=0}, \quad \lim_{a\to 0}\frac{D_1^{(i)}}{a} = \left.\frac{D_1^{(i)}}{a}\right|_{a=0},$$

$$\lim_{a\to 0} D_2^{(i)} = D_2^{(i)}|_{a=0} \quad (58)$$

exist, and will be used in the making of the solid sphere solution.

Solid Sphere Solution and Discussion

Now consider the solution for a solid sphere ($a = 0$). In this case, the initial propagating wave solution for the hollow sphere (Eqs. (15), (21), and (22)), still holds as an exact solution for the solid sphere, except at the central point $r = a = 0$, where the displacement and stress become unbounded and undefined. On account of this, it follows that the solid sphere solution should be sought via a limit process applied on the hollow sphere solution in which $a \to 0$.

Applying the limit process of $a \to 0$ on the hollow sphere solution (27), (30), and (31), which corresponds to the first reflected wave from $r = a$, the solid sphere solution for that reflected wave turns out to be

$$f^{(1)}(S) = -Ce^{-\beta S/b} - e^{a_0 S}[A \sin(b_0 S) + B\cos(b_0 S)], \quad (59)$$

$$u_r = \{C(1 - \beta r/b)e^{-\beta S/b} + e^{a_0 S}[(A - A_1 r)\sin(b_0 S) + (B - B_1 r)\cos(b_0 S)]\}/r^2, \quad (60)$$

$$\sigma_r = \Big\{[4\mu(\beta r/b - 1) - (\lambda + 2\mu)\beta^2 r^2/b^2]Ce^{-\beta S/b} + e^{a_0 S}[(A_3 r - A_2 - A_4 r^2)\sin(b_0 S) + (B_3 r - B_2 - B_4 r^2)\cos(b_0 S)] + 2(\lambda + 2\mu)C\left[a_0^2 + b_0^2 + \frac{\beta}{b}\left(\frac{\beta}{b} + 2a_0\right)\right]L(S)r^2\Big\}/r^3, \quad (61)$$

where $S = -r - b + ct$, A_i and B_i, $i = 1, 2, 3, 4$, have been given in Eq. (23) and $L(S)$ stands for an irregular function, defined for $S \geq 0$ and behaving such that

$$L(S) \equiv \lim_{a\to 0} e^{-S/a} = \begin{cases} 1, & S = 0, \\ 0, & S > 0. \end{cases} \quad (62)$$

Besides, in deriving Eqs. (59), (60), and (61), the power series expansion for $D_0^{(1)}$ in a,

$$D_0^{(1)} = 2C\left[a_0^2 + b_0^2 + \frac{\beta}{b}\left(\frac{\beta}{b} + 2a_0\right)\right]a^2 + \ldots, \quad (63)$$

has been used.

The limit value of the term $D_0^{(1)}e^{-S/a}$ in Eq. (27), as well as that of its first derivative with respect to r vanishes, whereas the limit value of the second derivative does not: it brings about a term containing $L(S)$ in Eq. (61), which represents a stress pulse of finite magnitude, instantaneously appearing and vanishing at the wave front.

Likewise, through the limit process of $a \to 0$, Eq. (35), which corresponds to the first reflection from $r = b$, becomes

$$g^{(1)}(R) = C_0^{(2)}e^{-\beta R/b} + e^{a_0 R}[(A_{0,0}^{(2)} + A_{1,0}^{(2)}R)\sin(b_0 R) + (B_{0,0}^{(2)} + B_{1,0}^{(2)}R)\cos(b_0 R)], \quad (64)$$

where $R = r - 3b + ct$ and

$$C_0^{(2)} = \frac{(\lambda + 2\mu)\beta^2 + 4\mu - 4\mu\beta}{(\lambda + 2\mu)\beta^2 + 4\mu + 4\mu\beta}C,$$

$$A_{1,0}^{(2)} = \frac{B_{7,0}}{2b^2 b_0(\lambda + 2\mu)}, \quad B_{1,0}^{(2)} = -\frac{A_{7,0}}{2b^2 b_0(\lambda + 2\mu)},$$

$$A_{7,0} = 4\mu[A + b(a_0 A - b_0 B)] + (\lambda + 2\mu)b^2[(a_0^2 - b_0^2)A - 2a_0 b_0 B],$$

$$B_{7,0} = 4\mu[B + b(a_0 B + b_0 A)] + (\lambda + 2\mu)b^2[(a_0^2 - b_0^2)B + 2a_0 b_0 A],$$

$$B_{0,0}^{(2)} = -C_0^{(2)}, \quad A_{0,0}^{(2)} = -(B_{0,0}^{(2)}a_0 + B_{1,0}^{(2)} - \beta C_0^{(2)}/b)/b_0. \quad (65)$$

Expressions for the associated displacement and stress can be obtained from the limit forms of Eqs. (38) and (40) and are written as

$$u_r = -\{(1 + \beta r/b)C_0^{(2)}e^{-\beta R/b} + e^{a_0 R}[A_{8,0}(r, R)\sin(b_0 R) + B_{8,0}(r, R)\cos(b_0 R)]\}/r^2, \quad (66)$$

$$\sigma_r = \Big\{[4\mu(1 + \beta r/b) + (\lambda + 2\mu)\beta^2 r^2/b^2]C_0^{(2)}e^{-\beta R/b} + e^{a_0 R}[A_{9,0}(r, R)\sin(b_0 R) + B_{9,0}(r, R)\cos b_0 R] - 2(\lambda + 2\mu)C\left[a_0^2 + b_0^2 + \frac{\beta}{b}\left(\frac{\beta}{b} + 2a_0\right)\right]L(R)r^2\Big\}/r^3, \quad (67)$$

where expressions for $A_{8,0}$, $B_{8,0}$, $A_{9,0}$, and $B_{9,0}$ can be obtained from Eqs. (39) and (41) by replacing $A_0^{(2)}$, $B_0^{(2)}$, $A_1^{(2)}$, and $B_1^{(2)}$ contained therein with $A_{0,0}^{(2)}$, $B_{0,0}^{(2)}$, $A_{1,0}^{(2)}$, and $B_{1,0}^{(2)}$, respectively.

The solutions for the solid sphere to the subsequent reflections can be obtained from the limit forms of Eqs. (45) and (51) as well as the limit forms of the expressions for the associated displacements and stresses.

Downloaded 04 May 2010 to 171.66.16.26. Redistribution subject to ASME license or copyright; see http://www.asme.org/terms/Terms_Use.cfm

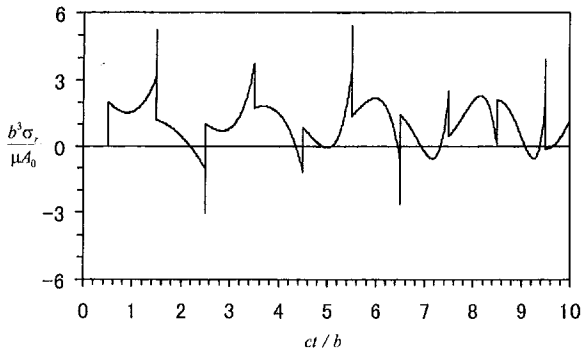


Fig. 1 Values of radial stress, hollow and solid sphere solution (r/b = 0.5)

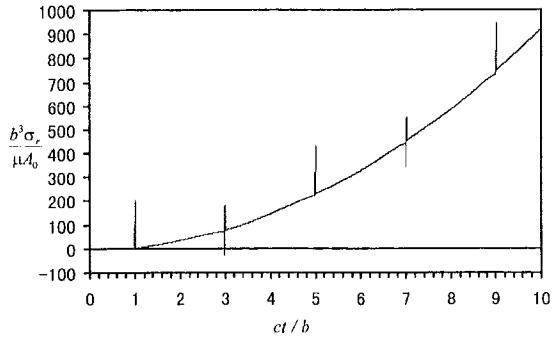


Fig. 2 Values of radial stress, hollow and solid sphere solution (r/b = 0.01)

Through the limit process, all terms with coefficients $D_j^{(i)}$'s in Eqs. (45) and (51) become zero. The limit values of the coefficients $C^{(i)}$, $A_j^{(i)}$, and $B_j^{(i)}$ in these two equations can be determined by using Eq. (56) and the like equations.

To obtain the limit forms of the associated displacements and stresses, the coefficients $C^{(i)}$, $A_j^{(i)}$, and $B_j^{(i)}$ in the displacement and stress expressions for the hollow sphere must be replaced by their limit values.

For displacement and stress components of form $e^{-S/a}(e^{-R/a})$ and with coefficient $D_j^{(i)}$, via simple analysis, it is shown that all such displacement components, as well as the stress components with coefficient $D_j^{(i)}, j \geq 3$, vanish through the limit process; in the meantime, stress components with coefficients $D_0^{(i)}$, $D_1^{(i)}$, and $D_2^{(i)}$ transform into stress pulses of finite magnitude at the wave front. These stress pulses form a portion of stress σ_r for the solid sphere, and can be expressed as

$$\sigma_{rD} = (\lambda + 2\mu)(d_0^{(2n+1)} - 2d_1^{(2n+1)} + 2d_2^{(2n+1)})\frac{L(S)}{r} \quad (68)$$

for the $(n + 1)$th reflection from the inner boundary, and

$$\sigma_{rD} = (\lambda + 2\mu)(d_0^{(2n+2)} - 2d_1^{(2n+2)} + 2d_2^{(2n+2)})\frac{L(R)}{r} \quad (69)$$

for the $(n + 1)$th reflection from the outer boundary, where (see Eq. (58))

$$d_0^{(i)} = \lim_{a\to 0}\frac{D_0^{(i)}}{a^2},\ d_1^{(i)} = \lim_{a\to 0}\frac{D_1^{(i)}}{a},\ d_2^{(i)} = \lim_{a\to 0} D_2^{(i)}. \quad (70)$$

The solution for the solid sphere has been provided. This solution is now discussed as follows.

Validity of the Solution. The solutions for the hollow and solid spheres are developed in the foregoing sections by elementary mathematics, and expressed in exact, explicit, and closed forms. Consequently, the validity of the solution can easily be confirmed either directly by analysis or by accurate numerical results. In the following, a hollow and a solid sphere with ν = 0.3 and under $\sigma_0 = -A_0 e^{-\beta ct/b}$, $\beta = 0$ (corresponding to a step temperature rise) will be referred in the following numerical examples for the dynamic response problem.

For a fixed value of r, say r_0, the dynamic response given by the solution of the hollow sphere solution, with a much smaller than r_0, should be nearly the same as that given by the solid sphere solution. The values of the radial stress during the dynamic response for a hollow (a/b = 0.00001, hollow sphere solution) and a solid sphere (a/b = 0, solid sphere solution) are calculated and presented graphically in Figs. 1 and 2 for r/b = 0.5 and 0.01, respectively. The two solutions agree very well in that they can only be represented by a single curve in each case.

Consider the solid sphere solution. The initial propagating wave arrives at r/b = 0.5 when ct/b = 0.5. This initial wave does not contain any stress pulse, and the stress discontinuity at the wave front is of value 2. At ct/b = 1.5, the first reflected wave from the inner boundary, r = 0, reaches r/b = 0.5, with stress discontinuity at the wave front being also of value 2. This reflected wave has a stress pulse of value 4 at r/b = 0.5. In Fig. 1, the stress discontinuity and the stress pulse are shown by a vertical line segment of length 4. Likewise, at ct/b = 2.5, when the first reflected wave from the outer boundary $r = b$ arrives at r/b = 0.5, the stress discontinuity and the stress pulse are of value −2 and −4, respectively. Similar remarks can be made for the subsequent period of the dynamic response, and also to the case of r/b = 0.01, which is shown in Fig. 2. However, stress discontinuities and stress pulses cannot clearly be seen in Fig. 2, due to the fact that they occur in a time period too small in comparison with the time unit of the figure.

Magnitude of Stress Discontinuity at the Wave Front. It is a general conclusion in spherical wave propagation that the magnitude of stress discontinuity at the wave front varies in proportion to $1/r$ (Milklowitz, 1978). Our analysis confirms this conclusion; besides, it can be visualized in Figs. 1 and 2, where radial stresses for the hollow and solid spheres at r/b = 0.5 and 0.01 are shown.

Stress Multiplication on the Inner Fixed Boundary. When an incoming wave (initial propagating or reflected from the outer boundary) in the hollow sphere reaches the inner fixed boundary $r = a$ at a certain moment, at that instant the reflected wave produces a radial stress of equal magnitude and same sign with respect to the radial stress carried by the incoming wave, at the same place $r = a$. This conclusion can be established by the use of an impulse-momentum equation (Milklowitz, 1978) to a hollow sphere. Similar phenomenon is known as stress multiplication in simple plane wave reflection at a fixed boundary (Graff, 1976). The conclusion also can be confirmed by an examination of Eqs. (22) and (31), as well as that which can be observed from Fig. 4, in which the radial stresses at the inner fixed boundary of hollow spheres with various values of a/b, during the inceptive period of the dynamic response, are depicted.

As stress multiplication invariably takes place at the inner fixed boundary of the hollow sphere, irrespective of how small the inner radius a may be, it also occurs at the ultimate end of the limit process, that is, at the center of the solid sphere. This can be seen from the fact that both Eqs. (22) and (61) yield the quantity $P = r\sigma_r$ of equal magnitude and the same sign at r = 0, the moment $t = (b - a)/c$, where $P = (\lambda + 2\mu)C[a_0^2 + b_0^2 + \beta(\beta/b + 2a_0)/b]$.

In the meantime the reflected wave from the outer free boundary produces a radial stress at $r = b$, which is equal in magnitude and opposite in sign to the radial stress carried by the incoming

Downloaded 04 May 2010 to 171.66.16.26. Redistribution subject to ASME license or copyright; see http://www.asme.org/terms/Terms_Use.cfm

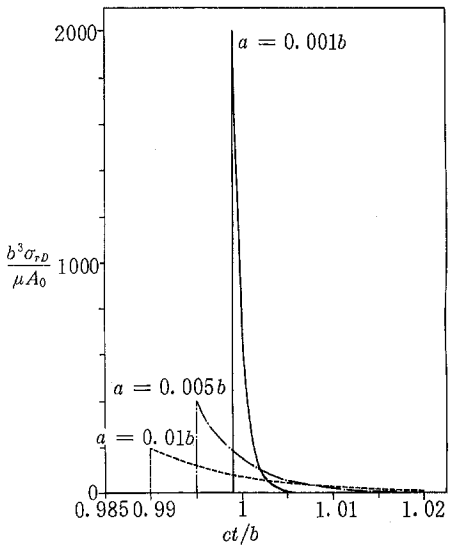


Fig. 3 Values of σ_{rD} at the fixed boundary

wave at the same place, $r = b$. Combining this stress adversal and the stress multiplication phenomena at the free and fixed boundaries, respectively, the following rule can be drawn for the stress discontinuity at the wave front when it is passing through a spherical surface of coordinate r_0. That is, the inwardly and outwardly going waves pass through the spherical surface at $t = (mb - r_0)/c$ and $(mb + r_0)/c$, $m = 1, 3, 5, \ldots$, respectively; both waves are with a stress discontinuity of value $(-1)^{(m+1)/2}b\sigma_0/r_0$, in the present numerical examples $\sigma_0 = -A_0$.

Radial Stress Component With Coefficient $D_j^{(i)}$. Equation (31), the expression for the radial stress of the elastic wave first reflected from $r = a$ in the hollow sphere, contains a component $[4\mu - 4\mu r/a + (\lambda + 2\mu)r^2/a^2]D_0^{(1)}e^{-S/a}/r^3$, which is necessary for the solution to be free of static elements. For a fixed r in the hollow sphere with small inner radius a, this component jumps to a certain value abruptly at the instant the wave front arrives, and after that instant decays very rapidly. This can be seen in Fig. 3, where this component, denoted by σ_{rD}, is shown for $r = a$ for various values of a.

For the solid sphere at the point $r = 0$, this component reduces to, as indicated in Eq. (61), a stress pulse, instantanonsly appearing and vanishing at the instant the wave front of the initial propagating wave arrives, and of a magnitude M of unbounded strength such as

$$\lim_{r\to 0} rM = 2C(\lambda + 2\mu)[a_0^2 + b_0^2 + \beta(\beta/b + 2a_0)/b]. \quad (71)$$

According to Eqs. (68), (69), and (70), for subsequent reflections stress components with coefficients $D_0^{(i)}$, $D_1^{(i)}$, and $D_2^{(i)}$ turn into stress pulses through the limit process. In addition, since the stress discontinuity at the wave front in the solid sphere solution is always of finite magnitude everywhere except at $r = 0$, the coefficient $D_j^{(i)}$ in the hollow sphere solution must take the form indicated in Eq. (57).

Discussion on a Previous Study. As indicated in the Introduction, the same problem and virtually the same numerical examples were investigated in Hata (1991a), where the first two ray integrals (radial displacements) were given by expressions containing functions of complex variables; and the further ray integrals, expressed in the form of definite integrals, were evaluated with numerical quadrature. Likewise, no explicit expressions for the stress were given in Hata (1991a).

However, from the numerical values of stresses (Figs. 2 and 4(*b*)) in Hata (1991a), it is seen that the stress discontinuities at the wave front do not vary in proportion to $1/r$; besides it was concluded there that the radial stress at the sphere center is bounded, and numerical values of the stress were presented there to confirm the conclusion. From the numerical values we see that while the radial stress carried by the incoming wave is positive, that which is induced by the reflected wave at the center is negative. Consequently, these results given in Hata (1991a) are entirely different from those obtained in this article; in the meantime, they are also inconsistent with the general conclusions drawn from the basic theory of elastodynamics.

Stress Singularity. The center point $r = 0$ is an essential singularity in stress for the solid sphere. This stress singularity is evolved from the abruptly changing stress component of form $e^{-S/a}$ at the inner fixed boundary of the hollow sphere. For a finite a the term representing this component in Eq. (27) has a regular Laplace transform. However, in the limit of $a \to 0$, the Laplace transform of the term itself, as well as that of its first derivative with respect to r vanishes, whereas the Laplace transform of its second derivative does not. This fact may be used to account for the possible fact that in solving this basic problem with the Laplace transform technique, something may inappropriately be missed in the resulted transformed equation.

Summary and Extension

The thermoelasticodynamic problem of a solid sphere thermally induced by a sudden uniform temperature rise is, with a simple reduction, reduced to an isothermal dynamic response problem of the solid sphere.

An exact solution for the dynamic response problem of a hollow sphere, whose inner boundary is fixed, is developed by using a solution in D'Alembert form and a technique of singularity extraction. The solution for the hollow sphere is then treated in a limit process in which the inner radius a approaches zero, and thereby creates a solution for the solid sphere. The solid sphere solution is exact and explicit, besides, it is closed for each wave propagation or reflection.

The above development is based on the assumption that σ_0 in Eq. (4) takes the form of an exponential function (see Eq. (9)), which includes the important case of a step loading ($\beta = 0$). For σ_0 of another pattern, write it in the following power series form

$$\sigma_0(t) = c_0 + c_1 t + c_2 t^2 + \ldots \quad (72)$$

and substituting (72) into (13) and other related equations, the resulting ordinary differential equations can be solved with equal exactness and ease. Furthermore, by the use of the principle of superposition, the solution when σ_0 takes a more complicated form, e.g., that contains some discontinuous points, can as well as be constructed straightforwardly.

Acknowledgment

This work was supported by a grant from the National Natural Foundation of PRC.

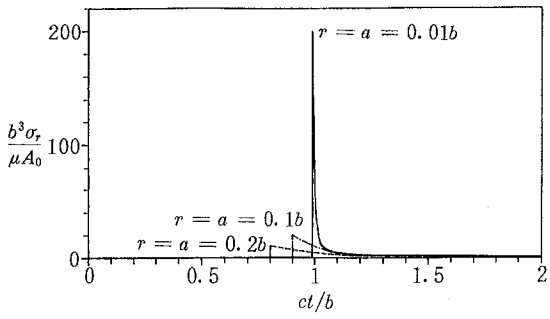


Fig. 4 Values of radial stress at the fixed boundary

Downloaded 04 May 2010 to 171.66.16.26. Redistribution subject to ASME license or copyright; see http://www.asme.org/terms/Terms_Use.cfm

References

Achenbach, J. D., 1973, *Wave Propagation in Elastic Solids,* North-Holland, Amsterdam.

Boley, B. A., and Weiner, J. H., 1960, *Theory of Thermal Stresses,* John Wiley and Sons, New York.

Eringen, A. C., and Suhubi, E. S., 1975, *Elastodynamics II: Linear Theory,* Academic Press, New York.

Graff, K. F., 1975, *Wave Motion in Elastic Solids,* Clarendon Press, Oxford.

Hata, T., 1991a, "Stress-Focusing Effect in a Uniformly Heated Solid Sphere," ASME JOURNAL OF APPLIED MECHANICS, Vol. 58, pp. 58–63.

Hata, T., 1991b, "Thermal Shock in a Hollow Sphere Caused by Rapid Uniform Heating," ASME JOURNAL OF APPLIED MECHANICS, Vol. 58, pp. 64–69.

Ho, C. H., 1976, "Stress-Focusing Effect in a Uniformly Heated Cylindrical Rod," ASME JOURNAL OF APPLIED MECHANICS, Vol. 43, pp. 464–468.

Ince, E. L., 1945, *Ordinary Differential Equations,* Dover, New York.

Milklowitz, J., 1978, *Elastic Waves and Waveguides,* North-Holland, Amsterdam.

Mann-Nachbar, P., and Nachbar, W., 1970, "Thermal shock Following Rapid Uniform Heating of Spheres and Long Cylindrical Rods," Aerospace Corp. Report TR-0066 (S5816-71)-1.

Pao, Y. H., and Ceranoglue, A. N., 1978, "Determination of Transient Response of a Thick-Walled Spherical Shell by Ray Theory," ASME JOURNAL OF APPLIED MECHANICS, Vol. 45, pp. 114–122.

Pao, Y. H., and Mow, C. C., 1973, *Diffraction of Elastic Waves and Dynamic Stress Concentrations,* Crane and Russak, New York.

Downloaded 04 May 2010 to 171.66.16.26. Redistribution subject to ASME license or copyright; see http://www.asme.org/terms/Terms_Use.cfm

Decomposition of the Deformation Gradient in Thermoelasticity

A. Imam
Assoc. Mem. ASME

G. C. Johnson
Mem. ASME

Department of Mechanical Engineering,
University of California at Berkeley,
Berkeley, CA 94720

The deformation gradient of a thermoelastic solid undergoing large deformations is decomposed into elastic and thermal components, corresponding to an intermediate configuration which is assumed to be stress-free. This decomposition is shown to be unique only to within a rigid-body motion of the intermediate configuration. An alternate decomposition is proposed in which this arbitrariness is removed. The thermoelastic theory developed on the basis of these decompositions is linearized, resulting in familiar expressions of linear thermoelasticity. The stress response function is further specialized for the particular case of isotropic linear solids.

1 Introduction

In the general theory of thermoelasticity the independent variables consist of the deformation gradient and the temperature field where the former is replaced, after imposition of the invariance requirements, by some measure of strain. It is sometimes advantageous to consider intermediate configurations, which the body may or may not actually occupy in the course of its motion, and analyze the various kinematical and thermodynamical fields at such intermediate configurations in order to gain a better understanding of the overall motion of the body. Examples of such intermediate configurations are those associated with the polar decomposition of the deformation gradient, or the intermediate configurations associated with finite deformation plasticity involving the multiplicative decomposition of the deformation gradient into elastic and plastic components as proposed by Lee (1969) and further discussed by Casey and Naghdi (1981).

Typically, it is desirable to separate the kinematic effects of the thermal portion of a thermoelastic process from the kinematic effects of the applied mechanical loading. In order to effect such a separation, the total deformation gradient is decomposed into "thermal" and "elastic" parts. The thermal part of the deformation gradient represents the deformation associated with a temperature change, but no mechanical loading, and takes the undeformed reference configuration into a stress-free intermediate configuration. The elastic part of the deformation gradient represents the deformation, due to the mechanical loading, from this intermediate configuration to the current configuration at constant temperature. This multiplicative decomposition allows natural definitions for all the relevant kinematic measures in terms of the thermal and elastic components of the deformation gradient, and permits relatively simple description for the free energy in terms of these measures.

In Section 2 we consider the multiplicative decomposition of the deformation gradient, corresponding to the deformation of a thermoelastic body, into two components representing the thermal part of the deformation and the purely elastic part of the deformation, respectively. The intermediate configuration, which results from the thermal part of the deformation, is assumed to be stress-free, thereby enabling us to define the strain at this configuration as the thermal strain. The notion of a stress-free configuration has a counterpart in the multiplicative decomposition of the deformation gradient for an elastic-plastic body proposed by Lee (1969). The intermediate configuration is shown to be nonunique under a rigid-body motion. Consequences of the requirement that the material response be invariant under rigid-body motions are explored and the principles of thermodynamics are employed to obtain constitutive relations for stress and entropy.

In order to circumvent the arbitrariness in the intermediate configuration, an alternate decomposition is proposed in Section 3 which involves two intermediate stress-free configurations. These configurations arise due to thermal stretching and rotation of the body, respectively, and are uniquely defined. Once again, principles of thermodynamics are invoked in order to obtain constitutive relations for the various thermomechanical fields in terms of the alternate kinematic measures.

In Section 4 we develop the linear version of the above formulations and recover results that are familiar from the study of the linear thermomechanical response of elastic bodies. In particular, we develop constitutive relations for stress and entropy using a procedure similar to the one employed by Carlson (1972). The multiplicative decomposition of the deformation gradient is now manifested as an additive decomposition of the strain into a thermal and an elastic component. We show that the stress in the linear theory is determined entirely by the elastic component of the strain. Finally, the stress response function for the special case of isotropic elastic solids is obtained, where the response of the body is characterized by three material constants.

2 General Theory of Thermoelasticity

Let the position vector to a point in a thermoelastic body B, in a fixed reference configuration κ_0, be denoted by $\mathbf{X}$. The position of the same material point in the current configuration κ at time t is denoted by $\mathbf{x}$, making it possible to define the deformation gradient as

$$\mathbf{F} = \frac{\partial \mathbf{x}}{\partial \mathbf{X}}, \quad \det \mathbf{F} > 0, \tag{1}$$

where det stands for the determinant.

We now assume the existence of an intermediate configuration $\bar{\kappa}$ and refer to the deformation gradient associated with this configuration relative to the reference configuration as $\mathbf{F}_\vartheta$.

Contributed by the Applied Mechanics Division of THE AMERICAN SOCIETY OF MECHANICAL ENGINEERS for publication in the ASME JOURNAL OF APPLIED MECHANICS.

Discussion on the paper should be addressed to the Technical Editor, Professor Lewis T. Wheeler, Department of Mechanical Engineering, University of Houston, Houston, TX 77204-4792, and will be accepted until four months after final publication of the paper itself in the ASME JOURNAL OF APPLIED MECHANICS.

Manuscript received by the ASME Applied Mechanics Division, Aug. 8, 1996; final revision, Aug. 10, 1997. Associate Technical Editor: R. Abeyaratne.

 Copyright © 1998 by ASME

Downloaded 04 May 2010 to 171.66.16.26. Redistribution subject to ASME license or copyright; see http://www.asme.org/terms/Terms_Use.cfm

Since $\bar{\kappa}$ is assumed to be an admissible configuration, $\det \mathbf{F}_\vartheta > 0$ and, consequently, $\mathbf{F}$ can be written as

$$\mathbf{F} = \mathbf{F}_e\mathbf{F}_\vartheta, \tag{2}$$

where $\mathbf{F}_e$ refers to the deformation gradient associated with the configuration κ relative to the configuration $\bar{\kappa}$. It follows from (2) that $\det \mathbf{F}_e > 0$. The deformation gradient $\mathbf{F}$ is a compatible field in the sense that if F_{iA} are components of $\mathbf{F}$ with respect to fixed Cartesian coordinates in κ and κ_0, then $\partial F_{iA}/\partial X_B = \partial F_{iB}/\partial X_A$. However, $\mathbf{F}_\vartheta$ and $\mathbf{F}_e$ need not, in general, be compatible.

In view of the above decomposition the various thermomechanical fields, prescribed by constitutive equations, depend on $\mathbf{F}_\vartheta$, $\mathbf{F}_e$ and the absolute temperature designated by ϑ. The tensor $\mathbf{F}_\vartheta$ is taken to be a function of ϑ alone. In particular, the Helmholtz free energy per unit mass, denoted by ψ, is written as

$$\psi = \psi_1(\mathbf{F}_e, \mathbf{F}_\vartheta, \vartheta) = \psi_2(\mathbf{F}, \mathbf{F}_\vartheta, \vartheta). \tag{3}$$

The polar decompositions corresponding to $\mathbf{F}$, $\mathbf{F}_e$, and $\mathbf{F}_\vartheta$ are

$$\mathbf{F} = \mathbf{RU} = \mathbf{VR}, \quad \mathbf{F}_e = \mathbf{R}_e\mathbf{U}_e = \mathbf{V}_e\mathbf{R}_e,$$
$$\mathbf{F}_\vartheta = \mathbf{R}_\vartheta\mathbf{U}_\vartheta = \mathbf{V}_\vartheta\mathbf{R}_\vartheta, \tag{4}$$

where $\mathbf{R}$, $\mathbf{R}_e$, and $\mathbf{R}_\vartheta$ are proper orthogonal tensors and $\mathbf{U}$, $\mathbf{U}_e$, and $\mathbf{U}_\vartheta$ as well as $\mathbf{V}$, $\mathbf{V}_e$, and $\mathbf{V}_\vartheta$ are symmetric positive-definite tensors. The deformation tensors $\mathbf{C}$, $\mathbf{C}_e$, and $\mathbf{C}_\vartheta$ and strain tensors $\mathbf{E}$, $\mathbf{E}_e$, and $\mathbf{E}_\vartheta$ are defined by

$$\mathbf{C} = \mathbf{F}^T\mathbf{F} = \mathbf{U}^2, \quad \mathbf{C}_e = \mathbf{F}_e^T\mathbf{F}_e = \mathbf{U}_e^2, \quad \mathbf{C}_\vartheta = \mathbf{F}_\vartheta^T\mathbf{F}_\vartheta = \mathbf{U}_\vartheta^2,$$
$$\mathbf{E} = \tfrac{1}{2}(\mathbf{C} - \mathbf{I}), \quad \mathbf{E}_e = \tfrac{1}{2}(\mathbf{C}_e - \mathbf{I}), \quad \mathbf{E}_\vartheta = \tfrac{1}{2}(\mathbf{C}_\vartheta - \mathbf{I}), \tag{5}$$

where $\mathbf{I}$ is the second-order identity tensor. We note that, because of (2), $\mathbf{E}$, $\mathbf{E}_e$, and $\mathbf{E}_\vartheta$ are not independent, and using (2) and (5) it readily follows that

$$\mathbf{E} = \mathbf{E}_\vartheta + \mathbf{F}_\vartheta^T\mathbf{E}_e\mathbf{F}_\vartheta. \tag{6}$$

Let us now explore the consequences of the invariance requirements in the presence of the intermediate configuration. To this end, following Casey and Naghdi (1983), we subject the current configuration as well as the intermediate configuration to the invariance requirements. This implies that when $\mathbf{F}$ and $\mathbf{F}_\vartheta$ are transformed into

$$\mathbf{F}^+ = \mathbf{Q}(t)\mathbf{F} \quad \text{and} \quad \mathbf{F}_\vartheta^+ = \bar{\mathbf{Q}}(t)\mathbf{F}_\vartheta, \tag{7}$$

where $\mathbf{Q}$ and $\bar{\mathbf{Q}}$ are two arbitrary proper orthogonal tensor-valued functions of time, the Helmholtz free-energy function remains unaltered, i.e.,

$$\psi = \psi^+ = \psi_1(\mathbf{F}_e^+, \mathbf{F}_\vartheta^+, \vartheta^+) = \psi_2(\mathbf{F}^+, \mathbf{F}_\vartheta^+, \vartheta^+), \tag{8}$$

where the rigid motions are superimposed at constant temperature resulting in $\vartheta^+ = \vartheta$. Furthermore, it follows from (2) and (7) that $\mathbf{F}_e$ transforms as

$$\mathbf{F}_e^+ = \mathbf{Q}\mathbf{F}_e\bar{\mathbf{Q}}^T, \tag{9}$$

and, using (5) and (7), $\mathbf{C}_\vartheta$ transforms as

$$\mathbf{C}_\vartheta^+ = \mathbf{F}_\vartheta^{+T}\mathbf{F}_\vartheta^+ = \mathbf{F}_\vartheta^T\mathbf{F}_\vartheta = \mathbf{C}_\vartheta. \tag{10}$$

In view of (7) and (9), Eq. $(8)_2$ implies that

$$\psi = \psi_1(\mathbf{F}_e^+, \mathbf{F}_\vartheta^+, \vartheta) = \psi_1(\mathbf{Q}\mathbf{F}_e\bar{\mathbf{Q}}^T, \bar{\mathbf{Q}}\mathbf{F}_\vartheta, \vartheta). \tag{11}$$

Since $\mathbf{Q}$ and $\bar{\mathbf{Q}}$ are arbitrary proper orthogonal tensors, we may let

$$\mathbf{Q} = \mathbf{R}_\vartheta^T\mathbf{R}_e^T \quad \text{and} \quad \bar{\mathbf{Q}} = \mathbf{R}_\vartheta^T \tag{12}$$

and use these in (11) to obtain

$$\psi = \psi_1(\mathbf{R}_\vartheta^T\mathbf{R}_e^T\mathbf{F}_e\mathbf{R}_\vartheta, \mathbf{R}_\vartheta^T\mathbf{F}_\vartheta, \vartheta) = \psi_1(\mathbf{R}_\vartheta^T\mathbf{U}_e\mathbf{R}_\vartheta, \mathbf{U}_\vartheta, \vartheta)$$
$$= \hat{\psi}_1(\mathbf{R}_\vartheta^T\mathbf{C}_e\mathbf{R}_\vartheta, \mathbf{C}_\vartheta, \vartheta) = \tilde{\psi}(\mathbf{R}_\vartheta^T\mathbf{E}_e\mathbf{R}_\vartheta, \mathbf{E}_\vartheta, \vartheta), \tag{13}$$

where (4) and (5) have been used. As expected, the arguments of $\hat{\psi}_1$ and $\tilde{\psi}$ in (13) are all invariant under rigid-body motions of $\bar{\kappa}$ and κ.

We can carry out a similar analysis for the Helmholtz free enegy written as a function of $\mathbf{F}$, $\mathbf{F}_\vartheta$ and ϑ as in $(8)_3$. Thus, using (7), $(8)_3$ can be written as

$$\psi = \psi_2(\mathbf{F}^+, \mathbf{F}_\vartheta^+, \vartheta) = \psi_2(\mathbf{QF}, \bar{\mathbf{Q}}\mathbf{F}_\vartheta, \vartheta). \tag{14}$$

If we choose

$$\mathbf{Q} = \mathbf{R}^T \quad \text{and} \quad \bar{\mathbf{Q}} = \mathbf{R}_\vartheta^T, \tag{15}$$

then (14) implies that

$$\psi = \psi_2(\mathbf{R}^T\mathbf{F}, \mathbf{R}_\vartheta^T\mathbf{F}_\vartheta, \vartheta) = \psi_2(\mathbf{U}, \mathbf{U}_\vartheta, \vartheta) = \hat{\psi}_2(\mathbf{C}, \mathbf{C}_\vartheta, \vartheta)$$
$$= \bar{\psi}(\mathbf{E}, \mathbf{E}_\vartheta, \vartheta), \tag{16}$$

where (4) and (5) were again employed. We note that the arguments of $\bar{\psi}$ are also invariant. Therefore, the Helmholtz free-energy function can be expressed in two distinct ways as given in (13) and (16).

To complete the thermodynamic development we need to obtain appropriate expressions for stress and entropy in terms of the free-energy function. This is accomplished following the formulation of Green and Naghdi (1977).[1]

To this end, we let $\mathbf{S}$ represent the symmetric Piola-Kirchhoff stress, η the entropy per unit mass, $\mathbf{q}$ the heat flux vector, and ξ the internal entropy production per unit mass. In what follows, we use the form of ψ given in (16) and assume that $\mathbf{S}$, η, and ξ depend on $\mathbf{E}$, $\mathbf{E}_\vartheta$, and ϑ while $\mathbf{q}$ has an additional dependence on the gradient of ϑ with respect to the reference configuration, denoted by $\nabla\vartheta$. The field quantities $\mathbf{S}$, η, and ξ remain unaltered under the transformations given in (7), while $\mathbf{q}^+ = \mathbf{Qq}$. Then, following Green and Naghdi (1977), the identity

$$-\rho(\dot{\psi} + \eta\dot{\vartheta}) + \frac{\rho}{\rho_0}\mathbf{S}\cdot\dot{\mathbf{E}} - \rho\vartheta\xi - \frac{1}{\vartheta}\mathbf{q}\cdot\nabla\vartheta = 0 \tag{17}$$

is required to hold for all thermomechanical processes. In (17), the superposed dot represents material time differentiation while ρ and ρ_0 denote the mass densities in κ and κ_0, respectively. Performing the differentiation of ψ in (17) we obtain

$$-\rho\left[\frac{\partial\bar{\psi}}{\partial\mathbf{E}}\cdot\dot{\mathbf{E}} + \frac{\partial\bar{\psi}}{\partial\mathbf{E}_\vartheta}\cdot\dot{\mathbf{E}}_\vartheta + \frac{\partial\bar{\psi}}{\partial\vartheta}\dot{\vartheta} + \eta\dot{\vartheta}\right]$$
$$+ \frac{\rho}{\rho_0}\mathbf{S}\cdot\dot{\mathbf{E}} - \rho\vartheta\xi - \frac{1}{\vartheta}\mathbf{q}\cdot\nabla\vartheta = 0. \tag{18}$$

As the above holds for all thermomechanical processes, $\dot{\mathbf{E}}$ and $\dot{\vartheta}$ can be chosen arbitrarily. Furthermore, the constitutive relations do not depend on $\dot{\mathbf{E}}$ and $\dot{\vartheta}$ and we recall that $\mathbf{E}_\vartheta$ depends only on ϑ. Then, it follows from (18) that

$$\mathbf{S} = \rho_0\frac{\partial\bar{\psi}}{\partial\mathbf{E}}, \quad \eta = -\frac{\partial\bar{\psi}}{\partial\vartheta} - \frac{\partial\bar{\psi}}{\partial\mathbf{E}_\vartheta}\cdot\frac{d\mathbf{E}_\vartheta}{d\vartheta},$$
$$\rho\vartheta\xi + \frac{1}{\vartheta}\mathbf{q}\cdot\nabla\vartheta = 0. \tag{19}$$

So far we have introduced $\mathbf{E}_\vartheta$ as the strain corresponding to the intermediate configuration but have not specified in what

[1] It is possible to use an alternative formulation involving the Clausius-Duhem inequality (Coleman and Noll, 1963), as a representation of the second law, to obtain results that are identical to what are presented here.

Downloaded 04 May 2010 to 171.66.16.26. Redistribution subject to ASME license or copyright; see http://www.asme.org/terms/Terms_Use.cfm

way it might be determined. In order to identify $\mathbf{E}_\vartheta$, we require the intermediate configuration to be stress-free. More precisely, since the total strain in the intermediate configuration is $\mathbf{E}_\vartheta$, we require that

$$\mathbf{S} = \bar{\mathbf{S}}(\mathbf{E}_\vartheta, \mathbf{E}_\vartheta, \vartheta) = 0. \tag{20}$$

The above equation serves to determine $\mathbf{E}_\vartheta$ which, we assume, can be done uniquely.

However, the stress tensor $\mathbf{S}$ and the thermal strain $\mathbf{E}_\vartheta$ remain unaltered under rigid-body motions of $\bar{\kappa}$. Consequently, (20) implies that the stress-free configuration is only unique up to a rigid-body motion. This nonuniqueness of the intermediate configuration is also suggested by the decomposition (2) and the definition of $\mathbf{E}_\vartheta$ in (5), whereupon changing $\mathbf{F}_e$ to $\mathbf{F}_e\hat{\mathbf{Q}}^T$ and $\mathbf{F}_\vartheta$ to $\hat{\mathbf{Q}}\mathbf{F}_\vartheta$, with $\hat{\mathbf{Q}}$ being any proper orthogonal tensor, $\mathbf{F}$ and $\mathbf{E}_\vartheta$ remain unaffected. Thus, while $\mathbf{E}_\vartheta$ can be identified in a unique way, the proposed decomposition of the deformation gradient remains nonunique.

3 An Alternate Decomposition

In order to avoid the nonuniqueness associated with the decomposition presented in Section 2, we consider an alternate decomposition of the deformation gradient analogous to the one proposed originally by Bammann and Johnson (1987) within the context of plasticity.

To this end, we first note that under the transformations given in (7), Eqs. $(5)_2$ and (9) imply that

$$\mathbf{C}_e^+ = \mathbf{F}_e^{+T}\mathbf{F}_e^+ = \bar{\mathbf{Q}}\mathbf{F}_e^T\mathbf{Q}^T\mathbf{Q}\mathbf{F}_e\bar{\mathbf{Q}}^T = \bar{\mathbf{Q}}\mathbf{C}_e\bar{\mathbf{Q}}^T. \tag{21}$$

Then using (21), (5), (7), and (9), the tensors in the polar decompositions of $\mathbf{F}_e$ and $\mathbf{F}_\vartheta$ are found to transform as

$$\mathbf{R}_e^+ = \mathbf{Q}\mathbf{R}_e\bar{\mathbf{Q}}^T, \quad \mathbf{U}_e^+ = \bar{\mathbf{Q}}\mathbf{U}_e\bar{\mathbf{Q}}^T, \quad \mathbf{V}_e^+ = \mathbf{Q}\mathbf{V}_e\mathbf{Q}^T,$$
$$\mathbf{R}_\vartheta^+ = \bar{\mathbf{Q}}\mathbf{R}_\vartheta, \quad \mathbf{U}_\vartheta^+ = \mathbf{U}_\vartheta, \quad \mathbf{V}_\vartheta^+ = \bar{\mathbf{Q}}\mathbf{V}_\vartheta\bar{\mathbf{Q}}^T, \tag{22}$$

where it is seen that $\mathbf{V}_e$ and $\mathbf{U}_\vartheta$ are independent of the orientation of the intermediate configuration. We now introduce a rotation

$$\bar{\mathbf{R}} = \mathbf{R}_e\mathbf{R}_\vartheta, \tag{23}$$

which, upon using (22), is found to transform as

$$\bar{\mathbf{R}}^+ = \mathbf{Q}\bar{\mathbf{R}}. \tag{24}$$

Therefore, $\bar{\mathbf{R}}$ is also independent of the orientation of $\bar{\kappa}$.

Using $\mathbf{V}_e$, $\mathbf{U}_\vartheta$, and $\bar{\mathbf{R}}$, the decomposition of the deformation gradient in (2) is written as

$$\mathbf{F} = \mathbf{V}_e\bar{\mathbf{R}}\mathbf{U}_\vartheta, \tag{25}$$

where $\mathbf{F}$ is decomposed into a thermal stretch, a rotation, and an elastic stretch. There are two unique intermediate configurations associated with the above decomposition. The first, κ_1, is obtained by mapping the reference configuration κ_0 through the thermal stretch $\mathbf{U}_\vartheta$, and the second intermediate configuration, κ_2, is obtained from κ_1 through the rotation $\bar{\mathbf{R}}$. As the strain in both κ_1 and κ_2 is $\mathbf{E}_\vartheta$, these intermediate configurations are stress-free.

We note that all intermediate configurations which may be obtained from $\bar{\kappa}$ through a rigid-body motion, correspond to the same intermediate configurations κ_1 and κ_2 and, as a consequence, the nonuniqueness associated with $\bar{\kappa}$ is removed when we consider the decomposition given in (25).

We now rewrite the decomposition in (25) as

$$\mathbf{F} = \bar{\mathbf{F}}_e\mathbf{U}_\vartheta, \tag{26}$$

where

$$\bar{\mathbf{F}}_e = \mathbf{V}_e\bar{\mathbf{R}}. \tag{27}$$

Then several measures of strain with respect to κ_1 are defined as

$$\bar{\mathbf{E}} = \mathbf{U}_\vartheta^{-1}\mathbf{E}\mathbf{U}_\vartheta^{-1}, \quad \bar{\mathbf{E}}_\vartheta = \mathbf{U}_\vartheta^{-1}\mathbf{E}_\vartheta\mathbf{U}_\vartheta^{-1},$$
$$\bar{\mathbf{E}}_e = \tfrac{1}{2}(\bar{\mathbf{F}}_e^T\bar{\mathbf{F}}_e - \mathbf{I}) = \tfrac{1}{2}(\bar{\mathbf{R}}^T\mathbf{V}_e^2\bar{\mathbf{R}} - \mathbf{I}). \tag{28}$$

The strain $\bar{\mathbf{E}}$ represents the change in length due to the overall deformation measured per unit length in κ_1, while $\bar{\mathbf{E}}_\vartheta$ represents the change in length due to the thermal stretch measured per unit length in κ_1. Similarly, the strain measure $\bar{\mathbf{E}}_e$ represents the change in length due to the elastic stretch measured per unit length in the intermediate configuration κ_1. Note also that (22) and (24) imply that $\bar{\mathbf{E}}_\vartheta$ and $\bar{\mathbf{E}}_e$ are invariant strain measures, i.e.,

$$\bar{\mathbf{E}}_\vartheta^+ = \bar{\mathbf{E}}_\vartheta \quad \text{and} \quad \bar{\mathbf{E}}_e^+ = \bar{\mathbf{E}}_e. \tag{29}$$

We also define an invariant stress measure $\bar{\mathbf{S}}$ as

$$\bar{\mathbf{S}} = \frac{1}{\det \mathbf{U}_\vartheta}\mathbf{U}_\vartheta\mathbf{S}\mathbf{U}_\vartheta. \tag{30}$$

In analogy to the Cauchy stress $\mathbf{T}$ defined in the current configuration by

$$\mathbf{T} = \frac{1}{\det \mathbf{F}}\mathbf{F}\mathbf{S}\mathbf{F}^T, \tag{31}$$

the stress tensor $\bar{\mathbf{S}}$ may be thought of as a measure of stress in the intermediate configuration κ_1.

In view of the decomposition given in (26), the thermomechanical fields are functions of $\bar{\mathbf{F}}_e$, $\mathbf{U}_\vartheta$, and ϑ, where it is recalled that $\mathbf{U}_\vartheta$ depends on ϑ. In particular, the Helmholtz free energy is expressed as

$$\psi = \psi_3(\bar{\mathbf{F}}_e, \mathbf{U}_\vartheta, \vartheta), \tag{32}$$

Then application of invariance requirements, as in Section 2, allows (32) to be rewritten as

$$\psi = \psi^+ = \hat{\psi}(\bar{\mathbf{E}}_e, \bar{\mathbf{E}}_\vartheta, \vartheta). \tag{33}$$

We now proceed to determine constitutive relations for the stress $\bar{\mathbf{S}}$ and entropy η. Using (4), (6), and (28), it can be shown that

$$\bar{\mathbf{E}} = \bar{\mathbf{E}}_\vartheta + \bar{\mathbf{E}}_e. \tag{34}$$

In addition, it can be shown that the stress power is given by

$$\mathbf{S}\cdot\dot{\mathbf{E}} = \mathrm{Tr}\,(\mathbf{S}\dot{\mathbf{E}}) = (\det \mathbf{U}_\vartheta)\,\mathrm{Tr}\,(2\dot{\mathbf{U}}_\vartheta\mathbf{U}_\vartheta^{-1}\bar{\mathbf{S}}\bar{\mathbf{E}} + \bar{\mathbf{S}}\dot{\bar{\mathbf{E}}}), \tag{35}$$

where Tr stands for the trace.

Once expressions (33) and (35) are substituted in the thermodynamic relation (17), using the same reasoning as employed in the previous section, it is found that

$$\bar{\mathbf{S}} = \bar{\rho}\,\frac{\partial\hat{\psi}}{\partial\bar{\mathbf{E}}_e}, \tag{36}$$

$$\bar{\rho}\eta = -\bar{\rho}\,\frac{\partial\hat{\psi}}{\partial\vartheta} - \bar{\rho}\,\frac{\partial\hat{\psi}}{\partial\bar{\mathbf{E}}_\vartheta}\cdot\frac{d\bar{\mathbf{E}}_\vartheta}{d\vartheta} + 2\,\mathrm{Tr}\left(\frac{d\mathbf{U}_\vartheta}{d\vartheta}\mathbf{U}_\vartheta^{-1}\bar{\mathbf{S}}\bar{\mathbf{E}}\right) + \mathrm{Tr}\left(\bar{\mathbf{S}}\,\frac{d\bar{\mathbf{E}}_\vartheta}{d\vartheta}\right), \tag{37}$$

where

$$\bar{\rho} \equiv \rho_0(\det \mathbf{U}_\vartheta)^{-1}. \tag{38}$$

Expression (36) is a constitutive relation in terms of the quantities defined relative to the intermediate configuration κ_1.

Downloaded 04 May 2010 to 171.66.16.26. Redistribution subject to ASME license or copyright; see http://www.asme.org/terms/Terms_Use.cfm

4 Linearized Theory of Thermoelasticity

In the previous sections we indicated how multiplicative decompositions of the deformation gradient can be achieved in the context of the general theory of thermoelasticity. In this section we develop the linear version of the theory and recover the familiar results of linear thermoelasticity using a procedure similar to that of Carlson (1972). Linearization is performed about the reference configuration by requiring that both $\overline{\vartheta} \equiv \vartheta - \vartheta_0$, where ϑ_0 represents the temperature in the reference configuration, and $\mathbf{u} \equiv \mathbf{x} - \mathbf{X}$ be of $O(\epsilon)$, where ϵ is some appropriate measure of smallness. Moreover, we assume that the time and space derivatives of $\overline{\vartheta}$ and $\mathbf{u}$ are of $O(\epsilon)$ and the deformation gradient in $\overline{\kappa}$ can be written as $\mathbf{F}_\vartheta = \mathbf{I} + O(\epsilon)$. The last assumption applies to the intermediate configurations κ_1 and κ_2 as well. Then, (6) implies that

$$\mathbf{e} = \mathbf{e}_\vartheta + \mathbf{e}_e. \tag{39}$$

Here, we have used lowercase letters for linearized strain measures. Equation (39) represents an additive decomposition of the total strain in the linear theory.

In the linearized theory, the Helmholtz free energy in (16) is a quadratic function of its arguments and can be expressed as

$$\rho_0\psi = \rho_0\overline{\psi}(\mathbf{e}, \mathbf{e}_\vartheta, \overline{\vartheta}) = \tfrac{1}{2}\mathbf{C}\mathbf{e}\cdot\mathbf{e} + \tfrac{1}{2}h\overline{\vartheta}^2 + \mathbf{A}\mathbf{e}_\vartheta\cdot\mathbf{e} + \tfrac{1}{2}\mathbf{B}\mathbf{e}_\vartheta\cdot\mathbf{e}_\vartheta + \mathbf{d}\cdot\mathbf{e}\overline{\vartheta} + \mathbf{g}\cdot\mathbf{e}_\vartheta\overline{\vartheta}, \tag{40}$$

where $\mathbf{A}$, $\mathbf{B}$, and $\mathbf{C}$ are fourth-order tensors, $\mathbf{d}$ and $\mathbf{g}$ are second-order tensors and h is a scalar. Subsequent work will show that $\mathbf{C}$ is the isothermal elasticity tensor.

In order to determine the stress, denoted by $\boldsymbol{\sigma}$ in the linearized theory, $(19)_1$ and (40) are used to find

$$\boldsymbol{\sigma} = \rho_0\frac{\partial\overline{\psi}}{\partial\mathbf{e}} = \mathbf{C}\mathbf{e} + \mathbf{A}\mathbf{e}_\vartheta + \mathbf{d}\overline{\vartheta}. \tag{41}$$

The above expression can be used to determine $\mathbf{e}_\vartheta$ by recalling that the stress in the stress-free configuration satisfies (20), whose linear analog is

$$\boldsymbol{\sigma} = \overline{\boldsymbol{\sigma}}(\mathbf{e}_\vartheta, \mathbf{e}_\vartheta, \overline{\vartheta}) = 0. \tag{42}$$

Combining (41) and (42), we obtain

$$\mathbf{C}\mathbf{e}_\vartheta + \mathbf{A}\mathbf{e}_\vartheta + \mathbf{d}\overline{\vartheta} = 0. \tag{43}$$

The above equation can be solved for $\mathbf{e}_\vartheta$ to yield

$$\mathbf{e}_\vartheta = -(\mathbf{C} + \mathbf{A})^{-1}\mathbf{d}\overline{\vartheta} \equiv \boldsymbol{\alpha}\overline{\vartheta}, \tag{44}$$

where

$$\boldsymbol{\alpha} = -(\mathbf{C} + \mathbf{A})^{-1}\mathbf{d} \tag{45}$$

is the second-order tensor of thermal expansion.

Using (44), the expression for Helmholtz free energy in (40) can be rewritten as

$$\rho_0\psi = \tfrac{1}{2}\mathbf{C}\mathbf{e}\cdot\mathbf{e} + \tfrac{1}{2}h\overline{\vartheta}^2 + \mathbf{A}\boldsymbol{\alpha}\cdot\mathbf{e}\overline{\vartheta} + \tfrac{1}{2}\mathbf{B}\boldsymbol{\alpha}\cdot\boldsymbol{\alpha}\overline{\vartheta}^2 + \mathbf{d}\cdot\mathbf{e}\overline{\vartheta} + \mathbf{g}\cdot\boldsymbol{\alpha}\overline{\vartheta}^2 = \tfrac{1}{2}\mathbf{C}\mathbf{e}\cdot\mathbf{e} - \mathbf{C}\boldsymbol{\alpha}\cdot\mathbf{e}\overline{\vartheta} + (\tfrac{1}{2}h + \tfrac{1}{2}\mathbf{B}\boldsymbol{\alpha}\cdot\boldsymbol{\alpha} + \mathbf{g}\cdot\boldsymbol{\alpha})\overline{\vartheta}^2, \tag{46}$$

where (43) was used in the last equality. Expression (46) is rewritten as

$$\rho_0\psi = \frac{1}{2}\mathbf{C}\mathbf{e}\cdot\mathbf{e} - \frac{c}{2\vartheta_0}\overline{\vartheta}^2 - \mathbf{C}\boldsymbol{\alpha}\cdot\mathbf{e}\overline{\vartheta}, \tag{47}$$

where

$$c \equiv -\vartheta_0(h + \mathbf{B}\boldsymbol{\alpha}\cdot\boldsymbol{\alpha} + 2\mathbf{g}\cdot\boldsymbol{\alpha}) \tag{48}$$

represents the specific heat of the solid and $\mathbf{C}$ is the fourth-order isothermal elasticity tensor.

Similarly, the expressions for $\mathbf{e}_\vartheta$, given in (44), and the total strain, given in (39), can be used to rewrite the stress in (41) as

$$\boldsymbol{\sigma} = \mathbf{C}\mathbf{e}_e. \tag{49}$$

This expression indicates that the stress is determined completely by the elastic component of the strain.

The corresponding expression for entropy can be obtained by substituting (40) into $(19)_2$ to find

$$\rho_0\eta = \frac{c}{\vartheta_0}\overline{\vartheta} + \mathbf{C}\boldsymbol{\alpha}\cdot\mathbf{e}. \tag{50}$$

Having determined the thermomechanical fields of interest using $\overline{\psi}$, next we consider the alternate representation of the Helmholtz free energy $\hat{\psi}$, given in (33), and determine the analogs of the constitutive relations (36) and (37) in the linear theory.

We first note that by (5),

$$\mathbf{U}_\vartheta = (\mathbf{I} + 2\mathbf{e}_\vartheta)^{1/2} = \mathbf{I} + \mathbf{e}_\vartheta + O(\epsilon^2) = \mathbf{I} + \boldsymbol{\alpha}\overline{\vartheta} + O(\epsilon^2). \tag{51}$$

As a result, taking (28) and (34) into account, the distinction between $\mathbf{e}_e$ and $\overline{\mathbf{e}}_e$ disappears in the linear case. Then, substituting (39) into (47) we obtain

$$\rho_0\psi = \rho_0\hat{\psi}(\mathbf{e}_e, \mathbf{e}_\vartheta, \overline{\vartheta}) = \frac{1}{2}\mathbf{C}(\mathbf{e}_e + \mathbf{e}_\vartheta)\cdot(\mathbf{e}_e + \mathbf{e}_\vartheta) - \frac{c}{2\vartheta_0}\overline{\vartheta}^2 - \mathbf{C}\boldsymbol{\alpha}\cdot(\mathbf{e}_e + \mathbf{e}_\vartheta)\overline{\vartheta}. \tag{52}$$

Neglecting terms of order two in ϵ, (36) is written as

$$\boldsymbol{\sigma} = \rho_0\frac{\partial\hat{\psi}}{\partial\mathbf{e}_e} = \mathbf{C}\mathbf{e}_e, \tag{53}$$

where (44) and (52) have been used in the last equality.

Alternatively, $\hat{\psi}$ can be expressed as a quadratic function of its arguments $\mathbf{e}_e$, $\mathbf{e}_\vartheta$, and $\overline{\vartheta}$. Then, imposing the requirement that the intermediate configuration be stress-free results in an expression that is equaivalent to (52).

We now develop the constitutive relation for entropy. Linearization of (37) results in

$$\rho_0\eta = -\rho_0\frac{\partial\hat{\psi}}{\partial\overline{\vartheta}} - \rho_0\frac{\partial\hat{\psi}}{\partial\mathbf{e}_\vartheta}\cdot\boldsymbol{\alpha} + \boldsymbol{\sigma}\cdot\boldsymbol{\alpha}. \tag{54}$$

Using (52) in the above expression we find

$$\rho_0\eta = \left(\frac{c}{\vartheta_0} + \mathbf{C}\boldsymbol{\alpha}\cdot\boldsymbol{\alpha}\right)\overline{\vartheta} + \boldsymbol{\sigma}\cdot\boldsymbol{\alpha} = \left(\frac{c}{\vartheta_0} + \mathbf{C}\boldsymbol{\alpha}\cdot\boldsymbol{\alpha}\right)\overline{\vartheta} + \mathbf{C}(\mathbf{e} - \boldsymbol{\alpha}\overline{\vartheta})\cdot\boldsymbol{\alpha} = \frac{c}{\vartheta_0}\overline{\vartheta} + \mathbf{C}\boldsymbol{\alpha}\cdot\mathbf{e}. \tag{55}$$

The last equality is exactly the same as the one obtained in (50) and represents the entropy density function in the linear theory.

Finally, as an example of the application of the foregoing results, we consider an isotropic solid for which $\boldsymbol{\alpha} = \alpha\mathbf{I}$. Then,

Downloaded 04 May 2010 to 171.66.16.26. Redistribution subject to ASME license or copyright; see http://www.asme.org/terms/Terms_Use.cfm

using the expression for isothermal elasticity tensor $\mathbf{C}$, (44) and (49) yield

$$\boldsymbol{\sigma} = \lambda \mathbf{I}\ \mathrm{Tr}\ \mathbf{e} + 2\mu\mathbf{e} - \alpha(3\lambda + 2\mu)\mathbf{I}\bar{\vartheta}, \qquad (56)$$

where μ and λ are Lame's constants.

The above expression for stress is familiar from linear isotropic thermoelasticity (Boley and Weiner, 1985). Here, it was obtained as a result of linearizing the general theory of thermoelasticity which incorporates a multiplicative decomposition of the deformation gradient into thermal and elastic components.

References

Bammann, D. J., and Johnson, G. C., 1987, "On the Kinematics of Finite-Deformation Plasticity," *Acta Mechanica,* Vol. 70, pp. 1–13.

Boley, B., and Weiner, J. H., 1985, *Theory of Thermal Stresses,* Krieger, Malabar, FL.

Carlson, D. E., 1972, *Linear Thermoelasticity,* Handbuch der Physik, Vol. Vla/2, pp. 297–345.

Casey, J., and Naghdi, P. M., 1981, "A Remark on the Use of the Decomposition $\mathbf{F} = \mathbf{F}_e\mathbf{F}_p$ in Plasticity," ASME JOURNAL OF APPLIED MECHANICS, Vol. 47, pp. 672–675.

Casey, J., and Naghdi, P. M., 1983, "On the Use of Invariance Requirements for Intermediate Configurations Associated With the Polar Decomposition of the Deformation Gradient," *Quarterly of Applied Math.,* pp. 339–342.

Coleman, B. D., and Noll, W., 1963, "The Thermodynamics of Elastic Materials with Heat Conduction and Viscosity," *Archive for Rational Mechanics and Analysis,* Vol. 13, No. 3, pp. 167–178.

Green, A. E., and Naghdi, P. M., 1977, "On Thermodynamics and the Nature of the Second Law," *Proceedings of the Royal Society of London,* Vol. A357, pp. 253–270.

Lee, E. H., 1969, "Elastic-Plastic Deformation at Finite Strains," ASME JOURNAL OF APPLIED MECHANICS, Vol. 36, pp. 1–8.

Downloaded 04 May 2010 to 171.66.16.26. Redistribution subject to ASME license or copyright; see http://www.asme.org/terms/Terms_Use.cfm

An Inverse Problem for Determination of Transient Surface Temperature From Piezoelectric Sensor Measurement

Fumihiro Ashida
Department of Electronics and Control Engineering
Tsuyama National College of Technology, Tsuyama, Okayama 708, Japan

T. R. Tauchert
Department of Mechanical Engineering, University of Kentucky, Lexington, KY 40506-0046
Mem. ASME

The time-varying ambient temperature on the face of a piezoelectric disk is inferred from a knowledge of the thermally induced electric potential difference across the disk thickness. The temperature-sensing disk has a circular planform, possesses hexagonal material symmetry properties, and is constrained by a rigid, thermally insulated, electrically charge-free ring. A potential function approach, together with Laplace transforms, is employed to solve the inverse problem for a particular form of electric potential difference. Also presented is a finite difference formulation which does not require specification of an analytical form for the potential difference. Numerical results are given for the predicted transient ambient temperatures corresponding to various combinations of disk thickness-to-radius ratios and surface heat transfer coefficients. Through-thickness distributions of temperature, stresses, and electric field intensities are shown, and a comparison of the exact and finite difference results is provided.

Introduction

Recent interest in piezoelectric materials stems from their potential use in intelligent structural systems. The coupling that exists between the thermal/elastic/electric fields in piezoelectric materials provides a mechanism for sensing thermomechanical disturbances from measurements of induced electric potentials, and for altering structural responses via applied electric fields. Fundamental studies dealing with nonisothermal behaviors of piezoelectric media include the works of Tiersten (1971), who derived nonlinear equations of thermoelectroelasticity, and Chandrasekharaiah (1988), who developed a generalized linear piezothermoelastic formulation. Investigations that consider piezoelectric elements as deformation sensors and/or actuators for structures operating in thermal environments include the recent works of Jonnalagadda et al. (1993), Rao and Sunar (1993), Tzou and Ye (1994), Shen and Weng (1995), Lee and Saravanos (1996), Reddy (1996) and Xu and Noor (1996), among others.

The concept of utilizing a piezoelectric element as a temperature sensor was explored in a recent investigation by the present authors (1997). An inverse problem was solved to predict the axisymmetric temperature distribution on the surface of a circular disk based on measurements of the electric potential distributions on the faces of the disk. Whereas this earlier analysis was restricted to stationary temperature fields, the present study treats transient conditions.

The circular disk considered here is initially at zero temperature, has a thermally insulated cylindrical boundary, and is subject to linear heat transfer on its plane surfaces. One face is exposed to zero ambient temperature, while the opposite face is subject to the unknown uniform ambient temperature. Under these conditions, heat flows in the thickness direction only.

For the elastic and electric fields, the faces of the disk are considered to be free of both traction and electric charge, while the cylindrical edge is constrained against radial deformation, and is free of transverse traction and electric charge.

The objective of the analysis is to determine the transient ambient temperature on the top surface of the disk from a knowledge of the induced electric potential difference across the disk thickness. This *inverse* problem is solved using a potential function approach similar to that employed by the authors for the solution of *direct* piezoelectric problems (1998), together with Laplace transforms. Inversion of the transform for the unknown ambient temperature requires specification of a particular form for the potential difference. In addition to the exact solution, a finite difference scheme which does not require specification of a particular analytical form for the potential difference is developed.

Governing Equations

We consider the axisymmetric response of a piezothermoelastic solid possessing hexagonal material symmetry of class 6 mm. Constitutive equations for the stresses σ_{ij}, expressed in cylindrical coordinates, are

$$\sigma_{rr} = c_{11}\epsilon_{rr} + c_{12}\epsilon_{\theta\theta} + c_{13}\epsilon_{zz} - e_1E_z - \beta_1 T$$

$$\sigma_{\theta\theta} = c_{12}\epsilon_{rr} + c_{11}\epsilon_{\theta\theta} + c_{13}\epsilon_{zz} - e_1E_z - \beta_1 T$$

$$\sigma_{zz} = c_{13}\epsilon_{rr} + c_{13}\epsilon_{\theta\theta} + c_{33}\epsilon_{zz} - e_3E_z - \beta_3 T$$

$$\sigma_{zr} = c_{44}\epsilon_{zr} - e_4E_r \qquad (1)$$

where ϵ_{ij} are the strain components, E_i are the electric field intensities, T denotes the temperature rise, c_{ij} are elastic stiffnesses, e_i

Contributed by the Applied Mechanics Division of THE AMERICAN SOCIETY OF MECHANICAL ENGINEERS for publication in the ASME JOURNAL OF APPLIED MECHANICS.

Discussion on this paper should be addressed to the Technical Editor, Professor Lewis T. Wheeler, Department of Mechanical Engineering, University of Houston, Houston, TX 77204-4792, and will be accepted until four months after final publication of the paper itself in the ASME JOURNAL OF APPLIED MECHANICS.

Manuscript received by the ASME Applied Mechanics Division, Feb. 20, 1997; final revision, Aug. 18, 1997. Associate Technical Editor: J. N. Reddy.

 Copyright © 1998 by ASME

Downloaded 04 May 2010 to 171.66.16.26. Redistribution subject to ASME license or copyright; see http://www.asme.org/terms/Terms_Use.cfm

are piezoelectric constants, and β_i are stress-temperature coefficients. The strains are related to the displacements u_i by

$$\epsilon_{rr} = u_{r,r}, \quad \epsilon_{\theta\theta} = \frac{1}{r} u_r, \quad \epsilon_{zz} = u_{z,z}, \quad \epsilon_{zr} = u_{z,r} + u_{r,z}. \quad (2)$$

Constitutive equations for the electric field are

$$D_r = e_4 \epsilon_{zr} + \eta_1 E_r,$$

$$D_z = e_1 \epsilon_{rr} + e_1 \epsilon_{\theta\theta} + e_3 \epsilon_{zz} + \eta_3 E_z + p_3 T \quad (3)$$

where D_i are the electric displacement components, η_i are dielectric permittivities, and p_3 is the pyroelectric constant. Although the properties of piezoelectric materials depend, in general, upon the magnitude of the temperature, for simplicity it is assumed here that the changes in temperature are sufficiently small that all properties are temperature independent.

The temperature T is governed by Fourier's heat conduction equation

$$\lambda_1 \left(T_{,rr} + \frac{1}{r} T_{,r} \right) + \lambda_3 T_{,zz} = c\rho T_{,t} \quad (4)$$

in which λ_i are coefficients of thermal conductivity, c is specific heat, and ρ denotes density.

The equations of equilibrium are

$$\sigma_{rr,r} + \sigma_{rz,z} + \frac{1}{r} (\sigma_{rr} - \sigma_{\theta\theta}) = 0,$$

$$\sigma_{zr,r} + \sigma_{zz,z} + \frac{1}{r} \sigma_{zr} = 0 \quad (5)$$

and the equation of electrostatics is

$$D_{r,r} + D_{z,z} + \frac{1}{r} D_r = 0. \quad (6)$$

Problem Statement

The circular disk considered in this study (Fig. 1) is initially at zero temperature, has a thermally insulated cylindrical boundary ($r = a$), and is subject to linear heat transfer on its plane surfaces. Surface $z = -b$ is exposed to zero ambient temperature with a relative heat transfer coefficient h_1 (ratio of heat convection coefficient and thermal conductivity coefficient λ_3), while face $z = +b$ is subject to uniform ambient temperature $\Theta(t)$ with heat transfer coefficient h_2; that is,

$$T_{,z} - h_1 T = 0 \quad \text{on} \quad z = -b \quad (7)$$

$$T_{,z} + h_2 T = h_2 \Theta(t) \quad \text{on} \quad z = b. \quad (8)$$

Under these conditions, heat flow occurs in the z-direction only, resulting in the one-dimensional temperature distribution $T(z, t)$ governed by

$$\kappa T_{,zz} = T_{,t} \quad (9)$$

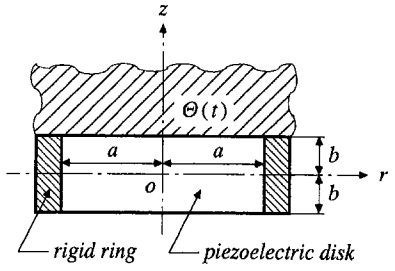


Fig. 1 Piezoelectric sensor

in which $\kappa \equiv \lambda_3 / c\rho$ denotes thermal diffusivity.

For the elastic and electric fields, the faces of the disk are considered to be free of both traction and electric charge, while the cylindrical edge is constrained against radial deformation (e.g., by a rigid ring), and is free of transverse traction and electric charge, i.e.,

$$\sigma_{rz} = \sigma_{zz} = D_z = 0 \quad \text{on} \quad z = \pm b \quad (10)$$

$$u_r = \sigma_{rz} = D_r = 0 \quad \text{on} \quad r = a. \quad (11)$$

The objective of the analysis is to determine the transient ambient temperature $\Theta(t)$ on the top surface of the disk from a knowledge of the induced electric potential difference across the disk thickness.

Solution Procedure

Following a procedure similar to that introduced earlier by the authors (1998), we express the displacement and electric field intensities induced by the temperature field $T(z, t)$ as

$$u_r = 0, \quad u_z = \Psi_{,z} \quad (12)$$

$$E_r = 0, \quad E_z = -\Phi_{,z} \quad (13)$$

where Ψ and Φ are potential functions which satisfy the relations

$$\Psi_{,zz} = \gamma_1 T(z, t) \quad (14)$$

$$\Phi_{,z} = \gamma_2 T(z, t) \quad (15)$$

in which

$$\gamma_1 = \frac{\beta_3 \eta_3 - e_3 p_3}{c_{33}\eta_3 + e_3^2}, \quad \gamma_2 = \frac{c_{33} p_3 + \beta_3 e_3}{c_{33}\eta_3 + e_3^2}. \quad (16)$$

Substitution of Eqs. (12)–(15) into (1)–(3) leads to

$$\sigma_{rr} = \sigma_{\theta\theta} = \gamma_3 T, \quad \sigma_{rz} = \sigma_{zz} = D_r = D_z = 0 \quad (17)$$

where

$$\gamma_3 = c_{13}\gamma_1 + e_1 \gamma_2 - \beta_1. \quad (18)$$

Note that the equations of equilibrium (5) and electrostatics (6), plus boundary conditions (10) and (11), are satisfied by the relations given above.

Integration of Eq. (15) gives

$$\Phi = \int \gamma_2 T(z, t) dz + C \quad (19)$$

so that the difference in electric potential across the disk thickness, say $V(t)$, becomes

$$V(t) = \left[\int \gamma_2 T(z, t) dz \right]_{z=b} - \left[\int \gamma_2 T(z, t) dz \right]_{z=-b}. \quad (20)$$

Next, we apply the Laplace transform to the heat conduction Eq. (9) and the thermal boundary condition (7), to obtain

$$\kappa T^*_{,zz} = pT^* \quad (21)$$

Downloaded 04 May 2010 to 171.66.16.26. Redistribution subject to ASME license or copyright; see http://www.asme.org/terms/Terms_Use.cfm

and

$$T_z^* - h_1 T^* = 0 \quad \text{on} \quad z = -b. \tag{22}$$

The general solution to Eq. (21) is given by

$$T^* = A \cosh\left(\sqrt{\frac{p}{\kappa}}\, z\right) + B \sinh\left(\sqrt{\frac{p}{\kappa}}\, z\right). \tag{23}$$

Condition (22) requires that constant B be related to A by the expression

$$B = \frac{\sqrt{\frac{p}{\kappa}} \sinh\left(\sqrt{\frac{p}{\kappa}}\, b\right) + h_1 \cosh\left(\sqrt{\frac{p}{\kappa}}\, b\right)}{\sqrt{\frac{p}{\kappa}} \cosh\left(\sqrt{\frac{p}{\kappa}}\, b\right) + h_1 \sinh\left(\sqrt{\frac{p}{\kappa}}\, b\right)} A. \tag{24}$$

We now apply the Laplace transform to Eq. (20), yielding

$$V^* = \left[\int \gamma_2 T^* dz\right]_{z=b} - \left[\int \gamma_2 T^* dz\right]_{z=-b}. \tag{25}$$

By substituting expression (23) into (25) and performing the integration, it is found that

$$A = \frac{\sqrt{\frac{p}{\kappa}}\, V^*}{2\gamma_2 \sinh\left(\sqrt{\frac{p}{\kappa}}\, b\right)}. \tag{26}$$

Introducing expressions (24) and (26) into (23) then gives

$$T^* = \frac{V^* \sqrt{\frac{p}{\kappa}}}{2\gamma_2 \sinh\left(\sqrt{\frac{p}{\kappa}}\, b\right)} \left\{ \cosh\left(\sqrt{\frac{p}{\kappa}}\, z\right) + \frac{\left[\sqrt{\frac{p}{\kappa}} \sinh\left(\sqrt{\frac{p}{\kappa}}\, b\right) + h_1 \cosh\left(\sqrt{\frac{p}{\kappa}}\, b\right)\right] \sinh\left(\sqrt{\frac{p}{\kappa}}\, z\right)}{\sqrt{\frac{p}{\kappa}} \cosh\left(\sqrt{\frac{p}{\kappa}}\, b\right) + h_1 \sinh\left(\sqrt{\frac{p}{\kappa}}\, b\right)} \right\}. \tag{27}$$

Inversion of T^* using the convolution theorem is not possible, since T^*/V^* does not necessarily converge when $p \to \infty$. Therefore, we shall assume a particular form for the function $V(t)$ prior to calculating the inverse Laplace transform.

Consider, for example, a potential difference given by

$$V = V_0(1 - e^{-\delta\kappa t/a^2}) \tag{28}$$

where δ is an arbitrary coefficient. The Laplace transform of V is

$$V^* = \frac{V_0 \delta \frac{\kappa}{a^2}}{p\left(p + \delta \frac{\kappa}{a^2}\right)}. \tag{29}$$

Substitution of Eq. (29) into (27) gives

$$T^* = \frac{V_0 \delta \frac{\kappa}{a^2}}{2\gamma_2 p\left(p + \delta \frac{\kappa}{a^2}\right) \frac{\sinh\left(\sqrt{\frac{p}{\kappa}}\, b\right) b}{\sqrt{\frac{p}{\kappa}}\, b}} \left\{ \cosh\left(\sqrt{\frac{p}{\kappa}}\, z\right) + \frac{\sqrt{\frac{p}{\kappa}} \sinh\left(\sqrt{\frac{p}{\kappa}}\, b\right) + h_1 \cosh\left(\sqrt{\frac{p}{\kappa}}\, b\right)}{\cosh\left(\sqrt{\frac{p}{\kappa}}\, b\right) + h_1 \frac{\sinh\left(\sqrt{\frac{p}{\kappa}}\, b\right) b}{\sqrt{\frac{p}{\kappa}}\, b}} \times \frac{z \sinh\left(\sqrt{\frac{p}{\kappa}}\, z\right)}{\sqrt{\frac{p}{\kappa}}\, z} \right\} \tag{30}$$

Inversion of T^* is performed using the method of residues. The residues of $e^{pt}T^*(p)$ at the poles of T^* are as follows:

(i) $p = 0$:

$$\text{Residue} = \lim_{p \to 0} (p - 0) e^{pt} T^*(p) = \frac{V_0}{2\gamma_2 b}\left(1 + \frac{h_1 z}{1 + h_1 b}\right). \tag{31}$$

(ii) $p = -\delta\kappa/a^2$:

$$\text{Residue} = -\frac{V_0 \sqrt{\delta} e^{-\delta\kappa t/a^2}}{2\gamma_2 a \sin\left(\sqrt{\delta}\, \frac{b}{a}\right)} \left\{ \cos\left(\frac{\sqrt{\delta} z}{a}\right) + \frac{-\sqrt{\delta} \sin\left(\sqrt{\delta}\, \frac{b}{a}\right) + h_1 a \cos\left(\sqrt{\delta}\, \frac{b}{a}\right)}{\sqrt{\delta} \cos\left(\sqrt{\delta}\, \frac{b}{a}\right) + h_1 a \sin\left(\sqrt{\delta}\, \frac{b}{a}\right)} \sin\left(\frac{\sqrt{\delta} z}{a}\right) \right\}. \tag{32}$$

(iii) $p_n = -\beta_n^2 \kappa$ where β_n are roots of $\sin(\beta b) = 0$ (poles corresponding to $\sinh(\sqrt{p/\kappa}\, b) = 0$):

$$\text{Residue} = \frac{V_0 \delta e^{-\kappa \beta_n^2 t}}{\gamma_2 b(\delta - \beta_n^2 a^2) \cos(\beta_n b)} \times \left\{ \cos(\beta_n z) + \frac{h_1}{\beta_n} \sin(\beta_n z) \right\}. \tag{33}$$

Downloaded 04 May 2010 to 171.66.16.26. Redistribution subject to ASME license or copyright; see http://www.asme.org/terms/Terms_Use.cfm

(iv) $p_m = -\eta_m^2\kappa$ where η_m are roots of $\eta \cos(\eta b) + h_1 \sin(\eta b) = 0$ (poles corresponding to $\sqrt{p/\kappa}\cosh(\sqrt{p/\kappa}b) + h_1 \sinh(\sqrt{p/\kappa}b) = 0$):

Residue

$$= \frac{V_0\delta e^{-\kappa\eta_m^2 t}[-\eta_m \sin(\eta_m b) + h_1 \cos(\eta_m b)] \sin(\eta_m z)}{\gamma_2(\delta - \eta_m^2 a^2) \sin(\eta_m b)[(1 + h_1 b)\cos(\eta_m b) - \eta_m b \sin(\eta_m b)]}. \quad (34)$$

The temperature $T(z, t)$, found by summing the residues given in Eqs. (31)–(34), now can be expressed as

$$T(z,t) = T_0 + T_1\frac{z}{b} + \left[T_3 \cos\left(\frac{\sqrt{\delta}z}{a}\right) + T_4 \sin\left(\frac{\sqrt{\delta}z}{a}\right)\right]e^{-\delta\kappa t/a^2} + \sum_{n=1}^{\infty}[T_5 \cos(\beta_n z) + T_6 \sin(\beta_n z)]e^{-\kappa\beta_n^2 t} + \sum_{m=1}^{\infty} T_7 \sin(\eta_m z)e^{-\kappa\eta_m^2 t} \quad (35)$$

in which

$$T_0 = \frac{V_0}{2\gamma_2 b}, \quad T_1 = \frac{V_0 h_1}{2\gamma_2(1 + h_1 b)}, \quad T_3 = \frac{-V_0\sqrt{\delta}}{2\gamma_2 a \sin\left(\sqrt{\delta}\frac{b}{a}\right)}$$

$$T_4 = \frac{V_0\sqrt{\delta}\left[\sqrt{\delta}\sin\left(\sqrt{\delta}\frac{b}{a}\right) - h_1 a \cos\left(\sqrt{\delta}\frac{b}{a}\right)\right]}{2\gamma_2 a \sin\left(\sqrt{\delta}\frac{b}{a}\right)\left[\sqrt{\delta}\cos\left(\sqrt{\delta}\frac{b}{a}\right) + h_1 a \sin\left(\sqrt{\delta}\frac{b}{a}\right)\right]}$$

$$T_5 = \frac{V_0\delta}{\gamma_2 b(\delta - \beta_n^2 a^2)\cos(\beta_n b)},$$

$$T_6 = \frac{V_0\delta h_1}{\gamma_2 b(\delta - \beta_n^2 a^2)\beta_n \cos(\beta_n b)}$$

$$T_7 = \frac{V_0\delta[-\eta_m \sin(\eta_m b) + h_1 \cos(\eta_m b)]}{\gamma_2(\delta - \eta_m^2 a^2)[-\eta_m b \sin(\eta_m b) + (1 + h_1 b)\cos(\eta_m b)]\sin(\eta_m b)} \quad (36)$$

and where

$$\sin(\beta_n b) = 0, \quad \eta_m \cos(\eta_m b) + h_1 \sin(\eta_m b) = 0. \quad (37)$$

Finally, substituting Eq. (35) into boundary condition (8) and solving for $\Theta(t)$ yields the desired expression for the ambient temperature, namely

$$\Theta(t) = T_0 + T_1\left(1 + \frac{1}{h_2 b}\right) + T_3\left[\cos\left(\sqrt{\delta}\frac{b}{a}\right) - \frac{\sqrt{\delta}}{h_2 a}\sin\left(\sqrt{\delta}\frac{b}{a}\right)\right]e^{-\delta\kappa t/a^2} + T_4\left[\sin\left(\sqrt{\delta}\frac{b}{a}\right) + \frac{\sqrt{\delta}}{h_2 a}\cos\left(\sqrt{\delta}\frac{b}{a}\right)\right]e^{-\delta\kappa t/a^2} + \sum_{n=1}^{\infty}\left[T_5 + T_6\frac{\beta_n}{h_2}\right]\cos(\beta_n b)e^{-\kappa\beta_n^2 t} + \sum_{m=1}^{\infty} T_7\left(\frac{h_2 - h_1}{h_2}\right)\sin(\eta_m b)e^{-\kappa\eta_m^2 t}. \quad (38)$$

Unknown ambient temperatures corresponding to electric potential differences described by expressions other than Eq. (28) can be obtained similarly.

Finite Difference Approximation

We next introduce a finite difference formulation which leads to a solution for $\Theta(t)$ without specification of a particular form for the electric potential difference $V(t)$. In this case the heat conduction Eq. (9) is written in terms of time increments $\Delta t_j = t_j - t_{j-1}$ as

$$\kappa T_{j,zz} - \frac{T_j}{\Delta t_j} = -\frac{T_{j-1}}{\Delta t_j} \quad (39)$$

in which T_j is the temperature at time t_j.

The general solution of Eq. (39) may be expressed as

$$T_j = \sum_{k=1}^{j} w_{jk} T_{kc} \quad (40)$$

where

$$w_{jk} = \delta_{jk} + (1 - \delta_{jk})\frac{\Delta t_k w_{(j-1)k}}{\Delta t_k - \Delta t_j} \quad (41)$$

in which δ_{jk} is the Kronecker delta, and the temperature coefficients T_{kc} are governed by the equation

$$\kappa T_{jc,zz} - \frac{T_{jc}}{\Delta t_j} = 0. \quad (42)$$

Thermal boundary conditions (7) and (8) then require that

$$T_{jc,z} - h_1 T_{jc} = 0 \quad \text{on} \quad z = -b \quad (43)$$

$$T_{jc,z} + h_2 T_{jc} = h_2 H_j \quad \text{on} \quad z = b \quad (44)$$

where

$$H_1 = \Theta_1, \quad H_j = \Theta_j - \sum_{k=1}^{j-1} w_{jk} H_k \quad (j \geq 2). \quad (45)$$

The general solution of Eq. (42) is

$$T_{jc} = A_j \cosh(z/\sqrt{\kappa\Delta t_j}) + B_j \sinh(z/\sqrt{\kappa\Delta t_j}). \quad (46)$$

Substitution of expression (46) into boundary condition (43) leads to the result

$$A_j\left[\frac{1}{\sqrt{\kappa\Delta t_j}}\sinh(b/\sqrt{\kappa\Delta t_j}) + h_1 \cosh(b/\sqrt{\kappa\Delta t_j})\right] - B_j\left[\frac{1}{\sqrt{\kappa\Delta t_j}}\cosh(b/\sqrt{\kappa\Delta t_j}) + h_1 \sinh(b/\sqrt{\kappa\Delta t_j})\right] = 0. \quad (47)$$

The electric potential at time t_j is, according to Eq. (19),

$$\Phi_j = \gamma_2 \int T_j dz + C = \gamma_2 \sum_{k=1}^{j} w_{jk}\Phi_{kc} + C \quad (48)$$

with

$$\Phi_{kc} = \sqrt{\kappa\Delta t_k}[A_k \sinh(z/\sqrt{\kappa\Delta t_k}) + B_k \cosh(z/\sqrt{\kappa\Delta t_k})]. \quad (49)$$

Downloaded 04 May 2010 to 171.66.16.26. Redistribution subject to ASME license or copyright; see http://www.asme.org/terms/Terms_Use.cfm

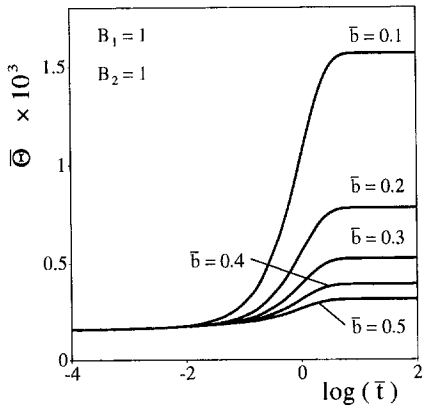


Fig. 2 Ambient temperature histories corresponding to various depth-to-radius ratios $\bar{b}$

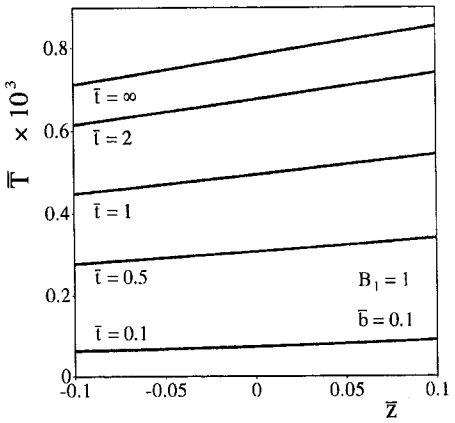


Fig. 4 Temperature distributions at selected times $\bar{t}$

The difference in electric potential V_j at time t_j is then given by

$$V_j = [\Phi_j]_{z=b} - [\Phi_j]_{z=-b} = \gamma_2 \sum_{k=1}^{j} w_{jk}\{[\Phi_{kc}]_{z=b} - [\Phi_{kc}]_{z=-b}\} \quad (50)$$

which can be written in the alternate form

$$\gamma_2\{[\Phi_{jc}]_{z=b} - [\Phi_{jc}]_{z=-b}\} = P_j \quad (51)$$

where

$$P_1 = V_1, \quad P_j = V_j - \sum_{k=1}^{j-1} w_{jk}P_k \quad (j \geq 2). \quad (52)$$

Substituting Eq. (49) into (51) and solving for coefficient A_j give

$$A_j = \frac{P_j}{2\gamma_2\sqrt{\kappa\Delta t_j}\,\sinh\,(b/\sqrt{\kappa\Delta t_j})}. \quad (53)$$

Equation (47) then yields

$$B_j = \frac{\sinh\,(b/\sqrt{\kappa\Delta t_j}) + h_1\sqrt{\kappa\Delta t_j}\,\cosh\,(b/\sqrt{\kappa\Delta t_j})}{\cosh\,(b/\sqrt{\kappa\Delta t_j}) + h_1\sqrt{\kappa\Delta t_j}\,\sinh\,(b/\sqrt{\kappa\Delta t_j})} \times \frac{P_j}{2\gamma_2\sqrt{\kappa\Delta t_j}\,\sinh\,(b/\sqrt{\kappa\Delta t_j})}. \quad (54)$$

The temperature coefficient T_{jc}, found by substituting Eqs. (53) and (54) into (46), becomes

$$T_{jc} = \frac{P_j}{2\gamma_2\sqrt{\kappa\Delta t_j}\,\sinh\,(b/\sqrt{\kappa\Delta t_j})}\left[\cosh\,(z/\sqrt{\kappa\Delta t_j}) + \frac{\sinh\,(b/\sqrt{\kappa\Delta t_j}) + h_1\sqrt{\kappa\Delta t_j}\,\cosh\,(b/\sqrt{\kappa\Delta t_j})}{\cosh\,(b/\sqrt{\kappa\Delta t_j}) + h_1\sqrt{\kappa\Delta t_j}\,\sinh\,(b/\sqrt{\kappa\Delta t_j})} \times \sinh\,(z/\sqrt{\kappa\Delta t_j})\right]. \quad (55)$$

Application of boundary condition (44) then leads to

$$H_j = \frac{P_j}{2\gamma_2 h_2\kappa\Delta t_j}\left[1 + h_2\sqrt{\kappa\Delta t_j}\,\coth\,(b/\sqrt{\kappa\Delta t_j}) + \frac{\tanh\,(b/\sqrt{\kappa\Delta t_j}) + h_1\sqrt{\kappa\Delta t_j}}{1 + h_1\sqrt{\kappa\Delta t_j}\,\tanh\,(b/\sqrt{\kappa\Delta t_j})} \times \{\coth\,(b/\sqrt{\kappa\Delta t_j}) + h_2\sqrt{\kappa\Delta t_j}\}\right]. \quad (56)$$

From Eq. (45) it follows that the ambient temperature Θ_j at time t_j is given by

$$\Theta_1 = H_1, \quad \Theta_j = H_j + \sum_{k=1}^{j-1} w_{jk}H_k \quad (j \geq 2). \quad (57)$$

Numerical Example

For illustrative purposes, the disk material is considered to be cadmium selenide, with the following properties (Berlincourt, et al., 1963):

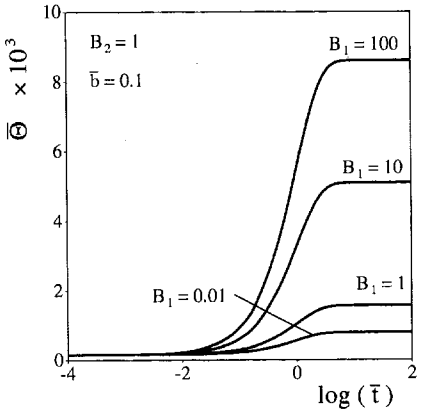


Fig. 3 Ambient temperature histories corresponding to various values of Biot number B_1

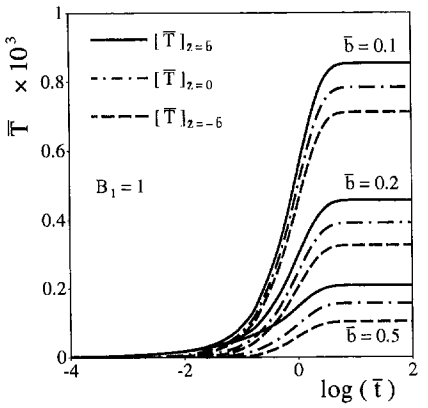


Fig. 5 Temperature histories at top, middle, and bottom of disk, corresponding to various depth-to-radius ratios $\bar{b}$

Downloaded 04 May 2010 to 171.66.16.26. Redistribution subject to ASME license or copyright; see http://www.asme.org/terms/Terms_Use.cfm

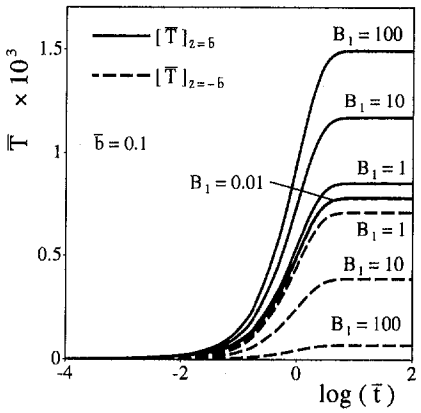


Fig. 6 Temperature histories at disk surfaces, corresponding to various values of Biot number B_1

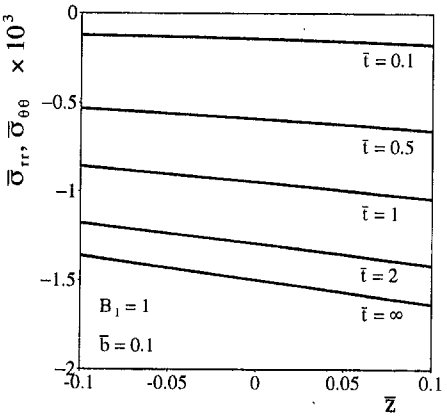


Fig. 8 Stress distributions at selected times $\bar{t}$

$$c_{13} = 39.3 \times 10^9\ \mathrm{Nm^{-2}},\quad c_{33} = 83.6 \times 10^9\ \mathrm{Nm^{-2}}$$

$$\beta_1 = 0.621 \times 10^6\ \mathrm{NK^{-1}m^{-2}},\quad \beta_3 = 0.551 \times 10^6\ \mathrm{NK^{-1}m^{-2}}$$

$$e_1 = -0.160\ \mathrm{Cm^{-2}},\quad e_3 = 0.347\ \mathrm{Cm^{-2}}$$

$$\eta_3 = 90.3 \times 10^{-12}\ \mathrm{C^2N^{-1}m^{-2}},$$

$$p_3 = -2.94 \times 10^{-6}\ \mathrm{CK^{-1}m^{-2}}\quad Y_r = 42.8 \times 10^9\ \mathrm{Nm^{-2}},$$

$$\alpha_r = 4.4 \times 10^{-6}\ \mathrm{K^{-1}},\quad d_1 = -3.92 \times 10^{-12}\ \mathrm{CN^{-1}} \qquad (58)$$

where Y_r is Young's modulus, α_r is the coefficient of linear thermal expansion, and d_1 is the piezoelectric coefficient. Since the values of the coefficients of heat conduction for cadmium selenide could not be found in the literature, the value $\lambda^2 = \lambda_z/\lambda_r = 1.5$ is assumed.

The following dimensionless quantities are introduced for convenience in presentation of numerical results:

$$\bar{b} = \frac{b}{a},\quad \bar{z} = \frac{z}{a},\quad \bar{t} = \frac{\kappa t}{a^2},\quad B_1 = ah_1,\quad B_2 = ah_2$$

$$\bar{\Theta} = \frac{a\alpha_r\Theta}{|d_1|V_0},\quad \bar{T} = \frac{a\alpha_r T}{|d_1|V_0},\quad \bar{u}_i = \frac{u_i}{|d_1|V_0},$$

$$\bar{\sigma}_{ij} = \frac{a\sigma_{ij}}{|d_1|Y_rV_0},\quad \bar{E}_z = \frac{aE_z}{V_0}. \qquad (59)$$

Response quantities were calculated for a disk subject to a potential difference described by Eq. (28) with $\delta = 1$, i.e.,

$$V = V_0(1 - e^{-\kappa t/a^2}). \qquad (60)$$

Calculations were performed by retaining the first 50 terms in each of the infinite series.

Figure 2 shows the time variation of the nondimensionalized ambient temperature $\bar{\Theta}(\bar{t})$ for disks with Biot numbers $B_1 = B_2 = 1$ and various depth-to-radius ratios $\bar{b} = b/a$. The effect of Biot number B_1 (bottom face) on the ambient temperature $\bar{\Theta}(\bar{t})$ (top face) for the case $B_2 = 1$ and $\bar{b} = 0.1$ is illustrated in Fig. 3. Note that a thin disk (small $\bar{b}$) with a large relative heat transfer coefficient (large B_1) corresponds to a large ambient temperature $\bar{\Theta}(\bar{t})$, and vice versa.

Figure 4 depicts the variation of temperature $\bar{T}$ with depth at selected times, when $B_1 = 1$ and $\bar{b} = 0.1$. Time histories of $\bar{T}$ at the top, middle, and bottom of the disk, associated with different combinations of B_1 and $\bar{b}$ are shown in Figs. 5 and 6.

Time variation of axial displacements $[\bar{u}_z]_{\bar{z}=\bar{b}} - [\bar{u}_z]_{\bar{z}=-\bar{b}}$, and through-thickness distributions of stresses $\bar{\sigma}_{rr}$ and $\bar{\sigma}_{\theta\theta}$ and electric field intensity $\bar{E}_z$ for the case $B_1 = 1$ and $\bar{b} = 0.1$, are presented in Figs. 7–9. The maximum (absolute) value of each response quantity is seen to occur when steady-state conditions ($t \to \infty$) have been reached.

A comparison of the exact solution (Eq. (38)) and the finite difference representation (Eq. (57)) for the inferred ambient temperature, with $B_1 = B_2 = 1$ and $\bar{b} = 0.1$, is shown in Table 1. The finite difference results were obtained using unequal, continuously increasing time increments $\Delta\bar{t}_j$. The table shows values of $\bar{\Theta}_j$ calculated using four different sets of time increments; time $\bar{t}_j = 100$ was reached in 36 time-steps for one set of increments (corresponding to $\bar{t}_j = 10^{[(j-1)/5]-5}$) and in 141 steps for another set (based on $\bar{t}_j = 10^{[(j-1)/20]-5}$). Each set of finite difference results is seen to be in excellent agreement

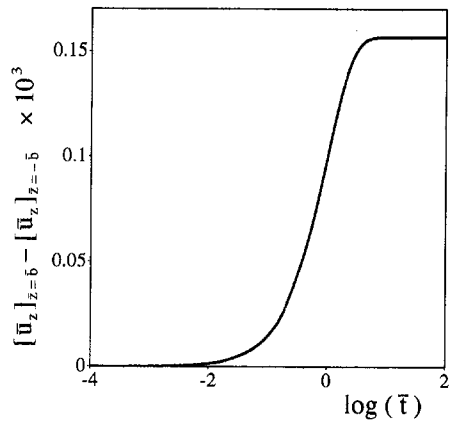


Fig. 7 Time variation of difference in surface displacements

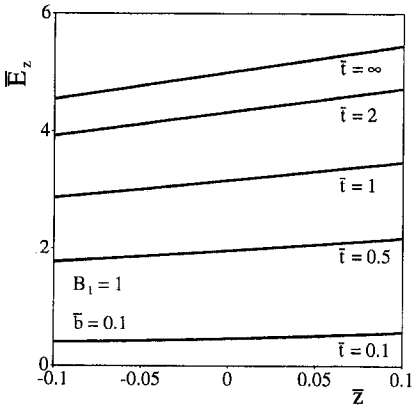


Fig. 9 Distributions of electric field intensity at selected times $\bar{t}$

Downloaded 04 May 2010 to 171.66.16.26. Redistribution subject to ASME license or copyright; see http://www.asme.org/terms/Terms_Use.cfm

Table 1 Inferred ambient temperature at selected times (Fourier numbers) $\bar{t}$

Fourier's Number	Exact Solution	Finite Difference Solution			
		$\bar{t}_j = 10^{\frac{j-1}{5}-5}$	$\bar{t}_j = 10^{\frac{j-1}{10}-5}$	$\bar{t}_j = 10^{\frac{j-1}{15}-5}$	$\bar{t}_j = 10^{\frac{j-1}{20}-5}$
10^{-5}	-157.2	-157.1	-157.1	-157.1	-157.1
10^{-4}	-158.3	-158.3	-158.3	-158.3	-158.3
10^{-3}	-162.0	-161.9	-162.0	-162.0	-162.0
10^{-2}	-175.8	-176.1	-176.0	-175.9	-175.9
10^{-1}	-295.4	-298.2	-297.0	-296.5	-296.2
10^{0}	-1049.4	-1061.9	-1056.0	-1053.9	-1052.8
10^{1}	-1565.9	-1566.0	-1565.9	-1565.9	-1565.9
10^{2}	-1566.0	-1566.0	-1566.0	-1566.0	-1566.0

with the exact solution, with the smaller set of increments yielding slightly more accurate results at intermediate times, where the time variation of temperature is greatest.

Conclusion

The results presented herein indicate that a time-varying ambient temperature can be determined from knowledge of the induced electric potential difference across a piezoelectric disk. It has been illustrated that an exact solution for the unknown temperature and the resulting stresses and electric field intensities can be found, providing the potential difference can be represented in analytical form. A finite difference formulation that does not require specification of an analytical form has been presented also. The results provide evidence that piezoelectric elements can be used effectively as temperature sensors for use in intelligent structural systems.

References

Ashida, F., and Tauchert, T. R., 1997, "Temperature determination for a contacting body based on an inverse piezothermoelastic problem," *International Journal of Solids and Structures,* Vol. 34, pp. 2549–2561.

Ashida, F., and Tauchert, T. R., 1998, "Transient response of a piezothermoelastic circular disk under axisymmetric heating," *Acta Mechanica,* Vol. 128, pp. 1–14.

Berlincourt, D., Jaffe, H., and Shiozawa, L. R., 1963, "Electroelastic properties of the sulfides, selenides, and tellurides of zinc and cadmium," *Physical Review,* Vol. 129, pp. 1009–1017.

Chandrasekharaiah, D. S., 1988, "A generalized linear thermoelasticity theory for piezoelectric media," *Acta Mechanica,* Vol. 71, pp. 39–49.

Jonnalagadda, K. D., Tauchert, T. R., and Blandford, G. E., 1993, "High-order displacement formulation for a piezothermoelastic laminate," *Mechanics of Electromagnetic Materials and Structures,* J. S. Lee, G. A. Maugin, and Y. Shindo, eds., ASME publication AMD-Vol. 161/MD-Vol. 42, ASME, New York, pp. 145–159.

Lee, H.-J., and Saravanos, D. A., 1996, "Coupled layerwise analysis of thermopiezoelectric composite beams," *AIAA Journal,* Vol. 34, pp. 1231–1237.

Rao, S. S., and Sunar, M., 1993, "Analysis of distributed thermopiezoelectric sensors and actuators in advanced intelligent structures," *AIAA Journal,* Vol. 31, pp. 1280–1286.

Reddy, J. N., 1996, "Refined theories and computational procedures for the modeling of smart composite structures," *Composite Science and Technology* (Proceedings of the First International Conference on Composite Science and Technology), S. Adali and V. E. Verijenko, eds., pp. 421–429.

Shen, Y. C., and Weng, C. I., 1995, "The deformation control of a laminated composite plate containing piezoelectric layers under thermal loading," *Journal of Thermal Stresses,* Vol. 18, pp. 449–464.

Tiersten, H. F., 1971, "On the nonlinear equations of thermoelectroelasticity," *International Journal of Engineering Science,* Vol. 9, pp. 587–604.

Tzou, H. S., and Ye, R., 1994, "Piezothermoelasticity and precision control of piezoelectric systems," *Journal of Vibration and Acoustics,* Vol. 116, pp. 489–495.

Xu, K., and Noor, A. K., 1996, "Three-dimensional solutions for coupled thermoelectroelastic response of multilayered cylindrical shells," *AIAA Journal,* Vol. 34, pp. 802–812.

Downloaded 04 May 2010 to 171.66.16.26. Redistribution subject to ASME license or copyright; see http://www.asme.org/terms/Terms_Use.cfm

Stress and Deformation Fields Around a Cylindrical Cavity Embedded in a Pressure-Sensitive Elastoplastic Medium

I. D. R. Bradford[1]
Schlumberger Cambridge Research,
High Cross,
Madingley Road,
Cambridge CB3 0EL
England

D. Durban
Faculty of Aerospace Engineering,
Technion-Israel Institute of Technology,
Haifa 32000, Israel
Mem. ASME

The problem of an internally pressurized cylindrical cavity under remote nonequibiaxial compression is examined within the framework of small strain theory. The cavity is embedded in a medium with a pressure-sensitive elastoplastic, strain-hardening and nonassociative response. The stress and deformation fields around the cavity are derived using a Drucker-Prager type deformation theory under the assumption of plane strain. The symmetry conditions allow the solution to be expanded as a Fourier cosine series in the circumferential direction. The Fourier coefficients are functions of the radial coordinate and are governed by a coupled system of ordinary differential equations. Numerical examples illustrate the evolution of the elastoplastic interface, together with the variation in both the stress concentration factor and the displacements at the cavity surface, due to increasing remote load.

1 Introduction

This paper analyses the stress and deformation fields around an internally pressurized cylindrical cavity, embedded in a pressure-sensitive elastoplastic medium, under remote nonequibiaxial compression. This problem is of considerable interest in the mechanics of geomaterials as it simulates the behavior of an oil well or a tunnel.

An oil well is internally pressurized by a liquid with suspended solids, which is known as a drilling fluid. This fluid transports waste material that has been generated during the drilling process to the surface. The internal pressure acts to support the borehole wall and can be controlled by modifying the fluid density. It is particularly important to minimize the fluid density in order to maximize the rate at which wells can be drilled. However, if the fluid density is too low then material adjacent to the borehole wall can deform plastically and can undergo high levels of deformation. This leads to the borehole wall contracting or the well collapsing and frequently results in drilling equipment becoming stuck (Last et al., 1995). Consequently, it is important to analyse the stress and deformation fields around wells in order to be able to select the most appropriate drilling fluid density.

Galin (1946) determined the stress and deformation fields around a cylindrical cavity embedded in an elastic-perfectly plastic Tresca material, under the assumption that the plastic region surrounds the cavity. In the case of remote nonequibiaxial loading, it was shown that the elastic-plastic interface is elliptical; its eccentricity is, however, curtailed by the requirement for statical determinancy (Hill, 1951). This restriction, together with the initial assumption, limits the deviation from equibiaxial remote loading for which this analysis applies.

Salençon (1966, 1969), under the same assumptions as Galin (1946), considered a cylindrical cavity embedded in an elastic-perfectly plastic Mohr-Coulomb solid and derived the stress field in the plastic region. Detournay and Fairhurst (1986, 1987) extended Salençon's (1966, 1969) analysis. They obtained the complete stress and deformation field around the cavity and showed, in the case of remote nonequibiaxial loading, that the elastic-plastic interface is approximately elliptical. The deviation from equibiaxial loading for which these analyses are valid is limited by the same restrictions that apply to Galin's (1946) study.

Huang (1972) used the J_2 deformation theory to derive the stress and deformation patterns around a cylindrical cavity, embedded in a medium obeying the Ramberg-Osgood (1943) response characteristic, under remote uniaxial tension or pure shear. No restrictions were placed on the plastic zone geometry, other than those which are implicit due to the use of the small-strain deformation theory. The symmetry conditions allow the solution to be expanded as a Fourier series in the circumferential direction. The Fourier coefficients are functions of the radial coordinate and are governed by a coupled set of ordinary differential equations. Wilner (1988) solved problems with spherical cavities, using a variational approach under remote nonequitriaxial tension.

In this paper, Huang's analysis is enhanced to account for pressure-sensitive elastoplasticity, strain-hardening and nonassociative response. The stress and deformation fields are determined around an internally pressurized cylindrical cavity under remote nonequibiaxial compressive loading specified below and in section four. The constitutive model, summarized in Section 2 follows Durban and Fleck's (1997) deformation theory formulation for a Drucker-Prager solid and is applicable for small strains. The governing equations are derived using this deformation theory in section three under the assumption of plane strain, with the associated boundary data given in Section 4. The solution, following Huang (1972), is expressed as a Fourier series in the circumferential direction. This leads to a governing system of coupled fourth-order ordinary differential equations. In Section 5, numerical examples illustrate the evolution of the elastoplastic interface, together with the variation in both the stress concentration factor and the displacements at the cavity surface, due to increasing remote load. It is also shown that the use of deformation theory is justifiable because the stress path does not deviate considerably from proportionality. Section 6 presents the conclusions.

[1] To whom correspondence should be addressed.

Contributed by the Applied Mechanics Division of THE AMERICAN SOCIETY OF MECHANICAL ENGINEERS for publication in the ASME JOURNAL OF APPLIED MECHANICS.

Discussion on the paper should be addressed to the Technical Editor, Professor Lewis T. Wheeler, Department of Mechanical Engineering, University of Houston, Houston, TX 77204-4792, and will be accepted until four months after final publication of the paper itself in the ASME JOURNAL OF APPLIED MECHANICS.

Manuscript received by the ASME Applied Mechanics Division, May 28, 1997; final revision, Dec. 8, 1997. Associate Technical Editor: S. Kyriakides.

 Copyright © 1998 by ASME

Downloaded 04 May 2010 to 171.66.16.26. Redistribution subject to ASME license or copyright; see http://www.asme.org/terms/Terms_Use.cfm

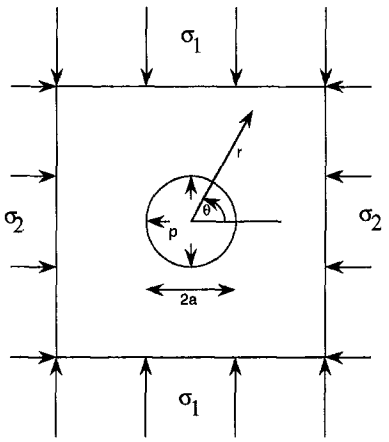


Fig. 1 Internally pressurized cavity under remote nonequibiaxial compression

Figure 1 depicts the schematics of the problem: a circular cylindrical cavity of radius a is embedded in a pressure-sensitive elastoplastic medium. The cavity is subjected to an internal pressure p and nonuniform loading at infinity comprising of perpendicular compressive normal stresses of magnitude σ_1 and σ_2, ordered such that $\sigma_1 \geq \sigma_2 \geq 0$. The normal stress σ_1 is applied along the axes $\theta = \pm\pi/2$, with σ_2 acting along the axes $\theta = 0$ and $\theta = \pi$. The deformation is restricted to the plane perpendicular to the cavity axis (z) and is symmetric with respect to the loading axes.

It is convenient to define, for later use, a parameter t where

$$t = \frac{\sigma_1 - \sigma_2}{\sigma_1 + \sigma_2}, \tag{1.1}$$

which measures the deviation of remote loading from uniformity. Thus, in uniform all-round compression, $\sigma_1 = \sigma_2$ and $t = 0$, while in remote uniaxial compression, $\sigma_2 = 0$ and $t = 1$. The problem lies in finding the stresses and deformation near the cavity under given loading conditions.

2 Constitutive Model

Drucker and Prager (1952) modified the von Mises yield function to account for pressure dependence of the yield surface. The Drucker-Prager yield surface is defined by the generalized stress

$$\sigma_e = \sqrt{\tfrac{3}{2} s_{ij} s_{ij}} + \tfrac{1}{3}\mu\sigma_{kk}, \tag{2.1}$$

where σ_{ij} and s_{ij} denote total and deviatoric stresses, respectively (by convention, tensile stresses and strains are positive), μ is a material parameter which reflects pressure sensitivity, and a repeated subscript implies summation in the usual manner. The von Mises yield stress is described by $\mu = 0$.

Durban and Fleck (1997) recently used the Drucker-Prager criterion in a theory for pressure sensitive materials which allows for strain hardening and nonassociated flow. This theory employs a plastic potential, ϕ, which is analogous to, but does not coincide with, the yield surface (2.1). The plastic potential is defined by

$$\phi = \sqrt{\tfrac{3}{2} s_{ij} s_{ij}} + \tfrac{1}{3}\eta\sigma_{kk}, \tag{2.2}$$

where η is a material constant which, like μ, expresses the influence of pressure sensitivity. For associated flow $\mu = \eta$.

Normality and plastic power equivalence generate the plastic strain rate tensor, d_{ij}^p (Durban and Fleck, 1997). Thus

$$d_{ij}^p = \frac{\sigma_e}{\phi}\dot{\epsilon}_p\left\{\frac{3s_{ij}}{2Q} + \frac{1}{3}\eta\delta_{ij}\right\}, \tag{2.3}$$

where $Q = \sqrt{3s_{ij}s_{ij}/2}$ is the Mises effective stress, δ_{ij} denotes the Kronecker delta, and the superposed dot represents differentiation with respect to a time-like parameter. The generalized plastic strain, ϵ_p, is a given function of the generalized stress (2.1). Durban and Papanastasiou (1997) assumed, in their study of cylindrical cavity problems, the power-law relation

$$\sigma_e = Y + \sigma_0\epsilon_p^n, \quad \text{for} \quad \sigma_e \geq Y, \tag{2.4}$$

where the yield stress Y and the parameters σ_0 and n are material constants.

It is assumed that the total strain, e_{ij}, is small and that the elastic strain rate, d_{ij}^e, is defined by the Hookean relation

$$d_{ij}^e = \frac{1+\nu}{E}\left\{\dot{\sigma}_{ij} - \frac{\nu}{1+\nu}\dot{\sigma}_{kk}\delta_{ij}\right\}, \tag{2.5}$$

where $\dot{\sigma}_{ij}$ is the stress rate, with ν and E denoting the Poisson's ratio and the Young's modulus, respectively.

The total strain rate, d_{ij}, is the sum of the d_{ij}^e and d_{ij}^p. Thus, for small strains the Drucker-Prager flow theory constitutive relations are

$$d_{ij} = \frac{1+\nu}{E}\left\{\dot{\sigma}_{ij} - \frac{\nu}{1+\nu}\dot{\sigma}_{kk}\delta_{ij}\right\} + \frac{\sigma_e}{\phi}\dot{\epsilon}_p\left\{\frac{3s_{ij}}{2Q} + \frac{1}{3}\eta\delta_{ij}\right\}. \tag{2.6}$$

The plastic part of (2.6) is active provided $\sigma_e \geq Y$ and $\dot{\epsilon}_p > 0$ to assure continuous plastic loading.

In proportional loading the ratios of the stress components remain constant. In our problem, it is expected that the loading path in stress space is nearly proportional, so we assume that it is admissible to replace Eq. (2.6) by the deformation theory relationship

$$e_{ij} = \frac{1+\nu}{E}\left\{\sigma_{ij} - \frac{\nu}{1+\nu}\sigma_{kk}\delta_{ij}\right\} + \frac{\sigma_e}{\phi}\epsilon_p\left\{\frac{3s_{ij}}{2Q} + \frac{1}{3}\eta\delta_{ij}\right\} + (1-2\nu)\frac{p_0}{E}\delta_{ij}, \tag{2.7}$$

where account has been taken of a background uniform hydrostatic stress, $\sigma_{ij} = -p_0\delta_{ij}$.

For plane-strain deformation patterns, (2.7) gives the four relations

$$e_{rr} = \frac{1}{E}\{\sigma_{rr} - \nu\sigma_{\theta\theta}\} + \frac{\Gamma}{3}\{2\sigma_{rr} - \sigma_{\theta\theta}\} + \Theta,$$

$$e_{\theta\theta} = \frac{1}{E}\{\sigma_{\theta\theta} - \nu\sigma_{rr}\} + \frac{\Gamma}{3}\{2\sigma_{\theta\theta} - \sigma_{rr}\} + \Theta,$$

$$e_{zz} = \left\{\frac{1+\nu}{E} + \Gamma\right\}\sigma_{zz} - \left\{\frac{\nu}{E} + \Gamma\right\}(\sigma_{rr} + \sigma_{\theta\theta}) + \Theta = 0,$$

$$e_{r\theta} = \left\{\frac{1+\nu}{E} + \Gamma\right\}\sigma_{r\theta}, \tag{2.8}$$

Downloaded 04 May 2010 to 171.66.16.26. Redistribution subject to ASME license or copyright; see http://www.asme.org/terms/Terms_Use.cfm

where

$$\Gamma = \frac{\sigma_e}{\phi}\epsilon_p \frac{3}{2Q}, \quad \Delta = \frac{\eta}{3}\frac{\sigma_e}{\phi}\epsilon_p \quad \text{and}$$

$$\Theta = \Delta - \left\{\frac{\nu}{E} + \frac{\Gamma}{3}\right\}\sigma_{zz} + (1 - 2\nu)\frac{p_0}{E}. \tag{2.9}$$

The axial stress, σ_{zz}, given implicitly from (2.8c), is

$$\sigma_{zz} = \frac{\{6\nu\phi\sigma_h - \frac{2}{3}\eta\sigma_e E\epsilon_p - 2(1-2\nu)\phi p_0\}(\sigma_e - \mu\sigma_h) + 3\sigma_h\sigma_e E\epsilon_p}{2(1+\nu)\phi(\sigma_e - \mu\sigma_h) + 3E\sigma_e\epsilon_p}, \tag{2.10}$$

where $\sigma_h = \sigma_{kk}/3$ is the hydrostatic (mean) stress.

3 Deformation Around the Circular Cavity

Huang (1972) employed the J_2 deformation theory to obtain the stress and deformation fields around a cylindrical cavity, embedded in a medium with the Ramberg-Osgood (1943) response characteristic, under remote uniaxial tension or pure shear. In this section Huang's (1972) analysis is extended in order to consider the problem of an internally pressurized cavity under remote nonequibiaxial compression (Fig. 1) embedded in a medium modeled by the deformation theory (2.7) for a Drucker-Prager solid with small strain response.

The transformation $x = a/r$ maps the infinite region exterior to the cavity, $r \geq a$, onto the finite domain $0 \leq x \leq 1$. The stress components, expressed in terms of a stress function $F(x, \theta)$ (Huang, 1972) are

$$\sigma_{rr} = 2F - x\frac{\partial F}{\partial x} + \frac{\partial^2 F}{\partial \theta^2},$$

$$\sigma_{\theta\theta} = 2F - 2x\frac{\partial F}{\partial x} + x^2\frac{\partial^2 F}{\partial x^2},$$

$$\sigma_{r\theta} = x\frac{\partial^2 F}{\partial x \partial \theta} - \frac{\partial F}{\partial \theta}. \tag{3.1}$$

The symmetry conditions allow F to be expanded as a Fourier cosine series of the form

$$F = \sum_{m=0,2,4,\ldots}^{\infty} f_m(x)\cos m\theta, \tag{3.2}$$

where the functions $f_m(x)$ are to be determined. Thus, the components of the radial profiles of the deformation and stress fields around the cavity are unknown functions of only one variable, x.

For plane-strain problems, the strain compatibility equation is

$$x^2\frac{\partial^2 e_{\theta\theta}}{\partial x^2} + \frac{\partial^2 e_{rr}}{\partial \theta^2} + x\frac{\partial e_{rr}}{\partial x} + 2x\frac{\partial^2 e_{r\theta}}{\partial \theta \partial x} - 2\frac{\partial e_{r\theta}}{\partial \theta} = 0. \tag{3.3}$$

Combining (2.8) to (3.3) gives

$$\sum_{m=0,2,4,\ldots}^{\infty}\left\{A_{4m}\frac{d^4 f_m}{dx^4} + A_{3m}\frac{d^3 f_m}{dx^3} + A_{2m}\frac{d^2 f_m}{dx^2} + A_{1m}\frac{df_m}{dx} + A_{0m}f_m\right\} = g. \tag{3.4}$$

The coefficients A_{im} and g, given in the Appendix, are even functions of θ and can be represented by cosine series as

$$A_{st} = \sum_{j=0,2,4,\ldots}^{\infty} B_{st}^j \cos j\theta, \quad g = \sum_{j=0,2,4,\ldots}^{\infty} G^j \cos j\theta. \tag{3.5}$$

It is easily shown that the coefficients B_{st}^j and G^j are

$$B_{st}^j = \frac{4}{(1+\delta_{0j})\pi}\int_0^{\pi/2} A_{st}\cos j\theta d\theta,$$

$$G^j = \frac{4}{(1+\delta_{0j})\pi}\int_0^{\pi/2} g\cos j\theta d\theta. \tag{3.6}$$

Substituting (3.5) into (3.4) and equating coefficients of $\cos j\theta$ gives the governing set of ordinary differential equations for the functions $f_m(x)$:

$$\sum_{m=0,2,4,\ldots}^{\infty}\left\{B_{4m}^j\frac{d^4 f_m}{dx^4} + B_{3m}^j\frac{d^3 f_m}{dx^3} + B_{2m}^j\frac{d^2 f_m}{dx^2} + B_{1m}^j\frac{df_m}{dx} + B_{0m}^j f_m\right\} = G^j, \tag{3.7}$$

for $j = 0, 2, 4, \ldots$.

If the remote stress field is uniform ($\sigma_1 = \sigma_2$), only the first term in the expansion (3.2) is required. The governing system (3.7) then reduces to the single equation defined by $j = m = 0$.

Let $1/\hat{x}$ denote the maximum radius of any elastoplastic interface. In the region $0 \leq x < \hat{x}$, where arcs of fixed radii lie entirely within elastic material, the system (3.7) reduces to the biharmonic equation $\nabla^2\Phi = 0$, where $\Phi = F/x^2$ is the Airy stress function, with the standard solution

$$F = \alpha_0 + \beta_0 \ln(x) + \gamma_0 x^2 + \chi_0 x^2 \ln(x) + \sum_{m=2,4,\ldots}^{\infty}\{\alpha_m x^m + \beta_m x^{-m} + \gamma_m x^{2+m} + \chi_m x^{2-m}\}\cos m\theta, \quad 0 \leq x < \hat{x}, \tag{3.8}$$

where α_m, β_m, γ_m and χ_m ($m = 0, 2, 4, \ldots$) are constants. Any stress field derived by substituting (3.8) into (3.1) is independent of γ_0. Hence, it is permissible to proceed with $\gamma_0 = 0$ without loss of generality.

4 Boundary Conditions

A unique solution of the system of fourth-order differential Eqs. (3.7) requires four boundary conditions for each function $f_m(x)$. In this section, two boundary conditions are derived at each of $x = 0$ and $x = 1$ for every $f_m(x)$.

The stresses at infinity (i.e., $x = 0$) are

$$\sigma_{rr} = -\tfrac{1}{2}\sigma_1(1 - \cos 2\theta) - \tfrac{1}{2}\sigma_2(1 + \cos 2\theta),$$

$$\sigma_{\theta\theta} = -\tfrac{1}{2}\sigma_1(1 + \cos 2\theta) - \tfrac{1}{2}\sigma_2(1 - \cos 2\theta),$$

$$\sigma_{r\theta} = -\tfrac{1}{2}(\sigma_1 - \sigma_2)\sin 2\theta. \tag{4.1}$$

Thus, from (3.1) and (3.2), the first boundary condition at $x = 0$ is

$$F = -\tfrac{1}{4}(\sigma_1 + \sigma_2) - \tfrac{1}{4}(\sigma_1 - \sigma_2)\cos 2\theta. \tag{4.2}$$

If the remote field is elastic, then (3.8) requires

$$\alpha_0 = -\tfrac{1}{4}(\sigma_1 + \sigma_2), \quad \chi_2 = -\tfrac{1}{4}(\sigma_1 - \sigma_2), \tag{4.3}$$

with $\beta_m = 0$ ($m \geq 0$) and $\chi_m = 0$ ($m \geq 4$).

The second boundary condition at $x = 0$ is deduced by following Huang's (1972) analysis. The strain compatibility condition (3.3) can be rewritten as

Downloaded 04 May 2010 to 171.66.16.26. Redistribution subject to ASME license or copyright; see http://www.asme.org/terms/Terms_Use.cfm

$$x\frac{\partial^2 e_{\theta\theta}}{\partial x^2}+\frac{\partial e_{rr}}{\partial x}+2\frac{\partial^2 e_{r\theta}}{\partial\theta\partial x}=\frac{1}{x}\left\{-\frac{\partial^2 e_{rr}}{\partial\theta^2}+2\frac{\partial e_{r\theta}}{\partial\theta}\right\}. \quad (4.4)$$

If the remote field is elastic, the stress strain relationships (2.6) together with (4.1) imply that $-\partial^2 e_{rr}/\partial\theta^2 + 2\partial e_{r\theta}/\partial\theta = 0$ at $x = 0$. Applying L'Hospital's rule to (4.4) at the limit of $x \to 0$, then gives

$$\frac{\partial^3 e_{rr}}{\partial\theta^2\partial x}+\frac{\partial e_{rr}}{\partial x}=0. \quad (4.5)$$

The symmetry conditions imply $e_{rr} = \sum_{m=0,2,4,\ldots}^{\infty} h_m(x)\cos m\theta$. Hence, from (4.5)

$$\frac{\partial e_{rr}}{\partial x}=0. \quad (4.6)$$

It follows from the stress strain relationships (2.6) that the second boundary condition at $x = 0$ is

$$\frac{dF}{dx}=0. \quad (4.7)$$

The cavity is subjected to an internal pressure p. Thus

$$\sigma_{rr}=-p,\quad \sigma_{r\theta}=0,\quad \text{at}\quad x=1. \quad (4.8)$$

Equations (3.1) and (3.2) therefore imply the following two boundary conditions at the cavity wall

$$2f_0-\frac{df_0}{dx}=-p,\quad f_m=\frac{df_m}{dx}=0\quad \text{for}$$

$$m=2,4,\ldots,\quad \text{at}\quad x=1. \quad (4.9)$$

The solution of the system (3.7) is required subject to boundary conditions defined by (4.2) and (4.7) in the far-field and by (4.9) at the cavity wall.

In the absence of plastic deformation, the well-known elastic solution, easily recovered from (3.8), (4.9), (4.2) together with (4.7), can be written in terms of F as

$$F=-\tfrac{1}{4}(\sigma_1+\sigma_2)+\{-\tfrac{1}{2}(\sigma_1+\sigma_2)+p\}x^2\ln(x)$$

$$-\tfrac{1}{4}(\sigma_1-\sigma_2)(1-x^2)^2\cos 2\theta. \quad (4.10)$$

In the case where plastic deformation occurs, the solution is derived iteratively using a shooting method. The unknown parameters in the far-field, namely χ_0, α_m and γ_m $(m \geq 2)$, are adjusted until the boundary conditions at the cavity wall (4.9) are satisfied. The elastic solution (4.10) provides initial estimates for these unknown parameters. Thus, $\chi_0 = p - (\sigma_1 + \sigma_2)/2$, $\alpha_2 = (\sigma_1 - \sigma_2)/2$, $\chi_2 = \gamma_2 = -(\sigma_1 - \sigma_2)/4$ and $\alpha_m = \gamma_m = 0$ $(m \geq 4)$. In the region $0 \leq x < \hat{x}$, where arcs of fixed radii lie entirely within elastic material, the solution is given by (3.8). In the region $\hat{x} \leq x \leq 1$, where the arcs can pass through both elastic and plastically yielded material, the solution is generated by integrating the system (3.7) using a fourth-order Runge-Kutta scheme, where quantities in (3.7) are normalized with respect to E in order to alleviate stiffness problems. It is notable that the fourth derivatives $d^4 f_m/dx^4 (m \geq 0)$ are present in the terms B^j_{0m}, B^j_{1m}, B^j_{2m} together with g and are therefore given implicitly by (3.7). The integrals (3.6) are evaluated through Gaussian quadrature.

The solution is deemed to be satisfactory when the addition of a further term in the Fourier expansion (3.2) changes the tangential stress, $\sigma_{\theta\theta}$, at the cavity wall by less than two percent (Huang, 1972). For the cases considered in the next section, convergence typically requires three or four terms. As the number of terms increases the solution oscillates but the magnitude of the error decreases monotonically.

5 Numerical Examples

Figures 2 and 3 display the evolution of the elastoplastic interface (i.e., contours of $\sigma_e = Y$) under increasing remote loading for the cases $t = 0.2$ and $t = 0.4$, respectively. The material behavior is representative of sandstones commonly encountered in oil and gas reservoirs and is described by the stress-strain relationship (2.4) with parameters $E = 10$ GPa, $\nu = 0.3$, $Y = 30$ MPa, $\sigma_0 = 100$ MPa, $n = 0.4$, $\mu = 0.9$, and $\eta = 0.8$. Plastic yielding first occurs at $x = 1$, $\theta = 0$. The plastic zone then grows as the remote load increases. The elastoplastic interface is, initially, convex and shaped like a section of an oval which expands under increasing load; the major axis is parallel to $\theta = 0$ and the eccentricity increases with t. This process does not, however, continue indefinitely as the interface becomes concave near the cavity surface when $\sigma_1 = 93.3$ MPa and $\sigma_2 = 40$ MPa. This effect is illustrated in Fig. 4, which shows the contours of generalized stress (2.1) for this case.

At the cavity surface, the stress with the largest magnitude is always $\sigma_{\theta\theta}$ at $\theta = 0$. The stress concentration factor, K, which quantifies the effect of inserting the cavity into the medium, is therefore

$$K=-\frac{(\sigma_{\theta\theta})_{x=1,\theta=0}}{\sigma_1}, \quad (5.1)$$

where $(\sigma_{\theta\theta})_{\theta=0} = -\sigma_1$ prior to the cavity insertion.

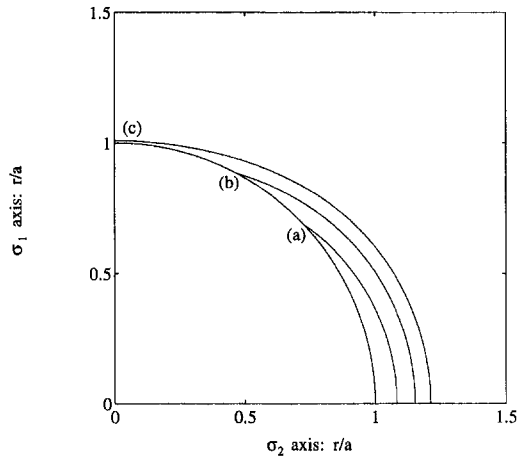


Fig. 2 Evolution of the elastoplastic interface in the case $t = 0.2$ and $p = 1$ MPa. The remote loading is (a) $\sigma_1 = 45$ MPa, $\sigma_2 = 30$ MPa, (b) $\sigma_1 = 60$ MPa, $\sigma_2 = 40$ MPa, and (c) $\sigma_1 = 75$ MPa, $\sigma_2 = 50$ MPa.

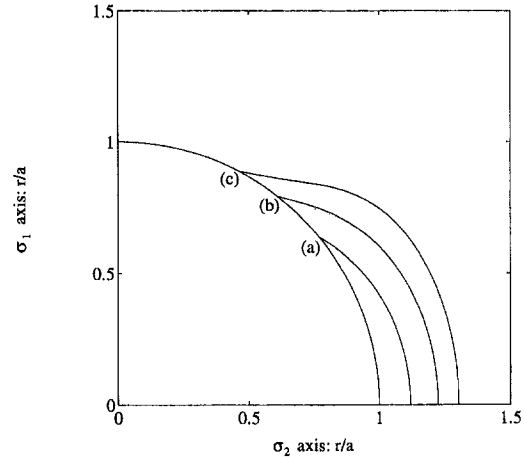


Fig. 3 Evolution of the elastoplastic interface in the case $t = 0.4$ and $p = 1$ MPa. The remote loading is (a) $\sigma_1 = 46.7$ MPa, $\sigma_2 = 20$ MPa, (b) $\sigma_1 = 70$ MPa, $\sigma_2 = 30$ MPa, and (c) $\sigma_1 = 93.3$ MPa, $\sigma_2 = 40$ MPa.

Downloaded 04 May 2010 to 171.66.16.26. Redistribution subject to ASME license or copyright; see http://www.asme.org/terms/Terms_Use.cfm

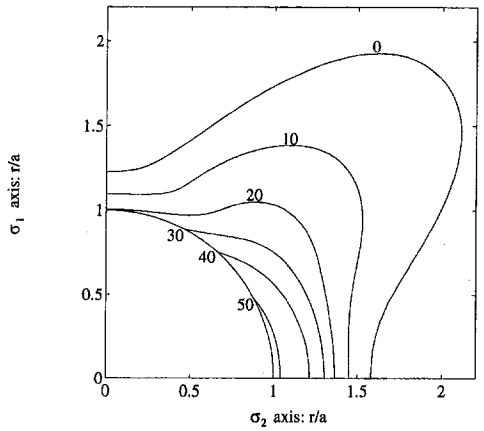


Fig. 4 Generalized stress, σ_e, contours, labelled in MPa, for the case σ_1 = 93.3 MPa, σ_2 = 40 MPa, and p = 1 MPa

Table 1 Stress concentration factors

σ_1 (MPa)	σ_2 (MPa)	t	$(\sigma_{\theta\theta})_{x=1,\theta=0}$ (MPa)	K	$(\epsilon_p)_{x=1,\theta=0}$ (×1000)
45	30	0.2	−94.2	2.1	1.7
60	40	0.2	−112.1	1.9	6.4
75	50	0.2	−122.2	1.6	10.8
46.7	20	0.4	−100.8	2.2	3.5
70	30	0.4	−123.0	1.8	11.9
93.3	40	0.4	−138.5	1.5	22.8

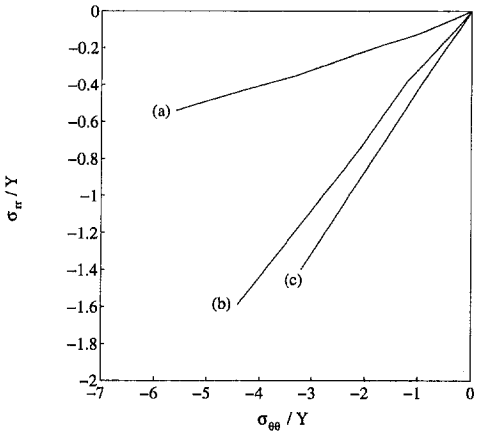


Fig. 5 Stress paths along θ = 0 at (*a*) a/r = 0.9, (*b*) a/r = 0.6 and (*c*) a/r = 0.2, in the case t = 0.4

Table 1 gives values of K for the cases considered above. These range from 1.5 to 2.2. At given values of σ_2, K is higher at t = 0.2 than at t = 0.4. This is due to plastic hardening, which is more pronounced when t = 0.4, partially suppressing the rise in $|(\sigma_{\theta\theta})_{x=1,\theta=0}|$ which accompanies any increase in t.

In order to confirm the validity of Drucker-Prager deformation theory, it is necessary to examine the stress paths along radial directions in the domain $0 \le \theta \le \pi/2$. The stress paths along the axis $\theta = 0$ (Fig. 5) appear to have the greatest deviation from proportional loading. This deviation is, however, slight supporting the validity of Drucker-Prager deformation theory (Budiansky, 1959).

Figure 6 displays the normalized radial displacement, u_r/a, at the cavity wall. It is evident that increasing the remote load at constant values of t causes the cavity to contract. The greatest contraction occurs at $\theta = \pi/2$, where the normal to the cavity surface is parallel to the line of action of σ_1. For a constant remote mean stress, increasing t induces greater constriction at $\theta = \pi/2$ and less contraction at $\theta = 0$. This effect is illustrated by curves (*b*) and (*c*), in the case $(\sigma_1 + \sigma_2)/2$ = 50 MPa.

Figure 7 displays the normalized tangential displacement, u_θ/a, at the cavity wall. It is remarkable that in all four cases u_θ is symmetric about $\theta = \pi/4$. It is evident that increasing the remote load induces a higher displacement towards $\theta = 0$.

The influence of plastic dilation can be seen in Table 2 for the cases η = 0.0, 0.4 and 0.8. Values of all other constitutive parameters remain as defined above. The more pronounced plastic dilation occurring at at higher values of η partially suppresses compression, reducing plastic hardening. This causes both the

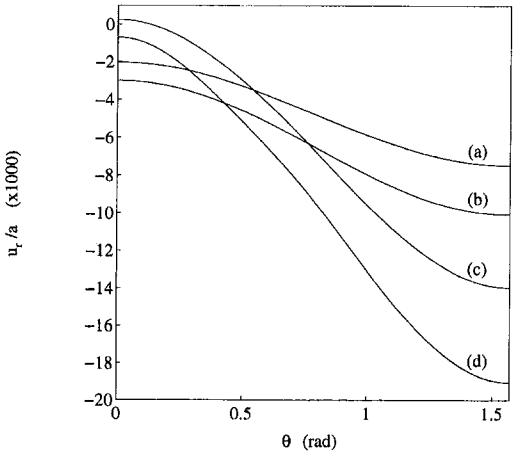


Fig. 6 Normalized radial displacement, u_r/a, at the cavity surface. The remote loading is (*a*) σ_1 = 45 MPa, σ_2 = 30 MPa, (*b*) σ_1 = 60 MPa, σ_2 = 40 MPa, (*c*) σ_1 = 70 MPa, σ_2 = 30 MPa, and (*d*) σ_1 = 93.3 MPa, σ_2 = 40 MPa. In all cases p = 1 MPa.

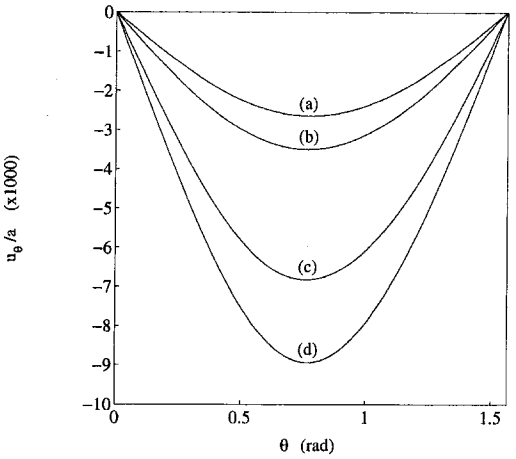


Fig. 7 Normalized tangential displacement, u_θ/a, at the cavity surface. The remote loading is (*a*) σ_1 = 45 MPa, σ_2 = 30 MPa, (*b*) σ_1 = 60 MPa, σ_2 = 40 MPa, (*c*) σ_1 = 70 MPa, σ_2 = 30 MPa, and (*d*) σ_1 = 93.3 MPa, σ_2 = 40 MPa. In all cases p = 1 MPa.

Table 2 Influence of dilation

σ_1 (MPa)	σ_2 (MPa)	η	$(\sigma_{\theta\theta})_{x=1,\theta=0}$ (MPa)	K	$(\epsilon_p)_{x=1,\theta=0}$ (×1000)
45	30	0.0	−93.1	2.1	2.1
45	30	0.4	−93.6	2.1	1.9
45	30	0.8	−94.2	2.1	1.7
70	30	0.0	−117.2	1.7	14.0
70	30	0.4	−120.1	1.7	13.1
70	30	0.8	−123.0	1.8	11.9

Downloaded 04 May 2010 to 171.66.16.26. Redistribution subject to ASME license or copyright; see http://www.asme.org/terms/Terms_Use.cfm

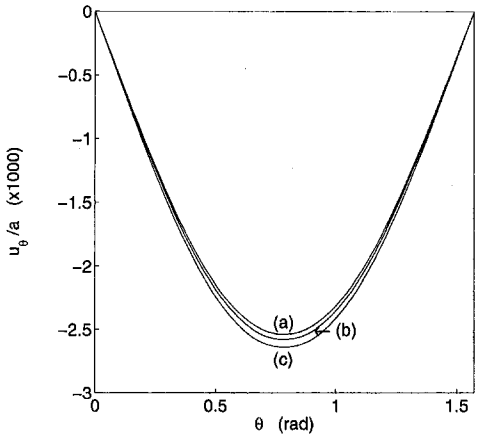


Fig. 8 Normalized tangential displacement, u_θ/a, at the cavity surface, for the cases (a) $\eta = 0.0$, (b) $\eta = 0.4$, and (c) $\eta = 0.8$. The remote loading is $\sigma_1 = 45$ MPa, $\sigma_2 = 30$ MPa, and $p = 1$ MPa.

hoop stress and hoop strain at the cavity wall to decrease, inducing higher tangential displacements towards $\theta = 0$ (Fig. 8). The minimum tangential displacement decreases by four percent as η increases from 0.0 to 0.8.

6 Conclusions

This paper presents an analysis the problem of an internally pressurized cylindrical cavity, embedded in a medium with a pressure-sensitive elastoplastic, strain-hardening, and nonassociative response, under remote nonequibiaxial compression. The constitutive model follows Durban and Fleck's (1997) deformation theory formulation for a Drucker-Prager solid and is applicable for small strains. The paper is an extension of Huang's (1972) analysis for a cylindrical cavity embedded in a medium obeying J_2 deformation theory together with a Ramberg-Osgood (1943) response characteristic.

The stress and deformation patterns around the cavity were derived under the assumption of plane strain. The symmetry conditions allowed the solution to be expanded as a Fourier series in the circumferential direction. The Fourier coefficients were functions of the radial coordinate and were governed by a coupled set of ordinary differential equations.

Numerical examples illustrated the evolution of the elastoplastic interface, together with the variation in both the stress concentration factor and the displacement at the cavity surface, under increasing remote loading, at constant values of the parameter, t. This parameter measures the deviation of remote loading from uniformity. The elastoplastic interface was, initially, convex and shaped like a section of an oval, which expands under increasing remote load; the major axis was parallel to $\theta = 0$ and the eccentricity increased with t. Under high remote compression, however, the interface became concave near the cavity surface. The tangential displacement, u_θ, at the cavity surface was symmetric about $\theta = \pi/4$. For a given remote mean stress, the stress concentration factor decreased as the remote stress deviation increased, because of the higher plastic deformation and hardening at the cavity surface. It was found that increasing plastic dilation alleviated the compression to a greater extent and this reduced the plastic hardening.

Acknowledgments

The authors wish to thank Schlumberger for giving permission to publish this work. Part of this study was supported by the fund for the promotion of research at the Technion.

References

Budiansky, B., 1959, "A Reassessment of Deformation Theories of Plasticity," ASME JOURNAL OF APPLIED MECHANICS, Vol. 26, pp. 259–264.

Detournay, E., 1986, "An Approximate Statical Solution of the Elastoplastic Interface for the Problem of Galin With a Cohesive-Frictional Material," *Int. J. Solids Structures,* Vol. 22, pp. 1434–1454.

Detournay, E., and Fairhurst, C., 1987, "Two-Dimensional Elastoplastic Analysis of a Long Cylindrical Cavity Under Non-Hydrostatic Loading," *Int. J. Rock Mech. Min. Sci. and Geomech.,* Vol. 24, No. 4, pp. 197–211.

Drucker, D. C., and Prager, W., 1952, "Soil Mechanics and Plastic Analysis or Limit Design," ASME JOURNAL OF APPLIED MECHANICS, Vol. 12, pp. 157–165.

Durban, D., and Fleck, N. A., 1997, "Spherical Cavity Expansion in a Drucker-Prager Solid," *Journal of Applied Mechanics,* Vol. 64, pp. 743–750.

Durban, D., and Papanastasiou, P. C., 1997, "Cylindrical Cavity Expansion and Contraction in Pressure Sensitive Geomaterials," *Acta Mechanica,* Vol. 122, pp. 99–122.

Galin, L. A., 1946, "Plane Elastic-Plastic Problem: Plastic Regions Around Circular Holes in Plates and Beams," *Prikl. Mat. Mekh,* Vol. 10, pp. 365–386.

Hill, R., 1951, *The Mathematical Theory of Plasticity,* Clarendon Press, Oxford, UK.

Huang, Wu-Cheng., 1972, "Theoretical Stress Concentrations at Circular Holes and Inclusions in Strain Hardening Materials," *Int. J. Solids Structures,* Vol. 8, pp. 149–192.

Last, N. C., Plumb, R. A., Harkness, R., Charlez, P., Alsen, J., and McLean, M. R., 1995, "An Integrated Approach to Evaluating and Managing Wellbore Instability in the Cusiana Field, South America, Columbia," *Proc. Society of Petroleum Engineers Annual Technical Conference and Exhibition,* Dallas, TX, Oct. 22–25, pp. 147–160.

Ramberg, W., and Osgood, W. R., 1943, "Description of Stress-Strain Curves by Three Parameters," NACA TN 902.

Salençon, J., 1966, "Expansion Quasi-Statique d'une Cavité a Sýmetrie Sphérique ou Cylindrique dans un Milieu Élastoplastique," *Annls Ponts Chauss,* Vol. 3, pp. 175–187.

Salençon, J., 1969, "Contraction Quasi-Statique d'une Cavité a Sýmetrie Sphérique ou Cylindrique dans un Milieu Élastoplastique," *Annls Ponts Chauss,* Vol. 4, pp. 231–236.

Wilner, B., 1988, "Stress Analysis of Particles in Metals," *J. Mech. Phys. Solids,* Vol. 36, No. 2, pp. 141–165.

APPENDIX

The Coefficients in (3.4)

The coefficients A_{im} and g are

$$A_{0m} = \{m^4c_1 + 2x(1 + 2m^2)c_2 + x^2(2 + m^2)c_4 + 2(1 - m^2)c_6 - m^2(c_8 + c_9)\} \cos m\theta + \{2m(2m^2 - 5)c_5 - xmc_7\} \sin m\theta,$$

$$A_{1m} = \{xc_1 - 2x^2(1 + 2m^2)c_2 - 2xm^2c_3 - 3x^4c_4 + xm^2c_8\} \cos m\theta + xm\{6c_5 - xc_7\} \sin m\theta,$$

$$A_{2m} = \{-x^2c_1 + x^3c_2 + 2x^2m^2c_3 + 2x^4c_4 - x^2c_6 - x^2m^2c_8\} \cos m\theta - 4x^2mc_5 \sin m\theta,$$

$$A_{3m} = 2x^3\{c_1 + 2xc_2\} \cos m\theta,$$

$$A_{4m} = x^4c_1 \cos m\theta,$$

$$g = -x\frac{\partial\Theta}{\partial x} - x^2\frac{\partial^2\Theta}{\partial x^2} - \frac{\partial^2\Theta}{\partial\theta^2}. \quad \text{(A1)}$$

The coefficients c_i are

$$c_1 = \frac{1}{E} + \frac{2\Gamma}{3}, \quad c_4 = \frac{1}{3}\frac{\partial^2\Gamma}{\partial x^2}, \quad c_7 = 2\frac{\partial^2\Gamma}{\partial x\partial\theta},$$

$$c_2 = \frac{1}{3}\frac{\partial\Gamma}{\partial x}, \quad c_5 = \frac{1}{3}\frac{\partial\Gamma}{\partial\theta}, \quad c_8 = 2\left\{\frac{1 + \nu}{E} + \Gamma\right\},$$

$$c_3 = \frac{\nu}{E} + \frac{\Gamma}{3}, \quad c_6 = \frac{1}{3}\frac{\partial^2\Gamma}{\partial\theta^2}, \quad c_9 = 2\left\{\frac{1 - \nu}{E} + \frac{\Gamma}{3}\right\}. \quad \text{(A2)}$$

Downloaded 04 May 2010 to 171.66.16.26. Redistribution subject to ASME license or copyright; see http://www.asme.org/terms/Terms_Use.cfm

D. L. Johnson

L. M. Schwartz

Schlumberger-Doll Research,
Old Quarry Road,
Ridgefield, CT 06877-4108

D. Elata[1]

J. G. Berryman

Earth Sciences Division,
Lawrence Livermore National Laboratory,
Mail Stop L-202,
P.O. Box 808,
Livermore, CA 94551

B. Hornby[2]

Schlumberger Cambridge Research,
High Cross,
Madingley Road,
Cambridge, CB3 0EL, UK

A. N. Norris

Department of Mechanical and
Aerospace Engineering,
Rutgers University,
Piscataway, NJ 08855-0909

Linear and Nonlinear Elasticity of Granular Media: Stress-Induced Anisotropy of a Random Sphere Pack

We develop an effective medium theory of the nonlinear elasticity of a random sphere pack based upon the underlying Hertz-Mindlin theory of grain-grain contacts. We compare our predictions for the stress-dependent sound speeds against new experimental data taken on samples with stress-induced uniaxial anistropy. We show that the second-order elastic moduli, C_{ijkl}, and therefore the sound speeds, can be calculated as unique path-independent functions of an arbitrary strain environment, $\{\epsilon_{kl}\}$, thus generalizing earlier results due to Walton. However, the elements of the stress tensor, σ_{ij}, are not unique functions of $\{\epsilon_{kl}\}$ and their values depend on the strain path. Consequently, the sound speeds, considered as functions of the applied stresses, are path dependent. Illustrative calculations for three cases of combined hydrostatic and uniaxial strain are presented. We show further, that, even when the additional applied uniaxial strain is small, these equations are not consistent with the usual equations of third-order hyperelasticity. Nor should they be, for the simple reason that there does not exist an underlying energy function which is simply a function of the current state of the strain. Our theory provides a good understanding of our new data on sound speeds as a function of uniaxial stress.

1 Introduction

Granular media exhibit a wide range of interesting properties. They are in some respects similar to solids and in other respects similar to fluids, although they are distinctly different from either. Consequently, the physics of granular media represents an active area of current research activity (Bideau and Dodds, 1991; Mehta, 1991; Nagel, 1992). A major area of interest is the manner by which applied forces are communicated from one grain to another, a subject with clear implications for the propagation of sound waves which is the topic of this article. Specifically, we present new theoretical and experimental results which clarify the way that sound speeds in granular media depend upon the applied stresses which, in general, may be anisotropic. The central issue here is that sound cannot propagate unless there is an applied stress because the "spring constants" between the grains vanish when the stress is eliminated. By measuring the effects of anisotropic stresses, we have extended earlier experimental work which had been limited to a consideration of applied stress which is strictly hydrostatic. Previous such studies are seriously inadequate, for reasons upon which we expand below.

Two related issues complicate the analysis of sound propagation in granular systems: nonlinearity and path dependence. Both effects originate with the contact forces exerted by one grain on another. Stress-induced changes in sound speeds are the fundamental signature of nonlinear elasticity. It is well known that granular media are highly nonlinear and that the rates at which sound speeds change with applied stress increase dramatically as the stress decreases. It is also known that stress versus strain experiments on such systems often show considerable hysteresis, which is due, in part, to the path-dependent nature of the contact forces. From a theoretical viewpoint, it is therefore necessary to develop nonperturbative methods of the kind employed in this paper.

We emphasize the importance of studying granular systems under the influence of anisotropic stresses. First, in conventional nonlinear *hyperelasticity* theory, there exists an energy density function which is strictly a function of the current state of strain, and not upon the past history of the deformation. Here, the so-called third-order elastic constants are used to describe the rate of change of sound speeds with applied stress or strain. (The values of the sound speeds themselves are given in terms of the second-order elastic constants, e.g., the Lamé constants λ and μ.) Even in the very simplest case of an isotropic hyperelastic medium there are three different third-order elastic constants: A, B, and C. A measurement of the change of longitudinal and of transverse sound speeds due to applied hydrostatic pressure can determine only two linearly independent combinations of these constants. Therefore, even in this simplest case, a measurement of the effects of nonhydrostatic stress is needed to complete the determination of the set A, B, C. Second, in granu-

[1] Present address: Faculty of Mechanical Engineering, Technion-I.I.T., Haifa 32000, Israel.

[2] Present address: ARCO Exp. and Prod. Tech., 2300 W. Plano Parkway, Plano, TX 75075-8499.

Contributed by the Applied Mechanics Division of THE AMERICAN SOCIETY OF MECHANICAL ENGINEERS for publication in the ASME JOURNAL OF APPLIED MECHANICS.

Discussion on the paper should be addressed to the Technical Editor, Professor Lewis T. Wheeler, Department of Mechanical Engineering, University of Houston, Houston, TX 77204-4792, and will be accepted until four months after final publication of the paper itself in the ASME JOURNAL OF APPLIED MECHANICS.

Manuscript received by the ASME Applied Mechanics Division, Mar. 19, 1997; final revision, Sept. 21, 1997. Associate Technical Editor: M. Shinozuka.

 Copyright © 1998 by ASME

Downloaded 04 May 2010 to 171.66.16.26. Redistribution subject to ASME license or copyright; see http://www.asme.org/terms/Terms_Use.cfm

lar systems the forces exerted at the individual grain-grain contacts are path dependent. It follows that the stress-induced changes in forces are also path dependent so that sound speeds depend on the order in which stresses are applied. (This is true even though there is *no hysteresis* along any given stress path.) This issue does not arise when only hydrostatic pressure is applied nor does it arise in hyperelastic materials. Third, in geophysical applications, sedimentary rocks, which are formed from granular media, often exhibit strong acoustic anisotropy due to their inherently anisotropic stress environment (Walsh, 1965; Nur and Simmons, 1969; Nur, 1971; Lockner et al., 1977; Berryman, 1979; Helbig, 1983; Thomsen, 1986; Sayers, 1988; Sayers et al., 1990; Yin and Nur, 1992). We view the understanding of the nonlinear acoustic properties of unconsolidated granular media and the associated stress-induced anisotropy as a paradigm problem for this more general class of materials.

As the issues considered here are complicated, it will be useful to summarize the structure of this paper. In Section 2 we review the equations that describe the Hertz-Mindlin forces exerted between two grains in contact. Each contact is assumed to be rough and static friction prevents tangential slipping. In general, such forces are *not* described by a well-defined strain-energy function and any discussion of the resulting acoustic properties of the granular composite must take account of the strain history (Mindlin, 1949; Elata, 1996). Because we focus our interests here upon the role of the strain history, we employ an effective medium theory (Walton, 1987; Norris and Johnson, 1997) to make the connection between the properties of the individual grain-grain contacts and those of the composite.

We use the term "random" to distinguish our samples from ordered packings. As with all effective medium theories, only some features of the true random nature of the sample are captured by our theory, such as the average number of grain-grain contacts. This particular effective medium theory is easily generalizable to other situations, such as different bead sizes, a nonisotropic distribution of contacts, a radial distribution of contacts, but we do not explicitly consider those examples here.

Within this context, there is, surprisingly, one important relation in the acoustics of granular systems that is *path independent.* Norris and Johnson (1997) (NJ) have shown that the additional work associated with incremental displacements of a contact around a given strain state are path *independent* to second order in the *additional* strain. The coefficients of these second-order terms are, in turn, path-*independent* functions of the current state of strain. This implies that the associated equations for the second-order elastic moduli (i.e., the sound speeds) considered as functions of the strain tensor are also path *independent.* By contrast, we show that the relation between *stress* and strain is explicitly path dependent. Therefore, the sound speeds are path *independent* functions of applied strain, but path-*dependent* functions of applied stress. To illustrate these findings we consider three cases of combined hydrostatic and uniaxial strain. In Section 3 we ask if the conventional theory of third-order hyperelasticity can be used to describe this system (Hughes and Kelly, 1953; Gol'dberg, 1961). Here we show that, even when the deviations from the isotropic state are small, the path dependent nature of the forces implies that the third-order formulation is not valid, precisely because of the lack of a strain-energy function and we illustrate this point with a numerical example. In Section 4 we discuss the comparison of our analysis with new experimental results on the stress dependence of longitudinal and transverse sound speeds in a granular packing under uniaxial compression. Generally, the level of agreement between theory and experiment is quite satisfactory. Our conclusions are presented in Section 5.

2 Theory of Combined Hydrostatic and Uniaxial Strain

In this section we derive results for the elastic constants and for the stress tensor, when the strain is a combination of both hydrostatic and uniaxial compression.

2.1 Path-Dependent Contact Forces. In a recent article, Norris and Johnson (1997) considered the linear and nonlinear elasticity of different models of granular aggregates. These models differ in the nature of the grain-grain contact but can be written in the context of a common formalism. Let us suppose $2w$, $2s$ are, respectively, the normal and the transverse components of the displacement of one sphere relative to another. Let N, T be the normal and transverse components of the restoring force. An infinitesimal change in displacement ($w \to w + \Delta w$, $s \to s + \Delta s$) leads to an infinitesimal change in restoring force ($N \to N + \Delta N$, $T \to T + \Delta T$). All models considered in Norris and Johnson (1997) can be written in the form

$$\Delta N = C_n a_n(w)\Delta w, \quad \Delta T = C_t a_t(w)\Delta s, \tag{1}$$

where C_n, C_t depend only on shear modulus, μ, and the Poisson ratio, ν, of the individual grains

$$C_n = \frac{4\mu_s}{1-\nu_s}, \quad C_t = \frac{8\mu_s}{2-\nu_s}. \tag{2}$$

The quantities a_n, a_t are different for the different models of grain-grain contact but they do not depend upon the elastic constants of the grains. For the specific no-slip case being considered in the present article, one has

$$a_n(w) = a_t(w) = (Rw)^{1/2}, \tag{3}$$

where R is the radius of the spherical grain.

Let $W(w, s)$ be the work needed to displace the two grains relative to each other. In general W is very much dependent upon the path of the deformation, $s = s(w)$, and not simply upon the final values of (w, s). Suppose, however, one asks the question: How much additional work is needed to take the contact from one state characterized by (w_0, s_0) to another $(w_0 + w_1, s_0 + s_1)$? For any of the models that can be brought into the form of Eq. (1), one has the result from (Norris and Johnson, 1997)

$$W(w_0 + w_1, s_0 + s_1)$$

$$= W_0(w_0, s_0) + N_0 w_1 + T_0 s_1 + \tfrac{1}{2}C_n a_n(w_0)w_1^2 + \tfrac{1}{2}C_t a_t(w_0)s_1^2$$

$$+ \text{path-dependent third-order terms in } (w_1, s_1), \tag{4}$$

where N_0 and T_0 are the normal and transverse components, respectively, of the force between the grains at the state of displacement (w_0, s_0). The terms quadratic in w_1, s_1 are independent of the path taken in (w_1, s_1) space. Moreover, because the coefficients of these terms depend only on w_0 and not upon s_0, these terms are independent of the path of the original deformation: $s_0 = s_0(w_0)$. For this reason, the elastic constants of the ensemble of grains are well-defined functions of the current state of strain $\boldsymbol{\epsilon}$; for any of the models that can be brought to the form (1) the elastic constants can be written, in the effective medium approximation, as Eq. (60) of Norris and Johnson (1997):

$$C_{ijkl}(\boldsymbol{\epsilon}) = (1-\phi)\frac{nR^2}{4V_0}\{\langle[4C_n a_n(\xi) - 4C_t a_t(\xi)]N_i N_j N_k N_l\rangle$$

$$+ \langle C_t a_t(\xi)(\delta_{ik}N_j N_l + \delta_{il}N_j N_k + \delta_{jl}N_i N_k + \delta_{jk}N_i N_l)\rangle\}. \tag{5}$$

Here $\mathbf{N}$ is a unit vector along the sphere centers, $\xi \equiv -\mathbf{N}\cdot\boldsymbol{\epsilon}\cdot\mathbf{N}R$, $\langle\cdots\rangle$ represents an average over solid angles, n is the average number of contacts per grain, ϕ is the porosity, and $V_0 = (\frac{4}{3})\pi R^3$ is the volume of a single grain. In addition to being an effective medium approximation, Eq. (5) also presumes that the relative change in sample dimensions is negligible compared against the relative change in stiffness. For sake of numerical definiteness, we shall assume the angular distribution of contacts is isotropic, although Jenkins et al. (1989) have

Downloaded 04 May 2010 to 171.66.16.26. Redistribution subject to ASME license or copyright; see http://www.asme.org/terms/Terms_Use.cfm

argued that there is evidence of anisotropy in the distribution of contacts due to the directionality imposed by gravity.

The effective medium theory of Norris and Johnson (1997) was derived by finessing the issue of the rotation of the grains. If a symmetric strain is applied to the sample, it was pointed out that the total torque on each grain will vanish and therefore the grains will not rotate. It is therefore possible to deduce the (properly symmetrized) elastic constants and stresses as a function of the strain history. These elastic constants are the relevant ones for long-wavelength wave propagation, even, say, for shear waves. In such a motion, the grains may rotate but they do so in such a manner that the torque vanishes and the relevant elastic constants are the "torque-free" ones. See Schwartz et al. (1984) for details.

Within the effective medium framework, the validity of Eq. (5) does *not* depend on the strain history of the composite system. In the special case appropriate to Hertz-Mindlin contacts, for which Eq. (3) holds, Eq. (5) reduces to

$$C_{ijkl} = \frac{3n(1-\phi)}{4\pi^2 R^{1/2} B_W (2B_W + C_W)} \langle \xi^{1/2} \{ 2C_W N_i N_j N_k N_l + B_W (\delta_{ik} N_j N_l + \delta_{il} N_j N_k + \delta_{jl} N_i N_k + \delta_{jk} N_i N_l) \} \rangle, \quad (6)$$

where

$$B_W = \frac{2}{\pi C_n}, \quad C_W = \frac{4}{\pi}\left[\frac{1}{C_t} - \frac{1}{C_n}\right]. \quad (7)$$

Equations (6) are identical with those derived by Walton (1987) who made the unnecessary assumption that all components of the strain ϵ_{pq} are simultaneously increased together, holding their ratios fixed. We emphasize, again, that these equations are valid for any applied strain, and are independent of the history of the granular medium.

2.2 Analytic Results for Specific Strain Paths. Let us consider a special case of interest in which the strain is a combination of hydrostatic and uniaxial compression:

$$\epsilon_{ij} = \epsilon \delta_{ij} + \epsilon_3 \delta_{i3} \delta_{j3}. \quad (8)$$

2.2.1 Sound Speeds. In this case it is clear that the system will exhibit the symmetries usually associated with transversely isotropic materials and, after some rearranging, we have from Eq. (6)

$$C_{11} \equiv C_{1111} = \frac{\gamma}{\alpha}\left\{ 2B_W [I_0(\alpha) - I_2(\alpha)] + \frac{3C_W}{4}[I_0(\alpha) - 2I_2(\alpha) + I_4(\alpha)] \right\},$$

$$C_{13} \equiv C_{1133} = \frac{\gamma}{\alpha}\{ C_W [I_2(\alpha) - I_4(\alpha)] \},$$

$$C_{33} \equiv C_{3333} = \frac{\gamma}{\alpha}\{ 4B_W I_2(\alpha) + 2C_W I_4(\alpha) \},$$

$$C_{44} \equiv C_{2323} = \frac{\gamma}{\alpha}\left\{ \frac{B_W}{2}[I_0(\alpha) + I_2(\alpha)] + C_W [I_2(\alpha) - I_4(\alpha)] \right\},$$

$$C_{66} \equiv C_{1212} = \frac{\gamma}{\alpha}\left\{ B_W [I_0(\alpha) - I_2(\alpha)] + \frac{C_W}{4}[I_0(\alpha) - 2I_2(\alpha) + I_4(\alpha)] \right\}, \quad (9)$$

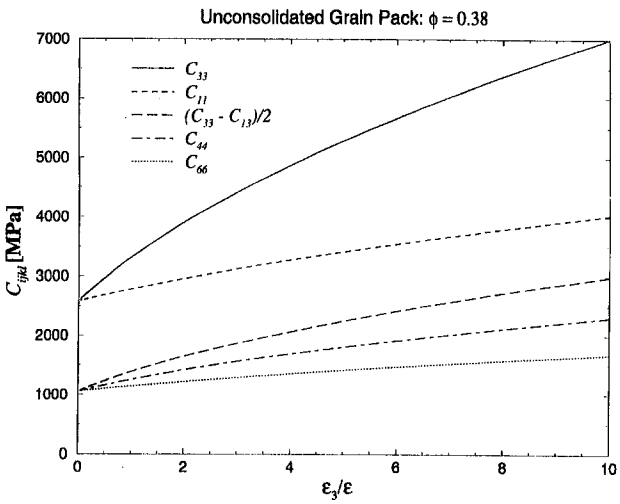


Fig. 1 The values of $\{C_{ij}\}$ are shown as functions of ϵ_3/ϵ. These are calculated from Eqs. (9) with the following parameter values: C_n = 95 GPa, C_t/C_n = 0.35, n = 6.5, ϕ = 0.38, ϵ = −0.0035.

where

$$\gamma \equiv \frac{3n(1-\phi)(-\epsilon)^{1/2}}{4\pi^2 B_W (2B_W + C_W)} = \frac{3}{32} C_n C_t n (1-\phi)(-\epsilon)^{1/2}, \quad (10)$$

$\alpha^2 \equiv \epsilon/\epsilon_3$ and $\{I_n(\alpha)\}$ denotes the integrals

$$I_n(\alpha) \equiv \int_0^1 x^n \sqrt{\alpha^2 + x^2}\, dx, \quad (11)$$

which can be evaluated analytically as

$$I_0(\alpha) = \frac{1}{2}\left[\sqrt{1+\alpha^2} + \alpha^2 \ln\left(\frac{1+\sqrt{1+\alpha^2}}{\alpha}\right)\right],$$

$$I_{2n+2}(\alpha) = \frac{1}{2n+4}[(1+\alpha^2)^{3/2} - (2n+1)\alpha^2 I_{2n}(\alpha)], \quad n \geq 0. \quad (12)$$

In Fig. 1 we show the behavior of the moduli C_{ij} calculated from Eqs. (9)–(12). The values of the parameter set were chosen in order to match our experimental data which we present later in Section 4. Instead of plotting C_{13} we show the combination $(C_{33} - C_{13})/2$ which reduces to the shear modulus, μ as $\epsilon_3/\epsilon \to 0$. (In this limit, C_{11} and C_{33} approach $\lambda + 2\mu$.) As might be expected on physical grounds, the quantity C_{33} shows the greatest variation as ϵ_3/ϵ increases. In Fig. 2 three high symmetry $(V_P/V_S)^2$ ratios are plotted against ϵ_3/ϵ. Shown also are the limiting behaviors as $\epsilon_3/\epsilon \to 0$ and $\epsilon_3/\epsilon \to \infty$. The first of the limits was discussed by Schwartz et al. (1994) within the framework of a simple perturbation expansion based on Walton's original Eq. (6). The second limit was considered by Walton, and Fig. 2 makes clear that the approach to this limiting regime is very slow. This approach is controlled by the logarithmic terms in Eqs. (12); indeed, when the results are replotted on a logarithmic scale (Fig. 3) the approach to the uniaxial limit is evident.

2.2.2 Stress Tensor. In the foregoing subsection we derived results for the second-order elastic constants as well-defined functions of the specific strain, Eq. (8). Experimentally it is difficult to monitor the strain in unconsolidated samples;

Downloaded 04 May 2010 to 171.66.16.26. Redistribution subject to ASME license or copyright; see http://www.asme.org/terms/Terms_Use.cfm

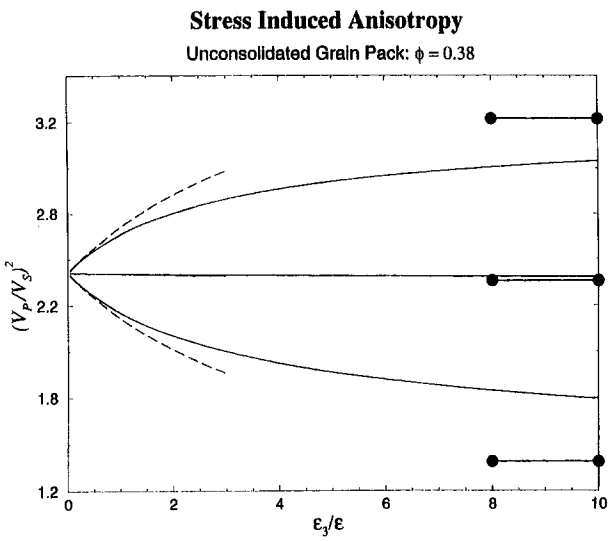


Fig. 2 Three squared sound speed ratios are plotted as functions of ϵ_3/ϵ. The upper and lower curves are the ratios C_{33}/C_{44} and C_{11}/C_{44}; the middle (nearly flat) curve is C_{11}/C_{66}. On the right-hand side the asymptotic values are shown with thick solid lines while the corresponding lines on the left-hand side give the three ratios of the initial slopes, Eqs. (27). Same parameter set as in Fig. 1.

generally it is one or more components of the stress tensor that are measured. Thus, we wish to formulate an equation relating stress to the strain elements. In order to do so, we must make a specific assumption regarding the strain history of the granular packing. In the present discussion we consider the three strain paths described in Fig. 4. In all cases the starting point is Eq. (55) of Norris and Johnson (1997), which we rewrite as

$$\sigma_{ij} = (1 - \phi)\frac{nR}{V_0}\left\{\frac{1}{2}\langle N_i T_j + N_j T_i\rangle - C_n\langle A_n(\xi)N_i N_j\rangle\right\}. \quad (13)$$

Here $\mathbf{T}$ is the path-dependent transverse force for a given contact:

$$T_i = C_t \int_{\text{path}} a_t(\xi)ds_i(\xi), \quad (14)$$

$\xi \equiv -\mathbf{N}\cdot\boldsymbol{\epsilon}\cdot\mathbf{N}R$ is the normal component of displacement, $\mathbf{s} = \mathbf{P}\boldsymbol{\epsilon}\mathbf{N}R$ is the transverse component, $\mathbf{P} = \mathbf{I} - \mathbf{NN}$ is a projection

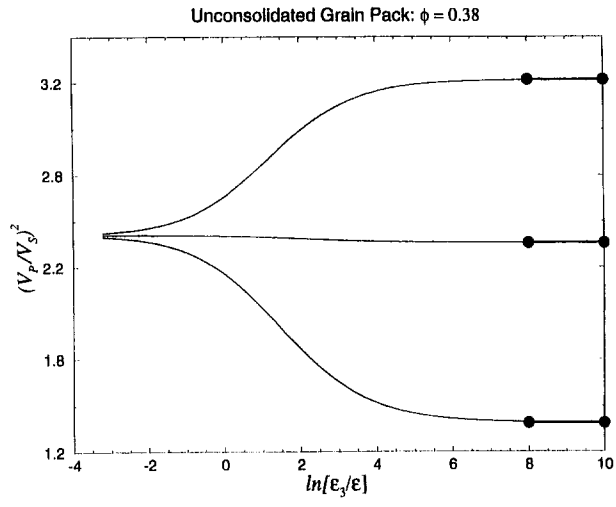


Fig. 3 The same curves shown in Fig. 2 are shown on a logarithmic scale to emphasize the slow approach to the large strain asymptote

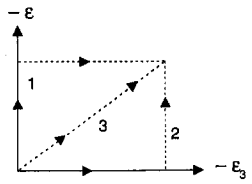


Fig. 4 Three distinct strain paths, all leading to the same final state, are illustrated schematically

operator, and $A_n(\xi) = (\frac{2}{3})R^{1/2}\xi^{3/2}$. The integral in (14) is dependent upon the path $\mathbf{s} = \mathbf{s}(\xi)$. In general, $\mathbf{T}$ and $\mathbf{s}$ are not parallel.

For the special class of deformation paths for which $\mathbf{s}$ for each contact always points in the same direction, we may write

$$\mathbf{ds} = \hat{\mathbf{s}}ds(\xi), \quad (15)$$

where $\hat{\mathbf{s}} = \mathbf{P}\boldsymbol{\epsilon}\mathbf{N}R/s$ is the (constant) unit vector in the direction of transverse displacement and $s = |\mathbf{P}\boldsymbol{\epsilon}\mathbf{N}|R$ is the magnitude of the final value of the transverse displacement. Under these restrictions, $\mathbf{T}$ and $\mathbf{s}$ are parallel and Eq. (13) becomes

$$\sigma_{ij} = (1 - \phi)\frac{nR}{V_0}\left\{C_t R\left\langle\left[\int_{\text{path}} a_t(\xi)ds(\xi)\right]\right.\right.$$
$$\left.\left.\times\frac{1}{2s}(N_i P_{jk} + N_j P_{ik})\epsilon_{kl}N_l\right\rangle - C_n\langle A_n(\xi)N_i N_j\rangle\right\}. \quad (16)$$

Let us consider path 1 in detail. Here the system is first hydrostatically compressed

$$\epsilon_{ij} = x\epsilon\delta_{ij} \quad 0 < x < 1. \quad (17)$$

Equation (17) implies $\xi = -x\epsilon R$ and $s \equiv 0$. The resulting stress is isotropic: $\sigma_{ij} = -p\delta_{ij}$ where the pressure p was first derived by Walton (1987):

$$p = -(1 - \phi)\frac{2nR^3C_n}{9V_0}(-x\epsilon)^{3/2}. \quad (18)$$

Next, an additional uniaxial compression is applied

$$\epsilon_{ij} = \epsilon\delta_{ij} + y\epsilon_3\delta_{i3}\delta_{j3}0 < y < 1. \quad (19)$$

For this path we have

$$\xi = -(\epsilon + y\epsilon_3 N_3^2)R,$$
$$s = -y\epsilon_3[N_3^2(1 - N_3^2)]^{1/2}. \quad (20)$$

At the end of this path, the deformation is that given by Eq. (8). It is straightforward to evaluate the path-dependent integrals implied by (16) as well as the angular averages. In terms of the final strain components the only nonzero stress components are σ_{33} and $\sigma_{11} = \sigma_{22}$:

$$\sigma_{33}(\epsilon, \epsilon_3) = -\frac{2(-\epsilon)^{3/2}(1 - \phi)nR^3}{3\alpha^3V_0}$$
$$\times\{C_t[\alpha^2 I_0(\alpha) + (1 - \alpha^2)I_2(\alpha) - I_4(\alpha) - 2\alpha^3/3]$$
$$+ C_n[\alpha^2 I_2(\alpha) + I_4(\alpha)]\}, \quad (21)$$

and

$$\sigma_{11}(\epsilon, \epsilon_3) = -\frac{(-\epsilon)^{3/2}(1 - \phi)nR^3}{3\alpha^3V_0}$$
$$\times\{-C_t[\alpha^2 I_0(\alpha) + (1 - \alpha^2)I_2 - I_4(\alpha) - 2\alpha^3/3]$$
$$+ C_n[\alpha^2 I_0(\alpha) + (1 - \alpha^2)I_2(\alpha) - I_4(\alpha)]\}. \quad (22)$$

In the second path described in Fig. 4, we have a uniaxial compression followed, rather than preceded, by an isotropic

Downloaded 04 May 2010 to 171.66.16.26. Redistribution subject to ASME license or copyright; see http://www.asme.org/terms/Terms_Use.cfm

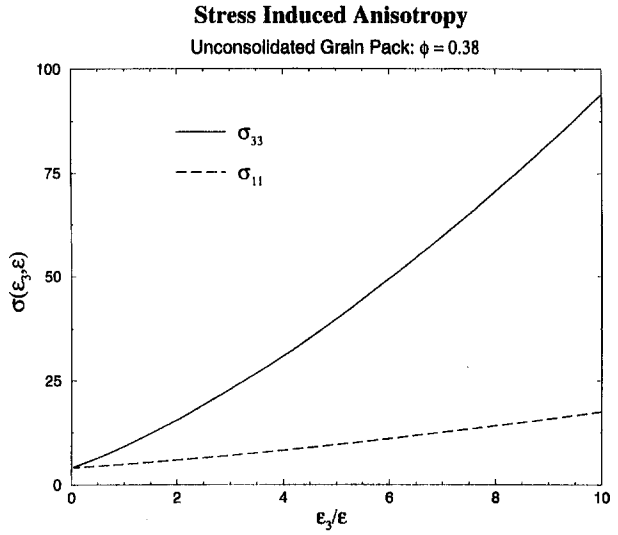


Fig. 5 The vertical and horizontal components of the stress tensor (based on Eqs. (21) and (22)) are plotted as functions of ϵ_3/ϵ. Same parameter set as in Fig. 1.

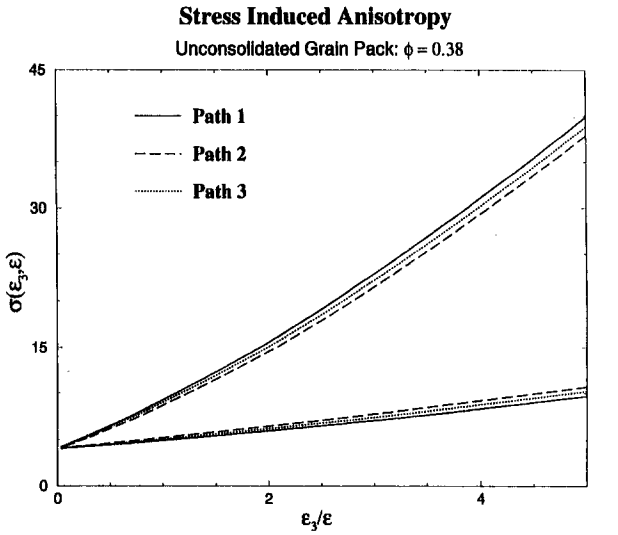


Fig. 6 The vertical and horizontal components of the stress tensor, based on the three paths shown in Fig. 4, are compared in the small strain regime. The three sets of curves remain very close for all values of ϵ_3/ϵ.

compression. The final strain configuration is the same as for path 1 but the corresponding stress is now given by

$$\sigma_{33}(\epsilon, \epsilon_3) = -\frac{2(-\epsilon)^{3/2}(1-\phi)nR^3}{3\alpha^3 V_0} \times \left\{\frac{1}{12}C_t + C_n[\alpha^2 I_2(\alpha) + I_4(\alpha)]\right\}, \quad (23)$$

and

$$\sigma_{11}(\epsilon, \epsilon_3) = -\frac{(-\epsilon)^{3/2}(1-\phi)nR^3}{3\alpha^3 V_0}\left\{-\frac{1}{12}C_t + C_n[\alpha^2 I_0(\alpha) + (1-\alpha^2)I_2(\alpha) - I_4(\alpha)]\right\}. \quad (24)$$

Finally, for the third path in Fig. 4, where the two strain components are applied simultaneously, we have

$$\sigma_{33}(\epsilon, \epsilon_3) = -\frac{2(-\epsilon)^{3/2}(1-\phi)nR^3}{3\alpha^3 V_0} \times \{C_t[I_2(\alpha) - I_4(\alpha)] + C_n[\alpha^2 I_2(\alpha) + I_4(\alpha)]\}, \quad (25)$$

and

$$\sigma_{11}(\epsilon, \epsilon_3) = -\frac{(-\epsilon)^{3/2}(1-\phi)nR^3}{3\alpha^3 V_0}\{-C_t[I_2(\alpha) - I_4(\alpha)] + C_n[\alpha^2 I_0(\alpha) + (1-\alpha^2)I_2(\alpha) - I_4(\alpha)]\}. \quad (26)$$

In each of these cases we have $\sigma_{11}(\epsilon, \epsilon_3) = \sigma_{22}(\epsilon, \epsilon_3)$. Note that the limit $\epsilon_3 \to 0$ leads to the result for hydrostatic pressure (Eq. (3.19) of Walton (1987)) and that in the opposite limit of purely uniaxial compression, $\epsilon \to 0$, the above equations all reduce to Eqs. (3.24) of Walton (1987). The stress components corresponding to the first strain path are plotted in Fig. 5. In Fig. 6, results for the different strain paths considered above are compared on an expanded scale; clearly, the differences between the three sets of curves are quite small.

3 Remarks on Third-Order Hyperelasticity Theory

Since the effective elastic constants are unique, path-independent functions of the strain tensor, it might be supposed that they are equivalent to the predictions of an effective, nonlinear hyperelastic medium. This is *not* so for the simple reason that the contact forces are path dependent, and certainly not derivable from a potential energy function. Thus the macroscopic equations of motion are not derivable from an elastic energy density function. At some point the analogy must break down. Here we demonstrate a specific contradiction between the two points of view.

It was shown in Norris and Johnson (1997) that the analogy breaks down at the third order in the expansion of the change in energy due to an incremental deformation. Although the second-order coefficients, the usual elastic constants, are path independent, the third-order terms are not. In conventional nonlinear elasticity theory, it is these third-order coefficients which determine how the sound speeds change under the application of an incremental strain applied to the system taken in some conveniently chosen reference state. Here we take the reference state to be *any* state of purely isotropic strain; this is always a valid choice for isotropic elastic systems. Let us therefore consider how the elastic constants change when a small uniaxial strain is superimposed upon a large isotropic strain, i.e., Eq. (8) to first order in ϵ_3/ϵ. It is straightforward to expand equations (9) to first order in $1/\sqrt{\alpha}$. These specific results had been reported by Schwartz et al. (1994).

$$C_{11} = \gamma\left[\frac{4B_W}{3} + \frac{2C_W}{5} + \frac{\epsilon_3}{\epsilon}\left(\frac{2B_W}{15} + \frac{C_W}{35}\right)\right],$$

$$C_{13} = \gamma\left[\frac{2C_W}{15} + \frac{\epsilon_3}{\epsilon}\left(\frac{C_W}{35}\right)\right],$$

$$C_{33} = \gamma\left[\frac{4B_W}{3} + \frac{2C_W}{5} + \frac{\epsilon_3}{\epsilon}\left(\frac{2B_W}{5} + \frac{C_W}{7}\right)\right],$$

$$C_{44} = \gamma\left[\frac{2B_W}{3} + \frac{2C_W}{15} + \frac{\epsilon_3}{\epsilon}\left(\frac{2B_W}{15} + \frac{C_W}{35}\right)\right],$$

$$C_{66} = \gamma\left[\frac{2B_W}{3} + \frac{2C_W}{15} + \frac{\epsilon_3}{\epsilon}\left(\frac{B_W}{15} + \frac{C_W}{105}\right)\right]. \quad (27)$$

Similarly, let us now consider the predictions of third-order elasticity theory for these same moduli under the same condi-

Downloaded 04 May 2010 to 171.66.16.26. Redistribution subject to ASME license or copyright; see http://www.asme.org/terms/Terms_Use.cfm

tions of small ϵ_3 but arbitary ϵ. The second and third-order elastic constants will, therefore, be seen to be functions of the isotropic strain, ϵ. Our derivation proceeds along the lines of Hughes and Kelly (1953), who considered the similar problem of the change of speeds under uniaxial *stress*; we use the Landau and Lifschitz (1986) notation as presented by Gol'dberg (1961). Thus, the second-order elastic constants are λ, μ while the third-order ones are A, B, C. Let us consider wave motion in which the propagation direction is confined to the x–z plane: $\mathbf{u} = [u(x, z), v(x, z), w(x, z)]$. We find

$$\rho_0 \frac{\partial^2 u}{\partial t^2} = C_{11} \frac{\partial^2 u}{\partial x^2} + C_{44} \frac{\partial^2 u}{\partial z^2} + (C_{13} + C_{44}) \frac{\partial^2 w}{\partial x \partial z},$$

$$\rho_0 \frac{\partial^2 w}{\partial t^2} = C_{44} \frac{\partial^2 w}{\partial x^2} + C_{33} \frac{\partial^2 w}{\partial z^2} + (C_{13} + C_{44}) \frac{\partial^2 u}{\partial x \partial z},$$

$$\rho_0 \frac{\partial^2 v}{\partial t^2} = C_{66} \frac{\partial^2 v}{\partial x^2} + C_{44} \frac{\partial^2 v}{\partial z^2}, \tag{28}$$

where (x, z) refer to the original (Lagrangian) position and, to first order in ϵ_3:

$$C_{11} = \lambda + 2\mu + \epsilon_3(\lambda + 2B + 2C),$$

$$C_{13} = \lambda + \epsilon_3(-\mu + 2B + 2C),$$

$$C_{33} = \lambda + 2\mu + \epsilon_3(3\lambda + 6\mu + 2A + 6B + 2C),$$

$$C_{44} = \mu + \epsilon_3(\lambda + 2\mu + A/2 + B),$$

$$C_{66} = \mu + \epsilon_3(\lambda + B). \tag{29}$$

Is there any way in which Eqs. (27) can be made to be equivalent to Eqs. (29)? First, we see that there is no problem with the zero-order terms which imply $\lambda = (\frac{2}{15})C_W\gamma$ and $\mu = ((\frac{2}{3})B_W + (\frac{2}{15})C_W)\gamma$. Second, the third-order constants must have a divergent term: $(A, B, C) \propto (-\epsilon)^{-(1/2)}$. Therefore, for small enough ϵ, we may neglect (λ, μ) as compared with (A, B, C) in the terms proportional to ϵ_3 because $(\lambda, \mu) \propto (-\epsilon)^{(1/2)}$. Similarly, we may neglect the distinction between the new density and the original $\rho' = (1 + \epsilon_3)\rho_0$ as well as that between the new coordinates and the old $z' = (1 + \epsilon_3)z$. There remains an unavoidable problem: If one sets the coefficient of ϵ_3 in each of Eqs. (27) equal to its counterpart in (29) (neglecting λ and μ as compared with A, B, C) we have five equations in only three unknowns. There is no set of the quantities (A, B, C) which can simultaneously satisfy these equations. This makes concrete the general demonstration that, for path-dependent contact forces, the second-order elastic constants are well-defined functions of the strain but the third-order constants are path dependent.

A careful inspection of (27) and (29) shows that the quantities dependent upon C_W can be made to match correctly but that the coefficients of B_W can not. This is a reflection of the fact that, within Walton's (1987) formulation, the normal component of stiffness for each contact is proportional to $2B_W + C_W$ whereas the tangential stiffness is proportional to $2B_W$; see Eqs. (2.13) and (2.14) of Walton (1987). It has been emphasized previously (Norris and Johnson, 1997) that the difficulty in reconciling models of path-dependent contact forces with nonlinear elasticity stems from the transverse components of the contact stiffness. Alternatively, we may say that the divergent parts of the changes in C_{ij} are predicted to obey the following relationships, according to third-order elasticity theory, Eqs. (29):

$$\Delta C_{11} - \Delta C_{13} = 0,$$

$$\Delta C_{11} + \Delta C_{33} - 2\Delta C_{13} - 4\Delta C_{44} = 0. \tag{30}$$

We see from Eqs. (27) that the second of these equations is satisfied by the predictions of the contact theory, but not the first. So to say, we have four equations (not five) in three unknowns. This is a specific manifestation of a more general property of this contact theory, derived in Norris and Johnson (1997), that changes in second-order elastic constants due to an imposed strain are governed, to first order, by four "third-order modulii," B_{111}, B_{112}, B_{123}, and $\tilde{B}$ and *not* the usual three (A, B, C).

Table 1 The quantities which determine the strain-induced anisotropy of the elastic constants for a random sphere pack, via Eqs. (27), as compared to the best fit values assuming the validity of third-order elasticity theory, equations (29). We assume $\lambda = \mu = 24$ GPa as appropriate for a silica glass. The best fit values are (ϵ/γ) $(A, B, C) = (27.2, 34.7, -17.2)$. All values in 10^{-4} $(\text{Pa})^{-1}$.

	Contact Theory		Third-Order Elasticity	
ΔC_{11}	$\left(\frac{2B_W}{15} + \frac{C_W}{35}\right)$	71.1	35.1	$\frac{\epsilon}{\gamma}(2B + 2C)$
ΔC_{13}	$\left(\frac{C_W}{35}\right)$	4.7	35.1	$\frac{\epsilon}{\gamma}(2B + 2C)$
ΔC_{33}	$\left(\frac{2B_W}{5} + \frac{C_W}{7}\right)$	222.6	228.3	$\frac{\epsilon}{\gamma}(2A + 6B + 2C)$
ΔC_{44}	$\left(\frac{2B_W}{15} + \frac{C_W}{35}\right)$	71.1	48.3	$\frac{\epsilon}{\gamma}(A/2 + B)$
ΔC_{66}	$\left(\frac{B_W}{15} + \frac{C_W}{105}\right)$	34.7	34.7	$\frac{\epsilon}{\gamma}(B)$

How serious an error might be made were one to assume the validity of third-order elasticity theory for a system such as this? Let us consider a hypothetical case of a granular medium whose strain dependent moduli are accurately given by Eq. (27) (for small ϵ_3). An experimental measurement of the change of elastic constants with uniaxial strain would be proportional to the quantities within parentheses in (27). Typical values are given in Table 1, assuming the beads are made of glass. If one were to make a best least-squares fit of Eqs. (29) to these values, the resultant values of these quantities are poorly fit by third-order elasticity theory; these values are also listed in Table 1. We see that there is an appreciable problem were one naively to apply third-order elasticity theory to the strain dependence of the sound speeds.

Winkler and Liu (1997) have already performed an experiment analogous to the *gedanken* experiment shown in Table 1. They have measured the changes in the speeds of sound as a function of applied stresses in a suite of nine rocks. They considered P and S speeds as a function of isotropic pressure and they considered P and both S speeds for waves propagating perpendicular to the axis of an applied uniaxial stress. From the initial slopes of these five measurements they determined a best fit set of values for the third-order elastic constants (A, B, C). The quality of their fit is much better than that indicated in our Table 1. Thus, we conclude that the concept of an elastic energy of deformation for sedimentary rocks may be a valid one, at least through third order in the applied strain—unlike the model of the present paper. For larger stress, though, it is known that rocks undergo hysteretic deformation (Brown et al., 1989; Hilbert et al., 1994).

4 Comparison With Experimental Data

Our measurements were made in a specialized compaction cell that was constructed to study the developing elastic properties of artificial sediments as a function of axial stress. A block diagram of the compaction cell is shown in Fig. 7. Anisotropic compressional and four-component shear wave velocities were recorded using transducers oriented parallel and perpendicular

Downloaded 04 May 2010 to 171.66.16.26. Redistribution subject to ASME license or copyright; see http://www.asme.org/terms/Terms_Use.cfm

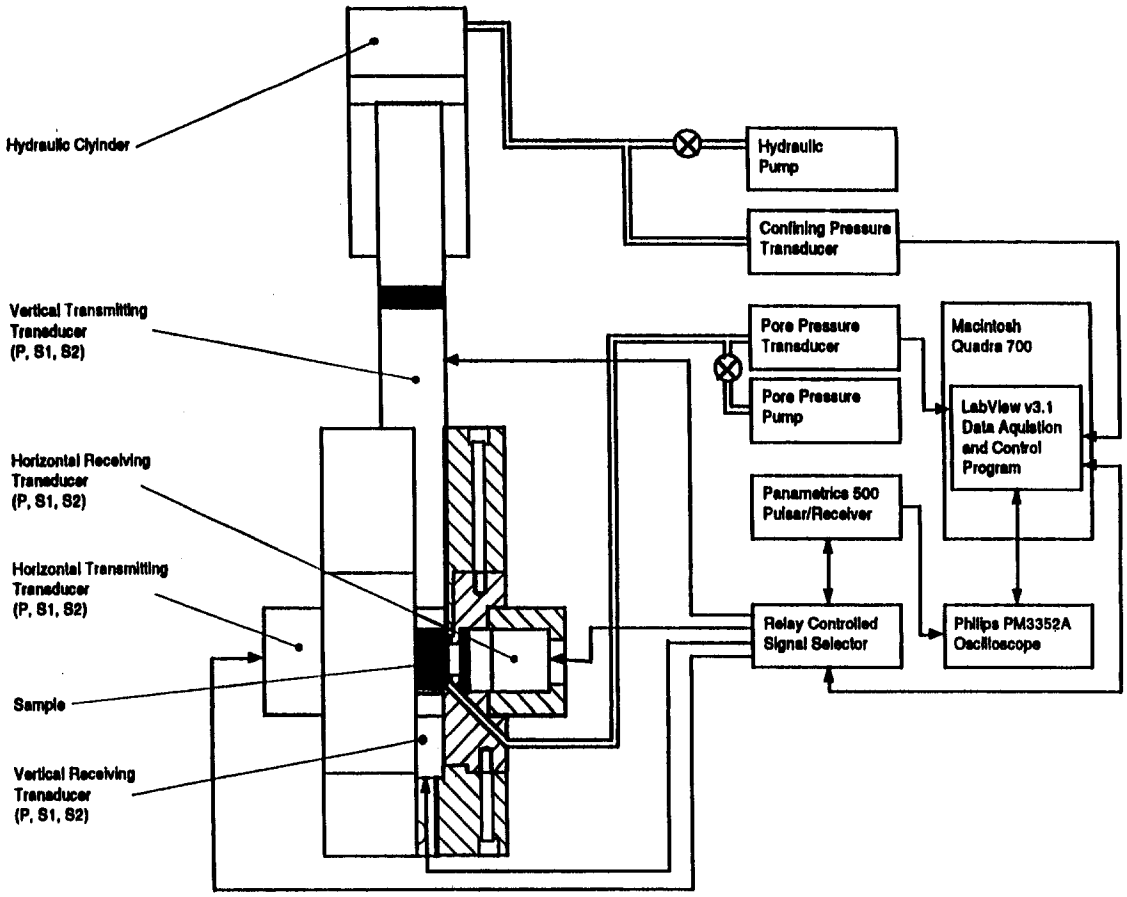


Fig. 7 Block diagram for the experimental setup used to measure the sound speeds as a function of applied stress

to the direction of axial stress. The compaction cell was constructed of EN303 stainless steel and the system has a maximum confining stress of 110 MPa. The cell is presumed to be rigid enough that the sample experiences a macroscopic uniaxial strain (negligible lateral motion). A Power Team 1826 25 ton hydraulic shop press applies the axial stress to the vertical piston. Transducers for elastic wave measurements are 4 × Verde GeoScience compressional and polarized shear wave 500 kHz ultrasonic transducers. Sample length is dynamically measured during the acquisition using a Schlumberger DC50 LVDT.

The sample we studied was comprised of dry mono-dispersed spherical glass beads with diameters of roughly 70 μm. The beads were placed in the chamber of the compaction cell and were uniaxially strained by the application of axial stresses up to 100 MPa applied over four separate cycles. To determine the P and S-wave velocities, we examined the corresponding waveforms as a function of stress for each of the four cycles. As expected, the most stable results were obtained for the last stress cycle. By this point the individual beads appear to have reached relatively stable configurations within the disordered packing. In almost all of the waveforms, the desired arrival is easily identified. However, properly locating the shear arrivals can be difficult, particularly at low applied stresses for the mode propagating normal to the direction of axial stress and polarized perpendicular to the direction of axial stress. We found that identification of weak arrivals was facilitated by examining the waveforms as a function of applied stress. While the best signal to noise ratios were obtained at the largest applied stress levels, the weaker arrivals could be identified by following the desired point of constant phase (first zero crossing) to lower stresses.

Figure 8 is a composite plot of the measured velocities for the fourth cycle of applied stress. Clearly, even for this simplest of granular media, the data show considerable hysteresis. The physical basis for this hysteresis is most likely small rearrangements in the positions of the grains during the *increasing* stress part of the cycle. Once the particles are tightly wedged together, one might assume that there are many fewer rearrangements in *decreasing* stress part of the cycle. Indeed, we believe that

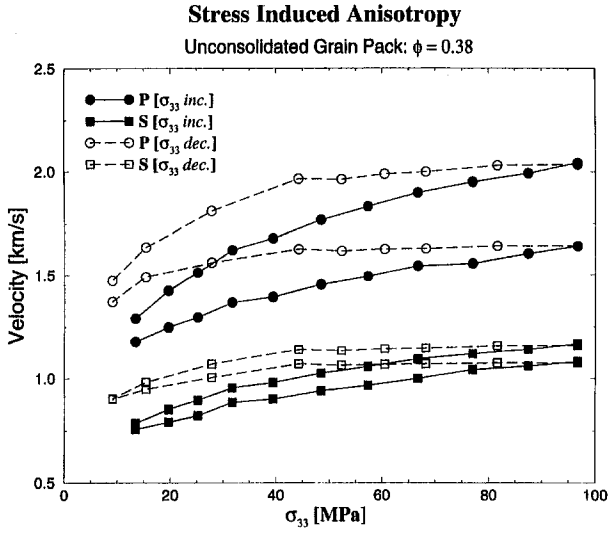
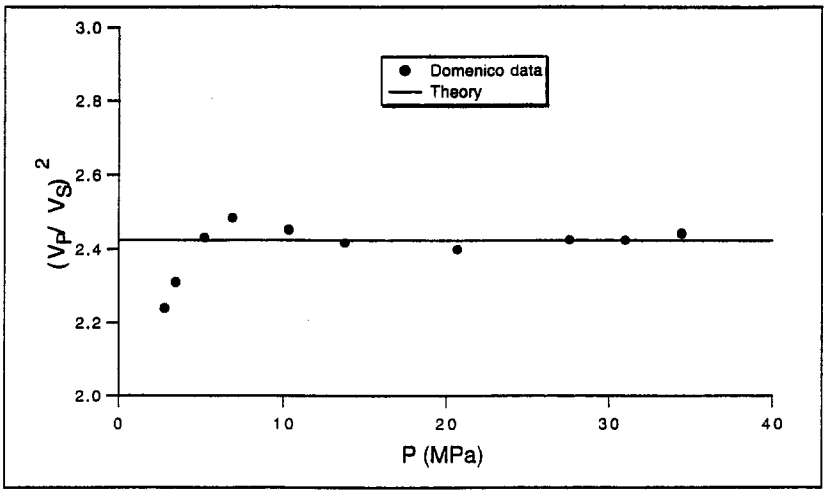


Fig. 8 Experimental results for two compressional mode (circles) and two shear mode (squares) speeds are plotted as a functions of applied vertical stress during the fourth stress cycle. The filled (open) symbols correspond to the increasing (decreasing) stress part of the cycle. The faster and slower *P* waves are associated with vertical and horizontal propagation, respectively. The faster *S* wave propagates vertically while the slower *S* wave propagates horizontally and is polarized horizontally.

Downloaded 04 May 2010 to 171.66.16.26. Redistribution subject to ASME license or copyright; see http://www.asme.org/terms/Terms_Use.cfm



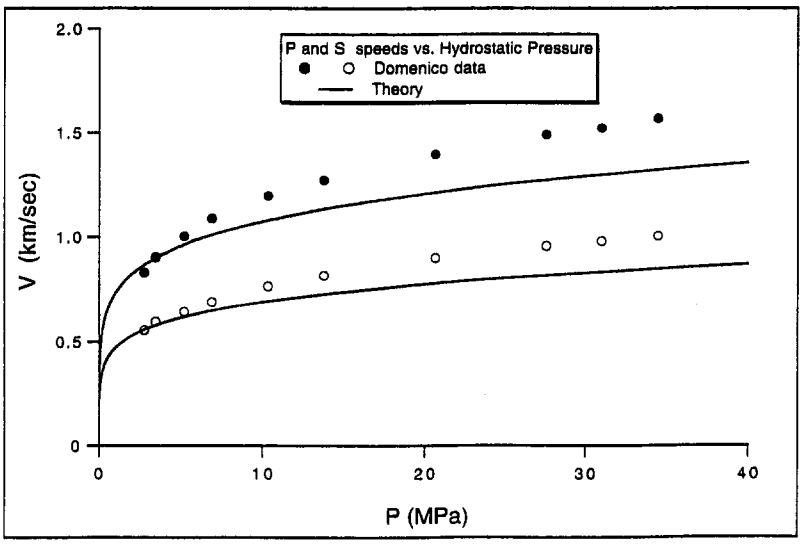


Fig. 9 V_P and V_S as a function of confining pressure for unconcolidated glass beads. The data are from Domenico (1977). The calculated value of the ratio V_P/V_S is very sensitive to the assumed value of C_t/C_n, here taken to be 0.35. The overall scale of the speeds is then set by C_n, here taken to be 95 GPa. We assume the average coordination number is n = 6.5.

this wedging of grains during the stress cycles contributes to a *residual* stress distribution in the packing even when the piston is removed and there is no applied stress. It is this residual stress that gives rise to the internal strain that we model with the parameter ϵ, the initial hydrostatic compression.

Because granular rearrangements involve breaking and reforming of contacts, they invalidate the assumption of our effective medium description of the packing. For this reason we compare our equations only with the decreasing stress part of the last cycle. To get a reasonable fit to the data we have treated the quantities n, C_n, C_t/C_n, and ϵ as adjustable parameters. We somewhat arbitrarily take n = 6.5, although only the products, nC_n and nC_t, enter in the theory. First, we demand consistency of our calculations with the data of Domenico (1977) who measured V_P and V_S as a function of *hydrostatic* confining pressure on unconsolidated glass beads. We see in Fig. 9 that the ratio V_P/V_S is essentially independent of pressure, as the theory predicts. This sets the value of the ratio C_t/C_n = 0.35. Then, the value C_n = 95 GPa was taken to ensure a reasonable overall fit to the actual speeds, as shown in Fig. 9. (For comparison, the first of Eqs. (2) yields C_n = 128 GPa and C_t/C_n = 0.857 if we take μ_s = 24 GPa and ν_s = 0.25 as appropriate for a silica glass. This would predict a value V_P/V_S that is significantly lower than the measured pressure-independent value.) Finally, the value ϵ = −0.0035 was chosen to get an acceptable fit to our own measured data. Our fit to the data is presented in Figs. 10 and 11. The calculated curves are faithful to the qualitative trends in the measured data and are in good overall agreement with the absolute values of the sound speeds and the V_P/V_S ratios. In connection with Fig. 11, we note that there is considerably less difference in the V_p/V_s ratios for the increasing and decreasing parts of the stress cycle than was seen for the absolute velocities shown in Fig. 8. We remind the reader that we have made two critical assumptions: the validity of the effective medium approximation and the assumption of no-slip between grains, either of which may be suspect. In the case of the former assumption we note that Liu et al. (1995) have given convincing theoretical and experimental arguments for the existence of a very broad (~exponential) distribution of contact forces. In the case of the latter assumption we note that our best-fit value of C_t/C_n is less than half that predicted from a literal interpretation of Eq. (2).

5 Conclusions

We have considered the elastic properties of granular media, specifically systems for which each grain-grain contact is de-

Downloaded 04 May 2010 to 171.66.16.26. Redistribution subject to ASME license or copyright; see http://www.asme.org/terms/Terms_Use.cfm

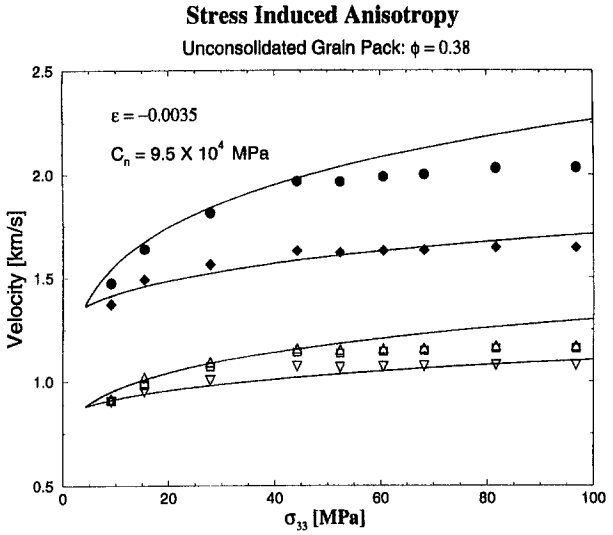


Fig. 10 The experimental speeds shown in Fig. 8 for *decreasing* applied stress are compared with the results of our calculations. Here the relation between stress and strain was calculated from Eqs. (21) and (22). Same parameter set as in Fig. 1.

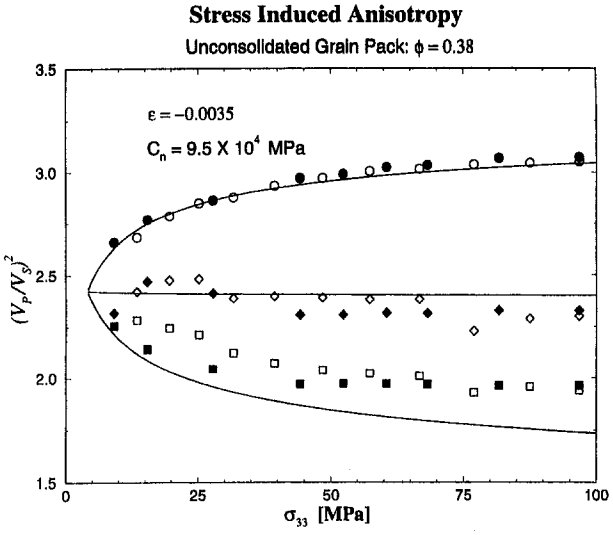


Fig. 11 Ratios of squared *P* to *S* speeds calculated as in Fig. 10 are shown together with experimental data for both the increasing and decreasing parts of the fourth stress cycle. (The relation between σ_{ij} and ϵ_{ij} is again calculated from Eqs. (21) and (22).) As in Fig. 2, the upper curve and the circles represent C_{33}/C_{44}, the middle curve and the diamonds represent C_{11}/C_{44}, and the lower curve and the squares represent C_{11}/C_{66}. In all three cases, the filled (open) symbols are the measured ratios for decreasing (increasing) stress.

scribed by a slight generalization of the Hertz-Mindlin theory. Within the context of a simple effective medium theory, we have derived expressions which describe each elastic constant as a function of a combined hydrostatic and uniaxial strain. This is a path-independent result. We have explored three different assumptions regarding the order in which the strain is applied and have calculated how the stress depends upon strain for each path. Although the second-order elastic constants are well-defined functions of the strain, the third-order constants are not. We have shown specifically how the concept of third-order elastic constants breaks down when a small uniaxial strain is applied to an unconsolidated granular medium that already has a large hydrostatic strain. Finally, we have shown how our experimental data on sound speeds measured as a function of applied stress can be understood if one assumes there is a remanent hydrostatic strain in the system.

Acknowledgments

The work of D. Elata and J. G. Berryman was performed under the auspices of the U. S. Department of Energy by the Lawrence Livermore National Laboratory under contract No. W-7405-ENG-48 and supported specifically by the Geosciences Research Program of the DOE Office of Energy Research within the Office of Basic Energy Sciences, Division of Engineering and Geosciences.

References

Berryman, J. G., 1979, "Long-wave elastic anisotropy in transversely isotropic media," *Geophysics,* Vol. 44, pp. 896–917.

Bideau, D., and Dodds, J., eds., 1991, *Physics of Granular Media,* Les Houches Series, Nova Science, Commack, NY.

Brown, E. T., Bray, J. W., and Santarelli, F. J., 1989, "Influence of Stress-Dependent Elastic Moduli on Stresses and Strains around Axisymmetric Boreholes," *Rock Mechanics and Rock Engineering,* Vol. 22, pp. 189–203.

Domenico, S. N., 1977, "Elastic properties of unconsolidated porous sand reservoirs," *Geophysics,* Vol. 42, pp. 1339–1368.

Elata, D., 1996, "On the Oblique Compression of Two Elastic Spheres," ASME JOURNAL OF APPLIED MECHANICS, Vol. 63, pp. 1039–1041.

Gol'dberg, Z. A., 1961, "Interaction of Plane Longitudinal and Transverse Elastic Waves," *Soviet Physics-Acoustics,* Vol. 6, pp. 306–310.

Helbig, K., 1983, "Elliptical anisotropy—Its significance and meaning," *Geophysics,* Vol. 48, pp. 825–832.

Hilbert, L. B., Hwong, T. K., Cook, N. G. W., Nihei, K. T., and Myer, L. R., 1994, "Effects of Strain Amplitude on the static and dynamic nonlinear deformation of Berea sandstone," *Rock Mechanics,* Nelson and Laubach, eds., Balkema, Rotterdam.

Hughes, D. S., and Kelly, J. L., 1953, "Second-Order Elastic Deformation of Solids," *Physical Review,* Vol. 92, pp. 1145–1149.

Jenkins, J. T., Cundall, P. A., and Ishibashi, I., 1989, "Micromechanical modeling of granular materials with the assistance of experiments and numerical simulations," *Powders and Grains,* Biarez and Gourvès, eds., Balkema, Rotterdam, pp. 257–264.

Landau, L. D., and Lifshitz, E. M., 1986, *Theory of Elasticity,* 3rd Ed., Pergamon, Oxford, pp. 106–107.

Liu, C.-h., Nagel, S. R., Schecter, D. A., Coppersmith, S. N., Majumdar, S., Narayan, O., and Witten, T. A., 1995, "Force Fluctuations in Bead Packs," *Science,* Vol. 269, pp. 513–515.

Lockner, D. A., Walsh, J. B., and Byerlee, J. D., 1977, "Changes in seismic velocity and attenuation during deformation of granite," *Journal of Geophysical Research,* Vol. 82, pp. 5374–5378.

Mehta, A., ed., 1991, *Granular Media: An Interdisciplinary Approach,* Springer, New York.

Mindlin, R. D., 1949, "Compliance of Elastic Bodies in Contact," ASME JOURNAL OF APPLIED MECHANICS, Vol. 71, pp. 259–268.

Mindlin, R. D., and Deresiewicz, H., 1953, "Elastic Spheres in Contact Under Varying Oblique Forces," ASME JOURNAL OF APPLIED MECHANICS, Vol. 75, pp. 327–344.

Nagel, S. R., 1992, "Instabilities in a Sandpile," *Reviews of Modern Physics,* Vol. 64, pp. 321–325.

Norris, A. N., and Johnson, D. L., 1997, "Nonlinear Elasticity of Granular Media," ASME JOURNAL OF APPLIED MECHANICS, Vol. 64, pp. 39–49.

Nur, A., and Simmons, G., 1969, "Stress-induced velocity anisotropy in rock: An experimental study," *Journal of Geophysical Research,* Vol. 74, pp. 6667–6674.

Nur, A., 1971, "Effects of stress on velocity anisotropy in rocks with cracks," *Journal of Geophysical Research,* Vol. 76, pp. 2022–2034.

Sayers, C. M., 1988, "Stress-induced ultrasonic wave velocity anisotropy in fractured rock," *Ultrasonics,* Vol. 26, pp. 311–317.

Sayers, C. M., van Munster, J. G., and King, M. S., 1990, "Stress-induced ultrasonic anisotropy in Berea sandstone," *International Journal of Rock Mechanics, Mining Science & Geomechanics Abstracts,* Vol. 27, pp. 429–436.

Schwartz, L. M., Johnson, D. L., and Feng, S., 1984, "Vibrational Modes in Granular Materials," *Physical Review Letters,* Vol. 52, pp. 831–834.

Schwartz, L. M., Murphy, W. M., and Berryman, J. G., 1994, "Stress-induced transverse isotropy in rocks," *SEG Technical Program Expanded Abstracts,* Sixty-Fourth Annual International Meeting and Exposition, p. 1081.

Thomsen, L. M., 1986, "Weak elastic anisotropy," *Geophysics,* Vol. 51, pp. 1954–1966.

Walsh, J. B., 1965, "The effects of cracks on the uniaxial elastic compression of rocks," *Journal of Geophysical Research,* Vol. 70, pp. 399–411.

Walton, K., 1987, "The effective elastic moduli of a random packing of spheres," *Journal of the Mechanics and Physics of Solids,* Vol. 35, pp. 213–226.

Winkler, K. W., and Liu, X., 1996, "Measurement of Third Order Elastic Constants in Rocks," *Journal of the Acoustical Society of America,* Vol. 100, pp. 1392–1398.

Yin, H., and Nur, A., 1992, "Stress-induced ultrasonic velocity and attenuation anisotropy of rocks," *SEG Technical Program Expanded Abstracts,* Sixty-Second Annual International Meeting and Exposition, pp. 1073–1076.

Downloaded 04 May 2010 to 171.66.16.26. Redistribution subject to ASME license or copyright; see http://www.asme.org/terms/Terms_Use.cfm

Rigid Stamp Indentation on a Curvilinear Hole Boundary of an Anisotropic Elastic Body

C. W. Fan
Former Ph.D. Student.

Chyanbin Hwu[1]
Professor.

Institute of Aeronautics and Astronautics,
National Cheng Kung University,
Tainan, Taiwan 70101 R.O.C.

A general solution for the problems of rigid stamp indentation on a curvilinear hole boundary of an anisotropic elastic body is obtained by employing the Stroh formalism, the method of analytical continuation, and the technique of mapping a closed curve to a unit circle. With this general solution, two typical curvilinear holes are studied. One is an ellipse, the other is a polygon. Since the transformation functions used in our solutions are not always one to one, some of the solutions are not exact but only approximate. For example, the solutions to the problems of anisotropic plates containing an elliptic hole and isotropic plates containing a polygonal hole are exact, but the solutions to the problems of anisotropic plates containing a polygonal hole are only approximate. Because the solutions presented in this paper are new and no other analytical solution has been found in the literature, the correctness of the present results can only be checked analytically by their reduced forms such as those for isotropic media or those for the stress boundary value problems. To show the generality of our solutions and to see clearly the physical behavior of the indentation problems two numerical examples are given, and their related hoop stress and stress contour are also plotted.

1 Introduction

Since the mechanics analysis of composite materials usually depends upon the model of linear anisotropic elasticity, the analytical study for the anisotropic elasticity becomes important for the understanding of the mechanical behavior of composite materials. Among various formulations, the complex variable formulations developed by Muskhelishvili (1954) for isotropic elasticity, and by Lekhnitskii (1963) and Stroh (1958) for anisotropic elasticity, have been proved to be powerful mathematical tools dealing with the infinite domain problems. Through these methods, many exact closed-form solutions have been obtained for the conventional elasticity problems.

However, due to the mathematical infeasibility, most of the effort was put on the first and second fundamental boundary value problems. For mixed boundary value problems of anisotropic elasticity, very few works have been done. Recently (Fan and Hwu, 1996), a type of the mixed boundary value problems with straight edges—punch problems for an anisotropic elastic half-plane—was solved in detail by employing the Stroh formalism (Ting, 1996) and the method of analytical continuation (Muskhelishvili, 1954). Through the successful experience in dealing with the straight edge boundaries, we now like to study a similar but more complicated problem with curvilinear boundaries. The typical example for this case is the problem of the rigid stamp indentation on a curvilinear hole boundary, which has never been solved analytically in the literature for the anisotropic elastic body. In engineering practice, the solutions to these kind of problems may be useful for the understanding of the mechanical behavior of a pin-loaded hole in composite materials. By surveying the literature, it was found that these kind of problems were usually solved numerically by treating it as a first fundamental problem with the pin-loaded pressure assumed to be a known function. The assumption of the pin-loaded pressure distribution may now be checked by using the analytical solution found in this paper.

In earlier works, Muskhelishvili (1954) and England (1971) developed a theoretical procedure by using the method of analytical continuation to deal with the mixed boundary value problem for an infinite isotropic body containing an elliptical hole which is loaded by a rigid stamp on the hole boundary. Besides the analytical works stated above, most of the effort is devoted to the numerical calculation by finite element or boundary element methods. For instance, Chang (1986) utilized a special finite element to evaluate the effect of the assumed pin-load distribution on the calculated strength and to predict the failure mode of pin-loaded holes in laminated composites. Mahajerin and Sikarskie (1986) developed an efficient boundary element to study loaded holes in composites. Wang (1994) investigated the effects of the clearance between pin and hole, the pin-load magnitude, the contact condition, and the relative pin/lug rigidities by using the finite element method.

In this paper we hope to find a unified analytical solution for general curvilinear hole boundaries and for general anisotropic elastic media. To deal with the curvilinear hole boundaries a one-to-one mapping, which may transform an awkwardly shaped region to a simpler one, is introduced—for example the problems of an anisotropic plate containing an elliptic hole and an isotropic plate containing a polygonal hole. However, there are some cases that a one-to-one mapping function cannot be found, such as a polygonal hole in an anisotropic body. These cases will all be discussed in this paper, and their associated solutions, hoop stress, and stress contour will also be provided.

2 Problem Formulation

Consider a set of rigid stamps of given profiles in contact with the curvilinear hole boundary of an anisotropic elastic body. It is assumed that the stamps indent the hole boundary in such a way that the stamps completely adhere to the elastic body on initial contact and during the subsequent indentation no slip occurs and the contact region does not change. It is

[1] To whom all correspondence should be addressed.

Contributed by the Applied Mechanics Division of THE AMERICAN SOCIETY OF MECHANICAL ENGINEERS for publication in the ASME JOURNAL OF APPLIED MECHANICS.

Discussion on the paper should be addressed to the Technical Editor, Professor Lewis T. Wheeler, Department of Mechanical Engineering, University of Houston, Houston, TX 77204-4792, and will be accepted until four months after final publication of the paper itself in the ASME JOURNAL OF APPLIED MECHANICS.

Manuscript received by the ASME Applied Mechanics Division, Mar. 3, 1997; final revision, Dec. 5, 1997. Associate Technical Editor: X. Markenscoff.

 Copyright © 1998 by ASME

Downloaded 04 May 2010 to 171.66.16.26. Redistribution subject to ASME license or copyright; see http://www.asme.org/terms/Terms_Use.cfm

hoped that a unified solution can be obtained for general curvilinear hole boundaries such as circles, ellipses, and polygonals, etc. In the theory of two-dimensional linear elasticity one of the most useful techniques for the solution of boundary value problems with awkwardly shaped regions is to transform the region into one of a simpler shape. Thus, a transformation $z = m(\zeta)$ is considered in the present problem, which maps the points of a region R_ζ with a circular hole boundary in the ζ-plane onto the points of a region R_z with a curvilinear hole boundary in the z-plane. To define a corresponding one-to-one mapping from R_z onto R_ζ, the transformation between R_z and R_ζ should be one to one and invertible. Hence, $m(\zeta)$ should be holomorphic in R_ζ and $m'(\zeta) \neq 0$ for all $\zeta \in R_\zeta$.

Since the body to be indented is linear anisotropic elastic, it must satisfy the following strain-displacement equations, the stress-strain laws, and the equations of equilibrium,

$$\epsilon_{ij} = \tfrac{1}{2}(u_{i,j} + u_{j,i}), \quad \sigma_{ij} = C_{ijks}\epsilon_{ks}, \quad \sigma_{ij,j} = 0, \tag{2.1}$$

where u_i, σ_{ij}, and ϵ_{ij} are, respectively, the displacement, stress, and strain; the repeated indices imply summation a comma stands for differentiation and C_{ijks} are the elastic constants which are assumed to be fully symmetric and positive definite.

For two-dimensional problems in which x_3 does not appear in the basic equations or the boundary conditions, the general solution to Eqs. (2.1) may be expressed in terms of three holomorphic functions of complex variables $z_\alpha (= x_1 + p_\alpha x_2)$ where p_α, $\alpha = 1, 2, 3$, are the material eigenvalues whose imaginary parts have been arranged to be positive (Stroh, 1958; Lekhnitskii, 1963). As stated in the first paragraph of this section, the function variable is better chosen to be ζ_α instead of z_α, which maps the points outside the curvilinear hole of the z_α-plane onto the points outside the unit circle of the ζ_α-plane according to a one-to-one transformation function,

$$z_\alpha = m_\alpha(\zeta_\alpha), \quad (\alpha \text{ not summed}). \tag{2.2}$$

For the later use of derivation, we now list a compact matrix form solution expressed in terms of the complex variable ζ_α which satisfies all the basic equations given in (2.1), (Stroh, 1958; Ting, 1996)

$$\begin{aligned} \mathbf{u} &= 2\,\mathrm{Re}\{\mathbf{A}\mathbf{f}(\zeta)\} = \mathbf{A}\mathbf{f}(\zeta) + \bar{\mathbf{A}}\overline{\mathbf{f}(\zeta)}, \\ \boldsymbol{\phi} &= 2\,\mathrm{Re}\{\mathbf{B}\mathbf{f}(\zeta)\} = \mathbf{B}\mathbf{f}(\zeta) + \bar{\mathbf{B}}\overline{\mathbf{f}(\zeta)}, \end{aligned} \tag{2.3a}$$

where

$$\begin{aligned} &\mathbf{A} = [\mathbf{a}_1 \quad \mathbf{a}_2 \quad \mathbf{a}_3], \quad \mathbf{B} = [\mathbf{b}_1 \quad \mathbf{b}_2 \quad \mathbf{b}_3], \\ &\mathbf{f}(\zeta) = [f_1(\zeta_1) \quad f_2(\zeta_2) \quad f_3(\zeta_3)]^T. \end{aligned} \tag{2.3b}$$

The superscript T denotes the transpose and the overbar represents the conjugate of a complex number. $\mathbf{u} = (u_1, u_2, u_3)$ is the vector form of displacement. $\boldsymbol{\phi} = (\phi_1, \phi_2, \phi_3)$ stands for the stress function vector which is related to the surface traction $\mathbf{t}$ by

$$\mathbf{t} = \frac{\partial \boldsymbol{\phi}}{\partial s}, \tag{2.4a}$$

where s is the arc length measured along the curved boundary in the direction such that when one faces the direction of increasing s, the material is located on the right-hand side. When the boundary is a plane parallel to the x_2-axis or the x_1-axis, Eq. (2.4a) reduces to

$$\sigma_{i1} = -\phi_{i,2}, \quad \sigma_{i2} = \phi_{i,1}, \tag{2.4b}$$

which can be used to calculate all the stress components at any point. $(\mathbf{a}_\alpha, \mathbf{b}_\alpha)$, $\alpha = 1, 2, 3$, of (2.3b) are the material eigenvectors associated with p_α. $f_\alpha(\zeta_\alpha)$, $\alpha = 1, 2, 3$, are three holomorphic complex functions to be determined by satisfying the boundary conditions of the problem.

Due to the assumption of rigid stamp indentation over the contact region of the hole boundary, the displacement $\mathbf{u}$ is known and set to be $\hat{\mathbf{u}}$. Over the remainder of the hole boundary, the surface traction is assumed to be free. On transforming to the region $|\zeta| \geq 1$ of the ζ-plane, the boundary conditions can then be expressed as

$$\begin{aligned} \mathbf{u}_{,n}(s) &= \hat{\mathbf{u}}'(s), \quad s \in L, \\ \mathbf{t}_m(s) &= \mathbf{0}, \quad s \notin L, \end{aligned} \tag{2.5}$$

where $s = e^{i\psi}$ denotes the points on the unit circle of the ζ-plane; L is the union of n arcs $L_k = (a_k, b_k)$, $k = 1, 2, \ldots, n$, of the unit circle; $\mathbf{t}_m$ is the surface traction along the boundary of which the normal is $\mathbf{m}$; $\hat{\mathbf{u}}'(s)$ is the prescribed function of the displacement gradient along the tangent direction $\mathbf{n}$; $\mathbf{m}^T(\theta) = (-\sin\theta, \cos\theta, 0)$, $\mathbf{n}^T(\theta) = (\cos\theta, \sin\theta, 0)$ are, respectively, the unit vectors normal and tangent to the boundary; and the angle θ is measured counterclockwise from the positive x_1-axis to the tangent vector $\mathbf{n}$ (Fig. 1).

3 General Solutions for Curvilinear Hole Boundaries

In order to find the holomorphic function $\mathbf{f}(\zeta)$ of the governing Eq. (2.3) which satisfies the boundary conditions set in (2.5), we first express the surface traction $\mathbf{t}_m$ in terms of $\mathbf{f}(\zeta)$, by employing (2.4a) and (2.3a)$_2$, as

$$\mathbf{t}_m = \frac{\partial \boldsymbol{\phi}}{\partial n} = \frac{\partial}{\partial n}[\mathbf{B}\mathbf{f}(\zeta) + \bar{\mathbf{B}}\overline{\mathbf{f}(\zeta)}], \quad \zeta \to s^+, \tag{3.1}$$

where the superscript + of s means that the boundary point $s = e^{i\psi}$ is approached from the region R^+ which is outside the unit circle of ζ-plane. Similarly, s^- will denote the boundary point s approached from the region R^- inside the unit circle of ζ-plane. Using the chain rule, we have

$$\begin{aligned} \mathbf{t}_m = \mathbf{B}\frac{\partial \mathbf{f}(\zeta)}{\partial \zeta}\frac{\partial \zeta}{\partial \psi}\frac{\partial \psi}{\partial z_\alpha}\left[\frac{\partial z_\alpha}{\partial x_1}\frac{\partial x_1}{\partial n} + \frac{\partial z_\alpha}{\partial x_2}\frac{\partial x_2}{\partial n}\right] \\ + \bar{\mathbf{B}}\frac{\partial \overline{\mathbf{f}(\zeta)}}{\partial \bar{\zeta}}\frac{\partial \bar{\zeta}}{\partial \psi}\frac{\partial \psi}{\partial \bar{z}_\alpha}\left[\frac{\partial \bar{z}_\alpha}{\partial x_1}\frac{\partial x_1}{\partial n} + \frac{\partial \bar{z}_\alpha}{\partial x_2}\frac{\partial x_2}{\partial n}\right], \quad \zeta \to s^+, \end{aligned} \tag{3.2}$$

where

$$\begin{aligned} &\frac{\partial \zeta}{\partial \psi} = ie^{i\psi} = is, \quad \frac{\partial x_1}{\partial n} = \cos\theta, \quad \frac{\partial x_2}{\partial n} = \sin\theta, \\ &\frac{\partial z_\alpha}{\partial x_1} = 1, \quad \frac{\partial z_\alpha}{\partial x_2} = p_\alpha. \end{aligned} \tag{3.3}$$

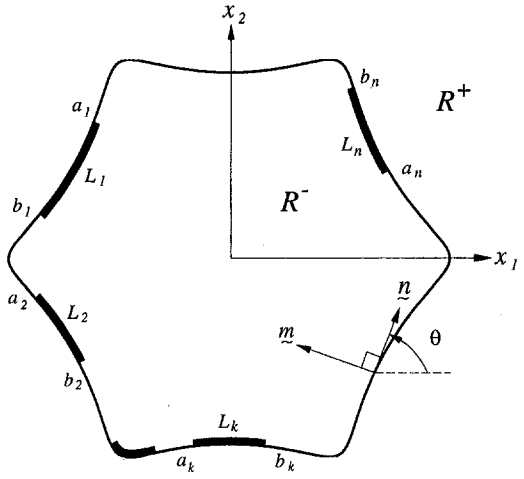


Fig. 1 A curvilinear hole indented by a set of rigid stamps (the hole boundary is represented by Eq. (5.1) with $a = c = 1$, $k = 5$, $\epsilon = 0.1$)

Downloaded 04 May 2010 to 171.66.16.26. Redistribution subject to ASME license or copyright; see http://www.asme.org/terms/Terms_Use.cfm

The term $\partial\psi/\partial z_\alpha$ is evaluated by using $z_\alpha = x_1 + p_\alpha x_2$ and

$$\frac{\partial x_1}{\rho\partial\psi} = -\cos\theta, \quad \frac{\partial x_2}{\rho\partial\psi} = -\sin\theta, \tag{3.4a}$$

where

$$\rho = \sqrt{\left|\frac{\partial x_1}{\partial\psi}\right|^2 + \left|\frac{\partial x_2}{\partial\psi}\right|^2}. \tag{3.4b}$$

The result is

$$\frac{\partial\psi}{\partial z_\alpha} = \frac{-1}{\rho(\cos\theta + p_\alpha \sin\theta)}. \tag{3.5}$$

Substituting (3.3) and (3.5) into (3.2), we obtain

$$\mathbf{t}_m = \lim_{\zeta\to s^+}\left\{-\frac{i}{\rho}\zeta\mathbf{B}\mathbf{f}'(\zeta) + \frac{i}{\rho\zeta}\bar{\mathbf{B}}\overline{\mathbf{f}'(\zeta)}\right\}, \tag{3.6}$$

which can be further expressed as

$$\mathbf{t}_m = -\frac{i}{\rho}s\mathbf{B}\mathbf{f}'(s^+) + \frac{i}{\rho s}\bar{\mathbf{B}}\overline{\mathbf{f}'(1/\bar{s})}. \tag{3.7}$$

From the theory of complex variable function, we know that if $\mathbf{f}'(\zeta)$ is holomorphic in R^+, then $\mathbf{f}'(1/\bar{\zeta})$ is holomorphic in R^-. With this in mind, we introduce $\boldsymbol{\theta}'(\zeta)$ such that

$$\boldsymbol{\theta}'(\zeta) = \begin{cases}\zeta\mathbf{B}\mathbf{f}'(\zeta), & \zeta\in R^+,\\ \dfrac{1}{\zeta}\bar{\mathbf{B}}\overline{\mathbf{f}'(1/\bar{\zeta})}, & \zeta\in R^-.\end{cases} \tag{3.8}$$

Since $\mathbf{f}'(\zeta)$ should be holomorphic in the elastic body R^+, $\boldsymbol{\theta}'(\zeta)$ is now holomorphic in R^+ and R^-, i.e., $\boldsymbol{\theta}'(\zeta)$ is sectionally holomorphic in the whole plane, except possibly on some segments along the unit circle.

By the definition given in (3.8), Eq. (3.6) can be rewritten as

$$\mathbf{t}_m = \frac{-i}{\rho}[\boldsymbol{\theta}'(s^+) - \boldsymbol{\theta}'(s^-)]. \tag{3.9}$$

In a similar way, the displacement gradients along the tangent direction $\mathbf{n}$ of the hole boundary can be formulated as

$$-\rho\mathbf{M}\mathbf{u}_{,n} = \boldsymbol{\theta}'(s^+) + \mathbf{M}\bar{\mathbf{M}}^{-1}\boldsymbol{\theta}'(s^-), \tag{3.10}$$

where $M = -i\mathbf{B}\mathbf{A}^{-1}$ is the impedance matrix. Substituting (3.9) and (3.10) into the boundary conditions (2.5), we obtain the following Hilbert problem:

$$\begin{aligned}&\boldsymbol{\theta}'(s^+) + \mathbf{M}\bar{\mathbf{M}}^{-1}\boldsymbol{\theta}'(s^-) = -\rho\mathbf{M}\hat{\mathbf{u}}', \quad s\in L,\\ &\boldsymbol{\theta}'(s^+) - \boldsymbol{\theta}'(s^-) = \mathbf{0}, \quad s\notin L.\end{aligned} \tag{3.11}$$

The solution to this Hilbert problem is (Hwu, 1992a)

$$\boldsymbol{\theta}'(\zeta) = -\frac{1}{2\pi i}\mathbf{X}_0(\zeta)\int_L \frac{\rho}{s-\zeta}[\mathbf{X}_0^+(s)]^{-1}\mathbf{M}\hat{\mathbf{u}}'(s)ds + \mathbf{X}_0(\zeta)\mathbf{p}(\zeta), \tag{3.12}$$

where $\mathbf{p}(\zeta)$ is an arbitrary polynomial vector to be determined by the loading conditions; $\mathbf{X}_0(\zeta)$ is the basic Plemelj function defined as

$$\mathbf{X}_0(\zeta) = \boldsymbol{\Lambda}\boldsymbol{\Gamma}(\zeta), \tag{3.13a}$$

where

$$\boldsymbol{\Lambda} = [\boldsymbol{\lambda}_1, \boldsymbol{\lambda}_2, \boldsymbol{\lambda}_3],$$

$$\boldsymbol{\Gamma}(\zeta) = \langle\langle\prod_{j=1}^{n}(\zeta - a_j)^{-(1+\delta_\alpha)}(\zeta - b_j)^{\delta_\alpha}\rangle\rangle. \tag{3.13b}$$

δ_α and $\boldsymbol{\lambda}_\alpha$, $\alpha = 1, 2, 3$ of (3.13b) are the eigenvalues and eigenvectors of

$$(\bar{\mathbf{M}}^{-1} + e^{2\pi i\delta}\mathbf{M}^{-1})\boldsymbol{\lambda} = \mathbf{0}. \tag{3.14}$$

The explicit solutions for the eigenvalues δ have been shown in Fan and Hwu (1996).

The determination of $\mathbf{p}(\zeta)$ may be done by the following force conditions which are derived by using (3.9):

$$\boldsymbol{\gamma}_k = -\int_{L_k}\frac{i}{\rho}[\boldsymbol{\theta}'(s^+) - \boldsymbol{\theta}'(s^-)]ds, \quad \text{for} \quad k = 1, 2, \ldots, n, \tag{3.15}$$

where $\boldsymbol{\gamma}_k$ is the known resultant force vector applied on the kth stamp. In addition to Eq. (3.15), which is the equilibrium equation for each stamp, the examination of the behavior of the stress and displacement fields at the infinity and origin may also be helpful for the determination of $\mathbf{p}(\zeta)$. If we consider the stresses are bounded at infinity, it may be shown that for large $|z|$, the complex function vector $\mathbf{f}(z)$ has the form

$$\mathbf{f}(z) = \langle\langle\log z_\alpha\rangle\rangle\boldsymbol{\gamma} + \langle\langle z_\alpha\rangle\rangle\mathbf{q} + \mathbf{O}(1), \tag{3.16}$$

where the angular brackets $\langle\langle\ \ \rangle\rangle$ stand for the diagonal matrix in which each component is varied according to the Greek index α; $\boldsymbol{\gamma}$ is related to the resultant force $\hat{\mathbf{p}}$ applied on the entired body, and $\mathbf{q}$ is related to the stresses σ_{ij}^∞ at infinity. The relations are (Eshelby et al., 1953; Ting, 1988)

$$\boldsymbol{\gamma} = \frac{1}{2\pi i}\mathbf{A}^T\hat{\mathbf{p}}; \tag{3.17}$$

$$\mathbf{q} = \mathbf{A}^T\mathbf{t}_2^\infty + \mathbf{B}^T\boldsymbol{\epsilon}_1^\infty, \tag{3.18a}$$

where

$$\mathbf{t}_2^\infty = \begin{Bmatrix}\sigma_{12}^\infty\\ \sigma_{22}^\infty\\ \sigma_{32}^\infty\end{Bmatrix}, \quad \boldsymbol{\epsilon}_1^\infty = \begin{Bmatrix}\epsilon_{11}^\infty\\ \epsilon_{12}^\infty\\ 2\epsilon_{13}^\infty\end{Bmatrix}. \tag{3.18b}$$

With the transformation $z_\alpha = m_\alpha(\zeta)$, and the definition given in (3.8), Eq. (3.16) is then used to derive the infinity and origin conditions for $\boldsymbol{\theta}'(\zeta)$. The results are

$$\boldsymbol{\theta}'(\zeta) = \mathbf{B}\left\{\left\langle\left\langle\frac{\zeta m_\alpha'(\zeta)}{m_\alpha(\zeta)}\right\rangle\right\rangle\boldsymbol{\gamma} + \langle\langle\zeta m_\alpha'(\zeta)\rangle\rangle\mathbf{q} + \mathbf{O}\left(\frac{1}{\zeta}\right)\right\}, \quad |\zeta|\to\infty, \tag{3.19a}$$

and

$$\boldsymbol{\theta}'(\zeta) = \frac{1}{\zeta}\bar{\mathbf{B}}\left\{\left\langle\left\langle\frac{\bar{m}_\alpha'\left(\frac{1}{\zeta}\right)}{\bar{m}_\alpha\left(\frac{1}{\zeta}\right)}\right\rangle\right\rangle\bar{\boldsymbol{\gamma}} + \left\langle\left\langle\bar{m}_\alpha'\left(\frac{1}{\zeta}\right)\right\rangle\right\rangle\bar{\mathbf{q}} + \mathbf{O}(\zeta)\right\}, \quad |\zeta|\to 0. \tag{3.19b}$$

4 Elliptical Hole Boundaries

Consider an infinite anisotropic body containing an elliptical hole of which the boundary can be expressed as

Downloaded 04 May 2010 to 171.66.16.26. Redistribution subject to ASME license or copyright; see http://www.asme.org/terms/Terms_Use.cfm

$$x_1 = a\cos\psi, \quad x_2 = b\sin\psi, \tag{4.1}$$

where a, b are the lengths of semi-axes of the elliptical hole. In order to map the elliptical hole onto a unit circle, the transformation function $m_\alpha(\zeta_\alpha)$ is chosen to be

$$z_\alpha = m_\alpha(\zeta_\alpha) = \frac{1}{2}\left\{(a - ibp_\alpha)\zeta_\alpha + (a + ibp_\alpha)\frac{1}{\zeta_\alpha}\right\},$$

(α not summed), (4.2)

which can be proved to be single-valued when the points outside the elliptical hole of the z_α-plane are designated to be mapped onto the points outside the unit circle of the ζ_α-plane. Thus, its inverse function should exist and could easily be found by solving (4.2), which is

$$\zeta_\alpha = m_\alpha^{-1}(z_\alpha) = \frac{z_\alpha + \sqrt{z_\alpha^2 - (a^2 + b^2p_\alpha^2)}}{a - ibp_\alpha},$$

(α not summed). (4.3)

Suppose that the hole is loaded by a rigid stamp along the segment between $(a\cos\phi, -b\sin\phi)$ and $(a\cos\phi, b\sin\phi)$, which is mapped onto an arc $L = (e^{-i\phi}, e^{i\phi})$ in the ζ_α-plane. If the profile of the stamp is compatible with that of the hole boundary, $\hat{\mathbf{u}}'(s) = \mathbf{0}$ when $s \in L$. With this specification, the general solution given in (3.12) may now be simplified to

$$\boldsymbol{\theta}'(\zeta) = \boldsymbol{\Lambda}\boldsymbol{\Gamma}(\zeta)\mathbf{p}(\zeta), \tag{4.4a}$$

where

$$\boldsymbol{\Gamma}(\zeta) = \langle\langle(\zeta - e^{-i\phi})^{-(1/2)-i\epsilon_\alpha}(\zeta - e^{i\phi})^{-(1/2)+i\epsilon_\alpha}\rangle\rangle, \tag{4.4b}$$

and the branch of $\boldsymbol{\Gamma}(\zeta)$ is selected so that $\zeta\boldsymbol{\Gamma}(\zeta) \to \mathbf{I}$ as $|\zeta| \to \infty$. To determine the polynomial $\mathbf{p}(\zeta)$, we first consider the infinity and origin conditions. Substituting (4.2) into (3.19), we obtain

$$\boldsymbol{\theta}'(\zeta) = \mathbf{B}\left\{\boldsymbol{\gamma} + \frac{\zeta}{2}\langle\langle a - ibp_\alpha\rangle\rangle\mathbf{q} + \mathbf{O}\left(\frac{1}{\zeta}\right)\right\}, \quad |\zeta| \to \infty,$$

$$\boldsymbol{\theta}'(\zeta) = \bar{\mathbf{B}}\left\{\bar{\boldsymbol{\gamma}} + \frac{1}{2\zeta}\langle\langle a + ib\bar{p}_\alpha\rangle\rangle\bar{\mathbf{q}} + \mathbf{O}(\zeta)\right\}, \quad |\zeta| \to 0. \tag{4.5}$$

Moreover, $\boldsymbol{\Gamma}(\zeta)$ given in (4.4b) can also be expanded for large $|\zeta|$ as

$$\boldsymbol{\Gamma}(\zeta) = \frac{1}{\zeta} + \left\langle\left\langle\left(\frac{1}{2} - i\epsilon_\alpha\right)e^{i\phi} + \left(\frac{1}{2} + i\epsilon_\alpha\right)e^{-i\phi}\right\rangle\right\rangle\frac{1}{\zeta^2} + O\left(\frac{1}{\zeta^3}\right), \tag{4.6a}$$

and for small $|\zeta|$ as

$$\boldsymbol{\Gamma}(\zeta) = -\langle\langle e^{-2\phi\epsilon_\alpha}\rangle\rangle - \langle\langle e^{-2\phi\epsilon_\alpha}[(\tfrac{1}{2} + i\epsilon_\alpha)e^{i\phi} + (\tfrac{1}{2} - i\epsilon_\alpha)e^{-i\phi}]\rangle\rangle\zeta + O(\zeta^2). \tag{4.6b}$$

With Eq. (4.4a), comparison of the infinity and origin conditions given in (4.5) and (4.6) now leads to

$$\mathbf{p}(\zeta) = \mathbf{d}_2\zeta^2 + \mathbf{d}_1\zeta + \mathbf{d}_0 + \mathbf{d}_{-1}\zeta^{-1}, \tag{4.7}$$

and

$$\mathbf{B}\langle\langle a - ibp_\alpha\rangle\rangle\mathbf{q} = 2\boldsymbol{\Lambda}\mathbf{d}_2,$$

$$\mathbf{B}\boldsymbol{\gamma} = \boldsymbol{\Lambda}\mathbf{d}_1 + \boldsymbol{\Lambda}\langle\langle(\tfrac{1}{2} - i\epsilon_\alpha)e^{i\phi} + (\tfrac{1}{2} + i\epsilon_\alpha)e^{-i\phi}\rangle\rangle\mathbf{d}_2,$$

$$\bar{\mathbf{B}}\langle\langle a + ib\bar{p}_\alpha\rangle\rangle\bar{\mathbf{q}} = -2\boldsymbol{\Lambda}\langle\langle e^{-2\phi\epsilon_\alpha}\rangle\rangle\mathbf{d}_{-1},$$

$$\bar{\mathbf{B}}\boldsymbol{\gamma} = -\boldsymbol{\Lambda}\{\langle\langle e^{-2\phi\epsilon_\alpha}\rangle\rangle\mathbf{d}_0 + \langle\langle e^{-2\phi\epsilon_\alpha}[(\tfrac{1}{2} + i\epsilon_\alpha)e^{i\phi} + (\tfrac{1}{2} - i\epsilon_\alpha)e^{-i\phi}]\rangle\rangle\mathbf{d}_{-1}\}. \tag{4.8}$$

Once the loading conditions are given (i.e., $\mathbf{q}$ and $\boldsymbol{\gamma}$ are known), the four unknowns $\mathbf{d}_{-1}$, $\mathbf{d}_0$, $\mathbf{d}_1$, and $\mathbf{d}_2$ can be obtained by solving (4.8). Thus, the problem is solved.

Now consider a particular loading condition that all the stresses vanish at infinity and a resultant force $\hat{\mathbf{p}} = (X, Y, 0)^T$ is applied on the rigid stamp. In this case, $\mathbf{q} = \mathbf{0}$ and $\boldsymbol{\gamma} = (1/2\pi i)\mathbf{A}^T\hat{\mathbf{p}}$ by Eqs. (3.17) and (3.18). The four unknowns $\mathbf{d}_{-1}$, $\mathbf{d}_0$, $\mathbf{d}_1$, $\mathbf{d}_2$, can then be determined from (4.8) as

$$\mathbf{d}_{-1} = \mathbf{0}, \quad \mathbf{d}_0 = -\langle\langle e^{2\phi\epsilon_\alpha}\rangle\rangle\boldsymbol{\Lambda}^{-1}\bar{\mathbf{B}}\bar{\boldsymbol{\gamma}},$$
$$\mathbf{d}_1 = \boldsymbol{\Lambda}^{-1}\mathbf{B}\boldsymbol{\gamma}, \quad \mathbf{d}_2 = \mathbf{0}. \tag{4.9}$$

The solution of $\mathbf{f}'(\zeta)$ can therefore be found by combining (3.8), (4.4), (4.7), and (4.9), which is

$$\mathbf{f}'(\zeta) = \frac{1}{2\pi i}\mathbf{B}^{-1}\boldsymbol{\Lambda}\boldsymbol{\Gamma}(\zeta)\left[\boldsymbol{\Lambda}^{-1}\mathbf{B}\mathbf{A}^T + \left\langle\left\langle\frac{e^{2\phi\epsilon_\alpha}}{\zeta}\right\rangle\right\rangle\boldsymbol{\Lambda}^{-1}\overline{\mathbf{B}\mathbf{A}}^T\right]\hat{\mathbf{p}}. \tag{4.10}$$

Note that during the derivation through the method of analytical continuation shown in Sections 3 and 4, the argument of each component function of $\mathbf{f}(\zeta)$ is written without referring to its associated eigenvalues p_α (Hwu, 1993). Once the solution of $\mathbf{f}(\zeta)$ is obtained for a given boundary value problem, a replacement of ζ_1, ζ_2, or ζ_3 should be made for each component function to calculate field quantities from (2.3). In other words, the function vector $\mathbf{f}(\zeta)$ of Eq. (4.10), which has the form of $\mathbf{f}(\zeta) = [f_1(\zeta), f_2(\zeta), f_3(\zeta)]^T$, is not consistent with the solution form shown in $(2.3b)_3$ and is valid only along the hole boundary $\zeta = s = e^{i\psi}$. To get the explicit full-field solution, a translating technique (Hwu, 1993) based upon the above statement is employed in (4.10), which leads to

$$\mathbf{f}'(\zeta) = \frac{1}{2\pi i}\sum_{k=1}^{3}\left[\langle\langle\boldsymbol{\Gamma}_k(\zeta_\alpha)\rangle\rangle\mathbf{B}^{-1}\boldsymbol{\Lambda}\mathbf{I}_k\boldsymbol{\Lambda}^{-1}\mathbf{B}\mathbf{A}^T + \left\langle\left\langle\boldsymbol{\Gamma}_k(\zeta_\alpha)\frac{e^{2\phi\epsilon_\alpha}}{\zeta_\alpha}\right\rangle\right\rangle\mathbf{B}^{-1}\boldsymbol{\Lambda}\mathbf{I}_k\boldsymbol{\Lambda}^{-1}\overline{\mathbf{B}\mathbf{A}}^T\right]\hat{\mathbf{p}}, \tag{4.11a}$$

where

$$\mathbf{I}_1 = \begin{bmatrix}1&0&0\\0&0&0\\0&0&0\end{bmatrix}, \quad \mathbf{I}_2 = \begin{bmatrix}0&0&0\\0&1&0\\0&0&0\end{bmatrix},$$

$$\mathbf{I}_3 = \begin{bmatrix}0&0&0\\0&0&0\\0&0&1\end{bmatrix}. \tag{4.11b}$$

Using the result of (4.11) and applying a correspondence relation between isotropic and anisotropic elasticity proposed by Hwu (1996), the complex potential function $\varphi'(\zeta)$ (Muskhelishvili, 1954) of the present problem with isotropic media can be found to be

Downloaded 04 May 2010 to 171.66.16.26. Redistribution subject to ASME license or copyright; see http://www.asme.org/terms/Terms_Use.cfm

$$\varphi'(\zeta) = -\frac{X + iY}{2\pi(1+\kappa)}\left(1 + \frac{\kappa e^{-2\phi\epsilon}}{\zeta}\right)$$

$$\times (\zeta - e^{-i\phi})^{-(1/2)+i\epsilon}(\zeta - e^{i\phi})^{-(1/2)-i\epsilon}, \quad (4.12)$$

where $\kappa = 3 - 4\nu$ for plane strain and $\kappa = (3 - \nu)/(1 + \nu)$ for generalized plane stress, and ν is the Poisson's ratio. The solution shown in (4.12) agrees with that presented in England (1971).

5 Polygonal Hole Boundaries

Consider a hole, the contour of which is represented by

$$\left.\begin{aligned} x_1 &= a(\cos\psi + \epsilon\cos k\psi) \\ x_2 &= a(c\sin\psi - \epsilon\sin k\psi) \end{aligned}\right\}, \quad (5.1)$$

where $0 < c \leq 1$, and k is an integer. When $\epsilon = 0$ we obtain an ellipse with semi-axes a and ac, which is the case discussed in the previous section. In the case of $\epsilon = 0$, $c = 1$ and $\epsilon = 0$, $c \to 0$, the contour represents, respectively, a circle and a crack. When $c = 1$ and $k = 2$ the opening has three symmetry axes. With an appropriate selection of the parameter ϵ, the opening will differ from an equilateral triangle with rounded corners. When $c = 1$ and $k = 3$ there are four symmetry axes and at some values of ϵ the opening will differ little from a square with rounded corners. When $c < 1$ and $k = 3$ we will obtain ovals of a special type. When $c = 1$ and $k = 4$, a pentagon may be obtained.

An infinite plane with a hole represented by (5.1) is transformed to the ζ_α-plane with a hole in the shape of a unit circle. The transformation function is (Hwu, 1990)

$$z_\alpha = m_\alpha(\zeta_\alpha) = \frac{a}{2}\left\{(1 - ip_\alpha c)\zeta_\alpha + (1 + ip_\alpha c)\frac{1}{\zeta_\alpha}\right.$$

$$\left. + \epsilon(1 + ip_\alpha)\zeta_\alpha^k + \epsilon(1 - ip_\alpha)\frac{1}{\zeta_\alpha^k}\right\}, \quad (\alpha \text{ not summed}), \quad (5.2)$$

which is one to one when the hole is in the shape of an ellipse ($\epsilon = 0$ which makes the last two terms vanish) or the medium is isotropic ($p_\alpha = i$ which makes the third term vanish). For an anisotropic plane containing a polygonal hole, the transformation is generally not one to one. However, if we designate the point outside and nearest the unit circle to be the mapped point, a one-to-one transformation with *cuts* passing through the critical points will be obtained. With this designation for nonsingle-valued transformation, the solutions obtained will be well approximated if the critical points are far away from the hole (see Appendix). Whether the transformation function given in (5.2) is single-valued or not, an explicit inverse function like that for the elliptic hole, Eq. (4.3), is difficult to be obtained due to the complexity of (5.2). Thus, the numerical calculation from z_α to ζ_α is necessary for the case of a general polygonal hole.

If we consider that the polygonal hole is loaded by a resultant force $\hat{\mathbf{p}} = (X, Y, 0)^T$ applied on a rigid stamp along the segment between $a(\cos\phi + \epsilon\cos k\phi, -c\sin\phi + \epsilon\sin k\phi)$ and $a(\cos\phi + \epsilon\cos k\phi, c\sin\phi - \epsilon\sin k\phi)$ which is mapped onto an arc $L = (e^{-i\phi}, e^{i\phi})$ in the ζ_α-plane and $\hat{\mathbf{u}}'(s) = \mathbf{0}$ when $s \in L$, the solution form to this problem will then be exactly the same as that shown in Eq. (4.11), except that the relation between ζ_α and z_α is now given in (5.2) instead of (4.2).

Since there is no analytical solution presented in the literature for the mixed boundary value problems with polygonal hole boundaries, for the purpose of verification we now study another special case which may be reduced from our general solution shown in Section 3. Consider an anisotropic body containing a polygonal hole loaded by a uniform stress σ_{ij} at infinity. If the entire boundary of the polygonal hole is traction-free, the displacement-prescribed segment L will vanish and the mixed boundary value problem reduces to a stress boundary value problem. Thus, the integral term of Eq. (3.12) will vanish and the Plemelj function $\mathbf{X}_0(\zeta) = \mathbf{\Lambda}/\zeta$ will be in the form of a polynomial. The solution shown in (3.12) can therefore be reduced to

$$\boldsymbol{\theta}'(\zeta) = \mathbf{p}(\zeta), \quad (5.3)$$

in which the polynomial vector $\mathbf{p}(\zeta)$ can be determined by substituting the transformation function (5.2) into the infinity and origin conditions shown in (3.19). The result is

$$\boldsymbol{\theta}'(\zeta) = \frac{a}{2}\left\{\mathbf{B}\langle\langle(1 - ip_\alpha c)\zeta + k\epsilon(1 + ip_\alpha)\zeta^k\rangle\rangle\mathbf{q}\right.$$

$$\left. + \bar{\mathbf{B}}\left\langle\left\langle(1 + i\bar{p}_\alpha c)\frac{1}{\zeta} + k\epsilon(1 - i\bar{p}_\alpha)\frac{1}{\zeta^k}\right\rangle\right\rangle\bar{\mathbf{q}}\right\}, \quad (5.4)$$

where $\mathbf{q}$ is related to the infinity stresses σ_{ij} by Eq. (3.18). The solution of $\mathbf{f}(\zeta)$ can then be found by applying $(3.8)_1$ to (5.4) and integrating the results with respect to ζ. If we ignore the integration constant which corresponds to the rigid-body motion, we get

$$\mathbf{f}(\zeta) = \frac{a}{2}\left\{\langle\langle(1 - ip_\alpha c)\zeta + \epsilon(1 + ip_\alpha)\zeta^k\rangle\rangle\mathbf{q}\right.$$

$$\left. - \mathbf{B}^{-1}\bar{\mathbf{B}}\left\langle\left\langle(1 + i\bar{p}_\alpha c)\frac{1}{\zeta} + \epsilon(1 - i\bar{p}_\alpha)\frac{1}{\zeta^k}\right\rangle\right\rangle\bar{\mathbf{q}}\right\}. \quad (5.5)$$

Again, Eq. (5.5) is valid only along the hole boundary $\zeta = s = e^{i\psi}$. To get an explicit full-field solution, a translating technique introduced by Hwu (1993) should be employed in (5.5). The result is

$$\mathbf{f}(\zeta) = \frac{a}{2}\left\{\langle\langle(1 - ip_\alpha c)\zeta_\alpha + \epsilon(1 + ip_\alpha)\zeta_\alpha^k\rangle\rangle\mathbf{q}\right.$$

$$- \left\langle\left\langle\frac{1}{\zeta_\alpha}\right\rangle\right\rangle\mathbf{B}^{-1}\bar{\mathbf{B}}\langle\langle 1 + i\bar{p}_\alpha c\rangle\rangle\bar{\mathbf{q}}$$

$$\left. + \left\langle\left\langle\frac{1}{\zeta_\alpha^k}\right\rangle\right\rangle\mathbf{B}^{-1}\bar{\mathbf{B}}\langle\langle\epsilon(1 - i\bar{p}_\alpha)\rangle\rangle\bar{\mathbf{q}}\right\}, \quad (5.6)$$

which can be proved to be identical to that obtained by Hwu (1990).

6 Numerical Calculation

Since the solutions presented in this paper are new and no other analytical solution has been found in the literature, the correctness of the present results can only be checked analytically by their reduced forms such as Eq. (4.12) for isotropic media in the case of an elliptical hole boundary and Eq. (5.6) for the stress boundary value problem in the case of a polygonal hole boundary. For the general case of anisotropic media containing an elliptic or a polygonal hole indented by a rigid stamp, numerical calculation will be done in this section to show its generality. Moreover, in order to see clearly the physical behavior of the indentation problems, the related hoop stress and stress contour will also be plotted.

The procedure for numerical calculation is as follows:

1 Calculate the material eigenvalues p_α, $\alpha = 1, 2, 3$ and material eigenvector matrices $\mathbf{A}$ and $\mathbf{B}$ from the elastic constants

Downloaded 04 May 2010 to 171.66.16.26. Redistribution subject to ASME license or copyright; see http://www.asme.org/terms/Terms_Use.cfm

C_{ijkl} (Ting, 1996). Note that the eigenvector matrices $\mathbf{A}$ and $\mathbf{B}$ are normalized by $\mathbf{A}^T\mathbf{B} + \mathbf{B}^T\mathbf{A} = \mathbf{I}$.

2 Calculate the eigenvalues δ and eigenvector $\boldsymbol{\lambda}$ from (3.14) and construct the matrices $\boldsymbol{\Lambda}$ and $\boldsymbol{\Gamma}(\zeta)$ by (3.13b) with the stamp location (a_j, b_j) given. Note that the eigenvector matrix $\boldsymbol{\Lambda}$ is normalized by $\frac{1}{2}\bar{\boldsymbol{\Lambda}}^T(\mathbf{M}^{-1} + \bar{\mathbf{M}}^{-1})\boldsymbol{\Lambda} = \mathbf{I}$.

3 For any particular point (x_1, x_2), calculate $z_\alpha (= x_1 + p_\alpha x_2)$ and its corresponding ζ_α by (4.3) for elliptic hole boundary or by solving (5.2) and designating the point outside and nearest the unit circle to be the mapped point for polygonal hole boundary.

4 Calculate $\mathbf{f}(\zeta)$ by (4.11) for the case of elliptic or polygonal hole boundary. Note that the solution form for the elliptic and polygonal hole boundary is the same except that the relations between ζ_α and z_α are different.

5 Calculate the displacements, stresses, and strains from (2.3) and (2.4). Note that the hoop stress σ_{nn} is related to the stress function vector $\boldsymbol{\phi}$ by, with the use of Eq. (2.4a), $\sigma_{nn} = -\mathbf{n}^T(\theta)\boldsymbol{\phi}_{,m}$.

During the numerical calculation, we encounter a problem about the determination of the complex variable function $\boldsymbol{\Gamma}(\zeta) = \langle\langle(\zeta - e^{-i\phi})^{-(1/2)-i\epsilon_\alpha}(\zeta - e^{i\phi})^{-(1/2)+i\epsilon_\alpha}\rangle\rangle$, which is multivalued if no special requirement was set. To deal with this problem, a special branch cut is introduced such that the complex variable function $\boldsymbol{\Gamma}(\zeta)$ keeps continuous across the entire boundary C: $|\zeta| = 1$ except the segment L in which $\boldsymbol{\Gamma}(\zeta)$ induces a jump.

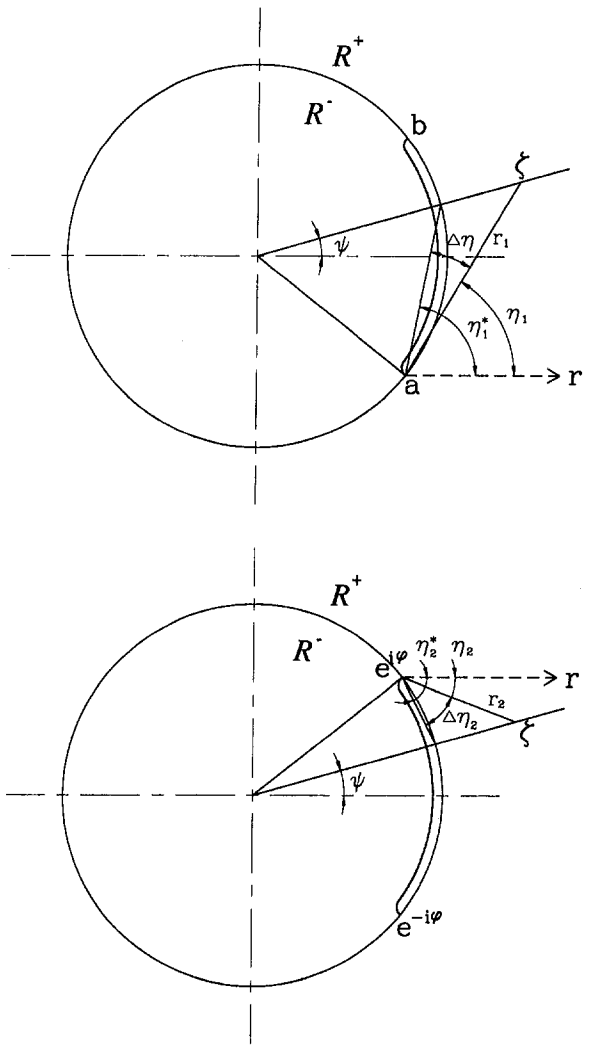


Fig. 2 A special polar coordinate system for the calculation of the complex variable function Γ(ζ)

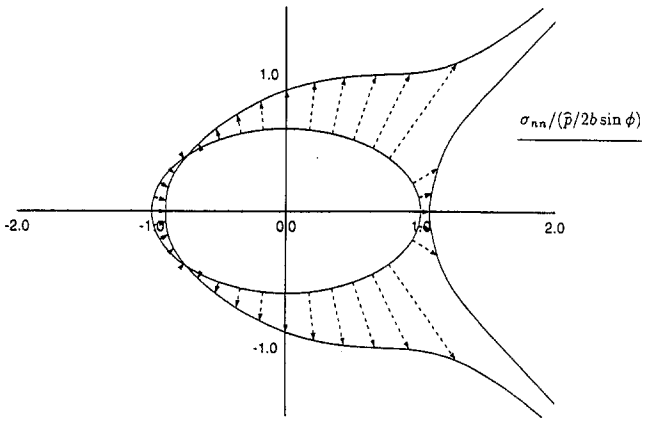


Fig. 3 The nondimensionalized hoop stress $\sigma_{nn}/(\hat{p}/2b \sin \phi)$ along the elliptic hole boundary indented by a rigid stamp

For this purpose, we construct a bipolar coordinate system (see Figs. 2(a), (b)), and let

$$\zeta - e^{-i\phi} = r_1 e^{i\eta_1}, \quad \zeta - e^{i\phi} = r_2 e^{i\eta_2}.$$

$\boldsymbol{\Gamma}(\zeta)$ can then be expressed as

$$\boldsymbol{\Gamma}(\zeta) = \left\langle\left\langle (r_1 r_2)^{-1/2}\left(\frac{r_2}{r_1}\right)^{i\epsilon_\alpha} e^{-(i/2)(\eta_1+\eta_2)} e^{\epsilon_\alpha(\eta_1-\eta_2)}\right\rangle\right\rangle. \quad (6.1)$$

For a boundary point $s = e^{i\psi}$, the branch cut for the term $(\zeta - e^{-i\phi})^{-(1/2)-i\epsilon_\alpha}$ will be set such that (see Fig. 2(a))

$$\arg(s^+ - e^{-i\phi}) = \eta_1^*, \quad \arg(s^- - e^{-i\phi}) = \eta_1^* - 2\pi, \quad (6.2)$$

across the entire boundary C. On the other hand, the branch cut for $(\zeta - e^{i\phi})^{-(1/2)+i\epsilon_\alpha}$ will be set such that (see Fig. 2(b))

$$\arg(s^+ - e^{i\phi}) = \eta_2^*, \quad \arg(s^- - e^{i\phi}) = \eta_2^* - 2\pi, \quad s \in C - L,$$

$$\arg(s^\pm - e^{i\phi}) = \eta_2^*, \quad s \in L. \quad (6.3)$$

By the definition given in (6.2) and (6.3), we find that when a point moves across the boundary from R^+ to R^-, the term $(\eta_1 + \eta_2)$ in (6.1) may undergo a decrease 4π and 2π for $s \in C - L$ and $s \in L$, respectively. Meanwhile, the term $(\eta_1 - \eta_2)$ in (6.1) may undergo a decrease 0 and 2π for $s \in C - L$ and $s \in L$, respectively. Thus by (6.1), the relation between $\boldsymbol{\Gamma}(s^+)$ and $\boldsymbol{\Gamma}(s^-)$ can be represented as

$$\boldsymbol{\Gamma}(s^+) = \boldsymbol{\Gamma}(s^-), \quad s \in C - L,$$

$$\boldsymbol{\Gamma}(s^+) = \langle\langle -e^{2\pi\epsilon_\alpha}\rangle\rangle \boldsymbol{\Gamma}(s^-), \quad s \in L. \quad (6.4)$$

Note that the term $\langle\langle -e^{2\pi\epsilon_\alpha}\rangle\rangle$ representing the jump when $\boldsymbol{\Gamma}(\zeta)$ moves across the segment L of the boundary is exactly the factor $e^{2\pi i\delta}$ of the eigenrelation (3.14). This implies that the definition given in (6.2) and (6.3) will provide us with the required values for the function $\boldsymbol{\Gamma}(\zeta)$.

For a point ζ not on the boundary and $\arg(\zeta) = \psi$ we use η_1^* as a reference to calculate the argument $\eta_1 = \arg(\zeta - e^{-i\phi})$, i.e.,

$$\eta_1 = \eta_1^* + \Delta\eta_1, \quad (6.5a)$$

Downloaded 04 May 2010 to 171.66.16.26. Redistribution subject to ASME license or copyright; see http://www.asme.org/terms/Terms_Use.cfm

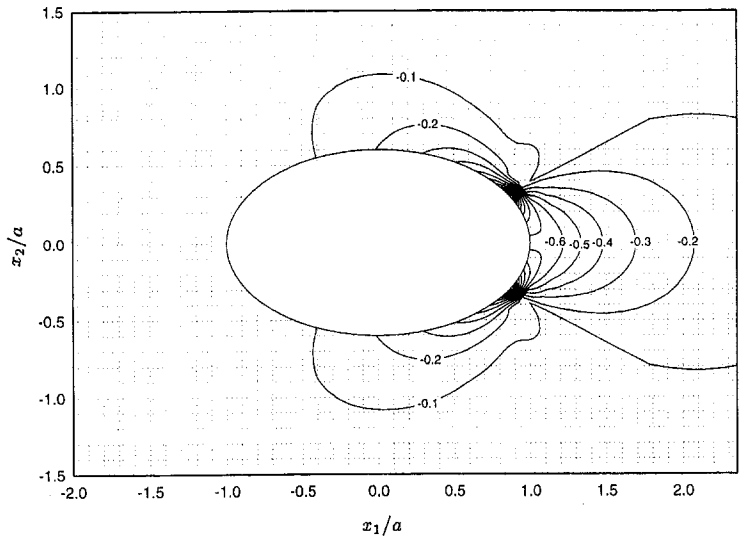


Fig. 4 Contour plot of the nondimensionalized stress $\sigma_{11}/(\hat{p}/2b \sin \phi)$ for the orthotropic body containing an elliptic hole indented by a rigid stamp

where

$$\Delta\eta_1 = \arg\left(\frac{\zeta - e^{-i\phi}}{\sigma - e^{-i\phi}}\right). \qquad (6.5b)$$

$\eta_2 = \arg(\zeta - e^{i\phi})$ can be obtained in a similar way. Thus, the complex variable function $\mathbf{\Gamma}(\zeta)$ can be uniquely determined by (6.1) for all points of the anisotropic body.

In the following examples, the infinite body is considered to be made of an orthotropic material whose mechanical properties are represented by

$$E_1 = 60.7 \text{ Gpa}, \quad E_2 = 24.8 \text{ Gpa},$$

$$G_{12} = 12.0 \text{ Gpa}, \quad \nu_{12} = 0.23,$$

where E, G, and ν are, respectively, the Young's modulus, shear modulus, and the Poisson's ratio. The subscript 1 and 2 denote the x and y-directions.

(i) Elliptic Hole Boundaries. The hole size, stamp location, and load magnitude for our numerical calculation are, respectively, $(a, b) = (1, 0.6)$, $\phi = 30$ deg and $\hat{\mathbf{p}} = (\hat{p}, 0, 0)$, $\hat{p} = 1000$ Nt, of which the size unit is selected to be the meter, which is just a reference for the infinite domain. The nondimensionalized hoop stress $\sigma_{nn}/(\hat{p}/2b \sin \phi)$ along the hole boundary is shown in Fig. 3. The stress singularity near the ends of the rigid stamp shown by Eq. (4.11) can be found in this figure. However, since the oscillatory zone is too small (about $10^{-4}a$), the oscillatory behavior near the ends of the rigid stamp cannot be revealed by this figure. To see the stresses in the full field, the contour plot of the nondimensionalized stress $\sigma_{11}/(\hat{p}/2a)$ shown in Fig. 4 may be helpful. Note that since the mapping function (4.2) used in this example is single-valued, all the solutions presented are exact.

(ii) Equilateral Triangular Hole Boundaries. Consider an infinite orthotropic elastic body containing an equilateral triangular hole which is represented by $a = c = 1$, $k = 2$ and $\epsilon = 0.25$. The stamp location and load magnitude are represented by $\phi = 30$ deg and $\hat{\mathbf{p}} = (\hat{p}, 0, 0)$, $\hat{p} = 1000$ Nt, respectively. Same as example (i), in Figs. 5 and 6 we show the nondimensionalized hoop stress $\sigma_{nn}/(\hat{p}/2a(c \sin \phi - \epsilon \sin 2\phi))$ along the hole boundary and the nondimensionalized stress contour of $\sigma_{11}/(\hat{p}/2a(c \sin \phi - \epsilon \sin 2\phi))$. Both of these reveal the stress singularity behavior at the ends of the rigid stamp. Note that since the mapping function (5.2) used in this example is nonsingle-valued, all the solutions presented are only approximate.

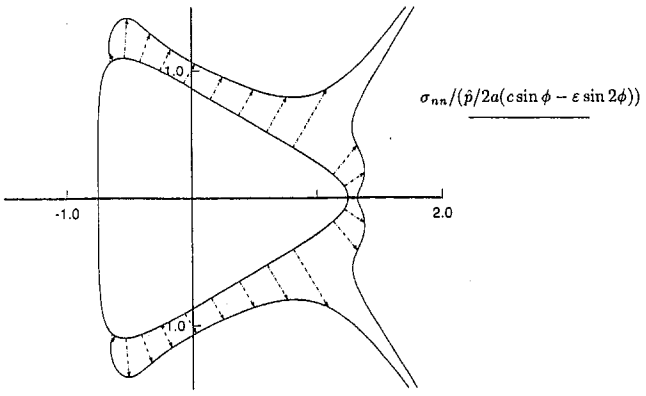


Fig. 5 The nondimensionalized hoop stress $\sigma_{nn}/(\hat{p}/2a(c \sin \phi - \epsilon \sin 2\phi))$ along the triangular hole boundary indented by a rigid stamp

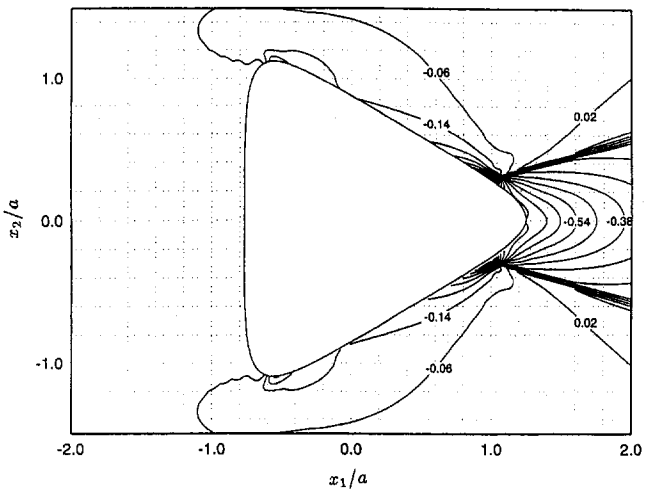


Fig. 6 Contour plot of the nondimensionalized stress $\sigma_{11}/(\hat{p}/2a(c \sin \phi - \epsilon \sin 2\phi))$ for the orthotropic body containing a triangular hole indented by a rigid stamp

Downloaded 04 May 2010 to 171.66.16.26. Redistribution subject to ASME license or copyright; see http://www.asme.org/terms/Terms_Use.cfm

7 Conclusions

The analytical solution obtained in (3.12) is general in the following sense:

1 The hole boundary can be any kind of curvilinear function. If its associated transformation function is one to one, the solution obtained will be exact. Otherwise, a special designation about the transformation should be given and the solution obtained is only approximate.

2 The material can be any kind of anisotropic material including the degenerate materials such as the isotropic materials which are treated by introducing a small perturbation of the material constants.

3 The shape, location, and number of the rigid stamps can be arbitrary.

When the hole boundary, material properties, loadings and the stamp shape, location, and number are specified, examination of the infinity and origin conditions may help us to solve (3.12) completely. A typical example is given in (4.10) which is valid for both of the elliptic and polygonal holes. However, without any annotation Eq. (4.10) can only be used along the hole boundary. The associated solution valid for the entire full field is shown in (4.11) which is derived by using the translating technique.

Since there are no such general analytical solutions found in the literature, the solutions presented in this paper are checked analytically by comparing the reduced special cases of which the solutions have been obtained in the literature. To help the readers see more clearly the physical behavior of the present problem, numerical examples are given and their related hoop stresses and stress contours are plotted. Moreover, the procedure for the numerical calculation is also described in detail in this paper.

Acknowledgments

The authors would like to thank the support by National Science Council, Republic of China, through Grant No. NSC 85-2212-E006-015.

References

Chang, F. K., 1986, "The Effect of Pin Load Distribution on the Strength of Pin Loaded Holes in Laminated Composites," *J. of Composite Materials,* Vol. 20, pp. 401–408.

England, A. H., 1971, *Complex Variable Methods in Elasticity,* Wiley Interscience, London.

Eshelby, J. D., Read, W. T., and Shockley, W., 1953, "Anisotropic Elasticity with Applications to Dislocation Theory," *Acta Met.,* Vol. 1, pp. 251–259.

Fan, C. W., and Hwu, C., 1996, "Punch Problems for an Anisotropic Elastic Half-Plane," ASME JOURNAL OF APPLIED MECHANICS, Vol. 63, pp. 69–76.

Hwu, C., 1990, "Anisotropic Plates With Various Openings Under Uniform Loading or Pure Bending," ASME JOURNAL OF APPLIED MECHANICS, Vol. 57, pp. 700–706.

Hwu, C., 1992a, "Thermoelastic Interface Crack Problems in Dissimilar Anisotropic Media," *International Journal of Solids and Structures,* Vol. 29, pp. 2077–2090.

Hwu, C., 1992b, "Polygonal Holes in Anisotropic Media," *Int. J. Solids and Structures,* Vol. 29, pp. 2369–2384.

Hwu, C., 1993, "Explicit Solutions for the Collinear Interface Crack Problems," *International Journal of Solids and Structures,* Vol. 30, pp. 301–312.

Hwu, C., 1996, "Correspondence Relations between Anisotropic and Isotropic Elasticity," *The Chinese Journal of Mechanics,* Vol. 12, No. 4, pp. 483–493.

Hwu, C., and Wang, W. Y., 1992, "Various Rigid Inclusions in Anisotropic Media," *Journal of the Chinese Society of Mechanical Engineers,* Vol. 13, No. 1, pp. 10–16.

Lekhnitskii, S. G., 1968, *Anisotropic plates,* Gordon and Breach, MIR, Moscow.

Mahajerin, E., and Sikarskie, D. L., 1986, "Boundary Element Study of a Loaded Hole in an Orthotropic Plate," *J. of Composite Materials,* Vol. 20, pp. 375–389.

Muskhelishvili, N. I., 1954, *Some Basic Problems of the Mathematical Theory of Elasticity,* Noordhoff, Groningen.

Stroh, A. N., 1958, "Dislocations and Cracks in Anisotropic Elasticity," *Philosophical Magazine,* Vol. 7, pp. 625–646.

Ting, T. C. T., 1988, "Some Identities and the Structures of $\mathbf{N}_i$ in the Stroh Formalism of Anisotropic Elasticity," *Quarterly Journal of Applied Mathematics,* Vol. 46, pp. 109–120.

Ting, T. C. T., 1996, *Anisotropic Elasticity: Theory and Applications,* Oxford Science Publications, New York.

Wang, G. S., 1994, "Stress Analysis for a Lug under Various Conditions," *J. of Strain Analysis,* Vol. 29, pp. 7–16.

APPENDIX

(The contents given below are extracted and modified from Hwu and Wang (1992), which are added for the convenience of the readers' reference.)

The mapping function given in (5.2) is single-valued only when all the branch points are located inside the unit circle $|\zeta| = 1$. This requirement is satisfied for the following two conditions (Hwu, 1992b): (*a*) an anisotropic plate containing an elliptic hole; (*b*) an isotropic plate with polygonal holes. Hence, the solutions presented in this paper are exact for these two cases. For the general anisotropic materials with polygonal holes, at least one of the branch points located outside the unit circle and (5.2) is nonsingle-valued. The occurrence of branch points outside the unit circle means that there will be multiple values of ζ, corresponding to one point z_α, located outside the unit circle. If we designate the point nearest the unit circle to be the mapped point, we will have one-to-one transformation. The hole boundary is then mapped onto the unit circle and $|\zeta_\alpha| \to \infty$ when $|z_\alpha| \to \infty$ is also satisfied. However, the ζ values may be discontinuous near the branch point, which may cause the discontinuity of displacements and stresses. To have a clear understanding of this phenomena, a typical example is shown below.

Example: $k = 2, , c = 1, a = 1, \epsilon = 0.25, p_\alpha = 0.712i$. The mapping function (5.2) becomes

$$z_\alpha = 0.856\zeta + 0.144\frac{1}{\zeta} + 0.036\zeta^2 + 0.214\frac{1}{\zeta^2}.$$

The branch points ζ_0 can then be calculated numerically by $dz_\alpha/$

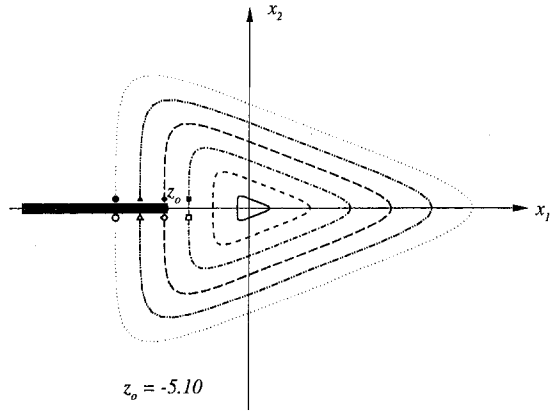


Fig. 7(*a*) The *z*-plane ($\epsilon = 0.25, a = 1, c = 1, k = 2, p_\alpha = 0.712i$)

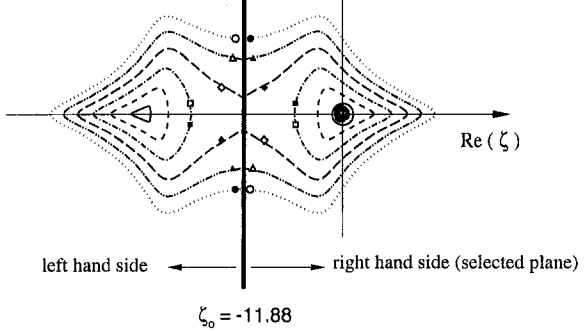


Fig. 7(*b*) The ζ-plane ($\epsilon = 0.25, a = 1, c = 1, k = 2, p_\alpha = 0.712i$)

Downloaded 04 May 2010 to 171.66.16.26. Redistribution subject to ASME license or copyright; see http://www.asme.org/terms/Terms_Use.cfm

$d\zeta = 0$. The results are $\zeta_0 = 0.84, -0.43 \pm 0.64i, -11.88$. The transformation from the z-plane to the ζ_α-plane is shown in Fig. 7. From this figure, we see that every point outside the hole boundary on the z-plane maps to four points on the ζ_α-plane. Two of them are located outside the unit circle and are on the right and left-hand sides of $\zeta_0 = -11.88$, the other two are inside the unit circle. The hole boundary is mapped to the unit circle and another triangular contour on the left side of ζ_0. The mapped plane (the ζ-plane) *looks* symmetric with respect to the axis of $\zeta_0 = -11.88$, except that the mapped hole boundary on the right side is a unit circle, not a triangle. To have a one-to-one transformation, the mapped plane is now selected to be the one nearest the unit circle, i.e., the plane on the right-hand side of $\zeta_0 = -11.88$. Discontinuity occurs at $\zeta_0 = -11.88$. The corresponding point in the z-plane is $z_0 = -5.10$. Figure 7 shows that the mapped points of $z = x_1^* + i0^\pm$ for $x_1^* > -5.10$, such as the points marked by (■) and (□), will be continuous when they approach to x_1-axis. However, the mapped point of $z = x_1^* + i0^\pm$ for $x_1^* < -5.10$, such as the points marked by (◆), (▲), (●) and (◇), (△), (○), will not be continuous when they approach to x_1-axis. The mapped points of $z = x_1^* + i0^\pm$ for $x_1^* < -5.10$ can be expressed as $-11.88 \pm i\zeta_I^*$ of which the discontinuity is $2i\zeta_I^*$. Therefore, the corresponding displacements and stresses will also be discontinuous near the branch point, which is not physical admissible for a continuum. However, this discontinuity will approach zero when x_1 approaches infinity, if the stress function is in negative power of ζ. The solution obtained will then approximate to the exact solution if the discontinuity along the whole branch cut approaches zero. This occurs when the branch points are far away from the hole since all the ζ values corresponding to the entire branch cut are large enough to let the negative power of ζ approach zero. This also means that the interaction between the branch cut and the hole is weak when they are far away from each other. The numerical results presented in Hwu and Wang (1992) and Hwu (1992b) for the stress boundary value problems show that they are really well approximated.

Although the approximation is based upon the argument that ϵ is very small and the branch point is far away from the hole, the present example ($\epsilon = 0.25$, $|\zeta_0| = 11.88$) shows that even for a not very small ϵ and not far away ζ_0, the approximation is still well enough. In addition to this example, there are other examples shown in Hwu and Wang (1992) and Hwu (1992b) indicating this approximation. Thus, we may say that if the distance from the branch point to the unit circle is greater than ten times of the radius of the unit circle, i.e., $|\zeta_0| \geq 10$, the approximation by using the transformation function (5.2) is well enough.

Downloaded 04 May 2010 to 171.66.16.26. Redistribution subject to ASME license or copyright; see http://www.asme.org/terms/Terms_Use.cfm

Probabilistic Representation and Transmission of Nonstationary Processes in Multi-Degree-of-Freedom Systems

S. F. Masri
Mem. ASME

A. W. Smyth

M.-I. Traina

Civil Engineering Department,
University of Southern California,
Los Angeles, CA 90089-2531

A relatively simple and straightforward procedure is presented for representing nonstationary random process data in a compact probabilistic format which can be used as excitation input in multi-degree-of-freedom analytical random vibration studies. The method involves two main stages of compaction. The first stage is based on the spectral decomposition of the covariance matrix by the orthogonal Karhunen-Loeve expansion. The dominant eigenvectors are subsequently least-squares fitted with orthogonal polynomials to yield an analytical approximation. This compact analytical representation of the random process is then used to derive an exact closed-form solution for the nonstationary response of general linear multi-degree-of-freedom dynamic systems. The approach is illustrated by the use of an ensemble of free-field acceleration records from the 1994 Northridge earthquake to analytically determine the covariance kernels of the response of a two-degree-of-freedom system resembling a commonly encountered problem in the structural control field. Spectral plots of the extreme values of the rms response of representative multi-degree-of-freedom systems under the action of the subject earthquake are also presented. It is shown that the proposed random data-processing method is not only a useful data-archiving and earthquake feature-extraction tool, but also provides a probabilistic measure of the average statistical characteristics of earthquake ground motion corresponding to a spatially distributed region. Such a representation could be a valuable tool in risk management studies to quantify the average seismic risk over a spatially extended area.

1 Introduction

A state-of-the-art review of current probabilistic methods and their structural and geotechnical applications indicates an active interest and growing recognition by designers of the significance of probabilistic approaches in engineering applications, particularly in the areas of structural reliability and risk analysis. Representative publications in the field of applied mechanics which deal with the stochastic response of dynamic systems include the work of Caughey and Stumpf (1961), Corotis and Vanmarke (1975), Spanos and Lutes (1980), DebChaudhury and Gasparini (1982), Iwan and Hou (1989), Soong and Grigoriu (1993), Lin and Cai (1995), and Lutes and Sarkani (1997). A major part of the impetus behind this strong interest in probabilistic methods is the need to quantify the safety margin in critical engineering facilities subjected to stochastic dynamic environments.

Among the major impediments to a more extensive use of probabilistic methods in structural dynamics applications are (1) the problems involved in the construction and representation of statistical models based on actual stochastic process excitation data, and (2) the computational difficulties encountered in subsequent analytical random vibration analyses to determine closed-form solutions for the response covariance.

For example, for an accurate analysis of the response of a dynamic system to earthquake excitation, it is imperative that the evolutionary nature of the seismic loads be properly represented as a nonstationary stochastic process. This fact has motivated a considerable amount of research into the simulation of, and response to, nonstationary random processes. (For appropriate bibliography, see the review paper by Vanmarcke (1979) and the work of Shinozuka and Deodatis (1988).) While these simulation studies have made available useful tools for the modeling of earthquakes in numerical computer studies, their format is not suitable for incorporation into an *analytical* random vibration analysis. The difficulty lies in the fact that the approximations that have been developed for the simulation procedures often lead to a characterization of the earthquake loads so complicated that analytical response calculations become unduly cumbersome.

A popular procedure for analytically representing earthquake ground-motion time histories is to model them as a zero-mean white noise process modulated by a deterministic envelope function. While this approach is a step in the right direction, it suffers from the deficiency of not being an authentic representation of actual earthquake spectral contents. On the other hand, models of earthquakes as filtered white noise, where the filter has constant or time-varying parameters, lead to analytical expressions that cannot be solved in a closed form for the nonstationary random vibration solutions of the covariance kernels of dynamic system response (Conte and Peng, 1996; Papadimitriou and Beck, 1990).

This paper presents a relatively straightforward procedure for representing stochastic process excitation data, in a compact probabilistic format that allows its convenient use later in analytical random vibration studies of general linear multi-degree-

Contributed by the Applied Mechanics Division of THE AMERICAN SOCIETY OF MECHANICAL ENGINEERS for publication in the ASME JOURNAL OF APPLIED MECHANICS.

Discussion on the paper should be addressed to the Technical Editor, Professor Lewis T. Wheeler, Department of Mechanical Engineering, University of Houston, Houston, TX 77204-4792, and will be accepted until four months after final publication of the paper itself in the ASME JOURNAL OF APPLIED MECHANICS.

Manuscript received by the ASME Applied Mechanics Division, Mar. 10, 1997; final revision, July 2, 1997. Associate Technical Editor: M. Shinozuka.

 Copyright © 1998 by ASME

Downloaded 04 May 2010 to 171.66.16.26. Redistribution subject to ASME license or copyright; see http://www.asme.org/terms/Terms_Use.cfm

of-freedom dynamic systems. The response solution is formulated in a state-variable form (Langley, 1986). In general, with the use of complex mathematical modeling of the excitation process, the response convolution integral could only be calculated for considerably simplified models (Hou, 1990). However, because of the form in which the excitation process data is analytically approximated, the response solution can be obtained analytically.

1.1 Background. The authors have previously presented (Masri and Miller, 1982) a procedure for the compact probabilistic representation of the covariance kernels of arbitrary random processes in a form that results in simplified analytical random vibration studies. This procedure was later improved by using a method based on the spectral decomposition of the random process by the orthogonal Karhunen-Loeve expansion and the subsequent use of least-squares approaches to develop an approximate analytical fit for the eigenvectors of the underlying random process. The resulting compact analytical representation of the random process was then used to derive a closed-form solution for the nonstationary response of a damped single-degree-of-freedom harmonic oscillator. The utility of the method for representing the excitation and calculating the mean-square response was illustrated by the use of an ensemble of synthetic acceleration records corresponding to a random process that is widely used in random vibration studies (Traina et al., 1986).

It is worth pointing out that there are two separate but complementary aspects to the above cited studies by the authors: (1) data condensation, and (2) the development of analytical expressions that govern the transmission of nonstationary random vibration in linear systems. Thus, while there are many classical and relatively new methods for data condensation that can, and are, being used (particularly in the image-processing and signal-analysis fields) for drastic data condensation, the format of the condensed representation in conventional methods precludes the use of these techniques for situations where the ultimate objective goes beyond mere condensation to the next stage where the condensed form is employed in deriving *analytical* expressions that yield the nonstationary response of linear dynamic systems to arbitrary random excitations. By contrast, the approach used by the authors results in a significant level of data reduction while still allowing the subsequent use of the compact format for analytical random vibration transmission studies.

The authors have also presented an application of the method using a relatively small ensemble of ground motion records from the Los Angeles region for the 1971 San Fernando earthquake (Masri et al., 1990). The estimation method yielded accurate correspondence with exact analytical results when used for single-degree-of-freedom system response simulation.

1.2 Scope. As mentioned above, the potential of the method under consideration has been previously demonstrated in the cited studies through the use of "synthetic" random excitation and also through the use of a relatively small ensemble of records from the 1971 San Fernando earthquake.

The previous formulation by the authors was restricted to single-degree-of-freedom system transmission studies. The general method is now extended to include multi-degree-of-freedom linear dynamic systems. The covariance kernels of the system response are obtained and subsequently used to determine the response features of a two-degree-of-freedom system which serves as a reduced order model of a problem widely encountered in the structural control field: an earthquake-excited building with a tuned mass damper. The approach under discussion can yield average measures of the system response which are useful in the design of such systems: e.g., the efficiency of the damping devices or the relative displacement (proximity spectra) requirements in order for base-excited structures to avoid impacting the rigid barriers commonly encountered in the design of such systems.

The occurrance of the 1994 Northridge earthquake and the corresponding wealth of high-quality ground motion records available from the Los Angeles region, furnishes an excellent data-set to be used as the excitation stochastic process in calculating the example multi-degree-of-freedom response solution.

2 Formulation

2.1 Orthogonal Decomposition and Representation of Covariance Kernel. The compaction of the probabilistic description of a system's input excitation is briefly reviewed in this section. The data condensation is performed in two steps: (1) the spectral decomposition of the input covariance matrix is calculated, and only the dominant eigenvectors are retained, and (2) those eigenvectors are least-squares fitted with a series of orthogonal polynomials. This method of data compaction permits closed-form probabilistic system response simulation studies.

2.1.1 Eigenvector Expansion of Covariance Matrix. The covariance matrix $[C]$ for a system with support acceleration $\ddot{s}(t)$ is defined as follows:

$$C_{\ddot{s}\ddot{s}}(t_1, t_2) = E[(\ddot{s}(t_1) - \mu_{\ddot{s}}(t_1))(\ddot{s}(t_2) - \mu_{\ddot{s}}(t_2))] \quad (1)$$

where $E[\cdot]$ is the expectation operator, and $\mu_{\ddot{s}}(t)$ is the mean value of the support acceleration at time t. Using the Karhunen-Loeve expansion, the spectral representation of $[C]$ may be expressed as

$$[C] = \sum_{i=1}^{k} \lambda_i \mathbf{p}_i \mathbf{p}_i^T + [E_k] = [C_k] + [E_k] \quad (2)$$

where $\lambda_1 \geq \lambda_2 \geq \ldots \geq \lambda_N \geq 0$, and thus $[C_k]$ represents the reconstruction of the covariance matrix by using the first (largest) k eigenvectors, and $[E_k]$ represents the truncation error.

2.1.2 Error Bounds on Truncation Effects. It can be shown (Treitel and Shanks, 1971) that the rate of convergence of $[C_k]$ to $[C]$ as measured by the dimensionless energy-related error term ϵ_k is given by

$$\epsilon_k = 1 - (\sum_{j=1}^{k} \lambda_j^2)/(\sum_{j=1}^{N} \lambda_j^2); \quad k = 1, 2, \ldots, N. \quad (3)$$

In practical cases, only a small number k of λ's is likely to be computed. The bounds for the case where $m \leq k$ (Traina et al., 1986) are

$$(\epsilon_m)_{\max} = 1 - \frac{\lambda_1^2 + \lambda_2^2 + \ldots + \lambda_m^2}{\lambda_1^2 + \lambda_2^2 + \ldots + (N - k + 1)\lambda_k^2}, \quad (4)$$

and

$$(\epsilon_m)_{\min} = 1 - \frac{\lambda_1^2 + \lambda_2^2 + \ldots + \lambda_m^2}{\lambda_1^2 + \lambda_2^2 + \ldots + \lambda_k^2}. \quad (5)$$

2.1.3 Least-Squares Fit of Covariance Matrix. The eigenvectors $\mathbf{p}_i$ of each $[C]$ can be least-squares fitted by orthogonal polynomials to produce $\hat{\mathbf{p}}_i$, whose vector components may be written as follows:

$$\mathbf{p}_i(t_l) \approx \hat{\mathbf{p}}_i(t_l) = \sum_{j=0}^{m_i - 1} H_{ij} T_j(t_l'), \quad (6)$$

where

$$t_l' = \frac{2t_l}{t_{\max}} - 1 \quad (7)$$

and m_i is the number of Chebyshev polynomials used in the series fit for $\hat{\mathbf{p}}_i$. The T's are Chebyshev polynomials, and H_{ij} is the coefficient of the Chebyshev polynomial of the order j

Downloaded 04 May 2010 to 171.66.16.26. Redistribution subject to ASME license or copyright; see http://www.asme.org/terms/Terms_Use.cfm

associated with eigenvector $\mathbf{p}_i$. The estimated covariance matrix $[\hat{C}_k]$ can then be constructed with the least-squares estimated eigenvectors, and expressed in terms of the Chebyshev polynomial series form (Masri et al., 1990):

$$[\hat{C}_k(t_1, t_2)] = \sum_{i=1}^{k} \lambda_i \sum_{j=0}^{m_i-1} \sum_{l=0}^{m_i-1} H_{ij} H_{il} T_j(t_1') T_l(t_2'), \quad (8)$$

where $0 \le t_i \le t_{\max}$; $i = 1, 2$. Chebyshev polynomials were chosen for the least-squares fitting, because in addition to being orthogonal, they have the desirable feature of equal-error ("equal-ripple") approximation within an interval of interest.

2.2 Nonstationary Response of a Multi-Degree-of-Freedom System to Nonstationary Excitation. The closed-form formulation of the multi-degree-of-freedom linear dynamic system response to the analytical estimate of the excitation covariance matrix given in Eq. (8) is presented below.

2.2.1 Formulation for General Excitation. By writing the system motions and excitation in the state-space form as follows,

$$\{x(t)\} = \begin{Bmatrix} q(t) \\ --- \\ \dot{q}(t) \end{Bmatrix}; \quad \{u(t)\} = \begin{Bmatrix} 0 \\ --- \\ F(t) \end{Bmatrix}, \quad (9)$$

the general n-degree-of-freedom system equation of motion may be written as

$$\{\dot{x}(t)\} = \mathbf{A}\{x(t)\} + \mathbf{B}\{u(t)\}. \quad (10)$$

The solution of this linear equation of motion is then

$$\{x(t)\} = e^{\mathbf{A}(t)}\{x(0)\} + \int_0^t e^{\mathbf{A}(t-\tau)}\mathbf{B}\{u(\tau)\}d\tau. \quad (11)$$

For convenience, the initial conditions will be assumed to be zero, i.e., $\{x(0)\} = \{0\}$. The general solution may then be reduced to

$$\{x(t_1)\} = \int_0^{t_1} e^{\mathbf{A}(t_1-\tau_1)}\mathbf{B}\{u(\tau_1)\}d\tau_1. \quad (12)$$

The response covariance (assuming a zero-mean response) is thus defined as follows:

$$E[\{x(t_1)\}\{x(t_2)\}^T] = \int_0^{t_1}\int_0^{t_2} e^{\mathbf{A}(t_1-\tau_1)}\mathbf{B}E[\{u(\tau_1)\}\{u(\tau_2)\}^T] \times \mathbf{B}^T(e^{\mathbf{A}(t_2-\tau_2)})^T d\tau_1 d\tau_2. \quad (13)$$

It can be shown that for a $(2n \times 2n)$ matrix $\mathbf{A}$ with distinct eigenvalues $\kappa_1, \kappa_2, \ldots, \kappa_{2n}$, it is computationally efficient to express $e^{\mathbf{A}t}$ using the following relationship (Moler and Van Loan, 1978):

$$e^{\mathbf{A}t} = \alpha_0(t)\mathbf{I} + \alpha_1(t)\mathbf{A} + \ldots + \alpha_{2n-1}(t)\mathbf{A}^{2n-1} \quad (14)$$

where

$$\begin{bmatrix} \alpha_0(t) \\ \alpha_1(t) \\ \vdots \\ \alpha_{2n-1}(t) \end{bmatrix} = \begin{bmatrix} 1 & \kappa_1 & \kappa_1^2 & \cdots & \kappa_1^{2n-1} \\ 1 & \kappa_2 & \kappa_2^2 & \cdots & \kappa_2^{2n-1} \\ \vdots & \vdots & \vdots & \vdots & \vdots \\ 1 & \kappa_{2n} & \kappa_{2n}^2 & \cdots & \kappa_{2n}^{2n-1} \end{bmatrix}^{-1} \begin{bmatrix} e^{\kappa_1(t)} \\ e^{\kappa_2(t)} \\ \vdots \\ e^{\kappa_{2n}(t)} \end{bmatrix}. \quad (15)$$

2.2.2 Formulation for Support Excitation. If the vector $\{y(t)\}$ is defined as the vector of nodal displacements relative to the support position, the equation of motion for a base-excited multi-degree-of-freedom system is

$$\mathbf{M}\{\ddot{y}(t)\} + \mathbf{C}\{\dot{y}(t)\} + \mathbf{K}\{y(t)\} = -\mathbf{M}\{e\}\ddot{s}(t), \quad (16)$$

and by introducing

$$\{x(t)\} = \begin{Bmatrix} y(t) \\ --- \\ \dot{y}(t) \end{Bmatrix}; \quad \{u(t)\} = \begin{Bmatrix} 0 \\ --- \\ F(t) \end{Bmatrix} \quad (17)$$

Eq. (16) can be expressed as

$$\{\dot{x}(t)\} = \mathbf{A}\{x(t)\} + \mathbf{B}\{u(t)\}, \quad (18)$$

thus leading to

$$\begin{Bmatrix} \dot{y}(t) \\ \ddot{y}(t) \end{Bmatrix} = \begin{bmatrix} 0 & \mathbf{I} \\ -\mathbf{M}^{-1}\mathbf{K} & -\mathbf{M}^{-1}\mathbf{C} \end{bmatrix} \begin{Bmatrix} y(t) \\ \dot{y}(t) \end{Bmatrix} + \begin{bmatrix} \mathbf{I} & 0 \\ 0 & \mathbf{I} \end{bmatrix} \begin{Bmatrix} 0 \\ -\{e\}\ddot{s}(t) \end{Bmatrix}. \quad (19)$$

Introducing the $(2n \times 2n)$ matrix

$$[\mathbf{h}(t)] = e^{\mathbf{A}(t)} = \begin{bmatrix} h_{11}(t) & \cdots & h_{12n}(t) \\ \vdots & \ddots & \vdots \\ h_{2n1}(t) & \cdots & h_{2n2n}(t) \end{bmatrix} \quad (20)$$

the general expression for the output covariance matrix can then be determined from

$$E[\{x(t_1)\}\{x(t_2)\}^T] = \int_0^{t_1}\int_0^{t_2} \begin{bmatrix} h_{11}(t_1-\tau_1) & \cdots & h_{12n}(t_1-\tau_1) \\ \vdots & \ddots & \vdots \\ h_{2n1}(t_1-\tau_1) & \cdots & h_{2n2n}(t_1-\tau_1) \end{bmatrix} \begin{bmatrix} 0 & \cdots & 0 & 0 & \cdots & 0 \\ \vdots & \ddots & \vdots & \vdots & \ddots & \vdots \\ 0 & \cdots & 0 & 0 & \cdots & 0 \\ 0 & \cdots & 0 & E[\ddot{s}(\tau_1)\ddot{s}(\tau_2)] & \cdots & E[\ddot{s}(\tau_1)\ddot{s}(\tau_2)] \\ \vdots & \ddots & \vdots & \vdots & \ddots & \vdots \\ 0 & \cdots & 0 & E[\ddot{s}(\tau_1)\ddot{s}(\tau_2)] & \cdots & E[\ddot{s}(\tau_1)\ddot{s}(\tau_2)] \end{bmatrix} \begin{bmatrix} h_{11}(t_1-\tau_1) & \cdots & h_{12n}(t_1-\tau_1) \\ \vdots & \ddots & \vdots \\ h_{2n1}(t_1-\tau_1) & \cdots & h_{2n2n}(t_1-\tau_1) \end{bmatrix}^T d\tau_1 d\tau_2. \quad (21)$$

For example, in the case where $n = 2$, Eq. (21) reduces to

$$E[y_2(t_1)y_1(t_2)] = \int_0^{t_1}\int_0^{t_2} (h_{23}(t_1-\tau_1) + h_{24}(t_1-\tau_1)) \times (h_{13}(t_2-\tau_2) + h_{14}(t_2-\tau_2)) \times E[\ddot{s}(\tau_1)\ddot{s}(\tau_2)]d\tau_1 d\tau_2. \quad (22)$$

The first and second terms in the integral above can be defined as $\hat{h}_2(t_1-\tau_1)$ and $\hat{h}_1(t_2-\tau_2)$, respectively. Thus, for arbitrary n,

$$\hat{h}_r(t) \equiv \sum_{s=n+1}^{2n} h_{rs}(t), \quad (23)$$

and can be thought of as the impulse response of a particular node r to support acceleration.

The nodal response due to the acceleration of each Chebyshev polynomial at the support is obtained from

$$I_l^{(r)}(t) = \frac{t_{\max}}{2}\int_{-1}^{((2t/t_{\max})-1)} \hat{h}_r\left(t - \frac{t_{\max}}{2}(\xi+1)\right)T_l(\xi)d\xi \quad (24)$$

and, recalling the form of the estimated covariance matrix of

Downloaded 04 May 2010 to 171.66.16.26. Redistribution subject to ASME license or copyright; see http://www.asme.org/terms/Terms_Use.cfm

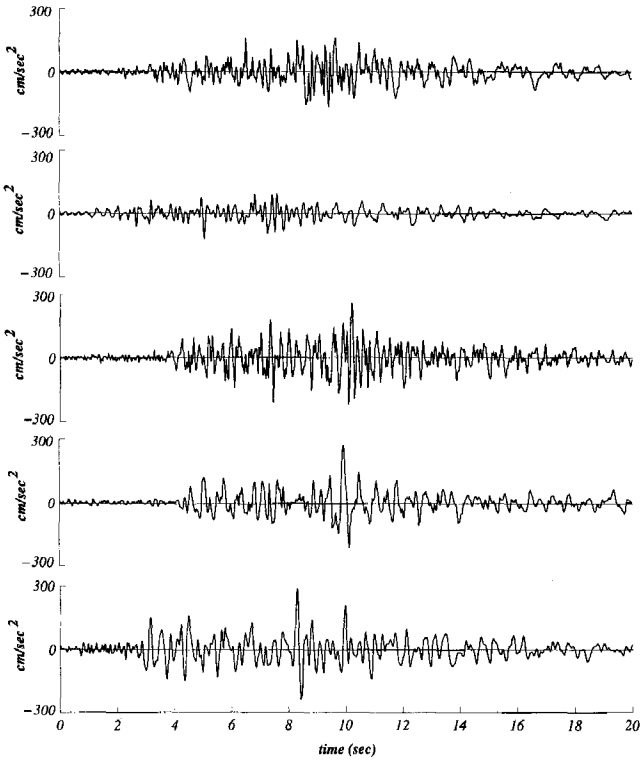


Fig. 1 Sample accelerograms used to generate the covariance matrix corresponding to the 1994 Northridge earthquake

the support excitation given in Eq. (8), estimates of the output covariance are obtained from

$$E[y_r(t_1)y_s(t_2)] \simeq E_m^{(k)}[y_r(t_1)y_s(t_2)] = \sum_{i=1}^{k} \lambda_i \sum_{j=0}^{m-1} \sum_{l=0}^{m-1} H_{ij}H_{il}Y_{jl}^{(rs)}(t_1, t_2) \quad (25)$$

where

$$Y_{jl}^{(rs)}(t_1, t_2) \equiv I_j^{(r)}(t_1)I_l^{(s)}(t_2). \quad (26)$$

2.2.3 Derivation of Closed-Form Response Solution. In order to obtain the closed-form solution of the response problem, one must evaluate the integral in Eq. (24) which defines the system functions $I_l^{(r)}(t)$. It is useful to note that the $\hat{h}_r(t)$ functions are simply summation of $e^{\kappa_j t}$ terms weighted by particular coefficients, and that the Chebyshev polynomials may also be written in a finite series form:

$$T_l(\xi) = \sum_{k=0}^{l} f_{lk}\xi^k \quad (27)$$

where the f_{lk}'s are given by the following recursion formulas

$$\left.\begin{aligned} f_{00} = 1, \quad f_{10} = 1, \; f_{11} = 1, \\ f_{l+1,0} = -f_{l-1,0}, \quad k = 0 \\ f_{l+1,k} = 2f_{l,k-1} - f_{l-1,k}, \quad k = 1, 2, \ldots, l-1 \\ f_{l+1,k} = 2f_{l,k-1}, \quad k = l, l+1 \end{aligned}\right\}. \quad (28)$$

Introducing coefficients $a_j^{(r)}$ where

$$\hat{h}_r(t) = \sum_{j=1}^{2n} a_j^{(r)} e^{\kappa_j t}, \quad (29)$$

then Eq. (24) may be written as

$$I_l^{(r)}(t) = \sum_{j=1}^{2n} a_j^{(r)} \frac{t_{\max}}{2} e^{\kappa_j (t-(t_{\max}/2))} \times \sum_{k=0}^{l} f_{lk} \int^{((2t/t_{\max})-1)} e^{p_j\xi}\xi^k d\xi \quad (30)$$

where

$$p_j = -\kappa_j \frac{t_{\max}}{2} = c_j + id_j. \quad (31)$$

Clearly for each r, the terms to the right of $a_j^{(r)}$ in Eq. (30) and the integral is computed identically. The $a_j^{(r)}$ terms simply dictate how the $2n$ time-dependent functions should be combined for a particular Chebyshev polynomial of order l. It is quite logical to then proceed with the relatively complicated integral operation on the exponential terms in Eq. (15), which through linear combination make up the $\hat{h}_r(t)$ terms. If the Vandermonde matrix in Eq. (15) is called $\mathbf{V}$, then this yields

$$\{\beta_l(t)\} = \mathbf{V}^{-1}\{\gamma_l(t)\} \quad (32)$$

where the jth term in $\{\gamma_l(t)\}$ is now

$$\begin{aligned} \gamma_{lj}(t) &= \frac{t_{\max}}{2} e^{\kappa_j(t-(t_{\max}/2))} \sum_{k=0}^{l} f_{lk} \int_{-1}^{((2t/t_{\max})-1)} e^{p_j\xi}\xi^k d\xi \\ &= \frac{t_{\max}}{2} e^{\kappa_j(t-(t_{\max}/2))} \sum_{k=0}^{l} f_{lk} \left[\int_{-1}^{((2t/t_{\max})-1)} e^{c_j\xi}\xi^k \cos(d_j\xi) d\xi \right. \\ &\quad \left. + i \int_{-1}^{((2t/t_{\max})-1)} e^{c_j\xi}\xi^k \sin(d_j\xi) d\xi \right] \\ &= \frac{t_{\max}}{2} e^{\kappa_j(t-(t_{\max}/2))} \\ &\quad \times \sum_{k=0}^{l} f_{lk} \left[e^{c_j\xi} \sum_{m=1}^{k+1} \frac{(-1)^{m+1}k!\xi^{k-m+1}}{(k-m+1)!(c_j^2+d_j^2)^{m/2}} \right. \\ &\quad \left. \times (\cos(d_j\xi + m\rho_j) + i\sin(d_j\xi + m\rho_j)) \right]_{-1}^{((2t/t_{\max})-1)} \end{aligned} \quad (33)$$

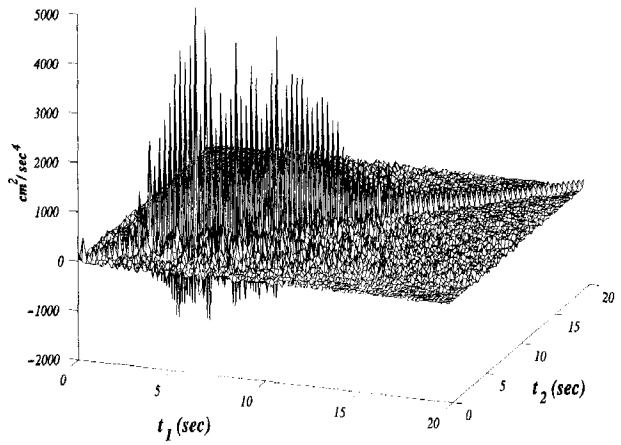


Fig. 2 Exact covariance matrix [C] representing the first 20 seconds of the ensemble corresponding to the 1994 Northridge earthquake accelerations

Downloaded 04 May 2010 to 171.66.16.26. Redistribution subject to ASME license or copyright; see http://www.asme.org/terms/Terms_Use.cfm

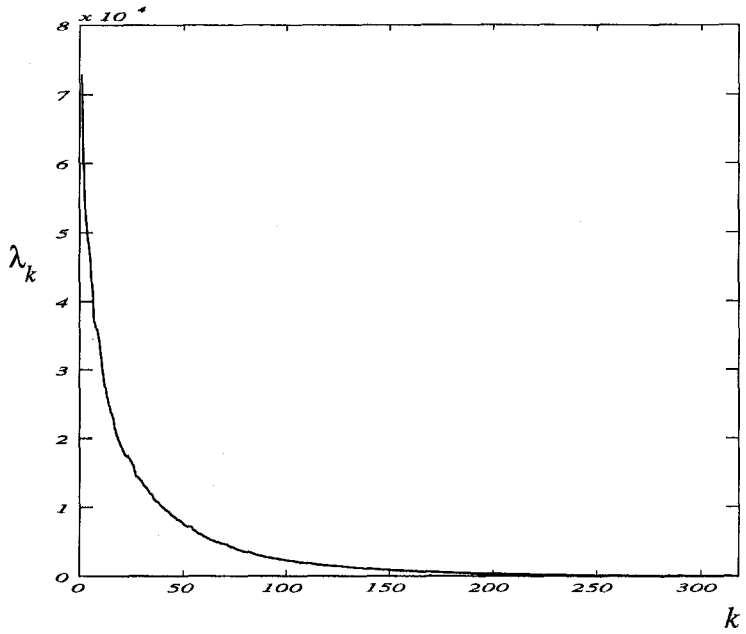


Fig. 3 Rate of convergence of the eigenvalues λ_k of the covariance matrix [C] for the 1994 Northridge earthquake data

where

$$\rho_j = \sin^{-1}\left(\frac{-d_j}{\sqrt{c_j^2 + d_j^2}}\right). \quad (34)$$

Following Eq. (14), but using the $\beta_l(t)$'s instead of the $\alpha(t)$'s, one may define a modified system matrix

$$[\mathbf{g}(l, t)] = \beta_{l0}(t)\mathbf{I} + \beta_{l1}(t)\mathbf{A} + \ldots + \beta_{l2n-1}(t)\mathbf{A}^{2n-1}. \quad (35)$$

Then, using the combination scheme of Eq. (23), one can write the system functions as

$$I_l^{(r)}(t) = \sum_{s=n+1}^{2n} g_{rs}(l, t). \quad (36)$$

Combining this result with Eq. (26) and Eq. (25), one obtains the closed-form analytical expression for the response covariance.

3 Applications

3.1 Ground Motion Records From the Northridge Earthquake. An ensemble of 318 accelerograms was selected from the 1994 Northridge earthquake data sets of the California

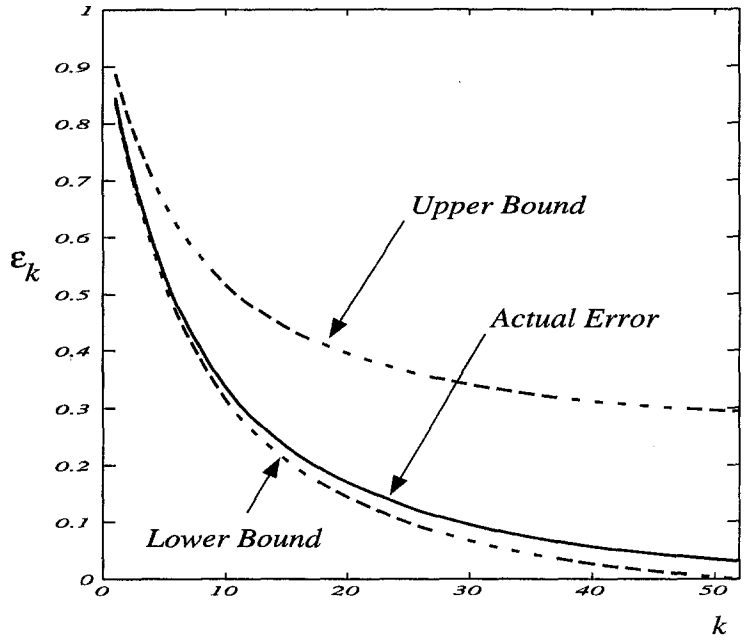


Fig. 4 Variation of the dimensionless energy-related error measure ϵ_k and its bounds with the number k of eigenvectors used to reconstruct $[C_k]$ for the 1994 Northridge earthquake

Downloaded 04 May 2010 to 171.66.16.26. Redistribution subject to ASME license or copyright; see http://www.asme.org/terms/Terms_Use.cfm

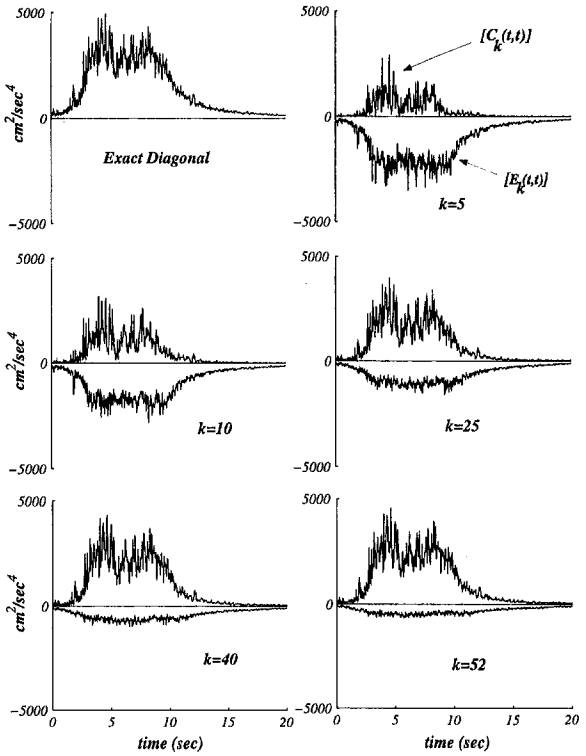


Fig. 5 Comparison between the diagonal elements of [C] and [C_k] for different values of truncation parameter k

Division of Mines and Geology (CDMG, 1994) and the USC Los Angeles Strong Motion Network (USC, 1996). Records belonging to the data sets have been digitized at 0.02 seconds, baseline-corrected, and band-pass filtered between 0.07–25 Hz. An effort was made to select a subset corresponding to all available free-field or building basement measurements included in the above referenced data sets. The validity of records from two of the available sites has been questioned, so these were omitted from the ensemble.

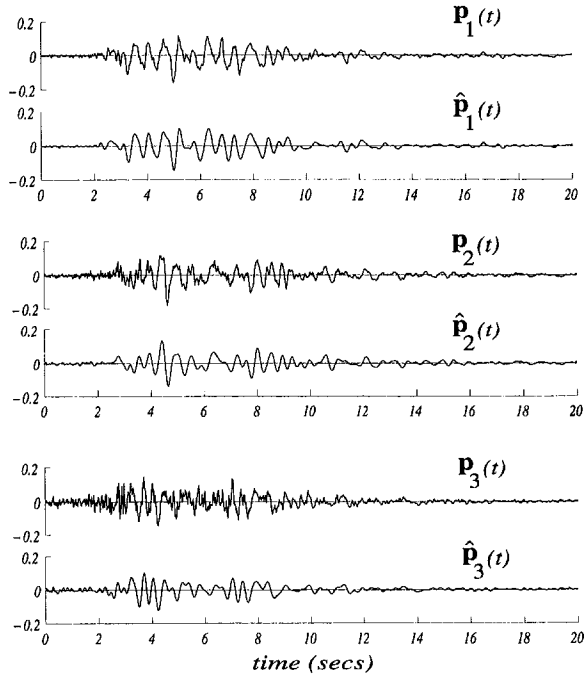


Fig. 6 The first three exact eigenvectors $p_i(t)$ of [C] and their corresponding least-squares fit $\hat{p}_i(t)$ for the 1994 Northridge earthquake, using 200 Chebyshev coefficients

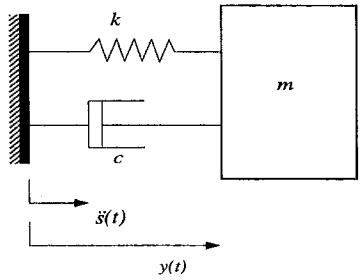


Fig. 7 Single-degree-of-freedom system

The available records were collected from locations reasonably spread out in and around the Los Angeles metropolitan area. In this study, vertical and horizontal records were included in the ensemble to be processed, and the records were synchronized from a one percent g trigger threshold in the horizontal direction at each site.

A representative sample of the 318 selected accelerograms is shown in Fig. 1. The time span shown corresponds to the first 20 seconds of ground shaking. For ease of comparison, identical acceleration scales are used for the plotted records. The considerable variation among the ensemble members is self-evident.

3.2 Construction of Covariance Kernels. The covariance matrix $[C]$ of order (1001×1001) representing the first 20 seconds of the ensemble of ground acceleration records discussed above, is shown in Fig. 2. Notice that the surface is symmetric with respect to the diagonal which represents the time variation of the mean square of the records.

The validity of collecting an ensemble of earthquake records from a spatially distributed region, and arguing that this may be representative of the average for that event is debatable. In this study, the main goal is to demonstrate the compaction and general response simulation method for a generic nonstationary random process.

3.3 Compact Probabilistic Representation of Earthquake Records.

3.3.1 Spectral Representation of Covariance Matrix. The 318 nonvanishing eigenvalues λ_k of $[C]$ for the Northridge data set were computed and their magnitudes are shown in Fig. 3. Note that the first (largest) eigenvalue is $\lambda_1 \approx 7.28 \times 10^4$ while

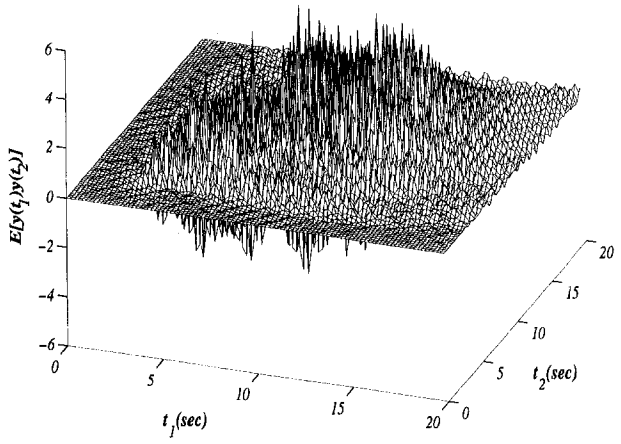


Fig. 8 Output covariance matrix $K_{yy}(t_1, t_2)$ of a representative single-degree-of-freedom system based on using 52 least-square fitted eigenvectors to reconstruct the input covariance matrix [$\hat{C}_{52}$]

Downloaded 04 May 2010 to 171.66.16.26. Redistribution subject to ASME license or copyright; see http://www.asme.org/terms/Terms_Use.cfm

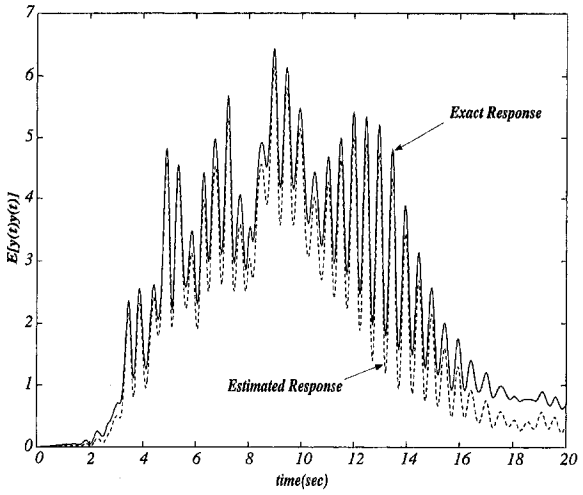


Fig. 9 Comparison of the transient mean-square response of a single-degree-of-freedom oscillator obtained by (1) direct numerical integration using the exact [C], and (2) using the analytical expression in Eq. (25), which incorporates truncation as well as least-squares fit errors corresponding to $[\hat{C}_{52}]$

$\lambda_{318} \approx 4.57 \times 10^{-11}$. Since $[C]$ in the present application was constructed from 318 distinct records, all eigenvalues beyond number 318 are zero (Treitel and Shanks, 1971).

For the Northridge data set, the number of eigenvalues chosen to approximate the exact matrix was 52. This cutoff value of k corresponds to an eigenvalue with ten percent of the magnitude of the maximum eigenvalue. The choice of ten percent is arbitrary.

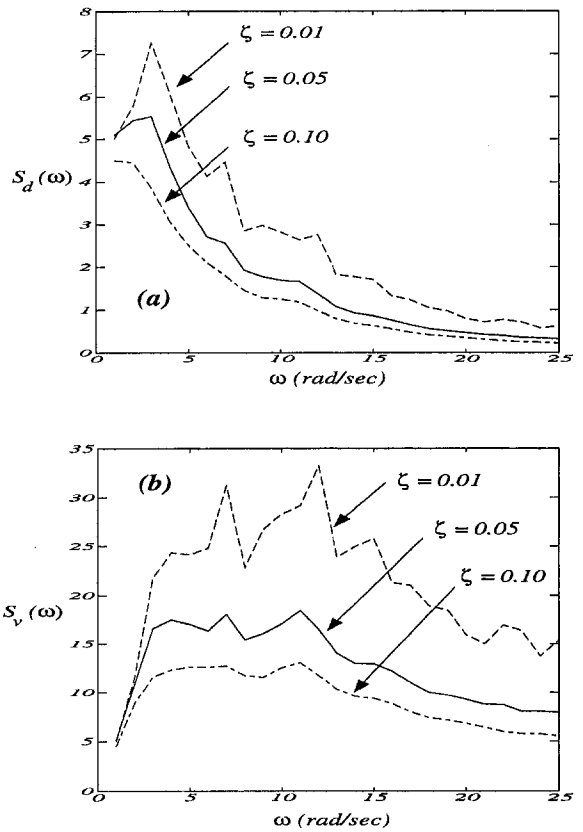


Fig. 10 Spectral plots of the influence of the ratio of critical damping ζ on the extreme values of the rms displacement and velocity of a representative single-degree-of-freedom system under the 1994 Northridge earthquake

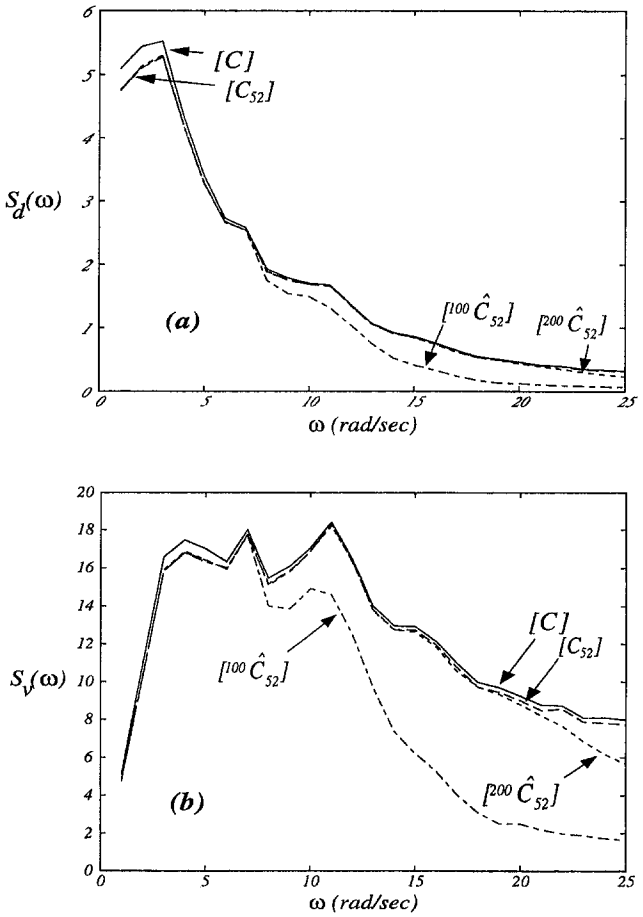


Fig. 11 Spectral plots of the influence of eigenvector truncation errors as well as least-squares fit errors on the extreme values of the rms displacement and velocity of a representative single-degree-of-freedom system having a unit mass and ζ = 0.05 under the excitation of the 1994 Northridge earthquake

3.3.2 Convergence Rates of the Eigenvector Expansion. The rate of convergence of $[C_k]$ to $[C]$ as measured by the dimensionless, energy-related error term ϵ_k as given by Eq. (3) is presented along with the respective upper and lower error bounds (Eq. (4) and Eq. (5)) in Fig. 4.

Although there is naturally some discrepancy between the truncated series and the exact energy value, these first 52 eigenvalues clearly capture most of the energy transmitted by the ground motion. Another illustration of the quality of fit achieved by using only the first 52 eigenvalues can be seen in Fig. 5 where the diagonals of $[C_k]$ are compared with that of $[C]$ for different k values which govern the truncation level. In each of the six panels shown in Fig. 5, the upper portion corresponds

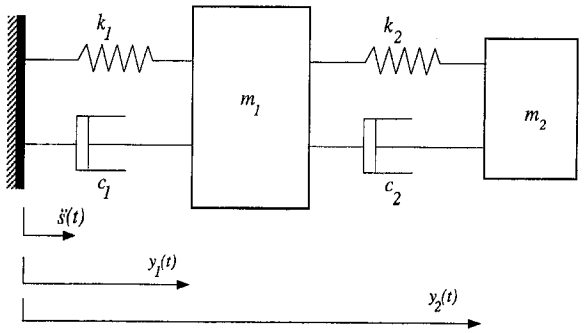


Fig. 12 Two-degree-of-freedom system

Downloaded 04 May 2010 to 171.66.16.26. Redistribution subject to ASME license or copyright; see http://www.asme.org/terms/Terms_Use.cfm

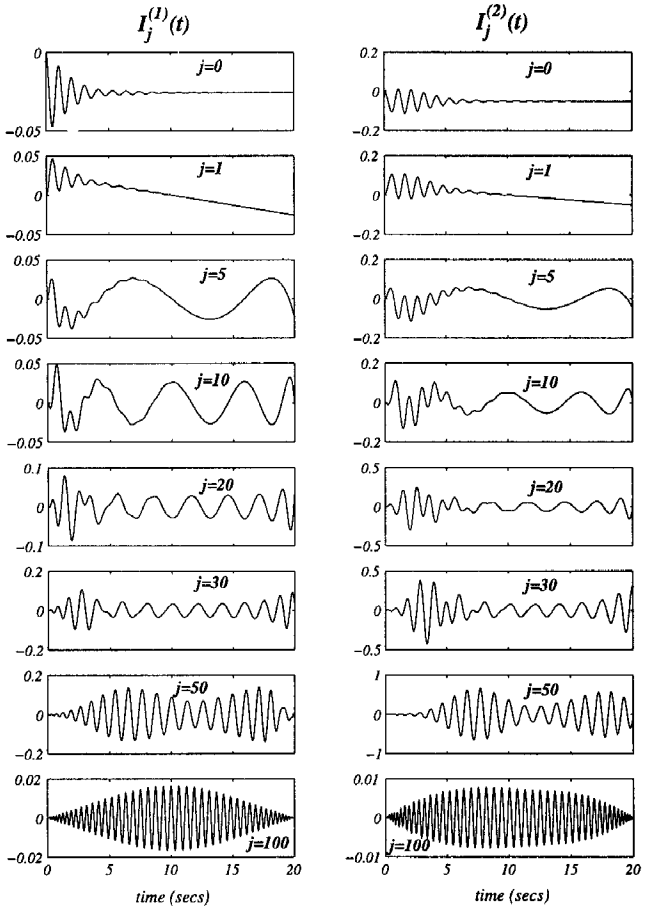


Fig. 13 Sample system functions $I_j^{(r)}(t)$ which represent the response of node r to base acceleration of a Chebyshev polynomial of order j. The system dynamic properties are $\omega_1 = \omega_2 = 2\pi$, $m_2/m_1 = 0.02$, $\zeta_1 = 0.05$, and $\zeta_2 = 0.1$.

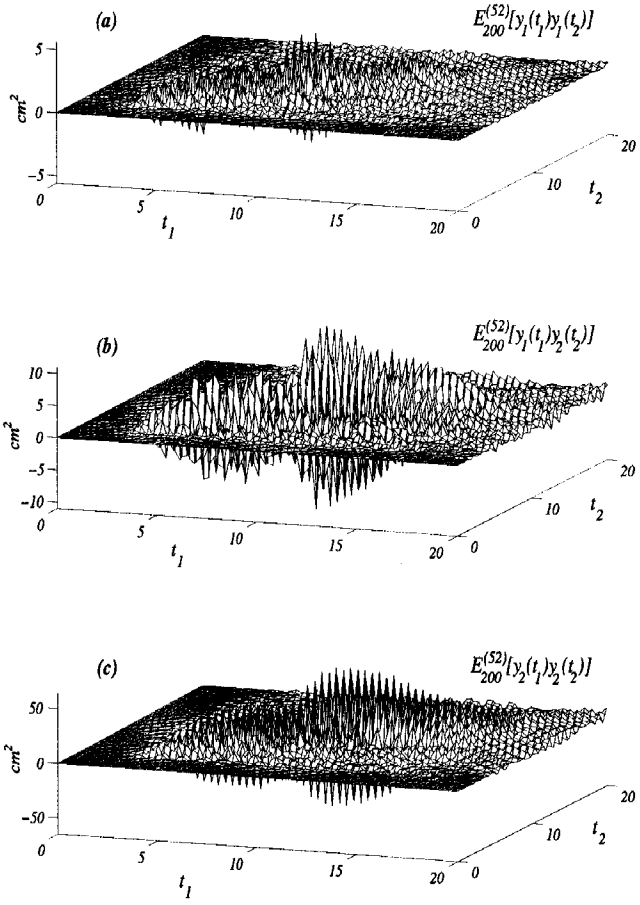


Fig. 14 Two-degree-of-freedom system response covariance matrices for Northridge excitation, (a) $E_m^{(k)}[y_1(t_1)y_1(t_2)]$, (b) $E_m^{(k)}[y_1(t_1)y_2(t_2)]$ and (c) $E_m^{(k)}[y_2(t_1)y_2(t_2)]$ where $k = 52$ and $m = 200$. The system dynamic properties are $\omega_1 = \omega_2 = 2\pi$, $m_2/m_1 = 0.02$, $\zeta_1 = 0.05$, and $\zeta_2 = 0.1$.

to the diagonal terms of the excitation covariance matrix when reconstructed from the first k eigenvectors, and the lower portion shows the corresponding truncation error.

3.3.3 Least-Squares Representation of Covariance Matrix. The second compaction step involves the least-squares fitting of the selected eigenvectors of the covariance matrix as indicated in Eq. (6). In this case the value of m_i (the order of the Chebyshev polynomial fit) was chosen to be 200.

Figure 6 shows the first three dominant eigenvectors $\mathbf{p}_i(t)$ of the excitation covariance matrix along with those $\hat{\mathbf{p}}_i(t)$ approximated by the Chebyshev polynomial fitting. Naturally, for eigenvectors with high-frequency content, higher orders of orthogonal polynomials are required for a better fit.

3.4 Response of a Single-Degree-of-Freedom System to Nonstationary Earthquake Inputs. To illustrate the validity and performance of the method under discussion for probabilistic structural dynamics, the procedure indicated by Eq. (25) is used to analytically determine the covariance matrix of the response of an example single-degree-of-freedom system (shown in Fig. 7) to the Northridge earthquake covariance matrix under discussion.

3.4.1 Transient Mean-Square Response Time History. Figure 8 shows a three-dimensional representation of the output covariance matrix $E[y(t_1)y(t_2)]$ of a single-degree-of-freedom system based on using the first 52 eigenvectors that have been least-squares fitted by approximating Chebyshev polynomials. The example single-degree-of-freedom system used in Fig. 8 has a natural frequency of 1.0 Hz and a damping ratio of ζ = 0.05. The time scale is in units of seconds and the amplitude scale is in units of cm^2.

The transient mean-square response of the single-degree-of-freedom system is obtained from Eq. (25) by letting $t_1 = t_2 = t$. The m.s. response of this example single-degree-of-freedom oscillator was also determined by direct numerical evaluation of the double integral appearing in Eq. (13), using the exact $[C]$ and the result is compared with the estimated response in

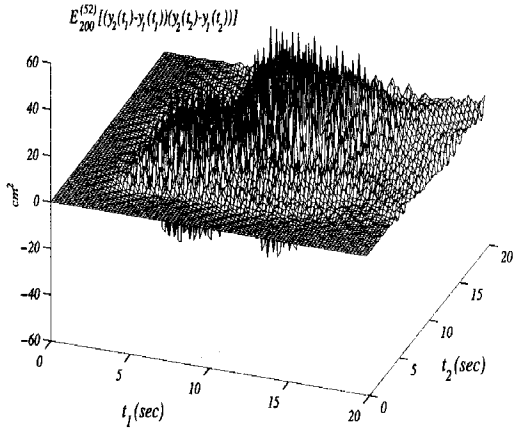


Fig. 15 Two-degree-of-freedom system relative response covariance matrix for Northridge excitation $E_m^{(k)}[(y_2(t_1) - y_1(t_1))(y_2(t_2) - y_1(t_2))]$. The system dynamic properties are $\omega_1 = \omega_2 = 2\pi$, $m_2/m_1 = 0.02$, $\zeta_1 = 0.05$, and $\zeta_2 = 0.1$.

Downloaded 04 May 2010 to 171.66.16.26. Redistribution subject to ASME license or copyright; see http://www.asme.org/terms/Terms_Use.cfm

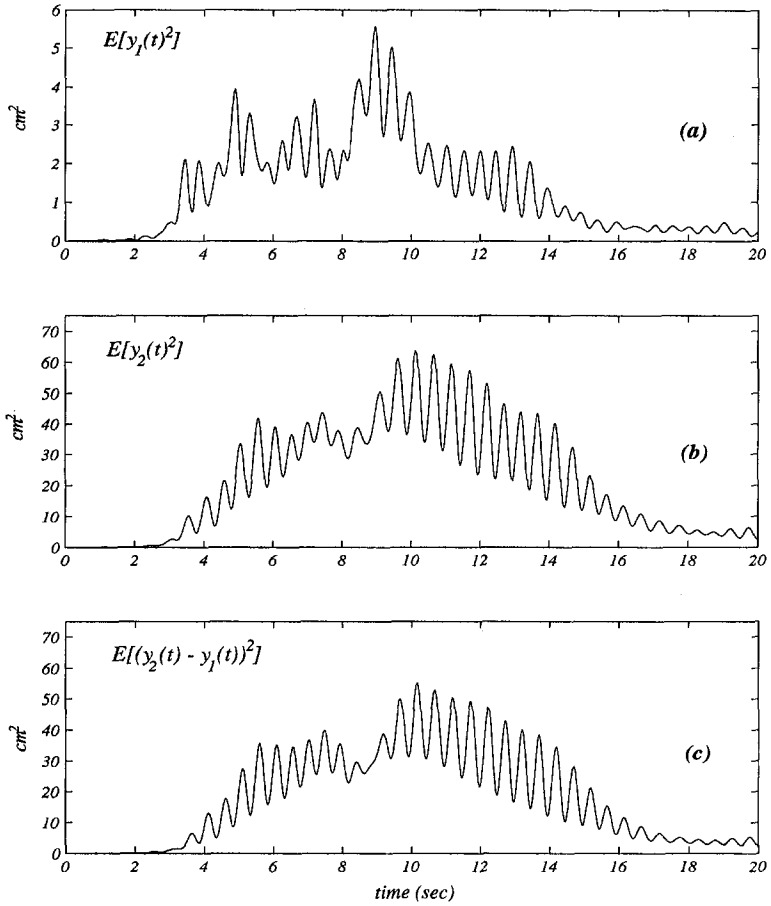


Fig. 16 Transient mean-square responses of (*a*) primary system m_1, (*b*) auxiliary mass m_2, and (*c*) the proximity between m_1 and m_2. For this example $\mu = 0.02$, $\omega_1 = \omega_2 = 2\pi$, $\zeta_1 = 0.05$, and $\zeta_2 = 0.1$.

Fig. 9. The estimated response includes eigenvector truncation errors (i.e., using only the first 52 eigenvectors) as well as least-squares fit errors in the selected eigenvectors. Although the estimated response also includes errors due to the order of the least-squares fit of the eigenvectors in the series in Eq. (6), in this case, where ω_n is relatively low, the small discrepancy between the two results can be mostly attributed to the truncation of the eigenvector expansion of the input covariance kernel. This error, resulting from the decreased input energy, should be considered when applying the method for the purposes of reliability analysis.

3.4.2 Extreme Values of the RMS Response. The extreme values of the r.m.s. response of a damped single-degree-of-freedom system, defined as

$$S_d(\omega, \zeta) \equiv \sqrt{\max_t \{E[y^2(t)]\}}, \tag{37}$$

where $E[y^2(t)]$ is the m.s. response of the corresponding single-degree-of-freedom system, are plotted in Fig. 10(a) in the form of S_d versus ω. The three curves shown correspond to $\zeta = 0.01$, 0.05, and 0.10. Figure 10(b) shows a corresponding plot for the extreme values of velocity calculated from

$$S_v(\omega, \zeta) \equiv \sqrt{\max_t \{E[\dot{y}^2(t)]\}}. \tag{38}$$

The values of $E[y^2(t)]$ and $E[\dot{y}^2(t)]$ shown in Fig. 10 were calculated by the analytical approach under consideration using the approximating matrix $[{}^{200}C_{52}]$ as input.

To separate errors from truncation (the use of 52 eigenfunctions), and least-squares fit inaccuracies (the use of 200 Chebyshev coefficients), the extreme values of displacement and velocity rms values are calculated from (1) Eq. (13) using the exact covariance matrix $[C]$ as input, (2) Eq. (13) using $[C_{52}]$ as input, (3) Eq. (25) using $k = 52$ and $m = 200$ (i.e., calculating $E^{(52)}_{200}[y(t_1)y(t_2)]$, and (4) also using Eq. (25) with $k = 52$ and $m = 100$. For illustration, a damping coefficient $\zeta = 0.05$ was used, and a unit mass was assumed. Figure 11 shows the results of these calculations. Note that most of the errors for $\omega > 7$ radians/sec are due to least-squares fit inaccuracies.

3.5 Response of a Two-Degree-of-Freedom System to Nonstationary Earthquake Inputs.

3.5.1 Simplified Model of a Building With a Tuned Mass Damper. The two-degree-of-freedom system considered for response simulation consists of a primary system with an attached auxiliary mass damper acting as a tuned dynamic vibration neutralizer. This system is shown in Fig. 12. Simulation of this case will yield probabilistic information on the effectiveness of such a tuned mass damper system, and a probabilistic description of the relative motions of the two masses. The primary system in the two-degree-of-freedom system is identical to the two-degree-of-freedom system used in the previous simulation with $\zeta = 0.05$ and a natural frequency of 1.0 Hz.

A representative sample of the system functions $I_j^{(r)}(t)$ are presented in Fig. 13. Recalling Eq. (24), the system functions yield the transient response of each degree-of-freedom r to a base acceleration of the Chebyshev polynomial of order j. The system functions depend only on the dynamic properties of the system (i.e., they are independent of the excitation). The left-hand side column of plots in Fig. 13 correspond to the system

Downloaded 04 May 2010 to 171.66.16.26. Redistribution subject to ASME license or copyright; see http://www.asme.org/terms/Terms_Use.cfm

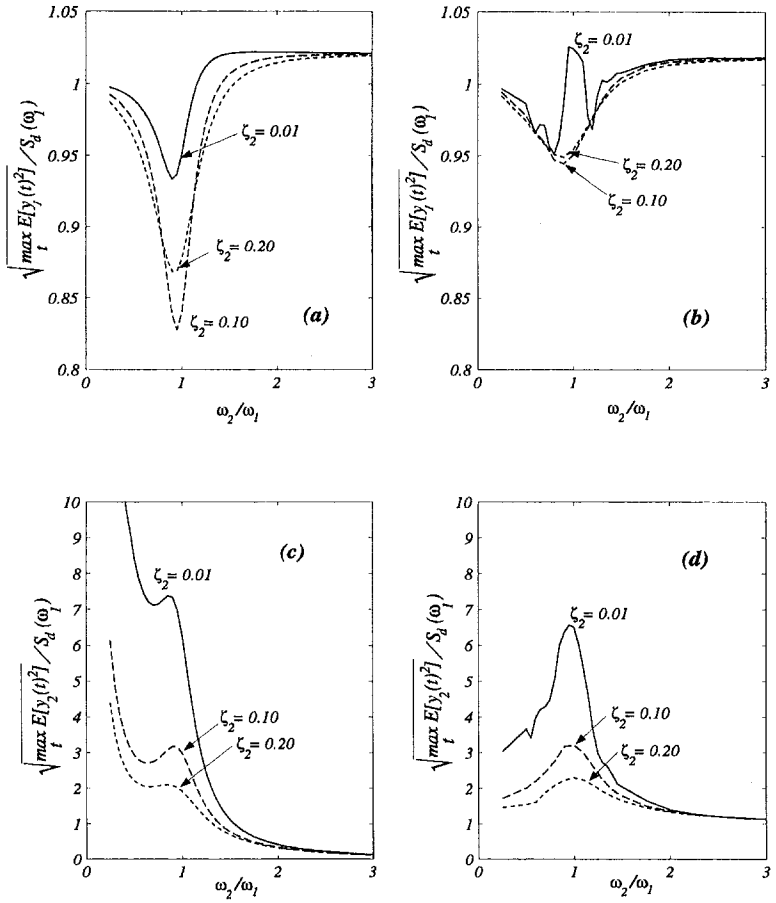


Fig. 17 Comparison of maximum rms response of $y_1(t)$ and $y_2(t)$ with varying ζ_2 for stationary response to white-noise excitation ((*a*) and (*c*)), and for the nonstationary response to the nonstationary Northridge excitation ((*b*) and (*d*)). For this example $\mu = 0.02$, $\omega_1 = 2\pi$, and $\zeta_1 = 0.05$.

functions associated with the primary system, while the right-hand column of plots correspond to those associated with the auxiliary mass damper. All of the plots have identical time scales but different amplitude scales. Note that the various functions exhibit differing spectral contents, and their amplitude scales have no consistent pattern. As can be seen from Eq. (25), the contribution of the various system functions to the system response is "scaled" by pairs that constitute term $Y_{jl}^{(rs)}$ which is subsequently scaled by $H_{ij}H_{il}$ terms and λ_i, which represent the excitation characteristics.

Figures $14(a)-14(c)$ show the response covariance matrix for $E_m^{(k)}[y_1(t_1)y_1(t_2)]$, $E_m^{(k)}[y_1(t_1)y_2(t_2)]$ and $E_m^{(k)}[y_2(t_1)y_2(t_2)]$. For added resolution, different amplitude scales are used for the three functions shown in Fig. 14. The first plot may be compared with the single-degree-of-freedom case (in Fig. 8), and it can clearly be seen that an auxiliary system, which is carefully tuned may reduce the overall response of the primary system. In this case the auxiliary mass was two percent of the primary mass.

To obtain the covariance matrix of the relative motion of the two masses, the following equivalence relationship is used:

$$E_m^{(k)}[(y_2(t_1) - y_1(t_1))(y_2(t_2) - y_1(t_2))]$$
$$= E_m^{(k)}[y_1(t_1)y_1(t_2)] - E_m^{(k)}[y_1(t_1)y_2(t_2)]$$
$$- E_m^{(k)}[y_2(t_1)y_1(t_2)] + E_m^{(k)}[y_2(t_1)y_2(t_2)]. \quad (39)$$

The covariance matrix evaluated in Eq. (39) is shown in Fig. 15. Notice that the r.m.s. value of the maximum relative displacement between the primary and auxiliary mass is much larger than the mean-square value of the maximum displacement of the primary mass. This fact has a significant impact on the design of realistic auxiliary mass dampers where practical relative motion constraints must be coped with.

The transient mean-square response of the two-degree-of-freedom system under consideration is presented in Fig. $16(a)-(c)$. Figure $16(a)$ may be compared with the response of the primary system alone in Fig. 9. Figure $16(c)$ gives the m.s. transient response of the relative displacement of the auxiliary mass with respect to the primary system. Note that the amplitude scale for the m.s. of the relative motion is an order-of-magnitude larger than the corresponding scale for the m.s. of the primary system.

3.5.2 Extreme Values of the Response Spectra. Numerous response evaluations were conducted using this compact analytical method on the primary/auxiliary-mass damper system with varying parameters. This permitted the study of the optimum values for a representative primary system subjected to this particular nonstationary support excitation. First, the effect of varying the values of ζ_2 is investigated. The results are shown in Fig. $17(b)$ and (d), along with corresponding stationary response obtained for identical systems experiencing stationary white-noise support excitation (Figs. $17(a)$ and (c)). The results for the stationary case were obtained from the analytical solution to this problem (Crandall and Mark, 1973). All of the extreme r.m.s. response quantities are normalized by the extreme r.m.s. response of the primary system alone to the respective excitation, denoted by $S_d(\omega_1)$. When comparing Fig. $17(b)$ with Fig. $17(a)$ it is clear that the effectiveness of passive mass

Downloaded 04 May 2010 to 171.66.16.26. Redistribution subject to ASME license or copyright; see http://www.asme.org/terms/Terms_Use.cfm

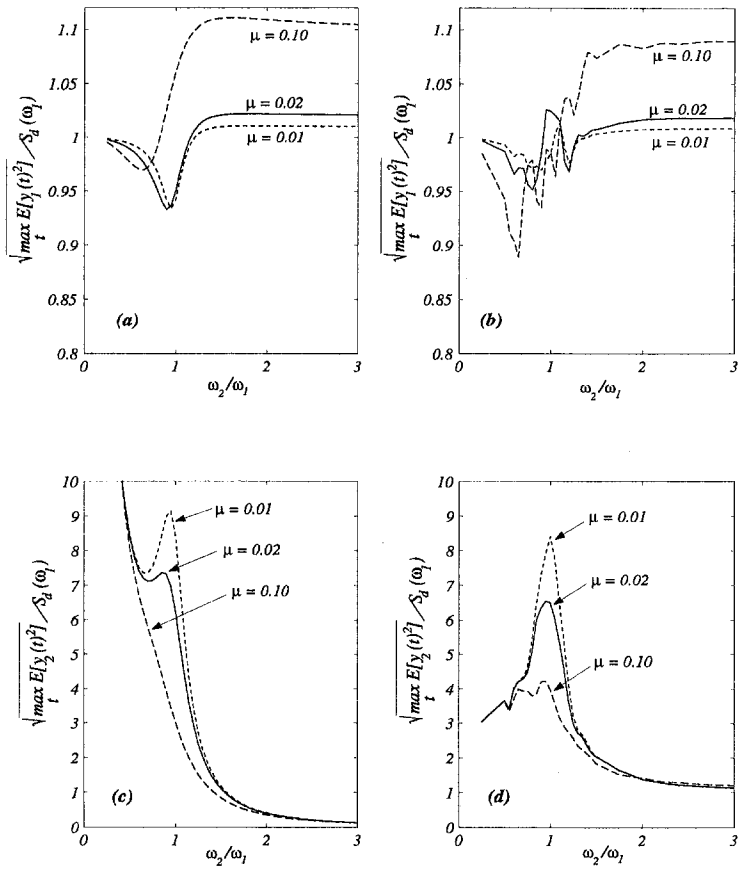


Fig. 18 Comparison of maximum rms response of $y_1(t)$ and $y_2(t)$ with varying $\mu = m_2/m_1$ for stationary response to white-noise excitation ((*a*) and (*c*)), and for the nonstationary response to the nonstationary Northridge excitation ((*b*) and (*d*)). For this example, $\omega_1 = 2\pi$, $\zeta_1 = 0.05$, and $\zeta_2 = 0.01$.

damper systems is greatly reduced for nonstationary excitation and response. In fact, with a poor choice of $\zeta_2 = 0.01$, the auxiliary damper causes the primary system to actually have a larger expected extreme response than it would have had on its own. Even a good choice of $\zeta_2 = 0.1$ and a ω_2/ω_1 ratio of slightly less than one, which reduces the response in the stationary case by about 17 percent, only yields a reduction of six percent in this particular nonstationary excitation case. The extreme response plots for the auxiliary system appear qualitatively similar to the extreme relative motion spectra due to the relative magnitudes of $y_2(t)$ and $y_1(t)$.

The results of varying the mass ratio $\mu = m_2/m_1$ are examined for a system with $\omega_1 = 2\pi$, $\zeta_1 = 0.05$ and $\zeta_2 = 0.01$. Again the results are contrasted in Fig. 18 with the analytical results of stationary response for stationary white noise excitations. Along with the other differences between the stationary excitation case and the nonstationary case, it is interesting to note, when comparing Fig. 18(b) with Fig. 18(a), that a choice of $\mu = 0.1$ and assumed $\zeta_2 = 0.01$ is not a particularly good choice in the stationary case for this system, but that it could, however, be a good choice for this particular nonstationary excitation and an optimum ω_2/ω_1 ratio.

4 Discussion

From the single-degree-of-freedom response comparisons between the exact response to a probabilistic input, and that obtained through the compact estimate of the input, it is clear that for well-chosen polynomial fit-orders and eigenvalue truncation quantities, response results are very accurate. In the compaction application presented here, there was only a three percent energy truncation error, while, with a polynomial fit of order 200, only $\frac{1}{30}$th of the original quantity of data was required to store the input process. It is important to reiterate, that after the estimate of the input covariance is made in Eq. (8), no further approximations are made in obtaining the system response.

Although the primary purpose of this study is not to present a detailed parametric study of the performance of a primary/auxiliary mass damper system from the structural control point of view, some interesting reminders of the limited effectiveness of passive auxiliary dampers are given for highly nonstationary support excitation.

It is useful to note also that a convenient by-product of the state-variable formulation of the response problem is that second-moment probabilistic descriptions of the velocity response are obtained directly with no additional computation.

5 Summary and Conclusions

A relatively straightforward method has been presented for the compaction of nonstationary random process realization data into an analytical form which may be used as input to general linear multi-degree-of-freedom dynamic systems with arbitrary characteristics (i.e., no restrictions on the damping elements) to obtain the exact closed-form response solution. The ensemble data covariance matrix compaction is done in two steps: (1) the spectral decomposition of the data covariance matrix by the Karhunen-Loeve expansion, and (2) the least-squares fitting of the dominant eigenvectors of the covariance matrix with orthogonal polynomials. The analytical approximation of the input data was used to obtain exact analytical expressions for the response of general linear multi-degree-of-freedom dynamic systems. Given reasonable choices of the parameters governing the accuracy of the approximation of the input, excellent accu-

Downloaded 04 May 2010 to 171.66.16.26. Redistribution subject to ASME license or copyright; see http://www.asme.org/terms/Terms_Use.cfm

racy was obtained for the system response. It is important to note also, that the derived closed-form response solution is suitable for general linear multi-degree-of-freedom systems, and relies in no way upon assumptions of classical normal modes.

Although the data used in this study was obtained from actual ground motion records, this method also has potential for simplifying and reducing the computational effort involved in numerical (Monte Carlo) simulation studies using synthetically generated input realizations. An ensemble of synthetically generated input records could be collected, processed using the proposed compaction method, and finally used to analytically obtain the second-moment probabilistic description of a dynamic system response.

In the context of the earthquake engineering field, the data compaction method in this study will become progressively more useful with the continuing proliferation in seismological instrumentation worldwide. The data-processing approach is not only a useful data-archiving and earthquake feature-extraction tool, but also provides a probabilistic measure of the average statistical characteristics of earthquake ground motion corresponding to a spatially distributed region. Such a representation could be a valuable tool in risk management studies to quantify the average seismic risk over a spatially extended area.

Acknowledgment

This study was supported in part by grants from the National Science Foundation and from the Air Force Office of Scientific Research. The assistance of Prof. George W. Housner is appreciated.

References

California Division of Mines and Geology, 1994, "Processed CSMIP Strong Motion Records from the Northridge, CA Earthquake of Jan. 17, 1994," Release 6 and 9.

Caughey, T. K., and Stumpf, H. J., 1961, "Transient Response of a Dynamic System under Random Excitation," ASME JOURNAL OF APPLIED MECHANICS, Vol. 28, pp. 563–566.

Conte, J. P., and Peng, B.-F., 1996, "An Explicit Closed-Form Solution for Linear Systems Subjected to Nonstationary Random Excitation," *Probabilistic Engineering Mechanics,* Vol. 11, pp. 37–50.

Corotis, R. B., and Vanmarcke, E. H., 1975, "Time-Dependent Spectral Content of System Response," *J. Engrg. Mech. Div., ASCE,* Vol. 101, No. 5, pp. 623–637.

Crandall, S. H., and Mark, W. D., 1973, *Random Vibration in Mechanical Systems,* Academic Press, New York.

DebChaudhury, A., and Gasparini, D. A., 1982, "Response of MDOF Systems to Vector Random Excitation," *J. Engrg. Mech. Div., ASCE,* Vol. 108, No. 2, pp. 367–385.

Graupe, D., 1976, *Identification of Systems,* Robert E. Kreiger, Huntington, NY.

Hou, Z. K., 1990, "Nonstationary Response of Structures and its Application to Earthquake Engineering," Report No. EERL 90-01, Cal. Institute of Technology, Pasadena, CA.

Iwan, W. D., and Hou, Z. K., 1989, "Explicit Solutions for the Response of Simple Systems subjected to Nonstationary Random Excitation," *Struct. Safety,* Vol. 6, pp. 77–86.

Langley, R. S., 1986, "Structural Response to Nonstationary Non-White Stochastic Ground Motions," *Earthquake Engrg. and Struc. Dyn.,* Vol. 14, pp. 909–924.

Lin, Y. K., and Cai, G. Q., 1995, *Probabilistic Structural Dynamics: Advanced Theory and Applications,* McGraw-Hill, New York.

Lutes, L. D., and Sarkani, S., 1997, *Stochastic Analysis of Structural and Mechanical Vibrations,* Prentice-Hall, Englewood Cliffs, NJ.

Masri, S. F., and Miller, R. K., 1982, "Compact Probabilistic Representation of Random Processes," ASME JOURNAL OF APPLIED MECHANICS, Vol. 49, pp. 871–876.

Masri, S. F., Miller, R. K., and Traina, M.-I., 1990, "Probabilistic Representation and Transmission of Earthquake Ground Motion Records," *Earthquake Eng. and Structural Dynamics,* Vol. 19, pp. 1025–1040.

Mercer, T., 1909, "Functions of Positive and Negative Type and Their Connection with Theory of Integral Equations," *Trans. London Phil. Soc.,* Vol. A209, pp. 415–446.

Moler, C., and Van Loan, C., 1978, "Nineteen Dubious Ways to Compute the Exponential of a Matrix," *SIAM Review,* Vol. 20, No. 4, Oct., pp. 801–836.

Papadimitriou, C., and Beck, J. L., 1990, "Nonstationary Stochastic Characterization of Strong-Motion Accelerograms," *Proc. of 4th U.S. National Conf. on Earthquake Engineering,* Vol. 1, pp. 477–86.

Papadimitriou, C., and Beck, J. L., 1994, "Approximate Random Vibration Analysis of Classically Damped MDOF Systems," *Journal of Engineering Mechanics,* Vol. 120, No. 1, Jan., pp. 75–96.

Scheid, F., 1968, *Numerical Analysis,* Schaum, New York.

Shinozuka, M., and Deodatis, G., 1988, "Stochastic Process Models for Earthquake Ground Motion," *Probabilistic Engineering Mechanics,* Vol. 3, No. 3, pp. 114–123.

Soong, T. T., and Grigoriu, M., 1993, *Random Vibration of Mechanical and Structural Systems,* Prentice-Hall, Englewood Cliffs, NJ.

Spanos, P. T. D., and Lutes, L. D., 1980, "Probability of Response to Evolutionary Process," *J. Engrg. Mech., ASCE,* Vol. 106, No. 2, pp. 213–224.

Thomas, J. B., 1981, *An Introduction to Applied Probability and Random Processes,* Robert E. Krieger, Huntington, NY.

Todorovska, M., 1996, "Strong Motion Records (Volume 1, Volume 2 and Volume 3) of the Northridge Earthquake (17 January, 1994, M = 6.7)," Los Angeles Strong Motion Network, University of Southern California, Los Angeles, CA.

Traina, M. I., Miller, R. K., and Masri, S. F., 1986, "Orthogonal Decomposition and Transmission of Nonstationary Random Processes," *Probabilistic Engineering Mechanics,* Vol. 1, No. 3, pp. 136–149.

Treitel, S., and Shanks, J. L., 1971, "The Design of Multistage Separable Planar Filters," *IEEE Trans. Geos. Electron.,* Vol. 9, No. 1, pp. 10–27.

Tumarkin, A., Tumarkin, A., and Archuleta, R., 1996, "The Strong Motion Data Base," Southern California Earthquake Center, Los Angeles, CA.

Vanmarke, E. H., 1979, "Some Recent Developments in Random Vibration," ASME *Applied Mechanics Reviews,* Vol. 32, No. 10, pp. 1197–1202.

Downloaded 04 May 2010 to 171.66.16.26. Redistribution subject to ASME license or copyright; see http://www.asme.org/terms/Terms_Use.cfm

V. H. Bulsara
Cummins Engine Company,
Box 3005, Mailcode 41618,
Columbus, IN 47202-3005
Mem. ASME.

Y. Ahn
Department of Mechanical Engineering,
Hanyang University,
Kyungki-Do 425-791, Korea

S. Chandrasekar
School of Industrial Engineering,
Purdue University,
1287 Grissom Hall,
West Lafayette, IN 47907-1287
Mem. ASME

T. N. Farris
School of Aeronautics and Astronautics,
Purdue University,
1282 Grissom Hall,
West Lafayette, IN 47907-1282

Mechanics of Polishing

A model has been developed to determine the number and sizes of abrasive particles involved in material removal in polishing, and the forces acting on these particles. The effect of particle size on these parameters has been simulated for a range of particle sizes. It is shown that when polishing with abrasive powders having relatively broad size distributions, only a very small percentage of the particles are involved in material removal. Further, these particles are comprised of the larger particles occurring in the tail end of the particle size distribution. The average force on a particle is found to be in the range of 5–200 mN under typical polishing conditions, which is of the order of loads used in micro-indentation hardness testing. These predictions of the model are consistent with observations pertaining to polished surfaces and the polishing process.

Introduction

A common method for making surfaces smooth is by rubbing them against a block with an abrasive slurry interspersed between them. This process is called polishing or sometimes, lapping. The block is typically made of a metal, e.g., cast iron, tin, or it consists of a soft flexible material such as cloth, nylon, or leather attached to the surface of a metal block. The polishing slurry is composed of hard, abrasive particles (e.g., diamond, silicon carbide, alumina) suspended in a fluid medium such as deionized water, glycol, or viscous oil. A force is applied to the work surface by the polishing block, this force typically corresponding to a polishing pressure of 7–14 kPa (1–2 p.s.i.), where polishing pressure is the polishing force divided by the work surface area. The relative sliding velocity between the block and the work surface is usually less than 0.5 m/s and randomly oriented through the course of the process so as to produce a smooth surface devoid of directional scratches. This velocity is one to two orders of magnitude less than the relative velocity between an abrasive wheel and workpiece in grinding. An early important application of polishing was in lens making and indeed it was for this reason that the process was studied by Newton, Herschel, and Rayleigh (Rayleigh, 1901). Since then, polishing has become a critical process in many applications ranging from the manufacture of precision mechanical components to electronic substrates and optical windows.

While the applied polishing force is low and in itself insufficient even to cause considerable elastic deformation of the work surface, this force is transmitted to the surface, not uniformly, but at the microscopic contacts between the abrasive particles and the work surface (Samuels, 1982; Rabinowicz, 1968). At these contacts the pressure imposed by a particle on the surface should be quite high, often comparable to the hardness of the work material. Consequently, the mechanism of material removal in polishing, which varies from brittle fracture to plastic microcutting, is not so much dictated by the applied polishing force as by the manner in which this force is transmitted locally by the particles to the work surface. This is consistent with microscopic observations of polished surfaces and polishing debris which indicate that the abrasive particles act like single-point cutting tools or indenters (Samuels, 1982; Aghan and Samuels, 1970). The force applied by an abrasive particle also plays a major role in determining polishing temperatures (Bulsara et al., 1997), and the extent of plastically deformed layers and residual stresses on polished surfaces (Samuels, 1982; Chandrasekar and Chaudhri, 1993; Hockey, 1971; Kinoshita et al., 1976). Because of the critical importance of these forces to the mechanics of polishing, it is of interest to deduce the magnitude and distribution of these forces and their dependence on polishing parameters.

Background

A preliminary step towards determining the force acting on an abrasive particle was taken by us in Chauhan et al. (1993) where a model describing the transmission of the polishing force to the work surface was formulated based on ideas introduced by Imanaka (1966). We showed there, that the size distribution of particles used in the polishing slurry had a major influence on the number of particles involved in material removal and on the forces acting on these particles. Further, our calculations (Chauhan et al., 1993) indicated that of the particles present on the work surface, only a small number were engaged in material removal and that these were the larger particles occurring in the tail end of the particle size distribution. While the analysis yielded several new results, a detailed study of the forces acting on the particles and their dependence on particle size was precluded by the way in which the particle size distribution was described in the model. Since a normal distribution, which is unbounded, was used to describe the particle sizes (or diameters) which always lie between a minimum and a maximum value, details about the tail end of the distribution could

Contributed by the Applied Mechanics Division of THE AMERICAN SOCIETY OF MECHANICAL ENGINEERS for publication in the ASME JOURNAL OF APPLIED MECHANICS.

Discussion on the paper should be addressed to the Technical Editor, Professor Lewis T. Wheeler, Department of Mechanical Engineering, University of Houston, Houston, TX 77204-4792, and will be accepted until four months after final publication of the paper itself in the ASME JOURNAL OF APPLIED MECHANICS.

Manuscript received by the ASME Applied Mechanics Division, Mar. 3, 1997; final revision, Aug. 25, 1997. Associate Technical Editor: R. Becker.

 Copyright © 1998 by ASME

Downloaded 04 May 2010 to 171.66.16.26. Redistribution subject to ASME license or copyright; see http://www.asme.org/terms/Terms_Use.cfm

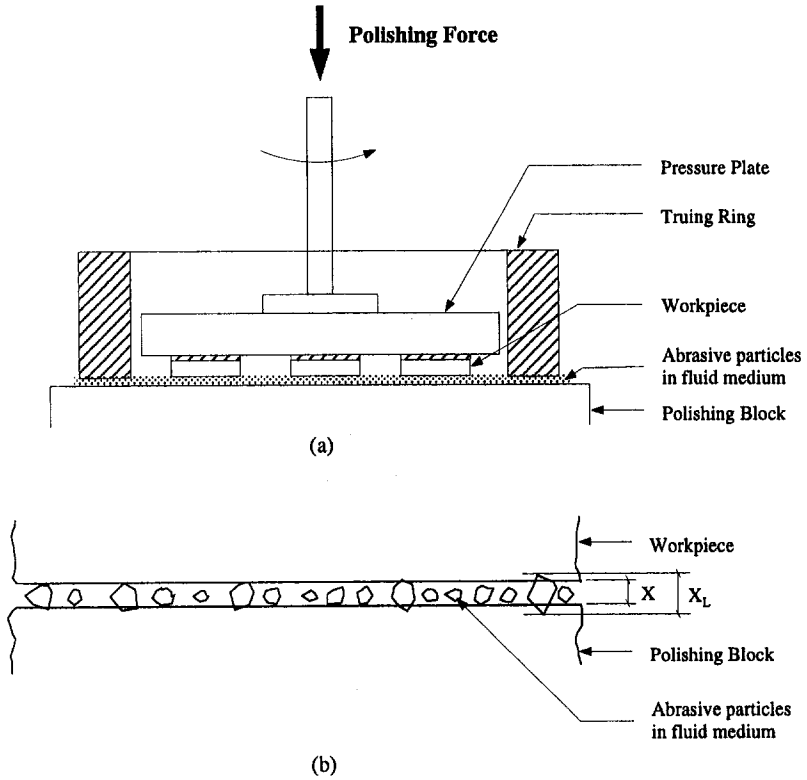


Fig. 1 Schematic of (*a*) polishing process, and (*b*) abrasive-workpiece contact in polishing

not be accurately represented, these details being the very ones which were shown to be of greatest significance to the mechanics of polishing in the analysis (Chauhan et al., 1993). Nor could a normal distribution, which is symmetric about its mean, be used to adequately represent particle sizes whose probability density function is skewed; such a density function is quite characteristic of fine grit size abrasives (see discussion later).

In this paper, we present an extensive refinement of the polishing force model described in Chauhan et al. (1993) which removes the limitations discussed above. A key step in the refinement is the use of a bounded lognormal distribution to accurately represent the variation in abrasive particle size. A detailed analysis is made of the number and sizes of particles involved in material removal, the forces acting on these particles, and the surface roughness on polished surfaces.

General Description of the Force Model

Figure 1 shows a schematic of a typical polishing process. The work surface and the polishing block are separated by a distance X which depends on the applied polishing force, P_{total}, and other parameters. The abrasive particles in the polishing slurry are not all of the same size but are usually statistically distributed with a mean diameter of d and variance of σ^2. The complex nature of the deformation and fracture processes occurring at the microscopic contacts between the particles and the work surface precludes a detailed modeling of polishing which takes into account the mechanism of material removal. Indeed, such a model has not been well developed even for the cutting of metals with single-point tools. The approach taken here seeks to move away from considering the details of the material removal mechanism(s) by assuming that the loading of an abrasive particle against a work surface resembles the quasi-static indentation of a half-space by a hard rigid indenter. By making this simplifying assumption, it becomes possible to formulate a model for calculating the normal force acting on a particle during polishing and for estimating the number of particles engaged in material removal at any given instant.

The major assumptions made in the model are (see Fig. 2):

1 the contact between an abrasive particle and the work surface resembles the quasi-static indentation of a half-space by a hard indenter. A fully developed plastic zone forms around this contact so that the mean contact pressure applied by the particle is equal to the hardness (H) of the workpiece material. In this zone, the elastic strains are a negligible fraction of the total strain and can be ignored.

2 the abrasive particle acts like a sharp conical indenter with a semiapical angle, θ. This geometry is consistent with observations showing abrasive particles to have negative rake angles (Samuels, 1982). The depth of penetration (δ) of such a conical indenter into the workpiece under the action of a force (P) can then be estimated.

3 the abrasive particle sizes are described by an appropriate probability density function. In our analysis a bounded, lognormal distribution is used.

4 only those abrasive particles having a mean diameter greater than the separation distance (X) between the work surface and the polishing block are involved in material removal (Fig. 1(b)). Such particles are, henceforth, referred to as *active* particles or as the particles involved in polishing.

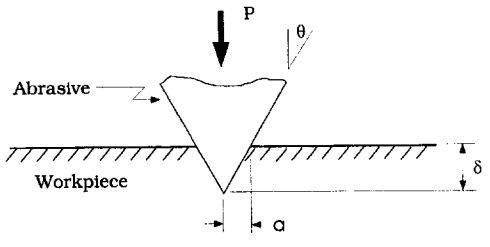


Fig. 2 Conical indenter model of the contact between an abrasive particle and the workpiece used to calculate polishing forces

Downloaded 04 May 2010 to 171.66.16.26. Redistribution subject to ASME license or copyright; see http://www.asme.org/terms/Terms_Use.cfm

5 The externally applied polishing force (P_{total}) is transmitted to the workpiece through the active particles, so that the sum of the individual forces (P_i) on these particles is equal to P_{total}.
6 there is no interaction between the stress fields of different abrasive-workpiece contacts.
7 particles flow into and out-of-the-work region in such a way that the distribution of particle size remains constant.

Formulation

Abrasive particles are usually available in different grit sizes (i.e., particle sizes) from the manufacturer. For each grit size, the particle diameters are distributed between a minimum size, x_{min}, and a maximum size, x_{max}, this distribution being typically described by a probability density function, $\phi(x)$. The probability density function, $\phi(x)$, is a measure of the probability of finding an abrasive particle in a given size range. In other words, the probability of finding a particle of size between x_1 and x_2 is given by $\int_{x_1}^{x_2} \phi(x)dx$ with $\int_{x_{min}}^{x_{max}} \phi(x)dx$ being equal to one. Since particles of different sizes are present in a slurry, the estimation of forces on the different particles may be done statistically using a suitable model to describe the contact between a particle and the work surface.

Assuming the contact between a particle and the work surface, and between a particle and the polishing block to be a hardness indentation by a rigid nondeformable indenter, the normal load, P, on an abrasive particle is given by

$$P = \Psi H \tan^2\theta\, \delta^2 = \Psi H' \tan^2\theta\, \delta'^2 \tag{1}$$

where H is the hardness of the work material, H' is the hardness of the polishing block, δ is the penetration of the indenter into the workpiece, δ' is the penetration of the indenter into the polishing block, Ψ is a shape factor for the indenter, and 2θ is the included angle of the indenter. For a conical indenter, $\Psi = \pi$ and 2θ is the apical or cone angle, while for a Vickers indenter, $\Psi = 4$ and $2\theta = 136$ deg.

If X is the distance separating the polishing block and the work surface, then we get for an active particle of diameter x, that

$$\delta + \delta' = x - X. \tag{2}$$

Eliminating δ' from Eqs. (1) and (2), we obtain

$$P = \frac{\Psi H \tan^2\theta}{\left(1 + \sqrt{\frac{H}{H'}}\right)^2}(x - X)^2. \tag{3}$$

In order to obtain the distribution of forces on the various abrasive particles present in the gap between the polishing block and the work surface, the first step is to estimate the total number of particles, N, present in the gap and the maximum abrasive size in this sample, X_L. X_L is not necessarily the same as the maximum abrasive size in the population, x_{max}, especially for small sample sizes of the population (or small workpiece areas). N can be taken as the number of particles present in a gap volume of AX_L. Consequently,

$$AX_L = \frac{M_a}{\rho_a}\left(1 + \frac{\rho_a}{m\rho_l}\right) = \frac{\pi N\overline{x^3}}{6}\left(1 + \frac{\rho_a}{m\rho_l}\right) \tag{4}$$

where A is the area of the work surface being polished, ρ_a is the density of the abrasive material, ρ_l is the density of the liquid used in the slurry, M_a is the mass of the abrasive in the slurry, m is the ratio of the mass of the abrasive to the mass of the liquid in the slurry, and $\overline{x^3}$ is the mean of the cube of the particle size. This gives

$$N = \frac{6AX_L}{\pi\overline{x^3}}\Big/\left(1 + \frac{\rho_a}{m\rho_l}\right). \tag{5}$$

It should be noted that in a sufficiently large sample size of abrasive particles, X_L will be equal to x_{max}, and $\overline{x^3}$ will be equal to $\int_{x_{min}}^{x_{max}} x^3\phi(x)dx$. How large the sample size should be for this to be valid can be determined by conducting simulation experiments wherein values of x are sampled from $\phi(x)$. If the sample size is sufficiently large, then the value of N can be obtained from Eq. (5).

For samples smaller than the critical size, in which case $X_L \neq x_{max}$, we can fit equations to the N versus X_L curve, and the N versus $\overline{x^3}$ curve using the results from the simulation experiments, and then solve for N and X_L using Eq. (5) and the above two fitted curves.

It is reasonable to assume that only those abrasive particles having a size larger than the separation distance, X, between the polishing block and the work surface actually take part in polishing. These particles, called *active particles,* transmit the polishing force, P_{total}, to the work surface. Hence, we can write

$$P_{total} = \sum_{x_i > X} P_i, \tag{6}$$

where P_i is obtained by replacing x with x_i in Eq. (3). This discrete sum can be approximated for a continuous distribution $\phi(x)$ by

$$P_{total} = \frac{\Psi H \tan^2\theta\, N}{\left(1 + \sqrt{\frac{H}{H'}}\right)^2}\int_X^{X_L}(x - X)^2\phi(x)dx. \tag{7}$$

The only unknown in this equation is the separation distance, X, between the polishing block and the work surface, which can be evaluated numerically.

The number of active particles, n, is then given by

$$n = N\int_X^{X_L}\phi(x)dx. \tag{8}$$

The average load, P_{ave}, and the maximum load, P_{max}, on the particles are then given by

$$P_{ave} = \frac{P_{total}}{n}, \tag{9}$$

and

$$P_{max} = \frac{\Psi H \tan^2\theta}{\left(1 + \sqrt{\frac{H}{H'}}\right)^2}(X_L - X)^2. \tag{10}$$

Finally, by assuming that the scratches generated on the surface of the work material are entirely plastic and neglecting any elastic recovery, the depth (d) of a scratch made by a particle of size x can be calculated from Eqs. (1) and (2) as

$$d = \frac{x - X}{1 + \sqrt{\frac{H}{H'}}} \tag{11}$$

from which the surface roughness parameters characterizing the polished surface may be derived.

Results

Abrasive Size Distribution. A bounded lognormal distribution was selected to fit the abrasive particle size distribution as it is known to be representative of many granulated powders

Downloaded 04 May 2010 to 171.66.16.26. Redistribution subject to ASME license or copyright; see http://www.asme.org/terms/Terms_Use.cfm

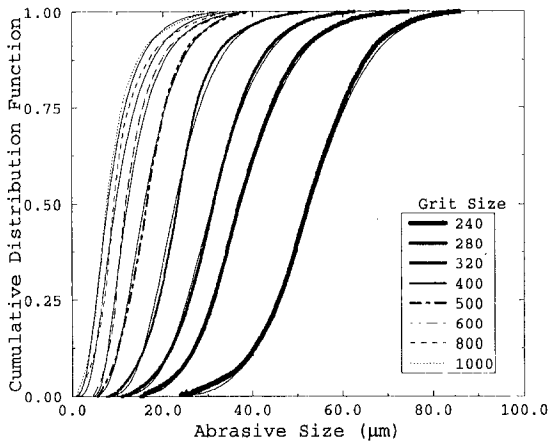


Fig. 3 Cumulative distribution functions ($\Phi(x)$) for silicon carbide abrasive. The curves denoted by the legend are the cumulative distribution functions supplied by the manufacturer. The solid lines overlapping these are those obtained by fitting a lognormal distribution function. Note the excellent quality of fit.

produced by milling fine-grained materials (Reed, 1995). The mathematical representation of an unbounded, lognormal probability density function is

$$f(x) = \frac{1}{(x - b_1)\sqrt{2\pi}\, b_3} e^{-(1/2)((\ln(x-b_1)-b_2)/b_3)^2}, \quad x > b_1 \quad (12)$$

where, b_1, b_2, and b_3 are the three parameters of the unbounded distribution, and x is the particle size in microns. Since the abrasive size distribution is bounded between a smallest size, $x_{\min}$ and a largest size, $x_{\max}$, the bounded lognormal probability density function of abrasive size, $\phi(x)$, is given by

$$\phi(x) = \left\{ \frac{1}{(x - b_1)\sqrt{2\pi}\, b_3} e^{-(1/2)((\ln(x-b_1)-b_2)/b_3)^2} \right\} \times \frac{1}{b_4} \quad (13)$$

where

$$b_4 = \int_{x_{\min}}^{x_{\max}} f(x)dx. \quad (14)$$

Hence, the bounded lognormal distribution for the abrasive size has four parameters, b_1, b_2, b_3, and b_4, which have to be determined for different abrasive grit sizes.

The measured particle size distribution for silicon carbide abrasive were made available to us by the manufacturer in the form of cumulative distribution curves, $\Phi(x)$, for the different grit sizes (see Fig. 3). The cumulative distribution value corresponding to any particle size, x, is the area under the probability density function between $x_{\min}$ and x, i.e., $\Phi(x) = \int_{x_{\min}}^{x} \phi(x)dx$. Bounded lognormal cumulative distribution functions were fitted to the manufacturer supplied data using a least-square error minimization technique, in order to obtain the parameters of the probability density function for the different grit sizes. The distribution functions were constrained to closely fit the tail ends of the data provided by the manufacturer. This was done using a modification of the fitdemo.m program in MATLAB. The mean abrasive size, $\bar{x}$, was then calculated for each grit size as $\int_{x_{\min}}^{x_{\max}} x\phi(x)dx$. The mean of the cube of the abrasive size, $\overline{x^3}$, was also calculated for each grit size as $\int_{x_{\min}}^{x_{\max}} x^3\phi(x)dx$.

The parameters of the probability density function and the mean particle size for the different grit sizes obtained using the above procedure, are given in Table 1 for silicon carbide abrasive. Plots of the corresponding cumulative distribution functions, $\Phi(x)$, and probability density functions, $\phi(x)$, are shown in Figs. 3 and 4, respectively. It is clear from these figures

Table 1 Abrasive size distribution parameters for silicon carbide

Grit Size	x_{min} (μm)	x_{max} (μm)	$\bar{x}$ (μm)	$\overline{x^3}$ ($\mu m^3 \times 10^{-3}$)	b_1	b_2	b_3	b_4
240	24.0	90.0	53.3	171.5	-60.6	4.7	0.10	0.996
280	15.0	75.0	38.3	68.7	-17.2	4.0	0.19	0.995
320	10.0	65.0	31.9	40.9	-13.7	3.8	0.20	0.997
400	7.0	55.0	23.9	18.1	-0.8	3.2	0.31	0.997
500	5.5	40.0	17.1	7.2	0.0	2.8	0.38	0.989
600	4.0	38.0	13.7	4.2	3.4	2.2	0.58	0.990
800	1.5	35.0	11.0	2.7	0.1	2.3	0.55	0.990
1000	1.0	35.0	9.2	1.8	-0.7	2.2	0.53	0.995

that the bounded lognormal distribution provides an accurate representation of particle sizes. It can also be observed from the probability density function plots (Fig. 4) that this function is no longer symmetric for the smaller particle sizes (i.e., larger grit size numbers) but is skewed to the left. This is a major correction to our earlier model (Chauhan et al., 1993) where the abrasive particle sizes were assumed to be distributed according to a normal probability density function which is unbounded.

Simulation Experiments for N Versus X_L and $\overline{x^3}$. Simulation experiments were conducted to study the variation of the largest particle size in the sample, X_L with the sample size, N. For each grit size, N values of x were sampled from the corresponding probability density function, $\phi(x)$, and the largest of these N values was determined. This procedure was repeated 100 times to get a mean and standard error (and hence a corresponding error bar) for the value of X_L corresponding to each N. The mean and standard error were obtained for N equal to 1, 10, 100, 1000, 10,000, 31,623, 100,000, 316,228, 500,000, 750,000 and 1,000,000. The plot of X_L versus N derived from the above simulation is shown in Fig. 5 for the different grit sizes. Similar experiments were conducted to study the variation of the average of the cubes of particle diameters, $\overline{x^3}$, with the sample size, N. The plot of $\overline{x^3}$ versus N for different grit sizes is shown in Fig. 6. It must be noted that when calculating x^3 in Eq. (4), the sum of the cubes (Σx^3) of the particle diameters is not approximated as the cube of the sum ($(\Sigma x)^3$) of the particle diameters. Such an approximation leads to errors as the number of particles between the polishing block and the work surface increases, especially for the smaller particle sizes (i.e., larger grit size numbers).

It can be seen from Fig. 5 that for a sample size exceeding about 10,000 particles, the maximum particle size in the sample reaches a constant value which is practically indistinguishable from the maximum abrasive size of the population. Also, from Fig. 6, for sample sizes exceeding 1000 particles, the average

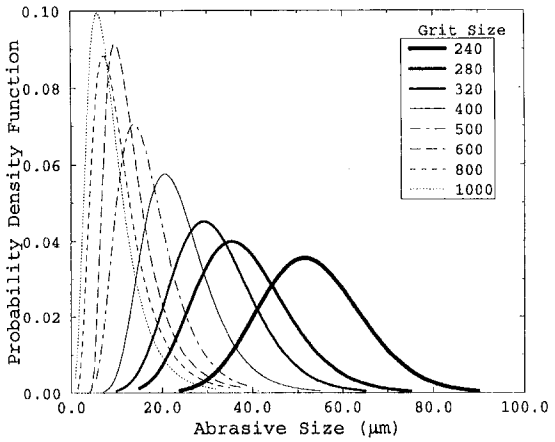


Fig. 4 Lognormal probability density function ($\phi(x)$) fitted to size distribution data provided by the manufacturer for silicon carbide

Downloaded 04 May 2010 to 171.66.16.26. Redistribution subject to ASME license or copyright; see http://www.asme.org/terms/Terms_Use.cfm

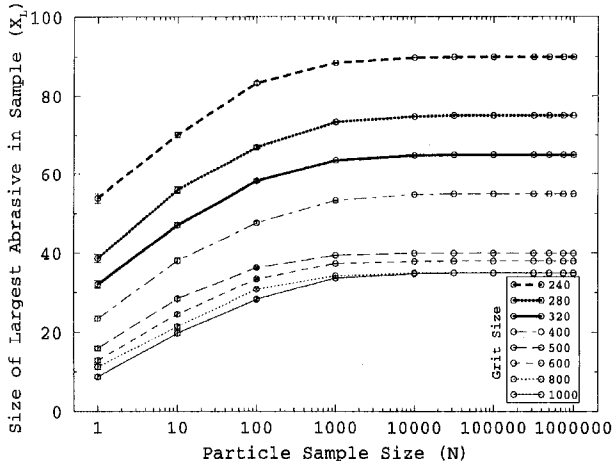


Fig. 5 The variation of the maximum particle size (X_L) with the number of particles (N) in the sample

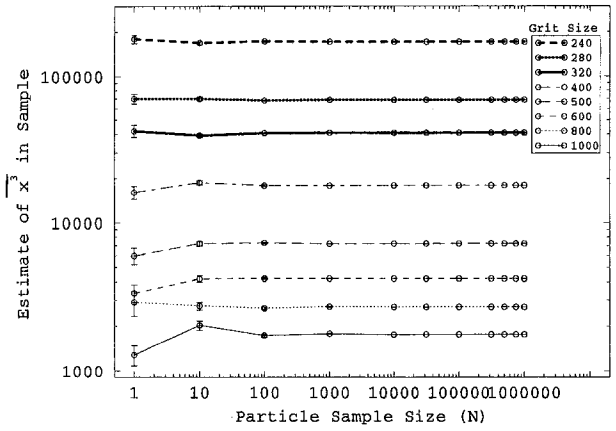


Fig. 6 The variation of the average of the cubes of particle diameters ($\overline{x^3}$) with the number of particles (N) in the sample

Table 2 Properties of abrasive and workpiece materials

Material	Density (kg/m^3)	Knoop* hardness (kg/mm^2)
Silicon carbide	3210	2300-2900
Y_2O_3-partially stabilized zirconia	6100	1100-1300
Ni-Zn ferrite	5300	750
Magnesium Oxide	3675	610
Soda lime glass	2500	520
1070 Steel	7840	220

* Where a range is given for a property, the average or mid-range value has been used in the calculation

value of x^3 reaches a constant value which is indistinguishable from that calculated directly from the probability density function, $\phi(x)$. Hence, X_L can be replaced with x_{max}, and $\overline{x^3}$ with $\int_{x_{min}}^{x_{max}} x^3\phi(x)dx$ in Eq. (5) for cases where the total number of particles in the polishing gap is greater than 10,000. It should be noted that this is actually the case for the typical polishing conditions considered in this study, and that these assumptions are hence used in the ensuing calculations.

Forces on Active Particles. The model was used to calculate the distribution of forces on active particles for the polishing of different work materials with silicon carbide abrasive. The relevant properties of the silicon carbide abrasive and the work materials of interest are given in Table 2.

The calculation of the forces was done for a slurry of silicon carbide abrasive in water with a concentration (m) of 0.25, work surface area of 1000 mm^2, and a polishing pressure of 14 kPa. This results in a polishing force (P_{total}) of 14 N, which is transmitted by the active particles. The polishing block was assumed to be nondeformable for simplicity, i.e., H' was assumed to be infinity. However, it should be noted that the forces can be calculated using the model for any finite hardness value for the polishing block; the forces in this case would be lower in value than those for which the polishing block is assumed to be nondeformable. An estimate of the apical angle for the abrasive particles, 2θ, was obtained as 122 deg from SEM photographs of the silicon carbide abrasive powder (Chauhan et al., 1993), and a corresponding value of 61 deg is used for θ in the ensuing calculations.

The total number of particles on the work surface, N, calculated using Eq. (5), and the number of active particles, n, from Eq. (8) are listed in Table 3 for different workpiece materials and silicon carbide grit sizes. Both of these quantities decrease fairly monotonically with increasing average particle size (or decreasing grit size numbers), with a greater number of active particles being present when polishing softer workpiece materials. The most interesting observation about the results reported in Table 3 is that only a very small percentage (<0.5 percent) of the abrasive particles distributed over the workpiece are actually engaged in material removal, that is the number of active particles (n) is a very small fraction of the total number of particles (N). This observation is seen to hold over a wide range of abrasive grit sizes and for workpiece materials of varying hardness values (Table 2). It is also seen in Table 2 that for any grit size, the value of n increases with decreasing workpiece hardness.

Figures 7(a) and 7(b) show the variation of the maximum and the average normal force on an abrasive particle, respectively, with particle size. These forces were calculated using Eqs. (9) and (10). The maximum and average normal force on a particle are seen to increase fairly monotonically with average particle size in Figs. 7(a) and 7(b). The maximum force on a particle (Fig. 7(a)) varies between 0.02 N and 0.65 N while the average force has a value between 0.007 N and 0.2 N (Fig. 7(b)) for the different work materials. These values are in the range of loads used typically in microhardness measurements. Similar values for the average force on a particle in polishing have been predicted by Buijs and Houten (1993) using a different approach.

Figure 7 shows that the highest values for the forces are obtained in the polishing of zirconia while the lowest values occur in the polishing of 1070 carbon steel. This can be explained with reference to the number of active particles, n, listed in Table 3. Since n has its smallest value for the polishing of zirconia, the average force per particle is also greatest in this case. The exact opposite is true in the polishing of 1070 steel for which n has the largest value in Table 3.

Discussion

A model has been developed to predict the number and sizes of abrasive particles involved in polishing, and the forces acting on these particles. In the model, the contact between an abrasive particle and the work surface has been represented as a hardness indentation. This has been combined with an accurate representation of the abrasive particle size distribution by a bounded lognormal probability density function, to determine the particles taking part in material removal and the forces transmitted by these particles.

The calculations made using the model have yielded interesting results. It has been found that only a very small percentage (less than 0.5 percent) of the abrasive particles present in the gap between the polishing block and the work surface are actually involved in polishing. Further, these particles are comprised

Downloaded 04 May 2010 to 171.66.16.26. Redistribution subject to ASME license or copyright; see http://www.asme.org/terms/Terms_Use.cfm

Table 3 Number of active particles (n) between the workpiece and the polishing block for different silicon carbide grit sizes

Grit Size →	240	280	320	400	500	600	800	1000
Mean Size (μm) →	53.3	38.3	31.9	23.9	17.1	13.7	11.0	9.2
Workpiece Material ↓								
Zirconia	88	135	184	263	829	1029	1305	1043
Ni-Zn Ferrite	106	161	220	313	978	1211	1535	1229
Magnesium Oxide	115	174	237	337	1052	1300	1648	1320
Soda lime Glass	123	185	252	358	1114	1376	1744	1398
1070 Steel	176	260	353	497	1517	1862	2357	1896
Total number of abrasive particles (N)	72610	151087	219837	421585	766998	1251523	1793761	2739087

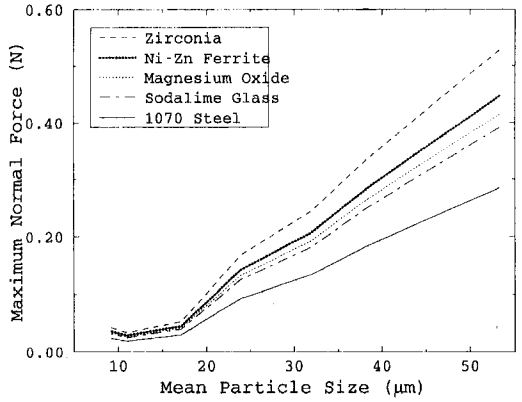


Fig. 7(*a*)

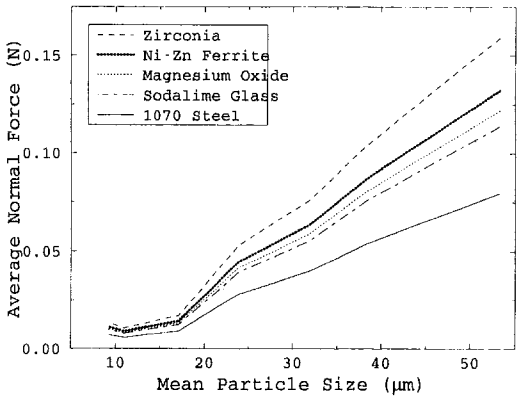


Fig. 7(*b*)

Fig. 7 Variation of normal force on a particle with mean particle size for the polishing of different work materials with silicon carbide abrasive (polishing pressure = 14 kPa, slurry concentration (m) = 0.25); (a) maximum force (P_{max}), and (b) average force per particle (P_{ave})

of the larger particles present in the tail end of the particle size distribution. This has been shown to hold over a wide range of abrasive grit sizes. These conclusions imply that the vast majority of abrasive particles present on the work surface do not take part in material removal and play only a passive role in polishing. Hence, instead of using abrasive particles with a broad size distribution (as is typical in practice), if one were to use a peaked size distribution, then a significantly greater number of particles would be involved in polishing. Further, in such a case, the polishing force could also be considerably increased compared to that used presently, since a greater number of particles will be transmitting this force to the work surface. The polishing action would then be significantly enhanced, the polishing process made more efficient, and further, the amount of abrasive used in polishing could also be significantly reduced. A theoretical and experimental investigation of these aspects using diamond polishing powders of different size distributions is in progress.

Our calculations have shown that under typical polishing conditions, the average normal force on an abrasive particle ranges from 0.007 N to 0.2 N while the maximum force on a particle is between 0.02 N and 0.65 N. These forces are relatively small and similar in magnitude to those applied in a microhardness test. While it is difficult to measure the forces acting on particles in polishing, and this has not been done to date, there are many indirect observations which support our estimate of these forces. The calculated average and maximum force on an abrasive particle are found to be within a factor of two of estimates derived (a) from microscopic observations of scratches and measured scratch widths on polished surfaces of ceramics (Chauhan et al., 1993), (b) from sizes of polishing wear particles (Lu, 1995), and (c) from depths of residually stressed and plastically deformed layers on polished surfaces (Hockey, 1971; Kinoshita et al., 1976; Namba and Tsuwa, 1978; Chandrasekar and Chaudhri, 1993). Our estimate of the percentage of particles involved in polishing is also consistent with estimates of this percentage derived from values of the polishing pressure at which crushing of the abrasive particles is observed to occur (Chauhan et al., 1993). Calculations are now being made with the model to systematically explore the effect of particle size on surface roughness for a wide range of particle sizes, including submicron-sized polishing powders. It is expected that such an analysis should reveal fundamental relationships that may exist between surface roughness and particle size in polishing.

In summary, the polishing force model provides a powerful analytical tool for predicting the polishing action of abrasive particles and the characteristics of polished surfaces. Further, it contains within it a framework for correlating the mechanics of polishing with the mechanics of deformation and fracture occurring about microindentations and scratches in solids.

Conclusions

A model has been developed to estimate the number and sizes of particles involved in material removal in polishing, and the average and maximum forces on these abrasive particles. The effect of the mean particle size on these values has been studied. These estimates are found to be consistent with observations pertaining to polished surfaces and the polishing process. It has been determined that when polishing with abrasive powders having relatively broad size distributions, only a very small percentage (less than 0.5 percent) of the abrasive particles present between the polishing block and work surface are actually engaged in material removal. Thus it would, perhaps, be more economical and efficient to use abrasives with peaked size distributions rather than those generally available.

Acknowledgments

We would like to acknowledge grants from the NSF (CMS9714604) and the Center for Collaborative Manufacturing at Purdue University.

References

Aghan, R. L., and Samuels, L. E., 1970, "Mechanisms of abrasive polishing," *Wear*, Vol. 16, pp. 293–301.

Downloaded 04 May 2010 to 171.66.16.26. Redistribution subject to ASME license or copyright; see http://www.asme.org/terms/Terms_Use.cfm

Buijs, M., and Houten, K. L., 1993, "Three-body abrasion of brittle materials as studied by lapping," *Wear,* Vol. 166, pp. 237–245.

Bulsara, V. H., Ahn, Y., Chandrasekar, S., and Farris, T. N., 1997, "Polishing and lapping temperatures," ASME *Journal of Tribology,* Vol. 119, pp. 163–170.

Chandrasekar, S., and Chaudhri, M. M., 1993, "Indentation cracking in soda-lime glass and Ni-Zn ferrite under Knoop and conical indenters and residual stress measurements," *Philosophical Magazine A,* Vol. 67, No. 5, pp. 1187–1218.

Chauhan, R., Ahn, Y., Chandrasekar, S., and Farris, T. N., 1993, "Role of indentation fracture in free abrasive machining of ceramics," *Wear,* Vol. 162, pp. 246–257.

Hockey, B. J., 1971, "Plastic deformation of alumina by indentation and abrasion," *Journal of the American Ceramic Society,* Vol. 54, No. 5, pp. 223–231.

Imanaka, O., 1966, "Lapping mechanisms of glass-especially on roughness of lapped surface," *Annals of CIRP,* Vol. 13, pp. 227–233.

Kinoshita, M., Murayama, T., Hoshina, N., and Kobayashi, A., 1976, "The surface damaged layer study of mn-zn single crystal using magnetic domain observation technique," *Annals CIRP,* Vol. 25, pp. 449–454.

Lu, L., 1995, "Formation of Wear Particles in Polishing of Brittle Solids and Grinding of Metals," Ph.D. thesis, Purdue University, West Lafayette, IN.

Namba, Y., and Tsuwa, H., 1978, "Mechanism and some applications of ultra-fine finishing," *Annals of the CIRP,* Vol. 27, No. 1, pp. 511–516.

Rabinowicz, E. C., 1968, "Polishing," *Scientific American,* Vol. 218, No. 6, pp. 91–99.

Rayleigh, L., 1901, "Polish," *Nature,* Vol. 64, p. 385.

Reed, J. S., 1995, "Particle Size and Shape," *Principles of Ceramics Processing,* 2nd ed., John Wiley and Sons, pp. 92–117.

Samuels, L. E., 1982, *Metallographic Polishing by Mechanical Methods,* 3rd ed., ASM, Materials Park, OH.

Downloaded 04 May 2010 to 171.66.16.26. Redistribution subject to ASME license or copyright; see http://www.asme.org/terms/Terms_Use.cfm

The Jamb (Self-Locking) Process in Three-Dimensional Collisions

J. A. Batlle
Mem. ASME.

S. Cardona

Department of Mechanical Engineering,
Polytechnical University of Catalunya,
Av. Diagonal, 647,
08028 Barcelona, Spain

For collisions that can be described by means of Routh's incremental model, the jamb or self-locking process, which is characterized by a negative slope of the plot of the normal (separating) velocity v_n as a function of the normal impulse P_n, is far more complicated in three dimensions than in planar collisions because its occurrence depends not only on the friction coefficient μ, but also on the direction of sliding $\boldsymbol{\sigma}$, which is variable. A thorough study of the jamb process as it occurs in Routh's model is presented. For a given collision configuration the system behavior concerning jamb can be fully characterized in the plane of vectors $\boldsymbol{\mu}\boldsymbol{\sigma}$, where four jamb-related domains are defined. Jamb is investigated in the plane of the sliding velocity—where it occurs in an angular sector—and in the $v_n(P_n)$ plots. When jamb starts during expansion, $v_n > 0$, a second compression-expansion phase can take place in some cases, and then the usual energetical restitution coefficient e_w may be ill-defined. A new formulation for the energy dissipated by the normal force is presented that can be consistently applied in all cases. The new concepts and procedures are illustrated by means of an application example.

1 Introduction

In rough collisions which are well described by Routh's incremental model (Routh, 1905), while a purely normal percussive force tends always to separate the colliding surfaces, the presence of a tangential percussive force may tend either to separate or to compress them. In the latter case if the approaching tendency is greater than the separating one, the normal approaching velocity increases (or the separating one decreases). However, such an increase cannot last forever. Eventually the end of sliding or the change in the sliding direction stops the increase of the normal approaching velocity, and the collision proceeds until its end with a normal velocity which increases monotonically in the separating direction. The self-locking phenomenon of normal approaching velocity increase is referred to as the *jamb process* (Stronge, 1990) or *percussive wedging* (Batlle, 1993). In certain cases the jamb process is responsible for the decrease of a normal separating velocity reached after a previous compression-expansion phase.

Beghin (1951) was aware of this and made an introductory analysis of it, under Routh's model, in the case of three-dimensional *tangential collisions* (collisions with negligible approaching initial velocity) between a moving body and a fixed surface. More recently, while three-dimensional rough collisions have received increasing attention, jamb in three-dimensional rough collisions has not yet been addressed. Most of the published work on three-dimensional rough collisions described by Routh's model (Batlle and Condomines, 1991; Batlle, 1993, 1996a, b; Ivanov, 1992; Marghitu and Hurmuzlu, 1995; Bhatt and Koechling, 1995a, b; Stronge, 1994) is related to their analytical formulation, to the energetical consistency of several restitution coefficients, and to the sliding velocity flow. Nor has jamb in three-dimensional rough collisions been addressed by means of more elaborate models that consider a finite area of contact instead of a single point (Jaeger, 1992, 1994; Cohen and Mac Sithigh, 1991; Villagio, 1996). Routh's model is a good starting point for studying jamb.

Jamb in planar rough collisions is not as complex as in the three-dimensional case, because the sliding velocity has a constant direction under jamb conditions. As a consequence, if jamb occurs it has to be necessarily from the beginning of the collision and last until the sliding stops. Furthermore, an analytical integration in three different steps—jamb, compression without sliding, and expansion without sliding—is always possible. Batlle (1993) and Stronge (1990) present examples of jamb in planar collisions as well as the values of the minimum required friction coefficient.

In this article a thorough analysis of the jamb process in three-dimensional rough collisions as it occurs in Routh's model is presented. The use of the plane of vectors $\boldsymbol{\mu} \equiv \mu\boldsymbol{\sigma}$ ($\boldsymbol{\sigma} \equiv \mathbf{v}_t/|\mathbf{v}_t|$ being the unit vector in the direction of sliding) and the plot of $\boldsymbol{\mu}_A(\boldsymbol{\sigma})$ corresponding to asymptotes, introduced by Batlle (1996), allow the definition of several domains of $\boldsymbol{\mu}$ related to the jamb process, which give a clear picture of all possibilities of the jamb process. Besides this it is shown that when jamb starts during expansion, $v_n > 0$, a second compression-expansion phase can take place in some cases and then the conventional energetic restitution coefficient may be ill-defined: compression work is not uniquely defined and, in some cases, more dissipative materials could predict a reduction in the energy dissipated by the normal force. A new approach for dealing with the energy dissipation associated with the normal force is presented.

The findings about jamb in three-dimensional rough collisions presented in this article are probably relevant to many other collision models, over and above Routh's model. This would be the case during gross sliding of collisions of objects with some finite tangential compliance, if contact deformations are strongly localized (i.e., "force-response rigid" objects as described in Chatterjee (1997)).

2 The Evolution of the Normal and Sliding Velocities at the Collision Point

For a single-point rough collision in a multibody system with frictionless constraints and n degree-of-freedom described by

Contributed by the Applied Mechanics Division of THE AMERICAN SOCIETY OF MECHANICAL ENGINEERS for publication in the ASME JOURNAL OF APPLIED MECHANICS.

Discussion on this paper should be addressed to the Technical Editor, Professor Lewis T. Wheeler, Department of Mechanical Engineering, University of Houston, Houston, TX 77204-4792, and will be accepted until four months after final publication of the paper itself in the ASME JOURNAL OF APPLIED MECHANICS.

Manuscript received by the ASME Applied Mechanics Division, Feb. 8, 1996; final revision, June 25, 1997. Associate Technical Editor: J. T. Jenkins.

 Copyright © 1998 by ASME

Downloaded 04 May 2010 to 171.66.16.26. Redistribution subject to ASME license or copyright; see http://www.asme.org/terms/Terms_Use.cfm

the generalized velocities $\{u\}^T = \{u_1, u_2, \ldots u_n\}$ for which $[M]$ is the inertia matrix and under the assumptions of Coulomb's friction with coefficient μ and infinite tangential stiffness at the collision point, the Lagrangian formulation leads to the following evolution equations for the tangential (sliding) velocity $\mathbf{v}_t$ and the normal (separating) velocity v_n at the collision point (Batlle and Condomines, 1991; Batlle, 1993, 1996a, 1996b)

$$d\mathbf{v}_t/dP_n = \mathbf{h} - \mu[b]\boldsymbol{\sigma}, \tag{1}$$

$$dv_n^s/dP_n = a - \mu\mathbf{h}^T\boldsymbol{\sigma}, \quad \text{for sliding conditions,} \tag{2}$$

$$dv_n^{ns}/dP_n = a - \mathbf{h}^T[b]^{-1}\mathbf{h} > 0,$$

$$\text{for nonsliding conditions,} \tag{3}$$

where P_n is the normal impulse and

$$\begin{bmatrix} a & \mathbf{h} \\ \mathbf{h}^T & [b] \end{bmatrix} = [K]^T[M][K], \tag{4}$$

$[K]$ being the matrix of kinematical coefficients relating v_n and $\mathbf{v}_t$ to the generalized velocities $\{u\}$,

$$\begin{Bmatrix} v_n \\ \mathbf{v}_t \end{Bmatrix} = [K]^T\{u\}. \tag{5}$$

Equation (1) is an autonomous flow whose integration gives the hodographs of $\mathbf{v}_t$—and, consequently, the sliding direction $\boldsymbol{\sigma}$—as a function of P_n. This result is used in (2) to calculate $v_n^s(P_n)$ under sliding conditions. If sliding stops, (3) must be used instead of (2) to proceed with the integration of v_n, which evolves with constant dv_n/dP_n under this condition. Obviously, the set of curves $v_n^s(P_n)$ for a given initial $\mathbf{v}_t^0$ and different values of initial v_n^0 are curves of the same shape though shifted along the v_n-axis. The end of the collision can be conveniently determined, in order to guarantee energetical consistency, by means of a termination criterion related to the work W_n done by the normal force. Energetical consistency requires that $W_n = 0$ for perfectly elastic collisions and $W_n < 0$ for partially plastic collisions.

For systems with drivers that guarantee the continuity of a set of generalized velocities, an analogous formulation is obtained in which "a", $\mathbf{h}$ and $[b]$ have different expressions but keep the same properties (Batlle and Condomines, 1991; and Batlle, 1993).

3 The End of the Collision: A New Energetical Approach

The concept of restitution of the work W_n done by the normal force was used by Beghin (1951) to predict the end of a rough collision. W_n can be expressed as

$$W_n = \int_0^{P_n} v_n dP_n. \tag{6}$$

Two extreme cases may occur: that of a *perfectly elastic* rough collision, with full restitution of the energy absorbed by the internal deformation ($W_n = 0$), and that of a *perfectly plastic* rough collision, which ends after a phase of compression when the condition $v_n = 0$ is reached. In this case there is no restitution at all of $W_n \equiv W_{\text{comp}}$, associated with the compression phase. For other intermediate cases a hypothesis on the amount of energy dissipated by the normal percussive force can be used.

If $W_n(P_n)$ has a single minimum, which corresponds to the compression work W_{comp}, the energy dissipated by the normal force has commonly been formulated as a known fraction λ of W_{comp} (Batlle et al., 1991; Stronge, 1991). If the ratio $\eta = dv_n/dP_n$ is constant (and consequently $v_n + v_a = \eta P_n$, where $v_a = -v_n^0$ is the normal approaching velocity at the beginning of the collision), $W_n(P_n)$ is a parabola

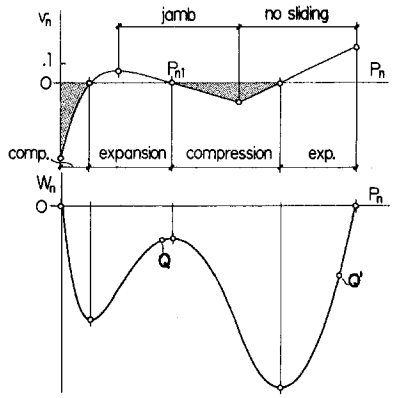


Fig. 1 Plots $v_n(P_n)$ and $W_n(P_n)$ for the application example with $\mu = 4$, and initial conditions $v_n^0 = -0.38$; $\mathbf{v}_t^{0T} = \{0.5, 1\}$

$$W_n = \frac{1}{\eta}\int_{-v_a}^{v_n} v_n dv_n = -\frac{1}{2\eta}[v_a^2 - v_n^2] = -v_a P_n + \frac{1}{2}\eta P_n^2, \tag{7}$$

and the Newton's and Poisson's rules are energetically consistent: $e_N = e_P = 1$ corresponds to $W_n = 0$, and $e_N = e_P < 1$ corresponds to $W_n < 0$ (Batlle, 1993). According to (7), $W_{\text{comp}} = -v_a^2/(2\eta)$, so it would be assumed that the collision ends when $W_n^e = -\lambda v_a^2/(2\eta)$. If the Newton's rule is applied, substitution of $v_n = e_N v_a$ in Eq. (7) leads to $W_n^e = -(1 - e_N^2)v_a^2/(2\eta)$, and hence $\lambda = 1 - e_N^2$. This result suggests the introduction of an energetical restitution coefficient e_w for general rough collisions such that $\lambda = 1 - e_w^2$.

However, in three-dimensional collisions $W_n(P_n)$ may have two local minima and then the hypothesis that a known fraction λ of the W_{comp} is dissipated by the normal force is ill-defined. $W_n(P_n)$ may have two local minima when jamb starts during an expansion phase change of $\boldsymbol{\sigma}$ may lead to this—as illustrated in Fig. 1 for the application example (the same presented in Batlle (1996b)) with $\mu = 4$, and initial conditions $v_n^0 = -0.38$ and $\mathbf{v}_t^{0T} = \{0.5, 1\}$. For sufficiently small dissipation, after a first compression-expansion phase, ($0 \le P_n \le P_{n1}$) jamb leads to a second compression-expansion phase. It can be assumed that dissipation occurs in both compression and expansion phases. So, as compared to a collision ending at point Q, a slightly less dissipative behaviour would lead to the second one ending for instance at Q' with an energy dissipation significantly greater than that of the former case, which proves the inconsistency of the usual hypothesis in which a more dissipative material would lead to a greater energy dissipation. Besides this there is the difficulty to define unambiguously the compression work in this case.

A convenient approach is to assume the energy dissipated by the normal force as the work done by a *normal friction force* F_{nf}.

$$W_{n\,\text{dis}} = -\int_0^{P_{nf}} |v_n|\,d|P_{nf}| = -\int_0^{P_n} |v_n|\frac{|F_{nf}|}{F_n}dP_n. \tag{8}$$

The simplest choice for $|F_{nf}|$ is $|F_{nf}| = \nu F_n$, and consequently

$$W_{n\,\text{dis}} = -\nu\int_0^{P_n} |v_n|\,dP_n. \tag{9}$$

The range for ν is between $\nu = 0$, for perfectly elastic collisions, to $\nu = 1$, for perfectly plastic ones. Another simple choice is to relate F_{nf} to the *normal elastic force* $F_e \equiv F_n - F_{nf}$: $F_{nf} = \rho F_e$ with $0 \le \rho \le \infty$ during compression and $F_{nf} = -\rho F_e$ for $0 \le \rho < 1$, while $F_{nf} = -F_e$ for $\rho > 1$, during expansion. $\rho =$

Downloaded 04 May 2010 to 171.66.16.26. Redistribution subject to ASME license or copyright; see http://www.asme.org/terms/Terms_Use.cfm

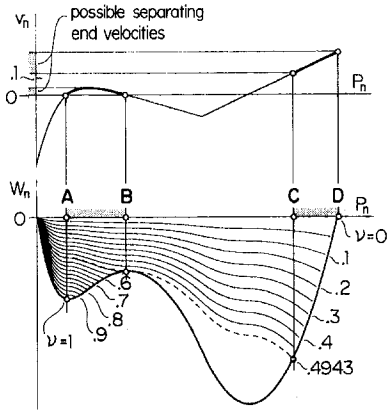


Fig. 2 Plots $v_n(P_n)$ and $W_n(P_n)$ for the application example with $\mu = 4$, and initial conditions $v_n^0 = -0.40$; $\mathbf{v}_t^{0T} = \{0.5, 1\}$. Plots of $W_{n\,\mathrm{dis}}$ calculated with Eq. (9) are shown for several values of ν.

0 and $\rho \geq 1$ correspond to perfectly elastic and perfectly plastic collisions, respectively.

The collision ends when $W_n = W_{n\,\mathrm{dis}}$, and hence, from (6) and (9)

$$\int_0^{P_n} v_n dP_n = -\nu \int_0^{P_n} |v_n|\, dP_n;$$

$$\text{or} \quad \int_0^{P_n} (v_n + \nu |v_n|) dP_n = 0. \tag{10}$$

Functions $W_n(P_n)$ and $W_{n\,\mathrm{dis}}(P_n)$ for several values of ν are shown in Fig. 2 for the application example with $\mu = 4$, and initial conditions $v_n^0 = -0.40$ and $\mathbf{v}_t^{0T} = \{0.5, 1\}$. Any point in spans AB and CD can correspond to a possible end condition. For $\nu = 1$ (perfectly plastic collision), the collision ends at the first minimum. The boundary value ν separating points B and C is $\nu = 0.4943$. These results show that, besides e_w, a generalized restitution coefficient e'_N for Newton's rule such that $v_s = e'_N v_a$ with $0 \leq e'_N \leq e'_{N\,\max} = v_{s\,\max}/v_a$, ($v_{s\,\max}$ corresponding to a perfectly elastic collision) is also inconsistent. The same happens for a generalized Poisson's restitution coefficient e'_P such that $P_{\mathrm{exp}} = e'_P P_{\mathrm{comp}}$ with $o \leq e'_P \leq e'_{P\,\max} = P_{\mathrm{exp}\,\max}/P_{\mathrm{comp}}$, ($P_{\mathrm{exp}\,\max}$ corresponding to a perfectly elastic collision).

The application of this new formulation to cases in which the Newton's rule is energetically consistent leads to

$$W_{n\,\mathrm{dis}}(P_n) = -\nu \int_0^{P_{\mathrm{comp}}} v_n dP_n + \nu \int_{P_{\mathrm{comp}}}^{P_n} v_n dP_n$$

$$= -\nu \left[\frac{1}{2} \eta P_n^2 - v_a P_n + \frac{v_a^2}{\eta} \right], \tag{11}$$

and, by equating $W_{n\,\mathrm{dis}} = W_n$, the dissipated energy at the end of the collision is found to be

$$W_n = W_{n\,\mathrm{dis}} = -W_{\mathrm{comp}} \frac{2\nu}{1+\nu}. \tag{12}$$

Equation (12) suggests the following relationship between ν and e_w:

$$1 - e_w^2 = \frac{2\nu}{1+\nu}; \quad \text{or} \quad \nu = \frac{1 - e_w^2}{1 + e_w^2}. \tag{13}$$

4 The Jamb Process

The jamb process is characterized by $dv_n^s < 0$ and according to (2) this requires $\mu \mathbf{h}^T \boldsymbol{\sigma} > a$. This condition shows that jamb occurrence depends upon μ and the sliding direction $\boldsymbol{\sigma}$. If vectors $\boldsymbol{\mu} \equiv \mu\boldsymbol{\sigma}$ and $\boldsymbol{\sigma}_h \equiv \mathbf{h}/|\mathbf{h}|$ are introduced, the condition for jamb may be written as

$$\boldsymbol{\sigma}_h^T \boldsymbol{\mu} > a/|\mathbf{h}| \equiv \mu_J. \tag{14}$$

In the polar plane of $\boldsymbol{\mu}$, introduced by Batlle (1996), vectors $\boldsymbol{\mu}$ verifying (14) lie in the half-plane, or *jamb domain*, separated from the origin by the straight line $\boldsymbol{\sigma}_h^T \boldsymbol{\mu} = \mu_J$, Fig. 3, which is perpendicular to $\mathbf{h}$ at a distance μ_J from the origin in the direction of $\mathbf{h}$. This straight line will be called *jamb boundary*.

For a given $\mu > \mu_J$, jamb occurs for sliding velocities $\mathbf{v}_t$ such that the angle defined by $\mathbf{v}_t$ and $\mathbf{h}$ is less than $\varphi = \arccos(\mu_J/\mu)$, (Fig. 3).

It is worth noting that critical $\boldsymbol{\mu}_c \equiv [b]^{-1}\mathbf{h}$, for which $d\mathbf{v}_t = 0$, always lies outside the jamb-domain because

$$\boldsymbol{\sigma}_h^T \boldsymbol{\mu}_c = \mathbf{h}^T [b]^{-1} \mathbf{h}/|\mathbf{h}|, \tag{15}$$

and according to (3), $\mathbf{h}^T[b]^{-1}\mathbf{h} < a$, which leads to

$$\boldsymbol{\sigma}_h^T \boldsymbol{\mu}_c < a/|\mathbf{h}| \equiv \mu_J. \tag{16}$$

In the $\boldsymbol{\mu}$-plane, distances from the jamb boundary are related to the slope dv_n/dP_n, Fig. 4. When there is sliding, according to (1), dv_n^s/dP_n is proportional to the distance δ from the jamb boundary to $\boldsymbol{\mu}$,

$$dv_n^s/dP_n = |\mathbf{h}|(\mu_J - \boldsymbol{\sigma}_h \boldsymbol{\mu}) = |\mathbf{h}|\delta. \tag{17}$$

Distances δ for points in the jamb domain are negative and lead to a negative slope in the plot $v_n^s(P_n)$, while δ is positive otherwise and leads to a positive slope in $v_n^s(P_n)$. In the absence of sliding, (3) leads to a uniform slope proportional to the distance δ_c from the jamb boundary to $\boldsymbol{\mu}_c$,

$$dv_n^{ns}/dP_n = |\mathbf{h}|(\mu_J - \boldsymbol{\sigma}_h \boldsymbol{\mu}_c) \equiv |\mathbf{h}|\delta_c. \tag{18}$$

5 Jamb-Related Domains in the μ-Plane

Jamb in three-dimensional rough collisions has a greater complexity than jamb in planar rough collisions because of the

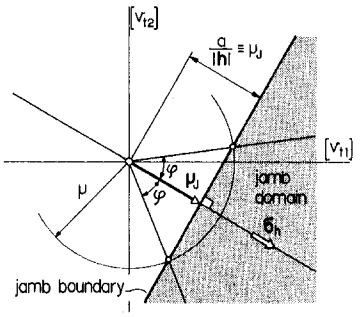


Fig. 3 Geometry of the jamb domain in the μ-plane

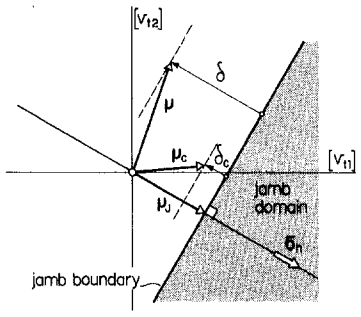


Fig. 4 For plots $v_n(P_n)$, the slope dv_n/dP_n under sliding and non sliding conditions is proportional to δ and δ_c, respectively

Downloaded 04 May 2010 to 171.66.16.26. Redistribution subject to ASME license or copyright; see http://www.asme.org/terms/Terms_Use.cfm

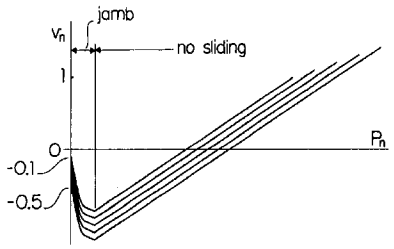


Fig. 5 Plots $v_n(P_n)$ under full jamb condition calculated for the application example with $\mu = 4$ and initial conditions $v_n^0 = -0.1, -0.2, \ldots -0.5$; $\mathbf{v}_t^{0T} = \{0.75, -1\}$

change of the sliding direction $\boldsymbol{\sigma}$ during the collision. On one hand, as $\boldsymbol{\sigma}_h$ and $\boldsymbol{\mu}$ have constant directions in planar collisions, if condition (14) is verified at the beginning of the collision it is verified during the full sliding phase of the collision. In other words: when there is jamb, it occurs until sliding necessarily stops. On the other hand in three-dimensional rough collisions, as the jamb occurrence depends upon μ and $\boldsymbol{\sigma}$, for a given μ the jamb condition given by (14) may be fulfilled over the full sliding interval or over a limited portion of it.

In order to fully characterize the jamb behavior for a given collision configuration of the system as a function of $\boldsymbol{\mu}$, the following jamb related domains in the $\boldsymbol{\mu}$ plane can be defined:

.FJ, domain of *full jamb*: for $v_n < 0$, jamb occurs until the sliding stops. Consequently, for collisions starting in this domain jamb occurs from the beginning of the collision, as illustrated in Fig. 5.

.PJ, domain of *partial jamb*: for $v_n < 0$, jamb occurs but ends before the sliding stops. Consequently, for collisions starting in this domain jamb occurs from the beginning of the collision, as shown in Fig. 6.

.AFJ, domain of *access to full jamb*: in this domain collisions start under no-jamb conditions but, if the initial normal approaching velocity is high enough, they will enter the domain of full jamb.

.APJ, domain of *access to partial jamb*: in this domain collisions start under no-jamb conditions but, if the initial normal approaching velocity is high enough, they will enter the domain of partial jamb.

To determine these domains it is useful to introduce the polar plot $\boldsymbol{\mu}_A(\boldsymbol{\sigma})$ corresponding to the value μ_A for which $\boldsymbol{\sigma}$ is an *asymptote* or an *invariant direction* ($d\mathbf{v}_t$, given by (1), is parallel to $\boldsymbol{\sigma}$ for points in an asymptote or invariant direction) (Batlle, 1996b; Bhatt and Koechling, 1995b). This plot is a hyperbola, Fig. 7, whose geometry is determined by $\mathbf{h}$ and $[b]$). It is worth noting that the hyperbola branch containing the origin, contains $\boldsymbol{\mu}_c$ as well. Point C corresponds to the *critical asymptote* ($\mathbf{v}_t$ remains unchanged during the collision). Points in the arc OC correspond to centrifugal asymptotes, which are of the *tangent* type. All other asymptotes are centripetal. Those associated with points in arcs CT and A*T′ are of the tangent type

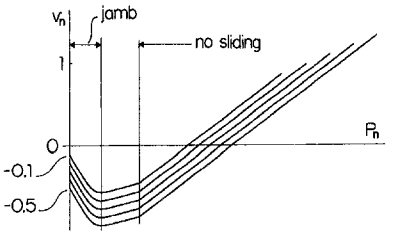


Fig. 6 Plots $v_n(P_n)$ under partial jamb condition calculated for the application example with $\mu = 2$ and initial conditions $v_n^0 = -0.1, -0.2, \ldots -0.5$,; $\mathbf{v}_t^{0T} = \{0.75, -1\}$

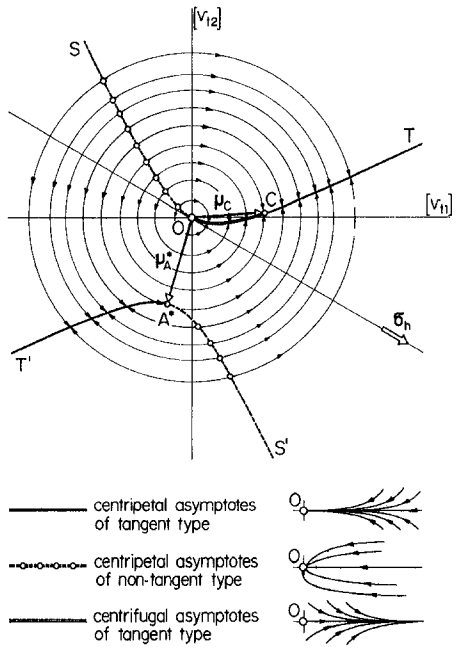


Fig. 7 Polar plot $\mu_A(\sigma)$ of μ vectors corresponding to the asymptotes, and evolution of vectors μ and the sliding directions σ

and those associated with arcs OS and A*S′ are of the *non-tangent* type. Point A* corresponds to the bifurcation asymptote (for $\mu < \mu_A^*$ there are two asymptotes only, while for $\mu > \mu_A^*$ there are four of them).

During the collision, $\boldsymbol{\mu}$ evolves over a centered circumference of radius μ which has two intersections (if $\mu < \mu_A^*$) or four (if $\mu > \mu_A^*$) with the plot $\boldsymbol{\mu}_A(\boldsymbol{\sigma})$. These intersections correspond to the asymptotes. Vector $\boldsymbol{\mu}$ evolves in the direction from a non-tangent asymptote towards a tangent asymptote, as shown in Fig. 7. Evolution of $\boldsymbol{\sigma}$ follows that of the direction of $\boldsymbol{\mu}$.

Superimposition of Fig. 3 and Fig. 7 defines the four domains related to the jamb process, as shown in Fig. 8. The FJ domain contains an arc of the hyperbola that corresponds to centripetal

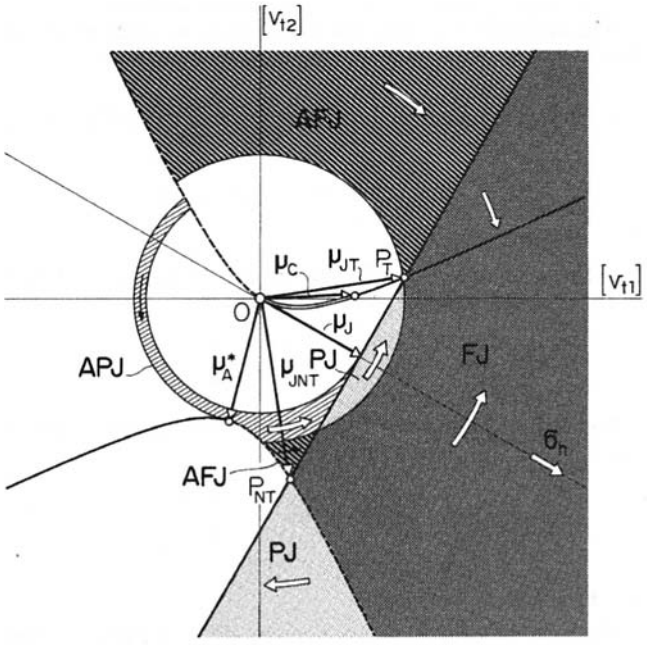


Fig. 8 The jamb related domains in the μ plane. FJ: full jamb. PJ: partial jamb. AFJ: access to full jamb. APJ: access to partial jamb.

Downloaded 04 May 2010 to 171.66.16.26. Redistribution subject to ASME license or copyright; see http://www.asme.org/terms/Terms_Use.cfm

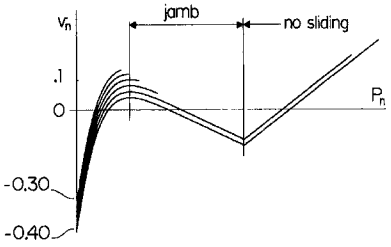


Fig. 9 Plots $v_n(P_n)$ under access to full jamb condition calculated for the application example with $\mu = 4$ and initial conditions $v_n^0 = -0.30, -0.32, \ldots -0.40$; $\mathbf{v}_t^{0T} = \{0.5, 1\}$

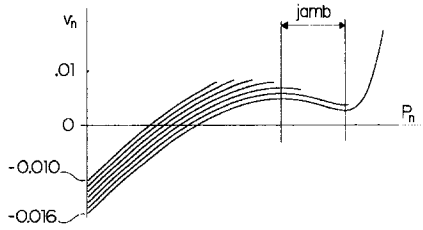


Fig. 10 Plots $v_n(P_n)$ under access to partial jamb condition calculated for the application example with $\mu = 1.114$ and initial conditions $v_n^0 = -0.010, -0.011, \ldots -0.016$; $\mathbf{v}_t^{0T} = \{0.25, -1\}$

asymptotes of tangent type and it is always connected, while some of the other domains may be split in two disjoint pieces according to the relative position of the jamb boundary and the hyperbola branches. The characteristic μ values that define the boundaries of these domains are μ_J, μ_A^*, and μ_{JT} and μ_{JNT} that correspond to the intersections P_T and P_{NT} of the jamb boundary with an hyperbola arc associated with tangent type asymptotes and with an hyperbola arc associated with non-tangent type asymptotes, respectively.

Vectors $\boldsymbol{\mu}_{JT}$ and $\boldsymbol{\mu}_{JNT}$ are orthogonal and can be analytically determined. If unit vector $\boldsymbol{\sigma}_T = [T]\boldsymbol{\sigma}$ perpendicular to $\boldsymbol{\sigma}$ is defined by means of matrix $[T]$

$$[T] = \begin{bmatrix} 0 & -1 \\ 1 & 0 \end{bmatrix}, \tag{19}$$

then, the condition for $\boldsymbol{\mu}_A \equiv \mu_A \boldsymbol{\sigma}_A$ to be an asymptote may be written, according to (1) as

$$\boldsymbol{\sigma}_{AT}^T \mathbf{h} - \boldsymbol{\sigma}_{AT}[b]\boldsymbol{\mu}_A = 0, \tag{20}$$

and (20) leads to

$$\boldsymbol{\mu}_A = \boldsymbol{\sigma}_A(\boldsymbol{\sigma}_{AT}^T \mathbf{h})/(\boldsymbol{\sigma}_{AT}^T[b]\boldsymbol{\sigma}_A). \tag{21}$$

Substitution of (21) into the equation of the jamb boundary

$$\boldsymbol{\sigma}_h^T \boldsymbol{\mu}_J = a/|\mathbf{h}|, \quad \text{or} \quad \mathbf{h}^T \boldsymbol{\mu}_J = a, \tag{22}$$

leads to the equation that determines $\boldsymbol{\sigma}_{JT}$ and $\boldsymbol{\sigma}_{JNT}$. If they are represented as $\boldsymbol{\sigma}_{J'}$.

$$(\boldsymbol{\sigma}_{J'}^T \mathbf{h})(\boldsymbol{\sigma}_{J'T}^T \mathbf{h})/(\boldsymbol{\sigma}_{J'T}^T[b]\boldsymbol{\sigma}_{J'}) = a. \tag{23}$$

The symmetry of $\boldsymbol{\sigma}_{J'}$ and $\boldsymbol{\sigma}_{J'T}$ in (23) shows that the vectors $\boldsymbol{\mu}_{JT}$ and $\boldsymbol{\mu}_{JNT}$ are orthogonal (It is worth noting that this orthogonality is a general property of the hyperbola because P_T and P_{NT} are the intersections of the hyperbola with a straight line perpendicular to a hyperbola tangent). To determine analytically these vectors the eigendirections of $[b]$ can be used as axes in the sliding velocity plane. If b_1 and b_2 are the eigenvalues of $[b]$ and $\mathbf{h}^T = \{\tilde{h}_1, \tilde{h}_2\}$, Eq. (23) with $\boldsymbol{\sigma}_{J'}^T = \{\cos \psi_{J'}, \sin \psi_{J'}\}$ translates into

$$(-\tilde{h}_1 \sin \psi_{J'} + \tilde{h}_2 \cos \psi_{J'})(\tilde{h}_1 \cos \psi_{J'} + \tilde{h}_2 \sin \psi_{J'}) = a(b_2 - b_1) \sin \psi_{J'} \cos \psi_{J'}, \tag{24}$$

and from (24)

$$\psi_{J'} = \frac{1}{2} \arctan \frac{2\tilde{h}_1 \tilde{h}_2}{\tilde{h}_1^2 - \tilde{h}_2^2 + a(b_2 - b_1)}. \tag{25}$$

Equation (25) leads to two values of $\psi_{J'}$, with $|\psi_{J'}| < \pi/2$, whose difference is $\pi/2$.

As far as the values of μ_{JT} and μ_{JNT} are concerned, from Eqs. (21) and (23)

$$\mu_{JN,JS} = (\boldsymbol{\sigma}_{J'T}^T \mathbf{h})/(\boldsymbol{\sigma}_{J'T}^T[b]\boldsymbol{\sigma}_J) = a/(\boldsymbol{\sigma}_{J'T}^T \mathbf{h}) = a/(\tilde{h}_1 \cos \psi_{J'} + \tilde{h}_2 \sin \psi_{J'}) = \mu_J/\cos(\psi_{J'} - \psi_h). \tag{26}$$

Collisions entering the FJ domain from the AFJ domain with $v_n < 0$ develop full jamb (the jamb occurs until the sliding stops). But if they enter the FJ domain with $v_n > 0$ (that is, during a first expansion phase) the collision may end before jamb succeeds in making $v_n < 0$, as illustrated in Fig. 9 by curves for initial $v_n^0 = -0.34$ and -0.36. However, if v_n becomes negative, a second compression phase starts and full jamb develops, as shown in Fig. 9 by curves for initial $v_n^0 = -0.38$ and -0.40.

For collisions entering the PJ domain from the APJ domain with $v_n < 0$, partial jamb fully develops to its end (jamb ends before the end of the collision and before the sliding stops). But if they enter the PJ domain with $v_n > 0$ the collision may end with $v_n > 0$ before the partial jamb fully develops, as illustrated in Fig. 10 by curve for initial $v_n^0 = -0.014$, or the partial jamb may fully develop ending either with $v_n > 0$, as illustrated in Fig. 10 by curves for initial $v_n^0 = -0.015$ and -0.016, or with $v_n < 0$, and is this case there is a second compression phase.

For collisions starting in the AFJ or APJ domains that develop a second compression phase, W_n has two minima, Figs. 1 and 2, and a formulation for $W_{n\,\mathrm{dis}}$ different from $W_{n\,\mathrm{dis}} = (1 - e_w^2)\, W_{comp}$, (Section 3), is required.

6 Application Example

The same application case as in Batlle (1996b) is used, Fig. 11, for which

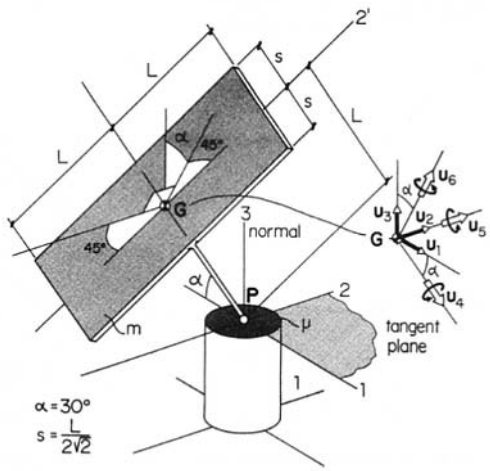


Fig. 11 Application example parameters and generalized velocities

Downloaded 04 May 2010 to 171.66.16.26. Redistribution subject to ASME license or copyright; see http://www.asme.org/terms/Terms_Use.cfm

$$a = m^{-1}6$$

$$\mathbf{h} = (m^{-1}/\sqrt{3})\begin{Bmatrix} 5 \\ -8 \end{Bmatrix}, \quad [b] = (m^{-1}/3)\begin{bmatrix} 7 & -8 \\ -8 & 23 \end{bmatrix}. \quad (27)$$

From these values $\mu_J = 1.1016$; $\mu_{JNT} = 1.207$; $\mu_{JT} = 2.691$; $\boldsymbol{\sigma}_h^T \boldsymbol{\mu}_c = 0.7249$ leading to $\delta_c = 0.3767$ and as it is found in the reference $\mu_A^* = 1.06$; $\mu_N = 1.114$.

The jamb related domains are shown in Fig. 12. Figure 13 shows the hodograph planes for several values of μ (as this application case was not specially chosen to illustrate the jamb process, it leads to the consideration of unusually high μ values). In the hodograph planes the sectors of partial jamb, full jamb, and access to full jamb, when appropriate, are shown. Plots of $v_n(P_n)$ illustrating cases of full and partial jamb as well as cases of access to full and partial jamb are shown in Figs. 5, 6, 9, and 10, respectively. Initial sliding velocities $\mathbf{v}_t^0$ and vectors $\boldsymbol{\mu}^0$ used are depicted in Figs. 13 and 12 as points 1, 2, 3, and 4, respectively. Plots $v_n(P_n)$ are represented until the end of the collision under the assumption of perfectly elastic normal force (point D in Fig. 2). As discussed in Section 3, perfectly plastic collisions end at the

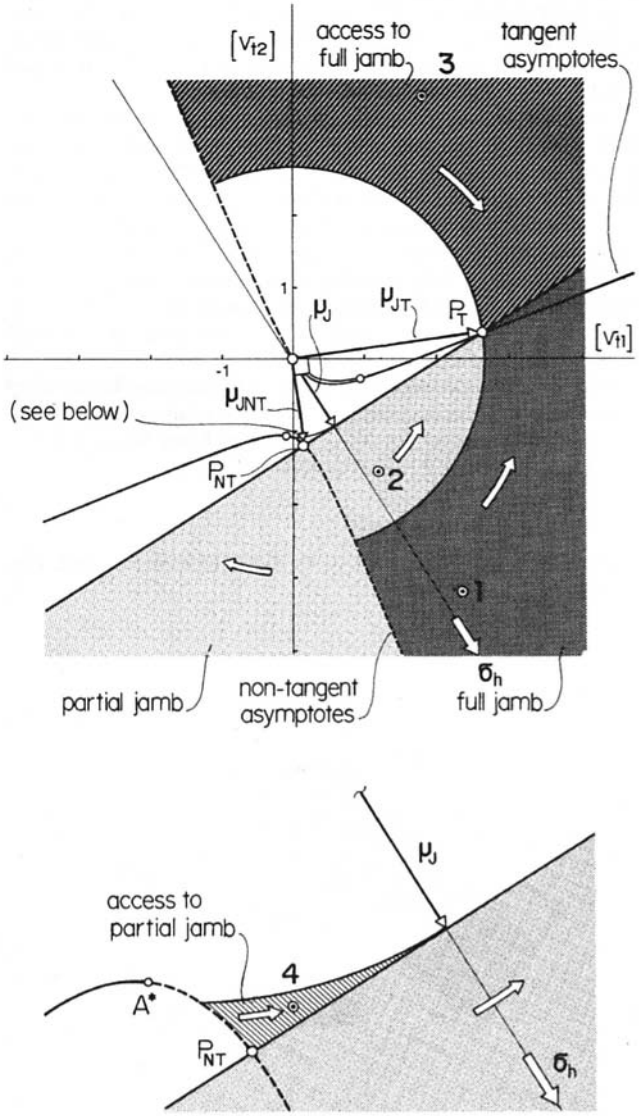


Fig. 12 The jamb related domains in the μ plane for the application example. Points 1, 2, 3, 4 correspond to initial vector μ^0 for Figs. 5, 6, 9, 10, respectively.

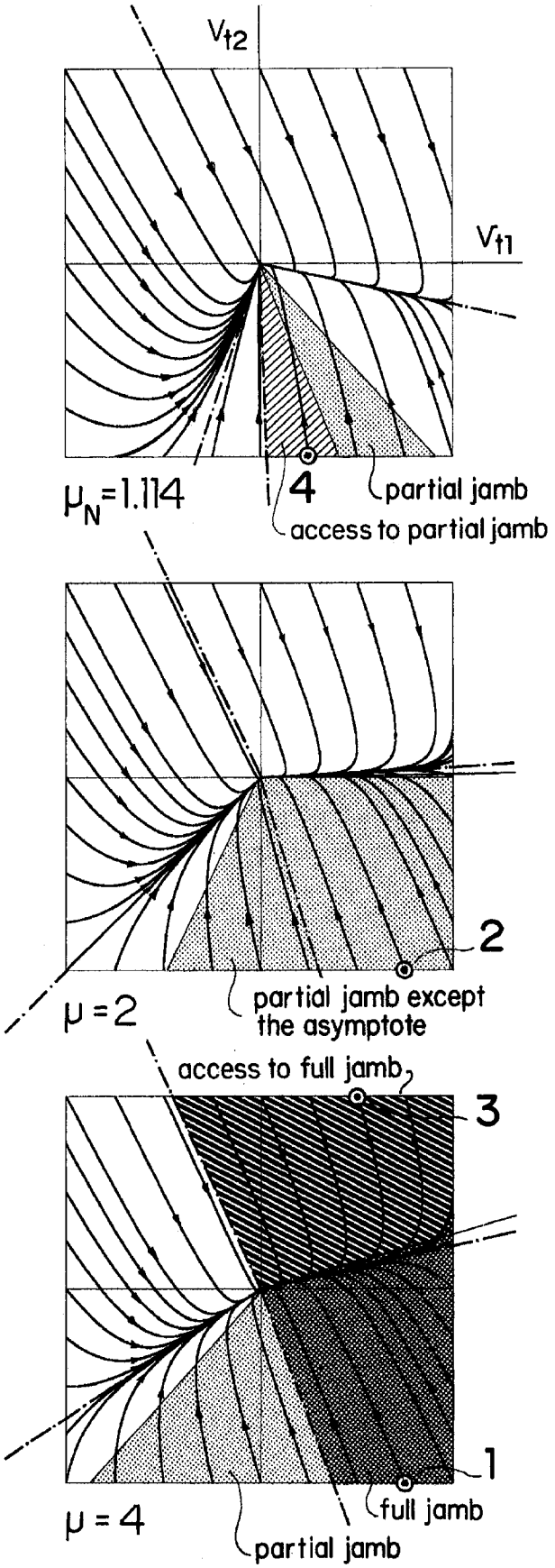


Fig. 13 Hodographs in the plane of v_t for several values of μ. Points 1, 2, 3, 4 correspond to initial v_t^0 for Figs. 5, 6, 9, 10, respectively.

Downloaded 04 May 2010 to 171.66.16.26. Redistribution subject to ASME license or copyright; see http://www.asme.org/terms/Terms_Use.cfm

first crossing with the $v_n = 0$-axis (point A in Fig. 2). For partially elastic collisions $v_n(P_n)$ may end at any point between zero and $v_{n\,\max}$ if $W_n(P_n)$ has a single minimum, and at certain spans of $v_n(P_n)$ if $W_n(P_n)$ has two minima as illustrated in Fig. 2 and discussed in Section 3.

7 Conclusions

A thorough study of the jamb process in three dimensions, characterized by $dv_n/dP_n < 0$, has been presented under Routh's incremental model. For a given collision configuration it has been shown that the jamb occurrence depends upon the friction coefficient and the sliding direction.

In the plane of vectors $\boldsymbol{\mu} = \mu\boldsymbol{\sigma}$, the conditions for jamb process are fulfilled in a half-plane, and the behavior of the system concerning jamb (for a given collision configuration) may be characterized by means of four jamb related domains. These domains are defined from the polar plot of $\boldsymbol{\mu}_A(\boldsymbol{\sigma})$, associated with the asymptotes of the sliding velocity flow, which is a hyperbola, and the jamb boundary, which is a straight line.

In the plane of the sliding velocity, for a given μ greater than μ_J (the threshold μ for jamb), jamb occurs in an angular sector symmetrical to the invariant direction for $\mu = 0$. The four jamb related domains in the $\boldsymbol{\mu}$-plane correspond to several (from zero to three) angular sectors.

Rough collisions developing jamb may be particularly complex when the jamb does not start from the beginning of the collision. If jamb starts during the expansion phase, $v_n > 0$, a second compression-expansion phase may develop. In such a case the usual energetical restitution coefficient is ill-defined. A new formulation of the energy dissipated by the normal force has been presented that can be consistently applied in all cases.

Acknowledgment

The author expresses his thanks to the referees, whose advice has been of great value to improve the final version of the article.

References

Batlle, J. A., and Condomines, A. B., 1991, "Rough Collisions in Multibody Systems," *Journal of Mechanism and Machine Theory,* Vol. 26, No. 6, pp. 565–577.

Batlle, J. A., 1993, "On Newton's and Poisson's Rules of Percussive Dynamics," ASME JOURNAL OF APPLIED MECHANICS, Vol. 60, pp. 376–381.

Batlle, J. A., 1996a, "Ballanced Rough Collisions," ASME JOURNAL OF APPLIED MECHANICS, Vol. 63, pp. 168–172.

Batlle, J. A., 1996b, "The Sliding Velocity Flow of Rough Collisions in Multibody Systems," ASME JOURNAL OF APPLIED MECHANICS, Vol. 63, pp. 804–809.

Beghin, H., 1951, *Cours de Mécanique Théorique et Appliquée,* Gauthier-Villars, Paris, pp. 477–783.

Bhatt, V., and Koechling, J. C., 1995a, "Partitioning the Parameter Space According to Different Behaviors During Three-Dimensional Impacts," ASME JOURNAL OF APPLIED MECHANICS, Vol. 62, pp. 740–746.

Bhatt, V., and Koechling, J. C., 1995b, "Three-Dimensional Frictional Rigid Body Impact," ASME JOURNAL OF APPLIED MECHANICS, Vol. 62, pp. 893–898.

Chatterjee, A., 1997, "Rigid Body Collisions: Some General Considerations, New Collision Laws, and Some Experimental Data," Ph.D. thesis, Cornell University, Ithaca, New York.

Cohen, M., and Mac Sithigh, G. P., 1991, "Impulsive Motions of Elastic Pseudo-Rigid Bodies," ASME JOURNAL OF APPLIED MECHANICS, Vol. 58, pp. 1042–1048.

Ivanov, A. P., 1992, "Energetics of a Collision with Friction," *Journal of Applied Mathematics and Mechanics,* Vol. 56, No. 4, pp. 527–534.

Jaeger, J., 1992, "Elastic Impact with Friction," Thesis, University of Delf, Delf, The Netherlands.

Jaeger, J., 1994, "Analytical Solutions of Contact Impact Problems," M. Okrouhlik, ed., ASME *Applied Mechanics Reviews,* Vol. 74, pp. 35–54.

Marghitu, D. B., and Hurmuzlu, Y., 1995, "Three-Dimensional Rigid-Body Collisions With Multiple Contact Points," ASME JOURNAL OF APPLIED MECHANICS, Vol. 62, pp. 725–732.

Routh, E. J., 1905, *Dynamics of a System of Rigid Bodies,* Vol. 1, MacMillan and Co., London.

Stronge, W. J., 1990, "Rigid Body Collisions with Friction," *Proc. Royal Society, London,* Vol. A431, pp. 169–181.

Stronge, W. J., 1994, "Swerve During Three-Dimensional Impact of Rough Rigid Bodies," ASME JOURNAL OF APPLIED MECHANICS, Vol. 60, pp. 605–611.

Downloaded 04 May 2010 to 171.66.16.26. Redistribution subject to ASME license or copyright; see http://www.asme.org/terms/Terms_Use.cfm

Guided Circumferential Waves in a Circular Annulus

Guoli Liu

Jianmin Qu
Assoc. Mem.

The George W. Woodruff School
of Mechanical Engineering,
Georgia Institute of Technology,
Atlanta, GA 30332-0405

A two-dimensional circular annulus is considered in this paper as a waveguide. The guided steady-state time-harmonic waves propagating in the circumferential direction are studied. It is found that the guided circumferential waves are dispersive. The dispersion equation is derived analytically and numerical examples are presented for the frequency dispersion curves. The displacement profiles across the wall thickness of the annulus are also obtained for the first five propagating modes. In addition, the analogy between a flat plate and an annulus in the asymptotic limit of infinite radius of curvature is discussed to reveal some interesting wave phenomena intrinsic to curved waveguides.

1 Introduction

Fatigue cracks have been found to initiate and grow in the radial direction in many annulus-shaped components in aging mechanical structures. For example, in a helicopter, the rotor drive system contains many components, such as the rotor hub, reservoir hub, pitch shaft, etc., that contain annulus-shaped parts. Currently, detection of such radial fatigue cracks relies mostly on visual inspection. More systematic, automated, and efficient methods to detect these cracks are needed.

Conventional ultrasonic imaging techniques can be used to detect such radial cracks. However, these techniques are impractical for real-time integrated diagnosis. Recently, it has been proposed (Nagy et al., 1994) that guided ultrasonic waves that propagate in the circumferential direction may be used for the detection of radial fatigue cracks in weep holes in airframes. In the case of annulus structural components, access to the inner surface is usually unavailable. One can only generate guided waves from the outside of the annulus. Since the radial cracks are often found to initiate from the inner surface, particular wave modes must be selectively generated so that the energy is concentrated near the inner surface to increase the signal to noise ratio. Before such guided waves can be effectively used for this purpose, their generation and propagation must be understood. The physics and mechanics of the wave fields must be carefully examined. However, solutions to circumferential wave propagation in annular structures are very few, although there exists a large body of literature on straight waveguides, such as bars and plates.

To provide the scientific foundation for the guided wave techniques for detecting radial cracks in annular structures, a two-dimensional circular annulus is considered in this paper as a waveguide. The guided steady-state time-harmonic waves propagating in the circumferential direction are studied. The dispersion equation is derived analytically and numerical examples are presented for the frequency dispersion curves and the displacement profiles across the wall thickness of the annulus. In addition, the analogy between a flat plate and an annulus in the asymptotic limit of infinite radius of curvature is discussed to reveal some interesting wave phenomena intrinsic to curved waveguides.

Intuitively, an annulus can be viewed as a waveguide in which elastic waves can propagate in the circumferential direction. Extensive studies have been conducted on other type of waveguides. For example, wave propagation in the axial direction of a circular cross section bar (Mindlin and McNiven, 1960), a rectangular cross section bar (Mindlin and Fox, 1960), a circular hollow cylinder (Gazis, 1959), and plates (Mindlin, 1960) are well understood. A comprehensive review of these studies can be found in Miklowitz (1978). A more recent work by Ditri and Rose (1992) solved the problem of transient wave propagation in the axial direction of a hollow cylinder subjected to surface tractions.

The difference between an annulus and a plate is that the annulus has a finite radius of curvature. In fact, a flat plate can be viewed as a limiting case of the annulus when the radius of the curvature of the annulus becomes infinite. This conjecture will be confirmed numerically in this paper. Nevertheless, the finite radius of curvature does complicate the wave fields and generate some interesting new phenomena.

In a sense, a surface can also be viewed as a waveguide. The most familiar example of such a guided wave is the Rayleigh surface wave (Rayleigh, 1885). Later, it was observed that a Rayleigh-type wave may also propagate along a cylindrical surface (Cook and Valkenburg, 1954). The analytical work on Rayleigh-type waves on a cylindrical surface was presented by Viktorov (1958), Grace and Goodman (1966), Keller and Karal (1960, 1964), Grimshaw (1968), Rulf (1969), and Gregory (1971). It was found that unlike the Rayleigh waves on a planar surface, frequency dispersion takes place for surface waves propagating along a curved surface. In addition, in the case of a curvilinear (convex) boundary of a solid, it is also possible for other modes of surface waves to propagate, confined near the curved boundary (Brekhovskikh, 1968). These waves are sometimes called the "whispering gallery" waves. Famous examples of such whispering gallery waves include the Temple of Heaven in Beijing and the dome of St. Paul's Cathedral in London, which was described in Rayleigh's classic book (Rayleigh, 1945).

The dispersion of elastic waves and Rayleigh-type waves in a thin disk was investigated by Červ (1988). The focus was to study the displacement amplitude of the various circumferential modes in a solid disk. Recently, Qu et al. (1996) derived the dispersion equation for the time-harmonic circumferential waves in a circular annulus. In the case of an annulus, multiple reflection may take place. Consequently, guided waves between the inner and outer surfaces can propagate in the circumferential direction.

The paper is arranged as follows. Section 2 presents the steady-state fundamental governing equations and boundary conditions for free waves in an annulus. This boundary value

Contributed by the Applied Mechanics Division of THE AMERICAN SOCIETY OF MECHANICAL ENGINEERS for publication in the ASME JOURNAL OF APPLIED MECHANICS.

Discussion on the paper should be addressed to the Technical Editor, Professor Lewis T. Wheeler, Department of Mechanical Engineering, University of Houston, Houston, TX 77204-4792, and will be accepted until four months after final publication of the paper itself in the ASME JOURNAL OF APPLIED MECHANICS.

Manuscript received by the ASME Applied Mechanics Division, Nov. 19, 1996; final revision, Sept. 12, 1997. Associate Technical Editor: V. K. Kinra.

 Copyright © 1998 by ASME

Downloaded 04 May 2010 to 171.66.16.26. Redistribution subject to ASME license or copyright; see http://www.asme.org/terms/Terms_Use.cfm

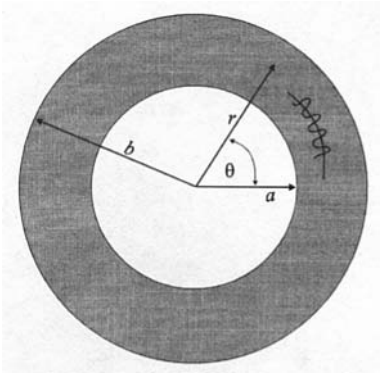


Fig. 1 A circular annulus with inner radius a, outer radius b, in the polar coordinate system (r, θ)

problem is solved in Section 3 for guided waves propagating in the circumferential direction. Section 4 shows some numerical results of the dispersion curves and displacement profiles across the thickness of the annulus. Several interesting features associated with the curved waveguide are also discussed in this section. Finally, some concluding remarks are given in Section 5.

2 Problem Statement

Consider steady-state time-harmonic waves in a circular annulus of inner radius a and outer radius b as shown in Fig. 1. It is assumed that the material is linearly elastic and isotropic. For the two-dimensional deformation studied here, assume that plane-strain deformation in the annulus prevails. Let ω and t be the circular frequency and time, respectively. Thus, without explicitly writing out the time factor $e^{i\omega t}$, which is common to all field quantities, the displacement components in the polar coordinate system (r, θ) shown in Fig. 1 can be written as

$$u_r = u_r(r, \theta), \quad u_\theta = u_\theta(r, \theta). \tag{1a, b}$$

According to the Hooke's law for linear elastic materials, the pertinent stress components corresponding to (1) are

$$\sigma_r = \lambda\left(\frac{\partial u_r}{\partial r} + \frac{u_r}{r} + \frac{1}{r}\frac{\partial u_\theta}{\partial \theta}\right) + 2\mu\frac{\partial u_r}{\partial r}, \tag{2a}$$

$$\sigma_\theta = \lambda\left(\frac{\partial u_r}{\partial r} + \frac{u_r}{r} + \frac{1}{r}\frac{\partial u_\theta}{\partial \theta}\right) + 2\mu\left(\frac{u_r}{r} + \frac{1}{r}\frac{\partial u_\theta}{\partial \theta}\right), \tag{2b}$$

$$\sigma_{r\theta} = \mu\left(\frac{\partial u_\theta}{\partial r} - \frac{u_\theta}{r} + \frac{1}{r}\frac{\partial u_r}{\partial \theta}\right), \tag{2c}$$

where λ and μ are the Lamé constants of the material.

Without body forces, the two-dimensional equations of motion in polar coordinates are

$$\frac{\partial \sigma_r}{\partial r} + \frac{\sigma_r - \sigma_\theta}{r} + \frac{1}{r}\frac{\partial \sigma_{r\theta}}{\partial \theta} + \rho\omega^2 u_r = 0, \tag{3a}$$

$$\frac{\partial \sigma_{r\theta}}{\partial r} + \frac{1}{r}\frac{\partial \sigma_\theta}{\partial \theta} + 2\frac{\sigma_{r\theta}}{r} + \rho\omega^2 u_\theta = 0, \tag{3b}$$

where ρ is the mass density. In addition, it is assumed that the surface of the annulus is traction free, i.e.,

$$\sigma_r = \sigma_{r\theta} = 0, \quad \text{at } r = a, b. \tag{4a, b}$$

Solutions to the boundary value problem posed by (2) – (4) are derived next.

3 Method of Solution

To solve the boundary value problem stated in the previous section, one may introduce the displacement potentials φ and ψ through

$$u_r = \frac{\partial \varphi}{\partial r} + \frac{1}{r}\frac{\partial \psi}{\partial \theta}, \quad u_\theta = \frac{1}{r}\frac{\partial \varphi}{\partial \theta} - \frac{\partial \psi}{\partial r}. \tag{5a, b}$$

It can be easily shown (Achenbach, 1984) that the equations of motion (3a, b) are automatically satisfied if φ and ψ satisfy the reduced wave equations

$$\left(\frac{\partial^2}{\partial r^2} + \frac{1}{r}\frac{\partial}{\partial r} + \frac{1}{r^2}\frac{\partial^2}{\partial \theta^2}\right)\varphi + \frac{\omega^2}{c_L^2}\varphi = 0, \tag{6a}$$

$$\left(\frac{\partial^2}{\partial r^2} + \frac{1}{r}\frac{\partial}{\partial r} + \frac{1}{r^2}\frac{\partial^2}{\partial \theta^2}\right)\psi + \frac{\omega^2}{c_T^2}\psi = 0, \tag{6b}$$

where c_L and c_T are, respectively, the longitudinal and shear wave velocities given by

$$c_L = \sqrt{\frac{\lambda + 2\mu}{\rho}}, \quad c_T = \sqrt{\frac{\mu}{\rho}}. \tag{7a, b}$$

For waves propagating in the θ-direction, one may write

$$\varphi = \Phi(r)\exp(ikb\theta), \quad \psi = \Psi(r)\exp(ikb\theta), \tag{8a, b}$$

where, for convenience, the wave number k is defined by

$$k = \frac{\omega}{c(b)}. \tag{9}$$

In (9), $c(r)$ is the linear phase velocity for material particles located at a distance r from the center and it should be a function of r. In fact, (8) represents a solution where the phase is constant along radial lines. Furthermore, for a given solution for (k, ω) the angular velocity is a constant along the radial lines so the velocity along the radial line varies linearly with r.

Substitution of (8a, b) into (6a, b), respectively, yields

$$\Phi'' + \frac{1}{r}\Phi' + \left[\left(\frac{\omega}{c_L}\right)^2 - \left(\frac{kb}{r}\right)^2\right]\Phi = 0, \tag{10a}$$

$$\Psi'' + \frac{1}{r}\Psi' + \left[\left(\frac{\omega}{c_T}\right)^2 - \left(\frac{kb}{r}\right)^2\right]\Psi = 0. \tag{10b}$$

These are Bessel equations. By introducing the nondimensional variables

$$\bar{r} = \frac{r}{b}, \quad \bar{k} = kh, \quad \bar{\omega} = \frac{\omega h}{c_T}, \quad h = b - a, \tag{11a, b, c, d}$$

$$\hat{k} = \frac{\bar{k}}{1 - \eta} = kb, \quad \hat{\omega} = \frac{\bar{\omega}}{1 - \eta} = \frac{\omega b}{c_T}, \quad \eta = \frac{a}{b}, \tag{12a, b, c}$$

their solutions are (Stakgold, 1979), respectively,

$$\Phi(\bar{r}) = A_1 J_{\hat{k}}\left(\frac{\hat{\omega}\bar{r}}{\kappa}\right) + A_2 Y_{\hat{k}}\left(\frac{\hat{\omega}\bar{r}}{\kappa}\right), \tag{13a}$$

$$\Psi(\bar{r}) = A_3 J_{\hat{k}}(\hat{\omega}\bar{r}) + A_4 Y_{\hat{k}}(\hat{\omega}\bar{r}), \tag{13b}$$

where $J_{\hat{k}}(x)$ and $Y_{\hat{k}}(x)$ are, respectively, the first and second-kind Bessel functions of order $\hat{k}$,

$$\kappa = \frac{c_L}{c_T} = \sqrt{\frac{2(1 - \nu)}{(1 - 2\nu)}}, \tag{14}$$

and ν is the Poisson's ratio; A_n, $n = 1, 2, 3, 4$, are constants to be determined by the boundary conditions.

Downloaded 04 May 2010 to 171.66.16.26. Redistribution subject to ASME license or copyright; see http://www.asme.org/terms/Terms_Use.cfm

Next, substituting (8) into (5), then into (2a, c) yields

$$\sigma_r = \frac{\mu \exp(ikb\theta)}{r^2}[\kappa^2 r^2\Phi'' + (\kappa^2 - 2)r\Phi' - (\kappa^2 - 2)k^2b^2\Phi + 2ikbr\Psi' - 2ikb\Psi],$$

$$\sigma_{r\theta} = \frac{\mu \exp(ikb\theta)}{r^2}[-r^2\Psi'' + r\Psi' - k^2b^2\Psi + 2ikbr\Phi' - 2ikb\Phi]. \quad (15a, b)$$

Enforcing the traction-free boundary conditions (4a, b) in conjunction with (13) yields a system of four homogeneous equations for the constants $\mathbf{A} = (A_1, A_2, A_3, A_4)^T$,

$$\mathbf{D}(\bar{k}, \bar{\omega})\mathbf{A} = \mathbf{0}, \quad (16)$$

where $\mathbf{D}(\bar{k}, \bar{\omega})$ is a known 4×4 matrix function of the nondimensional wave number $\bar{k}$, nondimensional frequency $\bar{\omega}$, and nondimensional wall thickness parameter η. Its components are given in the Appendix.

For nontrivial solutions, the determinant of the coefficient matrix of this system of equations must vanish, i.e.,

$$\text{Det}\,[\mathbf{D}(\bar{k}, \bar{\omega})] = 0. \quad (17)$$

The above equation provides the dispersion relationship between the wave number and the frequency, i.e., the $\bar{\omega}$–$\bar{k}$ relationship. The curve of $\bar{\omega}$ versus $\bar{k}$ is called the frequency dispersion curve. For each given $\bar{k}$ value, (17) may have many roots for $\bar{\omega}$. Therefore, solutions to (17) yield a family of dispersion curves. Each one is called a branch, which corresponds to a wave mode propagating in the circumferential direction.

Once a root corresponding to the given $\bar{k}$ is solved from (17), it can be substituted back into (16) to determine the corresponding eigenvector, $\mathbf{A}$. Obviously, $\mathbf{A}$ can only be determined up to an arbitrary multiplier. Without loss of generality, one may require $\|\mathbf{A}\| = 1$.

For a given $\bar{k}$ value, let the nth root of (17) be denoted by $\bar{\omega}_n$ and the corresponding eigenvector by $\mathbf{A}_n$. It then follows from (5)–(13) that the displacement components corresponding to this mode can be written as

$$u_r^{(n)} = W_r^{(n)}(\bar{r}) \exp(ikb\theta),$$
$$u_\theta^{(n)} = W_\theta^{(n)}(\bar{r}) \exp(ikb\theta), \quad (18a, b)$$

where the displacement amplitudes are

$$W_r^{(n)}(\bar{r}) = \frac{1}{b\bar{r}}\left[A_1^{(n)}\frac{\hat{\omega}_n\bar{r}}{\kappa}J_k'\left(\frac{\hat{\omega}_n\bar{r}}{\kappa}\right) + A_2^{(n)}\frac{\hat{\omega}_n\bar{r}}{\kappa}Y_k'\left(\frac{\hat{\omega}_n\bar{r}}{\kappa}\right) + i\hat{k}A_3^{(n)}J_k(\hat{\omega}_n\bar{r}) + i\hat{k}A_4^{(n)}Y_k(\hat{\omega}_n\bar{r})\right], \quad (19a)$$

$$W_\theta^{(n)}(\bar{r}) = \frac{1}{b\bar{r}}\left[i\hat{k}A_1^{(n)}J_k\left(\frac{\hat{\omega}_n\bar{r}}{\kappa}\right) + i\hat{k}A_2^{(n)}Y_k\left(\frac{\hat{\omega}_n\bar{r}}{\kappa}\right) - A_3^{(n)}\hat{\omega}_n\bar{r}J_k'(\hat{\omega}_n\bar{r}) - A_4^{(n)}\hat{\omega}_n\bar{r}Y_k'(\hat{\omega}_n\bar{r})\right]. \quad (19b)$$

It is clear from (18) that for the time-harmonic waves propagating in the θ-direction, all material particles located on the same radial line should have the same phase factor given by

$$\exp[i(kb\theta - \omega t)] = \exp\left[i\omega\left(\frac{kb\theta}{\omega} - t\right)\right] = \exp\left[i\omega\left(\frac{\theta}{\alpha} - t\right)\right], \quad (20)$$

where

$$\alpha = \frac{\omega}{kb} \quad (21)$$

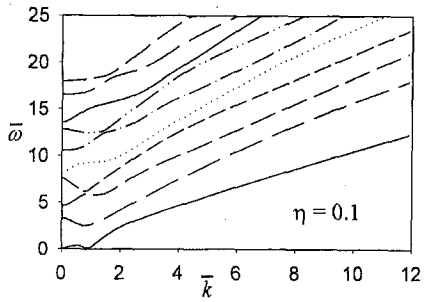


Fig. 2(*a*) The first ten branches of the $\bar{\omega}$–$\bar{k}$ relationship for $\eta = 0.1$

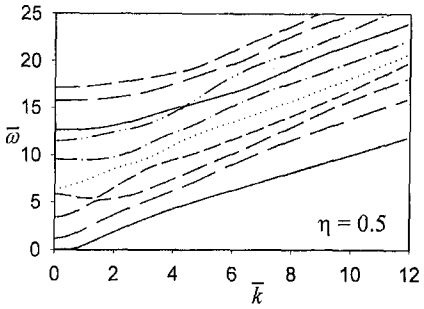


Fig. 2(*b*) The first ten branches of the $\bar{\omega}$–$\bar{k}$ relationship for $\eta = 0.5$

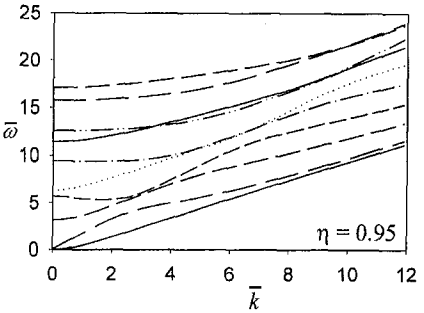


Fig. 2(*c*) The first ten branches of the $\bar{\omega}$–$\bar{k}$ relationship for $\eta = 0.95$

is called the "angular phase velocity" of the circumferential wave (Qu et al., 1996). In other words, each radial line of the annulus can be viewed as a wave front of the circumferential wave. Propagation of the circumferential wave can be described by the rotation of the radial line with an angular velocity α as defined by (21). Variation of the wave amplitude on each wavefront (radial line of the annulus) is characterized by the $W_r^{(n)}(r)$ and $W_\theta^{(n)}(r)$.

4 Numerical Examples and Discussions

In this section, some numerical examples of the steady-state circumferential waves are carried out for $\nu = 0.2817$, $c_T = 3200$ m/s, $c_L = 5660$ m/s, and $\eta = 0.1$, 0.5 and 0.95. The numerical solutions of the dispersion curves are obtained by giving a value of $\bar{k}$, then finding the root of (17) for the corresponding values of $\bar{\omega}$. An infinite number of real roots exits. Each represents a propagating mode. Note that care must be taken in the root-finding procedure, for the determinant (17) changes its value very rapidly.

The first ten modes, i.e., the first ten branches of the $\bar{\omega}$–$\bar{k}$ curves, are plotted in Figs. 2(a)–2(c) for $\eta = 0.1$, 0.5 and 0.95, respectively. Notice that at high frequencies, the first mode for all cases is almost a straight line, indicating that it is almost nondispersive.

It is also seen, for example, from Fig. 2(b) that there is a crossover point between the seventh and eighth modes around $\bar{k} = 4$ for the annulus with $\eta = 0.5$. For a thinner annulus, e.g., $\eta = 0.95$, there are more crossover points between different

Downloaded 04 May 2010 to 171.66.16.26. Redistribution subject to ASME license or copyright; see http://www.asme.org/terms/Terms_Use.cfm

modes. This crossover phenomenon also occurs in the case of a flat plate, where the symmetric and antisymmetric modes may have crossover points. Physically, a crossover point indicates that at that particular frequency, the mechanical energy may be exchangeable between the two neighboring modes (Meeker and Meitzler, 1964). However, unlike the plate case where the symmetric and antisymmetric modes are clearly defined, it is no longer possible to define the symmetric and antisymmetric modes in the annulus because of the curvature. For this reason, the modes are defined somewhat arbitrarily when two of them cross each other. Therefore, the concept of energy exchange between these two modes becomes somewhat of an artifact.

Once the frequency dispersion relationship is determined, one can compute the linear phase velocity in the circumferential direction for a material particle at distance r from the center

$$c(r) = r\alpha = \frac{\bar{\omega}}{\bar{k}} \frac{r}{b} c_T. \tag{22}$$

For example, the circumferential wave travels along the outer surface, $r = b$, with the speed of

$$c(b) = \frac{\bar{\omega}}{\bar{k}} c_T = \frac{\omega}{k}. \tag{23}$$

This is consistent with (9). Now the advantage of defining k through (9) is clear. Once the dispersion equation is solved, the propagating (phase) velocity at the outer surface of the annulus, $c(b)$, is obtained from (23). On the other hand, since $c(b)$ can be measured easily on the outer surface of the annulus, (23) provides a tool to determine the dispersion curves experimentally.

The phase velocities of the first ten modes are plotted in Figs. 3(*a*)–3(*c*) for $\eta = 0.1$, 0.5, and 0.95, respectively. For clarity, the different modes (branches) are named as labeled in these figures. The rational for such labeling will be discussed later. For now, it is seen, once again, from these results that at higher frequencies, the first modes are almost nondispersive for the three cases considered ($\eta = 0.1, 0.5, 0.95$). They all asymptotically approach the Rayleigh wave velocity which is nondispersive (here $c_R/c_T = 0.9214$ for $\nu = 0.2817$). Except for the first three modes, all higher modes have phase velocities greater than the shear wave speed in the wave number range considered. For the first mode at higher frequencies, the phase velocity $c(b)$ varies with the wall thickness: $c(b) > c_T$ for very thick annulus ($\eta = 0.1$), and $c(b) < c_T$ for very thin annulus ($\eta = 0.95$). It has been shown (Viktorov, 1958) that the phase velocity of the second mode should be greater than the Rayleigh wave velocity and approaches the Rayleigh wave velocity as $\bar{k} \to \infty$. However, the first two modes shown in Fig. 3 were not mentioned in (Viktorov, 1958; Červ, 1988), which seem to be the most complex modes to analyze.

Knowing the $\bar{\omega}$–$\bar{k}$ relationship, one can also compute the group velocity of the circumferential waves (Achenbach, 1984),

$$c_g = \frac{\partial \omega}{\partial k} = \frac{\partial \bar{\omega}}{\partial \bar{k}} c_T. \tag{24}$$

The group velocities of the first ten modes are plotted in Figs. 4(*a*)–4(*c*) for $\eta = 0.1$, 0.5 and 0.95, respectively. Unlike waves in a flat plate (Weaver and Pao, 1982), the group velocity may exceed the longitudinal wave speed c_L ($=1.814 c_T$ here) for a thicker annulus, see Figs. 4(*a*)–4(*b*). Since it is the overall wave group that propagates at the group velocity c_g, it can be interpreted that $c_g > c_L$ means that the waves will appear to originate at the front of the group, travel to the rear, and disappear (Graff, 1975).

Intuitively, one may expect that the size of the annulus (consequently, the curvature) would affect the dispersion relationship. However, the dispersion curves shown in Figs. 2–4 are

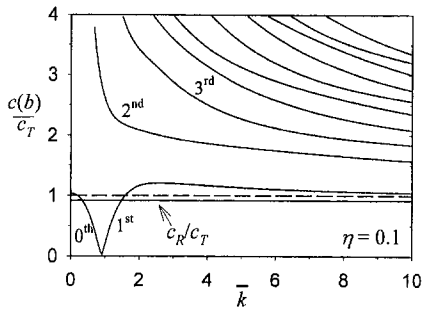


Fig. 3(*a*) The first ten branches of the $c(b)$–$\bar{k}$ relationship for $\eta = 0.1$

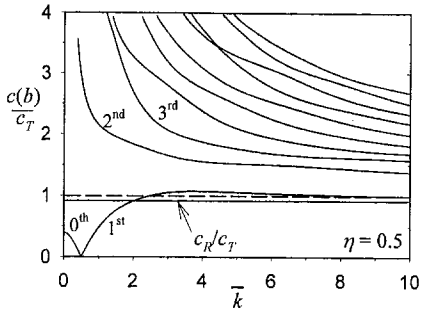


Fig. 3(*b*) The first ten branches of the $c(b)$–$\bar{k}$ relationship for $\eta = 0.5$

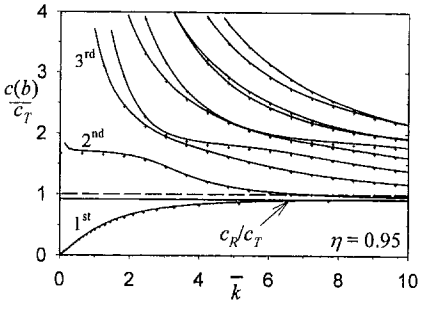


Fig. 3(*c*) The first ten branches of the $c(b)$–$\bar{k}$ relationship for $\eta = 0.95$. Solid lines are for the annulus and cross-hair symbols are for a flat plate of thickness h.

somewhat "curvature independent." This is because the $\bar{\omega}$–$\bar{k}$ curves obtained from (17) depend on only the shape factor η, which characterizes only the shape, not the radius of the annulus (e.g., the size). Consequently, the curves in Figs. 2–3 can be used for circular annuli of different radius, as along as they all have the same shape (e.g., the same η). The question is then "how does the curvature get involved?"

To this end, we return to the angular phase velocity defined in (21). Making use of the nondimensional variables introduced in (11)–(12), one can easily show that

$$\alpha = \frac{\omega}{kb} = \frac{\bar{\omega}}{\bar{k}} \frac{c_T}{b}. \tag{25}$$

Now, it is clear from (25) that, although the $\bar{\omega}$–$\bar{k}$ curves obtained from (17) depend on only the shape (not the radii of the annulus), the angular phase velocity of the circumferential waves does depend on the radius b. In other words, the curvature is involved through the angular phase velocity. Consequently, once the $\bar{\omega}$–$\bar{k}$ relationship is solved from (17) for a given shape factor, η, the angular phase velocity for annuli of different radii can be easily obtained from (25), as along as they all have the same shape factor, η. In this sense, the dispersion equation can be viewed as universal in that it provides the solutions for all annuli that have the same shape factor η.

Another point worth mentioning is the limits of the geometrical parameters. Note that in addition to the wavelength $2\pi/k$,

Downloaded 04 May 2010 to 171.66.16.26. Redistribution subject to ASME license or copyright; see http://www.asme.org/terms/Terms_Use.cfm

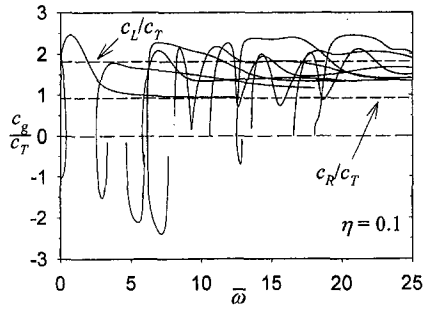


Fig. 4(*a*) The first ten branches of the c_g–$\bar{\omega}$ relationship for $\eta = 0.1$

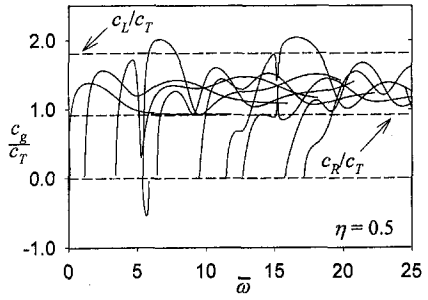


Fig. 4(*b*) The first ten branches of the c_g–$\bar{\omega}$ relationship for $\eta = 0.5$

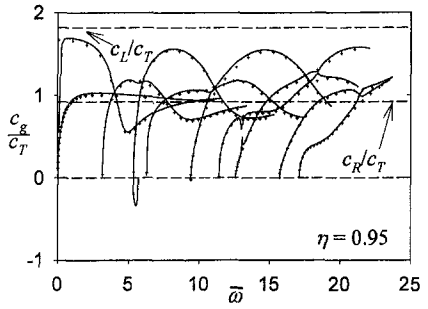


Fig. 4(*c*) The first ten branches of the c_g–$\bar{\omega}$ relationship for $\eta = 0.95$. Solid lines are for the annulus and cross-hair symbols are for a flat plate of thickness h.

there are two other independent length parameters in this problem. Although the choice is somewhat arbitrary, the outer radius b and the wall thickness h are taken to be the two independent parameters in this paper. For convenience, a nondimensional parameter $\eta = a/b$ was introduced in (12c) to characterize the shaper, or the aspect ratio of the annulus. The use of η in (17) makes the dispersion equation independent of the curvature as discussed in previous paragraphs. However, the limits of η must be carefully examined in order to correctly interpret the results.

It appears that $\eta = 0$ (i.e., $a = 0$ for finite b) corresponds to a solid disk. However, careful examination of the equations reveals that this is not the case. The limit of $a \to 0$ in (17) does not yield the dispersion equation for a solid disk. This may be understood physically by considering two disks, one that is solid and another that has a hole of infinitesimal radius at the center. For the solid disk, displacement at the center must be kept finite on physical grounds. Therefore, the displacement fields consists only the Bessel functions of the first kind. On the other hand, for the disk with a center hole, the free surface of the hole requires the Bessel function of the second kind in the displacement fields in order to satisfy the traction-free boundary condition. In fact, the multiple reflections between the outer surface and the surface of the hole form a caustics at the center. A strong stress concentration arises when the hole diameter becomes very small. The wave fields become unbounded in the limit of $a \to 0$. The unbounded displacement field is characterized by the singularity of the Bessel function of the second kind.

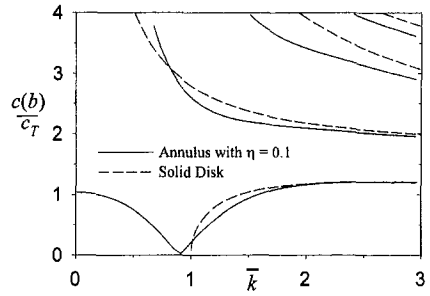


Fig. 5 Comparison of phase velocity dispersion curves between a solid disk and an annulus with $\eta = 0.1$

To illustrate the above argument, a comparison of the phase velocity dispersion curves between a solid disk and an annulus of $\eta = 0.1$ is shown in Fig. 5. It is seen that the cutoff wave number of the first mode is $\bar{k} = 1$ for the solid disk and $\bar{k} = 1-\eta$ for the annulus. In both cases, this corresponds to $\hat{k} = kb = 1$, which means that the wavelength on the outer surface is equal to $2\pi b$, the outer circumference. Since this mode is analogous to the first flexural mode (in the limit of $\eta \to 1$ it approaches to the first flexural mode in the plate, see Fig. 3(c)), its wavelength must be smaller than the circumference for it to propagate along the circumferential direction. However, the dispersion curves of the annulus have an extra branch extended from $\bar{k} = 0$ to $\bar{k} = 1-\eta = 0.9$, labeled as the 0th mode in this paper. This propagating mode is unique to the annulus due to the multiple reflections between the inner and outer surfaces. The outer surface of the annulus is a convex surface and the inner surface is a concave surface. The Rayleigh-type surface waves are different for these two cases (Viktorov, 1958). A convex surface admits a Rayleigh-type surface wave with real-valued wave number whose wave speed is slightly higher than the Rayleigh wave speed on a flat surface. On the other hand, a concave surface only admits a Rayleigh-type surface wave with complex wave number. Consequently, the surface wave on a concave surface propagates with attenuation due to the radiation of energy into the medium. This radiated energy will be reflected back to the center by the outer surface if there is one. Consequently, the attenuated surface wave on the inner surface is enhanced by this reflected energy to form a propagating wave. Thus, it is fair to say that the existence of the extra branch is to accommodate the inability of the concave surface to sustain propagating surface waves. As the wave number increases, the phase velocity of this extra mode decreases. The velocity (both phase and group), as well as the frequency, becomes zero when $\bar{k} = 1-\eta$ (see also Figs. 3(a)–3(c)). It follows from (12a) that this corresponds to $\hat{k} = kb = 1$, which means that the wavelength on the outer surface is equal to $2\pi b$, the outer circumference. In this case, no wave propagation takes place in the circumferential direction since the nodal points on the outer surface stay at the same position all the time due to the 2π periodicity. Since each radial line of the annulus is a wavefront propagating in the circumferential direction with the angular velocity defined by (25), one may conclude that there will be no wave propagation at any radius $a \leq r < b$ if there is no wave propagation on the outer surface $r = b$. Asymptotic analysis as $\hat{k} \to 1$, $\omega \to 0$ shows that the displacement field is indeed zero everywhere. Numerical computations also confirm this.

Next, consider the limit of $\eta \to 1$. Notice that

$$h = b - a = b(1 - \eta). \tag{26}$$

Therefore, two limiting cases may result.

Case (i) $\eta \to 1$ with h being a nonzero value;

Case (ii) $\eta \to 1$ with b being a finite value.

It follows from (26) that Case (i) yields $b \to \infty$. Consequently, this limiting case corresponds to a flat plate of thickness

Downloaded 04 May 2010 to 171.66.16.26. Redistribution subject to ASME license or copyright; see http://www.asme.org/terms/Terms_Use.cfm

h. On the other hand, Case (ii) yields $h \to 0$, which corresponds to a thin annulus (ring) of radius b.

Note from the preceding discussion that the two limiting cases are differentiated by only different values of b. Now recall that the dispersion Eq. (17) is independent of b. Therefore, one may conclude that the dispersion curves for guided waves in a plate and for the circumferential waves in a thin annulus are the same in the limit of $\eta \to 1$. For example, the dispersion relationship of a plate with thickness h represents an approximation to the dispersion relationship of an annulus with $\eta = 0.95$. This is demonstrated by the comparisons shown in Figs. 3(*c*)–4(*c*), where the phase and group velocities for the first ten modes in a plate of thickness h and that in an annulus of thickness h are plotted, respectively. The solid lines are from the annulus and the cross-hair symbols are from the plate. It is seen that the two cases are very close. Furthermore, based on the foregoing discussion, these are also approximate solutions to the velocity dispersion curves of a thin annulus of finite radius b. This discovery extends the utility of the Rayleigh-Lame dispersion equation for plates to annuli and cylindrical thin shells when circumferential waves are of interest. In other words, instead of going through complicated calculations to obtain the dispersion curves in the circumferential direction for a thin cylindrical shell, one can simply use the Rayleigh-Lame equation to obtain an approximate solution.

It seems that the above result is somewhat counterintuitive in that if the wave length is of the order of the circumference, there will still be a distinction between a thin cylindrical shell and a flat plate regardless of the value of η. This is indeed true. However, the above result simply states that in the limit of $\eta \to 1$, the dispersion curves for these two cases are the same when $\bar{k} = kh$ is used in the plot regardless of the value of b. Since the phase factor, $\exp[i(kb\theta - \omega t)]$, as shown in (20), does depend on b, the actual wave fields in the shell and in the plate are indeed different. The conclusion is, therefore, that although the wave fields may be quite different between a thin shell and a flat plate, their dispersion curves are identical if both are plotted versus $\bar{k} = kh$. For example, the dispersion curves for a thin shell are conventionally plotted as functions of $\hat{k} = kb$. From the above discussions, one can obtain these curves from the Rayleigh-Lame equations of a plate by converting $\bar{k} = kh$ to $\hat{k} = kb$ through (11)–(12).

Finally, consider the displacements. For the nth mode, the displacement variation as function of r is characterized by $W_r^{(n)}(\bar{r})$ and $W_\theta^{(n)}(\bar{r})$. Interestingly enough, our numerical solutions show that $W_r^{(n)}(\bar{r})$ is real and $W_\theta^{(n)}(\bar{r})$ is pure imaginary, which indicates that the two components are always 90 deg out of phase.

The first five modes of the displacement are computed at $\bar{\omega} = 10$. The corresponding radial variation $W_r^{(n)}(\bar{r})$ and $W_\theta^{(n)}(\bar{r})$ are obtained as functions of $\bar{r}$ from (19). Since $W_r^{(n)}(\bar{r})$ and $W_\theta^{(n)}(\bar{r})$ are, respectively, real and pure imaginary, the normalized displacement amplitude can be computed as

$$W_n(\bar{r}) = \frac{1}{H_n}\sqrt{|W_r^{(n)}(\bar{r})|^2 + |W_\theta^{(n)}(\bar{r})|^2}, \qquad (27)$$

where H_n is the maximum amplitude across the thickness for the nth mode, i.e.,

$$H_n = \max\{\sqrt{|W_r^{(n)}(\bar{r})|^2 + |W_\theta^{(n)}(\bar{r})|^2}, \quad \eta \le \bar{r} \le 1\}. \qquad (28)$$

The so normalized displacement amplitudes $W_n(\bar{r})$ are shown in Figs. 6(*a*)–6(*c*) for $\eta = 0.1$, 0.5 and 0.95, respectively. Generally speaking, for a fixed value of $\bar{\omega}$, higher modes have smaller wave numbers. The values of $\bar{k}$ corresponding to $\bar{\omega} = 10$ for each mode are indicated in these figures. In reading these figures, please note that the relative magnitude between different modes is meaningless because each mode is normalized by itself. The purpose of Fig. 6 is to show how each individual mode varies along the radial direction.

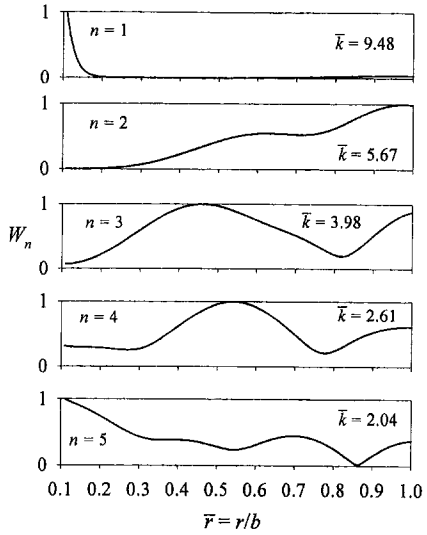


Fig. 6(*a*) Displacement profiles across the wall thickness of the first five modes for $\eta = 0.1$. They are normalized by their respective maximum amplitude through the thickness.

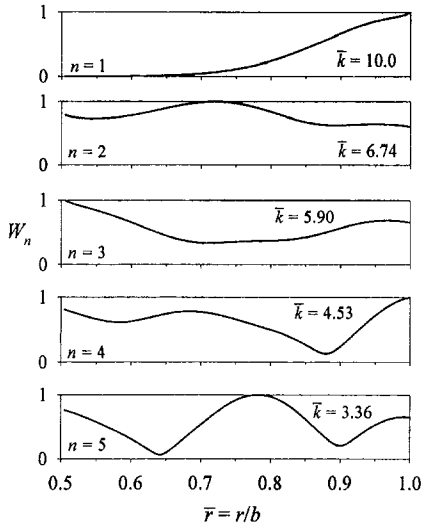


Fig. 6(*b*) Displacement profiles across the wall thickness of the first five modes for $\eta = 0.5$. They are normalized by their respective maximum amplitude through the thickness.

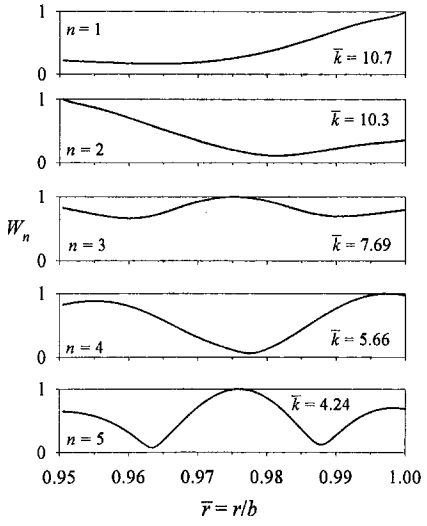


Fig. 6(*c*) Displacement profiles across the wall thickness of the first five modes for $\eta = 0.95$. They are normalized by their respective maximum amplitude through the thickness.

Downloaded 04 May 2010 to 171.66.16.26. Redistribution subject to ASME license or copyright; see http://www.asme.org/terms/Terms_Use.cfm

It is seen that in all three cases, the first mode is a Rayleigh-type surface wave either on the inner or outer surfaces, depending upon the shape factor of the annulus, η. Notice the large amplitude of the first mode near the inner surface, as shown in Fig. 6(a). This mode is primarily due to the presence of the inner free surface. Because the inner surface has such a small radius, the caustic effect previously mentioned gives rise to a large-displacement amplitude. For relatively thinner annulus, e.g., $\eta = 0.5$, the caustic effect becomes less important and the first mode becomes a Rayleigh-type surface wave on the outer surface. For the case $\eta = 0.95$, the annulus become even thinner and approaches to a plate. In this case, one may still call the first mode a Rayleigh-type surface wave on the outer surface, for its amplitude on the outer surface is still several times of that on the inner surface. However, the decay rate is much slower as shown in Fig. 6(c).

5 Summary

In this paper, the steady-state guided waves propagating in the circumferential direction of a circular annulus were considered. An analytical expression for the dispersion equation is derived. Numerical examples of the dispersion curves and the displacement fields of the first five propagating modes are presented. It was found that (i) the dispersion equation depends on the shape ($\eta = a/b$) not the size, b, of the annulus. (ii) the dispersion curves for a thin annulus can be approximated by that of a flat plate of the same thickness, (iii) the solution to a solid disk cannot be obtained by shrinking the inner diameter of an annulus to zero, (iv) the first mode is the Rayleigh-type of surface waves either on the inner surface or the outer surface, depending upon the shape of the annulus.

Acknowledgments

This work is supported by ONR through Grant N00014-95-1-0539.

References

Achenbach, J. D., 1984, *Wave Propagation in Elastic Solids,* North-Holland, Amsterdam.

Brekhovskikh, L. M., 1968, "Surface Waves Confined To The Curvature Of The Boundary In Solid," *Soviet Physics—Acoustics,* Vol. 13, pp. 462–472.

Červ, J., 1988, "Dispersion of Elastic Waves and Rayleigh-type Waves in a Thin Disc," *Acta Technica Csav,* Vol. 89, pp. 89–99.

Cook, E. G., and Valkenburg, H. E., 1954, "Surface Waves At Ultrasonic Frequencies," *ASTM, Bull.,* Vol. 3, pp. 81–84.

Ditri, J. J., and Rose, J. L., 1992, "Excitation of Guided Elastic Wave Modes in Hollow Cylinders by Applied Surface Traction," *J. Appl. Phys.,* Vol. 72, pp. 2589–2597.

Gazis, D., 1959, "Three Dimensional Investigation of the Propagation of Waves in Hollow Circular Cylinders, I. Analytical Foundation; II. Numerical Results," *J. Acoust. Soc. Am.,* Vol. 14, pp. 1869–1876.

Grace, O. D., and Goodman, R. R., 1966, "Circumferential Waves On Solid Cylinders," *J. Acoust. Soc. Am.,* Vol. 39, pp. 173–174.

Graff, K. F., 1975, *Wave Motion in Elastic Solids,* Ohio State University Press, Columbus, OH.

Gregory, R. D., 1971, "The Propagation of Rayleigh Waves over Curved Surfaces at High Frequency," *Proc. Cambridge Phil. Soc.,* Vol. 70, pp. 103–121.

Grimshaw, R., 1968, "Propagation of Surface Waves at High Frequency," *J. Inst. Maths Applics,* Vol. 4, pp. 174–193.

Keller, J. B., and Karal, F. C., 1960, "Surface Wave Excitation and Propagation," *J. Appl. Phys.,* Vol. 31, pp. 1039–1046.

Keller, J. B., and Karal, F. C., 1964, "Geometrical Theory of Elastic Surface-Wave Excitation and Propagation," *J. Acoust. Soc. Am.,* Vol. 36, pp. 32–40.

Meeker, T. R., and Meitzler, A. H., 1964, "Guided Waves Propagation In Elongated Cylinders and Plates," *Physical Acoustics,* W. P. Mason, ed., Vol. I–Part A, pp. 111–167.

Miklowitz, J., 1978, *The Theory of Elastic Waves and Wave Guides,* North-Holland, Amsterdam.

Mindlin, R. D., 1960, "Waves and Vibrations in Isotropic Elastic Plates," *Structural Mechanics,* J. N. Goodier and N. J. Hoff, eds., Pergamon Press, New York.

Mindlin, R. D., and Fox, E. A., 1960, "Vibrations and Waves in Elastic Bars of Rectangular Cross Section," *J. Appl. Mech.,* Vol. 27, pp. 152–158.

Mindlin, R. D., and McNiven, H. D., 1960, "Axially Symmetric Waves in Elastic Rods," ASME JOURNAL OF APPLIED MECHANICS, Vol. 27, pp. 145–151.

Nagy, P. B., Blodgett, M., and Golis, M., 1994, "Weep Hole Inspection by Circumferential Creeping Waves," *NDT & E International,* Vol. 27, pp. 131–142.

Qu, J., Berthelot, Y., and Li, Z., 1996, "Dispersion of Guided Circumferential Waves in Circular Annulus," *Review of Progress in Quantitative NDE,* Vol. 15, p. 169–176.

Rayleigh, J. W. S., 1885, "On Waves Propagated along the Plane Surface on an Elastic Solid," *Proc. Math. Soc. London,* Vol. 17, pp. 4–11.

Rayleigh, J. W. S., 1945, *The Theory of Sound,* Dover, New York.

Rulf, B., 1969, "Rayleigh Waves on Curved Surfaces," *J. Acoust. Soc. Am.,* Vol. 45, pp. 493–499.

Stakgold, I., 1979, *Green's Functions And Boundary Value Problems,* John Wiley and Sons, New York.

Viktorov, I. A., 1958, "Rayleigh-type Waves on a Cylindrical Surface," *Soviet Phys.—Acoust.,* Vol. 4, pp. 131–136.

Weaver, R. L., and Pao, Y. H., 1982, "Axisymmetric Elastic Waves Excited by a Point Source in a Plate," ASME JOURNAL OF APPLIED MECHANICS, Vol. 49, pp. 821–836.

APPENDIX

$$d_{11} = \frac{\hat{\omega}^2}{\kappa^2}\left[J_{k-2}\left(\frac{\hat{\omega}}{\kappa}\right) + J_{k+2}\left(\frac{\hat{\omega}}{\kappa}\right) - 2(\kappa^2 - 1)J_k\left(\frac{\hat{\omega}}{\kappa}\right)\right]$$

$$d_{12} = \frac{\hat{\omega}^2}{\kappa^2}\left[Y_{k-2}\left(\frac{\hat{\omega}}{\kappa}\right) + Y_{k+2}\left(\frac{\hat{\omega}}{\kappa}\right) - 2(\kappa^2 - 1)Y_k\left(\frac{\hat{\omega}}{\kappa}\right)\right]$$

$$d_{13} = i\hat{\omega}^2[J_{k-2}(\hat{\omega}) - J_{k+2}(\hat{\omega})]$$

$$d_{14} = i\hat{\omega}^2[Y_{k-2}(\hat{\omega}) - Y_{k+2}(\hat{\omega})]$$

$$d_{21} = \frac{\eta^2\hat{\omega}^2}{\kappa^2}\left[J_{k-2}\left(\frac{\eta\hat{\omega}}{\kappa}\right) + J_{k+2}\left(\frac{\eta\hat{\omega}}{\kappa}\right) - 2(\kappa^2 - 1)J_k\left(\frac{\eta\hat{\omega}}{\kappa}\right)\right]$$

$$d_{22} = \frac{\eta^2\hat{\omega}^2}{\kappa^2}\left[Y_{k-2}\left(\frac{\eta\hat{\omega}}{\kappa}\right) + Y_{k+2}\left(\frac{\eta\hat{\omega}}{\kappa}\right) - 2(\kappa^2 - 1)Y_k\left(\frac{\eta\hat{\omega}}{\kappa}\right)\right]$$

$$d_{23} = i\eta^2\hat{\omega}^2[J_{k-2}(\eta\hat{\omega}) - J_{k+2}(\eta\hat{\omega})]$$

$$d_{24} = i\eta^2\hat{\omega}^2[Y_{k-2}(\eta\hat{\omega}) - Y_{k+2}(\eta\hat{\omega})]$$

$$d_{31} = \frac{i\hat{\omega}^2}{\kappa^2}\left[J_{k-2}\left(\frac{\hat{\omega}}{\kappa}\right) - J_{k+2}\left(\frac{\hat{\omega}}{\kappa}\right)\right]$$

$$d_{32} = \frac{i\hat{\omega}^2}{\kappa^2}\left[Y_{k-2}\left(\frac{\hat{\omega}}{\kappa}\right) - Y_{k+2}\left(\frac{\hat{\omega}}{\kappa}\right)\right]$$

$$d_{33} = -\hat{\omega}^2[J_{k-2}(\hat{\omega}) + J_{k+2}(\hat{\omega})]$$

$$d_{34} = -\hat{\omega}^2[Y_{k-2}(\hat{\omega}) + Y_{k+2}(\hat{\omega})]$$

$$d_{41} = \frac{i\eta^2\hat{\omega}^2}{\kappa^2}\left[J_{k-2}\left(\frac{\eta\hat{\omega}}{\kappa}\right) - J_{k+2}\left(\frac{\eta\hat{\omega}}{\kappa}\right)\right]$$

$$d_{42} = \frac{i\eta^2\hat{\omega}^2}{\kappa^2}\left[Y_{k-2}\left(\frac{\eta\hat{\omega}}{\kappa}\right) - Y_{k+2}\left(\frac{\eta\hat{\omega}}{\kappa}\right)\right]$$

$$d_{43} = -\eta^2\hat{\omega}^2[J_{k-2}(\eta\hat{\omega}) + J_{k+2}(\eta\hat{\omega})]$$

$$d_{44} = -\eta^2\hat{\omega}^2[Y_{k-2}(\eta\hat{\omega}) + Y_{k+2}(\eta\hat{\omega})]$$

Downloaded 04 May 2010 to 171.66.16.26. Redistribution subject to ASME license or copyright; see http://www.asme.org/terms/Terms_Use.cfm

Interaction and Microfracturing Pattern for Successive Origination (Introduction) of Pores in Elastic Bodies: Finite Deformation

V. A. Levin
Department of Mechanics and Mathematics,
Moscow State University,
Moscow 119899, Russia
Mem. ASME

K. M. Zingerman
Department of Applied Mathematics
and Cybernetics,
Tver State University,
Tver 170000, Russia

The elastic interaction of holes, micropores, and narrow slots (cracks), introduced (originated) successively or simultaneously in previously loaded bodies, is analyzed under finite deformations. Their origination raises an additional finite deformations superimposed on the finite initial ones. The influence of mutual positions of holes, distances between them, their eccentricities and sizes on interaction is investigated. Qualitative and quantitative effects concerned with the finiteness of strains are considered.

1 Introduction

It is known that holes acting as stress concentrators reciprocally affect one another. Within the scope of linear elasticity (under the assumption that deformations are small and material properties are described by Hooke's law), two-dimensional problems of interacting holes are considered in a number of articles. The general technique for the solution of two-dimensional elastostatic problems with the use of functions, depending on complex variables, have been developed by Kolosov and Muskhelishvili and presented by Muskhelishvili (1953); Savin (1961) applied this technique to the problems of stress concentration near holes of different shapes (including some nonlinear problems).

Methods of the solution of two-dimensional problems for two interacting elliptical holes and some numerical results for the case of equal collinear holes have been considered by Sherman (1952). Kosmodamianskii (1975) considered a number of problems for arbitrarily located interacting holes, including a periodical arrangement, and presented numerical results. Neighboring elliptical holes with parallel axes were considered by Kosmodamianskii and Chernic (1981). The symmetric arrangement of holes was considered, for example, by Haddon (1967) and Horii and Nemat-Nasser (1985).

Arbitrarily located holes and cracks were considered also by Hu et al. (1993), Fond et al. (1995), and Xiwu et al. (1995). The extensive analysis of interaction between holes was performed by Tsukrov and Kachanov (1994, 1997). In these works, it is noted that in real materials pores have a substantially noncircular shape, and all the analyses are performed using simulation of defects by elliptical holes in the framework of linear elasticity.

Even for linear problems, in all the mentioned works, it is assumed that holes exist in a body before loading, and their initial shapes are given. The two-dimensional problems on stress concentration near a hole, which is originated (introduced) in a body undergoing large initial deformations and which has a prescribed circular or elliptical shape either at the moment of its origination (introduction) or in the final state, were considered by Levin and Tarasiev (1980) and Levin and Bulatov (1983). These problems have been solved with the use of the theory of repeatedly superimposed large deformations in elastic and viscoelastic bodies, formulated by Levin and Tarasiev (1980) and Levin (1988, 1996).

The present work is concentrated on the interaction of two or three successively or simultaneously introduced (originated) elliptical (at the moment of their introduction) holes in a body, undergoing finite initial deformations. The origination of holes induces additional finite deformations that are superimposed on the finite initial ones. It will describe how the interaction effects depend on the following:

- the location of holes at the moment when one of them is introduced and
- eccentricities of holes.

The work focuses also on the following issues:

- the interaction of a large hole with a small one,
- likely microfracturing patterns, and
- qualitative and quantitative effects associated with nonlinearity.

Only two-dimensional problems will be considered.

Because we consider the case of finite deformation, taking into account the order of origination (introduction) of holes, our analyses will be performed with the use of the above-mentioned theory of repeatedly superimposed large deformations.

To solve the system of nonlinear equilibrium equations with several displacement vectors (i.e., vectors of displacement from the initial to the first intermediate state, from the first intermediate to the second, etc.) which are not separable into isolated equations each depending on a single displacement vector, Signorini's technique is used. We realize that its application restricts the initial strains for which the problems may be solved. The advantages and limitations of this method in connection with the problems of usual nonlinear elasticity had been discussed in detail by Green and Adkins (1960), Truesdell (1972), and Lurie (1990). We only note that for the problem of introduction of a hole which becomes elliptical in the final state (i.e., a hole the shape of which is unknown at the moment of its origination) a

Contributed by the Applied Mechanics Division of THE AMERICAN SOCIETY OF MECHANICAL ENGINEERS for publication in the ASME JOURNAL OF APPLIED MECHANICS.

Discussion on the paper should be addressed to the Technical Editor, Professor Lewis T. Wheeler, Department of Mechanical Engineering, University of Houston, Houston, TX 77204-4792, and will be accepted until four months after final publication of the paper itself in the ASME JOURNAL OF APPLIED MECHANICS.

Manuscript received by the ASME Applied Mechanics Division, May 28, 1997; final revision, July 9, 1998. Associate Technical Editor: R. Abeyaratne.

 Copyright © 1998 by ASME

Downloaded 04 May 2010 to 171.66.16.26. Redistribution subject to ASME license or copyright; see http://www.asme.org/terms/Terms_Use.cfm

comparison was made between Signorini's and Newton-Kantorovich's (Kantorovich and Akilov, 1984) methods; and the difference in solutions, obtained for the initial strains considered in the paper, didn't exceed four to five percent.

Additionally, Levin (1987) obtained the necessary conditions of the perturbation method for the case of superimposed finite strains.

2 The Basic Equations of the Theory of Repeatedly Superimposed Large Deformations. The General Statement of Problem

The general statement of a problem is the following.

Assume large plane static strains and stresses are brought about by external forces in a nonlinear elastic body that was in the initial (unstressed) state. The body passes to the first intermediate state. Then a closed surface is imagined in the body, and its contents, bounded by this surface, is removed, and the effect of the removed part of the body on the remainder is replaced by forces, distributed over this closed surface (on the principle of releasing of braces). It is clear that this transformation doesn't change the stress and strain states in the body. Then these forces, changed to the category of external forces, are reduced to zero quasi-statically (for example, isothermally). It raises large (at the vicinity of the originated surface) strains and stresses that are superimposed on the large initial strains and stresses already existing in the body. The body passes to the second intermediate state. Naturally, the shape of the introduced boundary surface is changed, and one can predict the shape of this surface either in the first intermediate state or in the second intermediate state, and these two problems are different. Then this procedure is repeated for the origination of the second hole, etc.

The basic relations of the theory of repeatedly superimposed large deformations were presented by Levin and Tarasiev (1980), Levin (1988, 1996). Let us outline them here.

The equilibrium equation and the boundary conditions are

$$\overset{m}{\nabla}\cdot\overset{m}{\Sigma}_{0,n} - \overset{m}{\Sigma}_{0,n}\cdot\overset{m}{\nabla}\ln(1+\Delta_{0,n}) + \overset{m}{\Sigma}_{0,n}\cdot\cdot\,\overset{m}{\nabla}\Psi_{m,n}\cdot\Psi_{m,n}^{-1} - [\overset{m}{\nabla}\cdot\Psi_{m,n}^{T\,-1}\cdot\Psi_{m,n}^{T}]\cdot\overset{m}{\Sigma}_{0,n} + \overset{m}{F}_n\rho_m(1+\Delta_{0,m}) = 0. \quad (1)$$

$$\overset{(m)}{N}\cdot\overset{m}{\Sigma}_{0,n} = (1+\Delta_{0,n})\overset{m\,(n)}{P_{(m)}^{\ (n)}},$$

$$\overset{m\,(n)}{P_{(m)}^{\ (n)}} = (1+\Delta_{m,n})^{-1}\frac{|d\overset{m}{O}|}{|d\overset{n}{O}|}\overset{n\,(n)}{P_{(n)}^{\ (n)}}\cdot\Psi_{m,n}. \quad (2)$$

Hereafter the upper index over a quantity denotes the number of the state this quantity is given in or referred to.

$$\overset{m}{\Sigma}_{0,n} = (1+\Delta_{0,n})\Psi_{n,m}^{T}\cdot\sigma_{0,n}\cdot\Psi_{n,m}, \quad (3)$$

is the total (for the nth state) stress tensor referring to the base of the mth state; $\sigma_{0,n}$ is the true total (for the nth state) stress tensor ($\sigma_{0,1}$ is the Cauchy stress tensor); $\Delta_{0,n}$ is the relative volume change in transition from the initial to the nth state; $\Psi_{q,p}$ is the deformation gradient: $\Psi_{m,n} = \overset{m}{e}^{i}\overset{n}{e}_{i} = \Psi_{0,m}^{-1}\cdot\Psi_{0,n}$; $\overset{n}{e}_{i} = \partial\overset{n}{r}/\partial\xi^{i}$; $\overset{n}{r}$ is the radius vector of a particle in the nth state; ξ^{i} ($i = 1, \ldots, 3$) are the Lagrangian coordinates of a particle; $u_n = \overset{n}{r} - \overset{n-1}{r}$ is the displacement vector from the preceding ($n-1$)th to the subsequent nth state;

$$\Psi_{q,p} = I + \sum_{n=q+1}^{p}\overset{q}{\nabla}u_n = (I - \sum_{n=q+1}^{p}\overset{p}{\nabla}u_n)^{-1}, \quad (4)$$

$\overset{q}{\nabla} = (\partial/\partial\xi^{i})\overset{q}{e}^{i}$; $\overset{n\,(n)}{P_{(n)}^{\ (n)}}$ is the true stress vector on a surface element $d\overset{n}{O} = \overset{n}{N}|d\overset{n}{O}|$.

Note that if the shape of the first hole is given, for example, in the first intermediate state, and the shape of the second hole is prescribed at the moment of its introduction, then the system (1), (2) is not separable into some subsystems, one for each state (see Levin, 1988; Levin and Tarasiev, 1980).

Notation of constitutive equations (we shall use only well-known ones) in the space of an arbitrary state is obtained with the use of the procedure described by Levin (1996) and Levin and Tarasiev (1980). For example, if the relation

$$\overset{n}{\Sigma}_{0,n} = \overset{n}{a}_0(\overset{n}{E}_n^{(l)})I + \overset{n}{a}_1(\overset{n}{E}_n^{(l)})\overset{n}{E}_{0,n} + \overset{n}{a}_2(\overset{n}{E}_n^{(l)})(\overset{n}{E}_{0,n})^2 \quad (5)$$

is given [here $\overset{n}{E}_{0,n} = \frac{1}{2}(I - \Psi_{0,n}^{-1}\cdot\Psi_{0,n}^{T\,-1})$ is the strain tensor describing change of strains in transition from the initial to the nth state and referred to the base of the nth state; in general,

$$\overset{n}{E}_{q,p} = \tfrac{1}{2}(\Psi_{n,p}\cdot\Psi_{n,p}^{T} - \Psi_{n,q}\cdot\Psi_{n,q}^{T}), \quad (6)$$

$$\overset{n}{E}_{q,p} = \Psi_{n,m}\cdot\overset{m}{E}_{q,p}\cdot\Psi_{n,m}^{T} \quad (7)$$

$\overset{n}{E}_n^{(l)}$ ($l = 1, 2, 3$) are the algebraical invariants of the tensor $\overset{n}{E}_{0,n}$], then, using (3), (6), (7), one can obtain the representation for tensor $\overset{m}{\Sigma}_{0,n}$:

$$\overset{m}{\Sigma}_{0,n} = \overset{m}{a}_0(I + 2\overset{m}{E}_{m,n})^{-1} + \overset{m}{a}_1(I + 2\overset{m}{E}_{m,n})^{-1}\cdot\overset{m}{E}_{0,n}\cdot(I + 2\overset{m}{E}_{m,n})^{-1} + \overset{m}{a}_2[(I + 2\overset{m}{E}_{m,n})^{-1}\cdot\overset{m}{E}_{0,n}]^2\cdot(I + 2\overset{m}{E}_{m,n})^{-1} \quad (8)$$

where $\overset{m}{a}_i$, ($i = 0, 1, 2$) are the functions of simultaneous invariants of tensors $\overset{m}{E}_{0,n}$ and $\overset{m}{E}_{m,n}$.

It follows from (8) that, if the problem is solved in the space of a "later" state ($m > n$), then $\overset{m}{\Sigma}_{0,n}$ depends not only on $\overset{m}{E}_{0,n}$, but also on $\overset{m}{E}_{m,n}$, that complicates the solution of problems. But we can't avoid it, because boundary conditions may be given in the mth state.

The scheme of the solution of the problems stated above for the two-dimensional case is outlined in the Appendix.

3 Effect of Geometry of Successively or Simultaneously Introduced (Originated) Holes on Interaction

At first, we shall examine results of the solution (at finite deformations) of the two-dimensional problem of two holes successively originated (introduced) in a body undergoing initial finite deformations, when each hole assumes the shape of a narrow ellipse at the moment of its origination. Afterwards we shall consider the same problem of the introduction of a hole followed by the simultaneous introduction of two other holes. Specifically, we shall use Treloar's incompressible material (see Treloar, 1949):

$$\sigma_{0,n} = \mu\overset{n}{F}_{0,n} + p_{0,n}I \quad (9)$$

where $\overset{n}{F}_{0,n} = (I - 2\overset{n}{E}_{0,n})^{-1}$; at $n = 1$, $\overset{1}{F}_{0,1}$ is the Finger strain measure tensor; $p_{0,n}$ is the scalar.

The statement of the problem of two successively originated holes follows directly from the relations (1)–(8). In this problem and, for uniformity, for all the next problems we assume that the center of the second ellipse is marked at the moment when the first hole is originated. Here and below in the article we use for the solution of the specific problems the "superposition" program package developed by the authors which permits one to solve a set of two-dimensional and axially symmetric

Downloaded 04 May 2010 to 171.66.16.26. Redistribution subject to ASME license or copyright; see http://www.asme.org/terms/Terms_Use.cfm

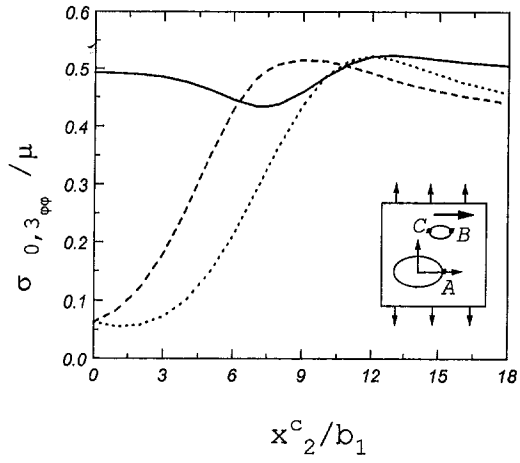


Fig. 1 Successive origination of two elliptical holes of different sizes with parallel axes. True hoop stress $\sigma_{0,3_{\varphi\varphi}}$ at the tip of the larger hole (point A) and at the tips of the smaller hole (points B, C) as a function of the x-coordinate of the center of the smaller hole x_2^c/b_1 (the smaller hole is "moved" parallel to its major axis). Nonlinear solution. —— point A, – – – point B, and --- point C.

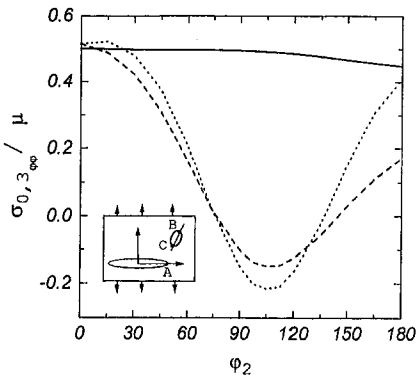


Fig. 3 Successive origination of two elliptical holes of different sizes. True hoop stress $\sigma_{0,3_{\varphi\varphi}}$ at the tip of the larger hole (point A) and at the tips of the smaller hole (points B, C) as a function of orientation φ_2 of the smaller hole (the smaller hole "slews" round point C). Nonlinear solution. —— point A, – – – point B, and --- point C.

problems of the theory of repeatedly superimposed large deformations in elastic and viscoelastic bodies (Appendix).

For uniformity, in all the particular examples presented above, a uniaxial initial load is given: $\sigma^{\infty}_{0,1_{11}} = \sigma^{\infty}_{0,1_{12}} = 0$, $\sigma^{\infty}_{0,1_{22}} = p$.

At first, the "large hole—small hole" interaction is considered for different positions of the center of a small hole, when the major axes of ellipses are parallel and the distance between them is fixed. Figures 1 and 2 present the total true hoop stress $\sigma_{0,3_{\varphi\varphi}}$ at the tip of the first (large) hole (point A) and at the tips of the second (small) hole (points B, C) as a function of a distance between the minor axes of ellipses $(x_2^c - x_1^c)$ for the case $p/\mu = 0.03$, $a_2/a_1 = 0.3$, $a_1/b_1 = a_2/b_2 = 8$, $(y_2^c - y_1^c)/b_1 = 4.5$, where a_1, b_1, a_2, b_2 are the major and minor semi-axes of the ellipses at the moments of their origination; x_1^c, y_1^c, x_2^c, y_2^c are the coordinates of the centers of the ellipses (for convenience, hereafter we assume $x_1^c = y_1^c = 0$).

Figure 1 presents the results for the nonlinear problem, Fig. 2 shows the same results under the assumption of small deformation. In partition, one can see from Fig. 1 that when x_2^c/b_1 is varied from 0 to 6, point A is the most dangerous from the point of view of fracturing; when x_2^c/b_1 is varied from 6 to 11, the most dangerous point is B; then for a relatively small interval $11 < x_2^c/b_1 < 12$ point C is the most dangerous; and at $x_2^c/b_1 > 12$ the most dangerous point is A again. One can see also that the introduction of the second hole leads either to increase (at $x_2^c/b_1 > 10$) or to decrease (at $x_2^c/b_1 < 10$) of the true hoop stress at point A, in comparison with the case when the second hole is absent, due to interaction effects. Comparing Figs. 1 and 2, one can see that taking into account interaction effects permits one to discover not only quantitative effects (in the nonlinear case, the stress concentration at point B is smaller by 28 percent, in comparison with the linear case) but also a qualitative effect. In the linear case, point A is the most dangerous from the point of view of fracturing at $0 < x_2^c/b_1 < 5$, and at $x_2^c/b_1 > 5$ points B and C will sequientally appear as the most dangerous. At the same time, as noted above, in the nonlinear case point A is the most dangerous as for $0 < x_2^c/b_1 < 5$, as for $x_2^c/b_1 > 12$. In addition, one can see from Figs. 1 and 2 that the correction for nonlinear effects at the tip of the first hole (point A) is significantly smaller than the corresponding correction at the tips of the second hole (points B, C).

A problem of interaction of two successively originated holes is presented in Figs. 3 and 4 for the case when the position of a tip of the small hole (point C in the figures) is fixed and an orientation of its axes is varied. The total hoop stresses $\sigma_{0,3_{\varphi\varphi}}$ at the tips of the first (point A) and the second (points B, C) holes are shown as a function of an orientation of the second hole for the case when point C is fixed, and the center of the second (small) hole slews round this point, at $p/\mu = 0.03$, $a_2/a_1 = 0.3$, $a_1/b_1 = a_2/b_2 = 8$, $(x_2^c - a_2 \cos\varphi_2)/b_1 = 8$; $(y_2^c - a_2 \sin\varphi_2)/b_1 = 4$; $a_2/a_1 = 0.3$, $\varphi_1 = 0$, $x_1^c = y_1^c = 0$. φ_i is the angle between the positive direction of the x-axis and the major axis of the ith ellipse. Figure 3 presents results for the nonlinear problem; Fig. 4 for the case of small deformations. One can see from Fig. 3 that for the nonlinear case point C is the most dangerous at 0 deg $< \varphi <$ 25 deg, and point A becomes the most dangerous at $\varphi >$ 25 deg. This is related to the well-

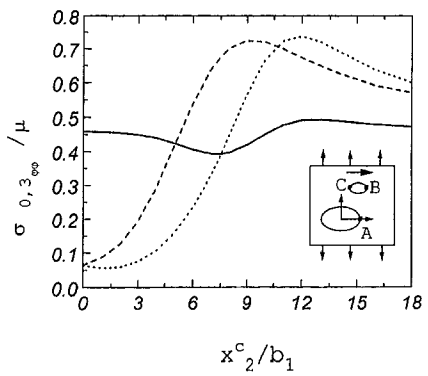


Fig. 2 The same problem as in Fig. 1. Linear approximation.

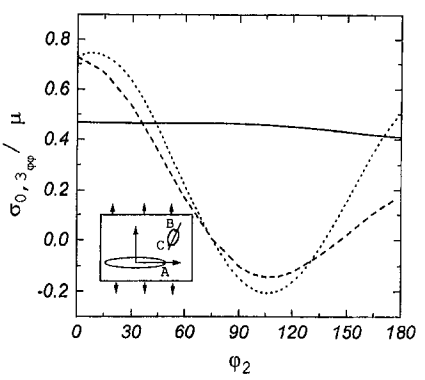


Fig. 4 The same problem as in Fig. 3. Linear approximation.

Downloaded 04 May 2010 to 171.66.16.26. Redistribution subject to ASME license or copyright; see http://www.asme.org/terms/Terms_Use.cfm

known fact that the stress distribution around an elliptical hole principally depends on its orientation with respect to an external stress field; when the major axis of an elliptic hole, which is introduced in the uniaxial external stress field, is oriented approximately in the direction of the external loading, the stress concentration at the tips of the hole is relatively small. Comparing Figs. 3 and 4, one can see the qualitative effects (in the linear case, point C is the most dangerous at two intervals: for 0 deg $< \varphi <$ 45 deg and for $\varphi >$ 170 deg) and also the quantitative ones: in the nonlinear case, the stress level at the point A is larger by seven percent and the stress level in point C, when this point is the most dangerous, is smaller by 30 percent.

Figure 5 shows some results of the solution of a problem of the simultaneous origination of two collinear narrow elliptical holes permitting one to examine the influence of size of the smaller hole on the stress level at the tips of the larger (point A) and the smaller (points B, C) holes when the distance between the nearest tips of holes is equal to the minor semi-axis of the larger hole, and the eccentricities of ellipses are fixed. One can see that for the case $p/\mu = 0.03$, $a_1/b_1 = a_2/b_2 = 8$, $(x_2^c - x_1^c - a_1 - a_2)/b_1 = 1$, $\varphi_1 = \varphi_2 = 0$, $x_1^c = y_1^c = y_2^c = 0$ the stresses at points B, C are decreased with the elevation of a_2/a_1, and the stress at point A is increased, and for $a_2 = a_1$, $\sigma_{0,3_{\varphi\varphi_A}} = \sigma_{0,3_{\varphi\varphi_B}}$. The correction for nonlinear effects in this case reaches 38 percent at point B in the direction of decreasing values of stress.

An interaction between two equal simultaneously originated collinear holes is examined in Fig. 6. Stress concentration at the tips of ellipses is plotted as a function of their eccentricities for the case when the distance between the nearest tips is equal to the minor semi-axis of each ellipse, and the eccentricity is varied because of variation of major semi-axes, at $p/\mu = 0.035$. For comparison, the stress concentration at the tip of a single elliptical hole is presented. One can see from Fig. 6 that a correction for nonlinear effects is increased with the elevation of a_1/b_1, reaching 60 percent for the linearized statement and 40 percent for the nonlinear statement at $a_1/b_1 = 7$. One can see also that a correction for nonlinear effects is increased with the elevation of a_1/b_1 (evidently because of increase of stress level), exceeding 30 percent at $a_1/b_1 = 7$.

The interaction of the larger elliptical hole with one or two smaller ones is examined in Fig. 7 for the case of successively introduced holes (it is assumed that the larger hole originates earlier than the smaller ones, and the latter are originated simultaneously with one another). The distribution of the true stress component σ_{22} along the major axis of the first hole near its tip

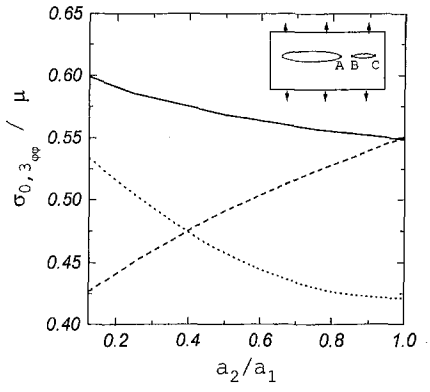


Fig. 5 Simultaneous origination of two collinear elliptical holes of different sizes with equal eccentricities. True hoop stress $\sigma_{0,3_{\varphi\varphi}}$ at the tip of the larger hole (point A) and at the tips of the smaller hole (points B, C) as a function of the size of the smaller hole a_2/a_1 (the distance between the nearest tips of holes is equal to the minor semi-axis of the larger hole). Nonlinear solution. —— point A, - - - point B, and --- point C.

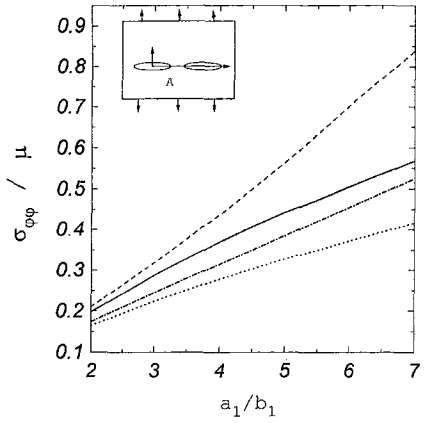


Fig. 6 Simultaneous origination of two equal collinear elliptical holes. True hoop stress $\sigma_{0,3_{\varphi\varphi}}$ at the tip of a hole (point A) as a function of the ratio of the semi-axes a_1/b_1 (the distance between the nearest tips of holes is equal to the minor semi-axis of a hole). —— nonlinear solution; - - - linear approximation; --- single hole, nonlinear solution (as a reference); and ---- single hole, linear approximation (as a reference).

is plotted for the case $p/\mu = 0.03$, $a_2/a_1 = 0.3$, $a_1/b_1 = a_2/b_2 = a_3/b_3 = 8$, $y_2^c = -y_3^c = 3b_1$, $x_2^c = x_3^c = 7b_1$, $x_1^c = y_1^c = 0$, $\varphi_1 = \varphi_2 = \varphi_3 = 0$ (the smaller holes are equal in size and are arranged symmetrically about the major axis of the larger hole). For comparison, the same plot is presented for the case of a single hole. One can see from Fig. 7 that the introduction of the smaller hole (holes) in a given arrangement leads to decrease of stresses at the neighborhood of the tip of the larger hole, and the correction at this tip is on the order of 24 percent for the case of one smaller hole and on the order of 43 percent for the case of two smaller holes.

4 Conclusion

The results of the solution of the problems of successive origination of two elliptical (at the moments of their origination) holes in an elastic body undergoing finite deformations, as presented in the paper, show that taking into account nonlinear effects permits one to obtain both qualitative differences (for example, for the analysis of the influence of mutual positions of holes, in nonlinear and linear cases different points are the most dangerous in the sense of fracturing, Figs. 1 and 2) and quantitative ones (the correction for nonlinear effects reaches 35 percent, Figs. 1–4). In addition, one can see from Figs. 1 and 3 that the most dangerous arrangement of holes (among the cases considered) is when their major axes are parallel and the distance between the nearest tips is the smallest of these

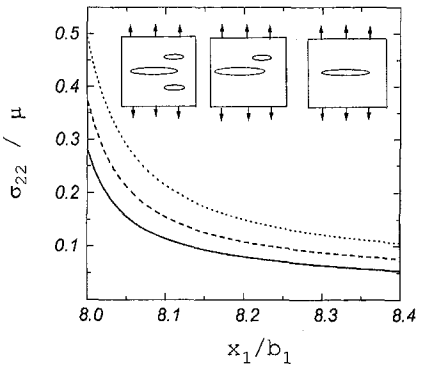


Fig. 7 Successive origination of two or three elliptical holes. Distribution of true stress component σ_{22} along the major axis of the larger hole near its tip. Nonlinear solution. —— 3 holes, - - - 2 holes, and --- 1 hole (as a reference).

Downloaded 04 May 2010 to 171.66.16.26. Redistribution subject to ASME license or copyright; see http://www.asme.org/terms/Terms_Use.cfm

cases. On the other hand, in this arrangement the smaller hole seems to "draw off" the stresses from the larger one.

From the analysis of simultaneous origination of two collinear holes (Fig. 5), one can see that with the enlargement of the smaller hole the stress concentration at its tips is increased, and the stress concentration at the nearest tip of the larger hole is decreased.

Considering the problem of simultaneous origination of two equal collinear holes (Fig. 6), one can see that with elevation of the ellipses' eccentricities (at a fixed distance between their nearest tips) a correction for interaction effects is increased, and a correction for nonlinear effects is increased too (by absolute value).

Analyzing the problem of the interaction between three successively originated holes, one can see that for the case considered the introduction of smaller holes leads to a decrease of the stress at the tip of the larger hole, and the total correction for influence of the smaller holes is a little smaller than the sum of corrections for influence of each of the smaller holes taken separately.

References

Fond, C., Flejou, J.-L., and Berthaud, Y., 1995, "Interaction Between Cracks and Circular Holes in Two-Dimensional Linear Elastic Media," *European Journal of Mechanics,* Vol. A14, No. 1, pp. 73–96.

Green, A. E., and Adkins, J. E., 1960, *Large Elastic Deformations and Non-Linear Continuum Mechanics,* Clarendon Press, Oxford, UK.

Haddon, R. A. W., 1967, "Stresses in an Infinite Plate With Two Unequal Circular Holes," *Quarterly Journal of Mechanics and Applied Mathematics,* Vol. 20, pp. 277–291.

Horii, H., and Nemat-Nasser, S., 1985, "Elastic Fields of Interacting Inhomogeneities," *International Journal of Solids and Structures,* Vol. 21, pp. 731–745.

Hu, K. X., Chandra, A., and Huang, Y., 1993, "Multiple Void-Crack Interaction," *International Journal of Solids and Structures,* Vol. 30, pp. 1473–1489.

Kantorovich, L. V., and Akilov, G. P., 1984, "*Functional Analysis,*" Nauka, Moscow (in Russian).

Kosmodamianskii, A. C., 1975, *Plane Problems of Theory of Elasticity for Plates With Holes, Cuts and Lugs,* Naukova Dumka, Kiev (in Russian).

Kosmodamianskii, A. C., and Chernic, U. I., 1981, "Stress State of a Plate Weakened by Two Elliptical Holes With Parallel Axes," *Soviet Applied Mechanics,* Vol. 17, pp. 576–581.

Levin, V. A., 1987, "Application of Method of Successive Approximations in the Problems of Superposition of Finite Strains," *Prikladnaia Mekhanika,* Vol. 23, No. 5, pp. 66–71 (in Russian).

Levin, V. A., 1988, "Stress Concentration Near a Hole, Which is Circular at the Time of Formation, in a Body Made of Viscoelastic Material," *Soviet Physics Doklady,* Vol. 33, No. 4, pp. 296–298.

Levin, V. A., 1996, "Repeatedly Superimposed Large Elastic Deformations," *International Journal of Fracture,* Vol. 79, No. 1, pp. R11–R15.

Levin, V. A., and Bulatov, L. A., 1983, "Concentration of Stresses Near the Circular Hole in the Body of Viscoelastic Material," *Mekhanika kompozitnykh materialov,* Vol. 3, pp. 423–426 (in Russian).

Levin, V. A., and Tarasiev, G. S., 1980, "Application of Large Elastic Deformations in the Space of Final States," *Soviet Physics Doklady,* Vol. 25, No. 3, pp. 217–219.

Lurie, A. I., 1990, *Non-Linear Theory of Elasticity,* North-Holland, Amsterdam.

Muskhelishvili, N. I., 1953, *Some Basic Problems of the Theory of Elasticity,* Noordhof, Groningen.

Savin, G. N., 1970, "Stress Distribution Around Holes," NASA Technical Translation TTF-607, Washington, DC.

Sherman, D. I., 1952, "On the Problem of Stressed State of Interchamber Pillars. Elastic Ponderable Medium Weakened by Two Holes of Elliptical Shape," *Izvestiya AN SSSR. Otdeleniye Tekhnicheskikh Nauk,* Part 1: No. 6, pp. 840–857; Part 2: No. 7, pp. 992–1010 (in Russian).

Treloar, L., 1949, *The Physics of Rubber Elasticity,* Clarendon Press, Oxford, UK.

Truesdell, C., 1972, *A First Course in Rational Continuum Mechanics,* The Johns Hopkins University, Baltimore, MD.

Tsukrov, I., and Kachanov, M., 1994, "Stress Concentrations and Microfracturing Patterns for Interacting Elliptical Holes," *International Journal of Fracture,* Vol. 68, pp. R89–R92.

Tsukrov, I., and Kachanov, M., 1997, "Stress Concentrations and Microfracturing Patterns in a Brittle-Elastic Solid With Interacting Pores of Diverse Shapes," *International Journal of Solids and Structures,* Vol. 34, No. 22, pp. 2887–2904.

Xiwu, X., Liangxin, S., and Xuqi, F., 1995, "Stress Concentration of Finite Composite Laminates Weakened by Multiple Elliptical Holes," *International Journal of Solids and Structures,* Vol. 32, pp. 3001–3014.

APPENDIX

Scheme of Solution of Problems Considered in the Paper

Signorini's expansion technique (method of small parameter) is used for the solution of the system of equilibrium equations depending on several displacement vectors (from the initial to the first state, from the first state to the second, etc.). This technique had been considered, among others, by Green and Adkins (1960), Truesdell (1972), and Lurie (1990). To solve the problem at each stage, Muskhelishvili's technique (Muskhelishvili, 1953) is used. In addition, Neumann-Schwartz' alternating technique is used (Muskhelishvili, 1953).

For computations, a specialized computer algebra system has been developed permitting one, among other computations, to implement this scheme in connection with the above-mentioned problems and to obtain a solution as a set of functions, depending on complex variables, with numerical coefficients. It permits one to obtain some qualitative results without an additional computations.

The problem of introduction of a single hole which becomes elliptical in the final state had previously been solved by Newton-Kantorovich's technique for the Mooney potential, and the difference by stresses at the points of maximal stress concentration had not exceeded four to five percent, in comparison with Signorini's technique for the initial loads and the ellipse's excentricity considered in the paper.

Downloaded 04 May 2010 to 171.66.16.26. Redistribution subject to ASME license or copyright; see http://www.asme.org/terms/Terms_Use.cfm

Response of a Nonconservative Continuous System to a Moving Concentrated Load

A. V. Pesterev
Institute of System Analysis,
Russian Academy of Sciences,
pr. 60-letiya Oktyabrya 9,
Moscow 117312, Russia

L. A. Bergman
Aeronautical and Astronautical
Engineering Department,
University of Illinois,
Urbana, IL 61821
Mem. ASME

The problem of calculating the response of a general class of nonconservative linear distributed parameter systems excited by a moving concentrated load is investigated. A method of solution based on the series expansion of the response in terms of complex eigenfunctions of the continuous system is proposed. A set of ordinary differential equations in the time-dependent coefficients of the expansion is established in terms of the unknown force of interaction on the continuum, which allows one to investigate different models of concentrated loads. For the case of a conservative oscillator moving with arbitrarily varying speed, the coefficients of the equations are obtained in explicit terms. Some results of numerical experiments involving a proportionally damped beam are presented.

1 Introduction

In this paper, we propose a method for calculating the response of a spatially one-dimensional, nonconservative linear distributed parameter system to a moving concentrated load. The term "moving concentrated load" is used here as a common name to denote various simple models of vehicles traversing the distributed system. By this we mean that the distributed system is subject to a concentrated force described by the Dirac delta-function, where the point of application of the force moves in time. The term is used to unify the discussion and to emphasize the fact that, for the most part, the presentation is not specific to a particular kind of vehicle-continuum interaction. In the following, we will address three kinds of these loads: "moving force," "moving mass," and "moving oscillator" models. The first model implies that the distributed system is subject to a given concentrated external force. The force magnitude may depend on time, and the point of its application moves along the continuum. One arrives at this problem considering, for example, a concentrated mass traversing the distributed system, neglecting the inertia of the mass. The remaining two models include, in addition to the continuum, a moving mass. The difference between the two lies in the interaction between the mass and distributed system. In the moving mass model, the mass is attached directly to the continuum (no elastic interaction force), while in the moving oscillator problem, it interacts with the distributed system through a spring (and, perhaps, a dashpot, though not in the present analysis).

The problem of calculating the response of a distributed parameter system to a moving concentrated load is very important in many engineering applications related, for example, to the analysis and design of highway and railway bridges, cable railways, etc. This problem has been of interest to engineering designers for many years. Most prior research has focused on the moving force and moving mass problems, and many methods for their solution have been proposed in the last three decades. These problems have been examined by "wave," finite element, and finite difference methods; by expansion of the solution in a series; by reduction to integro-differential equations; etc. The interested reader may find details of the aforementioned methods in Bolotin (1964), Frýba (1972, 1987), Lee (1996), Olson (1991), Pesterev and Bergman (1997c), Sadiku and Leipholz (1987), Stanišić (1985), and the references therein.

Some results concerning the moving oscillator problem may be found, e.g., in Bogacz and Szolc (1993), Delgado and dos Santos (1997), Pesterev and Bergman (1997a, b), Riemer (1987), and Yang, Tan, and Bergman (1997). The reasons why this model should be examined can be simply summarized. First, in some engineering applications, the moving oscillator model is more realistic (if, e.g., the vehicle is softly sprung to the distributed system); second, it may be viewed as the solution to the moving mass problem, in the limit; and third, the solution of the moving oscillator problem is obtained more easily than the solution of the moving mass problem.

It should be emphasized that most of the methods given in the above references are developed for particular kinds of distributed systems; e.g., for taut strings or Euler-Bernoulli beams with different boundary conditions. To the authors' knowledge, few examples of methods for analysis of nonconservative linear distributed systems subject to moving forces are available in the literature. Among specific applications, the response of damped annular plates subjected to circumferentially and radially moving point loads of prescribed magnitude has been studied by Weisensel and Schlack (1993); and the problem of a moving mass on a damped circular plate has been examined by Shen (1993). This paper is aimed at developing methods for calculating the response to moving concentrated loads, and in particular to a moving linear oscillator, of distributed systems governed by arbitrary linear non-self-adjoint operators.

The format of the paper is as follows. In the next section, a mathematical formulation of the problem is given. Then, using the modal representation for the Green's function of a general-type distributed system, we obtain the response of the continuum as a series expansion in terms of its complex eigenfunctions. In Section 4, the problem of finding the time-dependent coefficients of the expansion is reduced to that of solving a set of linear complex differential equations. These equations are obtained in their most general form, specific to neither the model of the moving concentrated load nor to the type of distributed system. The coefficients of the equations are given in terms of an unknown "interaction force" acting on the distributed system and in terms of direct and adjoint eigenfunctions of the

Contributed by the Applied Mechanics Division of THE AMERICAN SOCIETY OF MECHANICAL ENGINEERS for publication in the ASME JOURNAL OF APPLIED MECHANICS.

Discussion on the paper should be addressed to the Technical Editor, Professor Lewis T. Wheeler, Department of Mechanical Engineering, University of Houston, Houston, TX 77204-4792, and will be accepted until four months after final publication of the paper itself in the ASME JOURNAL OF APPLIED MECHANICS.

Manuscript received by the ASME Applied Mechanics Division, Apr. 3, 1997; final revision, Nov. 7, 1997. Associate Technical Editor: N. C. Perkins.

 Copyright © 1998 by ASME

Downloaded 04 May 2010 to 171.66.16.26. Redistribution subject to ASME license or copyright; see http://www.asme.org/terms/Terms_Use.cfm

distributed system. The cost of this generality is that the equations cannot be directly applied to any arbitrary problem, but require further specification of the moving load model and the type of non-self-adjointness inherent in the distributed system. In Section 5, a simple application, a moving conservative oscillator, is analyzed. The application to a particular type of distributed system requires finding the adjoint eigenfunctions that satisfy a certain normalization condition. This is discussed in Section 6. We show first that, in the case of a conservative distributed system, the equations obtained reduce to previously published results. Then, the case of a proportionally damped continuum is examined in detail. Finally, some results of numerical experiments related to the problem of a conservative oscillator traversing a proportionally damped beam are presented.

2 Problem Statement

The vibration of a spatially one-dimensional, linear non-self-adjoint distributed system is governed by the partial differential equation

$$Mw_{tt}(x, t) + Dw_t(x, t) + Kw(x, t) = f(x, t) \qquad (1)$$

subject to given boundary conditions, which are of no importance in this work and are omitted, and initial conditions

$$w(x, 0) = a_0(x), \quad w_t(x, 0) = b_0(x). \qquad (2)$$

Here, $x \in [0, L]$, L is the length of the continuum; $w(x, t)$ is the lateral displacement of the continuum; $a_0(x)$ and $b_0(x)$ are given initial disturbances; $f(x, t)$ is a given external force; $(\ )_t = \partial(\ )/\partial t$; and M, D, and K are spatial differential operators defined on functions satisfying necessary smoothness requirements and given boundary conditions. A positive definite operator M represents the inertia of the system; D can be represented as the sum of symmetric and skew-symmetric operators responsible for damping and gyroscopic effects, respectively; and K is the sum of a symmetric stiffness operator and a skew-symmetric operator associated with circulatory effects.

If the only external force acting on the continuum is a moving concentrated load, $f(x, t)$ can be represented in the form

$$f(x, t) = y(t)\delta(x - \zeta(t)), \qquad (3)$$

where function $\zeta(t)$ is the position of the concentrated load along the continuum in time, and the force $y(t)$ acting on the continuum is determined by the concentrated load model under consideration. In the simplest case, the moving force problem, $y(t)$ does not depend on the displacement of the continuum. In problems involving a mass m moving along the distributed system, $y(t)$ depends on the displacement of the continuum, and its particular form is determined by the law of interaction between the mass and continuum. For the case of the moving mass problem, the interaction force is the sum of the mass weight and the inertia force,

$$y(t) = mg - m\frac{d^2}{dt^2}w(\zeta(t), t). \qquad (4)$$

In the moving oscillator problem, examined in more detail in this paper, the mass interacts with the continuum through a spring (and perhaps a dashpot). As the emphasis of this paper is on the non-self-adjointness property of the distributed system rather than on the vehicle-structure interaction, we will consider the simplest case of the oscillator, namely, a conservative one. In this case, the interaction force is given by

$$y(t) = k(z(t) - w(\zeta(t), t)), \qquad (5)$$

where $z(t)$ is the coordinate of the mass along the axis perpendicular to the longitudinal axis of the continuum, and k is the stiffness of the spring connecting the mass to the distributed system (Fig. 1).

Usually, the case of constant speed is investigated, where $\zeta(t) = vt$. In fact, the method discussed herein does not depend on the law of the mass motion along the continuum, and we will assume that the mass speed may arbitrarily vary. Thus, in the following equations, either ζ should be replaced by vt if the mass traverses the continuum with a constant speed v, or the additional equation $\ddot{\zeta} = a(t)$ with appropriate initial conditions should be added, where $a(t)$ is the prescribed acceleration.

The goal of this paper is to develop a method for calculating the response of a general-type nonconservative continuum described by Eq. (1) due to a moving linear conservative oscillator. We will show that the response $w(x, t)$ can be expanded in a series in terms of complex eigenfunctions of the continuum and reduce the problem under consideration to that of solving a set of linear ordinary differential equations in the time-dependent coefficients of the series.

3 Modal Series Representation for the Continuum Response

To simplify the following equations, we will consider homogeneous boundary and initial conditions ($a_0(x) = b_0(x) = 0$ in (2)). The latter correspond to the case where the mass enters the left end of the continuum at $t = 0$ ($\zeta(0) = 0$), and the continuum is at rest for negative t. Clearly, the consideration of nonhomogeneous conditions presents no analytical problem but results in more cumbersome formulas.

It is well known (see, e.g., Yang, 1996) that the response of the distributed system to an external force $f(x, t)$ in the case of homogeneous initial and boundary conditions is given by

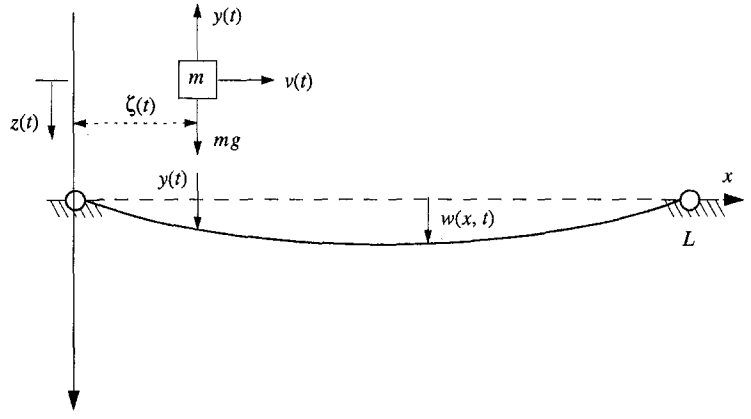


Fig. 1 A distributed elastic system carrying a moving linear conservative oscillator

Downloaded 04 May 2010 to 171.66.16.26. Redistribution subject to ASME license or copyright; see http://www.asme.org/terms/Terms_Use.cfm

$$w(x, t) = \int_0^t \int_0^L g(x, \xi, t - \tau) f(\xi, \tau) d\xi d\tau, \qquad (6)$$

where $g(x, \xi, t)$ is the Green's function of the continuum. To achieve the purpose of this section, we will take advantage of the modal expansion of the Green's function obtained by Yang (1996) for a general-type nonconservative distributed system. As shown in Yang (1996), if the distributed system lacks rigid-body modes (which is typical for the problem under consideration), the Green's function is given by

$$g(x, \xi, t) = \frac{1}{2} \sum_{n=\pm 1}^{\pm\infty} \frac{1}{\lambda_n} e^{\lambda_n t} \phi_n(x) \bar{\psi}_n(\xi). \qquad (7)$$

Here, complex λ_n and $\phi_n(x)$ are, respectively, the nth eigenvalue and eigenfunction of the distributed system, which are solutions to the eigenvalue problem associated with (1)

$$\{\lambda_n^2 M + \lambda_n D + K\} \phi_n(x) = 0. \qquad (8)$$

Functions $\psi_n(x)$ satisfy the adjoint eigenvalue problem

$$\{\bar{\lambda}_n^2 M + \bar{\lambda}_n D^* + K^*\} \psi_n(x) = 0; \qquad (9)$$

the overbar denotes complex conjugation, and the asterisk * denotes adjoint operators. Because the coefficients of Eq. (1) are real, the eigensolutions have the properties

$$\lambda_{-n} = \bar{\lambda}_n, \quad \phi_{-n} = \bar{\phi}_n, \quad \psi_{-n} = \bar{\psi}_n. \qquad (10)$$

In addition, $\phi_n(x)$ and $\psi_n(x)$ satisfy the normalization condition (Yang, 1996)

$$\int_0^L \bar{\psi}_n(x) M \phi_n(x) dx - \frac{1}{\lambda_n^2} \int_0^L \bar{\psi}_n(x) K \phi_n(x) dx = 2. \qquad (11)$$

Substituting (3) and (7) into (6), we obtain the modal expansion of the response of the distributed system

$$w(x, t) = \tfrac{1}{2} \sum_{n=\pm 1}^{\pm\infty} \phi_n(x) q_n(t), \qquad (12)$$

where

$$q_n(t) = \frac{1}{\lambda_n} \int_0^t e^{\lambda_n (t-\tau)} \bar{\psi}_n(\zeta(\tau)) y(\tau) d\tau. \qquad (13)$$

Substituting subscript $-n$ for n into (13) and taking into account (10) and the fact that $y(t)$ is a real function, we obtain the relation $q_{-n}(t) = \bar{q}_n(t)$; i.e., we only need to look for the coefficients $q_n(t)$ for positive n. In view of (10), it follows that $w(x, t)$ is a real function, and series (12) can be written in the form

$$w(x, t) = \tfrac{1}{2} \sum_{n=1}^{\infty} [\phi_n(x) q_n(t) + \bar{\phi}_n(x) \bar{q}_n(t)], \qquad (14)$$

or

$$w(x, t) = \sum_{n=1}^{\infty} \mathrm{Re}[\phi_n(x) q_n(t)]. \qquad (15)$$

In the general case (except for the case of the moving force problem), function $y(t)$ may depend on the unknowns $q_n(t)$ (and even on their derivatives). Thus, (13) is a set of coupled integral (or integro-differential) equations in $q_n(t)$. In the next section, we will reduce the problem of finding the coefficients q_n to that of solving a set of linear ordinary differential equations.

4 Equations Governing the Time-Dependent Coefficients of the Expansion

In this section, we will not specify the force $y(t)$ acting on the continuum, treating it instead as a certain unknown or given function. Under this assumption, we will obtain a set of formally uncoupled complex differential equations (as well as its real matrix form) that can be further applied to solving various problems with different models of the moving loads after specifying $y(t)$ in terms of the system response. It should also be emphasized that the equations to be obtained are valid for a general-type non-self-adjoint distributed system.

Differentiating both sides of Eq. (13), we obtain

$$\dot{q}_n(t) = \int_0^t e^{\lambda_n (t-\tau)} \bar{\psi}_n(\zeta(\tau)) y(\tau) d\tau + \frac{1}{\lambda_n} \bar{\psi}_n(\zeta(t)) y(t).$$

Taking (13) into account, we arrive at the set of complex ordinary differential equations in $q_n(t)$

$$\dot{q}_n(t) = \lambda_n q_n(t) + \frac{1}{\lambda_n} \bar{\psi}_n(\zeta(t)) y(t), \quad n = 1, 2, \ldots. \qquad (16)$$

Representing complex values in the standard form $q_n = q_n^R + i q_n^I$, $\phi_n = \phi_n^R + i\phi_n^I$, $\psi_n = \psi_n^R + i\psi_n^I$, and denoting $\lambda_n = \alpha_n + i\omega_n$, where i is the imaginary unit, we can write the nth complex equation of set (16) as the two real equations

$$\begin{aligned} \dot{q}_n^R &= \alpha_n q_n^R - \omega_n q_n^I + \gamma_n (\alpha_n \psi_n^R - \omega_n \psi_n^I) y(t), \\ \dot{q}_n^I &= \omega_n q_n^R + \alpha_n q_n^I - \gamma_n (\omega_n \psi_n^R + \alpha_n \psi_n^I) y(t), \end{aligned} \qquad (17)$$

where $\gamma_n = (\alpha_n^2 + \omega_n^2)^{-1}$.

For certain problems, in which the force $y(t)$ couples the equations, a matrix form of Eqs. (17) may be useful. In the following, we will use curly brackets to denote real vectors. Let N be the number of Eqs. (16) to be solved. We will denote by $\{\phi^R\}$, $\{\phi^I\}$, $\{\psi^R\}$, $\{\psi^I\}$, $\{q^R\}$, and $\{q^I\}$ the N-dimensional vectors composed of the components ϕ_n^R, ϕ_n^I, ψ_n^R, ψ_n^I, q_n^R, and q_n^I, respectively; and by A and Ω_1 the diagonal matrices of order N

$$A = \mathrm{diag}\,[\alpha_1, \ldots, \alpha_N], \quad \Omega_1 = \mathrm{diag}\,[\omega_1, \ldots, \omega_N].$$

Let us also introduce the $2N$-dimensional vectors

$$\{\phi\} = \begin{Bmatrix} \{\phi^R\} \\ \{\phi^I\} \end{Bmatrix}, \quad \{\psi\} = \begin{Bmatrix} \{\psi^R\} \\ \{\psi^I\} \end{Bmatrix}, \quad \{q\} = \begin{Bmatrix} \{q^R\} \\ \{q^I\} \end{Bmatrix},$$

and the $2N \times 2N$ block matrix

$$\Omega = \begin{bmatrix} A & -\Omega_1 \\ \Omega_1 & A \end{bmatrix}.$$

It can be verified directly that, in terms of the introduced notation, Eqs. (16) take the real matrix form

$$\{\dot{q}\} = \Omega\{q\} + \Omega^{-1}\{\bar{\psi}(\zeta)\} y(t). \qquad (18)$$

Note that the overbar here and in what follows means that the above component notation is applied to a complex conjugate function; i.e., $\{\bar{\psi}\} = \{\{\psi^R\}^T, -\{\psi^I\}^T\}^T$. In terms of this notation, Eq. (15) for the response of the distributed system can be written as

$$w(x, t) = \{\bar{\phi}(x)\}^T \{q(t)\}. \qquad (19)$$

5 Solution to the Moving Oscillator Problem

The equations obtained incorporate the (generally) unknown function $y(t)$. If the force $y(t)$ does not depend on the response of the distributed system, as in the case of the moving force problem, Eqs. (16) are uncoupled, and Eqs. (18), (19) immediately give a solution to the problem under consideration. However, if the force is due to a concentrated mass traversing the continuum, the situation becomes drastically different: the dynamics of the mass and its interaction with the distributed system result in coupling of the differential equations. To solve

Downloaded 04 May 2010 to 171.66.16.26. Redistribution subject to ASME license or copyright; see http://www.asme.org/terms/Terms_Use.cfm

the problem in the case where the force $y(t)$ depends on the unknowns $q_n(t)$, the equation for $y(t)$ is also required.

In this section, we will obtain the solution to the moving oscillator problem. We will examine the system depicted in Fig. 1 as an aggregate of two subsystems—the distributed nonconservative system and the mass—interacting through a linear spring. Let $z(t)$ be the lateral displacement of the mass and k the stiffness of the spring. For this problem, the interaction force is given by (5), and we have an additional unknown—the response of the mass $z(t)$. The mass is subject to two forces: its weight and the interaction force $-y(t)$. The equation governing the response of the mass is easy to obtain and is given by

$$m\ddot{z}(t) = mg - y(t).$$

Integration of this equation for the homogeneous initial conditions $z(0) = \dot{z}(0) = 0$ results in

$$z(t) = \frac{1}{2} gt^2 - \frac{1}{m} \int_0^t (t - \tau) y(\tau) d\tau.$$

For the sake of clarity, we write the response of the mass to the interaction force in a form similar to that for the distributed system,

$$z(t) = \tfrac{1}{2} gt^2 - \varphi_0 q_0(t), \tag{20}$$

where $\varphi_0 = 1/\sqrt{m}$ is the normalized (to unitary mass) rigid-body eigenfunction of the isolated mass, and $q_0 = \varphi_0 \int_0^t (t - \tau) y(\tau) d\tau$.

Now, in view of (19) and (20), Eq. (5) takes the form

$$y(t) = k[\tfrac{1}{2} gt^2 - \varphi_0 q_0(t) - \{\bar{\phi}(\zeta)\}^T \{q(t)\}]. \tag{21}$$

Appending this equation and the equation in the new unknown $q_0(t)$,

$$\ddot{q}_0 = \varphi_0 y(t), \tag{22}$$

to Eq. (18), we arrive at the set of equations of summary differential order $2N + 2$ in the time-dependent coefficients of the expansion of the system response

$$\begin{cases} \{\dot{q}\} = \Omega\{q\} + \Omega^{-1}\{\bar{\psi}(\zeta)\} y(t), \\ \ddot{q}_0 = \varphi_0 y(t), \\ y(t) = k\,[\tfrac{1}{2} gt^2 - \varphi_0 q_0(t) - \{\bar{\phi}(\zeta)\}^T \{q(t)\}], \end{cases} \tag{23}$$

with the homogeneous initial conditions

$$q_0(0) = \dot{q}_0(0) = 0, \quad \{q\} = 0. \tag{24}$$

Note that Eqs. (23) are not specific to a particular linear non-self-adjoint distributed system. Given normalized sets of the eigenfunctions $\phi_n(x)$ and $\psi_n(x)$ of the direct and adjoint eigenproblems, a solution to the moving oscillator problem can be obtained for any arbitrary non-self-adjoint distributed system.

As mentioned above, if the speed v of the mass along the continuum is constant, then substitution of $\zeta = vt$ results in the required set of equations. If the speed of the mass varies, then the additional equation

$$\ddot{\zeta}(t) = a(t) \tag{25}$$

with the initial conditions $\zeta(0) = 0$ and $\dot{\zeta}(0) = v_0$ should be added; here, $a(t)$ is a given law of variation of the mass speed along the continuum, and v_0 is the initial horizontal speed of the mass.

Thus, the response of an arbitrary non-self-adjoint distributed system due to a conservative oscillator traversing the continuum with an arbitrarily varying speed is given by Eq. (19), and the time-dependent coefficients $\{q\}$ are found to be solutions to the set of Eqs. (23) and (25) subject to initial conditions (24).

6 Application to Particular Kinds of Distributed Systems

In the previous section, we specialized the equations of Section 4 for a particular kind of moving load: namely, the case of a conservative oscillator. The application of the method discussed to a particular class of distributed system also requires discussion. The point to be made is that the coefficients of the equations obtained in the previous two sections are given in terms of eigenfrequencies and eigenfunctions of the direct and adjoint eigenproblems. While the eigenfrequencies and direct eigenfunctions (mode shapes) are available for certain kinds of homogeneous nonconservative distributed systems (or, in the case of nonhomogeneous systems, can be efficiently calculated), the adjoint eigenfunctions need to be found and normalized so that the normalization conditions (11) are satisfied.

The physical meaning of adjoint eigenfunctions is not a priori clear for a system with combined effects of damping, gyroscopic, and circulatory forces. This problem is discussed in Yang (1995, 1996), where the author showed that the adjoint eigenfunctions relate to the mode shapes of the distributed system. One can take advantage of his results to obtain the adjoint eigenfunctions in terms of the mode shapes of the distributed system and, thus, to obtain the coefficients of the differential equations in an explicit form (we assume that eigenfrequencies and eigenfunctions of the distributed system are available). It should be noted, however, that the adjoint eigenfunctions given in Yang (1995, 1996) are not normalized and, in the general case, do not satisfy (11). Hence, one should incorporate complex factors of the eigenfunctions. This point is illustrated further in this section by the example of a proportionally damped continuum.

In this section, we make specific the equations of the previous sections to two kinds of continua. As mentioned in the Introduction, the case of a conservative continuum is well examined, and various solutions to the moving mass and moving oscillator problems, obtained in the context of various approaches, are available in the literature. For the purpose of illustration, we will show first that certain sets of equations, corresponding to the conservative case obtained in earlier publications, follow from the equations established in the previous sections. Then, the case of proportionally damped continua will be examined in detail, and the coefficients of the equations will be obtained in explicit terms making it possible to numerically apply the method to particular distributed systems. To the authors' knowledge, the solution to this case is not available in the literature. Note here that the specialization of the equations to a particular kind of distributed system does not depend on the chosen model of moving load; therefore, we will mainly refer to the general equations discussed in Section 4.

In the following, we will use the notation $\varphi_n(x)$ to denote the nth real eigenfunction of the conservative system, or, in the case of a proportionally damped continuum, the eigenfunction of the associated conservative (undamped) continuum, that satisfies the normalization condition

$$\int_0^L \varphi_n(x) M \varphi_n(x) dx = 1 \tag{26}$$

(note that, for conservative systems, this condition coincides with (11)).

Conservative Systems. It is well known that a conservative ($D = 0$, $K = K^*$) system has purely imaginary eigenvalues $\lambda_n = i\omega_n$ (matrix A is zero) and real and orthogonal eigenfunctions. The direct and adjoint eigenvalue problems are the same, and, thus, the adjoint eigenfunctions coincide with the mode shapes $\varphi_n(x)$ of the system. Let $\{\varphi\}$ be the N-dimensional vector composed of $\varphi_n(\zeta)$. Then,

Downloaded 04 May 2010 to 171.66.16.26. Redistribution subject to ASME license or copyright; see http://www.asme.org/terms/Terms_Use.cfm

$$\{\bar{\psi}\} = \{\psi\} = \{\phi\} = \begin{Bmatrix} \{\varphi\} \\ \{0\} \end{Bmatrix}, \tag{27}$$

and Eq. (18) takes the form

$$\begin{Bmatrix} \{\dot{q}^R\} \\ \{\dot{q}^I\} \end{Bmatrix} = \begin{bmatrix} 0 & -\Omega_1 \\ \Omega_1 & 0 \end{bmatrix} \begin{Bmatrix} \{q^R\} \\ \{q^I\} \end{Bmatrix} + \begin{bmatrix} 0 & \Omega_1^{-1} \\ -\Omega_1^{-1} & 0 \end{bmatrix} \begin{Bmatrix} \{\varphi\} \\ \{0\} \end{Bmatrix} y(t), \tag{28}$$

or

$$\{\dot{q}^R\} = -\Omega_1\{q^I\}$$
$$\{\dot{q}^I\} = \Omega_1\{q^R\} - \Omega_1^{-1}\{\varphi\}y(t).$$

Differentiating the first of these two equations and substituting the second into the resulting equation, we arrive at the set of N second-order ordinary different equations

$$\{\ddot{q}^R\} = -\Omega_1^2\{q^R\} + \{\varphi(\zeta)\}y(t),$$

or

$$\ddot{q}_n^R = -\omega_n^2 q_n^R + \varphi_n(\zeta)y(t), \quad n = 1, 2, \ldots, N, \tag{29}$$

which coincides with the set of ordinary differential equations (39) in Pesterev and Bergman (1997a).

Returning to the moving oscillator problem, let us introduce the notation $\omega_0 = 0$ for the rigid-body eigenfrequency of the concentrated mass. It can be verified, noting (27)–(29), that the general system of Eqs. (23) can be rewritten in the simple form

$$\ddot{q}_n^R + \omega_n^2 q_n^R + k\varphi_n(\zeta)\sum_{m=0}^{N}\varphi_m(\zeta)q_m^R = \tfrac{1}{2}kgt^2\varphi_n(\zeta), \quad n = 0, 1, \ldots, N, \tag{30}$$

which coincides with Eqs. (1) in Pesterev and Bergman (1997b).

Finally, it should be noted that Eq. (29) can be applied directly to the examination of the moving mass problem. Actually, substituting (19) into (4) with regard to (27) and confining ourselves to the case of a constant speed v of the mass, we obtain

$$y(t) = m(g - \{\varphi\}^T\{\ddot{q}^R\} - 2v\{\varphi'\}^T\{\dot{q}^R\} - v^2\{\varphi''\}^T\{q^R\}). \tag{31}$$

Substituting this into Eq. (29), we arrive at the system of differential equations obtained by Lee (1996). This set can be resolved with respect to the second derivatives, as shown in Pesterev and Bergman (1997c).

Proportionally Damped Nongyroscopic Systems. It is well known (Caughey and O'Kelly, 1965; Yang, 1995) that if the system is proportionally damped (i.e., $K^* = K$, $D^* = D$, and $DM^{-1}K = KM^{-1}D$) the system eigenvalues are complex, and eigenfunctions of both direct and adjoint eigenvalue problem are real and coincide with the eigenfunctions $\varphi_n(x)$ of the associated classical self-adjoint problem

$$(\tilde{\lambda}_n^2 M + K)\varphi_n(x) = 0, \tag{32}$$

where $\tilde{\lambda}_n = i\tilde{\omega}_n$, and $\tilde{\omega}_n$ is the nth natural frequency of the associated undamped continuum. Note, however, that in the problem under consideration we cannot take $\varphi_n(x)$ for $\psi_n(x)$ since the normalization condition (11) will not be satisfied. As an eigenfunction can be multiplied by an arbitrary complex constant, we will look for the adjoint eigenfunctions in the form

$$\psi_n(x) = c_n\varphi_n(x), \tag{33}$$

where the complex numbers c_n should be chosen in order to satisfy (11) with $\phi_n(x) \equiv \varphi_n(x)$.

Before proceeding to the calculation of c_n, let us establish the formula that relates λ_n, $\bar{\lambda}_n$, and $\tilde{\lambda}_n$. Substituting $\varphi_n(x)$ into (8) and (9), multiplying the former by $\bar{\lambda}_n$ and the latter by λ_n, subtracting the second of the equations obtained from the first one, and taking into account that $K = K^*$ and $D = D^*$, we obtain

$$(\bar{\lambda}_n - \lambda_n)\{-\bar{\lambda}_n\lambda_n M + K\}\varphi_n(x) = 0. \tag{34}$$

Comparison of this equation with (32) while recalling that the λ_n have nonzero imaginary parts reveals that

$$\bar{\lambda}_n\lambda_n = -\tilde{\lambda}_n^2. \tag{35}$$

Now, substituting (33) and $\phi_n(x) = \varphi_n(x)$ into (11) and taking (32) and (26) into account, we arrive at

$$\bar{c}_n\int_0^L \varphi_n(x)M\varphi_n(x)dx - \frac{\bar{c}_n}{\lambda_n^2}\int_0^L \varphi_n(x)K\varphi_n(x)dx = \bar{c}_n\left\{\int_0^L \varphi_n(x)M\varphi_n(x)dx + \frac{\tilde{\lambda}_n^2}{\lambda_n^2}\int_0^L \varphi_n(x)M\varphi_n(x)dx\right\} = \bar{c}_n\left\{1 + \frac{\tilde{\lambda}_n^2}{\lambda_n^2}\right\} = 2.$$

In view of (35), it follows that

$$\bar{c}_n = \frac{2\lambda_n}{\lambda_n - \bar{\lambda}_n} = \frac{\lambda_n}{i\omega_n} \tag{36}$$

where, as before, ω_n is the imaginary part of λ_n.

Substituting $\bar{\psi}_n(\zeta) = \bar{c}_n\varphi_n(\zeta)$, where $\bar{c}_n$ is given by (36), into (16), we obtain

$$\dot{q}_n(t) = \lambda_n q_n(t) + \frac{1}{i\omega_n}\varphi_n(\zeta(t))y(t), \quad n = 1, 2, \ldots. \tag{37}$$

or

$$\dot{q}_n^R = \alpha_n q_n^R - \omega_n q_n^I,$$
$$\dot{q}_n^I = \omega_n q_n^R + \alpha_n q_n^I - \frac{1}{\omega_n}\varphi_n y(t). \tag{38}$$

As in the case of the conservative continuum, the unknowns q_n^I can be eliminated, and the above set can be reduced to a system of second-order differential equations. Indeed, differentiating the first of Eqs. (38) and substituting the second into the resulting equation, we arrive at a system of N ordinary differential equations similar to (29)

$$\ddot{q}_n^R = (\alpha_n^2 - \omega_n^2)q_n^R + \varphi_n(\zeta)y(t), \quad n = 1, 2, \ldots, N. \tag{39}$$

Equations (39) are not specific to a particular type of moving load. In the case of the moving force problem, they are, in fact, uncoupled and immediately give the required solution upon substitution of the form of the moving force $y(t)$. Furthermore, the system of equations corresponding to the moving oscillator problem is obtained in exactly the same way as that for the case of the conservative continuum,

$$\ddot{q}_n^R + (\omega_n^2 - \alpha_n^2)q_n^R + k\varphi_n(\zeta)\sum_{m=0}^{N}\varphi_m(\zeta)q_m^R = \tfrac{1}{2}kgt^2\varphi_n(\zeta), \quad n = 0, 1, \ldots, N, \tag{40}$$

where $\omega_0 = 0$ and $\alpha_0 = 0$.

Clearly, there is no difficulty obtaining the set of the equations corresponding to the moving mass case. This is achieved

Downloaded 04 May 2010 to 171.66.16.26. Redistribution subject to ASME license or copyright; see http://www.asme.org/terms/Terms_Use.cfm

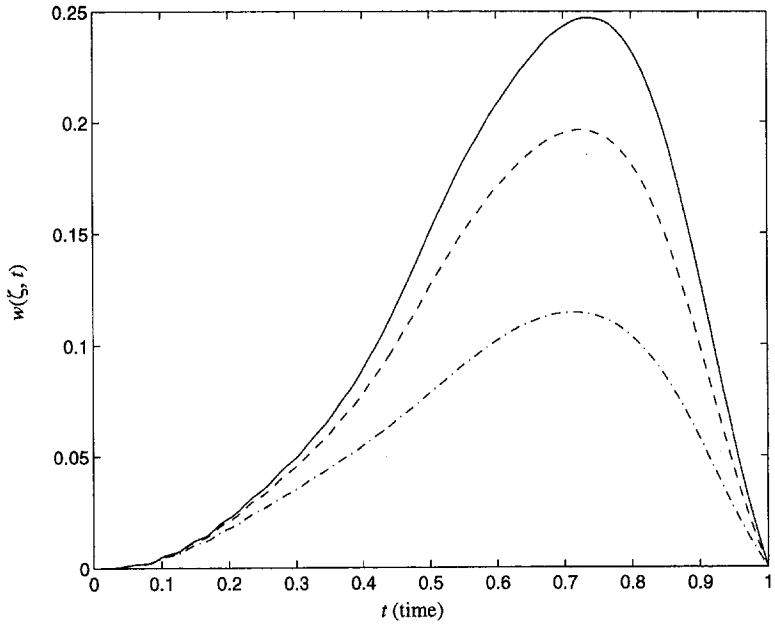


Fig. 2 Displacements of the mass moving with constant speed $v = 6$ m/s on the simply supported beam; (i) $c_d = 0$ (solid line), (ii) $c_d = 2$ (dashed line), and (iii) $c_d = 9$ (dash-dot line)

through substitution of (31) into (39) and results in equations similar to those in Lee (1996). The equations can then be resolved with respect to the second derivatives as was done in Pesterev and Bergman (1997c) for a conservative beam.

7 Numerical Results

In this section, we present some results of our numerical experiments related to the problem of an oscillator traversing a proportionally damped homogeneous beam. The equation governing vibration of such a beam is well known to be

$$\frac{\partial^2 w(x,t)}{\partial t^2} + c_d \frac{\partial w(x,t)}{\partial t} + \frac{EI}{\mu}\frac{\partial^4 w(x,t)}{\partial x^4} = f(x,t), \qquad 0 \le x \le L,$$

where $c_d = \tilde{c}_d/\mu$, $\tilde{c}_d$ is the damping coefficient, L is the beam length, and EI and μ are constant flexural rigidity and mass density per unit length, respectively.

Having no other published results involving damped continua at our disposal, we could only qualitatively compare the results obtained with those related to the conservative case. The Euler-Bernoulli beam considered in Sadiku and

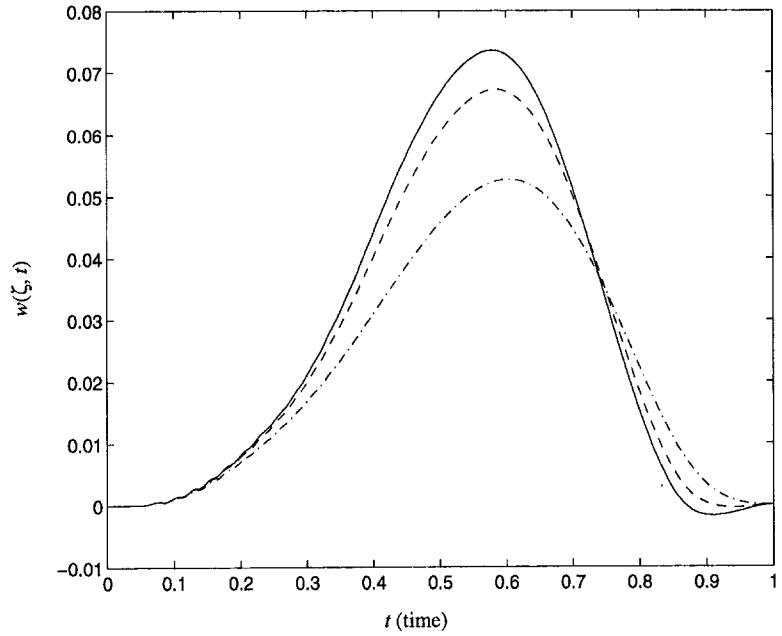


Fig. 3 Displacements of the mass moving with constant speed $v = 6$ m/s on the clamped-clamped beam; (i) $c_d = 0$ (solid line), (ii) $c_d = 2$ (dashed line), and (iii) $c_d = 9$ (dash-dot line)

Downloaded 04 May 2010 to 171.66.16.26. Redistribution subject to ASME license or copyright; see http://www.asme.org/terms/Terms_Use.cfm

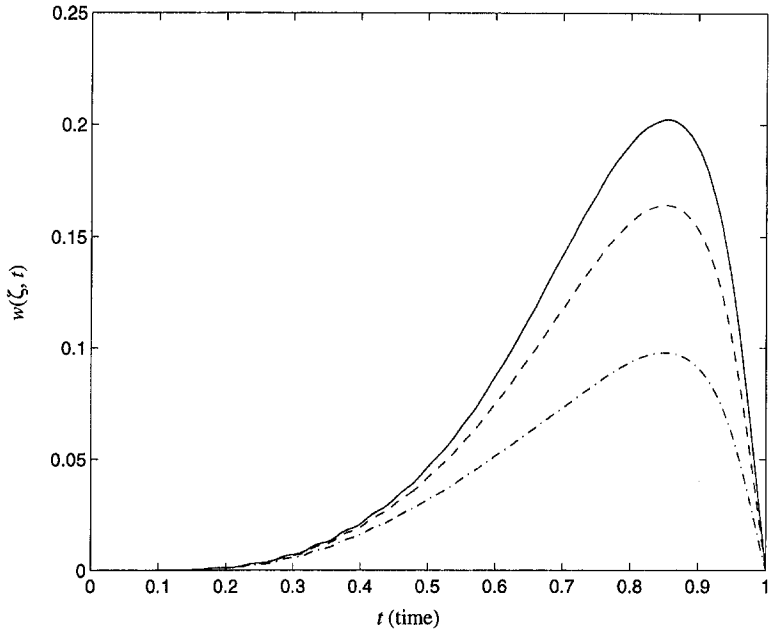


Fig. 4 Displacements of the accelerating mass ($\nu(0) = 0$, $a = 12$ m/s/s) on the simply supported beam; (i) $c_d = 0$ (solid line), (ii) $c_d = 2$ (dashed line), and (iii) $c_d = 9$ (dash-dot line)

Leipholz (1987) and in Pesterev and Bergman (1997a, b), with the addition of damping, was employed for the experiments. The numerical values of the beam parameters were as follows: $L = 6$ m, $EI/\mu = 275.4408$ m^4/s^2; the ratio of the mass of the oscillator to the beam mass was equal to $m/\mu L = 0.2$. Two cases of boundary conditions were considered: both ends either simply supported or clamped. The natural frequencies and orthonormal eigenfunctions of the associated conservative beam for both sets of boundary conditions are well known and are given, for example, in Sadiku and Leipholz (1987). As was mentioned, the eigenfunctions of the damped beam coincide with those of the undamped beam; the eigenvalues of the damped beam are given by

$$\lambda_n = -\frac{c_d}{2} + i\sqrt{\tilde{\omega}_n^2 - \frac{c_d^2}{4}},$$

where $\tilde{\omega}_n$ are natural frequencies of the undamped beam. The numerical values of first four $\tilde{\omega}_n$ for the beam under investigation are as follows. For the simply supported beam: 4.55, 18.2, 40.9, and 72.7 (rad/s); for the clamped-clamped beam: 10.3, 28.4, 55.7, and 92.1 (rad/s). Three variants of damping level were considered: (i) $c_d = 0$, (ii) $c_d = 2$, and (iii) $c_d = 9$. The curves corresponding to these cases are depicted in Figs. 2–5 by solid, dash, and dash-dot lines, respectively.

In Pesterev and Bergman (1997a, b), where the moving oscillator problem was considered, the stiffness of the spring con-

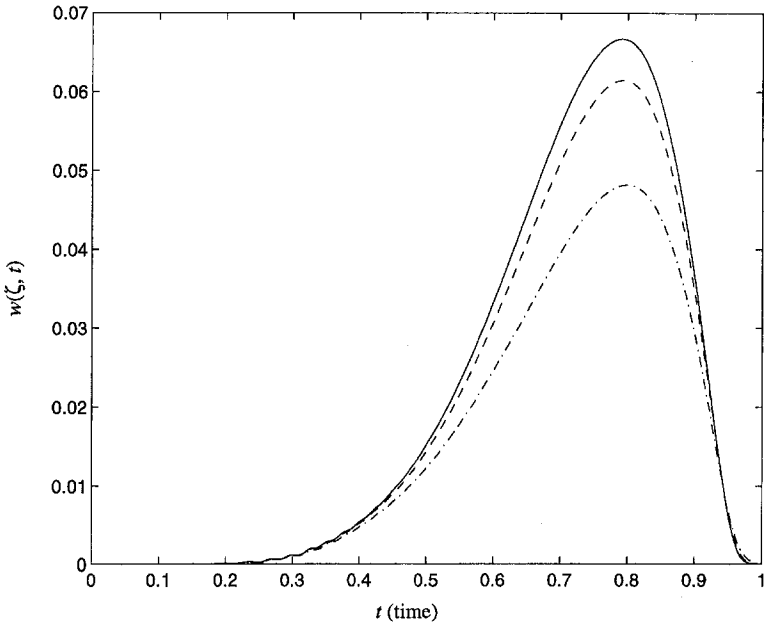


Fig. 5 Displacements of the accelerating mass ($\nu(0) = 0$, $a = 12$ m/s/s) on the clamped-clamped beam; (i) $c_d = 0$ (solid line), (ii) $c_d = 2$ (dashed line), and (iii) $c_d = 9$ (dash-dot line)

Downloaded 04 May 2010 to 171.66.16.26. Redistribution subject to ASME license or copyright; see http://www.asme.org/terms/Terms_Use.cfm

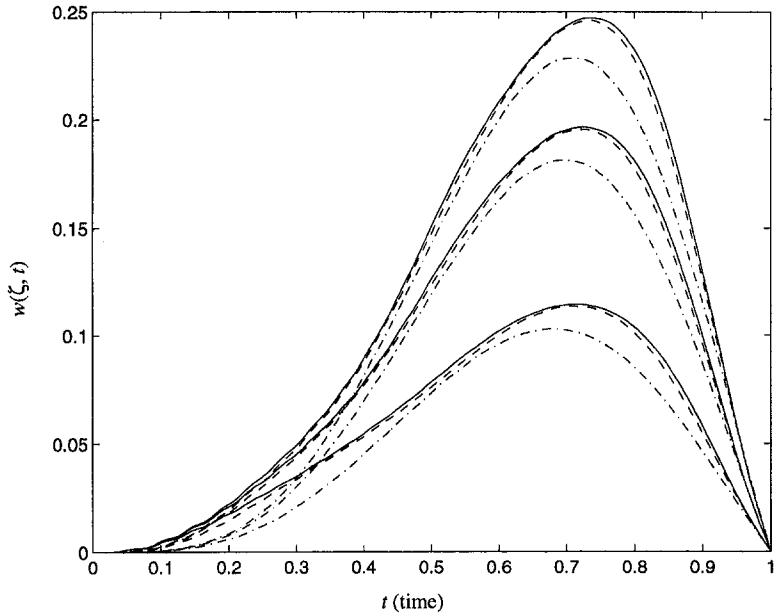


Fig. 6 Approximations of exact solutions depicted in Fig. 2 for different numbers N of terms of the expansion; (i) $N = 1$ (dash-dot lines), (ii) $N = 2$ (dash lines), and (iii) exact solutions (solid lines)

necting the mass and beam was chosen large in order to simulate the moving mass problem discussed in Sadiku and Leipholz (1987). In this work we used springs of stiffness $k = 2000$ N/m (for the simply supported beam) and $k = 5000$ N/m (for clamped-clamped beam), which ensured very good approximation to the solution of the moving mass problem.

All of the following figures present the deflections of the beam at the spring attachment point $w(\zeta(t), t)$ (in fact, since we considered very stiff springs, these curves also show the displacement of the moving mass on the beam). Figures 2 and 3 correspond to the case of the mass moving with constant speed $v = 6$ m/s along the simply supported and clamped-clamped beams, respectively. Figures 4 and 5 give the corresponding pictures of the displacements for accelerating motion, with zero initial speed $v_0 = 0$ and constant acceleration $a = 12$ m/s^2.

The numbers N of terms in expansion (19) were taken identical to those used in the experiments described in Pesterev and Bergman (1997a): $N = 4$, for the simply supported beam, and $N = 5$ for the clamped-clamped beam. These values of N ensured practically exact approximations of the desired solutions. To save space, we present here only one figure showing the convergence of the solutions in the case of the simply supported beam (note that the numerical results for the clamped-clamped beam were given in Pesterev and Bergman (1997a)). Figure 6 demonstrates rapid convergence of truncated series to the three exact solutions presented earlier in Fig. 2 and depicted in Fig. 6 by solid lines. Here, the dash-dot lines correspond to $N = 1$ and dash lines correspond to $N = 2$. Note that, for all three cases shown in Fig. 6, the use of any $N \geq 3$ resulted in the same curves.

To conclude this section, note that the solid lines in Figs. 2–5, which represent the case of the undamped beam, coincide with the corresponding curves in Pesterev and Bergman (1997a, b). Also note that, although the other curves cannot be compared with prior results, they look very reasonable and realistic when compared qualitatively with each other and with curves corresponding to the conservative case.

8 Concluding Remarks

A method for calculating the response of a nonconservative distributed parameter system to a moving concentrated load has been presented. It is based on expansion of the response in a series in terms of complex eigenfunctions of the distributed system. Assuming that the force acting on the distributed system from a moving vehicle is a given function of time, we have obtained the set of ordinary differential equations in the time-dependent coefficients of the expansion valid for various kinds of concentrated loads. To obtain the required set of ordinary differential equations given a particular model of the vehicle-structure interaction, one should express the force acting on the continuum in terms of the unknown coefficients of the expansion and substitute the resulting expression for the force into the above set of equations. In the paper, this has been done for the case of a moving conservative oscillator. When applied to a conservative distributed system, the set obtained is shown to coincide with that previously published in Pesterev and Bergman (1997a, b).

In the general case of a nonconservative distributed system, the coefficients of the differential equations obtained are given in terms of the eigenfrequencies and eigenfunctions of the adjoint system. To apply them to a particular non-self-adjoint system, the eigenfunctions of the corresponding adjoint problem satisfying the normalization conditions (11) should be found. In the paper, this is illustrated by the example of a proportionally damped continuum. A similar technique can be applied to other kinds of nonconservative continua. The results of some numerical experiments on the proportionally damped beam have been presented.

The case of a nonconservative moving oscillator (connected to the distributed system through a spring and dashpot) can be analyzed analogously. It should be noted that the interaction force in this case depends on the derivatives of the unknowns, and the differential equations are obtained in a form unresolved with respect to the derivatives. It can be shown, however, that the matrix of coefficients of the derivatives, which depends on time, can be inverted analytically. The appropriate technique is similar to that described in Pesterev and Bergman (1997c). We will defer the detailed discussion of this case to a later time, however.

References

Bogacz, R., and Szolc, T., 1992, "On Methods of Solution for the Discrete-Continuous System Under Moving Load," *ZAMM*, Vol. 72, pp. 16–19.

Downloaded 04 May 2010 to 171.66.16.26. Redistribution subject to ASME license or copyright; see http://www.asme.org/terms/Terms_Use.cfm

Bolotin, V. V., 1964, *The Dynamic Stability of Elastic Systems,* Holden-Day, San Francisco, CA.

Caughey, T. N., and O'Kelly, M. E., 1965, "Classical Normal Modes in Damped Linear Dynamic Systems," ASME JOURNAL OF APPLIED MECHANICS, Vol. 32, pp. 563–588.

Delgado, R. M., and dos Santos, S. M., 1997, "Modelling of Railway Bridge-Vehicle Interaction on High Speed Tracks," *Computers and Structures,* Vol. 63, pp. 511–523.

Frýba, L., 1972, *Vibration of Solids and Structures under Moving Loads,* Noordhoff, Groningen, The Netherlands.

Frýba, L., 1987, "Dynamic Interaction of Vehicles with Tracks and Roads," *Vehicle System Dynamics,* Vol. 16, pp. 129–138.

Lee, U., 1996, "Revisiting the Moving Mass Problem: Onset of Separation Between the Mass and Beam," ASME *Journal of Vibration and Acoustics,* Vol. 118, pp. 516–521.

Olson, M., 1991, "On the Fundamental Moving Load Problem," *Journal of Sound and Vibration,* Vol. 145, pp. 299–307.

Pesterev, A. V., and Bergman, L. A., 1997a, "Vibration of Elastic Continuum Carrying Moving Linear Oscillator," *ASCE Journal of Engineering Mechanics,* Vol. 123, pp. 878–884.

Pesterev, A. V., and Bergman, L. A., 1997b, "Vibration of Elastic Continuum Carrying Accelerating Oscillator," *ASCE Journal of Engineering Mechanics,* Vol. 123, pp. 886–889.

Pesterev, A. V., and Bergman, L. A., 1997c, "A Contribution to the Moving Mass Problem," ASME *Journal of Vibration and Acoustics,* in press.

Riemer, M., 1987, "Analitische Beschreibung von Fahrzeug/Fahrzeug-Modellen am Beispiel eines auf einer Saite laufenden Oszillators," *ZAMM,* Vol. 67, pp. 136–138.

Sadiku, S., and Leipholz, H. H. E., 1987, "On the Dynamics of Elastic Systems with Moving Concentrated Masses," *Ingenieur-Archiv,* Vol. 57, pp. 223–242.

Shen, I. Y., 1993, "Response of a Stationary, Damped, Circular Plate Under a Rotating Slider Bearing System," ASME *Journal of Vibration and Acoustics,* Vol. 115, pp. 65–69.

Stanišić, M. M., 1985, "On a New Theory of the Dynamic Behavior of the Structures Carrying Moving Masses," *Ingenieur-Archiv,* Vol. 55, pp. 176–185.

Weisensel, G. N., and Schlack, A. L. Jr., 1993, "Response of Annular Plates to Circumferentially and Radially Moving Loads," ASME JOURNAL OF APPLIED MECHANICS, Vol. 60, pp. 649–661.

Yang, B., 1995, "Modal Controllability and Observability of General Mechanical Systems," ASME *Journal of Vibration and Acoustics,* Vol. 117, pp. 510–515.

Yang, B., 1996, "Integral Formulas for Non-Self-Adjoint Distributed Dynamic Systems," *AIAA Journal,* Vol. 34, pp. 2132–2139.

Yang, B., Tan, C. A., and Bergman, L. A., 1997, "On the Problem of a Distributed Parameter System Carrying a Moving Oscillator," *Dynamics and Control of Distributed Systems,* H. Tzou and L. Bergman, eds., Cambridge University Press, in press.

Downloaded 04 May 2010 to 171.66.16.26. Redistribution subject to ASME license or copyright; see http://www.asme.org/terms/Terms_Use.cfm

How the Raleigh Flow Transits to Blasius Numerically

G. N. Sarma
Department of Mathematics,
University of Roorkee,
Roorkee (U.P.) 247667, India

This paper answers the question numerically how a two-dimensional incompressible Rayleigh boundary layer started impulsively past a semi-infinite flat plate with uniform velocity in the mainstream transits to steady Blasius flow. It is shown that the transition is a convective transition and smooth with no discontinuities. It is effected by the parameters called the convective and angular parameters. The velocity field gets disintegrated into discrete dissimilar diffusive layers of different convective orders. This is an example based on modified boundary layer theory of Sarma. Polynomial solutions are found using the theory of definite thickness boundary layers and the method of weighted residuals. This modifies the numerical works of Hall and Dennis, which are based on Stewartson's theory of propagation of disturbances.

1 Introduction

The Rayleigh-Blasius problem of propagation of disturbances in incompressible two-dimensional impulsively started boundary layer flow past a semi-infinite flat plate was analysed by Stewartson (1951, 1973). But his solution is based on essential singularities and so unrealistic for a continuous flow phenomenon. Stewartson's analysis (1951) does not speak anything about how the two asymptotic solutions for small and large times match. The theory given by Sarma (1991) modifies his theory. Based on that, this paper gives a smooth numerical solution (as expected by Stuart (1963) and Riley (1975)) different from that of Hall (1969) and Dennis (1972). As per the theory of Sarma (1991), the transition is due to convective parameter $U_M t/x$ and angular parameters c_x and c_t ($U_M = \delta(\partial u/\partial y)_o$; δ is the boundary layer thickness, x and y the distances along and normal to a wall, t time, u the velocity in the x direction, the suffix o indicates at $y = o$, and U_M can be made equal to the velocity in the mainstream (if it is nonzero). The angular parameters give the angular variations of the velocity vector or of the vorticity with respect to the convective coordinates x and t in the neighborhood of a wall. The angular parameters are defined with respect to the disturbing velocities u_{BE} and u_{RE} (u_{BE} the Blasius based eigen velocity due to spatial inertia force and u_{RE} is the Rayleigh-based eigen velocity due to local inertia force). They are defined by $\lim (x\partial u_{BE}/u_{BE}\partial x) = x\partial\tau_{BE}/\tau_{BE}\partial x = c_x(x, t)$ and $\lim (t\partial u_{RE}/u_{RE}\partial t) = t\partial\tau_{RE}/\tau_{RE}\partial t = c_t(x, t)$ as $y \to o$ ($\tau_{BE} = \mu(\partial u_{BE}/\partial y)_o$ and $\tau_{RE} = \mu(\partial u_{RE}/\partial y)_o$ are the skin frictions, μ coefficient of viscosity). As a first approximation, in the Rayleigh-Blasius problem the parameters are treated as constants and play the roles of eigenvalues. In the text of this paper, $c_x = l - 0.5$ and $c_t = m - 0.5$ where l and m are constants. With respect to the velocities u_R and u_B of the particular Rayleigh and Blasius flows, the parameters c_t and c_x assume the particular values given by $c_t = t\partial\tau_R/\tau_R\partial t = -0.5$ and $c_x = x\partial\tau_B/\tau_B\partial x = -0.5$ because the thicknesses are proportional to $\sqrt{t}$ and $\sqrt{x}$ (where $\tau_R = \mu(\partial u_R/\partial y)_o$ and $\tau_B = \mu(\partial u_B/\partial y)_o$).

From the definition for c_x, we have $\tau_{BE} = O((\mu U_M/\sqrt{\nu t})(U_M t/x)^{-c_x}) = O((\mu U_M/\sqrt{\nu x/U_M})(U_M t/x)^{-(c_x+0.5)})$ (where t-dependence is so adjusted to suit the behavior of the velocity u_{BE} as $t \to o$ and $x \to \infty$ and in the matching region when $c_x < -0.5$) and $\lim (v_{BE}/u_{BE})/(y/x) = -(\partial\tau_{BE}/\partial x)/(2\tau_{BE}/x) = -(c_x/2)$ as $y \to o$ (where v_{BE} is the velocity component in the y-direction corresponding to u_{BE}, ν Kinematic viscosity). This means $-(c_x/2)$ is just the relative measure of the gradient (v_{BE}/u_{BE}) of the disturbing velocity vector due to Blasius based eigenflow to that of the gradient (y/x) of the position vector in the neighborhood of a wall. The parameter c_x can also be interpreted as the ratio of two gradients $\partial\tau_{BE}/\partial x$ and τ_{BE}/x of the tangent and of the position vector, respectively, at a point (τ_{BE}, x) on a curve $\tau_{BE} = \tau_{BE}(x, t)$ for a given t. The negative character of c_x signifies that τ_{BE} is a decreasing function of x and the two gradients v_{BE}/u_{BE} and y/x have the same sign. Similarly from the definition for c_t, we have $\tau_{RE} = O((\mu U_M/\sqrt{\nu x/U_M})(x/U_M t)^{-c_t}) = O((\mu U_M/\sqrt{\nu t})(x/U_M t)^{-(c_t+0.5)})$ (where x-dependence is so adjusted to suit the behavior of the velocity u_{RE} as $t \to \infty$ and $x \to o$ and in the matching region when $c_t < -0.5$) and $\lim (v_{RE}/u_{RE})/(y/x) = -(\partial\tau_{RE}/\partial x)/(2\tau_{RE}/x) = 0.5(c_t + 0.5)$ as $y \to o$ (where v_{RE} is the velocity component in the y-direction corresponding to u_{RE}). This means $0.5(c_t + 0.5)$ is just the relative measure of the gradient v_{RE}/u_{RE} of the disturbing velocity vector due to Rayleigh based eigenflow to that of the gradient y/x of the position vector in the neighborhood of a wall. The parameter c_t can also be interpreted as the ratio of two gradients $\partial\tau_{BE}/\partial t$ and τ_{BE}/t of the tangent and of the position vector, respectively, at a point (τ_{RE}, t) on a curve $\tau_{RE} = \tau_{RE}(x, t)$ for a given x. The negative character of c_t (< -0.5) signifies that τ_{RE} is a decreasing function of t and an increasing function of x and the two gradients v_{RE}/u_{RE} and y/x have opposite signs in the limit. These characters of c_x and c_t are met in the present problem. The negative characters of c_x and c_t also assure the smooth convective behaviors mathematically and physically of the disturbing velocities and forces, in their respective regions of validity. From the definition for c_x, we have $u_{BE}/U_M = O((y/\sqrt{\nu x/U_M})(U_M t/x)^{-(c_x+0.5)})$. So we find that the disturbance u_{BE} to the velocity u_R (the Rayleigh velocity) and the disturbance $(t/U_M)(\partial u_{BE}/\partial t + u_R\partial u_{BE}/\partial x + v_{BE}\partial u_R/\partial y)$ to the force $(t/U_M)(\partial u_R/\partial t)$ die out as $U_M t/x \to o$ such that the ratio $(u_R\partial u_{BE}/\partial x + v_{BE}\partial u_R/\partial y)/(\partial u_{BE}/\partial t) = O(U_M t/x)$. Similarly from the definition for c_t, we have $u_{RE}/U_M = O((y/\sqrt{\nu t})(x/U_M t)^{-(c_t+0.5)})$. We find that the disturbance u_{RE} to the velocity u_B (the Blasius velocity) and the disturbance $(x/U_M^2)(\partial u_{RE}/\partial t + u_B\partial u_{RE}/\partial x + u_{RE}\partial u_B/\partial x + v_B\partial u_{RE}/\partial y + v_{RE}\partial u_B/\partial y)$ to the force $(x/U_M^2)(u_B\partial u_B/\partial x + v_B\partial u_B/\partial y)$ die out as $(x/U_M t) \to o$ such that the ratio $(u_B\partial u_{RE}/\partial x + u_{RE}\partial u_B/\partial x + v_B\partial u_{RE}/\partial y + v_{RE}\partial u_B/\partial y)/(\partial u_{RE}/\partial t) = O(U_M t/x)$ (where v_B is the velocity component in the y-direction corresponding to u_B).

Contributed by the Applied Mechanics Division of THE AMERICAN SOCIETY OF MECHANICAL ENGINEERS for publication in the ASME JOURNAL OF APPLIED MECHANICS.

Discussion on this paper should be addressed to the Technical Editor, Professor Lewis T. Wheeler, Department of Mechanical Engineering, University of Houston, Houston, TX 77204-4792, and will be accepted until four months after final publication of the paper itself in the ASME JOURNAL OF APPLIED MECHANICS.

Manuscript received by the ASME Applied Mechanics Division, Nov. 4, 1993; final revision, Oct. 10, 1994. Associate Technical Editor: S. Lichter.

 Copyright © 1998 by ASME

Downloaded 04 May 2010 to 171.66.16.26. Redistribution subject to ASME license or copyright; see http://www.asme.org/terms/Terms_Use.cfm

The parameters c_x and c_t are called angular parameters because they give in a way (as explained above) the relative measure of the tangent of the angle of the disturbing velocity to the tangent of the angle of the position vector. This leads to the definition of an eigenvector. That is, an eigenvector is that for which the gradient is proportional to that of the position vector in the neighbourhood of a wall. The physics of a flow will necessarily depend on the proportionality constant independent of y. This means the undisturbed velocity is not only disturbed in magnitude but also in direction. The disturbing velocity field gets disintegrated in terms of the directions. As seen in this paper, for a polynomial solution of Nth degree, there will be $(N-1)$ possible eigenvalues for $l\,(=l_r,\ r = 1, 2, 3, \ldots, N-1)$ and correspondingly $(N-1)$ possible eigen solutions, giving what is called a general Blasius-based eigen velocity u_{BE} as a linear combination of all these $(N-1)$ solutions, summed over all the $(N-1)$ eigenvalues. Similarly there will be a general Rayleigh-based eigen velocity u_{RE} corresponding to $(N-1)$ possible eigenvalues for $m\ (=m_r,\ r = 1, 2, 3, \ldots, N-1)$. Thus the disturbing velocity vector is broken into a discrete set of vectors corresponding to a set of angles or directions related to the discrete set of eigenvalues.

The convective parameter $U_M t/x$ which is defined as a relative measure of the spatial to local inertia force is not of order 1 in general. In Stewartson's work (1951), this parameter is not treated as a force parameter, but only as a dimensionless time variable. From Sarma (1991), the orders of x and t are $x = O(U_M \delta_B^2/\nu)$ and $t = O(\delta_R^2/\nu)$ (where $\nu = \mu/\rho$ and ρ density); δ_R and δ_B are the thicknesses in Rayleigh (1911) and Blasius (1908) flows. So the convective parameter is of order $(\delta_R/\delta_B)^2$. The disturbing part of the velocity as found in this paper is of the convective order $(\delta_R/\delta_B)^{2\lambda}$ (where λ is an eigenvalue). In Prandtl's theory (1904), neither the angular parameters nor the convective parameter nor the convective orders exist. These are new to the theory, which take care of the most important effect of convection on diffusion. With constant orders for x and t, in Prandtl's theory, it is assumed $U_M t/x = 1$ to be true everywhere in the flow against reality. For example, in the case of Rayleigh flow, the spatial inertia force is zero and so $U_M t/x = 0$ and in Blasius flow local inertia force is zero and so $U_M t/x = \infty$. In the disturbed flow $U_M t/x$ varies from 0 to ∞. If $U_M t/x = 1$ is taken, as in Prandtl's theory (1904) and as in Stewartson's work (1951), the local and spatial inertia forces when they occur together do not know how one dominates over the other convectively.

In this paper the flow field with respect to the magnitude of the convective parameter is divided into four regions or layers: (i) the Rayleigh layer where $u = u_R(\eta_R)$, $\eta_R = y/\delta_R$ for $\delta = \delta_R$; (ii) the Rayleigh-based disturbed layer where $u = u_{RB}(\eta_R, \eta_B, T, c_x)$, $\eta_B = y/\delta_B$, $T = U_M t/x = O(\delta_R^2/\delta_B^2)$ for $\delta_R \le \delta = \delta_{RB} \le \delta_J$, δ_J the thickness in the common region where all the forces are of the same order and δ_{RB} that in Rayleigh-based disturbed flow; (iii) the Blasius-based disturbed layer where $u = u_{BB}(\eta_R, \eta_B, T, c_t)$ for $\delta_J \le \delta = \delta_{BB} \le \delta_B$, δ_{BB} the thickness in Blasius-based disturbed flow; and (iv) the Blasius layer where $u = u_B(\eta_B)$ for $\delta = \delta_B$.

Each inertia force, spatial or local, has a dual role as a basic dominating force and as a small disturbing force. Whatever may be the role, the role can not change the physical character of a force. That is, the spatial inertia force together with the viscous force produces a Blasius layer and also a disturbing Blasius-based eigenlayer, both of the same thickness. Both these layers are determined as two parts of a general solution u_{GB} of the Blasius equation given by $u_{GB} = u_B(\eta_B) + u_{BE}(\eta_B) + u_{BE}(\eta_B, T, c_x)$. Similarly the local inertia force also produces two layers and the general solution u_{GR} of the Rayleigh equation is $u_{GR} = u_R(\eta_R) + u_{RE}(\eta_R, T, c_t)$. Now the question is, these eigen layers are disturbances to what and in continuity with what? In order to treat a general solution u_{GB} or u_{GR} as an approximate solution of the full boundary layer equation, the disturbing part can not be treated as a disturbance to undisturbed part if both the parts are due to the same force and due to the layers of the same thickness. In other words no disturbance is possible between forces of the same convective order. Just as a viscous flow cannot be treated as a perturbed non-viscous flow, it can not even be treated (when the flow is due to forces of different convective orders) as a perturbed viscous flow due to forces of equal convective orders. This is because, a force which produces an undisturbed state cannot act as a disturbing force to the same state and also because the convective behavior of the disturbance is not in continuity with the undisturbed part, but in continuity if the two parts are due to forces of different convective orders. So the disturbing Blasius based eigen velocity u_{BE} from the spatial inertia force is rightly treated as a disturbance to the basic Rayleigh velocity u_R from local inertia force and vice versa. This type of combination facilitates smooth local and global convective behaviors. Thus the Rayleigh-based disturbed velocity u_{RB} and the Blasius based disturbed velocity u_{BB} are taken as $u_{RB} = u_R + u_{BE}$ and $u_{BB} = u_B + u_{RE}$. Here the eigensolutions u_{BE} and u_{RE} act as trial solutions in u_{RB} and u_{BB}. The concept of layers, the combination of layers and various parameters indicate that the convective transition from Rayleigh to Blasius layer is not because of time t alone or of space x alone or of linearity or of nonlinearity but because of both space and time through the convective parameter $U_M t/x$ and through the angular parameters c_x and c_t whereas the diffusive transition from viscous to nonviscous takes place due to vorticity variation in the direction normal to a wall. This in a way also suggests the fact that both the inertia forces have equal chances to play their roles in every phenomenon in fluids through their varying magnitudes, keeping the physics in tact.

The velocities u_{RB} and u_{BB} still contain arbitrary eigen functions and eigenvalues. These are determined using the initial, boundary and matching conditions and the equations of motion by the method of weighted residuals. For all velocities fourth-degree polynomials are constructed, except for Blasius velocity u_B for which up to the 8th degree are found. To determine the coefficients in a polynomial, along with the essential conditions, instead of the differential equations their weighted integral equations are used treating the stream function and its powers as weight functions. Natural local conditions derived from the differential equations are not used as in Pohlhausen (1921). Integration of the equations suppresses the diffusive nature resulting in equations for convective balance. Such equations are used by Schtichting (1933) and Glauert (1956) in the analysis of free and wall jets. The friction term, in the integral equations used in this paper, at the edge of a layer is not omitted just as in Von Karman (1921), for the reasons of unknown magnitude of the error which will be introduced by omission. With the polynomial solutions, different thicknesses of order n are calculated numerically using the following integral definitions:

$$\delta_D^{(n)} = \int_0^\delta s^n(1-\bar{u})dy, \quad \delta_M^{(n)} = \int_0^\delta s^n\bar{u}(1-\bar{u})dy, \quad (1a)$$

$$\delta_V^{(n)} = -\frac{\mu\delta}{\tau}\int_0^\delta s^n\frac{\partial^2 u}{\partial y^2}\,dy, \quad \delta_E^{(n)} = \int_0^\delta s^n\bar{u}(1-\bar{u}^2)dy, \quad (1b)$$

where $s = \psi/U_M\delta$ (ψ the stream function), $\bar{u} = u/U_M$; $\delta_D^{(n)}$, $\delta_M^{(n)}$, $\delta_V^{(n)}$, and $\delta_E^{(n)}$ are displacement, momentum, vorticity, and energy thicknesses, respectively; and U_M a constant velocity in the main stream. The paper also modifies the concept of approximation and the numerical value of t in Rayleigh analogy (1911) to be $2.337x/U_M$ instead of x/U_M to get the skin friction in Blasius flow from that in Rayleigh flow. It establishes the fact that it is not the Reynolds number alone which distinguishes the magnitudes of various forces and which can control both the diffusive and convective phenomena in fluids and also modifies the Prandtl's assumption (1904) that all forces are of the

Downloaded 04 May 2010 to 171.66.16.26. Redistribution subject to ASME license or copyright; see http://www.asme.org/terms/Terms_Use.cfm

same order of magnitude and confirms the views of Seth (1960). The numerical behavior of the velocities explain how smooth transitions with no singularities can take place in fluids through convective and angular parameters.

2 Integral Equations and Polynomial Solutions of Blasius and Rayleigh Flows

The boundary layer equations of Blasius and Rayleigh flows are $u_{GB}\partial u_{GB}/\partial x + v_{GB}\partial u_{GB}/\partial y = \nu\partial^2 u_{GB}/\partial y^2$, $\partial u_{GB}/\partial x + \partial v_{GB}/\partial y = 0$ and $\partial u_{GR}/\partial t = \nu\partial^2 u_{GR}/\partial y^2$, $\partial u_{GR}/\partial x + \partial v_{GR}/\partial y = 0$ (v_{GB} and v_{GR} are the velocities in the y direction). The momentum integral equations of order n of these differential equations, using nth order stream function as a weight function, are

$$\frac{\partial}{\partial x}\int_0^{\delta_B} \frac{\psi_{GB}^{n+1}}{(n+1)}\frac{\partial u_{GB}}{\partial y}\,dy + \nu\int_0^{\delta_B}\psi_{GB}^{n}\frac{\partial^2 u_{GB}}{\partial y^2}\,dy = 0, \quad (2)$$

$$-\int_0^{\delta_R}\psi_{GR}^{n}\frac{\partial u_{GR}}{\partial t}\,dy + \nu\int_0^{\delta_B}\psi_{GR}^{n}\frac{\partial^2 u_{GR}}{\partial y^2}\,dy = 0. \quad (3)$$

These will be equations for convective balance. To find the solutions u_B, u_{BE}, u_R, and u_{RE} satisfying the Eqs. (2) and (3), let us assume Nth degree polynomials of the form

$$\frac{u_{GB}}{U_M} = \sum_{i=1}^{N} a_i(x,t)\eta_B^i, \quad \frac{u_B}{U_M} = \sum_{i=1}^{N} a_{i,o}\eta_B^i,$$

$$\frac{u_{BE}}{U_M} = x^l\sum_{i=1}^{N} a_{i,1}(t)\eta_B^i, \quad (4)$$

$$\frac{u_{GR}}{U_M} = \sum_{i=1}^{N} b_i(x,t)\eta_R^i, \quad \frac{u_R}{U_M} = \sum_{i=1}^{N} b_{i,o}\eta_R^i,$$

$$\frac{u_{RE}}{U_M} = t^m\sum_{i=1}^{N} b_{i,1}(x)\eta_R^i, \quad (5)$$

where $a_i(x,t) = a_{i,o} + x^l a_{i,1}(t)$, $b_i(x,t) = b_{i,o} + t^m b_{i,1}(x)$; $a_{i,o}$, $b_{i,o}$, l and m are constants; $a_{i,1}$ and $b_{i,1}$ are arbitrary functions of t and x, respectively. The explicit dependence on x and t is due to the unknown convective nature in a flow, but not due to pressure gradient or shape factor. In view of the algebraic dependence of δ_B on x and δ_R on t, power series in x for a_i and in t for b_i are assumed. As a first approximation, the terms of order x^l and t^m are only considered in Eqs. (4) and (5). The break ups of a_i and b_i automatically break the velocity fields into the basic and eigen parts based on convective nature. These parts have to satisfy the essential boundary conditions

$$u_B = v_B = u_R = v_R = u_{BE} = v_{BE} = u_{RE} = v_{RE} = 0 \text{ at } y = 0, \quad (6)$$

$$u_B = U_M, \quad u_{BE} = 0 \quad \text{at} \quad \eta_B = 1 \quad \text{and}$$

$$u_R = U_M, \quad u_{RE} = 0 \quad \text{at} \quad \eta_R = 1. \quad (7)$$

Subjecting the Eqs. (4) and (5) to the conditions in Eqs. (6) and (7) and then substituting in Eqs. (2) and (3) and equating the coefficients of various powers of x and t we get the equations for $a_{i,o}$, $a_{i,1}$, $b_{i,o}$, and $b_{i,1}$ given in the Appendix.

2.1 Blasius Velocity u_B and its Numerical Solution. The force constant Λ_B defined in the Appendix and the coefficients $a_{i,o}$ in the solution u_B in Eq. (4) are determined from the equations for $a_{i,o}$ given in the Appendix. The equations being nonlinear, they are solved numerically by Newton-Raphson iterative method. According to that method, it is assumed $a_{i,o} = \bar{a}_{i,o} + H_i$ where $\bar{a}_{i,o}$ are the approximate values and H_i are the correction factors to them. Linearizing the system by writing Taylor's series of g_i (which are defined in the Appendix) about $\bar{a}_{i,o}$, we get the system of linear equations for H_i given by $g_i + \sum_{q=1}^{N} H_q g_{iq} = 0$, $g_{iq} = \partial g_i/\partial \bar{a}_{q,o}$ for $i = 1, 2, \ldots, N$ and $g_o = 1/\Lambda_B$. These equations are solved numerically by Gauss elimination method and also by the method of steepest descent and the process is iterated to get the values of $a_{i,o}$ and Λ_B to the desired accuracy. According to the method of steepest descent the values of H_i are given by $H = -\bar{\mu}W'g$, $\bar{\mu} = g'WW'g/(WW'g)'(WW'g)$ where H and g are two column matrices with elements H_i and g_i, respectively, and W is a square matrix with elements g_{iq}, the dash being the transpose of a matrix. For a fourth-degree velocity profile, when $N = 4$, the starting values of $a_{i,o}$ are 2, 0, −2, 1 for $i = 1$ to 4 same as those given by Pohlhausen (1921). Table 2 given in the Appendix records the characteristic quantities: the force constant, the skin friction coefficient and the other dimensionless boundary layer, displacement, momentum, and vorticity thicknesses in Blasius flow are calculated as per the definitions in Eqs. (1). It is found that the Newton-Raphson method combined with the Gauss elimination gives more accurate results than those by the method of descent. But both are accurate in comparison with the Pohlhausen's method (1921). The inaccuracy in Pohlhausen's method may be due to the forcing natural condition $\nu(\partial u_B/\partial y)_{\delta_B} = 0$ at the finite distance $y = \delta_B$. The results for $N = 5$ to 8 by the method of descent improve the accuracy systematically. Table 1 given in Appendix gives the velocity profiles for polynomials of different degrees. It is also found that the exact value 0.01134 of $(\partial u_B/\partial y)_{\delta_B}\sqrt{\nu x/U_M^3}$ is more closer to the value 0.01061 as predicted in this paper than to the value zero assumed by Pohlhausen at $y = \delta_B$. From the Blasius solution, the exact value is calculated for $\delta_B = 5.2\sqrt{\nu x/U_M}$ for which $u_B = 0.99U_M$, sacrificing some accuracy because it is impossible to indicate the thickness in an unambiguous way.

2.2 Blasius-Based Eigen Velocity u_{BE} and its Polynomial. The solution of the linear homogeneous equations given in the Appendix for the functions $a_{i,1}(t)$ and for the constant l determine the polynomial solution u_{BE} in Eq. (4). These equations will have a nontrivial solution if

$$\begin{vmatrix} 1 & 1 & \cdots & 1 \\ E_{1,1} + lF_{1,1} & E_{2,1} + lF_{2,1} & \cdots & E_{N,1} + lF_{N,1} \\ \cdots & \cdots & \cdots & \cdots \\ \cdots & \cdots & \cdots & \cdots \\ E_{1,N-1} + lF_{1,N-1} & E_{2,N-1} + lF_{2,N-1} & \cdots & E_{N,N-1} + lF_{N,N-1} \end{vmatrix} = 0. \quad (8)$$

The roots of Eq. (8) $l = l_r$ ($r = 1, 2, \ldots, N-1$) are the eigenvalues. Because of Eq. (8) the N linearly independent equations get reduced to $N-1$ equations in N unknowns. If $a_{N,1} \neq 0$, the first $N-1$ equations, corresponding to an eigenvalue l_r, can be written in terms of $N-1$ ratios $a_{p,1}/a_{N,1}$ ($=a_p^{(r)}$), for $p = 1, 2, \ldots, N-1$ with $a_N^{(r)} = 1$. As explained in Sarma (1991), $a_{N,1}x^{l_r}$ is taken to be equal to $(\delta_R/\delta_B)^{-(2L_r+1)}$ for a smooth joining of the velocity fields in the common region of Blasius based and Rayleigh based flows, where $2l_r = (2L_r + 1)$, L_r being the angular parameters. Thus the general eigen solution is a linear combination of all eigen solutions given by Eq. (4) for $l = l_r$ ($r = 1, 2, 3, \ldots, N-1$). Summation over all r gives

$$\frac{u_{BE}}{U_M} = \sum_{r=1}^{N-1}\sum_{i=1}^{N} T_r a_i^{(r)}(\delta_R/\delta_B)^{-(2L_r+1)}\eta_B^i, \quad (9)$$

where T_r are arbitrary constants to be determined by matching conditions in the common region. For $N = 4$, the equations for $a_i^{(r)}$ are solved by the Gauss elimination method. The values of L_r and $a_i^{(r)}$ are found to be

$$L_1 = -1.700829,$$

$$a_i^{(1)} = 0.496985, 0.072580, -1.569565, 1.0,$$

Downloaded 04 May 2010 to 171.66.16.26. Redistribution subject to ASME license or copyright; see http://www.asme.org/terms/Terms_Use.cfm

$$L_2 = -6.066926,$$

$$a_i^{(2)} = 3.518291, -7.310884, 2.792593, 1.0,$$

$$L_3 = -18.740286,$$

$$a_i^{(3)} = -0.555414, 1.992418, -2.437005, 1.0.$$

The angular parameters are all negative and the eigen solution given by (9) goes to zero as $\delta_R/\delta_B\ (=0(\sqrt{U_M t/x}))$ goes to zero and so the region relevant to the solution is that for large x and small t. The Blasius equation which is supposed to be true for small x and large t induces an eigen solution valid for large x and small t. Thus the eigen solution given by (9) because of its convective behavior is treated as a trial solution in the Rayleigh-based disturbed solution u_{RB}. It is also important to note how the disturbing velocity is broken into diffusive layers of different convective orders $(\delta_R/\delta_B)^{-(2L_r+1)}$.

2.3 Rayleigh Velocity u_R and its Numerical Solution. To determine the solution u_R given by Eq. (5), the equations for $b_{i,o}$ given in the Appendix are solved numerically, exactly in the same way as explained in Section 2.1 for a Blasius solution u_B. For $N = 4$, the solution u_R as determined by the method of steepest descent is

$$\frac{u_R}{U_M} = 1.965185\eta_R - 0.015547\eta_R^2 - 1.987370\eta_R^3 + 1.037730\eta_R^4,$$
$$= \text{erf}\,(\bar{\eta}_R),\ \bar{\eta}_R = y/2\sqrt{\nu t}\ \text{(Exact Rayleigh solution)}. \tag{10}$$

Table 3 given in the Appendix contains the numerical values of the force constant $\Lambda_R\ (=\delta_R^2/2\nu t)$, the skin friction coefficient and the other thicknesses calculated as per the definitions in Eqs. (1). Again the Table 3 indicates that the higher order integral methods over those with local conditions give good accurate results, because the exact value 0.0314 of $(\partial u_R/\partial y)\sqrt{\nu t/U_M^2}\ (=\exp(-\bar{\eta}_R^2)/\sqrt{\pi}$ for $\bar{\eta}_R = \delta_R/2\sqrt{\nu t} = 1.7 \approx 1.718$ from Table 3) is closer to the value 0.0358 (given in Table 3 using three integral conditions as in Blasius flow) than to the local value zero (which is supposed to be one of the conditions to be used in constructing a fourth-degree velocity profile following Pohlhausen's technique).

2.4 Rayleigh-Based Eigen Velocity u_{RE} and its Polynomial. The solution of the linear homogeneous equations for $b_{i,1}$ given in the Appendix determine the Rayleigh-based eigen solution u_{RE} given in Eq. (5). As in the case of Blasius-based eigenflow in Section 2.2, the general eigen solution u_{RE} is given by a linear combination of all eigen solutions given by Eq. (5) for $m = m_r$ ($r = 1, 2, 3, \ldots, N-1$). Summation over all r gives

$$\frac{u_{RE}}{U_M} = \sum_{r=1}^{N-1}\sum_{i=1}^{N} X_r b_i^{(r)} (\delta_B/\delta_R)^{-(2M_r+1)} \eta_R^i, \tag{11}$$

where X_r are arbitrary constants to be determined by matching the Blasius-based and Rayleigh-based disturbed solutions. The constants $M_r\ (=m_r - 0.5)$ for $r = 1, 2, \ldots, N-1$ are the angular parameters, m_r being the eigenvalues. The numerical values of the constants M_r and $b_i^{(r)}$ are found to be

$$M_1 = -1.813992,$$

$$b_i^{(1)} = 1.373981, -1.508143, -0.865838, 1.0,$$

$$M_2 = -5.834829,$$

$$b_i^{(2)} = -0.641187, 2.417174, -2.775987, 1.0,$$

$$M_3 = -17.166608,$$

$$b_i^{(3)} = -0.212495, 1.210667, -1.998172, 1.0.$$

The solution (11) goes to zero as $\delta_B/\delta_R\ (=O(\sqrt{x/U_M t}))$ goes to zero. The local inertia force of order y induces an eigen solution valid for small x and large t and so it is used as a trial solution in Blasius-based disturbed solution u_{BB}. The disturbing velocity due to local inertia force is broken into diffusive layers of convective orders $(\delta_B/\delta_R)^{-(2M_r+1)}$.

3 Rayleigh and Blasius-Based Disturbed Velocities u_{RB} and u_{BB} and Their Numerical Solutions

Having determined the basic and the disturbing velocities, with the proper combination of those velocities as indicated in Section 1, the polynomial solutions of the disturbed velocities u_{RB} and u_{BB} will be of the form

$$u_{RB} = u_R + u_{BE} = U_M \sum_{i=1}^{N} R^{(i)} \eta_B^i,$$

$$u_{BB} = u_B + u_{RE} = U_M \sum_{i=1}^{N} B^{(i)} \eta_B^i, \tag{12}$$

$$v_{RB} = \frac{U_M \delta_B}{x} \sum_{r=1}^{N-1}\sum_{i=1}^{N} T_r \left(\frac{-2l_r + i}{2i+2}\right)\left(\frac{\delta_R}{\delta_B}\right)^{-2l_r} a_i^{(r)} \eta_B^{i+1}, \tag{13}$$

$$v_{BB} = \frac{U_M \delta_B}{x} \sum_{i=1}^{N} \frac{i a_{i,o}}{2i+2} \eta_B^{i+1} + \frac{U_M \delta_R}{x} \sum_{r=1}^{N-1}\sum_{i=1}^{N} \frac{X_r m_r}{i+1}\left(\frac{\delta_B}{\delta_R}\right)^{-2m_r} b_i^{(r)} \eta_R^{i+1}, \tag{14}$$

$$R^{(i)} = b_{i,o}\left(\frac{\delta_B}{\delta_R}\right)^i + \sum_{r=1}^{N-1} T_r \left(\frac{\delta_R}{\delta_B}\right)^{-2l_r} a_i^{(r)}, \tag{15}$$

$$B^{(i)} = a_{i,o} + \sum_{r=1}^{N-1} X_r \left(\frac{\delta_B}{\delta_R}\right)^{-2m_r+i} b_i^{(r)}, \quad \eta_R = (\delta_B/\delta_R)\eta_B. \tag{16}$$

These above forms for the solutions still contain unknown constants X_r and T_r and yet the solutions also have to satisfy the equations of motion:

$$\partial u_{RB}/\partial x + \partial v_{RB}/\partial y = 0,$$

$$\partial u_{RB}/\partial t + u_{RB}\partial u_{RB}/\partial x + v_{RB}\partial u_{RB}/\partial y = \nu \partial^2 u_{RB}/\partial y^2,$$

$$\partial u_{BB}/\partial x + \partial v_{BB}/\partial y = 0,$$

$$\partial u_{BB}/\partial t + u_{BB}\partial u_{BB}/\partial x + v_{BB}\partial u_{BB}/\partial y = \nu \partial^2 u_{BB}/\partial y^2.$$

Instead of using these differential equations directly, their nth-order integral equations which are given below are used:

$$-\int_0^{\delta_{RB}} \psi_{RB}^n \frac{\partial u_{RB}}{\partial t}\, dy + \frac{\partial}{\partial x}\int_0^{\delta_{RB}} \frac{\psi_{RB}^{n+1}}{n+1}\frac{\partial u_{RB}}{\partial y}\, dy + \nu \int_0^{\delta_{RB}} \psi_{RB}^n \frac{\partial^2 u_{RB}}{\partial y^2}\, dy = 0, \tag{17}$$

$$-\int_0^{\delta_{BB}} \psi_{BB}^n \frac{\partial u_{BB}}{\partial t}\, dy + \frac{\partial}{\partial x}\int_0^{\delta_{BB}} \frac{\psi_{BB}^{n+1}}{n+1}\frac{\partial u_{BB}}{\partial y}\, dy + \nu \int_0^{\delta_{BB}} \psi_{BB}^n \frac{\partial^2 u_{BB}}{\partial y^2}\, dy = 0. \tag{18}$$

The solutions (12) to (14) automatically satisfy the boundary conditions (6) and the continuity conditions (or the initial conditions) $u_{RB} \to u_R$ as $t \to o$ and $x \to \infty$ (or $\delta_R/\delta_B \to o$) and $u_{BB} \to u_B$ as $t \to \infty$ and $x \to o$ (or $\delta_B/\delta_R \to o$). And yet they have to satisfy the matching, the v-continuity condition in the main stream, and the boundary conditions (7) in addition to the inte-

Downloaded 04 May 2010 to 171.66.16.26. Redistribution subject to ASME license or copyright; see http://www.asme.org/terms/Terms_Use.cfm

gral conditions (17) and (18). When $N = 4$, there are eight constants T_r and X_r ($r = 1, 2, 3$), δ_R/δ_B and δ_J/δ_B to be determined numerically. So we use (i) four matching conditions $R^{(i)} = B^{(i)}$ for $i = 1$ to 4 (a consequence of $u_{RB} = u_{BB}$ for all $y = \delta_{RB} = \delta_{\cdot B} = \delta_J$ in the common region where all the forces and thicknesses are of the same order for some value of δ_R/δ_B), (ii) the v-continuity condition $v_{RB} = v_{BB}$ at $y = \delta_J$; (iii) one boundary condition $\sum_{i=1}^{N} R^{(i)}(\delta_J/\delta_B)^i = 1$ where $u_{RB} = U_M$ at $y = \delta_{RB} = \delta_J$ (the other condition $u_{BB} = U_M$ at $y = \delta_{BB} = \delta_J$ is satisfied automatically because of the matching conditions in (i)); and (iv) two linearized integral conditions (17) and (18) for order zero. Thus the numerical values calculated by iterative method are

$$T_r = 0.470113,\ 0.006825,\ -0.140581, \quad \delta_R/\delta_B = 0.999972.$$

$$X_r = 0.284966,\ -0.321377,\ 0.246562, \quad \delta_J/\delta_B = 0.999991.$$

The dimensionless boundary layer thickness (δ/δ_B) is

$$\frac{\delta}{\delta_B} = \frac{\delta_R}{\delta_B} = \sqrt{\frac{\Lambda_R}{\Lambda_B}\left(\frac{U_M t}{x}\right)} \quad \text{when} \quad \delta = \delta_R,$$

$$= \frac{\delta_{RB}}{\delta_B} = 1.0 \Big/ \sum_{i=1}^{N} R^{(i)}(\delta_{RB}/\delta_B)^{i-1} \quad \text{for} \quad \delta_R \le \delta_{RB} \le \delta_J,$$

$$= \frac{\delta_{BB}}{\delta_B} = 1.0 \Big/ \sum_{i=1}^{N} B^{(i)}(\delta_{BB}/\delta_B)^{i-1} \quad \text{for} \quad \delta_J \le \delta_{BB} \le \delta_B,$$

$$= 1 \quad \text{when} \quad \delta = \delta_B.$$

The skin friction coefficient ($\tau\sqrt{U_M x/\nu})/\rho U_M^2 =$) τ^* is

$$\tau^* = \tau_R^* = (b_{1,o}/\sqrt{2\Lambda_B})(\delta_B/\delta_R) \quad \text{when} \quad \delta = \delta_R,$$

$$= \tau_{RB}^* = \tau_R^* + \sum_{r=1}^{N-1} T_r\left(\frac{\delta_R}{\delta_B}\right)^{-2l_r} \frac{a_1^{(r)}}{\sqrt{2\Lambda_B}}$$

$$\text{for} \quad \delta_R \le \delta_{RB} \le \delta_J,$$

$$= \tau_{BB}^* = \tau_B^* + \sum_{r=1}^{N-1} X_r\left(\frac{\delta_B}{\delta_R}\right)^{-2m_r+1} \frac{b_1^{(r)}}{\sqrt{2\Lambda_B}}$$

$$\text{for} \quad \delta_J \le \delta_{BB} \le \delta_B,$$

$$= \tau_B^* = \frac{a_{1,o}}{\sqrt{2\Lambda_B}} \quad \text{when} \quad \delta = \delta_B.$$

Table 4 gives the behavior of skin friction coefficient and the boundary layer thickness as functions of the convective parameter T whereas Table 5 gives the velocity profiles along with those of Rayleigh (1911), Hall (1969), Pohlhausen (1921), and Blasius (1908) for comparison purposes.

4 Conclusions

The omission of the skin friction term at the edge of a layer in the integral equation of order zero leads to an ill-conditioned system of equations when we go for higher orders. As the degree of the polynomial increases, higher degree polynomials determined by higher order integral equations are becoming closer to the exact solution systematically. The spatial and local inertia forces which are of unequal convective orders in general become equal approximately when the convective parameter $T = 2.337$. This helps us to get approximately the skin friction in Blasius flow from that in Rayleigh flow by replacing t by $2.337x/U_M$ instead by x/U_M as in Rayleigh analogy (1911). The fact of unequal convective orders for inertia forces dispels the most important belief in Prandtl's boundary layer theory (1904). The convective parameter T cannot be taken even approximately to be of order 1 in the flow field as the independent variables x and t become dependent and introduce degeneracy.

As against one similarity variable η_R or η_B and the parameter T (Stewartson, 1951), the Rayleigh-Blasius flow is described simultaneously by both the similarity variables η_R and η_B, the convective parameter T, and the angular parameters L_r and M_r. The velocity goes to depend purely on y and t through the similarity variable η_R alone when t is small and x is large as $T \to 0$ and becomes the Rayleigh velocity. Similarly it goes to depend purely on y and x through η_B alone when t is large and x is small as $T \to \infty$ and becomes the Blasius velocity. The two limiting flows are achieved asymptotically but not in the finite part of the x, t plane mathematically. The Rayleigh flow is disturbed by x from $x = \infty$, the local inertia force keeps its dominance approximately up to the value $T = 2.337$ where a continuous change of dominance from local to spatial inertia force takes place through equal dominance and then the flow steadies down very slowly as expected by Hall (1969) to match with the Blasius flow, losing the dependence on t. There is a slow algebraic matching up to an accuracy of four decimal places when $T = 290$ unlike quick exponential rapidity of transition as predicted mathematically by Stewartson (1951) and Watson (in the Appendix to Dennis, 1972) and numerically by Hall (1969) and Dennis (1972). The approach and the rate of approach of velocity to the limiting states are all smooth and effected by the conditions in the upstream and down-stream directions. The points $T = 1, \infty$ are no more points of essential singularities as visualised by Stewartson (1951). At these points the velocities assume higher values than those predicted by Hall (1969) and Dennis (1972). Neither pure Rayleigh flow exists up to $T = 1$ nor pure Blasius flow for $T > 4$.

Acknowledgment

The author would like to record his sincere thanks to Referee A for his comments which helped to modify the presentation of some parts of the paper and to Referee B who made me explain the theoretical background of the paper.

References

Blasius, H., 1908, "Grenzschichten in Flussigkeiten mit kleiner Reibung," *Zeitschrift fur Mathematik und Physik,* Vol. 56, pp. 1–37.

Dennis, S. C. R., 1972, "The Motion of a Viscous Fluid Past an Impulsively Started Semi-Infinite Flat Plate," *Journal of the Institute of Mathematics and its Applications,* Vol. 10, pp. 105–117.

Glauert, M. B., 1956, "The Wall Jet," *Journal of Fluid Mechanics,* Vol. 1, pp. 625–643.

Hall, M. G., 1969, "The Boundary Layer Over an Impulsively Started Flat Plate," *Proceedings of the Royal Society, London,* Vol. A.310, pp. 401–414.

Pohlhausen, K., 1921, "Zur Naberungsweisen Integration Der Differential-Gleichung Der Laminaren Reibungsschicht," *Zeitschrift fur angewandte Mathematik und Mechanik,* Vol. 1, pp. 252–268.

Prandtl, L., 1904, "Uber Flussigkeitsbewegung Bei Sher Kleiner Reibung," *Verhandlungen des III. Internationalen Mathematiker-Kongresses,* Heidelberg, Leipzig, pp. 484–491.

Rayleigh, Lord, 1911, "On the Motion of Solid Bodies Through Viscous Liquids," *Philosophical Magazine,* Vol. 21, No. 6, pp. 697–711.

Riley, N., 1975, "Unsteady Laminar Boundary Layers," *SIAM Review,* Vol. 17, No. 2, pp. 274–297.

Sarma, G. N., 1991, "Modified Boundary Layer Theory and Theory of Diffusion and Convection of Vortices, Part I—Definite Thickness Boundary Layers (Abridged version)," *Proceedings of the 7th International Conference on Numerical Methods in Laminar and Turbulent Flow,* Vol. 7, Part I, Stanford University, Stanford, CA, pp. 634–644.

Schlichting, H., 1933, "Laminare Strahlausbreitung," *Zeitschrift fur Angewandte Mathematik und Mechanik,* Vol. 13, pp. 260–263.

Seth, B. R., 1960, "Boundary Layer Research," *The Journal of the Indian Mathematical Society,* Vol. XXIV, Nos. 3 and 4, pp. 527–550.

Stewartson, K., 1951, "On the Impulsive Motion of a Flat Plate in a Viscous Fluid," *The Quarterly Journal of Mechanics and Applied Mathematics,* Vol. 4, pp. 182–198.

Stewartson, K., 1973, "On the Impulsive Motion of a Flat Plate in a Viscous Fluid, II," *The Quarterly Journal of Mechanics and Applied Mathematics,* Vol. 26, pp. 143–152.

Stuart, J. T., 1963, "Unsteady Boundary Layers," *Laminar Boundary Layers,* L. Rosenhead, ed.: Clarendon Press, Oxford, pp. 349–408.

Downloaded 04 May 2010 to 171.66.16.26. Redistribution subject to ASME license or copyright; see http://www.asme.org/terms/Terms_Use.cfm

Von Karman, Th., 1921, "Uber Laminare und Turbulente Reibung," *Zeitschrift fur Angewandte Mathematik und Mechanik,* Vol. 1, pp. 233–253.

APPENDIX

A.1 The equations for $a_{i,o}$ are

$$g_o = \frac{1}{\Lambda_B} = -\frac{[a_{1,o}K_{1,o}^{(o)} + \sum_{i=o}^{N-2}(i+2)a_{i+2,o}K_{1,o}^{(i+1)}]}{[\sum_{i=o}^{N-2}(i+2)(i+1)a_{i+2,o}K_{o,o}^{(i)}]}$$

$$g_1 = \sum_{i=1}^{N} a_{i,o} - 1 = 0,$$

$$g_{n+1} = a_{1,o}K_{n+1,o}^{(o)} + \sum_{i=o}^{N-2}(i+2)a_{i+2,o}(K_{n+1,o}^{(i+1)} + (i+1)g_oK_{n,o}^{(i)}) = 0,$$

where

$$K_{n,o}^{(p)} = \text{the part independent of } x^l \text{ in } \left(\int_0^1 \left(\frac{\psi_{GB}}{U_M\delta_B}\right)^n \eta_B^p d\eta_B\right),$$

$$= \frac{1}{p+1} \quad \text{for} \quad n = 0,$$

$$= \sum_{i=1}^{N} \frac{a_{i,o}}{i+1} K_{n-1,o}^{(i+p+1)} \quad \text{for} \quad n = 1, 2, \ldots, N-1.$$

A.2 The equations for $a_{p,1}$ are

$$\sum_{p=1}^{N} a_{p,1} = 0,$$

$$\sum_{p=1}^{N}(E_{p,n+1} + lF_{p,n+1})a_{p,1} = 0 \quad \text{for} \quad n = 0, 1, 2, \ldots, N-2,$$

where

$$E_{p,n} = \Lambda_B B_{p,n} + D_{p,n}, \quad F_{p,n} = \frac{2\Lambda_B}{n} B_{p,n},$$

$$B_{p,n} = pK_{n,o}^{(p-1)} + \sum_{i=1}^{N} \frac{nia_{i,o}}{(p+1)} K_{n-1,o}^{(i+p)},$$

$$D_{p,n} = p(p-1)K_{n-1,o}^{(p-2)} + \sum_{i=1}^{N} \frac{(n-1)i(i-1)a_{i,o}}{(p+1)} K_{n-2,o}^{(i+p-1)},$$

$$\Lambda_B = \frac{U_M\delta_B}{\nu}\frac{d\delta_B}{dx} = \frac{U_M\delta_B^2}{2\nu x} = \text{a force constant.}$$

A.3 The equations for $b_{i,o}$ are

$$f_o = \frac{1}{\Lambda_R} = -\frac{[b_{1,o}S_{o,o}^{(1)} + \sum_{i=0}^{N-2}(i+2)b_{i+2,o}S_{o,o}^{(i+2)}]}{[\sum_{i=0}^{N-2}(i+2)(i+1)b_{i+2,o}S_{o,o}^{(i)}]},$$

$$f_1 = \sum_{i=1}^{N} b_{i,0} - 1 = 0,$$

$$f_{n+1} = b_{1,o}S_{n,o}^{(1)} + \sum_{i=0}^{N-2}(i+2)b_{i+2,o}(S_{n,o}^{(i+2)} + (i+1)f_oS_{n,o}^{(i)}) = 0,$$

where the expressions for $S_{n,o}^{(p)}$ and Λ_R similar to those of $K_{n,o}^{(p)}$ and Λ_B can be written down easily.

A.4 The equation for $b_{p,1}$ are

$$\sum_{p=1}^{N} b_{p,1} = 0$$

$$\sum_{p=1}^{N}(\bar{E}_{p,n} + m\bar{F}_{p,n})b_{p,1} = 0 \quad \text{for} \quad n = 0, 1, 2, \ldots, N-2,$$

where $\bar{E}_{p,n}$ and $\bar{F}_{p,n}$ are similar to those of $E_{p,n}$ and $F_{p,n}$.

A.5 Tables of velocity profiles and characteristic quantities.

Table 1 Velocity profiles of different degrees of the basic Blasius flow

Degree of a profile	Method	Velocity profile
4	Newton-Raphson-Gauss elimination method with the initial values of the Pohlhausen's profile	$\frac{u_B}{U_M} = 1.7556057\eta_B + 0.59700325\eta_B^2 - 2.5165927\eta_B^3 + 1.1639837\eta_B^4$
5	Newton-Raphson-Steepest method with the initial values of the lower degree profile	$\frac{u_B}{U_M} = 1.7556077\eta_B + 0.59700228\eta_B^2 - 2.5165915\eta_B^3 + 1.1639841\eta_B^4 - 0.00000252\eta_B^5$
6	Newton-Raphson-Steepest method with the initial values of the lower degree profile	$\frac{u_B}{U_M} = = 1.7556081\eta_B + 0.5969998\eta_B^2 - 2.5165886\eta_B^3 + 1.1639878\eta_B^4 - 0.00000171\eta_B^5 - 0.00000533\eta_B^6$
7	Newton-Raphson-Steepest method with the initial values of the lower degree profile	$\frac{u_B}{U_M} = 1.7556062\eta_B + 0.59699614\eta_B^2 - 2.5165852\eta_B^3 + 1.1639934\eta_B^4 + 0.0000023\eta_B^5 - 0.00000579\eta_B^6 - 0.00000699\eta_B^7$
8	Newton-Raphson-Steepest method with the initial values of the lower degree profile	$\frac{u_B}{U_M} = 1.7556043\eta_B + 0.59699395\eta_B^2 - 2.51655835\eta_B^3 + 1.1639967\eta_B^4 + 0.00000539\eta_B^5 - 0.00000428\eta_B^6 - 0.00000805\eta_B^7 - 0.00000439\eta_B^8$
4	Pohlhausen's profile	$\frac{u_B}{U_M} = 2\eta_B - 2\eta_B^3 + \eta_B^4$
—	Exact solution	$\frac{u_B}{U_M} = \varphi'(\bar{\eta}_B), \bar{\eta}_B = y\sqrt{\frac{U_M}{\nu x}}, 2\varphi''' + \varphi\varphi'' = 0, \varphi(o) = \varphi'(o) = 0, \varphi'(\infty) = 1, \varphi'(5.2) = 0.99425, \left(\frac{1}{U_M}\frac{\partial u_B}{\partial y}\sqrt{\frac{\nu x}{U_M}}\right)_{5.2} = \varphi''(5.2) = 0.01134$

Downloaded 04 May 2010 to 171.66.16.26. Redistribution subject to ASME license or copyright; see http://www.asme.org/terms/Terms_Use.cfm

Table 2 The characteristic quantities associated with the basic Blasius layer

Degree of a profile	4	5	6	7	8	Pohlhausen's 4th degree	Exact at $\bar{\eta}_B = 5.2$
Λ_B	13.806503	13.806758	13.807005	13.807148	13.807236	17.027027	13.52
$\frac{\tau_B}{\rho U_M^2}\sqrt{\frac{U_M x}{\nu}}$	0.33409513	0.33409241	0.33408950	0.33408741	0.33408600	0.34272484	0.332057
$\delta_B\sqrt{\frac{U_M}{\nu x}}$	5.2548079	5.2548569	5.2549034	5.2549307	5.2549474	5.8355851	5.2
$\delta_{D,B}^{(o)}\sqrt{\frac{U_M}{\nu x}}$	1.6791607	1.6791730	1.6791868	1.6791978	1.6792056	1.7506755	1.7208
$\delta_{D,B}^{(1)}\sqrt{\frac{U_M}{\nu x}}$	0.12513397	0.12513431	0.12513489	0.12513571	0.12513641	—	—
$\delta_{M,B}^{(o)}\sqrt{\frac{U_M}{\nu x}}$	0.64696433	0.64696858	0.64697367	0.64697818	0.64698149	0.68544968	0.664
$\delta_{M,B}^{(1)}\sqrt{\frac{U_M}{\nu x}}$	0.08792934	0.08792952	0.08792993	0.08793058	0.08793113	—	—
$\delta_{v,B}^{(o)}\sqrt{\frac{U_M}{\nu x}}$	5.0878823	5.0879517	5.0880231	5.0880725	5.0881063	—	—
$\delta_{v,B}^{(1)}\sqrt{\frac{U_M}{\nu x}}$	1.382995	1.383021	1.383051	1.383076	1.383094	—	—
$\frac{1}{U_M}\left(\frac{\partial U_B}{\partial y}\right)\delta_B\sqrt{\frac{\nu x}{U_M}}$	0.0106139	0.0106114	0.0106197	0.0106082	0.0106070	0.0000000	0.01134

Table 3 The characteristic quantities associated with the basic Rayleigh layer

Λ_R	$\frac{\tau_R}{\rho U_M^2}\sqrt{\frac{U_M^2 t}{\nu}}$	$\frac{\delta_R}{\sqrt{\nu t}}$	$\frac{\delta_{D,R}^{(o)}}{\sqrt{\nu t}}$	$\frac{\delta_{D,R}^{(1)}}{\sqrt{\nu t}}$
5.90696437	0.57175015	3.43713961	1.07200486	0.084927106
$\frac{\delta_{M,R}^{(o)}}{\sqrt{\nu t}}$	$\frac{\delta_{M,R}^{(1)}}{\sqrt{\nu t}}$	$\frac{\delta_{v,R}^{(o)}}{\sqrt{\nu t}}$	$\frac{\delta_{v,R}^{(1)}}{\sqrt{\nu t}}$	$\frac{1}{U_M}\left(\frac{\partial u_R}{\partial y}\right)_{\delta_R}\sqrt{\nu t}$
0.42783074	0.060997964	3.22222445	0.72660447	0.035750034

Downloaded 04 May 2010 to 171.66.16.26. Redistribution subject to ASME license or copyright; see http://www.asme.org/terms/Terms_Use.cfm

Table 4 Values of skin friction coefficient and boundary layer thickness as functions of the convective parameter T

$T = \frac{U_M t}{x}$	τ^*	δ/δ_B	$T = \frac{U_M t}{x}$	τ^*	δ/δ_B
	τ^*_R	δ_R/δ_B		τ^*_{BB}	δ_{BB}/δ_B
0.001	18.08033	0.02068	2.33720	0.43786	0.99999
0.01	5.71750	0.06541	2.4	0.43239	0.99809
			2.5	0.42338	0.80300
	τ^*_{RB}	δ_{RB}/δ_B	2.6	0.41498	0.78461
0.01	5.71757	0.06540	3.0	0.39048	0.76614
0.05	2.55738	0.14588	3.4	0.37624	0.76751
0.1	1.80904	0.20515	3.6	0.37128	0.77025
0.4	0.90935	0.38651	3.8	0.36725	0.77359
0.6	0.74681	0.45358	4.0	0.36392	0.77724
1.0	0.58783	0.54995	4.5	0.35766	0.78690
1.4	0.50751	0.62862	5.0	0.35332	0.79650
1.8	0.45984	0.70911	10.0	0.33944	0.86567
2.2	0.43500	0.93996	20.0	0.33561	0.92915
2.3	0.43587	0.98780	30.0	0.33482	0.95755
2.33720	0.43786	0.99999	50.0	0.33438	0.98024
			100.0	0.33418	0.99369
			200.0	0.33412	0.99808
			300.0	0.33411	0.99906
			400.0	0.33410	0.99943
			440.0	0.33410	0.99952
			440.0		
				τ^*_B	δ_B/δ_B
				0.33410	1.00000

Downloaded 04 May 2010 to 171.66.16.26. Redistribution subject to ASME license or copyright; see http://www.asme.org/terms/Terms_Use.cfm

Table 5 Velocity profiles for different values of the convective parameter T in different convective regions (where $\eta_B = \bar{\eta}_B/\sqrt{2\Lambda_B}$, $\eta_R = \bar{\eta}_B/2\sqrt{T}$, and $\bar{u} = u/U_M$) and those of the other authors

T:	0.01	0.01	0.01	1.0	1.5	2.0	2.33720
$\bar{\eta}_B$	erf ($\bar{\eta}_R$)	$\bar{u}_R$	$\bar{u}_{RB}$	$\bar{u}_{RB}$ (Hall)	$\bar{u}_{RB}$ (Hall)	$\bar{u}_{RB}$ (Hall)	$\bar{u}_{RB} = \bar{u}_{BB}$
0.0	0.00000	0.00000	0.00000	0.00000 (0.0000)	0.00000 (0.0000)	0.00000 (0.0000)	0.00000
0.2	0.84270	0.86566	0.86567	0.11714 (0.1125)	0.09842 (0.0920)	0.08858 (0.0804)	0.08699
0.4	0.99532	1.03704	1.05707	0.23194 (0.2227)	0.19548 (0.1827)	0.17612 (0.1600)	0.17234
0.6	0.99998			0.34240 (0.3286)	0.28996 (0.2711)	0.26171 (0.2383)	0.25537
0.8	1.00000			0.44684 (0.4284)	0.38080 (0.3562)	0.34458 (0.3145)	0.33547
1.0				0.54383 (0.5205)	0.46707 (0.4638)	0.42400 (0.3881)	0.41210
1.2				0.63226 (0.6039)	0.54798 (0.5124)	0.49936 (0.4584)	0.48479
1.4				0.71132 (0.6778)	0.62288 (0.5823)	0.57015 (0.5249)	0.55314
1.6				0.78047 (0.7421)	0.69126 (0.6461)	0.63592 (0.5873)	0.61681
1.8				0.83945 (0.7969)	0.75277 (0.7036)	0.69634 (0.6452)	0.67554
2.0				0.88843 (0.8427)	0.80718 (0.7547)	0.75114 (0.6983)	0.72915
2.2				0.92766 (0.8802)	0.85440 (0.7996)	0.80018 (0.7465)	0.77750
2.4				0.95783 (0.9103)	0.89449 (0.8383)	0.84337 (0.7896)	0.82054
2.6				0.97987 (0.9340)	0.92764 (0.8713)	0.88074 (0.8276)	0.85828
2.8				0.99503 (0.9523)	0.95421 (0.8990)	0.91239 (0.8607)	0.89081
3.0				1.00484 (0.9661)	0.97466 (0.9219)	0.93854 (0.8890)	0.91827
3.2					0.98962 (0.9406)	0.95947 (0.9129)	0.94090
3.4					0.99984 (0.9554)	0.97556 (0.9327)	0.95898
3.6					1.00624 (0.9671)	0.98729 (0.9488)	0.97287
3.8						0.99522 (0.9617)	0.98300
4.0						1.00001 (0.9718)	0.98987
4.2							0.99404
4.4							0.99616
4.6							0.99692
4.8							0.99711
5.0							0.99757
5.2							0.99922
5.4							1.00302

T:	3.0	4.0	6.0	290.0	∞	Exact
$\bar{\eta}_B$	$\bar{u}_{BB}$ (Hall)	$\bar{u}_{BB}$ (Hall)	$\bar{u}_{BB}$ (Hall)	$\bar{u}_{BB}$	$\bar{u}_B$ (Pohlhausen)	$\varphi'(\bar{\eta}_B)$
0.0	0.00000 (0.0000)	0.00000 (0.0000)	0.00000 (0.0000)	0.00000	0.00000 (0.0000)	0.00000
0.2	0.07825 (0.0698)	0.07329 (0.0669)	0.07020 (0.0664)	0.06755	0.06755 (0.0685)	0.06641
0.4	0.15629 (0.1393)	0.14707 (0.1337)	0.14118 (0.1327)	0.13603	0.13603 (0.1365)	0.13277
0.6	0.23340 (0.2084)	0.22059 (0.2002)	0.21219 (0.1989)	0.20470	0.20469 (0.2036)	0.19894
0.8	0.30891 (0.2765)	0.29315 (0.2663)	0.28255 (0.2647)	0.27287	0.27286 (0.2694)	0.26471
1.0	0.38222 (0.3435)	0.36413 (0.3315)	0.35161 (0.3297)	0.33991	0.33990 (0.3335)	0.32979
1.2	0.45279 (0.4088)	0.43295 (0.3957)	0.41881 (0.3937)	0.40526	0.40524 (0.3957)	0.39378
1.4	0.52014 (0.4721)	0.49911 (0.4582)	0.48365 (0.4562)	0.46840	0.46838 (0.4555)	0.45627
1.6	0.58385 (0.5329)	0.56215 (0.5187)	0.54565 (0.5167)	0.52888	0.52887 (0.5128)	0.51676
1.8	0.64358 (0.5907)	0.62170 (0.5767)	0.60444 (0.5747)	0.58632	0.58630 (0.5673)	0.57477
2.0	0.69903 (0.6452)	0.67742 (0.6316)	0.65968 (0.6297)	0.64037	0.64034 (0.6187)	0.62977
2.2	0.74997 (0.6959)	0.72904 (0.6830)	0.71109 (0.6812)	0.69076	0.69074 (0.6670)	0.68132
2.4	0.79624 (0.7426)	0.77637 (0.7305)	0.75845 (0.7289)	0.73727	0.73725 (0.7120)	0.72899
2.6	0.83773 (0.7848)	0.81925 (0.7738)	0.80162 (0.7723)	0.77976	0.77973 (0.7536)	0.77246
2.8	0.87441 (0.8225)	0.85761 (0.8127)	0.84048 (0.8114)	0.81810	0.81807 (0.7917)	0.81152
3.0	0.90629 (0.8557)	0.89142 (0.8471)	0.87502 (0.8459)	0.85227	0.85224 (0.8262)	0.84605
3.2	0.93346 (0.8844)	0.92071 (0.8769)	0.90523 (0.8759)	0.88229	0.88225 (0.8574)	0.87609
3.4	0.95607 (0.9087)	0.94559 (0.9024)	0.93122 (0.9016)	0.90822	0.90818 (0.8849)	0.90177
3.6	0.97432 (0.9291)	0.96622 (0.9239)	0.95311 (0.9231)	0.93020	0.93016 (0.9091)	0.92333
3.8	0.98849 (0.9458)	0.98280 (0.9415)	0.97110 (0.9409)	0.94843	0.94839 (0.9299)	0.94112
4.0	0.99891 (0.9592)	0.99564 (0.9558)	0.98546 (0.9553)	0.96316	0.96311 (0.9475)	0.95552
4.2	1.00597 (0.9693)	1.00506 (0.9671)	0.99649 (0.9668)	0.97469	0.97465 (0.9621)	0.96696
4.4			1.00458 (0.9757)	0.98341	0.98336 (0.9739)	0.97587
4.6				0.98972	0.98968 (0.9830)	0.98269
4.8				0.99414	0.99408 (0.9898)	0.98779
5.0				0.99718	0.99713 (0.9945)	0.99175
5.2				0.99947	0.99942 (0.9976)	0.99425
5.4				1.00167	1.00161 (0.9992)	0.99616
5.6						0.99748
5.8						0.99838

Downloaded 04 May 2010 to 171.66.16.26. Redistribution subject to ASME license or copyright; see http://www.asme.org/terms/Terms_Use.cfm

Y. Y. Lin
Graduate Student

J. C. Sung[1]
Professor

Department of Civil Engineering,
National Cheng Kung University,
Tainan, Taiwan 70101, R.O.C.

Stress Singularities at the Apex of a Dissimilar Anisotropic Wedge

The complex form of the characteristic equation for the stress singularities of the order $r^{\lambda-1}$ ($0 < Re\,[\lambda] < 1$) for the dissimilar anisotropic wedges is derived. Special attention is then focused on the problems that are composed by two orthotropic materials. For such problems the characteristic equation is expressed in real forms from which the dependence of the singularities on the material parameters and wedge angles is investigated. The case of a single free-fixed wedge problem is particularly studied in detail. Numerical results for several special wedge geometries are also presented.

1 Introduction

Investigation of the order of stress singularities at the apex of a homogeneous isotropic wedge was treated very early by Williams (1952). He employed the eigenfunction expansion technique to study the singular nature for a single wedge problem subjected to different boundary conditions. Bogy, employing Mellin transform, studied a series of elastic wedge problems. Among them, some of his works are related to isotropic material compositions (Bogy, 1968, 1970, 1971; Bogy and Wang, 1971) while others are related to problems composed by two orthotropic wedges where the characteristic equation developed is suitable only for a specially aligned material principal axes for both wedges (Bogy, 1972; Kuo and Bogy, 1974a, b).

In the present work, characteristic equation for the stress singularities of the order $r^{\lambda-1}$ ($0 < \mathrm{Re}[\lambda] < 1$), where r is the radial distance from the apex of wedges, is derived for the dissimilar anisotropic elastic wedges. Characteristic equation obtained is expressed in terms of a determinant of a 3×3 matrix which is usually in complex forms. Special attention is then given to the dissimilar wedges composed by two orthotropic materials where their material principal axes are aligned so that they have no inclinations relative to the interface bonded by the two wedges. For such a problem, the characteristic equation is further expressed in real forms where the dependence of the material parameters is shown explicitly. Many other characteristic equations corresponding to wedge problems that are composed by degenerated materials, e.g., wedge problems composed by two isotropic materials, can be obtained from present results. The case of a single free-fixed wedge problem is particularly discussed. For a single free-fixed wedge, it is found that when the wedge angle γ is equal to $\pi/2$ or $3\pi/2$, their characteristic roots are independent of the material parameter δ and they are only functions of the material parameters κ and β_0. Numerical results for several special geometries of the wedge problems are also presented where the effects of the material parameters and the wedge angles on the order of singularities are examined.

2 Stroh Formalism

Consider a two-dimensional deformation of a linear elastic solid whose field quantities are functions of x_1 and x_2 only. The general expressions for the displacement $\mathbf{u}$ and stress function ϕ for such a deformation are (Eshelby et al., 1953; Stroh, 1958)

$$\mathbf{u} = 2\,\mathrm{Re}\{\mathbf{A}\mathbf{f}(\mathbf{z})\} \tag{1}$$

$$\phi = 2\,\mathrm{Re}\{\mathbf{B}\mathbf{f}(\mathbf{z})\} \tag{2}$$

where Re{ } denotes real part,

$$\mathbf{f}(\mathbf{z}) = (f_1(z_1), f_2(z_2), f_3(z_3))^T \tag{3}$$

with $z_k = x_1 + p_k x_2$, ($k = 1, 2, 3$). Superscript T represents transpose. Matrix $\mathbf{A}$ with components denoted by a_{kj} and constants p_k are determined from the following eigenvalue problem

$$\{c_{i1k1} + p_j(c_{i1k2} + c_{i2k1}) + p_j^2 c_{i2k2}\}\, a_{kj} = 0 \quad (\text{no sum on } j) \tag{4}$$

where c_{ijkl} are the elastic constants. Without loss of generality, one may take the imaginary part of p_k to be positive. Matrix $\mathbf{B}$ in Eq. (2) is defined by

$$\mathbf{B} = \mathbf{R}^T\mathbf{A} + \mathbf{T}\mathbf{A}\mathbf{P} \tag{5}$$

where

$$R_{ik} = c_{i1k2} \tag{6}$$

$$T_{ik} = c_{i2k2} \tag{7}$$

and $\mathbf{P} = \mathrm{diag}\,\langle p_1, p_2, p_3\rangle$. Along a plane curve with unit normal vector $\mathbf{n}$, the stress function ϕ is related to the stress vector $\mathbf{t}_n$ by (see e.g., Ting 1986)

$$\mathbf{t}_n = \frac{\partial \phi}{\partial s} \tag{8}$$

where s is the arc length of the curve. Matrices $\mathbf{A}$ and $\mathbf{B}$ appearing in Eqs. (1) and (2) satisfy the following orthogonality relations (Stroh, 1958; Chadwick and Smith, 1977):

$$\begin{bmatrix} \mathbf{A} & \bar{\mathbf{A}} \\ \mathbf{B} & \bar{\mathbf{B}} \end{bmatrix} \begin{bmatrix} \mathbf{B} & \bar{\mathbf{B}} \\ \mathbf{A} & \bar{\mathbf{A}} \end{bmatrix}^T = \begin{bmatrix} \mathbf{I} & \mathbf{0} \\ \mathbf{0} & \mathbf{I} \end{bmatrix} \tag{9}$$

where $\mathbf{I}$ is a 3×3 unit matrix and a bar over a quantity represents the conjugate of that quantity.

[1] To whom correspondence should be addressed.

Contributed by the Applied Mechanics Division of THE AMERICAN SOCIETY OF MECHANICAL ENGINEERS for publication in the ASME JOURNAL OF APPLIED MECHANICS.

Discussion on the paper should be addressed to the Technical Editor, Professor Lewis T. Wheeler, Department of Mechanical Engineering, University of Houston, Houston, TX 77204-4792, and will be accepted until four months after final publication of the paper itself in the ASME JOURNAL OF APPLIED MECHANICS.

Manuscript received by the ASME Applied Mechanics Division, Sept. 5, 1996; final revision, Oct. 15, 1997. Associate Technical Editor: X. Markenscoff.

 Copyright © 1998 by ASME

Downloaded 04 May 2010 to 171.66.16.26. Redistribution subject to ASME license or copyright; see http://www.asme.org/terms/Terms_Use.cfm

3 Characteristic Equation for Dissimilar Anisotropic Wedges

Stress singularities at the apex of a dissimilar anisotropic wedge as depicted in Fig. 1 can be effectively studied by assuming the functions in each region as

$$\mathbf{f}^{(1)} = \frac{c^{(1)}}{2}\left(\frac{r}{\hat{r}}\right)^{\lambda}\mathbf{\Lambda}^{(1)}(\theta, +\gamma_1, \lambda)\mathbf{q}^{(1)} + \frac{\bar{c}^{(1)}}{2}\left(\frac{r}{\hat{r}}\right)^{\bar{\lambda}}\mathbf{\Lambda}^{(1)}(\theta, +\gamma_1, \bar{\lambda})\bar{\mathbf{q}}^{(1)} \quad (10a)$$

$$\mathbf{f}^{(2)} = \frac{c^{(2)}}{2}\left(\frac{r}{\hat{r}}\right)^{\lambda}\mathbf{\Lambda}^{(2)}(\theta, -\gamma_2, \lambda)\mathbf{q}^{(2)} + \frac{\bar{c}^{(2)}}{2}\left(\frac{r}{\hat{r}}\right)^{\bar{\lambda}}\mathbf{\Lambda}^{(2)}(\theta, -\gamma_2, \bar{\lambda})\bar{\mathbf{q}}^{(2)} \quad (10b)$$

where $c^{(1)}$ and $c^{(2)}$ are complex constants, $\mathbf{q}^{(1)}$ and $\mathbf{q}^{(2)}$ are undetermined complex vectors, γ_1 and γ_2 are the wedge angles, $\hat{r}$ is a certain characteristic length scale and $\mathbf{\Lambda}^{(1)}$ and $\mathbf{\Lambda}^{(2)}$ are defined by

$$\mathbf{\Lambda}^{(1)}(\theta, +\gamma_1, \lambda) = \left\langle\left(\frac{\zeta^{(1)}(\theta)}{\zeta^{(1)}(+\gamma_1)}\right)^{\lambda}\right\rangle\mathbf{B}^{(1)T} = \mathrm{diag}\left[\left(\frac{\zeta_1^{(1)}(\theta)}{\zeta_1^{(1)}(+\gamma_1)}\right)^{\lambda}, \left(\frac{\zeta_2^{(1)}(\theta)}{\zeta_2^{(1)}(+\gamma_1)}\right)^{\lambda}, \left(\frac{\zeta_3^{(1)}(\theta)}{\zeta_3^{(1)}(+\gamma_1)}\right)^{\lambda}\right]\mathbf{B}^{(1)T} \quad (11a)$$

$$\mathbf{\Lambda}^{(2)}(\theta, -\gamma_2, \lambda) = \left\langle\left(\frac{\zeta^{(2)}(\theta)}{\zeta^{(2)}(-\gamma_2)}\right)^{\lambda}\right\rangle\mathbf{B}^{(2)T} = \mathrm{diag}\left[\left(\frac{\zeta_1^{(2)}(\theta)}{\zeta_1^{(2)}(-\gamma_2)}\right)^{\lambda}, \left(\frac{\zeta_2^{(2)}(\theta)}{\zeta_2^{(2)}(-\gamma_2)}\right)^{\lambda}, \left(\frac{\zeta_3^{(2)}(\theta)}{\zeta_3^{(2)}(-\gamma_2)}\right)^{\lambda}\right]\mathbf{B}^{(2)T} \quad (11b)$$

where

$$\zeta_j^{(\alpha)}(\theta) = \cos\theta + p_j^{(\alpha)}\sin\theta \ (\alpha = 1, 2) \quad (11c)$$

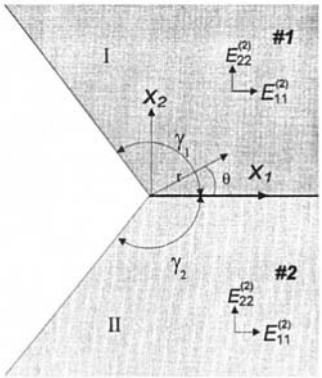


Fig. 1 Dissimilar anisotropic wedges

Substituting Eqs. (10) and (11) to Eqs. (1) and (2), the displacements, stress functions, and tractions in each wedge are given as follows:

$$\mathbf{u}^{(1)} = \mathrm{Re}\left\{c^{(1)}\left(\frac{r}{\hat{r}}\right)^{\lambda}\mathbf{h}^{(1)}(\theta, +\gamma_1, \lambda)\right\} \quad (12a)$$

$$\boldsymbol{\phi}^{(1)} = \mathrm{Re}\left\{c^{(1)}\left(\frac{r}{\hat{r}}\right)^{\lambda}\mathbf{g}^{(1)}(\theta, +\gamma_1, \lambda)\right\} \quad (12b)$$

$$\mathbf{t}_r^{(1)} = -\frac{\partial\boldsymbol{\phi}^{(1)}}{\partial r} = -\mathrm{Re}\left\{c^{(1)}\lambda\left(\frac{r}{\hat{r}}\right)^{\lambda-1}\mathbf{g}^{(1)}(\theta, +\gamma_1, \lambda)\right\} \quad (12c)$$

$$\mathbf{u}^{(2)} = \mathrm{Re}\left\{c^{(2)}\left(\frac{r}{\hat{r}}\right)^{\lambda}\mathbf{h}^{(2)}(\theta, -\gamma_2, \lambda)\right\} \quad (13a)$$

$$\boldsymbol{\phi}^{(2)} = \mathrm{Re}\left\{c^{(2)}\left(\frac{r}{\hat{r}}\right)^{\lambda}\mathbf{g}^{(2)}(\theta, -\gamma_2, \lambda)\right\} \quad (13b)$$

$$\mathbf{t}_r^{(2)} = -\frac{\partial\boldsymbol{\phi}^{(2)}}{\partial r} = -\mathrm{Re}\left\{c^{(2)}\lambda\left(\frac{r}{\hat{r}}\right)^{\lambda-1}\mathbf{g}^{(2)}(\theta, -\gamma_2, \lambda)\right\} \quad (13c)$$

where

$$\mathbf{h}^{(1)}(\theta, +\gamma_1, \lambda) = (\mathbf{A}^{(1)}\mathbf{\Lambda}^{(1)}(\theta, +\gamma_1, \lambda) + \overline{\mathbf{A}^{(1)}\mathbf{\Lambda}^{(1)}(\theta, +\gamma_1, \bar{\lambda})})\mathbf{q}^{(1)}$$

$$\mathbf{g}^{(1)}(\theta, +\gamma_1, \lambda) = (\mathbf{B}^{(1)}\mathbf{\Lambda}^{(1)}(\theta, +\gamma_1, \lambda) + \overline{\mathbf{B}^{(1)}\mathbf{\Lambda}^{(1)}(\theta, +\gamma_1, \bar{\lambda})})\mathbf{q}^{(1)}$$

$$\mathbf{h}^{(2)}(\theta, -\gamma_2, \lambda) = (\mathbf{A}^{(2)}\mathbf{\Lambda}^{(2)}(\theta, -\gamma_2, \lambda) + \overline{\mathbf{A}^{(2)}\mathbf{\Lambda}^{(2)}(\theta, -\gamma_2, \bar{\lambda})})\mathbf{q}^{(2)}$$

$$\mathbf{g}^{(2)}(\theta, -\gamma_2, \lambda) = (\mathbf{B}^{(2)}\mathbf{\Lambda}^{(2)}(\theta, -\gamma_2, \lambda) + \overline{\mathbf{B}^{(2)}\mathbf{\Lambda}^{(2)}(\theta, -\gamma_2, \bar{\lambda})})\mathbf{q}^{(2)} \quad (14)$$

Note that tractions given by Eqs. (12c) and (13c) vanish on planes $\theta = \gamma_1$ and $\theta = -\gamma_2$, respectively. The enforcement of the continuity of displacements and tractions on the perfectly joined interface produces

$$\left[\mathbf{A}^{(1)}\left\langle\left(\frac{1}{\zeta^{(1)}(+\gamma_1)}\right)^{\lambda}\right\rangle\mathbf{B}^{(1)T} + \overline{\mathbf{A}^{(1)}\left\langle\left(\frac{1}{\zeta^{(1)}(+\gamma_1)}\right)^{\lambda}\right\rangle\mathbf{B}^{(1)T}}\right]\hat{\mathbf{q}}^{(1)} = \left[\mathbf{A}^{(2)}\left\langle\left(\frac{1}{\zeta^{(2)}(-\gamma_2)}\right)^{\lambda}\right\rangle\mathbf{B}^{(2)T} + \overline{\mathbf{A}^{(2)}\left\langle\left(\frac{1}{\zeta^{(2)}(-\gamma_2)}\right)^{\lambda}\right\rangle\mathbf{B}^{(2)T}}\right]\hat{\mathbf{q}}^{(2)} \quad (15a)$$

Downloaded 04 May 2010 to 171.66.16.26. Redistribution subject to ASME license or copyright; see http://www.asme.org/terms/Terms_Use.cfm

$$\left[\mathbf{B}^{(1)}\left\langle\left(\frac{1}{\zeta^{(1)}(+\gamma_1)}\right)^{\lambda}\right\rangle\mathbf{B}^{(1)T} + \overline{\mathbf{B}^{(1)}\left\langle\left(\frac{1}{\zeta^{(1)}(+\gamma_1)}\right)^{\lambda}\right\rangle\mathbf{B}^{(1)T}}\right]\hat{\mathbf{q}}^{(1)}$$

$$= \left[\mathbf{B}^{(2)}\left\langle\left(\frac{1}{\zeta^{(2)}(-\gamma_2)}\right)^{\lambda}\right\rangle\mathbf{B}^{(2)T} + \overline{\mathbf{B}^{(2)}\left\langle\left(\frac{1}{\zeta^{(2)}(-\gamma_2)}\right)^{\lambda}\right\rangle\mathbf{B}^{(2)T}}\right]\hat{\mathbf{q}}^{(2)} \quad (15b)$$

where $\hat{\mathbf{q}}^{(1)} = c^{(1)}\mathbf{q}^{(1)}$ and $\hat{\mathbf{q}}^{(2)} = c^{(2)}\mathbf{q}^{(2)}$. Eliminating $\hat{\mathbf{q}}^{(1)}$ from Eq. (15a, b) and using the orthogonality properties of Eq. (9), one obtains

$$2[\mathbf{K}^1(\lambda) + \mathbf{K}^2(\lambda)]\hat{\mathbf{q}}^{(2)} = \mathbf{0} \quad (16)$$

where

$$\mathbf{K}^1(\lambda) = \frac{1}{2}\sum_{k=1}^{3}\sum_{j=1}^{3}\left[\left(\frac{\zeta_k^{(1)}(+\gamma_1)}{\zeta_j^{(2)}(-\gamma_2)}\right)^{\lambda}\mathbf{B}^{(1)}\mathbf{I}_k\mathbf{B}^{(1)T}\mathbf{M}_1\mathbf{B}^{(2)}\mathbf{I}_j\mathbf{B}^{(2)T} + \left(\overline{\frac{\zeta_k^{(1)}(+\gamma_1)}{\zeta_j^{(2)}(-\gamma_2)}}\right)^{\lambda}\overline{\mathbf{B}^{(1)}\mathbf{I}_k\mathbf{B}^{(1)T}\mathbf{M}_1\mathbf{B}^{(2)}\mathbf{I}_j\mathbf{B}^{(2)T}}\right] \quad (17a)$$

$$\mathbf{K}^2(\lambda) = \frac{1}{2}\sum_{k=1}^{3}\sum_{j=1}^{3}\left[\left(\frac{\zeta_k^{(1)}(+\gamma_1)}{\zeta_j^{(2)}(-\gamma_2)}\right)^{\lambda}\mathbf{B}^{(1)}\mathbf{I}_k\mathbf{B}^{(1)T}\mathbf{M}_2\overline{\mathbf{B}^{(2)}\mathbf{I}_j\mathbf{B}^{(2)T}} + \left(\overline{\frac{\zeta_k^{(1)}(+\gamma_1)}{\zeta_j^{(2)}(-\gamma_2)}}\right)^{\lambda}\overline{\mathbf{B}^{(1)}\mathbf{I}_k\mathbf{B}^{(1)T}\mathbf{M}_2}\mathbf{B}^{(2)}\mathbf{I}_j\mathbf{B}^{(2)T}\right] \quad (17b)$$

$$\mathbf{M}_1 = -i\bar{\mathbf{F}}$$
$$\mathbf{M}_2 = -i\bar{\mathbf{G}} \quad (18)$$

Matrices $\mathbf{F}$ and $\mathbf{G}$ appearing above are defined, respectively, by

$$\mathbf{F} = (i\mathbf{A}^{(1)}\mathbf{B}^{(1)-1}) + \overline{(i\mathbf{A}^{(2)}\mathbf{B}^{(2)-1})}$$
$$\mathbf{G} = (i\mathbf{A}^{(1)}\mathbf{B}^{(1)-1}) - (i\mathbf{A}^{(2)}\mathbf{B}^{(2)-1}). \quad (19)$$

For nontrivial solutions of $\hat{\mathbf{q}}^{(2)}$, the determinant of the coefficient matrix of Eq. (16) has to be zero, i.e.,

$$\det[\mathbf{K}_1(\lambda) + \mathbf{K}_2(\lambda)] = 0, \quad 0 < \mathrm{Re}\{\lambda\} < 1 \quad (20)$$

This is the characteristic equation for the power of singularities λ. Note that this eq. is reduced to that studied by Wu and Chang (1993) when a homogeneous wedge problem is considered. Also note that for the interfacial crack problem, i.e., $\gamma_1 = \gamma_2 = \pi$, the characteristic roots obtained from Eq. (20) are the same as those given by Ting (1986).

4 Dissimilar Orthotropic Wedge Problems

In this section, we shall consider wedge problems that are composed by two orthotropic materials. Material principal axes of both materials are specially oriented so that they have no inclinations relative to the interface as shown in Fig. 1. For orthotropic materials, matrices appearing in Eqs. (17a) and (17b) can be expressed by the Krenk's parameters κ, E, ν, and κ as follows (Sung et al., 1996):

$$\mathbf{B}^{(\alpha)}\mathbf{I}_1\mathbf{B}^{(\alpha)T} = \frac{E^{(\alpha)}}{8\omega_-^{(\alpha)}}\begin{bmatrix} i\delta^{(\alpha)}\omega_+ & -1 \\ -1 & -i(\delta^{(\alpha)}\omega_+)^{-1}\end{bmatrix}$$

$$\mathbf{B}^{(\alpha)}\mathbf{I}_2\mathbf{B}^{(\alpha)T} = \frac{E^{(\alpha)}}{8\omega_-^{(\alpha)}}\begin{bmatrix} -i\delta^{(\alpha)}\omega_- & 1 \\ 1 & i(\delta^{(\alpha)}\omega_-)^{-1}\end{bmatrix} \quad (21)$$

where

$$\omega_+^{(\alpha)} = \sqrt{(1+\kappa^{(\alpha)})/2}$$
$$\omega_-^{(\alpha)} = \sqrt{|1-\kappa^{(\alpha)}|/2}, \quad \alpha = 1, 2 \quad (22)$$

Similarly, matrices $\mathbf{D}$, $\mathbf{U}$, $\mathbf{W}$ defined below will take the following forms:

$$\mathbf{D} = \mathrm{Re}\{\mathbf{F}\} = \begin{bmatrix} \frac{2\omega_+^{(1)}}{E^{(1)}\delta^{(1)}} + \frac{2\omega_+^{(2)}}{E^{(2)}\delta^{(2)}} & 0 \\ 0 & \frac{2\omega_+^{(1)}\delta^{(1)}}{E^{(1)}} + \frac{2\omega_+^{(2)}\delta^{(2)}}{E^{(2)}}\end{bmatrix} \quad (23)$$

$$\mathbf{U} = \mathrm{Re}\{\mathbf{G}\} = \begin{bmatrix} \frac{2\omega_+^{(1)}}{E^{(1)}\delta^{(1)}} - \frac{2\omega_+^{(2)}}{E^{(2)}\delta^{(2)}} & 0 \\ 0 & \frac{2\omega_+^{(1)}\delta^{(1)}}{E^{(1)}} - \frac{2\omega_+^{(2)}\delta^{(2)}}{E^{(2)}}\end{bmatrix} \quad (24)$$

$$\mathbf{W} = \mathrm{Im}\{\mathbf{F}\} = \mathrm{Im}\{\mathbf{G}\} = \begin{bmatrix} 0 & (1-\nu^{(1)})E^{(1)-1} - (1-\nu^{(2)})E^{(2)-1} \\ -(1-\nu^{(1)})E^{(1)-1} + (1-\nu^{(2)})E^{(2)-1} & 0\end{bmatrix} \quad (25)$$

Using results of (21) to (25), elements of $\mathbf{K}^1$ and $\mathbf{K}^2$ can be further expressed in real forms as follows:

$$K_{11}^1 = \{-[(\delta^{(2)}q_+^{(2)} - \delta^{(1)}q_+^{(1)})S_1 + (\delta^{(1)}q_+^{(1)} - \delta^{(2)}q_-^{(2)})S_2 + (\delta^{(1)}q_-^{(1)} - \delta^{(2)}q_+^{(2)})S_3 + (\delta^{(2)}q_-^{(2)} - \delta^{(1)}q_-^{(1)})S_4]\beta_1 - [-S_1 + S_2 + S_3 - S_4]d_5 - [q_+^{(1)}q_+^{(2)}S_1 - q_+^{(1)}q_-^{(2)}S_2 - q_-^{(1)}q_+^{(2)}S_3 + q_-^{(1)}q_-^{(2)}S_4]\delta^{(1)}\delta^{(2)}\}/(4\omega_-^{(1)}\omega_-^{(2)}d_3d_4)$$

$$K_{22}^1 = \{[(\delta^{(1)-1}q_-^{(1)} - \delta^{(2)-1}q_-^{(2)})S_1 + (\delta^{(2)-1}q_+^{(2)} - \delta^{(1)-1}q_-^{(1)})S_2 + (\delta^{(2)-1}q_-^{(2)} - \delta^{(1)-1}q_+^{(1)})S_3 + (\delta^{(1)-1}q_+^{(1)} - \delta^{(2)-1}q_+^{(2)})S_4]\beta_1 - [q_-^{(1)}q_-^{(2)}S_1 - q_-^{(1)}q_+^{(2)}S_2 - q_+^{(1)}q_-^{(2)}S_3 + q_+^{(1)}q_+^{(2)}S_4]d_5\delta^{(1)-1}\delta^{(2)-1} - [-S_1 + S_2 + S_3 - S_4]\}/(4\omega_-^{(1)}\omega_-^{(2)}d_3d_4)$$

$$K_{12}^1 = \{-[(1-\delta^{(1)}\delta^{(2)-1}q_+^{(1)}q_-^{(2)})C_1 + (\delta^{(1)}\delta^{(2)-1}q_+^{(1)}q_+^{(2)} - 1)C_2 + (\delta^{(1)}\delta^{(2)-1}q_-^{(1)}q_-^{(2)} - 1)C_3 + (1-\delta^{(1)}\delta^{(2)-1}q_-^{(1)}q_+^{(2)})C_4]\beta_1 - [-q_-^{(2)}C_1 + q_+^{(2)}C_2 + q_-^{(2)}C_3 - q_+^{(2)}C_4]d_5\delta^{(2)-1} + [-q_+^{(1)}C_1 + q_+^{(1)}C_2 + q_-^{(1)}C_3 - q_-^{(1)}C_4]\delta^{(1)}\}/(4\omega_-^{(1)}\omega_-^{(2)}d_3d_4)$$

Downloaded 04 May 2010 to 171.66.16.26. Redistribution subject to ASME license or copyright; see http://www.asme.org/terms/Terms_Use.cfm

$$K_{21}^1 = \{[(1 - \delta^{(1)^{-1}}\delta^{(2)}q_-^{(1)}q_+^{(2)})C_1 + (\delta^{(1)^{-1}}\delta^{(2)}q_-^{(1)}q_-^{(2)} - 1)C_2 + (\delta^{(1)^{-1}}\delta^{(2)}q_+^{(1)}q_+^{(2)} - 1)C_3 + (1 - \delta^{(1)^{-1}}\delta^{(2)}q_+^{(1)}q_-^{(2)})C_4]\beta_1 + [q_-^{(1)}C_1 - q_-^{(1)}C_2 - q_+^{(1)}C_3 + q_+^{(1)}C_4]d_5\delta^{(1)^{-1}} - [q_+^{(2)}C_1 - q_-^{(2)}C_2 - q_+^{(2)}C_3 + q_-^{(2)}C_4]\delta^{(2)}\}/(4\omega_-^{(1)}\omega_-^{(2)}d_3d_4) \quad (26a)$$

and

$$K_{11}^2 = \{-[q_+^{(1)}q_+^{(2)}S_1 - q_+^{(1)}q_-^{(2)}S_2 - q_-^{(1)}q_+^{(2)}S_3 + q_-^{(2)}q_-^{(1)}S_4]\alpha_1\delta^{(1)}\delta^{(2)} + [-S_1 + S_2 + S_3 - S_4]\alpha_2d_5 - [-(\delta^{(1)}q_+^{(1)} + \delta^{(2)}q_+^{(2)})S_1 + (\delta^{(1)}q_+^{(1)} + \delta^{(2)}q_-^{(2)})S_2 + (\delta^{(1)}q_-^{(1)} + \delta^{(2)}q_+^{(2)})S_3 - (\delta^{(1)}q_-^{(1)} + \delta^{(2)}q_-^{(2)})S_4]\beta_1\}/(4\omega_-^{(1)}\omega_-^{(2)}d_3d_4)$$

$$K_{22}^2 = \{[-S_1 + S_2 + S_3 - S_4]\alpha_1 + [-q_-^{(1)}q_-^{(2)}S_1 + q_-^{(1)}q_+^{(2)}S_2 + q_+^{(1)}q_-^{(2)}S_3 - q_+^{(2)}q_+^{(1)}S_4]\alpha_2d_5\delta^{(1)^{-1}}\delta^{(2)^{-1}} - [-(\delta^{(1)^{-1}}q_-^{(1)} + \delta^{(2)^{-1}}q_-^{(2)})S_1 + (\delta^{(1)^{-1}}q_-^{(1)} + \delta^{(2)^{-1}}q_+^{(2)})S_2 + (\delta^{(1)^{-1}}q_+^{(1)} + \delta^{(2)^{-1}}q_-^{(2)})S_3 - (\delta^{(1)^{-1}}q_+^{(1)} + \delta^{(2)^{-1}}q_+^{(2)})S_4]\beta_1\}/(4\omega_-^{(1)}\omega_-^{(2)}d_3d_4)$$

$$K_{12}^2 = \{-[-q_+^{(1)}C_1 + q_+^{(1)}C_2 + q_-^{(1)}C_3 - q_-^{(1)}C_4]\alpha_1\delta^{(1)} - [-q_-^{(2)}C_1 + q_+^{(2)}C_2 + q_-^{(2)}C_3 - q_+^{(2)}C_4]\alpha_2d_5\delta^{(2)^{-1}} + [-(\delta^{(1)}\delta^{(2)^{-1}}q_+^{(1)}q_-^{(2)} + 1)C_1 + (\delta^{(1)}\delta^{(2)^{-1}}q_+^{(1)}q_+^{(2)} + 1)C_2 + (\delta^{(1)}\delta^{(2)^{-1}}q_-^{(1)}q_-^{(2)} + 1)C_3 - (\delta^{(1)}\delta^{(2)^{-1}}q_-^{(1)}q_+^{(2)} + 1)C_4]\beta_1\}/(4\omega_-^{(1)}\omega_-^{(2)}d_3d_4)$$

$$K_{21}^2 = \{-[q_+^{(2)}C_1 - q_-^{(2)}C_2 - q_+^{(2)}C_3 + q_-^{(2)}C_4]\alpha_1\delta^{(2)} - [q_-^{(1)}C_1 - q_-^{(1)}C_2 - q_+^{(1)}C_3 + q_+^{(1)}C_4]\alpha_2d_5\delta^{(1)^{-1}} - [-(\delta^{(1)^{-1}}\delta^{(2)}q_-^{(1)}q_+^{(2)} + 1)C_1 + (\delta^{(1)^{-1}}\delta^{(2)}q_-^{(1)}q_-^{(2)} + 1)C_2 + (\delta^{(1)^{-1}}\delta^{(2)}q_+^{(1)}q_+^{(2)} + 1)C_3 - (\delta^{(1)^{-1}}\delta^{(2)}q_+^{(1)}q_-^{(2)} + 1)C_4]\beta_1\}/(4\omega_-^{(1)}\omega_-^{(2)}d_3d_4) \quad (26b)$$

where

$$\gamma_1' = \tan^{-1}(\delta^{(1)}(\omega_+^{(1)} + \omega_-^{(1)})\tan\gamma_1)$$

$$\gamma_1'' = \tan^{-1}(\delta^{(1)}(\omega_+^{(1)} - \omega_-^{(1)})\tan\gamma_1)$$

$$\gamma_2' = \tan^{-1}(\delta^{(2)}(\omega_+^{(2)} + \omega_-^{(2)})\tan\gamma_2)$$

$$\gamma_2'' = \tan^{-1}(\delta^{(2)}(\omega_+^{(2)} - \omega_-^{(2)})\tan\gamma_2) \quad (27a)$$

$$q_+^{(\alpha)} = \omega_+^{(\alpha)} + \omega_-^{(\alpha)} \quad q_-^{(\alpha)} = \omega_+^{(\alpha)} - \omega_-^{(\alpha)} \quad (27b)$$

$$d_1 = (\sqrt{\cos^2\gamma_1 + (\delta^{(1)}(\omega_+^{(1)} + \omega_-^{(1)})\sin\gamma_1)^2})^\lambda$$

$$d_2 = (\sqrt{\cos^2\gamma_1 + (\delta^{(1)}(\omega_+^{(1)} - \omega_-^{(1)})\sin\gamma_1)^2})^\lambda$$

$$d_3 = (\sqrt{\cos^2\gamma_2 + (\delta^{(2)}(\omega_+^{(2)} + \omega_-^{(2)})\sin\gamma_2)^2})^\lambda$$

$$d_4 = (\sqrt{\cos^2\gamma_2 + (\delta^{(2)}(\omega_+^{(2)} - \omega_-^{(2)})\sin\gamma_2)^2})^\lambda$$

$$d_5 = \frac{\beta_1}{\beta_2} = \frac{\delta^{(2)}(1 + \alpha_0) + \delta^{(1)}(1 - \alpha_0)}{\delta^{(2)^{-1}}(1 + \alpha_0) + \delta^{(1)^{-1}}(1 - \alpha_0)} \quad (27c)$$

$$S_1 = \sin(\lambda(\gamma_1' \pm \gamma_2'))d_1d_4$$

$$S_2 = \sin(\lambda(\gamma_1' \pm \gamma_2''))d_1d_3$$

$$S_3 = \sin(\lambda(\gamma_1'' \pm \gamma_2'))d_2d_4$$

$$S_4 = \sin(\lambda(\gamma_1'' \pm \gamma_2''))d_2d_3 \quad (27d)$$

$$C_1 = \cos(\lambda(\gamma_1' \pm \gamma_2'))d_1d_4$$

$$C_2 = \cos(\lambda(\gamma_1' \pm \gamma_2''))d_1d_3$$

$$C_3 = \cos(\lambda(\gamma_1'' \pm \gamma_2'))d_2d_4$$

$$C_4 = \cos(\lambda(\gamma_1'' \pm \gamma_2''))d_2d_3 \quad (27e)$$

The constants α_1, β_1, α_2, and β_2 appearing in Eqs. (26) and (27) are generalized Dundurs' constants which are defined as

$$\alpha_1 = \frac{(1 + \alpha_0) - (1 - \alpha_0)\Delta^{-1}}{(1 + \alpha_0) + (1 - \alpha_0)\Delta^{-1}}$$

$$\alpha_2 = \frac{(1 + \alpha_0) - (1 - \alpha_0)\Delta}{(1 + \alpha_0) + (1 - \alpha_0)\Delta}$$

$$\beta_1 = \delta^{(2)}\frac{2\beta_0}{(1 + \alpha_0) + (1 - \alpha_0)\Delta^{-1}}$$

$$\beta_2 = \delta^{(2)^{-1}}\frac{2\beta_0}{(1 + \alpha_0) + (1 - \alpha_0)\Delta} \quad (28)$$

where

$$\alpha_0 = \frac{\frac{\omega_+^{(2)}}{E^{(2)}} - \frac{\omega_+^{(1)}}{E^{(1)}}}{\frac{\omega_+^{(2)}}{E^{(2)}} + \frac{\omega_+^{(1)}}{E^{(1)}}} \quad \beta_0 = \frac{\frac{1 - \nu^{(2)}}{E^{(2)}} - \frac{1 - \nu^{(1)}}{E^{(1)}}}{2\left(\frac{\omega_+^{(2)}}{E^{(2)}} + \frac{\omega_+^{(1)}}{E^{(1)}}\right)} \quad (29)$$

Several special wedge geometries are discussed in the following.

(I) $\gamma_1 = \gamma_2 = \pi$. By letting $\gamma_1 = \gamma_2 = \pi$, we have the interfacial crack problem. For such a case, $\gamma_1' = \gamma_1'' = \pi$ and $\gamma_2' = \gamma_2'' = \pi$ (see Eq. (27)). Therefore, elements of $\mathbf{K}^1$ and $\mathbf{K}^2$ are reduced to

$$K_{11}^1 = -\delta^{(1)}\delta^{(2)}\sin(2\lambda\pi)$$

$$K_{22}^1 = -\delta^{(1)^{-1}}\delta^{(2)^{-1}}\sin(2\lambda\pi)d_5$$

$$K_{12}^1 = -\delta^{(1)}\delta^{(2)^{-1}}\cos(2\lambda\pi)\beta_1$$

$$K_{21}^1 = \delta^{(1)^{-1}}\delta^{(2)}\cos(2\lambda\pi)\beta_1 \quad (30)$$

and

$$K_{11}^2 = 0$$

$$K_{22}^2 = 0$$

$$K_{12}^2 = \delta^{(1)}\delta^{(2)^{-1}}\beta_1$$

$$K_{21}^2 = -\delta^{(1)^{-1}}\delta^{(2)}\beta_1 \quad (31)$$

Hence the corresponding characteristic equation is

$$\cos^2(\lambda\pi) - \beta_1\beta_2\sin^2(\lambda\pi) = 0 \quad 0 \le \mathrm{Re}\{\lambda\} \le 1 \quad (32)$$

where the roots are found to be

$$\lambda = \frac{1}{2} \pm \frac{1}{2\pi}i\ln\frac{1 + \sqrt{\beta_1\beta_2}}{1 - \sqrt{\beta_1\beta_2}} \quad (33)$$

which is the same as that given by Sung et al. (1996). Using the definitions of β_1 and β_2 given by (28), the above roots can be rewritten in terms of parameters α_0, β_0, and Δ as

$$\lambda = \frac{1}{2} \pm \frac{1}{2\pi}i \times \ln\frac{1 + 2\beta_0/\sqrt{2(1 + \alpha_0^2) + (1 - \alpha_0^2)(\Delta + \Delta^{-1})}}{1 - 2\beta_0/\sqrt{2(1 + \alpha_0^2) + (1 - \alpha_0^2)(\Delta + \Delta^{-1})}} \quad (34)$$

Downloaded 04 May 2010 to 171.66.16.26. Redistribution subject to ASME license or copyright; see http://www.asme.org/terms/Terms_Use.cfm

Thus, if the two orthotropic materials have the property that $\Delta = 1$, i.e., $\delta^{(1)} = \delta^{(2)}$, then the roots λ are simplified to

$$\lambda = \frac{1}{2} \pm \frac{1}{2\pi} i \ln \frac{1 + \beta_0}{1 - \beta_0} \tag{35}$$

which depend on parameter β_0 only.

(II) $E^{(1)} \gg E^{(2)}$ (or $\alpha_0 = 1$). Consider the case of $E^{(1)} \gg E^{(2)}$ (or equivalently the case of $\alpha_0 = 1$). For this case, the generalized Dundurs' constants become

$$\alpha_1 = \alpha_2 = 1$$

$$\delta^{(2)^{-1}}\beta_1 = \beta^{(2)}\beta_2 = \beta_0 = \frac{1 - \nu^{(2)}}{2\omega_+^{(2)}} \tag{36}$$

Hence, it can be shown that the combinations of the elements of $\mathbf{K}^1$ and $\mathbf{K}^2$ are

$$\begin{aligned}
K_{11}^1 + K_{11}^2 &= -2\delta^{(1)}\delta^{(2)}[d_4 \cos(\lambda\gamma_2')(q_+^{(2)} - \beta_0) - d_3 \\
&\times \cos(\lambda\gamma_2'')(q_-^{(2)} - \beta_0)](d_1 q_+^{(1)} \sin(\lambda\gamma_1') - d_2 q_-^{(1)} \\
&\times \sin(\lambda\gamma_1'')) + 2\delta^{(2)^2}[d_4 \sin(\lambda\gamma_2')(1 - q_+^{(2)}\beta_0) - d_3 \\
&\times \sin(\lambda\gamma_2'')(1 - q_-^{(2)}\beta_0)](d_1 \cos(\lambda\gamma_1') - d_2 \cos(\lambda\gamma_1'')) \\
K_{22}^1 + K_{22}^2 &= 2\delta^{(1)^{-1}}\delta^{(2)}[d_4 \cos(\lambda\gamma_2')(\beta_0 - q_-^{(2)}) - d_3 \\
&\times \cos(\lambda\gamma_2'')(\beta_0 - q_+^{(2)})](d_1 q_-^{(1)} \sin(\lambda\gamma_1') - d_2 q_+^{(1)} \\
&\times \sin(\lambda\gamma_1'')) - 2[d_4 \sin(\lambda\gamma_2')(q_-^{(2)}\beta_0 - 1) - d_3 \\
&\times \sin(\lambda\gamma_2'')(q_+^{(2)}\beta_0 - 1)](d_1 \cos(\lambda\gamma_1') - d_2 \cos(\lambda\gamma_1'')) \\
K_{12}^1 + K_{12}^2 &= 2\delta^{(2)}[d_4 \cos(\lambda\gamma_2')(q_-^{(2)} - \beta_0) \\
&- d_3 \cos(\lambda\gamma_2'')(q_+^{(2)} - \beta_0)](d_1 \cos(\lambda\gamma_1') \\
&- d_2 \cos(\lambda\gamma_1'')) + 2\delta^{(1)}[d_4 \sin(\lambda\gamma_2')(1 - q_-^{(2)}\beta_0) \\
&- d_3 \sin(\lambda\gamma_2'')(1 - q_+^{(2)}\beta_0)](d_1 q_+^{(1)} \sin(\lambda\gamma_1') \\
&- d_2 q_-^{(1)} \sin(\lambda\gamma_1'')) \\
K_{21}^1 + K_{21}^2 &= -2\delta^{(2)}[d_4 \cos(\lambda\gamma_2')(q_+^{(2)} - \beta_0) \\
&- d_3 \cos(\lambda\gamma_2'')(q_-^{(2)} - \beta_0)](d_1 \cos(\lambda\gamma_1') \\
&- d_2 \cos(\lambda\gamma_1'')) - 2\delta^{(1)^{-1}}\delta^{(2)^2}[d_4 \sin(\lambda\gamma_2')(1 - q_+^{(2)}\beta_0) \\
&- d_3 \sin(\lambda\gamma_2'')(1 - q_-^{(2)}\beta_0)](d_1 q_-^{(1)} \sin(\lambda\gamma_1') \\
&- d_2 q_+^{(1)} \sin(\lambda\gamma_1'')) \qquad (37)
\end{aligned}$$

Using these results, the characteristic equation becomes

$$D_1 D_2 = 0 \tag{38}$$

where

$$\begin{aligned}
D_1 &= (\omega_-^{(1)} d_1 d_2)^{-1}\{d_1^2 + d_2^2 - 2d_1 d_2[\sin(\lambda\gamma_1') \\
&\times \sin(\lambda\gamma_1'')\kappa^{(2)} + \cos(\lambda\gamma_1')\cos(\lambda\gamma_1'')]\} \qquad (39) \\
D_2 &= \delta^{(2)^2}(\omega_-^{(2)} d_3 d_4)^{-1}[(d_4^2 + d_3^2)(1 + \beta_0^2 - 2\beta_0\omega_+^{(2)}) \\
&- 2d_3 d_4 \cos(\lambda\gamma_2')\cos(\lambda\gamma_2'')(\kappa^{(2)} + \beta_0^2 - 2\beta_0\omega_+^{(2)}) \\
&- 2d_3 d_4 \sin(\lambda\gamma_2')\sin(\lambda\gamma_2'') \\
&\times (1 + \beta_0^2\kappa^{(2)} - 2\beta_0\omega_+^{(2)})] \qquad (40)
\end{aligned}$$

It is noted that the characteristic equation corresponding to $D_2 = 0$ is the problem of a single wedge where the extended wedge angle is γ_2. On the radial direction of this problem one of the faces of the wedge is fixed while the other is traction free (free-fixed problem). The case of $D_1 = 0$ corresponds to another single wedge problem where the extension of the wedge angle is γ_1 while the boundary conditions on the faces of this wedge are both traction free (free-free problem). In the paper by Kuo and Bogy (1974*b*), they have treated a free-free single wedge problem. By appropriate arranging the material principal axes in their results (i.e., letting $b = a - \pi/2$, where $2a$ is the extended angle of the wedge while b is a certain reference angle of the material principal axes. Here, a and b are their notations), one will find that their results coincide with our case of $D_1 = 0$. In the following, several special situations corresponding to the case of $D_2 = 0$ (single free-fixed wedge problem) which are not discussed previously are further addressed.

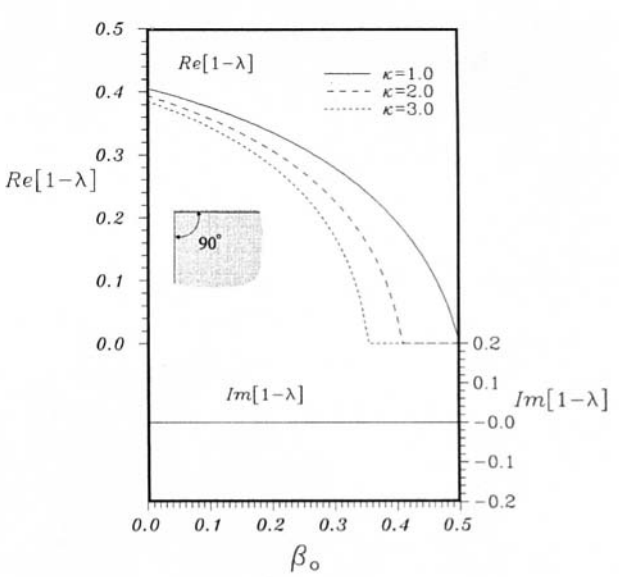


Fig. 2 Roots λ for single free-fixed wedge problem for $\gamma = 90$ deg

(a) $D_2 = 0$ with $\gamma_2 = \pi/2$. At this special wedge angle, we find from (27) that

$$\begin{aligned}
\gamma_2' = \pi/2 \quad d_3 &= (\delta^{(2)}(\omega_+^{(2)} + \omega_-^{(2)}))^{\lambda} \\
\gamma_2'' = \pi/2 \quad d_4 &= (\delta^{(2)}(\omega_+^{(2)} - \omega_-^{(2)}))^{\lambda}. \qquad (41)
\end{aligned}$$

Hence,

$$\begin{aligned}
D_2 &= \delta^{(2)^{2(\lambda+1)}}(\omega_-^{(2)} d_3 d_4)^{-1}[((\omega_+^{(2)} + \omega_-^{(2)})^{2\lambda} \\
&+ (\omega_+^{(2)} - \omega_-^{(2)})^{2\lambda})(1 + \beta_0^2 - 2\beta_0\omega_+^{(2)}) \\
&- 2\cos^2\left(\frac{\lambda\pi}{2}\right)(\kappa^{(2)} + \beta_0^2 - 2\beta_0\omega_+^{(2)}) \\
&- 2\sin^2\left(\frac{\lambda\pi}{2}\right)(1 + \beta_0^2\kappa^{(2)} - 2\beta_0\omega_+^{(2)})] = 0. \qquad (42)
\end{aligned}$$

It is seen that at the wedge angle $\gamma_2 = \pi/2$ the characteristic root depends only on the parameters $\kappa^{(2)}$ and β_0. It is not related to the parameter $\delta^{(2)}$ at all. The dependence of the roots on β_0 for several values of $\kappa^{(2)}$ is shown in Fig. 2. It is seen that these roots presented are all real (In plotting those figures corresponding to a single wedge problem, all the superscripts or subscripts relevant to parameters are suppressed for simplicity).

(b) $D_2 = 0$ with $\gamma_2 = \pi$. In this case, we find from (27) that

$$\gamma_2' = \gamma_2'' = \pi \quad d_3 = d_4 = 1. \tag{43}$$

Downloaded 04 May 2010 to 171.66.16.26. Redistribution subject to ASME license or copyright; see http://www.asme.org/terms/Terms_Use.cfm

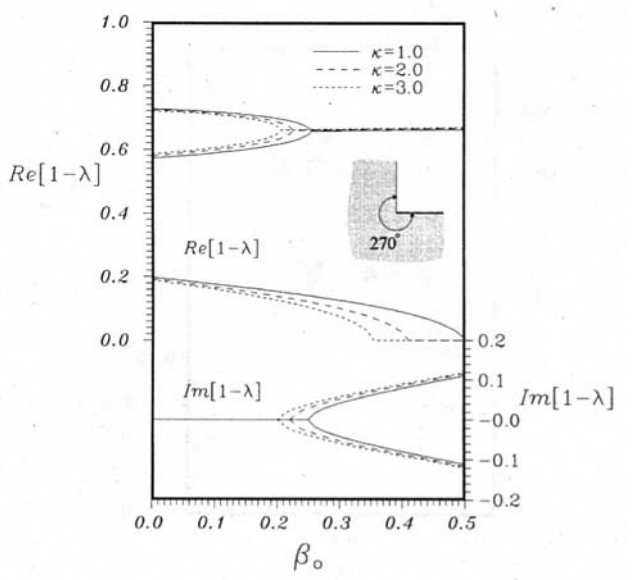


Fig. 3 Roots λ for single free-fixed wedge problem for $\gamma = 270$ deg

Hence

$$D_2 = -\delta^{(2)}\omega_-^{(2)}(\cos^2(\lambda\pi) + \beta_0^2 \sin^2(\lambda\pi)) = 0 \quad (44)$$

The solutions of above characteristic roots λ, depending on β_0 only, are

$$\lambda = \frac{1}{2} \pm \frac{1}{2\pi} i \ln \frac{1+\beta_0}{1-\beta_0} \quad (45)$$

which are independent of $\delta^{(2)}$ and $\kappa^{(2)}$. In the treatment of two general anisotropic interfacial crack problems, Ting (1986) has found that the roots are

$$\lambda = \frac{1}{2} \pm i \frac{1}{2\pi} \ln \frac{1+\beta}{1-\beta}$$

where

$$\beta = [-\tfrac{1}{2} \text{ tr } (\mathbf{S})^2]^{1/2} \quad (46)$$

Matrix $\mathbf{S}$ appearing above is defined by $\mathbf{S} = i(2\mathbf{A}\mathbf{B}^T - \mathbf{I})$ for general anisotropic materials. The corresponding elements of matrix $\mathbf{S}$ for orthotropic materials have been given by Ting (1988) and with his results one can show that the parameter β in Eq. (46) is reduced to our parameter β_0.

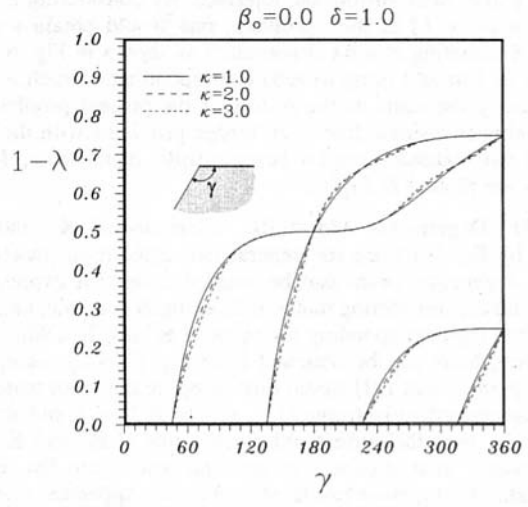


Fig. 4 Roots λ versus wedge angle γ for single free-fixed wedge problem ($\delta = 1$)

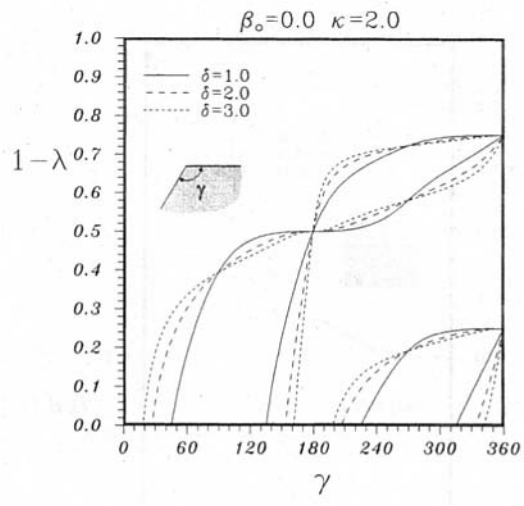


Fig. 5 Roots λ versus wedge angle γ for single free-fixed wedge problem ($\kappa = 2$)

(c) $D_2 = 0$ *with* $\gamma_2 = 3\pi/2$. At this wedge angle, we find that

$$\gamma_2' = 3\pi/2 \quad d_3 = (\delta^{(2)}(\omega_+^{(2)} + \omega_-^{(2)}))^\lambda$$
$$\gamma_2'' = 3\pi/2 \quad d_4 = (\delta^{(2)}(\omega_+^{(2)} - \omega_-^{(2)}))^\lambda \quad (47)$$

and hence

$$D_2 = \delta^{(2)^{2(\lambda+1)}}(\omega_-^{(2)} d_3 d_4)^{-1}[((\omega_+^{(2)} + \omega_-^{(2)})^{2\lambda} + (\omega_+^{(2)} - \omega_-^{(2)})^{2\lambda})(1 + \beta_0^2 - 2\beta_0\omega_+^{(2)}) - 2\cos^2\left(\frac{3\lambda\pi}{2}\right)(\kappa^{(2)} + \beta_0^2 - 2\beta_0\omega_+^{(2)}) - 2\sin^2\left(\frac{3\lambda\pi}{2}\right)(1 + \beta_0^2\kappa^{(2)} - 2\beta_0\omega_+^{(2)})] = 0 \quad (48)$$

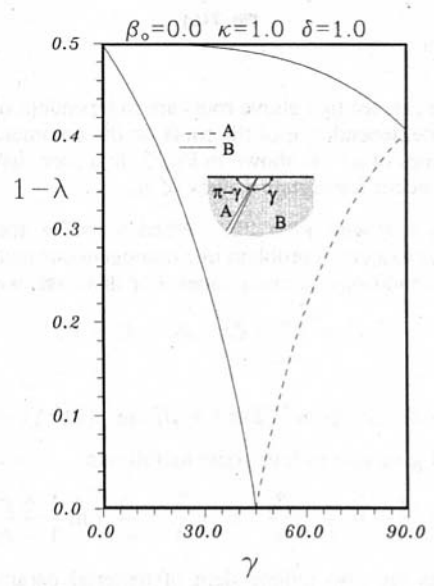


Fig. 6 Two free-fixed wedge problems combined together with total wedge angles equal to π

Downloaded 04 May 2010 to 171.66.16.26. Redistribution subject to ASME license or copyright; see http://www.asme.org/terms/Terms_Use.cfm

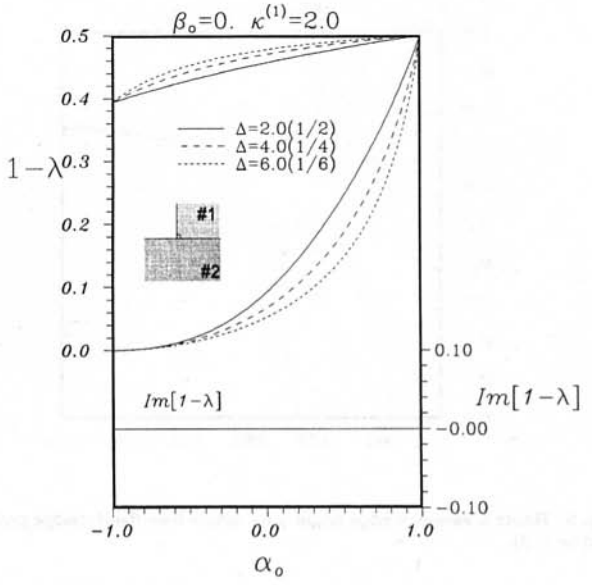


Fig. 7(a)

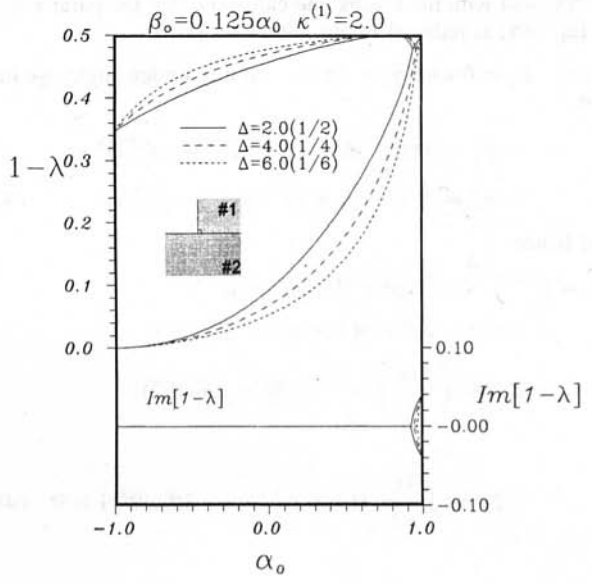


Fig. 7(b)

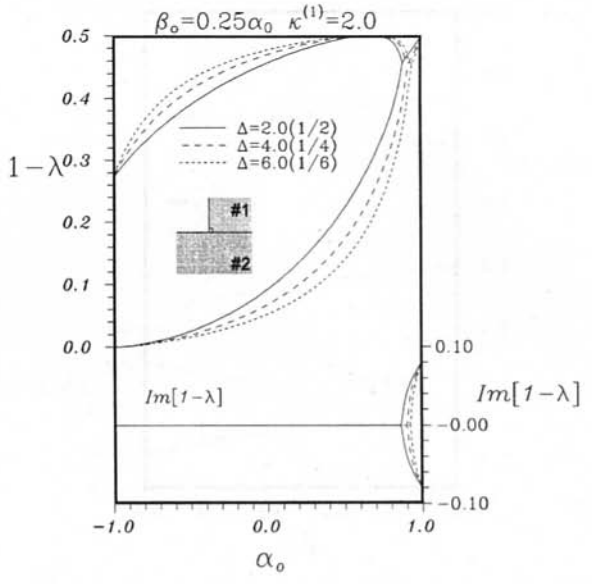


Fig. 7(c)

Figs. 7 Roots λ versus α_0 for $\beta_0 = m\alpha_0$ where m = 0, 0.125 and 0.25, respectively ($\gamma_1 = \pi/2$, $\gamma_2 = \pi$)

Again, one can see that above roots are independent of parameter $\delta^{(2)}$. The dependence of the roots on the parameter β_0 with several values of $\kappa^{(2)}$ is shown in Fig. 3. It is seen that complex roots may occur for certain values of β_0.

(d) $D_2 = 0$ with $\gamma_2 = 2\pi$. When $\gamma_2 = 2\pi$, the problem corresponds to a crack problem in a homogeneous medium with free-fixed conditions on crack faces. For this case, we find that

$$\gamma_2' = \gamma_2'' = 2\pi \quad d_3 = d_4 = 1 \tag{49}$$

and

$$D_2 = -\delta^{(2)}\omega^{(2)}(\cos^2(2\lambda\pi) + \beta_0^2 \sin^2(2\lambda\pi)) = 0 \tag{50}$$

which will give rise to four roots as follows:

$$\lambda_1 = \frac{1}{4} \pm \frac{1}{4\pi} i \ln\frac{1+\beta_0}{1-\beta_0} \quad \lambda_2 = \frac{3}{4} \pm \frac{1}{4\pi} i \ln\frac{1+\beta_0}{1-\beta_0}. \tag{51}$$

These roots are also independent of material parameter $\delta^{(2)}$. Ting (1986) has also investigated above free-fixed crack problem for general anisotropic materials. Six characteristic roots are given. Two of them are real which correspond to the roots for antiplane problem. The rest in complex conjugate forms are the results for in-plane deformation, which are the same as those presented in Eq. (51) except β_0 should be replaced by β.

(e) $D_2 = 0$ with arbitrary angle of γ_2. Above discussions are all for certain special wedge angles ($\gamma_2 = \pi/2$, π, $3\pi/2$ and 2π). As to arbitrary wedge angles, the order of singularities will depend in general on material parameters $\delta^{(2)}$, $\kappa^{(2)}$, and β_0. Fig. 4 presents the results of $1 - \lambda$ versus γ_2 (γ_2 = 0, ~360 deg) for the choice of $\beta_0 = 0.0$ and $\delta^{(2)} = 1.0$. It is seen that no roots of λ ($0 < \mathrm{Re}[\lambda] < 1$) are found when wedge angle γ_2 is below certain values. There may correspond to one, two or even four real roots for other wedge angles γ_2. The effect of material parameter $\delta^{(2)}$ on the roots λ is shown in Fig. 5. It is seen that curves corresponding to different values of $\delta^{(2)}$ will produce the same values of λ at several special wedge angles (i.e., at $\gamma_2 = \pi/2$, π, $3\pi/2$ or 2π), as has been discussed previously.

It should be noted that in the paper by Lin and Sung (1996), they have treated the singularities of an inclined crack terminating at a dissimilar anisotropic interface. By considering $E^{(1)} \gg E^{(2)}$ (or $\alpha_0 = 1$) in their problem, one would obtain a slant crack terminating at a fixed boundary as shown in Fig. 6. The results of Lin and Sung (1996) corresponding to such a case are exactly the same as the results of the present problem by combining two single free-fixed wedge problems with the sum of the two extended angles being always equal to π. These results are plotted in Fig. 6.

(III) Degenerate Materials. Elements of $\mathbf{K}^1$ and $\mathbf{K}^2$ given by Eq. (26) are for general two orthotropic materials. Many degenerate cases can be studied from that expression. For instance, considering material #2 being degenerate, i.e., $\kappa^{(2)} = 1$, then the corresponding elements of $\mathbf{K}^1$ and $\mathbf{K}^2$, which are not given here, can be obtained from Eq. (26) by taking the limiting process of L'Hospital rule. Suppose that both materials are degenerated to isotropic (i.e., $\kappa^{(1)} = \delta^{(1)} = 1$ and $\kappa^{(2)} = \delta^{(2)} = 1$), then the corresponding elements of $\mathbf{K}^1$ and $\mathbf{K}^2$ can be obtained in a similar way and the results are list in the Appendix. Using those results shown in the Appendix, one can show that the corresponding characteristic equation is reduced to that given by Bogy (1971).

Downloaded 04 May 2010 to 171.66.16.26. Redistribution subject to ASME license or copyright; see http://www.asme.org/terms/Terms_Use.cfm

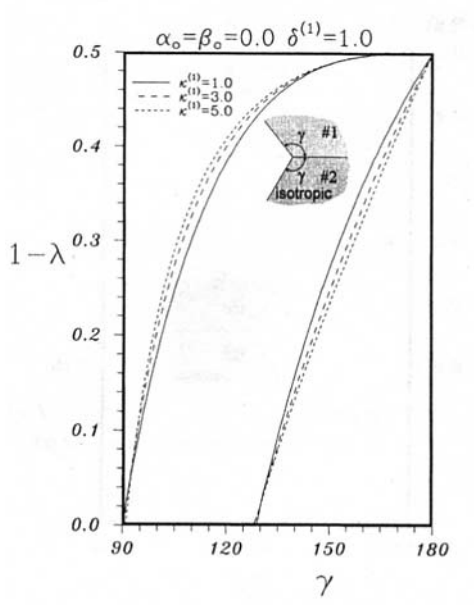


Fig. 8 Roots λ versus γ for equal angle wedge problem ($\delta^{(1)} = 1$, $\alpha_0 = \beta_0 = 0$)

5 Some Further Numerical Results

The case of $\gamma_1 = \gamma_2 = \pi/2$ corresponds to a free-edge problem which is encountered frequently in many engineering applications. The singular nature for such a problem has been investigated by Sung et al. (1996) for orthotropic materials. The characteristic equation is developed from the consideration of the singular behavior of a system of singular integral equations (Sung et al., 1996). Their result is equivalent to the present one by letting $\gamma_1 = \gamma_2 = \pi/2$. Hence, the free-edge problem will not be addressed in the following. Instead, we select several special configurations of the dissimilar wedge problems for the numerical investigations which are discussed below:

(I) $\gamma_1 = \pi/2$, $\gamma_2 = \pi$. Consider the case of $\gamma_1 = \pi/2$ and $\gamma_2 = \pi$. For this case, those quantities defined in Eq. (27) are

$$\gamma_1' = \pi/2 = \gamma_1'' \quad d_1 = (\delta^{(1)} q_+^{(1)})^\lambda$$

$$\gamma_2' = \pi = \gamma_2'' \quad d_2 = (\delta^{(1)} q_-^{(1)})^\lambda \quad d_3 = d_4 = 1.$$

Therefore the elements of $\mathbf{K}^1$ and $\mathbf{K}^2$ become

$$K_{11}^1 + K_{11}^2 = -\delta^{(2)}[\delta^{(1)}(q_+^{(1)} d_1 - q_-^{(1)} d_2)(\sin(3\lambda\pi/2) + \alpha_1 \sin(-\lambda\pi/2)) + \beta_1(d_1 - d_2)(\sin(3\lambda\pi/2) - \sin(-\lambda\pi/2))]/(2\omega_-^{(1)})$$

$$K_{22}^1 + K_{22}^2 = \delta^{(2)^{-1}}[\delta^{(1)^{-1}} d_5(q_-^{(1)} d_1 - q_+^{(1)} d_2)(\sin(3\lambda\pi/2) + \alpha_2 \sin(-\lambda\pi/2)) + \beta_1(d_1 - d_2)(\sin(3\lambda\pi/2) - \sin(-\lambda\pi/2))]/(2\omega_-^{(1)})$$

$$K_{12}^1 + K_{12}^2 = -\delta^{(2)^{-1}}[\delta^{(1)}\beta_1(q_+^{(1)} d_1 - q_-^{(1)} d_2)(\cos(3\lambda\pi/2) - \cos(-\lambda\pi/2)) + d_5(d_1 - d_2)(\cos(3\lambda\pi/2) + \alpha_2 \cos(-\lambda\pi/2))]/(2\omega_-^{(1)})$$

$$K_{21}^1 + K_{21}^2 = -\delta^{(2)}[\delta^{(1)^{-1}}\beta_1(q_-^{(1)} d_1 - q_+^{(1)} d_2)(\cos(3\lambda\pi/2) - \cos(-\lambda\pi/2)) + (d_1 - d_2)(\cos(3\lambda\pi/2) + \alpha_1 \cos(-\lambda\pi/2))]/(2\omega_-^{(1)}) \quad (52)$$

It is interesting to note that parameter $\kappa^{(2)}$ doesn't enter into these expressions. Therefore, the singular nature will be independent of parameter $\kappa^{(2)}$. Moreover, it is found that the singular nature will remain the same when Δ is replaced by Δ^{-1}. This fact can be verified by considering the characteristic equation which is given by

$$\begin{aligned}
&(q_+^{(1)\lambda+1} - q_-^{(1)\lambda+1})(q_+^{(1)\lambda-1} - q_-^{(1)\lambda-1})(\sin(3\lambda\pi/2) \\
&\quad + \alpha_1 \sin(-\lambda\pi/2))(\sin(3\lambda\pi/2) + \alpha_2 \sin(-\lambda\pi/2)) \\
&\quad + (q_+^{(1)\lambda+1} - q_-^{(1)\lambda+1})(q_+^{(1)\lambda-1} - q_-^{(1)\lambda-1})\beta_1\beta_2(\cos(3\lambda\pi/2) \\
&\quad - \cos(-\lambda\pi/2))^2 + (q_+^{(1)\lambda} - q_-^{(1)\lambda})^2\beta_1\beta_2(\sin(3\lambda\pi/2) \\
&\quad - \sin(-\lambda\pi/2))^2 + (q_+^{(1)\lambda} - q_-^{(1)\lambda})^2(\cos(3\lambda\pi/2) \\
&\quad + \alpha_1 \cos(-\lambda\pi/2))(\cos(3\lambda\pi/2) + \alpha_2 \cos(-\lambda\pi/2)) \\
&\quad + \frac{4\beta_0(1-\alpha_0)(q_+^{(1)\lambda} - q_-^{(1)\lambda})}{((1+\alpha_0) + (1-\alpha_0)\Delta^{-1})((1+\alpha_0) + (1-\alpha_0)\Delta)} \\
&\quad \times (q_+^{(1)\lambda+1} - q_-^{(1)\lambda+1} + q_+^{(1)\lambda-1} - q_-^{(1)\lambda-1}) \\
&\qquad \times (1 - \cos(\lambda\pi)) = 0 \quad (53)
\end{aligned}$$

It is noted that when Δ is replaced by Δ^{-1}, the following relationships hold:

$$\alpha_1(\Delta) = \alpha_2(\Delta^{-1}), \ \beta_1(\Delta) = \beta_2(\Delta^{-1}) \quad (54)$$

Hence, it is seen that equation (53) will remain the same when Δ is replaced by Δ^{-1}. The effect of the material parameters on the singularities can be studied from Eq. (53). We choose $\beta_0 = m\alpha_0$ where $m = 0$, 0.125 and 0.25 ($|\alpha_0| \leq 1.0$) for the presentations. Results are presented in Figs. 7(a) to 7(c) with $\kappa^{(1)} = 2.0$. It is noted that real roots are always observed for the case of $\beta_0 = 0.0$.

(II) $\gamma_1 = \gamma_2 = \gamma$ ($\pi/2 < \gamma < \pi$). The second configuration considered is the problem of equal angle wedges, i.e., $\gamma_1 = \gamma_2 = \gamma$. For simplicity, we consider only the case of an isotropic material (#2) ($\kappa^{(2)} = 1 = \delta^{(2)}$) joined to an orthotropic material (#1). First we select the material combinations are such that $\alpha_0 = \beta_0 = 0$. Hence, only material parameters $\kappa^{(1)}$ and $\delta^{(1)}$ have to be considered. Figure 8 are the results of ($1 - \lambda$) versus γ for various values of $\kappa^{(1)}$ with $\delta^{(1)} = 1.0$ while those shown in Fig. 9 are the results of the influence of $\delta^{(1)}$. It is observed that for such a material compositions, the roots are found to be always real. It is also seen that the effect of the

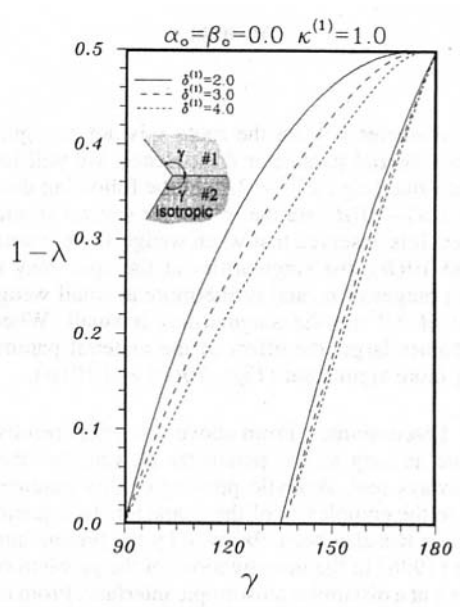


Fig. 9 Roots λ versus γ for equal angle wedge problem ($\kappa^{(1)} = 1$, $\alpha_0 = \beta_0 = 0$).

Downloaded 04 May 2010 to 171.66.16.26. Redistribution subject to ASME license or copyright; see http://www.asme.org/terms/Terms_Use.cfm

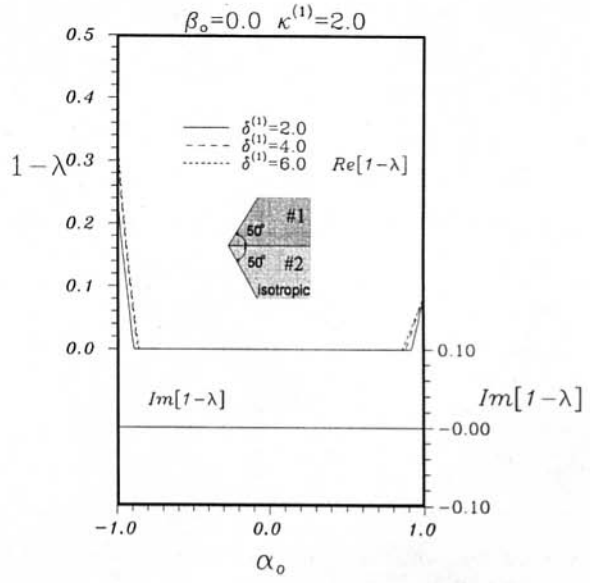


Fig. 10(*a*)

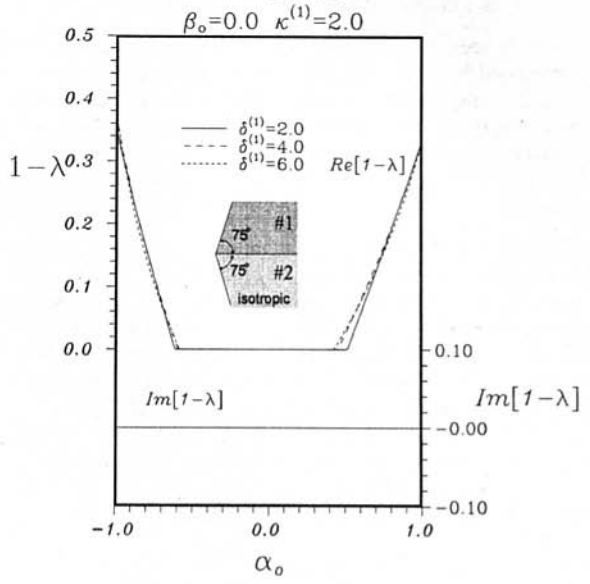


Fig. 10(*b*)

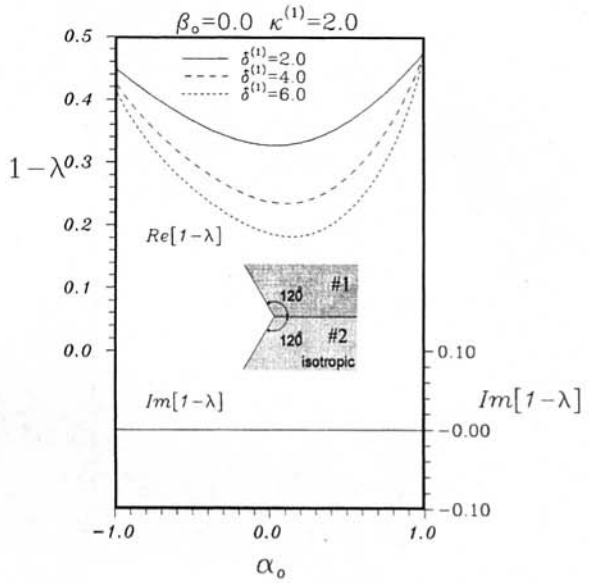


Fig. 10(*c*)

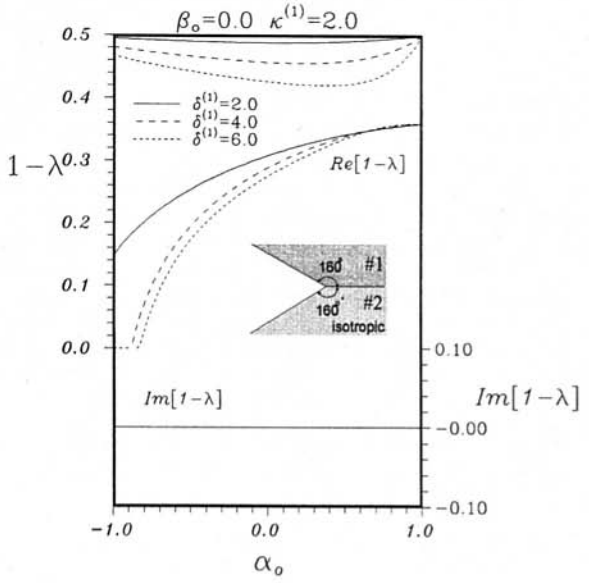


Fig. 10(*d*)

Figs. 10 Roots λ versus α_0 for equal angle wedge problems with γ = 50 deg, 75 deg, and 160 deg, respectively

material parameter $\kappa^{(1)}$ on the roots λ is not as significant as that of the material parameter $\delta^{(1)}$. Hence, we will let $\kappa^{(1)}$ be a constant value (e.g., $\kappa^{(1)} = 2.0$) in the following discussions. Figures $10(a)-10(d)$ are the results for several special wedge geometries. It is observed that when wedge angle is small (Figs. $10(a)$ and $10(b)$, the singularities at the apex may not exist for certain ranges of α_0 and furthermore at small wedge angles the effect of $\delta^{(1)}$ on the singularities is small. When wedge angle becomes large, the effect of the material parameter $\delta^{(1)}$ is getting more significant (Figs. $10(c)$ and $10(d)$.

(III) Discussions. From above numerical results, we observed that as long as the parameter β_0 vanishes the roots λ will be always real. Analytic proving of this statement is not easy due to the complexity of the characteristic equation. Same phenomenon has also been observed by the present authors Lin and Sung (1996) in the investigations of the problem of a crack terminating at a dissimilar anisotropic interface. From the results of both analyses, it appears that parameter β_0 plays some definite role in the determination of whether a root is real or complex.

6 Conclusions

A characteristic equation for the stress singularities has been derived for a dissimilar anisotropic wedge problem. Explicit forms of this equation expressed in terms of material parameters are then given for wedge problems composed by two orthotropic materials. The characteristic equation corresponding to degenerate cases can be obtained from present results. The case of a single free-fixed wedge problem is particularly studied. The stress singularities for several special wedge geometries are investigated and the dependence of the order of the singularity on the wedge angle and material parameters is also examined.

References

Bogy, D. B., 1968, "Edge-Bonded Dissimilar Orthogonal Elastic Wedges Under Normal and Shear Loading," ASME JOURNAL OF APPLIED MECHANICS, Vol. 35, p. 460.

Bogy, D. B., 1970, "On the Problem of Edge-Bonded Elastic Quarter-Planes Loaded At The Boundary," *International Journal of Solid and Structures*, Vol. 6, pp. 1287–1313.

Downloaded 04 May 2010 to 171.66.16.26. Redistribution subject to ASME license or copyright; see http://www.asme.org/terms/Terms_Use.cfm

Bogy, D. B., 1971, "Two Edge-Bonded Elastic Wedges of Different Materials Wedge Angles Under Surface Tractions," ASME JOURNAL OF APPLIED MECHANICS, Vol. 38, pp. 377–386.

Bogy, D. B., 1972, "The Plane Solution for Anisotropic Elastic Wedges under Normal and Shear Loading," ASME JOURNAL OF APPLIED MECHANICS, Vol. 39, pp. 1103–1109.

Bogy, D. B., and Wang, K. C., 1971, "Stress Singularities at Interface Corners in Bonded Dissimilar Isotropic Elastic Materials," *International Journal of Solids and Structures,* Vol. 7, pp. 993–1005.

Chadwick, P., and Smith, G. D., 1977, "Foundations of the Theory of Surface Wave in Anisotropic Elastic Materials," *Advances in Applied Mechanics,* Vol. 17, pp. 303–376.

Eshelby, J. D., Read, W. T., and Shockley, W., 1953, "Anisotropic Elasticity With Application to Dislocation Theory," *Acta Metall,* Vol. 1, pp. 251–259.

Kuo, M. C., and Bogy, D. B., 1974a, "Plane Solutions for the Displacement and Traction-Displacement Problems for Anisotropic Elastic Wedges," ASME JOURNAL OF APPLIED MECHANICS, Vol. 41, pp. 197–202.

Kuo, M. C., and Bogy, D. B., 1974b, "Plane Solutions for Traction Problems on Orthotropic Unsymmetrical Wedges and Symmetrically Twinned Wedges," ASME JOURNAL OF APPLIED MECHANICS, Vol. 41, pp. 203–208.

Lin, Y. Y., and Sung, J. C., 1996, "Singularities of an Inclined Crack Terminating at an Anisotropic Bimaterial Interface" *International Journal of Solids and Structures,* accepted for publication.

Stroh, A. N., 1958, "Dislocations and Cracks in Anisotropic Elasticity," *Philos. Mag.,* Vol. 7, pp. 625–646.

Sung, J. C., Liou, J. Y., and Lin, Y. Y., 1996, "Some Phenomena of Cracks Perpendicular to an Interface Between Dissimilar Orthotropic Materials," ASME JOURNAL OF APPLIED MECHANICS, Vol. 63, pp. 190–203.

Ting, T. C. T., 1986, "Explicit Solution and Invariance of the Singularities at an Interface Crack in Anisotropic Composites," *International Journal of Solids and Structures,* Vol. 22, pp. 965–983.

Ting, T. C. T., 1988, "Some Identities and the Structure Ni in the Stroh Formalism of Anisotropic Elasticity," *Quarterly of Applied Mathematics,* Vol. 46, pp. 109–120.

Williams, M. L., 1952, "Stress Singularities Resulting From Various Boundary Conditions in Angular Corners of Plates in Extension," ASME JOURNAL OF APPLIED MECHANICS, Vol. 19, pp. 526–528.

Wu, K. C., and Chang, F. T., 1993, "Near-Tip Fields in a Notched Body With Dislocations and Body Forces," ASME JOURNAL OF APPLIED MECHANICS, Vol. 60, pp. 936–941.

APPENDIX

The elements of $K^{\gamma}_{\alpha\beta}$ $(\alpha, \beta, \gamma = 1, 2)$ for wedges composed by two isotropic materials are as follows:

$$K^1_{11} = -\lambda[\cos(\lambda(\gamma_1+\gamma_2))(\sin\gamma_1\cos\gamma_1 - \sin\gamma_2\cos\gamma_2) + \sin(\lambda(\gamma_1+\gamma_2))(\sin^2\gamma_1 + \sin^2\gamma_2)]\beta - [\lambda\sin(\lambda(\gamma_1+\gamma_2))(\sin^2\gamma_1 - \sin^2\gamma_2) + \sin(\lambda(\gamma_1+\gamma_2)) + \lambda\cos(\lambda(\gamma_1+\gamma_2))(\sin\gamma_1\cos\gamma_1 + \sin\gamma_2\cos\gamma_2)]$$

$$K^1_{22} = \lambda[\cos(\lambda(\gamma_1+\gamma_2))(\sin\gamma_1\cos\gamma_1 - \sin\gamma_2\cos\gamma_2) + \sin(\lambda(\gamma_1+\gamma_2))(\sin^2\gamma_1 + \sin^2\gamma_2)]\beta + [\lambda\sin(\lambda(\gamma_1+\gamma_2))(\sin^2\gamma_1 - \sin^2\gamma_2) - \sin(\lambda(\gamma_1+\gamma_2)) + \lambda\cos(\lambda(\gamma_1+\gamma_2))(\sin\gamma_1\cos\gamma_1 + \sin\gamma_2\cos\gamma_2)]$$

$$K^1_{12} = [-\lambda\cos(\lambda(\gamma_1+\gamma_2))(\sin^2\gamma_1 + \sin^2\gamma_2) - \cos(\lambda(\gamma_1+\gamma_2)) + \lambda\sin(\lambda(\gamma_1+\gamma_2))(\sin\gamma_1\cos\gamma_1 - \sin\gamma_2\cos\gamma_2)]\beta + \lambda[\sin(\lambda(\gamma_1+\gamma_2))(\sin\gamma_1\cos\gamma_1 + \sin\gamma_2\cos\gamma_2) - \cos(\lambda(\gamma_1+\gamma_2))(\sin^2\gamma_1 - \sin^2\gamma_2)]$$

$$K^1_{21} = [-\lambda\cos(\lambda(\gamma_1+\gamma_2))(\sin^2\gamma_1 + \sin^2\gamma_2) + \cos(\lambda(\gamma_1+\gamma_2)) + \lambda\sin(\lambda(\gamma_1+\gamma_2))(\sin\gamma_1\cos\gamma_1 - \sin\gamma_2\cos\gamma_2)]\beta + \lambda[\sin(\lambda(\gamma_1+\gamma_2))(\sin\gamma_1\cos\gamma_1 + \sin\gamma_2\cos\gamma_2) - \cos(\lambda(\gamma_1+\gamma_2)) \times (\sin^2\gamma_1 - \sin^2\gamma_2)] \quad \text{(A1)}$$

and

$$K^2_{11} = [2\lambda^2\cos(\lambda(\gamma_1-\gamma_2))(\sin^2\gamma_2\sin\gamma_1\cos\gamma_1 + \sin^2\gamma_1\sin\gamma_2\cos\gamma_2) + 2\lambda^2\sin(\lambda(\gamma_1-\gamma_2))(\sin\gamma_1\cos\gamma_1\sin\gamma_2\cos\gamma_2 - \sin^2\gamma_1\sin^2\gamma_2) - \lambda\cos(\lambda(\gamma_1-\gamma_2))(\sin\gamma_1\cos\gamma_1 - \sin\gamma_2\cos\gamma_2) + \lambda\sin(\lambda(\gamma_1-\gamma_2))(\sin^2\gamma_1 - \sin^2\gamma_2)](\alpha-\beta) + \sin(\lambda(\gamma_1-\gamma_2))\alpha$$

$$K^2_{22} = [2\lambda^2\cos(\lambda(\gamma_1-\gamma_2))(\sin^2\gamma_2\sin\gamma_1\cos\gamma_1 + \sin^2\gamma_1\sin\gamma_2\cos\gamma_2) + 2\lambda^2\sin(\lambda(\gamma_1-\gamma_2))(\sin\gamma_1\cos\gamma_1\sin\gamma_2\cos\gamma_2 - \sin^2\gamma_1\sin^2\gamma_2) + \lambda\cos(\lambda(\gamma_1-\gamma_2))(\sin\gamma_1\cos\gamma_1 - \sin\gamma_2\cos\gamma_2) - \lambda\sin(\lambda(\gamma_1-\gamma_2))(\sin^2\gamma_1 - \sin^2\gamma_2)](\alpha-\beta) + \sin(\lambda(\gamma_1-\gamma_2))\alpha$$

$$K^1_{12} = [-2\lambda^2\sin(\lambda(\gamma_1-\gamma_2))(\sin^2\gamma_2\sin\gamma_1\cos\gamma_1 + \sin^2\gamma_1\sin\gamma_2\cos\gamma_2) + 2\lambda^2\cos(\lambda(\gamma_1-\gamma_2))(\sin\gamma_1\cos\gamma_1\sin\gamma_2\cos\gamma_2 - \sin^2\gamma_1\sin^2\gamma_2) - \lambda\sin(\lambda(\gamma_1-\gamma_2))(\sin\gamma_1\cos\gamma_1 + \sin\gamma_2\cos\gamma_2) - \lambda\cos(\lambda(\gamma_1-\gamma_2))(\sin^2\gamma_1 + \sin^2\gamma_2)](\alpha-\beta) - \cos(\lambda(\gamma_1-\gamma_2))\beta$$

$$K^2_{21} = [2\lambda^2\sin(\lambda(\gamma_1-\gamma_2))(\sin^2\gamma_2\sin\gamma_1\cos\gamma_1 + \sin^2\gamma_1\sin\gamma_2\cos\gamma_2) - 2\lambda^2\cos(\lambda(\gamma_1-\gamma_2))(\sin\gamma_1\cos\gamma_1\sin\gamma_2\cos\gamma_2 - \sin^2\gamma_1\sin^2\gamma_2) - \lambda\sin(\lambda(\gamma_1-\gamma_2))(\sin\gamma_1\cos\gamma_1 + \sin\gamma_2\cos\gamma_2) - \lambda\cos(\lambda(\gamma_1-\gamma_2))(\sin^2\gamma_1 + \sin^2\gamma_2)](\alpha-\beta) - \cos(\lambda(\gamma_1-\gamma_2))\beta \quad \text{(A2)}$$

where α and β are Dundurs' constants.

Downloaded 04 May 2010 to 171.66.16.26. Redistribution subject to ASME license or copyright; see http://www.asme.org/terms/Terms_Use.cfm

Physical Restrictions on the Impulse Acting During Three-Dimensional Impact of Two "Rigid" Bodies

M. B. Rubin
Faculty of Mechanical Engineering,
Technion—Israel Institute of Technology,
32000 Haifa, Israel
Mem. ASME

It is well known that the impulse of the contact force acting during impact of two rigid bodies determines the abrupt change in the motions of the two bodies. Much recent work has been focused on determining a constitutive equation for this impulse which models the complicated phenomena occurring during the actual deformations of the two bodies. The objective of this paper is to discuss a set of physical conditions which impose nontrivial restrictions on general constitutive equations for the impulse. Due to the general nature of these restrictions they can be used to determine the range of validity of various proposals for the impulse. For the general case of three-dimensional impact, the impulse depends on an energetic coefficient of restitution and two angles defining its direction. However, when there are no directional properties of the roughness of the two impacting bodies, it is reasonable to propose a simpler form for the direction of the impulse which depends only on this coefficient of restitution and a single friction angle. An example of impact of two finite spheres is considered which shows that the condition that the two bodies have a tendency to separate after impact imposes nontrivial bounds on this friction angle.

1 Introduction

A number of complicated phenomena occur when two bodies collide. Since no materials are infinitely stiff this collision causes elastic waves to propagate from the contact region into each of the bodies. It also causes deformation of the surfaces of the bodies in contact and spreading of the contact region. Moreover, if the relative velocity of the points which initiate the contact is large enough then the deformation of the bodies can dissipate energy due to inelastic effects. Additional dissipation can be caused by slipping of the two bodies in the contact region.

In spite of the complicated nature of the deformations that occur in each body during impact it is sometimes possible to model the impact using rigid-body dynamics. Such models usually make the following two assumptions.

(A1) The time interval (t_1, t_2) of the impulsive contact is so short that the centers of mass and angular orientations of the two rigid bodies are presumed not to change during the impulsive event.

(A2) The contact region remains small enough relative to the sizes of the two bodies that the impulsive loads acting in this contact region are considered to act at a single point of contact of the two bodies.

Within the context of such assumptions, the complicated phenomena associated with actual deformations of the bodies are modeled by equations for the magnitude and direction of the impulse of the force acting in the contact region. Also, assumption (A2) precludes a discussion of penetration-type problems where large plastic deformations cause significant changes in the shape of one or both of the impacting bodies.

Contributed by the Applied Mechanics Division of THE AMERICAN SOCIETY OF MECHANICAL ENGINEERS for publication in the ASME JOURNAL OF APPLIED MECHANICS.

Discussion on the paper should be addressed to the Technical Editor, Professor Lewis T. Wheeler, Department of Mechanical Engineering, University of Houston, Houston, TX 77204-4792, and will be accepted until four months after final publication of the paper itself in the ASME JOURNAL OF APPLIED MECHANICS.

Manuscript received by the ASME Applied Mechanics Division, Nov. 22, 1996; final revision, Sept. 12, 1997. Associate Technical Editor: S. W. Shaw.

Rigid-body dynamics provides algebraic equations that connect the impulse with the discontinuities in the velocities of the centers of mass and the angular velocities of the two bodies before and after the impact event. However, rigid-body dynamics does not provide a constitutive equation for this impulse. To motivate constitutive equations for this impulse many researchers are modeling details of the complicated interactions that occur and are integrating equations of motion over a finite period of the impact event. Such an approach provides integral expressions for the total impulse applied during the impact. Therefore, in either case, the final expression for the impulse can be analyzed within the context of the restrictions discussed in this paper.

For the simple case of collinear impact of two point masses it is well known that the velocities after impact can be determined in terms of a phenomenological quantity called the coefficient of restitution e. For this simple case, the quantity e can be interpreted in three ways: (a) as the separation velocity divided by the approach velocity; (b) as the impulse applied during restitution divided by the impulse applied during compression; and (c) as the square root of the change in kinetic energy during restitution divided by the change in kinetic energy during compression. This latter interpretation causes e to be a measure of the amount of kinetic energy that is dissipated during the impact event, with $e = 1$ for no dissipation and $e = 0$ for maximum dissipation. In this regard, it should be mentioned that Calladine (1990) has proposed a graphical representation that explains these three interpretations of the coefficient of restitution.

Much recent work has been concerned with the more complicated problem of contact of multibody linkages (e.g., Moreau, 1994; Ivanov, 1995; Pfeiffer, 1996). Particular reference should be made to the monograph of Brogliato (1996) on nonsmooth impact which discusses many of the complicated features of modeling a number of unilateral constraints characterizing contact of multibody systems. In spite of the mathematical difficulties in modeling multibody contact, there still appears to be no real consensus on how to model the general problem of

 Copyright © 1998 by ASME

Downloaded 04 May 2010 to 171.66.16.26. Redistribution subject to ASME license or copyright; see http://www.asme.org/terms/Terms_Use.cfm

three-dimensional impact of only two rigid bodies (Mac Sithigh, 1995; Chatterjee, 1997a).

The historical review by Goldsmith (1960) indicates that the initial discussion of rigid-body impact is due to Galileo and that Newton introduced the notion of the coefficient of restitution e. Most recent work on the impact of two "rigid" bodies uses Hertz theory of contact to determine the magnitude of the normal contact force. Keller (1986) used the coefficient of restitution e and analyzed the problem of impact with Coulomb friction to provide a relationship between the normal and tangential impulses. Moreover, the effects of different definitions of e have been considered by Smith and Liu (1992) and Marghitu and Hurmuzlu (1995), and the effect of plastic deformation on the value of e has been considered by Stronge (1995). Also, modifications of the Hertz theory which include the effect of local curvature have been discussed by Villaggio (1996).

From the point of view of rigid-body dynamics the value of e can be less than unity with kinetic energy loss in the impact event even if the two bodies remain elastic. This is because wave propagation effects can cause elastic strain energy and kinetic energy to be trapped in vibrational modes of the bodies after impact (e.g., Hunter, 1957; Stronge, 1995; Stoianovici and Hurmuzlu, 1996).

Much of the previous work on rigid-body impact attempts to propose quantitative functional forms for the coefficient of restitution and the direction of impulse applied. These functional forms are thought of here as constitutive equations which depend on the material and geometric properties of the two bodies as well as on the relative velocity of impact. The objective of this paper is to discuss a set of physical conditions which impose nontrivial restrictions on general constitutive equations for the impulse. Due to the general nature of these restrictions, they must be satisfied by all constitutive equations for the impulse. Consequently, it is expected that these restrictions will provide useful guidance for limiting functional forms proposed for the impulse which attempt to model complicated features of the impact event due to inelasticity, friction and wave propagation. In particular, they can be used to determine the range of validity of various proposals for the impulse.

Restrictions for specific classes of problems are discussed in the book by Brach (1991) which include the common notion that the dissipation of kinetic energy during the impact event must be non-negative. Brach (1991, p. 36) also mentions a less well-known restriction that the tangential component of the impulse must be limited. In addition, some general considerations of rigid-body collision laws together with a number of relevant references has been presented in an expanded form by Chatterjee (1997a) and in a more concise form by Chatterjee and Ruina (1997b, c).

A brief outline of the paper is as follows. Section 2 presents the basic formulation and equations and Section 3 presents physical restrictions on the impulse. Section 4 summarizes the main results, which are formulated in terms of an energetic definition of the coefficient of restitution for three-dimensional impact and two angles that characterize the direction of impulse. Also, in Section 4, a simpler form for the direction of the impulse is proposed in terms of this coefficient of restitution and a single friction angle, and an example of impact of two finite spheres is considered.

Throughout the text, vectors and tensors are denoted by boldfaced symbols and no summation convention is implied for repeated capital indices. The dot, cross, and tensor product operations are denoted by the symbols $(\cdot)$, $(\times)$, and $(\otimes)$, respectively, and some tensor operations needed for the mathematical development presented here are reviewed in the Appendix.

2 Basic Formulation and Equations

Consider two rigid bodies A and B which are moving so that at the instant of impact point C on the surface of body A coincides with point D on the surface of body B (Fig. 1). Just before the beginning of impact ($t = t_1$), body A has absolute angular velocity $\boldsymbol{\omega}_{A1}$, its center of mass (point A) has absolute velocity $\mathbf{v}_{A1}$, and point C has absolute velocity $\mathbf{v}_{C1}$. At this same time ($t = t_1$), body B has absolute angular velocity $\boldsymbol{\omega}_{B1}$, its center of mass (point B) has absolute velocity $\mathbf{v}_{B1}$, and point D has absolute velocity $\mathbf{v}_{D1}$. Just after the end of the impact ($t = t_2$), these physical quantities attain the values $\{\boldsymbol{\omega}_{A2}, \mathbf{v}_{A2}, \mathbf{v}_{C2}, \boldsymbol{\omega}_{B2}, \mathbf{v}_{B2}, \mathbf{v}_{D2}\}$, respectively. Also, let m_A be the mass of body A; $\mathbf{I}_A$ be the inertia tensor of body A about its center of mass; $\mathbf{r}_{C/A}$ be the position vector of point C relative to point A; m_B be the mass of body B; $\mathbf{I}_B$ be the inertia tensor of body B about its center of mass; and $\mathbf{r}_{D/B}$ be the position vector of point D relative to point B. It follows that in view of the assumption (A1) the quantities $\{\mathbf{I}_A, \mathbf{r}_{C/A}, \mathbf{I}_B, \mathbf{r}_{D/B}\}$ remain constant during the impact.

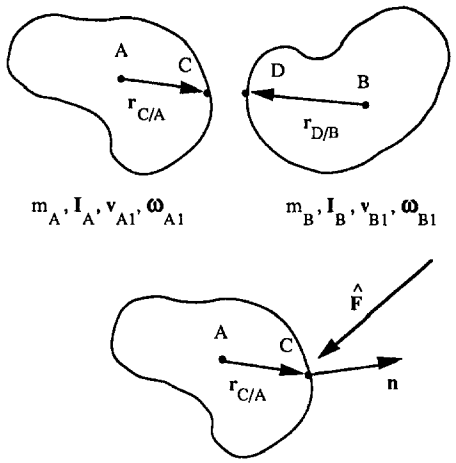


Fig. 1 Sketch of two rigid bodies just before impact at points C and D. Also shown are the unit outward normal n to body A and the impulse $\hat{\mathbf{F}}$ applied by body B on body A.

Letting $\mathbf{F}(t)$ be the force applied by body B on body A during the impact event it follows that the impulse $\hat{\mathbf{F}}$ due to this force is defined by (see Fig. 1)

$$\hat{\mathbf{F}} = \int_{t_1}^{t_2} \mathbf{F}(t)\,dt. \tag{1}$$

Next, using the above definitions and integrating the equations of linear momentum and angular momentum (about the center of mass) of the two bodies yields the equations

$$\hat{\mathbf{F}} = m_A(\mathbf{v}_{A2} - \mathbf{v}_{A1}), \quad \mathbf{r}_{C/A} \times \hat{\mathbf{F}} = \mathbf{I}_A(\boldsymbol{\omega}_{A2} - \boldsymbol{\omega}_{A1}),$$
$$-\hat{\mathbf{F}} = m_B(\mathbf{v}_{B2} - \mathbf{v}_{B1}), \quad -\mathbf{r}_{D/B} \times \hat{\mathbf{F}} = \mathbf{I}_B(\boldsymbol{\omega}_{B2} - \boldsymbol{\omega}_{B1}), \tag{2}$$

where use has also been made of assumptions (A1) and (A2) to write the impulse (in $(2)_{2,4}$) due to the moments applied by the force $\mathbf{F}(t)$ about the centers of mass of the bodies. In addition, Eqs. (2) reflect the fact that $(-\hat{\mathbf{F}})$ is the impulse applied by body A on body B.

Since the inertia tensors $\mathbf{I}_A$ and $\mathbf{I}_B$ are symmetric positive definite tensors they can be inverted and Eqs. (2) can be rewritten in the forms

$$\mathbf{v}_{A2} = \mathbf{v}_{A1} + \frac{1}{m_A}\hat{\mathbf{F}}, \quad \boldsymbol{\omega}_{A2} = \boldsymbol{\omega}_{A1} + \mathbf{I}_A^{-1}(\mathbf{r}_{C/A} \times \hat{\mathbf{F}}),$$
$$\mathbf{v}_{B2} = \mathbf{v}_{B1} - \frac{1}{m_B}\hat{\mathbf{F}}, \quad \boldsymbol{\omega}_{B2} = \boldsymbol{\omega}_{B1} - \mathbf{I}_B^{-1}(\mathbf{r}_{D/B} \times \hat{\mathbf{F}}). \tag{3}$$

Moreover, since the bodies are rigid, the velocities of points C and D are given by

Downloaded 04 May 2010 to 171.66.16.26. Redistribution subject to ASME license or copyright; see http://www.asme.org/terms/Terms_Use.cfm

$$\mathbf{v}_{C1} = \mathbf{v}_{A1} + \boldsymbol{\omega}_{A1} \times \mathbf{r}_{C/A}, \quad \mathbf{v}_{C2} = \mathbf{v}_{A2} + \boldsymbol{\omega}_{A2} \times \mathbf{r}_{C/A},$$

$$\mathbf{v}_{D1} = \mathbf{v}_{B1} + \boldsymbol{\omega}_{B1} \times \mathbf{r}_{D/B}, \quad \mathbf{v}_{D2} = \mathbf{v}_{B2} + \boldsymbol{\omega}_{B2} \times \mathbf{r}_{D/B}. \quad (4)$$

Now, substitution of (3) into (4) yields the expressions

$$\mathbf{v}_{C2} = \mathbf{v}_{C1} + \frac{1}{m_A}\hat{\mathbf{F}} - [\mathbf{r}_{C/A} \times \mathbf{I}_A^{-1}(\mathbf{r}_{C/A} \times \hat{\mathbf{F}})],$$

$$\mathbf{v}_{D2} = \mathbf{v}_{D1} - \frac{1}{m_B}\hat{\mathbf{F}} + [\mathbf{r}_{D/B} \times \mathbf{I}_B^{-1}(\mathbf{r}_{D/B} \times \hat{\mathbf{F}})]. \quad (5)$$

Thus, the relative velocities of the contact points C and D can be defined by the expressions

$$\Delta\mathbf{v}_1 = \mathbf{v}_{C1} - \mathbf{v}_{D1}, \quad \Delta\mathbf{v}_2 = \mathbf{v}_{C2} - \mathbf{v}_{D2}, \quad (6)$$

so that

$$\Delta\mathbf{v}_2 = \Delta\mathbf{v}_1 + \left[\frac{m_A + m_B}{m_A m_B}\right]\hat{\mathbf{F}} - [\mathbf{r}_{C/A} \times \mathbf{I}_A^{-1}(\mathbf{r}_{C/A} \times \hat{\mathbf{F}}) + \mathbf{r}_{D/B} \times \mathbf{I}_B^{-1}(\mathbf{r}_{D/B} \times \hat{\mathbf{F}})]. \quad (7)$$

Furthermore, with the help of the result (A3) of the Appendix, Eq. (7) can be written in the simplified form

$$\Delta\mathbf{v}_2 = \Delta\mathbf{v}_1 + \frac{1}{m}\mathbf{A}\hat{\mathbf{F}}, \quad (8)$$

where the effective mass m and the symmetric positive definite inertia tensor $\mathbf{A}$ have been defined by

$$m = \frac{m_A m_B}{m_A + m_B},$$

$$\mathbf{A} = \mathbf{I} + m[(\boldsymbol{\epsilon}\mathbf{r}_{C/A})^T\mathbf{I}_A^{-1}(\boldsymbol{\epsilon}\mathbf{r}_{C/A}) + (\boldsymbol{\epsilon}\mathbf{r}_{D/B})^T\mathbf{I}_B^{-1}(\boldsymbol{\epsilon}\mathbf{r}_{D/B})]. \quad (9)$$

Next, it is recalled that the total kinetic energy of the two-body system just before impact T_1 and that just after impact T_2 are given by

$$T_1 = \tfrac{1}{2} m_A \mathbf{v}_{A1} \cdot \mathbf{v}_{A1} + \tfrac{1}{2}\mathbf{I}_A \cdot (\boldsymbol{\omega}_{A1} \otimes \boldsymbol{\omega}_{A1}) + \tfrac{1}{2} m_B \mathbf{v}_{B1} \cdot \mathbf{v}_{B1} + \tfrac{1}{2}\mathbf{I}_B \cdot (\boldsymbol{\omega}_{B1} \otimes \boldsymbol{\omega}_{B1}),$$

$$T_2 = \tfrac{1}{2} m_A \mathbf{v}_{A2} \cdot \mathbf{v}_{A2} + \tfrac{1}{2}\mathbf{I}_A \cdot (\boldsymbol{\omega}_{A2} \otimes \boldsymbol{\omega}_{A2}) + \tfrac{1}{2} m_B \mathbf{v}_{B2} \cdot \mathbf{v}_{B2} + \tfrac{1}{2}\mathbf{I}_B \cdot (\boldsymbol{\omega}_{B2} \otimes \boldsymbol{\omega}_{B2}). \quad (10)$$

However, with the help of the expressions (3)–(9) and those in the Appendix it can be shown that

$$T_1 - T_2 = \left[-\hat{\mathbf{F}} \cdot \Delta\mathbf{v}_1 - \frac{1}{2m}\mathbf{A} \cdot (\hat{\mathbf{F}} \otimes \hat{\mathbf{F}})\right]. \quad (11)$$

Also, it should be mentioned that equations of the types (8) and (11), and the importance of a tensor related to (9), have previously been considered by other authors (Smith, 1991; Ivanov, 1992; Mac Sithigh, 1995; Chatterjee, 1997a).

The critical value of energy dissipation is attained when the impulse $\hat{\mathbf{F}}$ satisfies the equation

$$\frac{d(T_1 - T_2)}{d\hat{\mathbf{F}}} = -\Delta\mathbf{v}_1 - \frac{1}{m}\mathbf{A}\hat{\mathbf{F}} = 0. \quad (12)$$

Moreover, since the second derivative of the energy dissipation with respect to the impulse is negative definite

$$\frac{d^2(T_1 - T_2)}{d\hat{\mathbf{F}} \otimes d\hat{\mathbf{F}}} = -\frac{1}{m}\mathbf{A}, \quad (13)$$

it follows that this value of $\hat{\mathbf{F}}$ causes the energy dissipation to attain a local maximum. Also, with the help of (8), (11), and (12) it can be shown that for this maximum value of energy dissipation

$$\hat{\mathbf{F}} = -m\mathbf{A}^{-1}\Delta\mathbf{v}_1, \quad \Delta\mathbf{v}_2 = 0,$$

$$T_1 - T_2 = \frac{m}{2}\mathbf{A}^{-1} \cdot (\Delta\mathbf{v}_1 \otimes \Delta\mathbf{v}_1) > 0. \quad (14)$$

Physically, the result $(14)_2$ means that the contact points on the two bodies tend to stick together after impact.

3 Restrictions on the Impulse

In order to limit the magnitude and direction of the impulse it seems reasonable to make the following four physical assumptions:

(P1) The impulse is not orthogonal to the relative velocity of the contact points just before impact

$$\hat{\mathbf{F}} \cdot \Delta\mathbf{v}_1 \neq 0, \quad (15)$$

(P2) The impulse has a component that resists penetration and aids separation of the two bodies

$$\hat{\mathbf{F}} \cdot (-\mathbf{n}) > 0, \quad (16)$$

(P3) The two bodies have a tendency to separate after the impact event

$$\Delta\mathbf{v}_2 \cdot (-\mathbf{n}) \geq 0, \quad (17)$$

(P4) The dissipation of kinetic energy during the impact event is non-negative

$$T_1 - T_2 \geq 0. \quad (18)$$

These assumptions place restrictions on the impulse $\hat{\mathbf{F}}$ because with the help of (8) and (11) the conditions (17) and (18) can be rewritten as functions of $\hat{\mathbf{F}}$. Moreover, it is noted that the impact event will not occur unless the bodies have a tendency to penetrate each other with

$$\Delta\mathbf{v}_1 \cdot \mathbf{n} > 0. \quad (19)$$

To analyze these restrictions it is convenient to write the impulse $\hat{\mathbf{F}}$ in terms of its magnitude f and its direction $\mathbf{f}$ such that

$$\hat{\mathbf{F}} = f\mathbf{f}, \quad f > 0, \quad \mathbf{f} \cdot \mathbf{f} = 1, \quad (20)$$

where the trivial case of zero impulse has been excluded. It then follows from (15) and the positive definite character of $\mathbf{A}$, that without loss in generality, the magnitude f can be written in terms of the scalar η such that

$$f = (1 + \eta)\left[\frac{-m\mathbf{f} \cdot \Delta\mathbf{v}_1}{\mathbf{A} \cdot (\mathbf{f} \otimes \mathbf{f})}\right]. \quad (21)$$

Now, substitution of (20) and (21) into (11) yields the expression

$$T_1 - T_2 = (1 - \eta^2)\left[\frac{m(\mathbf{f} \cdot \Delta\mathbf{v}_1)^2}{2\mathbf{A} \cdot (\mathbf{f} \otimes \mathbf{f})}\right], \quad (22)$$

which will satisfy the energy dissipation restriction (18) provided that η is limited to the range

$$-1 < \eta \leq 1, \quad (23)$$

with the value $\eta = -1$ being excluded because of $(20)_2$ and (21). Also, by substituting (23) into (21) it is possible to develop a stronger restriction than (15) which requires

$$\mathbf{f} \cdot (-\Delta\mathbf{v}_1) > 0, \quad (24)$$

and indicates that the impulse resists the relative velocity of the

Downloaded 04 May 2010 to 171.66.16.26. Redistribution subject to ASME license or copyright; see http://www.asme.org/terms/Terms_Use.cfm

contact points just before impact (this result was also obtained by Chatterjee, 1997a). Next, by using (20) and (21) and taking the dot product of (8) with the direction of $\mathbf{f}$ it follows that

$$\eta = -\frac{\mathbf{f}\cdot\Delta\mathbf{v}_2}{\mathbf{f}\cdot\Delta\mathbf{v}_1}. \tag{25}$$

This last expression indicates that η is the same coefficient of restitution that was introduced by Ivanov (1992) who used a different method of analysis. Furthermore, it is noted from (25) that η relates the changes in the components of the relative velocities in the direction $\mathbf{f}$ of impulse instead of the components in the normal direction $\mathbf{n}$ as is indicated by the formula for the case of collinear impact of two point masses. Also, it is noted that Brogliato (1996, Sec. 6.2) has recorded generalizations of Eqs. (21) and (22) for frictionless impacts of multibody systems.

To expand on the interpretation of η, it can be shown that when $\mathbf{f}$ is taken in the direction of maximum energy dissipation $(14)_1$ that (8) reduces to

$$\Delta\mathbf{v}_2 = -\eta\Delta\mathbf{v}_1 \quad \text{for} \quad \mathbf{f} = -\frac{\mathbf{A}^{-1}\Delta\mathbf{v}_1}{|\mathbf{A}^{-1}\Delta\mathbf{v}_1|}. \tag{26}$$

This means that for this direction of impulse the relative velocity after impact remains in the same direction as that before impact. Also, for this value of $\mathbf{f}$ and for η restricted to the range (23), the conditions (18) and (24) are automatically satisfied and the conditions (16) and (17) require

$$\mathbf{n}\cdot\mathbf{A}^{-1}\Delta\mathbf{v}_1 > 0, \quad \eta \geq 0. \tag{27}$$

Thus, the specification $(26)_2$ is only possible if $\Delta\mathbf{v}_1$ satisfies the restriction $(27)_1$.

4 Discussion

Examination of the expressions (22) and (26) suggests that the scalar η is a natural generalization to three-dimensional impact of the energetic interpretation of the coefficient of restitution for one-dimensional impact. In particular, it follows from (22) that the energy dissipation vanishes when $\eta = 1$ and for the special case when $\eta = 0$ and $\mathbf{f}$ is oriented in the direction $(26)_2$, the bodies remain in contact just after impact since $\Delta\mathbf{v}_2 = 0$. In this regard it should be emphasized that when $\eta = 0$ and $\mathbf{f}$ is not oriented in the direction $(26)_2$ then the bodies do not remain in contact just after impact. However, the value of $\eta = 0$ is still associated with maximum energy dissipation for any specific $\mathbf{f}$. Also, since the expression (22) is unchanged by replacing the unit vector $\mathbf{f}$ with the impulse $\hat{\mathbf{F}}$ it can be shown that the energy dissipation attains its maximum value for constant η and $\Delta\mathbf{v}_1$ when $\mathbf{f}$ is in the direction $(26)_2$.

Although the energy dissipation will be non-negative when η is restricted to the range (23), the expression (25) indicates that negative values of η would cause the components $\mathbf{f}\cdot\Delta\mathbf{v}_1$ and $\mathbf{f}\cdot\Delta\mathbf{v}_2$ of the relative velocities in the direction of impulse to have the same signs, which does not seem physically reasonable. Moreover, when $\mathbf{f}$ is oriented in the direction $(26)_2$ then η must be non-negative $(27)_2$. For these reasons it is assumed that η remains non-negative. Consequently, with the help of the representation (20) for the impulse and the expression (8), the restrictions (24) and (16)–(18) are satisfied, provided that

$$\mathbf{f}\cdot(-\Delta\mathbf{v}_1) > 0, \quad \mathbf{f}\cdot(-\mathbf{n}) > 0,$$

$$(-\mathbf{n})\cdot\mathbf{A}\mathbf{f} \geq \frac{(\Delta\mathbf{v}_1\cdot\mathbf{n})\mathbf{A}\cdot(\mathbf{f}\otimes\mathbf{f})}{(1+\eta)\mathbf{f}\cdot(-\Delta\mathbf{v}_1)}, \quad 0 \leq \eta \leq 1. \tag{28}$$

It also follows that if the bodies are smooth and there is no frictional component of the impulse, then $(28)_3$ requires

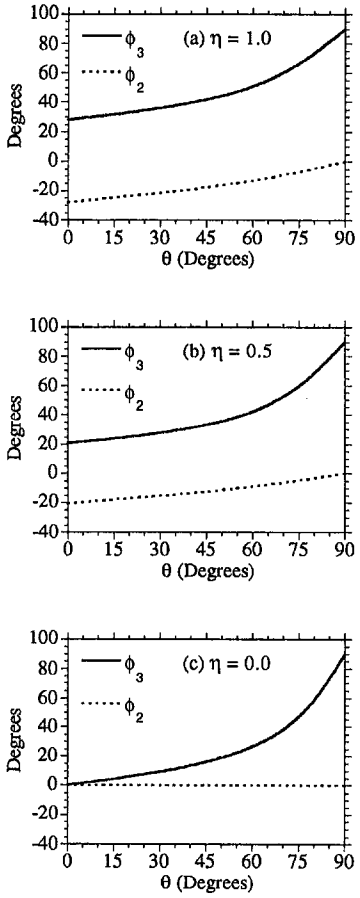


Fig. 2 Impact of two spheres. Plots of the minimum ϕ_2 and maximum ϕ_3 friction angles versus the angle θ of the initial relative velocity for three values of the coefficient of restitution η.

$$1 \geq \frac{1}{1+\eta} \quad \text{for} \quad \mathbf{f} = -\mathbf{n}, \tag{29}$$

which provides additional justification for omitting negative values of η.

From the point of view of applications it is necessary to propose constitutive equations for the generalized coefficient of restitution η and two angles that characterize the unit vector $\mathbf{f}$ describing the direction of the impulse. If these constitutive equations are restricted so that the inequalities (28) are satisfied then the physical restrictions (15)–(18) and (24) will also be satisfied. Consequently, it is desirable to use these inequalities to limit proposed functional forms for the impulse.

The previous results are general and are presumed to be valid for all constitutive equations. However, when there are no directional properties of the roughness of the two impacting bodies, it is reasonable to propose a simpler form for the direction of the impulse which depends only on the coefficient of restitution and a single friction angle. For this case it is assumed that the impulse acts in the plane defined by the normal $\mathbf{n}$ and the direction of the vector $\mathbf{A}^{-1}\Delta\mathbf{v}_1$ which causes maximum energy dissipation for a fixed value of η (see $(26)_2$) (this same plane was considered as collision law II in Chatterjee (1997a) and Chatterjee and Ruina, (1997c)). Thus, $\mathbf{f}$ is specified by

$$\mathbf{f} = -\cos\phi\,\mathbf{n} - \sin\phi\left[\frac{\mathbf{A}^{-1}\Delta\mathbf{v}_1 - (\mathbf{n}\cdot\mathbf{A}^{-1}\Delta\mathbf{v}_1)\mathbf{n}}{|\mathbf{A}^{-1}\Delta\mathbf{v}_1 - (\mathbf{n}\cdot\mathbf{A}^{-1}\Delta\mathbf{v}_1)\mathbf{n}|}\right], \tag{30}$$

where ϕ is the friction angle. Here, it is tacitly assumed that if

Downloaded 04 May 2010 to 171.66.16.26. Redistribution subject to ASME license or copyright; see http://www.asme.org/terms/Terms_Use.cfm

$\mathbf{A}^{-1}\Delta\mathbf{v}_1$ is in the direction of $\mathbf{n}$ then $\mathbf{f}$ also is in the direction of $\mathbf{n}$ with $\phi = 0$.

Within the context of the assumption (30) the impulse is characterized by only two constitutive equations: one for the coefficient of restitution η and one for the friction angle ϕ. By defining the angle ϕ_1,

$$\phi_1 = -\tan^{-1}\left[\frac{(\mathbf{n}\cdot\Delta\mathbf{v}_1)|\mathbf{A}^{-1}\Delta\mathbf{v}_1 - (\mathbf{n}\cdot\mathbf{A}^{-1}\Delta\mathbf{v}_1)\mathbf{n}|}{\Delta\mathbf{v}_1\cdot\{\mathbf{A}^{-1}\Delta\mathbf{v}_1 - (\mathbf{n}\cdot\mathbf{A}^{-1}\Delta\mathbf{v}_1)\mathbf{n}\}}\right], \quad (31)$$

it can be shown that the inequalities $(28)_1$ and $(28)_2$ are satisfied provided that ϕ is limited to the range

$$\phi_1 < \phi < \frac{\pi}{2}. \quad (32)$$

The condition $(28)_3$ further limits the range of ϕ but at present it does not appear that this condition can be simplified. Also, η is limited to the range $(28)_4$.

As a simple example consider the collision of two homogeneous spheres of radii R_A and R_B, respectively, and take

$$\mathbf{n} = \mathbf{e}_1, \quad \Delta\mathbf{v}_1 = \Delta v_1[\cos\theta\mathbf{e}_1 + \sin\theta\mathbf{e}_2],$$
$$\Delta v_1 > 0, \quad 0 \le \theta < \frac{\pi}{2}. \quad (33)$$

It follows from the geometric properties of spheres that

$$\mathbf{r}_{C/A} = R_A\mathbf{e}_1, \quad \mathbf{I}_A = \frac{2m_AR_A^2}{5}\mathbf{I},$$
$$\mathbf{r}_{D/B} = -R_B\mathbf{e}_1, \quad \mathbf{I}_B = \frac{2m_BR_B^2}{5}\mathbf{I}, \quad (34)$$

which can be used to deduce that

$$\mathbf{A} = \mathbf{e}_1\otimes\mathbf{e}_1 + \tfrac{7}{2}(\mathbf{e}_2\otimes\mathbf{e}_2 + \mathbf{e}_3\otimes\mathbf{e}_3),$$
$$\mathbf{A}^{-1} = \mathbf{e}_1\otimes\mathbf{e}_1 + \tfrac{2}{7}(\mathbf{e}_2\otimes\mathbf{e}_2 + \mathbf{e}_3\otimes\mathbf{e}_3). \quad (35)$$

Thus, with the help of (30) it can be shown that

$$\mathbf{f} = -(\cos\phi\mathbf{e}_1 + \sin\phi\mathbf{e}_2), \quad \phi_1 = \theta - \frac{\pi}{2}, \quad (36)$$

and that the restriction $(28)_3$ reduces to

$$\cos\phi \ge \frac{\cos\theta(2 + 5\sin^2\phi)}{2(1+\eta)\cos(\phi - \theta)}. \quad (37)$$

In order to determine the range of ϕ allowed by the restriction (37), the values of ϕ^* which satisfy the equality are determined by the equation

$$2(1+\eta)[\cos^2\phi^* + \tfrac{1}{2}\sin(2\phi^*)\tan\theta] = 2 + 5\sin^2\phi^*,$$
$$2(1+\eta)\cos^2\phi^* - 2 - 5\sin^2\phi^* = -(1+\eta)\sin(2\phi^*)\tan\theta. \quad (38)$$

Now, expressing $\cos^2\phi^*$ and $\sin^2\phi^*$ in terms of $\cos(2\phi^*)$ and squaring both sides of $(38)_2$ yields a quadratic equation for $\cos(2\phi^*)$ of the form

$$[(7+2\eta)^2 + 4(1+\eta)^2\tan^2\theta]\cos^2(2\phi^*) - 2(49 - 4\eta^2)\cos(2\phi^*) + [(7-2\eta)^2 - 4(1+\eta)^2\tan^2\theta] = 0, \quad (39)$$

which can be solved to obtain the two relevant solutions

$$\phi_2 = -\frac{1}{2}\cos^{-1}\left[\frac{(49-4\eta^2) + 4(1+\eta)\tan\theta\{14\eta + (1+\eta)^2\tan^2\theta\}^{1/2}}{(7+2\eta)^2 + 4(1+\eta)^2\tan^2\theta}\right] \le 0,$$
$$\phi_3 = \frac{1}{2}\cos^{-1}\left[\frac{(49-4\eta^2) - 4(1+\eta)\tan\theta\{14\eta + (1+\eta)^2\tan^2\theta\}^{1/2}}{(7+2\eta)^2 + 4(1+\eta)^2\tan^2\theta}\right] \ge 0. \quad (40)$$

Moreover, it can be shown that

$$\phi_1 < \phi_2 \le \phi \le \phi_3 < \frac{\pi}{2}. \quad (41)$$

This result indicates that the range of the friction angle is totally determined by the restriction $(28)_3$ which requires the two bodies to have a tendency to separate after the impact event. Consequently, the acceptable range of ϕ can be shown graphically in Fig. 2 by plotting ϕ_2 and ϕ_3 as functions of the angle θ of the initial relative impact velocity for various values of the coefficient of restitution η. These results reveal that the extent of this acceptable range decreases with decreasing values of η. Also, it should be mentioned that when η is positive the friction angle ϕ can be negative. However, the physical significance of negative values of ϕ is unclear.

In summary, the physical conditions (15)–(18) impose restrictions on constitutive equations for the impulse that acts during the impact event. These conditions have been reformulated (28) in terms of a generalized coefficient of restitution η and the direction $\mathbf{f}$ of the impulse (see (20) and (21)). It is hoped that the compact tensorial form (28) will be useful in determining the range of validity of various proposals of constitutive equations for the impulse.

Acknowledgments

The author would like to thank Prof. D. Pai for calling his attention to this problem and for a number of helpful discussions. Also, the author would like to thank Dr. A. Chatterjee for helpful discussions and for supplying a number of references which were unknown to the author during the preparation of the original manuscript.

References

Brach, R. M., 1991, *Mechanical Impact Dynamics: Rigid Body Collisions,* John Wiley and Sons, New York.

Brogliato, B., 1996, *Nonsmooth Impact Mechanics, Models, Dynamics and Controls* (Lecture Notes in Control and Information Sciences 220), Springer-Verlag, New York.

Calladine, C. R., 1990, "The teaching of some aspects of the theory of inelastic collisions," *International Journal of Mechanical Engineering Education,* Vol. 18, pp. 301–310.

Chatterjee, A., 1997a, "Rigid body collisions: Some general considerations, new collision laws, and some experimental data," Ph.D. thesis supervised by A. Ruina at Cornell University, Ithaca, New York.

Chatterjee, A., and Ruina, A., 1997b, "Rigid body collision laws: Some general considerations," presented at the Fifth Pan American Congress of Applied Mechanics, Jan. 2–4, San Juan, Puerto Rico.

Chatterjee, A., and Ruina, A., 1997c, "Some new algebraic rigid body collision laws," Presented at the Fifth Pan American Congress of Applied Mechanics, Jan. 2–4, San Juan, Puerto Rico.

Downloaded 04 May 2010 to 171.66.16.26. Redistribution subject to ASME license or copyright; see http://www.asme.org/terms/Terms_Use.cfm

Goldsmith, W., 1960, *Impact,* Edward Arnold Publishers, London.
Hunter, S. C., 1957, "Energy absorbed by elastic waves during impact," *Journal of the Mechanics and Physics of Solids,* Vol. 5, pp. 162–171.
Ivanov, A. P., 1992, "Energetics of a collision with friction," *J. Appl. Maths. Mechs.,* Vol. 56, pp. 527–534.
Ivanov, A. P., 1995, "On multiple contact," *J. Appl. Maths. Mechs.,* Vol. 59, pp. 887–902.
Keller, J. B., 1986, "Impact With Friction," ASME JOURNAL OF APPLIED MECHANICS, Vol. 53, pp. 1–4.
Mac Sithigh, G. P., 1995, "Rigid-body impact with friction: Various approaches compared," *Impact, Waves and Fracture,* R. C. Batra, A. K. Mal, and G. P. Mac Sithigh, eds., ASME, New York, pp. 307–317.
Marghitu, D. B., and Hurmuzlu, Y., 1995, "Three-Dimensional Rigid-Body Collisions With Multiple Contact Points," ASME JOURNAL OF APPLIED MECHANICS, Vol. 62, pp. 725–732.
Moreau, J. J., 1994, "Some numerical methods in multibody dynamics: Application to granular materials," *Eur. J. Mech. A/Solids,* Vol. 13, No. 4 suppl., pp. 93–114.
Pfeiffer, F., 1996, "The multiple contact problem of multibody dynamics," *EUROMECH—2nd European Nonlinear Oscillations Conference,* Prague, Sept., 9–13, pp. 17–46.
Smith, C. E., 1991, "Predicting Rebounds Using Rigid-Body Dynamics," ASME JOURNAL OF APPLIED MECHANICS, Vol. 58, pp. 754–758; and discussion, 1992, Vol. 59, p. 700.
Smith, C. E., and Liu, P. P., 1992, "Coefficients of Restitution," ASME JOURNAL OF APPLIED MECHANICS, Vol. 59, pp. 963–969.
Stoianovici, D., and Hurmuzlu, Y., 1996, "A Critical Study of the Applicability of Rigid-Body Collision Theory," ASME JOURNAL OF APPLIED MECHANICS, Vol. 63, pp. 307–316.
Stronge, W. J., 1995, "Theoretical coefficient of restitution for planar impact of rough elasto-plastic bodies," *Impact, Waves and Fracture* R. C. Batra, A. K. Mal, and G. P. Mac Sithigh, eds., ASME, New York, pp. 351–362.
Villaggio, P., 1996, "The Rebound of an Elastic Sphere Against a Rigid Wall," ASME JOURNAL OF APPLIED MECHANICS, Vol. 63, pp. 259–263.

APPENDIX

For convenience of the reader this Appendix reviews some tensor operations that are relevant to the mathematical developments of this paper. To this end, let $\mathbf{a}$, $\mathbf{b}$, $\mathbf{c}$, and $\mathbf{d}$ be arbitrary vectors, $\mathbf{I}$ be the unit second-order tensor, $\mathbf{B}$ be an arbitrary second-order tensor, and $\boldsymbol{\epsilon}$ be the third-order permutation symbol. Now, the tensor product operation ($\otimes$) is defined such that

$$(\mathbf{a}\otimes\mathbf{b})\mathbf{c}=\mathbf{a}(\mathbf{b}\cdot\mathbf{c})=(\mathbf{b}\cdot\mathbf{c})\mathbf{a},\quad \mathbf{c}(\mathbf{a}\otimes\mathbf{b})=(\mathbf{c}\cdot\mathbf{a})\mathbf{b},$$
$$\mathbf{I}\cdot(\mathbf{a}\otimes\mathbf{b})=\mathbf{a}\cdot\mathbf{b},$$
$$\mathbf{B}\cdot(\mathbf{a}\otimes\mathbf{b})=\mathbf{a}\cdot(\mathbf{B}\mathbf{b})=(\mathbf{B}^T\mathbf{a})\cdot\mathbf{b}, \tag{A1}$$

where $\mathbf{B}^T$ denotes the transpose of $\mathbf{B}$. Also, $\boldsymbol{\epsilon}$ is related to the cross product operation ($\times$) and has the properties that

$$\boldsymbol{\epsilon}^T=-\boldsymbol{\epsilon},\quad (\boldsymbol{\epsilon}\mathbf{a})^T=-(\boldsymbol{\epsilon}\mathbf{a}),$$
$$\mathbf{a}\times\mathbf{b}=\boldsymbol{\epsilon}\cdot(\mathbf{a}\otimes\mathbf{b})=(\boldsymbol{\epsilon}^T\mathbf{a})\mathbf{b}=-(\boldsymbol{\epsilon}\mathbf{a})\mathbf{b}=(\boldsymbol{\epsilon}\mathbf{a})^T\mathbf{b}, \tag{A2}$$

where $(\boldsymbol{\epsilon}\mathbf{a})$ is a second-order tensor. It then follows that

$$\begin{aligned}\mathbf{a}\times\mathbf{B}(\mathbf{c}\times\mathbf{d})&=(\boldsymbol{\epsilon}\mathbf{a})^T\mathbf{B}(\mathbf{c}\times\mathbf{d})\\&=(\boldsymbol{\epsilon}\mathbf{a})^T\mathbf{B}(-\boldsymbol{\epsilon}\mathbf{c})\mathbf{d}=-(\boldsymbol{\epsilon}\mathbf{a})^T\mathbf{B}(\boldsymbol{\epsilon}\mathbf{c})\mathbf{d},\\[(\boldsymbol{\epsilon}\mathbf{a})^T\mathbf{B}(\boldsymbol{\epsilon}\mathbf{c})]\cdot(\mathbf{b}\otimes\mathbf{d})&=\mathbf{b}\cdot(\boldsymbol{\epsilon}\mathbf{a})^T\mathbf{B}(\boldsymbol{\epsilon}\mathbf{c})\mathbf{d}\\&=[(\boldsymbol{\epsilon}\mathbf{a})\mathbf{b}]\cdot\mathbf{B}[(\boldsymbol{\epsilon}\mathbf{c})\mathbf{d}]\\&=(-\mathbf{a}\times\mathbf{b})\cdot\mathbf{B}\,(-\mathbf{c}\times\mathbf{d})\\&=(\mathbf{a}\times\mathbf{b})\cdot\mathbf{B}(\mathbf{c}\times\mathbf{d}).\end{aligned} \tag{A3}$$

Also, if $\mathbf{B}$ is a symmetric positive definite second-order tensor then

$$\mathbf{B}\cdot(\mathbf{a}\otimes\mathbf{a})>0\quad\text{whenever}\quad|\mathbf{a}|>0. \tag{A4}$$

Downloaded 04 May 2010 to 171.66.16.26. Redistribution subject to ASME license or copyright; see http://www.asme.org/terms/Terms_Use.cfm

Steady Sliding of Two Elastic Half-Spaces With Friction Reduction due to Interface Stick-Slip

G. G. Adams
Professor,
Department of Mechanical Engineering,
Northeastern University,
Boston, MA 02115
e-mail: adams@neu.edu
Fellow ASME

The sliding of two perfectly flat elastic half-spaces with a constant interfacial coefficient of friction is investigated. Previous work has demonstrated that this configuration is dynamically unstable due to the destabilization of frictional slip waves. It was speculated that this dynamic instability could lead to stick-slip motion at the sliding interface. It is shown here that stick-slip motion at the interface can exist with a speed-independent interface coefficient of friction. Steady motion persists sufficiently far from the interface and thus gives the impression of uniform sliding. This type of stick-slip motion is due to interfacial slip waves and allows the bodies to slide with an apparent coefficient of friction which is less than the interface coefficient of friction. Furthermore it is shown that the apparent friction coefficient decreases with increasing speed even if the interface friction coefficient is speed-independent. Finally, it is shown that the presence of slip waves may make it possible for two frictional bodies to slide without a resisting shear stress and without any interface separation. No distinction is made between static and kinetic friction.

1 Introduction

The sliding of two surfaces upon each other is such a common occurrence. Yet this phenomenon remains one which is not well understood. The relative motion of two surfaces is resisted by a tangential force which is called the frictional force. The ratio of this tangential force to the normal force is called the coefficient of kinetic friction (μ) and this coefficient can easily be determined experimentally. However, the mechanics of contact and friction is quite complex. Ibrahim (1994a) reviewed the experimental and theoretical results which relate the dependence of friction upon time of contact, sliding velocity, normal load, and temperature. Nonuniform sliding, in the form of stick-slip motion or tangential oscillations, have been attributed to any of three causes—the difference between the coefficients of static and kinetic friction, a decrease in the coefficient of kinetic friction with increased sliding velocity, or variations in the friction coefficient along the contacting surfaces. Such nonuniform motion is particularly undesirable in machine tool and robotic applications. The review article by Ibrahim (1994b) pertains to the dynamics and modeling of frictional sliding in various industrial applications. Tworzydlo, Becker, and Oden (1994) discuss numerical modeling of friction-induced vibrations and dynamic instabilities. The role of friction in automatic control systems is reviewed by Armstrong-Hélouvry, Dupont, and Canudas de Wit (1994).

Tolstoi (1967) investigated the effect of the normal degree-of-freedom of sliding surfaces. His experiments indicated the existence of natural normal microvibrations which strongly affects the magnitude of the frictional force as well as the stability of sliding. During sliding the nonuniformities in the tangential motion are accompanied by synchronous nonuniformities in the normal motion. The mechanism responsible for the coupling between normal and tangential motion relies on two effects—the friction force decreases with increased separation of the rough surfaces, and increased sliding velocities lead to greater separations. The experimental work of Soom and Kim (1983a, b) measured the oscillations in the normal and tangential contact forces during sliding. These contact vibrations are induced by surface irregularities which move into the contact region. Although the friction force fluctuations are in phase with the normal force variations, their ratio is greater than the measured kinetic coefficient of friction. Soom and Chen (1986) performed a numerical simulation, the results of which were in good agreement with the measurements of Soom and Kim (1983a).

Rice and Ruina (1983) investigated steady frictional sliding under the assumption of a shear stress which depends on slip velocity and on state. "State" refers to a functional dependence with fading memory on prior interface slip velocities. The instantaneous dependence of shear stress on slip velocity was taken to be positive. Nonetheless instabilities in sliding were shown to occur and a critical tangential stiffness for the existence of a flutter instability was determined. The analysis pertained to both a single-degree-of-freedom system of a sliding block and to elastic bodies.

Oden and Martins (1985) and Martins, Oden, and Simões (1990) investigated dynamic friction phenomena and included extensive reviews of previous works. They presented a nonlinear contact law based upon the deformation of a rough surface. No distinction was made between static and kinetic friction coefficients; nor was it assumed that the friction coefficient decreases with increasing sliding speed. Variational principles were established and applied in order to develop numerical methods. The sliding of a rigid block was modeled as a three-degree-of-freedom system. Stick-slip motion was shown to occur as a consequence of a dynamic instability involving the coupling between normal and tangential motions. Tworzydlo and Becker (1991) applied a numerical method to the model of Oden and Martins and showed that sliding can initiate at a lower value of the friction force than a purely static analysis would indicate.

Contributed by the Applied Mechanics Division of THE AMERICAN SOCIETY OF MECHANICAL ENGINEERS for publication in the ASME JOURNAL OF APPLIED MECHANICS.

Discussion on the paper should be addressed to the Technical Editor, Professor Lewis T. Wheeler, Department of Mechanical Engineering, University of Houston, Houston, TX 77204-4792, and will be accepted until four months after final publication of the paper itself in the ASME JOURNAL OF APPLIED MECHANICS.

Manuscript received by the ASME Applied Mechanics Division, Apr. 3, 1997; final revision, Dec. 9, 1997. Associate Technical Editor: J. T. Jenkins.

 Copyright © 1998 by ASME

Downloaded 04 May 2010 to 171.66.16.26. Redistribution subject to ASME license or copyright; see http://www.asme.org/terms/Terms_Use.cfm

Rayleigh waves can propagate along the free surface of a semi-infinite elastic body and have amplitudes which decay exponentially with distance from the free surface. Similar waves can travel along the interface of two contacting elastic bodies. Such waves were investigated by Stoneley (1924) for bonded contact and are known as Stoneley waves. Stoneley waves exist only if the shear wave speeds of the two materials do not differ greatly. Achenbach and Epstein (1967) and Murty (1975) investigated interface waves in unbonded frictionless contacts in which separation does not occur. These "smooth contact Stoneley waves" (also known as slip waves) differ from those for bonded contact and occur for a wider range of material combinations. Slip waves with interface separation were found by Comninou and Dundurs (1977). Those waves are inherently nonlinear due to the existence of both contact and separation regions whose locations are a priori unknown. Comninou and Dundurs (1978a) also investigated the possibility of separation waves and/or stick-slip waves in the sliding of two identical half-spaces with friction. Their analysis showed that such waves could exist only with singularities at the tips of the slip zones. Freund (1978) pointed out that the singularities encountered by Comninou and Dundurs (1977, 1978a) would require energy sources and sinks. Comninou and Dundurs (1978b) also investigated the possible sliding motion of two identical bodies without interface slipping. Such motion is analogous to a carpet being moved across the floor by the propagation of a "carpet fold." Singularities were also encountered in that analysis.

Martins, Guimarães, and Faria (1995) investigated the sliding of elastic and viscoelastic half-spaces against a rigid surface. Dynamic instabilities were found for cases in which the friction coefficient and the Poisson's ratio were sufficiently large. These instabilities were thought to play a role in Schallamach waves (Schallamach, 1971). Adams (1995) showed that the steady sliding of two elastic half-spaces is dynamically unstable. The instability mechanism is due to destabilization of interfacial slip waves and gives rise to a dynamic instability in the form of self-excited motion. These self-excited oscillations are generally confined to a region near the sliding interface. It was speculated that the instability would eventually lead to either partial loss of contact or to regions of stick-slip motion. It is noted that the cases investigated by Comninou and Dundurs (1977, 1978a, b) were those of frictionless sliding of different materials and frictional sliding of identical materials. Neither of those cases would lead to the dynamic instabilities encountered by Adams (1995).

It is the purpose of the present investigation to determine whether the unstable sliding of two different elastic half-spaces can lead to a motion in which regions of stick and slip propagate along the sliding interface. Furthermore, that type of sliding would allow the coefficient of friction at the interface to differ from the friction coefficient that would be measured at a large distance from the sliding interface. Also the observed friction coefficient could have a velocity-dependence even if the interface coefficient of friction is constant. Some of the algebraic manipulations in this work are quite complicated and have been accomplished with the help of the symbolic interpreter language Mathematica (Wolfram, 1991).

2 Problem Description

Consider two perfectly flat elastic half-spaces sliding with respect to each other (Fig. 1) with an *interfacial* coefficient of sliding friction μ. Far away from the interface, the shear stress τ_{12}^* and the normal stress τ_{22}^* are related through an *apparent* coefficient of friction (μ^*), i.e.,

$$\tau_{12}^* = -\mu^* \tau_{22}^*. \tag{1}$$

For reasons which will be shown later on, the value of μ^*, which is the ratio of the magnitudes of the remote shear stress to the remote normal stress, is not necessarily the same as the value of μ. Also, sufficiently far from the interface, the bodies move with a *constant* relative velocity v_0 (the sliding velocity) in the x_1-direction. However, the relative motion at the interface need not be uniform (steady) sliding.

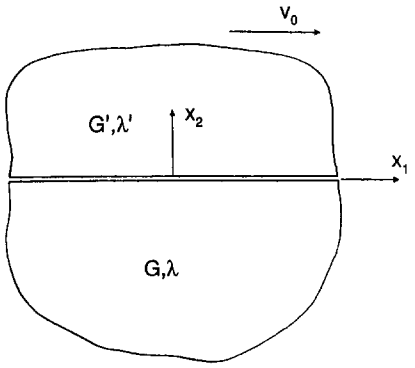


Fig. 1 Two elastic half-spaces sliding against each other

The solution for *steady* sliding is given by $\mu^* = \mu$, the uniform stress state (1) throughout the two bodies, all points on the lower body stationary, and all points on the upper body moving to the right with constant velocity v_0. However, it was shown by Adams (1995) that steady sliding is dynamically unstable due to the destabilization of interface slip waves. Thus consider the following displacement fields (Comninou and Dundurs, 1977) which satisfy the plane-strain equations of dynamic linear elasticity and are associated with interface waves traveling with phase velocity c,

$$\bar{u}_1 = \mathrm{Re}\{\sum_{m=1}^{\infty} [D_{1m} \exp(mk\zeta_1 x_2) + D_{2m} \exp(mk\zeta_2 x_2)] \exp[imk(x_1 - ct)]\} \tag{2}$$

$$\bar{u}_2 = \mathrm{Re}\{\sum_{m=1}^{\infty} [-i\zeta_1 D_{1m} \exp(mk\zeta_1 x_2) - i\zeta_2^{-1} D_{2m} \exp(mk\zeta_2 x_2)] \exp[imk(x_1 - ct)]\} \tag{3}$$

$$\bar{u}_1' = \mathrm{Re}\{\sum_{m=1}^{\infty} [D_{3m} \exp(-mk\zeta_3 x_2) + D_{4m} \exp(-mk\zeta_4 x_2)] \exp[imk(x_1 - ct)]\} \tag{4}$$

$$\bar{u}_2' = \mathrm{Re}\{\sum_{m=1}^{\infty} [i\zeta_3 D_{3m} \exp(-mk\zeta_3 x_2) + i\zeta_4^{-1} D_{4m} \exp(-mk\zeta_4 x_2)] \exp[imk(x_1 - ct)]\} \tag{5}$$

where

$$\zeta_1 = \sqrt{1 - (c/c_1)^2}, \quad \zeta_2 = \sqrt{1 - (c/c_2)^2}$$
$$\zeta_3 = \sqrt{1 - (c/c_1')^2}, \quad \zeta_4 = \sqrt{1 - (c/c_2')^2} \tag{6}$$

and

$$c_1 = \sqrt{\frac{\lambda + 2G}{\rho}}, \quad c_2 = \sqrt{\frac{G}{\rho}}, \quad c_1' = \sqrt{\frac{\lambda' + 2G'}{\rho'}},$$
$$c_2' = \sqrt{\frac{G'}{\rho'}}, \quad \beta = \frac{c_1}{c_2} = \sqrt{\frac{2(1-\nu)}{1-2\nu}},$$
$$\beta' = \frac{c_1'}{c_2'} = \sqrt{\frac{2(1-\nu')}{1-2\nu'}}, \quad \kappa = \frac{c_2'}{c_2}. \tag{7}$$

In Eqs. (2)–(5) k is the wave number, and in (7) c_1 and c_2 are the phase velocities of longitudinal and shear waves, respectively; G is the shear modulus, λ is the Lamé's constant,

Downloaded 04 May 2010 to 171.66.16.26. Redistribution subject to ASME license or copyright; see http://www.asme.org/terms/Terms_Use.cfm

and ρ is the mass density. Furthermore, the primes ($'$) refer to the upper half-space (Fig. 1). The displacements given by $\bar{u}_1$, $\bar{u}_2$, $\bar{u}_1'$, $\bar{u}_2'$ are *perturbation* displacements and are measured from the nominal steady-state sliding condition. Furthermore, the wave form given by (2) – (5) is appropriate for *real* waves which travel with phase velocity c without distortion. In addition to the primary wave number k in (2) – (5) is the index m. Thus the solutions sought are periodic in space with wavelength $2\pi/k$ and consists of an infinite number of components, each with wave number mk. The choice of the form for wave solutions (2) – (5) is appropriate for interface waves only. An analysis for steady sliding (Adams, 1995) included the possibility of body waves. However, it was found that the only waves generated by the sliding of two *flat* elastic half-spaces were interface waves. Hence the present analysis looks only for interface wave solutions. In addition, it has been assumed that the sliding speed is much less than any of the wave speeds of the two bodies.

The continuity conditions at the sliding interface pertain to the complete solution (i.e., the sum of the steady and perturbation solutions). Written in terms of a dimensionless moving coordinate η, the complete solution satisfies

$$u_2(\eta, 0) = u_2'(\eta, 0), \quad \tau_{12}(\eta, 0) = \tau_{12}'(\eta, 0)$$

$$\tau_{22}(\eta, 0) = \tau_{22}'(\eta, 0), \ \eta = k(x_1 - ct), \ -\pi \le \eta \le \pi \quad (8)$$

where

$$\tau_{12} = G\left(\frac{\partial \bar{u}_1}{\partial x_2} + \frac{\partial \bar{u}_2}{\partial x_1}\right) + \tau_{12}^*,$$

$$\tau_{22} = (\lambda + 2G)\frac{\partial \bar{u}_2}{\partial x_2} + \lambda \frac{\partial \bar{u}_1}{\partial x_1} + \tau_{22}^*.$$

We look for periodic regions of slip separated from regions of stick, i.e.,

$$v_S = \dot{\bar{u}}_1'(\eta, 0) - \dot{\bar{u}}_1(\eta, 0) + v_0 = 0, \quad |\eta| < a, \quad \text{stick region}$$

$$\tau_S = \tau_{12}(\eta, 0) + \mu\tau_{22}(\eta, 0) = 0, \quad a < |\eta| < \pi, \quad \text{slip region} \quad (10)$$

where v_S and τ_S pertain to the *complete* solution and are termed the slip velocity and slip stress, respectively. The conditions represented by (10) arise from the requirements that the slip velocity vanishes in the stick region ($|\eta| < a$) and that the slip stress vanishes in the slip region ($a < |\eta| < \pi$).

In addition, certain inequality constraints must be satisfied. In the slip region the complete slip velocity must be positive in order for sliding $(10)_2$ to occur, in the stick region the complete slip stress must be negative for the stick condition $(10)_1$ to prevail, and the complete normal stress must be negative everywhere. Thus

$$v_S \ge 0, \quad a < |\eta| < \pi,$$

$$\tau_S \le 0, \quad |\eta| < a, \quad \tau_{22} \le 0, \quad |\eta| < \pi. \quad (11)$$

Furthermore, the *complete* reverse slip stress (τ_R) must satisfy

$$\tau_R = \tau_{12}(\eta, 0) - \mu\tau_{22}(\eta, 0) \ge 0, \quad |\eta| < a \quad (12)$$

in the stick region in order to avoid slip in the negative x_1-direction. It is noted that the slip velocity is not constant along the interface. Thus the case under investigation consists of steady motion away from the interface along with periodic stick-slip motion propagating along the interface with phase velocity c.

Satisfaction of the continuity conditions (8) yields

$$D_{1m} = e_1 D_{4m}, \quad D_{2m} = e_2 D_{4m},$$

$$D_{3m} = e_3 D_{4m}, \quad m = 1, 2, 3, \ldots \quad (13)$$

where e_1, e_2, e_3 are independent of m and are given by

$$\begin{aligned} e_1 = (G'/G)[&-((\beta')^2(1 + \zeta_2^2)(-1 + \zeta_3^2)) \\ &+ 2(-1 - \zeta_2^2 - \zeta_2\zeta_3 + \zeta_3\zeta_4 + \zeta_2^2\zeta_3\zeta_4 + \zeta_2\zeta_3\zeta_4^2) \\ &+ (G'/G)(2 - 4\zeta_3\zeta_4 + 2\zeta_4^2 \\ &+ (\beta')^2(-1 + \zeta_3^2)(1 + \zeta_4^2))]/ \\ &\{[(2 - 4\zeta_1\zeta_2 + 2\zeta_2^2 + \beta^2(-1 + \zeta_1^2)(1 + \zeta_2^2))\zeta_3 \\ &+ (G'/G)(2(-2 + \beta^2)\zeta_3 - 2\beta^2\zeta_1^2\zeta_3 \\ &+ \zeta_1(-2 + (\beta')^2 + 2\zeta_2^2 - (\beta')^2\zeta_2^2 + 4\zeta_2\zeta_3 \\ &- (\beta')^2\zeta_3^2 + (\beta')^2\zeta_2^2\zeta_3^2))]\zeta_4\} \end{aligned} \quad (14)$$

$$\begin{aligned} e_2 = -\{&(G'/G)\zeta_2[\zeta_1(-4 + 2(\beta')^2 - 2(\beta')^2\zeta_3^2 + 4\zeta_3\zeta_4) \\ &- (-2 + \beta^2)\zeta_3(-1 + \zeta_4^2) + \beta^2\zeta_1^2\zeta_3(-1 + \zeta_4^2) \\ &+ (G'/G)\zeta_1(2 - 4\zeta_3\zeta_4 + 2\zeta_4^2 \\ &+ (\beta')^2(-1 + \zeta_3^2)(1 + \zeta_4^2))]\}/ \\ &\{[(2 - 4\zeta_1\zeta_2 + 2\zeta_2^2 + \beta^2(-1 + \zeta_1^2)(1 + \zeta_2^2))\zeta_3 \\ &+ (G'/G)(2(-2 + \beta^2)\zeta_3 - 2\beta^2\zeta_1^2\zeta_3 \\ &+ \zeta_1(-2 + (\beta')^2 + 2\zeta_2^2 - (\beta')^2\zeta_2^2 + 4\zeta_2\zeta_3 \\ &- (\beta')^2\zeta_3^2 + (\beta')^2\zeta_2^2\zeta_3^2))]\zeta_4\} \end{aligned} \quad (15)$$

$$\begin{aligned} e_3 = \{&-2 + 4\zeta_1\zeta_2 - 2\zeta_2^2 - \beta^2(-1 + \zeta_1^2)(1 + \zeta_2^2) \\ &+ (G'/G)[\beta^2(-1 + \zeta_1^2)(1 + \zeta_4^2) \\ &- 2(-1 + \zeta_1\zeta_2 - \zeta_1\zeta_4 + \zeta_1\zeta_2^2\zeta_4 - \zeta_4^2 + \zeta_1\zeta_2\zeta_4^2)]\}/ \\ &\{[(2 - 4\zeta_1\zeta_2 + 2\zeta_2^2 + \beta^2(-1 + \zeta_1^2)(1 + \zeta_2^2))\zeta_3 \\ &+ (G'/G)(2(-2 + \beta^2)\zeta_3 - 2\beta^2\zeta_1^2\zeta_3 \\ &+ \zeta_1(-2 + (\beta')^2 + 2\zeta_2^2 - (\beta')^2\zeta_2^2 + 4\zeta_2\zeta_3 \\ &- (\beta')^2\zeta_3^2 + (\beta')^2\zeta_2^2\zeta_3^2))]\zeta_4\}. \end{aligned} \quad (16)$$

The slip condition $(10)_2$ will now be satisfied. From (2), (3), and (13), the slip stress becomes

$$\tau_S = Gk \operatorname{Re}\{\sum_{m=1}^{\infty} (\delta_1 - i\mu\delta_2)mD_{4m} \exp(im\eta)\} + \tau_{12}^* + \mu\tau_{22}^* \quad (17)$$

where

$$\delta_1 = 2e_1\zeta_1 + e_2(\zeta_1 + \zeta_2^{-1}),$$

$$\delta_2 = 2e_1 + \beta^2\zeta_1^2 e_1 + 2e_2 - \beta^2 e_1. \quad (18)$$

In order to satisfy the slip condition, we use the integral transformation given by

$$D_{4m} = \frac{1}{m\pi k(\delta_1 - i\mu\delta_2)} \int_{-a}^{a} \phi(\xi) \exp(-im\xi) d\xi, \quad m = 1, 2, 3, \ldots, \infty. \quad (19)$$

It will be shown that $(10)_2$ will be automatically satisfied for a suitable choice of $\phi(\xi)$. The use of (1), (17), and (19) results in

$$\tau_S/G = -\frac{1}{2\pi}\int_{-a}^{a} \phi(\xi) d\xi + \phi(\eta)H(a - |\eta|) + (\mu - \mu^*)\tau_{22}^*/G \quad (20)$$

Downloaded 04 May 2010 to 171.66.16.26. Redistribution subject to ASME license or copyright; see http://www.asme.org/terms/Terms_Use.cfm

where $H(\cdot)$ is the Heaviside function. The identity (Gel'fand and Shilov, 1964)

$$\sum_{n=1}^{\infty} \cos nx = -\tfrac{1}{2} + \pi \sum_{n=-\infty}^{\infty} \delta(x - 2\pi n) \tag{21}$$

was used in obtaining (20) where $\delta(\cdot)$ is the Dirac delta function. It is noted that no assumption of symmetry is implied by the symmetric limits in the integral (19). The choice of the limits $(-a, a)$ merely fixes the origin of the η-coordinate in the middle of a stick region. Equation (20) will satisfy the slip condition $(10)_2$ provided that the resultant condition

$$\int_{-a}^{a} \phi(\xi)d\xi = -2\pi(\mu^* - \mu)\frac{\tau_{22}^*}{G} \tag{22}$$

is satisfied.

The slip velocity is given by

$$v_S = v_0 + ce_0k \operatorname{Re}\{\sum_{m=1}^{\infty} miD_{4m} \exp(im\eta)\},$$

$$e_0 = e_1 + e_2 - e_3 - 1. \tag{23}$$

Finally, (23) subject to $(10)_1$, with (19) and the identity (Gel'fand and Shilov, 1964)

$$\sum_{n=1}^{\infty} \sin nx = \frac{1}{2}\cot\frac{x}{2} \tag{24}$$

yields the singular integral equation

$$\frac{\delta_1}{2\pi}\int_{-a}^{a} \cot\left(\frac{\eta - \xi}{2}\right)\phi(\xi)d\xi - \frac{\mu\delta_2}{2\pi}\int_{-a}^{a}\phi(\xi)d\xi$$

$$+ \mu\delta_2\phi(\eta) = \frac{(v_0/c_2)(\delta_1^2 + \mu^2\delta_2^2)}{e_0(c/c_2)}, \quad -a < \eta < a. \tag{25}$$

The solution of (25) is subject to the resultant condition (22). In addition, the inequality constraints (11) – (12) must be satisfied. In an experiment, one would measure the apparent friction coefficient (μ^*) and its variation with sliding speed (v_0) and infer that these numbers are the same as the corresponding quantities at the interface. However, due to interfacial stick-and-slip, these quantities are not necessarily equal.

2.1 Search for Solutions: $\delta_1 \neq 0$. For $\delta_1 \neq 0$, the singular integral Eq. (25) was analyzed in order to determine the order of the singularities at $\eta = \pm a$ using the method of Muskhelishvili (1958). The numerical solution of (25) and (22) was then sought using the procedure of Erdogan and Gupta (1972). Any prospective solution must also satisfy the inequality conditions (11) – (12) and avoid the problem of energy sources and sinks (Freund, 1978). No such solutions were found for $\delta_1 \neq 0$.

2.2 Search for Solutions: $\delta_1 = 0$. The condition $\delta_1 = 0$ corresponds to the speed of *frictionless* slip waves (Achenbach and Epstein, 1967) and (25) simplifies considerably. The solution is simply

$$\phi(\eta) = \frac{\mu\delta_2(v_0/c_2)}{(1 - a/\pi)e_0(c/c_2)} \tag{26}$$

and the resultant condition (22) gives

$$\mu^* = \mu\left[1 - \frac{a\delta_2(v_0/c_2)}{(\pi - a)e_0(c/c_2)(\tau_{22}^*/G)}\right]. \tag{27}$$

The solution (26) – (27) must now be checked to ensure that the inequality conditions (11) – (12) are satisfied. Condition $(11)_1$ with (26) becomes

$$v_S = \left(\frac{\pi}{\pi - a}\right)v_0 \geq 0, \quad a < |\eta| < \pi \tag{28}$$

which, in view of $0 < a < \pi$, is automatically satisfied. Condition $(11)_2$ with (26) – (27) becomes

$$\frac{\tau_S}{G} = \left(\frac{\pi}{\pi - a}\right)\frac{\mu v_0\delta_2}{e_0c} \leq 0, \quad |\eta| < a. \tag{29}$$

A necessary and sufficient condition for the satisfaction of (29) is that $\delta_2/(e_0c) < 0$. The range $0 < \kappa < 1$ and $0.1 \leq G'/G \leq 10$ was investigated for material combinations such that frictionless slip waves exist. The quantity δ_2/e_0 was found to be negative everywhere in that range. The value of the wave speed (i.e., the frictionless slip wave speed) is determined from $\delta_1 = 0$ and has an arbitrary sign. Thus for all material combinations, (29) can be satisfied by choosing the appropriate sign for the wave speed "c." It is noted from this discussion that "c" is always positive in the parameter range defined above.

Condition $(11)_3$ along with (26) gives

$$\frac{\tau_{22}}{G} = [\pi H(a - |\eta|) - a]\frac{v_0\delta_2}{(\pi - a)e_0c} + \frac{\tau_{22}^*}{G} \leq 0 \tag{30}$$

which is automatically satisfied in the stick region. Satisfaction of (30) in the slip region requires

$$-\frac{(v_0/c_2)}{(\tau_{22}^*/G)} \leq -\left(\frac{\pi - a}{a}\right)\frac{e_0(c/c_2)}{\delta_2}. \tag{31}$$

Thus (31) gives a maximum sliding speed in order for these slip-and-stick waves to occur for a given a. Alternatively, (31) may be viewed as giving a maximum a for specified sliding speed. Although (31) was obtained from the condition that the complete contact pressure remain positive, it can be shown to be equivalent to the requirement that the apparent friction coefficient be positive. The condition of avoiding reverse slip (12) leads to

$$\frac{\tau_R}{G} = -\frac{\delta_2(v_0/c_2)\mu}{e_0(c/c_2)} - (\mu + \mu^*)\frac{\tau_{22}^*}{G} \geq 0 \tag{32}$$

which is automatically satisfied in the parameter range considered.

3 Results and Discussion

The fact that the slip velocity is *constant* in the slip region (28) allows the solution (26) – (27) to be re-interpreted in order to be valid even if the interface coefficient of friction is speed-dependent. The value of μ simply needs to be chosen to correspond to the slipping speed v_S. The perturbation solution (26) – (27) represents a series of frictionless slip waves which combine to form a normal stress ($\bar{\tau}_{22}$) in the form of a rectangular wave train. The corresponding perturbation in slip velocity is *in phase* with $\bar{\tau}_{22}$. Thus the stick region is formed by a change in slip velocity which cancels the sliding velocity. Along with the perturbation in v_S, the in-phase change in τ_{22} increases the magnitude of the contact pressure ($-\tau_{22}$) in the stick region (allowing $(11)_2$ to be satisfied). Also the contact pressure decreases by a constant amount in the slip region allowing for a constant ratio of the complete shear stress to the complete contact pressure. That ratio is the interfacial coefficient of sliding friction (μ) which will therefore be greater than the observed coefficient of friction (μ^*).

Downloaded 04 May 2010 to 171.66.16.26. Redistribution subject to ASME license or copyright; see http://www.asme.org/terms/Terms_Use.cfm

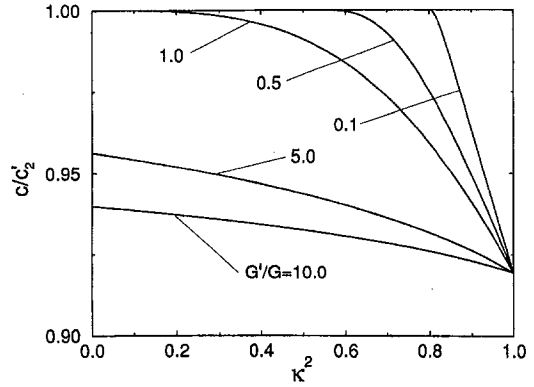


Fig. 2 Phase velocity (c/c_2') of stick-and-slip waves versus square of shear wave speed ratio (κ^2) for various values of the shear stiffness ratio (G'/G)

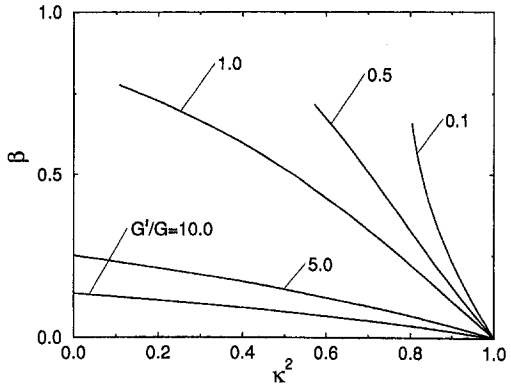


Fig. 3 Parameter β versus square of shear wave-speed ratio (κ^2) for various values of the shear stiffness ratio (G'/G)

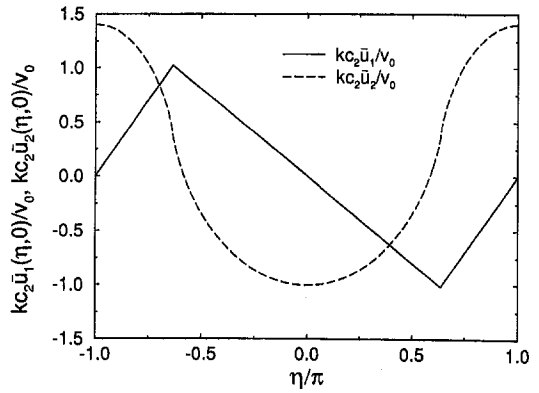


Fig. 4 Perturbations in the interface displacements $kc_2\bar{u}_1(\eta, 0)/v_0$, $kc_2\bar{u}_2(\eta, 0)/v_0$

All of the results in Figs. 2–5 are for $\nu = \nu' = 0.25$. Without loss of generality we assume that the material of the upper body has the lower shear wave speed, i.e., $\kappa < 1$. In Fig. 2 is shown the phase velocity of the stick-and-slip waves divided by c_2' versus the square of the shear wave-speed ratio (κ^2) for different stiffness ratios (G'/G). As κ decreases, the phase velocity increases. For some material combinations, slip waves are not possible. This condition is reflected by the phase velocity approaching the shear wave speed c_2' (Fig. 2). Furthermore, for fixed κ^2, as the shear stiffness ratio (G'/G) increases the phase velocity decreases. It is noted that increasing G'/G with κ^2 constant results in an increase in the density ratio (ρ'/ρ).

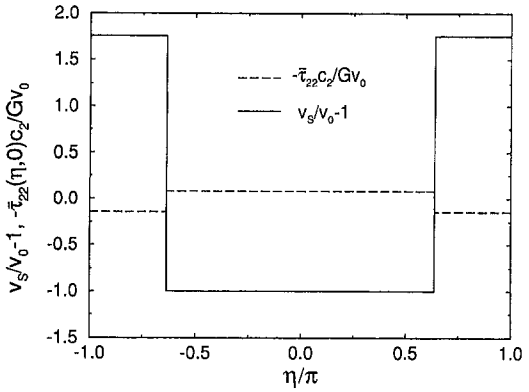


Fig. 5 Perturbations in the interface slip velocity ($v_s/v_0 - 1$) and in the interface contact pressure ($-\bar{\tau}_{22}(\eta, 0)c_2/Gv_0$)

It is convenient now to rewrite (27) as

$$\mu^* = \mu\left[1 - \beta\left(\frac{a}{\pi - a}\right)\frac{v_0/c_2'}{(-\tau_{22}^*/G')}\right],$$

$$\beta = -\delta_2/[(G'/G)(c/c_2')e_0] \tag{33}$$

where δ_2 is evaluated at the slip speed v_s. The parameter β is positive and provides a measure of the decrease in the apparent friction coefficient with increasing sliding speed. Alternatively the parameter β can be viewed as a measure of the decrease in μ^* with decreasing contact pressure. Note the factor $a/(\pi - a)$ where "$2a$" is the length of the stick zone and $2(\pi - a)$ is the length of the slip zone. Furthermore "a" is arbitrary and controls both the amplitude and the shape of the rectangular wave. In Fig. 3 is shown the variation of β with κ^2 for different values of G'/G. As the mismatch in the shear wave speeds increases (i.e., as κ^2 decreases), the parameter β increases until the point is reached at which slip waves no longer exist. Furthermore, as the stiffness ratio increases (with κ fixed) the parameter β decreases. Thus the decrease in the apparent friction coefficient is enhanced by low-shear stiffness ratio and by low-shear wave-speed ratio provided that slip waves remain possible for that material pair.

It is especially interesting to note that it is possible that $\mu^* = 0$ and thus that sliding of frictional bodies could occur without a resisting frictional force. As was noted in the previous section, the condition that $\mu^* = 0$ is equivalent to zero contact pressure in the slip zone. Hence the slip zones would have zero shear stress. Also, if $\mu^* = 0$ the stick zones apparently would have zero shear stress. In order to better understand this behavior, consider the sliding of a pair of bodies with a zero interface friction coefficient ($\mu = 0$). Superimpose on that steady sliding a rectangular slip-wave train such that the contact pressure vanishes in ($a < |\eta| < \pi$) and that the complete slip velocity vanishes in ($-a, a$). Such a solution then also satisfies the Coulomb friction law for any interface coefficient of sliding friction (μ) and also has a vanishing shear stress.

The results in Figs. 4–5 are for $a = 2$ and for $\kappa^2 = 0.9$ and $G'/G = 0.5$. In Fig. 4 is shown the perturbations in the normalized interface displacements $kc_2\bar{u}_1(\eta, 0)/v_0$ and $kc_2\bar{u}_2(\eta, 0)/v_0$. It is the saw-tooth shape of these tangential displacements which gives rise to the rectangular wave of slip velocity. Similarly Fig. 5 shows the perturbations in the normalized interface contact pressure and slip velocity. Both of these quantities are in the shape of a rectangular wave. Qualitatively similar results exist for other material combinations and different values of a.

4 Conclusions

The sliding of two different elastic half-spaces has been investigated under the condition that the sliding speed sufficiently

Downloaded 04 May 2010 to 171.66.16.26. Redistribution subject to ASME license or copyright; see http://www.asme.org/terms/Terms_Use.cfm

far from the interface is uniform. It is found that stick-and-slip waves (i.e., a superposition of slip waves which forms a rectangular wave in the contact pressure and in the slip velocity) can propagate along the interface (in the direction of sliding of the body with the lower shear wave speed) and allow for the interface sliding conditions to differ from the observed sliding conditions. The slip waves may be generated by the instability mechanism of steady sliding (Adams, 1995). The interface coefficient of friction can be constant or an increasing/decreasing function of slip velocity. However, it has been found that the *apparent* coefficient of friction can be less than the *interface* friction coefficient. Furthermore, the apparent coefficient of friction can decrease with sliding speed even though the interface friction coefficient is constant. Thus the measured coefficient of friction does not necessarily represent the behavior of the sliding interface. Finally, the presence of slip waves may make it possible for two frictional bodies to slide without a resisting shear stress and without any interface separation.

It is emphasized that there are many other effects which may influence the negative slope of the apparent-coefficient-of-friction versus velocity curve. Nonetheless it has been shown here that the presence of slip waves can at least partially explain this commonly encountered friction phenomenon.

Acknowledgments

This material is based upon work supported by the National Science Foundation under Grant No. CMS-9622196 of the Surface Engineering and Tribology Program.

References

Achenbach, J. D., and Epstein, H. I., 1967, "Dynamic Interaction of a Layer and a Half-Space," *ASCE Journal of the Engineering Mechanics Division,* Vol. EM5, pp. 27–42.

Adams, G. G., 1995, "Self-Excited Oscillations of Two Elastic Half-Spaces Sliding With a Constant Coefficient of Friction," ASME JOURNAL OF APPLIED MECHANICS, Vol. 62, pp. 867–872.

Armstrong-Hélouvry, B., Dupont, P., and Canudas de Wit, C., 1994, "Friction in Servo Machines: Analysis and Control Methods," ASME *Applied Mechanics Reviews,* Vol. 47, pp. 275–305.

Comninou, M., and Dundurs, J., 1977, "Elastic Interface Waves Involving Separation," ASME JOURNAL OF APPLIED MECHANICS, Vol. 44, pp. 222–226.

Comninou, M., and Dundurs, J., 1978a, "Elastic Interface Waves and Sliding Between Two Solids," ASME JOURNAL OF APPLIED MECHANICS, Vol. 45, pp. 325–330.

Comninou, M., and Dundurs, J., 1978b, "Can Two Solids Slide Without Slipping?" *International Journal of Solids and Structures,* Vol. 14, pp. 251–260.

Erdogan, F., and Gupta, G. D., 1972, "On the Numerical Solution of Singular Integral Equations," *Quarterly of Applied Mathematics,* Vol. 29, pp. 525–534.

Freund, L. B., 1978, "Elastic Waves Involving Separation," discussion, ASME JOURNAL OF APPLIED MECHANICS, Vol. 45, pp. 226–228.

Gel'fand, I. M., and Shilov, G. E., 1964, *Generalized Functions,* Academic Press, New York.

Ibrahim, R. A., 1994a, "Friction-Induced Vibration, Chatter, Squeal, and Chaos, Part I: Mechanics of Contact and Friction," ASME *Applied Mechanics Reviews,* Vol. 47, pp. 209–226.

Ibrahim, R. A., 1994b, "Friction-Induced Vibration, Chatter, Squeal, and Chaos, Part II: Dynamics and Modeling," ASME *Applied Mechanics Reviews,* Vol. 47, pp. 227–253.

Martins, J. A. C., Guimarães, J. and Faria, L. O., 1995, "Dynamic Surface Solutions in Linear Elasticity and Viscoelasticity With Frictional Boundary Conditions," ASME *Journal of Vibration and Acoustics,* Vol. 117, pp. 445–451.

Martins, J. A. C., Oden, J. T., and Simões, F. M. F., 1990, "A Study of Static and Kinetic Friction," *International Journal of Engineering Science,* Vol. 28, pp. 29–92.

Murty, G. S., 1975, "Wave Propagation at an Unbonded Interface Between Two Elastic Half-Spaces," *Journal of the Acoustical Society of America,* Vol. 58, pp. 1094–1095.

Muskhelishvili, N. I., 1958, *Singular Integral Equations,* P. Noordhoff, Groningen, The Netherlands.

Oden, J. T., and Martins, J. A. C., 1985, "Models and Computational Methods for Dynamic Friction Phenomena," *Computer Methods in Applied Mechanics and Engineering,* Vol. 52, pp. 527–634.

Rice, J. R., and Ruina, A. L., 1983, "Stability of Steady Frictional Sliding," ASME JOURNAL OF APPLIED MECHANICS, Vol. 50, pp. 343–349.

Schallamach, A., 1971, "How Does Rubber Slide?" *Wear,* Vol. 17, pp. 301–312.

Soom, A., and Chen, J. W., 1986, "Simulation of Random Surface Roughness-Induced Contact Vibrations at Hertzian Contacts During Steady Sliding," ASME *Journal of Tribology,* Vol. 108, pp. 123–127.

Soom, A., and Kim, C., 1983a, "Interactions Between Dynamic Normal and Frictional Forces During Unlubricated Sliding," ASME *Journal of Lubrication Technology,* Vol. 105, pp. 221–229.

Soom, A., and Kim, C., 1983b, "Roughness-Induced Dynamic Loading at Dry and Boundary-Lubricated Sliding Contacts," ASME *Journal of Lubrication Technology,* Vol. 105, pp. 514–517.

Stoneley, R., 1924, "Elastic Waves at the Surface of Separation of Two Solids," *Proceedings of the Royal Society of London,* Vol. A106, pp. 416–428.

Tolstoi, D. M., 1967, "Significance of the Normal Degree of Freedom and Natural Normal Vibrations in Contact Friction," *Wear,* Vol. 10, pp. 199–213.

Tworzydlo, W. W., and Becker, E., 1991, "Influence of Forced Vibrations on the Static Coefficient of Friction—Numerical Modeling," *Wear,* Vol. 143, pp. 175–196.

Tworzydlo, W. W., Becker, E. B., and Oden, J. T., 1994, "Numerical Modeling of Friction-Induced Vibrations and Dynamic Instabilities," ASME *Applied Mechanics Reviews,* Vol. 47, pp. 255–274.

Wolfram, S., 1991, *Mathematica, A System for Doing Mathematics by Computer,* 2nd Ed., Addison-Wesley, Reading, MA.

Downloaded 04 May 2010 to 171.66.16.26. Redistribution subject to ASME license or copyright; see http://www.asme.org/terms/Terms_Use.cfm

The Problem on Dynamical Loading of Plane Elastic Regions With Irregular Boundaries

N. Morozov
Professor,
e-mail: morozov@mnf.usr.pu.ru

I. Sourovtsova
e-mail: is@slk.usr.pu.ru

Elasticity Department,
State University, St. Petersburg,
Bibliotechnaja pl. 2,
St. Petersburg 198904,
Russia

The study of the problem of wave propagation in elastic wedge meets considerable difficulties, which are intensified by the presence of waves of two types that interact with each other through boundary conditions. However, some special surface loading permits separation of the potentials in the boundary conditions, but even in this case the problem cannot be simply reduced to two acoustic ones. The reason for this is that the edge condition cannot be satisfied if the disturbances are limited to a single type (longitudinal or shear). In spite of this the problem, such a special boundary loading nevertheless turns out to be very similar to the acoustic one, which makes it possible to find a closed analytical solution by means of the modified Kostrov method (Kostrov, 1966) and the idea of extension of operators. A similar approach is used for the study of the general problem of loading of the body with several angles.

The Lame equations are sufficiently complicated for direct investigation. In order to simplify this problem the representation of a displacement vector as a sum of some vectors, which satisfy more simple equations, is used. In the elasticity the Green-Lame representation is used:

$$u = \nabla\Phi + \nabla \times \bar{\Psi},$$

where potentials Φ and $\bar{\Psi}$ are solutions of waves equations.

The advantage of such representation is that the wave potentials satisfy two separate equations, the connection remains only in the boundary conditions.

The completeness theorem of the Green-Lame representation was first formulated by Klebsh in 1863. The accurate proof of this fact is given, for instance, in the paper by Sternberg (1960). According to the completeness theorem any waves process in a bounded or unbounded elastic body can be described as the superposition of two waves of motion, of longitudinal and shear waves, which propagate with different velocities. In the case of an unbounded body the waves of both types propagate independently. The presence of the boundary leads to the interaction of these waves with each other.

Let us consider the time-harmonic plane motion of an elastic medium, with a time-harmonic factor $\exp(i\omega t)$. The potentials Φ and Ψ of longitudinal and shear waves are, in this case, solutions of the Helmholz equations:

$$\Delta\Phi + k_1^2\Phi = 0, \tag{1}$$

$$\Delta\Psi + k_2^2\Psi = 0, \tag{2}$$

where $k_i = \omega^2/c_i^2$, $c_1(c_2)$—longitudinal (shear) velocities.

The displacements u_r, u_θ according to these potentials in the polar coordinates, are given by the following formulas:

$$u_r = \frac{\partial\Phi}{\partial r} + \frac{1}{r}\frac{\partial\Psi}{\partial\theta}; \quad u_\theta = \frac{1}{r}\frac{\partial\Phi}{\partial\theta} - \frac{\partial\Psi}{\partial r}.$$

In general, each boundary condition involves both potentials Φ and Ψ, but there are two realistic cases when each boundary condition involves only one potential, either Φ or Ψ. One special case specifies the normal displacement and shear traction on the boundary. In the second case the region is loaded by forces normal to the edges and in this case the shear displacement on the boundary of the surface vanishes identically.

For a correct formulation of our problem we have to add to Eqs. (1), (2) and the boundary conditions, specifying the behavior of wave fields in the neighborhoods of singular points of regions, namely, near the origins of the angles and at infinity.

The so-called "edge-condition" has to be satisfied near each origin:

$$u = O(r^p), \quad p > 0, \quad r \to 0 \tag{3}$$

Physically it guarantees finiteness of the elastic energy of any compact region. Without this auxiliary condition, the displacement components could be infinite at the tip. Mathematically it ensures a unique solution.

At infinity we apply the classical Sommerfeld's radiation conditions.

As shown by Kostrov (1966) (later by Zemell, 1975), it will not be possible to simply reduce the entire problem for a wedge even in the case of special boundary conditions to two acoustic ones, because this solution fails to satisfy the edge condition. In Kostrov's paper the problem of an incident plane wave at a rigid wedge in an unbounded elastic medium with frictionless contact was considered. We will consider the problem with other special boundary conditions which admit separations of the potentials.

1 First, let us consider a homogeneous isotropic medium which fills a wedge-shaped region

$$\Omega(-\alpha, \alpha) = \{r, \theta: r \geq 0, -\alpha \leq \theta \leq \alpha\}.$$

The wedge is loaded by time-harmonic surface forces which are normal to the edges. The shear displacement on the boundary of the surface should vanish identically:

$$\sigma_{\theta\theta}(r, \pm\alpha) = h_\pm(r), \quad 0 < r < \infty,$$

$$u_r(r, \pm\alpha) = 0.$$

This problem can be simplified by splitting it into two independent problems—symmetric and antisymmetric:

$$\text{(a)} \quad \sigma_{\theta\theta}(r, \pm\alpha) = h(r),$$

$$\text{(b)} \quad \sigma_{\theta\theta}(r, \pm\alpha) = \pm h(r).$$

Contributed by the Applied Mechanics Division of THE AMERICAN SOCIETY OF MECHANICAL ENGINEERS for publication in the ASME JOURNAL OF APPLIED MECHANICS.

Discussion on the paper should be addressed to the Technical Editor, Professor Lewis T. Wheeler, Department of Mechanical Engineering, University of Houston, Houston, TX 77204-4792, and will be accepted until four months after final publication of the paper itself in the ASME JOURNAL OF APPLIED MECHANICS.

Manuscript received by the ASME Applied Mechanics Division, May 28, 1997; final revision, Oct. 30, 1997. Associate Technical Editor: X. Markenscoff.

 Copyright © 1998 by ASME

Downloaded 04 May 2010 to 171.66.16.26. Redistribution subject to ASME license or copyright; see http://www.asme.org/terms/Terms_Use.cfm

Let us consider the symmetric problem. It can be shown that the boundary conditions can be formulated as

$$\Phi|_{\theta=\pm\alpha} = \frac{1}{\omega^2\rho} h(r), \tag{4}$$

$$\left.\frac{\partial\Psi}{\partial\theta}\right|_{\theta=\pm\alpha} = -\frac{1}{\omega^2\rho} rh'(r), \tag{5}$$

where Φ, Ψ are separated.

Thus we get the following problem: To find the wave fields Φ and Ψ we satisfy the Helmholz Eqs. (1), (2), the boundary conditions (4), (5), the condition at the vertex (3), and the radiation conditions in the region Ω.

Let us note that the boundary conditions are formulated in terms of potentials, whereas the edge condition is only derived for the displacement vector. First, let us try to find two independent solutions of the two acoustic problems for longitudinal and shear potentials not taking into account the edge condition.

Let us search the solutions of the Helmholz equations of $W_2^1(\bar{\Omega})$ class which yield the radiation conditions. Both acoustic problems have unique solutions in this class. Thus we obtain the Dirichlet problem for potential Φ and the Neuman problem for Ψ. The exact solutions of such problems can be derived, for instance, by means of the integral transformation of Kontorovich-Lebedev (1938). Use of this transform provides the fulfillment of the radiation condition.

In the case of a symmetrical loading the exact solutions of the acoustic problems can be written as the following double integrals:

$$\Phi_a(r, \theta) = \int_0^\infty \int_{-i\infty}^{i\infty} \frac{\mu h(x) \cos \mu\theta \kappa_1(\mu, x, r, \theta)}{x} dx d\mu,$$

$$\Psi_a(r, \theta) = \int_0^\infty \int_{-i\infty}^{i\infty} h'(x) \sin \mu\theta \kappa_2(\mu, x, r, \theta) dx d\mu,$$

$$\kappa_i(\mu, x, r, \theta) = \frac{\sin \pi\mu e^{-i\pi\mu} H_\mu^{(2)}(k_i r) H_\mu^{(2)}(k_i x)}{4i\omega^2\rho \cos \mu\alpha}, \quad i = 1, 2.$$

Using the formula of integral representation for a product of Hankel's functions (Dixon and Ferrar, 1933), we can obtain the asymptotics of the solution near the vertex:

$$\Phi_a(r, \theta) = Ar^{\pi/2\alpha} \cos\left(\frac{\pi\theta}{2\alpha}\right) + o(r^{\pi/2\alpha}),$$

$$\Psi_a(r, \theta) = Br^{\pi/2\alpha} \sin\left(\frac{\pi\theta}{2\alpha}\right) + o(r^{\pi/2\alpha}),$$

$$A = \frac{2\pi i k_1^{\pi/2\alpha}}{\rho\alpha\omega^2 2^{\pi/2\alpha}\Gamma(\pi/2\alpha + 1)} \int_\delta^\infty \frac{h(x)}{x} H_{\pi/2\alpha}^{(2)}(k_1 x) dx,$$

$$B = -\frac{2\pi i k_2^{\pi/2\alpha}}{\rho\alpha\omega^2 2^{\pi/2\alpha}\Gamma(\pi/2\alpha + 1)} \int_\delta^\infty h'(x) H_{\pi/2\alpha}^{(2)}(k_2 x) dx.$$

For the sake of simplicity let us assume that the loading $h(r)$ is applied at some distance from the tip, and provides convergence of the last integrals.

The displacement vectors according to acoustic potentials have the following asymptotics near the origin:

$$u_r^a = \frac{\pi}{2\alpha}(A + B) r^{\pi/2\alpha - 1} \cos\frac{\pi\theta}{2\alpha} + o(1),$$

$$u_\theta^a = -\frac{\pi}{2\alpha}(A + B) r^{\pi/2\alpha - 1} \sin\frac{\pi\theta}{2\alpha} + o(1).$$

So, the solution of the acoustic problems fails to satisfy the edge condition for re-entrant angles ($\alpha > \pi/2$) and, hence, the displacement components are infinite at the tip.

To resolve the problem with $2\alpha > \pi$ note that is not necessary to have potentials Φ and Ψ bounded at the edge—only displacements must be bounded. Let us replace the condition $\Phi, \Psi \in W_{2\text{loc}}^1(\bar{\Omega})$ by the condition $\Phi, \Psi \in L_{2\text{loc}}(\bar{\Omega})$.

The solution for the potentials of the L_2-class can be written as a sum of the acoustic terms and the homogeneous solutions of the Helmholz equations $\zeta(r, \theta) \in L_{2\text{loc}}(\bar{\Omega})$ for the Dirichlet and Neuman problems (Kondratiev, 1967). In the case of the wedge the function ζ coincides with the Hankel function $H_{\pi/2\alpha}^{(2)}(k_i r)$, multiplying by the corresponding trigonometric function. And so let us introduce such potentials

$$\Phi^0 = A_1 H_{\pi/2\alpha}^{(2)}(k_1 r) \cos\left(\frac{\pi\theta}{2\alpha}\right),$$

$$\Psi^0 = A_2 H_{\pi/2\alpha}^{(2)}(k_2 r) \sin\left(\frac{\pi\theta}{2\alpha}\right).$$

It is clear from the asymptotics of the Hankel functions near 0 that

$$H_\nu^{(2)}(x) \approx i\left(\frac{2}{x}\right)^\nu \frac{\Gamma(\nu)}{\pi}, \quad x \to 0, \quad \nu > 0,$$

$$2\frac{dH_\nu^{(2)}(z)}{dz} = H_{\nu-1}^{(2)}(z) - H_{\nu+1}^{(2)}(z),$$

and if $A_1 = (k_1/k_2)^{\pi/2\alpha} A_2$, then the corresponding displacements have such asymptotics near the origin

$$u_r^0 = \frac{\pi}{2\alpha} A_1 r^{\pi/2\alpha - 1} \cos\left(\frac{\pi\theta}{2\alpha}\right) + o(1),$$

$$u_\theta^0 = -\frac{\pi}{2\alpha} A_1 r^{\pi/2\alpha - 1} \sin\left(\frac{\pi\theta}{2\alpha}\right) + o(1).$$

Since the order of the dominant terms in u_r^0, u_θ^0 coincide with the order of the displacements u_r^a, u_θ^a corresponding to the acoustic potentials, then the potentials

$$\Phi = \Phi^0 + \Phi_a; \quad \Psi = \Psi^0 + \Psi_a$$

solve the initial problem of elasticity. We can find the constant A_1 from the condition (3) of the finiteness of the displacement components near the origin:

$$A_1 = -\frac{ik_1^{\pi/2\alpha - 2}}{4\Gamma(\pi/2\alpha - 1)} \left(A \int_\delta^\infty \frac{h(x)}{x} H_{\pi/2\alpha}^{(2)}(k_1 x) dx - B \int_\delta^\infty h'(x) H_{\pi/2\alpha}^{(2)}(k_2 x) dx \right).$$

Let us note that in the case of antisymmetrical loading each wave potential satisfies the edge condition and so the elasticity problem can be simply reduced to two acoustic ones.

2 We use such an idea for the solution of the general problem on the loading of the unbounded body with "m" reentrant angles.

Let us consider the problem in region Q which contains m re-entrant angles $\{\alpha_1, \ldots, \alpha_m\}$. We suppose that outside the sphere of the big radius the region coincides with a wedge. As before, let us suppose that the contour is loaded by forces normal to the edges, which have a time-harmonic factor $\exp(i\omega t)$ and the shear displacement on the boundary of the surface vanishes identically:

Downloaded 04 May 2010 to 171.66.16.26. Redistribution subject to ASME license or copyright; see http://www.asme.org/terms/Terms_Use.cfm

$$\sigma_{\theta\theta}|_{\partial Q} = h(r),$$

$$u_r|_{\partial Q} = 0.$$

At infinity the radiation conditions are fulfilled.

As shown by Kondratiev (1967), the main term in asymptotics of acoustic potentials of $W^1_{2\text{loc}}(\bar{Q})$-class near the i reentrant angles is as follows:

$$\Phi_a = A_i r_i^{\pi/2\alpha_i} \cos\left(\frac{\pi\theta_i}{2\alpha_i}\right) + o(r^{\pi/2\alpha}), \tag{6}$$

$$\Psi_a = B_i r_i^{\pi/2\alpha_i} \sin\left(\frac{\pi\theta_i}{2\alpha_i}\right) + o(r^{\pi/2\alpha}), \tag{7}$$

here (r_i, θ_i)—the polar coordinate with the center in the vertex of re-entrant angle i.

One can see that the corresponding displacement vector is infinite near the tip of each re-entrant angle.

To determinate the unknown constant A_i let us introduce the function $\zeta_i(r, \theta) \in L_{2\text{loc}}(\bar{Q})$, which satisfies the Helmholz equation in region Q, the homogeneous Dirichlet conditions on the entire boundary (except the tips of reentrant angles), and which can be written as (Kondratiev, 1967):

$$\zeta_i(r) = r_i^{-\pi/2\alpha_i} \cos\left(\frac{\pi\theta_i}{2\alpha_i}\right)\chi(r_i) + Z_i, \quad Z_i \in W^1_{2\text{loc}}(Q)$$

$$Z_i = \sum_{j=1}^{m} c_{ij} r_j^{\pi/2\alpha_j} \cos\left(\frac{\pi\theta_j}{2\alpha_j}\right)\chi(r_j) + R_i, \quad R_i \in W^2_{2\text{loc}}(\bar{Q}).$$

$\chi(r)$ is a smooth cutoff function, $\chi(0) = 1$.

Using the Green formula for functions ζ_i and Φ_a in the whole region Q except for the tips of reentrant angles, we arrive at some calculations (Mazija and Plamenevskij, 1976)—the expression for constants A_i in terms of the loading function $h(r)$ and function $\zeta_i(r, \theta)$:

$$A_i = \frac{1}{\pi\omega^2\rho}\int_{\partial Q} \frac{\partial\zeta_i}{\partial n} h(x)dx.$$

In a similar way, we can find the coefficients B_i in the asymptotical representation (7):

$$B_i = -\frac{1}{\pi\omega^2\rho}\int_{\partial Q} \tilde{\zeta}_i h'(r) r dr,$$

where $\tilde{\zeta}_i \in L_{2\text{loc}}(\bar{Q})$ satisfy the homogeneous Neuman problem for the Helmholz equation in region Q:

$$\tilde{\zeta}_i(r) = r_i^{-\pi/2\alpha_i} \sin\left(\frac{\pi\theta_i}{2\alpha_i}\right)\chi(r_i)$$

$$+ \sum_{j=1}^{m} e_{ij} r_j^{\pi/2\alpha_j} \sin\left(\frac{\pi\theta_j}{2\alpha_j}\right)\chi(r_j) + \tilde{R}_i, \quad \tilde{R}_i \in W^2_{2\text{loc}}(\bar{Q}).$$

Let us remind ourselves that in the case of the wedge

$$\zeta_i(r, \theta) = H^{(2)}_{\pi/2\alpha}(k_1 r)\cos\left(\frac{\pi\theta}{2\alpha}\right),$$

$$\tilde{\zeta}_i(r, \theta) = H^{(2)}_{\pi/2\alpha}(k_2 r)\sin\left(\frac{\pi\theta}{2\alpha}\right).$$

In order to construct the energetic solution let us extend the domain of the definition of functions Φ, Ψ to $L_{2\text{loc}}(\bar{Q})$. The set of all possible solutions for potential Φ in the area $L_{2\text{loc}}(\bar{Q})$ contains the acoustic solution and the sum of the auxilary functions

$$\Phi = \Phi_a + \sum_{i=1}^{m} b_i \zeta_i(x).$$

There is one main difficulty: the auxiliary function, which corrects the situation near one corner point, worsens the situations near the other corners. In order to avoid this we must construct the auxiliary matrix $\{c_{ij}\}$, which solves the problem on the whole.

In order to construct it we can use, as before, the Maziia-Plamenevsky method for the functions ζ_i, Z_j. And so we will get the matrix $\{c_{ij}\}$ in the form of the integral of functions ζ_i, Z_j.

$$c_{ij} = \frac{1}{\pi}\int_Q \zeta_i(r)\Gamma Z_j dQ.$$

Here Γ denotes the Helmholz operator.

It can be easily shown that $\{c_{ij}\}$ is a symmetric matrix.

In the similar way, we get the set of all possible solutions of the $L_{2\text{loc}}(\bar{Q})$ class for the shear potential Ψ:

$$\Psi = \Psi_a + \sum_{i=1}^{m} d_i \tilde{\zeta}_i(x).$$

The matrix $\{e_{ij}\}$ in the representation of function $\tilde{\zeta}_i(r)$ is a symmetric matrix also, and can be written as follows:

$$e_{ij} = \frac{1}{\pi}\int_Q \tilde{\zeta}_j(r)\Gamma\tilde{Z}_i dQ.$$

To find the solution with bounded energy we have m relations near the re-entrant angles:

$$\frac{\partial\Phi_i}{\partial r_i} + \frac{1}{r_i}\frac{\partial\Psi_i}{\partial\theta_i} = O(r_i^p), \quad p > 0, \quad r_i \to 0, \quad i = 1, \ldots, m.$$

Substituting the expressions for the sets of solutions for Φ and Ψ at the edge conditions we get m relations for determination of constants b_i, d_i:

$$b_i = d_i, \quad i = 1 \ldots m,$$

$$A_i + B_i + \sum_{j=1}^{m} (c_{ji} b_j + e_{ji} d_j) = 0$$

or

$$b = -(C + E)^{-1}(A + B),$$

where b, A, B—m-dimensional vectors, C, E, are the symmetric matrices $m \times m$.

Let us note that in the case of absence of the re-entrant angles on the contour each of the potentials satisfies the edge conditions and, hence, the problem can be reduced to two acoustic ones.

References

Dixon, A., and Ferrar, W., 1933, "Integrals for the product of two Bessel functions," *Quart. J. of Math.*, Vol. 4, pp. 193–208; 297–304.

Kondratiev, V., 1967, "Boundary problems for elliptic equations in domains with conical or angular points," *Trans. Math. Soc.*, Vol. 16, pp. 227–313.

Kontorovich, M., and Lebedev, N., 1938, "On the method of solution of some problems of the diffraction theory," *Journ. Phys.*, Vol. 1, pp. 229–241 (Russian, 1935).

Kostrov, B., 1966, "Diffraction of plane wave by a smooth rigid wedge in an unbounded elastic medium in absence of friction," *J. Appl. Math. Mech.*, Vol. 30, pp. 244–250.

Mazija, V., and Plamenevskij, B., 1976, "On the coefficients in the asymptotics of solutions of elliptical boundary value problems near edge," *Soviet Math. Dokl.*, Vol. 17, pp. 970–974.

Sternberg, E., 1960, "On the integration of the equations of motion in the classical theory of elasticity," *Arch. Rat. Mech. Anal.*, Vol. 6, No. 1, pp. 34–50.

Zemell, S. H., 1975, "Diffraction of elastic waves by a rigid-smooth wedge," *SIAM. J. Appl. Math.*, Vol. 5, No. 4, pp. 582–596.

Downloaded 04 May 2010 to 171.66.16.26. Redistribution subject to ASME license or copyright; see http://www.asme.org/terms/Terms_Use.cfm

Effects of Flexibility and Damping on Momentum Transfer During Locking of Two Moving Links, Part I: Numerical Simulation

W. Szyszkowski
Professor,
e-mail: szyszkow@engr.usask.ca,
Mem. ASME.

K. Fielden
Graduate Student,
e-mail: kmf230@engr.usask.ca.

Mechanical Engineering Department,
University of Saskatchewan,
57 Campus Drive,
Saskatoon, SK S7N 5A9,
Canada

The system consisting of two links and two joints is examined. The joints are idealy frictionless when unlocked. Due to flexibility of the links, the locking generates some damped vibrations. It is demonstrated that the presence of these vibrations, even of very small and seemingly neglegible amplitudes, have dramatic effects on the after-locking motion of the links. Depending on the level of flexibility and damping involved, the locking triggers a large-scale "slow" motion that may have either oscillatory or circular (clockwise or counterclockwise) characters. The links will stop at some resting configuration only at certain "critical" values of damping. The set of "critical dampings" seems to be infinite, though only two degrees-of-freedom are used to model the system. Governing equations for these phenomena are derived and discussed in Part II of this paper.

1 Introduction

In the kinetics of mechanisms, it is generally assumed that the motion of structural members experiencing small elastic deformation can be approximated with good accuracy by the equations derived from the rigid-body dynamics. Such an assumption is typically used to analyze maneuvers of manipulators or booms consisting of moderately flexible links connected at joints. However, this assumption appears to be unacceptable when one of the joints is suddenly locked while the links are still in motion. While analyzing the deployment of a satellite boom with relatively rigid links (Fielden, 1997), it was found that the locking action and the subsequent motion was substantially influenced by even relatively small and seemingly negligible flexibility and damping, although the solution of the rigid-body equations of motion for the links gave satisfactory answers with unlocked joints. Consequently, considering the whole maneuver, solutions of the rigid-body equations rendered inaccurate trajectories, internal forces, etc.

In order to focus on the locking effects only, a self-locking boom deploying from the folded to straight configurations is considered. The boom is made up of two links connected together by the elbow joint at B and anchored to a rigid surface of the satellite by the shoulder joint at A (Szyszkowski et al., 1996) as shown in Fig. 1. The two links have lengths l_1 and l_2. The centers of mass of each link includes the link itself and all the masses rigidly attached to it, thus for example, a tip mass M is incorporated in m_1. The mass moment of inertias about the centers of gravity are given by I_1 and I_2 and the rigid-body orientation of the two links is specified by the two angles θ_1 and θ_2.

Both links are allowed to move freely without friction (Szyszkowski and Johnson, 1997) at the joints until link 2 becomes vertical. At $\theta_2 = \pi/2$ the shoulder joint will lock. Before locking the motion of the system depends on the forces driving the boom. For the purpose of this analysis we assume that the trajectory of the center of mass of link 1 and the velocity along this trajectory just before the moment of locking are known. We also assume that no external forces are present at the moment of locking and in the post-locking motion (the driving forces that sped up the boom have been removed and the links are moving freely in space).

First, we use the rigid-body dynamics (the impulse-momentum relations) to predict the motion of link 1 after locking. Next we re-examine the locking process and the post-locking motion of the system by solving the equations that include some small deflections and damping due to flexibility of the link and the locked shoulder joint.

2 Locking by Rigid-Body Dynamics

For free-moving links before locking, the following relations hold:

$$v_a = l_2 \sin(\theta_1 + \theta_2)\dot{\theta}_2 \quad v_t = f\dot{\theta}_1 + l_2 \cos(\theta_1 + \theta_2)\dot{\theta}_2 \qquad (1)$$

where v_a and v_t are the components of the velocity of C that are axial and transverse to link 1 (Fig. 2).

The angular momentum of link 1 about point B is equal to

$$H_B = m_1 f v_t + I_1\dot{\theta}_1$$
$$= m_1 f[f\dot{\theta}_1 + l_2 \cos(\theta_1 + \theta_2)\dot{\theta}_2] + I_1\dot{\theta}_1. \qquad (2)$$

Since there is no angular impulse applied to link 1, this angular momentum must be conserved at locking, which occurs at $\theta_2 = \pi/2$ and at a given $\theta_1 = \theta_{1L}$. We assume that just before locking, the angular velocities of both links are given as $\dot{\theta}_{1i}$ and $\dot{\theta}_{2i}$. Immediately after locking the angular velocity of link 2 becomes zero since this joint is locked, while the velocity of link 1, denoted as $\dot{\theta}_{1r}$, can be determined from the conservation of angular momentum, (2), in the form

Contributed by the Applied Mechanics Division of THE AMERICAN SOCIETY OF MECHANICAL ENGINEERS for publication in the ASME JOURNAL OF APPLIED MECHANICS.

Discussion on the paper should be addressed to the Technical Editor, Professor Lewis T. Wheeler, Department of Mechanical Engineering, University of Houston, Houston, TX 77204-4792, and will be accepted until four months after final publication of the paper itself in the ASME JOURNAL OF APPLIED MECHANICS.

Manuscript received by the ASME Applied Mechanics Division, Feb. 12, 1997; final revision, Sept. 30, 1997. Associate Technical Editor: N. C. Perkins.

 Copyright © 1998 by ASME

Downloaded 04 May 2010 to 171.66.16.26. Redistribution subject to ASME license or copyright; see http://www.asme.org/terms/Terms_Use.cfm

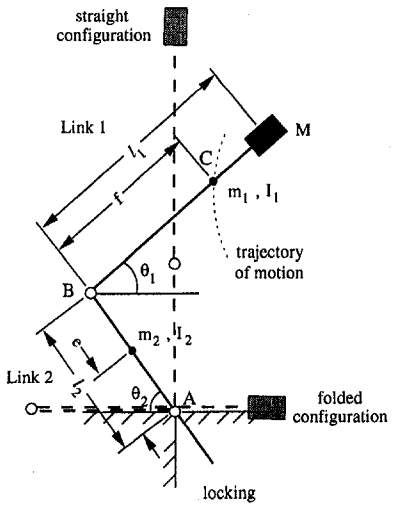


Fig. 1 The two-link system

$$\dot{\theta}_{1r} = \dot{\theta}_{1i} - \frac{l_2}{f} \frac{\sin(\theta_{1L})}{1 + \dfrac{I_1}{m_1 f^2}} \dot{\theta}_{2i}. \tag{3}$$

Substituting (1), this expression can also be written, in terms of the initial axial and transverse velocities of the mass center of link 1, as follows:

$$v_r = v_t + v_a \frac{\tan(\theta_{1L})}{1 + \dfrac{m_1 f^2}{I_1}} \tag{4}$$

where v_r is the velocity of the after-locking circular motion of link 1 (see Fig. 3). Thus, assuming no external forces during and after locking, any arbitrary motion of the links is converted into a circular motion of link 1 with its velocity being constant and defined by (4). This final velocity can be positive or negative depending on the values v_a, v_t, and θ_{1L}.

As can be seen from Eq. (4), a transverse component of the velocity before locking, v_t, is carried unchanged to the post-locking motion of link 1 along the circular trajectory. However, the contribution of axial component, v_a, depends on the angle θ_{1L} and the mass properties of link 1. This contribution, as demonstrated in the chapter that follows, appears to be very sensitive to any flexibility present in the system.

In order to analyze the flexibility effects, the initial transverse velocity, v_t, is assumed zero. This is equivalent to considering only the trajectories that are tangential to link 1 at the moment

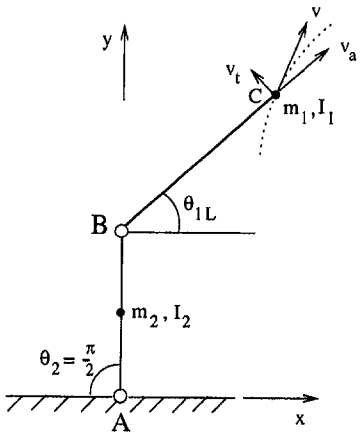


Fig. 2 The locking configuration

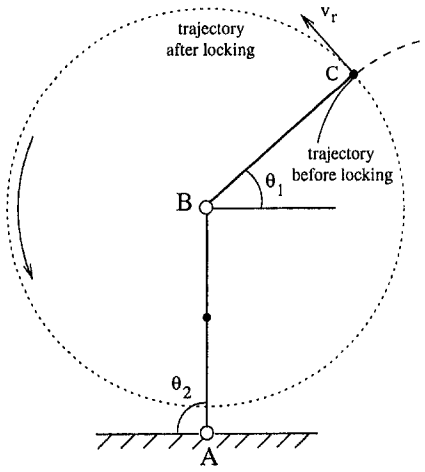


Fig. 3 Rigid links after-locking motion

of locking (Fig. 3). The required relation between the angular velocities before locking is obtained from (1):

$$\dot{\theta}_{1i} = \dot{\theta}_{2i} \frac{l_2}{f} \sin(\theta_{1L}). \tag{5}$$

Substituting to (3), the angular velocity after locking becomes dependent only on $\dot{\theta}_{1i}$ and is equal to

$$\dot{\theta}_{1r} = \frac{\dot{\theta}_{1i}}{1 + \dfrac{m_1 f^2}{I_1}}. \tag{6}$$

For example, when link 1 is uniform and $M = 0$, the final angular velocity of link 1 calculated from (6) becomes

$$\dot{\theta}_{1r} = \tfrac{1}{4} \dot{\theta}_{1i}. \tag{7}$$

If the mass of link 1 is negligible in comparison with M, then the center of mass is close to the tip of the link, that is $f \cong l_1$. Also, if $I_1 \cong I_M = Mr^2$, where r is the radius of gyration of mass M, the final angular velocity is given by

$$\dot{\theta}_{1r} \cong \frac{\dot{\theta}_{1i}}{1 + \left(\dfrac{l_1}{r}\right)^2}. \tag{8}$$

For example, if the tip mass is a cylindrical block, as in Szyszkowski et al. (1996), with

$$M = 1.0 \text{ kg} \quad I_M = 0.0048 \text{ kg} \cdot \text{m}^2$$

and if $l_1 = 0.61$ m, then the final angular velocity is

$$\dot{\theta}_{1r} \cong \frac{1}{78.5} \dot{\theta}_{1i}. \tag{9}$$

3 Locking of Flexible Links With Damping

For comparison, the dynamic behavior of the links during locking has been analyzed by the nonlinear finite element method using the ANSYS software. The links were modeled by ten beam elements with the bending and axial stiffness as in the real links taken from (Szyszkowski et al., 1996), while the joints by the control elements available from the ANSYS elements library. The finite element method model contains about 30 degrees-of-freedom and uses the Newmark procedure for time-integration combined with the Newton-Raphson method for securing the dynamic equilibrium at every time step (ANSYS, 1995). This solution routine is essentially capable of

Downloaded 04 May 2010 to 171.66.16.26. Redistribution subject to ASME license or copyright; see http://www.asme.org/terms/Terms_Use.cfm

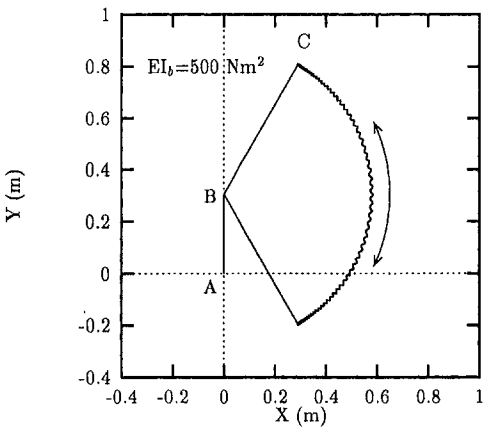


Fig. 4 Pendulum-like trajectory for EI_b = 500 Nm^2

solving large-motion dynamics of arbitrary flexible elements (Szyszkowski and Youck, 1993), though small time-steps, that can be required for accuracy, may necessitate a substantial computational effort (for example, in order to obtain a complete trajectory about 15,000 time-steps and four hours on a Sun SPARCstation 5 under Solaris was required).

It was expected that the results obtained in the previous section could be recreated if a sufficiently high stiffness for the beam elements was assumed. Surprisingly, despite raising the stiffness of the links and obtaining seemingly negligible elastic deformations in the system, it has been found that the post-locking behavior of link 1 was substantially different from that derived from the rigid-body dynamics. For example, for the boom with the bending stiffness EI_b = 500 Nm, the after-locking motion is shown in Fig. 4. The details of this behavior will be discussed later in Sections 3.2 and 3.3.) It was apparent that, in the locking process, flexibility was playing a more important role than intuitively predicted. As opposite to our case in which small elastic deflections are expected, Simo and Vu-Quoc (1986), using the FEAP program analyzed the case of locking of two very flexible links (Example 2.3.1). In their case, the deflections of the elbow joint were much bigger. Besides stating that the elbow link underwent a complete revolution, no particular pattern of the motion of that link was reported.

3.1 Locking Analysis by Two-Degree-of-Freedom Model. In order to understand the dynamics of the locking process in the presence of small elastic deflections of the links, a two-degree-of-freedom model which includes a rotational spring and a damper at the shoulder joint as shown in Fig. 5 is examined. The spring is to simulate the bending flexibility of the links. In typical links this flexibility is usually several orders

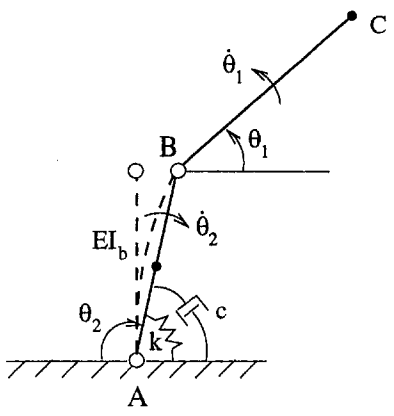


Fig. 5 Flexible system

higher than the axial flexibility (which is neglected here). To simulate the deflection of link 2 at B due to bending, the stiffness of the spring is assumed as

$$k = \frac{3EI_b}{l_2}, \tag{10}$$

where E is Young's modulus and I_b is the area moment of inertia of the link. Note that this model reflects the main characteristic of the system flexibility. Large forces occuring during locking in the elbow joint will cause only negligible axial deformations in link 1. This negligible effect of axial deformations in both links and absence of bending in link 1 can also be observed for much more flexible links considered in (Simo and Vu-Quoc, 1986).

The equations of motion for this system are developed using the Lagrange formulation. The kinetic energy, T, of the system is obtained as

$$T = \tfrac{1}{2} m_1[l_2^2\dot{\theta}_2^2 + f^2\dot{\theta}_1^2 + 2fl_2\dot{\theta}_1\dot{\theta}_2 \cos(\theta_1 + \theta_2)] + \tfrac{1}{2} m_2e^2\dot{\theta}_2^2 + \tfrac{1}{2} I_1\dot{\theta}_1^2 + \tfrac{1}{2} I_2\dot{\theta}_2^2. \tag{11}$$

The elastic energy, V, stored in the spring is

$$V = \frac{1}{2} k\left(\theta_2 - \frac{\pi}{2}\right)^2. \tag{12}$$

Here the angle of deflection is $\theta_2 - (\pi/2)$ because the spring is unloaded at $\theta_2 = \pi/2$.

Rayleigh's dissipation function for the system with a rotational damper at the shoulder joint is

$$I = \tfrac{1}{2} c\dot{\theta}_2^2 \tag{13}$$

where c is the damping constant.

The resulting Lagrange's equations are given by

$$\frac{d}{dt}\left(\frac{\partial L}{\partial \dot{\theta}_1}\right) - \frac{\partial L}{\partial \theta_1} = 0 \tag{14}$$

$$\frac{d}{dt}\left(\frac{\partial L}{\partial \dot{\theta}_2}\right) - \frac{\partial L}{\partial \theta_2} + \frac{\partial I}{\partial \dot{\theta}_2} = 0 \tag{15}$$

where $L = T - V$.

Substituting for L and I produces the following equations of motion for the system:

$$\begin{bmatrix} m_1f^2 + I_1 & m_1fl_2\cos(\theta_1 + \theta_2) \\ m_1fl_2\cos(\theta_1 + \theta_2) & m_1l_2^2 + m_2e^2 + I_2 \end{bmatrix} \begin{bmatrix} \ddot{\theta}_1 \\ \ddot{\theta}_2 \end{bmatrix} = \begin{bmatrix} m_1fl_2\dot{\theta}_2^2\sin(\theta_1 + \theta_2) \\ m_1fl_2\dot{\theta}_1^2\sin(\theta_1 + \theta_2) - k\left(\theta_2 - \frac{\pi}{2}\right) - c\dot{\theta}_2 \end{bmatrix}. \tag{16}$$

These equations can be integrated in time from the known values of the angles and angular velocities at the start of locking. The numerical solutions presented here are obtained using a fourth order Runge-Kutta algorithm. It takes about five minutes on a Sun SPARCstation 5 to run the complete simulation.

For the analysis we consider the links that were used in the self-locking satellite boom presented in (Szyszkowski et al., 1996). These links were made of a light composite (unit mass 0.14 kg/m) with their mass very small in comparison with the end mass (mass of the sensor) which was about 1 kg. In terms of the notation used here, the following parameters (SI units) are used to define this system.

Downloaded 04 May 2010 to 171.66.16.26. Redistribution subject to ASME license or copyright; see http://www.asme.org/terms/Terms_Use.cfm

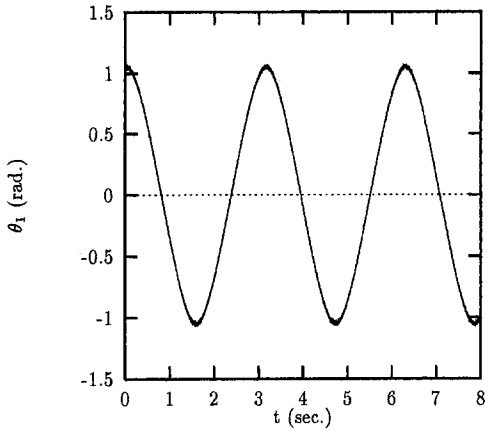


Fig. 6 Angular position of link 1 for EI_b = 500 Nm^2

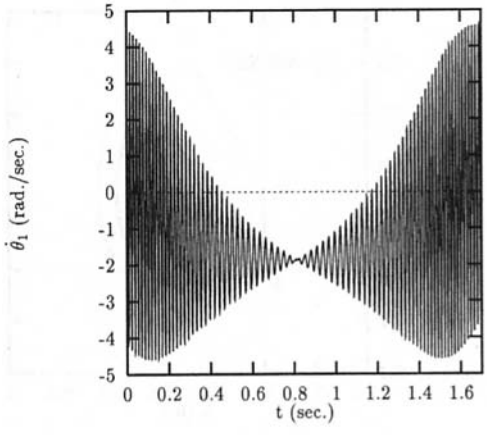


Fig. 7 Angular velocity of link 1 for EI_b = 500 Nm^2

$$m_1 = 1.1130 \quad l_1 = 0.610 \quad I_1 = 0.01296 \quad e = 0.153$$
$$m_2 = 0.05667 \quad l_2 = 0.306 \quad I_2 = 0.000447 \quad f = 0.579. \qquad (17)$$

Here we assume that the trajectory just before locking is tangential to link 1 ($v_t = 0$) and that $v_a = 1.5$ m/s. We also assume that at the moment of locking link 1 is positioned at $\theta_{1L} = 60$ deg from the horizontal.

Formally these assumptions translate into the following initial conditions for Eqn. (16) (the time is set to zero at the start of locking):

$$\begin{bmatrix} \theta_1(0) \\ \dot{\theta}_1(0) \\ \theta_2(0) \\ \dot{\theta}_2(0) \end{bmatrix} = \begin{bmatrix} \theta_{1L} \\ \dot{\theta}_{1i} \\ \frac{\pi}{2} \\ \dot{\theta}_{2i} \end{bmatrix} = \begin{bmatrix} 1.0472 \\ 4.4869 \\ 1.5708 \\ 9.8039 \end{bmatrix}. \qquad (18)$$

Note that if flexibility is neglected, link 1 after locking should, according to (6), be moving counterclockwise (see Fig. 3) with constant angular velocity equal to

$$\dot{\theta}_{1r} \cong 0.1506 \frac{1}{\text{sec.}}. \qquad (19)$$

3.2 Effects of Flexibility. First, consider the system without damping ($c = 0$) and with the following bending stiffness of the links

$$EI_b = 500.0 \text{ Nm}^2.$$

This approximately represents the stiffness of the links of the satellite boom used in Szyszkowski et al. (1996).

With the flexibility included the resulting motion after locking is essentially indistinguishable from the finite element method results shown in Fig. 4. Note that, in comparison with the finite element method calculations, at least for the links considered, our two-dimensional model has given almost identical results with a substantial saving in the computation time. This model was used to obtain the response of the system for a wide range of the link's stiffnesses and dampings. Figure 4 shows the position in space of the center of mass of link 1. The angular position of link 1 in time is plotted in Fig. 6. It is obvious that the circular motion predicted by the rigid-body model, Eq. (6), is not present at all.

Instead, the motion of link 1 is *dominated by a large pendulum-like slow oscillation* about the horizontal position $\theta_1 = 0$. Fast vibrations of small amplitudes that are present in the system become more visible when plotting the angular velocity of link 1 as in Fig. 7 and the angular position of link 2 as in Fig. 8. Analyzing Fig. 4, 6, and 7, it can be seen that the centre of mass of link 1 starts at the upper edge of the arc with a positive "average" $\dot{\theta}_1$ approximately equal to $\dot{\theta}_{1r}$. This velocity reduces to zero and then reverses direction. Link 1 speeds up gradually as it moves toward the horizontal position and begins slowing down after $\theta_1 = 0$ is reached until it stops at the bottom of the arc. It then begins moving upward again to the top of the arc where it stops and begins the cycle again. The period of this slow oscillation, T_s, is about 3.14 sec. and its amplitude is approximately $\pm\theta_{1L}$. Link 2, as expected, vibrates quickly back and forth around $\theta_2 = \pi/2$ (Fig. 8). The amplitude of these vibrations measured at B is about 6.5 mm ($\Delta\theta_2 \cong 0.025$ rad.) and the period of vibrations, T_f, changing slowly from about 0.016 sec. at $\theta_1 \cong \theta_{1L}$ to about 0.029 sec. at $\theta_1 = 0$.

Interestingly, *if the system is made more rigid, the period and the amplitude of the slow oscillations seems to be unaffected.* Figures 9 and 10 show the resulting motion for the same initial conditions but for the beams with EI_b = 5000 Nm^2 and EI_b = 50000 Nm^2 respectively. The $\theta_1(t)$ plots for these stiffnesses coincide with the plot shown in Fig. 6. The increasing stiffness affects only the amplitude and the period of the fast oscillations.

For the last case, the motion of link 2 is plotted in Fig. 11. Initially the link vibrates with the amplitude at B of about 0.65 mm ($\Delta\theta_2 \cong 0.0025$ rad.) and a period of $T_f \cong 0.002$ sec. Note that these vibrations, the amplitude of which represents only about 0.2 percent of the link length, would usually be neglected. Here, however, these very small elastic deformations change drastically the character of after-locking motion from circular with constant velocity to a slow oscillatory one with a pendulum-like pattern.

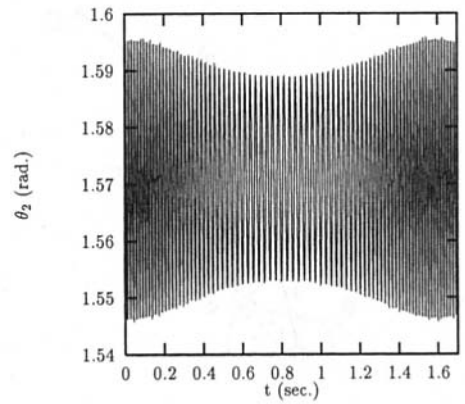


Fig. 8 Angular position of link 2 for EI_b = 500 Nm^2

Downloaded 04 May 2010 to 171.66.16.26. Redistribution subject to ASME license or copyright; see http://www.asme.org/terms/Terms_Use.cfm

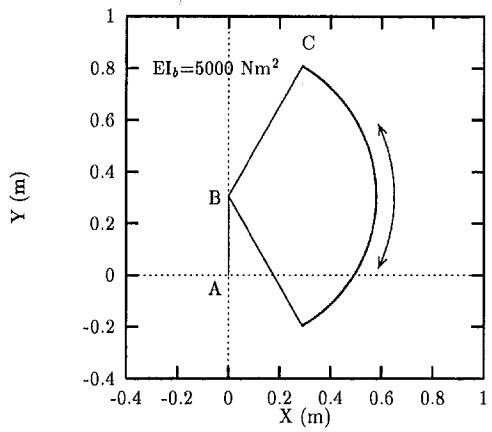


Fig. 9 Pendulum-like trajectory for EI_b = 5000 Nm^2

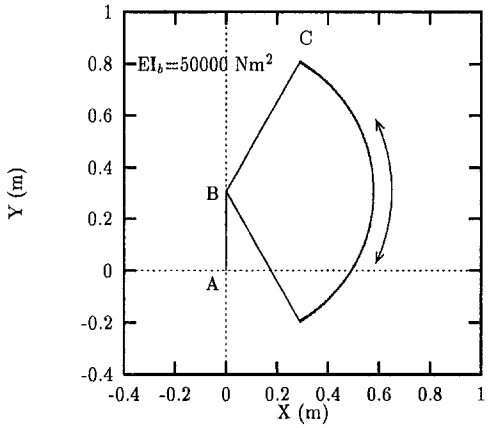


Fig. 10 Pendulum-like trajectory for EI_b = 50000 Nm^2

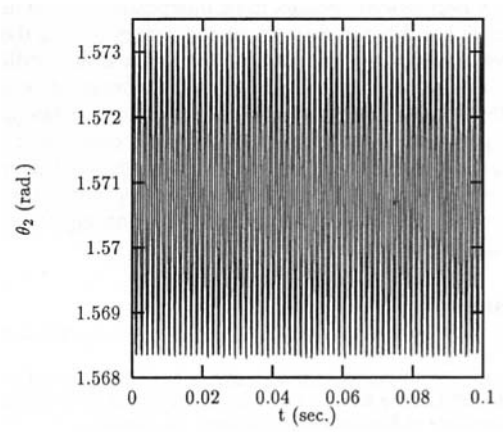


Fig. 11 Angular position of link 2 for EI_b = 50000 Nm^2

3.3 Effects of Damping. As was shown in the previous section, even small flexibility of this system produces behavior of the links that is much different than predicted by rigid-body mechanics. Including some damping modifies further this behavior. The following examples show that these modifications depend on the levels of damping and are quite substantial. The links with EI_b = 500 Nm^2 are analyzed to demonstrate these effects.

The location of link 1 in time for various damping values is plotted in Fig. 12. For reference purposes, the relation presented in Fig. 6 is replotted here as the case c = 0.

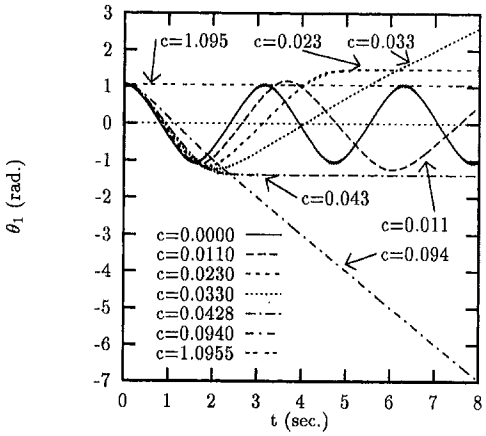


Fig. 12 Effect of damping on the angular position of link 1

Interestingly, the plots become *divergent* when damping is introduced. For example, see cases c = 0.011, c = 0.033 and c = 0.094 for which the amplitudes of slow oscillations are increasing with time (the meaning of the numerical values of c, given in Nms, is discussed in Part II of this paper). For certain magnitudes of damping (c = 0.0428 or c = 0.0230), referred to as the "critical damping," the plots asymptotically tend to some values representing the final locations of the link at rest.

For c = 0.033 the motion is shown in Fig. 13. The fast vibration is gradually damped out when link 1 makes one swing around the horizontal position and then starts rotating *counter-clockwise* with constant angular velocity $\dot{\theta}_1^\infty$ of about 0.61 rad./sec. (see the slope of line for c = 0.033 in Fig. 12). It should be emphasized that $\dot{\theta}_1^\infty$ is not related to the velocity $\dot{\theta}_{1r}$ given by (6) and resulting from the rigid-body dynamics.

If c = 0.094, link 1 ends up circulating *clockwise* with the angular velocity of 0.997 rad./sec. (or $\dot{\theta}_1^\infty = -0.997$ rad./sec.) as indicated in Fig. 14.

Since the velocity $\dot{\theta}_1^\infty$ is changing sign when c is changed from 0.033 to 0.094, one can conclude that there is a "critical" damping such that $\dot{\theta}_1^\infty = 0$. This damping will cause link 1 to stop.

Indeed if c = 0.042751, *the system comes to rest* at the location *below* the horizontal line as shown in Fig. 15. However, for c = 0.023018 it stops again, this time at the location *above* the horizontal as shown in Fig. 16.

In order to examine how many "critical values" of damping may exist for this two-degree-of-freedom system the analysis was performed for a wide range of c. The highest value of

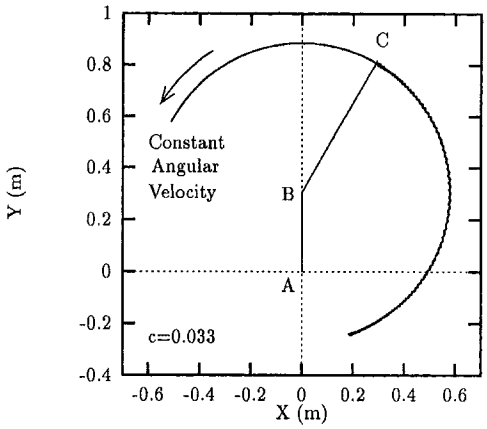


Fig. 13 Trajectory of link 1 for c = 0.033 Nms

Downloaded 04 May 2010 to 171.66.16.26. Redistribution subject to ASME license or copyright; see http://www.asme.org/terms/Terms_Use.cfm

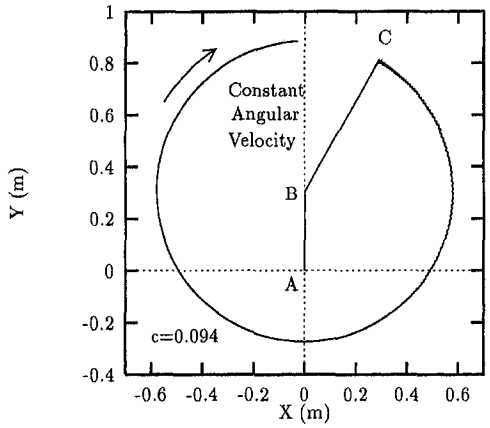


Fig. 14 Trajectory of link 1 for c = 0.094 Nms

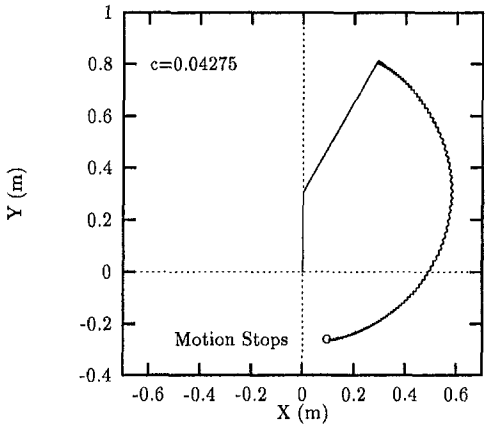


Fig. 15 Trajectory of link 1 for c = 0.042751 Nms

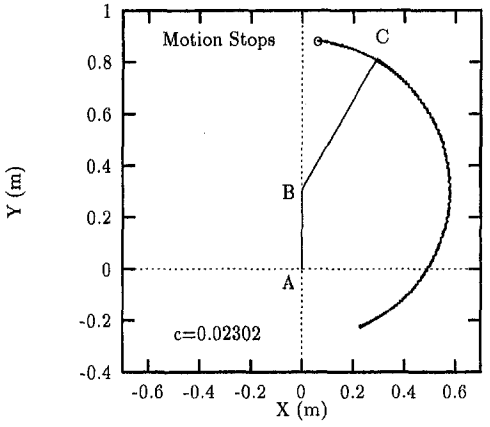


Fig. 16 Trajectory of link 1 for c = 0.023018 Nms

damping at which the system stops was found to be c_1^{cr} = 1.0955 (as indicated in Fig. 12), and next in the descending order were the above-mentioned c_2^{cr} = 0.042751 and c_3^{cr} = 0.023018. Then there seemed to be an infinite number of successive values of critical damping approximately satisfying the following formula:

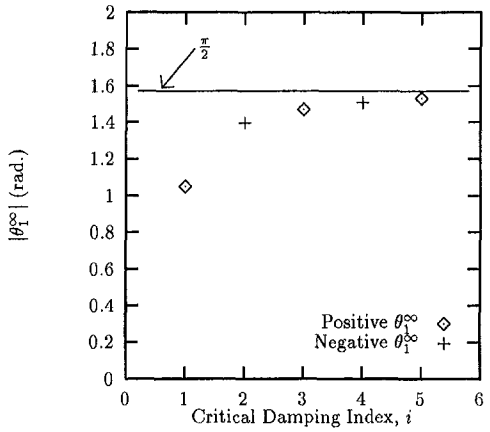


Fig. 17 Effect of critical damping on the asymptotic position of link 1

$$\frac{1}{c_{i+1}^{cr}} - \frac{1}{c_i^{cr}} = 0.1508i + 19.7651 \quad i \geq 3. \tag{20}$$

In the set of critical damping values, the sequential numbers i will be referred to as the critical damping indices.

The corresponding values of $\theta_1^{\infty}(c_i^{cr})$ at rest as a function of i are shown in Fig. 17. These final configurations alternate with increasing c_i and seem to be approaching the angle of ± 90 deg.

4 Concluding Comments

Even if the links are relatively rigid and any vibrations excited during the locking process seem to be negligibly small, the after-locking motion of the links is significantly affected by these vibrations and their damping characteristics.

Examination of the two-link damping-free system presented reveals that if the shoulder link (link 2) is suddenly locked at the end joint, the elbow link (link 1), somewhat surprisingly, begins moving in a pendulum-like *slow oscillatory motion* around the horizontal position. The period and amplitude of these slow oscillations appears to be independent of the flexibility of the links. What is even more surprising, adding damping to the system *increases* the amplitudes of the slow oscillations. Asymptotically, after a sufficient time, the damped slow motion of the elbow link becomes a circular one with a constant angular velocity dependent on the value of damping coefficient.

For certain discrete values of the damping coefficient, the link comes to rest. However, its final resting configuration *is not* horizontal (this is the configuration the damping-free system was oscillating about).

References

ANSYS, 1995, *ANSYS User's Manual, Revision 5.2, Theory,* Vol. 4, Chapters 15–17.

Fielden, K., 1997, "The Numerical Simulation of the Dynamics of a Satellite Boom With Self-Locking Joints," M.Sc. thesis, Department of Mechanical Engineering, University of Saskatchewan, Saskatoon, SK, Canada.

Simo, J. C., and Vu-Quoc, L., 1986, "On the Dynamics of Flexible Beams Under Large Overall Motion, The Plane Case: Part I and Part II," ASME JOURNAL OF APPLIED MECHANICS, Vol. 53, pp. 849–863.

Szyszkowski, W., and Johnson, D. W., 1997, "A Self-Locking Satellite Boom With Flexure-Made Joints," *Proceedings of PACAM V,* Puerto Rico, pp. 367–370.

Szyszkowski, W., and Youck, D., 1993, "Optimal Control of a Flexible Manipulator," *Computers and Structures,* Vol. 47, pp. 801–813.

Szyszkowski, W., Youck, D., and Johnson, D., 1996, "The Dynamics of Deployment of a Satellite Boom With Self-Locking Joints," *Proceedings of the 15th Canadian Congress of Applied Mechanics,* CANCAM 95, Victoria, BC, Canada, pp. 310–311.

Downloaded 04 May 2010 to 171.66.16.26. Redistribution subject to ASME license or copyright; see http://www.asme.org/terms/Terms_Use.cfm

Effects of Flexibility and Damping on Momentum Transfer During Locking of Two Moving Links, Part II: Analytical Approach

W. Szyszkowski
Professor,
e-mail: szyszkow@engr.usask.ca,
Mem. ASME.

K. Fielden
Graduate Student,
e-mail: kmf230@engr.usask.ca.

Mechanical Engineering Department,
University of Saskatchewan,
57 Campus Drive,
Saskatoon, SK S7N 5A9,
Canada

The numerical analysis presented in Part I of this paper revealed that small and seemingly negligible flexibility and damping effects influence significantly the post-locking motion of the assembly consisting of two joint-connected links. Here we concentrate on a more physical understanding and explanation of the phenomenon observed. It is shown that the main characteristic features of the post-locking motion can be recovered by decomposing it into the "fast" and "slow" modes. The governing equations of these two modes of motion are derived and discussed in detail.

1 Approximate Analysis of the After-Locking Motion

The after-locking behavior of the links as presented in Part I of this paper seems to be composed of two distinct types of motion. The locking triggers a relatively fast vibration with small amplitudes around an "average" location of the link. In turn, the "average" location of the link is moving much slower. In order to decompose these two modes of motion, one can write

$$\theta_i(t) = \theta_i^s(t) + \theta_i^f(t) \quad i = 1, 2 \tag{1}$$

where superscripts s and f denote the components related to the *slow* and *fast motions*, respectively. Due to the above-mentioned nature of these two modes of motion it can be assumed that

$$|\theta_i^f(t)| \le \Delta\theta_i^f \ll 1 \quad |\dot\theta_i^s| \ll |\dot\theta_i^f|$$
$$|\ddot\theta_i^s| \ll |\ddot\theta_i^f| \quad \left|\theta_2^s - \frac{\pi}{2}\right| \ll 1 \tag{2}$$

where $\Delta\theta_i^f$ are amplitudes of the fast vibrations. Using these assumptions, the horizontal motion of the elbow joint, δ_B, and the motion of point C in the direction of the elbow link, δ_C, can be approximated as

$$\delta_B = \theta_2^f l_2 \quad \delta_C = \delta_B \cos\theta_1^s. \tag{3}$$

Also, the following approximate relation holds:

$$\theta_1^f = \frac{l_2}{f}\theta_2^f \sin\theta_1^s. \tag{4}$$

Note that (3) and (4) indicate that fast vibrations are almost perpendicular to the trajectory of slow motion (Fig. 1).

Using the physical sense of (2), that is neglecting the inertia forces related to the slow motion, the governing equations of the fast motion will be derived first. Next, the equation of slow motion will be obtained by extracting and analyzing small unbalanced effects generated during the fast vibration cycle. This strategy has been chosen (instead of using (2) directly in the governing Eqs. (16), Part I) due to its simplicity and straightforward physical interpretations.

1.1 Fast-Mode Motion. The equation of dynamic equilibrium of link 2 in the fast-mode motion is derived balancing the moment about A and omitting inertial effects resulting from the slow motion. Using the notation from Fig. 1, one obtains

$$(e^2m_2 + I_2)\ddot\theta_2^f = F_B^x l_2 - k\theta_2^f - c\dot\theta_2^f - F_B^y\delta_B \tag{5}$$

where F_B are the forces at joint B.

Similar equations of the mass center of link 1 in the fast motion can be written as

$$m_1\ddot\delta_C = -F_B^x\cos\theta_1^s - F_B^y\sin\theta_1^s$$
$$I_1\ddot\theta_1^f = (-F_B^x\sin\theta_1^s + F_B^y\cos\theta_1^s)f. \tag{6}$$

Combining (5), (6) and using (3), (4) we derive the equation describing the fast motion of C in the form

$$\hat m_1\ddot\delta_C + \hat c\dot\delta_C + \hat k\delta_C = 0 \tag{7}$$

where

$$\hat m_1 = m_1 + \frac{I_2 + e^2m_2}{\hat L^2}; \quad \hat c = \frac{c}{\hat L^2}; \quad \hat k = \frac{k}{\hat L^2} \tag{8}$$

and where

$$\hat L^2 = l_2^2\left(\cos^2\theta_1^s + \frac{I_1}{m_1f^2}\sin^2\theta_1^s\right). \tag{9}$$

Equation (7) can also be obtained substituting (1) into Eq. (16), Part I, and omitting small terms resulting from (2).

Since θ_1^s is changing very slowly we can approximate the solution to this equation by

$$\delta_C \cong \frac{v_a}{\omega}e^{-\xi\omega_f t}\sin\omega t \tag{10}$$

where

Contributed by the Applied Mechanics Division of THE AMERICAN SOCIETY OF MECHANICAL ENGINEERS for publication in the ASME JOURNAL OF APPLIED MECHANICS.

Discussion on the paper should be addressed to the Technical Editor, Professor Lewis T. Wheeler, Department of Mechanical Engineering, University of Houston, Houston, TX 77204-4792, and will be accepted until four months after final publication of the paper itself in the ASME JOURNAL OF APPLIED MECHANICS.

Manuscript received by the ASME Applied Mechanics Division, Oct. 10, 1997; final revision, Dec. 8, 1997. Associate Technical Editor: N. C. Perkins.

 Copyright © 1998 by ASME

Downloaded 04 May 2010 to 171.66.16.26. Redistribution subject to ASME license or copyright; see http://www.asme.org/terms/Terms_Use.cfm

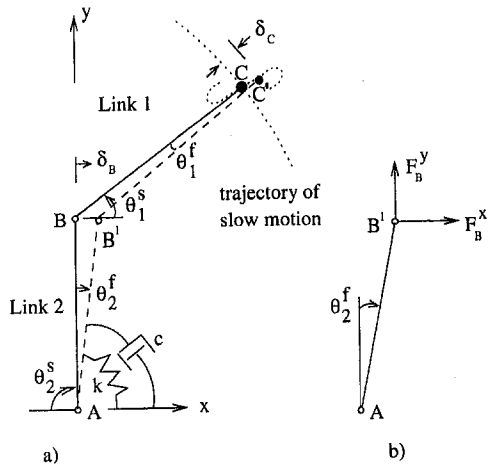


Fig. 1 Deformation and forces in the flexible system

$$\omega_f^2 = \frac{\hat{k}}{\hat{m}_1}$$

$$\xi = \frac{\hat{c}}{2\sqrt{\hat{m}_1 \hat{k}}}$$

$$\omega = \omega_f \sqrt{1 - \xi^2}.$$

In deriving (10), we assumed that $\xi < 1$ and used the initial conditions at the start of locking, that is $\delta_C(0) = 0$ and $\dot{\delta}_C(0) = v_a$.

Note also that now the parameter c can be related to the usual damping coefficient ξ.

Obviously, for large damping, the nonharmonic solutions become valid, that is

$$\delta_C = v_a t e^{-\omega_f t} \quad \text{for} \quad \xi = 1$$

$$\delta_C = \frac{v_a}{\omega_f \sqrt{\xi^2 - 1}} e^{-\xi \omega_f t} \sinh\left(\omega_f \sqrt{\xi^2 - 1}\, t\right) \quad \text{for} \quad \xi > 1. \quad (11)$$

Here, in the detailed derivations, we will use the harmonic solution (10) only. Formally, the same procedure may be followed when using the nonharmonic functions (11).

Equation (10) can be verified against the results presented in Part I and obtained from the integration of the complete equations of motion (Eq. (17) in Part I). If $c = 0$ the period and the amplitude of fast vibrations are defined from (10) as

$$T_f = \frac{2\pi}{\omega_f} = 2\pi l_2 \sqrt{\frac{m_1\left(\cos^2 \theta_1^s + \dfrac{I_1}{m_1 f^2} \sin^2 \theta_1^s\right) + \dfrac{I_2 + e^2 m_2}{l_2^2}}{k}} \quad (12)$$

and

$$\Delta\delta_C = \frac{T_f}{2\pi} v_a. \quad (13)$$

Substituting the parameters used in the numerival integration, for $EI_b = 500$ Nm^2 we obtain the following values from (12), (13), and (3): amplitude $\Delta\delta_B \cong 7.5$ mm (or $\Delta\theta_2^f = \Delta\delta_B / l_2 = 0.0245$) and $T_f \cong 0.0157$ sec. at $\theta_1 = 60$ deg, and $\Delta\delta_B \cong 6.97$ mm (or $\Delta\theta_2^f = 0.0228$) and $T_f \cong 0.0292$ sec. at $\theta_1 = 0$ deg. These results compare very favorably with the results shown in Fig. 8 (Part I), (see the amplitudes of vibrations at $t = 0$ and $t \cong 0.8$ sec., respectively) and obtained from numerical integrations of the complete nonlinear equations of motion.

1.2 Slow-Mode Motion. In order to understand the after-locking motion of link 1, consider the force F_C exerted on the mass center C (see Fig. 2(*a*)). This force can be calculated projecting the forces at joint B (see Fig. 1(*b*)) on the direction of link 1 to obtain

$$F_C = F_B^x \cos \theta_1^s + F_B^y \sin \theta_1^s. \quad (14)$$

Using (2), (3), (4), (5), and (6), this force can be rewritten in the form

$$F_C = \frac{F_B^x}{\cos \theta_1^s \left(1 + \dfrac{I_1}{m_1 f^2} \tan^2 \theta_1^s\right)} = \hat{m}_2 \ddot{\delta}_C + \hat{c}\dot{\delta}_C + \hat{k}\delta_C \quad (15)$$

where $\hat{m}_2 = (m_2 e^2 + I_2)/\hat{L}^2$.

Substituting from (10) we obtain

$$F_C = \frac{v_a}{\omega} e^{-\xi \omega_f t} \{[\hat{k} - \omega_f^2(\hat{m}_2 + 2\xi^2 m_1)] \sin \omega t + 2\xi \sqrt{1 - \xi^2}\, m_1 \omega_f^2 \cos \omega t\}. \quad (16)$$

This is the force driving the motion of link 1. Its component perpendicular to the trajectory of slow motion essentially causes the fast vibrations with frequency ω_f.

What is more interesting is the component F_C^t, tangential to the trajectory of slow motion, that can be calculated from

$$F_C^t \cong F_C \cdot \theta_1^f \quad \text{where} \quad \theta_1^f = \frac{\delta_C}{f} \tan \theta_1^s. \quad (17)$$

Substituting from (10) and (16) we get

$$F_C^t = F_0 \cdot \psi(\xi) \cdot e^{-2\xi \omega_f t} \cdot [1 - \cos 2\omega t + \eta(\xi) \sin 2\omega t] \quad (18)$$

where

$$F_0 = \frac{m_1 v_a^2}{2f} \cdot \tan \theta_1^s$$

$$\psi(\xi) = \frac{1 - 2\xi^2}{1 - \xi^2}$$

$$\eta(\xi) = \frac{2\xi\sqrt{1 - \xi^2}}{1 - 2\xi^2}.$$

Note the pulsating character of F_C^t which is plotted in Fig. 2(*b*).

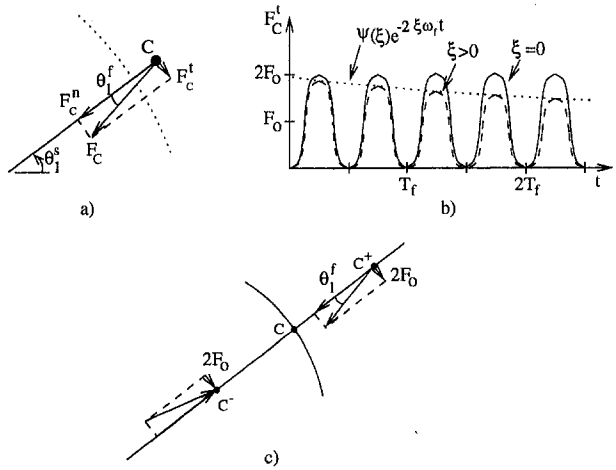


Fig. 2 Driving force of slow motion

Downloaded 04 May 2010 to 171.66.16.26. Redistribution subject to ASME license or copyright; see http://www.asme.org/terms/Terms_Use.cfm

This tangential force, as shown in Fig. 2(*c*), is always pushing link 1 towards the horizontal configuration, $\theta_1^s = 0$, independently of whether the mass center of link 1, indicated by $C^{\pm}$, is on the inside or outside of the average trajectory C (or whether θ_1^s is positive or negative).

The "average" tangential force over the period of fast vibrations is approximated by

$$F_t^{\text{avg}} = F_0 \cdot \psi(\xi) e^{-2\xi\omega_f t} \tag{19}$$

Note that F_t^{avg}, which depends on θ_1^s, should be considered as a restoring force in the slow pendulum-like motion of link 1 shown in Figs. 4, 9, and 10 of Part I of this paper.

Now using this force and considering the slow-mode motion only, the equation of dynamic equilibrium about point B for link 1 can be written in the form

$$(m_1 f^2 + I_1)\ddot{\theta}_1^s = -f F_t^{\text{avg}}. \tag{20}$$

Substituting (19) we finally obtain

$$\ddot{\theta}_1^s + \omega_s^2 \psi(\xi) e^{-2\xi\omega_f t} \tan \theta_1^s = 0 \tag{21}$$

where $\omega_s^2 = v_a^2 m_1/(2(m_1 f^2 + I_1))$.

This equation governs the slow motion of link 1 and can be integrated in time from the start of locking at which $\theta_s^1(0) = \theta_{1L}$ and $\dot{\theta}_1^s(0) = \dot{\theta}_{1r}$. The last condition results from the fact that during the first half of the cycle the effect of F_t^{avg} on the rotation of link 1 is negligible and its response is essentially governed by the rigid-body dynamics.

There are several interesting features of Eqn. (21):

(a) Since the stiffness k is not present in it, the slow after-locking motion is essentially independent of the flexibility of the system. It explains the trajectories presented in Figs. 4, 9, and 10 of Part 1 which look very similar though for each case the stiffnesses of the links were substantially different. These stiffnesses seem to be required only for triggering the slow-mode motion by producing some fast-mode oscillations.

(b) For undamped system ($c = \xi = 0$) and assuming small amplitudes of slow motion of link 1, that is $\tan \theta_1 \cong \theta_1$, we obtain the following solution to (21):

$$\theta_1^s = \theta_{1L} \cos \omega_s t + \frac{\dot{\theta}_{1r}}{\omega_s} \sin \omega_s t \tag{22}$$

where ω_s represents the frequency of slow pendulum-like oscillation (as presented in Figs. 4, 9, and 10 of Part I). Substituting the parameters used in the numerical integration, one obtains the period of slow-mode motion $T_s = (2\pi/\omega_s) \cong 3.49$ sec. The period of slow oscillations as shown in Fig. 6 (Part I) and obtained from integrating directly Eq. (16) of Part I was equal to about 3.14 sec. Taking into account that for the case considered ($\theta_{1L} = 60$ deg) the small-amplitude assumption is poorly met, these two results compare reasonably well.

Some effects resulting from large amplitudes of slow motion can be easily predicted. Note that if $\tan \theta_1^s$ is replaced by $\sin \theta_1^s$, the equation of undamped slow motion would be similar to the equation describing the motion of a pendulum for large rotations. Since $|\sin \theta_1^s| < |\theta_1^s|$, larger rotations in the pendulum motion make the system softer and reduce the frequency of oscillation (or increase the period of vibrations). Here, because $|\theta_1^s| < |\tan \theta_1^s|$, the opposite effect should be observed, that is, larger θ_1^s stiffens the system and, in comparison to the linear solution, enlarges its frequency (or reduce the period of vibrations). This explains why T_s calculated from (22) was bigger than the period of motion shown in Fig. 6 (Part I).

(c) For damped motion and for small θ_1^s, the closed-form solution to linearized Eq. (21) is in the form (Polyanin and Zaitsev, 1995):

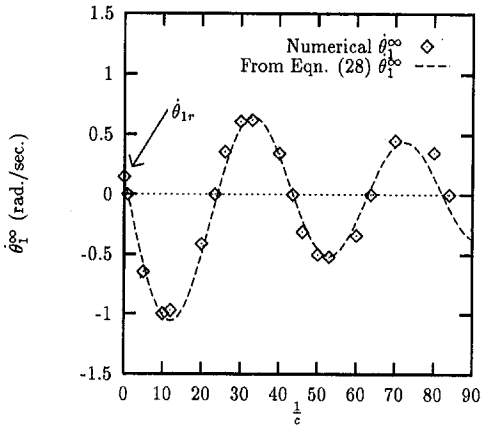


Fig. 3 Effect of damping on asymptotic velocity of link 1

$$\theta_1^s = a_1 J_0(\tau) + a_2 Y_0(\tau) \tag{23}$$

where J_n and Y_n are Bessel functions of the first and second kind and

$$\tau = \frac{\omega_s}{\xi\omega_f} e^{-\xi\omega_f t}. \tag{24}$$

The integration constants are determined from the initial conditions at $t = 0$ (the start of locking) and are equal to

$$a_1 = \frac{\pi}{2}\tau_0\left[-\theta_{1L} Y_1(\tau_0) + \frac{\dot{\theta}_{1r}}{\omega_s} Y_0(\tau_0)\right]$$

$$a_2 = \frac{\pi}{2}\tau_0\left[\theta_{1L} J_1(\tau_0) - \frac{\dot{\theta}_{1r}}{\omega_s} J_0(\tau_0)\right] \tag{25}$$

where $\tau_0 = \tau(0) = \omega_s/\xi\omega_f$.

In deriving (25), we make use of the Wronskian defined as

$$W_0(\tau_0) = J_1(\tau_0)Y_0(\tau_0) - J_0(\tau_0)Y_1(\tau_0) = \frac{2}{\pi\tau_0}. \tag{26}$$

Using Eq. (25), one can predict the asymptotic behavior of the system when time tends to infinity. Note that for $t \to \infty$, the parameter $\tau(t) \to 0$. Since $J_0(0) = 1$ and $Y_0(0) \to -\infty$, the system will either *diverge* if $a_2 \neq 0$ or *converge* to a finite configuration θ_1^{∞} if $a_2 = 0$.

First consider the case of *divergence*. From (23), the angular velocity of the slow motion of link 1 is

$$\dot{\theta}_1^s = \xi\omega_f \tau [a_1 J_1(\tau) + a_2 Y_1(\tau)]. \tag{27}$$

Since $J_1(\tau) \to 0$ and $Y_1(\tau) \to -2/\pi\tau$ when $\tau \to 0$, the angular velocity of link 1 will asymptotically tend to

$$\dot{\theta}_1^{\infty} = -\frac{2}{\pi} a_2 \xi\omega_f = -\omega_s \theta_{1L} J_1(\tau_0) + \dot{\theta}_{1r} J_0(\tau_0). \tag{28}$$

For example, for the case $c = 0.094$ Nms presented in Part I in Figs. 12 and 14, we have $\xi \cong 0.003156$ and $\tau_0 \cong 1.73$. Substituting into (28) results in $\dot{\theta}_1^{\infty} = -1.036$ 1/sec. which agrees very well with the exact solution shown there. Note that, despite a small value of the damping coefficient, ξ, link 1 makes only about half of the slow oscillation cycle. It indicates a great sensitivity of the system behavior to damping present in it.

For fixed initial conditions, and since $\tau_0 = \tau_0(\xi)$, Eq. (28) gives the effect of damping, ξ, on the final angular velocity $\dot{\theta}_1^{\infty}$. This relation is plotted in Fig. 3. Also, the results obtained from the numerical integration presented in Part I are shown. As can be seen Eq. (28) agrees well with the "exact" solution. Note that in this plot the abscisa represents the inverse of damp-

Downloaded 04 May 2010 to 171.66.16.26. Redistribution subject to ASME license or copyright; see http://www.asme.org/terms/Terms_Use.cfm

ing, that is damping is infinite at the origin and decreasing when moving away from it. Interestingly, it has been observed that $\dot{\theta}_1^\infty \to \dot{\theta}_{1r}$ for large c (in Part I we used $c = 10{,}000$). Thus the rigid-body motion, represented here by $\dot{\theta}_{1r}$ and defined by (19) in Part I, can be approached by assuming infinite damping irrespectively of the value of the bending stiffness of the links. The Bessel functions involved in this equation explain the oscillatory character of the plot. Note that for $\tau_0 \to 0$ that requires $\xi \to \infty$, Eq. (28) gives $\dot{\theta}_1^\infty \to \dot{\theta}_{1r}$ as observed from the numerical analysis.

The form of Eq. (28) indicates that there must be an infinite number of distinct values of ξ_i for which $\dot{\theta}_1^\infty = 0$. These values correspond to zeroes of the equation

$$\omega_s \theta_{1L} J_1\left(\frac{\omega_s}{\xi_i \omega_f}\right) - \dot{\theta}_{1r} J_0\left(\frac{\omega_s}{\xi_i \omega_f}\right) = 0$$

$$i = 1 \ldots \infty. \tag{29}$$

It justifies the infinite number and the regular character of the critical values of damping obtained in Part I and approximated by the formula (20). Note that for $\xi = \xi_i$ the integration constant $a_2 = 0$ and the system converges to the final configuration defined by

$$\theta_1^\infty(\xi_i) = \frac{\pi}{2} \tau_0^i \left[-\theta_{1L} Y_1(\tau_0^i) + \frac{\dot{\theta}_{1r}}{\omega_s} Y_0(\tau_0^i) \right] = \frac{\theta_{1L}}{J_0(\tau_0^i)} \tag{30}$$

where $\tau_0^i = \omega_s / \xi_i \omega_f$.

The last form of the above equation was obtained using (29) that must be satisfied for the critical damping.

For $i = 1$ and $c_1 = 1.0955$ Nms ($\xi \cong 0.0448$) Eq. (30) gives $\theta_1^\infty = 1.0498$ which compares very well with the result obtained from integration of the exact Eqs. (16) in Part I (see Fig. 12). However, for $i = 2$ and $c_2 = 0.042751$ Nms ($\xi \cong 0.00144$), from (30) one obtains $\theta_1^\infty = -2.60$, while from (16) and the direct integration we have $\theta_1^\infty = -1.5$ (see Fig. 12). This discrepancy can be explained again by the nonlinear stiffening effect due to large rotations. Since the "stiffness" of a system, the motion of which is governed by Eq. (21), is proportional to $\tan \theta_1^s$, the restoring force contributing to oscillations tends to infinity when $\theta_1^s \to \pm(\pi/2)$. Thus, whenever link 1 approaches either of its vertical configurations, an infinitely large repulsive force is developed which pushes away from those configurations and effectively imposes the limit $|\theta_1^\infty| < (\pi/2)$ on the magnitude of the final angle. On the other hand, for small θ_1^s, one can conclude from (30) that $|\theta_1^\infty| > |\theta_{1L}|$ (since $|J_0(\tau_0^i)| < 1$). Combining these two observations results in the following limits:

$$|\theta_{1L}| < |\theta_1^\infty| < \frac{\pi}{2} \tag{31}$$

which explains the results obtained from the exact integration of the complete equations and plotted in Fig. 17 of Part I.

Finally, using the asymptotic expansions of the Bessel functions, it is easy to show that for $\xi \to 0$ (which is equivalent to $\tau \to (\omega_s/\xi\omega_f) - \omega_s t$) the solution (23) becomes identical with the solution (22).

2 Concluding Remarks

As shown in Part I of this paper, the after-locking motion of the assembly consisting of two jointed links is extremely sensitive to small elastic deformations and small damping that may be present in the system. Here, by decomposing the motion into the fast and slow modes, the main features of such a behavior is explained, at least partially. The impact during locking generates a force in link 1, the components of which are responsible for both the fast and slow motions. Without damping, this force causes pendulum-like slow oscillations. Damping continuously reduces the amplitude of the force to the point where it effectively disappears. If it happened when link 1 was rotating clockwise or counterclockwise it will continue moving in that direction. If the driving force is reduced to zero when link 1 is at the turning point, it will stop moving. Finally, the transfer of momentum seems to follow the rigid dynamics rules only if the damping of the system becomes infinitely large, irrespectively of the stiffness of the links.

References

Polyanin, A. D., and Zaitsev, V. F., 1995, *Handbook of Exact Solutions for Ordinary Differential Equations*, CRC Press, Boca Raton, FL.

Downloaded 04 May 2010 to 171.66.16.26. Redistribution subject to ASME license or copyright; see http://www.asme.org/terms/Terms_Use.cfm

Boundary Effects in Penetration or Perforation

L. M. Keer
Fellow ASME.

Yonglin Xu

Department of Civil Engineering,
Northwestern University,
Evanston, IL 60208

V. K. Luk
Sandia National Laboratories,
Albuquerque, MN 87185
Mem. ASME

For the analysis of stress distributions around a projectile tip in penetration or perforation, a point force P *associated with an expansion source* E_z, *which depends on the geometry of the projectile, is employed to simulate the projectile. Using the method of half-space analysis by Mindlin (1936), the boundary effects on the projectile are analyzed. The analytical solutions of an expansion source associated with a concentrated force are derived for the prediction of the damage zones in a target, as the projectile either approaches or leaves the boundary. As a projectile perforates a target, it forms a cratering area at the impact surface and leaves a cone-like spalling area at the exit surface. The presence of these two areas and the fact that the spalling area is larger than the cratering area in perforation, can be explained by the stress analysis of boundary effects. Solution of the cavity expansion source in a half-space is derived. This solution provides a theoretical evidence for the conclusion obtained from the empirical analysis by Forrestal et al. (1994). Their conclusion states that when the projectile is at about twice its shank diameters, it can be approximately treated as though it were in the infinite medium.*

1 Introduction

Stress distribution around the projectile plays an important role in the prediction of the resistance in the perforation. Because of the different geometry of the projectiles and complicated physics phenomena involved in penetration and perforation, much effort is required to estimate the asymptotic stress field around the tip of a projectile.

In penetration, a great deal of interest has been directed towards evaluating the projectile resistance using the cavity expansion method proposed earlier by Hopkins (1960). With this simplified method, the problem is theoretically considered as a spherical symmetry problem, which differs from the actual stresses at the projectile tip. In this paper, a method for penetration simulation is proposed, in which the projectile is simulated as a point force and an expansion source for estimating stress distributions around the projectile. Thus, the damage zone around its tip can be determined in terms of the magnitudes of these two sources.

The boundary effects of the free surfaces in a target are significant because they affect the spalling and cratering phenomena in penetration and perforation. The method for analysis of a point force in the half-space by Mindlin (1936) is employed to derive the cavity expansion force and the circular expansion source in a half-space. In general, boundary effects near the free surface can be treated by applying imaginary sources at an imaginary point. As the source point approaches the free surface, these two points become closer and thus the higher stresses along the free surface may give rise to a significant damage of the target material. The calculation shows that the damage zone around the projectile exhibits a cone-like area open to the free surface which is very similar to the spalling zone in the perforation. In addition, the results of the boundary effects and the superposition of an expansion source and a concentrated force can be used to explain the observation that the cratering zone is smaller than the spalling zone.

The phenomena in penetration and perforation events involve very complicated material and structural responses, especially in dealing with cratering and spalling damage zones. The models documented herein represent a first-order attempt to capture a qualitative understanding of the mechanics involved in these phenomena. Additional research efforts are needed for more comprehensive models of these dynamic events.

2 Projectile Simulation

The distribution of the stresses around a projectile, in general, depends on the velocity and shape of the projectile. The magnitudes of the stresses around the projectile tip are greatly affected by the projectile velocity V since the resistance formula derived by Luk and Forrestal (1987) is $A + BV^2$, where A and B are constants determined by the material properties of the target. On the other hand, their distribution is influenced by the factors $\beta_j = \sqrt{1 - (V/C_j)^2}$ $(j = 1, 2)$, where C_j are wave velocities for longitudinal wave and transverse wave, respectively. In the range of one tenth of wave velocity (such as 300 m/sec), $V/C_j = 0.1$, and $\beta_j = 0.995$ very close to 1 (the static case). Moreover, the wave speed is larger than 3000 m/sec in the experimental materials such as concrete targets. Thus, the quasi-static analysis of the projectile should be sufficient to explore the stress distribution around the projectile.

A projectile can be simulated as a concentrated force P and a circular expansion source E_z as shown in Fig. 1. It is not sufficient to represent the penetration resistance by a concentrated force only. The damage zone caused by the concentrated force is symmetric to the x-y plane (see Fig. 1) by using the maximum shear stress criterion (Mises criterion). However, the experimental results show a larger damage zone ahead of the projectile than behind. The expansion source concepts may help explain the geometry of the damage zone.

For an ogival projectile as shown in Fig. 1, the resultant resistance in the z direction can be written as

$$F_z = 2\pi s^2 \int_{\phi_0}^{\pi/2} \sigma_n [\sin \phi - \sin \phi_0] \cos \phi d\phi \quad (2.1)$$

where $\sin \phi_0 = (s - a)/s$, and s, a, and ϕ are defined in Fig. 1. With the assumption (Luk and Forrestal, 1987)

$$\sigma_n = A + BV^2 \cos^2 \phi \quad (2.2)$$

Contributed by the Applied Mechanics Division of THE AMERICAN SOCIETY OF MECHANICAL ENGINEERS for publication in the ASME JOURNAL OF APPLIED MECHANICS.

Discussion on this paper should be addressed to the Technical Editor, Professor Lewis T. Wheeler, Department of Mechanical Engineering, University of Houston, Houston, TX 77204-4792, and will be accepted until four months after final publication of the paper itself in the ASME JOURNAL OF APPLIED MECHANICS.

Manuscript received by the ASME Applied Mechanics Division, Feb. 25, 1997; final revision, Aug. 13, 1997. Associate Technical Editor: W. K. Liu.

 Copyright © 1998 by ASME

Downloaded 04 May 2010 to 171.66.16.26. Redistribution subject to ASME license or copyright; see http://www.asme.org/terms/Terms_Use.cfm

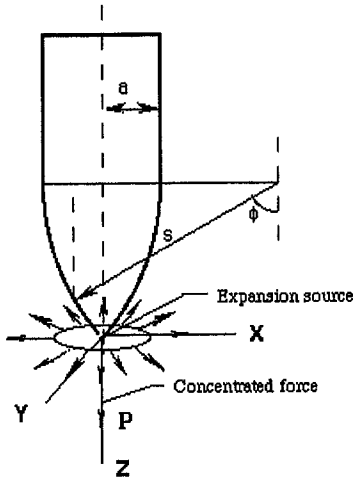


Fig. 1 Simulation of a projectile as a concentrated force and an circular expansion source

the resistance of the projectile is

$$F_z = \pi a^2\left[A + B\,\frac{8\psi - 1}{24\psi^2}\,V^2\right] \tag{2.3}$$

where $\psi = s/2a$ is the caliber radius head for the projectile with an ogival nose. Equations (2.2) and (2.3) were used for predicting depth of a penetrator by using an elastic-cracked model (Xu, Keer, and Luk, 1996a).

The force in the r direction ($r = \sqrt{x^2 + y^2}$) for a projectile is, of course, self-equilibrated. However, for each couple of tractions, the expansion source can be formed around the axis of the projectile. The circular expansion source can be written as

$$E_z = \int_\Omega rT_r d\Omega \tag{2.4a}$$

where Ω represents the surface of the projectile (Fig. 2). For the ogival projectile, the expansion source is

$$E_z = 2\pi s^3 \int_{\varphi_0}^{\pi/2} \sigma_n[\sin\phi - \sin\phi_0]^2 \sin\phi d\phi. \tag{2.4b}$$

Using the assumption of (2.2), the expansion source can be written as

$$E_z = 2\pi s^3\left\{\left[\cos\phi_0\left(1 - \frac{1}{3}\cos^2\phi_0\right) - \left(\frac{\pi}{2} - \phi_0\right)\sin\phi_0\right]A + \left[\frac{1}{3}\cos^3\phi_0(1 + \sin^2\phi_0) - \frac{1}{5}\cos^5\phi_0 - \frac{1}{4}\sin^2\phi_0\cos^3\phi_0 - \frac{1}{4}\left(\frac{\pi}{2} - \phi_0\right)\right]B\right\}. \tag{2.5}$$

For example, a uniform traction q on the hemispherical projectile with radius a can be simplified as a concentrated force $F_z = \pi a^2 q$ and an expansion source $E_z = (4\pi/3)a^3 q$. It can be seen that the concentrated force is related to the cross section of the projectile, and the expansion sources is related to its volume. The ratio of the expansion source E_z to the concentrated force F_z, denoted by k, is a function of $\psi = s/2a$ (geometry of the projectile). This functional relationship is shown in Fig. 3. The point source F_z and the expansion source E_z are calculated by integrating force on a spherical symmetric surface, which implies the shear stresses are neglected. The sharper the ogival projectile, the larger the expansion source E_z.

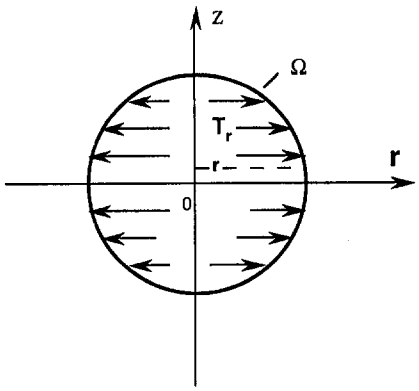


Fig. 2 Circular expansion source

3 Concentrated Force and Expansion Source for a Line Notch

As the projectile enters the target, the projectile can be simulated as a concentrated force and an expansion source in a line notch as shown in Fig. 1. The concentrated force P at a cone tip with cone angle φ_0 as shown in Fig. 4 has been studied by Little (1973). The general axially symmetric displacement expression in the spherical coordinate system is derived by Xu et al. (1996a) as

$$2\mu u_R = \sum_{-\infty}^{\infty} R^{\lambda_n}\left\{E_n[4(1-\nu) - (\lambda_n + 1)]\cos\varphi P_{\lambda_n} + F_n(\lambda_n + 1)P_{\lambda_n+1}\right\} - \frac{1}{R}B_0^*$$

$$2\mu u_\varphi = \sum_{-\infty}^{\infty} R^{\lambda_n}\left\{-E_n[4(1-\nu) + \lambda_n]\sin\varphi P_{\lambda_n} + (F_n - E_n)\frac{d}{d\varphi}P_{\lambda_n+1}\right\} + \frac{1}{R}B_0^*\frac{\sin\varphi}{1 + \cos\varphi} \tag{3.1}$$

where P_{λ_n} is Legendre function with complex index λ_n, which depends on the notch angle and can be obtained from an eigenvalue equation. Here, φ is the polar angle. Coefficients E_n, F_n,

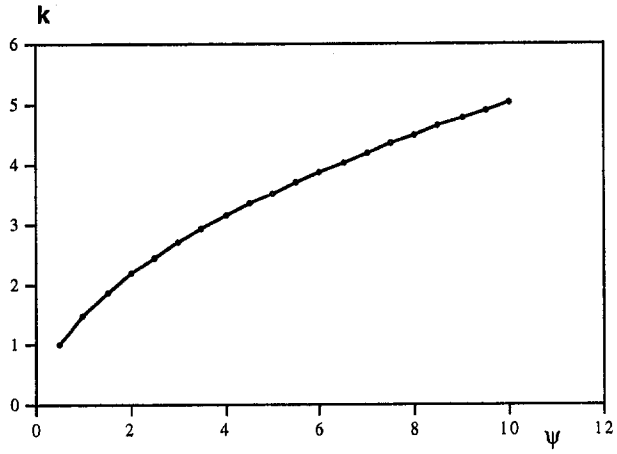


Fig. 3 Expansion source increases with the caliber radius head for ogival projectile

Downloaded 04 May 2010 to 171.66.16.26. Redistribution subject to ASME license or copyright; see http://www.asme.org/terms/Terms_Use.cfm

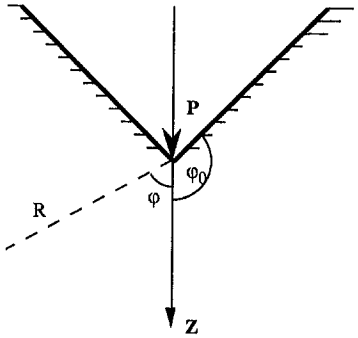


Fig. 4 A concentrated force *P* at the tip of a three-dimensional conical notch

and B_0^* are determined from the boundary and equilibrium conditions. For a conical notch under a concentrated force, the eigenvalue $\lambda_n = -1$, and the stress field around the tip of the conical notch line can be written as

$$\sigma_{RR} = \frac{P}{2\pi\alpha_0 R^2}(1-2\nu)\left[(1+\cos\varphi_0) - \frac{2(2-\nu)}{1-2\nu}\cos\varphi\right]$$

$$\sigma_{R\varphi} = \frac{P}{2\pi\alpha_0 R^2}(1-2\nu)\sin\varphi\left(1 - \frac{1+\cos\varphi_0}{1+\cos\varphi}\right)$$

$$\sigma_{\varphi\varphi} = \frac{P}{2\pi\alpha_0 R^2}(1-2\nu)\cos\varphi\left(1 - \frac{1+\cos\varphi_0}{1+\cos\varphi}\right)$$

$$\sigma_{\theta\theta} = \frac{P}{2\pi\alpha_0 R^2}(1-2\nu)\cos\varphi\left(1 - \frac{1+\cos\varphi_0}{1+\cos\varphi}\right) \quad (3.2a)$$

and the displacements are

$$2\mu u_R = \frac{P}{2\pi\alpha_0 R}[4(1-\nu)\cos\varphi - (1-2\nu)(1+\cos\varphi_0)]$$

$$2\mu u_\varphi = \frac{P}{2\pi\alpha_0 R}\left[(1-2\nu)\frac{1+\cos\varphi_0}{1+\cos\varphi}\sin\varphi - (3-4\nu)\sin\varphi\right] \quad (3.2b)$$

where the constant α_0 is

$$\alpha_0 = (1-\cos^3\varphi_0) - 2(1-\nu)\cos\varphi_0(1-\cos\varphi_0).$$

The special case of a line notch is taking $\varphi_0 = \pi$.

When the projectile enters a target, its tip can be simulated as a concentrated force for a dull flat projectile. However, for an ogival projectile as shown in Fig. 1, the tractions on the projectile surface give rise to an expansion source field around the projectile tip. The expansion source may be resulted from the concentrated couple around the z-axis. For an expansion source E_z in the notch line, the stress field around the notch tip was derived by Xu et al. (1996a) as

$$\sigma_{RR} = \frac{E_z}{2\pi\beta_0 R^3}[2(5-\nu)\cos^2\varphi - 6(1-\nu)]$$

$$\sigma_{R\varphi} = \frac{E_z}{2\pi\beta_0 R^3}2(1+\nu)\sin\varphi\cos\varphi$$

$$\sigma_{\varphi\varphi} = \frac{E_z}{2\pi\beta_0 R^3}(1-2\nu)\sin^2\varphi$$

$$\sigma_{\theta\theta} = \frac{E_z}{2\pi\beta_0 R^3}3(1-2\nu)\sin^2\varphi \quad (3.3)$$

and the displacements are

$$2\mu u_R = \frac{E_z}{\beta_0 R^2}\left\{\left[1 + \frac{1}{4(1-\nu)}\right]\cos^2\varphi - (3-4\nu)\right\}$$

$$2\mu u_\varphi = \frac{E_z}{\beta_0 R^2}\left\{-\left[1 - \frac{1}{4(1-\nu)}\right]\sin\varphi\cos\varphi\right\} \quad (3.4)$$

where the constant $\beta_0 = [4(6-5\nu)]/5$.

The analysis above indicates that, (1) the stress field induced by a concentrated force is antisymmetric and the field induced by the expansion source is symmetric to the x-y plane; (2) The asymptotic field induced by an expansion source E_z has higher singularity (R^{-3}) in comparison with one induced by a concentrated force with singularity (R^{-2}); and (3) under the loading of a concentrated force or an expansion source, the displacement for the line notch is of continuity, $u_\varphi|_{\varphi=\pi} = 0$. This fact implies that the boundary effects may be estimated by considering a half-space. A projectile can be simulated as a concentrated force P and a circular expansion source E_z.

4 Boundary Effects for a Cavity Expansion Source

As observed from the qualitative analysis of the penetration mechanism, when a high-velocity projectile strikes a target, a strong compressive wave propagates toward the exit surface. The reflected waves will then propagate from these free boundaries and create a region of tensile stress. This tensile region can cause fracture in a brittle target, such as concrete.

The boundary effects on the exit surface actually can be treated by applying image sources at the image point. The well-known analytical solution was early studied by Mindlin (1936). Here the solution of the cavity expansion source in a half-space is obtained by the image source method (Mindlin and Cheng, 1950).

The concept of cavity expansion source comes from the cavity expansion method proposed by Hopkins (1960). Shown in Fig. 5 is a cavity under a uniform pressure q on the spherical surface with radius a. The stress $\sigma_R = a^3 q/R^3$ results in the integral for any spherical surface when the same center is a constant E. Therefore

$$E = \iint \sigma_n R ds. \quad (4.1)$$

This constant is defined as a cavity expansion source at the center of the spherical cavity. The stress field induced by this cavity expansion source E in a spherical coordinate system is

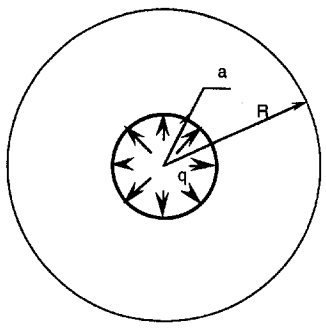


Fig. 5 Cavity expansion source induced by the uniform pressure on the cavity surface

Downloaded 04 May 2010 to 171.66.16.26. Redistribution subject to ASME license or copyright; see http://www.asme.org/terms/Terms_Use.cfm

$$\sigma_{RR} = -\frac{E}{4\pi R^3}, \quad \sigma_{R\varphi} = 0$$

$$\sigma_{\varphi\varphi} = \frac{E}{8\pi R^3}, \quad \sigma_{\theta\theta} = \frac{E}{8\pi R^3}. \tag{4.2}$$

This solution can be generated by a spherical cavity with radius a under the surface pressure $q = E/4\pi a^3$. The displacement on the spherical surface is $u_R = E/16\pi\mu R^2$.

For the problem of an expansion source in a half-space, we can put another source E at the image point as shown in Fig. 6. At the boundary ($z = 0$), the stress components in a cylindrical coordinate system can be written as

$$\sigma_{rr} = \sigma_{RR}\sin^2\varphi + 2\sigma_{R\varphi}\sin\varphi\cos\varphi + \sigma_{\varphi\varphi}\cos^2\varphi$$

$$\sigma_{rz} = (\sigma_{RR} - \sigma_{\varphi\varphi})\sin\varphi\cos\varphi + \sigma_{R\varphi}(\cos^2\varphi - \sin^2\varphi)$$

$$\sigma_{zz} = \sigma_{RR}\cos^2\varphi - 2\sigma_{R\varphi}\sin\varphi\cos\varphi + \sigma_{\varphi\varphi}\sin^2\varphi. \tag{4.3}$$

Therefore, on the boundary the shear stress vanishes and the normal stress is

$$\sigma_{zz} = \frac{E}{8\pi}\left(\frac{1}{R_0^3} - \frac{3h^2}{R_0^5}\right) \tag{4.4}$$

where $R_0 = \sqrt{x^2 + y^2 + h^2}$. Introducing the axially symmetric function $f(r, z)$ as used by Kassir and Sih (1975),

$$\sigma_{rr} = 2\mu\left[(1-2\nu)\frac{\partial^2 f}{\partial r^2} - 2\nu\frac{\partial^2 f}{\partial z^2} + z\frac{\partial^3 f}{\partial r^2\partial z}\right]$$

$$\sigma_{rz} = 2\mu z\frac{\partial^3 f}{\partial r\partial z^2}$$

$$\sigma_{zz} = 2\mu\left[-\frac{\partial^2 f}{\partial z^2} + z\frac{\partial^3 f}{\partial z^3}\right]$$

$$\sigma_{\theta\theta} = 2\mu\left[\frac{1}{r}\frac{\partial f}{\partial r} + 2\nu\frac{\partial^2 f}{\partial r^2} + \frac{z}{r}\frac{\partial^2 f}{\partial r\partial z}\right] \tag{4.5a}$$

and

$$u_r = (1-2\nu)\frac{\partial f}{\partial r} + z\frac{\partial^2 f}{\partial r\partial z}$$

$$u_z = -2(1-\nu)\frac{\partial f}{\partial r} + z\frac{\partial^2 f}{\partial z^2} \tag{4.5b}$$

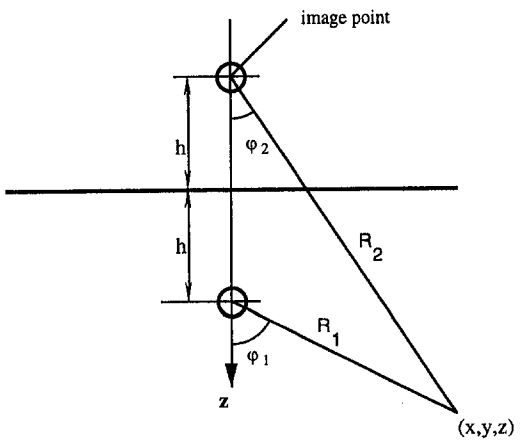


Fig. 6 Image sources for traction free on the boundary

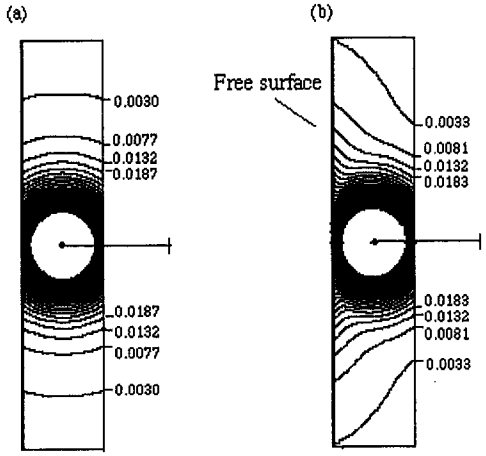


Fig. 7 Cavity expansion source in an infinite medium (*a*) and near the free boundary (*b*)

where f is a harmonic function, and the shear stress σ_{rz} vanishes at the surface $z = 0$. As compared to (4.3), the normal traction elimination requires

$$f = -\frac{E}{8\pi\mu R_2}. \tag{4.6}$$

Therefore the stresses in the cylindrical coordinate system can be written as

$$\sigma_{rr} = \frac{E}{8\pi R_1^3}[3\cos^2\varphi_1 - 2] + \frac{E}{8\pi R_2^3}[3\cos^2\varphi_2 - 2] + \left[(1-2\nu)\frac{\partial^2 F}{\partial r^2} - 2\nu\frac{\partial^2 F}{\partial z^2} + z\frac{\partial^3 F}{\partial r^2\partial z}\right]$$

$$\sigma_{rz} = -\frac{3E}{8\pi R_1^3}\sin\varphi_1\cos\varphi_1 - \frac{3E}{8\pi R_2^3}\sin\varphi_2\cos\varphi_2 + z\frac{\partial^3 F}{\partial r\partial z^2}$$

$$\sigma_{zz} = \frac{E}{8\pi R_1^3}[1 - 3\cos^2\varphi_1] + \frac{E}{8\pi R_2^3}[1 - 3\cos^2\varphi_2] - \frac{\partial^2 F}{\partial z^2} + z\frac{\partial^3 F}{\partial z^3}$$

$$\sigma_{\theta\theta} = \frac{E}{8\pi R_1^3} + \frac{E}{8\pi R_2^3} + \frac{1}{r}\frac{\partial F}{\partial r} + 2\nu\frac{\partial^2 F}{\partial r^2} + \frac{z}{r}\frac{\partial^2 F}{\partial r\partial z} \tag{4.7}$$

where function $F = E/4\pi R_2$, $R_1 = \sqrt{x^2 + y^2 + (z-h)^2}$, $R_2 = \sqrt{x^2 + y^2 + (z+h)^2}$ and $\cos\varphi_1 = (z-h)/R_1$, $\cos\varphi_2 = (z+h)/R_2$.

The contour plot of the Mises stresses, $k_2/(E/h^3)$, for a cavity expansion source exhibits spherical symmetry in an infinite space as shown in Fig. 7(a) and diverges toward the free surface in the half-space as shown in Fig. 7(b). For convenient comparison, the plot area for the infinite space is also taken as the region between two planes with distance h from the point source. The damage zone of a cavity expansion source in the full space exhibits spherical symmetry while the damage zone of a cavity expansion source in the half-space exhibits a horn open to the free surface. The rectangular area is taken as 5 units long and 2 units wide.

The displacement induced by a cavity expansion source approaching a free surface, in general, is larger than that in an infinite medium. As the expansion source goes far from the boundary, the displacement tends to the solution of infinite

Downloaded 04 May 2010 to 171.66.16.26. Redistribution subject to ASME license or copyright; see http://www.asme.org/terms/Terms_Use.cfm

medium. Figure 8(a) shows the displacements u_z at points A ($z = h - a$) and B ($z = h + a$). Curves of r_A ($r_A = \delta u_A/u_A$) and r_B ($r_B = \delta u_B/u_B$) represent the ratios of the displacement differences at points A and B, respectively, due to boundary effects. It is clear that as the $h = 4a$, the boundary effect on the displacements can be reduced to less than six percent. This result can be employed to explain the empirical assumption for the penetration by Forrestal et al. (1994), that as the penetration depth is larger than $4a$ (a is the radius of projectile), the projectile can be treated as though it were in the infinite medium. Figure 8(b) shows the Mises stress varies with the distance between the observation point and the source point. As the distance (h-z) increases or the boundary is approached, the Mises stress decreases. The function f_M in Fig. 8(b) represents the Mises stress, $f_M = k_2/(E/h^3)$. Here, $k_2 = \sqrt{I_2}$ (I_2 is the second principle invariance).

5 Boundary Effects for a Concentrated Force and an Expansion Source

Solutions of a concentrated force or a circular expansion source in a line notch indicate that the displacements on the surface of the line notch are continuous. This fact implies the possibility of considering the full space with certain sources instead of the line notch in a half-space. This method, to approximately describe the line notch in the half-space, will be used in this section. Therefore, the boundary effects due to the concentrated force and expansion source can be estimated using a similar way as in Section 4.

The analysis in Section 2 indicates that the solution of a concentrated force in the line notch is composed of a concentrated force and a center of dilatation lying along the negative z-axis in the infinite medium. Here it is intended to calculate the solution of these two sources in the half-space. The stress

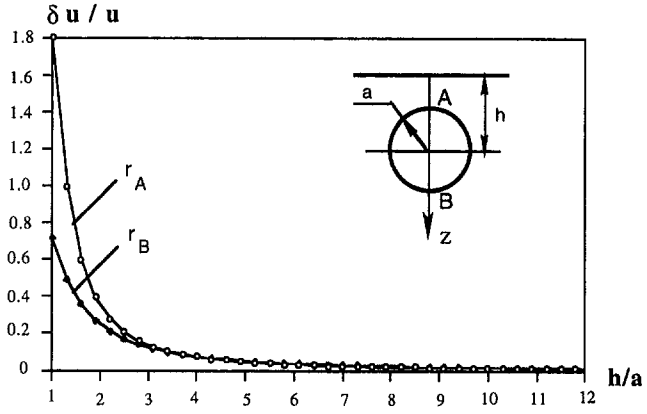


Fig. 8(a) Displacement of cavity expansion source in the half-space

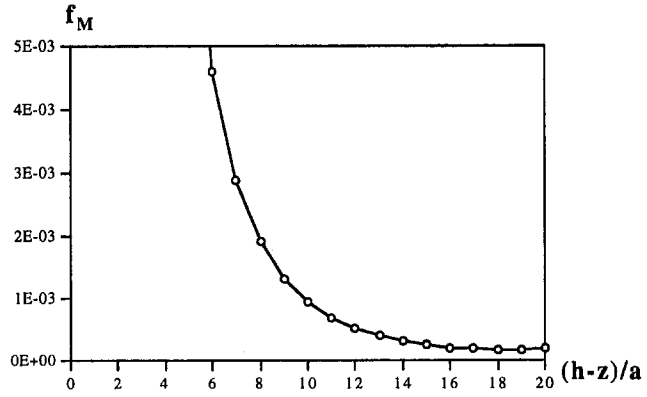


Fig. 8(b) The Mises stress varies with the distance h-z

field induced by a concentrated force P at the tip of the line notch can be written as

$$\sigma_{RR} = -\frac{P}{2\pi\alpha_0 R^2} 2(2-\nu)\cos\varphi$$

$$\sigma_{R\varphi} = \frac{P}{2\pi\alpha_0 R^2}(1-2\nu)\sin\varphi$$

$$\sigma_{\varphi\varphi} = \frac{P}{2\pi\alpha_0 R^2}(1-2\nu)\cos\varphi$$

$$\sigma_{\theta\theta} = \frac{P}{2\pi\alpha_0 R^2}(1-2\nu)\cos\varphi \tag{5.1}$$

and the displacements are

$$2\mu u_R = \frac{P}{2\pi\alpha_0 R} 4(1-\nu)\cos\varphi$$

$$2\mu u_\varphi = -\frac{P}{2\pi\alpha_0 R}(3-4\nu)\sin\varphi. \tag{5.2}$$

The normal stress on the line notch surface should be zero at $\varphi = \pi$ since the stress near the notch surface is discontinuous. For the half-space problem, the symmetric source in the other half-space makes the shear stress vanish on the boundary ($z = 0$), while the normal stress on the boundary is

$$\sigma_{zz} = \frac{P}{4\pi(3-2\nu)}\left[(1-2\nu)\frac{h}{R_0^3} + \frac{3h^3}{R_0^5}\right]. \tag{5.3}$$

Using the stress expression in (4.4) and (4.5) to eliminate the normal stress on the boundary gives

$$F_1 = \frac{P}{4\pi\mu(3-2\nu)}\left[-2(1-\nu)lg(R_2+z+h) + \frac{h}{R_2}\right] \tag{5.4}$$

where F_1 is a harmonic function corresponding to function f in (4.5). Therefore the stress field in cylindrical coordinates for a concentrated force in a half-space can be written as

$$\sigma_{rr} = \frac{P}{4\pi(3-2\nu)R_1^2}[3\cos^2\varphi_1 - 2(1+\nu)\cos\varphi_1]$$
$$- \frac{P}{4\pi(3-2\nu)R_2^2}[3\cos^2\varphi_2 - 2(1+\nu)\cos\varphi_2]$$
$$+ \left[(1-2\nu)\frac{\partial^2 F_1}{\partial r^2} - 2\nu\frac{\partial^2 F_1}{\partial z^2} + z\frac{\partial^3 F_1}{\partial r^2\partial z}\right]$$

$$\sigma_{rz} = \frac{P}{4\pi(3-2\nu)R_1^2}[-3\cos^2\varphi_1\sin\varphi_1$$
$$- (1-2\nu)\sin\varphi_1] - \frac{P}{4\pi(3-2\nu)R_2^2}[-3\cos^2\varphi_2$$
$$- (1-2\nu)\sin\varphi_2] + z\frac{\partial^3 F_1}{\partial r\partial z^2}$$

$$\sigma_{zz} = -\frac{P}{4\pi(3-2\nu)R_1^2}[3\cos^2\varphi_1 + (1-2\nu)\cos\varphi_1]$$
$$+ \frac{P}{4\pi(3-2\nu)R_2^2}[3\cos^2\varphi_2 + (1-2\nu)\cos\varphi_2]$$
$$+ \left[(1-2\nu)\frac{\partial^2 F_1}{\partial r^2} - 2\nu\frac{\partial^2 F_1}{\partial z^2} + z\frac{\partial^3 F_1}{\partial r^2\partial z}\right]$$

Downloaded 04 May 2010 to 171.66.16.26. Redistribution subject to ASME license or copyright; see http://www.asme.org/terms/Terms_Use.cfm

$$\sigma_{\theta\theta} = \frac{P}{4\pi(3-2\nu)R_1^2}(1-2\nu)\cos\varphi_1 - \frac{P}{4\pi(3-2\nu)R_2^2}(1-2\nu)\cos\varphi_2 + \frac{1}{r}\frac{\partial F_1}{\partial r} + 2\nu\frac{\partial^2 F_1}{\partial r^2} + \frac{z}{r}\frac{\partial^2 F_1}{\partial r \partial z}. \quad (5.5)$$

The contour plot of the Mises stresses, $k_2/(P/h^2)$, for the concentrated force in an infinite medium is shown in Fig. 9(a), and the corresponding solution for the half-space is shown in Fig. 9(b), where P is the concentrated force at the projectile tip and h is the distance from the projectile tip to the free surface. The analysis results indicated that as the projectile approaches the free surface, the damage zone takes the shape of a horn toward the surface. It is very similar to the spalling area in the case of a penetration or perforation.

The circular expansion source on the spherical surface covering the source point is defined as the integral in (2.4a), or

$$E_z = 2\pi\int_0^{\pi}(\sigma_{RR}\sin\varphi + \sigma_{R\varphi}\cos\varphi)(R\sin\varphi) \times R^2\sin\varphi\, d\varphi. \quad (5.6)$$

Therefore, the stress field should decay with distance $1/R^3$, that is

$$\sigma_{RR} = \frac{1}{R^3}\{[-2(5-\nu)\cos^2\varphi + 2\nu]C + 2D\}$$

$$\sigma_{R\varphi} = \frac{1}{R^3}\{-2(1+\nu)\sin\varphi\cos\varphi]C\}$$

$$\sigma_{\varphi\varphi} = \frac{1}{R^3}\{[(1-2\nu)\cos^2\varphi + 2(1-\nu)]C - D\}$$

$$\sigma_{\theta\theta} = \frac{1}{R^3}\{[3(1-2\nu)\cos^2\varphi + 2\nu]C - D\} \quad (5.7)$$

where C and D are constants determined by (5.6), and

$$2\pi\int_0^{\pi/2}(\sigma_{RR}\cos\varphi - \sigma_{R\varphi}\sin\varphi)R^2\sin\varphi d\varphi = 0. \quad (5.8)$$

Equation (5.8) means that the resultant traction in the z-direction on the semispherical surface vanishes. Thus, the solution for the circular expansion source is

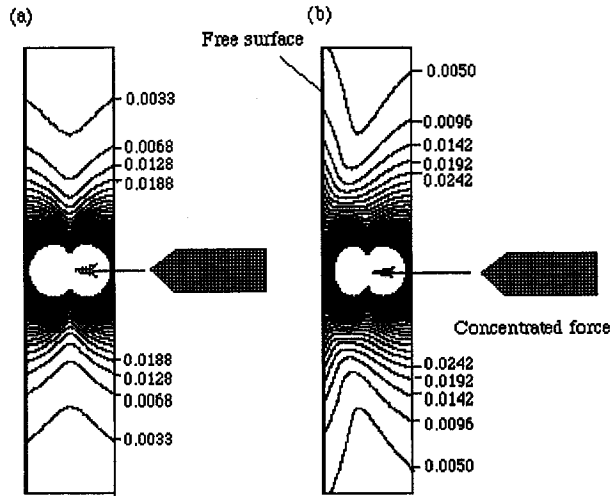


Fig. 9 Concentrated force in an infinite medium (a) and near the free boundary (b)

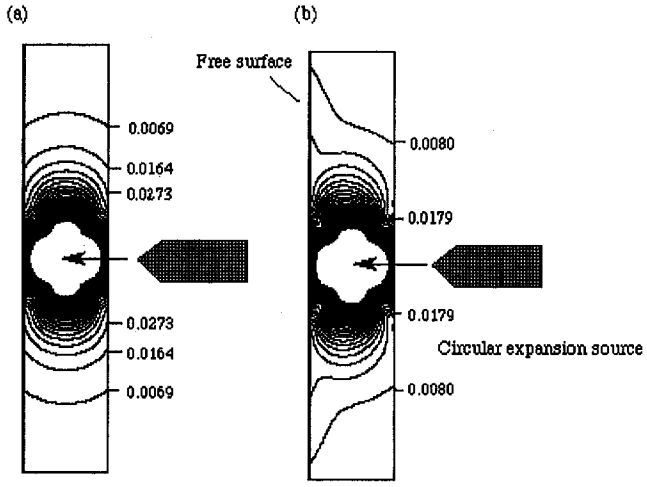


Fig. 10 Circular expansion source in an infinite medium (a) and near the free boundary (b)

$$\sigma_{RR} = \frac{E_z}{2\pi\beta_0 R^3}\{2(5-\nu)\cos^2\varphi - 6(1-\nu)\}$$

$$\sigma_{R\varphi} = \frac{E_z}{2\pi\beta_0 R^3}\{2(1+\nu)\sin\varphi\cos\varphi\}$$

$$\sigma_{\varphi\varphi} = \frac{E_z}{2\pi\beta_0 R^3}\{(1-2\nu)\sin^2\varphi\}$$

$$\sigma_{\theta\theta} = \frac{E_z}{2\pi\beta_0 R^3}\{3(1-2\nu)\sin^2\varphi\}, \quad (5.9)$$

where constant $\beta_0 = (4-5\nu)/15$. If another source is put at the image point, the normal stress on the boundary is

$$\sigma_{zz} = \frac{E_z}{2\pi\beta_0}\left[(1-2\nu) - \frac{6(2+\nu)h^2}{R_0^5} + \frac{15h^4}{R_0^7}\right]. \quad (5.10)$$

In the same way to eliminate the normal stress on the boundary gives the harmonic function F_2 in the expression of (4.5) as

$$F_2 = \frac{E_z}{2\pi\mu\beta_0}\left[\frac{3\nu}{h}lg(R_2+z+h) - (1+\nu)\frac{1}{R_2} + \frac{h(z+h)}{R_2^3}\right] \quad (5.11)$$

Thus, the stress filed induced by the circular expansion source is

$$\sigma_{rr} = \frac{E_z}{2\pi\beta_0 R_1^3}[15\cos^2\varphi_1 - 2(1-\nu)]\sin^2\varphi_1 + \frac{E_z}{2\pi\beta_0 R_2^3}[15\cos^2\varphi_2 - 2(1-\nu)]\sin^2\varphi_2 + \left[(1-2\nu)\frac{\partial^2 F_1}{\partial r^2} - 2\nu\frac{\partial^2 F_1}{\partial z^2} + z\frac{\partial^3 F_1}{\partial r^2\partial z}\right]$$

$$\sigma_{rz} = \frac{E_z}{2\pi\beta_0 R_1^3}\sin\varphi_1\cos\varphi_1[15\cos^2\varphi_1 - 3(3-2\nu)] + \frac{E_z}{2\pi\beta_0 R_2^3}\sin\varphi_2\cos\varphi_2[15\cos^2\varphi_2 - 3(3-2\nu)] + z\frac{\partial^3 F_2}{\partial r\partial z^2}$$

Downloaded 04 May 2010 to 171.66.16.26. Redistribution subject to ASME license or copyright; see http://www.asme.org/terms/Terms_Use.cfm

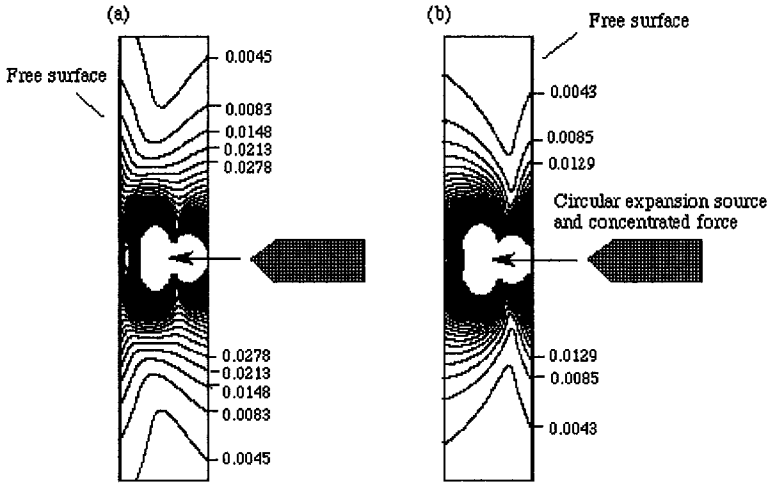


Fig. 11 Boundary effects of entrance surface and exiting surface to the circular expansion source and concentrated force

$$\sigma_{zz} = \frac{E_z}{2\pi\beta_0 R_1^3}[(1-2\nu) - 2(6-7\nu)\cos^2\varphi_1 + (15-8\nu)\cos^4\varphi_1] + \frac{E_z}{2\pi\beta_0 R_2^3}[(1-2\nu) - 2(6-7\nu)\cos^2\varphi_2 + (15-8\nu)\cos^4\varphi_2] + \left[(1-2\nu)\frac{\partial^2 F_2}{\partial r^2} - 2\nu\frac{\partial^2 F_2}{\partial z^2} + z\frac{\partial^3 F_2}{\partial r^2 \partial z}\right]$$

$$\sigma_{\theta\theta} = \frac{E_z}{2\pi\beta_0 R_1^3}[3(1-2\nu)\sin^2\varphi_1] + \frac{E_z}{2\pi\beta_0 R_2^3}[3(1-2\nu)\sin^2\varphi_2] + \left[\frac{1}{r}\frac{\partial F_2}{\partial r} + 2\nu\frac{\partial^2 F_2}{\partial r^2} + \frac{z}{r}\frac{\partial^2 F_2}{\partial r \partial z}\right] \quad (5.12)$$

The contour plot of the Mises stresses, $k_2/(E_z/h^3)$, for the circular expansion source E_z in an infinite medium and in a half-space is shown in Figs. 10(a) and (b). The plot also shows the cone-like shape as the projectile approaches the free surface.

When a projectile is simulated by a concentrated force and an expansion source, the contour plot of the shear stress is plotted as shown in Fig. 11. It shows that the shear stress ahead of the projectile is larger than that behind the projectile. As the projectile approaches the exit surface, Fig. 11(a), the damage zone is cone-like to open and radiate from the projectile tip to the free surface. When the projectile moves away from the free surface as shown in Fig. 11(b), the damage zone is much less than the that of approaching the surface. It is clear that Fig. 11(a) represents a superposition of an expansion source with a positive concentrated force (spalling), and Fig. 11(b) is for that with a negative concentrated force (cratering). Figures 12(a) and 12(b) show the Mises stress varies along the free surface (entrance surface and exit surface), compared to the same situation without boundary effects, where D is the distance from a point on the free surface to the axis of the projectile, and the function f_M in Figs. 12(a) and (b) represents $k_2(p/h^2)$. It indicates that, (1) under the same loading, the Mises stress becomes larger due to the boundary effects, due to the fact that besides the real sources (the concentrated force and expansion source) the imaginary sources also play an important role; (2) the Mises stress along the entrance surface is smaller than that along the exit surface, which accounts for such experimental observed phenomenon that the spalling area is larger than the cratering area in the perforation.

6 Conclusion

A projectile can be simulated by a concentrated force P and a circular expansion source E_z in terms of the geometry of the projectile. The damage zone ahead of the projectile tip exhibits a larger area than that behind it.

The solution of the cavity expansion source is useful in estimating the resistance of the projectile near the free surface. The results indicate that, as the depth of the projectile increases, the boundary effects on the projectile decrease. As the depth of the projectile is four time the radius of the projectile, the boundary effects can be less than six percent, and therefore the boundary has a negligible effect on the projectile.

The use of image sources on the image point is an effective way to calculate the boundary effects on the concentrated force or circular expansion source. The calculations show that when

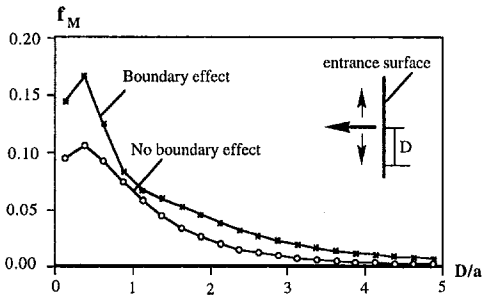


Fig. 12(a) The Mises stress along the entrance surface

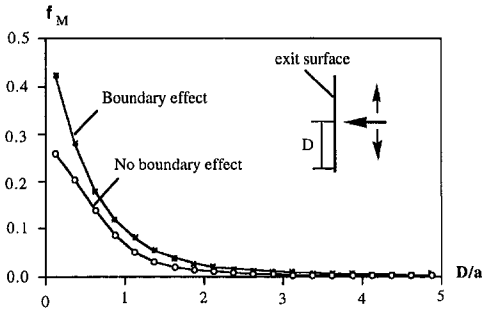


Fig. 12(b) The Mises stress along the exit surface

Downloaded 04 May 2010 to 171.66.16.26. Redistribution subject to ASME license or copyright; see http://www.asme.org/terms/Terms_Use.cfm

the projectile approaches a free surface, the contour plot of the stress distribution is often cone-like in shape, open toward the free surface, and that the spalling area is larger than the cratering area. These analyses results agree well with the post-test observation on perforation experiments.

Acknowledgment

The research conducted by Drs. L. M. Keer and X. Yu at Northwestern University was supported by a contract PR No. AF-6802 from Sandia National Laboratories. The work by Dr. V. K. Luk was performed at Sandia National Laboratories, which is operated for the U.S. Department of Energy under contract DE-AC04-94AL85000.

References

Forrestal, M. J., Atman, B. S., Cargile, J. D., and Hanchak, S. J., 1994, "An empirical equation for penetration depth of ogival-nose projectiles into concrete target," *Int. J. Impac. Engg.* Vol. 15, No. 4, pp. 395–405.

Hopkins, H. G., 1960, "Dynamic expansion of spherical cavities in metals," *Progress in Solid Mechanics,* Vol. 1, I. N. Sneddon and R. Hill, eds., North-Holland, Amsterdam.

Little, R. W., 1973, *Elasticity,* Prentice-Hall, Englewood Cliffs, NJ, p. 390.

Luk, V. K., and Forrestal, M. J., 1987, "Penetration into semi-infinite reinforced concrete targets with spherical and ogival nose projectiles," *Int. J. Impac. Engg.,* Vol. 6, No. 4, pp. 291–301.

Kassir, M. K., and Sih, G. C., 1975, "Three-dimensional crack problems," *Mechanics of Fracture,* Vol. 2, Noordhoff International Publishing, Dordrecht, The Netherlands.

Mindlin, R. D., 1936, "Force at a point in the interior of a semi-infinite solid," *Physics,* Vol. 7, pp. 195–202.

Mindlin, R. D., and Cheng, D. H., 1950, "Nuclei of strain in the semi-infinite solid," *J. Applied Phys.,* Vol. 21, pp. 926–930.

Xu, Y., Keer, L. M., and Luk, V. K., 1996a, "Elastic-cracked model for penetration into unreinforced concrete targets with ogival nose projectiles," *International Journal of Solids and Structures,* Vol. 34, No. 12, pp. 1479–1491.

Xu, Y., Keer, L. M., and Luk, V. K., 1996b, "Stress properties at the tip of a conical notch," *International Journal of Solids and Structures,* Vol. 34, No. 12, pp. 1531–1546.

Downloaded 04 May 2010 to 171.66.16.26. Redistribution subject to ASME license or copyright; see http://www.asme.org/terms/Terms_Use.cfm

Dynamic Response Control of Thin-Walled Beams to Blast Pulses Using Structural Tailoring and Piezoelectric Actuation

L. Librescu
Department of Engineering Science and Mechanics,
Virginia Polytechnic Institute and State University,
Blacksburg, VA 24061-0219

Sungsoo Na
Department of Automation Engineering,
Korea Polytechnic University,
Shihung, Keongki-do 429-450, Korea

An integrated dual approach aimed at controlling the dynamic response of anisotropic cantilevered thin-walled beams to blast and sonic-boom loading is presented. The approach is based upon the simultaneous implementation of structural tailoring and adaptive materials technology. Whereas structural tailoring uses the anisotropy properties of advanced composite materials, the adaptive materials technology exploits the converse effect of piezoactuators bonded or embedded into the host structure. A combined dynamic control law relating the piezoelectrically bending moment induced at the beam tip with the various kinematic response quantities is implemented and its effects upon the closed-loop dynamic response characteristics are investigated. The obtained results reveal the powerful role played by abovementioned integrated control methodology towards enhancing the dynamic response of thin-walled beam cantilevers to transient loading.

1 Introduction

During their operational life, the flight vehicle structures may be exposed to a variety of time-dependent loads induced by nuclear blast, gust, sonic boom, shock wave, fuel explosion, etc.

Having in view the damaging effects caused by the blast pulses on structural integrity and operational life of flight vehicle, adequate methods to predict and control their structural dynamic response have to be devised. This is more imperative as the next generations of aeronautical and space vehicle are likely to feature increasing structural flexibility and operate in severe environmental conditions.

Among all the geometrical structural configurations, the ones of a cylindrical cross section are most commonly used as parts of such vehicles. In this paper the control of the dynamic response of cantilevered anisotropic thin-walled beams of arbitrary cylindrical cross sections is considered.

In order to enhance the dynamic response characteristics of such structures when subjected to transient loadings, advanced concepts must be developed and implemented.

One of the possible options is to use a tailored anisotropic composite laminate. As a result, elastic couplings of a beneficial influence on the dynamic response characteristics can be generated.

However, such a technique is passive in nature in the sense that, once implemented, the structure cannot respond to the variety of factors under which it must operate.

As a complementary option, the adaptive materials technology can be applied.

In a structure with adaptive capabilities the dynamic response characteristics can be controlled in a known and predictable manner and, as a result, one can avoid the occurrence of the structural resonance and of any dynamic instability, and one can enhance the dynamic response to transient loadings.

The adaptive capability can be achieved through the converse piezoelectric effect, which consists of the generation of localized strains in response to an applied voltage. This induced strain field produces, in turn, a change in the dynamic response characteristics of the structure. Herein, a study of the enhancement of the dynamic response of cantilevered structures to transient loadings via the implementation of both techniques, namely, of the adaptive capability (referred to as *induced strain actuation*), and of the *structural tailoring* is addressed. Employment of a control law relating the applied electric field with one of the kinematical response quantities according to a prescribed functional relationship, results in a dynamic boundary value problem whose solution yields the closed-loop dynamic response characteristics.

The study is carried out in the context of an important structural entity, a thin-walled cantilever beam.

This type of structure can serve as a basic model for a number of constructions used in aeronautical and space industries, such as airplane wings, helicopter blades, robotic manipulator arms, and space booms, and in many mechanical engineering applications as well.

In spite of its practical importance, studies of the control of the dynamic response of thin-walled beams to transient loadings via implementation of abovementioned dual technology are virtually absent in the specialized literature. The aim of the present paper is to supply information in this field and reveal the efficiency of this dual control methodology as applied to the problem at hand.

In this sense, three related issues will be addressed, namely: (i) the development of a powerful mathematical methodology for determining the closed-loop response of thin-walled anisotropic cantilevers to time-dependent external excitations, (ii) to reveal the efficiency of the dual control methodology, and (iii) to highlight the influence of the various effects, including those related with the character of the considered pressure pulses on closed-loop dynamic response of thin-walled beam cantilevers.

It should be mentioned that the theory of anisotropic thin-walled beams as used in this paper was developed in the papers by Librescu and Song (1992) and Song and Librescu (1993).

Contributed by the Applied Mechanics Division of THE AMERICAN SOCIETY OF MECHANICAL ENGINEERS for publication in the ASME JOURNAL OF APPLIED MECHANICS.

Discussion on the paper should be addressed to the Technical Editor, Professor Lewis T. Wheeler, Department of Mechanical Engineering, University of Houston, Houston, TX 77204-4792, and will be accepted until four months after final publication of the paper itself in the ASME JOURNAL OF APPLIED MECHANICS.

Manuscript received by the ASME Applied Mechanics Division, Mar. 24, 1997; final revision, Aug. 13, 1997. Associate Technical Editor: W. K. Liu.

 Copyright © 1998 by ASME

Downloaded 04 May 2010 to 171.66.16.26. Redistribution subject to ASME license or copyright; see http://www.asme.org/terms/Terms_Use.cfm

However, in order to be reasonably self-contained, a number of basic steps yielding the pertinent governing equations will be shortly displayed.

2 Structural Model: Basic Equations

The structural model of single-cell thin-walled beams used in this study incorporates a number of nonclassical features such as: (i) anisotropy of constituent material layers, (ii) transverse shear, (iii) nonuniform twist, in the sense that the rate of twist $d\Theta/dz$ is no longer assumed to be constant as in the Saint-Venant torsional model, but a function of the spanwise coordinate, and (iv) primary and secondary warping effects.

In accordance with the above statements and in order to reduce the three-dimensional problem to an equivalent one-dimensional one, the components of the displacement vector are expressed as (see Song and Librescu, 1993):

$$u(x, y, z, t) = u_0(z, t) - y\Theta(z, t),$$

$$v(x, y, z, t) = v_0(z, t) + x\Theta(z, t), \qquad (1a, b)$$

$$w(x, y, z, t) = w_0(z, t) + \theta_x(z, t)\left[y(s) - n\frac{dx}{ds}\right] + \theta_y(z, t)\left[x(s) + n\frac{dy}{ds}\right] - \Theta'(z, t)[F_\omega(s) + na(s)], \qquad (1c)$$

where

$$\theta_x(z, t) = \gamma_{yz}(z, t) - v_0'(z, t),$$

$$\theta_y(z, t) = \gamma_{xz}(z, t) - u_0'(z, t), \qquad (2a, b)$$

and

$$a(s) = -y(s)\frac{dy}{ds} - x(s)\frac{dx}{ds}. \qquad (2c)$$

Here $\theta_x(z, t)$ and $\theta_y(z, t)$ denote the rotations about axes x and y, respectively, $\Theta(z, t)$ the twist about the z-axis, while γ_{yz} and γ_{xz} denote the transverse shear strains in the planes yz and xz, respectively.

In addition,

$$F_\omega(s) = \int_0^s [r_n(s) - \psi]ds, \qquad (3)$$

plays the role of the primary warping function, $na(s)$ that of the secondary warping, whereas ψ and $r_n(s)$ denote the torsional function and a geometric quantity defined in the paper by Song and Librescu (1993).

Equations (1) and (2) reveal that six kinematic variables: $u_0(z, t)$, $v_0(z, t)$, $w_0(z, t)$, $\theta_x(z, t)$, $\theta_y(z, t)$, and $\Theta(z, t)$ representing three translations in the x, y, z-directions and three rotations about the x, y, and z-axes, respectively, are used to define the displacement vector of components u, v, and w in the x, y, and z-directions, respectively.

Based on the kinematic representations, Eqs. (1) and (2), the strain measures assume the following form (see Librescu and Song (1992) and Song and Librescu (1993)):

Axial Strain:

$$\epsilon_{zz}(n, s, z, t) = \bar{\epsilon}_{zz}(s, z, t) + n\bar{\bar{\epsilon}}_{zz}(s, z, t), \qquad (4a)$$

where

$$\bar{\epsilon}_{zz}(s, z, t) = w_0'(z, t) + \theta_y'(z, t)x(s) + \theta_x'(z, t)y(s) - \Theta''(z, t)F_\omega(s), \qquad (4b)$$

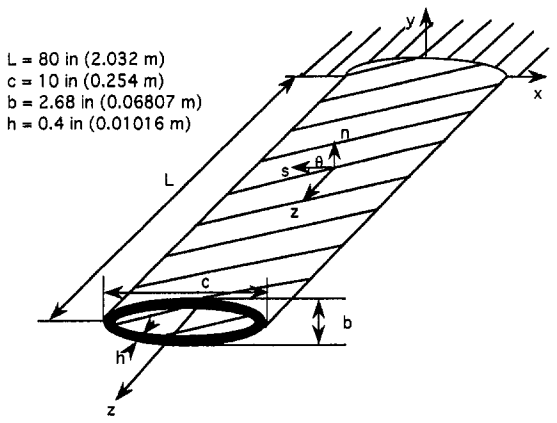


Fig. 1 Geometry of the cantilevered beam

and

$$\bar{\bar{\epsilon}}_{zz}(s, z, t) = \theta_y'(z, t)\frac{dy}{ds} - \theta_x'(z, t)\frac{dx}{ds} - \Theta''(z, t)a(s), \qquad (4c)$$

are the axial strains associated with the primary and secondary warping, respectively.

Tangential Shear Strain:

$$\epsilon_{sz}(s, z, t) = \bar{\epsilon}_{sz}(s, z, t) + 2\frac{A_c}{\beta}\Theta'(z, t), \qquad (5a)$$

where

$$\bar{\epsilon}_{sz}(s, z, t) = [\theta_y(z, t) + u_0'(z, t)]\frac{dx}{ds} + [\theta_x(z, t) + v_0'(z, t)]\frac{dy}{ds}. \qquad (5b)$$

Transverse Shear Strain:

$$\epsilon_{nz}(s, z, t) = [\theta_y(z, t) + u_0'(z, t)]\frac{dy}{ds} - [\theta_x(z, t) + v_0'(z, t)]\frac{dx}{ds}. \qquad (6)$$

Here, and in the following developments (x, y, z) is the *global* coordinate system, (see Fig. 1), where the z-axis coincides with the locus of symmetrical points of the cross sections along the wing span; (n, s, z) is a *local* coordinate system, while $(\cdot)' \equiv \partial(\cdot)/\partial z$.

For the problem considered herein, $u_0(z, t)$, $v_0(z, t)$, $w_0(z, t)$, and $\theta_x(z, t)$, $\theta_y(z, t)$ and $\Theta(z, t)$ constitute the basic one-dimensional unknown functions of the problem. When the transverse shear is ignored, $\theta_x \to -v_0'$ and $\theta_y \to -u_0'$ and, as a result, the number of unknowns is reduced to only four.

3 Constitutive Equations of Thin-Walled Beam Structures Incorporating Adaptive Capabilities

Intelligent structures are composed of materials with structurally integrated and highly distributed networks of sensors and actuators linked through a centralized multiprocessor. Such a structure would possess the ability to adapt to changing environments. Moreover, due to the distributed nature of the actuators present in such a structure, modern control methodologies are possible to be implemented. Piezoelectric materials exhibit two

Downloaded 04 May 2010 to 171.66.16.26. Redistribution subject to ASME license or copyright; see http://www.asme.org/terms/Terms_Use.cfm

basic phenomena which make them appropriate for the role of sensors and actuators in a control system. The first phenomenon is called the *direct piezoelectric effect* which consists of the generation of electrical charge or voltage in response to a mechanical deformation. Conversely, when an electric charge or voltage is applied, the piezoelectric material reacts by generating a mechanical strain. This phenomenon is called the *converse piezoelectric effect.* The direct and converse piezoelectric effects are basic towards the use of piezoelectric materials as sensors and actuators, respectively. Comprehensive reviews and assessments of the achievements reached by the use of intelligent structures in aerospace applications and in flexible structures, in general, can be found in the papers by Crawley (1994) and of Rao and Sunar (1994). For the problem at hand one considers the piezoelectric anisotropy to be of a transversal-isotropic type, where the surface of isotropy is parallel to the midsurface of the structure.

As a result, the n-axis of the structure constitutes an axis of rotary symmetry which coincides with the direction of polarization (thickness polarization).

One assumes that the piezoactuators are bonded on the upper and lower faces of the beam, that are spread over its entire span and, that the host structure is composed of r layers exhibiting monoclinic anisotropic properties. By reducing the three-dimensional constitutive equations of the entire structure to a two-dimensional counterpart and assuming that the hoop stress-resultant N_{ss} is negligibly small when compared with the remaining two-dimensional stress resultants, the two-dimensional constitutive equations can be written as (see Librescu et al., 1993, 1996):

$$N_{zz}(s, z, t) = K_{11}\bar{\epsilon}_{zz} + K_{12}\bar{\epsilon}_{sz} + K_{13}\Theta' + K_{14}\bar{\bar{\epsilon}}_{zz} - \hat{N}_{zz}$$

$$N_{sz}(s, z, t) = K_{21}\bar{\epsilon}_{zz} + K_{22}\bar{\epsilon}_{sz} + K_{23}\Theta' + K_{24}\bar{\bar{\epsilon}}_{zz}$$

$$N_{zn}(s, z, t) = A_{44}\epsilon_{zn}$$

$$L_{zz}(s, z, t) = K_{41}\bar{\epsilon}_{zz} + K_{42}\bar{\epsilon}_{sz} + K_{43}\Theta' + K_{44}\bar{\bar{\epsilon}}_{zz} - \hat{L}_{zz}$$

$$L_{sz}(s, z, t) = K_{51}\bar{\epsilon}_{zz} + K_{52}\bar{\epsilon}_{sz} + K_{53}\Theta' + K_{54}\bar{\bar{\epsilon}}_{zz}. \quad (7a\text{–}e)$$

In these equations N_{zz} and N_{sz} denote the tangential stress resultants; N_{zn} denotes the transverse shear stress resultant; L_{zz} and L_{sz} denote the stress couples; $\hat{N}_{zz}$ and $\hat{L}_{zz}$ denote the piezoelectrically induced-stress resultant and stress couple, respectively, while K_{ij} denote the modified local stiffness coefficients whose definition can be found in the paper by Song and Librescu (1993).

4 The Governing Equations of Adaptive Cantilevered Structures

Following the results of Librescu and Song (1992), the one-dimensional stress resultants and stress couples are defined as

$$T_z(z, t) = \oint N_{zz} ds,$$

$$Q_x(z, t) = \oint \left(N_{sz}\frac{dx}{ds} + N_{zn}\frac{dy}{ds}\right) ds, \quad (8a, b)$$

$$Q_y(z, t) = \oint \left(N_{sz}\frac{dy}{ds} - N_{zn}\frac{dx}{ds}\right) ds,$$

$$M_x(z, t) = \oint \left(yN_{zz} - L_{zz}\frac{dx}{ds}\right) ds \quad (8c, d)$$

$$M_y(z, t) = \oint \left(xN_{zz} + L_{zz}\frac{dy}{ds}\right) ds,$$

$$M_z(z, t) = \oint N_{sz}\frac{2A_C}{\beta} ds, \quad (8e, f)$$

$$B_\omega(z, t) = \oint [F_\omega(s)N_{zz} + a(s)L_{zz}] ds, \quad (8g)$$

where T_z is the axial force, Q_x and Q_y are the shear forces in the x and y-directions; M_x, M_y, and M_z denote the moments about the x, y, and z-axes, respectively, while B_ω denotes the biomoment. In view of Eqs. (7) and (8), the one-dimensional stress measures T_z, M_x, M_y, and B_ω can be cast in the form

$$T_z = \bar{T}_z - \hat{T}_z, \quad M_x = \bar{M}_x - \hat{M}_x,$$

$$M_y = \bar{M}_y - \hat{M}_y, \quad B_\omega = \bar{B}_\omega - \hat{B}_\omega \quad (9a\text{–}d)$$

where the overbars and overcarets identify the purely mechanical and piezoelectrically induced terms, respectively.

Assuming that the electric field vector $\mathcal{E}_i$ is represented in terms of the component $\mathcal{E}_3$, the piezoelectrically induced stress resultants and stress couples are proportional to the applied electric field $\mathcal{E}_3$. Having in view the distribution of piezoactuators over the entire beam span and the fact that $\mathcal{E}_3$ is assumed to be spatially uniform but time-dependent, one can infer that the piezoelectrically induced terms in Eq. (9) are independent on the spanwise z-coordinate. This explains why their contributions in the governing equations is immaterial and why they intervene as nonhomogeneous terms in the boundary conditions at the beam tip.

Consistent with the kinematical equations, Eqs. (1), the one-dimensional version of the equations of motion and the associated boundary conditions can be obtained by means of Hamilton's variational principle.

Replacement in the obtained equations of motion (not displayed here) of constitutive equations, Eqs. (7), and of strain-displacement relations, Eqs. (4)–(6), results in the governing equations expressed in terms of displacement quantities.

These equations feature, in general, a full coupling between the various elastic modes, i.e., between extension, twist, transversal bending (flapping), lateral bending (lagging), extension, and transverse shear. However, as it was revealed in a number of recent works, (see, e.g., Weisshaar (1987), Librescu and Simovich (1988), and Librescu and Thangjitham (1991)), flapping-twist cross-coupling turns out to be of an exceptional importance towards the enhancement of the response behavior of aircraft wings and helicopter blades.

As it was shown by Rehfield and Atilgan (1989) and Smith and Chopra (1991), the ply-angle distribution with respect to the spanwise z-axis inducing such a cross-coupling is

$$\theta(y) = -\theta(-y). \quad (10)$$

As a result of this ply-angle scheme, the governing equations expressed in terms of displacement quantities and featuring bending-twist cross-coupling are

$$\delta v_0: \quad a_{55}(v_0'' + \theta_x') + a_{56}\Theta''' + \underline{p_y = b_1\ddot{v}_0},$$

$$\delta\theta_x: \quad a_{33}\theta_x'' + a_{37}\Theta'' - a_{55}(v_0' + \theta_x) - a_{56}\Theta'' = \underline{(b_4 + b_{14})\ddot{\theta}_x},$$

$$\delta\Theta: \quad \underline{-a_{66}\Theta''''} + a_{77}\Theta'' - a_{56}(v_0''' + \theta_x'') + a_{73}\theta_x'' + m_z = (b_4 + b_5)\ddot{\Theta} - \underline{(b_{10} + b_{18})\ddot{\Theta}''}. \quad (11a\text{–}c)$$

For cantilevered beams, the boundary conditions to be prescribed are as follows.

At $z = 0$,

$$v_0 = 0, \quad \theta_x = 0, \quad \Theta = 0, \quad \underline{\Theta' = 0}, \quad (12a\text{–}d)$$

and at $z = L$,

Downloaded 04 May 2010 to 171.66.16.26. Redistribution subject to ASME license or copyright; see http://www.asme.org/terms/Terms_Use.cfm

$$\delta v_0: \quad a_{55}(v_0' + \theta_x) + a_{56}\Theta'' = 0,$$

$$\delta\theta_x: \quad a_{33}\theta_x' + a_{37}\Theta' = \hat{M}_x,$$

$$\delta\Theta: \quad -a_{66}\Theta''' + a_{77}\Theta' - a_{56}(v_0'' + \theta_x') + a_{37}\theta_x' = -(b_{10} + b_{18})\ddot{\Theta}',$$

$$\delta\Theta': \quad a_{56}(v_0' + \theta_x) + a_{66}\Theta'' = 0. \qquad (13a\text{–}d)$$

The terms underscored in Eqs. (11)–(13) by single and double dotted lines are associated with the warping inhibition and the warping inertia, respectively, whereas the term underscored by a solid line is associated with the rotatory inertia.

The infinitely rigid in transverse shear counterpart of Eqs. (11)–(13) is

$$\delta v_0: \quad a_{33}v_0^{IV} - a_{37}\Theta''' + p_y = -b_1\ddot{v}_0 + (b_4 + b_{14})\ddot{v}_0'',$$

$$\delta\Theta: \quad -a_{66}\Theta^{IV} + a_{77}\Theta'' - a_{73}v_0''' + m_z = (b_4 + b_5)\ddot{\Theta} - (b_{10} + b_{18})\ddot{\Theta}'', \qquad (14a, b)$$

and the boundary conditions are

at $z = 0$,

$$\Theta = \Theta' = v_0 = v_0' = 0, \qquad (15a\text{–}d)$$

and at $z = L$,

$$\delta v_0: \quad a_{33}v_0''' = (b_4 + b_{14})\ddot{v}_0'$$

$$\delta v_0': \quad a_{37}\Theta' - a_{33}v_0'' = \hat{M}_x$$

$$\delta\Theta: \quad -a_{66}\Theta''' + a_{77}\Theta' - a_{37}v_0'' = -(b_{10} + b_{18})\ddot{\Theta}'$$

$$\delta\Theta': \quad \Theta'' = 0. \qquad (16a\text{–}d)$$

The coefficients a_{ij} ($\equiv a_{ij}$) and b_i appearing in Eqs. (11)–(13) stand for the stiffness and inertia quantities, respectively. Their expression can be found in the papers by Librescu and Song (1992) and Song and Librescu (1993). From Eqs. (9)–(11) is readily seen that in addition to the transverse bending stiffness (a_{33}), twist stiffness (a_{77}) and transverse shear stiffness in the y-direction (a_{55}), the system is governed by the warping stiffness (a_{66}), twist-transverse shear (a_{56}), and bending-twist (a_{37}) cross-couplings. From Eqs. (14)–(16) it becomes also evident that for nonshearable beams, the stiffness quantities a_{55} and a_{56} become immaterial.

In the boundary conditions, Eqs. (13b) and (16b), $\hat{M}_x$ is the piezoelectrically induced bending moment, which, for already mentioned reasons, appears as a nonhomogeneous term in the boundary conditions at $z = L$. It should be noticed that $\hat{M}_x$ is different from zero only if external voltages of opposite signs are applied in the upper and bottom piezoactuator layers (out-of-phase activation—see, e.g., Birman (1994) and Lin and Crawley (1995)).

In the governing equations $p_y(z, t)$ and $m_z(z, t)$ denote the distributed force per unit span length and the twist moment about the z-axis. For the problem at hand, only the distributed force will be considered, implying that in the forthcoming developments $m_z(z, t) = 0$.

5 Time-Dependent Loads Associated With Blast and Sonic-Boom Pulses

Herein, the dynamic response control of thin-walled beams to explosive blast and sonic boom overpressure signatures will be addressed. For the case of blast loadings, various analytical expressions have been proposed and discussed (see, e.g., Crocker (1966), Birman and Bert (1987), and Librescu and Nosier (1990a, b)). As it was clearly established, the blast pulse reaches the peak value in such a short time that the structure can be assumed to be loaded instantly. Based on the experimental evidence, it may also be assumed that the pressure is uniformly distributed over the plate. This fact is also assumed in the case of sonic boom pulses. In accordance with the abovementioned references, the overpressure associated with the blast pulses can be described in terms of the modified Friedlander exponential decay equation as

$$p_y(s, z, t)(\equiv p_y(t)) = P_m\left(1 - \frac{t}{t_p}\right)e^{-a't/t_p}, \qquad (17)$$

where the negative phase of the blast is included. In Eq. (17), P_m denotes the peak reflected pressure in excess of the ambient one; t_p denotes the positive phase duration of the pulse measured from the time of impact of the structure and a' denotes a decay parameter which has to be adjusted to approximate the overpressure signature from the blast tests. As it could be inferred, the triangular load may be viewed as a limiting case of Eq. (17), occurring when $a'/t_p \to 0$.

As concerns the sonic-boom loading, this can be modeled as an N-shaped pressure pulse arriving at a normal incidence. Such a pulse corresponds to an idealized far-field overpressure produced by an aircraft flying supersonically in the earth's atmosphere or by any supersonic projectile rocket or missile (see Gotlieb and Ritzel (1988) and Crocker (1966, 1970)). The overpressure signature of the N-wave shock pulse can be described by

$$p_y(s, z, t)(\equiv p_y(t)) = \begin{cases} P_m\left(1 - \dfrac{t}{t_p}\right) \text{ for } 0 < t < rt_p \\ 0 \text{ for } t < 0 \text{ and } t > rt_p \end{cases} \qquad (18)$$

where r denotes the shock pulse length factor, and P_m and t_p maintain the same meaning as in the case of blast pulses. It may easily be seen that (i) for $r = 1$ the N-shaped pulse degenerates into a triangular pulse; (ii) for $r = 2$ a symmetric N-shaped pressure pulse is obtained; while (iii) for $1 < r < 2$ the N-shaped pulse becomes an asymmetric one as shown in Fig. 1(b). The dynamic response of composite flat panels to such shock pulses was analyzed by Librescu and Nosier (1990a, b).

Another special case corresponds to a step-pulse. Its analytic description can be either obtained from Eq. (17), when $t_p \to \infty$, and from Eq. (18) when $r = 1$ and $t_p \to \infty$.

In addition, there are recorded also the cases of the sine and rectangular pressure pulses described as

$$p_y(s, z, t) \equiv p_y(t) = \begin{cases} P_m \sin \pi t/t_p & 0 \le t \le t_p \\ 0 & t > t_p \end{cases} \text{ sine pulse}$$

$$= \begin{cases} P_m & 0 \le t \le t_p \\ 0 & t > t_p \end{cases} \text{ rectangular pulse.} \qquad (19)$$

The pressure pulses described above are also used in the present study.

6 The Control Law

One of the possible ways enabling one to control the dynamic response of cantilevered beams to transient loads is via the generation and use of a dynamic bending moment acting at the beam tip. This method which was substantiated mathematically by Lagnese and Lions (1988) and Lagnese (1989) is referred to as the *boundary moment control.*

For feedback control, the applied electric field $\mathcal{E}_3$ upon which the piezoelectrically induced boundary bending moment $\hat{M}_x$ depends, should be expressed through a prescribed functional rela-

Downloaded 04 May 2010 to 171.66.16.26. Redistribution subject to ASME license or copyright; see http://www.asme.org/terms/Terms_Use.cfm

tionship with the mechanical quantities characterizing the beam's response.

For the problem at hand, the goal of the control is to enhance the dynamic response to time-dependent external excitation. In order to increase control authority, a combined feedback control law is implemented in the form

$$\hat{M}_x(L, t) = k_V \dot{\theta}_x(L, t) + k_A \ddot{\theta}_x(L, t) \tag{20}$$

where k_V and k_A are the feedback gains. The control law, Eq. (20), expresses the fact the bending moment at the beam tip induced by piezoelectric strain actuation is proportional to the velocity and acceleration of rotation of the beam tip. Use of Eq. (20) into Eq. (13*b*) results in the boundary condition at $z = L$, including the feedback control as

$$\theta_x'(L, t) + f_3\Theta'(L, t) = [k_V \dot{\theta}_x(L, t) + k_A \ddot{\theta}_x(L, t)]/a_{33}, \quad (f_3 \equiv a_{37}/a_{33}). \tag{21}$$

The stiffness parameters f_3 in Eq. (21) reveals that due to the anisotropy of constituent materials of the structure, the piezoelectrically induced bending moment at the beam tip will also generate twist.

Under this form, the control law constitutes a generalization of those considered in a number of special cases in Bailey and Hubbard (1988) Tzou and Zhong (1992), Zhou (1993)), Baz (1995), and Librescu et al. (1993, 1996).

A number of successive steps aiming to solve the open/closed-loop boundary value problem have to be implemented. As a first step, Hamilton's variational principle stating that

$$\int_{t_1}^{t_2} (\delta T - \delta V + \delta W)dt = 0, \quad \delta v_0 = \delta\theta_x = \delta\Theta = 0 \quad \text{at } t = t_0, t_1 \tag{22}$$

will be used.

Herein T and V denote the kinetic and strain energies, respectively, while W is the work done by the external distributed loads; t_1 and t_2 denote two arbitrary instants of the time t while δ denotes the sign variation.

For the problem at hand for which the ply-angle configuration defined by Eq. (10) was adopted, one can express

$$\int_{t_1}^{t_2} \delta T dt = -\int_{t_1}^{t_2} \int_0^L (I_1\delta v_0 + I_2\delta\Theta + I_3\delta\theta_x)dzdt \tag{23}$$

where I_i denote inertia terms defined in Song and Librescu (1993), while

$$\delta V = -\int_0^L [(M_x' - Q_y)\delta\theta_x + (B_\omega'' + M_z')\delta\Theta + Q_y'\delta v_0]dz + [M_x\delta\theta_x - B_\omega\delta\Theta' + (B_\omega' + M_z)\delta\Theta + Q_y\delta v_0]|_0^L \tag{24}$$

and

$$\delta W = \int_0^L p_y\delta v_0 dt. \tag{25}$$

From Eq. (22) considered in conjunction with the Eqs. (23)–(25), with the definitions of one-dimensional stress-resultants Q_y, stress-couples M_x, M_z, and biomoment B_ω, and the two-dimensional constitutive equations, (Eqs. (7)), for independent and arbitrary variations $\delta\theta_x$, δv_0, and $\delta\Theta$, from (22), the equations of motion in terms of displacement quantities, as well as the boundary conditions can be obtained. However, in order to implement the Extended Galerkin Method, one uses Eq. (22), which in conjunction with Eqs. (23)–(25) can be written in a compact form as

$$\int_{t_1}^{t_2} \left[\int_0^L [(11a)\delta v_0 + (11b)\delta\theta_x + (11c)\delta\Theta]dz + [(13a)\delta v_0 + (13b)\delta\theta_x + (13c)\delta\Theta + (11d)\delta\Theta']|_0^L \right] dt = 0. \tag{26}$$

The numbers in brackets identify the left-hand expressions of the equations of motion and boundary conditions at $z = L$, displayed in the paper under the same numbers and modified by passing the right-hand side members in the left-hand side. Within the second step one assumes for the displacement quantities the representation

$$[v_0(z, t); \theta_x(z, t); \Theta(z, t)] = \sum_{j=1}^{N} [v_j(z)q_j(t); w_j(z)q_j(t); W_j(z)q_j(t)] \tag{27}$$

where $v_j(z)$, $w_j(z)$, and $W_j(z)$ are the trial functions which have to fulfill all the kinematic boundary conditions and are assumed to be known, while $q_i(t)$ are the generalized coordinates whose determination constitutes the central goal of the dynamic response problem. For the problem at hand the trial functions are represented as polynomials in the spanwise z variable which fulfill exactly the boundary conditions at $z = 0$. Representations (27), together with that of the bending control moment, Eq. (20), as well as that of the overpressure signatures are replaced in Eq. (26) and the integration with respect to the spanwise z-coordinate is performed. For the present problem the boundary conditions at $z = L$ being in general not fulfilled, corrective terms instead of zero-valued ones appear in the process of integration in Eq. (26), terms which compensate the nonfulfillment of the nonessential boundary conditions. As a result, an equation expressed in matrix form as

$$\mathbf{D} = 0 \tag{28}$$

is obtained where

$$\mathbf{D} \equiv \mathbf{M}\ddot{\mathbf{q}} + \mathbf{C}\dot{\mathbf{q}} + \mathbf{K}\mathbf{q} - \mathbf{F}. \tag{29}$$

Herein $\mathbf{q}$ is a $3N \times 1$ column matrix whose elements are $q_i(t)$; $\mathbf{M}$, $\mathbf{C}$, and $\mathbf{K}$ are $3N \times 3N$ square matrices, the latter one containing also the corrective boundary terms, while $\mathbf{F}$ ($\equiv \mathbf{F}(t)$) is the input $3N \times 1$ column matrix. It should be remarked that for the nonactivated beam or when only acceleration feedback control is only implemented $\mathbf{C}$ becomes immaterial.

Equation

$$\mathbf{M}\ddot{\mathbf{q}} + \mathbf{C}\dot{\mathbf{q}} + \mathbf{K}\mathbf{q} = \mathbf{F} \tag{30}$$

constitutes a set of coupled ordinary differential equations.

Multiplying Eq. (30) by $\mathbf{M}^{-1}$, introducing the generalized velocities $\dot{\mathbf{q}}$ as auxiliary variables by means of the matrix identity $\dot{\mathbf{q}} - \dot{\mathbf{q}} = \mathbf{0}$ and defining the state space vector

$$\mathbf{X} = \begin{Bmatrix} \mathbf{q} \\ \dot{\mathbf{q}} \end{Bmatrix} \tag{31}$$

one can express Eq. (30) in state space form as

$$\dot{\mathbf{X}} = \mathbf{A}\mathbf{X} + \mathbf{B}\mathbf{F} \tag{32}$$

Downloaded 04 May 2010 to 171.66.16.26. Redistribution subject to ASME license or copyright; see http://www.asme.org/terms/Terms_Use.cfm

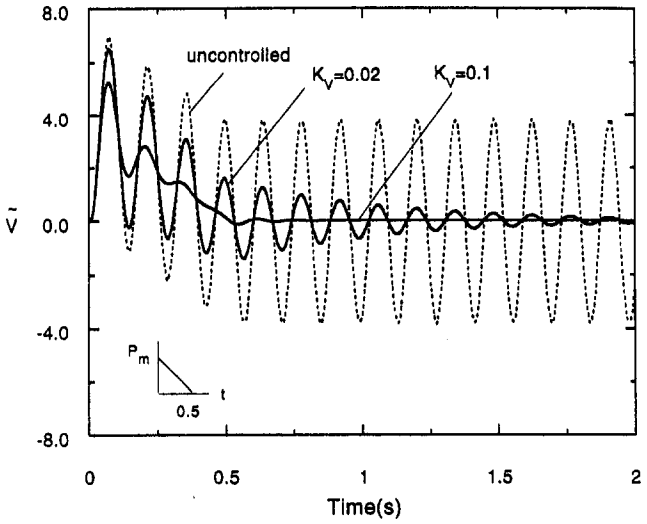


Fig. 2 Open and closed-loop nondimensional transversal deflection time-history to a blast loading; nonshearable and free-warping beam model; $\theta = 0$ deg; $t_p = 0.5$ s, $\mathcal{AR} = 16$

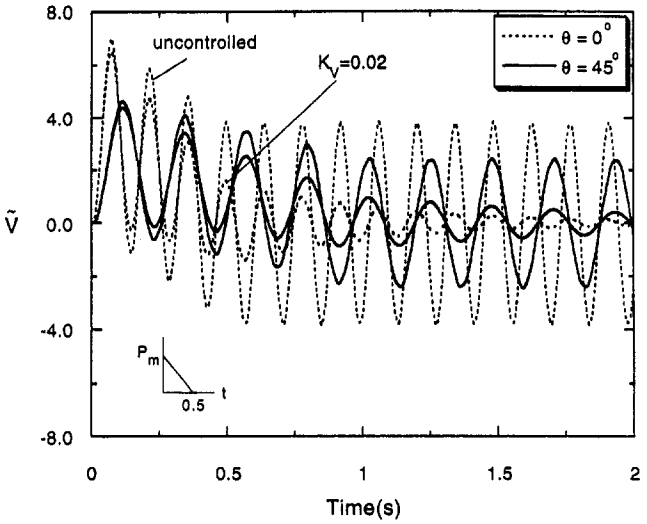


Fig. 3 Influence of ply-angle on open and closed-loop nondimensional transverse deflection time-history to a blast loading; nonshearable and free-warping beam model; $t_p = 0.5$ s, $\mathcal{AR} = 16$

where

$$\mathbf{A} = \begin{bmatrix} \mathbf{0} & \mathbf{I} \\ -\mathbf{M}^{-1}\mathbf{K} & -\mathbf{M}^{-1}\mathbf{C} \end{bmatrix} \text{ and } \mathbf{B} = \begin{Bmatrix} \mathbf{0} \\ \mathbf{M}^{-1} \end{Bmatrix}. \quad (33)$$

In this way, the determination of the open/closed-loop dynamic response has been reduced to the solution of the state-space Eq. (32). From the multitudes of methods available for its solution, the Laplace transform method was used.

7 Numerical Illustrations and Discussion

The numerical illustrations concern the open and closed-loop dynamic response of a cantilevered thin-walled beam of a biconvex cross-section profile (see Fig. 1) subjected to transient loadings. This cross-section profile was used in the study of the aeroelastic behavior of an advanced aircraft wing in Librescu et al. (1996).

The material of the host structure is considered to consist of a graphite-epoxy material whose on-axis properties have been supplied in the paper by Librescu and Song (1992) and Song and Librescu (1993).

The properties of piezoactuators are made of *PZT*–4 piezoceramic as provided by Berlincourt et al. (1964) can be found also in Librescu et al., (1993). The associated open and closed-loop boundary value problem has been solved via the use of the Extended Galerkin Method, which in other contexts was used in Song and Librescu (1993) and shown to provide excellent results when compared with the exact solution based on Laplace transform method, devised in Librescu and Thangjitham (1991).

The displayed results have been generated for the case of zero initial conditions and of $P_m = 500$ lb/L. In the following numerical illustrations, nondimensional feedback gains, related with their dimensional counterparts, are defined as

$$K_V = k_V \bar{\omega} L/a_{33},\ K_A = k_A \bar{\omega}^2 L/a_{33} \quad (34)$$

where $\bar{\omega} = 40.32$ rad/s is the lowest open-loop natural frequency associated with an unshearable free-warping beam model characterized by $\theta = 0$ deg and $\mathcal{AR} = 16$, where $\mathcal{AR}$ $(=2L/c)$ defines beam aspect ratio.

In Figs. 2–4 the effects of the dual control methodology on the dynamic response of the beam when subjected to a blast loading are highlighted. In these figures the case of a nonshearable beam freely to warp is considered. The results in

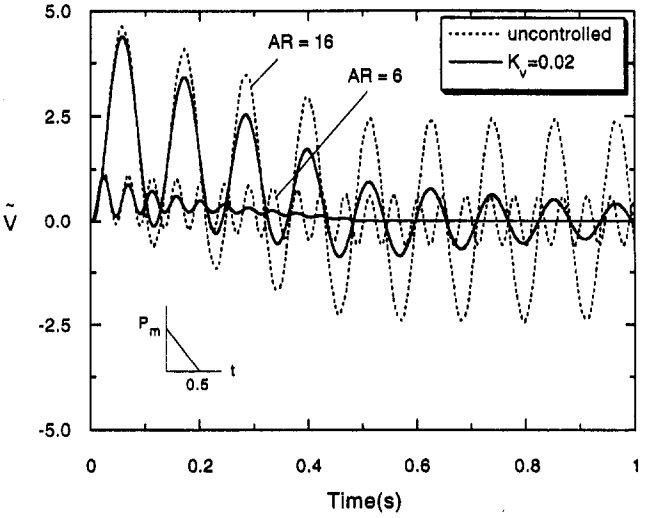


Fig. 4 Influence of the beam aspect ratio on the nondimensional transversal deflection time-history to a blast loading. Nonshearable and free-warping beam model; $\theta = 45$ deg, $t_p = 0.5$ s.

these plots reveal the strong beneficial influence played by the adaptive technology and by the combined tailoring and adaptive technology resulting in a reduction of the deflections in both the forced and free-motion ranges. The results supplied by these figures also reveal that implementation of a ply-angle yielding an increase of the bending stiffness a_{33} results not only in a dramatic reduction of the deflection in the free motion range, but also in a shift of the deflection peaks towards larger times.

One should remark that within the velocity feedback control methodology, the closedloop eigenvalues are complex valued quantities, and, as a result, damping is generated. This explains why in the free-motion range, for the activated structure and in contrast to the nonactivitated one, the response amplitudes decay as time unfolds. The effect of the beam aspect ratio on the control of the dynamic response is illustrated in Fig. 4. The results reveal the evident fact that for the same feedback gain, the response amplitudes are much larger for higher aspect ratio beams than for their low-aspect ratio counterparts.

In Figs. 5 and 6 the open and closed-loop dynamic response to a rectangular pressure pulse are considered. The results reveal

Downloaded 04 May 2010 to 171.66.16.26. Redistribution subject to ASME license or copyright; see http://www.asme.org/terms/Terms_Use.cfm

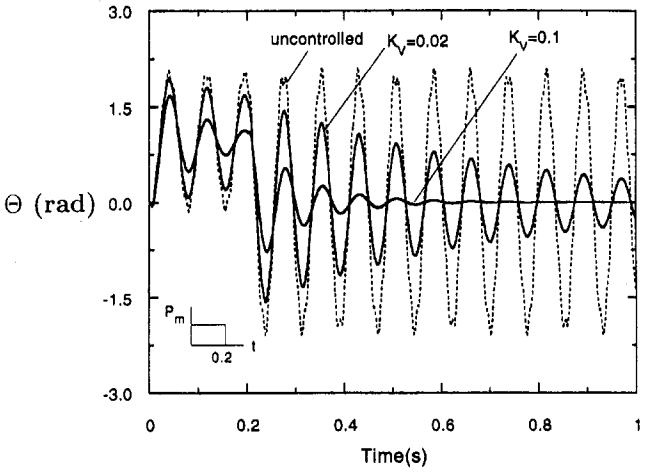


Fig. 5 Open and closed-loop twist time-history to a rectangular pressure pulse. Nonshearable and warping restraint beam model, $\theta = 60$ deg, $\bar{R} = 16$.

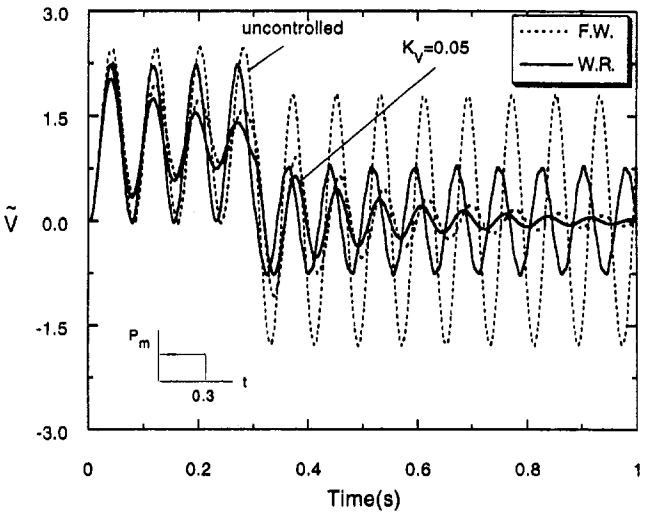


Fig. 6 Free and warping restraint effect on open and closed-loop transversal deflection time-history to a rectangular pressure pulse. Nonshearable beam model, $\theta = 60$ deg, $\bar{R} = 16$.

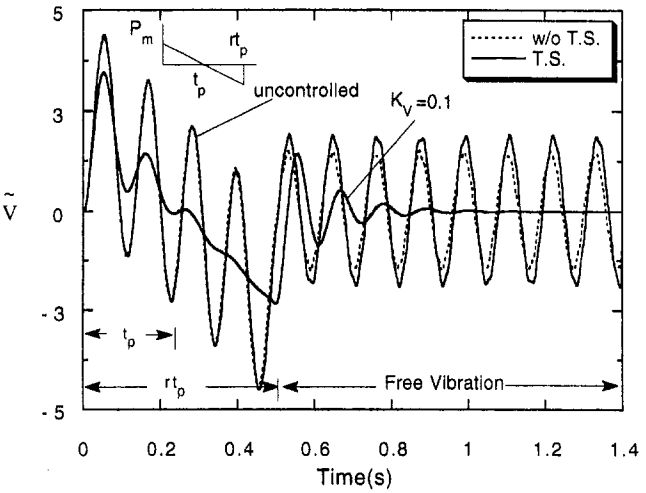


Fig. 7 Influence of the transverse shear effect on open and closed-loop transversal deflection time-history under a sonic-boom pressure pulse. Free-warping beam model, $\theta = 45$ deg, $\bar{R} = 16$, $r = 2$, $t_p = 0.25$ s.

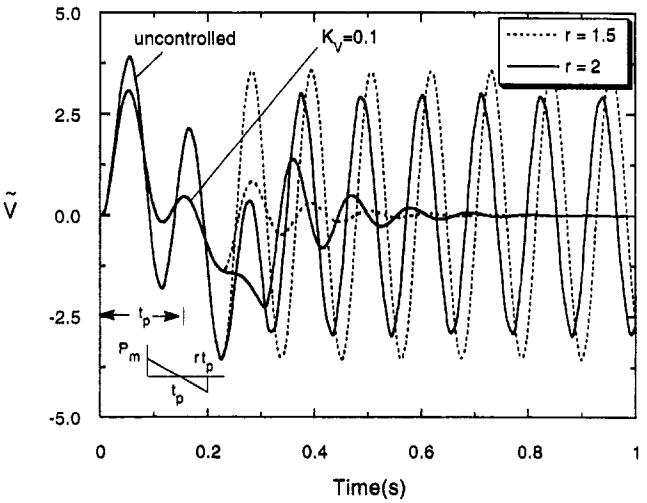


Fig. 8 Effect of the extent of the negative phase of the sonic-boom pressure pulse on the open and closed-loop transversal deflection time-history to a sonic-boom pulse. Nonshearable and warping restraint beam model $\theta = 45$ deg, $t_p = 0.15$ s, $\bar{R} = 16$.

that with the increase of the velocity feedback gain a dramatic reduction of the deflection and twist throughout the forced and free-motion ranges, and specially within the latter one, can be achieved. Figure 6 highlights the effects played by the warping restraint upon the open and closed-loop dynamic response of the beam subjected to a rectangular pressure pulse. The results reveal that in the forced motion range, although the warping restraint yields a reduction of the deflection amplitudes as compared to their free-warping counterpart, the reduction is less dramatic as compared to that experienced in the free-motion regime. However, when the beam is activitated, for the same feedback gain, the differences of the deflection amplitudes as experienced in the free and constrained warping beam models are more modest in the free motion regime than in the forced-motion one.

In Figs. 7–9 the open and closed-loop dynamic response of cantilevers exposed to a sonic-boom signature are displayed.

The results reveal again the powerful effect played by the velocity feedback control in reducing the dynamic deflection in the forced and free-motion regimes. The results in Fig. 7 show that the effect of transverse shear flexibility is slightly manifested in the free-motion range only. In this respect, transverse shear effect results in an increase of the dynamic deflection amplitudes as compared to the unshearable beam model counterpart.

In Fig. 8 the influence of the extent of the negative phase of the sonic-boom pulse measured in terms of the parameter r, on the open and closed-loop dynamic response is highlighted. The results show that for the unactivated beam, an increased extent of the negative phase of the pulse has a beneficial influence on the dynamic response in the free-motion range. However, for the activitated beam, as time unfolds, this influence becomes totally negligible. Figure 9 depicts the open and closed-loop dynamic responses to a step-pulse. It clearly appears that the implementation of both velocity and acceleration feedback control laws results in both a reduction of response amplitudes and of the shift of their maxima towards larger times.

Finally, Fig. 10 depicts the dynamic response to a sinusoidal pressure pulse. The results from this plot reveal that implementation of the dual control methodology can play a powerful role in controlling the response in both the forced-motion range where the tailoring technique plays a more stronger role, and in the free-motion range, where the strain actuation technology becomes more efficient.

Downloaded 04 May 2010 to 171.66.16.26. Redistribution subject to ASME license or copyright; see http://www.asme.org/terms/Terms_Use.cfm

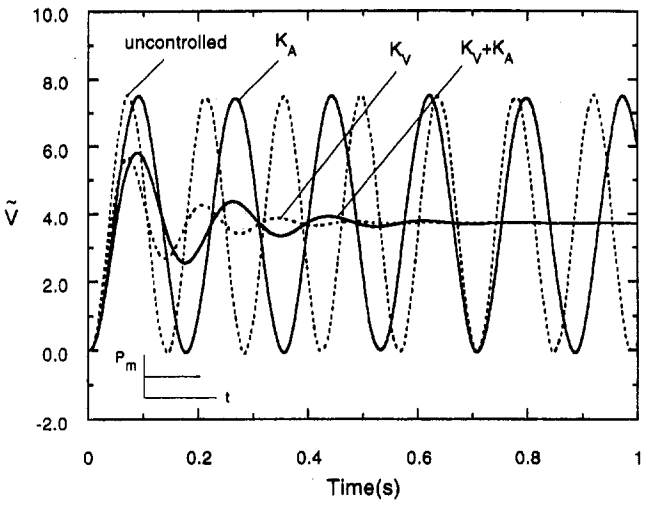


Fig. 9 Influence of the velocity and acceleration feedback control on the dimensionless transversal deflection time-history response to a step-pulse. Free-warping and nonshearable beam model $\theta = 0$ deg, $K_V = 0.1$, $K_A = 0.005$, $\mathcal{R} = 16$.

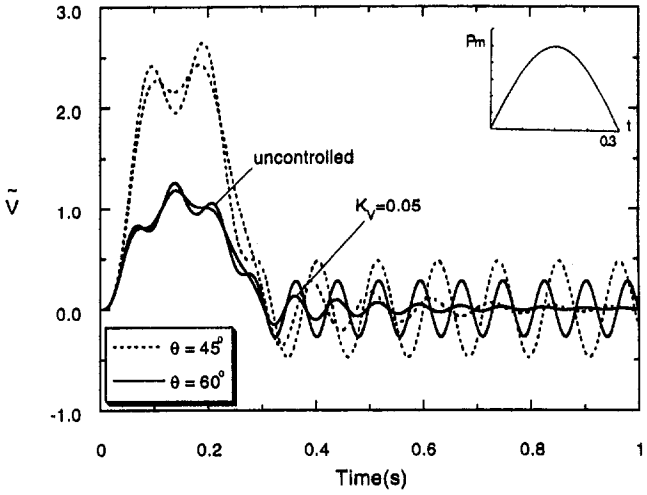


Fig. 10 Influence of the ply-angle and velocity feedback control upon the time-history transversal deflection to a sinusoidal pressure pulse. Nonshearable and warping restraint beam model, $\mathcal{R} = 16$.

Conclusions

A dual technology aimed at controlling the dynamic response of anisotropic thin-walled beam cantilevers to transient loadings was developed. The control is achieved through the simultaneous implementation of the tailoring technique and adaptive materials technology. The obtained results reveal the efficiency of this dual control methodology towards the enhancement of the dynamic response, in general, and of the combined feedback control law, in particular.

At the same time, the influence of a number of nonclassical effects featuring the beam model on the open and closed-loop dynamic responses, such as transverse shear and warping restraint, have been illustrated and their role assessed.

Last but not least, a powerful solution methodology enabling one to determine the open/closed-loop dynamic response of the structure was devised.

References

Bailey, T., and Hubbard, J. E., Jr., 1985, "Distributed Piezoelectric-Polymer Active Vibration Control of a Cantilever Beam," *Journal of Guidance, Control and Dynamics,* Vol. 8, No. 5, Sept.–Oct., pp. 605–611.

Baz, A., 1997, "Boundary Control of Beams Using Active Constrained Layer Damping," ASME *Journal of Vibration and Acoustics,* Vol. 9, pp. 166–172.

Berlincourt, D. A., Curran, D. R., and Jaffee, H., 1964, "Piezoelectric and Piezomagnetic Materials and Their Function in Transducers," *Physical Acoustics—Principles and Methods,* W. P. Mason, ed., Vol. 1, Part A, Academic Press, New York, pp. 169–270.

Birman, V., and Bert, C. W., 1987, "Behavior of Laminated Plates Subjected to Conventional Blast," *International Journal of Impact Engng.,* Vol. 6, No. 3, pp. 145–155.

Birman, V., 1994, "Analytical Models of Sandwich Plates with Piezoelectric Strip Stiffeners," *International Journal of Mechanical Sciences,* Vol. 36, No. 6, pp. 567–578.

Crawley, E. F., 1994, "Intelligent Structures for Aerospace; A Technology Overview and Assessment," *AIAA Journal,* Vol. 32, No. 8, pp. 1689–1699.

Crocker, M. J., 1966, "Theoretical and Experimental Response of Panels to Traveling Sonic Boom and Blast Waves," Wyle Laboratories, Research Staff, Rept. WR 66-2.

Crocker, M. J., 1970, Multimode Response of Panels to Normal and to Travelling Sonic Booms, *Journal Acoustical Society America.,* Vol. 42.

Gottlieb, J. J., and Ritzel, D. V., 1988, "Analytical Study of Sonic Boom From Supersonic Projectiles," *Progress in Aerospace Sciences,* Vol. 25, pp. 131–188.

Lagnese, J. E., and Lions, J. L., 1988, "Boundary Stabilization of Thin Plates," *Collection RMA,* Masson, Paris.

Lagnese, J. E., 1989, "Boundary Stabilization of Thin Plates," *SIAM Studies in Applied Mechanics,* SIAM, Philadelphia.

Librescu, L., and Nosier, A., 1990a, "Response of Laminated Composite Flat Panels to Sonic Boom and Explosive Blast Loadings," *AIAA Journal,* Vol. 28, No. 2, pp. 345–352.

Librescu, L., and Nosier, A., 1990b, "Dynamic Response of Anisotropic Composite Panels to Time-Dependent External Excitations," Paper ICAS-90-1.4R, *17th Congress of the International Council of the Aeronautical Sciences,* Stockholm, Sweden, Sept. pp. 2134–2144.

Librescu, L., and Simovich, J., 1988, "General Formulation for the Aeroelastic Divergence of Composite Swept Forward Wing Structures," *Journal of Aircraft,* Vol. 25, No. 4, pp. 364–371.

Librescu, L., and Thangjitham, S., 1991, "Analytical Studies on Static Aeroelastic Behavior of Forward-Swept Composite Wing Structures," *Journal of Aircraft,* Vol. 28, No. 2, pp. 151–157.

Librescu, L., and Song, O., 1992, "On the Static Aeroelastic Tailoring of Composite Aircraft Swept Wings Modelled as Thin-Walled Beam Structures," *Composites Engineering,* Vol. 2, No. 5–7 (Special Issue: *Use of Composites in Rotorcraft and Smart Structures*), pp. 497–512.

Librescu, L., Song, O., and Rogers, C. A., 1993, "Adaptive Vibrational Behavior of Cantilevered Structures Modeled as Composite Thin-Walled Beams," *International Journal of Engineering Science,* Vol. 31, No. 5, pp. 775–792.

Librescu, L., Meirovitch, L., and Song, O., 1996, "Integrated Structural Tailoring and Adaptive Materials Control for Advanced Aircraft Wings," *Journal of Aircraft,* Vol. 33, No. 1, Jan.–Feb. pp. 203–213.

Lin, C. Y., and Crawley, E. F., 1995, "Aeroelastic Actuation Using Elastic and Induced Strain Anisotropy," *Journal of Aircraft,* Vol. 32, No. 5, pp. 1130–1137.

Rao, S. S., and Sunar, M., 1994, "Piezoelectricity and its Use in Disturbance Sensing and Control of Flexible Structures: A Survey," ASME *Applied Mechanics Reviews,* Vol. 31, pp. 113–123.

Rehfield, L. W., and Atilgan, A. R., 1989, "Toward Understanding the Tailoring Mechanisms for Thin-Walled Composite Tubular Beams," Proceedings of the First USSR-U.S. Symposium on Mechanics of Composite Materials, S. W. Tsai, J. M. Whitney, T.-W. Chou, and R. M. Jones, eds., May 23–26, Riga, Latvia SSR, ASME, New York, pp. 187–196.

Smith, E. C., and Chopra, I., 1991, "Formulation and Evaluation of an Analytical Model for Composite Box-Beams," *Journal of the American Helicopter Society,* Vol. 36, No. 3, pp. 23–35.

Song, O., and Librescu, L., 1993, "Free Vibration of Anisotropic Composite Thin-Walled Beams of Closed Cross-Section Contour," *Journal of Sound and Vibration,* Vol. 167, No. 1, pp. 129–147.

Tzou, H. S., and Zhong, J. P., 1992, "Adaptive Piezoelectric Structures: Theory and Experiment," *Active Materials and Adaptive Structures, Materials and Structures Series,* G. J. Knowles, ed., Institute of Physics, pp. 219–224.

Tzou, H. S., 1993, *Piezoelectric Shells, Distributed Sensing and Control of Continua,* Kluwer, Dordrecht, The Netherlands.

Weisshaar, T. A., 1987, "Aeroelastic Tailoring—Creative Use of Unusual Materials," AIAA/ASME/ASCE/AHS 28th Structures, Structural Dynamics, and Materials Conference, Apr. 9–10, AIAA Paper 87-9076.

Downloaded 04 May 2010 to 171.66.16.26. Redistribution subject to ASME license or copyright; see http://www.asme.org/terms/Terms_Use.cfm

Dynamics of a Simple Model for a Wind-Loaded Nonlinear Structure: Bifurcations of Codimension One and Two

K. Yagasaki
Associate Professor,
Department of Mechanical and Systems Engineering,
Gifu University,
Gifu, Gifu 501-1193, Japan

The motion induced by vortex shedding of a structure with nonlinear restoring force is investigated. In particular, a conclusion about nonexistence of bounded motions obtained for a similar problem in the previous study is improved by taking into account the nonlinear restoring force characteristic. The vortex shedding frequency is assumed to be close to the natural frequency of the cross-wind oscillation and the along-wind oscillation is not excited, so that a single-degree-of-freedom model representing the cross-wind motions is obtained. The averaging method is applied to the single-degree-of-freedom system, and the normal form and center manifold theories are used to discuss bifurcations of codimension one, saddle-node and Hopf bifurcations. Moreover, it is shown that a multiple bifurcation of codimension two, called the Bogdanov-Takens bifurcation, occurs in the averaged system. The implications of the averaging results on the dynamics of the original single-degree-of-freedom system are described. Numerical examples are also given with numerical simulation results for both the averaged and original systems to demonstrate our theoretical predictions.

1 Introduction

Holmes and Lin (1978) studied a deterministic (turbulent-free) wind loading problem in which a structure with linear restoring force is excited by vortex shedding (Blevins, 1990). They showed that the cross-wind motions are likely to be more dangerous than the along-wind motions and analyzed the primary resonance case in which the vortex shedding frequency is close to the natural frequency of the cross-wind oscillations. The occurrence of saddle-node bifurcations at which two periodic orbits coalesce was detected and nonexistence of bounded motions was predicted in some parameter regions (see Section 3). To discuss the fate of the structure for the parameter regions, higher-order terms neglected in their model have to be taken into account.

The third-order subharmonic resonance behavior in their model was also studied by Holmes (1979). He discussed the possibility of the domain of stability to have an extremely complex boundary, so-called *fractal basin boundary* (e.g., Moon, 1992), when there exists an open set of initial points for which orbits tend to the infinity as $t \to \infty$, although a further careful treatment is now proven to be needed to reach this conclusion (cf. Section 4.7 of Guckenheimer and Holmes, 1983; and Holmes et al., 1988). See also Holmes (1981). Moreover, influences of a stochastic term representing the turbulent wind component were described in Vaicaitis et al. (1973) and Lin and Holmes (1978).

In this paper, the motion of a structure induced by vortex shedding is also investigated. Our model is similar to that of Holmes and Lin (1978) but has a nonlinear restoring force characteristic. The case in which their model has no bounded motions is treated appropriately. The approaches used here contain the averaging method and modern dynamical systems theory including the normal form and center manifold techniques. The use of dynamical systems theory developed for two decades reveals the occurrence of some different dynamical phenomena from the linear restoring force case. See the books of Guckenheimer and Holmes (1983), Wiggins (1990), and Kuznetsov (1995) for the necessary information on the dynamical systems theory.

This paper is organized as follows. In Section 2 an analytical model for a wind-loaded structure is described. The vortex shedding frequency is assumed to be close to the natural frequency of the cross-wind oscillations and the along-wind oscillation is not excited, so that a single-degree-of-freedom model representing the cross-wind motions is obtained. In Section 3 the result of Holmes and Lin (1978) is reviewed. In Section 4 simple bifurcations of codimension one, saddle-node and Hopf bifurcations, in the averaged system are analyzed. Roughly speaking, the codimension of bifurcations indicates the number of parameters required for describing the bifurcations. See the above references for details. In Section 5 a multiple bifurcation of codimension two called the Bogdanov-Takens bifurcation is discussed. In Section 6 numerical examples are given with numerical simulation results for both the averaged and original systems to demonstrate our theoretical predictions. Finally a summary and some comments are stated in Section 7.

2 Analytical Model

The model considered here is a box-type structure shown in Fig. 1. We assume that the structure moves only in the x and y-directions and the mean wind is directed in the x-direction. Holmes and Lin (1978) studied a similar problem and reduced it to a two-degree-of-freedom system

$$\ddot{x} + \bar{\delta}_1\dot{x} - \bar{\alpha}\dot{x}^2 + \omega_1^2 x = 0,$$

$$\ddot{y} + \bar{\delta}_2\dot{y} - \bar{\beta}y^2\cos\omega t + \omega_2^2 y = 2\bar{\beta}(U - \dot{x})^2\cos\omega t, \quad (1)$$

Contributed by the Applied Mechanics Division of THE AMERICAN SOCIETY OF MECHANICAL ENGINEERS for publication in the ASME JOURNAL OF APPLIED MECHANICS.

Discussion on the paper should be addressed to the Technical Editor, Professor Lewis T. Wheeler, Department of Mechanical Engineering, University of Houston, Houston, TX 77204-4792, and will be accepted until four months after final publication of the paper itself in the ASME JOURNAL OF APPLIED MECHANICS.

Manuscript received by the ASME Applied Mechanics Division, May 7, 1997; final revision, Nov. 15, 1997. Associate Technical Editor: S. W. Shaw.

 Copyright © 1998 by ASME

Downloaded 04 May 2010 to 171.66.16.26. Redistribution subject to ASME license or copyright; see http://www.asme.org/terms/Terms_Use.cfm

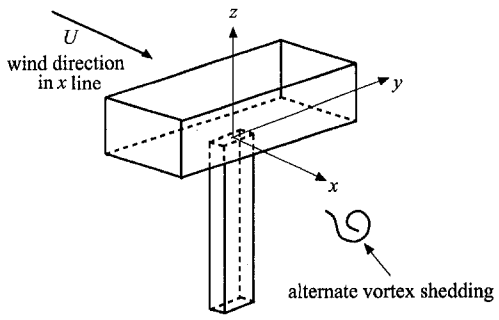


Fig. 1 A wind-loaded structure

where a dot denotes the differentiation with respect to t. The positive constants $\bar{\delta}_j$ and $\omega_j, j = 1, 2$, are the damping constants and natural angular frequencies, $\bar{\alpha}$ and $\bar{\beta}$ are aerodynamic and physical constants, U is the mean wind speed, and ω is the vortex-shedding frequency. Note that parametric excitation also appears in the linear damping term unless the y-component of the mean-wind velocity is zero (see Lin and Holmes, 1978). To take into account a nonlinear characteristic of the restoring force of the structure, we modify (1) as

$$\ddot{x} + \bar{\delta}_1 \dot{x} - \bar{\alpha}\dot{x}^2 + f_1(x, y) = 0,$$

$$\ddot{y} + \bar{\delta}_2 \dot{y} - \bar{\beta}\dot{y}^2 \cos \omega t + f_2(x, y) = 2\bar{\beta}(U - \dot{x})^2 \cos \omega t, \quad (2)$$

where $f_j(x, y)$, $j = 1, 2$, are nonlinear functions of x and y representing the nonlinear restoring force.

Moreover, we assume that the along-wind oscillation is not excited and $x \to 0$ as $t \to +\infty$. This means that one can set $x = \dot{x} = 0$ in the second equation of (2) if only steady-state responses are of interest. In addition, it is assumed that y is small and the restoring force has a symmetry about $y = 0$. So we choose a cubic function as $f_2(0, y)$ and obtain equation of motion

$$\ddot{y} + \bar{\delta}_2 \dot{y} - \bar{\beta}\dot{y}^2 \cos \omega t + y + \epsilon y^3 = \bar{\gamma} \cos \omega t \quad (3)$$

for the cross-wind oscillation, where ϵ is a small parameter and $\bar{\gamma} = 2\bar{\beta}U^2$. Here the time t was also scaled with the natural angular frequency ω_2, and the same notations were used for the parameters before and after scaling. In the following sections we study the dynamics of (3) under the primary resonance $\omega \approx 1$. The Hopf bifurcation behavior in (3) was also analyzed by a perturbation technique called Melnikov's method in Yagasaki (1996). Here the averaging method is used and other bifurcations of codimension one and two as well as the Hopf bifurcations are analyzed.

The above assumption on the along-wind oscillation holds for linear restoring force under an appropriate condition (see Holmes and Lin, 1978) but may not hold for a nonlinear restoring force due to the presence of the coupling terms in the nonlinear forcing. The coupled motion in the along and cross-wind directions is also of interest, but we do not pursue the problem and concentrate on the effect of the nonlinear restoring force characteristic on the dynamical behavior of the structure.

3 The Linear Restoring Force Case

The result of Holmes and Lin (1978) for the case of linear restoring force is first reviewed from the view point of dynamical systems theory. When the restoring force is linear, i.e., $\epsilon = 0$, Eq. (3) becomes

$$\ddot{y} + \bar{\delta}_2 \dot{y} - \bar{\beta}\dot{y}^2 \cos \omega t + y = \bar{\gamma} \cos \omega t. \quad (4)$$

Introduce a small parameter ϵ again and assume that $\bar{\delta}_2$, $\bar{\beta}$, $\bar{\gamma} = O(\epsilon)$ and $\omega = 1 + O(\epsilon)$. Let $\bar{\delta}_2 = \epsilon\delta$, $\bar{\beta} = \epsilon\beta$, $\bar{\gamma} = \epsilon\gamma$ and $\epsilon\Omega = \omega^2 - 1$. By using the van der Pol transformation

$$\begin{pmatrix} u \\ v \end{pmatrix} = \begin{pmatrix} \cos \omega t & -\frac{1}{\omega} \sin \omega t \\ -\sin \omega t & -\frac{1}{\omega} \cos \omega t \end{pmatrix} \begin{pmatrix} y \\ \dot{y} \end{pmatrix} \quad (5)$$

and applying the averaging method (e.g., Guckenheimer and Holmes, 1983), Eq. (4) becomes

$$\dot{u} = -\delta u + \Omega v - \frac{\beta}{2} uv,$$

$$\dot{v} = -\Omega u - \delta v - \frac{\beta}{4}(u^2 + 3v^2) - \gamma, \quad (6)$$

where the time t was rescaled from t to $\epsilon t/2$.

Let $(u, v) = (u_0, v_0)$ be a fixed point of the averaged system (6), i.e.,

$$-\delta u_0 + \Omega v_0 - \frac{\beta}{2} u_0 v_0 = 0,$$

$$-\Omega u_0 - \delta v_0 - \frac{\beta}{4}(u_0^2 + 3v_0^2) - \gamma = 0. \quad (7)$$

By the averaging theorem (Guckenheimer and Holmes, 1983), the fixed point corresponds to a harmonic orbit in the original system (4) approximately given by

$$y = u_0 \cos \omega t - v_0 \sin \omega t \quad (8)$$

if it is hyperbolic. The stability type of the harmonic orbit in (4) is the same as that of the fixed point in (6). Moreover, a hyperbolic periodic orbit in (6) corresponds to a two-dimensional normally hyperbolic invariant torus consisting of quasi-periodic orbits with the same stability type in (4).

If the fixed point (u_0, v_0) is nonhyperbolic, i.e., the Jacobian matrix of the right-hand side of (6) at $(u, v) = (u_0, v_0)$,

$$\begin{pmatrix} -\delta - \beta v_0/2 & \Omega - \beta u_0/2 \\ -\Omega - \beta u_0/2 & -\delta - 3\beta v_0/2 \end{pmatrix}, \quad (9)$$

has a zero eigenvalue or a pair of purely imaginary eigenvalues, then a bifurcation of codimension one, which can be generically observed with only one control parameter, can occur in (6) under a nondegenerate condition. See the references on dynamical systems theory cited in Section 1 for details. Near the parameter values at which the bifurcations of fixed points occur in the averaged system (6), the corresponding bifurcations of harmonic orbits also occur in the original system (4) (see Guckenheimer and Holmes, 1983).

Choose γ as a control parameter and let the other parameters be fixed. Suppose that

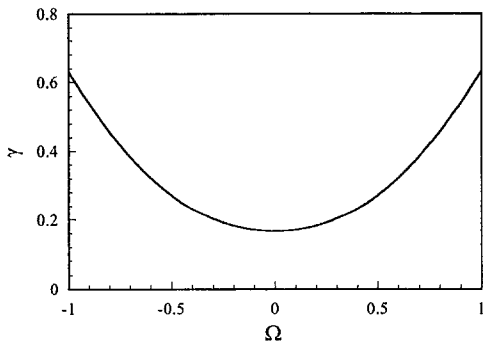


Fig. 2 A saddle-node bifurcation set for Eq. (6) with $\delta = 1$ and $\beta = 2$

Downloaded 04 May 2010 to 171.66.16.26. Redistribution subject to ASME license or copyright; see http://www.asme.org/terms/Terms_Use.cfm

$$\delta^2 + \Omega^2 + 2\beta\delta v_0 - \frac{\beta^2}{4}(u_0^2 - 3v_0^2) = 0 \qquad (10)$$

and

$$\delta + \beta v_0 \neq 0 \qquad (11)$$

as well as condition (7) holds for $\gamma = \gamma_0$. Then the Jacobian matrix (9) has a zero eigenvalue and Eq. (6) becomes

$$\dot{\xi} = \frac{a_0}{\lambda_0}\xi^2 + \frac{1}{\lambda_0}(\gamma - \gamma_0), \quad \dot{\eta} = \lambda_0\eta - \frac{1}{\lambda_0}(\gamma - \gamma_0) \qquad (12)$$

under a linear transformation such that the coefficient matrix is diagonalized, where the higher-order terms are eliminated and

$$a_0 = \frac{\beta}{4}\left[3\left(\delta + \frac{\beta}{2}v_0\right)^2 + \left(\Omega - \frac{\beta}{2}u_0\right)^2 + 2\left(\delta + \frac{\beta}{2}v_0\right)\left(\delta + \frac{3\beta}{2}v_0\right)\right],$$

$$\lambda_0 = -2(\delta + \beta v_0) \neq 0. \qquad (13)$$

It is not difficult to show from (7) and (10) that a_0 is positive. Equation (12) including the eliminated higher-order terms has a center manifold $\eta = O(\xi^2, \xi(\gamma - \gamma_0), (\gamma - \gamma_0)^2)$ at $(\xi, \eta) = (0, 0)$ for $\gamma \approx \gamma_0$. Hence, by the center manifold theorem, the dynamics of (12) with the higher-order terms and hence of (6) are determined by the first equation of (12) near $(\xi, \eta, \gamma) = (0, 0, \gamma_0)$. So two fixed points appear at $\gamma = \gamma_0$ as the control parameter γ is decreased, i.e., a subcritical saddle-node bifurcation occurs. For $\gamma < \gamma_0$, one of the fixed points is stable and the other is unstable if $\lambda_0 < 0$, and both are unstable if $\lambda_0 > 0$. It is also shown that the Jacobian matrix (9) never has purely imaginary eigenvalues.

Figure 2 shows the saddle-node bifurcation set in the (Ω, γ)-space for $\delta = 1$ and $\beta = 2$, and Fig. 3 shows the phase portraits in two regions of Fig. 2. Here the bifurcation curve was obtained by using a computer software called "AUTO" (Doedel and Kernévez, 1986) and solving (7) and (10), and the numerically computed solutions of (6) were obtained by a computer software called "Dynamics" (Nusse and Yorke, 1994). Thus, there is a parameter region in which no bounded solutions exist, and nonlinear terms ignored in this model may be dominant there. Our object is to describe how the dynamics of a structure of Fig. 1 change in such a parameter region owing to its nonlinear restoring force characteristic.

4 Bifurcations of Codimension One

We turn to the case of nonlinear restoring force. Again, set $\bar{\delta}_2 = \epsilon\delta$, $\bar{\beta} = \epsilon\omega$, $\bar{\gamma} = \epsilon\gamma$ and $\epsilon\Omega = \omega^2 - 1$. Application of the van der Pol transformation (5) and the averaging method to (3) yields

$$\dot{u} = -\delta u + \Omega v - \frac{\beta}{2}uv - \frac{3}{4}(u^2 + v^2)v,$$

$$\dot{v} = -\Omega u - \delta v - \frac{\beta}{4}(u^2 + 3v^2) + \frac{3}{4}(u^2 + v^2)u - \gamma, \qquad (14)$$

where the time t was also rescaled as $t \to \epsilon t/2$. Let (u_0, v_0) be a fixed point of (14),

$$-\delta u_0 + \Omega v_0 - \frac{\beta}{2}u_0v_0 - \frac{3}{4}(u_0^2 + v_0^2)v_0 = 0,$$

$$-\Omega u_0 - \delta v_0 - \frac{\beta}{4}(u_0^2 + 3v_0^2) + \frac{3}{4}(u_0^2 + v_0^2)u_0 - \gamma = 0. \qquad (15)$$

The Jacobian matrix of the right-hand side of (14) at $(u, v) = (u_0, v_0)$ is given by

$$\begin{pmatrix} -\delta - \beta v_0/2 - 3u_0v_0/2 & \Omega - \beta u_0/2 - 3(u_0^2 + 3v_0^2)/4 \\ -\Omega - \beta u_0/2 + 3(3u_0^2 + v_0^2)/4 & -\delta - 3\beta v_0/2 + 3u_0v_0/2 \end{pmatrix}. \qquad (16)$$

Choose γ as a control parameter and let the other parameters be fixed.

Suppose that

$$16(\delta^2 + \Omega^2) + 32\beta\delta v_0 - 48\Omega(u_0^2 + v_0^2) - 4\beta^2(u_0^2 - 3v_0^2) + 12\beta(u_0^2 + v_0^2)u_0 + 27(u_0^2 + v_0^2)^2 = 0 \qquad (17)$$

and condition (11) holds at the fixed point when $\gamma = \gamma_{sn}$. Then just one of the eigenvalues of the Jacobian matrix (16) is zero, and Eq. (14) can be rewritten as

$$\dot{\xi} = \frac{a_{sn}}{\lambda_0}\xi^2 + \frac{1}{\lambda_0}(\gamma - \gamma_{sn}), \quad \dot{\eta} = \lambda_0\eta - \frac{1}{\lambda_0}(\gamma - \gamma_{sn}) \qquad (18)$$

under a change of coordinate as in (12), where the higher-order terms are eliminated and

$$a_{sn} = \frac{\beta}{4}(3d_{11}^2 + d_{12}^2 + 2d_{11}d_{22}) - \frac{3u_0}{4}(d_{11}^2 + 3d_{12}^2 - 2d_{11}d_{22}) - \frac{3v_0}{4d_{12}}(3d_{11}^2d_{22} + d_{12}^2d_{22} - 2d_{11}d_{12}^2), \qquad (19)$$

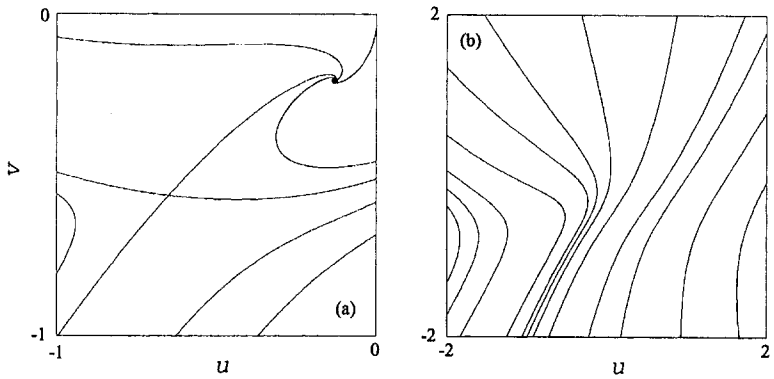


Fig. 3 Phase portraits of Eq. (6) for $\delta = 1$, $\beta = 2$ and $\Omega = 0.5$. (a) $\gamma = 0.2$; (b) $\gamma = 0.5$.

Downloaded 04 May 2010 to 171.66.16.26. Redistribution subject to ASME license or copyright; see http://www.asme.org/terms/Terms_Use.cfm

with d_{ij} the (i, j)-element of the Jacobian matrix (16). If $a_{sn} \neq 0$, then a saddle-node bifurcation occurs at $\gamma = \gamma_{sn}$. The bifurcation is supercritical if $a_{sn} < 0$, and subcritical if $a_{sn} > 0$. Moreover, one of the fixed points born at the bifurcation is stable and the other is unstable if $\lambda_0 < 0$, and both are unstable if $\lambda_0 > 0$.

In polar coordinates $r = \sqrt{u^2 + v^2}$ and $\theta = \arctan(v/u)$, Eq. (14) becomes

$$\dot{r} = -\delta r - \left(\gamma + \frac{3}{4}\beta r^2\right)\sin\theta,$$

$$\dot{\theta} = -\Omega + \frac{3}{4}r^2 - \left(\gamma + \frac{1}{4}\beta r^2\right)\frac{\cos\theta}{r}. \tag{20}$$

Suppose that

$$\gamma = \gamma_\pm = \frac{\beta}{18}\left[(\beta^2 + 6\Omega) \pm \sqrt{\beta^4 + 12\beta^2\Omega - 9\delta^2}\right] \tag{21}$$

and

$$\gamma > \frac{\beta(2\Omega + \sqrt{4\Omega^2 + \delta^2})}{12}, \tag{22}$$

where

$$\Omega \geq \frac{9\delta^2 - \beta^4}{12\beta^2}. \tag{23}$$

(Note that condition (21) holds if equality holds in (11) and that condition (17) holds if equality holds in (22).) Then the point

$$(r_0, \theta_0) = \left(2\sqrt{\frac{\gamma_\pm}{\beta}}, \arctan\frac{\beta\delta}{2(\beta\Omega - 3\gamma_\pm)}\right) \tag{24}$$

is a fixed point of (20) at which the Jacobian matrix of the right-hand side of (20),

$$\begin{pmatrix} -\delta - 3\beta r\sin\theta/2 & -(\gamma_\pm + 3\beta r^2/4)\cos\theta \\ -3r/2 + (\gamma_\pm/r^2 - \beta/4)\cos\theta & (\gamma_\pm + \beta r^2/4)\sin\theta/r \end{pmatrix} \tag{25}$$

has a pair of purely imaginary eigenvalues. Furthermore, under a change of coordinates, Eq. (20) is transformed into

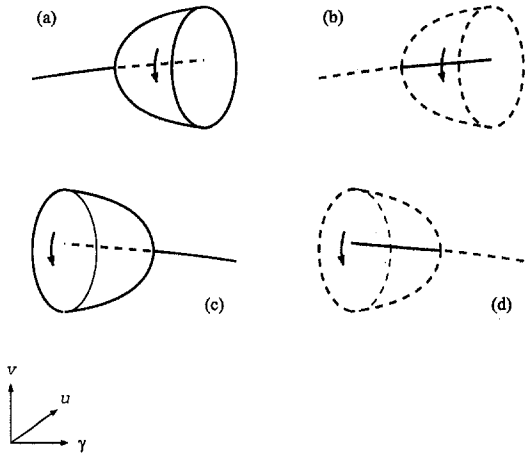


Fig. 4 Bifurcation diagrams near the Hopf bifurcation points for Eq. (26) with $\nu_\pm > 0$, where $u = \rho\cos\phi$ and $v = \rho\sin\phi$. (a) $a_\pm < 0$ and $d_\pm > 0$; (b) $a_\pm > 0$ and $d_\pm < 0$; (c) $a_\pm < 0$ and $d_\pm < 0$; (d) $a_\pm > 0$ and $d_\pm > 0$. Solid curves represent stable orbits and broken curves unstable orbits.

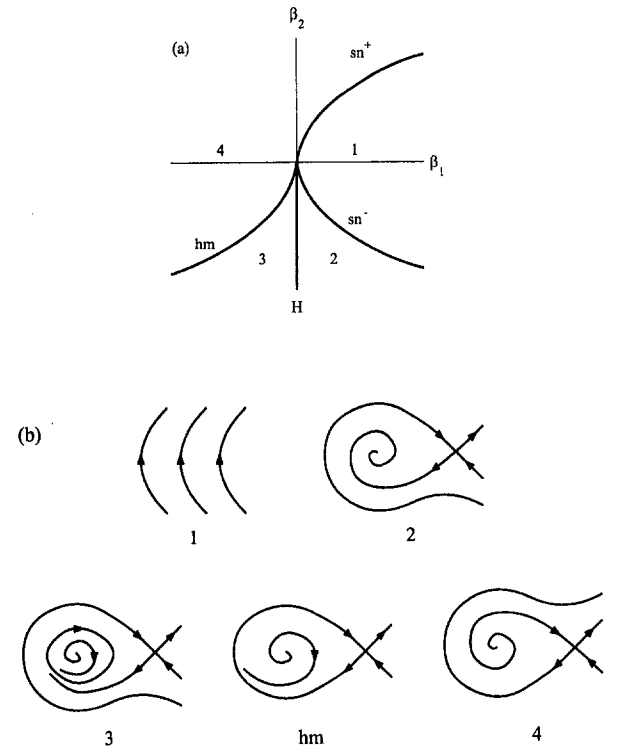


Fig. 5 The Bogdanov-Takens bifurcation with $s = -1$. (a) Bifurcation sets for Eq. (32); (b) phase portraits in regions of Fig. 5(a). "sn$^\pm$", "H" and "hm" represent saddle-node, Hopf, and homoclinic bifurcation sets, respectively.

$$\dot{\rho} = [d_\pm(\gamma - \gamma_\pm) + a_\pm\rho^2]\rho, \quad \dot{\phi} = \nu_\pm, \tag{26}$$

where

$$a_\pm = -\frac{3\delta}{32\beta^3\nu_\pm^2}(648\gamma_\pm^3 - 396\beta\Omega\gamma_\pm^2 + 48\beta^2\Omega^2\gamma_\pm + \beta^3\Omega(4\Omega^2 + \delta^2),$$

$$d_\pm = -\frac{\delta[36\gamma_\pm^2 - \beta^2(4\Omega^2 + \delta^2)]}{2\gamma(144\gamma_\pm^2 - 48\beta\Omega\gamma_\pm - \beta^2\delta^2)},$$

$$\nu_\pm = \frac{1}{4\beta}\sqrt{144\gamma_\pm^2 - 48\beta\Omega\gamma_\pm - \beta^2\delta^2}, \tag{27}$$

and the higher-order terms are eliminated. See Guckenheimer

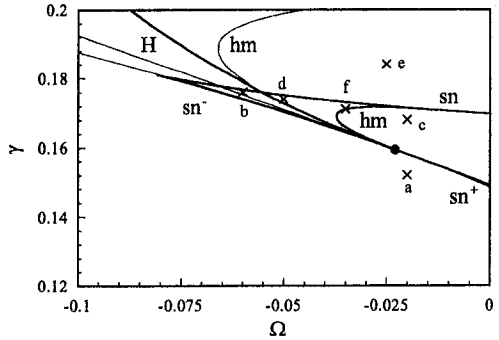


Fig. 6 Bifurcation sets for the averaged system (14) with $\delta = 1$ and $\beta = 2$. The curve "sn" represents a saddle-node bifurcation set and the other curves represent the same bifurcation sets as in Fig. 5. ● represents the Bogdanov-Takens bifurcation point. The thin curves were obtained from the normal form (32) of the Bogdanov-Takens bifurcation. The points "a" to "f" refer to parameter choices for the phase portraits of Fig. 7.

Downloaded 04 May 2010 to 171.66.16.26. Redistribution subject to ASME license or copyright; see http://www.asme.org/terms/Terms_Use.cfm

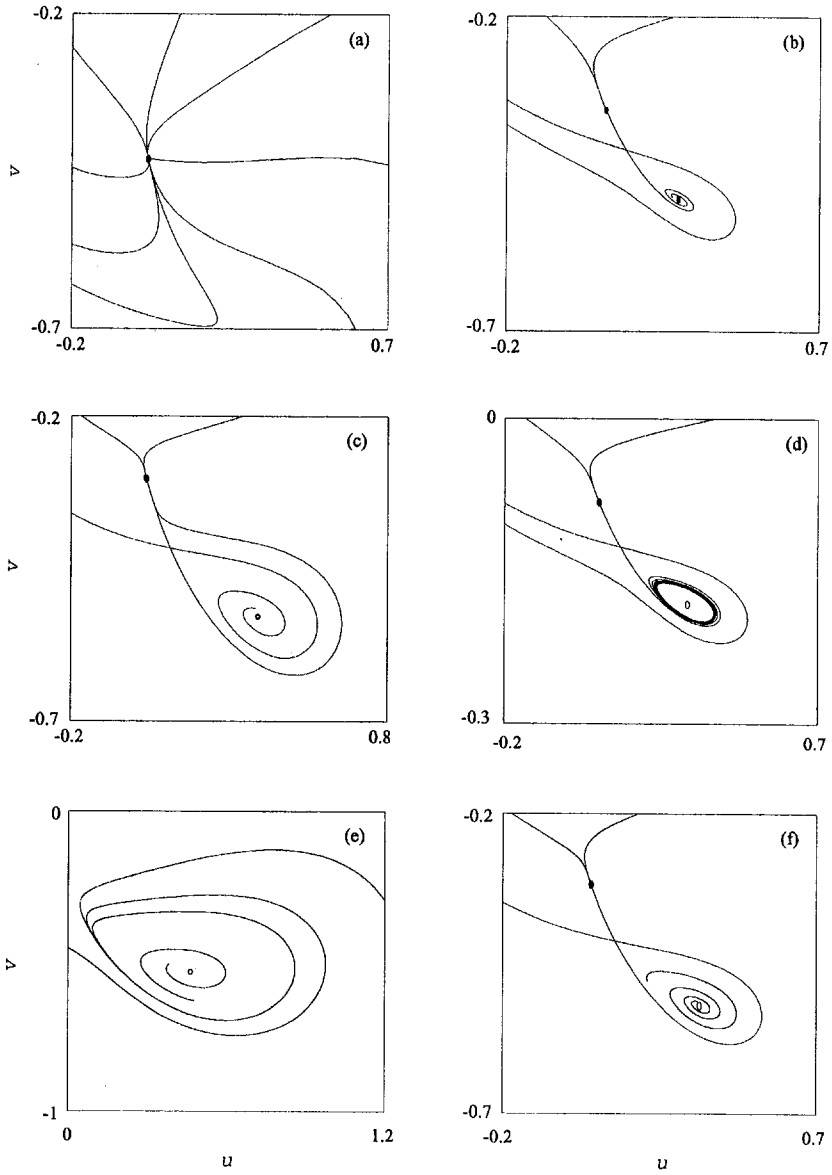


Fig. 7 Phase portraits of the averaged system (14) with $\delta = 1$ and $\beta = 2$. (*a*) $\gamma = 0.152$ and $\Omega = -0.02$; (*b*) $\gamma = 0.176$ and $\Omega = -0.06$; (*c*) $\gamma = 0.168$ and $\Omega = -0.02$; (*d*) $\gamma = 0.174$ and $\Omega = -0.05$; (*e*) $\gamma = 0.184$ and $\Omega = -0.025$; (*f*) $\gamma = 0.1710034$ and $\Omega = -0.03491334$. ● and ○ represent a sink and source, respectively.

and Holmes (1983) for the details on the necessary computation. Thus, we see that if $a_\pm, d_\pm \neq 0$, then the Hopf bifurcation occurs. When $a_\pm d_\pm < 0$ (respectively, $a_\pm d_\pm > 0$), it is supercritical (respectively, subcritical) and a periodic orbit appears (respectively, disappears) at $\gamma = \gamma_\pm$ as γ is increased. Moreover, the periodic orbit is stable (respectively, unstable) if $a_\pm < 0$ (respectively, > 0). See Fig. 4.

It is easily shown that $d_+ > 0$ and $d_- < 0$ if the inequality holds in (23) while $d_\pm = 0$ if the equality holds in (23). Substitution of (21) into the first equation of (27) also reveals that a_+ is negative. In addition, condition (22) holds for $\gamma = \gamma_+$. So the subcritical Hopf bifurcation occurs and a stable periodic orbit is born at $\gamma = \gamma_+$. However, the Hopf bifurcation at $\gamma = \gamma_-$ can be both supercritical and subcritical, and the periodic orbit born there can also be both stable and unstable. More precisely, if

$$648\gamma^3 - 396\beta\Omega\gamma^2 + 40\beta^2\Omega^2\gamma + \beta^3\Omega(4\Omega^2 + \delta^2) < 0 \quad \text{(respectively, } > 0\text{)}, \tag{28}$$

then the supercritical (respectively, subcritical) Hopf bifurcation occurs at $\gamma = \gamma_-$ and the periodic orbit born there is stable (respectively, unstable). These Hopf bifurcation results were also obtained by using Melnikov's method in Yagasaki (1996).

5 Bifurcations of Codimension Two: The Bogdanov-Takens Bifurcations

If condition (21) holds and equality holds in (22) instead of inequality, i.e.,

$$\gamma = \frac{\beta(2\Omega + \sqrt{4\Omega^2 + \delta^2})}{12}, \tag{29}$$

then the Jacobian matrix (25) has two zero eigenvalues. In such a case, a bifurcation of codimension two called the Bogdanov-Takens bifurcation may occur in (20) and hence (14). Here "codimension two" means that two control parameters are required to observe the bifurcation in general. Now we analyze the degenerate case.

Denote by γ_{BT} and Ω_{BT} the values of γ and Ω such that (21) and (29) hold. It follows that $\Omega = \Omega_{BT}$ is a root of the cubic equation

Downloaded 04 May 2010 to 171.66.16.26. Redistribution subject to ASME license or copyright; see http://www.asme.org/terms/Terms_Use.cfm

$$768\beta^2\Omega^3 - 576\delta^2\Omega^2 + 336\beta^2\delta^2\Omega + \delta^2(16\beta^4 - 225\delta^2) = 0 \quad (30)$$

such that Eq. (23) holds. By (23), only γ_- in (21) has to be considered as γ_{BT}, i.e.,

$$\gamma_{BT} = \frac{\beta}{18}\left[(\beta + 6\Omega_{BT}) - \sqrt{\beta^2 + 12\beta^2\Omega_{BT} - 9\delta^2}\right]. \quad (31)$$

The saddle-node and Hopf bifurcation curves given in Section 4 meet at the point $(\Omega_{BT}, \gamma_{BT})$ in the (Ω, γ)-space. After a lengthy manipulation, it is shown that Eq. (20) can be rewritten in the normal form of the Bogdanov-Takens bifurcation as

$$\dot{\eta} = \eta_2, \quad \dot{\eta}_2 = \beta_1 + \beta_2\eta_1 + \eta_1^2 + s\eta_1\eta_2, \quad (32)$$

near the fixed point (24) with $\gamma_\pm = \gamma_{BT}$ under a change of coordinates, where the higher-order terms are eliminated and

$$\beta_1 = \frac{B^4}{A^3}\left[\mu_{1,\gamma}(\gamma - \gamma_{BT}) + \mu_{1,\Omega}(\Omega - \Omega_{BT})\right],$$

$$\beta_2 = \frac{B^2}{A^2}\left[\mu_{2,\gamma}(\gamma - \gamma_{BT}) + \mu_{2,\gamma}(\Omega - \Omega_{BT})\right],$$

$$s = \text{sgn}\,(AB), \quad (33)$$

with

$$A = \frac{\beta^3\delta^5}{13824\gamma_{BT}^3} - \frac{\beta\delta^3}{32\gamma_{BT}} - \frac{6\delta\gamma_{BT}}{\beta}, \quad B = \frac{\beta\delta^2}{24\gamma_{BT}},$$

$$\mu_{1,\gamma} = \frac{3\delta}{2\beta} + \frac{\beta\delta^3}{192\gamma_{BT}^2}, \quad \mu_{1,\Omega} = \frac{\delta}{2},$$

$$\mu_{2,\gamma} = \frac{\beta^6\delta^8}{382205952\gamma_{BT}^7} - \frac{7\beta^4\delta^6}{2654208\gamma_{BT}^5} - \frac{\beta^2\delta^4}{9216\gamma_{BT}^3} + \frac{\delta^2}{8\gamma_{BT}},$$

$$\mu_{2,\Omega} = \frac{\beta^5\delta^6}{3981312\gamma_{BT}^5} - \frac{\beta^3\delta^4}{3072\gamma_{BT}^3} + \frac{\beta\delta^2}{12\gamma_{BT}} + \frac{24\gamma_{BT}}{\beta}. \quad (34)$$

Here the relation (29) was used and sgn is the signum function such that

$$\text{sgn}\,(x) = \begin{cases} 1 & \text{if } x > 0; \\ -1 & \text{if } x < 0; \\ 0 & \text{if } x = 0. \end{cases} \quad (35)$$

See Kuznetsov (1995) for the details on the necessary computation.

Figure 5 shows bifurcation sets of (32) in the (β_1, β_2)-space and its phase portraits for $s = -1$. The curves "sn$^\pm$" in Fig. 5(a)

$$4\beta_1 - \beta_2^2 = 0, \quad \beta_2 > 0 \quad \text{or} \quad < 0 \quad (36)$$

represent saddle-node bifurcations. There are a saddle and sink (respectively, source) in regions 2 (respectively, region 4) while there are no equilibria and limit cycles in region 1 (see Fig. 5(b)). The lower vertical axis "H,"

$$\beta_1 = 0, \quad \beta_2 < 0, \quad (37)$$

represents the Hopf bifurcations and in region 3 there are a saddle, source and stable limit cycle. The curve "hm" approximately given by

$$\beta_1 = -\frac{6}{25}\beta_2^2, \quad \beta_2 < 0 \quad (38)$$

represents new behavior which was not detected in Section 4, a homoclinic bifurcation: A homoclinic orbit exists and the limit cycle is broken. The higher-order terms eliminated in (32) do not affect the qualitative behavior of the untruncated system. For $s = 1$ a similar result is obtained except that the stability of equilibria and limit cycles is changed. See, e.g., Kuznetsov (1995) for more details.

The dynamics of the averaged system (14) near the fixed point (24) for $(\Omega, \gamma) \approx (\Omega_{BT}, \gamma_{BT})$ are qualitatively the same as those of the normal form (32). In addition, as stated in Section 3, hyperbolic fixed points (respectively, limit cycles) in the averaged system (14) correspond to hyperbolic harmonic orbits (respectively, two-dimensional normally hyperbolic invariant tori) with the same stability type in the original system (3). Near the saddle-node and Hopf bifurcation sets of fixed points in (14) there are also the corresponding bifurcation sets of harmonic orbits in (3). Furthermore, it can be shown on the basis of the results of Guckenheimer and Holmes (1983) and Holmes et al. (1988) that in a very narrow region of order $e^{-c/\epsilon}$ with c some constant near the homoclinic bifurcation set for (14), the stable and unstable manifolds of a saddle-type periodic orbit intersect transversely in (3). Such intersection implies the existence of chaotic orbits, which may be transient and unobservable in steady state. See the references cited in Section 1.

6 Numerical Examples

To demonstrate the above theoretical results, numerical examples are now given for $\epsilon = 0.1$, $\delta = 1$, and $\beta = 2$ (or, equivalently, $\bar{\delta}_2 = 0.1$ and $\bar{\beta} = 0.2$).

Figure 6 shows the bifurcation sets in the (Ω, γ)-space for the averaged system (14). The thick curves represent saddle-node and homoclinic bifurcation sets obtained by using the computer software "AUTO" as well as the Hopf bifurcation set given by (21)–(23), and the thin curves represent the bifurcation sets obtained from the analysis of Section 5. Both results are in good agreement near the Bogdanov-Takens bifurcation point although a saddle-node bifurcation curve "sn" cannot be detected by the analysis of Section 5. Note that the saddle-node bifurcation sets plotted as the thick curves can also be computed by solving (15) and (17). One also has $s = -1$ for the parameter values (see Eq. (34)), and the dynamics of (14) are the same as those of (32) in Fig. 5 near the Bogdanov-Takens bifurcation point. When γ is a control parameter, the lower saddle-node bifurcation curves "sn$^\pm$", for which $a_{sn} < 0$, represent supercritical ones and the upper curve "sn," for which $a_{sn} > 0$, represents subcritical one (see Eq. (19)). Condition $a_\pm > 0$ also holds on the Hopf bifurcation curve, and consequently a stable periodic orbit is born there.

Figure 7 shows the phase portraits of (14) obtained by the computer software "Dynamics." In Fig. 7(a) there is just one sink to all trajectories converge it as $t \to \infty$. Besides the sink, a sink and saddle appear in Fig. 7(b) and a saddle and source appear in Fig. 7(c). These fixed points are born upon passing

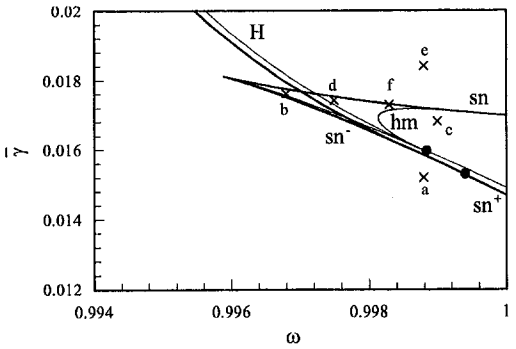


Fig. 8 Bifurcation sets of periodic orbits for the original system (3) with $\bar{\delta}_2 = 0.1$, $\bar{\beta} = 0.2$, and $\epsilon = 0.1$. The thick curves were obtained by direct application of AUTO while the thin curves were obtained from the averaging results of Fig. 6. The points "*a*" to "*f*" refer to parameter choices for the phase portraits of Fig. 9. See also the caption of Figs. 5 and 6.

Downloaded 04 May 2010 to 171.66.16.26. Redistribution subject to ASME license or copyright; see http://www.asme.org/terms/Terms_Use.cfm

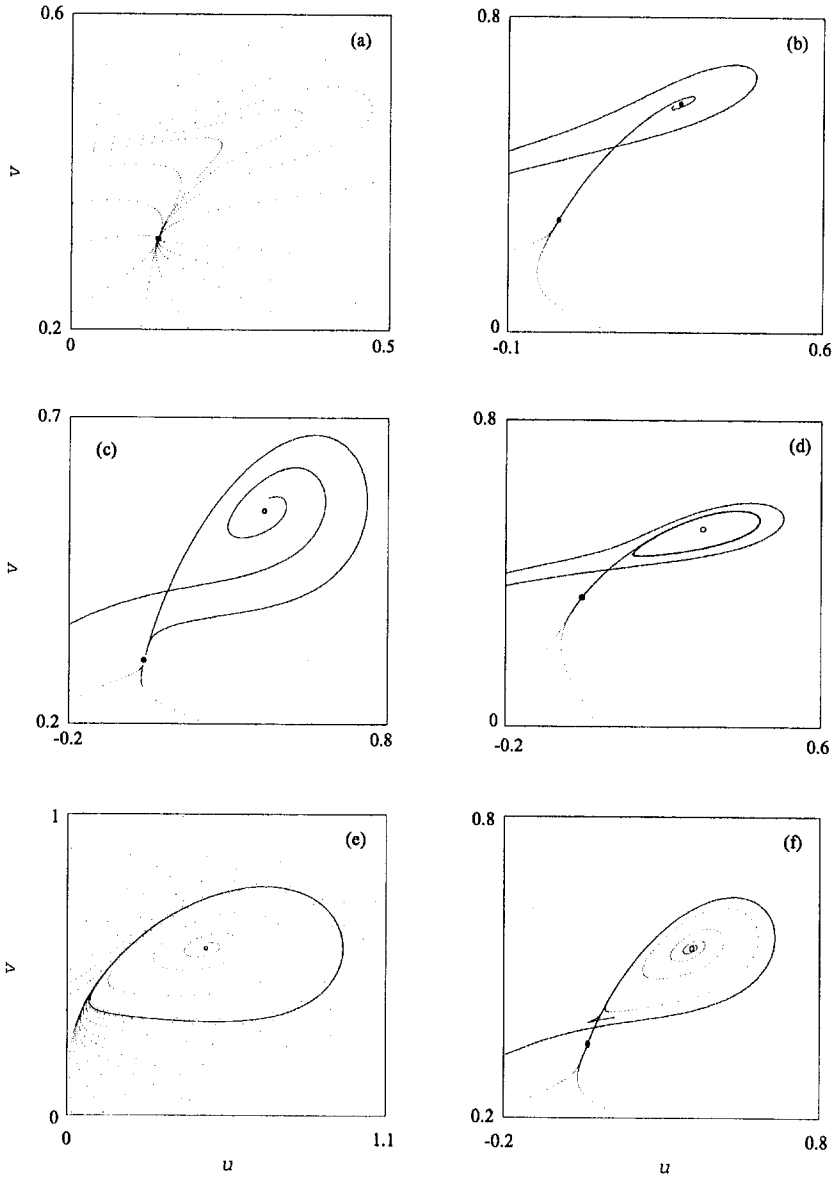


Fig. 9 Phase portraits of the Poincaré map of the original system (3) with $\bar{\delta}_2 = 0.1$, $\bar{\beta} = 0.2$ and $\epsilon = 0.1$. (*a*) $\gamma = 0.0152$ and $\omega = 0.9988$; (*b*) $\gamma = 0.0176$ and $\omega = 0.9968$; (*c*) $\gamma = 0.0168$ and $\omega = 0.999$; (*d*) $\gamma = 0.0174$ and $\omega = 0.9975$; (*e*) $\gamma = 0.0184$ and $\omega = 0.9988$; (*f*) $\gamma = 0.01727833$ and $\omega = 0.9983$. ● and ○ represent a sink and source, respectively.

through the saddle-node bifurcation curves "$\text{sn}^{\pm}$" in Fig. 6. Upon passing through the Hopf bifurcation curve "H" one of the two stable fixed points in Fig. 7(*b*) becomes unstable and a periodic orbit appears (see Fig. 7(*d*)). Moreover, upon passing through the saddle-node bifurcation curve "sn," the sink and saddle in Fig. 7(*b*) disappear (see Fig. 7(*e*)). The periodic orbit in Fig. 7(*d*) is also annihilated at a homoclinic bifurcation in Fig. 7(*f*). (cf. Figs. 7(*c*) and (*d*)). Thus, the results of the nonlinear restoring force case are very different from those of the linear restoring force case.

Direct numerical simulations were also performed for the original system (3). Figure 8 shows bifurcation sets of (3) obtained by the computer software "AUTO" as well as the averaging results of Fig. 6 in the $(\omega, \bar{\gamma})$-space. The direct simulation results are plotted as thick curves and the averaging results as thin curves. A good agreement is also found between both results although the homoclinic bifurcation curve could not be obtained by direct simulations.

Figure 9 shows numerically computed orbits of the Poincaré map of (3) defined by

$$P_\epsilon: (y(0), \dot{y}(0)) \to (y(T), \dot{y}(T)), \tag{39}$$

where $y(t)$ is a solution of (3) and $T = 2\pi/\omega$ is the forcing period. Again, the computer software "Dynamics" was used to obtain the orbits. Periodic orbits and two-dimensional invariant tori of (3) correspond to fixed points and invariant cycles of P_ϵ, respectively. It follows from the averaging theorem and the van der Pol transformation (5) that the Poincaré map P_ϵ has an orbit near

$$(y_n, \dot{y}_n) = (u(2t_n/\epsilon), -\omega v(2t_n/\epsilon)), \tag{40}$$

where $(u(t), v(t))$ is a solution of (14) and $t_n = 0 \bmod T$. Taking account of this relationship, one can predict the phase-space structure of the Poincaré map P_ϵ from that of the averaged system (14). By comparing Fig. 7 with Fig. 9, the result is seen to be fairly good. Moreover, the stable and unstable manifolds of a fixed point of P_ϵ intersect transversely in Fig. 9(*f*). The transverse intersection occurs only in a very narrow region of the parameter space. Figure 10 shows two types of stable periodic orbits and a stable quasi-periodic orbit of (3), which corre-

Downloaded 04 May 2010 to 171.66.16.26. Redistribution subject to ASME license or copyright; see http://www.asme.org/terms/Terms_Use.cfm

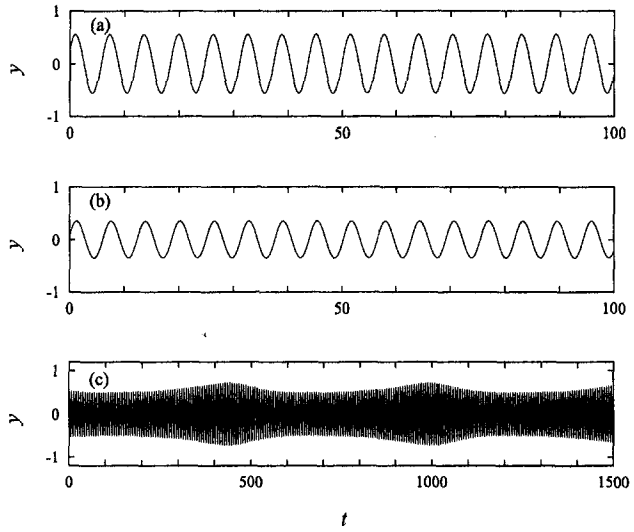


Fig. 10 Time series of stable periodic and quasiperiodic solutions of the original system (3) with $\bar{\delta}_2 = 0.1$, $\bar{\beta} = 0.2$ and $\epsilon = 0.1$. (*a*) and (*b*) $\gamma = 0.0176$ and $\omega = 0.9968$; (*c*) $\gamma = 0.0174$ and $\omega = 0.9975$.

spond to stable fixed points and invariant cycle shown in Figs. 9(*b*) and 9(*d*), respectively.

7 Conclusions

In this paper we have studied the dynamics induced by vortex shedding in a nonlinear structure. Under certain conditions, the cross-wind motion was modeled as a single-degree-of-freedom system. By using the averaging method and dynamical systems theory, it was shown that saddle-node and Hopf bifurcations, and more complicated behavior, the Bogdanov-Takens bifurcation, which was also accompanied by homoclinic bifurcations implying chaos, occur in the single-degree-of-freedom model. Thus, in comparison with the earlier work of Holmes and Lin (1978), nonlinear restoring force characteristic brings about drastic changes in the motion of the wind loaded structure. Numerical examples were also given to illustrate the theory, and good agreement is found between theoretical predictions and numerical simulation results for both the averaged and original systems.

Our result indicates that ignoring nonlinear properties may lead to inaccurate predictions for the dynamics of mechanical and structural systems even if the nonlinearity is very weak. Such complicated behavior as detected here also seems almost hopeless to be correctly described by using classical approaches. Dynamical systems theory can also be expected to be useful in analyzing these essentially nonlinear systems. Other examples of applications of the dynamical systems theory to flow-induced vibrations of structures are found in Païdoussis (1993).

The model considered here is a simple one for a structure excited by vortex shedding. In some situations more realistic models will be required. For example, a two-degree-of-freedom model is necessary for analyzing coupled motions in the along and cross-wind directions. This problem is challenging: Internal resonance behavior will play an important role in understanding the coupled motions. Moreover, it may be possible to treat nonlinear vibrations of wind loaded structures as coupled motion between elastic bodies and fluid owing to recent progress in the ability of computers. Many open problems remain in this field.

Acknowledgments

The author thanks Satoshi Araishi for his assistance with numerical work.

References

Blevins, R. D., 1990, *Flow-Induced Vibration,* Krieger, Malabar, FL.

Doedel E., and Kernévez J., 1986, "AUTO: Software for Continuation and Bifurcation Problems in Ordinary Differential Equations," Applied Mathematics Reports, California Institute of Technology, Pasadena, CA.

Guckenheimer, J., and Holmes, P., 1983, *Nonlinear Oscillations, Dynamical Systems, and Bifurcations of Vector Fields,* Springer-Verlag, New York.

Holmes, P. J., 1979, "Domains of Stability in a Wind-Induced Oscillation Problem," ASME JOURNAL OF APPLIED MECHANICS, Vol. 46, pp. 672–676.

Holmes, P. J., 1980, "Averaging and Chaotic Motions in Forced Oscillations," *SIAM Journal on Applied Mathematics,* Vol. 38, pp. 65–80.

Holmes, P. J., and Lin, Y. K., 1978, "Deterministic Stability Analysis of a Wind Loaded Structure," ASME JOURNAL OF APPLIED MECHANICS, Vol. 45, pp. 165–169.

Holmes, P., Marsden, J., and Scheurle, J., 1988, "Exponentially Small Splitting of Separatrices with Applications to KAM Theory and Degenerate Bifurcations," *Hamiltonian Dynamical Systems,* K. R. Meyer and D. G. Saari, eds., American Mathematical Society, Providence, RI.

Kuznetsov, Y. A., 1995, *Elements of Applied Bifurcation Theory,* Springer-Verlag, New York.

Lin, Y. K., and Holmes, P. J., 1978, "Stochastic Analysis of a Wind Loaded Structure," *Proceedings of ASCE Journal of the Engineering Mechanics Division,* Vol. 104, pp. 421–440.

Moon, F. C., 1992, *Chaotic and Fractal Dynamics,* John Wiley and Sons, New York.

Nusse, E. H., and Yorke, J. A., 1994, *Dynamics: Numerical Explorations,* Springer-Verlag, New York.

Païdoussis, M. P., 1993, "Some Curiosity-Driven Research in Fluid Structure Interactions and Its Current Applications," ASME *Journal of Pressure Vessel Technology,* Vol. 115, pp. 2–14.

Vaicaitis, R., Shinozuka, M., and Takeno, M., 1973, "Parametric Study of Wind Loading on Structures," *Proceedings of ASCE Journal of the Structural Division,* Vol. 99, pp. 453–468.

Wiggins, S., 1990, *Introduction to Applied Nonlinear Dynamical Systems and Chaos,* Springer-Verlag, New York.

Yagasaki, K., 1996, "The Melnikov Theory for Subharmonics and Their Bifurcations in Forced Oscillations," *SIAM Journal on Applied Mathematics,* Vol. 56, pp. 1720–1765.

Downloaded 04 May 2010 to 171.66.16.26. Redistribution subject to ASME license or copyright; see http://www.asme.org/terms/Terms_Use.cfm

Modeling and Identification of Inelastic Systems Using the Endochronic Model

Dar-Yun Chiang
Associate Professor,
Institute of Aeronautics
and Astronautics,
National Cheng Kung University,
Tainan, Taiwan 70101, R.O. China

An effective modeling method is proposed for the endochronic model based on the concept of plastic equilibrium points, which reduces the number of parameters involved and greatly simplifies the modeling process for practical applications. A systematic, optimization-based parameter estimation procedure for the proposed class of endochronic models is also presented for identification studies. Validity of the proposed modeling technique in both modeling and identification of inelastic systems is demonstrated by biaxial tension-torsion applications using experimental results available in the literature.

1 Introduction

In the current literature, various constitutive models have been proposed for structural or material systems exhibiting inelastic behavior. In contrast to those models formulated on the basis of the classical theory of plasticity (Mroz, 1967; Dafalias and Popov, 1976; Chiang and Beck, 1994a, b), endochronic models (Valanis, 1971, 1980) are formulated without employing the concept of a yield surface and are based on the internal variable theory of thermodynamics. Endochronic theory can be viewed as a generalization of the theory of viscoelasticity in which the real-time variable is replaced by a material variable, called the *intrinsic time,* which is a monotonically increasing measure of the deformation history of a material. The major contribution of endochronic theory is that it provides a unifying approach for describing the elastic-plastic behavior of materials without the requirement of introducing a yield surface and a loading function which distinguishes between loading and unloading.

Although the endochronic theory has been applied to model constitutive behavior of various materials (Bazant and Bhat, 1976; Valanis and Read, 1982) or structural components (Gu and Lee, 1997), its numerical implementation generally requires the determination of many parameters involved in the model. For an endochronic model, the memory kernel $\rho(z)$ and the hardening function $f(\eta)$ (see next section for details) can, in general, be determined from a simple shear (or tension) test and a cyclic test, respectively. However, even if the analytical expressions for representing these functions are determined, there remains the task of finding the appropriate constants associated with these functions. From the identification point of view, the large number of parameters involved in an endochronic model poses a severe problem for optimal estimation of the parameters from test data.

In the following, basic formulations of the endochronic theory and some inherent properties of the endochronic model will be addressed for cyclically stabilized elastic-plastic behavior. An effective modeling technique is then proposed for the endochronic model, which not only simplifies the modeling process, but also makes the model parsimonious in parameters so that its applicability to identification studies is improved. Numerical validations are performed through identification analysis using biaxial tension-torsion test results available in the literature. Favorable results demonstrate the modeling validity and predictive capability of the proposed modeling method for cyclically multi-axial material behavior based upon the endochronic theory.

2 Endochronic Theory and Its Implementation

The endochronic theory was originally formulated based on the internal variable theory of irreversible thermodynamics and the concept of intrinsic time which acts as a measure of the memory of the past deformation history of a material. A complete set of constitutive equations for plastically incompressible rate-independent materials, based on the modified endochronic theory (Valanis, 1980) can be summarized as follows:

$$\sigma_{ij} = C_{ijkl}\epsilon^e_{kl}, \tag{1}$$

$$\epsilon_{ij} = \epsilon^e_{ij} + \epsilon^p_{ij}, \tag{2}$$

$$s_{ij} = \int_0^z \rho(z - z')\,\frac{d\epsilon^p_{ij}}{dz'}\,dz', \tag{3}$$

$$s_{ij} = \sigma_{ij} - \tfrac{1}{3}\sigma_{kk}\delta_{ij}, \tag{4}$$

$$dz = \frac{d\eta}{f(\eta)}, \quad f(\eta) > 0, \tag{5}$$

$$d\eta = (d\epsilon^p_{ij}d\epsilon^p_{ij})^{1/2}, \tag{6}$$

where ϵ^e_{ij} and ϵ^p_{ij} are, respectively, the elastic and plastic components of the total strain tensor ϵ_{ij}, C_{ijkl} is the elastic modulus tensor, and s_{ij} is the deviatoric part of the total stress tensor σ_{ij}. $\rho(z)$ and $f(\eta)$ are positive material functions called the kernel (or memory) function and the (cyclic) hardening function, respectively. The physical nature of $\rho(z)$ pertains to kinematic hardening while $f(\eta)$ pertains to isotropic hardening. The differential quantity $d\eta$ represents the distance between two consecutive *plastic*-strain states, so that η defines a memory path in the *plastic*-strain space through which history-dependent effects of a material are introduced into the endochronic model. By introducing different forms for the two material functions $\rho(z)$ and $f(\eta)$, various types of elastic-plastic behavior of materials can be modeled. An important feature of the kernel function $\rho(z)$ in (3) is that the function must be singular at the origin, that is

Contributed by the Applied Mechanics Division of THE AMERICAN SOCIETY OF MECHANICAL ENGINEERS for publication in the ASME JOURNAL OF APPLIED MECHANICS.

Discussion on the paper should be addressed to the Technical Editor, Professor Lewis T. Wheeler, Department of Mechanical Engineering, University of Houston, Houston, TX 77204-4792, and will be accepted until four months after final publication of the paper itself in the ASME JOURNAL OF APPLIED MECHANICS.

Manuscript received by the ASME Applied Mechanics Division, May 22, 1997; final revision, Nov. 14, 1997. Associate Technical Editor: M. Ortiz.

 Copyright © 1998 by ASME

Downloaded 04 May 2010 to 171.66.16.26. Redistribution subject to ASME license or copyright; see http://www.asme.org/terms/Terms_Use.cfm

$$\rho(z) \to \infty \quad \text{as} \quad z \to 0, \tag{7}$$

and must be integrable so that the model can account appropriately for the elastic behavior at the onset of initial loading and unloading response.

There are basically two major classes of endochronic models, depending on the assumed form of the kernel function $\rho(z)$. The first one utilizes the Dirac delta function $\delta(z)$ to give

$$\rho(z) = s_y^0 \delta(z) + \rho_1(z), \tag{8}$$

where $\rho_1(z)$ is a regular (analytic) function and s_y^0 is a material constant that is related to the initial yield stress in simple tension. This formulation leads from (3) to

$$s_{ij}(z) = s_y^0 \frac{d\epsilon_{ij}^p}{dz} + r_{ij}(z), \tag{9}$$

where

$$r_{ij}(z) = \int_0^z \rho_1(z - z') \frac{d\epsilon_{ij}^p}{dz'} dz'. \tag{10}$$

Note that Eqs. (5), (6), and (9) imply

$$\|\tilde{s}(z) - \tilde{r}(z)\| = s_y^0 f(\eta), \tag{11}$$

where $\tilde{s}(z)$ and $\tilde{r}(z)$ denote, the two tensors with components s_{ij} and r_{ij}, respectively, and $\|\tilde{s}\| = (s_{ij}s_{ij})^{1/2}$. It can be deduced from (11) that this formulation results in a generalization of the classical theory of plasticity in such a way that the hardening function $f(\eta)$ signifies *isotropic* hardening behavior (yield-surface expansion), while the tensor $r_{ij}(z)$ denotes *kinematic* hardening behavior (yield-surface translation). Furthermore, it can be shown (Watanabe and Atluri, 1986) that by a suitable choice of $\rho_1(z)$ as a sum of exponential functions, the theory becomes similar to the classical multiyield-surface theory in which nested yield surfaces translate in the stress space according to some kinematic hardening rule.

Although the above formulation leads to a generalization of the classical plasticity theory, the original idea of avoiding the concept of yield surfaces and hardening rules is lost. Moreover, when the hardening function $f(\eta)$ saturates to a limit value, a "limit surface" exists which can move around in the stress space, as can be deduced from (11). As indicated by experimental observations (Lamba and Sidebottom, 1978), however, materials such as metals which have been cyclically stabilized, in general exhibit response behavior with *fixed* limit surfaces (in the stress space) beyond which the stress state never goes.

Another class of endochronic models has been developed (Valanis and Fan, 1984) in which the kernel function is, as a consequence of thermodynamics of discrete internal variables, of the form

$$\rho(z) = \sum_{k=1}^{\infty} c_k e^{-\alpha_k z}, \tag{12}$$

where the non-negative constants c_k and α_k satisfy

$$\sum_{k=1}^{\infty} c_k = \infty, \quad \sum_{k=1}^{\infty} \alpha_k < \infty, \tag{13}$$

so that (7) is satisfied and the integrability of $\rho(z)$ can be guaranteed. Two effective algorithms with formulations in *differential* and *incremental* forms, respectively, have been proposed to implement the endochronic constitutive equations. The differential form has been used by Watanabe and Atluri (1985), while the incremental form has been employed by Valanis and Fan (1983) and Hsu et al. (1991). It can be shown (Gu and Lee, 1997) that with the same memory function $\rho(z)$, the two forms differ from each other only by a factor whose value is close to one provided that the incremental steps are small.

3 Inherent Properties of the Endochronic Formulation

To implement the endochronic theory based upon a truncated form of the kernel function given in (12), it is required to determine the parameters involved in the model (c_k and α_k, $k = 1, 2, \ldots$) for the material of interest. In practice, the process of determining these constants could be rather cumbersome and difficult. It is the aim of the present study that through understanding of inherent properties of the above formulation, we can simplify the modeling process by reducing the number of parameters and thus make the model more suitable for identification studies.

Based on Eqs. (3) and (12), a recursive formula can be derived (Hsu et al., 1991):

$$s_{ij}(z_m) = \sum_{k=1}^{\infty} s_{ij}^k(z_m), \tag{14}$$

and

$$s_{ij}^k(z_m) \approx e^{-\alpha_k \Delta z_m} s_{ij}^k(z_{m-1}) + \frac{c_k}{\alpha_k}(1 - e^{-\alpha_k \Delta z_m}) \left.\frac{\Delta \epsilon_{ij}^p}{\Delta z}\right|_{z_{m-1}}, \tag{15}$$

where Δ denotes an increment of finite size and z_m denotes the value of z at the mth response step. Equation (15) may be rewritten as

$$(\Delta s_{ij}^k)_m \approx \left[\frac{c_k}{\alpha_k} \left.\frac{\Delta \epsilon_{ij}^p}{\Delta z}\right|_m - s_{ij}^k(z_{m-1})\right](1 - e^{-\alpha_k \Delta z_m}). \tag{16}$$

If the stress state reaches an "equilibrium state" (a stability limit under load control), at which the stress increments approach zero for appreciable *unidirectional* strain increments (Chiang and Beck, 1994b), i.e.,

$$(\Delta s_{ij}^k)_{eq} = 0 \quad \forall\, k = 1, 2, \ldots, n \tag{17}$$

then by (14), (16) we have

$$(s_{ij})_{eq} = \left(\sum_{k=1}^{\infty} \frac{c_k}{\alpha_k}\right) \left.\frac{\Delta \epsilon_{ij}^p}{\Delta z}\right|_{eq}. \tag{18}$$

It is seen from (18) that the stress state will remain at the equilibrium state until the plastic-strain path changes its direction. In the case of no cyclic hardening, $(\Delta z)^2 = \Delta \epsilon_{ij}^p \Delta \epsilon_{ij}^p$, and we get, from (18),

$$(s_{ij})_{eq}(s_{ij})_{eq} = \left(\sum_{k=1}^{\infty} \frac{c_k}{\alpha_k}\right)^2 \equiv k_u^2, \tag{19}$$

where k_u is a finite model constant (as implied by (13)) that can be related to some material constant. Equation (19) signifies that all the equilibrium states $(s_{ij})_{eq}$ form a hypersurface in the six-dimensional stress space (considering the symmetry of a stress tensor). This hypersurface is actually a "limit" surface associated with an endochronic model based on the kernel function given by (12). This can be shown by considering cyclically stabilized behavior (i.e., $f(\eta) \equiv 1$) as follows. From (5) and (6) we can put

$$\frac{d\epsilon_{ij}^p(z)}{dz} = n_{ij}(z), \tag{20}$$

where $n_{ij}(z)$ satisfies

$$\|n_{ij}(z)\| \equiv (n_{ij}(z)n_{ij}(z))^{1/2} = 1, \tag{21}$$

and therefore $|n_{ij}(z)| \leq 1$,. Thus, it follows from (3) that

Downloaded 04 May 2010 to 171.66.16.26. Redistribution subject to ASME license or copyright; see http://www.asme.org/terms/Terms_Use.cfm

$$s_{ij}(z) = \int_0^z \rho(z - z')n_{ij}(z')dz'. \tag{22}$$

Thus

$$\begin{aligned} s_{ij}(z)s_{ij}(z) &= \int_0^z \rho(z - z')n_{ij}(z')dz' \int_0^z \rho(z - z'')n_{ij}(z'')dz'' \\ &= \int_0^z \int_0^z \rho(z - z')\rho(z - z'')n_{ij}(z')n_{ij}(z'')dz'dz'' \\ &\le \int_0^z \int_0^z \rho(z - z')\rho(z - z'') \\ &\quad \times \|n_{ij}(z')\|\|n_{ij}(z'')\|dz'dz'' \\ &= \int_0^z \int_0^z \rho(z - z')\rho(z - z'')dz'dz'' \\ &= \left[\int_0^z \rho(z - z')dz\right]^2. \end{aligned} \tag{23}$$

If the kernel function $\rho(z)$ is given by (12), then one can show

$$\left[\int_0^z \rho(z - z')dz'\right]^2 \le \left[\sum_{k=1}^{\infty} \frac{c_k}{\alpha_k}\right]^2 = k_u^2. \tag{24}$$

Thus, from (23), (24) we obtain

$$s_{ij}(z)s_{ij}(z) \le k_u^2. \tag{25}$$

This proves that Eq. (19) represents a limit surface associated with an endochronic model so that no stress state of the model can lie outside the limit surface. In other words, the set of the stress points associated with different equilibrium states of an endochronic model represents the limit surface of that model for cyclically stabilized behavior.

Another interesting point about the endochronic model is the resemblance of (19) to the von Mises yield criterion in the classical theory of plasticity, given by

$$s_{ij}s_{ij} = \tfrac{2}{3}\sigma_0^2, \tag{26}$$

where σ_0 is the yield stress of a material in the uniaxial tension test. Actually, considering the uniaxial tension case where $s_{11} = 2\sigma_{11}/3 = -2s_{22} = -2s_{33}$, and $s_{ij} = 0$, $i \neq j$, (19) implies

$$(s_{ij})_{eq}(s_{ij})_{eq} = \tfrac{2}{3}\sigma_0^2 = k_u^2,$$

since we have $(\sigma_{11})_{eq} = \sigma_0$. Thus, we obtain the relation

$$\sum_{k=1}^{\infty} \frac{c_k}{\alpha_k} = k_u = \sqrt{\frac{2}{3}}\,\sigma_0, \tag{27}$$

which relates the model constants to the material constant σ_0. Equation (27) provides a guideline for choosing the model constants c_k and α_k, in addition to the constraints given in (13). This relation motivates a new effective modeling technique for endochronic models based on the formulation of the kernel function given by (12), as presented in the next section.

4 A Modeling Technique for the Endochronic Model

In the following, we assume that the material has been cyclically stabilized so that the hardening function $f(\eta) \equiv 1$. Thus, to apply an endochronic model to a real material with known elasticity constants, it remains to choose proper values for the model parameters involved in the definition of the kernel function given by (12). According to previous experiences with modeling of the kernel function (Hsu et al., 1991; Valanis and Fan, 1984), at least three exponential terms in the series representation of $\rho(z)$ are required to adequately describe the smooth yielding behavior of inelastic systems. In previous studies (Hsu et al. (1991) and Valanis and Fan (1984), for example) the model parameters involved in the three-term kernel function were chosen exclusively based on a trial-and-error procedure, which may be very difficult and inefficient in practical situations. Furthermore, from the system identification point of view where the parameters are estimated systematically from the data, such a model involving at least eight model parameters (c_k and α_k, $k = 1, 2, 3$, in addition to at least two other parameters of elasticity, E and ν, say) would cause problems of lack of parameter identifiability, that is, nonuniqueness or ill-conditioning for the inverse estimation problem. Thus, it is desirable that the modeling procedure for the kernel function of an endochronic model be simplified so that the number of parameters involved can be reduced and each parameter has clear physical significance.

Starting with the three-term representation for the kernel function $\rho(z)$, we introduce the following additional conditions consistent with (27):

$$\frac{c_k}{\alpha_k} = \frac{k_u}{3} \quad \forall\, k = 1, 2, 3. \tag{28}$$

The generality of the model behavior is not lost by introducing these constraints because numerical simulations indicate that it is the parameters α_k that primarily control the shape of yielding curves. To introduce further conditions on the model parameters we consider a uniaxial loading test. In this one-dimensional (uniaxial) case, we can derive the following equation for the nth branch of the response curve:

$$\sigma(z) = \sqrt{\frac{3}{2}} \sum_{k=1}^{3} \frac{c_k}{\alpha_k} [(-1)^n - e^{-\alpha_k z} + 2 \sum_{i=1}^{n} (-1)^{i-1} e^{-\alpha_k (z - z_i)}], \tag{29}$$

for $z > z_n$, where z_n corresponds to the nth load reversal point. Thus, for initial loading curve ($n = 0$), we have

$$\sigma(z) = \sqrt{\frac{3}{2}} \sum_{k=1}^{3} \frac{c_k}{\alpha_k} [1 - e^{-\alpha_k z}] = \sigma_0 - \sqrt{\frac{3}{2}} \sum_{k=1}^{3} \frac{c_k}{\alpha_k} e^{-\alpha_k z}, \tag{30}$$

where we made use of (27). In this case, $dz = \sqrt{3/2}\, d\epsilon^p$ where $d\epsilon^p$ is the uniaxial plastic strain increment; and so from (30), the instantaneous "plastic stiffness" on initial loading is given by

$$\frac{d\sigma}{d\epsilon^p} = \frac{3}{2} \sum_{k=1}^{3} c_k e^{-\sqrt{3/2}\alpha_k \epsilon^p}. \tag{31}$$

The instantaneous elastic stiffness is, of course,

$$\frac{d\sigma}{d\epsilon^e} = E. \tag{32}$$

Since the c_k's are related to the plastic stiffness, we introduce dimensionless parameters β_k defined by

$$c_k = \beta_k E, \quad k = 1, 2, 3, \tag{33}$$

then from (27), (28) we get

$$\alpha_k = \sqrt{\frac{27}{2}}\, \beta_k \frac{E}{\sigma_0}, \quad k = 1, 2, 3. \tag{34}$$

Using (2), (31), (32), the instantaneous total stiffness on initial loading is therefore given by

$$\frac{d\sigma}{d\epsilon} = E\left[1 + 1 \Big/ \left(\frac{3}{2} \sum_{k=1}^{3} \beta_k e^{-\sqrt{3/2}\alpha_k \epsilon^p}\right)\right]^{-1}. \tag{35}$$

Thus, if we select β_1 to be very large, which is consistent with

Downloaded 04 May 2010 to 171.66.16.26. Redistribution subject to ASME license or copyright; see http://www.asme.org/terms/Terms_Use.cfm

the first requirement in (13), then the initial total stiffness at $\epsilon^p = 0$ is E as desired. We may thus choose $\beta_1 = 10^{12}$. Moreover, as suggested by results of numerical simulations, we may fix the ratio of β_2 to β_3 (or, equivalently, α_2 to α_3) as $\beta_2 = \gamma\beta_3$, where γ can be optimally determined by fitting the uniaxial stress-strain curve. For many structural or material systems, it appears that we may set $\gamma = 3$, so that a smooth yielding curve can always be attained regardless of the shape of the hysteresis loops. Finally, we reparameterize so that β_3 is expressed in terms of a dimensionless parameter p by

$$\beta_3 = \sqrt{\frac{2}{27}}\, 2^p. \tag{36}$$

To summarize, we have the following parsimonious model for the endochronic kernel function using three exponential terms:

$$\rho(z) = \sum_{k=1}^{3} c_k e^{-\alpha_k z}, \tag{37}$$

$$c_1 = 10^{12}E, \quad c_2 = 3c_3, \quad c_3 = \sqrt{\frac{2}{27}}\, 2^p E, \tag{38}$$

$$\alpha_1 = \sqrt{\frac{2}{27}}\, 10^{12}\, \frac{E}{\sigma_0}, \quad \alpha_2 = 3\alpha_3, \quad \alpha_3 = 2^p\, \frac{E}{\sigma_0}. \tag{39}$$

The parameter p controls the degree of smoothness of yielding behavior. As $p \to \infty$, a yielding curve corresponding to the elasto-perfectly plastic behavior is obtained. Thus, only three parameters, E, σ_0, and p, are needed in the modeling process for general uniaxial inelastic behavior. In the case where multi-axial response behavior of *isotropic* materials is of interest, only one additional parameter, Poisson's ratio ν, is needed for the endochronic models based on the preceding formulation. This simplifies the application of endochronic models to general multi-axial response problems of cyclic plasticity, especially in the case where system identification is of interest, that is, the model is to be selected to match the behavior of a certain material. In this case, E, ν, and σ_0 could be determined by standard approaches and then the value of the parameter p could be chosen to give a least-squares match of the stress-strain curve for uniaxial loading. Although this is a nonlinear estimation problem, it is numerically straightforward because it is simply an optimization with respect to only a single variable.

Note that the parameter σ_0 can be interpreted as the limit stress (attainable at small strains) in the uniaxial case where only cyclically stabilized behavior is considered. This definition of σ_0 may be viewed as an extension of defining σ_0 as the yield stress of simple tension, since for engineering applications, structural systems do not, in general, exhibit hysteretic behavior with prominent yielding point (Jayakumar, 1987). It is assumed above that uniaxial tests to a limit state (at small strains) have been performed, so that σ_0 can be determined directly. However, this may not be possible, particularly for structural systems, so in this case, both σ_0 and p should be estimated from uniaxial stress-strain data.

5 Identification Algorithm

With the proposed class of endochronic models whose mathematical structure is specified, the system identification problem reduces to a parameter estimation problem. In the present study we consider a prescribed strain path as input loading, and the corresponding stress response as output. By employing the *least-squares output-error* method, the objective function to be minimized is simply the sum-of-square errors between the model stress and the test data, which is, in the biaxial tension-torsion case, defined as

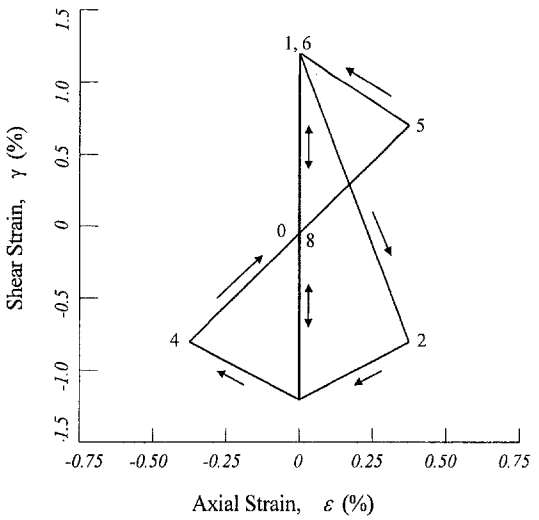


Fig. 1 Prescribed biaxial strain path for the identification study of the endochronic model with cyclically stabilized behavior

$$J(\boldsymbol{\theta}) = \frac{1}{V_\sigma}\sum_{i=1}^{M}\left[\sigma_i(\boldsymbol{\theta}, \epsilon, \gamma) - \sigma_i^*\right]^2 + \frac{1}{V_\tau}\sum_{i=1}^{M}\left[\tau_i(\boldsymbol{\theta}, \epsilon, \gamma) - \tau_i^*\right]^2, \tag{40}$$

where $\boldsymbol{\theta}$ denotes the vector of parameters and M is the number of measured data points in the response history. V_σ and V_τ are two normalizing constants, and ϵ and γ denote the axial strain (ϵ_{11}) and shear strain ($2\epsilon_{12}$) components, respectively.

For solving the nonlinear optimization problem of minimizing J with respect to $\boldsymbol{\theta}$, Powell's *conjugate-direction* method (Press et al., 1992) is employed in this study. The major advantage of this method lies in the fact that it does not require explicit evaluation of the function's *gradient,* which is usually difficult for identification of elastic-plastic systems. It should be remarked, however, that most traditional optimization methods (including Powell's method employed here) only search for a solution of *local* optimum close to the initial estimate of parameters. It is thus important for a model to have few parameters and each has clear physical meaning, so that initial estimate of parameters can be made easily and appropriately.

6 Application to Biaxial Tension-Torsion Loading

To illustrate the effectiveness of the proposed modeling technique we conducted identification studies under some general biaxial loading conditions involving axial and torsional loading. The experimental data employed was obtained from a series of strain-controlled tests conducted on OFHC copper by Lamba and Sidebottom (1978a, b). For identification purposes, the input/output data are the prescribed nonproportional strain path and the corresponding measured stress response, which are shown in Fig. 1 and Fig. 2, respectively. The model stress response fitted using the endochronic model based on the proposed modeling method is also shown in Fig. 2 for direct comparison. The parameter values identified are compared with those reported by Lamba and Sidebottom (1978a) in Table 1, where the "shape" parameter p has no direct comparison.

Comparing the correlated model stress with the experimental result we observe that the response behavior described by endochronic model is in good agreement with the experimental results in almost every aspect. Transition between the elastic and plastic regimes is smooth and well behaved, while the complicated biaxial Bauschinger effect is also well accounted for. Moreover, the model behavior clearly shows the existence of

Downloaded 04 May 2010 to 171.66.16.26. Redistribution subject to ASME license or copyright; see http://www.asme.org/terms/Terms_Use.cfm

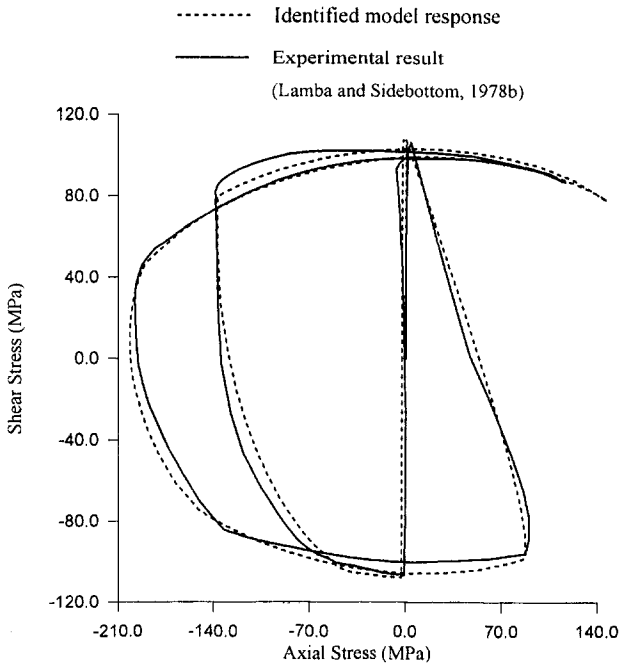


Fig. 2 Fitted stress response of the endochronic model compared with experimental result (from Lamba and Sidebottom, 1978b)

Table 1 Comparison of identified parameter values for the endochronic model with experimental results (Lamba and Sidebottom, 1978a)

Parameters	E (GPa)	ν	σ_u (MPa)	p
Experimental values	115	0.33	213	—
Identified values	116	0.34	209	0.91

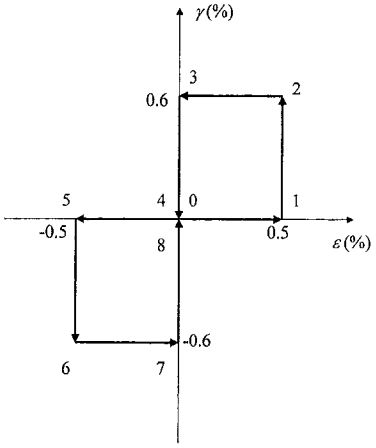


Fig. 3 Prescribed biaxial strain path for cross validation of the endochronic model

equilibrium points and a limit surface. Thus, the proposed parsimonious endochronic model, involving only four model parameters for isotropic materials, appears to be capable of modeling the biaxial response of thin-walled copper tubes very well.

To further validate the predictive capability of the endochronic model another set of experimental results is employed, which was obtained by McDowell et al. (1982) on the same metal (OFHC copper). The prescribed biaxial strain loading path involves several sharp direction changes as shown in Fig. 3, and the corresponding cyclically stabilized stress response

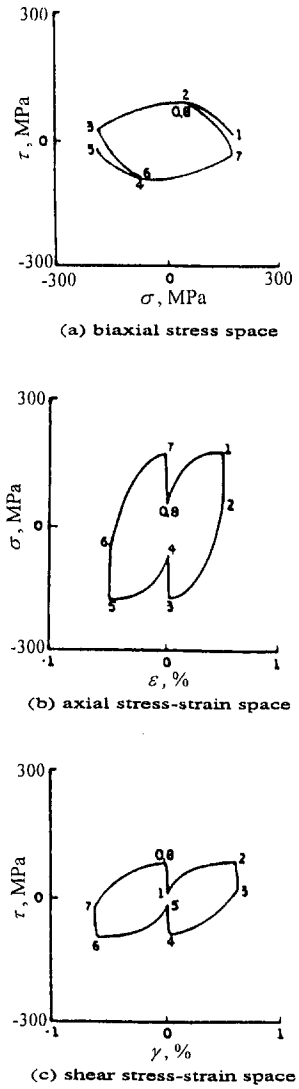


Fig. 4 Experimentally observed stress response of copper to the prescribed stain path given in Fig. 3 (from McDowell et al., 1982)

observed experimentally is shown in Fig. 4. The predicted stress response based on the endochronic model with previously identified parameters is shown in Fig. 5. It is observed that most important features of the response behavior, such as the peak stresses and the biaxial Bauschinger effect, are well predicted by the identified endochronic model. The modeling validity and predictive capability of the endochronic model for cyclically stabilized behavior is thus demonstrated. It is remarkable that cyclic hardening behavior of materials can also be modeled using the endochronic models provided that appropriate choice of the hardening function $f(\eta)$ in (5) has been made.

It is remarkable that the endochronic theory will not capture precisely the subcycles of hysteresis without further modification of the intrinsic time. The theory presented, thus, is particularly limited to describing completely reversed hysteresis or encounter with limit states during nonproportional loading, as shown in Fig. 2. Furthermore, the issue of generality associated with introducing constraints on the model constants merits further investigation. Based on previous experiences with the distributed-element models (Chiang and Beck, 1994a; Chiang, 1997) in modeling cyclic elastic-plastic behavior for various metals, the parameters proposed in the present paper are expected to result in good correlation of behavior for a range of initially isotropic polycrystalline materials.

Downloaded 04 May 2010 to 171.66.16.26. Redistribution subject to ASME license or copyright; see http://www.asme.org/terms/Terms_Use.cfm

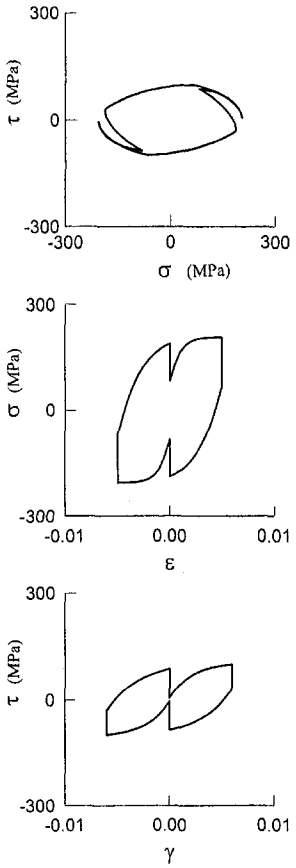


Fig. 5 Stress response predicted by the endochronic model with previously identified parameters to the prescribed stain path given in Fig. 3

7 Conclusions

Although the endochronic theory and its algorithmic implementation have been developed for quite a few years, the modeling process is, in general, complicated and needs special experience. This limits the applicability of the otherwise well-behaved models to practical engineering problems, especially when the model is to be matched to actual material behavior. An effective modeling technique is proposed based on a formulation of the endochronic theory and the concept of plastic equilibrium points to simplify the modeling process. This technique greatly reduces the number of parameters involved, and the parameters can be identified easily from test data of real structural or material systems. Applicability of the model to identification analysis of cyclically stabilized inelastic systems is demonstrated by using different sets of experimental data obtained from biaxial tension-torsion tests, and favorable results obtained confirm the validity of the proposed modeling technique for endochronic models.

Acknowledgment

The author gratefully acknowledges the support provided by the National Science Council of the Republic of China under Grant Number NSC 85-2212-E-006-014.

References

Bazant, Z. P., and Bhat, P. D., 1976, "Endochronic Theory of Inelasticity and Failure of Concrete," *ASCE Journal of Engineering Mechanics,* Vol. 102, No. EM4, pp. 701–722.

Chiang, D. Y. and Beck, J. L., 1994a, "A New Class of Distributed-Element Models for Cyclic Plasticity—I. Theory and Application," *Int. J. Solids and Structures,* Vol. 31, No. 4, pp. 469–484.

Chiang, D. Y. and Beck, J. L., 1994b, "A New Class of Distributed-Element Models for Cyclic Plasticity—II. On Important Properties of Material Behavior," *Int. J. Solids and Structures,* Vol. 31, No. 4, pp. 485–496.

Chiang, D. Y., 1997, "A Phenomenological Model for Cyclic Plasticity," ASME *ASME Journal of Engineering Materials and Technology,* Vol. 119, No. 1, pp. 7–11.

Dafalias, Y. F., and Popov, E. P., 1976, "Plastic Internal Variables Formalism of Cyclic Plasticity," ASME JOURNAL OF APPLIED MECHANICS, Vol. 98, p. 645.

Gu, R. J., and Lee, Y.-L., 1997, "A New Method for Estimating Nonproportional Notch-Root Stresses and Strains," ASME *Journal of Engineering Materials and Technology,* Vol. 119, pp. 40–45.

Hsu, S. Y., Jain, S. K., and Griffin, O. H., 1991, "Verification of Endochronic Theory for Nonproportional Loading Paths," ASCE *Journal of Engineering Mechanics,* Vol. 117, pp. 110–131.

Jayakumar, P., 1987, "Modeling and Identification in Structural Dynamics," Report No. EERL 87-01, California Institute of Technology, Pasadena, CA.

Lamba, H. S., and Sidebottom, O. M., 1978a, "Cyclic Plasticity for Nonproportional Paths: Part 1—Cyclic Hardening, Erasure of Memory, and Subsequent Strain Hardening Experiments," ASME *Journal of Engineering Materials and Technology,* Vol. 100, pp. 96–103.

Lamba, H. S., and Sidebottom, O. M., 1978b, "Cyclic Plasticity for Nonproportional Paths: Part 2—Comparison with Predictions of Three Incremental Plasticity Models," ASME *Journal of Engineering Materials and Technology,* Vol. 100, pp. 104–111.

McDowell, D. L., Socie, D. F., and Lamba, H. S., 1982, "Multiaxial Nonproportional Cyclic Deformation," *Low-Cycle Fatigue and Life Prediction,* ASTM, STP 770, pp. 500–518.

Mroz, Z., 1967, "On the Description of Anisotropic Workhardening," *J. Mech. and Phys. Solids,* Vol. 15, pp. 163–175.

Press, W. H., Teukolsky, S. A., Vetterling, W. T., and Flannery, B. P., 1992, *Numerical Recipes in Fortran: The Art of Scientific Computing,* 2nd Ed., Cambridge University Press, New York.

Valanis, K. C., 1971, "A Theory of Viscoplasticity Without a Yield Surface, Part 1: General Theory; Part 2: Application to Mechanical Behavior of Metals," *Archive of Mechanics,* Vol. 23, No. 4, pp. 517–551.

Valanis, K. C., 1980, "Fundamental Consequences of a New Intrinsic Time Measure: Plasticity as a Limit of the Endochronic Theory," *Archive of Mechanics,* Vol. 23, No. 2, pp. 171–191.

Valanis, K. C., and Read, H., 1982, "New Endochronic Plasticity Models for Soils," *Soil Mechanics—Transient and Cyclic Loads,* edited by G. N. Pande and O. C. Zienkiewicz, eds., Wiley, New York. John Wiley and Sons, New York.

Valanis, K. C., and Fan, J., 1984, "A Numerical Algorithm for Endochronic Plasticity and Comparison with experiment," *Computers and Structures,* Vol. 19, No. 516, pp. 714–724.

Watanabe, O., and Atluri, S. N., 1986, "Internal Time, General Internal Variable, and Multi-Yield-Surface Theories of Plasticity and Creep: A Unification of Concepts," *Int. J. Plasticity,* Vol. 2, No. 1, pp. 37–57.

Downloaded 04 May 2010 to 171.66.16.26. Redistribution subject to ASME license or copyright; see http://www.asme.org/terms/Terms_Use.cfm

P. Lancaster

P. Zizler

Department of Mathematics and Statistics,
The University of Calgary,
Calgary, Alberta T2N 1N4, Canada

On the Stability of Gyroscopic Systems

Gyroscopic systems considered here have the form $A\ddot{y} + G\dot{y} + Ky = 0$ where A, G, K are real $n \times n$ matrices with $A > 0$, $G^T = -G$, $K^T = K$, and the stiffness matrix K has some negative eigenvalues; i.e., the equilibrium position is unstable (when $G = 0$). A new necessary condition for stability is established. It is also shown that gyroscopic systems with $K < 0$ and G singular are always unstable for G sufficiently large.

1 Introduction

We define a gyroscopic system to be a time-invariant linear differential system:

$$A\ddot{y}(t) + G\dot{y}(t) + Ky(t) = 0 \tag{1.1}$$

with real matrix coefficients having the properties $A > 0$ (positive definite), $G^T = -G$ (skew-symmetric), $K^T = K$ (symmetric). Those systems for which K (the stiffness matrix) satisfies $K > 0$ or $K \geq 0$ are relatively well understood (see Lancaster (1966), for example) and this note contains contributions to the following problem types:

Case 1. $G^T = -G$ and $K^T = K$ with K *indefinite*, i.e., K may have both positive and negative eigenvalues. Physically, this generally means that the equilibrium position about which the system evolves is unstable. A new and simple *necessary* condition for the stability of (1.1) is established in Theorem 2. (Stability here means that all possible solutions of (1.1) are bounded for all $t \geq 0$).

Case 2. (a special case of Case 1). $G^T = -G$, $\det G = 0$, and $K < 0$ (K has only negative eigenvalues). If, on the other hand, we have $\det G \neq 0$ then this is again a relatively well-understood case (see Lakhadanov (1975), Barkwell et al. (1992), Seyranian et al. (1995), Walker (1991), Wu and Tsao (1994), and references there). The condition $K < 0$ implies that the equilibrium position is "completely unstable" and the interest here lies in the possibility of stabilizing such a system with a sufficiently large *singular* G. The asymptotic behavior of such systems for large G is the second contribution (Theorem 3).

All solutions of (1.1) can be characterized algebraically using properties of the matrix transfer function

$$L_0(\lambda) = \lambda^2 A + \lambda G + K \tag{1.2}$$

which arises on seeking solutions in the form $y(t) = p(t)e^{\lambda t}$ where $p(t)$ is a polynomial. Stability of the system then means that

(a) $L_0(\lambda)$ has no eigenvalues in the open right half of the complex plane and,
(b) if $L_0(\lambda)$ has eigenvalues on the imaginary axis (admitting zero eigenvalues) they are semi-simple (have no associated generalized eigenvectors).

These two statements are together necessary and sufficient for stability of a system (1.1).

2 Problem Reduction and First Properties

Reduction of (1.1) or $L_0(\lambda)$ of (1.2) to the case $A = I$ (the identity matrix) can be achieved in a familiar way using the positive definite matrix $A^{1/2}$. As our interests are largely in the case $K < 0$ it is also convenient to write $K = -C$ and define

$$L(\lambda) = \lambda^2 I + \lambda G - C \tag{2.1}$$

where $G^T = -G$ and $C^T = C$ are real matrices. We also refer to the transfer function $L(\lambda)$ as a "gyroscopic system". Initially, C may have both positive and negative eigenvalues but, in Section 4, we focus on Case 2 and assume $C > 0$.

By the spectrum of $L(\lambda)$, written $\sigma(L)$, we mean the set of all eigenvalues of $L(\lambda)$, i.e., all the zeros of the determinant $\det L(\lambda)$. We present two well-known facts which will be needed subsequently.

Proposition 1 *The spectrum of a gyroscopic system is symmetric with respect to both the real and imaginary axes of the complex plane.*

This double symmetry is frequently described as "Hamiltonian." To verify the proposition note that

$$L(\lambda)^* = L(-\bar{\lambda}), \quad L(\lambda)^T = L(-\lambda).$$

Thus, $L(\lambda)$, $L(\bar{\lambda})$, $L(-\lambda)$, and $L(-\bar{\lambda})$ are either all singular (when λ, $\bar{\lambda}$, $-\lambda$, $-\bar{\lambda}$ are all eigenvalues) or all nonsingular.

Consider a rotation of the parameter λ through a right angle and write $\beta = i\lambda$. Then define

$$M(\beta) = \beta^2 I + \beta(iG) + C, \tag{2.2}$$

($= -L(\lambda)$), then $\sigma(M) = i\sigma(L)$ and $\sigma(M)$ also has Hamiltonian symmetry. One advantage of this transformation is that $M(\beta)$ has *Hermitian* coefficients, $(iG)^* = iG$, $C^T = C^* = C$, and $M(\beta)$ is a self-adjoint matrix polynomial; a class of matrix functions which is relatively well understood (see Gohberg et al., 1982, for example).

Proposition 2 *The scalar polynomial $\det M(\beta)$ contains only even powers of β.*

The proof follows from Proposition 1 and the additional fact that Hamiltonian symmetry also includes the eigenvalue multiplicities.

Recall that the eigenvalues of the real skew-symmetric matrix G are pure-imaginary and symmetric about the real axis. In other words, the Hermitian matrix $B := iG$ has only real eigenvalues, and there is unitary matrix U (i.e., $U^*U = I$) for which

$$U^*BU = U^*(iG)U = \text{diag}\,[0, \ldots, 0, b_1, -b_1, b_2, -b_2, \ldots, b_k, -b_k] \tag{2.3}$$

Contributed by the Applied Mechanics Division of THE AMERICAN SOCIETY OF MECHANICAL ENGINEERS for publication in the ASME JOURNAL OF APPLIED MECHANICS.

Discussion on the paper should be addressed to the Technical Editor, Professor Lewis T. Wheeler, Department of Mechanical Engineering, University of Houston, Houston, TX 77204-4792, and will be accepted until four months after final publication of the paper itself in the ASME JOURNAL OF APPLIED MECHANICS.

Manuscript received by the ASME Applied Mechanics Division, June 17, 1997; final revision, Sept. 24, 1997. Associate Technical Editor: W. K. Liu.

 Copyright © 1998 by ASME

Downloaded 04 May 2010 to 171.66.16.26. Redistribution subject to ASME license or copyright; see http://www.asme.org/terms/Terms_Use.cfm

where $b_j > 0$ for $j = 1, 2, \ldots, k$. Furthermore, the number of zeros in this diagonal matrix is even or odd according as n is even or odd. Now $U^*M(\beta)U$ has the same spectrum (and multiplicities) as $M(\beta)$, so it can be assumed without loss of generality that

$$M(\beta) = \beta^2 I + \beta B + C \tag{2.4}$$

where B has the diagonal form of (2.3), but now we admit an Hermitian matrix C (since U is generally not a real matrix).

3 Necessary Conditions for Stability

There is a well-known condition of Hagedorn (see Hagedorn (1975) and Huseyin (1978)) which ensures that a gyroscopic system is *unstable.* To get a deeper insight we present it here with Huseyin's proof. The reductions of Section 2 are not required here and we consider a gyroscopic system of the form (1.2). Indeed, we can admit the more general case of complex coefficients with $A > 0$, $G^* = -G$, $K^* = K$. The hypotheses of Theorem 1 imply that problems of Case 2 are included. This is because $4K < GA^{-1}G$ and $G^* = -G$ imply that $K < 0$, but note that G may be singular or nonsingular.

Theorem 1 *If $4K < GA^{-1}G$ then the system (1.2) has no eigenvalues on the imaginary axis.*

Proof. We use the notation $(\ ,\ )$ for the standard inner-product on $\mathbb{C}^n$. The first steps take advantage of the real-symmetric square root $A^{1/2} > 0$ and the Cauchy-Schwarz inequality. For any nonzero vector u in $\mathbb{C}^n$,

$$\begin{aligned} |(u, Gu)|^2 &= |(A^{1/2}u, A^{-1/2}Gu)|^2 \\ &\le (A^{1/2}u, A^{1/2}u)(A^{-1/2}Gu, A^{-1/2}Gu) \\ &= -(u, Au)(u, GA^{-1}Gu). \end{aligned} \tag{3.1}$$

Now $G^T = -G$ implies (u, Gu) is pure imaginary, say $(u, Gu) = ig$ where $g \in \mathbb{R}$. We also write $(u, Au) = a > 0$ and obtain from (3.1)

$$g^2 + a(u, GA^{-1}Gu) \le 0.$$

Write $k = (u, Ku) \in \mathbb{R}$ and the hypothesis $4K < GA^{-1}G$ implies $4k < (u, GA^{-1}Gu)$. Thus,

$$g^2 + 4ak < g^2 + a(u, GA^{-1}Gu) \le 0. \tag{3.2}$$

Now suppose that u is an eigenvector of $L_0(\lambda_0)$, i.e., $L_0(\lambda_0)u = 0$ with $u \neq 0$ for some eigenvalue λ_0. Then

$$(u, L_0(\lambda_0)u) = \lambda_0^2 a + i\lambda_0 g + k = 0$$

implies

$$2a\lambda_0 = i(-g \pm \sqrt{g^2 + 4ak}).$$

The inequality $g^2 + 4ak < 0$ of (3.2) implies that λ_0 has a nonzero real part; and this is the case for *all* eigenvalues λ_0. □

Note that instability would occur if only one eigenvalue has a nonzero real part, but the condition $4K < GA^{-1}G$ implies that *all* eigenvalues have nonzero real parts. In contrast, when Theorem 2 below is violated (inequality (3.5) is not satisfied), there is at least one eigenvalue *off* the imaginary axis and instability is implied. Theorem 2 is a new criterion for instability and it will be shown by example that neither Theorem 1 nor Theorem 2 implies the other one. However, if C is indefinite, then Theorem 2 holds, but not Theorem 1. We first formulate a lemma.

Lemma 1 *Let $M(\beta)$ be defined as in (2.4) and assume that $p_n(\beta) := \det M(\beta)$ contains only even powers of β, with*

$$p_n(\beta) = \beta^{2n} + r_n\beta^{2n-2} + \ldots. \tag{3.3}$$

Then

$$r_n = \mathrm{Tr}\,(C) - \tfrac{1}{2}\|B\|_2^2. \tag{3.4}$$

The real number $\mathrm{Tr}\,(C) = \sum_{j=1}^{n} c_{jj}$ is the *trace* of C and $\|B\|_2^2 = \sum_{i,j=1}^{n} |b_{ij}|^2$, where $B = (b_{ij})_{i,j=1}^n$.

Proof. First consider the case $n = 2k$ and write

$$B = \mathrm{diag}\,[b_1, -b_1, \ldots, b_k, -b_k]$$

where $b_j \gtrless 0$, $j = 1, \ldots, k$. (It is convenient to admit $b_j = 0$ here.) Observe that $\|B\|_2^2 = 2\sum_{j=1}^{k} b_j^2$. Then (3.4) can be established by induction on k using the Laplace expansion for $\det M(\beta)$ associated with the first $2k - 2$ rows (see Section 2.4 of Lancaster and Tismenetsky (1985), for example).

In the case $n = 2l - 1$ write B in the form (2.3). Since a skew-symmetric matrix of odd size is necessarily singular, $M(\beta)$ has the partitioned form

$$M(\beta) = \begin{bmatrix} \beta^2 + c_{11} & \vdots & c_{12} \ldots c_{1n} \\ \cdots\cdots & \vdots & \cdots\cdots \\ \bar{c}_{12} & & \\ & \vdots & \\ \vdots & \vdots & M_1(\beta) \\ & \vdots & \\ \bar{c}_{1n} & & \end{bmatrix}$$

where, since the block $M_1(\beta)$ has even size, $2(l - 2) = n - 1$, the first part of the proof applies and

$$\det M_1(\beta) = \beta^{2n-2} + r_{n-1}\beta^{2n-4} + \ldots$$

where $r_{n-1} = \mathrm{Tr}\,(C_1) - \frac{1}{2}\|B\|_2^2$ (and C_1 is the obvious submatrix of C of size $n - 1$).

Note that the cofactors of $c_{12}, \ldots, c_{1n}$ in $M(\beta)$ have degree at most $2n - 4$ in β. It follows that

$$\begin{aligned} &\det M(\beta) \\ &\quad = \beta^{2n} + (r_{n-1} + c_{11})^{2n-2} + (\text{terms of lower degree}), \end{aligned}$$

i.e., $r_n = r_{n-1} + c_{11}$. Equation (3.4) follows. □

Theorem 2 *Let $L(\lambda)$ be a gyroscopic system with $C \neq 0$. If all eigenvalues of $L(\lambda)$ are pure imaginary, then*

$$\mathrm{Tr}\,(C) < \tfrac{1}{2}\|G\|_2^2. \tag{3.5}$$

Proof. Clearly, $L(\lambda)$ has all eigenvalues pure imaginary if and only if $M(\beta)$ of (2.4) has all real eigenvalues. By Proposition 2, $p_n(\beta) = \det M(\beta)$ contains only even powers of β, so the lemma can be used. Thus, all eigenvalues of $p_n(\beta)$ are real and are located symmetrically with respect to the imaginary axis. We claim that, in (3.3), we have $r_n < 0$. This follows from another easy induction proof using a factorization

$$p_n(\beta) = \prod_{j=1}^{n/2} (\beta^2 - \beta_j^2).$$

The hypothesis $C \neq 0$ is used to ensure that $\beta_1 \neq 0$.

Notice also that, because U is unitary, $\|B\|_2$ $(= \|G\|_2)$ and $\mathrm{Tr}\,(C)$ are not changed in the reduction process leading to (2.4). Consequently, $r_n < 0$ together with (3.4) leads to (3.5). □

Downloaded 04 May 2010 to 171.66.16.26. Redistribution subject to ASME license or copyright; see http://www.asme.org/terms/Terms_Use.cfm

Example 1 Let

$$L(\lambda) = \lambda^2\begin{bmatrix}1 & 0\\ 0 & 1\end{bmatrix} + \lambda\begin{bmatrix}0 & 2\\ -2 & 0\end{bmatrix} + \begin{bmatrix}2 & 1.5\\ 1.5 & 2\end{bmatrix}.$$

We have $G^2 = -\left[\begin{smallmatrix}4 & 0\\ 0 & 4\end{smallmatrix}\right]$, $4C = \left[\begin{smallmatrix}8 & 6\\ 6 & 8\end{smallmatrix}\right]$, and $4C + G^2 = \left[\begin{smallmatrix}4 & 6\\ 6 & 4\end{smallmatrix}\right] \not> 0$ so that Theorem 1 does not apply. However, Tr $(C) = 4$, $\frac{1}{2}\|G\|_2^2 = 4$, and (3.5) does not hold. Thus, there are eigenvalues of $L(\lambda)$ *off* the imaginary axis. It follows that $L(\lambda)$ is unstable.

Example 2 Let

$$L(\lambda) = \lambda^2\begin{bmatrix}1 & 0\\ 0 & 1\end{bmatrix} + \lambda\begin{bmatrix}0 & 2\\ -2 & 0\end{bmatrix} + \begin{bmatrix}1.5 & 0\\ 0 & 1.5\end{bmatrix}.$$

We have Tr $(C) = 3$, $\frac{1}{2}\|G\|_2^2 = 4$ and Theorem 2 tells us nothing. However, $4C + G^2 = \left[\begin{smallmatrix}2 & 0\\ 0 & 2\end{smallmatrix}\right] > 0$, and instability follows from Theorem 1.

For completeness, we note the well-known result that, for stability, it is necessary that C has an even number of positive eigenvalues. However, it is clear that *sufficient* conditions for stability are generally more useful than necessary conditions. We see the following as a major unsolved problem in this area:

Problem 1 Find easily verified sufficient conditions for the stability of gyroscopic systems of the form (2.1) (or 1.1) with an indefinite matrix C (or K).

4 The Case $C > 0$ and det $G = 0$

In contrast to the necessary conditions for stability of Section 3, some sufficient conditions for stability are known when $C > 0$ and det $G \neq 0$. For example, Barkwell et al. (1992) show that

$$|G| > kI + k^{-1}C, \quad k > 0 \tag{4.1}$$

implies stability (where $|G| = (-G^2)^{1/2} > 0$). Other sufficient conditions have been proposed by Lakhadanov (1975), Walker (1991), Wu and Tsao (1994), and Seyranian et al. (1995).

Observe that the definition of Case 1 admits some stable systems with C indefinite. For example, if $L(\lambda)$ of (2.1) satisfies (4.1) and $\hat{L}(\lambda) = \lambda^2 I + \lambda\hat{G} - \hat{C}$ satisfies $\hat{G}^T = -\hat{G}$ and $\hat{C} < 0$ then the system

$$L_1(\lambda) := \begin{bmatrix}L(\lambda) & 0\\ 0 & \hat{L}(\lambda)\end{bmatrix}$$

is gyroscopic with indefinite constant (stiffness) term diag $[-C, -\hat{C}]$, and is stable because both $L(\lambda)$ and $\hat{L}(\lambda)$ are stable. Furthermore, $\hat{G}$ may be singular (even zero) in which case the gyroscopic term of $L_1(\lambda)$ is also singular. However, this device does not produce stable systems $L_1(\lambda)$ admissible under the conditions of Case 2.

Lakhadanov (1975) has devised an example of a gyroscopic system with det $G = 0$ and $C > 0$ which is stable. He takes

$$G = \begin{bmatrix}0 & 1 & 10 & 0\\ -1 & 0 & 0 & 10\\ -10 & 0 & 0 & 10^2\\ 0 & -10 & -10^2 & 0\end{bmatrix},$$

$$C = \begin{bmatrix}10^{-6} & 0 & 0 & 0\\ 0 & 10^{-6} & 0 & 0\\ 0 & 0 & 10^3 & 0\\ 0 & 0 & 0 & 10^3\end{bmatrix}$$

and it can be confirmed computationally that the eight eigenvalues of $M(\beta)$ are real and distinct. Hence $L(\lambda)$ is stable. (Although the appearance of 10^{-6} in C looks a little strange, it can be verified numerically that the conclusion is not highly sensitive to changes in these entries.) This suggests the second unsolved problem:

Problem 2 Find easily verified sufficient conditions for the stability of gyroscopic systems with $C > 0$ (or $K < 0$) and det $G = 0$.

It is a classical result that when n, the size of $L(\lambda)$, is odd the system is *unstable*. To see this recall that det $L(\lambda)$ is a monic polynomial of degree $2n$ with real coefficients and the constant term is det $L(0) = (-1)^n$ det C. Thus, $C > 0$ and n odd imply that the constant term is negative. Thus det $L(\lambda)$ has at least one positive zero. Consequently, there are real eigenvalues and $L(\lambda)$ cannot be stable.

Our next result concerns gyroscopic systems of Problem 2 with an additional parameter ξ:

$$L_\xi(\lambda) = \lambda^2 I + \lambda\xi G - C.$$

We consider the eigenvalues $\lambda(\xi)$ as (necessarily) continuous functions of ξ for $\xi \geq 0$.

When $\xi = 0$, $L_0(\lambda)$ is unstable (all eigenvalues are real and nonzero). When det $G \neq 0$, $L_\xi(\lambda)$ is stable for ξ large enough (as in (4.1)) (all eigenvalues are on the imaginary axis). We are to examine the asymptotic behavior of the eigenvalues as $\xi \to \infty$ when det $G = 0$ and will show that, in the limit, there are nonzero real eigenvalues. Thus, the resolution of Problem 2 must include some upper bound on the size of G.

To formulate the theorem we recast the matrix polynomial as in Section 2 and consider

$$M_\xi(\beta) = \beta^2 I + \beta\xi B + C \tag{4.2}$$

where $B^* = B$, $C^* = C > 0$. It is convenient to introduce the "inertia triple" for B, (π, ν, δ) where $\pi + \nu + \delta = n$,

π is the number of positive eigenvalues of B,

ν is the number of negative eigenvalues of B,

δ is the number of zero eigenvalues of B.

We assume $\delta > 0$ and note that, for gyroscopic systems $B = iG$ and $\pi = \nu$.

Let P be the orthogonal projection on the nullspace of B. Thus, $\delta = \text{rank } P$. Notice that instability of $L_\xi(\lambda)$ for ξ large enough follows from statement (b) below. Pure imaginary nonzero eigenvalues of $M_\xi(\beta)$ correspond to nonzero real eigenvalues of $L_\xi(\lambda)$ and imply instability of the system. Thus, when G (or B) is singular, then $\delta > 0$ and there is instability when either ξ is small and positive, or ξ is large and positive. As Lakhadanov's example shows, there may be intermediate values of $\xi > 0$ for which the system is stable. The gist of Problem 2 is, therefore, the clarification of these intermediate stable regimes.

In statements (c) and (d) below we use the notation

$$\|C\|_\infty = \max_i \sum_{j=1}^{n} |c_{ij}|.$$

Theorem 3 *In the limit as $\xi \to \infty$ the eigenvalues of $M_\xi(\beta)$ of (4.2) behave as follows:*

(a) $n - \delta$ eigenvalues converge to zero.

(b) 2δ eigenvalues have limits of the form $\pm ia$ where a is a nonzero (real) eigenvalue of $(PCP)^{1/2}$.

(c) ν eigenvalues lie in circular disks with centers at points ξb_j, $b_j > 0$ and radius $\|C\|_\infty$.

(d) π eigenvalues lie in circular disks with centres at points $-\xi b_j$, $b_j > 0$ and radius $\|C\|_\infty$.

The proof is established in a sequence of three lemmas.

Lemma 2 *Statements (c) and (d) hold and the remaining $n + \delta$ eigenvalues are bounded as $\xi \to \infty$.*

Downloaded 04 May 2010 to 171.66.16.26. Redistribution subject to ASME license or copyright; see http://www.asme.org/terms/Terms_Use.cfm

Proof. Consider the companion matrix of $M_\xi(\beta)$:

$$C_M = \begin{bmatrix} 0 & I \\ -C & -\xi B \end{bmatrix}$$

and recall that $\sigma(M_\xi(\beta)) = \sigma(\beta I - C_M)$. By applying a suitable unitary similarity transformation to $M_\xi(\beta)$ it may be assumed that

$$B = \text{diag}\,[0, \ldots, 0, b_1, \ldots, b_\pi, -b_{\pi+1}, \ldots, -b_{\pi+\nu}] \quad (4.3)$$

where $b_j > 0$ for $j = 1, 2, \ldots, \pi + \nu$. The Gersgorin circles for C_M (see Lancaster and Tismenetsky, 1985, for example) all have radii independent of ξ, $\pi + \nu$ centers are at the points $-\xi b_j$, $\gamma = 1, \ldots, \pi + \nu$, and $n + \delta$ centres are at the origin. Since the eigenvalues of $M_\xi(\beta)$ are necessarily in the disks bounded by these circles the lemma is proved. □

Lemma 3 *Of the $n + \delta$ eigenvalues of $M_\xi(\beta)$ which remain bounded as $\xi \to \infty$, 2δ have finite nonzero limits and $n - \delta$ converge to zero.*

Proof. Consider the "reverse" polynomial

$$\tilde{M}_\xi(\beta) = \beta^2 M_\xi(1/\beta) = \beta^2 C + \beta\xi B + I.$$

The eigenvalues of $M_\xi(\beta)$ are the reciprocals of the eigenvalues of $\tilde{M}_\xi(\beta)$. Since $C > 0$ there is a nonsingular S such that $S^*CS = I$ and

$$\tilde{B} := S^*BS = \text{diag}\,[0, \ldots, 0, \tilde{b}_1, \ldots, \tilde{b}_\pi, -\tilde{b}_{\pi+1}, \ldots, -\tilde{b}_{\pi+\nu}]$$

where $b_j > 0$ for $j = 1, 2, \ldots, \pi + \nu$. Writing $C = S^*S > 0$, the polynomial

$$S^*\tilde{M}_\xi(\beta)S = \beta^2 I + \beta\xi\tilde{B} + \tilde{C}$$

has the same eigenvalue distribution as $\tilde{M}_\xi(\beta)$.

Now apply the Gersgorin argument to $S^*\tilde{M}_\xi(\beta)S$ to show that there are exactly $\pi + \nu$ eigenvalues of $\tilde{M}_\xi(\beta)$ whose absolute values go to infinity as $\xi \to \infty$. Hence, there are exactly $\pi + \nu$ $(= n - \delta)$ eigenvalues of $M_\xi(\beta)$ which converge to zero as $\xi \to \infty$. By Lemma 2 there are $n + \delta$ eigenvalues of $M_\xi(\beta)$ which remain bounded in the limit, and so $(n + \delta) - (n - \delta) = 2\delta$ eigenvalues have finite nonzero limits when $\xi \to \infty$. □

Lemma 4 *An eigenvalue of $M_\xi(\beta)$ having a nonzero finite limit as $\xi \to \infty$ converges to a pure imaginary number ia where a is an eigenvalue of $C_{11}^{1/2}$ and $C_{11} = PCP$.*

Proof. Without loss of generality, suppose that $B = \text{diag}\,[0, B_2, B_3]$ where $B_2 > 0$, $B_3 < 0$ (cf. (4.2)). Form a consistent partition of C:

$$C = \begin{bmatrix} C_{11} & C_{12} & C_{13} \\ C_{12}^* & C_{22} & C_{23} \\ C_{13}^* & C_{23}^* & C_{33} \end{bmatrix}.$$

Let $M_\xi(\beta)x(\xi) = 0$ where $\|x(\xi)\| = 1$ and continuous dependence of β and x on ξ may be assumed. Let y, z, w be consistent partitions of x and we obtain

$$M_\xi(\beta)x(\xi) = \begin{bmatrix} \lambda^2 I + C_{11} & C_{12} & C_{13} \\ C_{12}^* & \lambda^2 I + \lambda\xi B_2 + C_{22} & C_{23} \\ C_{13}^* & C_{23}^* & \lambda^2 I + \lambda\xi B_3 + C_{33} \end{bmatrix} \times \begin{bmatrix} y(\xi) \\ z(\xi) \\ w(\xi) \end{bmatrix} = 0. \quad (4.4)$$

Consider the second row of this equation and take the inner product (in $\mathbb{C}^n$) with $z(\xi)$ to obtain

$$((\lambda^2 I + C_{22})z, z) + (C_{23}w, z) + (C_{12}^* y, z) = -\lambda(\xi)\xi(B_2 z, z).$$

When $\lambda(\xi)$ has a finite limit as $\xi \to \infty$ the left-hand side is bounded. If, in addition, $\lambda(\infty) \neq 0$, we must have $(B_2 z, z) \to 0$ as $\xi \to \infty$, or the right-hand side is unbounded. But $B_2 > 0$ so $z(\xi) \to 0$ as $\xi \to \infty$.

A similar argument shows that $w(\xi) \to 0$ as $\xi \to \infty$. Thus, it follows from (4.4) that

$$(\lambda^2(\infty)I + C_{11})y(\infty) = 0, \quad \|y(\infty)\| = \|x(\infty)\| = 1.$$

The lemma follows. □

The statements of Theorem 3 simply combine the results of Lemmas 2, 3, and 4.

References

Barkwell, L., Lancaster, P., and Markus, A., 1992, "Gyroscopically Stabilized Systems: A Class of Quadratic Eigenvalue Problems With Real Spectrum," *Canadian Jour. of Math.*, Vol. 44, pp. 42–53.

Gohberg, I., Lancaster, P., and Rodman, L., 1982, *Matrix Polynomials*, Academic Press, New York.

Hagedorn, P., 1975, "Über die Instabilität Konservativer Systeme mit Gyroskopishen Kräften," *Ard. Rat. Mechn. Anal.*, Vol. 58, pp. 1–9.

Huseyin, K., 1978, *Vibrations and Stability of Multiple Parameter Systems*, North-Holland, Amsterdam.

Lakhadanov, V. M., 1975, "On Stabilization of Potential Systems," *J. of Applied Math. and Mech. (PMM)*, Vol. 39, No. 1, pp. 45–50.

Lancaster, P., 1966, *Lambda-matrices and Vibrating Systems*, Pergamon Press, Oxford, UK.

Lancaster, P., and Tismenetsky, M., 1985, *The Theory of Matrices*, Academic Press, Orlando.

Seyranian, A., Stoustrop, J., and Kliem, W., 1995, "On Gyroscopic Stabilization," *Z. angew. Math. Phys.*, Vol. 46, pp. 255–267.

Walker, J. A., 1991, "Stability of Linear Conservative Gyroscopic Systems," ASME JOURNAL OF APPLIED MECHANICS, Vol. 58, pp. 229–232.

Wu, J.-W., and Tsao, T.-C., 1994, "A Sufficient Stability Condition for Linear Conservative Gyroscopic Systems," ASME JOURNAL OF APPLIED MECHANICS, Vol. 61, pp. 715–717.

Downloaded 04 May 2010 to 171.66.16.26. Redistribution subject to ASME license or copyright; see http://www.asme.org/terms/Terms_Use.cfm

M. Ahmer Wadee

G. W. Hunt
M. I. Struct. E., F.I.M.A.

Department of Mechanical Engineering,
Faculty of Engineering & Design,
University of Bath,
Claverton Down,
Bath BA2 7AY,
England

Interactively Induced Localized Buckling in Sandwich Structures With Core Orthotropy

Recent work on the interactive buckling behavior of compressed sandwich structures (Hunt and Wadee, 1998) is extended to orthotropic core materials. The variation of the material properties can tend to maximize the interactive effect such that overall and secondary localized modes are triggered almost simultaneously, giving rise to highly unstable post-buckling behavior in systems of practical dimensions.

1 Introduction

Sandwich design, comprising two stiff flanges separated by a soft core material, is increasingly popular as a provider of structural strength combined with weight efficiency. However, recent developments have highlighted that, because it is a highly optimized structural form, it tends to exhibit complicated collapse mechanisms; in particular the spotlight has recently fallen on modal interactions which induce localized buckling onto a small section of one flange as shown in Fig. 1 (Hunt and Wadee, 1998). This recent work introduces a variational model, derived from a large-deflection (small-strain) potential energy formulation, for sandwich structures with isotropic cores—simple to model, but not covering a wide range of available core materials. The greater proportion of available core materials may be modeled more precisely by assuming orthotropic material properties (Allen, 1969; Gibson et al., 1982; Kodiyalam et al., 1996). Previous work on periodic Rayleigh-Ritz models has indicated that core orthotropy can adversely affect the post-buckling performance of the sandwich structure (Da Silva and Hunt, 1990).

In this paper the earlier variational formulation is extended to include orthotropic cores. A parametric study to determine the effect of varying the respective core axial and shear moduli on the proximity of the critical bifurcation, which leads to overall buckling, and secondary bifurcation, which leads to localized buckling, is performed by the use of the numerical continuation package *AUTO94* (Doedel et al., 1995). It is found that orthotropic properties can, in certain configurations, lead to highly complex interactive buckling phenomena such that critical and secondary modes of buckling are triggered virtually simultaneously (Thompson and Hunt, 1973; Budiansky and Hutchinson, 1979).

2 Variational Formulation

The sandwich panel under consideration is shown in Fig. 2, comprising two flanges separated by a softer core material. Although ultimately strains grow to be reasonably large, small-strain assumptions are used throughout, on the basis that the phenomenology of buckle pattern initiation is unlikely to be altered by the choice of alternative large-strain measures.

2.1 Overall Buckling. Classical work on compressed sandwich structures shows that buckling first takes place at an initial critical bifurcation point, C, shown in Fig. 3 as part of a typical equilibrium diagram for a sandwich strut, in an Euler-type overall mode (Allen, 1969). We allow for this by introducing separate "sway" and "tilt" components, whereby a linear combination of these components gives the overall mode profile. This two-degree-of-freedom formulation for the overall mode of buckling (Fig. 4) ensures that the shear strain γ_{xy} is not ignored, as in engineers' bending theory where plane sections are assumed to remain plane ($q_s = q_t$). Linear theory shows that the sway component $W(x)$ and the tilt component $\theta(x)$ are successfully modeled by

$$W(x) = q_s L \sin\frac{\pi x}{L}, \quad \theta(x) = q_t \pi \cos\frac{\pi x}{L}. \tag{1}$$

The corresponding shear strain is given by

$$\gamma_{xy} = (q_s - q_t)\pi \cos\frac{\pi x}{L}. \tag{2}$$

2.2 Interactive Buckling. Once the sandwich structure buckles in an overall mode, its flanges carry different compressive stresses. Also, physically, the greatest compressive stress occurs at the midspan of one flange. This allows the possibility of a secondary bifurcation S (Fig. 3) manifesting itself as a local instability occurring at midspan, as a result of the overall mode forcing the flange locally to exceed its local buckling load. The interaction of overall and local modes thus leads to localized buckling. The corresponding modeshape is defined by functions $w(x)$ and $u(x)$, to represent lateral and in-plane flange displacements, respectively, as shown in Fig. 5.

2.2.1 Bending Energy. The bending energy components arise from the overall bending of both flanges, coupled with extra local bending of the bottom flange of Fig. 5. Linear curvature expressions suffice, giving

$$U_b = \tfrac{1}{2}EI\int_0^L (2W''^2 + w''^2)dx$$
$$= \tfrac{1}{2}EI\int_0^L \left(2q_s^2\frac{\pi^4}{L^2}\sin^2\frac{\pi x}{L} + w''^2\right)dx, \tag{3}$$

where E and ν, respectively, are the Young's modulus and Poisson's ratio of the flange material, and primes represent differentiation with respect to the spatial variable x. Here, EI is the flexural rigidity of one flange:

$$EI = \frac{Ect^3}{12(1-\nu^2)}. \tag{4}$$

2.2.2 Membrane Energy. The membrane strain energy arises from axial displacement of the flanges. The top flange simply contributes the tensile strain resulting from overall buck-

Contributed by the Applied Mechanics Division of THE AMERICAN SOCIETY OF MECHANICAL ENGINEERS for publication in the ASME JOURNAL OF APPLIED MECHANICS.

Discussion on the paper should be addressed to the Technical Editor, Professor Lewis T. Wheeler, Department of Mechanical Engineering, University of Houston, Houston, TX 77204-4792, and will be accepted until four months after final publication of the paper itself in the ASME JOURNAL OF APPLIED MECHANICS.

Manuscript received by the ASME Applied Mechanics Division, June 24, 1997; final revision, Oct. 30, 1997. Associate Technical Editor: S. Kyriakides.

 Copyright © 1998 by ASME

Downloaded 04 May 2010 to 171.66.16.26. Redistribution subject to ASME license or copyright; see http://www.asme.org/terms/Terms_Use.cfm

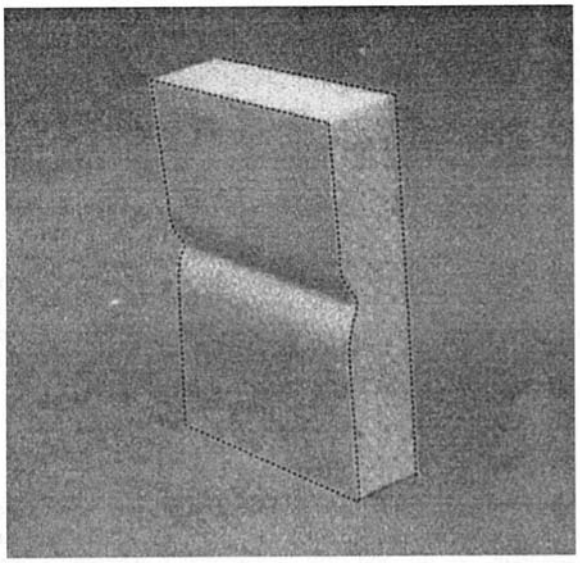


Fig. 1 Localized buckling in an axially compressed sandwich panel caused by interaction with overall buckling

ling, along with a component coming from the pure squash end-shortening Δ,

$$\epsilon_{xt} = -\frac{b}{2}\theta' - \Delta = q_t \frac{b\pi^2}{2L}\sin\frac{\pi x}{L} - \Delta, \tag{5}$$

while the bottom flange adds as extra contributions to the corresponding strains, terms familiar from von Kármán large-deflection plate theory (Timoshenko and Gere, 1961):

$$\epsilon_{xb} = \frac{b}{2}\theta' - \Delta + u' + \tfrac{1}{2}w'^2$$

$$= -q_t \frac{b\pi^2}{2L}\sin\frac{\pi x}{L} - \Delta + u' + \tfrac{1}{2}w'^2. \tag{6}$$

The membrane strain energy is therefore ($D = Etc/2$):

$$U_m = D\int_0^L (\epsilon_{xt}^2 + \epsilon_{xb}^2)dx,$$

$$= D\int_0^L \left[2\Delta^2 + q_t^2\frac{b^2\pi^4}{2L^2}\sin^2\frac{\pi x}{L} + u'^2 + \tfrac{1}{4}w'^4\right.$$

$$\left. - \left(2\Delta + q_t\frac{b\pi^2}{L}\sin\frac{\pi x}{L}\right)(u' + \tfrac{1}{2}w'^2) + u'w'^2\right]dx. \tag{7}$$

2.2.3 Core Energy. The core provides only a small proportion of the axial resistance, but the main resistance to local transverse displacement and shear deformation. A plane-stress assumption is used to model the strain energy of the core. For compatibility, it is also assumed that local displacements $w_c(x, y)$ and $u_c(x, y)$ vary linearly through the core breadth b, such that the top flange has no local displacement and displacements match $w(x)$ and $u(x)$ on the bottom flange. Thus

$$u_c(x, y) = \left(\frac{b - 2y}{2b}\right)u(x),$$

$$w_c(x, y) = \left(\frac{b - 2y}{2b}\right)w(x). \tag{8}$$

Axial strains in the core are then compatible with axial strains in the flanges,

$$\epsilon_x = \frac{\partial u_c}{\partial x} + \frac{1}{2}\left(\frac{\partial w_c}{\partial x}\right)^2 - y\left(\frac{d\theta}{dx}\right) - \Delta$$

$$= \left(\frac{b - 2y}{2b}\right)u' + \frac{1}{2}\left(\frac{b - 2y}{2b}\right)^2 w'^2$$

$$+ q_t y\frac{\pi^2}{L}\sin\frac{\pi x}{L} - \Delta. \tag{9}$$

Remaining strains can be written from small deflection theory,

$$\epsilon_y = \nu_x\Delta + \frac{\partial w_c}{\partial y} = \nu_x\Delta - \frac{w}{b}, \tag{10}$$

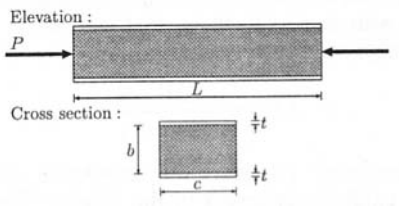


Fig. 2 Typical sandwich panel and cross section

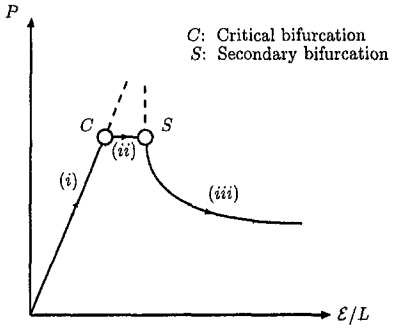


Fig. 3 Equilibrium diagram for sandwich struts: (*i*) fundamental path; (*ii*) critical bifurcation of overall buckling; (*iii*) secondary path of localized buckling. Here, *P* represents the applied load, and $\mathcal{E}$ is its corresponding deflection or end shortening.

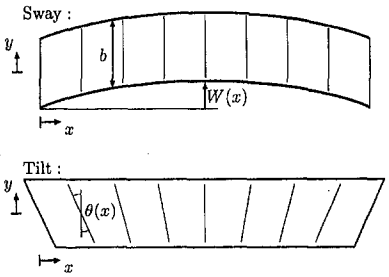


Fig. 4 Sway and tilt components of overall mode

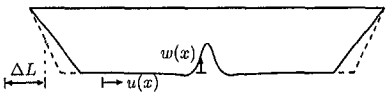


Fig. 5 Displacement functions used to model localized buckling

Downloaded 04 May 2010 to 171.66.16.26. Redistribution subject to ASME license or copyright; see http://www.asme.org/terms/Terms_Use.cfm

$$\gamma_{xy} = (q_s - q_t)\pi \cos\frac{\pi x}{L} + \frac{\partial w_c}{\partial x} + \frac{\partial u_c}{\partial y}$$

$$= (q_s - q_t)\pi \cos\frac{\pi x}{L} + \left(\frac{b - 2y}{2b}\right)w' - \frac{u}{b}. \quad (11)$$

The core is in a state of plane stress ($\sigma_z = \tau_{xz} = \tau_{yz} = 0$), which implies that the strain energy of the core is

$$U_c = \frac{1}{2}\int_S (\sigma_x\epsilon_x + \sigma_y\epsilon_y + \tau_{xy}\gamma_{xy})dS \quad (12)$$

where S is the solid domain of the integral. Hooke's law for an orthotropic material gives the constitutive relations (Jones, 1975; Da Silva and Hunt, 1990)

$$\sigma_x = \frac{E_x}{(1 - \nu_x\nu_y)}(\epsilon_x + \nu_y\epsilon_y) \quad (13)$$

$$\sigma_y = \frac{E_y}{(1 - \nu_x\nu_y)}(\epsilon_y + \nu_x\epsilon_x) \quad (14)$$

$$\tau_{xy} = G_c\gamma_{xy}, \quad (15)$$

where E_x and E_y are the orthogonal core Young's moduli, and G_c is the core shear modulus; the reciprocal relationship of the constitutive law is

$$E_x\nu_y = E_y\nu_x, \quad (16)$$

where ν_x and ν_y are the orthogonal core Poisson's ratios. The strain energy of the core is thus

$$U_c = \int_0^L \int_{-b/2}^{b/2} \left[\frac{c}{2(1 - \nu_x\nu_y)}(E_x\epsilon_x^2 + E_y\epsilon_y^2 + 2\nu_x E_y\epsilon_x\epsilon_y) + \frac{G_c c}{2}\gamma_{xy}^2\right]dydx. \quad (17)$$

Performing the integration with respect to y after substituting for ϵ_x, ϵ_y, and γ_{xy} gives

$$U_c = \int_0^L \left\{C_x\left[\Delta^2 + q_t^2\frac{b^2\pi^4}{12L^2}\sin^2\frac{\pi x}{L} + \tfrac{1}{3}u'^2 + \tfrac{1}{20}w'^4 - \Delta u' - \tfrac{1}{3}\Delta w'^2 + \tfrac{1}{4}u'w'^2 - q_t\frac{b\pi^2}{6L}\sin\frac{\pi x}{L}(u' + \tfrac{1}{2}w'^2)\right]\right.$$

$$+ \tfrac{1}{2}kw^2 - \tfrac{1}{3}k_1w^3 + \tfrac{1}{4}k_2w^4 + G\left[\frac{u^2}{b^2} + \tfrac{1}{3}w'^2 - \frac{uw'}{b}\right.$$

$$+ (q_s - q_t)^2\pi^2\cos^2\frac{\pi x}{L} + (q_s - q_t)\pi\cos\frac{\pi x}{L}$$

$$\left.\times\left(w' - \frac{2}{b}u\right)\right] + C_y[\nu_x^2\Delta b(u' - \Delta + \tfrac{1}{3}w'^2)$$

$$\left. - \nu_x(u'w + \tfrac{1}{3}ww'^2)]\right\}dx, \quad (18)$$

where

$$G = \frac{G_c c b}{2}, \quad k = \frac{E_y c}{2(1 - \nu_x\nu_y)b},$$

$$C_x = \frac{E_x b c}{2(1 - \nu_x\nu_y)}, \quad C_y = \frac{E_y c}{2(1 - \nu_x\nu_y)}. \quad (19)$$

Parameters k_1 and k_2 are included to adjust the transverse core stiffness properties to simulate real (nonlinear) core situations (Gibson et al., 1982; Gibson and Ashby, 1982) with an initially linear constitutive relationship for small displacement, followed by a destabilization ($k_1 > 0$) and then restabilization ($k_2 > 0$) as displacement grows. Polystyrene and polyurethane foams exhibit this type of nonlinear elastoplastic constitutive behavior in compression when strains become moderately large. Longitudinal and shear strains are small in comparison with the transverse core strain; and so the above nonlinearities are included only in the transverse direction. A full elastoplastic analysis of the core is avoided to limit unnecessary complexity in the model.

2.2.4 Work Done by Load. The final component of energy to be identified is the work done by the load P moving through its corresponding displacement $\mathcal{E}$. The contribution from the local buckling of a single flange at midsection is just one-half of the end shortening of the flange itself. Together with the contributions from pure squash and sway from overall buckling (Fig. 4), this gives

$$P\mathcal{E} = P\int_0^L \left(\frac{q_s^2\pi^2}{2}\cos^2\frac{\pi x}{L} - \tfrac{1}{2}u' + \Delta\right)dx. \quad (20)$$

2.2.5 Total Potential Energy. The total potential energy of the structure is given by the summation of U_c, U_m, and U_b, minus the work done by load,

$$V = \int_0^L \left\{C_x\left[\Delta^2 + q_t^2\frac{b^2\pi^4}{12L^2}\sin^2\frac{\pi x}{L} + \tfrac{1}{3}u'^2 + \tfrac{1}{20}w'^4 - \Delta u' - \tfrac{1}{3}\Delta w'^2 + \tfrac{1}{4}u'w'^2 - q_t\frac{b\pi^2}{6L}\sin\frac{\pi x}{L}(u' + \tfrac{1}{2}w'^2)\right]\right.$$

$$+ \tfrac{1}{2}kw^2 - \tfrac{1}{3}k_1w^3 + \tfrac{1}{4}k_2w^4 + G\left[\frac{u^2}{b^2} - \frac{uw'}{b} + \tfrac{1}{3}w'^2\right.$$

$$+ (q_s - q_t)^2\pi^2\cos^2\frac{\pi x}{L} + (q_s - q_t)\pi\cos\frac{\pi x}{L}$$

$$\left.\times\left(w' - \frac{2}{b}u\right)\right] + C_y[\nu_x^2\Delta b(u' - \Delta + \tfrac{1}{3}w'^2)$$

$$- \nu_x(u'w + \tfrac{1}{3}ww'^2)] + D\left[2\Delta^2 + q_t^2\frac{b^2\pi^4}{2L^2}\sin^2\frac{\pi x}{L}\right.$$

$$- \left(2\Delta + q_t\frac{b\pi^2}{L}\sin\frac{\pi x}{L}\right)(u' + \tfrac{1}{2}w'^2) + u'^2 + \tfrac{1}{4}w'^4$$

$$\left. + u'w'^2\right] + \tfrac{1}{2}EI\left(w''^2 + 2q_s^2\frac{\pi^4}{L^2}\sin^2\frac{\pi x}{L}\right)$$

$$\left. - P\left(\frac{q_s^2\pi^2}{2}\cos^2\frac{\pi x}{L} - \tfrac{1}{2}u' + \Delta\right)\right\}dx. \quad (21)$$

The analysis of this functional is in two distinct parts, the first to obtain differential equations for $w(x)$ and $u(x)$ along with suitable boundary conditions to minimize the potential energy using the calculus of variations, and the second to minimize the energy with respect to the generalized coordinates q_s, q_t, and Δ. The process is detailed in Hunt and Wadee (1998), and so only the results are presented here.

Downloaded 04 May 2010 to 171.66.16.26. Redistribution subject to ASME license or copyright; see http://www.asme.org/terms/Terms_Use.cfm

After determining the first variation of V and integrating by parts, we obtain the following differential equations:

$$EIw'''' + D\left[2\Delta w'' + q_t\frac{b\pi^2}{L}\left(\sin\frac{\pi x}{L}w'' + \frac{\pi}{L}\cos\frac{\pi x}{L}w'\right) - (2u''w' + 2u'w'' + 3w'^2w'')\right] + G\left[\frac{u'}{b} - \tfrac{2}{3}w'' + (q_s - q_t)\frac{\pi^2}{L}\sin\frac{\pi x}{L}\right] + kw - k_1w^2 + k_2w^3 + C_x\left[\tfrac{2}{3}\Delta w'' - (\tfrac{1}{2}u''w' + \tfrac{1}{2}u'w'' + \tfrac{3}{5}w'^2w'') + q_t\frac{b\pi^2}{6L}\left(\sin\frac{\pi x}{L}w'' + \frac{\pi}{L}\cos\frac{\pi x}{L}w'\right)\right] + C_y[\tfrac{2}{3}\nu_x(ww'' + w'^2) - \tfrac{2}{3}\nu_x^2\Delta bw'' - \nu_x(u' + \tfrac{1}{3}w'^2)] = 0 \quad (22)$$

$$\left(D + \frac{C_x}{3}\right)u'' - \frac{G}{b^2}u + \frac{G}{2b}w' + \left(D + \frac{C_x}{4}\right)w'w'' + \pi\cos\frac{\pi x}{L}\left[G\frac{(q_s - q_t)}{b} - q_t\frac{b\pi^2}{2L^2}\left(D + \frac{C_x}{6}\right)\right] - \frac{C_y\nu_x}{2}w' = 0, \quad (23)$$

subject to physical boundary conditions; simply supported ends are assumed,

$$w(0) = w''(0) = w(L) = w''(L) = 0, \quad (24)$$

and matching the applied stress at the ends,

$$-\frac{P}{4D} = \left(1 + \frac{C_x}{3D}\right)u'(x_0) + \left(1 + \frac{C_x}{4D}\right)\frac{1}{2}w'^2(x_0) - \left(1 + \frac{C_x}{2D} - \frac{C_y\nu_x^2 b}{2D}\right)\Delta, \quad (25)$$

where $x_0 = 0$ and L. These boundary conditions arise naturally from minimizing the potential energy functional (Hunt and Wadee, 1998). Finally, minimizing the energy with respect to the degrees-of-freedom lead to

$$P = \frac{2\pi^2 EI}{L^2} + \frac{2G}{q_s}\left[(q_s - q_t) + \frac{1}{\pi L}\int_0^L \cos\frac{\pi x}{L}\left(w' - \frac{2}{b}u\right)dx\right], \quad (26)$$

$$s(q_s - q_t) = q_t + \int_0^L\left[\frac{s}{\pi L}\cos\frac{\pi x}{L}\left(\frac{2}{b}u - w'\right) - \frac{1}{b\pi^2}\sin\frac{\pi x}{L}(u' + \tfrac{1}{2}w'^2)\right]dx, \quad (27)$$

$$\Delta = \frac{P + \int_0^L\left[\frac{2D}{L}(u' + \frac{1}{2}w'^2) + \left(\frac{C_x - C_y b\nu_x^2}{L}\right)(u' + \frac{1}{3}w'^2)\right]dx}{4D + 2C_x - 2C_y\nu_x^2 b}. \quad (28)$$

where

$$s = \frac{2GL^2}{b^2\pi^2}\left(D + \frac{C_x}{6}\right)^{-1}. \quad (29)$$

2.3 Linear Eigenvalue Analysis for Overall Buckling. A simple linear eigenvalue analysis yields the critical load for overall buckling P^C, arising on the pure squash fundamental path F at which $q_s = q_t = w = u = 0$. The potential energy is nondiagonalized with respect to q_s and q_t, and so this critical load C occurs when the matrix

$$\mathbf{V}_{ij}^F = \begin{pmatrix} \left.\frac{\partial^2 V}{\partial q_s^2}\right|^F & \left.\frac{\partial^2 V}{\partial q_s \partial q_t}\right|^F \\ \left.\frac{\partial^2 V}{\partial q_t \partial q_s}\right|^F & \left.\frac{\partial^2 V}{\partial q_t^2}\right|^F \end{pmatrix} \quad (30)$$

is singular. Rearranging the resulting equation to find P^C gives

$$P^C = \frac{2\pi^2 EI}{L^2} + \frac{2Gb^2\pi^2}{L^2}\left[\frac{\left(D + \frac{C_x}{6}\right)}{2G + \frac{b^2\pi^2}{L^2}\left(D + \frac{C_x}{6}\right)}\right]. \quad (31)$$

2.4 Nondimensionalization. The variables are rescaled such that the equations can be solved numerically in the numerical continuation package *AUTO94* (Doedel et al., 1995). The scalings for the principal variables used are as follows:

$$\tilde{x} \to \frac{2}{L}x, \quad \tilde{w} \to \frac{2}{L}w, \quad \tilde{u} \to \frac{2}{L}u. \quad (32)$$

3 Numerical Solution

The numerical results are given for a sandwich structure of practical dimensions and is performed by solving the interactive buckling Eqs. (22) and (23), subject to integral Eqs. (26), (27), and (28), rescaled in terms of the nondimensional variables (32), in the numerical continuation package *AUTO94*. Overall symmetry of the system is encapsulated by imposing the so-called *symmetric section* condition at $\tilde{x} = 1$:

$$w' = w''' = u = 0. \quad (33)$$

The purpose is to evaluate how core orthotropy can adversely affect the post-buckling performance of a perfect sandwich structure, with some of the consequences for real (imperfect) structures being highlighted. This is performed by varying material property parameters and noting the effect these have on the proximity of the critical and secondary bifurcations, measured by the magnitude of the sway mode (q_s); a value of zero at secondary bifurcation means the critical and secondary bifurcations would coincide.

Solutions are presented thus: first the core shear modulus, G_c, is varied independently of the core Young's moduli, E_x and E_y, which are kept constant; secondly, G_c is kept constant so that E_x and E_y can be varied one at a time; finally, we compare the difference between the isotropic and the most severe orthotropic modes thus found.

3.1 Numerical Results. For comparison purposes we choose a sandwich section which has received earlier attention (Da Silva and Hunt, 1990). For the flanges: Young's modulus: $E = 68947.57$ N/mm^2, Poisson's ratio: $\nu = 0.3$, thickness: $t = 0.508$ mm. For the core: breadth: $b = 50.8$ mm; strut width: $c = 254$ mm, strut length: $L = 508$ mm. Other properties are initially taken from an isotropic panel and are varied later to obtain results for the orthotropic core. Preliminary isotropic

Downloaded 04 May 2010 to 171.66.16.26. Redistribution subject to ASME license or copyright; see http://www.asme.org/terms/Terms_Use.cfm

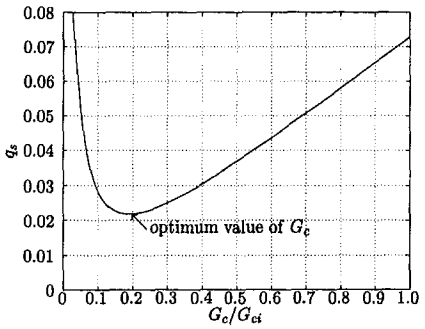
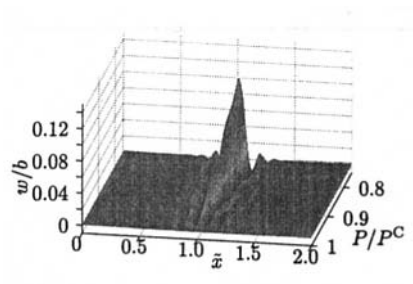


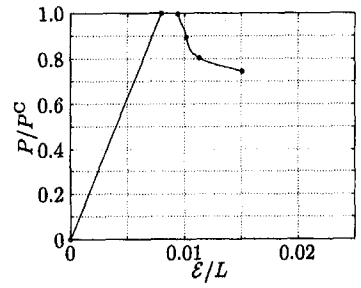
Fig. 6 Effect of varying G_c on the proximity of critical and secondary bifurcations

core properties are: Young's modulus: $E_{xi} = E_{yi} = 198.57$ N/mm^2, shear modulus: $G_{ci} = 82.74$ N/mm^2, Poisson's ratio: $\nu_{xi} = \nu_{yi} = 0.2$. In addition, nonlinearities are added to the core transverse resistance $F = kw - k_1w^2 + k_2w^3$, where k is given by Eq. (19) with $k_1 = 538$ N/mm^3 and $k_2 = 75$ N/mm^4. All modulus units hence will be in N/mm^2.

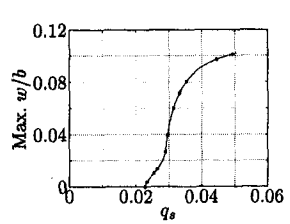
3.1.1 Variation of Core Shear Modulus. Orthotropy in the core means that the modulus of the core in shear can be altered independently of the Young's modulus components. Varying the shear modulus has a substantial influence on the critical load for overall buckling and thus has an important effect on the proximity of the critical and secondary bifurcations. Figure 6 shows the magnitude of sway at the secondary bifurcation (q_s) plotted against G_c.



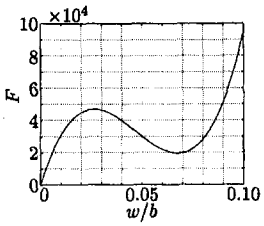
(a) Flange localization profiles



(b) Load–end-shortening curve



(c) Relative magnitudes of overall and localized modal amplitudes



(d) Transverse resistance of core

Fig. 7 Post-buckling response of a severe orthotropic case

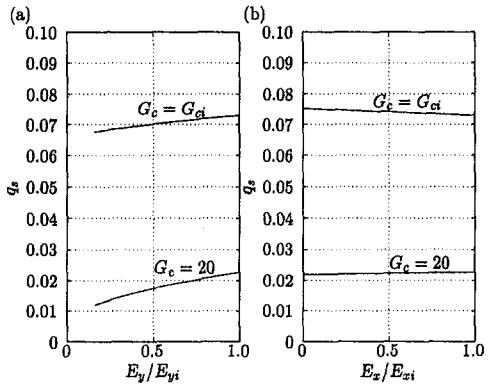


Fig. 8 Effects of varying direct core moduli on the position of the secondary bifurcation S: (a) E_y variation, (b) E_x variation

In the isotropic case $q_s = 0.073$, whereas when $G_c = 20$, $q_s = 0.023$. This shows that reducing the shear modulus in this case has a marked adverse effect on the post-buckling by bringing the two bifurcations much closer together. The post-buckling response of the severe configuration where $G_c = 20$ is shown in Fig. 7.

3.1.2 Variation of Direct Core Moduli. Varying the core transverse modulus, E_y, while keeping $\nu_x\nu_y = 0.04$ and G_c constant, we obtain Fig. 8(a). The two curves represent the cases of $G_c = G_{ci}$ (upper curve), and $G_c = 20$ (lower curve). Both curves show q_s dropping monotonically with a shallow gradient. Similarly, varying the core axial modulus, E_x while keeping $\nu_x\nu_y = 0.04$ and G_c constant, we obtain Fig. 8(b) (lower curve). It is thus found that the reduction in the relative strains required for localized buckling are not significantly affected by either E_y or E_x.

3.1.3 Comparison of Isotropy and Orthotropy. It is interesting to monitor the change in core shear modulus that will maximize the interaction between local and overall buckling. Figure 9(a) compares the maximized interactive effect, measured again by the value of q_s at secondary bifurcation, with the equivalent for an isotropic core, as direct core stiffness is altered. The curves touch at $E_c = 25$, indicating that, for a system of these particular dimensions and material characteristics, isotropy maximizes the interaction. When $E_c > 25$, decreasing G_c while holding E_c constant brings the bifurcations together. This is because, as G_c increases in relation to E_c, the strut tends to the engineers' bending theory situation of *plane sections remaining plane;* in the limit this denies the shearing displacements in the core that are part and parcel of localized buckling (Hunt and Wadee, 1998).

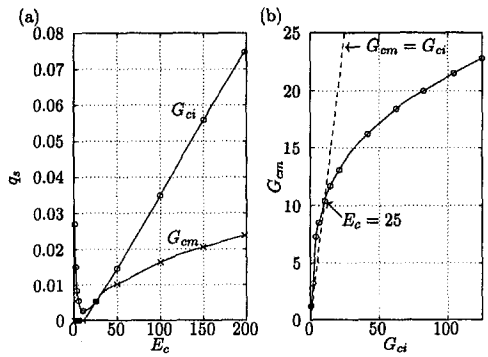


Fig. 9 (a) Comparison of secondary bifurcation position in isotropic cores (○) and orthotropic cores where G_c is varied to maximize the interaction (×). (b) Values of G_c which maximize the interaction.

Downloaded 04 May 2010 to 171.66.16.26. Redistribution subject to ASME license or copyright; see http://www.asme.org/terms/Terms_Use.cfm

On the other hand, when $E_c < 25$, the bifurcations are brought together by increasing G_c; indeed, q_s tends rapidly to zero as E_c reduces, indicating that primary and secondary bifurcations become virtually coincident, a phenomenon which is often associated with a high degree of imperfection sensitivity (Thompson and Hunt, 1984). This is the opposite situation: as G_c drops the strut loses shear resistance and the overall mode tends to pure sway with no tilt; this implies there is little or no differential compression in the flanges and hence little or no tendency for the response to localize to one flange. The full interactive effect is thus found for cores that allow just the optimum amount of shearing deformation.

4 Concluding Remarks

The introduction of orthotropy in the core of sandwich structure opens the application of this model to more widely available core materials. Moreover, it has highlighted the fact that the mode interaction that induces localized buckling can be greatly exaggerated by varying the material properties in an orthotropic manner. The variation of shear stiffness is identified as a key parameter in maximizing the interactive effect. It must be large enough for sway mode to bring with it a significant tilt component, but also small enough for shear deformations to be allowed in the core. Thus an optimum shear modulus exists for each different value of direct core stiffness.

The extent of this adverse exaggeration of the interactive post-buckling performance of the sandwich structure is such that the perfect strut buckles in an overall mode and then almost immediately (with < one percent additional axial strain) in a secondary localized mode. This is very likely to lead to a real strut with similar properties being very sensitive to initial imperfections such that the strut may not reach its linearly determined critical load.

Work is now proceeding to obtain experimental evaluation of this strut behavior in the laboratory. Preliminary comparisons of buckle patterns and wavelength are encouraging.

References

Allen, H. G., 1969, *Analysis and Design of Structural Sandwich Panels,* Pergamon, Oxford, UK.

Budiansky, B., and Hutchinson, J. W., 1979, "Buckling: Progress and Challenge," J. F. Besseling and A. M. J. van der Heijden, eds., *Trends in Solid Mechanics 1979: Proceedings of the symposium dedicated to the 65th birthday of W. T. Koiter,* Delft University Press, Delft, The Netherlands.

Da Silva, L. S., and Hunt, G. W., 1990, "Interactive Buckling in Sandwich Structures With Core Orthotropy," *Mech. Struct. & Mach.,* Vol. 18, No. 3, pp. 353–372.

Doedel, E. J., Wang, X. J., and Fairgrieve, T. F., 1995, "*AUTO94:* Software for Continuation and Bifurcation Problems in Ordinary Differential Equations," Tech. Rept. CRPC-95-2. California Institute of Technology, Pasadena, CA.

Gibson, L. J., and Ashby, M. F., 1982, "The Mechanics of Three-Dimensional Cellular Materials," *Proc. R. Soc. Lond.,* Vol. A382, pp. 43–59.

Gibson, L. J., Ashby, M. F., Schjaer, G. S., and Robertson, C. I., 1982, "The Mechanics of Two-Dimensional Cellular Materials," *Proc. R. Soc. Lond.,* Vol. A382, pp. 25–42.

Hunt, G. W., and Wadee, M. Ahmer, 1998, "Localization and Mode Interaction in Sandwich Structures," *Proc. R. Soc. Lond.,* Vol. A454, pp. 1197–1216.

Jones, R. M., 1975, *Mechanics of Composite Materials,* Hemisphere, New York.

Kodiyalam, S., Nagendra, S., and DeStefano, J., 1996, "Composite Sandwich Structure Optimization With Application to Satellite Components," *A.I.A.A. J.,* Vol. 34, No. 3, pp. 614–621.

Thompson, J. M. T., and Hunt, G. W., 1973, *A General Theory of Elastic Stability,* John Wiley and Sons, London.

Thompson, J. M. T., and Hunt, G. W., 1984, *Elastic Instability Phenomena.* John Wiley and Sons, Chichester, UK.

Timoshenko, S. P., and Gere, J. M., 1961, *Theory of Elastic Stability,* McGraw-Hill, New York.

Downloaded 04 May 2010 to 171.66.16.26. Redistribution subject to ASME license or copyright; see http://www.asme.org/terms/Terms_Use.cfm

Journal of Applied Mechanics

Brief Notes

A Brief Note is a short paper that presents a specific solution of technical interest in mechanics but which does not necessarily contain new general methods or results. A Brief Note should not exceed 1500 words *or equivalent* (a typical one-column figure or table is equivalent to 250 words; a one line equation to 30 words). Brief Notes will be subject to the usual review procedures prior to publication. After approval such Notes will be published as soon as possible. The Notes should be submitted to the Technical Editor of the JOURNAL OF APPLIED MECHANICS. Discussions on the Brief Notes should be addressed to the Editorial Department, ASME, United Engineering Center, 345 East 47th Street, New York, N. Y. 10017, or to the Technical Editor of the JOURNAL OF APPLIED MECHANICS. Discussions on Brief Notes appearing in this issue will be accepted until two months after publication. Readers who need more time to prepare a Discussion should request an extension of the deadline from the Editorial Department.

Cruciform Rigid Line Problem in an Infinite Plate

Y. Z. Chen[1]

1 Introduction

Recently there has been a resurgence of interest in the rigid line problem. Many works in this field were presented by Wang, Zhang, and Chou (1985), Hasebe and Takeuchi (1985), Dunders and Markenscoff (1989), Dunders (1989), Ballarini (1990), Chen and Hasebe (1992a), and Markenscoff and Li (1996). Characteristics of the stress field near the tip of a rigid line inhomogeneity can be found from an earlier investigation by England (1971). England analyzed the singular behavior of a wedge with the wedge angle $\alpha = \pi$ when the two edges are fixed. The analysis invariably leads to the conclusion that the stresses are singular with the asymptotic expression $\sigma_{ij} \approx O(r^{-1/2})$, where r denotes the distance between the rigid line tip and a point in the vicinity of the tip. The stress singularity coefficient (abbreviated as SSC) was defined and the leading term of stresses was also introduced by Hasebe and Takeuchi (1985).

For the simple reason that the definition used for SSC has the same expression with the crack problem, we use the following definition:

$$K_{1R} - iK_{2R} = 2\sqrt{2\pi} \lim_{z \to a} \sqrt{z - a}\phi'(z) \tag{1}$$

where the rigid line tip is located at the point $z = a$ and $\phi'(z)$ is a complex potential defined by Muskhelishvili (1953).

In this note the cruciform rigid line problem is studied. The objective of this paper is to provide the singular integral equation approach for the problem. Secondly, numerical results are present to show the interaction between rigid branches. In addition, some particular features in the rigid line problem are compared with those in the crack problem.

2 Analysis

The following analysis depends on the complex variable function method in plane elasticity (Muskelishvili, 1953). In this method the stresses $(\sigma_x, \sigma_y, \sigma_{xy})$, the displacements (u, v), and the resultant force function (X, Y) are expressed in terms of two complex potentials $\phi(z)$, $\psi(z)$ such that

$$\sigma_x + \sigma_y = 4\,\mathrm{Re}\phi'(z)$$

$$\sigma_y - \sigma_x + 2i\sigma_{xy} = 2[\bar{z}\phi''(z) + \psi'(z)] \tag{2}$$

$$f = -Y + iX = \phi(z) + z\overline{\phi'(z)} + \overline{\psi(z)} \tag{3}$$

$$2G(u + iv) = \kappa\phi(z) - z\overline{\phi'(z)} - \overline{\psi(z)} \tag{4}$$

where G is the shear modulus of elasticity, $\kappa = (3 - \nu)/(1 + \nu)$ for the plane stress problem, and ν is the Poisson's ratio. In addition, the following two derivatives in a specified direction are useful (Chen and Hasebe 1992b):

$$J_1\left(z, \frac{\overline{dz}}{dz}\right) = \lim_{\Delta z \to 0} \frac{1}{\Delta z}\{(f)_{z+\Delta z} - (f)_z\}$$

$$= \phi'(z) + \overline{\phi'(z)} + \frac{\overline{dz}}{dz}(z\overline{\phi''(z)} + \overline{\psi'(z)})$$

$$= N + iT \tag{5}$$

$$J_2\left(z, \frac{\overline{dz}}{dz}\right) = 2G \lim_{\Delta z \to 0} \frac{1}{\Delta z}\{(u + iv)_{z+\Delta z} - (u + iv)_z\}$$

$$= \kappa\phi'(z) - \overline{\phi'(z)} - \frac{\overline{dz}}{dz}(z\overline{\phi''(z)} + \overline{\psi'(z)}). \tag{6}$$

Physically, the J_1 value represents the traction $N + iT$ applied along the interval z, $z + \Delta z$ in Fig. 1.

In the analysis, the solution of the cruciform rigid line problem depends on the potential for a single rigid line problem. The appropriate complex potential for the single rigid line problem has been obtained previously by Chen and Hasebe (1992a), which is as follows:

[1] Laboratory for Nonlinear Mechanics of Continuous Media, Institute of Mechanics, Chinese Academy of Sciences, Beijing 100080, P. R. China. (Permanent address: Division of Engineering Mechanics, Jiangsu University of Science and Technology, Zhenjiang, Jiangsu 212013, P. R. China.)

Contributed by the Applied Mechanics Division of THE AMERICAN SOCIETY OF MECHANICAL ENGINEERS for publication in the ASME JOURNAL OF APPLIED MECHANICS. Manuscript received by the ASME Applied Mechanics Division, Dec. 5, 1996; final revision, Aug. 14, 1997. Associate Technical Editor: J. N. Reddy.

 Copyright © 1998 by ASME

Downloaded 04 May 2010 to 171.66.16.26. Redistribution subject to ASME license or copyright; see http://www.asme.org/terms/Terms_Use.cfm

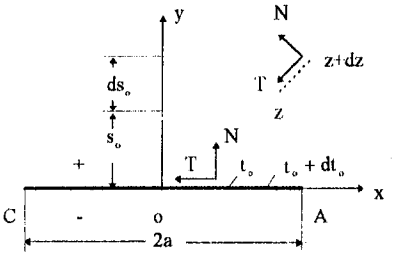


Fig. 1 A single rigid line problem in an infinite plate

$$\phi(z) = -\frac{1}{2\pi}\int_{-a}^{a} \text{Log}\,(z-t)h(t)dt$$

$$\psi(z) = \frac{\kappa}{2\pi}\int_{-a}^{a} \text{Log}\,(z-t)h(t)dt - \frac{1}{2\pi}\int_{-a}^{a}\frac{th(t)dt}{t-z} \quad (7)$$

where $h(t)$, $t \in (-a, a)$ takes the complex value in general. Physically, the function $h(t)$ represents the body force density. In this note only the normal mode case with the remote stresses σ_x^∞, σ_y^∞ is considered. In this case, the function $h(t)$ is an odd one and takes the real value.

Substituting (7) into (5) and (6), letting $z \to t_0^+$ and $z \to t_0^-$ $t_0 \in (-a, a)$ (Fig. 1), and using some results obtained previously (Chen and Hasebe, 1992b) along the line CA we can get

$$[J_1(t_0, 1)]^+ - [J_1(t_0, 1)]^- = [N(t_0) + iT(t_0)]^+ - [N(t_0) + iT(t_0)]^- = i(\kappa + 1)h(t_0), \quad |t_0| < a \quad (8)$$

$$[J_2(t_0, 1)]^+ = [J_2(t_0, 1)]^- = J_2(t_0, 1) = \frac{\kappa}{\pi}\int_{-a}^{a}\frac{h(t)dt}{t - t_0}, \quad |t_0| < a. \quad (9)$$

Equation (8) shows that the J_1 contribution has a jump when a moving point is passing through the line CA in Fig. 1. On the contrary, Eq. (9) shows that the J_2 contribution is continuous in the same condition.

The J_2 contribution along the interval $\overline{is_0,\ i(s_0 + ds_0)}$ in Fig. 1 can be obtained by simply substituting $z = is_0$, $dz = ids_0$, $\overline{dz}/dz = -1$, in (6), and it can be expressed in the form

$$J_2 = \frac{\kappa}{2\pi}\int_{-a}^{a}\frac{2is_0h(t)dt}{t^2 + s_0^2} - \frac{1}{2\pi}\int_{-a}^{a}\frac{2th(t)dt}{(t + is_0)^2}$$

(for a point along the y-axis in Fig. 1). (10)

Since the rigid line is in equilibrium, from Eq. (8) we obtain the following constraint equation:

$$\int_{-a}^{a} h(t)dt = 0. \quad (11)$$

From Eqs. (2) and (7), the SSC at the right tip A in Fig. 1 can be evaluated from

$$K_{1R} = -(2\pi)^{1/2}\operatorname*{Lim}_{t\to a}\sqrt{|t-a|}h(t). \quad (12)$$

The original stress field for the cruciform rigid line problem (Fig. 2(a)) can be considered as a superposition of the uniform stress field (Fig. 2(b)) and the perturbation field (Fig. 2(c)). Clearly, the original stress field has the following solution (Muskhelishvili, 1953):

$$2G(u + iv) = (\kappa - 1)\Gamma z - \Gamma_1\bar{z} \quad (13)$$

where

$$\Gamma = (\sigma_x^\infty + \sigma_y^\infty)/4, \quad \Gamma_1 = (\sigma_y^\infty - \sigma_x^\infty)/2. \quad (14)$$

Actually, the J_2 contribution caused by the uniform stress field should be canceled by the J_2 contribution caused by the perturbation field. Secondly, the cruciform rigid line problem is considered as a superposition of two single rigid line problems. With this in mind, letting the body force density $h_1(s_1)$, $(h_2(s_2))$ be placed along the horizontal portion (the vertical portion) of the cruciform configuration, and considering the J_2 contributions as shown by (9) and (10), we obtain the following system of singular integral equations:

$$\frac{2\kappa}{\pi}\int_0^a \frac{th_1(t)dt}{t^2 - s_1^2} + \frac{2}{\pi}\int_0^b \frac{t(s_1^2 - t^2)h_2(t)dt}{(t^2 + s_1^2)^2} = (1-\kappa)\Gamma + \Gamma_1, \quad (0 < s_1 < a) \quad (15)$$

$$\frac{2\kappa}{\pi}\int_0^b \frac{th_2(t)dt}{t^2 - s_2^2} + \frac{2}{\pi}\int_0^a \frac{t(s_2^2 - t^2)h_1(t)dt}{(t^2 + s_2^2)^2} = (1-\kappa)\Gamma - \Gamma_1, \quad (0 < s_2 < b). \quad (16)$$

In the studied case, since the functions $h_1(s_1)$, $(h_2(s_2))$ are odd real functions, the condition like Eq. (11) is satisfied automatically. It is of interest to point out that substituting $\kappa = -1$ into Eqs. (15) and (16) will yield the singular integral equation for the cruciform crack problem (Boiko and Karpenko, 1981).

After solving the integral equation, the SSCs at two tips A and B (Fig. 2) can be evaluated by

$$K_{1R,A} = -(2\pi)^{1/2}\operatorname*{Lim}_{t\to a}\sqrt{|t-a|}h_1(t) \quad \text{(for the tip A in Fig. 2)} \quad (17)$$

$$K_{1R,B} = -(2\pi)^{1/2}\operatorname*{Lim}_{t\to b}\sqrt{|t-b|}h_2(t) \quad \text{(for the tip B in Fig. 2)}. \quad (18)$$

3 Numerical Example

In the numerical solution, a semi-open quadrature rue is most suitable to solve the singular integral Eq. (15) and (16). The quadrature rule suggested by Boiko and Karpenko (1981) is used to solve the singular integral equation.

In the numerical solution we let

$$h_1(t) = \sqrt{\frac{t}{a-t}}H_1(t), \quad (0 \le t \le a)$$

$$h_2(t) = \sqrt{\frac{t}{b-t}}H_2(t), \quad (0 \le t \le b). \quad (19)$$

Finally, by using (17), (18), and (19) the SSCs at two rigid line tips A and B can be evaluated by

$$K_{1R,A} = -(2\pi a)^{1/2}H_1(a), \quad K_{1R,B} = -(2\pi b)^{1/2}H_2(b). \quad (20)$$

Under the following conditions (1) the plane stress condition

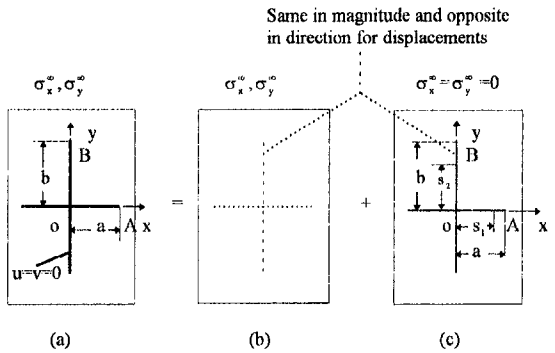


Fig. 2 Utilization of the superposition principle (a) the original stress field, (b) the uniform stress field, (c) the perturbation stress field

Downloaded 04 May 2010 to 171.66.16.26. Redistribution subject to ASME license or copyright; see http://www.asme.org/terms/Terms_Use.cfm

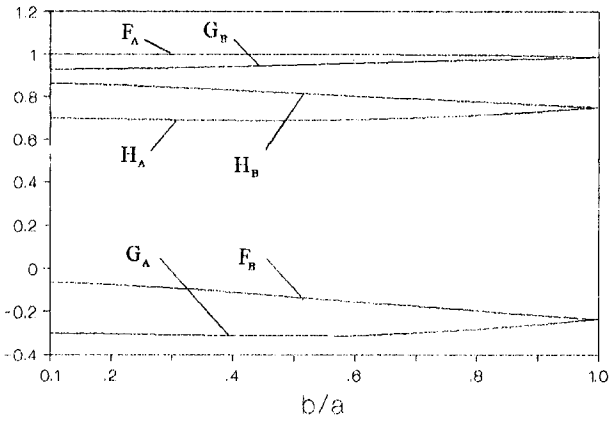


Fig. 3 Normalized SSCs at two rigid line tips A and B (see Fig. 2 and Eqs. (21), (22), (23), (24))

and $\nu = 0.3$ are assumed, and (b) the remote stresses σ_x^∞, σ_y^∞ are applied at infinity. The SSCs at two rigid line tips are expressed by

$$K_{1R,A} = (F_A(b/a)\sigma_x^\infty + G_A(b/a)\sigma_y^\infty)\frac{\kappa + 1}{4\kappa}\sqrt{\pi a}$$

(for the tip A in Fig. 2) (21)

$$K_{1R,B} = (F_B(b/a)\sigma_x^\infty + G_B(b/a)\sigma_y^\infty)\frac{\kappa + 1}{4\kappa}\sqrt{\pi b}$$

(for the tip B in Fig. 2). (22)

Finally, the calculated $F_A(b/a)$, $G_A(b/a)$, $F_B(b/a)$, $G_B(b/a)$ values are plotted in Fig. 3.

In the case of $\sigma_x^\infty = \sigma_y^\infty = p$, the SSCs can be expressed by

$$K_{1R,A} = H_A(b/a)p\frac{\kappa + 1}{4\kappa}\sqrt{\pi a}, \quad H_A = F_A + G_A$$

(for the tip A in Fig. 2) (23)

$$K_{1R,B} = H_B(b/a)p\frac{\kappa + 1}{4\kappa}\sqrt{\pi b}, \quad H_B = F_B + G_B$$

(for the tip B in Fig. 2). (24)

The calculated results for F_A, F_B, G_A, G_B, H_A, H_B values are listed plotted in Fig. 3. From Fig. 3 we see that, in the remote stress σ_x^∞ case, F_A values are dominant and $|F_A| > |F_B|$. In the meantime, in the remote stress σ_y^∞ case, G_B values are dominant and $|G_B| > |G_A|$.

4 Remarks

A comparison has been made between the rigid inclusion problem with the cavity problem (Dunders, 1989). Similarly, we also make a comparison for two problems. In the cruciform crack case with the remote stress σ_x^∞, the stress intensity factors at the tips A and B can be expressed by (Chen, 1993)

$$K_{1A} = f_A(b/a)\sigma_x^\infty\sqrt{\pi a}, \quad K_{1B} = f_B(b/a)\sigma_x^\infty\sqrt{\pi b}. \quad (25)$$

The calculated F_A, F_B (for the cruciform rigid line problem) and f_A, f_B (for the cruciform crack problem) values are listed in Table 1. From Table 1 we see that in the cruciform rigid line case F_A values are dominant and $|F_A| > |F_B|$, and in the cruciform crack case f_B values are dominant and $|f_B| > |f_A|$.

Table 1 Comparison results for the cruciform rigid line problem and the cruciform crack problem

	b/a =		
	0.1	0.2	1.0
F_A	1.000	1.000	0.985
F_B	−0.064	−0.075	−0.235
f_A	0.003	0.001	−0.217
f_B	0.997	0.998	1.081

Acknowledgment

The research project is support by National Natural Science Fund of China.

References

Ballarini, R., 1990, "A Rigid Line Inclusion at a Bimeterial Interface," *Engineering Fracture Mechanics,* Vol. 37, pp. 1–5.

Boiko, A. V., and Karpenko, L. N., 1981, "On Some Numerical Methods for the Solution of Plane Elasticity Problems for Bodies with Cracks by Means of Singular Integral Equations," *International Journal of Fracture,* Vol. 17, pp. 381–388.

Chen, Y. Z., and Hasebe, N., 1992a, "Integral Equation Approaches for Curved Rigid Line Problem in an Infinite Plate," *International Journal of Fracture,* Vol. 58, pp. 1–20.

Chen, Y. Z., and Hasebe, N., 1992b, "Interaction of Two Curved Cracks in an Infinite Plate," *Archive of Applied Mechanics,* Vol. 62, pp. 147–157.

Chen, Y. Z., 1993, "Numerical Solution for a Cruciform Crack Problem," *International Journal of Fracture,* Vol. 63, pp. R31–R34.

Dundurs, J., and Markenscoff, X., 1989, "A Green's Function Formulation of Anticracks and Their Interaction with Load-induced Singularities," ASME JOURNAL OF APPLIED MECHANICS, Vol. 56, pp. 550–555.

Dundurs, J., 1989, "Cavities vis-a-vis Rigid Inclusion and Some Related General Results in Plane Elasticity," ASME JOURNAL OF APPLIED MECHANICS, Vol. 56, pp. 786–790.

England, A. H., 1971, "On Stress Singularities in Linear Elasticity," *International Journal of Engineering Science,* Vol. 9, pp. 571–585.

Hasebe, N., and Takeuchi, T., 1985, "Stress Analysis a Semi-infinite Plate with a Thin Rigid Body," *International Journal of Engineering Science,* Vol. 23, pp. 531–539.

Markenscoff, X., and Li, N., 1996, "The Debonded Interface Anticrack," ASME JOURNAL OF APPLIED MECHANICS, Vol. 63, pp. 621–627.

Muskhelishvili, N. I., 1953, *Some Basic Problems in the Theory of Elasticity,* Noorhoff, Leyden, The Netherlands.

Wang, Z. Y., Zhang, H. T., and Chou, Y. T., 1985, "Characteristics of Elastic Field of a Rigid line Inhomogeneity," ASME JOURNAL OF APPLIED MECHANICS, Vol. 52, pp. 818–822.

A Modified Element-by-Element Preconditioner for Elastostatics

M. Barboteu[2], P. Alart[2], and F. Lebon[2]

In this paper we present in detail a modified element-by-element strategy. This kind of method is well known to be effective for large-scale problems because of its implicit parallelism. Numerical experiments described in this paper confirm the efficiency of this solver.

1 Introduction

Hughes, Levit, and Winget (1983) and also Hughes and Winget (1985) have introduced an element-by-element precon-

[2] Laboratoire de Mécanique et Génie Civil, UMR 5508 Université Montpellier 2-CNRS, Pl. E. Bataillon, 34095 Montpellier Cedex 5, France.

Contributed by the Applied Mechanics Division of THE AMERICAN SOCIETY OF MECHANICAL ENGINEERS for publication in the ASME JOURNAL OF APPLIED MECHANICS. Manuscript received by the ASME Applied Mechanics Division, Feb. 27, 1997; final revision, Aug. 11, 1997. Associate Technical Editor: W. K. Liu.

Downloaded 04 May 2010 to 171.66.16.26. Redistribution subject to ASME license or copyright; see http://www.asme.org/terms/Terms_Use.cfm

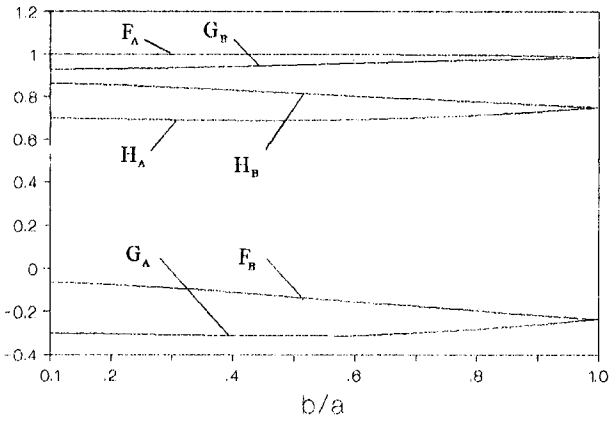


Fig. 3 Normalized SSCs at two rigid line tips A and B (see Fig. 2 and Eqs. (21), (22), (23), (24))

and $\nu = 0.3$ are assumed, and (b) the remote stresses σ_x^∞, σ_y^∞ are applied at infinity. The SSCs at two rigid line tips are expressed by

$$K_{1R,A} = (F_A(b/a)\sigma_x^\infty + G_A(b/a)\sigma_y^\infty)\frac{\kappa + 1}{4\kappa}\sqrt{\pi a}$$

(for the tip A in Fig. 2) (21)

$$K_{1R,B} = (F_B(b/a)\sigma_x^\infty + G_B(b/a)\sigma_y^\infty)\frac{\kappa + 1}{4\kappa}\sqrt{\pi b}$$

(for the tip B in Fig. 2). (22)

Finally, the calculated $F_A(b/a)$, $G_A(b/a)$, $F_B(b/a)$, $G_B(b/a)$ values are plotted in Fig. 3.

In the case of $\sigma_x^\infty = \sigma_y^\infty = p$, the SSCs can be expressed by

$$K_{1R,A} = H_A(b/a)p\frac{\kappa + 1}{4\kappa}\sqrt{\pi a}, \quad H_A = F_A + G_A$$

(for the tip A in Fig. 2) (23)

$$K_{1R,B} = H_B(b/a)p\frac{\kappa + 1}{4\kappa}\sqrt{\pi b}, \quad H_B = F_B + G_B$$

(for the tip B in Fig. 2). (24)

The calculated results for F_A, F_B, G_A, G_B, H_A, H_B values are listed plotted in Fig. 3. From Fig. 3 we see that, in the remote stress σ_x^∞ case, F_A values are dominant and $|F_A| > |F_B|$. In the meantime, in the remote stress σ_y^∞ case, G_B values are dominant and $|G_B| > |G_A|$.

4 Remarks

A comparison has been made between the rigid inclusion problem with the cavity problem (Dunders, 1989). Similarly, we also make a comparison for two problems. In the cruciform crack case with the remote stress σ_x^∞, the stress intensity factors at the tips A and B can be expressed by (Chen, 1993)

$$K_{1A} = f_A(b/a)\sigma_x^\infty\sqrt{\pi a}, \quad K_{1B} = f_B(b/a)\sigma_x^\infty\sqrt{\pi b}. \quad (25)$$

The calculated F_A, F_B (for the cruciform rigid line problem) and f_A, f_B (for the cruciform crack problem) values are listed in Table 1. From Table 1 we see that in the cruciform rigid line case F_A values are dominant and $|F_A| > |F_B|$, and in the cruciform crack case f_B values are dominant and $|f_B| > |f_A|$.

Table 1 Comparison results for the cruciform rigid line problem and the cruciform crack problem

	b/a =		
	0.1	0.2	1.0
F_A	1.000	1.000	0.985
F_B	−0.064	−0.075	−0.235
f_A	0.003	0.001	−0.217
f_B	0.997	0.998	1.081

Acknowledgment

The research project is support by National Natural Science Fund of China.

References

Ballarini, R., 1990, "A Rigid Line Inclusion at a Bimeterial Interface," *Engineering Fracture Mechanics,* Vol. 37, pp. 1–5.

Boiko, A. V., and Karpenko, L. N., 1981, "On Some Numerical Methods for the Solution of Plane Elasticity Problems for Bodies with Cracks by Means of Singular Integral Equations," *International Journal of Fracture,* Vol. 17, pp. 381–388.

Chen, Y. Z., and Hasebe, N., 1992a, "Integral Equation Approaches for Curved Rigid Line Problem in an Infinite Plate," *International Journal of Fracture,* Vol. 58, pp. 1–20.

Chen, Y. Z., and Hasebe, N., 1992b, "Interaction of Two Curved Cracks in an Infinite Plate," *Archive of Applied Mechanics,* Vol. 62, pp. 147–157.

Chen, Y. Z., 1993, "Numerical Solution for a Cruciform Crack Problem," *International Journal of Fracture,* Vol. 63, pp. R31–R34.

Dundurs, J., and Markenscoff, X., 1989, "A Green's Function Formulation of Anticracks and Their Interaction with Load-induced Singularities," ASME JOURNAL OF APPLIED MECHANICS, Vol. 56, pp. 550–555.

Dundurs, J., 1989, "Cavities vis-a-vis Rigid Inclusion and Some Related General Results in Plane Elasticity," ASME JOURNAL OF APPLIED MECHANICS, Vol. 56, pp. 786–790.

England, A. H., 1971, "On Stress Singularities in Linear Elasticity," *International Journal of Engineering Science,* Vol. 9, pp. 571–585.

Hasebe, N., and Takeuchi, T., 1985, "Stress Analysis a Semi-infinite Plate with a Thin Rigid Body," *International Journal of Engineering Science,* Vol. 23, pp. 531–539.

Markenscoff, X., and Li, N., 1996, "The Debonded Interface Anticrack," ASME JOURNAL OF APPLIED MECHANICS, Vol. 63, pp. 621–627.

Muskhelishvili, N. I., 1953, *Some Basic Problems in the Theory of Elasticity,* Noorhoff, Leyden, The Netherlands.

Wang, Z. Y., Zhang, H. T., and Chou, Y. T., 1985, "Characteristics of Elastic Field of a Rigid line Inhomogeneity," ASME JOURNAL OF APPLIED MECHANICS, Vol. 52, pp. 818–822.

A Modified Element-by-Element Preconditioner for Elastostatics

M. Barboteu[2], P. Alart[2], and F. Lebon[2]

In this paper we present in detail a modified element-by-element strategy. This kind of method is well known to be effective for large-scale problems because of its implicit parallelism. Numerical experiments described in this paper confirm the efficiency of this solver.

1 Introduction

Hughes, Levit, and Winget (1983) and also Hughes and Winget (1985) have introduced an element-by-element precon-

[2] Laboratoire de Mécanique et Génie Civil, UMR 5508 Université Montpellier 2-CNRS, Pl. E. Bataillon, 34095 Montpellier Cedex 5, France.

Contributed by the Applied Mechanics Division of THE AMERICAN SOCIETY OF MECHANICAL ENGINEERS for publication in the ASME JOURNAL OF APPLIED MECHANICS. Manuscript received by the ASME Applied Mechanics Division, Feb. 27, 1997; final revision, Aug. 11, 1997. Associate Technical Editor: W. K. Liu.

Downloaded 04 May 2010 to 171.66.16.26. Redistribution subject to ASME license or copyright; see http://www.asme.org/terms/Terms_Use.cfm

ditioner to overcome the excessive cost of the preconditioning matrix, especially when the scale of the system is very large. In this note we present a special element-by-element preconditioner for a symmetric system arising from elastostatics.

In Section 2, we give in detail our modified element-by-element preconditioner algorithm for elasticity. In Section 3, two classicals test are presented: a beam test and plate test. We describe the numerical features of our special preconditioner; efficiency is discussed and the comparison is made between our element-by-element and standard preconditioners such as the incomplete Cholesky factorization (see Alart and Lebon (1995) for references), diagonal, and classical element-by-element method. The interest of this paper is to illustrate the advantages of our preconditioner versus the classical element-by-element method.

2 Element-by-Element Preconditioner for Symmetric Systems

In elasticity, the stiffness matrix $\mathbf{A}$ is symmetric and positive definite. It is then appropriate to use a Crout $\mathbf{LDL}^t$ decomposition. Some modifications and detailed information are introduced in comparison with the original method of Hughes and Winget (1985). Element-by-element preconditioners are motivated by a desire to maintain the element-based data structure of current finite element codes. In order to obtain the Crout element-by-element preconditioner, we start from the standard finite element assembly operation. If we denote the eth element contribution to the global matrix $\mathbf{A}$ by $\mathbf{A}_e$, we have the following decomposition:

$$\mathbf{A} = \prod_{e=1}^{Nel} \mathbf{A}_e = \mathbf{W} + \prod_{e=1}^{Nel} [\mathbf{A}_e - \mathbf{W}_e]$$
$$= \mathbf{W}^{1/2}\left(\mathbf{I} + \mathbf{W}^{-1/2} \prod_{e=1}^{Nel} [\mathbf{A}_e - \mathbf{W}_e]\mathbf{W}^{-1/2}\right)\mathbf{W}^{1/2}, \quad (1)$$

where $\mathbf{W}$ (resp. $\mathbf{W}_e$) is the diagonal part of $\mathbf{A}$ (resp. $\mathbf{A}_e$) and *Nel* is the number of elements. The last factorization with the diagonal matrix $\mathbf{W}$ has a regularizing effect. Indeed, for diagonal scaling preconditioners, this regularization nondimensionalizes the equation system, ensuring that the residual norm used to monitor convergence is well defined. The first approximation for reaching the element-by-element preconditioner consists in extracting the gathering operation out of the round brackets of Eq. (1). For this purpose, let $\mathbf{C}_1$ be the preconditioner matrix obtained after this first approximation:

$$\mathbf{C}_1 = \mathbf{W}^{1/2} \prod_{e=1}^{Nel} [\bar{\mathbf{A}}_e]\mathbf{W}^{1/2}, \quad (2)$$

$$\text{with} \quad \bar{\mathbf{A}}_e = \mathbf{I}_e + \mathbf{W}_{ge}^{-1/2}(\mathbf{A}_e - \mathbf{W}_e)\mathbf{W}_{ge}^{-1/2}. \quad (3)$$

$\mathbf{W}_{ge}$ is the restriction of the diagonal *global* matrix $\mathbf{W}$ to the degrees-of-freedom of the eth element and it must be distinguished from the *elementary* diagonal $\mathbf{W}_e$. $\bar{\mathbf{A}}_e$ is the Winget regularized elementary matrix. This regularization ensures $\bar{\mathbf{A}}_e$ is positive-definite, hence a Crout $\mathbf{LDL}^t$ factorization is well defined. So the preconditioner $\mathbf{C}_1$ may be written as follows:

$$\mathbf{C}_1 = \mathbf{W}^{1/2} \prod_{e=1}^{Nel} [\mathcal{L}_e \cdot \mathcal{D}_e \cdot \mathcal{L}_e^t]\mathbf{W}^{1/2}, \quad (4)$$

$$\text{with} \quad \mathcal{L}_e = \mathbf{P}_e\bar{\mathbf{L}}_e\mathbf{P}_e, \quad \mathcal{D}_e = \mathbf{P}_e\bar{\mathbf{D}}_e\mathbf{P}_e \quad \text{and} \quad \bar{\mathbf{L}}_e\bar{\mathbf{D}}_e\bar{\mathbf{L}}_e^t = \mathbf{P}_e\bar{\mathbf{A}}_e\mathbf{P}_e \quad (5)$$

where $\bar{\mathbf{L}}_e$ and $\bar{\mathbf{D}}_e$ are given by the Crout factorization of the product matrix $\mathbf{P}_e\bar{\mathbf{A}}_e\mathbf{P}_e$. $\mathbf{P}_e$ is a permutation matrix whose role is to interchange rows and columns of $\bar{\mathbf{A}}_e$ such that they are consistent with the *local* nodal ordering.

It is convenient to express the Crout factorization by using a decomposition into lower-triangular ($\mathbf{E}_e$), upper-triangular ($\mathbf{E}_e^t$), and diagonal ($\mathbf{D}_e$) matrices, with respect to the *global* ordering:

$$\mathcal{L}_e = \mathbf{E}_e + \mathbf{I}_e, \quad \mathcal{D}_e = \mathbf{D}_e \quad \text{and} \quad \mathcal{L}_e^t = \mathbf{I}_e + \mathbf{E}_e^t. \quad (6)$$

Consequently, the matrices $\mathbf{E}_e$, $\mathbf{E}_e^t$ are not necessarily triangular according to the local nodal ordering. From a computational point of view, the matrices $\mathcal{L}_e$, $\mathcal{L}_e^t$, and $\mathcal{D}_e$ are stored in a single array as a matrix; the identity matrix is implicit. The gathering operation deals with $\mathbf{E}_e$, $\mathbf{E}_e^t$, and $\mathbf{D}_e$ as a single standard matrix, hence the global splitting $\mathbf{E}$, $\mathbf{D}$, $\mathbf{E}^t$ is relevant:

$$\mathbf{C}_2 = \mathbf{W}^{1/2} \prod_{e=1}^{Nel} [\mathbf{E}_e + \mathbf{D}_e + \mathbf{E}_e^t]\mathbf{W}^{1/2}$$
$$= \mathbf{W}^{1/2}(\mathbf{E} + \mathbf{D} + \mathbf{E}^t)\mathbf{W}^{1/2}. \quad (7)$$

Since the sum decomposition $\mathbf{E} + \mathbf{D} + \mathbf{E}^t$ corresponds to the computational storage of the $\mathbf{LDL}^t$ decomposition, we can approximate the preconditioner $\mathbf{C}_2$ by the new one noted $\mathbf{C}_3$:

$$\mathbf{C}_3 = (\mathbf{W}^{1/2}\mathbf{E}) + \mathbf{D} + (\mathbf{E}^t\mathbf{W}^{1/2}). \quad (8)$$

This last sum decomposition (8) may be identified with an approximation based upon the global Crout factorization. This allows us to define a Crout element-by-element preconditioner $\mathbf{C}_4$:

$$\mathbf{C}_4 = (\mathbf{W}^{1/2}\mathbf{L})\mathbf{D}(\mathbf{L}^t\mathbf{W}^{1/2}) = \mathcal{L} \cdot \mathbf{D} \cdot \mathcal{L}^t. \quad (9)$$

Some experiments show that a final modification improves the behavior of the preconditioner: the diagonal part, noted $\mathbf{D}$, is replaced by the initial diagonal part of $\mathbf{A}$ (noted $\mathbf{W}$). This last approximation is a main advance added to the Crout element-by-element preconditioner. Then we postulate the final element-by-element preconditioner $\mathbf{C}_5$ as

$$\mathbf{C}_5 = \mathcal{L} \cdot \mathbf{W} \cdot \mathcal{L}^t. \quad (10)$$

It seems that this modified preconditioner takes advantage of the classical element-by-element preconditioner and the standard diagonal one. Indeed the convergence of the residual norm in the conjugate gradient algorithm is more stable; i.e., this norm decrease is monotonic.

3 Numerical Results

We test the previous element-by-element preconditioner algorithm on two classical examples: an elastostatic bidimensional beam (see Fig. 1) and a plate problem.

The elastostatic beam is embedded on the edge AD and a transversal force is applied on the opposed edge CB. We have realized the numerical tests with six meshes: the coarser is

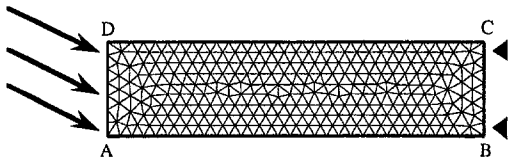


Fig. 1 Beam test (coarser mesh)

Table 1 Conjugate gradient iterations according to the different preconditioners and (between brackets) gain with respect to the method without preconditioner (example with classical bidimensional elements)

degrees of freedom	WP	DIAG	ILU	EBE	MEBE
360	202	178 (12%)	54 (74%)	103 (50%)	74 (63%)
1230	409	374 (9%)	106 (74%)	190 (53%)	140 (65%)
4730	830	789 (5%)	218 (73%)	373 (55%)	274 (66%)
18244	1671	1628 (2%)	458 (72%)	749 (55%)	551 (67%)
72298	3336	3242 (2%)	929 (72%)	1501 (55%)	1077 (67%)
287150	6707	6641 (1%)	2003 (70%)	3150 (53%)	2258 (66%)

Downloaded 04 May 2010 to 171.66.16.26. Redistribution subject to ASME license or copyright; see http://www.asme.org/terms/Terms_Use.cfm

Table 2 Conjugate gradient iterations according to the different preconditioners and (between brackets) gain with respect to the method without preconditioner (example with plate elements)

degrees of freedom	WP	DIAG	ILU	EBE	MEBE
8230	4917	2608 (47%)	664 (86%)	4173 (15%)	1286 (74%)
33174	22624	10887 (51%)	4028 (82%)	> WP	5311 (77%)

characterized by 360 degrees-of-freedom and the finer by around 290,000 degrees-of-freedom.

To appreciate the efficiency of our element-by-element method we compare our modified element-by-element preconditioner (noted MEBE) with four "classical" preconditioners which are the usual element-by-element (noted EBE), the incomplete Cholesky factorization (noted ILU), the diagonal preconditioning (noted DIAG), and the method without preconditioner (noted WP). This comparison have been made in terms of conjugate gradient (noted CG) iterations numbers (Table 1). The numerical tests seem to show that the modified element-by-element method is more efficient than element-by-element preconditioner. The difference is sensitive: our element-by-element algorithm requires around 28 percent of conjugate gradient iterations less than the element-by-element method, whatever the problem size may be (see Table 1). On the other hand, the difference between the incomplete Cholesky factorization method and the modified element-by-element algorithm decreases according to the number of degrees-of-freedom: 27 percent more than incomplete Cholesky factorization preconditioner for 360 degrees-of-freedom and only 11 percent more for 287,150 degrees-of-freedom.

The second example is a poor conditioned plate problem. The bidimensional squared plate is embedded on the four edges and we apply a vertical force on the upper surface. Contrary to the traditional element-by-element method, the behavior of our preconditioner is as good as in the previous example. So our preconditioner is more and more comparable to the incomplete Cholesky factorization preconditioner when the problem becomes larger in terms of degrees-of-freedom (Table 2). These comments are confirmed by the study of CPU time.

4 Conclusion

Our results indicate that our improved element-by-element algorithm is more efficient than the classical element-by-element preconditioner. It can be competitive with the incomplete Cholesky factorization preconditioner in terms of conjugate gradient iterations and CPU time (see Alart, Barboteu, and Lebon (1997) for a nonsymmetric extension). Through the two numerical examples, the modified element-by-element preconditioner seems to deliver an enhanced rate of convergence compared to the classical element-by-element method.

Moreover, the element-by-element procedure has been introduced for vectorized computation (see, for example, Muller (1985), Nour-Omid and Parlett (1985), and Hughes, Ferencz, and Hallquist (1987)) and, presently, have been implemented in parallel with a high degree of parallel granularity. This algorithm is particularly well adapted to computers with a large number of processors. In fact, most parallel element-by-element methods rely on the ability to place many elements on a single processor.

References

Alart, P., Barboteu, M., and Lebon, F. 1997, "Solutions of frictional contact problems by an EBE preconditioner," *Computational Mechanics,* to appear.

Alart, P., and Lebon, F. 1995, "Solutions of frictional contact problems using ILU and coarse/fine preconditioners," *Computational Mechanics,* Vol. 16, pp. 98–105.

Hughes, T. J. R., Ferencz, R. M., and Hallquist, J. O., 1987, "Large-scale vectorized implicit calculations in solid mechanics on a Cray X-MP/48 utilizing EBE preconditioned conjugate gradients," *Computer Methods in Applied Mechanics and Engineering,* Vol. 61, pp. 215–248.

Hughes, T. J. R., Levit, I., and Winget, J. M. 1983, "An element by element solution algorithm for problems of structural and solid mechanics," *Computer Methods in Applied Mechanics and Engineering,* Vol. 36, pp. 241–254.

Hughes, T. J. R., and Winget, J. M., 1985, "Solution algorithms for non linear transient heat conduction analysis employing element by element iteratives strategies," *Computer Methods in Applied Mechanics and Engineering,* Vol. 52, pp. 711–815.

Nour-Omid, B., and Parlett, B. N. 1985, "Element preconditioning using splitting techniques," *SIAM Journal on Scientific and Statistical Computing,* Vol. 6, pp. 761–770.

Large Deflection of a Rigid-Plastic Circular Plate Pressed by a Sphere

Ge Wang,[3] Hideomi Ohtsubo,[4] and Kikuo Arita[5]

A rigid-plastic circular plate deflected by a rigid sphere is investigated. The behavior at large deflection is considered; the contribution from a bending moment is neglected. Approximate formulas for the load-deflection relationship are derived. Experiments are conducted and the test data compare well with the prediction results. It is revealed that the size of the rigid sphere has a strong effect on the resistance of the compressed plate.

1 Introduction

The load-carrying capacity of a plate has been investigated by many researchers. Onat and Haythornthwaite (1956) demonstrated the increase in the load-carrying capacity of a loaded plate due to finite deflection. Zaid (1958) discussed the limit load of a plate of general shape and variable fixity under a concentrated load. Reid and Reddy (1978) estimated the effect of strain hardening on the large plastic deformation of a cantilever. Jones and Oliveira (1979) discussed the influence of rotatory inertia and transverse shear on the dynamic plastic behavior of beams. Liu and Stronge (1996) investigated the shear and bending deformation of circular plates by a central pressure pulse.

Recently, the safety of occupants during an automobile collision accident and ocean pollution due to cargo spillage from a struck or grounded ship have received increasing attention. The striking object is often of similar size to the struck object. Different from the existing researches as those introduced above, it is not appropriate to model the interaction of the striking and struck structures as a concentrated load. There are two different load types in structural mechanics, which are concentrated load and distributed load. External force is usually idealized as either one of these two types, or their combinations. In an automobile collision accident or in a ship-ship collision accident, the tip of the striking object is neither small nor large compared to the struck object. Hence, this kind of structural impact problem can be modeled by neither concentrated load nor distributed load.

[3] American Bureau of Shipping, Yokohama, Urban Square Yokohama, Sakaecho 1-1, Kanagawa-ku, Yokohama 221, Japan.

[4] Department of Naval Architecture and Ocean Engineering, The University of Tokyo, Hongo 7-3-1, Bunkyo-ku, Tokyo 113, Japan.

[5] Faculty of Structural Engineering, Kumamoto Institute of Technology, Ikeda 4-22-1, Kumamoto-shi 860, Japan.

Contributed by the Applied Mechanics Division of THE AMERICAN SOCIETY OF MECHANICAL ENGINEERS for publication in the ASME JOURNAL OF APPLIED MECHANICS. Manuscript received by the ASME Applied Mechanics Division, May 28, 1997; final revision, Aug. 25, 1997. Associate Technical Editor: W. J. Drugan.

Downloaded 04 May 2010 to 171.66.16.26. Redistribution subject to ASME license or copyright; see http://www.asme.org/terms/Terms_Use.cfm

Table 2 Conjugate gradient iterations according to the different preconditioners and (between brackets) gain with respect to the method without preconditioner (example with plate elements)

degrees of freedom	WP	DIAG	ILU	EBE	MEBE
8230	4917	2608 (47%)	664 (86%)	4173 (15%)	1286 (74%)
33174	22624	10887 (51%)	4028 (82%)	> WP	5311 (77%)

characterized by 360 degrees-of-freedom and the finer by around 290,000 degrees-of-freedom.

To appreciate the efficiency of our element-by-element method we compare our modified element-by-element preconditioner (noted MEBE) with four "classical" preconditioners which are the usual element-by-element (noted EBE), the incomplete Cholesky factorization (noted ILU), the diagonal preconditioning (noted DIAG), and the method without preconditioner (noted WP). This comparison have been made in terms of conjugate gradient (noted CG) iterations numbers (Table 1). The numerical tests seem to show that the modified element-by-element method is more efficient than element-by-element preconditioner. The difference is sensitive: our element-by-element algorithm requires around 28 percent of conjugate gradient iterations less than the element-by-element method, whatever the problem size may be (see Table 1). On the other hand, the difference between the incomplete Cholesky factorization method and the modified element-by-element algorithm decreases according to the number of degrees-of-freedom: 27 percent more than incomplete Cholesky factorization preconditioner for 360 degrees-of-freedom and only 11 percent more for 287,150 degrees-of-freedom.

The second example is a poor conditioned plate problem. The bidimensional squared plate is embedded on the four edges and we apply a vertical force on the upper surface. Contrary to the traditional element-by-element method, the behavior of our preconditioner is as good as in the previous example. So our preconditioner is more and more comparable to the incomplete Cholesky factorization preconditioner when the problem becomes larger in terms of degrees-of-freedom (Table 2). These comments are confirmed by the study of CPU time.

4 Conclusion

Our results indicate that our improved element-by-element algorithm is more efficient than the classical element-by-element preconditioner. It can be competitive with the incomplete Cholesky factorization preconditioner in terms of conjugate gradient iterations and CPU time (see Alart, Barboteu, and Lebon (1997) for a nonsymmetric extension). Through the two numerical examples, the modified element-by-element preconditioner seems to deliver an enhanced rate of convergence compared to the classical element-by-element method.

Moreover, the element-by-element procedure has been introduced for vectorized computation (see, for example, Muller (1985), Nour-Omid and Parlett (1985), and Hughes, Ferencz, and Hallquist (1987)) and, presently, have been implemented in parallel with a high degree of parallel granularity. This algorithm is particularly well adapted to computers with a large number of processors. In fact, most parallel element-by-element methods rely on the ability to place many elements on a single processor.

References

Alart, P., Barboteu, M., and Lebon, F. 1997, "Solutions of frictional contact problems by an EBE preconditioner," *Computational Mechanics,* to appear.

Alart, P., and Lebon, F. 1995, "Solutions of frictional contact problems using ILU and coarse/fine preconditioners," *Computational Mechanics,* Vol. 16, pp. 98–105.

Hughes, T. J. R., Ferencz, R. M., and Hallquist, J. O., 1987, "Large-scale vectorized implicit calculations in solid mechanics on a Cray X-MP/48 utilizing EBE preconditioned conjugate gradients," *Computer Methods in Applied Mechanics and Engineering,* Vol. 61, pp. 215–248.

Hughes, T. J. R., Levit, I., and Winget, J. M. 1983, "An element by element solution algorithm for problems of structural and solid mechanics," *Computer Methods in Applied Mechanics and Engineering,* Vol. 36, pp. 241–254.

Hughes, T. J. R., and Winget, J. M., 1985, "Solution algorithms for non linear transient heat conduction analysis employing element by element iteratives strategies," *Computer Methods in Applied Mechanics and Engineering,* Vol. 52, pp. 711–815.

Nour-Omid, B., and Parlett, B. N. 1985, "Element preconditioning using splitting techniques," *SIAM Journal on Scientific and Statistical Computing,* Vol. 6, pp. 761–770.

Large Deflection of a Rigid-Plastic Circular Plate Pressed by a Sphere

Ge Wang,[3] Hideomi Ohtsubo,[4] and Kikuo Arita[5]

A rigid-plastic circular plate deflected by a rigid sphere is investigated. The behavior at large deflection is considered; the contribution from a bending moment is neglected. Approximate formulas for the load-deflection relationship are derived. Experiments are conducted and the test data compare well with the prediction results. It is revealed that the size of the rigid sphere has a strong effect on the resistance of the compressed plate.

1 Introduction

The load-carrying capacity of a plate has been investigated by many researchers. Onat and Haythornthwaite (1956) demonstrated the increase in the load-carrying capacity of a loaded plate due to finite deflection. Zaid (1958) discussed the limit load of a plate of general shape and variable fixity under a concentrated load. Reid and Reddy (1978) estimated the effect of strain hardening on the large plastic deformation of a cantilever. Jones and Oliveira (1979) discussed the influence of rotatory inertia and transverse shear on the dynamic plastic behavior of beams. Liu and Stronge (1996) investigated the shear and bending deformation of circular plates by a central pressure pulse.

Recently, the safety of occupants during an automobile collision accident and ocean pollution due to cargo spillage from a struck or grounded ship have received increasing attention. The striking object is often of similar size to the struck object. Different from the existing researches as those introduced above, it is not appropriate to model the interaction of the striking and struck structures as a concentrated load. There are two different load types in structural mechanics, which are concentrated load and distributed load. External force is usually idealized as either one of these two types, or their combinations. In an automobile collision accident or in a ship-ship collision accident, the tip of the striking object is neither small nor large compared to the struck object. Hence, this kind of structural impact problem can be modeled by neither concentrated load nor distributed load.

[3] American Bureau of Shipping, Yokohama, Urban Square Yokohama, Sakaecho 1-1, Kanagawa-ku, Yokohama 221, Japan.

[4] Department of Naval Architecture and Ocean Engineering, The University of Tokyo, Hongo 7-3-1, Bunkyo-ku, Tokyo 113, Japan.

[5] Faculty of Structural Engineering, Kumamoto Institute of Technology, Ikeda 4-22-1, Kumamoto-shi 860, Japan.

Contributed by the Applied Mechanics Division of THE AMERICAN SOCIETY OF MECHANICAL ENGINEERS for publication in the ASME JOURNAL OF APPLIED MECHANICS. Manuscript received by the ASME Applied Mechanics Division, May 28, 1997; final revision, Aug. 25, 1997. Associate Technical Editor: W. J. Drugan.

Downloaded 04 May 2010 to 171.66.16.26. Redistribution subject to ASME license or copyright; see http://www.asme.org/terms/Terms_Use.cfm

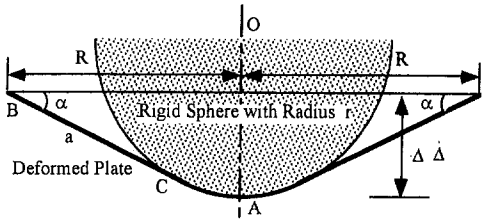


Fig. 1 Kinematic model for a plate deflected by a rigid sphere

There is a need to develop a new load type which can model the loading object as well.

Low (1981) used a rigid cylinder to indent a rigid-plastic beam of rectangular section and derived the load-deflection relationships at deflections not large. Zhu and Faulkner (1994) and Zhu et al. (1994) reported experimental and numerical investigations on plates under line-impact load. Shen (1995) examined the dynamic plastic response of thin circular plates struck transversely by a nonblunt mass. In these investigations the external load was not concentrated in a local zone; the loading object was a cylinder, a line segment or a mass with round tip. However, the effect of the geometry of the striking object on the resistance of the striking plate at large deflections has not yet been investigated.

As a first attempt to investigate the effects of the size of loading object, the behavior of a plate deflected by a rigid sphere is discussed in this paper. Only one geometric parameter is introduced to model the striking object, that is, the radius of the rigid sphere. The direct aim of this study is to examine whether the size of the striking object has an effect on the resistance of the struck structure or not. Approximate formulas are derived for the load-deflection relationship at large deflection. Experiments are carried out to check the derived formulas.

2 Kinematic Model

A simply supported circular thin plate with radius R is subjected to lateral indentation by a rigid sphere with radius r. The first contact of the rigid indenter is at the center of the plate. The process is quasi-static: dynamic effects are neglected. The material is assumed to be rigid-perfectly plastic. A kinematic model is proposed and shown in Fig. 1. The rigid indenter forces plasticity to spread in the plate. It is assumed that the deformed plate is on a conical surface, and that material remains rigid after wrapping around the surface of the indenter. The radial displacement is assumed to be zero.

For small deflections (of the order of plate thickness), the bending moment plays an important role. After a car crash accident or a ship collision accident, the permanent deformation of the struck structure may be very large, which is far beyond the order of plate thickness and is comparable in size to the dimension of the struck structure. As deflection increases, the importance of the bending moment diminishes and the membrane force develops rapidly. At sufficiently large deflections the membrane force dominates the behavior of the plate. The purpose of this paper is to investigate deflections that are not too small; the bending moment is therefore neglected in the following analysis.

The following two equations are geometrical relationships (Fig. 1),

$$\Delta = a \sin \alpha + r(1 - \cos \alpha) \tag{1}$$

$$R = a \cos \alpha + r \sin \alpha \tag{2}$$

where a is the instantaneous meridian distance from the plate's boundary to the position where the plate touches the rigid sphere, Δ is the deflection of the plate at the center, which is also the displacement of the indenter, and α is the angular deflection of the plate. The following equation is obtained from the above two equations:

$$\Delta = R\left(\tan \alpha + \frac{r}{R}\left(1 - \frac{1}{\cos \alpha}\right)\right). \tag{3}$$

The velocity of the indenter is then

$$\dot{\Delta} = \frac{R}{\cos^2 \alpha}\left(1 - \frac{r}{R} \sin \alpha\right)\dot{\alpha}. \tag{4}$$

The material is stretched mainly in the meridian plane. The principal strain is assumed to be in the meridian direction, which is

$$\epsilon = \frac{a - a \cos \alpha}{a \cos \alpha} = \frac{1}{\cos \alpha} - 1. \tag{5}$$

The strain rate is

$$\dot{\epsilon} = \frac{\sin \alpha}{\cos^2 \alpha}\dot{\alpha}. \tag{6}$$

The rate of the membrane energy of the plate is obtained by integrating $N_0\dot{\epsilon}$ over the annular dimension from C to B in the meridian direction,

$$\dot{E}_m = \int N_0 \dot{\epsilon}\, dA = N_0 \dot{\epsilon} \pi (R^2 - (r \sin \alpha)^2), \tag{7}$$

where N_0 is the plastic membrane load for a unit width of the plate, $N_0 = \sigma_0 t$ (σ_0 is the yield stress and t is the thickness). Substituting Eq. (6) into the above equation gives

$$\dot{E}_m = \pi N_0 R^2\left(1 - \left(\frac{r}{R}\right)^2 \sin^2 \alpha\right)\frac{\sin \alpha}{\cos^2 \alpha}\dot{\alpha}. \tag{8}$$

Equilibrium of the loaded plate can be expressed via virtual work as

$$F\dot{\Delta} = \dot{E}_m. \tag{9}$$

Therefore F, the resistance force of the plate, is

$$F = \frac{\dot{E}_m}{\dot{\Delta}} = \pi N_0 R \sin \alpha\left(1 + \frac{r}{R} \sin \alpha\right). \tag{10}$$

Equations (3) and (10) constitute the formulas for the load-deflection relationship of the plate at large deflections when it is compressed by a rigid ball. The dimensionless expressions are as follows:

$$\frac{F}{\sigma_0 t R} = \pi \sin \alpha\left(1 + \frac{r}{R} \sin \alpha\right) \tag{11}$$

$$\frac{\Delta}{R} = \tan \alpha + \frac{r}{R}\left(1 - \frac{1}{\cos \alpha}\right). \tag{12}$$

In Eqs. (3), (10), (11), and (12) the second terms involve the parameter r/R, which is the relative size of the indenter over that of the plate.

If bending stress is taken into account one can derive the following expression using similar methods to those used in this paper:

$$\frac{F^*}{F} = 1 + \frac{t}{2R}\frac{\cos^3 \alpha}{(1 + (r/R) \sin \alpha) \sin \alpha}, \tag{13}$$

where F^* is plate resistance taking bending stress into account. In deriving this equation it is assumed that plastic yielding is

Downloaded 04 May 2010 to 171.66.16.26. Redistribution subject to ASME license or copyright; see http://www.asme.org/terms/Terms_Use.cfm

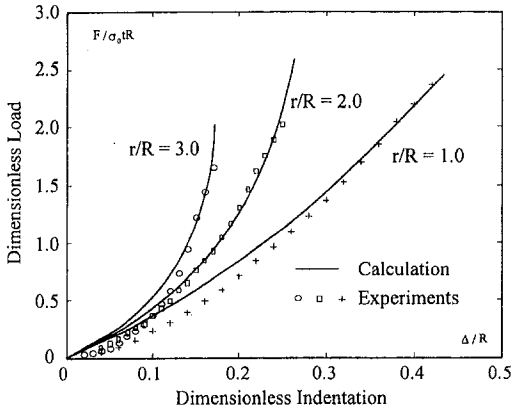


Fig. 2 Experimental data and prediction results

controlled independently in radial and in circumferential directions.

For small α, the second term of Eq. (13) is very large. Compared to F^*, F is negligibly small. Thus, bending stress dominates the behavior at small deflections. However, the second term is a quickly declining function of α. With the increase of α, that is, with the increase of deflection, the second term decreases rapidly. For a thin plate the ratio of $t/2R$ is small, usually less than one several tenth or even smaller. At sufficiently large deflections the second term becomes negligibly smaller than the first term. Therefore, if the deflection is not too small, one can consider membrane force only and neglect the contribution from the bending moment. As a result, Eqs. (3) and (10) or Eqs. (11) and (12) are used for calculating the load-deflection relationship.

3 Experiments and Discussions

A series of experiments was designed to investigate the effect of the indenter's size. The tested steel plate had a yield point of about 350 N/mm^2. The thickness was 2.3 mm and the ratio $2R/t$ was 87.0. The indenter was a cone fitted with round tips of different radii. The ratio of the indenter's tip radius to the radius of the plate, r/R, was 1.0, 2.0, and 3.0. Load was increased very slowly in order for the process to be quasi-static. The measured data are shown in Fig. 2. Clearly the larger the radius of the rigid sphere, the larger will be the resistance of the plate. For example, at dimensionless deflection $\Delta/R = 0.15$, the resistance for $r/R = 3.0$ is approximately three times that for $r/R = 1.0$. The increase in the plate's resistance curve is more rapid for larger tip radius. It is revealed that the indenter size has a strong effect on the resistance of the plate.

The calculations based on the derived prediction formulas (Eqs. (11) and (12)) are plotted in the same figure as well. The uppermost curve is associated with the largest tip radius, while the lowest curve belongs to the smallest tip radius. The calculated curves compare well with the experimental results, especially for large radius and large deflection.

In the literature on structural impact there is a trend to consider the case of nonblunt or sharp indenter with small likelihood (e.g., Ohtsubo and Wang, 1995). The blunt shape of a striking object is often neglected even thought this is the most common in practice. The structural strength may be greatly underestimated. This may lead to designs with unnecessarily large safety margin. The investigation of this paper intends to emphasize that in order to evaluate the damage extent more realistically, attention should be paid to modeling the striking object as well.

4 Conclusions

The behavior of a rigid-plastic plate deflected by a rigid sphere at large deflections is investigated. It is revealed that the resistance of the plate depends strongly on the roundness of the indenter. The plate provides larger resistance against a bigger ball or blunter indenter. In analyzing structural impact problems such as automobile or ship collision accidents, it is important to take into account the shape of the striking object.

Approximate formulas for the load-deflection relationship are derived. The prediction results based on the formulas compare well with the experimental curves. Therefore, the proposed kinematic model and the calculation formulas grasp the main features of the deflection process.

References

Jones, N., and de Oliveira, J. G., 1979, "The Influence of Rotatory Inertia and Transverse Shear on the Dynamic Plastic Behavior of Beams," ASME JOURNAL OF APPLIED MECHANICS, Vol. 23, pp. 303–310.

Liu, D., and Stronge, W., 1996, "Shear and Bending Deformation of Rigid-Plastic Circular Plates by Central Pressure Pulse," *International Journal of Impact Engineering,* Vol. 18, No. 4, 383–402.

Low, H. Y., 1981, "Behavior of a Rigid-Plastic Beam Loaded to Finite Deflections by a Rigid Circular Indenter," *International Journal of Mechanical Science,* Vol. 23, pp. 387–393.

Ohtsubo, H., and Wang, G., 1995, "An Upper-Bound Solution to the Problem of Plate Tearing," *Journal of Marine Science and Technology,* Vol. 1, pp. 46–51.

Onat, E. T., and Haythornthwaite, R. M., 1956, "The Load-Carrying Capacity of Circular Plates at Large Deflection," ASME *Journal of Applied Mechanics,* Vol. 23, pp. 75–103.

Reid, S. R., and Reddy, T. Y., 1978, "Effect of Strain Hardening on the Large Plastic Deformation of a Cantilever," ASME JOURNAL OF APPLIED MECHANICS, Vol. 45, pp. 953–955.

Shen, W. Q., 1995, "Dynamic Plastic Response of Thin Circular Plates Struck by Transversely by Nonblunt Masses," *International Journal of Impact Engineering,* Vol. 16, 2009–2021.

Zaid, M., 1958 "On the Carrying Capacity of Plates of Arbitrary Shape and Variable Fixity Under a Concentrated Load," ASME JOURNAL OF APPLIED MECHANICS, Vol. 25, pp. 598–602.

Zhu, L., and Faulkner, D., 1994, "Dynamic Inelastic Behavior of Plates in Minor Ship Collisions," *International Journal of Impact Engineering,* Vol. 15, No. 2, pp. 165–178.

Zhu, L., Faulkner, D., and Atkins, A. G., 1994, "The Impact of Rectangular Plates Made From Strain-Rate Sensitive Materials," *International Journal of Impact Engineering,* Vol. 15, No. 3, pp. 243–255.

On Love-Type Magnetoelastic Surface Waves

S. Chakraborty[6] and M. Chattopadhyay[7]

Introduction

Different aspects of waves in magnetoelasticity were investigated by several authors including Knopoff (1955), Dunkin and Eringen (1963), Yu and Tang (1965), Tomita and Shindo (1979), Maugin (1981, 1988), and Lee and Its (1992). Here we have investigated the possibility of magnetoelastic SH-waves in a semi-infinite perfectly conducting medium having a superficial layer and found that the magnetic field may cause such waves, even where they are absent in the purely elastic case.

[6] Lecturer, Department of Mathematics, St. Xavier's College, 30 Park Street, Calcutta 700016, India.

[7] Junior Research Fellow, Department of Mathematics, University of Burdwan, Burdwan 713104.

Contributed by the Applied Mechanics Division of THE AMERICAN SOCIETY OF MECHANICAL ENGINEERS for publication in the ASME JOURNAL OF APPLIED MECHANICS. Manuscript received by the ASME Applied Mechanics Division, June 17, 1997; final revision, Aug. 18, 1997. Associate Technical Editor: V. K. Kinra.

Downloaded 04 May 2010 to 171.66.16.26. Redistribution subject to ASME license or copyright; see http://www.asme.org/terms/Terms_Use.cfm

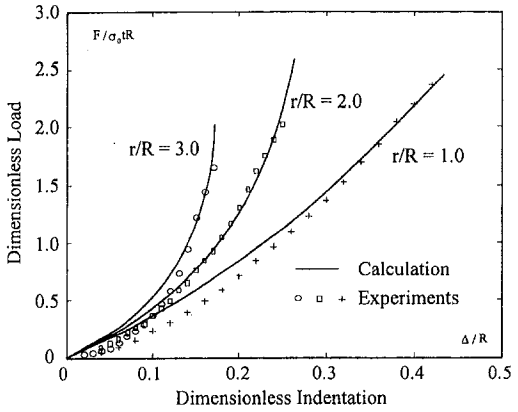


Fig. 2 Experimental data and prediction results

controlled independently in radial and in circumferential directions.

For small α, the second term of Eq. (13) is very large. Compared to F^*, F is negligibly small. Thus, bending stress dominates the behavior at small deflections. However, the second term is a quickly declining function of α. With the increase of α, that is, with the increase of deflection, the second term decreases rapidly. For a thin plate the ratio of $t/2R$ is small, usually less than one several tenth or even smaller. At sufficiently large deflections the second term becomes negligibly smaller than the first term. Therefore, if the deflection is not too small, one can consider membrane force only and neglect the contribution from the bending moment. As a result, Eqs. (3) and (10) or Eqs. (11) and (12) are used for calculating the load-deflection relationship.

3 Experiments and Discussions

A series of experiments was designed to investigate the effect of the indenter's size. The tested steel plate had a yield point of about 350 N/mm^2. The thickness was 2.3 mm and the ratio $2R/t$ was 87.0. The indenter was a cone fitted with round tips of different radii. The ratio of the indenter's tip radius to the radius of the plate, r/R, was 1.0, 2.0, and 3.0. Load was increased very slowly in order for the process to be quasi-static. The measured data are shown in Fig. 2. Clearly the larger the radius of the rigid sphere, the larger will be the resistance of the plate. For example, at dimensionless deflection $\Delta/R = 0.15$, the resistance for $r/R = 3.0$ is approximately three times that for $r/R = 1.0$. The increase in the plate's resistance curve is more rapid for larger tip radius. It is revealed that the indenter size has a strong effect on the resistance of the plate.

The calculations based on the derived prediction formulas (Eqs. (11) and (12)) are plotted in the same figure as well. The uppermost curve is associated with the largest tip radius, while the lowest curve belongs to the smallest tip radius. The calculated curves compare well with the experimental results, especially for large radius and large deflection.

In the literature on structural impact there is a trend to consider the case of nonblunt or sharp indenter with small likelihood (e.g., Ohtsubo and Wang, 1995). The blunt shape of a striking object is often neglected even thought this is the most common in practice. The structural strength may be greatly underestimated. This may lead to designs with unnecessarily large safety margin. The investigation of this paper intends to emphasize that in order to evaluate the damage extent more realistically, attention should be paid to modeling the striking object as well.

4 Conclusions

The behavior of a rigid-plastic plate deflected by a rigid sphere at large deflections is investigated. It is revealed that the resistance of the plate depends strongly on the roundness of the indenter. The plate provides larger resistance against a bigger ball or blunter indenter. In analyzing structural impact problems such as automobile or ship collision accidents, it is important to take into account the shape of the striking object.

Approximate formulas for the load-deflection relationship are derived. The prediction results based on the formulas compare well with the experimental curves. Therefore, the proposed kinematic model and the calculation formulas grasp the main features of the deflection process.

References

Jones, N., and de Oliveira, J. G., 1979, "The Influence of Rotatory Inertia and Transverse Shear on the Dynamic Plastic Behavior of Beams," ASME JOURNAL OF APPLIED MECHANICS, Vol. 23, pp. 303–310.

Liu, D., and Stronge, W., 1996, "Shear and Bending Deformation of Rigid-Plastic Circular Plates by Central Pressure Pulse," *International Journal of Impact Engineering,* Vol. 18, No. 4, 383–402.

Low, H. Y., 1981, "Behavior of a Rigid-Plastic Beam Loaded to Finite Deflections by a Rigid Circular Indenter," *International Journal of Mechanical Science,* Vol. 23, pp. 387–393.

Ohtsubo, H., and Wang, G., 1995, "An Upper-Bound Solution to the Problem of Plate Tearing," *Journal of Marine Science and Technology,* Vol. 1, pp. 46–51.

Onat, E. T., and Haythornthwaite, R. M., 1956, "The Load-Carrying Capacity of Circular Plates at Large Deflection," ASME *Journal of Applied Mechanics,* Vol. 23, pp. 75–103.

Reid, S. R., and Reddy, T. Y., 1978, "Effect of Strain Hardening on the Large Plastic Deformation of a Cantilever," ASME JOURNAL OF APPLIED MECHANICS, Vol. 45, pp. 953–955.

Shen, W. Q., 1995, "Dynamic Plastic Response of Thin Circular Plates Struck by Transversely by Nonblunt Masses," *International Journal of Impact Engineering,* Vol. 16, 2009–2021.

Zaid, M., 1958 "On the Carrying Capacity of Plates of Arbitrary Shape and Variable Fixity Under a Concentrated Load," ASME JOURNAL OF APPLIED MECHANICS, Vol. 25, pp. 598–602.

Zhu, L., and Faulkner, D., 1994, "Dynamic Inelastic Behavior of Plates in Minor Ship Collisions," *International Journal of Impact Engineering,* Vol. 15, No. 2, pp. 165–178.

Zhu, L., Faulkner, D., and Atkins, A. G., 1994, "The Impact of Rectangular Plates Made From Strain-Rate Sensitive Materials," *International Journal of Impact Engineering,* Vol. 15, No. 3, pp. 243–255.

On Love-Type Magnetoelastic Surface Waves

S. Chakraborty[6] and M. Chattopadhyay[7]

Introduction

Different aspects of waves in magnetoelasticity were investigated by several authors including Knopoff (1955), Dunkin and Eringen (1963), Yu and Tang (1965), Tomita and Shindo (1979), Maugin (1981, 1988), and Lee and Its (1992). Here we have investigated the possibility of magnetoelastic SH-waves in a semi-infinite perfectly conducting medium having a superficial layer and found that the magnetic field may cause such waves, even where they are absent in the purely elastic case.

[6] Lecturer, Department of Mathematics, St. Xavier's College, 30 Park Street, Calcutta 700016, India.

[7] Junior Research Fellow, Department of Mathematics, University of Burdwan, Burdwan 713104.

Contributed by the Applied Mechanics Division of THE AMERICAN SOCIETY OF MECHANICAL ENGINEERS for publication in the ASME JOURNAL OF APPLIED MECHANICS. Manuscript received by the ASME Applied Mechanics Division, June 17, 1997; final revision, Aug. 18, 1997. Associate Technical Editor: V. K. Kinra.

Downloaded 04 May 2010 to 171.66.16.26. Redistribution subject to ASME license or copyright; see http://www.asme.org/terms/Terms_Use.cfm

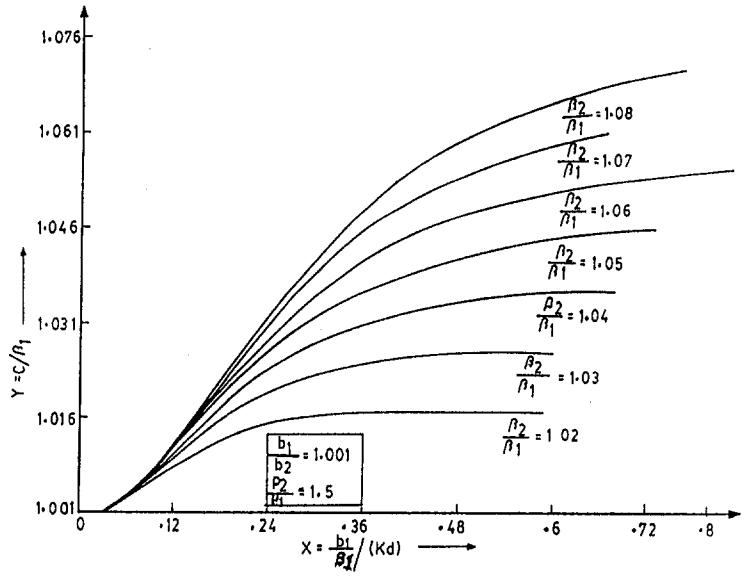


Fig. 1 Dispersion curves showing (c/β_1) against $X = (b_1/\beta_1)/kd$ for $\beta_2/\beta_1 = 1.02, 1.03, \ldots, 1.08$ with $b_1/b_2 = 1.001$, $\rho_2/\rho_1 = 1.5$

Basic Equations

Maxwell's equations of the electromagnetic field are

$$\text{div } D = 0; \quad \text{div } B = 0;$$

$$\text{curl } H = J; \quad \text{curl } E = -\frac{\partial B}{\partial t} \tag{1}$$

where the displacement current is neglected and D, B, H, E, and J have their standard meanings.

The equations of motion are

$$\tau_{ij,j} + [J \times B]_i = \rho \frac{\partial^2 u_i}{\partial t^2} \quad i = 1, 2, 3, \tag{2}$$

τ_{ij} being the usual elastic stress tensor in the medium.

The constitutive equations are

$$B = \mu H \tag{3}$$

$$J = \sigma(E + \dot{u} \times B) \tag{4}$$

where μ is the magnetic permeability, σ the electrical conductivity, and $\dot{u}$ the particle velocity.

$$\tau_{ij} = \lambda u_{k,k}\delta_{ij} + 2Ge_{ij} \tag{5}$$

where e_{ij} are the strain components and

$$2e_{ij} = u_{i,j} + u_{j,i}.$$

λ, G are Lamé constants.

The electromagnetic boundary conditions are

$$n \cdot \|B\| = 0$$

$$n \times \|H\| = 0$$

$$n \cdot \|E + \dot{u} \times B\| = 0 \tag{6}$$

where n is normal to the interfaces $x_3 =$ constant. $\|\cdot\|$ discontinuity jump at the boundary of the vector within.

Stress continuity conditions across the boundaries $x_3 =$ constant are

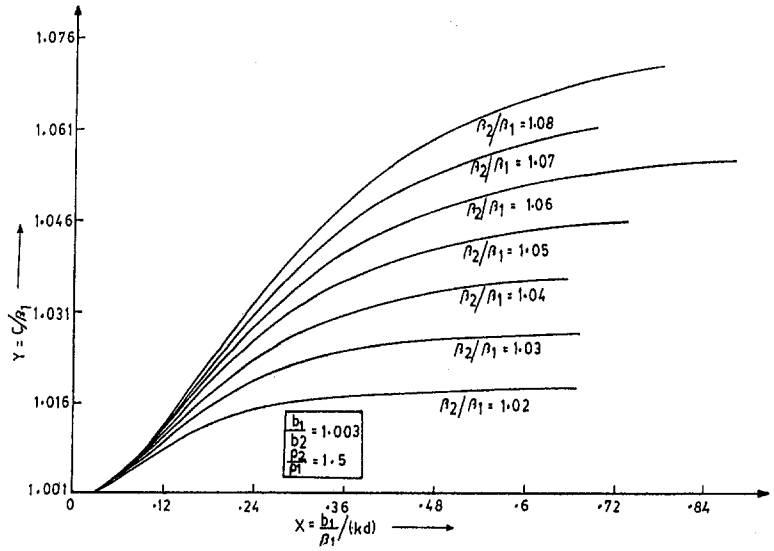


Fig. 2 Dispersion curves showing c/β_1 against X for $\beta_2/\beta_1 = 1.02, 1.03, \ldots, 1.08$ with $b_1/b_2 = 1.003$, $\rho_2/\rho_1 = 1.5$

Downloaded 04 May 2010 to 171.66.16.26. Redistribution subject to ASME license or copyright; see http://www.asme.org/terms/Terms_Use.cfm

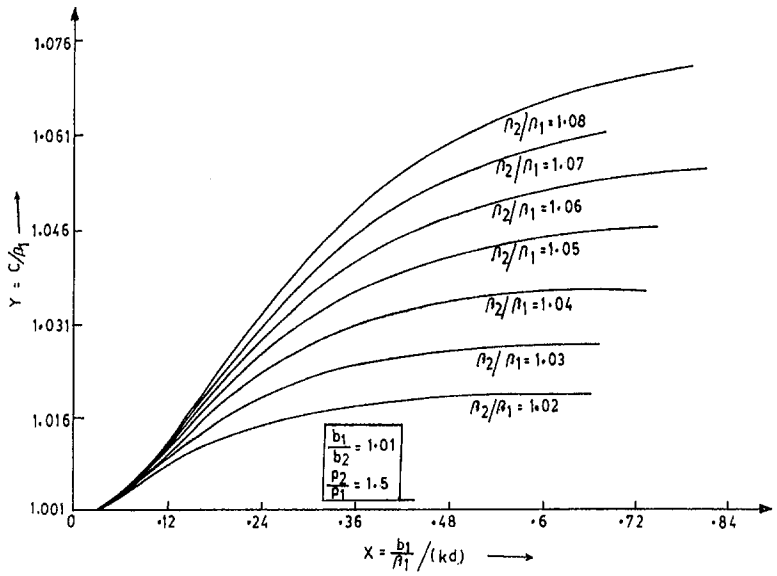


Fig. 3 Dispersion curves showing c/β_1 against X for $\beta_2/\beta_1 = 1.02, 1.03, \ldots, 1.08$ with $b_1/b_2 = 1.01$, $\rho_2/\rho_1 = 1.5$

$$(\tau_{3j} + \tau^E_{3j})_+ - (\tau_{3j} + \tau^E_{3j})_- = 0, \quad j = 1, 2, 3 \qquad (7)$$

where τ^E_{3j} are Maxwell's stress tensor components.

Formulation

In rectangular coordinates (x, y, z) the medium $(-d < z < \infty)$ consists of a layer $M_1(-d < z < 0)$ lying on a semi-infinite medium $M_2(0 < z < \infty)$ with moduli of rigidity and magnetic permeabilities (G_1, G_2), (μ_1, μ_2) in M_1, M_2, respectively. The bias magnetic fields in vacuo, M_1 and M_2 are, respectively, $(H_1^{(0)}, H_3^{(0)})$, $(H_1^{(1)}, 0, H_3^{(1)})$, and $(H_1^{(2)}, 0, H_3^{(2)})$. The perturbed magnetic fields are

$$(H_1^{(\alpha)} + h_1^{(\alpha)}, h_2^{(\alpha)}, H_3^{(\alpha)} + h_3^{(\alpha)}) \quad \text{with} \quad \alpha = 1, 2 \text{ for } M_1, M_2 \text{ respectively.} \qquad (8)$$

The displacement field is given by

$$u^{(\alpha)} = (0, v^{(\alpha)}(x, z, t), 0) \qquad (9)$$

with $\alpha = 1$ for M_1, $\alpha = 2$ for M_2.

For a perfectly conducting medium $\sigma \to \infty$ and (4) gives the perturbed electric field, which on substitution in (1) gives

$$\dot{h}^{(\alpha)} = \left(0, H_3^{(\alpha)} \frac{\partial \dot{v}^{(\alpha)}}{\partial z} + H_1^{(\alpha)} \frac{\partial \dot{v}^{(\alpha)}}{\partial z}, 0\right) \qquad (10)$$

neglecting second-order terms. Integrating (10) with respect to time t

$$h^{(\alpha)} = \left(0, H_3^{(\alpha)} \frac{\partial v^{(\alpha)}}{\partial z} + H_1^{(\alpha)} \frac{\partial v^{(\alpha)}}{\partial z}, 0\right). \qquad (11)$$

The Lorentz force is

$$J^{(\alpha)} \times B^{(\alpha)} = (0, \mu_\alpha H_1^{(\alpha)} h_{2_x}^{(\alpha)} + \mu_\alpha H_1^{(\alpha)} h_{2_x}^{(\alpha)}, 0) \qquad (12)$$

The boundary conditions (6) on $z = 0$ and $z = -d$ give

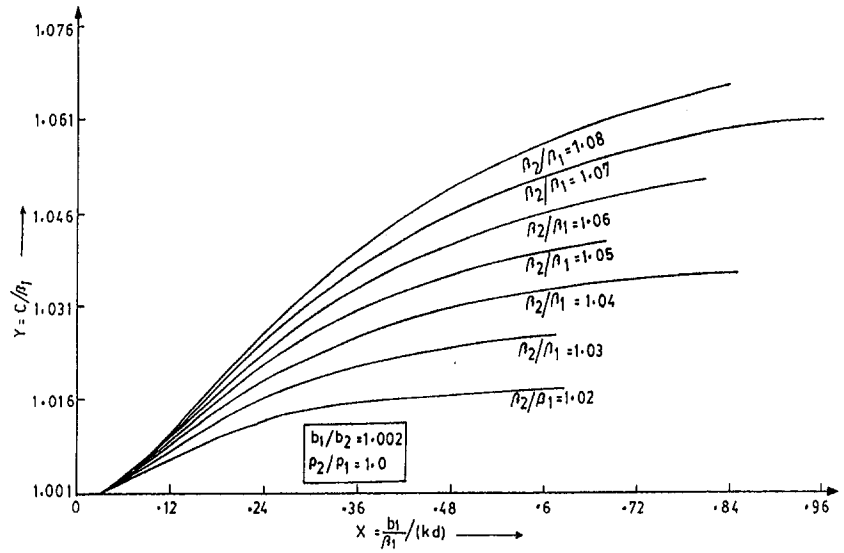


Fig. 4 Dispersion curves showing c/β_1 against X for $\beta_2/\beta_1 = 1.02, 1.03, \ldots, 1.08$ with $b_1/b_2 = 1.002$, $\rho_2/\rho_1 = 1.0$

Downloaded 04 May 2010 to 171.66.16.26. Redistribution subject to ASME license or copyright; see http://www.asme.org/terms/Terms_Use.cfm

$$H_1^{(0)} = H_1^{(1)} = H_1^{(2)} \tag{13}$$

and

$$\mu_0 H_3^{(0)} = \mu_1 H_3^{(1)} = \mu_2 H_3^{(2)}. \tag{14}$$

Hence,

$$\mathbf{H}^{(2)} = (H_1, 0, rH_3) \tag{15}$$

where we have written

$$\mathbf{H} = (H_1^{(1)}, 0, H_3^{(1)}) = (H_1, 0, H_3) \tag{16}$$

and

$$r = \mu_1/\mu_2. \tag{17}$$

Finally, the equation of motion in (2) which is not identically satisfied is

$$(1 + a_1^2/b_1^2)v_{xx}^{(1)} + (1 + a_3^2/b_1^2)v_{zz}^{(1)} + (2a_1a_3/b_1^2)v_{xz}^{(1)} = (1/b_1^2)v_{tt}^{(1)} \quad \text{for } M_1 \tag{18}$$

and

$$(1 + a_2^2/b_2^2)v_{xx}^{(2)} + (1 + r^2a_4^2/b_2^2)v_{zz}^{(2)} + (2ra_2a_4/b_2^2)v_{xz}^{(2)} = (1/b_2^2)v_{tt}^{(2)} \quad \text{for } M_2, \tag{19}$$

where we have introduced the symbols

$$\mu_1 H_1^2/\rho_1 = a_1^2, \quad \mu_2 H_1^2/\rho_2 = a_2^2, \quad \mu_1 H_3^2/\rho_1 = a_3^2, \quad \mu_2 H_3^2/\rho_2 = a_4^2, \quad G_1/\rho_1 = b_1^2, \quad G_2/\rho_2 = b_2^2. \tag{20}$$

a_1, a_3 and a_2, a_4 are Alfvén wave velocities in M_1 M_2, and b_1, b_2 are the S-wave velocities in M_1, M_2.

Stress Boundary Conditions. From (7) the stress-free condition leads to

$$G_1 v_z^{(1)} = 0 \quad \text{at} \quad z = -d \tag{21a}$$

$$[G_1 v_z^{(1)}]_{z=0^-} = [G_2 v_z^{(2)}]_{z=0^+}. \tag{21b}$$

The displacement being continuous at $z = 0$, we have

$$[v^{(1)}]_{z=0^-} = [v^{(2)}]_{z=0^+}. \tag{21c}$$

Wave Solution. For a SH surface wave traveling in the x-direction, the solutions to (18) and (19) are in the form:

$$v^{(1)} = (A_1 \exp(ikn_1 z) + A_2 \exp(ikn_2 z)) \exp\{ik(x - ct)\} \tag{22}$$

$$v^{(2)} = B \exp\{-k(im_1 + m_2)z\} \exp(ik(x - ct)) \tag{23}$$

where the real part of the wave velocity c satisfies the inequality

$$\beta_1 < \mathrm{Re}(c) < \beta_2 \tag{24}$$

and

$$n_{1,2} = -L \pm N$$

$$L = a_1a_3/(b_1^2 + a_3^2) \tag{25}$$

$$N = b_1(b_1^2 + a_1^2 + a_3^2)^{1/2}(c^2/\beta_1^2 - 1)^{1/2}(b_1^2 + a_3^2)^{-1} \tag{26}$$

$$\beta_1^2 = b_1^2(1 + a_1^2(b_1^2 + a_3^2)^{-1}) \tag{27}$$

$$m = im_1 + m_2 \tag{28}$$

$$m_1 = ra_2a_4(b_2^2 + r^2a_4^2)^{-1} \tag{29}$$

$$m_2 = b_2(1 - c^2/\beta_2^2)^{1/2}(b_2^2 + a_2^2 + r^2a_4^2)^{1/2}m_1/(ra_2a_4) \tag{30}$$

$$\beta_2^2 = b_2^2 + a_2^2 - r^2a_2^2a_4^2(b_2^2 + r^2a_4^2)^{-1}. \tag{31}$$

Frequency Equation. The Eqs. (22), (23) represent a wave provided the boundary conditions (21a), (21b), and (21c) are satisfied. On eliminating $A_1 : A_2 : B$ from these conditions we obtain the frequency equation

$$[G_1(N^2 - L^2) + G_2m_1L] \sin Nkd - m_2G_2N \cos Nkd - i[m_2LG_2 \sin Nkd + m_1G_2N \cos Nkd] = 0. \tag{32}$$

Real Wave Velocity. For a surface wave with the wave velocity c real, the quantities m, N are real. Hence, in this case on equating real and imaginary parts in (32) to zero, the following two equations are satisfied by the wave velocity c:

$$[G_1(N^2 - L^2) + G_2m_1L] \sin Nkd - m_2G_2N \cos Nkd = 0 \tag{33}$$

$$m_2LG_2 \sin Nkd + m_1G_2N \cos Nkd = 0. \tag{34}$$

For Eqs. (33) and (34) to be consistent, the following equation is to be satisfied:

$$[G_1(N^2 - L^2)m_1 + G_2L(m_1^2 + m_2^2) = 0, \tag{35}$$

which holds if

$$m_1 = L = 0, \tag{36}$$

or, if

$$c^2 = \frac{G_1ra_2a_4(b_1^2 + a_1^2) - G_2a_1a_3(b_2^2 + a_2^2)}{G_1ra_2a_4 - G_2a_1a_3}. \tag{37}$$

We conclude from (37) that $c^2 > \beta_2^2$ when $b_2^2 + a_2^2 > b_1^2 + a_1^2$ and

$$\rho_2G_2 > \rho_1G_1. \tag{38}$$

Condition (37) is therefore not suitable for a real surface wave. We therefore examine the first alternative, namely condition (36) which is valid in either of the following two cases:

Case I: $H_3 = 0$, $H_1 \neq 0$.
Here $a_3 = a_4 = 0$, $m_1 = L = 0$,

$$\beta_1 = (b_1^2 + a_1^2)^{1/2}, \quad \beta_2 = (b_2^2 + a_2^2)^{1/2}$$

$$n_1 = kN = \frac{k}{b_1}(b_1^2 + a_1^2)^{1/2}(c^2/\beta_1^2 - 1)^{1/2}$$

$$m_2 = \frac{1}{b_1}(b_2^2 + a_2^2)^{1/2}(1 - c^2/\beta_2^2)^{1/2}. \tag{39}$$

The frequency equation is obtained from (33) as

$$\tan\left[\frac{kd}{b_1}(b_1^2 + a_1^2)^{1/2}(c^2/\beta_1^2 - 1)^{1/2}\right] = \frac{G_2}{G_1}\frac{\frac{1}{b_2}(b_2^2 + a_2^2)^{1/2}(1 - c^2/\beta_2^2)^{1/2}}{\frac{1}{b_1}(b_1^2 + a_1^2)^{1/2}(c^2/\beta_1^2 - 1)^{1/2}}. \tag{40}$$

Hence, magnetoelastic Love waves are propagated with velocity c such that $\beta_1 < c < \beta_2$ provided $\beta_1 < \beta_2$. Since $\beta_1 > b_1$ and $\beta_2 > b_2$, the effect of the magnetic field in this case is to alter the range of possible values of c. Other properties such as dispersion hold as usual.

Since $\beta_2^2 - \beta_1^2 = b_2^2 + a_2^2 - b_1^2 - a_1^2$, it is interesting to note that magnetoelastic Love waves may exist if $b_2^2 + a_2^2 - b_1^2 - a_1^2 > 0$, even if ordinary Love waves do not exist. Hence the presence of a magnetic field in this case is responsible for the existence of Love waves. Figures 1, 2, 3, and 4 give the nature of dispersion curves for this case corresponding to different values of β_2/β_1, ρ_2/ρ_1 when $b_1/b_2 > 1$.

Downloaded 04 May 2010 to 171.66.16.26. Redistribution subject to ASME license or copyright; see http://www.asme.org/terms/Terms_Use.cfm

Again, in the case when M_1, M_2 are elastically homogeneous but magnetic permeabilities are different, i.e., $\mu_1 < \mu_2$ then $\beta_1 < \beta_2$, and consequently magnetoelastic SH-waves exist in this case as well.

Case II: $H_1 = 0, H_3 \neq 0$.

In this case the frequency Eq. (32) becomes

$$\tan\left[\frac{kb_1 d}{(b_1^2 + a_3^2)^{1/2}}(c^2/b_1^2 - 1)^{1/2}\right] = \frac{G_2}{G_1}\frac{(1 + a_3^2/b_1^2)^{1/2}T}{(1 + r^2a_4^2/b_2^2)^{1/2}} \quad (41)$$

where

$$T = \frac{(1 - c^2/b_2^2)^{1/2}}{(c^2/b_1^2 - 1)^{1/2}}. \quad (42)$$

Equation (41) shows the existence of surface waves in the medium with velocity c, such that $b_1 < c < b_2$.

Numerical Results

From the frequency Eq. (40) of Case I numerical values of the velocity c/β_1 has been plotted against $(b_1/\beta_1)/kd$ for the cases where b_1/b_2 is greater than one, but β_2/β_1 is greater than one in Figs. 1, 2, 3, and 4.

Acknowledgment

This work was done jointly by the authors during their tenures of fellowships, respectively, as a Senior Research Fellow of CSIR, India under Prof. A. Chakraborty of Jadavpur University, and as a Junior Research Fellow (UGC-DRS) under Prof. S. K. Chakraborty of Burdwan University.

References

Dunkin, J. W., and Eringen, A. C., 1963, "On the Propagation of Waves in a Electromagnetic Elastic solid," *International Journal of Engineering Science,* Vol. 1, pp. 461–495.

Knopoff, L., 1955, "The Interaction between Elastic wave Motion and a Magnetic Field in Electrical Conductors," *Journal of Geophysical Research,* Vol. 60, pp. 441–456.

Lee, Jong S., and Its, Elizabeth N., 1992, "Propagation of Rayleigh Waves in Magneto-Elastic Media," ASME JOURNAL OF APPLIED MECHANICS, Vol. 59, pp. 812–818.

Maugin, G. A., 1981, "Wave Motion in Magnetizable Deformable Solids," *International Journal of Engineering Science,* Vol. 19, pp. 321–388.

Maugin, G. A., 1988, "Shear Horizontal Surface Acoustic Waves on Solids," *Recent Advances in Surface Acoustic Waves,* D. F. Parker and G. A. Maugin, eds., Springer-Verlag, Berlin, pp. 158–172.

Tomita, S., and Shindo, Y., 1979, "Rayleigh Waves in Magneto-Thermo-Elastic Solid with Thermal Relaxation," *International Journal of Engineering Science,* Vol. 17, pp. 227–232.

Yu, Chia P., and Tang, Sam, 1966, "Magneto-elastic Waves in Initially stressed Conductors," *ZAMP,* Vol. 17, pp. 766–775.

A Nonspectral Stability Criterion for Linear Conservative Gyroscopic Systems

R. M. Bulatovic[8]

Using a Lyapunov-type approach, a simple sufficient stability condition for linear conservative gyroscopic systems with negative definite stiffness matrix is derived. The condition is nonspectral; it involves only the definiteness of certain combinations of the system's coefficient matrices.

[8] Department of Mechanical Engineering, University of Montenegro, Cetinski put b b, 81 000 Podgorica, Montenegro, Yugoslavia.

Contributed by the Applied Mechanics Division of THE AMERICAN SOCIETY OF MECHANICAL ENGINEERS for publication in the ASME JOURNAL OF APPLIED MECHANICS. Manuscript received by the ASME Applied Mechanics Division, May 19, 1997; final revision, Nov. 17, 1997. Associate Technical Editor: N. C. Perkins.

1 Introduction and Previous Results

We consider a linear mechanical system described by the equation

$$M\ddot{q} + B\dot{q} + Cq = 0, \quad (1)$$

where M, B, and C are real $n \times n$ matrices, q is the n-vector, $\cdot = d/dt$, and

- M is symmetric and positive definite ($M = M^T > 0$);
- B is skew-symmetric ($B = -B^T$);
- C is symmetric and negative definite ($C = C^T < 0$).

The vector q represents the generalized coordinates, M is the mass matrix, B describes the gyroscopic forces, and C the potential forces.

The stability properties of such a system have been investigated for many years. The first general treatment was by Thomson and Tait (1879). For the potential system, which can be formally obtained from (1) by setting $B = 0$, it is well known that the system is unstable. If gyroscopic forces are introduced, then the system (1) may be stable or unstable. According to classical result, given by Thomson and Tait (1879) and Chetayev (1961), the system $M\ddot{q} + Cq = 0$, $C < 0$ may be gyroscopically stabilized if and only if the degree-of-freedom is even.

As $M > 0$, one can utilize the positive definite square root in a familiar way to transform Eq. (1) to the form

$$\ddot{x} + G\dot{x} + Kx = 0 \quad (2)$$

where $G = M^{-1/2}BM^{-1/2}$, $K = M^{-1/2}CM^{-1/2}$ and $x = M^{1/2}q$. It is clear that $G^T = -G$ and $K^T = K$.

It is well known that the system of equations (1) or (2) is stable if and only if the eigenvalues associated with (2) are purely imaginary and semisimple, i.e., the eigenvalues have only linear elementary divisors. Eigenvalue (spectral) analysis is not useful for the stability investigation for systems with large numbers of degrees-of-freedom. Therefore, nonspectral stability conditions (necessary and/or sufficient) for system (2) are of practical interest and importance. References on the subject can be found in Bulatovic (1997) and Seyranian, Stoustrup, and Kliem (1995).

Several investigations have been made to clarify the role of the matrix $4K - G^2$ concerning stability of system (2). Pozharicki (1956) and Hagedorn (1975) showed that $4K - G^2 < 0$ implies instability. For a two-degree-of-freedom system, Teschner (1977) showed that $4K - G^2 > 0$ implies stability. Inman and Saggio (1985) extended this result and showed that if the trace of $(4K - G^2)$ is positive, then the system is stable. Huseyin, Hagedorn, and Teschner (1983) proved that if $KG = GK$, then $4K - G^2 > 0$ is necessary and sufficient for the stability of system (2). On the other hand, $4K - G^2 > 0$ does not generally ensure stability (see, for instance, the example in Barkwell and Lancaster (1992)). Inman (1988) proposed that the system (2) is stable if

$$4K - G^2 - \epsilon I > 0 \quad (3)$$

where $2\epsilon = \lambda_{max}(-G^2) > 0$ is the largest eigenvalue of $-G^2$ and I is identity matrix. Unfortunately, Inman's proof is not rigorous as pointed out by Walker (1991). However, there is no counter example for the condition (3). In the last decade Inman's paper stimulated some investigations published in ASME *Journal of Applied Mechanics* (see the list of references), but in these investigations criterion (3) has not been proved.

Downloaded 04 May 2010 to 171.66.16.26. Redistribution subject to ASME license or copyright; see http://www.asme.org/terms/Terms_Use.cfm

Again, in the case when M_1, M_2 are elastically homogeneous but magnetic permeabilities are different, i.e., $\mu_1 < \mu_2$ then $\beta_1 < \beta_2$, and consequently magnetoelastic SH-waves exist in this case as well.

Case II: $H_1 = 0, H_3 \neq 0$.

In this case the frequency Eq. (32) becomes

$$\tan\left[\frac{kb_1 d}{(b_1^2 + a_3^2)^{1/2}}(c^2/b_1^2 - 1)^{1/2}\right] = \frac{G_2}{G_1}\frac{(1 + a_3^2/b_1^2)^{1/2}T}{(1 + r^2a_4^2/b_2^2)^{1/2}} \quad (41)$$

where

$$T = \frac{(1 - c^2/b_2^2)^{1/2}}{(c^2/b_1^2 - 1)^{1/2}}. \quad (42)$$

Equation (41) shows the existence of surface waves in the medium with velocity c, such that $b_1 < c < b_2$.

Numerical Results

From the frequency Eq. (40) of Case I numerical values of the velocity c/β_1 has been plotted against $(b_1/\beta_1)/kd$ for the cases where b_1/b_2 is greater than one, but β_2/β_1 is greater than one in Figs. 1, 2, 3, and 4.

Acknowledgment

This work was done jointly by the authors during their tenures of fellowships, respectively, as a Senior Research Fellow of CSIR, India under Prof. A. Chakraborty of Jadavpur University, and as a Junior Research Fellow (UGC-DRS) under Prof. S. K. Chakraborty of Burdwan University.

References

Dunkin, J. W., and Eringen, A. C., 1963, "On the Propagation of Waves in a Electromagnetic Elastic solid," *International Journal of Engineering Science,* Vol. 1, pp. 461–495.

Knopoff, L., 1955, "The Interaction between Elastic wave Motion and a Magnetic Field in Electrical Conductors," *Journal of Geophysical Research,* Vol. 60, pp. 441–456.

Lee, Jong S., and Its, Elizabeth N., 1992, "Propagation of Rayleigh Waves in Magneto-Elastic Media," ASME JOURNAL OF APPLIED MECHANICS, Vol. 59, pp. 812–818.

Maugin, G. A., 1981, "Wave Motion in Magnetizable Deformable Solids," *International Journal of Engineering Science,* Vol. 19, pp. 321–388.

Maugin, G. A., 1988, "Shear Horizontal Surface Acoustic Waves on Solids," *Recent Advances in Surface Acoustic Waves,* D. F. Parker and G. A. Maugin, eds., Springer-Verlag, Berlin, pp. 158–172.

Tomita, S., and Shindo, Y., 1979, "Rayleigh Waves in Magneto-Thermo-Elastic Solid with Thermal Relaxation," *International Journal of Engineering Science,* Vol. 17, pp. 227–232.

Yu, Chia P., and Tang, Sam, 1966, "Magneto-elastic Waves in Initially stressed Conductors," *ZAMP,* Vol. 17, pp. 766–775.

A Nonspectral Stability Criterion for Linear Conservative Gyroscopic Systems

R. M. Bulatovic[8]

Using a Lyapunov-type approach, a simple sufficient stability condition for linear conservative gyroscopic systems with negative definite stiffness matrix is derived. The condition is nonspectral; it involves only the definiteness of certain combinations of the system's coefficient matrices.

[8] Department of Mechanical Engineering, University of Montenegro, Cetinski put b b, 81 000 Podgorica, Montenegro, Yugoslavia.

Contributed by the Applied Mechanics Division of THE AMERICAN SOCIETY OF MECHANICAL ENGINEERS for publication in the ASME JOURNAL OF APPLIED MECHANICS. Manuscript received by the ASME Applied Mechanics Division, May 19, 1997; final revision, Nov. 17, 1997. Associate Technical Editor: N. C. Perkins.

1 Introduction and Previous Results

We consider a linear mechanical system described by the equation

$$M\ddot{q} + B\dot{q} + Cq = 0, \quad (1)$$

where M, B, and C are real $n \times n$ matrices, q is the n-vector, $\cdot = d/dt$, and

- M is symmetric and positive definite ($M = M^T > 0$);
- B is skew-symmetric ($B = -B^T$);
- C is symmetric and negative definite ($C = C^T < 0$).

The vector q represents the generalized coordinates, M is the mass matrix, B describes the gyroscopic forces, and C the potential forces.

The stability properties of such a system have been investigated for many years. The first general treatment was by Thomson and Tait (1879). For the potential system, which can be formally obtained from (1) by setting $B = 0$, it is well known that the system is unstable. If gyroscopic forces are introduced, then the system (1) may be stable or unstable. According to classical result, given by Thomson and Tait (1879) and Chetayev (1961), the system $M\ddot{q} + Cq = 0$, $C < 0$ may be gyroscopically stabilized if and only if the degree-of-freedom is even.

As $M > 0$, one can utilize the positive definite square root in a familiar way to transform Eq. (1) to the form

$$\ddot{x} + G\dot{x} + Kx = 0 \quad (2)$$

where $G = M^{-1/2}BM^{-1/2}$, $K = M^{-1/2}CM^{-1/2}$ and $x = M^{1/2}q$. It is clear that $G^T = -G$ and $K^T = K$.

It is well known that the system of equations (1) or (2) is stable if and only if the eigenvalues associated with (2) are purely imaginary and semisimple, i.e., the eigenvalues have only linear elementary divisors. Eigenvalue (spectral) analysis is not useful for the stability investigation for systems with large numbers of degrees-of-freedom. Therefore, nonspectral stability conditions (necessary and/or sufficient) for system (2) are of practical interest and importance. References on the subject can be found in Bulatovic (1997) and Seyranian, Stoustrup, and Kliem (1995).

Several investigations have been made to clarify the role of the matrix $4K - G^2$ concerning stability of system (2). Pozharicki (1956) and Hagedorn (1975) showed that $4K - G^2 < 0$ implies instability. For a two-degree-of-freedom system, Teschner (1977) showed that $4K - G^2 > 0$ implies stability. Inman and Saggio (1985) extended this result and showed that if the trace of $(4K - G^2)$ is positive, then the system is stable. Huseyin, Hagedorn, and Teschner (1983) proved that if $KG = GK$, then $4K - G^2 > 0$ is necessary and sufficient for the stability of system (2). On the other hand, $4K - G^2 > 0$ does not generally ensure stability (see, for instance, the example in Barkwell and Lancaster (1992)). Inman (1988) proposed that the system (2) is stable if

$$4K - G^2 - \epsilon I > 0 \quad (3)$$

where $2\epsilon = \lambda_{max}(-G^2) > 0$ is the largest eigenvalue of $-G^2$ and I is identity matrix. Unfortunately, Inman's proof is not rigorous as pointed out by Walker (1991). However, there is no counter example for the condition (3). In the last decade Inman's paper stimulated some investigations published in ASME *Journal of Applied Mechanics* (see the list of references), but in these investigations criterion (3) has not been proved.

Downloaded 04 May 2010 to 171.66.16.26. Redistribution subject to ASME license or copyright; see http://www.asme.org/terms/Terms_Use.cfm

In the following section, with the help of Lyapunov's direct method, it will be proven that in condition (3), ϵ can be chosen in a way that this condition guarantees stability. In our approach ϵ is equal to the double difference of the maximal and minimal eigenvalues of the matrix K.

2 A Stability Criterion Based on the Matrix $4K - G^2$

We denote by δ_1 and δ_2 the maximal and minimal eigenvalues of $-K$, respectively. It is clear that $\delta_1 \geq \delta_2 > 0$.

Theorem. If $G^T = -G$ and $K^T = K < 0$, the system described by Eq. (2) is stable if

$$4K - G^2 - \delta I > 0 \tag{4}$$

where $\delta = 2(\delta_1 - \delta_2)$.

Proof. Along with energy integral

$$H = \tfrac{1}{2}\dot{x}^T\dot{x} + \tfrac{1}{2}x^TKx \tag{5}$$

there exists the first integral (Lakhadanov, 1978)

$$\Gamma = \dot{x}^T(K - G^2)\dot{x} - 2\dot{x}^TGKx + x^TK^2x \tag{6}$$

of the system (2). We select auxiliary function $V(x, \dot{x})$ as a combination of the above integrals having the form

$$V = \Gamma - 2\delta_1 H$$
$$= \dot{x}^T(K - G^2 - \delta_1 I)\dot{x} - 2\dot{x}^TGKx + x^T(K^2 - \delta_1 K)x. \tag{7}$$

It is clear that $dV/dt = 0$. Since

$$\dot{x}^TK\dot{x} \leq -\delta_2\dot{x}^T\dot{x}, \tag{8}$$

we conclude that

$$V \geq \dot{x}^T\left(2K - \frac{G^2}{2} - (\delta_1 - \delta_2)I\right)\dot{x} + V_1(x, \dot{x}) \tag{9}$$

where

$$2V_1 = \dot{x}^T(-G^2)\dot{x} - 4\dot{x}^TGKx + 2x^T(K^2 - \delta_1 K)x. \tag{10}$$

Setting

$$y = (-G^2)^{1/2}\dot{x} - 2(-G^2)^{-1/2}GKx \tag{11}$$

where $(-G^2)^{1/2}$ is the unique positive definite square root of $-G^2$, we can rewrite $2V_1$ as

$$2V_1 = y^Ty - 2x^T(K^2 + \delta_1 K)x. \tag{12}$$

From $K^2 + \delta_1 K \leq 0$ and $K^2 - \delta_1 K > 0$, according to (10) and (12), we see that V_1 is positive semidefinite and the set

$$\{(x, \dot{x}): \dot{x} = 0, V_1 = 0\} \tag{13}$$

is trivial. Consequently, according to (9), $V(x, \dot{x})$ is positive definite if the condition (4) holds; hence, the Theorem follows from Lyapunov's stability theorem (see, for instance, Meirovitch (1970)).

3 Illustrative Example

Consider a simplified model of a disk mounted on a noncircular weightless rotating shaft which is also subjected to a constant axial compression force. By using a reference frame rotating with the shaft the problem can readily be formulated, resulting in an equation of the form (2) with the matrices

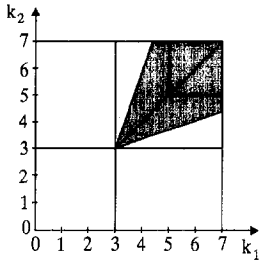


Fig. 1 Stability region of system (14) predicted by criteria based on the matrix $4K - G^2$.

$$G = 2\xi\begin{pmatrix} 0 & -1 \\ 1 & 0 \end{pmatrix},$$

$$K = \begin{pmatrix} k_1 - \xi^2 - \eta & 0 \\ 0 & k_2 - \xi^2 - \eta \end{pmatrix}, \tag{14}$$

where ξ is the shaft angular velocity, η is the axial force, and k_1, k_2 are elastic rigidities in the two principle directions (see Huseyin (1976)). We fix the values of ξ^2 and η as those in Inman (1988), $\xi^2 = 4$, $\eta = 3$ and we assume that $0 < k_1 < 7$ and $0 < k_2 < 7$, i.e., K is negative definite.

Each of the earlier stability criteria based on the matrix $4K - G^2$ mentioned in the first section, as well as the condition obtained here, are next applied to the above system and compared.

An elementary calculation shows that

$$4K - G^2 = 4\begin{pmatrix} k_1 - 3 & 0 \\ 0 & k_2 - 3 \end{pmatrix}$$

and $\lambda_{\max}(-G^2) = 16$ and $\lambda_{\max}(-K) - \lambda_{\min}(-K) = |k_1 - k_2|$. The condition $KG = GK$ is equivalent to $k_1 = k_2$. The stability regions predicted by various stability criteria formulated for n-degree-of-freedom systems are displayed in Fig. 1. Each region is defined by inequalities in the two parameters k_1 and k_2 as indicated in the following:

(A) Pozharicki-Hagedorn Instability Criterion. The system is unstable if $k_1 < 3$ and $k_2 < 3$. This corresponds to the square in the lower left corner of the figure.

(B) Huseyin-Hagedorn-Teschner Criterion. The system is stable if $k_1 = k_2 > 3$. This result is represented by the line segment between (3, 3) and (7, 7).

(C) Inman Conjecture. The system is stable if $5 < k_1 < 7$ and $5 < k_2 < 7$. This corresponds to the smaller square in the upper right corner of the figure.

(D) Proposed Theorem. The system is stable if $2(k_1 - 3) - |k_1 - k_2| > 0$ and $2(k_2 - 3) - |k_1 - k_2| > 0$. This criterion is represented by the shaded trapezoidal area in the figure.

4 Concluding Remarks

We have been interested in clarifying the role of the matrix $4K - G^2$ concerning the stability of multidimensional linear gyroscopic conservative systems with $K < 0$. In Section 2 a theorem has been derived via appropriate Lyapunov function. The Theorem provides sufficient condition for stability. This condition is easy to use, and may yield useful design constraints. The present Theorem is the same type as the conjecture in Inman (1988), but the value of ϵ in condition (3) is equal to the double difference of the maximal and minimal eigenvalue of the matrix K. In the special case of $K = kI$ this condition reduces to the criterion $4K - G^2 > 0$ which is necessary and

Downloaded 04 May 2010 to 171.66.16.26. Redistribution subject to ASME license or copyright; see http://www.asme.org/terms/Terms_Use.cfm

sufficient for stability for this class of systems (necessity follows from the Huseyin-Hagedorn-Teschner Theorem). Figure 1 indicates that present condition is superior to the Inman's conjecture for the system considered in the example (14), but this does not yield the exact stability region.

References

Barkwell, L., and Lancaster, P., 1992, "Overdamped and Gyroscopic Vibrating Systems," ASME JOURNAL OF APPLIED MECHANICS, Vol. 59, pp. 176–181.

Bulatovic, R. M., 1997, "On Stability of Linear Potential Gyroscopic Systems in a Case When Potential Energy Possesses Maximum," *Prikl. Math. Mekh. (PMM)*, Vol. 61, pp. 385–389 (in Russian).

Chetayev, N. G., 1961, *The Stability of Motion*, Pergamon Press, New York.

Hagedorn, P., 1975, "Über die Instabilit ät konservativer Systeme mit gyroskopischen Kräften," *Archive for Rational Mechanics and Analysis*, Vol. 58, No. 1, pp. 1–9.

Huseyin, K., 1978, *Vibrations and Stability of Multiple Parameter Systems*, Nordhoff International Publishing.

Huseyin, K., Hagedorn, P., and Teschner, W., 1983, "On the Stability of Linear Conservative Gyroscopic Systems," *Journal of Applied Mathematics and Physics (ZAMP)*, Vol. 34, pp. 807–815.

Inman, D. J., 1988, "A Sufficient Condition for the Stability of Conservative Gyroscopic Systems," ASME JOURNAL OF APPLIED MECHANICS, Vol. 55, pp. 895–898.

Inman, D. J., and Saggio, F., 1985, "Stability Analysis of Gyroscopic Systems by Matrix Methods," *AIAA Journal of Guidance, Control and Dynamics*, Vol. 8, No. 1, pp. 150–152.

Wu, Jinn-Wen, and Tsao, Tsu-Chin, 1994, "A Sufficient Stability Condition for Linear Conservative Gyroscopic Systems," ASME JOURNAL OF APPLIED MECHANICS, Vol. 61, pp. 715–717.

Lakhadanov, V. M., 1978, "On the Quadratic Integrals of Linear Autonomous Systems," *Prikl. Math. Mekh. (PMM)*, Vol. 42, pp. 555–557, (in Russian).

Meirovitch, L., 1970, *Methods of Analytical Dynamics*, McGraw-Hill, New York.

Pozharicki, G. K., 1956, "On the Instability of Motions of Conservative Systems," *Prikl. Math. Mekh. (PMM)*, Vol. 20, pp. 429–433, (in Russian).

Seyranian, A., Stoustrup, J., and Kliem, W., 1995, "On Gyroscopic Stabilization," *Journal of Applied Mathematics and Physics (ZAMP)*, Vol. 46, pp. 255–264.

Teschner, W., 1977, "Instabilität bei nichtlinearen konservativen Systemen mit gyroskopischen Kräften," Ph.D. thesis, TH Darmstadt.

Thomson, W., and Tait, G., 1879, *A Treatise on Natural Philosophy*, Vol. 1, Part 1, Cambridge University Press, Cambridge, UK.

Walker, J., 1991, "Stability of Linear Conservative Gyroscopic Systems," ASME JOURNAL OF APPLIED MECHANICS, Vol. 58, pp. 229–232.

On the Stability of Schapery Beams

D. Touati[9] and G. Cederbaum[9]

Introduction

The buckling and post-buckling of linear viscoelastic beams has been studied in the past in several works. The creep buckling of nonlinear viscoelastic beams was analyzed, e.g., by Distefano and Sackman (1968) and by Chung and Chung-Li (1986). Investigations of the problem within the linear theory (geometrically and viscoelastically) showed that, for solids, there is a safe load below which the creep buckling process stabilizes in time. Above this load the beam will buckle in the sense that the deflection may increase without bound. When considering the nonlinear *geometrical* effects, the problem solution predicts no such infinite increase of the lateral deflections with time for any practical loading. From this point of view, it can be said that the geometrical nonlinearity stabilizes the system.

The post-buckling behavior of imperfect nonlinear viscoelastic beams was investigated by the authors of this paper (Touati and Cederbaum, 1997a), using the Leaderman (1962) nonlinear constitutive model. In the present paper we extend that work and analyze the post-buckling behavior of imperfect beams by using the Schapery (1969) nonlinear viscoelastic model. This model for the characterization of the behavior of nonlinear viscoelastic materials was found in several studies to be the most general and convenient one (see, for example, Smart and Williams (1972), Dillard et al. (1987), and Scott et al. (1995)). Yet, its application in structural analysis and design was mainly within the finite element method. The main reason, probably, is due to the need of performing several time-dependent experiments in order to obtain the four functions needed for the complete description of the material, and it is easier to perform creep tests, which are needed for the finite element analysis, rather than the relaxation ones. However, for the formulation of the problem by a set of first-order differential equations, one needs the Schapery description of the material within the relaxation version; and this, in most cases, is not available. A way to resolve this obstacle is by predicting stress relaxation from known creep. A method of how to perform such prediction within the Schapery nonlinear viscoelastic model was suggested recently by the authors of this paper (Touati and Cederbaum, 1997b).

Problem Formulation

Consider an initially imperfect, simply supported beam of length l and cross-sectional area A, subjected to a constant compressive load, p, as shown in Fig. 1(*a*).

The beam material is nonlinearly viscoelastic, modeled by Schapery (1969) as

$$\sigma(t) = E_\infty h_\infty \epsilon + h_1 \int_{0^-}^{t} \Delta E(\rho - \rho') \frac{d}{d\tau} [h_2 \epsilon] d\tau. \quad (1)$$

E_∞ is the final value of the relaxation modulus and $\Delta E(t)$ is the transient component of modulus given by

$$\Delta E(t) = \sum_{i=1}^{n} E_i e^{-t/\alpha_i}, \quad (2)$$

where E_i and α_i are constants. The strain-dependent properties can be expressed as

$$h_m = 1 + \gamma_m \epsilon^2, \quad m = 1, 2, \infty \quad (3)$$

where γ_m are the material nonlinearity parameters. Finally, ρ is the so-called reduced time defined by

$$\rho = \int_{0^-}^{t} \frac{dt'}{a_\epsilon[\epsilon(t')]}, \quad \text{and} \quad \rho' = \int_{0^-}^{\tau} \frac{dt'}{a_\epsilon[\epsilon(t')]} \quad (4)$$

where

$$a_\epsilon = \begin{cases} 1, & \epsilon \le \epsilon_0 \\ c e^{-\gamma_a \epsilon}, & \epsilon > \epsilon_0 \end{cases} \quad (5)$$

and c, γ_a, and ϵ_0 are constants.

For convenience, Eq. (1) is rewritten as

$$\sigma(t) = \epsilon(E_\infty h_\infty + \Delta E_0 h_1 h_2) + h_1 \int_{0^+}^{t} \frac{d[\Delta E(\rho - \rho')]}{d(t - \tau)} h_2 \epsilon d\tau \quad (6)$$

where $\Delta E_0 = \Delta E(0) = \sum_{i=1}^{n} E_i$.

Within the elastica, the bending strain, ϵ, in a fiber at a distance z from the neutral axis of the imperfect beam is

[9] The Pearlstone Center for Aeronautical Engineering Studies, Department of Mechanical Engineering, Ben-Gurion University of the Negev, Beer Sheva 84105, Israel.

Contributed by the Applied Mechanics Division of THE AMERICAN SOCIETY OF MECHANICAL ENGINEERS for publication in the ASME JOURNAL OF APPLIED MECHANICS. Manuscript received by the ASME Applied Mechanics Division, May 22, 1997; final revision, Dec. 1, 1997. Associate Technical Editor: I. M. Daniel.

Downloaded 04 May 2010 to 171.66.16.26. Redistribution subject to ASME license or copyright; see http://www.asme.org/terms/Terms_Use.cfm

sufficient for stability for this class of systems (necessity follows from the Huseyin-Hagedorn-Teschner Theorem). Figure 1 indicates that present condition is superior to the Inman's conjecture for the system considered in the example (14), but this does not yield the exact stability region.

References

Barkwell, L., and Lancaster, P., 1992, "Overdamped and Gyroscopic Vibrating Systems," ASME JOURNAL OF APPLIED MECHANICS, Vol. 59, pp. 176–181.

Bulatovic, R. M., 1997, "On Stability of Linear Potential Gyroscopic Systems in a Case When Potential Energy Possesses Maximum," *Prikl. Math. Mekh. (PMM)*, Vol. 61, pp. 385–389 (in Russian).

Chetayev, N. G., 1961, *The Stability of Motion*, Pergamon Press, New York.

Hagedorn, P., 1975, "Über die Instabilit ät konservativer Systeme mit gyroskopischen Kräften," *Archive for Rational Mechanics and Analysis*, Vol. 58, No. 1, pp. 1–9.

Huseyin, K., 1978, *Vibrations and Stability of Multiple Parameter Systems*, Nordhoff International Publishing.

Huseyin, K., Hagedorn, P., and Teschner, W., 1983, "On the Stability of Linear Conservative Gyroscopic Systems," *Journal of Applied Mathematics and Physics (ZAMP)*, Vol. 34, pp. 807–815.

Inman, D. J., 1988, "A Sufficient Condition for the Stability of Conservative Gyroscopic Systems," ASME JOURNAL OF APPLIED MECHANICS, Vol. 55, pp. 895–898.

Inman, D. J., and Saggio, F., 1985, "Stability Analysis of Gyroscopic Systems by Matrix Methods," *AIAA Journal of Guidance, Control and Dynamics*, Vol. 8, No. 1, pp. 150–152.

Wu, Jinn-Wen, and Tsao, Tsu-Chin, 1994, "A Sufficient Stability Condition for Linear Conservative Gyroscopic Systems," ASME JOURNAL OF APPLIED MECHANICS, Vol. 61, pp. 715–717.

Lakhadanov, V. M., 1978, "On the Quadratic Integrals of Linear Autonomous Systems," *Prikl. Math. Mekh. (PMM)*, Vol. 42, pp. 555–557, (in Russian).

Meirovitch, L., 1970, *Methods of Analytical Dynamics*, McGraw-Hill, New York.

Pozharicki, G. K., 1956, "On the Instability of Motions of Conservative Systems," *Prikl. Math. Mekh. (PMM)*, Vol. 20, pp. 429–433, (in Russian).

Seyranian, A., Stoustrup, J., and Kliem, W., 1995, "On Gyroscopic Stabilization," *Journal of Applied Mathematics and Physics (ZAMP)*, Vol. 46, pp. 255–264.

Teschner, W., 1977, "Instabilität bei nichtlinearen konservativen Systemen mit gyroskopischen Kräften," Ph.D. thesis, TH Darmstadt.

Thomson, W., and Tait, G., 1879, *A Treatise on Natural Philosophy*, Vol. 1, Part 1, Cambridge University Press, Cambridge, UK.

Walker, J., 1991, "Stability of Linear Conservative Gyroscopic Systems," ASME JOURNAL OF APPLIED MECHANICS, Vol. 58, pp. 229–232.

On the Stability of Schapery Beams

D. Touati[9] and G. Cederbaum[9]

Introduction

The buckling and post-buckling of linear viscoelastic beams has been studied in the past in several works. The creep buckling of nonlinear viscoelastic beams was analyzed, e.g., by Distefano and Sackman (1968) and by Chung and Chung-Li (1986). Investigations of the problem within the linear theory (geometrically and viscoelastically) showed that, for solids, there is a safe load below which the creep buckling process stabilizes in time. Above this load the beam will buckle in the sense that the deflection may increase without bound. When considering the nonlinear *geometrical* effects, the problem solution predicts no such infinite increase of the lateral deflections with time for any practical loading. From this point of view, it can be said that the geometrical nonlinearity stabilizes the system.

The post-buckling behavior of imperfect nonlinear viscoelastic beams was investigated by the authors of this paper (Touati and Cederbaum, 1997a), using the Leaderman (1962) nonlinear constitutive model. In the present paper we extend that work and analyze the post-buckling behavior of imperfect beams by using the Schapery (1969) nonlinear viscoelastic model. This model for the characterization of the behavior of nonlinear viscoelastic materials was found in several studies to be the most general and convenient one (see, for example, Smart and Williams (1972), Dillard et al. (1987), and Scott et al. (1995)). Yet, its application in structural analysis and design was mainly within the finite element method. The main reason, probably, is due to the need of performing several time-dependent experiments in order to obtain the four functions needed for the complete description of the material, and it is easier to perform creep tests, which are needed for the finite element analysis, rather than the relaxation ones. However, for the formulation of the problem by a set of first-order differential equations, one needs the Schapery description of the material within the relaxation version; and this, in most cases, is not available. A way to resolve this obstacle is by predicting stress relaxation from known creep. A method of how to perform such prediction within the Schapery nonlinear viscoelastic model was suggested recently by the authors of this paper (Touati and Cederbaum, 1997b).

Problem Formulation

Consider an initially imperfect, simply supported beam of length l and cross-sectional area A, subjected to a constant compressive load, p, as shown in Fig. 1(*a*).

The beam material is nonlinearly viscoelastic, modeled by Schapery (1969) as

$$\sigma(t) = E_\infty h_\infty \epsilon + h_1 \int_{0^-}^{t} \Delta E(\rho - \rho') \frac{d}{d\tau} [h_2 \epsilon] d\tau. \quad (1)$$

E_∞ is the final value of the relaxation modulus and $\Delta E(t)$ is the transient component of modulus given by

$$\Delta E(t) = \sum_{i=1}^{n} E_i e^{-t/\alpha_i}, \quad (2)$$

where E_i and α_i are constants. The strain-dependent properties can be expressed as

$$h_m = 1 + \gamma_m \epsilon^2, \quad m = 1, 2, \infty \quad (3)$$

where γ_m are the material nonlinearity parameters. Finally, ρ is the so-called reduced time defined by

$$\rho = \int_{0^-}^{t} \frac{dt'}{a_\epsilon[\epsilon(t')]}, \quad \text{and} \quad \rho' = \int_{0^-}^{\tau} \frac{dt'}{a_\epsilon[\epsilon(t')]} \quad (4)$$

where

$$a_\epsilon = \begin{cases} 1, & \epsilon \le \epsilon_0 \\ c e^{-\gamma_a \epsilon}, & \epsilon > \epsilon_0 \end{cases} \quad (5)$$

and c, γ_a, and ϵ_0 are constants.

For convenience, Eq. (1) is rewritten as

$$\sigma(t) = \epsilon(E_\infty h_\infty + \Delta E_0 h_1 h_2) + h_1 \int_{0^+}^{t} \frac{d[\Delta E(\rho - \rho')]}{d(t - \tau)} h_2 \epsilon d\tau \quad (6)$$

where $\Delta E_0 = \Delta E(0) = \sum_{i=1}^{n} E_i$.

Within the elastica, the bending strain, ϵ, in a fiber at a distance z from the neutral axis of the imperfect beam is

[9] The Pearlstone Center for Aeronautical Engineering Studies, Department of Mechanical Engineering, Ben-Gurion University of the Negev, Beer Sheva 84105, Israel.

Contributed by the Applied Mechanics Division of THE AMERICAN SOCIETY OF MECHANICAL ENGINEERS for publication in the ASME JOURNAL OF APPLIED MECHANICS. Manuscript received by the ASME Applied Mechanics Division, May 22, 1997; final revision, Dec. 1, 1997. Associate Technical Editor: I. M. Daniel.

Downloaded 04 May 2010 to 171.66.16.26. Redistribution subject to ASME license or copyright; see http://www.asme.org/terms/Terms_Use.cfm

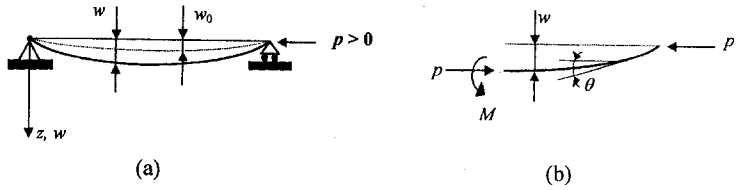


Fig. 1 Deflection of an imperfect simply supported beam

$$\epsilon = -z(\theta_{,x} - \theta_{0,x}) \tag{7}$$

where θ_0 is the initial rotation of the beam cross section, and θ is the angle of rotation of the beam cross section, given by

$$\theta = \sin^{-1}(w_{,x}). \tag{8}$$

From Eq. (8) one obtains

$$\theta_{,x} = \frac{w_{,xx}}{\cos\theta} \tag{9}$$

where $\cos\theta = \sqrt{1 - \sin^2\theta} \cong 1 - \frac{1}{2}w_{,x}^2$ for moderate geometrical nonlinearity, so that

$$\frac{1}{\cos\theta} \cong 1 + \frac{1}{2}w_{,x}^2, \tag{10}$$

and the expression derived for $\theta_{,x}$ is thus

$$\theta_{,x} \cong w_{,xx} + \tfrac{1}{2}w_{,x}^2 w_{,xx}. \tag{11}$$

It is assumed that the imperfection is small so that

$$\theta_{0,x} \cong w_{0,xx} \tag{12}$$

For further usage we record the following expression:

$$\theta_{,x}^3 \cong w_{,xx}^3(1 + \tfrac{3}{2}w_{,x}^2) \tag{13}$$

and note that $\theta_{0,x}^3$ is negligible.

For a simply supported beam (see Fig. 1(*b*))

$$M = -pw, \tag{14}$$

where the time-dependent moment resultant is given by

$$M(t) = -\int_A z\sigma(t)dA. \tag{15}$$

By substituting Eqs. (2)–(13), (15) into (14), and using the following dimensionless quantities

$$\xi = \frac{x}{l}, \quad 0 \le \xi \le 1$$

$$\omega = \frac{w}{l}, \quad \omega_0 = \frac{w_0}{l}, \quad \eta = \frac{h}{l}, \tag{16}$$

one obtains the equilibrium equation

$$\left(\omega_{,xx} - \omega_{0,xx} + \frac{1}{2}\omega_{,xx}\omega_{,x}^2\right)(1 + \Delta D_0)$$

$$+ [(\gamma_1 + \gamma_2)\Delta D_0 + \gamma_\infty]$$

$$\times \frac{I_1}{Il^2}\eta^2(\omega_{,xx} - \omega_{0,xx})^3 + \pi^2\frac{p}{p_e}(1 + \Delta D_0)\omega$$

$$= \int_A \sum_{i=1}^{n} [F_{1i} + (\omega_{,xx} - \omega_{0,xx})^2 F_{2i}]dA \tag{17}$$

where

$$I = \int_A z^2 dA, \quad I_1 = \int_A z^4 dA, \quad \Delta D_0 = \frac{\Delta E_0}{E_\infty},$$

$$D_i = \frac{E_i}{E_\infty}, \quad p_e = \frac{E_0 I\pi^2}{l^2}\left(= \frac{E_0 A\pi^2}{12}\eta^2\right)$$

is the Euler buckling load, and

$$F_{1i} = \frac{D_i}{\alpha_i I}\int_{0^+}^{t} e^{-(\rho-\rho')/\alpha_i}\frac{1}{a_\epsilon}\left[\left(\omega_{,xx} - \omega_{0,xx} + \frac{1}{2}\omega_{,x}^2\omega_{,xx}\right)z^2 + \frac{z^4\gamma_2}{l^2}(\omega_{,xx} - \omega_{0,xx})^3\right]d\tau \tag{18}$$

$$F_{2i} = \frac{D_i}{\alpha_i I}\int_{0^+}^{t} e^{-(\rho-\rho')/\alpha_i}\frac{1}{a_\epsilon}\left[\frac{z^4\gamma_1}{l^2}(\omega_{,xx} - \omega_{0,xx})\right]d\tau \tag{19}$$

(high order terms in Eq. (17) have been omitted).

Method of Solution

By differentiating Eqs. (18), (19) via the Leibnitz rule, the following set of ordinary differential equations are derived:

$$\dot{F}_{1i} = -\frac{1}{\alpha_i a_\epsilon}\left\{F_{1i} - D_i\left[\left(\omega_{,xx} - \omega_{0,xx} + \frac{1}{2}\omega_{,x}^2\omega_{,xx}\right)\frac{z^2}{I} + \frac{z^4\gamma_2}{Il^2}(\omega_{,xx} - \omega_{0,xx})^3\right]\right\} \tag{20}$$

$$\dot{F}_{2i} = -\frac{1}{\alpha_i a_\epsilon}\left[F_{2i} - D_i\frac{z^4\gamma_1}{Il^2}(\omega_{,xx} - \omega_{0,xx})\right] \tag{21}$$

where

$$\frac{1}{a_\epsilon} = 1 + (e^{\gamma_a\epsilon}/c - 1)U(\epsilon - \epsilon_0)$$

$$\cong 1 + \left[\left(1 + \gamma_a\epsilon + \frac{1}{2}\gamma_a^2\epsilon^2\right)\Big/ c - 1\right]U(\epsilon - \epsilon_0)$$

$$= 1 + \left\{\left[1 - \frac{\gamma_a z}{l}\left(\omega_{,xx} - \omega_{0,xx} + \frac{1}{2}\omega_{,x}^2\omega_{,xx}\right) + \frac{\gamma_a^2 z^2}{2l^2}\left(\omega_{,xx} - \omega_{0,xx} + \frac{1}{2}\omega_{,x}^2\omega_{,xx}\right)^2\right]\Big/ c - 1\right\}U(\epsilon - \epsilon_0) \tag{22}$$

and $U(\epsilon - \epsilon_0)$ is the unit step function. Equation (17) together with Eqs. (20), (21) represent a nonlinear initial and boundary value problem. Its solution here is based on the assumption that the time response of the first mode dominates the total beam

Downloaded 04 May 2010 to 171.66.16.26. Redistribution subject to ASME license or copyright; see http://www.asme.org/terms/Terms_Use.cfm

response (see, e.g., Minahen and Knauss, 1993). Thus the following solution functions are considered:

$$\omega = f(t) \sin \pi\xi \tag{23}$$

$$F_{1i} = H_{1i}(z, t) \sin \pi\xi \tag{24}$$

$$F_{2i} = H_{2i}(z, t) \sin \pi\xi. \tag{25}$$

The initial imperfection is also assumed to have a sinusoidal function

$$\omega_0 = e \sin \pi\xi \tag{26}$$

where e is a small positive constant. By substituting Eqs. (23)–(26) into (20), (21), and then using the Galerkin method, the following equations are derived:

$$\dot{H}_{1i}(z, t) = -\frac{1}{\alpha_i}\left\langle 1 + \left\{\left[1 + \frac{8\gamma_a\pi}{3l}\left(f - e + \frac{\pi^2}{8}f^3\right)z + \frac{3\gamma_a^2\pi^4}{8l^2}(f-e)^2z^2\right]\Big/ c - 1\right\}U(\epsilon - \epsilon_0)\right\rangle \times \left\{H_{1i} + \left[\left(f - e + \frac{\pi^2}{8}f^3\right)z^2 + \frac{3\pi^4\gamma_2}{4l^2}(f-e)^3z^4\right]\frac{\pi^2 D_i}{I}\right\} \tag{27}$$

$$\dot{H}_{2i}(z, t) = -\frac{1}{\alpha_i}\left\langle 1 + \left\{\left[1 + \frac{8\gamma_a\pi}{3l}\left(f - e + \frac{\pi^2}{8}f^3\right)z + \frac{3\gamma_a^2\pi^4}{8l^2}(f-e)^2z^2\right]\Big/ c - 1\right\}U(\epsilon - \epsilon_0)\right\rangle \times \left\{H_{2i} + \frac{\pi^2 D_i\gamma_1 z^4}{l^2 I}(f-e)\right\} \tag{28}$$

and by employing the same procedure with respect to Eq. (17), and then differentiating the resulting equation with respect to time, we obtain

$$\dot{f} = \frac{-\sum_{i=1}^{n}\left[\frac{1}{\pi^2}\int_A \dot{H}_{1i}\,dA + \frac{3\pi^2}{4}(f-e)^2\int_A \dot{H}_{2i}\,dA\right]}{\left(1 - \frac{p}{p_e} + \frac{3\pi^2}{8}f^2\right)(1 + \Delta D_0) + [\gamma_\infty + (\gamma_1 + \gamma_2)\Delta D_0]\frac{9\gamma_\infty I_1\pi^4}{4Il^2}(f-e)^2 + \frac{3\pi^2}{2}(f-e)\int_A H_{2i}\,dA}. \tag{29}$$

The initial conditions for Eqs. (27), (28) are $H_{1i}(z, 0^+) = H_{2i}(z, 0^+) = 0$. The initial condition for Eq. (29) is the instantaneous static deflection f_0 at $t = 0^+$, and is given by the relation

$$\frac{p}{p_e} = 1 - \frac{e}{f_0} + \frac{\pi^2}{8}f_0^2 + \frac{3\pi^4 I_1[(\gamma_1 + \gamma_2)\Delta D_0 + \gamma_\infty]}{4Il^2(1 + \Delta D_0)}\frac{(f_0 - e)^3}{f_0} \tag{30}$$

as derived from Eq. (17). It is noted that the nature of the response predicted by Eq. (30) depends on whether $(\gamma_1 + \gamma_2)\Delta D_0 + \gamma_\infty \geq 0$. If this is the case the beam will be stable. Otherwise, it may lose its stability, depending on the other parameters involved.

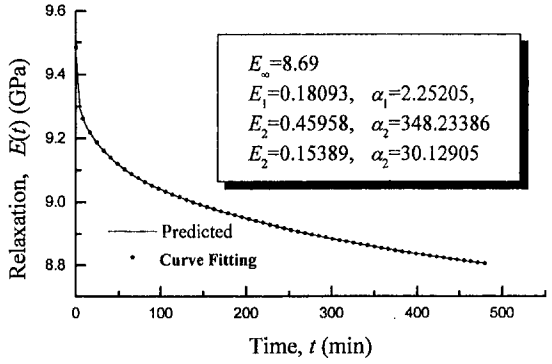


Fig. 2 Relaxation function versus time for graphite/epoxy in the transverse (22) direction

Numerical Example

Equations (27)–(29) constitute a set of first-order differential equations that can be solved numerically. In the following example we consider a beam with a rectangular cross section, $l = 20$ and $h = 1$ ($\eta = 0.05$). Within the Schapery *creep* model

$$\epsilon(t) = D_0 g_0 \sigma + g_1 \int_{0^-}^{t} \Delta D(\psi - \psi')\frac{d}{d\tau}[g_2\sigma]\,d\tau$$

$$\psi = \int_{0^-}^{t}\frac{dt'}{a_\sigma[\sigma(t')]}, \quad \psi' = \int_{0^-}^{\tau}\frac{dt'}{a_\sigma[\sigma(t')]}. \tag{31}$$

The creep compliance parameters D_0 and ΔD, and the nonlinear stress-dependent properties g_0, g_1, g_2, and a_s, in our case, are those reported by Tuttle and Brinson (1986) for the creep of graphite/epoxy laminates in the transverse (22) direction. This data enable us to predict the Schapery *relaxation* model (Eq. (1)) for this material by the method developed by the authors (Touati and Cederbaum, 1997b). The results of this prediction are shown in Fig. 2 for the relaxation modulus and in Fig. 3 for the nonlinear functions. It is noted that for this material $(\gamma_1 + \gamma_2)\Delta D_0 + \gamma_\infty < 0$.

Figure 4 shows the deflection, $f(t)$, versus t (the full lines) for different ratios of p/p_e. The results were obtained by solving Eqs. (27)–(29) within the computer program Matlab version 4.2c, utilizing the high-order Runge-Kutta method. The integration over the cross section appears in Eq. (29) is performed by Simpson's 1/3 method with 0.1 step size over the cross section height. From this figure it follows that there is a certain value of p/p_e below which the deflections are monotonically increasing towards final asymptotic values. For higher values of p/p_e the beam will become unstable in the sense that very large deflections are developed. This behavior is similar to that predicted within the linear viscoelastic and linear geometrical theory (see, e.g., Vinogradov, 1987), and contrary to the results obtained when considering nonlinear geometric effects (but linearly viscoelastic, see, e.g., Vinogradov, 1985). However, this kind of behavior may change by considering, for example, a material with the same characterizations as before except that γ_2 and γ_∞ are ≥ 0. In this case the material nonlinearity plays the same role as that of the geometric nonlinearity—to stabilize the sys-

Downloaded 04 May 2010 to 171.66.16.26. Redistribution subject to ASME license or copyright; see http://www.asme.org/terms/Terms_Use.cfm

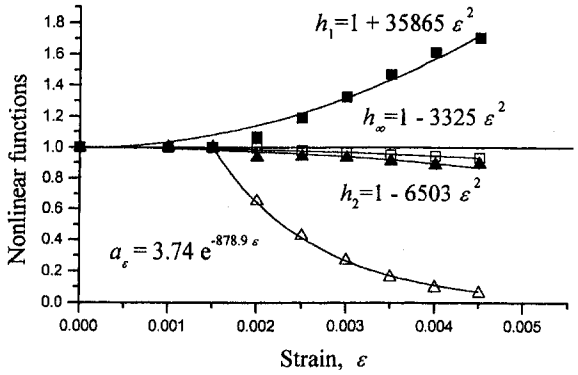


Fig. 3 Nonlinear relaxation properties h_∞, h_1, h_2, a_ε versus strain for graphite/epoxy in the transverse (22) direction

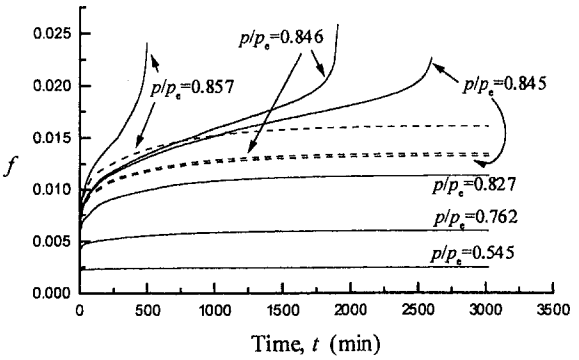


Fig. 4 The central deflection f versus time at different values of the load ratio, p/p_e

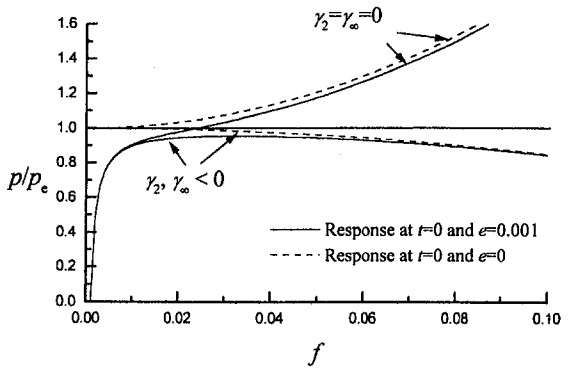


Fig. 5 The load ratio p/p_e versus the central deflection f, at $t = 0^+$

tem. This can be seen in Fig. 4 by the dashed lines (representing the case of $\gamma_2 = \gamma_\infty = 0$), which are the counterparts of those lines of instability (where γ_2 and $\gamma_\infty < 0$). An example of such material (where γ_2 and γ_∞ are non-negative) is the high-density polyethylene (Popelar et al., 1990). Finally, the response of the beam, $f(t)$, versus the loading ratio, p/p_e, at $t = 0^+$ is shown in Fig. 5. The cases considered are with and without imperfection and for negative and non-negative values of γ_2 and γ_∞. We may conclude from this figure, together with Fig. 4, that cases with γ_2 and $\gamma_\infty \geq 0$ will always be stable, while when γ_2 and $\gamma_\infty < 0$ instability may occur for some loading.

Summary

The post-buckling behavior of imperfect beams made of a nonlinear viscoelastic material is investigated. The material is modeled according to the Schapery strain-based representation of nonlinear viscoelasticity. Solutions within a nonlinear geometrical theory are developed to calculate the growth of the deflection in time. The numerical results show that beyond a certain value of the compressed loading large deflections are developed and the beam become unstable. This occurs for nonlinear materials which at $t = 0^+$ are of the "soft" type.

References

Chang, W. P., and Chung-Li, T., 1986, "Creep buckling of nonlinear viscoelastic columns," *Acta Mechanica,* Vol. 60, pp. 199–215.

Dillard, D. A., Straight, M. R., and Brinson, H. F., 1987, "The nonlinear viscoelastic characterization of Graphite/Epoxy composites," *Polymers Engineering and Science,* Vol. 27, No. 2, pp. 116–123.

Distefano, J. N., and Sackman, J. L., 1968, "On the stability of an initially imperfect, nonlinearly viscoelastic column," *Int. J. Solids and Structures,* Vol. 4, pp. 341–354.

Leaderman, H., 1962, "Large longitudinal retarded elastic deformation of rubberlike network polymers," *Transaction of the Society of Rheology,* Vol. 6, pp. 361–382.

Minahen, T. M., and Knauss, W. G., 1993, "Creep buckling of viscoelastic structures," *Int. J. Solids and Structures,* Vol. 30, No. 8, pp. 1057–1092.

Popelar, C. F., Popelar, C. H., and Kenner, V. H., 1990, "Viscoelastic material characterization and modeling for polyethylen," *Plymer Engineering and Science,* Vol. 30, No. 10, pp. 577–586.

Schapery, R. A., 1969, "On the characterization of nonlinear viscoelastic materials," *Polymers Engineering and Science,* Vol. 9, No. 4, pp. 295–310.

Scott, D. W., Lai, J. S., and Zureick, A. H., 1995, "Creep behavior of fiber reinforced polymeric composites: A review of the technical literature," *J. Reinforced Plastics and Composites,* Vol. 14, pp. 588–617.

Smart, J., and Williams, J. G., 1972, "A comparison of single integral nonlinear viscoelastic theories," *J. Mechanics Physics Solids,* Vol. 20, pp. 313–324.

Touati, D., and Cederbaum, G., 1997a, "Post buckling analysis of imperfect nonlinear viscoelastic columns," *Int. J. Solids and Structures,* Vol. 34, No. 14, pp. 1751–1760.

Touati, D., and Cederbaum, G., 1997b, "On the Prediction of Stress Relaxation From Known Creep of Nonlinear Materials," ASME *Journal of Engineering Materials and Technology,* Vol. 119, No. 2, pp. 121–124.

Tuttle, M. E., and Brinson, H. F., 1986, "Prediction of the long-term creep compliance of general composite laminates," *Experimental Mechanics,* Vol. 26, No. 1, pp. 89–102.

Vinogradov, A. M., 1985, "Nonlinear effects in creep buckling analysis of columns," *J. Engineering Mechanics,* Vol. 111, No. 6, pp. 757–767.

Vinogradov, A. M., 1987, "Buckling of viscoelastic beam columns," *AIAA J.,* Vol. 25, No. 3, pp. 479–483.

Boundary Spectral Strip for Elastodynamics Using Analytical Integration Along a Circular Path

O. Michael[10], J. Avrashi[11], and G. Rosenhouse[12]

The two-dimensional elastodynamics boundary integral equation is solved by using a spectral harmonic series. The frequency domain kernel is expanded into a Taylor series enabling the integration of each term of the series analytically along a circular integration path. The application of the method is demonstrated by solving two simple problems having a known analyti-

[10] Department of Aerospace and Mechanical Engineering, Boston University, 110 Cummington Street, Boston, MA 02215.

[11] Faculty of Mechanical Engineering, Technion–Israel Institute of Technology, Haifa, 32000, Israel

[12] Faculty of Civil Engineering, Technion–Israel Institute of Technology, Haifa, 32000, Israel.

Contributed by the Applied Mechanics Division of THE AMERICAN SOCIETY OF MECHANICAL ENGINEERS for publication in the ASME JOURNAL OF APPLIED MECHANICS. Manuscript received by the ASME Applied Mechanics Division, Apr. 18, 1997; final revision, Nov. 14, 1997. Associate Technical Editor: M. Ortiz.

Downloaded 04 May 2010 to 171.66.16.26. Redistribution subject to ASME license or copyright; see http://www.asme.org/terms/Terms_Use.cfm

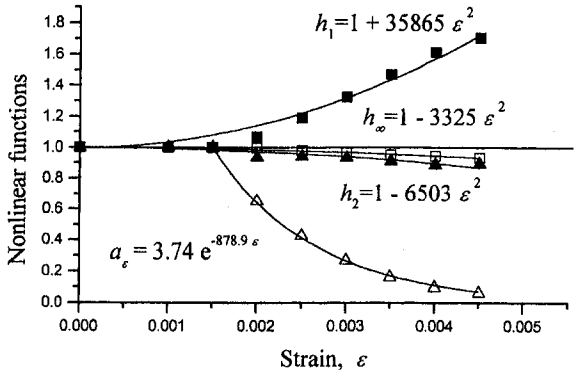


Fig. 3 Nonlinear relaxation properties h_∞, h_1, h_2, a_ε versus strain for graphite/epoxy in the transverse (22) direction

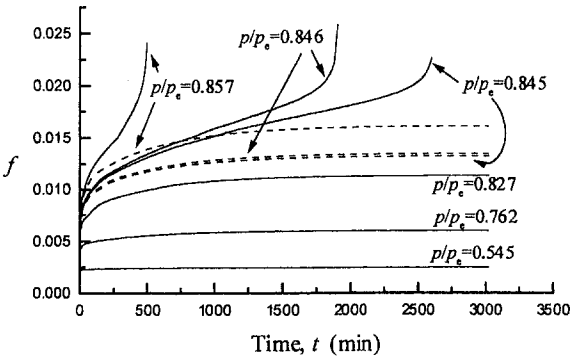


Fig. 4 The central deflection f versus time at different values of the load ratio, p/p_e

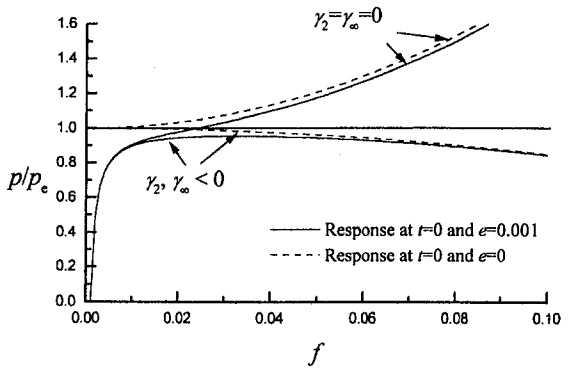


Fig. 5 The load ratio p/p_e versus the central deflection f, at $t = 0^+$

tem. This can be seen in Fig. 4 by the dashed lines (representing the case of $\gamma_2 = \gamma_\infty = 0$), which are the counterparts of those lines of instability (where γ_2 and $\gamma_\infty < 0$). An example of such material (where γ_2 and γ_∞ are non-negative) is the high-density polyethylene (Popelar et al., 1990). Finally, the response of the beam, $f(t)$, versus the loading ratio, p/p_e, at $t = 0^+$ is shown in Fig. 5. The cases considered are with and without imperfection and for negative and non-negative values of γ_2 and γ_∞. We may conclude from this figure, together with Fig. 4, that cases with γ_2 and $\gamma_\infty \geq 0$ will always be stable, while when γ_2 and $\gamma_\infty < 0$ instability may occur for some loading.

Summary

The post-buckling behavior of imperfect beams made of a nonlinear viscoelastic material is investigated. The material is modeled according to the Schapery strain-based representation of nonlinear viscoelasticity. Solutions within a nonlinear geometrical theory are developed to calculate the growth of the deflection in time. The numerical results show that beyond a certain value of the compressed loading large deflections are developed and the beam become unstable. This occurs for nonlinear materials which at $t = 0^+$ are of the "soft" type.

References

Chang, W. P., and Chung-Li, T., 1986, "Creep buckling of nonlinear viscoelastic columns," *Acta Mechanica,* Vol. 60, pp. 199–215.

Dillard, D. A., Straight, M. R., and Brinson, H. F., 1987, "The nonlinear viscoelastic characterization of Graphite/Epoxy composites," *Polymers Engineering and Science,* Vol. 27, No. 2, pp. 116–123.

Distefano, J. N., and Sackman, J. L., 1968, "On the stability of an initially imperfect, nonlinearly viscoelastic column," *Int. J. Solids and Structures,* Vol. 4, pp. 341–354.

Leaderman, H., 1962, "Large longitudinal retarded elastic deformation of rubberlike network polymers," *Transaction of the Society of Rheology,* Vol. 6, pp. 361–382.

Minahen, T. M., and Knauss, W. G., 1993, "Creep buckling of viscoelastic structures," *Int. J. Solids and Structures,* Vol. 30, No. 8, pp. 1057–1092.

Popelar, C. F., Popelar, C. H., and Kenner, V. H., 1990, "Viscoelastic material characterization and modeling for polyethylen," *Plymer Engineering and Science,* Vol. 30, No. 10, pp. 577–586.

Schapery, R. A., 1969, "On the characterization of nonlinear viscoelastic materials," *Polymers Engineering and Science,* Vol. 9, No. 4, pp. 295–310.

Scott, D. W., Lai, J. S., and Zureick, A. H., 1995, "Creep behavior of fiber reinforced polymeric composites: A review of the technical literature," *J. Reinforced Plastics and Composites,* Vol. 14, pp. 588–617.

Smart, J., and Williams, J. G., 1972, "A comparison of single integral nonlinear viscoelastic theories," *J. Mechanics Physics Solids,* Vol. 20, pp. 313–324.

Touati, D., and Cederbaum, G., 1997a, "Post buckling analysis of imperfect nonlinear viscoelastic columns," *Int. J. Solids and Structures,* Vol. 34, No. 14, pp. 1751–1760.

Touati, D., and Cederbaum, G., 1997b, "On the Prediction of Stress Relaxation From Known Creep of Nonlinear Materials," ASME *Journal of Engineering Materials and Technology,* Vol. 119, No. 2, pp. 121–124.

Tuttle, M. E., and Brinson, H. F., 1986, "Prediction of the long-term creep compliance of general composite laminates," *Experimental Mechanics,* Vol. 26, No. 1, pp. 89–102.

Vinogradov, A. M., 1985, "Nonlinear effects in creep buckling analysis of columns," *J. Engineering Mechanics,* Vol. 111, No. 6, pp. 757–767.

Vinogradov, A. M., 1987, "Buckling of viscoelastic beam columns," *AIAA J.,* Vol. 25, No. 3, pp. 479–483.

Boundary Spectral Strip for Elastodynamics Using Analytical Integration Along a Circular Path

O. Michael[10], J. Avrashi[11], and G. Rosenhouse[12]

The two-dimensional elastodynamics boundary integral equation is solved by using a spectral harmonic series. The frequency domain kernel is expanded into a Taylor series enabling the integration of each term of the series analytically along a circular integration path. The application of the method is demonstrated by solving two simple problems having a known analyti-

[10] Department of Aerospace and Mechanical Engineering, Boston University, 110 Cummington Street, Boston, MA 02215.

[11] Faculty of Mechanical Engineering, Technion–Israel Institute of Technology, Haifa, 32000, Israel

[12] Faculty of Civil Engineering, Technion–Israel Institute of Technology, Haifa, 32000, Israel.

Contributed by the Applied Mechanics Division of THE AMERICAN SOCIETY OF MECHANICAL ENGINEERS for publication in the ASME JOURNAL OF APPLIED MECHANICS. Manuscript received by the ASME Applied Mechanics Division, Apr. 18, 1997; final revision, Nov. 14, 1997. Associate Technical Editor: M. Ortiz.

Downloaded 04 May 2010 to 171.66.16.26. Redistribution subject to ASME license or copyright; see http://www.asme.org/terms/Terms_Use.cfm

cal solution. The results show a good agreement between the numerical and the analytical solutions. As in the elastostatic formulation, the boundary spectral strip dynamic formulation shows an exponential convergence rate.

1 Introduction

The boundary integral equation method is considered an attractive method for the solution of wave propagation problems. It enables a solution procedure that is carried on the boundaries alone. The direct formulation and solutions for the general transient two and three-dimensional elastodynamics problem is presented in Cruse and Rizzo (1968) and Cruse (1968). These include solutions in the Laplace transform space which can be converted easily into the frequency domain. The numerical evaluation of integrals with the elastodynamic kernel for formation of the coefficient matrix seems to be more problematic as compared to elastostatics or to potential equations. The main existing approach to overcome this difficulty is to subtract the elastostatics kernel from the elastodynamics kernel and to remain with a nonsingular expression as suggested in Rizzo et al. (1985).

Recently, a new nonelement "semi-analytical" method for solution of the boundary integral equation was developed. It was defined as the boundary spectral strip method (BSM). This method was implied and tested for potential and elastostatic equations (Michael et al., 1996a, b). In the present work we expand the two-dimensional elastodynamics fundamental solution into a series of terms which depend on geometry only, multiplied each by a term which depends on physical properties only. This technique enables us to integrate over the hypersingular elastodynamics kernel analytically for circular geometries.

2 Kernel Expansion

The fundamental solution for the two-dimensional steady-state elastodynamics equation was first presented in Cruse et al. (1968) and Cruse (1968) in the form of displacements and tractions kernels. These kernels can be written as

$$u^*_{kl} = \frac{1}{2\pi\mu}(A_{kl} - B_{kl}); \quad p^*_{kl} = \frac{1}{2\pi}(C_{kl} + D_{kl} + E_{kl}) \quad (1)$$

where A_{kl}, B_{kl}, C_{kl}, D_{kl}, and E_{kl} are five fundamental terms, defined as

$$A_{kl} = T_1\delta_{kl} = \{\psi\}\delta_{kl}; \quad B_{kl} = T_2 r_{,k} r_{,l} = \{\chi\} r_{,k} r_{,l}$$

$$C_{kl} = T_3 \frac{1}{r}\left(\frac{\partial r}{\partial n}\delta_{kl} + r_{,k}n_l + r_{,l}n_k\right)$$

$$= \left\{S\frac{d\psi}{dS} - \chi\right\}\frac{1}{r}\left(\frac{\partial r}{\partial n}\delta_{kl} + r_{,k}n_l + r_{,l}n_k\right)$$

$$D_{kl} = T_4\left(\frac{1}{r}\frac{\partial r}{\partial n} r_{,k} r_{,l}\right) = \left\{2\left(2\chi - S\frac{d\psi}{dS}\right)\right\}\left(\frac{1}{r}\frac{\partial r}{\partial n} r_{,k} r_{,l}\right)$$

$$E_{kl} = T_5\left(\frac{1}{r} r_{,k} n_l\right)$$

$$= \{S[K_1(S) + \Lambda(2\Lambda^2 - 1)K_1(\Lambda S)]\}\left(\frac{1}{r} r_{,k} n_l\right). \quad (2)$$

Here C_T and C_L are the transverse shear wave and the longitudinal pressure wave velocities, respectively. $S = i\omega r/C_T$, $\Lambda = C_T/C_L$, and the two functions ψ and χ are

$$\psi = K_0\left(\frac{i\omega r}{C_T}\right) + \frac{C_T}{i\omega r}\left[K_1\left(\frac{i\omega r}{C_T}\right) - \frac{C_T}{C_L}K_1\left(\frac{i\omega r}{C_L}\right)\right];$$

$$\chi = K_2\left(\frac{i\omega r}{C_T}\right) - \left(\frac{C_T}{C_L}\right)^2 K_1\left(\frac{i\omega r}{C_L}\right). \quad (3)$$

K_n is the modified Bessel function of the second kind of order n. Note that all the terms T_1 to T_5 in Eqs. (2) are purely physical and they are multiplied by purely geometrical terms. Using the expansion for K_n given in Abramowitz and Stegun (1965), we rewrite the physical terms T_i of Eqs. (2) as

$$T_i = t_{0_i} + t_{1_i}\ln S + \sum_{n=1}^{N_t}\{t_{2n_i}S^{2n}\ln S + t_{3n_i}S^{2(n-1)}\ln S + t_{4n_i}S^{2n} + t_{5n_i}S^{2(n-1)}\}. \quad (4)$$

Here N_t is the number of terms used in the approximation of K_n. The subterms t_{n_i} can be found in Michael et al. (1997). Note that all the terms of Eq. (4) yield singularities only for $n = 1$ and they combine a $\ln S$ multiplied by a geometrical term. The boundary spectral strip method allows us to perform analytically all the integrations with terms of the form S^{2n}, $S^{2n}\ln S$ for a pure circular geometry (other means of numerical integration can be used in cases of noncircular geometries).

3 Analytical Integrations for a Circular Path

Most of the integrals needed for the elastodynamics solution exist in the elastostatic solution (Michael et al., 1996a). The exceptions are integrals of the form

$$I_m = \int_0^{2\pi}\frac{\ln\bar{r}}{\bar{r}^{2m}}\cos n\theta d\theta \quad m = 1, 2 \quad (5)$$

where $\bar{r}$ is the distance r normalized by the radius of the integration path R. These integrals are not available in integrals handbooks, and therefore it was necessary to develop a technique to solve integrals of this kind. The technique is demonstrated here for the I_1 integral where $m = 1$. The solution for the I_2 integral is given as well. Generally this technique can be used for any value of positive m.

Using the fact that for an arc geometry $\bar{r}^2 = 1 - 2p\cos\theta + p^2$ (where $p = a/R$ and a is the distance between the arc center and the collocation point), the I_1 integral can be written as

$$I_1 = \int_0^{2\pi}\frac{\ln\bar{r}}{\bar{r}^2}\cos n\theta d\theta$$

$$= \frac{1}{2}\int_0^{2\pi}\frac{\ln(1 - 2p\cos\theta + p^2)}{(1 - 2p\cos\theta + p^2)}\cos n\theta d\theta. \quad (6)$$

In the case where $|p| < 1$, the $\ln r^2$ term in the nominator can be expanded into the following infinite series:

$$\ln(1 - 2p\cos\theta + p^2) = -2\sum_{\nu=1}^{\infty}\frac{p^\nu}{\nu}\cos\nu\theta. \quad (7)$$

Substituting this expansion into I_1 yields

$$I_1 = -\sum_{\nu=1}^{\infty}\frac{p^\nu}{\nu}\int_0^{2\pi}\frac{\cos\nu\theta\cos n\theta}{(1 - 2p\cos\theta + p^2)}d\theta$$

$$= -\frac{1}{2}\sum_{\nu=1}^{\infty}\frac{p^\nu}{\nu}\int_0^{2\pi}\frac{\cos(n-\nu)\theta + \cos(n+\nu)\theta}{(1 - 2p\cos\theta + p^2)}d\theta. \quad (8)$$

Using the integral $\int_0^{2\pi}(\cos a\theta/r^2)d\theta$, which is given in Gröber and Hofreiter (1961), the last integral can be written as

Downloaded 04 May 2010 to 171.66.16.26. Redistribution subject to ASME license or copyright; see http://www.asme.org/terms/Terms_Use.cfm

$$I_1 = -\sum_{\nu=1}^{\infty} \frac{p^\nu}{\nu} \frac{\pi}{1-p^2} [p^{|n-\nu|} + p^{|n+\nu|}]$$
$$= -\frac{\pi}{1-p^2} \left\{ p^n \sum_{\nu=1}^{\infty} \frac{p^{2\nu}}{\nu} + p^n \sum_{\nu=1}^{n} \frac{1}{\nu} + p^{-n} \sum_{\nu=n+1}^{\infty} \frac{p^{2\nu}}{\nu} \right\}. \quad (9)$$

Adding and subtracting the term $p^{-n}\Sigma_{\nu=1}^{n} p^{2\nu}/\nu$ yields

$$I_1 = -\frac{\pi}{1-p^2} \left\{ (p^n + p^{-n}) \sum_{\nu=1}^{\infty} \frac{p^{2\nu}}{\nu} - p^n \sum_{k=1}^{n} \frac{1}{k} [1 - p^{2(k-n)}] \right\}, \quad (10)$$

and since $\Sigma_{\nu=1}^{\infty} p^{2\nu}/\nu = -\ln(1-p^2)$, we finally find the result for the integral as

$$I_1 = \frac{\pi}{1-p^2} \left\{ (p^n + p^{-n}) + \ln(1-p^2) + p^n \sum_{k=1}^{n} \frac{1}{k} [1 - p^{2(k-n)}] \right\}. \quad (11)$$

In the case where $|p| > 1$, we define $\bar{p} = 1/p$ and obtain the analytical results by a simple change of variables.

The I_2 integral can be derived in a similar way, and it is given for the case of $|p| < 1$ as

$$I_2 = \frac{\pi}{(1-p^2)^3} \left\{ [(p^n + p^{-n})(1+p^2) + n(p^n - p^{-n})(1-p^2)] \ln(1-p^2) + p^2(p^n + p^{-n}) - \sum_{k=1}^{n} \frac{1}{k} [(p^n - p^{2k-n})(1+p^2) + (n-k)(1-p^2)(p^n + p^{2k-n})(1-p^2)] \right\}. \quad (12)$$

We note here that this method can also be used for other values of positive integer m.

4 Numerical Results

Two problems are solved here in order to demonstrate the method. Both are involved with a circular cavity embedded in an infinite domain. In the first case we apply a normal excitation which, generates radial plane waves, while in the second case we apply a tangential excitation, which results in rotational shear waves. Figures 1(a) and 1(b) depict the amplitude of the pressure wave (P-wave) and the rotary shear wave (RS-wave), respectively. The analytical solutions are presented by the bold-type lines, while the numerical results for the different number of approximation terms are marked on those graphs. For all cases, Poisson's ratio is $\nu = 0.3$, and only one trigonometric term is needed for the solution. It can be observed that for values of $S \leq 1i$, the four-terms approximation provides excellent results, while for higher values of S, a higher number of terms is needed. Figure 2 shows the number of terms needed in order to provide an error less than five percent and one percent for the two problems. It can be seen that there is almost a linear relation between the number of terms needed to overcome prescribed error and the value of S. In fact, Fig. 2 can help figure out what is the number of terms needed for the approximation for a given value of S. From the investigation of more complex problems, where more trigonometric terms are needed for the solution, we found that the method converges exponentially, as was expected, when using a spectral method.

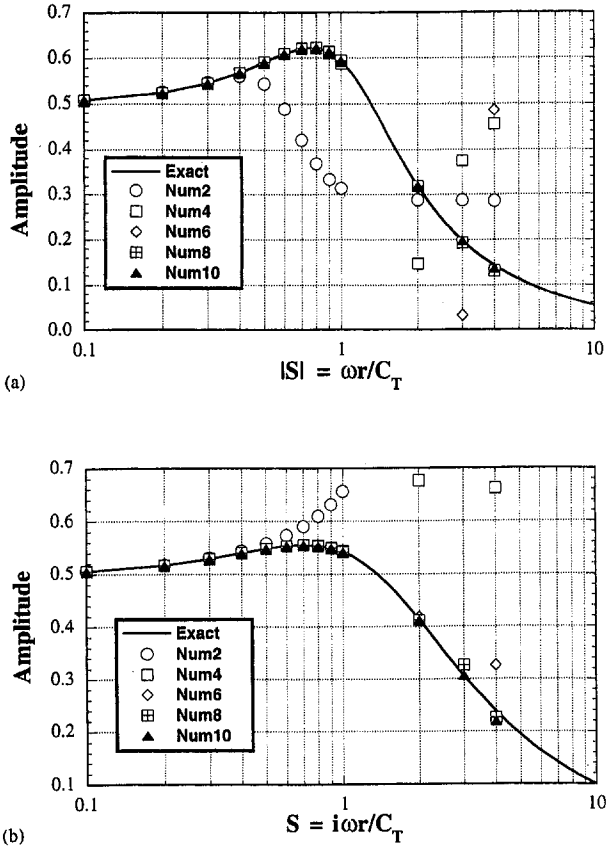


Fig. 1 Amplitude as a function of S with varying number of approximation terms N_t for the fundamental solution; (a) P-Wave, (b) RS-Wave

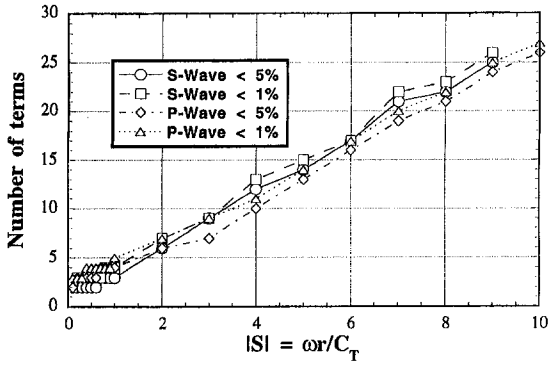


Fig. 2 Number of terms required to obtain a given error as a function of S

5 Remarks and Conclusions

The elastodynamics kernel was expanded in the present work by using a Taylor series. Analytical expressions were developed for the integrations along a circular path. These results can be used for the solution of problems involved with circular boundaries or used to reduce singularity in problems with other geometries.

References

Abramowitz, M., and Stegun, I. A., 1965, *Handbook of Mathematical Functions,* Dover, New York.

Cruse, T. A., 1968, "A Direct Formulation and Numerical Solution of General Transient Elastodynamics, II," *J. Math. Anal. Appl.* Vol. 22, pp. 341–355.

Cruse, T. A., and Rizzo, F. J., 1968, "A Direct Formulation and Numerical Solution of General Transient Elastodynamics, I," *J. Math Anal. Appl.,* Vol. 22, pp. 224–259.

Downloaded 04 May 2010 to 171.66.16.26. Redistribution subject to ASME license or copyright; see http://www.asme.org/terms/Terms_Use.cfm

Gröber, W., and Hofreiter, N., 1961, *Bestimmte Integrale*, Zweiter teil, Wein, Dritte, Verbesserte Aiflage, Wein Springer-Verlag, Wein, Austria.

Michael, O., Avrashi, J., and Rosenhouse, G., 1996a, "The Boundary Strip Method in Elastostatics and Potential Equations," *Int. J. for Num. Meth. in Engng.*, Vol. 39, pp. 527–544.

Michael, O., Avrashi, J., and Rosenhouse, G., 1996b, "A New Boundary Spectral Strip Method for Non-periodical Geometrical Entities Based on Analytical Integrations," *Computer Method in Appl. Mech. and Engng.*, Vol. 135, pp. 327–342.

Michael, O., Avrashi, J., and Rosenhouse, G., 1997, "Steady State Elastodynamics Solutions Using Boundary Spectral Line Strips," *Engineering Computations*, accepted for publication.

Rizzo, F. J., Shippy, D. J., and Rezayat, M., 1985, "A Boundary Integral Equation Method for Time-Harmonic Radiation and Scattering in an Elastic Half-Space," *Advanced Topics in Boundary Element Analysis*, T. A. Cruse, A. B. Pifko, and H. Armen, eds., ASME, New York, pp. 83–90.

Downloaded 04 May 2010 to 171.66.16.26. Redistribution subject to ASME license or copyright; see http://www.asme.org/terms/Terms_Use.cfm

Journal of Applied Mechanics

Book Review

Solution of Crack Problems: The Distributed Dislocation Technique, by D. A. Hills, P. A. Kelly, D. N. Dai, and A. M. Korsunsky. Kluwer Academic Publishers, Dordrecht, The Netherlands, 1996.

REVIEWED BY L. M. KEER[1]

Fracture mechanics applications using dislocation theory have now been in the literature for a number of years. Many such solutions have appeared and been catalogued in the seminal book by Mura (*Micromechanics of Defects in Solids,* Martinus Nijhoff, 1982). There, the application of dislocation theory towards the solution of significant problems in materials science has been demonstrated by two and three-dimensional examples.

The book by Hills et al., using the distributed dislocation method, formulates problems appropriate to two-dimensional and three-dimensional elasticity. Solutions given in this volume are in the context of linear, isotropic elasticity, and except for a brief mention of crack-tip plasticity, there is no attempt to include nonlinear fracture mechanics into the scope of this book.

The list of two-dimensional topics chosen by the authors include cracks in monolithic plane bodies that can be arbitrary in shape, interfacial cracks and cracks that have a kinking geometry. These solutions represent important applications to areas of engineering interest, such as tribology (fretting, contact fatigue, inclusions), composite materials (interfacial cracking), and others. Recently, considerable interest has been given to planar three-dimensional cracks. The theory associated with such problems is developed cleanly in three chapters, the last revealing the mathematical foundations behind the hypersingular integrals that appear in such three-dimensional formulations. The reader is given a sound introduction to this subject, and with the framework given here, will obtain the insight to carry through more difficult research examples.

Finally, the reader is provided with several useful appendices containing tables of exact analytical results that provide influence functions for dislocation systems of particular geometries, recipes for solution of singular integral equations of the first kind, and results for plane and ring dipole influence functions.

The book would be suitable as a graduate level text for students who have already taken an elasticity course and who understand some of the mathematical and physical concepts concerned with integral equations.

[1] Professor, Departments of Civil and Mechanical Engineering, Northwestern University, Evanston, IL 60208. Fellow ASME.

 Copyright © 1998 by ASME

Downloaded 04 May 2010 to 171.66.16.26. Redistribution subject to ASME license or copyright; see http://www.asme.org/terms/Terms_Use.cfm